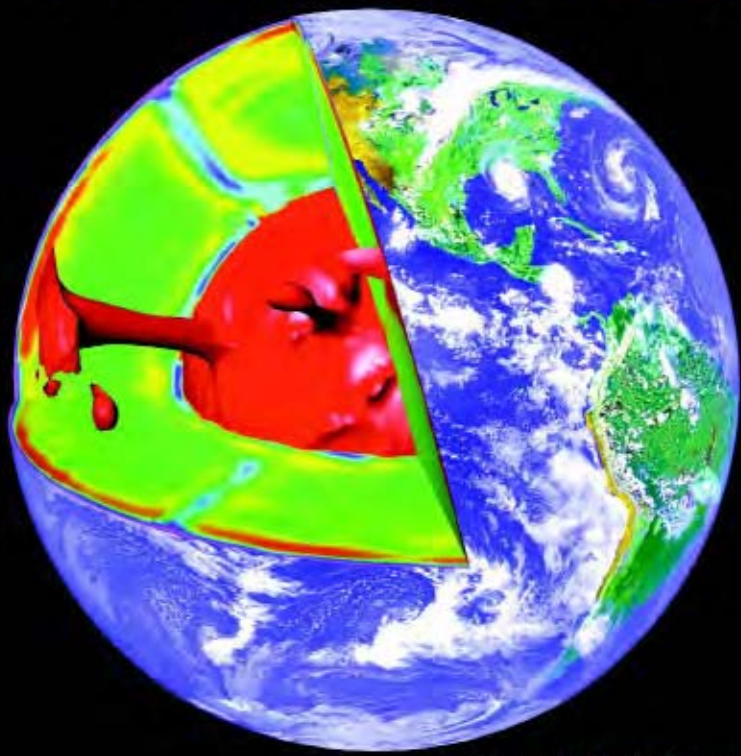


Mantle Convection in the Earth and Planets



*Gerald Schubert
Donald L. Turcotte
Peter Olson*

This page intentionally left blank

Mantle Convection in the Earth and Planets

Mantle Convection in the Earth and Planets is a comprehensive synthesis of all aspects of mantle convection within the Earth, the terrestrial planets, the Moon, and the Galilean satellites of Jupiter.

Mantle convection sets the pace for the evolution of the Earth as a whole. It influences Earth's topography, gravitational field, geodynamo, climate system, cycles of glaciation, biological evolution, and formation of mineral and hydrocarbon resources. It is the primary mechanism for the transport of heat from the Earth's deep interior to its surface. Mantle convection is the fundamental cause of plate tectonics, formation and drift of continents, volcanism, earthquakes, and mountain building. This book provides both a connected overview and an in-depth analysis of the relationship between these phenomena and the process of mantle convection. Complex geodynamical processes are explained with simple mathematical models.

The book includes up-to-date discussions of the latest research developments that have revolutionized our understanding of the Earth and the planets. These developments include:

- the emergence of mantle seismic tomography which has given us a window into the mantle and a direct view of mantle convection;
- progress in measuring the thermal, mechanical, and rheological properties of Earth materials in the laboratory;
- dramatic improvements in computational power that have made possible the construction of realistic numerical models of mantle convection in three-dimensional spherical geometry;
- spacecraft missions to Venus (Magellan), the Moon (Clementine and Lunar Prospector), Mars (Mars Global Surveyor), and the Galilean moons of Jupiter (Galileo) that have enormously increased our knowledge of these planets and satellites.

Mantle Convection in the Earth and Planets is suitable as a text for a graduate course in geophysics and planetary physics, and as a supplementary reference for use at the undergraduate level. It is also an invaluable review for researchers in the broad fields of the Earth and planetary sciences including seismologists, tectonophysicists, geodesists, mineral physicists, volcanologists, geochemists, geologists, mineralogists, petrologists, paleomagnetists, planetary geologists, and meteoriticists. The book features a comprehensive index, an extensive reference list, numerous illustrations (many in color), and major questions that focus the discussion and suggest avenues of future research.

Gerald Schubert is a Professor in the Department of Earth and Space Sciences and the Institute of Geophysics and Planetary Physics at the University of California, Los Angeles. He is co-author with Donald L. Turcotte of *Geodynamics* (John Wiley and Sons, 1982), and co-author of over 400 research papers. He has participated in a number of NASA's planetary missions and has been on the editorial boards of many journals, including *Icarus*, *Journal of Geophysical Research*, *Geophysical Research Letters*, and *Annual Reviews of Earth and Planetary Sciences*. Professor Schubert is a Fellow of the American Geophysical Union and a recipient of the Union's James B. Macelwane Medal.

Donald L. Turcotte is Maxwell Upson Professor of Engineering, Department of Geological Sciences, Cornell University. He is co-author of three books, including *Geodynamics* (with Gerald Schubert, John Wiley and Sons, 1982), and *Fractals and Chaos in Geology and Geophysics* (Cambridge University Press, 1992 and 1997). He is co-author of over 300 research papers. Professor Turcotte is a Fellow of the American Geophysical Union, Honorary Fellow of the European Union of Geosciences, and Fellow

of the Geological Society of America. He is the recipient of several medals, including the Day Medal of the Geological Society of America and the Wegener Medal of the European Union of Geosciences.

Peter Olson is a Professor of Geophysical Fluid Dynamics, Department of Earth and Planetary Sciences, Johns Hopkins University. He is a Fellow of the American Geophysical Union and an Honorary Fellow of the European Union of Geosciences. He has served on the editorial boards of many journals, including *Science*, *Journal of Geophysical Research*, *Reviews of Geophysics*, *Geophysical Research Letters*, and *Geochemistry, Geophysics, Geosystems*. Professor Olson has been a NASA Principal Investigator and President of the Tectonophysics Section, American Geophysical Union. He has co-authored over 100 research papers.

Mantle Convection in the Earth and Planets

GERALD SCHUBERT

University of California, Los Angeles

DONALD L. TURCOTTE

Cornell University

PETER OLSON

The Johns Hopkins University



CAMBRIDGE
UNIVERSITY PRESS

PUBLISHED BY THE PRESS SYNDICATE OF THE UNIVERSITY OF CAMBRIDGE
The Pitt Building, Trumpington Street, Cambridge, United Kingdom

CAMBRIDGE UNIVERSITY PRESS

The Edinburgh Building, Cambridge CB2 2RU, UK
40 West 20th Street, New York, NY 10011-4211, USA
477 Williamstown Road, Port Melbourne, VIC 3207, Australia
Ruiz de Alarcón 13, 28014 Madrid, Spain
Dock House, The Waterfront, Cape Town 8001, South Africa

<http://www.cambridge.org>

© Cambridge University Press 2004

First published in printed format 2001

ISBN 0-511-03719-8 eBook (Adobe Reader)

ISBN 0-521-35367-X hardback

ISBN 0-521-79836-1 paperback

Contents

<i>Preface</i>	<i>page</i> xiii
1 Historical Background	1
1.1 Introduction	1
1.2 Continental Drift	5
1.3 The Concept of Subsolidus Mantle Convection	8
1.4 Paleomagnetism	11
1.5 Seafloor Spreading	12
1.6 Subduction and Area Conservation	13
2 Plate Tectonics	16
2.1 Introduction	16
2.2 The Lithosphere	25
2.3 Accretional Plate Margins (Ocean Ridges)	26
2.4 Transform Faults	28
2.5 Subduction	29
2.5.1 Rheology of Subduction	33
2.5.2 Dip of Subduction Zones	34
2.5.3 Fate of Descending Slabs	35
2.5.4 Why are Island Arcs Arcs?	35
2.5.5 Subduction Zone Volcanism	36
2.5.6 Back-arc Basins	38
2.6 Hot Spots and Mantle Plumes	39
2.7 Continents	42
2.7.1 Composition	42
2.7.2 Delamination and Recycling of the Continents	44
2.7.3 Continental Crustal Formation	47
2.8 Plate Motions	48
2.9 The Driving Force for Plate Tectonics	52
2.10 The Wilson Cycle and the Time Dependence of Plate Tectonics	57
3 Structure and Composition of the Mantle	63
3.1 Introduction	63
3.2 Spherically Averaged Earth Structure	63
3.3 The Crust	68
3.3.1 Oceanic Crust	69

3.3.2	Continental Crust	71
3.4	The Upper Mantle	74
3.4.1	Radial Structure of the Upper Mantle	75
3.4.2	Upper Mantle Composition	80
3.5	The Transition Zone	84
3.5.1	The 410 km Seismic Discontinuity	84
3.5.2	The 660 km Seismic Discontinuity	86
3.6	The Lower Mantle	92
3.7	The D'' Layer and the Core–Mantle Boundary	94
3.8	The Core	97
3.9	Three-dimensional Structure of the Mantle	101
3.9.1	Upper Mantle Seismic Heterogeneity and Anisotropy	103
3.9.2	Extensions of Subducted Slabs into the Lower Mantle	106
3.9.3	Lower Mantle Seismic Heterogeneity	113
3.9.4	Topography of the Core–Mantle Boundary	116
4	Mantle Temperatures and Thermodynamic Properties	118
4.1	Heat Conduction and the Age of the Earth	118
4.1.1	Cooling of an Isothermal Earth	118
4.1.2	Cooling of a Molten Earth	123
4.1.3	Conductive Cooling with Heat Generation	125
4.1.4	Mantle Convection and Mantle Temperatures	127
4.1.5	Surface Heat Flow and Internal Heat Sources	128
4.2	Thermal Regime of the Oceanic Lithosphere	132
4.2.1	Half-space Cooling Model	132
4.2.2	Plate Cooling Model	139
4.3	Temperatures in the Continental Lithosphere	143
4.4	Partial Melting and the Low-velocity Zone	151
4.5	Temperatures, Partial Melting, and Melt Migration Beneath Spreading Centers	153
4.5.1	Melt Migration by Porous Flow	154
4.5.2	Melt Migration in Fractures	166
4.6	Temperatures in Subducting Slabs	176
4.6.1	Frictional Heating on the Slip Zone	176
4.6.2	Phase Changes in the Descending Slab	180
4.6.3	Metastability of the Olivine–Spinel Phase Change in the Descending Slab	185
4.7	The Adiabatic Mantle	188
4.8	Solid-state Phase Transformations and the Geotherm	191
4.9	Temperatures in the Core and the D'' Layer	200
4.10	Temperatures in the Transition Zone and Lower Mantle	204
4.11	Thermodynamic Parameters	207
4.11.1	Thermal Expansion	207
4.11.2	Specific Heat	209
4.11.3	Adiabatic Temperature Scale Height	209
4.11.4	Thermal Conductivity and Thermal Diffusivity	210
5	Viscosity of the Mantle	212
5.1	Introduction	212

5.1.1	Isostasy and Flow	212
5.1.2	Viscoelasticity	212
5.1.3	Postglacial Rebound	213
5.1.4	Mantle Viscosity and the Geoid	215
5.1.5	Mantle Viscosity and Earth Rotation	215
5.1.6	Laboratory Experiments	215
5.2	Global Isostatic Adjustment	216
5.2.1	Deformation of the Whole Mantle by a Surface Load	217
5.2.1.1	Half-space Model	217
5.2.1.2	Spherical Shell Model	222
5.2.1.3	Postglacial Relaxation Time and Inferred Mantle Viscosity	223
5.2.2	Ice Load Histories and Postglacial Sea Levels	224
5.2.3	Evidence for a Low-viscosity Asthenosphere Channel	227
5.3	Changes in the Length of Day	230
5.4	True Polar Wander	231
5.5	Response to Internal Loads	232
5.6	Incorporation of Surface Plate Motion	237
5.7	Application of Inverse Methods	238
5.8	Summary of Radial Viscosity Structure	240
5.9	Physics of Mantle Creep	240
5.10	Viscosity Functions	248
6	Basic Equations	251
6.1	Background	251
6.2	Conservation of Mass	251
6.3	Stream Functions and Streamlines	253
6.4	Conservation of Momentum	254
6.5	Navier–Stokes Equations	255
6.6	Vorticity Equation	257
6.7	Stream Function Equation	257
6.8	Thermodynamics	259
6.9	Conservation of Energy	262
6.10	Approximate Equations	265
6.11	Two-Dimensional (Cartesian), Boussinesq, Infinite Prandtl Number Equations	274
6.12	Reference State	274
6.13	Gravitational Potential and the Poisson Equation	279
6.14	Conservation of Momentum Equations in Cartesian, Cylindrical, and Spherical Polar Coordinates	280
6.15	Navier–Stokes Equations in Cartesian, Cylindrical, and Spherical Polar Coordinates	281
6.16	Conservation of Energy Equation in Cartesian, Cylindrical, and Spherical Polar Coordinates	286
7	Linear Stability	288
7.1	Introduction	288
7.2	Summary of Basic Equations	288
7.3	Plane Layer Heated from Below	290

7.4	Plane Layer with a Univariant Phase Transition Heated from Below	297
7.5	Plane Layer Heated from Within	303
7.6	Semi-infinite Fluid with Depth-dependent Viscosity	307
7.7	Fluid Spheres and Spherical Shells	308
7.7.1	The Internally Heated Sphere	313
7.7.2	Spherical Shells Heated Both from Within and from Below	316
7.7.3	Spherical Shell Heated from Within	318
7.7.4	Spherical Shell Heated from Below	320
7.8	Spherical Harmonics	323
8	Approximate Solutions	330
8.1	Introduction	330
8.2	Eigenmode Expansions	331
8.3	Lorenz Equations	332
8.4	Higher-order Truncations	337
8.5	Chaotic Mantle Mixing	344
8.6	Boundary Layer Theory	350
8.6.1	Boundary Layer Stability Analysis	350
8.6.2	Boundary Layer Analysis of Cellular Convection	353
8.7	Single-mode Mean Field Approximation	361
8.8	Weakly Nonlinear Stability Theory	367
8.8.1	Two-dimensional Convection	367
8.8.2	Three-dimensional Convection, Hexagons	370
9	Calculations of Convection in Two Dimensions	376
9.1	Introduction	376
9.2	Steady Convection at Large Rayleigh Number	378
9.3	Internal Heat Sources and Time Dependence	382
9.4	Convection with Surface Plates	385
9.5	Role of Phase and Chemical Changes	390
9.6	Effects of Temperature- and Pressure-dependent Viscosity	393
9.7	Effects of Temperature-dependent Viscosity: Slab Strength	396
9.8	Mantle Plume Interaction with an Endothermic Phase Change	401
9.9	Non-Newtonian Viscosity	404
9.10	Depth-dependent Thermodynamic and Transport Properties	405
9.11	Influence of Compressibility and Viscous Dissipation	408
9.12	Continents and Convection	408
9.13	Convection in the D'' Layer	413
10	Numerical Models of Three-dimensional Convection	417
10.1	Introduction	417
10.2	Steady Symmetric Modes of Convection	418
10.2.1	Spherical Shell Convection	418
10.2.2	Rectangular Box Convection	428
10.3	Unsteady, Asymmetric Modes of Convection	440
10.4	Mantle Avalanches	454
10.5	Depth-dependent Viscosity	470
10.6	Two-layer Convection	473
10.7	Compressibility and Adiabatic and Viscous Heating	477

10.8	Plate-like Rheology	488
10.9	Three-dimensional Models of Convection Beneath Ridges and Continents	498
11	Hot Spots and Mantle Plumes	499
11.1	Introduction	499
11.2	Hot Spot Tracks	501
11.3	Hot Spot Swells	505
11.4	Hot Spot Basalts and Excess Temperature	508
11.5	Hot Spot Energetics	510
11.6	Evidence for Mantle Plumes from Seismology and the Geoid	514
11.7	Plume Generation	518
11.8	Plume Heads and Massive Eruptions	525
11.9	Plume Conduits and Halos	529
11.10	Instabilities and Waves	533
11.11	Dynamic Support of Hot Spot Swells	537
11.12	Plume–Ridge Interaction	543
11.13	Massive Eruptions and Global Change	545
12	Chemical Geodynamics	547
12.1	Introduction	547
12.2	Geochemical Reservoirs	547
12.3	Oceanic Basalts and Their Mantle Reservoirs	549
12.4	Simple Models of Geochemical Evolution	551
12.4.1	Radioactivity	551
12.4.2	A Two-reservoir Model with Instantaneous Crustal Differentiation	553
12.4.3	Application of the Two-reservoir Model with Instantaneous Crustal Addition to the Sm–Nd and Rb–Sr Systems	555
12.4.4	A Two-reservoir Model with a Constant Rate of Crustal Growth	556
12.4.5	Application of the Two-reservoir Model with Crustal Growth Linear in Time to the Sm–Nd System	558
12.4.6	A Two-reservoir Model with Crustal Recycling	561
12.4.7	Application of the Two-reservoir Model with Crustal Recycling to the Sm–Nd System	563
12.5	Uranium, Thorium, Lead Systems	565
12.5.1	Lead Isotope Systematics	565
12.5.2	Application to the Instantaneous Crustal Differentiation Model	569
12.6	Noble Gas Systems	573
12.6.1	Helium	574
12.6.2	Argon	577
12.6.3	Xenon	579
12.7	Isotope Systematics of Ocean Island Basalts	580
12.8	Summary	583
13	Thermal History of the Earth	586
13.1	Introduction	586

13.2	A Simple Thermal History Model	587
13.2.1	Initial State	587
13.2.2	Energy Balance and Surface Heat Flow Parameterization	588
13.2.3	Temperature Dependence of Mantle Viscosity and Self-regulation	590
13.2.4	Model Results	591
13.2.5	Surface Heat Flow, Internal Heating, and Secular Cooling	594
13.2.6	Volatile Dependence of Mantle Viscosity and Self-regulation	596
13.3	More Elaborate Thermal Evolution Models	602
13.3.1	A Model of Coupled Core–Mantle Thermal Evolution	602
13.3.2	Core Evolution and Magnetic Field Generation	607
13.4	Two-layer Mantle Convection and Thermal Evolution	611
13.5	Scaling Laws for Convection with Strongly Temperature Dependent Viscosity	617
13.6	Episodicity in the Thermal Evolution of the Earth	625
13.7	Continental Crustal Growth and Earth Thermal History	627
14	Convection in the Interiors of Solid Planets and Moons	633
14.1	Introduction	633
14.1.1	The Role of Subsolidus Convection in the Solar System	634
14.1.2	Surface Ages and Hypsometry of the Terrestrial Planets	635
14.2	Venus	640
14.2.1	Comparison of Two Sisters: Venus versus Earth	640
14.2.2	Heat Transport in Venus	647
14.2.3	Venusian Highlands and Terrestrial Continents	656
14.2.4	Models of Convection in Venus	657
14.2.5	Topography and the Geoid: Constraints on Convection Models	661
14.2.6	Convection Models with a Sluggish or Stagnant Lid	664
14.2.7	Convection Models with Phase Changes and Variable Viscosity	667
14.2.8	Thermal History Models of Venus	672
14.2.9	Why is There no Dynamo in Venus?	678
14.3	Mars	681
14.3.1	Surface Tectonic and Volcanic Features	681
14.3.2	Internal Structure	686
14.3.3	The Martian Lithosphere	687
14.3.4	Radiogenic Heat Production	690
14.3.5	Martian Thermal History: Effects of Crustal Differentiation	691
14.3.6	Martian Thermal History: Magnetic Field Generation	698
14.3.7	Martian Thermal History Models with a Stagnant Lid	706
14.3.8	Convection Patterns in Mars	708
14.3.9	Summary	715
14.4	The Moon	716
14.4.1	The Lunar Crust: Evidence from the Apollo Missions	716
14.4.2	Differentiation of the Lunar Interior: A Magma Ocean	718
14.4.3	Lunar Topography and Gravity	719
14.4.4	Early Lunar History	722
14.4.5	Is There a Lunar Core?	726

14.4.6	Crustal Magnetization: Implications for a Lunar Core and Early Dynamo	726
14.4.7	Origin of the Moon	727
14.4.8	Lunar Heat Flow and Convection	727
14.4.9	Lunar Thermal Evolution with Crustal Differentiation	728
14.4.10	Lunar Isotope Ratios: Implications for the Moon's Evolution	731
14.5	Io	736
14.5.1	Volcanism and Heat Sources: Tidal Dissipation	736
14.5.2	Some Consequences of Tidal Dissipation	739
14.5.3	Io's Internal Structure	740
14.5.4	Models of Tidal Dissipation in Io	742
14.5.5	Models of the Thermal and Orbital Dynamical History of Io	746
14.6	Mercury	748
14.6.1	Composition and Internal Structure	748
14.6.2	Accretion, Core Formation, and Temperature	750
14.6.3	Thermal History	752
14.7	Europa, Ganymede, and Callisto	756
14.7.1	Introduction	756
14.7.2	Europa	756
14.7.3	Ganymede	760
14.7.4	Callisto	761
14.7.5	Convection in Icy Satellites	763
15	Nature of Convection in the Mantle	767
15.1	Introduction	767
15.2	Form of Downwelling	774
15.2.1	Subduction	774
15.2.2	Delamination	778
15.3	Form of Upwelling	778
15.3.1	Accretional Plate Margins	778
15.3.2	Mantle Plumes	780
15.4	Horizontal Boundary Layers	782
15.4.1	The Lithosphere	782
15.4.2	The D'' Layer	783
15.4.3	Internal Boundary Layers	784
15.5	The General Circulation	784
15.6	Time Dependence	786
15.7	Special Effects in Mantle Convection	787
15.7.1	Solid-state Phase Transformations	788
15.7.2	Variable Viscosity: Temperature, Pressure, Depth	789
15.7.3	Nonlinear Viscosity	789
15.7.4	Compressibility	790
15.7.5	Viscous Dissipation	791
15.8	Plates and Continents	791
15.8.1	Plates	791
15.8.2	Continents	792
15.9	Comparative Planetology	792
15.9.1	Venus	793

15.9.2 Mars	794
15.9.3 The Moon	794
15.9.4 Mercury and Io	795
15.9.5 Icy Satellites	795
<i>References</i>	797
<i>Appendix: Table of Variables</i>	875
<i>Author Index</i>	893
<i>Subject Index</i>	913

Preface

This book gives a comprehensive and connected account of all aspects of mantle convection within the Earth, the terrestrial planets, the Moon, and the Galilean satellites of Jupiter. Convection is the most important process in the mantle, and it sets the pace for the evolution of the Earth as a whole. It controls the distribution of land and water on geologic time scales, and its influences range from the Earth's climate system, cycles of glaciation, and biological evolution to the formation of mineral and hydrocarbon resources. Because mantle convection is the primary mechanism for the transport of heat from the Earth's deep interior to its surface, it is the underlying cause of plate tectonics, formation and drift of continents, volcanism, earthquakes, and mountain building processes. It also shapes the gravitational and magnetic fields of the Earth. Mantle convection plays similar, but not identical, roles in the other planets and satellites.

This book is primarily intended as a research monograph. Our objective is to provide a thorough treatment of the subject appropriate for anyone familiar with the physical sciences who wishes to learn about this fascinating subject. Some parts of the book are quite mathematical, but other parts are qualitative and descriptive. Accordingly, it could be used as a text for advanced coursework in geophysics and planetary physics, or as a supplementary reference for introductory courses.

The subject matter has been selected quite broadly because, as noted above, mantle convection touches on so many aspects of the Earth and planetary sciences. A comprehensive index facilitates access to the content and an extensive reference list does the same for the relevant literature. A list of symbols eases their identification. We highlight major unanswered questions throughout the text, to focus the discussion and suggest avenues of future research. There are numerous illustrations, some in color, of results from advanced numerical models of mantle convection, laboratory experiments, and global geophysical and planetary data sets. Many complex geodynamical processes are explained using simple, idealized mathematical models.

We begin with a historical background in Chapter 1. Qualitative evidence for the drift of the continents over the Earth's surface was available throughout much of the first half of the twentieth century, while at the same time a physical understanding of thermal convection was being developed. However, great insight was required to put these together, and this happened only gradually, within an atmosphere of enormous controversy. The pendulum began to swing towards acceptance of continental drift and mantle convection in the 1950s and 1960s as a result of paleomagnetic data indicating that continents move relative to one another and seafloor magnetic data indicating that new seafloor is continually created at mid-ocean ridges.

The concepts of continental drift, seafloor spreading, and mantle convection became inseparably linked following the recognition of plate tectonics in the late 1960s. Plate tectonics unified a wide range of geological and geophysical observations. In plate tectonics the surface of the Earth is divided into a small number of nearly rigid plates in relative motion. Chapter 2 presents an overview of plate tectonics, including the critical processes beneath ridges and deep-sea trenches, with emphasis on their relationship to mantle convection. This chapter also introduces some other manifestations of convection not so closely related to plate tectonics, including volcanic hot spots that mark localized plume-like mantle upwellings, and the evidence for delamination, where dense lower portions of some plates detach and sink into the underlying mantle.

To understand mantle convection we need to know what the Earth is like inside. In Chapter 3 we discuss the internal structure of the Earth and describe in detail the properties of its main parts: the thin, solid, low-density silicate crust, the thick, mostly solid, high-density silicate mantle, and the central, partially solidified, metallic core. Seismology is the source of much of what we know about the Earth's interior. Chapter 3 summarizes both the average radial structure of the Earth and its lateral heterogeneity as revealed by seismic tomography. The chapter also describes the pressure-induced changes in the structure of mantle minerals, including the olivine–spinel and spinel–perovskite + magnesiowüstite transitions that occur in the mantle transition zone and influence the nature of mantle convection.

Radiogenic heat sources and high temperatures at depth in the Earth drive mantle convection, and the cooling of the Earth by convective heat transfer in turn controls the Earth's temperature. The Earth's thermal state is the subject of Chapter 4. Here we discuss the geothermal heat flow at the surface, the sources of heat inside the Earth, the thermal properties of the mantle including thermal conductivity and thermal expansivity, and the overall thermal state of the Earth. Chapter 4 includes analysis of the oceanic lithosphere as the upper thermal boundary layer of mantle convection and considers the thermal structure of the continental lithosphere. The adiabatic nature of the vigorously convecting mantle is discussed and the D'' layer at the base of the mantle is analyzed as the lower thermal and compositional boundary layer of mantle convection. The thermal structure of the core is reviewed. Mechanisms of magma migration through the mantle and crust are treated in considerable detail.

Mantle convection requires that the solid mantle behave as a fluid on geological time scales. This implies that the solid mantle has a long-term viscosity. In Chapter 5, the physical mechanisms responsible for viscous behavior are discussed and the observations used to deduce the mantle viscosity are reviewed, along with the relevant laboratory studies of the viscous behavior of mantle materials.

In Chapter 6, the equations that govern the fluid behavior of the mantle are introduced. The equations that describe thermal convection in the Earth's mantle are nonlinear, and it is not possible to obtain analytical solutions under conditions fully applicable to the real Earth. However, linearized versions of the equations of motion provide important information on the onset of thermal convection. This is the subject of Chapter 7. A variety of approximate solution methods are introduced in Chapter 8, including the boundary layer approximation that explains the basic structure of the oceanic lithosphere. Concepts of dynamical chaos are introduced and applied to mantle convection. Numerical solutions of the mantle convection equations in two and three dimensions are given in Chapters 9 and 10, respectively. Observations and theory relevant to mantle plumes are presented in Chapter 11. In Chapter 12, geochemical observations pertinent to mantle convection are given along with the basic concepts of chemical geodynamics. Chapter 13 discusses the thermal history of the Earth

and introduces the approximate approach of parameterized convection as a tool in studying thermal evolution.

Mantle convection is almost certainly occurring within Venus and it may also be occurring, or it may have occurred, inside Mars, Mercury, the Moon, and many of the satellites of the outer planets. Observations and theory pertaining to mantle convection in planets and satellites are given in Chapter 14. Mercury, Venus, Mars, the Moon, and the Galilean satellites of Jupiter – Io, Europa, Ganymede, and Callisto – are all discussed in detail. Each of these bodies provides a unique situation for the occurrence of mantle convection. Tidal heating, unimportant in the Earth and the terrestrial planets, is the primary heat source for Io. The orbital and thermal evolutions of Io, Europa, and Ganymede are strongly coupled, unlike the orbital and thermal histories of the Earth and inner planets. The rheology of ice, not rock, controls mantle convection in the icy satellites Ganymede and Callisto. Among the many questions addressed in Chapter 14 are why Venus does not have plate tectonics and whether Mars once did. Methods of parameterized convection are employed in Chapter 14 to study the thermal evolution of the planets and satellites.

The results presented in this book are summarized in Chapter 15. Throughout the book questions are included in the text to highlight and focus discussion. Some of these questions have generally accepted answers whereas other answers remain controversial. The discussion given in Chapter 15 addresses the answers, or lack of answers, to these questions.

Our extensive reference list is a testimony to several decades of substantial progress in understanding mantle convection. Even so, it is not possible to include all the pertinent literature or to acknowledge all the significant contributions that have led to our present level of knowledge. We apologize in advance to our colleagues whose work we may have unintentionally slighted. We point out that this oversight is, in many cases, simply a consequence of the general acceptance of their ideas.

Many of our colleagues have read parts of various drafts of this book and their comments have substantially helped us prepare the final version. We would like to acknowledge in this regard the contributions of Larry Cathles, Robert Kay, David Kohlstedt, Paul Tackley, John Vidale, Shun Karato, and Orson Anderson. A few of the chapters of this book were used in teaching and our students also provided helpful suggestions for improving the text. Other colleagues generously provided figures, many of which are prominently featured in our book. Illustrations were contributed by David Sandwell, Paul Tackley, Henry Pollack, David Yuen, Maria Zuber, Todd Ratcliff, William Moore, Sami Asmar, David Smith, Alex Konopliv, Sean Solomon, Louise Kellogg, Laszlo Keszthelyi, Peter Shearer, Yanick Ricard, Brian Kennett, and Walter Mooney. The illustration on the cover of this book was prepared by Paul Tackley. Paul Roberts diligently worked on the weakly nonlinear stability theory of Section 8.8 and provided the solution for hexagonal convection presented in Section 8.8.2.

Credit for the preparation of the manuscript is due to Judith Hohl, whose patience, dedication, and hard work were essential to the completion of this book. Her TeX skills and careful attention to detail were invaluable in dealing with the often complicated equations and tables. She is also responsible for the accuracy and completeness of the large reference list and was helped in the use of TeX and BibTeX by William Moore, whose ability to modify the TeX source code enhanced the quality of the manuscript and rescued us from a number of dire situations. Others who assisted in manuscript preparation include Sue Peterson, Nanette Anderson, and Nik Stearn. Cam Truong and Kei Yauchi found and copied hundreds of references. Richard Sadakane skillfully prepared the majority of the figures.

1

Historical Background

1.1 Introduction

The origin of mountain ranges, volcanoes, earthquakes, the ocean basins, the continents, and the very nature of the Earth's interior are questions as old as science itself. In the development of modern science, virtually every famous Natural Philosopher has conjectured on the state of the deep interior and its relationship to the Earth's surface. And every one of these thinkers has come to essentially the same general conclusion: despite the obvious solidity of the Earth beneath our feet, the interior must have flowed, in order to create the complex surface geology we see today. Although we can trace this idea as far back as written scientific record permits, it nevertheless remained a strictly qualitative hypothesis until the early part of the twentieth century. Then several timely developments in physics, fluid mechanics, geophysics, and geology finally established a true physical paradigm for the Earth's interior, mantle convection.

In reviewing the development of the concept of mantle convection, we find it is impossible to identify one particular time or event, or one particular individual, as being decisive in either its construction or its acceptance. Instead, the subject's progress has followed a meandering course, assisted along by the contributions of many. Still, there are a few scientific pioneers whose insights were crucial at certain times. These insights deserve special recognition and, when put together, provide some historical context with which future progress can be measured.

The idea of flow in the Earth's interior was popular among the early Natural Philosophers, as it was commonly assumed that only the outermost portion of the Earth was solid. Descartes imagined the Earth to consist of essentially sedimentary rocks (the crust) lying over a shell of denser rocks (the mantle) with a metallic center (the core). Leibniz proposed that the Earth cooled from an initially molten state and that the deep interior remained molten, a relic of its formation. Edmond Halley argued that the flow of liquids in a network of subsurface channels would explain his discovery of the secular variation of the geomagnetic field. Both Newton and Laplace interpreted the equatorial bulge of the Earth to be a consequence of a fluid-like response to its rotation. The idea that the Earth's interior included fluid channels and extensive molten regions, as expressed in the artist's drawing in Figure 1.1, was the dominant one until the late nineteenth century, when developments in the theory of elasticity and G. H. Darwin's (1898) investigation of the tides indicated that the Earth was not only solid to great depths, but also "more rigid than steel."

In the eighteenth and early nineteenth centuries, resolution of an old controversy led geologists to accept the idea of a hot and mobile Earth interior. This controversy centered on

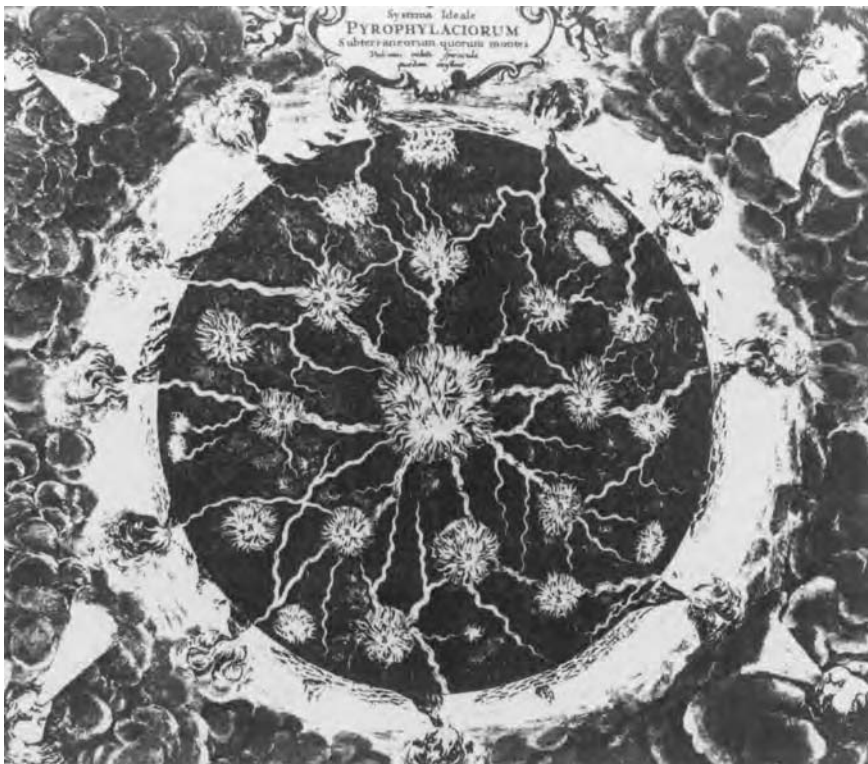


Figure 1.1. An early depiction of the Earth's interior, showing channels of fluid connected to a molten central core. This was the prevailing view prior to the nineteenth century.

the origin of rocks and pitted the so-called Neptunists, led by Abraham Werner, who thought all rocks were derived by precipitation from a primeval ocean, against others who held that igneous rocks crystallized from melts and were to be distinguished from sedimentary rocks formed by surficial processes. Their most influential member was an amateur scientist, James Hutton (Figure 1.2), who advanced the concept of uniformitarianism, that the processes evident today were those that shaped the Earth in the past. He also held to the idea of a molten, flowing interior, exerting forces on the solid crust to form mountain ranges, close to the modern view based on mantle convection. Ultimately Hutton's view prevailed, and with it, an emphasis on the idea that the fundamental physical process behind all major geological events is heat transfer from the deep interior to the surface. Thus, geologists were receptive to the idea of a hot, mobile Earth interior. However, most of the geological and geophysical evidence obtained from the continental crust seemed to demand vertical motions, rather than horizontal motions. For example, in the mid-nineteenth century it was discovered that mountain ranges did not have the expected positive gravity anomaly. This was explained by low-density continental roots, which floated on the denser mantle like blocks of wood in water, according to the principle of hydrostatic equilibrium. This implied, in turn, that the mantle behaved like a fluid, allowing vertical adjustment. However, the notion that the crust experiences far larger horizontal displacements was less well supported by evidence and was not widely held.

Figure 1.2. James Hutton (1726–1797), the father of Geology and proponent of internal heat as the driving force for Earth’s evolution.



The idea that flow in the Earth’s interior is a form of thermal convection developed slowly. Recognition of the significance of thermal convection as a primary fluid mechanical phenomenon in nature came from physicists. Count Rumford is usually given credit for recognizing the phenomenon around 1797 (Brown, 1957), although the term convection (derived from *convectio*, to carry) was first used by Prout (1834) to distinguish it from the other known heat transfer mechanisms, conduction and radiation. Subcrustal convection in the Earth was first suggested by W. Hopkins in 1839 and the first interpretations of geological observations using convection were made by Osmond Fisher (1881). Both of these presumed a fluid interior, so when the solidity of the mantle was established, these ideas fell out of favor.

The earliest experiments on convection in a layer of fluid heated from below and cooled from above were reported by J. Thompson (1882), who observed a “tesselated structure” in the liquid when its excess temperature, compared to that of the overlying air, was sufficiently large. But the name most closely associated with convection is Henri Bénard (Figure 1.3). Bénard (1900, 1901) reported the first quantitative experiments on the onset of convection, including the role of viscosity, the cellular planform, and the relationship between cell size and fluid layer depth. Bénard produced striking photographs of the convective planform in thin layers of viscous fluids heated from below (Figure 1.4). The regular, periodic, hexagonal cells in his photographs are still referred to as Bénard cells. Since Bénard used fluid layers in contact with air, surface tension effects were surely present in his experiments, as he himself recognized. It has since been shown that Bénard’s cells were driven as much by surface tension gradients as by gradients in buoyancy. Still, he correctly identified the essentials of thermal convection, and in doing so, opened a whole new field of fluid mechanics. Motivated by the “interesting results obtained by Bénard’s careful and skillful experiments,” Lord Rayleigh (1916; Figure 1.5) developed the linear stability theory for the onset of convection



Figure 1.3. Henri Bénard (1880–1939) (on the left) made the first quantitative experiments on cellular convection in viscous liquids. The picture was taken in Paris about 1920 with Reabouchansky on the right.

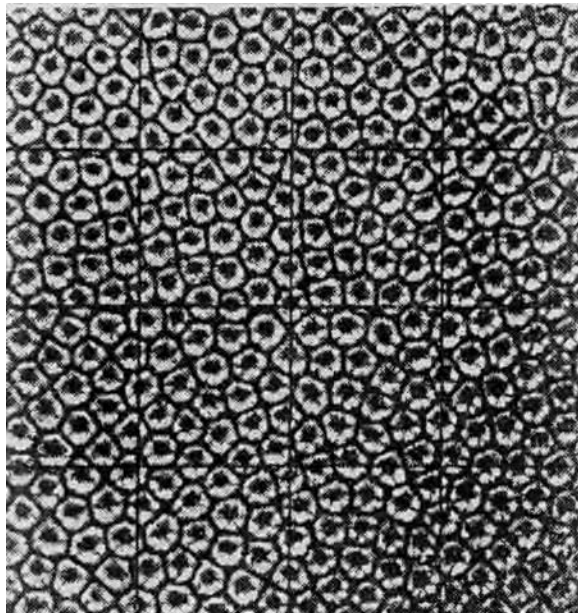


Figure 1.4. Photograph of hexagonal convection cells in a viscous fluid layer heated from below, taken by Bénard (1901).

in a horizontally infinite fluid layer between parallel surfaces heated uniformly from below and cooled uniformly from above, and isolated the governing dimensionless parameter that now bears his name. It was unfortunate that these developments in fluid mechanics were not followed more widely in Earth Science, for they might have removed a stumbling block to acceptance of the milestone concept of continental drift.



Figure 1.5. Lord Rayleigh (1842–1919) developed the theory of convective instability in fluids heated from below.

1.2 Continental Drift

The earliest arguments for continental drift were largely based on the fit of the continents. Ever since the first reliable maps were available, the remarkable fit between the east coast of South America and the west coast of Africa has been noted (e.g., Carey, 1955). Indeed, the fit was pointed out as early as 1620 by Francis Bacon (Bacon, 1620). North America, Greenland, and Europe also fit as illustrated in Figure 1.6 (Bullard et al., 1965).

Geological mapping in the southern hemisphere during the nineteenth century revealed that the fit between these continents extends beyond coastline geometry. Mountain belts in South America match mountain belts in Africa; similar rock types, rock ages, and fossil species are found on the two sides of the Atlantic Ocean. Thus the southern hemisphere geologists were generally more receptive to the idea of continental drift than their northern hemisphere colleagues, where the geologic evidence was far less conclusive.

Further evidence for continental drift came from studies of ancient climates. Geologists recognized that tropical climates had existed in polar regions at the same times that arctic climates had existed in equatorial regions. Also, the evolution and dispersion of plant and animal species was best explained in terms of ancient land bridges, suggesting direct connections between now widely separated continents.

As previously indicated, most geologists and geophysicists in the early twentieth century assumed that relative motions on the Earth's surface, including motions of the continents relative to the oceans, were mainly vertical and generally quite small – a few kilometers in extreme cases. The first serious advocates for large horizontal displacements were two visionaries, F. B. Taylor and Alfred Wegener (Figure 1.7). Continental drift was not widely discussed until the publication of Wegener's famous book (Wegener, 1915; see also Wegener, 1924), but Taylor deserves to share the credit for his independent and somewhat earlier account (Taylor, 1910). Wegener's book includes his highly original picture of the breakup

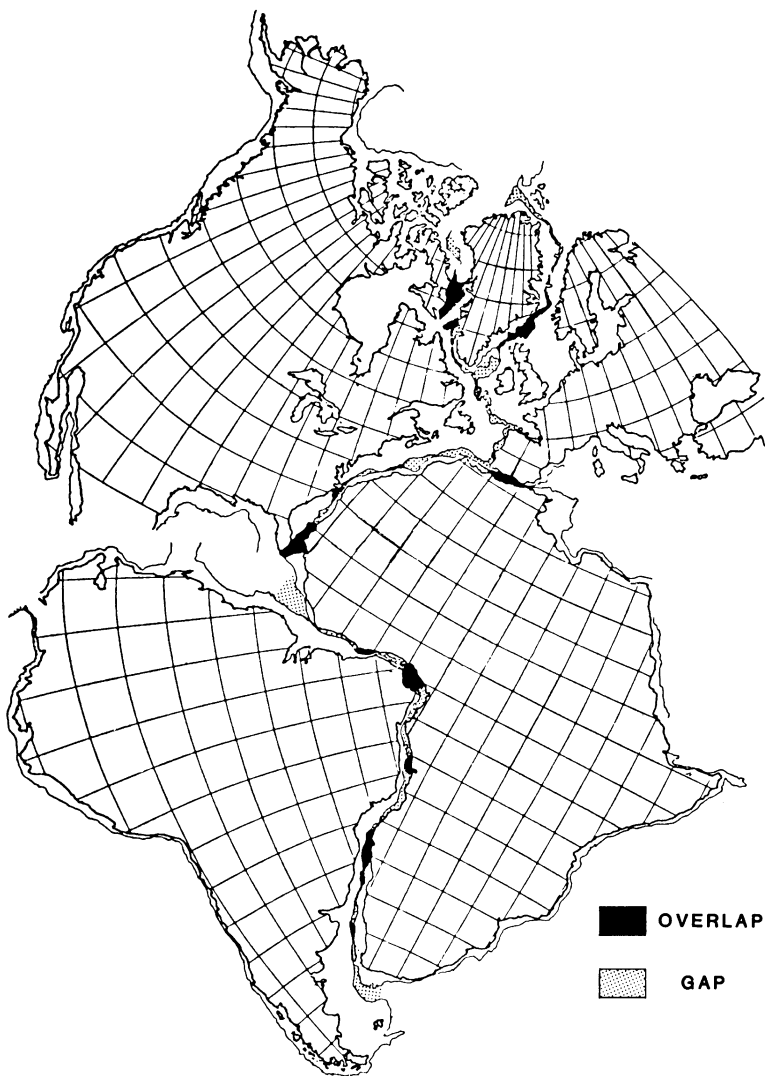


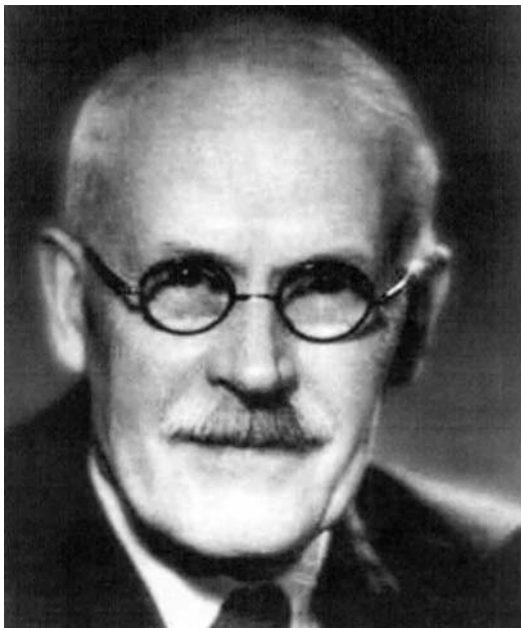
Figure 1.6. The remarkable “fit” between the continental margins of North and South America and Greenland, Europe, and Africa (from Bullard et al., 1965). This fit was one of the primary early arguments for continental drift.

and subsequent drift of the continents, and his recognition of the supercontinent Pangaea (all Earth). (Later it was argued (du Toit, 1937) that there had formerly been a northern continent, Laurasia, and a southern continent, Gondwanaland, separated by the Tethys ocean.) Wegener assembled a formidable array of facts and conjecture to support his case, including much that was subsequently discredited. This partially explains the hostile reception his book initially received. However, the most damaging criticisms came from prominent geophysicists such as H. Jeffreys in England and W. Bowie in the U.S., who dismissed the idea because the driving forces for continental drift proposed by Taylor and Wegener (tidal and differential centrifugal forces, respectively) were physically inadequate. (Wegener was a meteorologist and recognized that the Earth’s rotation dominated atmospheric flows. He proposed that these

Figure 1.7. Alfred Wegener (1880–1930), the father of continental drift.



Figure 1.8. Harold Jeffreys (1891–1989), the most influential theorist in the early debate over continental drift and mantle convection.



rotational forces were also responsible for driving the mantle flows resulting in continental drift.) At the same time, seismologists were exploring the Earth's deep interior, and were impressed by the high elastic rigidity of the mantle. In his influential book, *The Earth* (Jeffreys, 1929), Sir Harold Jeffreys (Figure 1.8) referred to the mantle as the "shell," arguing that this term better characterized its elastic strength. Paradoxically, Jeffreys was at the same

time making fundamental contributions to the theory of convection in fluids. For example, he showed (Jeffreys, 1930) that convection in a compressible fluid involved the difference between the actual temperature gradient and the adiabatic temperature gradient. This result would later figure prominently in the development of the theory of whole mantle convection. But throughout his illustrious career, Jeffreys maintained that the idea of thermal convection in the highly rigid mantle was implausible on mechanical grounds. The realization that a solid could exhibit both elastic and viscous properties simultaneously was just emerging from the study of materials, and evidently had not yet come fully into the minds of geophysicists.

The failure of rotational and tidal forces meant that some other mechanism had to be found to drive the motion of the continents with sufficient power to account for the observed deformation of the continental crust, seismicity, and volcanism. In addition, such a mechanism had to operate in the solid, crystalline mantle.

Question 1.1: *What is the source of energy for the tectonics and volcanism of the solid Earth?*

Question 1.2: *How is this energy converted into the tectonic and volcanic phenomena we are familiar with?*

The mechanism is thermal convection in the solid mantle, also referred to as subsolidus mantle convection. A fluid layer heated from below and cooled from above will convect in a gravitational field due to thermal expansion and contraction. The hot fluid at the base of the layer is less dense than the cold fluid at the top of the layer; this results in gravitational instability. The light fluid at the base of the layer ascends and the dense fluid at the top of the layer descends. The resulting motion, called thermal convection, is the fundamental process in the Earth's tectonics and volcanism and is the subject of this book. We will see that the energy to drive subsolidus convection in the mantle and its attendant geological consequences (plate tectonics, mountain building, volcanic eruptions, earthquakes) derives from both the secular cooling of the Earth's hot interior and the heat produced by the decay of radioactive elements in the rocks of the mantle.

The original proposal for subsolidus convection in the mantle is somewhat obscure. Bull (1921, 1931) suggested that convection in the solid mantle was responsible for continental drift, but he did not provide quantitative arguments in support of his contention. About the same time, Wegener came to realize that his own proposed mechanism was inadequate for continental drift. He apparently considered the possibility of mantle convection, and made passing reference to it as a plausible driving force in the final edition of his book (Wegener, 1929). It was during this era that the importance of convection was first being recognized in his own field of meteorology. But Wegener chose not to promote it as the cause of continental drift, and the idea languished once again.

1.3 The Concept of Subsolidus Mantle Convection

Arthur Holmes (1931, 1933; Figure 1.9) was the first to establish quantitatively that thermal convection was a viable mechanism for flow in the solid mantle, capable of driving continental drift. Holmes made order of magnitude estimates of the conditions necessary for convection, the energetics of the flow, and the stresses generated by the motion. He concluded that the available estimates of mantle viscosity were several orders of magnitude less



Figure 1.9. Arthur Holmes (1890–1965), the first prominent advocate for subsolidus mantle convection.

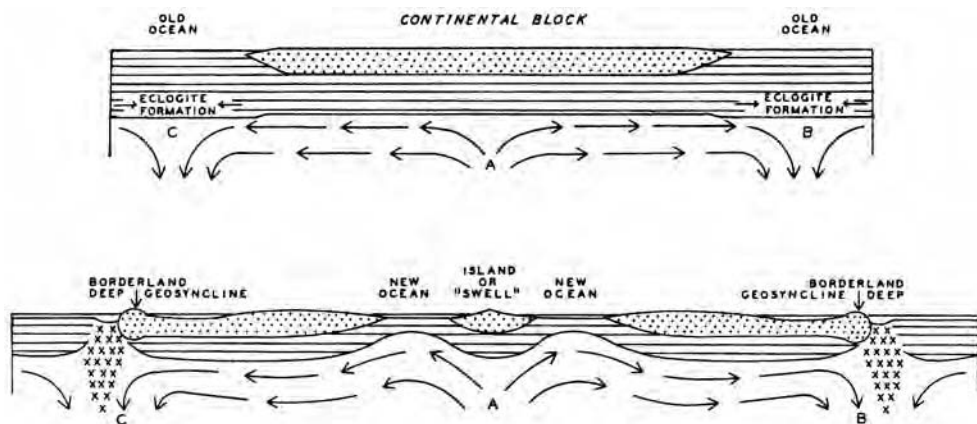


Figure 1.10. Arthur Holmes' (1931) depiction of mantle convection as the cause of continental drift, thirty years prior to the discovery of seafloor spreading.

than that required for the onset of convection. He also outlined a general relation between the ascending and descending limbs of mantle convection cells and geological processes, illustrated in Figure 1.10. Holmes argued that radioactive heat generation in the continents acted as a thermal blanket inducing ascending thermal convection beneath the continents. Holmes was one of the most prominent geologists of the time, and in his prestigious textbook *Principles of Physical Geology* (Holmes, 1945), he articulated the major problems of mantle convection much as we view them today.

The creep viscosity of the solid mantle was first determined quantitatively by Haskell (1937). Recognition of elevated beach terraces in Scandinavia showed that the Earth's surface

is still rebounding from the load of ice during the last ice age. By treating the mantle as a viscous fluid, Haskell was able to explain the present uplift of Scandinavia if the mantle has a viscosity of about 10^{20} Pa s. Remarkably, this value of mantle viscosity is still accepted today. Although an immense number (water has a viscosity of 10^{-3} Pa s), it predicts vigorous mantle convection on geologic time scales.

The viscous fluid-like behavior of the solid mantle on long time scales required an explanation. How could horizontal displacements of thousands of kilometers be accommodated in solid mantle rock?

Question 1.3: Why does solid mantle rock behave like a fluid?

The answer was provided in the 1950s, when theoretical studies identified several mechanisms for the very slow creep of crystalline materials thereby establishing a mechanical basis for the mantle's fluid behavior. Gordon (1965) showed that solid-state creep quantitatively explained the viscosity determined from observations of postglacial rebound. At temperatures that are a substantial fraction of the melt temperature, thermally activated creep processes allow hot mantle rock to flow at low stress levels on time scales greater than 10^4 years. In hindsight, the flow of the crystalline mantle should not have been a surprise for geophysicists since the flow of crystalline ice in glaciers had long been recognized and accepted.

In the 1930s a small group of independent-minded geophysicists including Pekeris (1935), Hales (1936), and Griggs (1939) attempted to build quantitative models of mantle convection. Figure 1.11 shows an ingenious apparatus built by Griggs to demonstrate the effects of mantle convection on the continental crust. Griggs modeled the crust with sand–oil mixtures, the mantle with viscous fluids, and substituted mechanically driven rotating cylinders for the thermal buoyancy in natural convection. His apparatus produced crustal roots and near-surface thrusting at the convergence between the rotating cylinders; when only one cylinder was rotated, an asymmetric root formed with similarities to a convergent plate margin, including a model deep sea trench. The early work of Pekeris and Hales were attempts at finite amplitude theories of mantle convection. They included explanations for dynamic surface topography, heat flow variations, and the geoid based on mantle convection that are essentially correct according to our present understanding.

In retrospect, these papers were far ahead of their time, but unfortunately their impact was much less than it could have been. In spite of all the attention given to continental drift, the solid foundation of convection theory and experiments, and far-sighted contributions of a few to create a framework for convection in the mantle, general acceptance of the idea came slowly. The vast majority of the Earth Sciences community remained unconvinced about the significance of mantle convection. We can identify several reasons why the Earth Science community was reluctant to embrace the concept, but one stands out far above the others: the best evidence for mantle convection comes from the seafloor, and until the middle of the twentieth century the seafloor was virtually unknown. The situation began to change in the 1950s, when two independent lines of evidence confirmed continental drift and established the relationship between the continents, the oceans, and mantle convection. These were paleomagnetic pole paths and the discovery of seafloor spreading. We will consider each of these in turn.

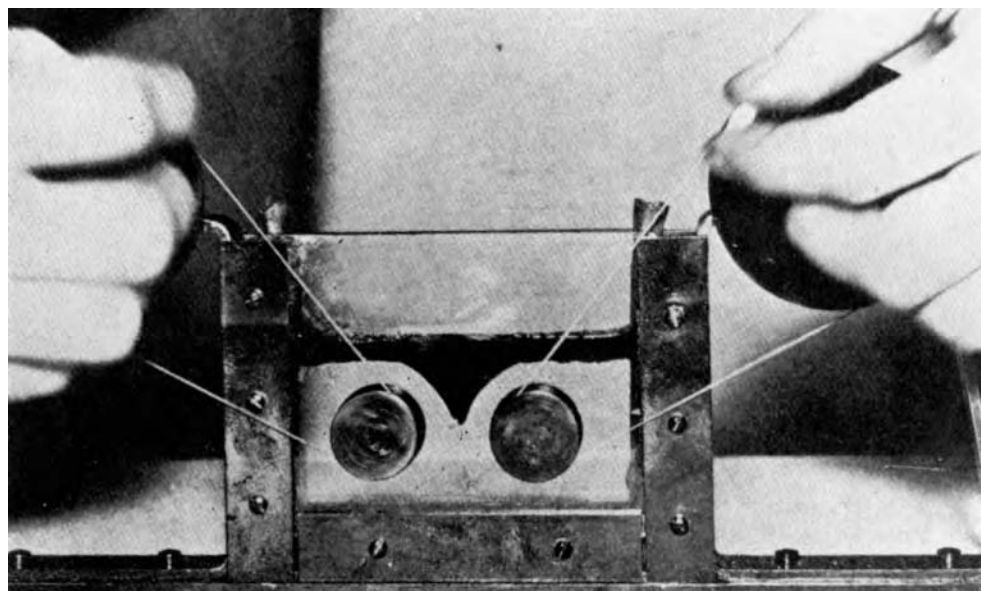


Figure 1.11. Early experiment on mantle convection by David Griggs (1939), showing styles of deformation of a brittle crustal layer overlying a viscous mantle. The cellular flow was driven mechanically by rotating cylinders.

1.4 Paleomagnetism

Many rocks contain small amounts of magnetic and paramagnetic minerals that acquire a weak remnant magnetism at the time of crystallization of the rock. Thus igneous rocks preserve evidence of the direction of the Earth's magnetic field at the time they were formed. In some cases sedimentary rocks also preserve remnant magnetism. Studies of the remnant magnetism in rocks are known as paleomagnetism and were pioneered in the early 1950s by Blackett (1956) and his colleagues.

This paleomagnetic work demonstrated inconsistencies between the remnant magnetic field orientations found in old rocks and the magnetic field in which the rocks are found today. In some cases, corrections had to be made for the effects of the local tilting and rotation that the rocks had undergone since their formation. Even so, having taken into account these and other possible effects, discrepancies remained. Several explanations for these discrepancies were given: (1) variations in the Earth's magnetic field, (2) movement of the entire outer shell of the Earth relative to the axis of rotation (i.e., polar wander), and (3) continental drift.

The systematic variations in the remnant magnetism strongly favored the third explanation. When the remnant magnetic vectors for a series of rocks with different ages from the same locality were considered together, the orientation had a regular and progressive change with age, with the most recent rocks showing the closest alignment with the present field. This is shown graphically by plotting a series of "virtual magnetic poles." For each rock in the time series, a "pole position" is derived from its magnetic inclination and declination. If sufficient points are plotted, they form a curved line terminating near the present pole for the youngest rocks; when rocks in North America and Europe are compared, the opening of the North Atlantic is clearly illustrated as shown in Figure 1.12. In the late 1950s these studies were taken by their proponents as definitive evidence supporting continental drift.

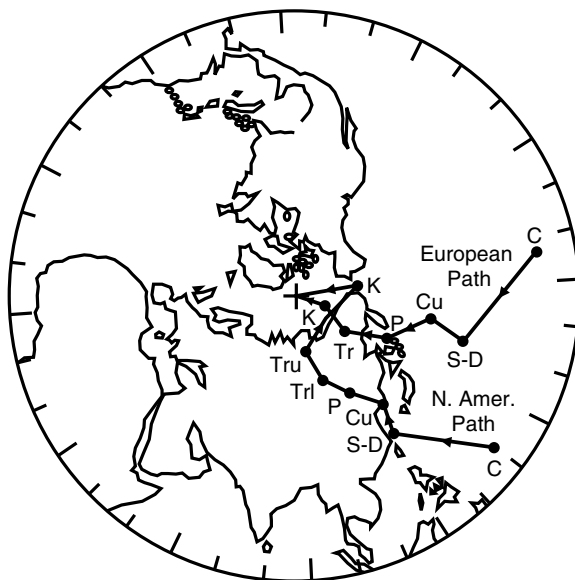


Figure 1.12. Polar wander paths based on observations from North America and Europe. Points on the path are identified by age in millions of years (C = Cambrian 540–510; S-D = Silurian/Devonian 440–290; Cu = Upper Carboniferous 325–290; P = Permian 290–245; Tr, I, u = Triassic, lower, upper 225–190; K = Cretaceous 135–65). The shapes of the paths are approximately the same until the Triassic when the continents began to separate.

(Runcorn, 1956, 1962a). The opponents of continental drift argued that the results could be due to variations in the structure of the Earth's magnetic field.

There was another important result of the paleomagnetic studies. Although consistent and progressive changes in the magnetic inclination and declination were observed for each continent, the polarity of the remnant magnetic field was highly variable and in some cases agreed with the polarity of the present field and in others was reversed (Cox et al., 1963, 1964). The recognition that virtually all rocks with reversed polarity had formed within specific time intervals, regardless of latitude or continent, led to the conclusion that the reversed magnetic polarities were the result of aperiodic changes in the polarity of the Earth's magnetic field. These reversals were to play a key role in quantifying the seafloor spreading hypothesis, discussed in the next section.

1.5 Seafloor Spreading

In the decades leading up to the 1950s, extensive exploration of the seafloor led to the discovery of a worldwide range of mountains on the seafloor, the mid-ocean ridges. Of particular significance was the fact that the mid-Atlantic ridge bisects the entire Atlantic Ocean. The crests of the ridges have considerable shallow seismic activity and volcanism. Ridges also display extensional features suggesting that the crust is moving away on both sides. These and other considerations led to the hypothesis of seafloor spreading (Dietz, 1961; Hess, 1962, 1965), wherein the seafloor moves laterally away from each side of a ridge and new seafloor is continuously being created at the ridge crest by magma ascending from the mantle.

It was immediately recognized that the new hypothesis of seafloor spreading is entirely consistent with the older idea of continental drift. New ocean ridges form where continents break apart, and new ocean crust is formed symmetrically at this ocean ridge, creating a new ocean basin. The classic example is the Atlantic Ocean, with the mid-Atlantic ridge being the site of ocean crust formation. In the process of seafloor spreading, the continents are transported with the ocean floor as nearly rigid rafts.

This realization was a critical advance in defining the role of mantle convection. It shifted the emphasis from the continents to the seafloor. The drifting blocks of continental crust came to be seen as nearly passive participants in mantle convection, whereas the dynamics of the process were to be found in the evolution of the ocean basins.

Striking direct evidence for the seafloor spreading hypothesis came from the linear magnetic field anomalies that parallel the ocean ridges (Mason, 1958). Vine and Matthews (1963) proposed that these linear anomalies represent a fossilized history of the Earth's magnetic field. As the oceanic crust is formed at the crest of the ocean ridge, the injected basaltic magmas crystallize and cool through the Curie temperature, and the newly formed rock is magnetized with the polarity of the Earth's magnetic field.

The magnetic anomaly produced by the magnetized crust as it spreads away from the ridge is a record of the Earth's magnetic field at the time the crust formed (Figure 1.13). Since it had just been shown that the Earth's magnetic field is subject to aperiodic reversals and these reversals had been dated from studies of volcanics on land (Cox et al., 1964), the rate of movement of the crust away from the ridge crest was determined from the spacing of the magnetic stripes (Vine and Wilson, 1965; Pitman and Heirtzler, 1966; Vine, 1966; Dickson et al., 1968). A comprehensive summary of the worldwide distribution of magnetic stripes was given by Heirtzler et al. (1968).

A typical space–time correlation for the East Pacific Rise is given in Figure 1.13. The data correlate the distance from the ridge crest to the position where the magnetic anomaly changes sign with the time when the Earth's magnetic field is known from independent evidence to have reversed. For this example, with 3.3 Myr seafloor lying 160 km from the ridge axis, the spreading rate is 48 mm yr^{-1} , and so new seafloor is being created at a rate of 96 mm yr^{-1} .

The Vine–Matthews interpretation of the magnetic anomalies was confirmed by the drilling program of the Glomar Challenger (Maxwell et al., 1970). After drilling through the layer of sediments on the ocean floor, the sediment immediately overlying the basaltic crust was dated. The ages of the basal sediments as a function of distance from the mid-Atlantic ridge are compared with the magnetic anomaly results for the same region in Figure 1.14. The agreement is excellent, and the slope of the correlation gives a constant spreading rate of 20 mm yr^{-1} . The conclusion is that the Atlantic Ocean is widening at a rate of 40 mm yr^{-1} .

1.6 Subduction and Area Conservation

The observed rates of seafloor spreading are large when compared with those of many other geological processes. With the present distribution of ridges, they would be sufficient to double the circumference of the Earth in several hundred million years (5% of its age). If the seafloor spreading hypothesis is correct, the Earth must either be expanding very rapidly or surface area must in some way be consumed as rapidly as it is generated by the spreading process. Each of these alternatives had a champion: S. Warren Carey chose the former and Harry Hess chose the latter.

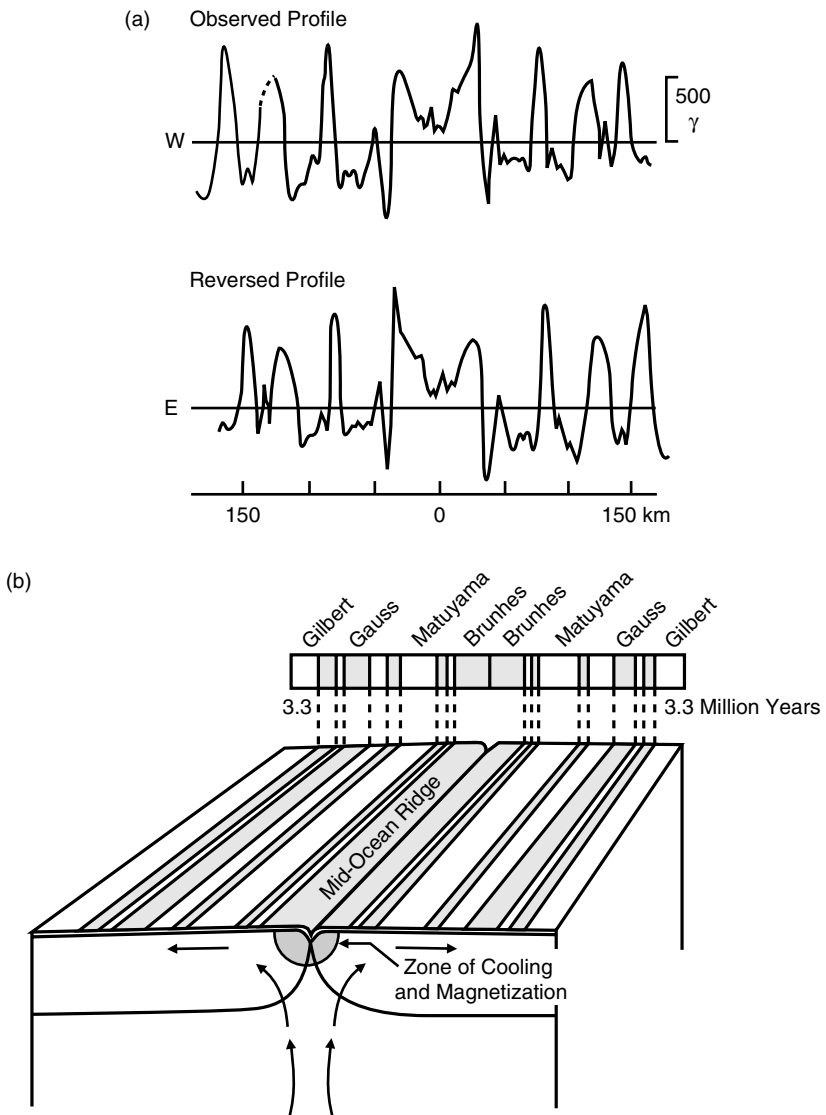
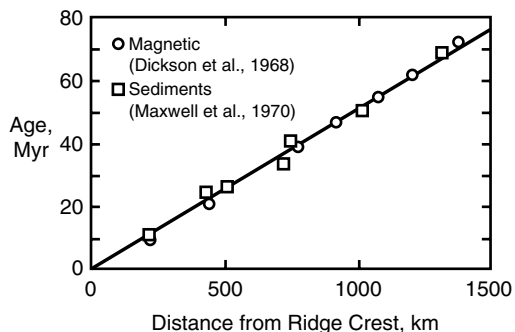


Figure 1.13. (a) Magnetic profile across the East Pacific Rise at 51°S; the lower profile shows the observed profile reversed for comparison. (b) The spreading ocean floor. Hot material wells up along the oceanic ridge. It acquires a remanent magnetism as it cools and travels horizontally away from the ridge. At the top of the diagram are shown the known intervals of normal (gray) and reversed (white) polarity of the Earth's magnetic field, with their names. The width of the ocean-floor stripes is proportional to the duration of the normal and reversed time intervals.

Carey (1958, 1976) had been concerned about the geometrical reconstruction of former continental masses. These studies led him to view the Earth as undergoing rapid expansion. This view did not receive wide support and it will not be considered further. There is no satisfactory physical explanation of how such a large volume expansion might have occurred and it is inconsistent both with estimates of the change in the Earth's rate of rotation and with paleomagnetic constraints on changes in the Earth's radius.

Figure 1.14. Age of the oceanic crust versus distance from the crest of the mid-Atlantic ridge, as inferred from the magnetic anomaly pattern and from the oldest sediments.



Hess (1962) favored an Earth of constant volume and believed that there were zones in the oceans where the evidence suggested that surface area might be lost. He drew attention to the deep ocean trenches of the Pacific and other oceans, which had been studied for many years.

It had been recognized in the thirties by the Dutch geophysicist Vening Meinesz (1937, 1948) that very large gravity anomalies were associated with trenches. The trenches were also associated with unusual seismic activity. Over most of the Earth, earthquakes are restricted to the outer fifty or so kilometers; at ocean trenches, however, earthquakes lie within an inclined zone that intersects the surface along the line of the trench and dips downward into the mantle at angles ranging from 30 to 80°. Along these zones, seismic activity extends for many hundreds of kilometers, in some cases as deep as 700 km.

Hess's view, and he was followed by Vine and Matthews (1963), was that trenches were the sites of crustal convergence; new ocean floor is created at mid-ocean ridges, travels laterally and is consumed at ocean trenches. The loss of surface area at trenches subsequently became known and understood as subduction. Hess also proposed a fundamental difference between oceanic and continental crust. The former was being continuously created at ocean ridges and lost at ocean trenches. Because oceanic crust is relatively thin, the buoyant body forces which would resist subduction are relatively small. The crust of the continents, however, is 5–6 times as thick and has a slightly greater density contrast with the underlying mantle. As a consequence it cannot be subducted. This view was certainly influenced by the failure to identify any part of the floors of the deep oceans older than 200 million years and the recognition that continents commonly contained rocks several billion years old.

The concepts of continental drift, seafloor spreading, and subduction were combined into the plate tectonics model that revolutionized geophysics in the mid-to-late 1960s. The essentials of the plate tectonics model will be discussed in the next chapter. Although plate tectonics is an enormously successful model, it is essentially kinematic in nature. As the accounts in this chapter indicate, the search for a fully dynamic theory for tectonics has proven to be a far more difficult task. It has involved many branches of Earth Science, and continues to this day. This book describes the achievements as well as the questions remaining in this search.

2

Plate Tectonics

2.1 Introduction

During the 1960s there were a wide variety of studies on continental drift and its relationship to mantle convection. One of the major contributors was J. Tuzo Wilson. Wilson (1963a, b, 1965a, b) used a number of geophysical arguments to delineate the general movement of the ocean floor associated with seafloor spreading. He argued that the age progression of the Hawaiian Islands indicated movement of the Pacific plate. He showed that earthquakes on transform faults required seafloor spreading at ridge crests. During this same period other geophysicists outlined the general relations between continental drift and mantle convection (Orowan, 1964, 1965; Tozer, 1965a; Verhoogen, 1965). Turcotte and Oxburgh (1967) developed a boundary layer model for thermal convection and applied it to the mantle. According to this model, the oceanic lithosphere is associated with the cold upper thermal boundary layer of convection in the mantle; ocean ridges are associated with ascending convection in the mantle and ocean trenches are associated with the descending convection of the cold upper thermal boundary layer into the mantle. Despite these apparently convincing arguments, it was only with the advent of plate tectonics in the late 1960s that the concepts of continental drift and mantle convection became generally accepted.

Plate tectonics is a model in which the outer shell of the Earth is broken into a number of thin rigid plates that move with respect to one another. The relative velocities of the plates are of the order of a few tens of millimeters per year. Volcanism and tectonism are concentrated at plate boundaries. The basic hypothesis of plate tectonics was given by Morgan (1968); the kinematics of rigid plate motions were formulated by McKenzie and Parker (1967) and Le Pichon (1968). Plate boundaries intersect at triple junctions and the detailed evolution of these triple junctions was given by McKenzie and Morgan (1969). The concept of rigid plates with deformations primarily concentrated near plate boundaries provided a comprehensive understanding of the global distribution of earthquakes (Isacks et al., 1968).

The distribution of the major surface plates is given in Figure 2.1; ridge axes, subduction zones, and transform faults that make up plate boundaries are also shown. Global data used to define the plate tectonic model are shown in Figures 2.2–2.9. The distribution of global shallow and deep seismicity is shown in Figure 2.2, illustrating the concept of shallow seismicity defining plate boundaries. Figure 2.3 shows the distribution of ages of the ocean crust obtained from the pattern of magnetic anomalies on the seafloor. The distribution of crustal ages confirms that ridges are the source of ocean crust and also establishes the rates of seafloor spreading in plate tectonics. Figures 2.4–2.6 show geoid height variations – the topography of the equilibrium sea surface, which correlates closely with seafloor topography

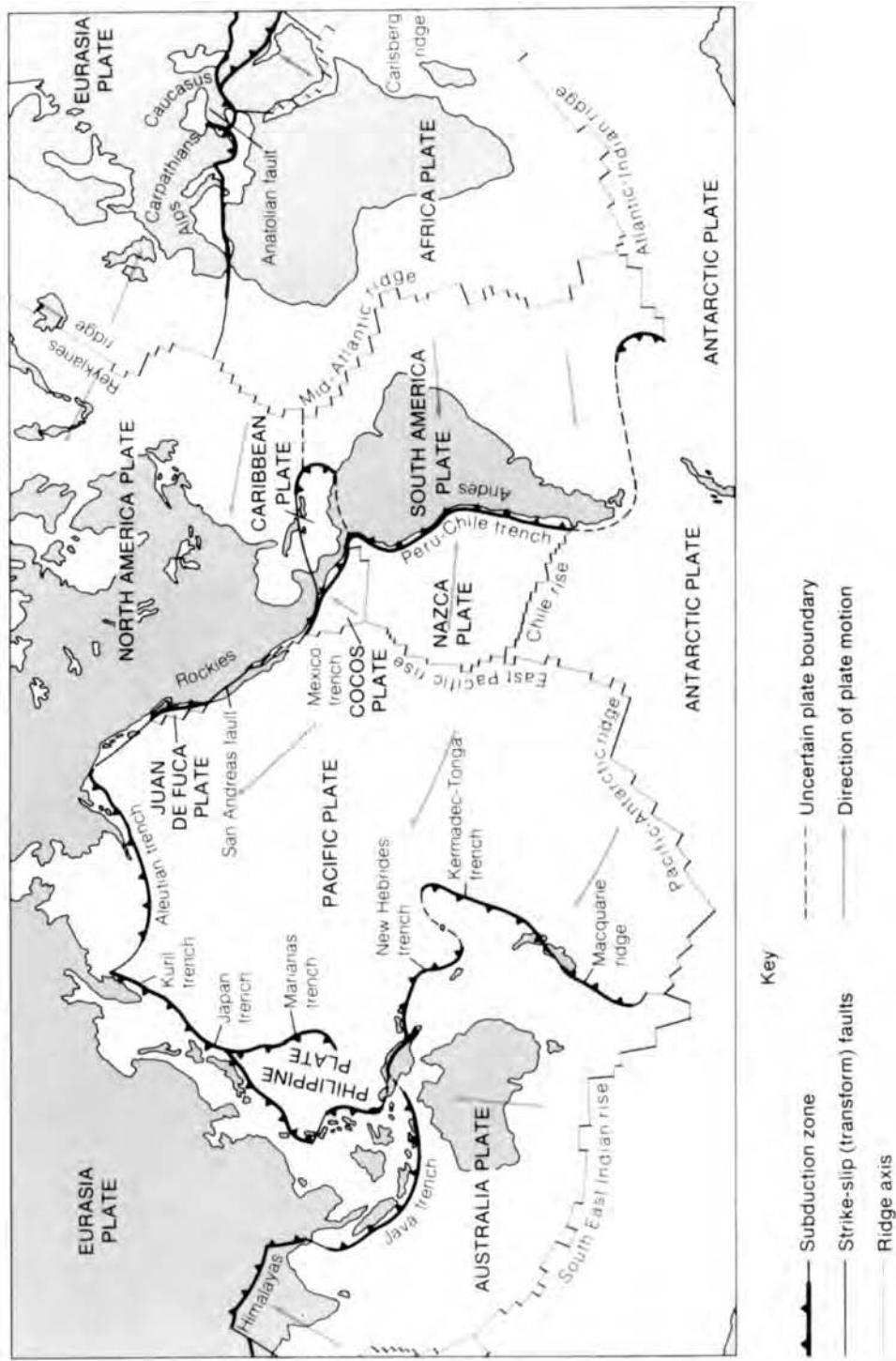


Figure 2.1. Distribution of the major surface plates. The ridge axes, subduction zones, and transform faults that make up the plate boundaries are shown. After Bolt (1993).

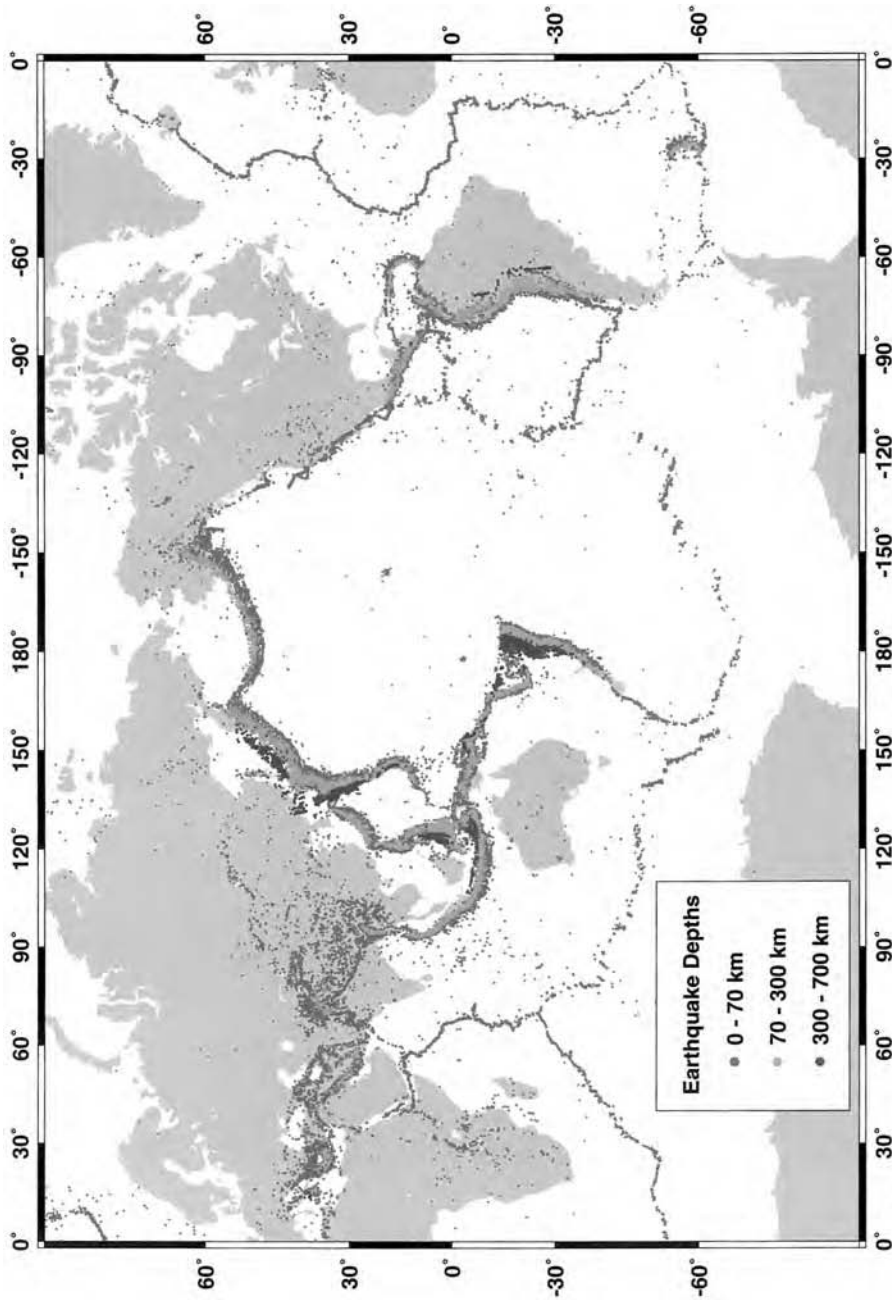


Figure 2.2. The global distribution of both shallow and deep seismicity for well-located earthquakes with magnitude > 5.1 . The shallow seismicity closely delineates plate boundaries. Based on Engdahl et al. (1998).

For a color version of this figure, see plate section.

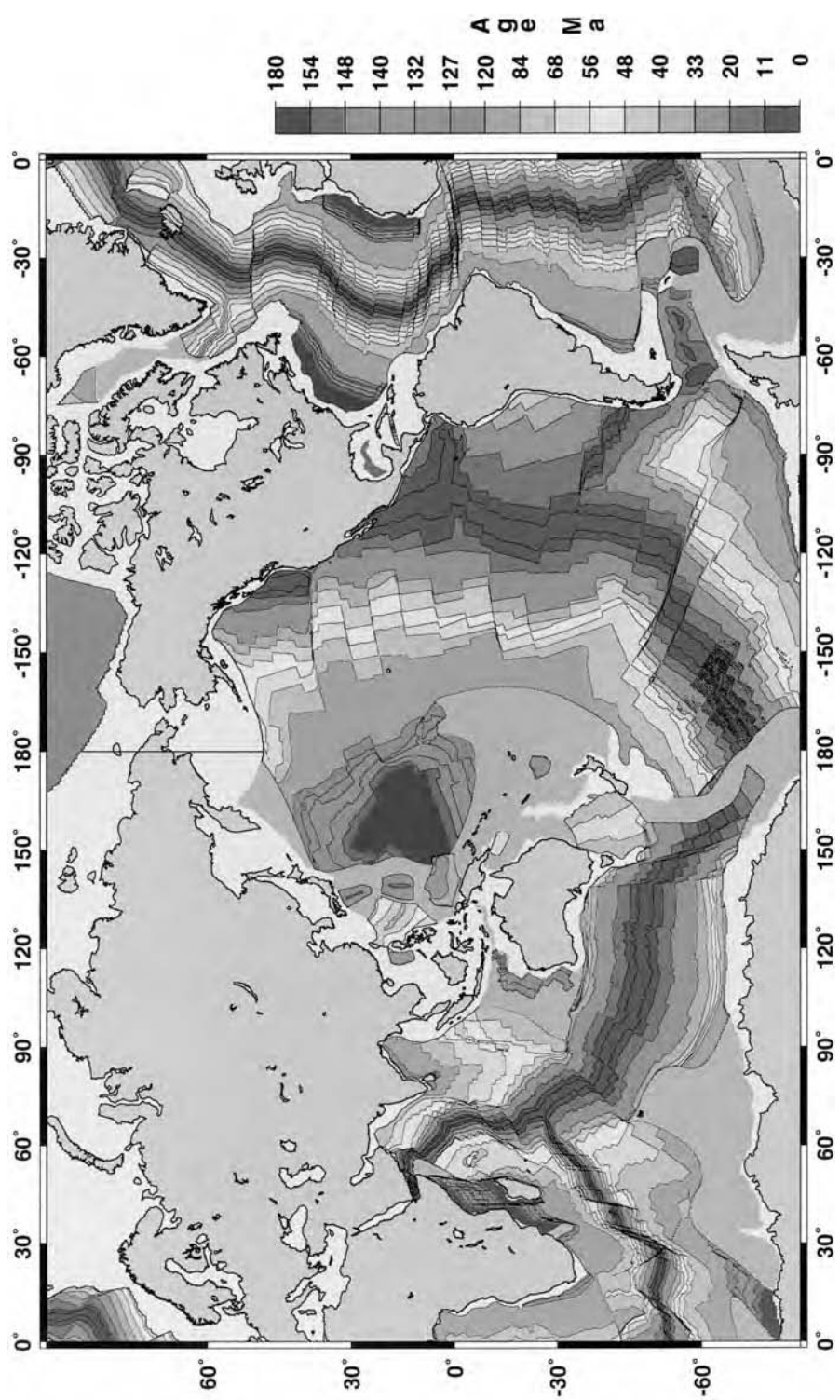
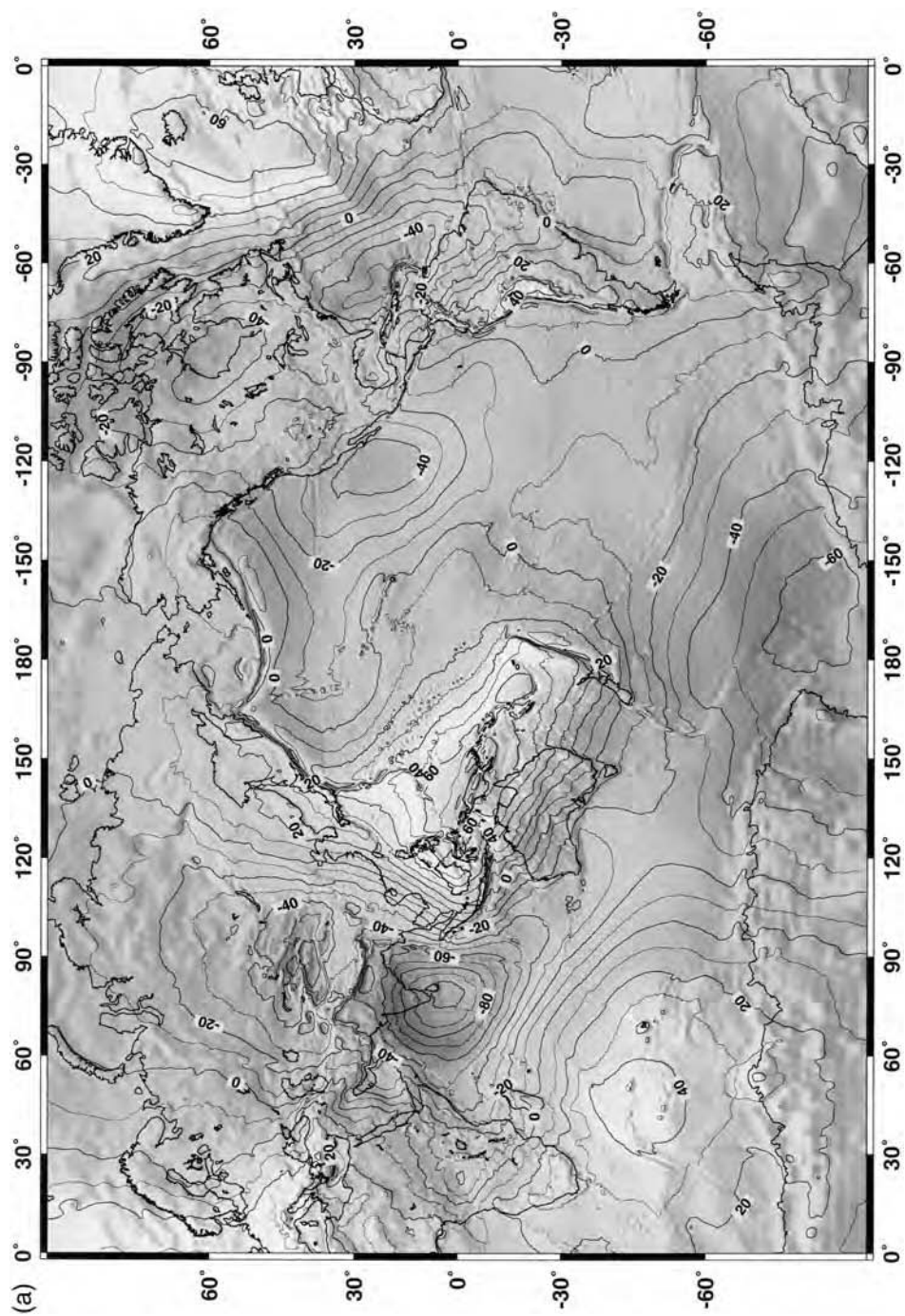


Figure 2.3. Age distribution of the oceanic crust as determined by magnetic anomalies on the seafloor. Based on Mueller et al. (1997).

For a color version of this figure, see plate section.



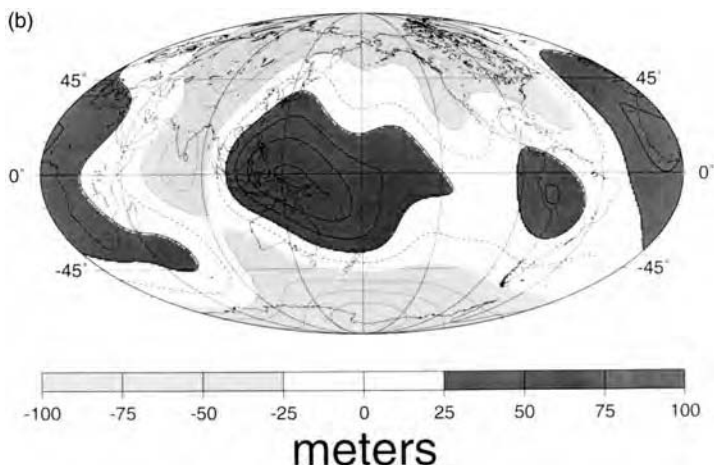


Figure 2.4. (a) Global geoid variations (after Lemoine et al., 1998) and (b) geoid variations complete to spherical harmonic degree 6 (after Ricard et al., 1993). (a) is model EGM96 with respect to the reference ellipsoid WG584. In (b), dotted contours denote negative geoid heights and the dashed contour separates areas of positive and negative geoid height.

For a color version of part (a), see plate section.

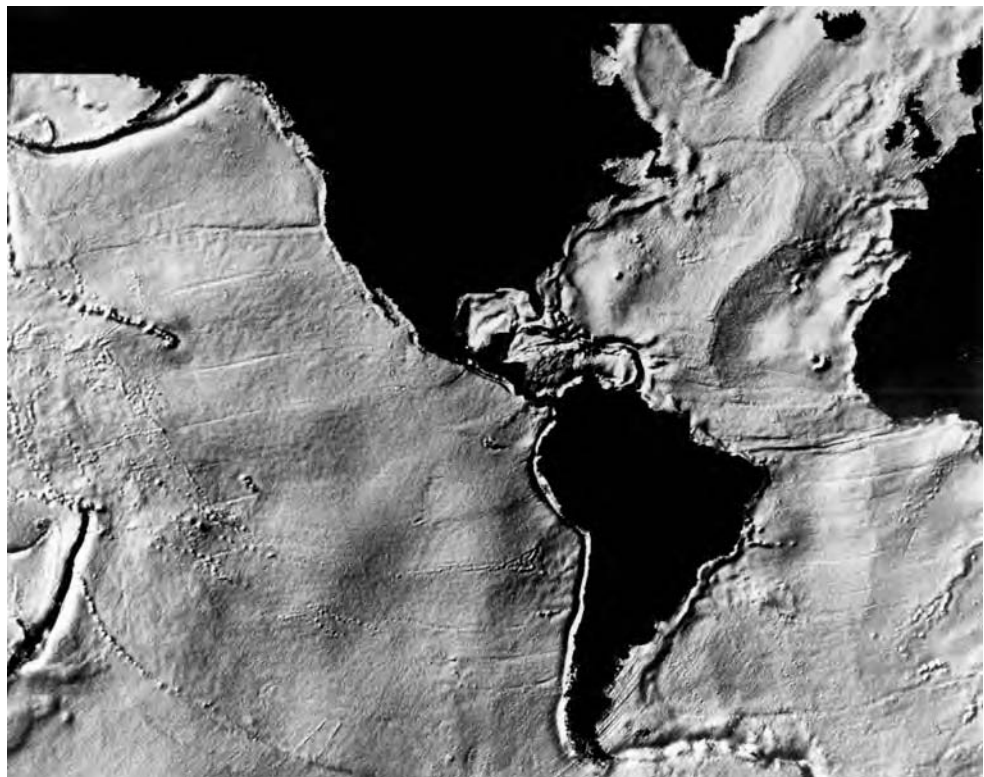


Figure 2.5. Geoid variations over the Atlantic and the eastern Pacific. The long-wavelength components of the global geoid shown in Figure 2.4b (to spherical harmonic degree 6) have been removed. After Marsh (1983).

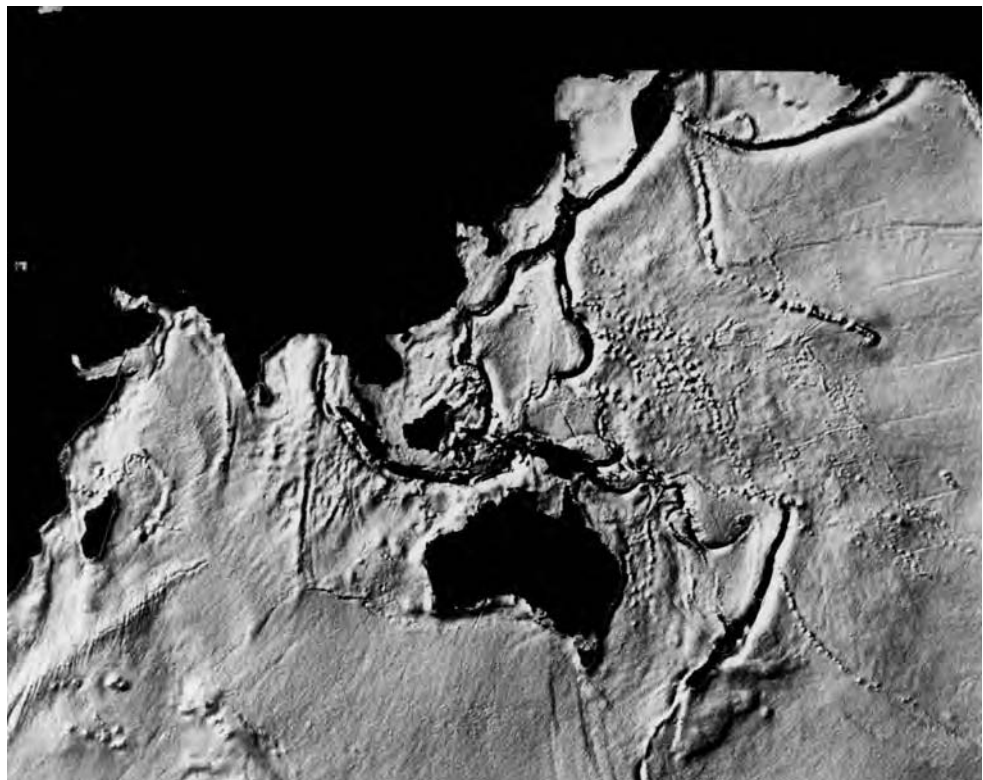


Figure 2.6. Western Pacific geoid. The long-wavelength components of the global geoid shown in Figure 2.4b (to spherical harmonic degree 6) have been removed. After Marsh (1983).

(Figure 2.7). The three types of structures used to define plate boundaries in Figure 2.1 – ridges, trenches, and transform faults – are evident in the geoid and the topography. Figure 2.8 shows the global pattern of heat flow, and Figure 2.9 gives the global locations of volcanoes. Volcanoes, like earthquakes, are strongly clustered at plate boundaries, mainly subduction zones. There are also numerous intraplate volcanoes, many at sites known as hot spots.

The essence of plate tectonics is as follows. The outer portion of the Earth, termed the lithosphere, is made up of relatively cool, stiff rocks and has an average thickness of about 100 km. The lithosphere is divided into a small number of mobile plates that are continuously being created and consumed at their edges. At ocean ridges, adjacent plates move apart in a process known as seafloor spreading. As the adjacent plates diverge, hot mantle rock ascends to fill the gap. The hot, solid mantle rock behaves like a fluid because of solid-state creep processes. As the hot mantle rock cools, it becomes rigid and accretes to the plates, creating new plate area. For this reason ocean ridges are also known as accretionary plate boundaries.

Because the surface area of the Earth is essentially constant, there must be a complementary process of plate consumption. This occurs at ocean trenches. The surface plates bend and descend into the interior of the Earth in a process known as subduction. At an ocean trench the two adjacent plates converge, and one descends beneath the other. For this reason ocean trenches are also known as convergent plate boundaries. A cross-sectional view of the creation and consumption of a typical plate is illustrated in Figure 2.10. As the plates move away from ocean ridges, they cool and thicken and their density increases due to thermal

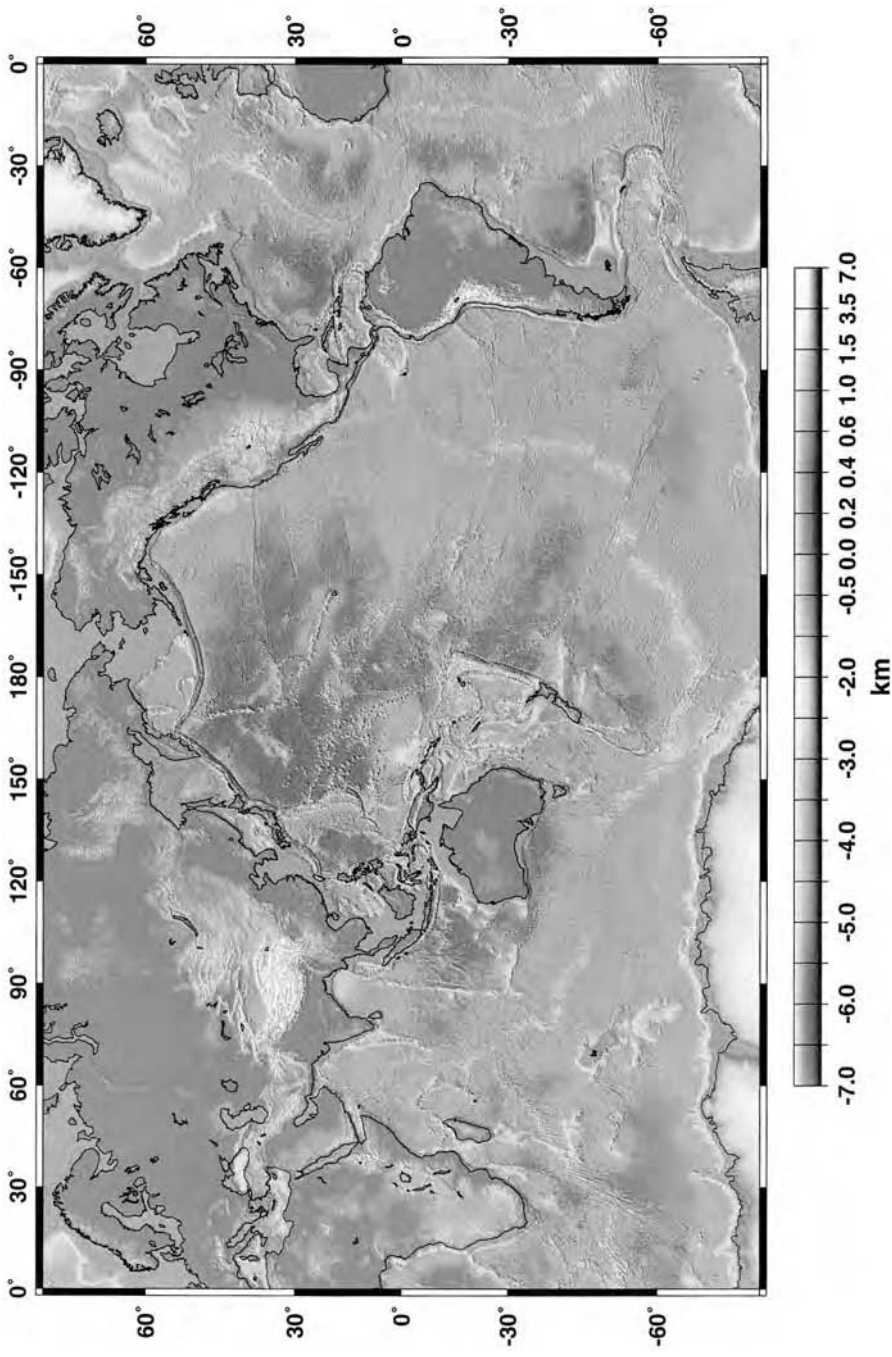


Figure 2.7. Global topography. The mountain range on the seafloor, the system of mid-ocean ridges, is a prominent feature of the Earth's topography. Based on Smith and Sandwell (1997).

For a color version of this figure, see plate section.

Heat Flow

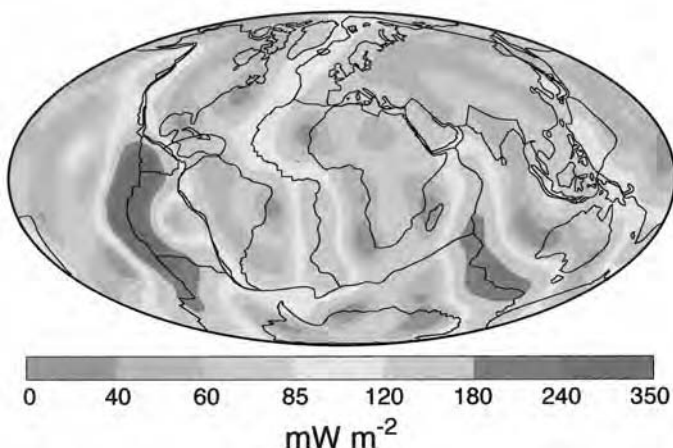


Figure 2.8. Pattern of global heat flux variations complete to spherical harmonic degree 12. After Pollack et al. (1993).

For a color version of this figure, see plate section.

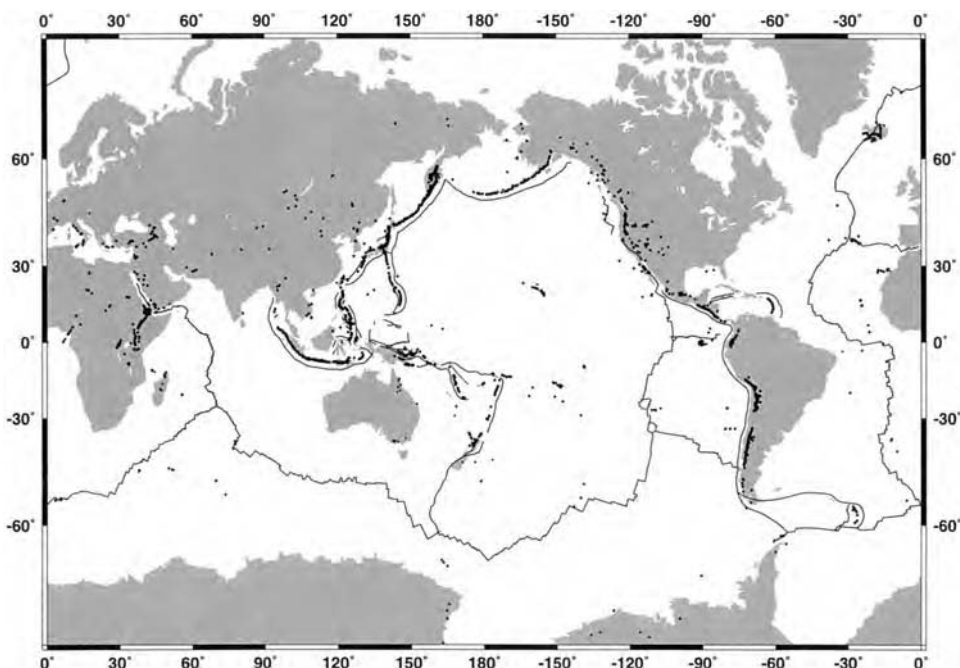


Figure 2.9. Global distribution of volcanoes active in the Quaternary.

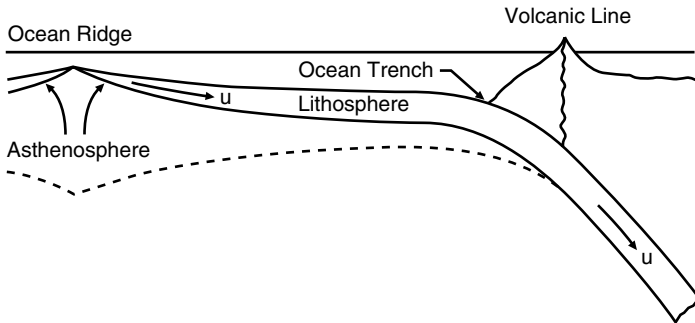


Figure 2.10. Accretion of a lithospheric plate at an ocean ridge (accretionary plate margin) and its subduction at an ocean trench (subduction zone). The asthenosphere, which lies beneath the lithosphere, and the volcanic line above the subducting lithosphere are also shown. The plate migrates away from the ridge crest at the spreading velocity u . Since there can be relative motion between the ocean ridge and ocean trench, the velocity of subduction can, in general, be greater or less than u .

contraction. As a result, the lithosphere becomes gravitationally unstable with respect to the warmer asthenosphere beneath. At an ocean trench, the lithosphere bends and sinks into the interior of the Earth because of its negative buoyancy.

2.2 The Lithosphere

An essential feature of plate tectonics is that only the outer shell of the Earth, the lithosphere, remains rigid during long intervals of geologic time. Because of their low temperature, rocks in the lithosphere resist deformation on time scales of up to 10^9 yr. In contrast, the rock beneath the lithosphere is sufficiently hot that solid-state creep occurs. The lithosphere is composed of both mantle and crustal rocks. The oceanic lithosphere has an average thickness of 100 km with the uppermost 6–7 km being the oceanic crust. The oceanic lithosphere participates in the plate tectonic cycle. The continental lithosphere has a typical thickness of about 200 km (some authors argue that the thickness may be twice this value; further discussion will be given in Chapters 3 and 4). Typically, the upper 30 km of the continental lithosphere is continental crust. Because of the buoyancy of the continental crust, the continental lithosphere does not subduct, although it does participate in plate motions.

Because of their higher temperatures, rocks beneath the lithosphere can flow by subsolidus viscous creep. This region is called the asthenosphere. Because the silicic rocks of the continental crust are softer than both mantle rocks and the basaltic rocks of the oceanic crust, rocks within the continental crust, particularly within the lower crust, can also flow viscously while the mantle rocks below behave rigidly. The result is an intracrustal asthenosphere layer within the continental lithosphere.

Although the concept of a lithosphere is straightforward, there is in fact considerable confusion because the precise definition depends on the property being considered. We speak of the mechanical lithosphere, the thermal lithosphere, and the elastic lithosphere. Here each is considered in turn.

(1) *Mechanical lithosphere*. The mechanical lithosphere is defined to be those rocks that remain a coherent part of the plates on geological time scales. A typical definition would be rocks that cannot be deformed more than 1% in 10^8 yr at typical mantle stress levels

(say 1 MPa). The deformation of the mantle is determined by its viscosity, and its viscosity is, in turn, determined by its temperature. Thus the base of the mechanical lithosphere is prescribed by an isotherm, typically 1,400 K. Rocks shallower than the level of this isotherm are sufficiently cool to behave rigidly, whereas rocks lying deeper than this isotherm are sufficiently hot to deform and flow viscously in response to long-term forces. The term “tectonic plate” is most closely related to this definition of the lithosphere.

(2) *Thermal lithosphere*. We will consider the thermal structure of both the oceanic and continental lithospheres in Chapter 4. The oceanic lithosphere is taken to be the upper thermal boundary layer of mantle convection. Since the thermal boundary layer has a continuous variation in temperature, the definition of its thickness is arbitrary. If the temperature difference across the oceanic lithosphere (the thermal boundary layer) is $T_m - T_s$, where T_s is the surface temperature and T_m is the mantle temperature beneath the boundary layer, a typical definition of the base of the thermal boundary layer is the depth at which the temperature T is $T_s + 0.9(T_m - T_s)$. If this temperature is equal to the rheological temperature determining the base of the mechanical lithosphere, then the mechanical and thermal lithospheres are the same. In the remainder of this book we will assume that this is the case, and we will refer to both the mechanical and thermal lithospheres as the lithosphere.

(3) *Elastic lithosphere*. The rigidity of the lithosphere also allows it to flex when subjected to a load. An example is the load applied by a volcanic island. The load of the Hawaiian Islands causes the lithosphere to bend downward around the load, resulting in a moat, i.e., a region of deeper water around the islands. The elastic bending of the lithosphere under vertical loads can also explain the structure of ocean trenches and some sedimentary basins. However, the entire lithosphere is not effective in transmitting elastic stresses. Only about the upper half of it is sufficiently rigid that elastic stresses are not relaxed on time scales of 10^9 yr. This fraction of the lithosphere is referred to as the elastic lithosphere. Solid-state creep processes relax stresses in the lower, hotter part of the lithosphere. This lower part of the lithosphere, however, remains a coherent part of the plates.

The strength of the lithosphere allows the plates to transmit elastic stresses over geologic time intervals. The plates act as stress guides. Stresses that are applied at the boundaries of a plate can be transmitted throughout the interior of the plate. The ability of the plates to transmit stress over large distances is a key factor in driving tectonic plates.

2.3 Accretional Plate Margins (Ocean Ridges)

Lithospheric plates are created at ocean ridges (Figures 2.1, 2.5, 2.7, and 2.10). The two plates on either side of an ocean ridge move away from each other with nearly steady velocities of a few tens of millimeters per year. As the two plates diverge, hot mantle rock flows upward to fill the gap. The upwelling mantle rock cools by conductive heat loss to the surface. The cooling rock accretes to the base of the spreading plates, becoming part of them; the structure of an accreting plate margin is illustrated in Figure 2.11.

As the plates move away from the ocean ridge, they continue to cool and thicken. The elevation of the ocean ridge as a function of distance from the ridge crest, shown in the images of the geoid in Figures 2.5 and 2.6 and in the topography of Figure 2.7, can be explained in terms of the temperature distribution in the lithosphere. As the lithosphere cools, it contracts thermally and its upper surface – the ocean floor – sinks relative to the ocean surface. The topographic elevation of the ridge is due to the lower-density, thinner, and hotter lithosphere near the axis of accretion at the ridge crest. The elevation of

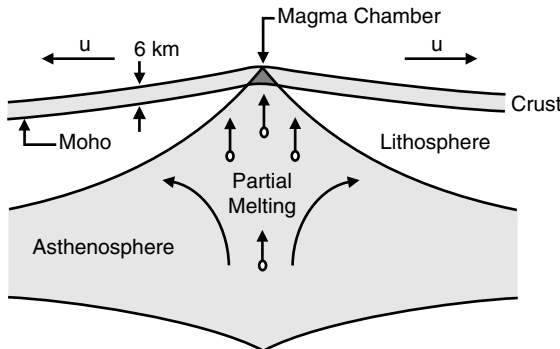


Figure 2.11. Structure at and beneath an accreting plate margin (ocean ridge). Hot flowing mantle rock (asthenosphere) ascends beneath the ridge axis. Pressure-release melting occurs and the resulting magma migrates upward to form the axial magma chamber. The basaltic rocks in this magma chamber solidify to form the 6 km thick ocean crust. Heat loss to the seafloor cools and thickens the oceanic lithosphere and hot asthenospheric rock accretes to it.

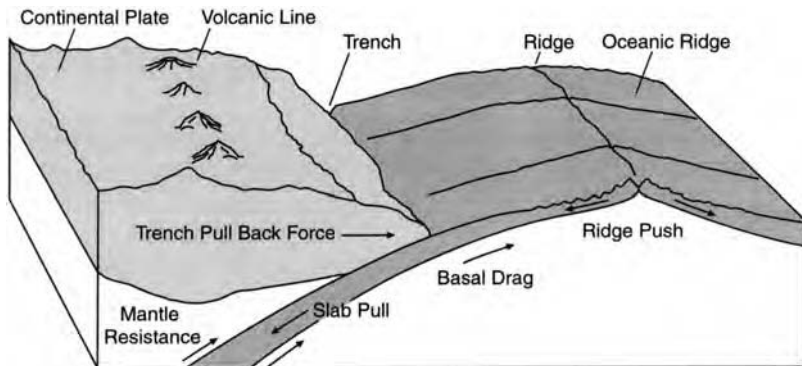


Figure 2.12. Illustration of the major forces acting on the plates.

the ridge also exerts a gravitational body force that drives the lithosphere away from the accretional boundary; it is one of the important forces driving the plates and is known as gravitational sliding or ridge push (Figure 2.12). Conductive cooling of the lithosphere also causes a decrease in the geothermal gradient, which is evident in the pattern of global heat flow (Figure 2.8); heat flow is highest at the ridges and decreases with increasing plate age.

The volume occupied by the ocean ridges displaces seawater. Rates of seafloor spreading vary in time. When rates of seafloor spreading are high, ridge volume is high, seawater is displaced, and the result is an increase in the global sea level. Variations in rates of seafloor spreading are the primary cause for changes in sea level on geological time scales (Hays and Pitman, 1973; Turcotte and Burke, 1978; Schubert and Reymer, 1985). During the Cretaceous (≈ 80 Ma) the rate of seafloor spreading was about 30% greater than at present, sea level was about 200 m higher than today, and a substantial fraction of the continental interiors was covered by shallow seas.

Ocean ridges generate a large fraction of the Earth's volcanism. Because almost all the ridge system is below sea level, only a small part of this volcanism can be readily observed. Ridge volcanism can be seen in Iceland, where the oceanic crust is sufficiently thick that the ridge crest rises above sea level. The volcanism at ocean ridges is caused by pressure-release melting. The diverging plates induce an upwelling in the mantle. The temperature of the ascending rock decreases slowly with decreasing pressure along an adiabat. The solidus temperature for melting decreases with decreasing pressure at a much faster rate. When the temperature of the ascending mantle rock equals the solidus temperature, melting begins. The ascending mantle rock contains a low-melting-point basaltic component; this component melts first to form the oceanic crust (Figure 2.11).

2.4 Transform Faults

One of the striking features of accretional plate margins is the orthogonal system of ridge segments and transform faults. The ridge segments lie nearly perpendicular to the spreading

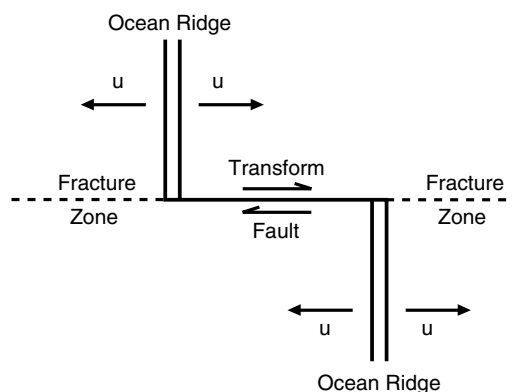


Figure 2.13. Segments of an ocean ridge offset by a transform fault. The fracture zones are extensions of the transform faults into the adjacent plates.

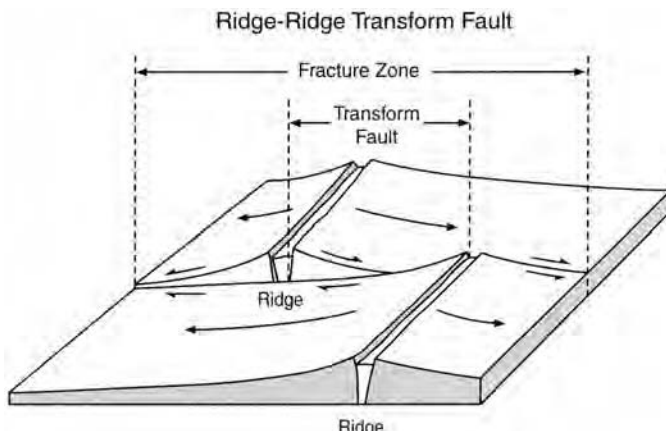


Figure 2.14. Sketch of a ridge-ridge transform fault showing exaggerated differential vertical subsidence across the fault.

direction, whereas the transform faults lie parallel to the spreading direction. This structure is illustrated in Figures 2.1, 2.5, 2.7, 2.13, and 2.14. The relative velocity across a transform fault is twice the spreading velocity. This relative motion results in seismicity on the transform fault between the adjacent ridge segments.

There is also differential vertical motion on transform faults (Figure 2.14). As the seafloor spreads away from a ridge crest, it also subsides. Since the adjacent points on each side of a transform fault usually lie at different distances from the ridge crest where the crust was formed, the rates of subsidence on the two sides differ. The extensions of the transform faults into the adjacent plates are known as fracture zones. Fracture zones are often deep valleys in the seafloor. Transform faults and fracture zones are prominently visible in Figures 2.5, 2.6, and 2.7.

Question 2.1: Why do accretional plate margins develop the orthogonal ridge segment–transform fault geometry?

Ocean ridges do not form obliquely to the direction of seafloor spreading. Instead they form the orthogonal ridge–transform system described above. This orthogonal system has been reproduced in laboratory experiments using freezing wax (Oldenburg and Brune, 1972, 1975). Despite the ability to reproduce the orthogonal pattern in the laboratory, the physical reason for the orthogonal pattern remains unclear. A number of authors have suggested that the pattern is associated with the thermal stresses that develop in the cooling oceanic lithosphere (Collette, 1974; Turcotte, 1974; Parmentier and Haxby, 1986; Sandwell, 1986).

A transform fault that connects two segments of an ocean ridge is known as a ridge–ridge transform (Figures 2.13 and 2.14). Transform faults can also connect two segments of an ocean trench or a segment of a ridge with a segment of a trench (Figure 2.15). In some cases one end of a transform fault terminates in a triple junction of three surface plates. An example is the San Andreas fault in California, which accommodates lateral sliding between the Pacific and North American plates (Figure 2.16).

A variety of other complex geometrical patterns are associated with accretional plate margins. In some cases ridge jumps occur and ridge segments propagate (Hey et al., 1980). If the direction of seafloor spreading changes due to plate interactions, the accretional margin can break up into a number of microplates until a new orthogonal pattern of ridges and transforms is established.

2.5 Subduction

As the oceanic lithosphere moves away from an ocean ridge, it cools, thickens, and becomes more dense because of thermal contraction. Even though the basaltic rocks of the oceanic crust are lighter than the underlying mantle rocks, the colder subcrustal rocks in the lithosphere become sufficiently dense to make old oceanic lithosphere heavy enough to be gravitationally unstable with respect to the hot mantle rocks beneath the lithosphere. As a result of this gravitational instability, the oceanic lithosphere founders and begins to sink into the interior of the Earth, creating the ocean trenches shown in Figures 2.5 and 2.6.

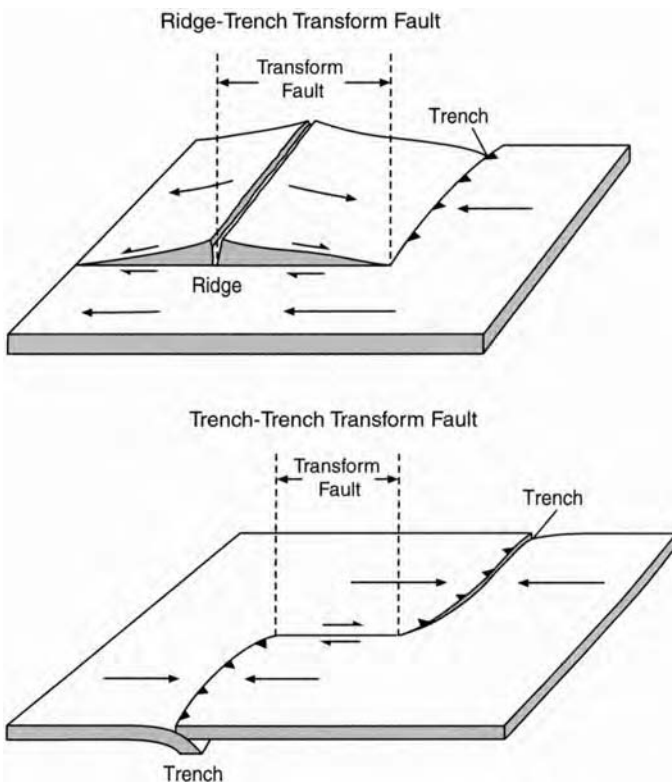


Figure 2.15. Sketch of ridge–trench and trench–trench transform faults.



Figure 2.16. The San Andreas transform fault system accommodates lateral sliding between the Pacific and North American plates. The northern terminus of the San Andreas fault is the Mendocino triple junction at the intersection of the Juan de Fuca, Pacific, and North American plates.

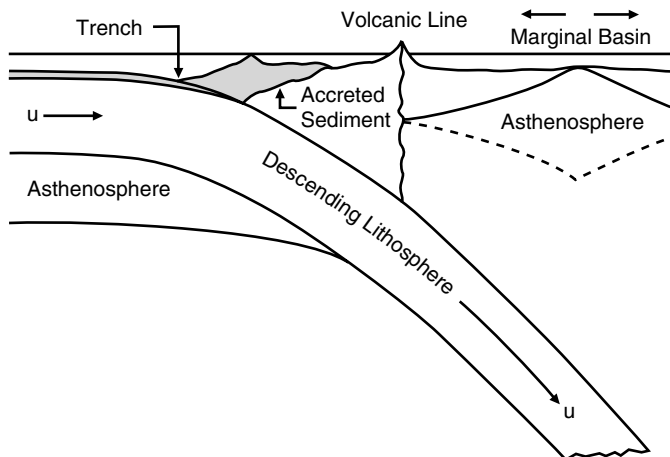


Figure 2.17. Illustration of the subduction of oceanic lithosphere at an ocean trench. The line of volcanic edifices associated with most subduction zones is shown. A substantial fraction of the sediments that coat the basaltic oceanic crust is scraped off during subduction to form an accretionary prism of sediments. Back-arc spreading forms a marginal basin behind some subduction zones.

The subduction of the oceanic lithosphere at an ocean trench is illustrated schematically in Figure 2.17. A chain of volcanoes which lie parallel to the ocean trench is generally associated with subduction. A substantial fraction of the sediments that coat the oceanic crust is scraped off during subduction to form an accretionary prism of sediments (von Huene and Scholl, 1991). In some cases back-arc seafloor spreading forms a marginal basin behind the subduction zone.

The excess density of the rocks of the descending lithosphere results in a downward buoyancy force. Because the lithosphere behaves elastically, it can transmit stresses, i.e., it can act as a stress guide. A portion of the negative buoyancy force acting on the descending plate is transmitted to the surface plate, which is pulled toward the ocean trench. This is slab pull, one of the important forces driving plate tectonics (Figure 2.12).

Ocean trenches are the sites of most of the largest earthquakes. At depths of less than about 55 km, the earthquakes occur on the dipping fault plane that separates the descending lithosphere from the overlying lithosphere (Ruff, 1996). Below about 55 km depth, the earthquakes probably occur within the subducting lithosphere (Comte et al., 1999). Earthquakes at ocean trenches can occur to depths of 660 km or more, depending on variations in the depth of the 660 km seismic discontinuity. Where the mantle is expected to be warmer, earthquakes do not extend as deep (Green and Houston, 1995; Kirby et al., 1996) in accordance with the expected upwarping of the 660 km seismic discontinuity (see Chapters 4, 9, 10, and 13). This seismogenic region, known as the Wadati–Benioff zone (Wadati, 1928, 1934/35; Benioff, 1949; Utsu, 1971), delineates the approximate structure of the descending plate. An early example of the geometry of the Wadati–Benioff zone at two locations along the Tonga arc is shown in Figure 2.18. The projection of the Wadati–Benioff zone onto the surface of the Earth is shown by the systematic horizontal trends in the locations of earthquakes of different depths on the global seismicity map of Figure 2.2. The shapes of the upper boundaries of several descending lithospheres are given in Figure 2.19, on the assumption that the earthquakes in the Wadati–Benioff zone lie on or near the top of the descending slab. The positions of the trenches and the volcanic

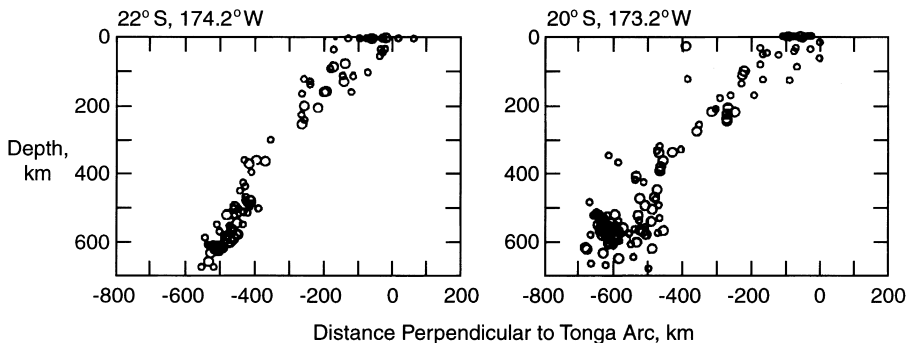


Figure 2.18. Earthquake foci beneath the Tonga arc at two sections oriented perpendicular to the arc. The geographic position corresponds to zero distance on the abscissa. Larger symbols represent more accurate hypocenter locations. The earthquakes were recorded by seismograph stations between 1959 and 1962. Hypocenters are projected from distances ± 125 km of each line. The earthquake hypocenters delineate a nearly linear dipping structure, the Wadati–Benioff zone. After Sykes (1966).

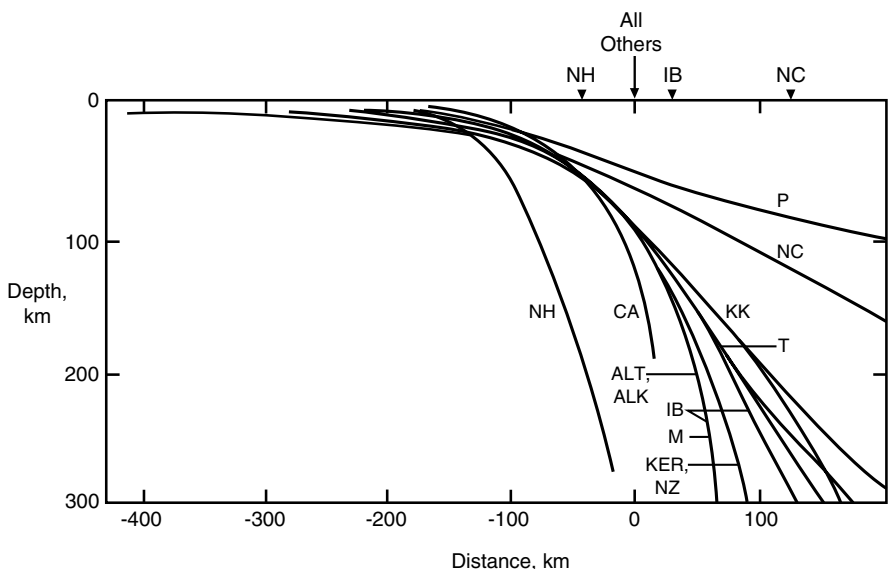


Figure 2.19. The shapes of the upper boundaries of descending lithospheric slabs at several oceanic trenches based on the distributions of earthquakes. The names of the trenches are abbreviated for clarity (NH = New Hebrides, CA = Central America, ALT = Aleutian, ALK = Alaska, M = Mariana, IB = Izu Bonin, KER = Kermadec, NZ = New Zealand, T = Tonga, KK = Kurile-Kamchatka, NC = North Chile, P = Peru). The locations of the volcanic lines are shown by solid triangles (Isacks and Barazangi, 1977); all except NH, IB, and NC lie at a common point (all others).

lines are also shown. Many subducted lithospheres have an angle of dip near 45° . In the New Hebrides the dip is significantly larger, and in Peru and North Chile the angle of dip is smaller.

Along localized segments of some subduction zones, earthquakes at depths of 70–150 km are concentrated on two parallel dipping planes vertically separated by 20–40 km

(Engdahl and Scholz, 1977; Hasegawa et al., 1978a, b; Kawakatsu, 1986; Abers, 1992, 1996; Gorbatov et al., 1994; Kao and Chen, 1994, 1995; Comte et al., 1999) (Figure 2.20). The upper plane of these double seismic zones seems to lie just below the top of the descending slab; the lower plane, therefore, must lie within the slab (Abers, 1996; Comte et al., 1999).

2.5.1 Rheology of Subduction

Question 2.2: What is the rheology of the lithosphere at a subduction zone?

The mechanical behavior of the lithosphere at subduction zones has received considerable attention. Two extreme modes of lithospheric deformation that might be associated with subduction are flexure and rupture. Flexure appears to be the best approximation. The oceanic lithosphere bends continuously and maintains its structural integrity as it passes through the subduction zone and creates the large geoid anomalies seen at the trenches in Figures 2.5 and 2.6. Studies of elastic bending at subduction zones are in good agreement with the morphology of some subduction zones seaward of the trench axis (Caldwell et al., 1976; Levitt and Sandwell, 1995). However, there are clearly significant deviations from a simple elastic rheology. Some trenches exhibit a sharp “hinge” near the trench axis; this has been attributed to an elastic–perfectly plastic rheology (McAdoo et al., 1978). Extensional shallow seismicity is generally observed on the forebulge seaward of ocean trenches. Thus the shallow bending lithosphere is undergoing brittle failure, but this failure does not propagate through the lithosphere and it appears to have little effect on the general flexural behavior.

The paired belts of deep seismicity in some subducting slabs (Figure 2.20) provide information on the rheology of these slabs. The upper seismic zone near the upper boundary of the descending lithosphere exhibits down-dip compressional focal mechanisms. The lower seismic zone near the center of the descending lithosphere exhibits down-dip extensional focal mechanisms. These double seismic zones are attributed to the “unbending,” i.e., straightening out, of the descending lithosphere (Samowitz and Forsyth, 1981; Kawakatsu, 1986). The double seismic zones are further evidence of the rigidity of the subducted lithosphere. They also indicate that forces on the subducted lithosphere are straightening it out so it usually descends at nearly 45°.

An alternative explanation of the bending of the lithosphere as it approaches a subduction zone is that the bending is a viscous effect (De Bremaecker, 1977; McKenzie, 1977a; Melosh and Raefsky, 1980). Viscous deformation can produce the same morphology of flexure as an elastic rheology so that studies of flexure at trenches cannot differentiate between the two approaches. However, viscous flexure relaxes at long times. The fact that lithospheric flexure is observed in sedimentary basins with ages greater than 10^8 yr (compared with 10^6 yr for subduction) is evidence that the concept of a viscous rheology for lithospheric flexure is inappropriate (Turcotte, 1979). Nevertheless, application of a viscous rheology to the lithosphere may be appropriate for investigating other aspects of the subduction process (Zhang et al., 1985; Vassiliou and Hager, 1988; Zhong and Gurnis, 1994a; Gurnis et al., 1996).

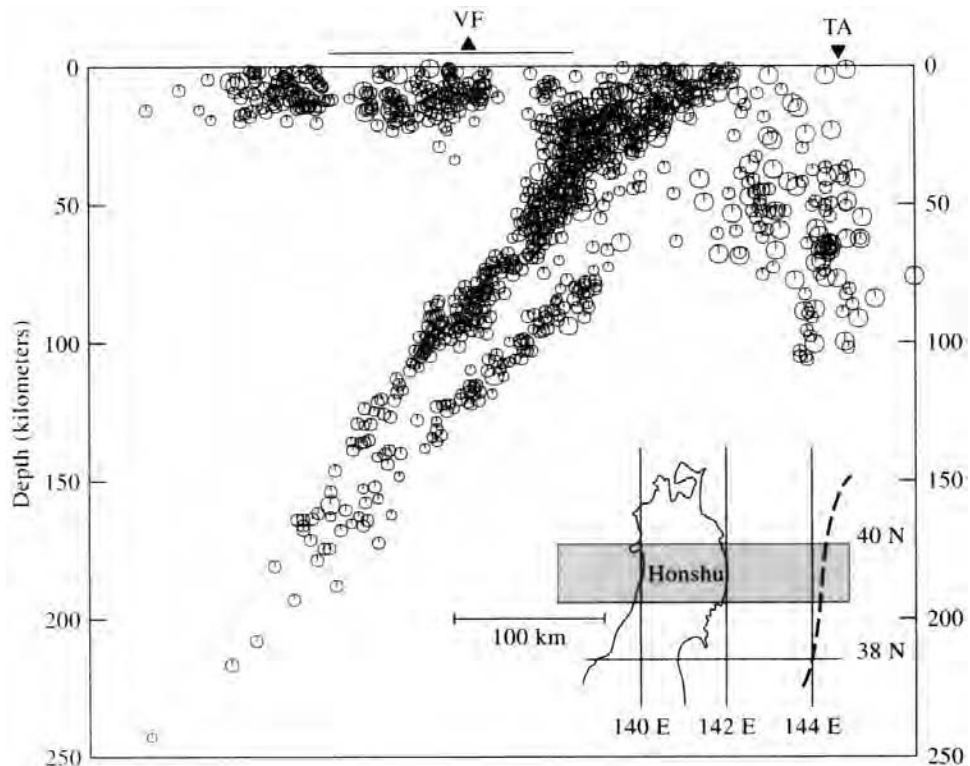


Figure 2.20. Double Benioff zone marking subduction at the Japan arc. Circles are foci of earthquakes recorded in 1975 and 1976. VF – volcanic front, TA – Japan Trench axis. After Hasegawa et al. (1978b). Redrawn from Bolt (1993).

2.5.2 Dip of Subduction Zones

Question 2.3: What determines the subduction dip angle?

Since the gravitational body force on the subducted lithosphere is downward, it would be expected that the subduction dip angle would tend toward 90° . In fact, as shown in Figure 2.19, the typical dip angle for a subduction zone is near 45° . One explanation is that the oceanic lithosphere is “foundering” and the trench is migrating oceanward. In this case the dip angle is determined by the flow kinematics (Hager and O’Connell, 1981). While this explanation is satisfactory in some cases, it has not been established that all slab dip angles can be explained by the kinematics of mantle flows.

An alternative explanation has been given by Stevenson and Turner (1977), Tovish et al. (1978), and Yokokura (1981). These authors argue that the subducted slab is supported by the induced flow above the slab. The descending lithosphere induces a corner flow in the mantle wedge above it and the pressure forces associated with this corner flow result in a dip angle near 45° .

2.5.3 Fate of Descending Slabs

Question 2.4: What is the fate of descending slabs?

One of the key questions in mantle convection is the fate of the descending slab. Earthquakes on the Wadati–Benioff zone terminate near a depth of about 660 km, but termination of seismicity does not imply cessation of slab descent. As will be discussed in the next chapter, 660 km is near the depth of a major seismic discontinuity associated with the solid–solid phase change from spinel to perovskite and magnesiowüstite; this phase change could act as a barrier to the descending lithosphere. In some cases seismic activity spreads out at this depth, and in some cases it does not. Studies of seismic focal mechanisms in the Wadati–Benioff zone give extensional stresses in the upper part of the zone and compressional stresses in the lower part of the zone (Isacks and Molnar, 1971).

Another major mantle phase transition at a depth of about 410 km is associated with the phase change from olivine to β spinel. Theoretical studies indicate that this shallower exothermic phase change will enhance convection (Turcotte and Schubert, 1971). However, similar studies of the effect on convection of the deeper endothermic phase change from spinel to perovskite and magnesiowüstite show that it could inhibit flow through 660 km depth, particularly if there is also a significant stabilizing compositional change at this depth (Schubert et al., 1975; Christensen and Yuen, 1984). The effects of major solid–solid phase transitions on convection in the mantle will be discussed in detail in Chapters 4, 9, and 10.

One of the principal goals of mantle seismic tomography has been to determine the fate of subducted slabs. Numerous seismic investigations of deep earthquakes and mantle structure around subduction zones have sought to resolve the maximum depth subducted lithosphere can be traced into the mantle. There is still much disagreement on this issue, perhaps because there is, in fact, no single depth where all slab penetration terminates. Indeed, surveys of all the pertinent seismic evidence (Lay, 1994a, b, c) come to the conclusion that some slabs penetrate through the transition zone into the lower mantle, while others do not.

An additional question about the fate of descending slabs is the maximum depth of penetration of slabs that enter the lower mantle.

Question 2.5: Do slabs that cross 660 km depth sink all the way to the core–mantle boundary or do they come to rest at some shallower depth?

Seismic tomographic evidence that at least some slabs descend all the way to the bottom of the mantle will be presented in Chapter 3.

2.5.4 Why Are Island Arcs Arcs?

Question 2.6: Why do subduction zones have arcuate structures?

One of the striking features of subduction zones is their arcuate structure in map view or planform. Subduction zones are made up of a sequence of arc structures with a clear

planform curvature; this is the origin of the term “island arc.” A good example is the Aleutian arc, shown in Figures 2.1 and 2.5. Just as accretionary margins are characterized by their orthogonal ridge–transform geometry, subduction zones are characterized by their arc configuration.

Frank (1968a) proposed a simple model for the curvature of island arcs based on a ping-pong ball analogy. If an indentation is made on a ping-pong ball, there is a simple analytical relation between the angle of dip and the radius of the indentation. Frank proposed that this relation also could be used to relate the dip angle of the subducted lithosphere to the planform radius of curvature of the island arc. The assumption was that the rigidity of the subducted lithosphere controlled the geometry of subduction in direct analogy to a ping-pong ball. Clearly this problem is related to the problem of the angle of dip considered in the previous section.

Several authors have tested Frank’s hypothesis (DeFazio, 1974; Tovich and Schubert, 1978) and have found that it is a fair approximation in some cases and a poor approximation in other cases. It is generally accepted that the arcuate structure of island arcs can be attributed to the rigidity of the descending plate (Laravie, 1975), but the detailed mechanism remains controversial. Yamaoka et al. (1986) and Yamaoka and Fukao (1987) attribute the island arc cusps to lithospheric buckling. It is clear from seismic observations that the cusps represent tears in the descending lithosphere.

Any completely successful numerical model for mantle convection must reproduce the observed arcuate structure of subduction zones.

2.5.5 Subduction Zone Volcanism

Question 2.7: What is the mechanism for subduction zone volcanism?

Volcanism is also associated with subduction (Tatsumi and Eggins, 1995). A line of regularly spaced volcanoes closely parallels the trend of almost all the ocean trenches. These volcanoes may result in an island arc or they may occur within continental crust (Figure 2.21). The volcanoes generally lie above where the descending plate is 125 km deep, as illustrated in Figure 2.17. It is far from obvious why volcanism is associated with subduction. The descending lithosphere is cold compared with the surrounding mantle, and thus it acts as a heat sink rather than as a heat source. The downward flow of the descending slab is expected to entrain flow in the overlying mantle wedge. However, this flow will be primarily downward; thus, magma cannot be produced by pressure-release melting. One possible source of heat is frictional dissipation on the fault plane between the descending lithosphere and the overlying mantle (McKenzie and Sclater, 1968; Oxburgh and Turcotte, 1968; Turcotte and Oxburgh, 1968). However, there are several problems with generating island arc magmas by frictional heating. When rocks are cold, frictional stresses can be high and significant heating can occur. However, when the rocks become hot, the stresses are small, and it may be difficult to produce significant melting simply by frictional heating (Yuen et al., 1978). On the other hand, Kanamori et al. (1998) have used the unusual properties of the 1994 Bolivian earthquake, including a slow rupture velocity, a high stress drop (about 100 MPa), and a low ratio of radiated seismic energy to total strain energy, to infer that melting may have occurred on the fault plane during this earthquake. They suggested a minimum frictional stress of about 55 MPa and calculated a minimum amount of nonradiated seismic

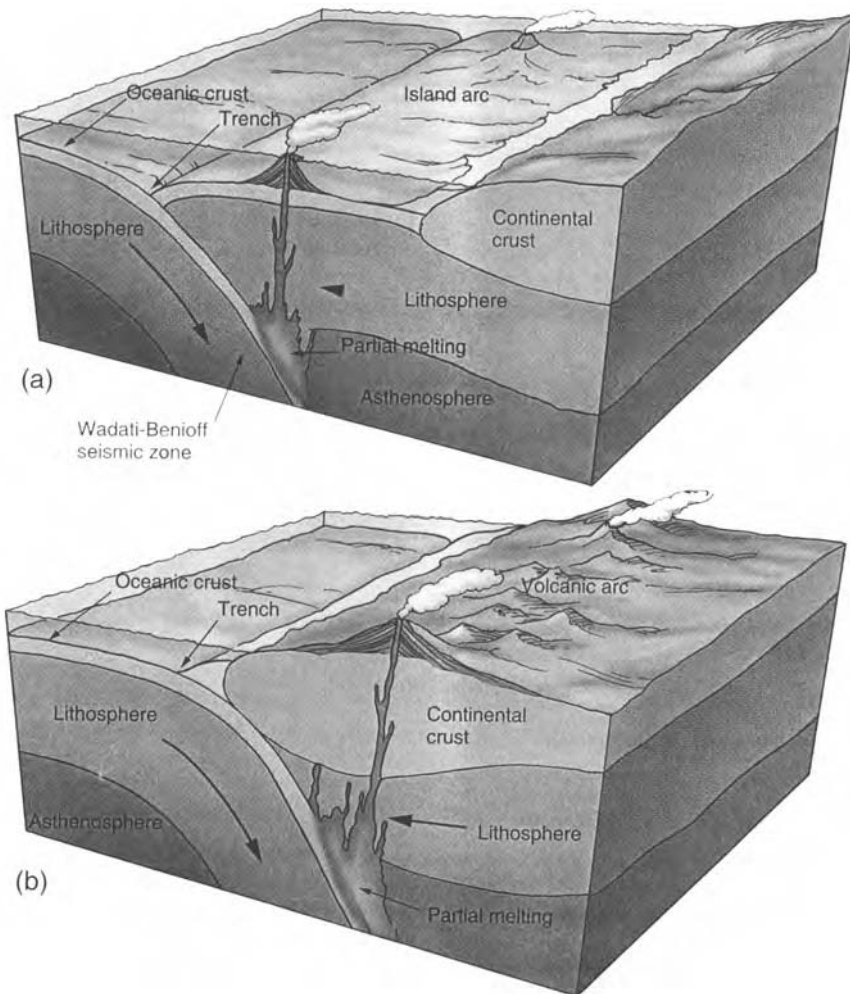


Figure 2.21. Schematic of (a) oceanic lithosphere subducting beneath oceanic lithosphere and the creation of a volcanic island arc, and (b) oceanic lithosphere subducting beneath continental lithosphere and creation of a volcanic chain on the continent. After Tarbuck and Lutgens (1988).

energy equal to about 10^{18} J, sufficient to have melted a layer on the fault plane about 300 mm thick.

One proposed explanation for arc volcanism involves interactions between the descending slab and the induced flow in the overlying mantle wedge, leading to heating of the descending oceanic crust and melting (Marsh, 1979). Many thermal models of the subduction zone have been produced (e.g., Oxburgh and Turcotte, 1970; Toksöz et al., 1971; Turcotte and Schubert, 1973; Hsui and Toksöz, 1979; Hsui et al., 1983; Peacock et al., 1994; Ponko and Peacock, 1995; Iwamori, 1997; Kincaid and Sacks, 1997). All these models show that there is great difficulty in producing enough heat to generate the observed volcanism, since the subducted cold lithospheric slab is a very strong heat sink and depresses the isotherms above the slab.

Water released when hydrated minerals in the subducted oceanic crust are heated can contribute to melting by depressing the solidus temperature of the crustal rocks and adjacent mantle wedge rocks (Anderson et al., 1976; Ringwood, 1977a; Bird, 1978a). However, the bulk of the volcanic rocks at island arcs have near-basaltic compositions and erupt at temperatures very similar to eruption temperatures at accretional margins. Studies of the petrology of island arc magmas (Hawkesworth et al., 1994) indicate that they are primarily the result of the partial melting of fertile mantle rocks in the mantle wedge above the descending slab.

Nevertheless, there is geochemical evidence that the subducted oceanic crust does play an important role in island arc volcanism. Beryllium isotopic studies of volcanic rocks in subduction settings have revealed ^{10}Be enrichments relative to mid-ocean ridge and ocean island basalts that are attributed to sediment subduction (Tera et al., 1986; Sigmarsson et al., 1990). One way to incorporate ^{10}Be from subducted sediments into island arc magmas is through dehydration of the sediments and transport of beryllium with the liberated water (Tatsumi and Isoyama, 1988). Thus, direct melting of the subducted oceanic crust and lithosphere is not required to explain the ^{10}Be excess in island arc volcanic rocks. Other evidence that the subducted oceanic crust is important in island arc magmatism is the location of the surface volcanic lines, which has a direct relationship to the geometry of subduction. In some cases two flaps of slab subduct at different angles, as in the Aleutians. For the shallower dipping slab, the volcanic line is further from the trench, keeping the depth to the slab beneath the volcanic line nearly constant (Kay et al., 1982).

The basic physical processes associated with subduction zone volcanism remain enigmatic, though it is apparent that the subducted oceanic crust triggers this volcanism. However, substantial melting of the subducted crust only occurs when young and relatively hot lithosphere is being subducted (Drummond and Defant, 1990; Kay et al., 1993). The bulk of the volcanism is directly associated with the melting of the mantle wedge similar to the melting beneath an accretional plate margin. A possible explanation for island arc volcanism has been given by Davies and Stevenson (1992). They suggest that “fluids” from the descending oceanic crust induce melting and create sufficient buoyancy in the partially melted mantle wedge rock to generate an ascending flow and further melting through pressure release. This process may be three dimensional with along-strike ascending diapirs associated with individual volcanic centers. Sisson and Bronto (1998) have analyzed the volatile content of primitive magmas from Galunggung volcano in the Indonesian arc and concluded that the magmas were derived from the pressure-release melting of hot mantle peridotite. There is no evidence that volatiles from the subducted oceanic crust were directly involved in the formation of these magmas. We conclude that many aspects of island arc volcanism remain unexplained.

2.5.6 Back-arc Basins

Question 2.8: Why do back-arc basins form?

In some subduction zones, a secondary accretionary plate margin lies behind the volcanic line (Karig, 1971). This back-arc spreading is similar to the seafloor spreading that is occurring at ocean ridges. The composition and the structure of the ocean crust that is being created are the same. Behind-arc spreading has created marginal basins such as the Sea of Japan.

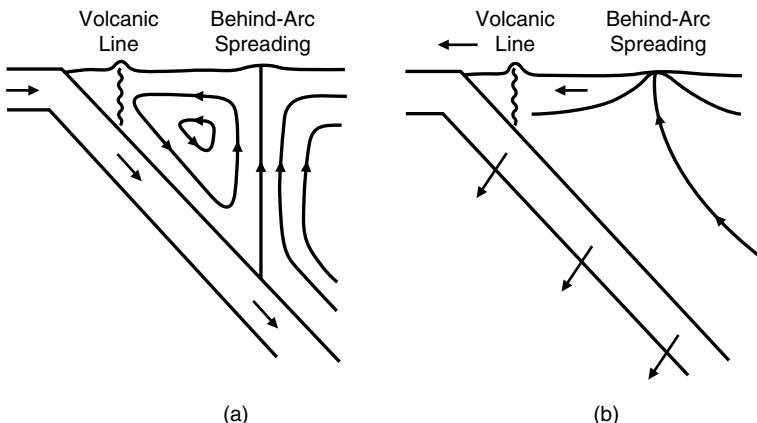


Figure 2.22. Models for the formation of marginal basins. The descending slab, volcanic line, and behind-arc spreading axis are shown. The mantle wedge is the region above the descending slab. (a) Secondary mantle convection induced by the descending lithosphere. (b) Ascending convection generated by the foundering of the sinking lithosphere and the seaward migration of the trench.

A number of explanations have been given for behind-arc spreading (Hynes and Mott, 1985). One hypothesis is that the descending lithosphere induces a secondary convection cell, as illustrated in Figure 2.22a (Toksoz and Hsui, 1978a; Hsui and Toksoz, 1981). An alternative hypothesis is trench rollback, where the ocean trench migrates away from an adjacent continent because of the transverse motion of the descending lithosphere. Behind-arc spreading occurs in response to the rollback, as illustrated in Figure 2.22b (Chase, 1978; Garfunkel et al., 1986).

A number of authors have proposed that there are basically two types of subduction zones (Wilson and Burke, 1972; Molnar and Atwater, 1978; Uyeda and Kanamori, 1979). If the adjacent continent is being driven up against the trench, as in Chile, marginal basins do not develop. If the adjacent continent is stationary relative to the trench, as in the Marianas, the foundering of the lithosphere leads to a series of marginal basins as the trench migrates seaward. Jarrard (1986) has provided a more extensive classification of subduction zones. There is evidence that behind-arc spreading centers are initiated at volcanic lines (Karig, 1971). The lithosphere at the volcanic line may be sufficiently weakened by heating that it fails under tensional stress.

2.6 Hot Spots and Mantle Plumes

Question 2.9: Are there plumes in the mantle beneath hot spots, and if so, from what depth(s) do they originate?

Not all volcanism is restricted to the plate margins. Figures 2.4a, 2.5, and 2.6 show large geoid highs over regions of intraplate volcanism, such as Hawaii and Iceland, known as hot spots. The locations of some major hot spots around the globe are given in Figure 2.23. Morgan (1971) attributed hot spot volcanism to mantle plumes. Mantle plumes are quasi-cylindrical concentrated upflows of hot mantle material and they represent a basic form of

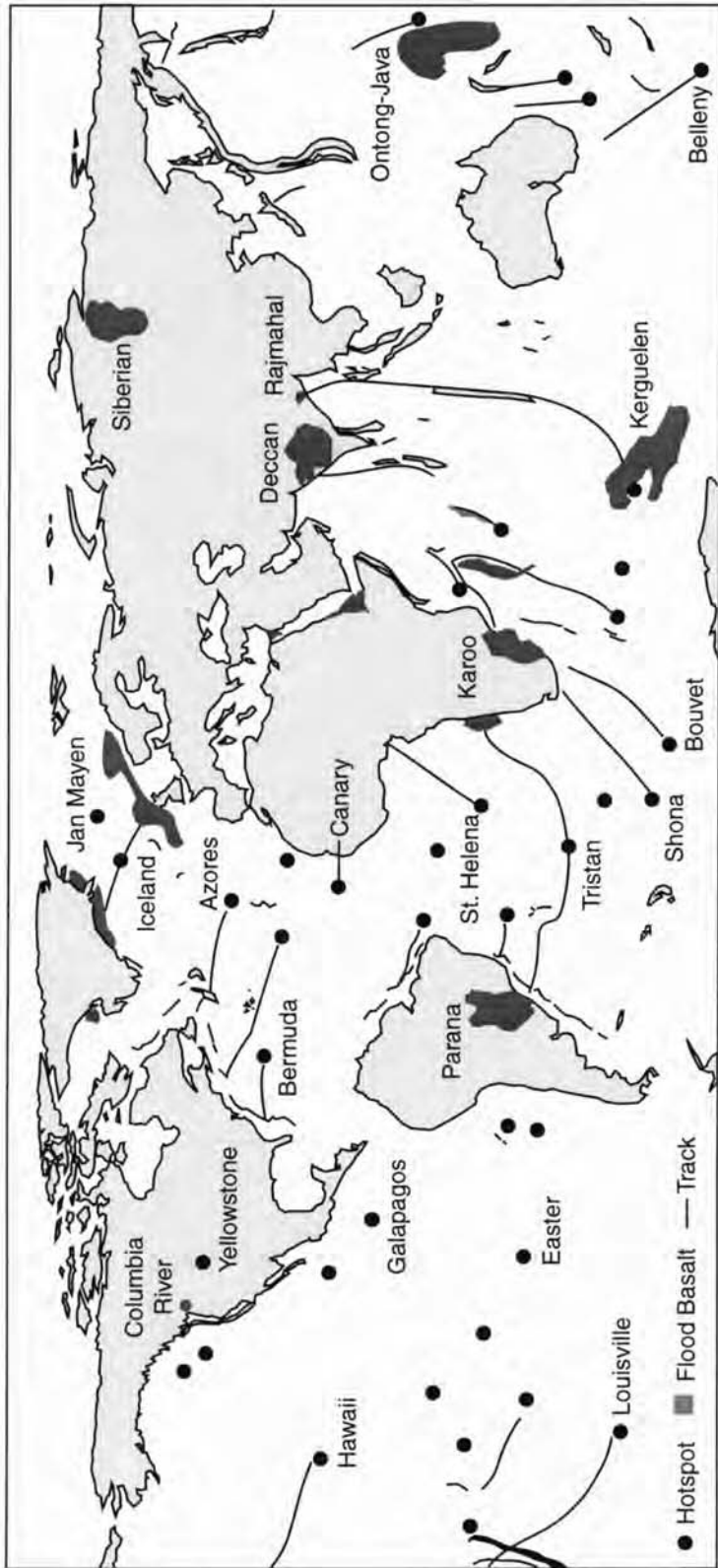


Figure 2.23. Map of major hot spots, hot spot tracks, and flood basalt provinces.

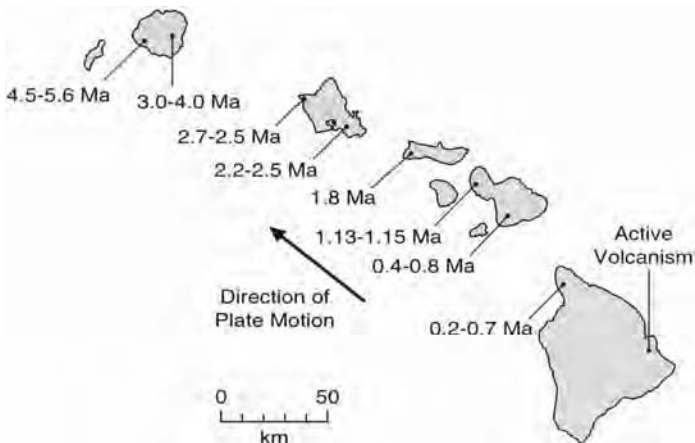
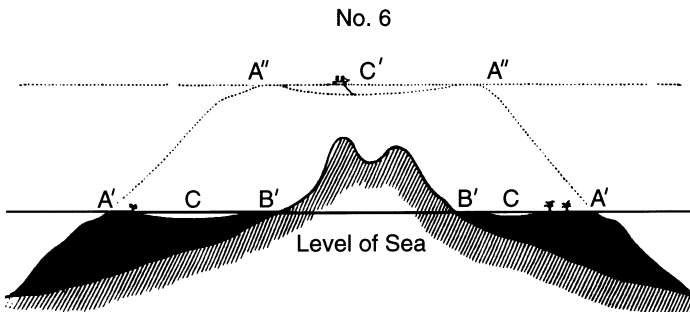


Figure 2.24. Ages in Ma of volcanic rocks on the Hawaiian Island chain. The volcanic rocks on the islands age systematically to the northwest, parallel to the direction of plate motion. The islands are also more eroded to the northwest.

upwelling in the convecting mantle (Bercovici et al., 1989a). Pressure-release melting in the hot ascending plume rock produces the basaltic volcanism that is forming the Hawaiian Island chain. The hypothesis of fixed mantle plumes beneath overriding plates explains the systematic age progression of the Hawaiian-Emperor island-seamount chain (Figure 2.24) and the deepening of the seafloor with increasing age along the chain. Although the ideas of plate tectonics and mantle plumes were unknown to him in the 1830s, Charles Darwin concluded from his geologic observations of ocean islands and their coral reefs (Figure 2.25) that coral reefs and atolls formed through the aging and subsidence of the islands. Darwin's insightful observations and coral reef theory are presented in *The Geology of the Voyage of H.M.S. Beagle, Part I: Structure and Distribution of Coral Reefs* (see Barrett and Freeman, 1987).

It is remarkable that more than 150 years ago, Darwin inferred the subsidence of the ocean floor with age along island chains. He wrote, "Finally, when the two great types of structure, namely barrier-reefs and atolls on the one hand, and fringing-reefs on the other, are laid down on a map, they offer a grand and harmonious picture of the movements which the crust of the earth has undergone within a late period. We there see vast areas rising, with volcanic matter every now and then bursting forth. We see other wide spaces sinking without any volcanic outbursts; and we may feel sure that the movement has been so slow as to have allowed the corals to grow up to the surface, and so widely extended as to have buried over the broad face of the ocean every one of those mountains, above which the atolls now stand like monuments, marking the place of their burial." In an introduction to *The Works of Charles Darwin* (Barrett and Freeman, 1987), J. W. Judd (in 1890) refers to the following excerpt from Darwin's correspondence: "It still seems to me a marvellous thing that there should not have been much, and long-continued, subsidence in the beds of the great oceans. I wish some doubly rich millionaire would take it into his head to have borings made in some of the Pacific and Indian atolls, and bring home cores for slicing from a depth of 500 or 600 feet." While marine geologists and geophysicists of our day may not be the millionaires of Darwin's musings, they have brought home the cores that Darwin hoped for and have confirmed his theory.



A'A': Outer edges of the barrier-reef at the level of the sea. The cocoa-nut trees represent coral-islets formed on the reef.

C C: The lagoon-channel.

B'B': The shores of the island, generally formed of low alluvial land and of coral detritus from the lagoon-channel.

A''A'': The outer edges of the reef, now forming an atoll.

C': The lagoon of the newly-formed atoll. According to the scale the depth of the lagoon and of the lagoon-channel is exaggerated.

Figure 2.25. A sketch from Darwin's coral reef theory illustrating the formation of a barrier reef through island subsidence.

Plates and plumes are both consequences of mantle convection, but plumes are not required in plate tectonic theory per se. Although mantle plumes are expected to exist on theoretical grounds, and plumes do occur in relevant laboratory and numerical experiments on convection, direct observational evidence that mantle plumes exist beneath hot spots remains elusive. Seismic tomography holds the best promise to discover mantle plumes through the seismic velocity anomaly that must be associated with the hot upwelling plume material. An example of the use of seismic tomography to image mantle plumes, which illustrates the promise as well as the practical difficulties involved, is shown in Figure 2.26 from a study of mantle structure beneath the Iceland hot spot by Wolfe et al. (1997). The most likely source of mantle plumes is the hot material in the thermal boundary layer at the base of the mantle. Alternatively, if the phase transition at 660 km depth is a boundary that physically separates the upper mantle from the lower mantle, then upper mantle plumes could also originate at this depth. Chapter 11 will be devoted to a detailed discussion of hot spots and mantle plumes.

2.7 Continents

2.7.1 Composition

As described in the previous sections, the development of plate tectonics involved primarily the ocean basins. Yet the vast majority of geological data concerns the continents. There is little evidence for plate tectonics in the continents, and this is certainly one reason why most geologists did not accept the arguments in favor of continental drift and mantle convection for so long.

Question 2.10: How were the continents formed?

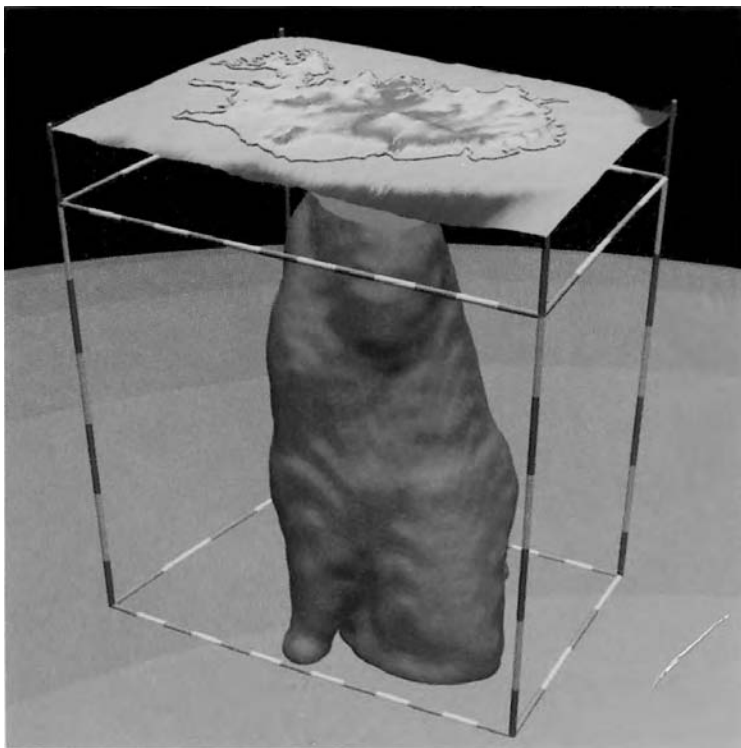


Figure 2.26. Seismically delineated plume structure beneath central Iceland (Wolfe et al., 1997).

For a color version of this figure, see plate section.

The surface rocks of the continental crust are much older than the rocks of the oceanic crust. They also have a much more silicic composition. The continents include not only the area above sea level but also the continental margins. It is difficult to provide an absolute definition of the division between oceanic and continental crust. In most cases it is appropriate to define the transition to occur at an ocean depth of 3 km. The area of the continents including the margins is about $1.9 \times 10^8 \text{ km}^2$, or 37% of the surface of the Earth. Schubert and Sandwell (1989) have provided estimates for the volume of the continents.

The rocks that make up the continental crust are, in bulk, more silicic and therefore less dense than the basaltic rocks of the oceanic crust. This difference makes the continental lithosphere gravitationally stable and prevents it from being subducted. Although continental crust is not destroyed by subduction, it can be recycled indirectly by the subduction of sediments or by delamination.

It is relatively easy to estimate the composition of the upper continental crust but it is difficult to estimate the composition of the crust as a whole. Direct evidence for the composition of the lower continental crust comes from surface exposures of high-grade metamorphic rocks and lower crustal xenoliths transported to the surface in diatremes and magma flows. Indirect evidence for the composition of the lower crust comes from comparisons between seismic velocities and laboratory studies of relevant minerals (Gao et al., 1998). Estimates of the bulk composition of the continental crust are given in Table 2.1. In Table 2.2 the average composition from Table 2.1 is compared with a typical basalt composition. Also included

Table 2.1. Estimates for the Composition of the Bulk Continental Crust

	1	2	3	4	5	6	7	8	9	10	Average
SiO ₂	61.9	63.9	57.8	61.9	62.5	63.8	63.2	57.3	63.2	59.1	61.5
TiO ₂	1.1	0.8	1.2	0.8	0.7	0.7	0.6	0.9	0.7	0.7	0.8
Al ₂ O ₃	16.7	15.4	15.2	15.6	15.6	16.0	16.1	15.9	14.8	15.8	15.7
FeO	6.9	6.1	7.6	6.2	5.5	5.3	4.9	9.1	5.6	6.6	6.4
MgO	3.5	3.1	5.6	3.1	3.2	2.8	2.8	5.3	3.15	4.4	3.7
CaO	3.4	4.2	7.5	5.7	6.0	4.7	4.7	7.4	4.66	6.4	5.5
Na ₂ O	2.2	3.4	3.0	3.1	3.4	4.0	4.2	3.1	3.29	3.2	3.3
K ₂ O	4.2	3.0	2.0	2.9	2.3	2.7	2.1	1.1	2.34	1.9	2.5

Note: 1. Goldschmidt (1933), 2. Vinogradov (1962), 3. Pakiser and Robinson (1966), 4. Ronov and Yaroshevsky (1969), 5. Holland and Lambert (1972), 6. Smithson (1978), 7. Weaver and Tarney (1984), 8. Taylor and McLennan (1985), 9. Shaw et al. (1986), 10. Rudnick and Fountain (1995).

Table 2.2. Average Composition of Basalts (Nockolds, 1954), the Mean Composition of the Continental Crust from Table 2.1, and the Mean Composition of Archean and Post-Archean Clastic Sediments (Taylor and McLennan, 1985, p. 99)

	Basalt	Average Continental Crust	Archean Clastic Sediments	Post-Archean Clastic Sediments
SiO ₂	50.8	61.5	65.9	70.4
TiO ₂	2.0	0.8	0.6	0.7
Al ₂ O ₃	14.1	15.7	14.9	14.3
FeO	9.0	6.4	6.4	5.3
MgO	6.3	3.7	3.6	2.3
CaO	10.4	5.5	3.3	2.0
Na ₂ O	2.2	3.3	2.9	1.8
K ₂ O	0.8	2.5	2.2	3.0

in Table 2.2 are the mean compositions of very old Archean ($\sim 2 +$ Gyr) and post-Archean clastic sediments. Estimates of the mean composition of the continental crust are clearly more basic (less silicic) than the composition of the upper continental crust, but they do not approach a basaltic composition. The fact that upper continental crust is more silicic than lower continental crust is consistent with the remelting hypothesis for the origin of granites. However, if the only mantle melt responsible for forming the continental crust is basalt, then the mean composition of the continental crust should be basaltic. This is clearly not the case. There is also some evidence that the continental crust has become more silicic with time (Ronov, 1972). This change is supported by the comparison between Archean and post-Archean sediments given in Table 2.2.

2.7.2 Delamination and Recycling of the Continents

Question 2.11: Does delamination play an important role in recycling continental crust and lithosphere?

There is no evidence that continental lithosphere is subducted. This is generally attributed to the buoyancy of the continental crust, which results in the continental lithosphere being gravitationally stable. However, the mantle portion of the continental lithosphere is sufficiently cold and dense to be gravitationally unstable. Thus it is possible for the lower part of the continental lithosphere, including the lower continental crust, to delaminate and sink into the lower mantle. This is partial subduction.

Continental delamination was proposed and studied by Bird (1978b, 1979) and Bird and Baumgardner (1981). These authors suggested that delamination is occurring beneath the Himalaya and Zagros collision zones and is also responsible for the elevation of the Colorado Plateau. Hildebrand and Bowring (1999) have argued in favor of delamination at collision zones. McKenzie and O’Nions (1983) have suggested that delamination occurs at island arcs. The zone of high seismic velocities found beneath the Transverse Ranges in California by Humphreys and Clayton (1990) can be interpreted to be the result of delamination. The structure of the Alps can also be associated with crustal and lithospheric delamination (Butler, 1986; Laubscher, 1988). Sacks and Secor (1990) have suggested delamination in continental collision zones. Delamination can be associated with certain types of magmatism (Kay and Kay, 1991, 1993).

There are a number of continental areas in which the mantle lithosphere is absent. One example is the western United States. Crustal doubling such as in Tibet has also been attributed to the absence of mantle lithosphere beneath Asia (Molnar and Tapponnier, 1981). Plateau uplifts such as the Altiplano in the Andes are associated with the absence of mantle lithosphere. In the Puna section of the Altiplano there is direct geochemical evidence supporting the delamination of the lower continental crust (Kay and Kay, 1993). Delamination is an efficient mechanism for the removal of continental lithosphere – for example, in the western United States. Alternative mechanisms for thinning the lithosphere include heat transfer from an impinging plume and heat transport by magmas. The former process may be very slow (Emerson and Turcotte, 1983) and the latter one requires very large volumes of magma (Lachenbruch and Sass, 1978). Moore et al. (1998b) have modeled the plume–lithosphere interaction at the Hawaiian Swell and have shown how three-dimensional drip instabilities of the lower lithosphere can lead to rapid (10 Myr time scale) lithospheric thinning by a mantle plume.

A major unknown is whether delamination includes the lower continental crust. It is well documented that a soft intracrustal zone exists in orogenic zones (Hadley and Kanamori, 1977; Mueller, 1977; Eaton, 1980; Yeats, 1981; Turcotte et al., 1984). The presence of a soft layer at an intermediate depth in the crust can be attributed to the presence of quartz (Kirby and McCormick, 1979). Delamination at this intracrustal weak zone can explain intracrustal decollements in the Alps (Oxburgh, 1972) and in the southern Appalachians (Cook et al., 1979).

Direct estimates for the rate of recycling of continental crust on the Earth have been given by several authors based on various lines of reasoning. Armstrong (1981) gave a rate of $2 \pm 1 \text{ km}^3 \text{ yr}^{-1}$, DePaolo (1983) gave $2.5 \pm 1.2 \text{ km}^3 \text{ yr}^{-1}$, Reymer and Schubert (1984) gave $0.59 \text{ km}^3 \text{ yr}^{-1}$, and Turcotte (1989a) gave $1.49 \text{ km}^3 \text{ yr}^{-1}$. These rates are about 10% of the rate of production of oceanic crust on the Earth, which is $17 \pm 2 \text{ km}^3 \text{ yr}^{-1}$ (Turcotte and Schubert, 1982, p. 166). The only mechanism that can recycle these relatively large volumes of continental crust is crustal delamination (Turcotte, 1989a, b).

Bird (1979) hypothesized that delamination occurred in a manner like subduction as a consequence of lithospheric flexure beneath a decollement similar to the flexure of the oceanic lithosphere seaward of an ocean trench. However, this type of delamination would result in

large surface gravity signatures that are not observed. Another model for delamination has been given by Houseman et al. (1981), Houseman and England (1986), and England and Houseman (1986). These authors treat the continental lithosphere as a viscous fluid which thickens in a collision zone. The thick cold lithosphere is gravitationally unstable and sinks or delaminates. Pari and Peltier (1996) proposed that continuous mantle downwelling occurs beneath the continents.

Turcotte (1983) proposed the alternative mechanism of lithospheric stoping illustrated in Figure 2.27. Soft mantle rock penetrates the continental crust in a zone of volcanism; possible sites would be the volcanic lines associated with subduction zones adjacent to continents and continental rifts; this penetration occurs at mid-crustal levels where the rocks have the softest rheology (Figure 2.27a). Eventually the continental lithosphere fails along a pre-existing zone of weakness (e.g., a fault) (Figure 2.27b). The decoupled block of continental lithosphere (including the lower crust) sinks into the mantle and is replaced by hot asthenosphere mantle rock. This lithospheric stoping process continues away from the initial zone of volcanism.

There are other mechanisms by which continental crust can be recycled into the mantle (McLennan, 1988). Several are associated with subduction zones. Sediments from the continental crust coat the oceanic crust that is being subducted. Some of these sediments are scraped off in the oceanic trench and form the accretionary prism as illustrated in Figure 2.17, but some sediments are entrained in the subducted oceanic crust (Karig and Kay, 1981). There is also some evidence that the subducted lithosphere can erode and entrain some of the overlying continental crust; however, the estimated volume is small. Also some of the subducted entrained material is returned to the crust in the island arc volcanism. Schubert and Sandwell (1989) have suggested that slivers of continental crust broken off from the

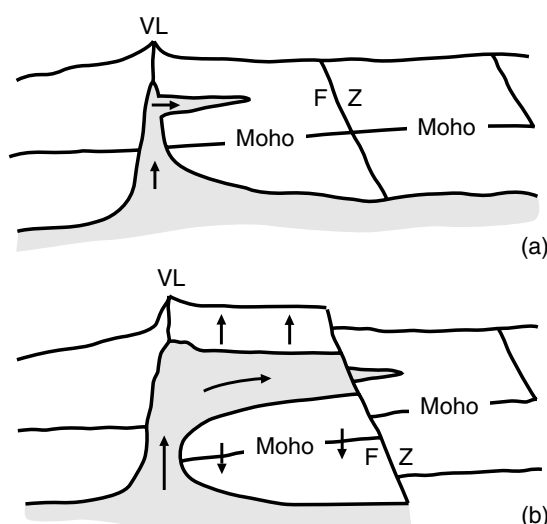


Figure 2.27. Delamination of the continental crust by a lithospheric stoping process. (a) The asthenosphere penetrates into the continental crust along a volcanic line (VL) associated with a subduction zone. It then splits the crust behind the volcanic line along an intracrustal (horizontal) zone of weakness. (b) The lower continental crust and mantle lithosphere beneath the penetrating asthenosphere break away along a pre-existing fault (FZ) and delaminate.

continents and trapped in the seafloor could, if sufficiently small, be subducted with the oceanic lithosphere.

2.7.3 *Continental Crustal Formation*

Question 2.12: How is continental crust formed?

Can currently observed processes, i.e., subduction-related volcanism and continental rift or hot spot volcanism, lead to the formation of continental crust, or was the continental crust primarily formed by processes in the Archean that are no longer active? A related question is whether the formation of the continental crust is continuous or episodic. A primary constraint on models for the generation of the continental crust is its silicic composition. As discussed above, the crust has a mean composition that is more silicic than magmas produced in the mantle today. One hypothesis for the formation of the continental crust is that silicic magmas were generated in the mantle in the Archean and that these magmas are responsible for the silicic composition of the continental crust. Brown (1977) suggested that the direct addition of silicic magmas was primarily responsible for the formation of the silicic continental crust.

An alternative hypothesis for the generation of the continental crust has been given by Kay and Kay (1988). The hypothesis consists of three parts: (1) Basaltic volcanism from the mantle associated with island arc volcanics, continental rifts, and hot spots is responsible for the formation of the continental crust. (2) Intracrustal melting and high-temperature metamorphism is responsible for the differentiation of the crust so that the upper crust becomes more silicic and the lower crust becomes more basic. In a paper entitled “No water, no granites – no oceans, no continents,” Campbell and Taylor (1983) argue that basaltic magmas from the mantle intruded into a basaltic continental crust in the presence of water can produce the granitic rocks associated with the continental crust. (3) Delamination of substantial quantities of continental lithosphere including the mantle and lower crust returns a substantial fraction of the more basic lower crust to the mantle. The residuum, composed primarily of the upper crust, thus becomes more silicic.

In this model, the basic cycle responsible for the evolution of the continental crust is as follows. The oceanic crust is created at mid-ocean ridges. Selected elements from the continental crust are added to the oceanic crust by solution and deposition. For example, sediments derived from the continents coat the oceanic crust. Some fraction of the sediments and the altered oceanic crust are subducted at ocean trenches. The remainder of the sediments is returned to the continental crust in accretionary prisms. The subducted oceanic crust and entrained sediments are partially melted beneath island arc volcanoes inducing partial melting in the overlying mantle wedge. The result is a near-basaltic composition with trace element and isotopic compositions contaminated with the signature of the altered oceanic crust and entrained continental sediments.

Island arcs can contribute to the formation of continental crust, in two ways. (1) If an island arc stands on oceanic crust, it generates thick crust. If this island arc subsequently collides with a continent, it can add material in the form of exotic terranes. (2) If a subduction zone is adjacent to a continent, then the subduction zone can add mantle-derived magmas directly to the crust (Figure 2.21). This is happening today in the Andes. The importance of island arc processes in forming continental crust has been discussed in detail by Taylor and White (1965), Taylor (1967, 1977), Jakeš and White (1971), Jakeš and Taylor (1974),

and Taylor and McLennan (1985). Flood and rift volcanics and hot spots have added a considerable volume of mantle-derived magmas to the continental crust. McKenzie (1984a) argues that the continental crust is being continuously underplated by extensive intrusive magmas.

It is widely accepted that the silicic rocks associated with continents are produced when basaltic magma intrusions partially melt basaltic or other more silicic continental crustal rocks in the presence of water (Huppert and Sparks, 1988; Luais and Hawkesworth, 1994). In order to produce a continental crust that has a mean composition that is more silicic than basalt, it is necessary to remove the residual basic rock. This is done by the delamination of the lower continental crust.

2.8 Plate Motions

The surface plates are rigid to a first approximation and are in relative motion with respect to each other. The relative motion between two adjacent rigid plates can be described by Euler's theorem. The theorem states that any line on the surface of a sphere can be translated to any other position and orientation on the sphere by a single rotation about a suitably chosen axis passing through the center of the sphere. In terms of the Earth this means that a rigid surface plate can be shifted to a new position by a rotation about a uniquely defined axis. The point where this axis intercepts the surface of the Earth is known as the pole of rotation. This is illustrated in Figure 2.28, where plate B is rotating counterclockwise with respect to plate A at the angular velocity ω about the pole of rotation P. Ridge segments lie on lines of longitude emanating from the pole of rotation. Transform faults lie on small circles with their centers at the pole of rotation.

The relative motion between two adjacent plates is completely specified when the latitude and longitude of the pole of rotation together with the angular velocity of rotation are given. These quantities for the NUVEL-1 model of DeMets et al. (1990) are given in Table 2.3. The plate geometry upon which this model is based consists of the 12 rigid plates illustrated in Figure 2.29. The plate rotation vectors are also shown. The best-fitting plate rotation vectors in this model were obtained using 1,122 data points from 22 plate boundaries. The

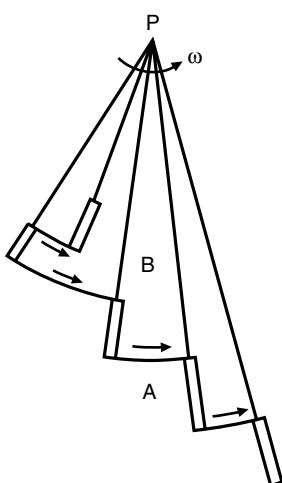


Figure 2.28. Illustration of Euler's theorem. Plate B is moving counterclockwise relative to plate A. The motion is defined by the angular velocity ω about the pole of rotation P. Double lines are ridge segments, and arrows denote direction of motion on transform faults.

data include 277 spreading rate determinations based on magnetic anomalies. An example of the magnetic profiles for the spreading boundary between the Cocos and Pacific plates is given in Figure 2.30. The NUVEL-1 model also uses 232 transform fault azimuths and 724 earthquake slip vectors. The authors found, however, that earthquake slip vectors at ocean trenches systematically misfit whenever convergence is oblique.

Revisions to the geomagnetic time scale have necessitated some recalibration of the NUVEL-1 global plate motion model. The changes consist largely in a reduction of the angular velocities. The revised plate motion model is referred to as NUVEL-1A (DeMets et al., 1994). Angular velocities for model NUVEL-1A are given in Table 2.3.

Table 2.3. Euler Vectors for Pairs of Plates Sharing a Boundary Based on the NUVEL-1 Model of DeMets et al. (1990) and the NUVEL-1A Model of DeMets et al. (1994); the First Plate Moves Counterclockwise Relative to the Second Plate

Plate Pair	Latitude (°N)	Longitude (°E)	ω , NUVEL-1 (deg Myr ⁻¹)	ω , NUVEL-1A
EU-NA	62.4	135.8	0.22	0.21
AF-NA	78.8	38.3	0.25	0.24
AF-EU	21.0	-20.6	0.13	0.12
NA-SA	16.3	-58.1	0.15	0.15
AF-SA	62.5	-39.4	0.32	0.31
AN-SA	86.4	-40.7	0.27	0.26
NA-CA	-74.3	-26.1	0.11	0.10
CA-SA	50.0	-65.3	0.19	0.18
NA-PA	48.7	-78.2	0.78	0.75
CO-PA	36.8	-108.6	2.09	2.00
CO-NA	27.9	-120.7	1.42	1.36
CO-NZ	4.8	-124.3	0.95	0.91
NZ-PA	55.6	-90.1	1.42	1.36
NZ-AN	40.5	-95.9	0.54	0.52
NZ-SA	56.0	-94.0	0.76	0.72
AN-PA	64.3	-84.0	0.91	0.87
PA-AU	-60.1	-178.3	1.12	1.07
EU-PA	61.1	-85.8	0.90	0.86
CO-CA	24.1	-119.4	1.37	1.31
NZ-CA	56.2	-104.6	0.58	0.55
AU-AN	13.2	38.2	0.68	0.65
AF-AN	5.6	-39.2	0.13	0.13
AU-AF	12.4	49.8	0.66	0.63
AU-IN	-5.6	77.1	0.31	0.30
IN-AF	23.6	28.5	0.43	0.41
AR-AF	24.1	24.0	0.42	0.40
IN-EU	24.4	17.7	0.53	0.51
AR-EU	24.6	13.7	0.52	0.50
AU-EU	15.1	40.5	0.72	0.69
IN-AR	3.0	91.5	0.03	0.03

Abbreviations: PA, Pacific; NA, North America; SA, South America; AF, Africa; CO, Cocos; NZ, Nazca; EU, Eurasia; AN, Antarctica; AR, Arabia; IN, India; AU, Australia; CA, Caribbean. See Figures 2.1 and 2.29 for plate geometries.

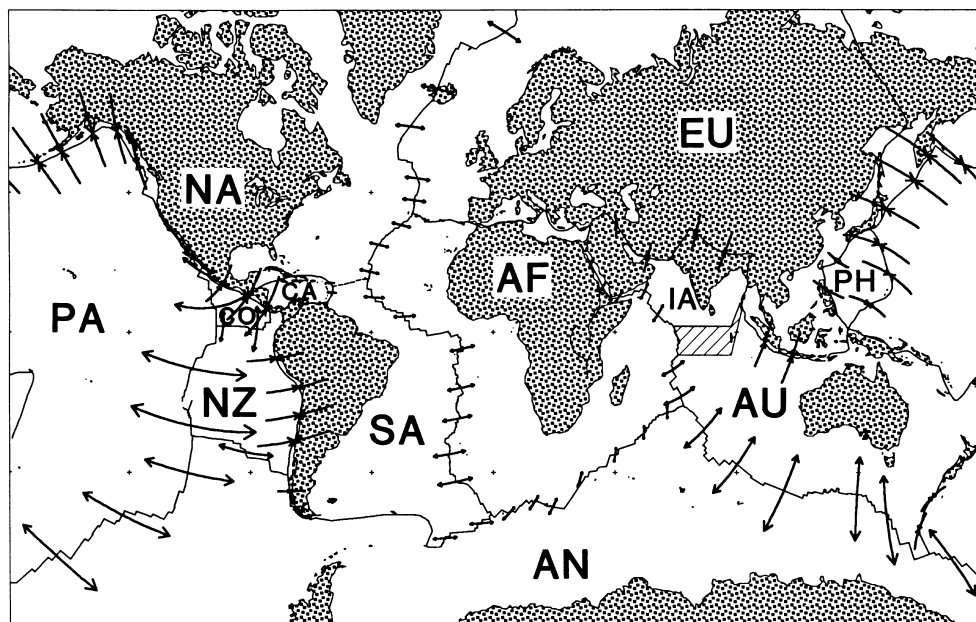


Figure 2.29. The 12 rigid plates used in the NUVEL-1 model of DeMets et al. (1990) are shown. The plate rotation vectors are also shown.

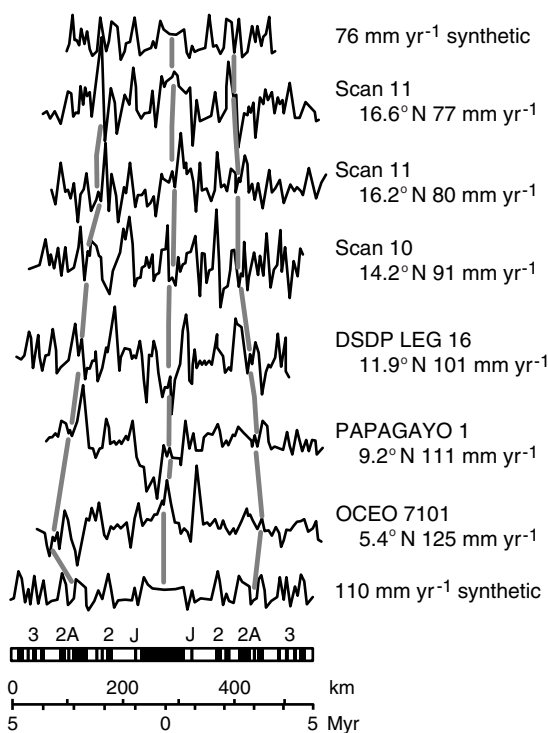


Figure 2.30. Cocos–Pacific magnetism profiles from the National Geodetic Data Center (NGDC) archives. Six profiles are shown with (half) spreading rates from 77 mm yr^{-1} to 125 mm yr^{-1} . Synthetic profiles for spreading rates of 76 mm yr^{-1} and 110 mm yr^{-1} are shown. Also shown are the sequence of reversals and the time scale for a spreading rate of 110 mm yr^{-1} .

The reduced angular velocities agree better with plate speeds deduced from space geodetic measurements.

The magnitude of the relative velocity u_{rel} between plates at any boundary is

$$u_{\text{rel}} = \omega a \sin \Delta \quad (2.8.1)$$

where a is the radius of the Earth and Δ is the angle subtended at the center of the Earth by the pole of rotation P and the point A on the plate boundary (Figure 2.31a). The angle Δ is related to the colatitude Θ and east longitude Ψ of the rotation pole and the colatitude Θ' and east longitude Ψ' of the point on the plate boundary A by

$$\cos \Delta = \cos \Theta \cos \Theta' + \sin \Theta \sin \Theta' \cos(\Psi - \Psi') \quad (2.8.2)$$

The geometry is illustrated in Figure 2.31b, where s is the surface arc between points A and P , and O is the center of the Earth. With (2.8.1) and (2.8.2) one can find the magnitude of the relative velocity between two plates at any point on the boundary between the two plates, once the latitude and longitude of the point on the boundary have been specified. As a specific example let us determine the magnitude of the relative velocity across the San Andreas fault at San Francisco (37.8°N , 122°W). We assume that the entire relative velocity between the rigid Pacific and North American plates is accommodated on this fault. From the NUVEL-1 model (Table 2.3), we find $\Theta = 41.3^{\circ}$ and $\Psi = -78.2^{\circ}$. Since $\Theta' = 52.2^{\circ}$

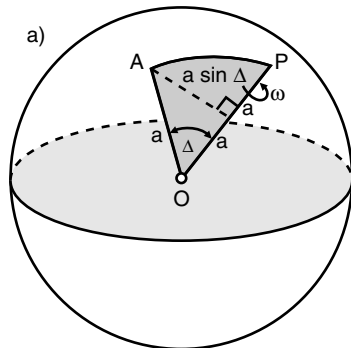
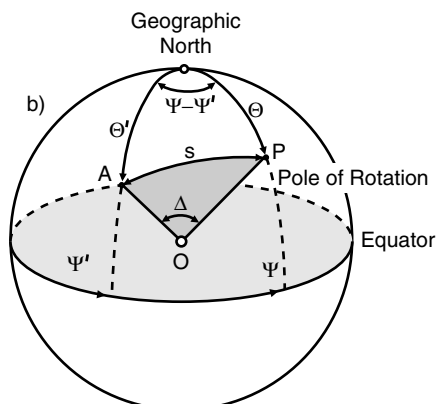


Figure 2.31. (a) Geometry for the determination of the magnitude of the relative plate velocity u_{rel} at a point A on the boundary between two plates in terms of the rate of rotation ω about a pole P . (b) Geometry for determining the angle between a point A on a plate and a pole of rotation.



and $\Psi' = 238^\circ$, we find from (2.8.2) that $\Delta = 33.7^\circ$; with $\omega = 0.78^\circ \text{ Myr}^{-1}$ we find from (2.8.1) that the magnitude of the relative velocity across the fault is 48 mm yr^{-1} .

Global plate motions show that new oceanic crust is being created at accretional margins at the rate of $2.8 \text{ km}^2 \text{ yr}^{-1}$ (Parsons, 1981); due to the conservation of plate area, the rate of subduction of oceanic crust is very close to $2.8 \text{ km}^2 \text{ yr}^{-1}$. Slight differences can be associated with changes in the area of the continents due to continental collisions or continental rifting.

The discussion given above implies that the plates are rigid. This is a reasonable approximation at any instant in time, but as the plates evolve in time, deformation must take place in the interiors of the plates (Dewey, 1975; Gordon, 1998). A configuration of rigid plates with boundaries made up of accretionary margins, subduction zones, and transform faults cannot evolve in time without overlaps and holes. The required interior deformations are generally accommodated by relatively broad plate boundaries. The western United States is an example. Interior plate deformations occur primarily in the “softer” continents.

2.9 The Driving Force for Plate Tectonics

The motions of the surface plates were described in the last section. We now show that these motions provide some information on the forces that drive plate tectonics. The basic question we address is:

Question 2.13: *What are the forces that drive plate tectonics?*

There are three primary candidates for the forces that drive plate tectonics. These are:

- (i) *Slab pull.* The cold subducted lithosphere at ocean trenches is denser than the hotter mantle adjacent to it. This negative buoyancy results in a downward body force. As we have discussed above, the descending lithosphere is attached to the adjacent surface plate. The resulting body force on the surface plate is known as slab pull (Figure 2.12).
- (ii) *Ridge push.* The mid-ocean ridges are elevated above the adjacent ocean basins. This results in a body force pushing the adjacent ridge segments apart. This force is also known as gravitational sliding (Figure 2.12).
- (iii) *Basal tractions.* If the mantle flow beneath a surface plate is faster than the motion of the plate, the mantle will drag the plate along; the result is a basal traction that will drive the motion of the plate.

Forsyth and Uyeda (1975) summarized the statistics of present-day plate motions and their results are given in Table 2.4. This table gives the perimeter of each plate, the length of plate boundary occupied by ridges and trenches, plate area, and the speed of each plate. By virtue of its size and speed, the Pacific plate alone contains more than two-thirds of the entire kinetic energy of the lithosphere relative to the hot spot reference frame. Together, the Pacific and Indian plates contain more than 90% of the lithospheric kinetic energy, and the three fast-moving large plates, Pacific, India and Nazca, contain in excess of 95% of the kinetic energy of the plates, while occupying only slightly more than half of the Earth’s surface area.

Why is the kinetic energy so unevenly partitioned among the plates? A partial explanation is found in Figure 2.32, which shows total plate area, plate area occupied by continents, and

Table 2.4. Summary of Major Plate Dimensions

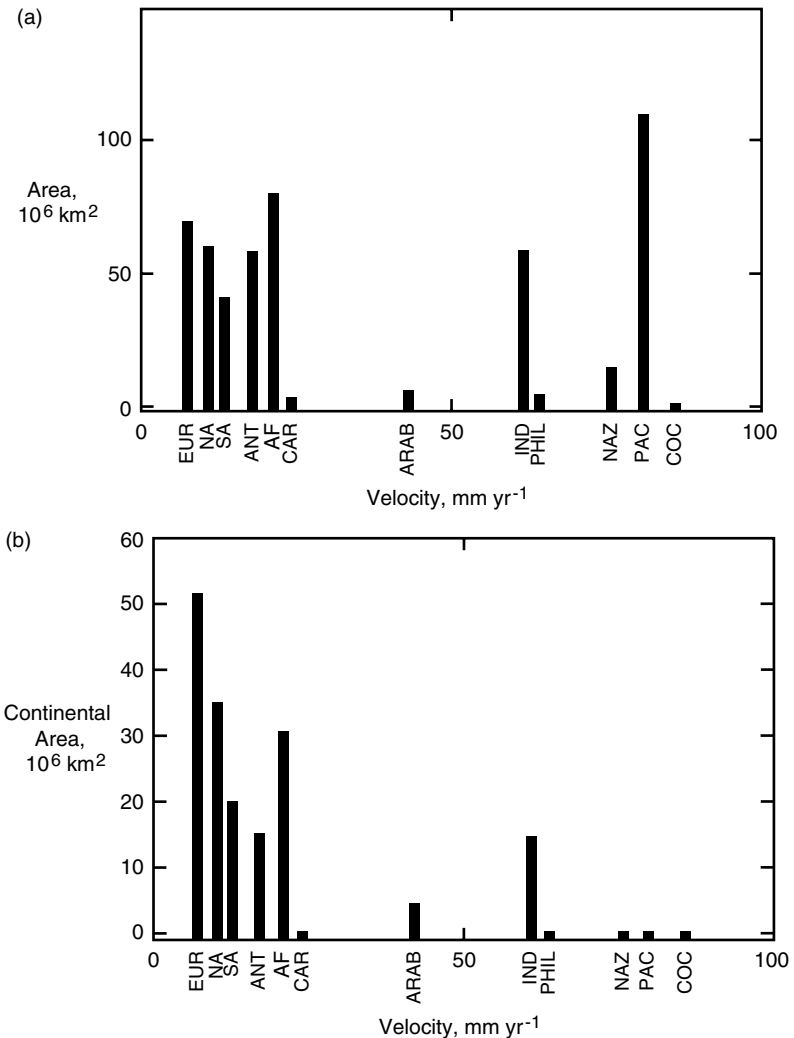
Plate	Area (10^6 km^2)	Continental Area (10^6 km^2)	Average Absolute Velocity (mm yr^{-1})	Circumference (10^2 km)	Length	
					Ridge (10^2 km)	Trench (10^2 km)
NA	60	36	11	388	146	12
SA	41	20	13	305	87	5
PA	108	—	80	499	152	124
AN	59	15	17	356	208	—
IN	60	15	61	420	124	91
AF	79	31	21	418	230	10
EU	69	51	7	421	90	—
NZ	15	—	76	187	76	53
CO	2.9	—	86	88	40	25
CA	3.8	—	24	88	—	—
PH	5.4	—	64	103	—	41
AR	4.9	4.4	42	98	30	—

Note: For plate abbreviations, see Table 2.3. PH, Philippine plate.

fraction of plate circumference occupied by ridges and trenches versus plate velocity for each plate (Forsyth and Uyeda, 1975). According to Figures 2.32b and d, plate velocity is sensitive to the fraction of the plate occupied by continental crust and to the length of subducting slabs attached to the plate. In general, continents occupy slow-moving plates, while fast-moving plates are connected to descending slabs. As seen in Figure 2.32d, the length of subducting boundaries clearly divides the major plates into two groups: the “energy-containing” plates attached to subducting slabs and the “energy-deficient” plates that lack major subducting slabs.

These associations imply that trench pull is the main driving force for plate motions, and that continents tend to slow plates down, probably through increased basal drag. In contrast, Figure 2.32c indicates that ridges do not control plate speeds. This leads to the conclusion that the ridge push force is small compared to the trench pull force. Further conclusions can be drawn from the fact that the small Nazca and Cocos plates are subducted at about the same rates as the large Pacific plate. This is evidence that the basal traction forces on the plates are negligible since all three plates are totally oceanic. The similar velocity of subduction of these oceanic plates is taken as evidence that the downward buoyancy force on the descending lithosphere is nearly balanced by the viscous resistance to its downward motion (Figure 2.12). This near-balance acts as a “velocity governor” on the rate of subduction and the slab pull represents the small excess force between the downward gravitational body force and the viscous resisting force. These conclusions regarding the forces that drive the plates have been generally confirmed by the study of Jurdy and Stefanick (1991), who showed that the stress distributions in the plates inferred from earthquake focal mechanisms and other sources are generally consistent with this picture.

As pointed out above, the plates containing continents move more slowly than the purely oceanic plates. An important question is whether this is due to the lack of subduction zones on the “continental” plates or due to basal tractions associated with the continents. As we will discuss in Chapters 3 and 4, the thickness of the continental lithosphere remains a subject of controversy. If the continental lithosphere has a thickness of $\sim 400 \text{ km}$ rather than $\sim 200 \text{ km}$, basal tractions would be expected to be important. Stoddard and Abbott (1996)



have addressed this problem and have concluded that basal continental tractions are not important.

Most studies of the forces that drive the plates have tested various assumptions against either plate velocities or inferred stress directions (e.g., Richardson et al., 1979). Bird (1998) has used a global model of laterally heterogeneous plates of nonlinear rheology separated by faults with low friction to test hypotheses on plate driving mechanisms against both plate velocities and stresses. He concludes that a model in which plates move over a resisting mantle at velocities dictated by their attached subducting slabs does not predict correct stress directions. He also finds that a model in which driving forces result only from elevation differences between rises and trenches and are balanced by basal drag and fault friction fails to predict correct plate velocities. A better match of model predictions to plate velocity and stress measurements occurs for a model in which the mantle supplies a forward basal

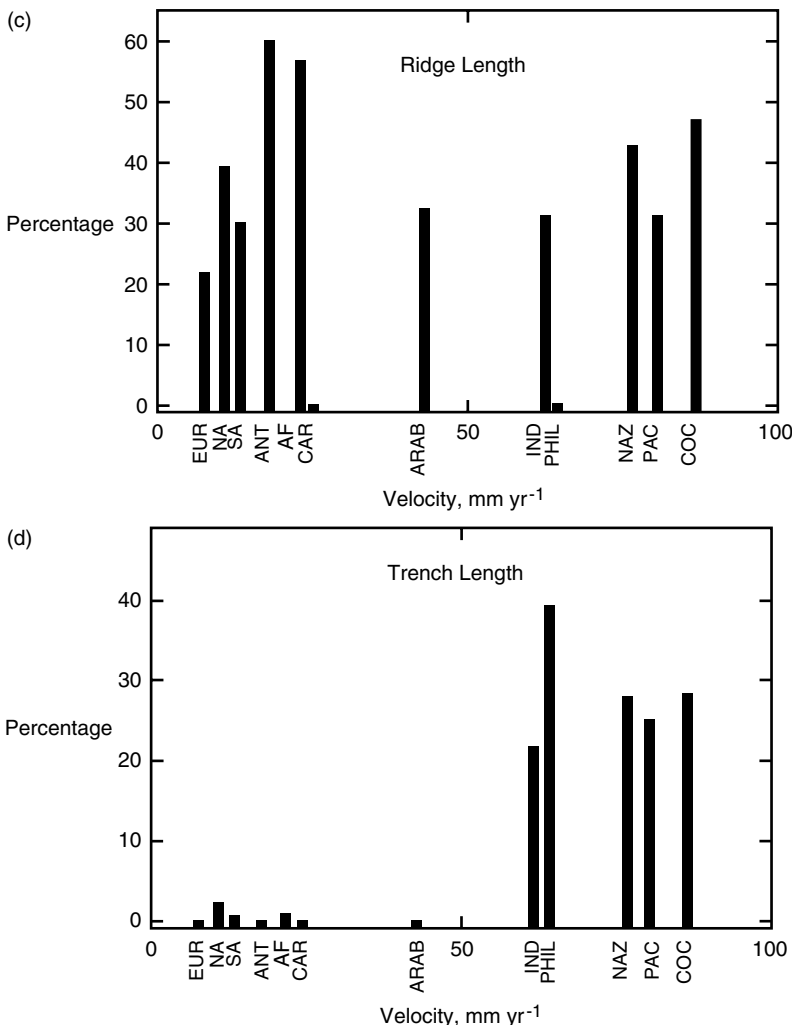


Figure 2.32. Plate tectonic statistics: (a) plate velocity versus area; (b) plate velocity versus continental area; (c) plate velocity versus percentage of perimeter that is ridge; (d) plate velocity versus percentage of perimeter that is trench.

traction to plates with continents, while oceanic plates experience negligible basal shear tractions. Bird's (1998) plate model is coupled to the underlying mantle in an artificial way, i.e., through imposed lower boundary conditions. A complete understanding of the forces that drive the plates will likely require a coupled and self-consistent model of both plates and mantle convection, i.e., a multi-rheological mantle convection model in which plates arise naturally as part of the model.

The rigidity of the surface plates also has a profound effect on the convective flows at depth. As will be shown, the thermal convection of an isoviscous fluid contains only the poloidal surface flows associated with sources of fluid at ascending sites of convection and sinks of fluid at descending regions of convection. With rigid surface plates the surface motion also has a toroidal component consisting of horizontal shearing and rotations about local vertical axes. Analysis of present plate motions by Hager and O'Connell (1978) showed

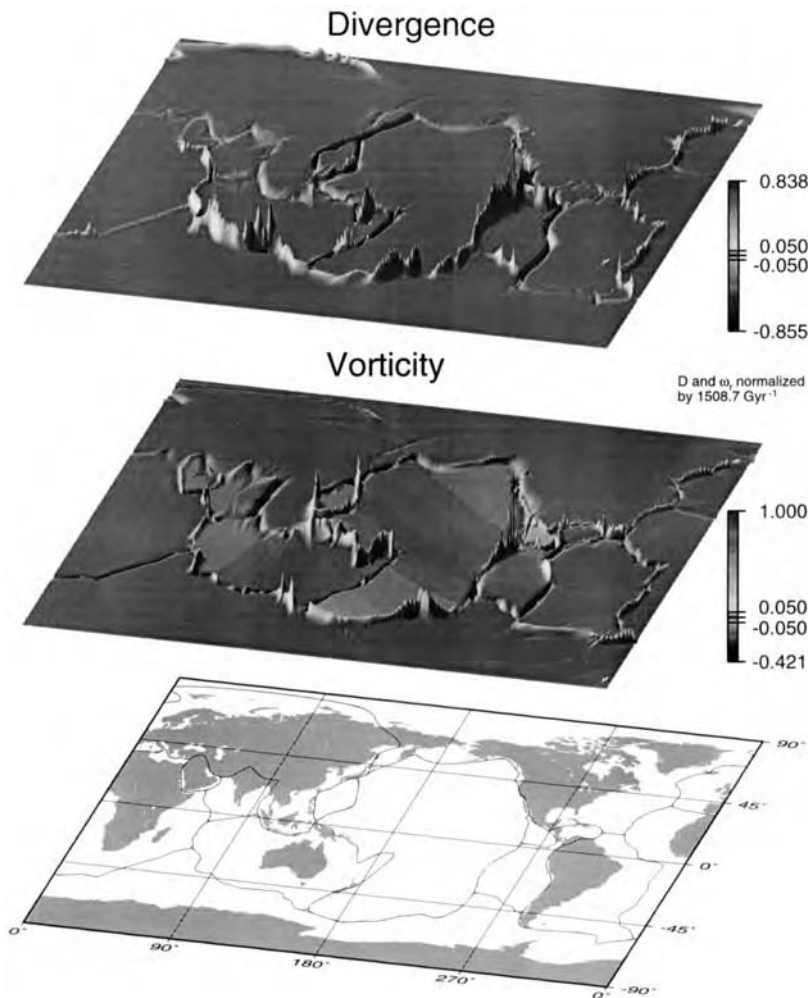


Figure 2.33. The pattern of horizontal divergence and the radial component of vorticity in present plate motions, calculated by Dumoulin et al. (1998).

that the kinetic energy of the toroidal part (strike-slip motion and oblique convergence) of present plate motions is nearly as large as the energy in the poloidal part (normal spreading and convergence).

Question 2.14: How is toroidal motion generated in mantle convection?

The origin of the toroidal kinetic energy and the manner in which mantle convection adapts to the presence of this component of kinetic energy are major unsolved problems. Figure 2.33 shows the fields of plate divergence (convergence) and radial vorticity calculated from present plate motions by Dumoulin et al. (1998). Positive and negative divergences are concentrated at ridges and trenches, respectively, as expected. The radial vorticity, a

measure of shearing motions and the toroidal energy density, is also concentrated along plate margins, rather than being broadly distributed in plate interiors. This demonstrates that the toroidal motion is associated with plate boundary deformations – shear at transform faults and at oblique subduction zones – rather than spin of plates as a whole. This type of toroidal motion requires strongly nonlinear rheology at plate boundaries, where the energy is drawn from the poloidal motion, shown in the pattern of surface divergence. The question has been the subject of many papers (Gable et al., 1991; O’Connell et al., 1991; Olson and Bercovici, 1991; Ribe, 1992; Lithgow-Bertelloni et al., 1993; Bercovici, 1995a; Weinstein, 1998).

2.10 The Wilson Cycle and the Time Dependence of Plate Tectonics

Wilson (1966) proposed that continental drift is cyclic. In particular he proposed that oceans open and close; this is now known as the Wilson cycle and was based on the opening and closing of the Atlantic Ocean. The Wilson cycle, in its simplest form, is illustrated in Figure 2.34.

Question 2.15: How are accretional plate margins formed?

The first step in the Wilson cycle, illustrated in Figure 2.34, is the breakup of a continent. This occurs on continental rift zones. Present examples are the East African Rift system and the Rio Grande graben. These may or may not break apart to form future oceans. Aulacogens (triple junctions with three rifts connected at about 120°) are believed to play a key role in the initiation of rifting and the breakup of continents (Burke, 1977). Aulacogens are associated with lithospheric swells (Burke and Dewey, 1973). An example of a lithospheric swell on a continent is the Ethiopian swell on the East African Rift. An example of a triple junction is at the southern end of the Red Sea; the three arms are the Red Sea, the Gulf of Aden, and the East African Rift. When a continent opens, two of the rifts separate and become part of an ocean. The third rift aborts and is known as a “failed” arm. Examples of failed arms associated with the opening of the Atlantic Ocean are the St. Lawrence River Valley Rift and the Niger Rift in Africa.

Continental rifts are tensional failures of the continental lithosphere. Both active and passive mechanisms for continental rifting have been proposed (Turcotte and Emerman, 1983). The passive mechanism hypothesizes that the continental lithosphere fails under tensional stresses transmitted through the elastic lithosphere by plate margin forces such as trench pull. In this mechanism volcanism and uplift associated with rifting are secondary processes. The active mechanism hypothesizes that a mantle plume impinges on the base of the continental lithosphere causing volcanism and uplift. In this mechanism the tensional failure of the lithosphere is a secondary process.

The second step in the Wilson cycle is the opening of the ocean illustrated in Figure 2.34. The rift valley splits apart and oceanic crust is formed at an accretional plate boundary. The Red Sea is an example of the initial stages of the opening of an ocean, while the Atlantic Ocean is an example of a mature stage. The margins of an opening ocean are known as passive continental margins in contrast to active continental margins, where subduction is occurring.

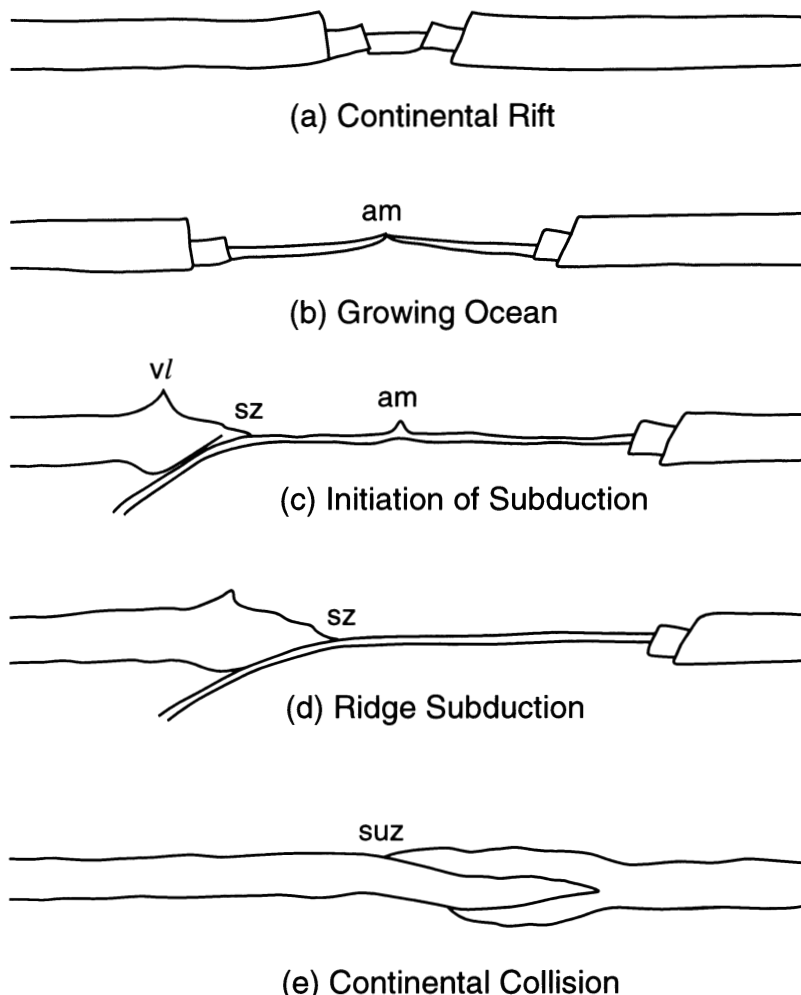


Figure 2.34. Illustration of the Wilson cycle. (a) Initiation of new ocean at a continental rift zone. (b) Opening of the ocean. am – accretional margin. (c) Initiation of subduction. sz – subduction zone, vl – volcanic line. (d) Ridge subduction. (e) Continental collision. suz – suture zone.

Question 2.16: How are subduction zones formed?

The third step in the Wilson cycle is the initiation of subduction (Figure 2.34). A passive continental margin is a favored site for the initiation of subduction because it is already a zone of weakness established during rifting. The differential subsidence between aging seafloor and the continental lithosphere provides a source of stress. A further source of stress is the gravitational loading by continental sediments deposited at the passive margin (Cloetingh et al., 1984, 1989; Erickson, 1993; Erickson and Arkani-Hamed, 1993).

Several mechanisms have been proposed for the actual initiation of subduction. McKenzie (1977b) proposed failure of the lithosphere under compressional stress. Thrust faulting at a

continental margin leads to the downthrusting of the oceanic lithosphere beneath the continental margin and the initiation of subduction. Turcotte et al. (1977), Kemp and Stevenson (1996), and Schubert and Zhang (1997) have proposed failure of the lithosphere under tension and the foundering of the oceanic lithosphere to generate a subduction zone. Faccenna et al. (1999) have discussed the initiation of subduction at a passive margin. Mueller and Phillips (1991) suggested that in some cases the creation of a new subduction zone could be triggered by the subduction of an aseismic ridge with thick and buoyant oceanic crust at an existing trench causing the cessation of further subduction there. Casey and Dewey (1984) have proposed a complex mechanism for the initiation of subduction involving accretional ridge segments and transform faults when the spreading direction shifts (see also Toth and Gurnis, 1998).

The fourth step in the Wilson cycle, illustrated in Figure 2.34, is ridge subduction. If the velocity of subduction is greater than the velocity of seafloor spreading, the ocean will close and eventually the accretional plate margin will be subducted. A number of authors have considered the thermal consequences of ridge subduction and have examined the geological record for effects on subduction zone volcanism and morphology (DeLong et al., 1978, 1979; Hsui, 1981). Ridge subduction played an important role in the recent geological evolution of the western United States and in the development of the San Andreas fault system (Atwater, 1970).

The fifth and final stage in the Wilson cycle, illustrated in Figure 2.34, is the continental collision that occurs when the ocean closes. This terminates the Wilson cycle. Continental collision is one of the primary mechanisms for the creation of mountains in the continents; the other is subduction (Dewey and Bird, 1970). The Himalayas and the Alps are examples of mountain belts caused by continental collisions, and the Andes is a mountain belt associated with subduction. The boundary between the two plates within the collision zone is known as a suture zone (Burke et al., 1977; Dewey, 1977).

The Himalayas are the result of the continental collision between the Indian subcontinent and Asia. This collision occurred about 45 Ma ago and has been continuing since. The initial collision resulted in a major global reorganization of plate motions that is best documented by the bend in the Hawaiian-Emperor seamount chain seen in Figures 2.6 and 2.7.

Many models have been proposed for the deformation that has resulted in the elevation of the Himalayas and the Tibetan Plateau. A viscous “snowplow” model has been suggested (England and Houseman, 1986). Another is the “flake tectonic” model (Oxburgh, 1972) in which the upper Asian continental crust overrides the Indian continental crust, the lower Asian crust and mantle having been previously delaminated. An additional model has been proposed by Molnar and Tapponnier (1975, 1978) in which India acts as an “indentor” that has driven Asian crust eastward into southeast Asia. Lenardic and Kaula (1995a) argue against the fluid “snowplow” model and in favor of a delayed removal of thickened lithosphere. In fact, the actual deformation associated with continental collision may be some complex combination of all these models.

There is evidence that plate tectonic processes are cyclic and correlate with the Wilson cycle. The evidence, which includes variations in sea level, in the strontium isotope ratios of seawater, and in continental volcanism associated with subduction of continental crust, has been summarized by Worsley et al. (1984), Nicolaysen (1985), Veevers (1989), and Unrug (1992). The summary cartoon given by Veevers (1989), partially reproduced in Figure 2.35, shows cyclic variability in the Paleozoic to recent geological record. Rates of crustal subduction and arc magma production increased during times of continental dispersal and decreased during times of continental aggregation; this is indicated by the correlation of low stand of

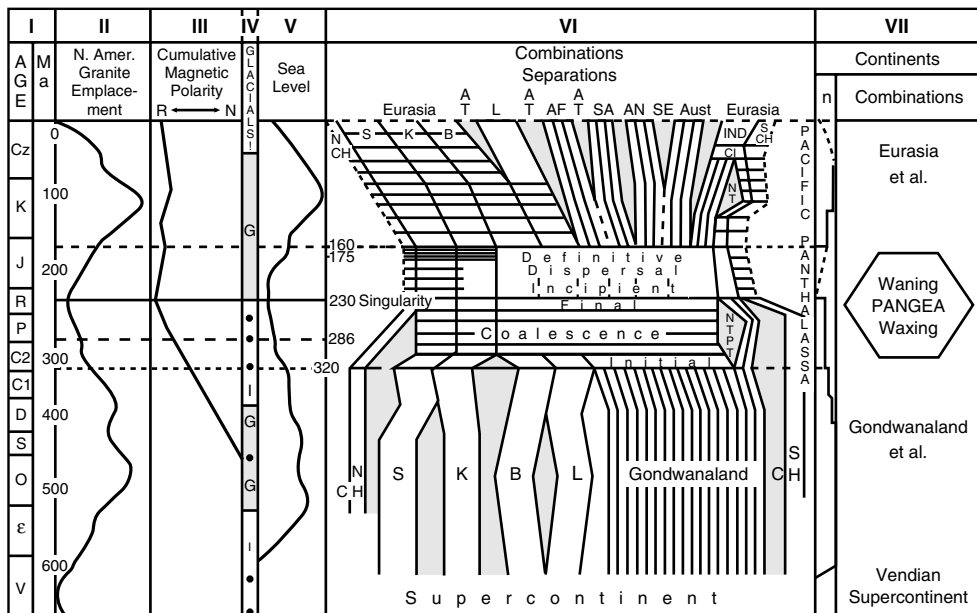


Figure 2.35. Illustration of the plate tectonic cycle (after Veevers, 1989). I. Age before present and geological epochs. II. Rates of emplacement of granitic rocks in North America. III. Cumulative polarity of the Earth's magnetic field; N normal and R reversed. IV. Periods of glaciations. V. Sea level variations. High stands of sea level correspond to high rates of seafloor spreading, which in turn correspond to high rates of subduction and production of granitic rocks. VI. Illustration of coalescence and dispersal of continental blocks. VII. Number of continents n .

sea level and implied low ridge volume. A minimum in continental granitoid production rates in North America (South America is similar) during the time of Pangea has also been noted (Figure 2.35).

The period 500–440 Ma (Ordovician) featured the breakup of the Vendian supercontinent. This was a time of high sea level, extensive island arc volcanism, and large compressional and tensional stresses in the continental crust. The period 380–340 Ma (late Devonian to lower Carboniferous) was a time of continental coalescence and collisions between large continental blocks. Sea level and oceanic spreading rates were decreasing and arc deformation was associated with major collisions during this period. The interval 340–260 Ma (upper Carboniferous to Permian) represented the peak of continental coalescence. There were collisions of large continental blocks and the sweeping up of small blocks. Much of the growing supercontinent was surrounded by subduction zones. Sea level was dropping and there were extensive regions of high continental relief associated with continental collisions. During the period 260–225 Myr before present (late Permian to Triassic) the Pangea supercontinent was at its maximum size. Rates of seafloor spreading and subduction reached their lowest levels, sea level was low, and the oceanic crust was relatively old. During this period clear evidence for subduction is missing along much of the Pangean margin.

The breakup of Pangea began in the early Triassic and continued into the Jurassic and Cretaceous. As emphasized by Veevers (1989), this period was marked by important flood basalts. Larson and Olson (1991) have shown that ocean plateau production occurred during the Cretaceous. As spreading in the ocean basins reinitiated, important subduction zones

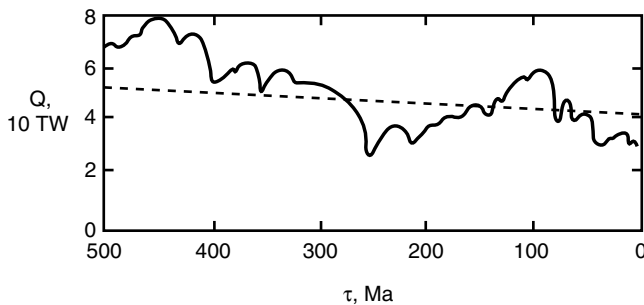


Figure 2.36. Global heat flow Q as a function of time before the present for the last 500 Myr. Solid curve – heat loss inferred from sea level variations. Dashed line – heat loss based on the decay of radioactive elements and secular cooling.

reappeared in oceanic arcs and along continental margins. Continental flood basalts, whose origin could lie in the partial melting of plume heads upwelling near the surface (Richards et al., 1989), were associated with continental breakup (Burke and Dewey, 1973). The positions of many plumes correlate with the position of Pangea at the time of its breakup (Anderson, 1982; Ashwal and Burke, 1989). Magmatism of both oceanic and continental arc type occurred frequently. A number of small terranes can be recognized in the geologic record and deformation associated with very active plates was common. The high stand of sea level during the Cretaceous is well documented and can be associated with excess ridge volume and a large plate tectonic flux, i.e., the area rate of plate formation was high (Hays and Pitman, 1973). This period not only coincides with a peak in ocean plateau formation, it is also coincident with the Cretaceous magnetic polarity superchron, suggesting an association with the core as well (Larson and Olson, 1991).

Fluctuations in sea level over geologic time have been used to deduce variations in the Earth's global heat flow Q (Hallam, 1977, 1992; Turcotte and Burke, 1978), as shown by the solid curve in Figure 2.36. The dashed line is the heat flow expected from the decay of radioactive elements and the secular cooling of the Earth. The plate tectonic cycle, as expressed in sea level variations, is associated with about a 30% fluctuation in global heat flow. Since the subduction of cold oceanic lithosphere is responsible for some 80% or more of the heat loss from the interior of the Earth, variations in the plate flux may influence (or be influenced by) mantle temperature and dynamics as follows (Figure 2.37):

- (i) When continents are dispersed, the plate flux is high so that sea level is high, seawater $^{87}\text{Sr}/^{86}\text{Sr}$ is low, and Andean-type volcanism is extensive. The high plate flux cools the mantle and may impede the formation of mantle plumes by emplacing relatively cold material on the core–mantle boundary, the likely site of plume formation. The net result is a reduction in the mantle plume flux.
- (ii) The breakup of continents can be attributed to a high plume flux. With a reduction in this flux the rate of continental breakup decreases. Due to simple kinematics the dispersed continents coalesce to form a supercontinent. A consequence of the resulting continental collisions and the reduction in the number of oceans is a reduction in the plate flux.
- (iii) With a single supercontinent and a low plate flux, the mantle heats up due to the decay of radioactive isotopes. The increase in mantle temperature and the warming near the

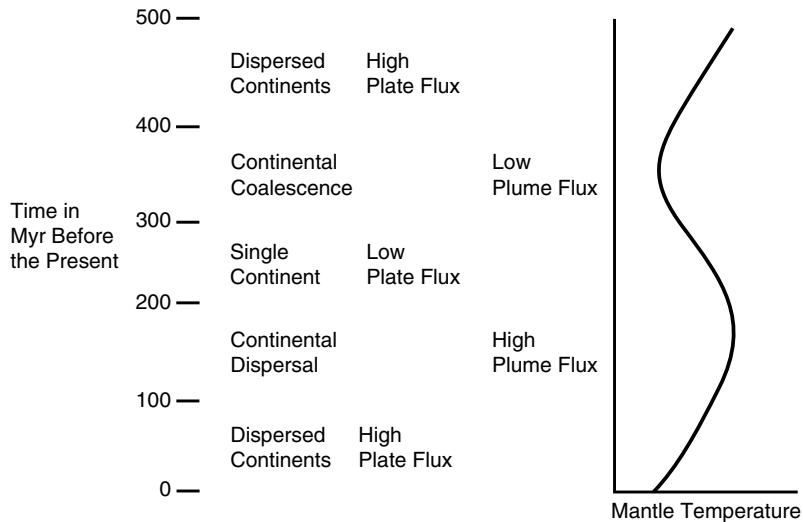


Figure 2.37. A scenario for the cyclic behavior of plate tectonics over the last 500 Myr.

core–mantle boundary leads to an increase in the plume flux and the breakup of the supercontinent (Yale and Carpenter, 1998).

- (iv) The cycle repeats.

Question 2.17: *Is the temporal variability of plate tectonics stochastic or is it driven by episodicity in mantle convection?*

Several plausible explanations for temporal variability in plate tectonics have been advanced, including the one just described. A second explanation is that it is completely stochastic and is associated with continental collisions and randomly generated plumes (Duncan and Turcotte, 1994). A third explanation is that mantle convection exhibits a quasi-periodicity or episodicity perhaps associated with mantle overturns that generate surface orogenic events (Stein and Hofmann, 1994; Condie, 1998). All of these proposed causes remain highly speculative, and there are very few critical observations with which to test them. But at least we can say that temporal variability in plate tectonics is fully expected on theoretical grounds, since the convection in the mantle that drives plate tectonics is unquestionably time-dependent. The nature of time dependence in mantle convection, its underlying causes, and its consequences for the thermal and tectonic history of the Earth are discussed in Chapters 10 and 13.

3

Structure and Composition of the Mantle

3.1 Introduction

In this chapter we review what is currently known about the structure and the bulk composition of the mantle, with emphasis on how these may influence the style of convection, and how they may be influenced by it. Brief descriptions of the crust and the core are also included, again with an emphasis on those aspects of each region most germane to mantle convection. There are several monographs dealing with Earth structure and composition in a general context, e.g., Ringwood (1975, 1979) and Anderson (1989).

The study of mantle structure is by tradition the province of seismology, while mantle composition has historically been a subject for high-pressure and high-temperature mineralogy, petrology, and geochemistry. A great many important advances have recently been made in these areas, with the result that the studies of mantle composition, structure, and dynamics are now closely related. New findings from seismology, mineral physics, and isotope geochemistry are quickly applied as constraints on models of mantle dynamics. There are also interactions in the other direction. Each new step in understanding the physics of convection is quickly incorporated into new interpretations of mantle structure. This interdisciplinary style of research is perhaps the single most important reason for the emerging view of the deep Earth as a unified physical and chemical system.

3.2 Spherically Averaged Earth Structure

The determination of elastic parameters and density throughout the Earth using observations of seismic waves and other constraints is the prototype inverse problem in geophysics. Like many inverse problems, it is formally nonunique and suffers from practical difficulties such as incomplete sampling and errors in the data. In spite of this, it is remarkable how much is now known about mantle structure, and this is particularly true of spherically averaged properties.

The major divisions of the Earth's interior are shown in Figure 3.1. The crust, mantle, and core were recognized in the early part of this century following Mohorovicic's 1909 discovery of the crust–mantle boundary (Moho) and Gutenberg's (1913) determination of the outer core radius. Lehmann (1936) inferred the existence of the inner core in 1936 and by 1939 Jeffreys (1939) had produced compressional and shear wave velocity profiles featuring a transition zone between about 400 km and 1,000 km depth. Thus, a nearly complete picture of the first-order spherical structure of the Earth was obtained prior to 1940. This period

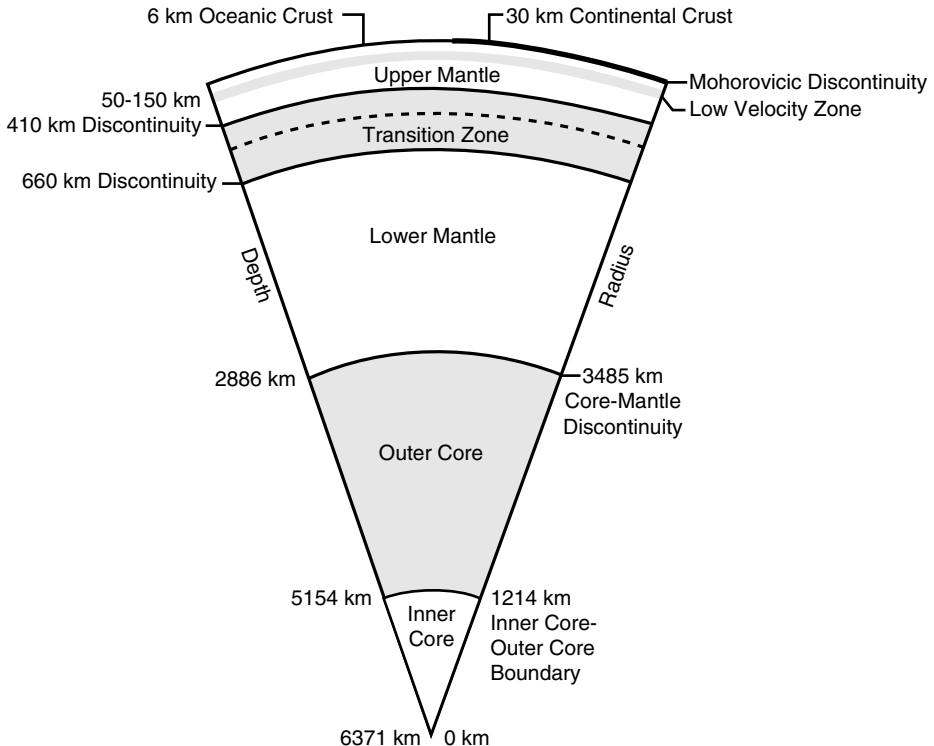


Figure 3.1. The major components of the Earth's interior are the crust, the mantle, and the core. The oceanic crust has a basaltic composition and a mean thickness of about 6km. The continental crust has a more silicic composition and a mean thickness of about 30km. The mantle has an ultrabasic composition; the compositional boundary between the crust and mantle is the Mohorovicic seismic discontinuity (the Moho). The mantle has major seismic discontinuities at depths of about 410 and 660km. The core is primarily iron; the outer core is liquid and the inner core is solid. The depths and radii of major boundaries are shown assuming spherical symmetry.

culminated with the publication of standard travel time curves for major seismic body wave phases, the JB tables (Jeffreys and Bullen, 1940), which are still in use today.

A method for obtaining radial density variations from radial profiles of compressional and shear wave velocities was developed by Williamson and Adams (1923). It provides a simple equation of state for describing compressibility in chemically homogeneous layers. Within such a layer, the radial variation in density ρ can be expressed in terms of any other two state variables. In particular we consider the pressure p and the entropy s and write

$$\frac{d\rho}{dr} = \left(\frac{\partial \rho}{\partial p} \right)_s \frac{dp}{dr} + \left(\frac{\partial \rho}{\partial s} \right)_p \frac{ds}{dr} \quad (3.2.1)$$

where r is the radial coordinate and the subscripts s and p refer to isentropic and isobaric variations, respectively. An isentropic process is a reversible process in which there is no heat transfer (adiabatic) and an isobaric process is a process at constant pressure. Applications of thermodynamics to the mantle will be discussed in greater detail in Section 6.8.

The thermodynamic derivative on the right side of (3.2.1), $(\partial\rho/\partial p)_s$, is related to the adiabatic compressibility χ_a of a material. The definition of χ_a is

$$\chi_a \equiv \frac{1}{\rho} \left(\frac{\partial \rho}{\partial p} \right)_s = \frac{1}{K_a} \quad (3.2.2)$$

where K_a is the adiabatic bulk modulus. The connection with elasticity comes from the relation between K_a and the velocities of the seismic compressional and shear waves, V_P and V_S , respectively, where

$$V_P = \left(\frac{K_a + 4\mu/3}{\rho} \right)^{1/2} \quad (3.2.3)$$

$$V_S = \left(\frac{\mu}{\rho} \right)^{1/2} \quad (3.2.4)$$

and μ is the shear modulus or rigidity of the solid. Elimination of the shear modulus from (3.2.3) and (3.2.4) gives

$$\Phi \equiv V_P^2 - \frac{4}{3} V_S^2 = \frac{K_a}{\rho} \quad (3.2.5)$$

where Φ is the seismic parameter. From (3.2.2) and (3.2.5), we can write the thermodynamic derivative $(\partial\rho/\partial p)_s$ simply as

$$\left(\frac{\partial \rho}{\partial p} \right)_s = \frac{1}{\Phi} \quad (3.2.6)$$

The radial profiles of V_P and V_S determined from seismology also give $\Phi(r)$ and $(\partial\rho/\partial p)_s$ as a function of r .

For a homogeneous layer that is well mixed, e.g., by convection, it is appropriate to assume that the layer is isentropic and $ds/dr = 0$. With this assumption and (3.2.6), the variation of density in (3.2.1) can be written as

$$\frac{d\rho}{dr} = \frac{1}{\Phi} \frac{dp}{dr} \quad (3.2.7)$$

The radial pressure derivative dp/dr in (3.2.7) is given to a good approximation throughout the mantle by the hydrostatic equation

$$\frac{dp}{dr} = -\rho g \quad (3.2.8)$$

where g is the acceleration of gravity. Substitution of (3.2.8) into (3.2.7) gives the Adams–Williamson equation for the variation of density with radius in the mantle:

$$\left(\frac{d\rho}{dr} \right)_s = \frac{-\rho g}{\Phi} \quad (3.2.9)$$

The subscript s on the left of (3.2.9) indicates that the process is isentropic. It should be emphasized that this result is valid only if the composition is uniform.

The acceleration of gravity g in the mantle also varies with radius. For a spherically symmetric Earth model $g(r)$ satisfies the Poisson equation

$$\frac{1}{r^2} \frac{d}{dr} (r^2 g) = 4\pi G\rho \quad (3.2.10)$$

where G is the universal constant of gravitation. Integration of (3.2.9) and (3.2.10), with $\Phi(r)$ known from seismology, gives a spherical Earth model, consisting of the radial variation of spherically averaged density and gravity. Integration of these coupled first-order differential equations requires two boundary conditions or constraints which are provided by the Earth's mass and moment of inertia; the densities of crustal and upper mantle rocks are also used to fix the densities at the tops of individual spherical layers. With $\rho(r)$ and $g(r)$ determined, the variation with radius of the adiabatic bulk modulus and rigidity can readily be found from (3.2.5) and (3.2.4), for example. The spherical Earth model also consists of $\mu(r)$ and $K_a(r)$.

Bullen (1936, 1940) first used the above procedure to obtain a six-layer Earth model, consisting of the crust (layer A), from the Earth's surface to the Moho (at a mean depth of 6 km beneath the oceans and 30 km beneath the continents), an adiabatic upper mantle (layer B), from the Moho to a depth of 400 km, an adiabatic lower mantle (layer D), from a depth of 1,000 km to a depth of 2,900 km, an adiabatic outer core (layer E), from a depth of 2,900 km to 5,100 km, and an adiabatic inner core (layer F), from 5,100 km depth to the center of the Earth. He found that the adiabatic approximation was not appropriate for the transition zone (layer C), from a depth of 400 km to 1,000 km, and instead used a polynomial function of radius to represent the density variation in this layer.

The resulting model A, as it was called, was an immediate success. Later, Bullen published model B, in which he added the assumption of continuity in the bulk modulus and its pressure derivative across the core–mantle boundary. This allowed him to further subdivide the lower mantle into layers D', to a depth of 2,700 km, and D'', between 2,700 km and 2,900 km depth. Bullen's models A and B are masterpieces of inductive science. They have been superseded by Earth models derived from larger data sets, and among all of his layer notation, only D'' has survived. However, these models were remarkably accurate. Perhaps more importantly, they introduced a new subject into geophysics – the use of spherical Earth models to infer mantle and core composition.

Modern Earth models are based on vastly larger seismic body wave data sets than were available to Bullen, and we now have normal mode frequencies from both toroidal oscillations (the mode equivalent of seismic Love waves) and spheroidal oscillations (equivalent to seismic Rayleigh waves) of the whole Earth. Normal mode frequencies are sensitive to the density distribution as well as the distribution of V_P and V_S , and incorporating them into Earth models substantially tightens the constraints on density, particularly in the lower mantle and outer core. The mathematics of the inversion procedure can be found in a number of review papers and texts, including Gilbert and Dziewonski (1975), Aki and Richards (1980), and Dziewonski and Anderson (1981). Spherically symmetric Earth models such as Dziewonski and Anderson's 1981 Preliminary Reference Earth Model (PREM) are derived using 2×10^6 P-wave (compressional wave) and 2×10^5 S-wave (shear wave) travel times and approximately 10^3 normal mode frequencies. The technique used in constructing these models is to apply body wave data to resolve fine structure and normal modes to determine the average density in each layer of the model. Uncertainties in density are quite low for averages over a finite depth interval. In the lower mantle and outer core, the uncertainty is less than 2% for averaging intervals of 400 km or more (Masters, 1979). This is somewhat

misleading, however, because the uncertainty increases rapidly as the averaging interval is reduced. In particular, the spherical Earth models are not able to accurately resolve discontinuities. The procedure for treating seismic and density discontinuities is to prescribe their depth a priori and allow the inversion procedure to determine the best-fitting values for properties in the layers on either side. Because precision decreases as the averaging interval decreases, it is difficult to resolve accurately the fine structure in important regions like the transition zone, where there are several closely spaced discontinuities. This limitation should always be kept in mind when interpreting the fine structure in spherical Earth models.

Profiles of V_P , V_S , and density ρ from model PREM are shown in Figure 3.2 for the whole Earth, and in detail for the upper mantle in Figure 3.3. The variations in bulk modulus

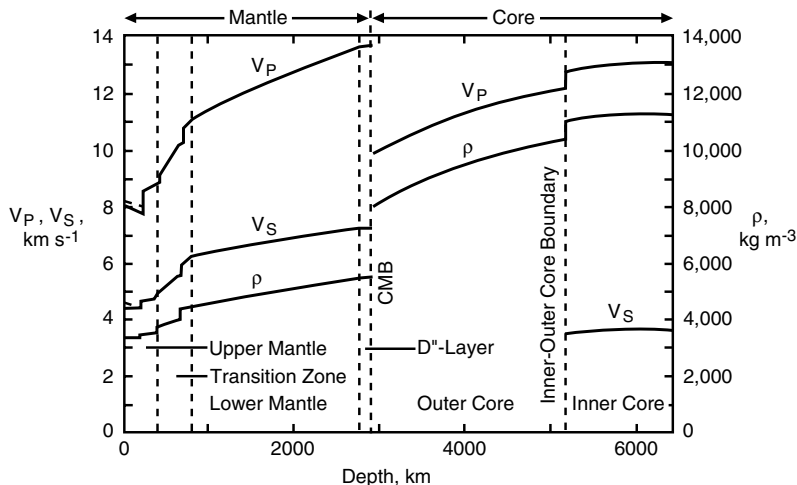


Figure 3.2. Spherical Earth model PREM (Dziewonski and Anderson, 1981). The seismic velocities V_P , V_S and density ρ are given as a function of depth.

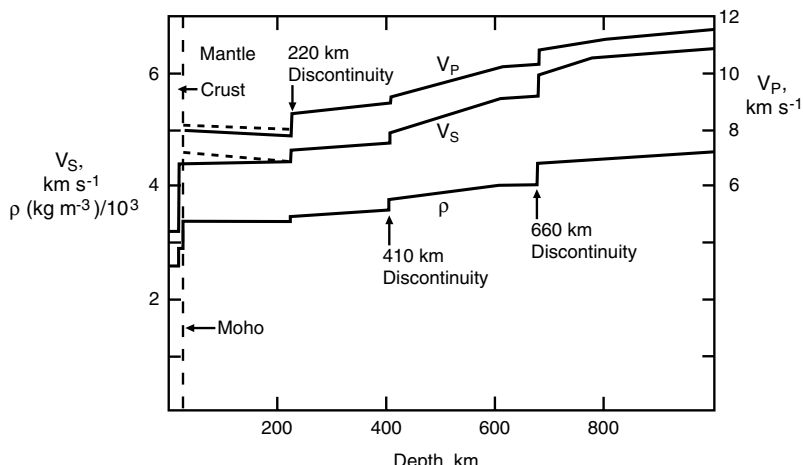


Figure 3.3. Structure of the upper mantle from the spherical Earth model PREM (Dziewonski and Anderson, 1981).

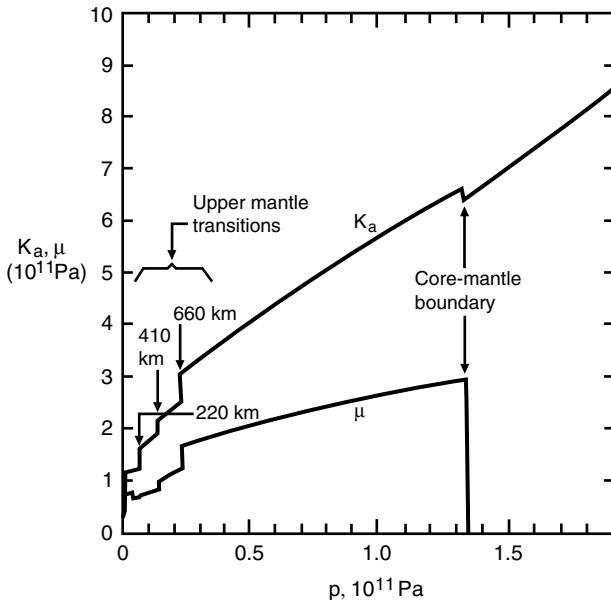


Figure 3.4. Dependences of the Earth's adiabatic bulk modulus K_a and shear modulus or rigidity μ on pressure in the spherical Earth model PREM (Dziewonski and Anderson, 1981).

and rigidity with pressure through the mantle are shown in Figure 3.4. PREM is constructed assuming three first-order discontinuities in the upper mantle, at depths of 220 km, 400 km, and 650 km. Like its predecessor PEM (Parametric Earth Model, Dziewonski et al., 1975), the profiles consist of polynomials within each layer. PREM assumes isotropy everywhere except between the Moho and 220 km depth, where transverse anisotropy is permitted. PREM also contains anelasticity, through the quality factor Q (inverse attenuation), and frequency-dependent elastic moduli. A major improvement over earlier models, such as Bullen's, is the presence of fine structure. Despite the fact that fine structure is the least certain component, it is the main feature that distinguishes one spherical model from another. Small differences in fine structure can lead to different interpretations regarding composition and its variation with depth in the mantle, which in turn may lead to grossly different inferences about the style of convection. Modern spherical Earth models (e.g., IASPEI 1991, see Kennett, 1991) have verified the major subdivisions listed in Table 3.1. These divisions provide the basis for discussions of the Earth's composition.

3.3 The Crust

In terms of its mass, the crust is a negligible part of the Earth, comprising less than 0.5% of the total (Table 3.1). But the significance of the crust for mantle convection is far greater than its fraction of the Earth's mass. The crust is the end product of mantle differentiation. Since differentiation of the mantle occurs primarily by partial melting, which is itself a product of convection, the crust yields information on the history of convection which is not obtainable by any other means. The crust also contains the most extreme lateral heterogeneities in the Earth, and this has a direct influence on the style of mantle convection. The continental

Table 3.1. Major Divisions of the Earth

Region	Depth Range (km)	Mass (10^{21} km)	Mass Fraction (%)	Average Density (kg m^{-3})
Oceanic crust	0–6	6	0.1	3,000
Continental crust	0–30	19	0.3	2,700
Upper mantle	(6,30)–410	615	10.3	3,350
Transition zone	410–660	415	7.0	3,860
Lower mantle	660–2,886	2,955	49.6	4,870
Outer core	2,886–5,140	1,867	31.1	11,000
Inner core	5,140–6,371	98	1.6	12,950
Whole Earth	0–6,371	5,975	100	5,515

crust contains a substantial fraction of the Earth's incompatible elements including the heat-producing elements uranium, thorium, and potassium. This fractionation strongly influences the strength of mantle convection.

The crust (continental and oceanic) is bimodal in nearly every respect: thickness, age, density, and composition. It is not possible to overemphasize this distinction, particularly with regard to the role of the crust in mantle convection. On average, the continental crust is old (mean age \simeq 2,000 Myr) while the oceanic crust is young (mean age \simeq 80 Myr). Oceanic crust is created continuously at spreading centers, the present rate of creation being $2.8 \text{ km}^2 \text{ yr}^{-1}$ (volumetrically about $17 \text{ km}^3 \text{ yr}^{-1}$), and is subducted back into the mantle at approximately the same rate. It is formed, almost entirely, by a single process – partial melting of an upper mantle composed of olivine, pyroxene, and garnet – resulting in a remarkably homogeneous product, mid-ocean ridge basalt (MORB). In contrast, most of the continental crust has resided on Earth's surface long enough to have experienced a sequence of collision events, intrusions of melts from below, episodes of loading and unloading, infiltration of metamorphic fluids, erosion and alterations in its thermal regime. One of the primary factors that accounts for the complexities of the continental crust and the relative simplicity of oceanic crust is the great disparity in ages. However, the silicic rocks of the continental crust are much weaker than the mafic rocks of the oceanic crust. Thus intraplate deformation is largely restricted to the continents as indicated by the distribution of earthquakes given in Figure 2.2. The relative weakness of continental rocks may have important implications for the tectonic evolution of the Earth and other planets. The history of plate tectonics requires the internal deformation of plates (Dewey, 1975); the required deformation occurs within the continents. As will be discussed in Chapter 14, the absence of "soft" continents on Venus may be the reason that Venus does not have plate tectonics.

3.3.1 Oceanic Crust

The same sequence of structural and lithologic units characterizes the oceanic crust on a global scale. Figure 3.5 shows the major layers in a typical cross-section, and Table 3.2 summarizes their properties. This stratigraphy was first identified from reflection and refraction seismic profiles; the connection between the seismic structure and the petrologic units was established through comparisons with ophiolite sequences, believed to be sections of oceanic crust and upper mantle thrust onto the continental crust. There are a number of excellent reviews of this subject, for example, Orcutt et al. (1984), and Purdy and Ewing

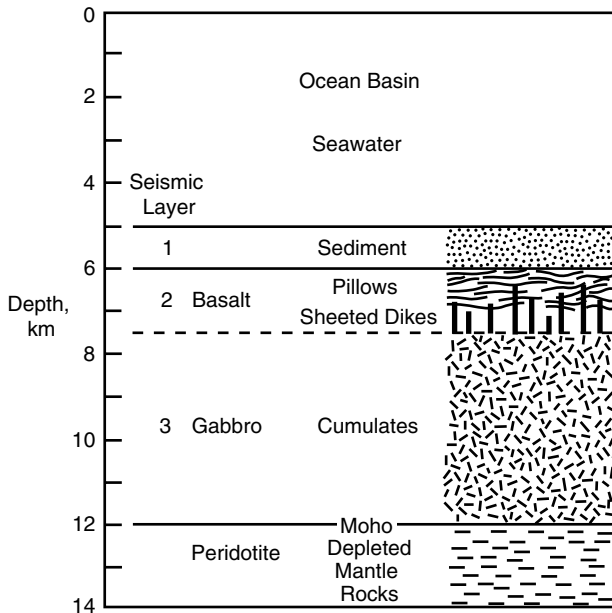


Figure 3.5. Idealized cross-section of the oceanic crust. Layer 1 is composed of sediments which have been deposited on the igneous layers 2 and 3. Layers 2 and 3 have essentially the same basaltic composition. Layer 2 is made up of the extrusive pillow basalts and the intrusive sheeted dike complex. Both have a fine-grained basaltic structure due to rapid cooling and have been extensively altered by hydrothermal flows. Layer 3 is made up of coarse-grained gabbros which cooled slowly in the magma chambers in the crust at the ridge axis.

Table 3.2. Oceanic Crust Structure

Seismic Layer	Average Thickness (km)	V_P (km s^{-1})	Average Density (kg m^{-3})
Seawater	4.6	1.5	1,026
Sediments	Variable	2.1 ± 0.7	2,000
Basaltic	1.6 ± 0.7	5.1 ± 0.6	3,000
Gabbroic	4.7 ± 1.4	6.8 ± 0.2	3,000
Upper mantle	—	8.15 ± 0.2	3,350

(1986). There are three important lithologic units in ocean crust between the water column (4.6 km average depth) and the upper mantle. Layer 1 is deep-sea sediments, about 0.5 km thick on average, but highly variable, with a statistical increase in thickness with increasing crustal age. The sediments are a fine-grained mixture of clays and various oozes, except where contaminated by terrigenous sediments delivered to the deep ocean by large river systems. Poorly consolidated, and with a high pore water content, their average V_P velocity and density are only 2.1 km s^{-1} and $2,000 \text{ kg m}^{-3}$, respectively. Layer 2 is composed of fine-grained tholeiitic basalts and basaltic glasses. The upper part of layer 2 is composed of pillow basalts, which are the products of basaltic magma extrusions onto the seafloor and their interactions with seawater. The lower part of layer 2 is made up of the coarser-grained basaltic sheeted dike complex. During each eruption the basaltic magma flows from the magma chamber at depth to the surface through a vertical crack or dike. The solidification

of the magmas in these dikes produces the sheeted dike complex. The average thickness of layer 2 is 1.6 km and it is considered to be the major source of seafloor magnetic anomalies (Smith and Banerjee, 1986). It is also seismically anisotropic, with the fast axis perpendicular to the direction of seafloor spreading where the crust was formed. This property has been ascribed to cracks and fissures oriented perpendicular to the original spreading direction, acquired during cooling at the ridge crest (Stephen, 1985). Layer 3 contains coarse-grained gabbros and related cumulates with essentially the same basaltic composition as layer 2. The coarse-grained structure is the result of slow cooling in the magma chamber at the base of the ocean crust at the ridge crest. Layer 3 averages 4.7 km in thickness.

The complete oceanic crust is typically 6–7 km thick. There is no systematic variation in thickness of layers 2 and 3 with age, in accord with the source of MORB being localized at spreading centers. Oceanic crust can range in thickness from 2 to 37 km; the partitioning of the crust into layer 2 and layer 3 characterizes even the thickest oceanic crust (Mutter and Mutter, 1993). Variations in the total thickness of oceanic crust result primarily from changes in the thickness of the lower oceanic crust, Layer 3 (Mutter and Mutter, 1993). The greatest thickness variations in oceanic crust occur along hot spot tracks, and at rifted margins where hot spots appear to have been initiated (White and McKenzie, 1989). The significance of these facts for the mantle plume theory of hot spot formation will be discussed in Chapter 11.

Numerous dredge samples have demonstrated the remarkable uniformity of the MORB bulk composition (Basaltic Volcanism Study Project, 1981). MORB is a tholeiitic basalt, slightly oversaturated in silica (see Table 2.2) with a relatively simple mineralogy – labradorite, calcic pyroxene, and minor amounts of olivine. The density of MORB lies between 2,900 and 3,000 kg m⁻³. Chemical analyses show a high concentration of Al₂O₃ and high Na/K ratios, relative to continental basalts (Hall, 1987). The geochemistry of MORB indicates it is derived from mantle material that is depleted, relative to chondritic meteorites, in incompatible elements such as K, Rb, Sr, U, Th, and in the rare earth elements. This pattern indicates that the parent mantle material is not “primitive,” but rather it has been differentiated, and has thereby lost some of its original inventory of low melting point components. It is generally accepted that the continental crust is the major complementary reservoir for the depleted mantle (O’Nions and Pankhurst, 1974; Zindler and Hart, 1986). The degree of differentiation of MORB parent material, its relationship to the continental crust, and the fraction of the mantle involved in producing MORB all bear on the question of the structure of mantle convection, and will be treated more fully in Chapter 12.

3.3.2 *Continental Crust*

The continental crust is distinctive from the oceanic crust in many ways. Its bulk composition is more silicic and this results in its bulk density being less than that of the oceanic crust. This low density and its greater thickness provide a gravitational stability to the continental lithosphere. Thus, continental crust is not readily recycled into the Earth’s interior as the oceanic crust is at subduction zones. As a result the mean age of the continental crust is more than one order of magnitude greater than the mean age of the oceanic crust. The continental crust is made up of igneous, metamorphic, and sedimentary components. Some of the igneous rocks have a basaltic composition similar to that of the oceanic crust, but most of them have a more silicic composition. Examples of silicic volcanism are the intrusive and extrusive volcanics of Andean-type subduction zones. A long-standing debate in geology concerns the origin of these granitic volcanics. Are they products of the mantle or of crustal fractionation? The current consensus favors crustal fractionation.

The hydrologic cycle plays an essential role in the evolution of the continents. Mountain ranges erode to mean sea level in relatively short geological times (≈ 50 Myr) generating sediments that collect on the continents, in internal sedimentary basins, and on the ocean floor. Some of the sediments on the ocean floor are recycled into the interior of the Earth at subduction zones but a substantial fraction are added to the continents in accretional prisms. Sediment piles can have thicknesses of 10 km or more and the high temperatures and pressures at the base of the piles can result in chemical compositional changes. These become the metamorphic rocks of the continental crust.

Unlike the oceanic crust, which has a single dominant mode of origin and a nearly universal stratigraphy, the continental crust is a heterogeneous aggregation of blocks, each having a very individual structure and history. It is somewhat misleading to discuss the continental crust in terms of its “average” properties, since it is possible that such an average may not occur. With this reservation in mind, we show in Figure 3.6 a sequence of representative seismic cross-sections through hypothetical examples of continental crust. The mean depth to Moho is about 35 km, and varies from 20 km or less beneath the continental slope at passive margins to 70–80 km beneath collision zones such as the Himalayas.

Until recently the structure of the deep continental crust was relatively unexplored, and this is reflected in the shortage of quantitative information on the deep crust in the older literature. This situation is rapidly changing, with organized exploration programs on every continent producing reflection and refraction data. In addition to an extensive survey literature on the continental crust as a whole (Burchfiel, 1983; Taylor and McLennan, 1985; Meissner, 1986; Windley, 1995), there are some interesting models of the lower crust (Fuchs, 1986; Mooney and Brocher, 1987) motivated by findings from deep seismic profiling experiments (Barazangi and Brown, 1986; Matthews and Smith, 1987).

Distinct layering can be found in the continental crust but it is more variable than in the oceanic crust. Much of the continental crust is covered with a thin veneer of sediments. The boundary between these sediments and the igneous and metamorphic rocks of the upper continental crust is known as basement. The basement rocks are exposed principally in the Archean shields and have an overall composition roughly equivalent to a granodiorite. The continental crust is generally divided into an upper crust and a lower crust. The upper

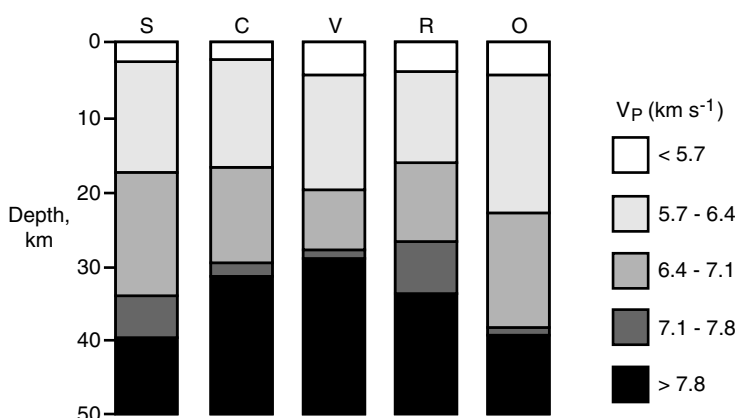


Figure 3.6. Idealized cross-sections of continental crust, showing the variations of V_P with depth. S = shields, C, V = Precambrian and Paleozoic platforms, R = rift zones, O = Mesozoic and Cenozoic orogenic belts. After Meissner (1986).

crust includes both the sediments and the crystalline basement rocks. Typical thicknesses of the upper crust are in the range 20–25 km and the basement rocks have seismic velocities V_P ranging from 5.7 to 6.3 km s^{-1} . The lower crust has thicknesses in the range 15–20 km and seismic velocities V_P in the range $6.3\text{--}7.5 \text{ km s}^{-1}$ (Rudnick and Fountain, 1995). The boundary between upper and lower crust is often indistinct; where it is observed it sometimes coincides with the Conrad seismic discontinuity, a feature in many older models of deep crustal structure. Depth profiles of seismic velocities, including the Conrad seismic discontinuity, have been inferred from the refraction of earthquake-generated seismic waves.

Deep seismic reflection profiling studies have provided additional information on the structure of the continental crust (Brown, 1991). Deep crustal reflection studies have demonstrated that the two-layer model of the continental crust is generally applicable, and furthermore it now appears that the structural contrast between the layers mirrors a contrast in rheology, which has important implications for continental tectonics. In stable shield and platform regions, Archean age crust is rather transparent to high-frequency seismic waves, particularly in the lower crust, suggesting the absence of sharp gradients in composition. Indeed, the Moho beneath shields and platforms is often not observed in reflection profiles. Regions that have experienced more recent deformation have a much different reflectivity. The upper crust in these regions is also relatively transparent to seismic reflections, a property attributed to the general lack of horizontal layering. This is an indication of brittle deformation in response to long-term tectonic forces and a general absence of pervasive ductile flow. Fine structure is generally oriented vertically, and probably consists of dikes, vertical shear zones, and plug-like intrusions. In contrast, the lower Phanerozoic crust is highly reflective at seismic exploration wavelengths. The most probable explanation is the presence of many fine-scale (100 m thick) horizontal laminations of various rock types. This is an indication of pervasive ductile deformation. The lower crust, composed of granulite facies metamorphic rocks, is ductile and generally more deformable than the granitic upper crust, and it is also more deformable than the underlying mantle. The resulting “sandwich” rheological structure may explain why continental deformation is generally more diffuse than deformation in the oceanic lithosphere. In particular, the weak lower crust probably accounts for the thin-skin style of deformation, including low-angle thrust faults that characterize continental tectonics in convergence zones.

The continental Moho is not a first-order seismic discontinuity in many locations, as was traditionally thought. Rather, it appears to extend over a broad depth range in which the composition changes progressively from crustal metamorphic rocks to upper mantle peridotites. Reflectivity studies suggest that the Moho zone includes interlayered strips of both crustal and upper mantle rocks (Fuchs, 1986; Mooney and Brocher, 1987; Jarchow and Thompson, 1989). The influence of the Moho on mantle convection is profound. Among all of the interfacial regions within the Earth, only the core–mantle boundary supports a larger density increase. The density of the continental crust averages $2,600\text{--}2,700 \text{ kg m}^{-3}$ while the density of the uppermost mantle is about $3,350 \text{ kg m}^{-3}$. Surface topography and Moho depth are well correlated at long wavelengths, indicating that continental topography is mirrored at the Moho. Buoyancy of continental rocks with respect to the mantle is the main reason why the continental crust resists subduction and remains on the Earth’s surface for billions of years.

On the basis of tectonic history, continental regions are classified as shields, platforms, and mountain belts or orogens. Shields and platforms are also referred to as cratons. This division is reflected to some degree in the deep structure, but it is most evident in the surface geology. Shields are ancient, stable, slightly elevated regions, nearly free of sedimentation, and primarily composed of Precambrian igneous and metamorphic rocks that have remained



Figure 3.7. Age provinces of the continental crust. a = Mesozoic and Cenozoic tectonic belts, b = Paleozoic tectonic belts, c = Proterozoic platforms, d = Proterozoic shields, e = Archean shields. Adapted from figures in Miyashiro et al. (1982) and Meissner and Wever (1989).

undisturbed for 1 Gyr or longer. Platforms are areas covered by a relatively thin veneer of flat-lying sediments of Proterozoic and younger age, again with little or no deformation. The primary difference between shields and platforms is that platforms occasionally have subsided below sea level. Orogenic mountain belts with Phanerozoic age deformation tend to form curved sections surrounding shields and platforms, as shown in Figure 3.7. This concentric pattern of crustal ages is usually interpreted as evidence for continental growth by accretion.

A global model of the Earth's crust based on seismic refraction data published between 1948 and 1995 and a detailed compilation of ice and sediment thickness has been presented by Mooney et al. (1998). Crustal thicknesses from this model are shown in Figure 3.8, which prominently displays the difference in thickness of oceanic and continental crust. The thickest crust is found beneath the Tibetan Plateau (70 km) and the Andes. Anomalously thick crust in the oceans is associated with oceanic plateaus and hot spots.

3.4 The Upper Mantle

As discussed above, the existence of the Moho as the boundary between the crust and the mantle was inferred from seismic velocity observations early in this century. Until the 1960s there were two competing hypotheses for the nature of the Moho. The first was a compositional boundary between the silicic and basaltic rocks of the crust and the ultrabasic rocks of the mantle, principally peridotite, that have the appropriate seismic velocity for the

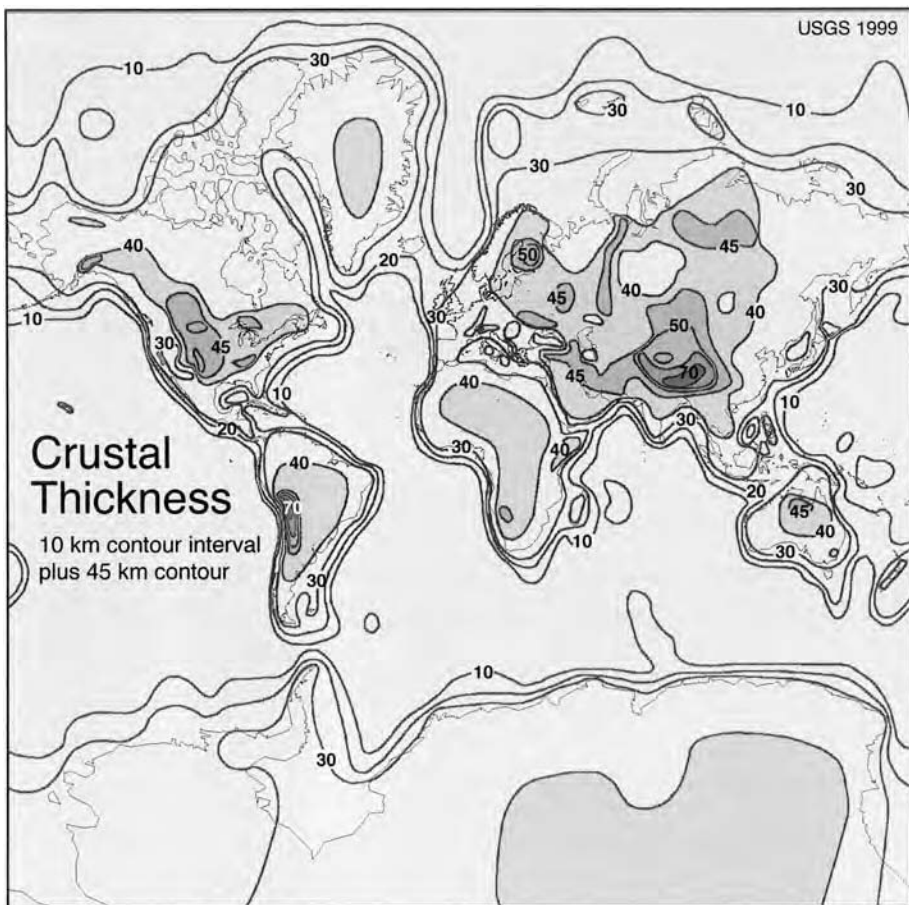


Figure 3.8. Global map of the thickness of the Earth's crust from the CRUST 5.1 model of Mooney et al. (1998). Crust thickness includes topography above sea level but not bathymetry.

For a color version of this figure, see plate section.

upper mantle. The second hypothesis was a phase boundary between basalt and its high-pressure equivalent eclogite. Like peridotite, eclogite has seismic velocities appropriate for the upper mantle.

With the general acceptance of plate tectonics, the compositional hypothesis for the Moho became favored. Confirmation came with the recognition of ophiolitic complexes as exposed sections of the oceanic crust. In Newfoundland, Cypress, Oman, and other places where the Moho is exposed at the Earth's surface, the basaltic and gabbroic rocks of the former oceanic crust are underlain by ultrabasic rocks with a mostly peridotitic composition.

3.4.1 Radial Structure of the Upper Mantle

Regional models of upper mantle structure derived from seismic surface waves commonly show very little increase in seismic velocities with depth for the first few tens of kilometers beneath the Moho. At greater depths, down to about 200 km, seismic velocities often decrease

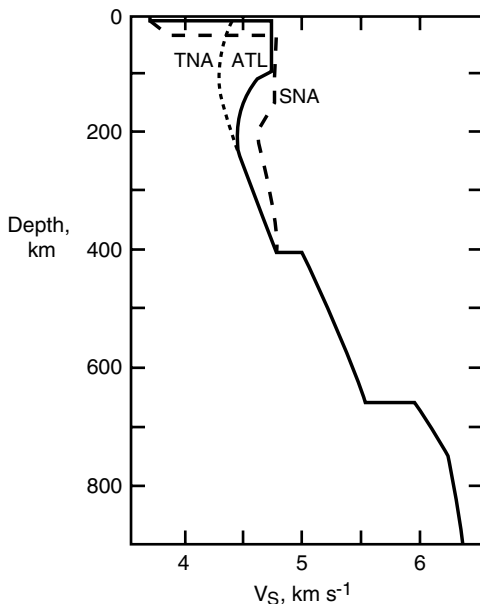


Figure 3.9. Regionalized upper mantle profiles of V_S from Grand and Helmberger (1984a,b). SNA = Canadian shield, TNA = tectonic western North America and East Pacific Rise, ATL = northeastern Atlantic.

with depth. We refer to the depth interval with nearly uniform velocity as the seismic lid (LID), and the depth interval with negative velocity gradients as the low-velocity zone (LVZ). This combination of structures is particularly evident in the oceanic upper mantle. Regional shear wave velocity profiles exhibiting these structures are shown in Figure 3.9.

The seismic LID roughly corresponds to the Earth's surface thermal boundary layer, the lithosphere. It has been speculated that the top of the low-velocity zone marks the transition in long-term rheology from the rigid lithosphere to the viscous asthenosphere. The upper part of the mantle LID has been depleted by the removal of the basaltic component to form the oceanic crust. The observed increase in seismic velocity with depth through the LID is attributed to this compositional change which dominates over the decrease in seismic velocity due to the temperature increase with depth through the LID. The mean density in the LID is known to be $3,300\text{--}3,400 \text{ kg m}^{-3}$ from the isostatic balance between oceanic and continental lithosphere.

The LID and the LVZ are seismically anisotropic, particularly beneath the oceans, and this fact complicates the problem of determining their structure and depth extent. Seismic anisotropy in the upper mantle is determined by a variety of methods, including azimuthal variations of P_n (P waves critically refracted along the Moho), shear wave birefringence (the dependence of wave speed on polarization direction), and comparisons between the dispersion of Rayleigh and Love surface waves.

The seismic anisotropy of the oceanic upper mantle was first measured by refraction studies (Morris et al., 1969; Raitt et al., 1969), which demonstrated that P_n is about 5% faster in the direction of seafloor spreading than in the direction parallel to the ridge. This azimuthal seismic anisotropy is attributed to the statistical alignment of olivine crystals, with the fast a -axes parallel to the spreading direction and the b - and c -axes concentrated in a vertical plane parallel to the spreading axis (Christensen and Salisbury, 1979). A preferential grain alignment is thought to result from the strain field at spreading centers (see Chapter 4).

An implication of this hypothesis is that anisotropy is “frozen” into the oceanic LID at the time of its formation.

Seismic anisotropy is also present in the upper mantle beneath the continents, as revealed by shear wave splitting, a phenomenon analogous to optical birefringence. When a seismic shear wave propagates through anisotropic regions of the crust and upper mantle, it splits into two waves with orthogonal polarizations and slightly different propagation speeds. Observations of shear wave splitting have demonstrated that anisotropy in the upper mantle beneath tectonic regions is often consistent with the regional pattern of crustal deformation, an indication that the upper mantle is coupled to tectonic events on the continents (Silver, 1996).

On even larger scales, seismologists observe a systematic discrepancy between the dispersion of Love and Rayleigh surface waves, which can be explained if horizontally polarized shear waves propagate faster than vertically polarized shear waves in the upper 200 km of the mantle. The global average of this difference is small, about 2% (Forsyth, 1975; Dziewonski and Anderson, 1981), but it is nonetheless significant. It implies that the isotropy of the upper mantle is, on average, transverse. This form of seismic anisotropy is defined by a single axis of symmetry, with isotropic behavior in planes perpendicular to the axis, and is described by five independent elastic parameters. In the upper mantle, the symmetry axis is oriented in the vertical (radial) direction, so the isotropic surfaces are the horizontal (spherical) surfaces. Transverse isotropy can be produced by crystals oriented randomly on spherical surfaces, but aligned in the radial direction, or alternatively, by a structure consisting of fine-scale horizontal laminations.

Azimuthal anisotropy in Rayleigh waves provides a means for mapping the direction of anisotropy in the LID and LVZ worldwide. Whereas the LID seismic anisotropy records the fossil spreading direction, the direction of seismic anisotropy in the LVZ is probably not frozen, but instead reflects grain alignment in the present field of flow. In principle then, LVZ directional seismic anisotropy provides a tool for determining the direction of shear beneath plates. We shall return to this topic in our discussion of seismic tomography later in this chapter.

The importance of seismic anisotropy to the problem of determining vertical structure is due to the tradeoff between anisotropy and LID thickness in the inversion of surface wave data. Figure 3.10 shows the variation in oceanic LID thickness as a function of crustal age, as determined from surface wave dispersion with and without anisotropy. Isotropic models yield apparently thick LIDs (Forsyth, 1975), whereas anisotropic models give LID thicknesses only about one-half as large (Regan and Anderson, 1984; Kawasaki, 1986). The isotropic LID is very close to the predicted thermal boundary layer thickness (see Chapter 4), whereas the anisotropic LID is closer to the mechanical thickness determined from lithosphere flexure studies (Levitt and Sandwell, 1995) (see Chapter 5).

The LVZ is present as a global feature for S waves, although its most important characteristic is its regional variability, as shown in Figure 3.9. Shield regions have high shear velocity LIDs to a depth of about 300 km and little or no LVZ. Tectonically active areas on continents, on the other hand, may not have a well-defined LID, and instead have low velocities extending to about 200 km depth. The most systematic variations in LVZ structure are found beneath ocean basins, where the LID thickness increases approximately as the square root of crustal age (Figure 3.10), similar to the increase in thermal boundary layer and elastic flexure thicknesses. This trend indicates a direct connection between seismic and thermal structure in the oceanic upper mantle. In the oceanic LID, temperature, pressure, and compositional gradients combine to produce a nearly constant seismic velocity depth

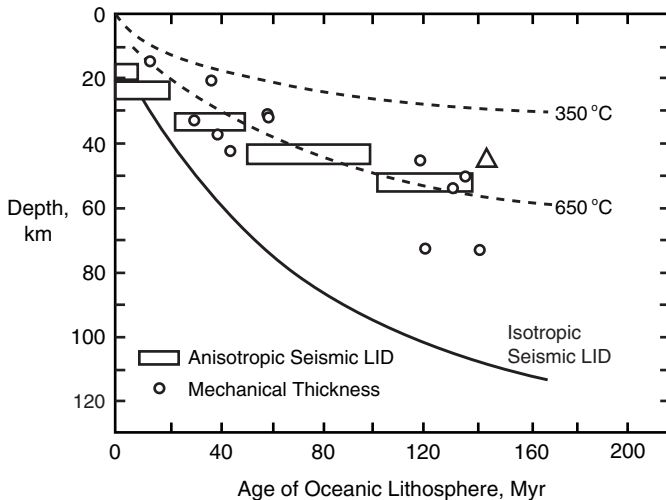


Figure 3.10. Oceanic LID thicknesses and mechanical lithosphere thicknesses versus crustal age (modified from Regan and Anderson, 1984). Boxes are LID thicknesses obtained by Regan and Anderson (1984) from surface wave dispersion assuming transverse anisotropy and anelastic dispersion. The solid curve represents seismic LID thickness estimates assuming isotropy. Circles are the thicknesses of the mechanical lithosphere computed by Levitt and Sandwell (1995) from elastic flexure analysis of lithospheric bending at subduction zones. Mechanical thicknesses represent thicknesses of the part of the lithosphere with long-term strength to resist deformation and are obtained from elastic thicknesses using a yield strength envelope model. The isotherms are from the thermal boundary layer model for the oceanic lithosphere given in Chapter 4.

profile; the thickness of the LID increases with increasing crustal age due to the conductive cooling of the lithosphere.

The LVZ beneath ocean basins is often interpreted as the intersection of the geotherm with the solidus of mantle rocks, and hence it marks the depth of partial melting. Partial melting in the LVZ is consistent with the distribution of seismic attenuation in the upper mantle. The quality factor Q (inverse attenuation rate) has a sharp minimum in the LVZ, particularly for S waves, as shown in Figure 3.11. Partial melts, even in low concentrations, strongly increase attenuation (decrease Q), particularly for seismic shear waves. The melt phase is concentrated at grain boundaries and tends to form an interconnected fluid network, which can drastically increase the rate of energy dissipation in seismic shear waves.

Question 3.1: Is the LVZ partially molten?

We have already noted that seismic shear wave velocities are much larger beneath continental cratonic regions (shields and platforms) than beneath tectonically active areas. Cratons evidently have “roots” extending into the upper mantle. There are a number of important unsolved problems concerning these roots, including their depth extent, possible compositional and rheological differences with respect to the rest of the upper mantle, and the implication that they are tightly bound to the overlying crust. Jordan (1975, 1981, 1988) introduced the term tectosphere to distinguish these roots from the rest of the lithosphere,

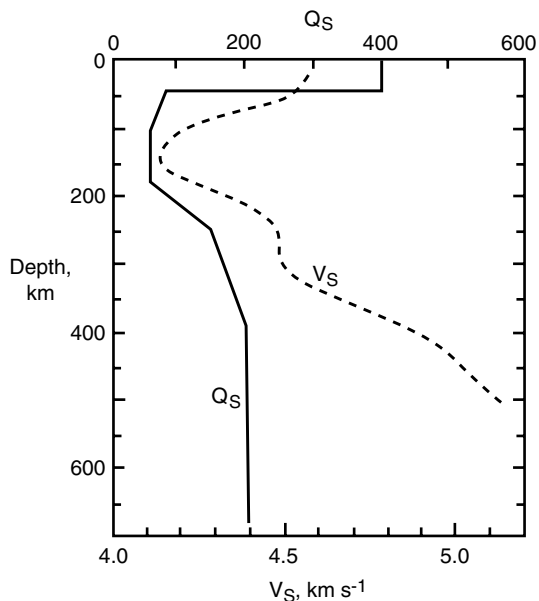


Figure 3.11. Profiles of shear wave velocity V_S and shear wave attenuation factor Q_S versus depth, showing oceanic LID–LVZ structure (after Anderson and Given, 1982).

and has argued that they must be cold and basalt depleted in comparison with surrounding mantle. Low temperatures provide the mechanical strength to bind the root to the overlying crust, and basalt depletion results in a residual harzburgite composition with a lower density than the less depleted mantle. Since isostatic compensation of the continental crust is nearly complete at the Moho, the tectosphere must have the same average density as less depleted mantle, and this requires cancellation of the effects of temperature and basalt depletion on density in the tectosphere. While there are strong indications of mantle roots beneath cratons, their depth extent remains controversial. Sacks and Snee (1984) have reviewed the evidence from seismology, in an attempt to detect patterns in continental root thickness. They find root thicknesses in the range 150–250 km, certainly greater than the oceanic LID thickness, but not as great as the 400–600 km originally proposed by Jordan (1975). Global seismic tomographic images show continental roots extending 300 km or more into the upper mantle, but the maximum depth of these structures is still poorly resolved (e.g., Su et al., 1994).

Question 3.2: What is the thickness of the continental lithosphere? Do the continents have roots that extend to depths of several hundred kilometers in the mantle?

One problem in detecting deep continental roots is that they may be masked by the Lehmann seismic discontinuity at about 220 km depth. The Lehmann seismic discontinuity is given in Earth model PREM (Figure 3.3) as an approximately 2% increase in velocity. It is often missing in profiles derived from body waves (Shearer, 1990), suggesting that it may be absent in some places, particularly beneath ocean basins. Gaherty and Jordan (1995) have

proposed that the Lehmann discontinuity represents the base of the anisotropic portion of the continental root, which would account for its absence in the oceanic upper mantle. The disappearance of anisotropy with depth could be a rheological effect (Karato, 1992; Gaherty and Jordan, 1995).

Question 3.3: *What is the nature of the Lehmann seismic discontinuity at a depth of 220 km?*

3.4.2 Upper Mantle Composition

The composition of the upper mantle is constrained by density, seismic velocities, and seismic anisotropy. It is also constrained by compositions found in ophiolite complexes and mantle xenoliths carried to the surface in kimberlitic and alkali basaltic eruptions. Furthermore, the compositions of the crust, mantle, and core must be consistent with cosmological estimates and, in addition, it is usually assumed that the upper mantle composition produces MORB upon 10–20% partial melting.

First, it is necessary that any model for mantle composition satisfy cosmochemical constraints. It is generally accepted that the meteorites classified as CI chondrites represent primordial building blocks of the Earth. Their mean bulk composition, with the exception of the volatile elements, is generally consistent with a mantle that is primarily peridotite and a core that is primarily iron, as shown in Table 3.3 (McDonough and Sun, 1995). Table 3.4 compares the average composition of CI chondrites with the so-called pyrolite composition, a peridotite model of the mantle introduced by Ringwood (1975) to explain the seismic, petrologic, and mineralogic properties of the upper mantle. Except for small differences in silicon and magnesium, the two compositions are very similar.

Relatively few silicate and oxide compounds are structurally stable at mantle pressures and temperatures, and this restricts the bulk composition to a mixture of olivine, pyroxenes, garnet, magnesiowüstite and the quartz polymorph stishovite. Chemical formulas and estimated

Table 3.3. Bulk Earth Composition^a

Element	Mantle wt (%)	Core wt (%)	Bulk Earth wt (%)
Al	2.35		1.59
Ca	2.53		1.71
Mg	22.8		15.4
Si	21.0		14.2
Fe	6.26	87.5	32.7
Cr	0.263	0.95	0.49
Ni	0.196	5.40	1.89
Mn	0.105	0.50	0.24
Na (ppm)	2,670		1,800
V (ppm)	82	120	95
Co	0.0105	0.26	0.0915
P	0.009	0.050	0.17

^a McDonough and Sun (1995).

Table 3.4. Chondrite Versus Pyrolite Composition^a

Component	CI Chondrites wt (%)	Pyrolite wt (%)
SiO ₂	49.9	45.0
TiO ₂	0.16	0.201
Al ₂ O ₃	3.65	4.45
Cr ₂ O ₃	0.44	0.384
MnO	0.13	0.135
FeO	8.0	8.05
NiO	0.25	0.25
MgO	35.15	37.8
CaO	2.90	3.55
Na ₂ O	0.34	0.36
K ₂ O	0.022	0.029

^a McDonough and Sun (1995).

Table 3.5. Pyrolite Model for Upper Mantle Composition^a

Minerals	Compositions	Pyrolite wt (%)
Olivine	(Mg, Fe) ₂ SiO ₄	57.9
Orthopyroxene	(Mg, Fe)SiO ₃	13.5
Clinopyroxene	([Ca, Mg] ₂ , NaAl)Si ₂ O ₆	16.3
Garnet	(Mg, Fe, Ca) ₃ Al ₂ Si ₃ O ₁₂	12.3

^a Ringwood (1975); Green and Falloon (1998).

mantle abundances of these minerals are listed in Table 3.5. Olivine is a complete solid solution of Mg and Fe silicates with end members fayalite, Fe₂SiO₄, and forsterite, Mg₂SiO₄. Mantle pyroxenes are orthopyroxene and clinopyroxene. Orthopyroxene is the limited solid solution, (Mg, Fe)SiO₃. The magnesium end member is enstatite; the iron end member is unstable. Clinopyroxene is a pyroxene solid solution including Ca and Al. End members are diopside, MgCaSi₂O₆, hedenbergite, FeCaSi₂O₆, and jadite, NaAlSi₂O₆. The chemical formula for garnet is (Mg, Fe, Ca)₃Al₂Si₃O₁₂. Among all possible rock assemblages composed of these minerals, only peridotites (olivine + pyroxene) and eclogites (pyroxene + garnet) are commonly found in mantle-derived samples. Eclogite is isochemical with basalt, and transforms to basalt at depths of less than about 80 km within the Earth.

The problem of determining the upper mantle composition from the composition of mantle xenoliths, plus the geophysical constraints, has been thoroughly treated (Boyd and Meyer, 1979; Ringwood, 1979; Anderson, 1989), although there is some disagreement on the most likely composition. Xenoliths from diamond-bearing kimberlite pipes, with source depths of 150 km or greater, are mostly peridotites; only a small fraction are eclogites. The most common peridotitic xenoliths are garnet lherzolites (about 60% olivine, the remainder orthopyroxene + clinopyroxene + garnet) and harzburgites (olivine + orthopyroxene), with eclogites and spinel lherzolites (spinel in place of garnet) being widespread but less abundant. If one assumes that the sampling by kimberlites is unbiased, then the upper mantle is composed primarily of peridotite, with eclogite an important but less abundant constituent.

This inference is consistent with seismic velocities and densities, and the abundance of olivine provides an explanation for seismic anisotropy in the upper 200 km of the mantle. In contrast, eclogite has a density of $3,500 \text{ kg m}^{-3}$ and is only weakly seismically anisotropic. It is therefore unlikely that eclogite is a dominant upper mantle assemblage.

For the purpose of determining the physical properties of the upper mantle, garnet peridotite is probably a good first-order approximation to the bulk composition. However, it is not completely satisfactory as a chemical model, because upper mantle rocks must be able to produce MORB upon partial melting. It is necessary to include some eclogite in the upper mantle composition in order that it serve as a source for basalt. A mantle rock that can produce MORB by 10–20% partial melting is said to be fertile. Mantle rocks from which the basaltic component has been extracted are said to be infertile. Most peridotites found in xenoliths are too refractory to produce large amounts of basaltic magma, i.e., they are too depleted in the pyroxenes due to prior partial melting (Hawkesworth et al., 1990).

There are basically two classes of models for upper mantle composition that can satisfy the geophysical constraints and also explain the origin of MORB. One class of models is based on the assumption that the dominant upper mantle rock type is a mixture of peridotite and eclogite. Ringwood (1975) proposed that its bulk composition corresponds to about three parts refractory peridotite plus one part eclogite, a hypothetical assemblage he termed pyrolite. The upper mantle abundances of minerals according to the pyrolite hypothesis are given in Table 3.5 (Ringwood, 1975; Green and Falloon, 1998). Partial melting of pyrolite beneath oceanic spreading centers leads to a compositionally stratified oceanic lithosphere, with basaltic ocean crust overlying refractory peridotites, which grade downward into pyrolite.

A second class of models for upper mantle composition is based on the assumption that the upper mantle is stratified. Dickinson and Luth (1971) proposed that the subducted oceanic crust transformed to eclogite and gravitationally separated to form the lower mantle beneath 700 km depth. A primary problem with this model is that the upper mantle would be so depleted that the oceanic crust could not be produced from it. A variant on this hypothesis has been proposed by Anderson and Bass (1984). They suggest that the entire mantle above the 410 km seismic discontinuity has the composition of the kimberlite xenoliths – mostly refractory peridotites – and that the source layer for MORB lies deeper in an eclogite-rich layer within the transition zone. In their model, the bulk composition of the upper mantle is too depleted to produce voluminous basaltic magmas and the transition zone is assumed to be the MORB source region. However, there are serious problems with any stratified mantle model. In order to maintain the stratification each layer would have to convect essentially independently. Significant transport of material across a stratification boundary would rapidly mix and homogenize the mantle. Also, it is difficult to envision a stratified mantle that could generate a basaltic oceanic crust of near-uniform composition. Such a crust is a natural consequence of ascending convection in an upper mantle that is a mixture of peridotite and eclogite.

Figure 3.12 is a comparison of several regionalized seismic velocity depth profiles with velocities calculated by Anderson and Bass (1984) along adiabats for the pyrolite model of upper mantle composition. Compressional V_P and shear V_S wave velocities are given for continental shields, the northwest Atlantic, the western Pacific, and tectonic rises (northern part of the East Pacific Rise, Gulf of California, and southern California). The expected seismic velocities for a pyrolite composition mantle at various potential (zero pressure) temperatures are plotted. The adiabatic pressure dependence of these velocities is obtained without taking into account partial melting. The portions of these curves beneath the solidus curves are in the partial melt field. The high velocities in the seismic lid and the low velocities

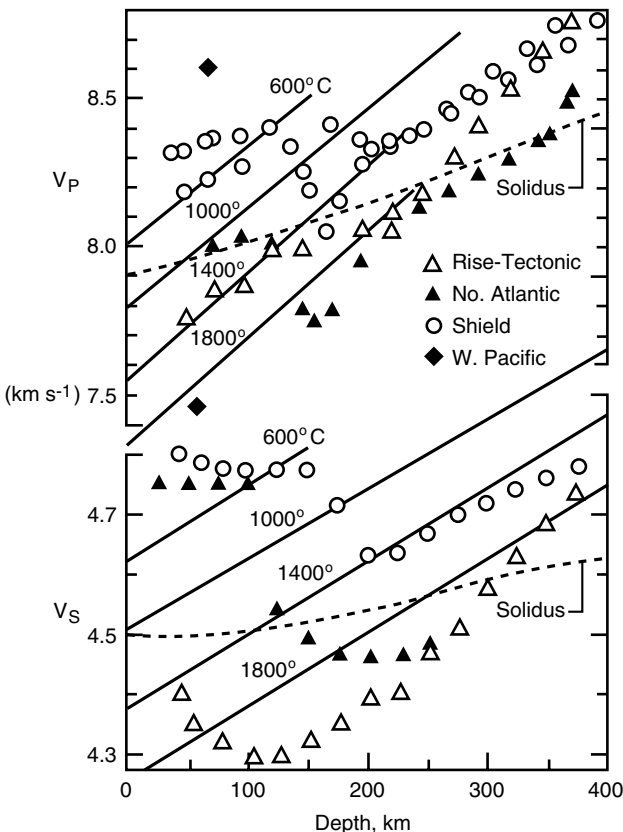


Figure 3.12. Compressional and shear wave velocities (V_P , V_S) are given as a function of depth for several regions (Anderson and Bass, 1984). The solid lines are the expected seismic velocities for a pyrolite composition mantle at various potential (zero pressure) temperatures. The adiabatic pressure dependence of these calculated velocities does not take into account partial melting. The portions of the data and curves beneath the dashed solidus lines lie in the partial melt field. The symbols are regionalized upper mantle seismic velocity profiles.

in the asthenosphere (LVZ) are clearly illustrated. The increase in velocity, from the LVZ down to 400 km depth, is reasonably consistent with a homogeneous composition under isentropic compression.

Another point revealed by the comparison in Figure 3.12 is the likelihood that the LVZ is caused by partial melting. In general, steep thermal gradients reduce V_P more than V_S , while small amounts of intergranular melts tend to reduce V_S more than V_P (Anderson, 1989). As shown in Figure 3.12, the LVZ is more pronounced for V_S , which is consistent with partial melting being the cause of the velocity decrease, rather than steep thermal gradients. Furthermore, the temperature distributions implied by the data in Figure 3.12 seem to require the presence of partial melts. Adiabats fitted to the seismic velocity profiles for spreading centers and tectonically active areas in Figure 3.12 lie above the solidus in the interval 50–300 km depth. It is worth emphasizing that this interpretation suggests that mid-ocean ridges and tectonically active regions such as western North America are underlain by a partially molten layer. Regardless of whether it is due to steep thermal boundary layer temperature gradients, or partial melts, or both, the LVZ is a product of mantle convection.

3.5 The Transition Zone

3.5.1 The 410km Seismic Discontinuity

In 1926 Byerly (1926) discovered a decrease in slope of the P-wave travel time curve at angular distances near 20° . It implied a sharp jump in V_P , which became known as the “ 20° seismic discontinuity.” Bullen’s early Earth models included this seismic discontinuity, and Bernal (1936) suggested it marked a solid-state phase transformation from the olivine to the denser spinel structure. Francis Birch took up the problem of interpreting mantle seismic structure in terms of composition; his efforts culminated in a landmark 1952 paper in which he applied an equation of state, derived from finite-strain theory, to Bullen’s Earth model B. Birch (1952) concluded that an upper mantle composition of olivine, pyroxene, and garnet is consistent with the seismic data, and proposed that the lower mantle is composed of a mixture of dense oxides such as periclase (MgO). He also concluded that the transition zone represents a succession of pressure-induced polymorphic phase changes. At the time there was neither the seismic nor the mineral physics data to fully test Birch’s proposals. In the 1960s, seismic array studies revealed that the transition zone has a fine structure including two sharp discontinuities near depths of 410 and 660km (Johnson, 1967). At nearly the same time, the olivine–spinel phase transformation was observed in laboratory experiments at approximately the correct pressure to explain the 410km seismic discontinuity (Akimoto and Fujisawa, 1968; Ringwood and Major, 1970). The presently accepted properties of this phase change include a 0.5 km s^{-1} jump in V_P and a $0.2\text{--}0.3 \text{ km s}^{-1}$ jump in V_S , centered near a depth of 410km and distributed over a depth interval of 15km or less (Fukao, 1977; Leven, 1985; Shearer, 1990, 1991). The lateral variation in depth is rather small, generally within ± 10 km of the global average depth (Shearer, 1991). The accompanying density jump is in the range $200\text{--}300 \text{ kg m}^{-3}$, as shown in Figure 3.3.

Phase relations in the transition zone and in the lower mantle are primarily controlled by two mineralogies, olivine and pyroxene–garnet. Garnet peridotite, the dominant upper mantle assemblage, consists of these in roughly a 3 : 1 proportion, implying that the phase transformation of olivine should control the character of the 410km seismic discontinuity.

The solid solution in olivine is usually expressed in terms of the magnesium number X_{Mg} , the molar concentration of Mg normalized by the molar concentration of Mg plus Fe, expressed as a percent. The upper mantle density $3,350 \text{ kg m}^{-3}$ is matched by olivine with a composition $(\text{Mg}_{0.89}, \text{Fe}_{0.11})_2\text{SiO}_4$, or $X_{\text{Mg}} \simeq 89$. Early experiments on the iron end member fayalite verified the transformation from the low-pressure α phase, with orthorhombic structure, to the cubic structure γ phase at about 7GPa. The phase diagram for olivine is shown in Figure 3.13. At transition zone temperatures of 1,600–1,900K, $X_{\text{Mg}} = 89$, olivine transforms to an intermediate β -modified spinel phase at 13–14GPa, and from the β -modified spinel phase to the γ -spinel phase at 17–18GPa. The transformation α olivine \rightarrow β -modified spinel occurs near 13.5GPa, 405km depth, at about 1,700K (Akaogi et al., 1989; Katsura and Ito, 1989), and is the most likely candidate to explain the 410km seismic discontinuity.

In addition to depth, the width of the mixed-phase region, where α olivine and β -modified spinel coexist, is crucial in identifying it with the 410km seismic discontinuity. Experimental evidence indicates that the α olivine \rightarrow β -modified spinel transformation occurs over a narrow pressure interval. For olivine with magnesium number 89, Katsura and Ito’s (1989) measurements indicate a 10–20km thickness for the α olivine \rightarrow β -modified spinel phase change in the temperature range 1,600–1,900K, with the width of the two-phase loop

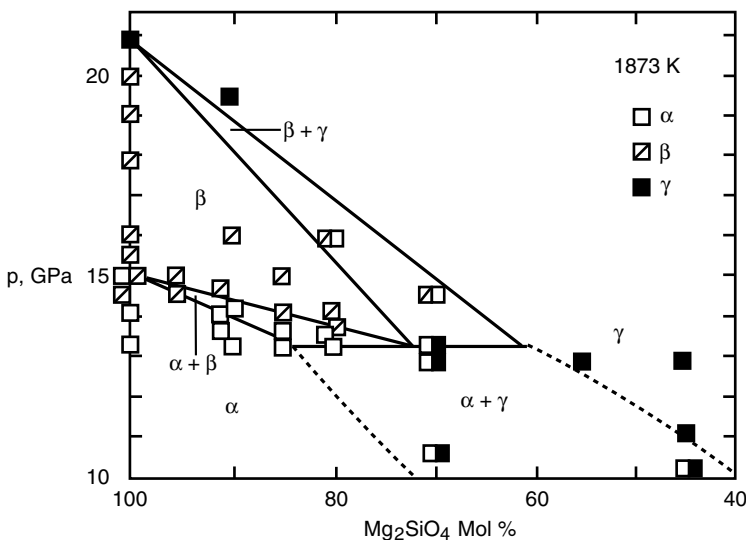


Figure 3.13. Phase diagram for the system $(\text{Mg}, \text{Fe})_2\text{SiO}_4$ at pressures of 10–21 GPa and $T = 1,873$ K (Katsura and Ito, 1989).

decreasing with increasing temperature. This is slightly thicker than most estimates of the depth interval of the 410 km seismic discontinuity, but within the present uncertainties. The experimentally determined Clapeyron slopes are positive, indicating that this reaction is exothermic. Estimates of the Clapeyron slope vary from $dp/dT \simeq 2.5 \text{ MPa K}^{-1}$ (Katsura and Ito, 1989) to $dp/dT \simeq 1.5 \text{ MPa K}^{-1}$ (Akaogi et al., 1989).

The P-wave velocity jump accompanying α olivine \rightarrow β -modified spinel has been estimated at 6.6% by Bina and Wood (1987); it is possible to account for the observed seismic velocity increase if the upper mantle is about 75% olivine. Thus, the experimental evidence supports the interpretation of the 410 km seismic discontinuity as the α olivine \rightarrow α olivine + β -modified spinel \rightarrow β -modified spinel phase transformation. The topography of the 410 km seismic discontinuity has been mapped by Flanagan and Shearer (1998a, b, 1999) as discussed further below.

The degree to which the olivine composition accounts for seismic velocities through the transition zone is shown in Figure 3.14, which compares equation of state calculations by Bina and Wood (1987) with PREM seismic velocities. The variation in seismic velocity can be well represented by a uniform composition from a depth of 410 km to the depth of the 660 km seismic discontinuity. A similar comparison has been made by Weidner (1985) using a pyrolite model composition, with the same result: there is no compelling reason to invoke compositional variation to explain the transition zone structure above a depth of 660 km.

However, this does not mean that compositional variations are necessarily absent in the transition zone. The seismic properties of other mantle compounds are similar to those of olivine at transition zone pressures. This is the case for pyroxenes, the second most abundant mineral in the upper mantle. There are several pressure-induced phase transformations in pyroxenes that are relevant to transition zone structure (Akaogi et al., 1987). At high temperatures, enstatite transforms to majorite, an Al-deficient garnet structure; at low temperatures, the transformation is from enstatite to β spinel plus stishovite (the high-pressure quartz polymorph, SiO_2 with Si in sixfold coordination), then to γ spinel plus stishovite.

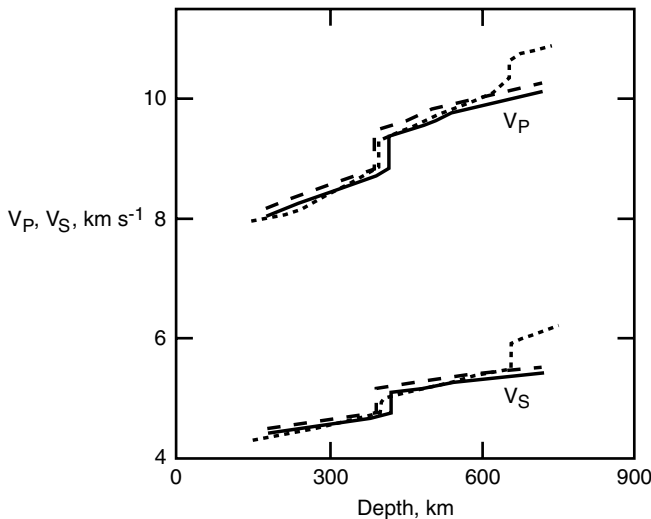


Figure 3.14. Depth profiles of V_P and V_S in the transition zone given by Bina and Wood (1987) for $X_{\text{Mg}} = 90$ olivine composition along 1,700 K (dashed) and 2,000 K (solid) isotherms. Dotted curves are the regionalized velocity profiles for North America given by Grand and Helmberger (1984a,b).

The approximate stability fields are shown in Figure 3.15. Elastic velocities are not as well determined for the pyroxene system as for the olivine system, but it is likely that pyroxenes would not appreciably change the seismic velocity profiles in Figure 3.14 if they were present in levels less than 30%. Thus, small variations in the relative abundance of olivine and pyroxene through the transition zone cannot be excluded.

Phase transformations in the pyroxene system are not expected to be as sharp as those in the olivine system, because pyroxene compounds accommodate greater amounts of “minor abundant” cations, such as Ca and Al, and these tend to spread out phase changes over a wider pressure interval. By virtue of their sharpness, transformations in olivine compounds can produce seismic discontinuities in the mantle, whereas transformations in pyroxenes are too gradual. Thus, the phase changes in olivine may be responsible for the 410 km and 660 km seismic discontinuities, while phase changes in pyroxene may account for the steep velocity gradients elsewhere in the transition zone (Figure 3.3).

3.5.2 The 660 km Seismic Discontinuity

The seismic discontinuity near 660 km depth contains the sharpest changes in seismic properties within the mantle. Over an interval of about 5 km or perhaps even less, V_P and V_S increase by 0.4–0.6 and 0.3–0.4 km s^{-1} , respectively, and the density ρ increases by about 400 kg m^{-3} , or about 9% according to Earth model PREM.

The sharpness of this interface was originally inferred from observations of underside reflections, precursors to the seismic phase $P'P'$ (PKPPKP). Richards (1972) and Benz and Vidale (1993) have used $P'P'$ precursor amplitudes to infer a thickness of 4 km or less for the seismic discontinuity. Lees et al. (1983) argued that such reflections would not occur if the thickness of the seismic discontinuity were much greater than a few kilometers. The interpretation of $P'P'$ precursors as underside reflections from the 660 km seismic discontinuity

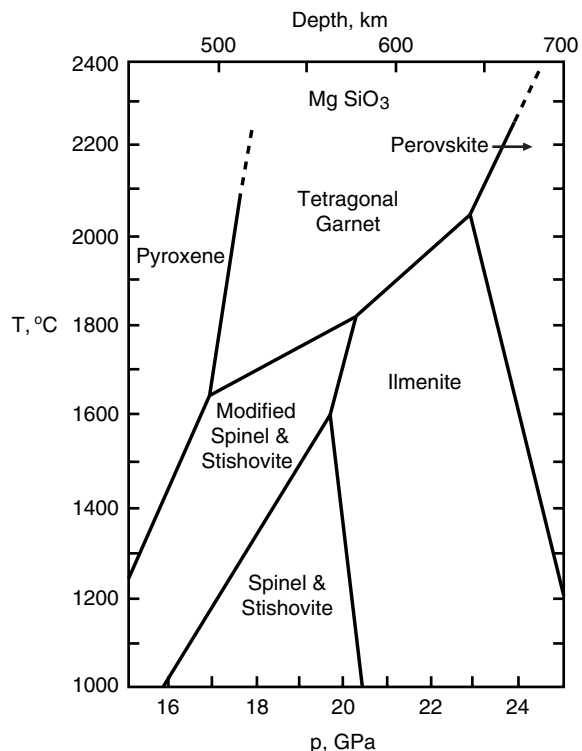


Figure 3.15. Phase stability fields in temperature-pressure coordinates for MgSiO₃. After Sawamoto (1987).

has been questioned (Estabrook and Kind, 1996), but the conclusion that this discontinuity occurs over a very narrow pressure range persists.

In the literature, this seismic discontinuity is variously located between depths of 650 km and 670 km. The discrepancy is partly an indication of the difficulty in determining its absolute depth precisely, and partly due to lateral variations in its absolute depth (Shearer and Masters, 1992). In this text, we shall refer to it simply as the “660 km seismic discontinuity.”

Question 3.4: What is the nature of the 660 km seismic discontinuity?

The composition of the transition zone in general, and the nature of the 660 km seismic discontinuity in particular, represents one of the most important constraints on any model of mantle convection. No other part of the structure of the mantle has been subject to as much interpretation and conjecture. The seismicity of the Earth terminates abruptly near this depth, a fact that many geophysicists interpreted to mean that subducted lithospheric slabs are unable to penetrate across the discontinuity, and thus remain in the upper mantle. This interpretation led to the idea of a two-layer mantle, in which the 660 km seismic discontinuity divides the mantle into two convecting regions, with only limited mass transfer occurring across the discontinuity.

What property of the 660 km seismic discontinuity would make it possible to stop subducted slabs from entering the lower mantle? Models of mantle convection described in Chapter 9 indicate that the endothermic pressure-induced phase transformations near 660 km

depth inhibit slab penetration, but do not provide a permanent barrier. In addition, the inferred increase in viscosity near this depth discussed in Chapter 5 may affect the structure of the flow by causing slabs to decelerate and buckle, but would not prevent them from sinking into the lower mantle. Only an intrinsic density increase, due to changes in bulk composition, can provide a sufficiently strong restoring force to keep negatively buoyant lithosphere in the upper mantle. Thus, the dynamical significance of the 660 km seismic discontinuity revolves around the question of whether it is simply a phase transformation, or whether there is also a change in bulk composition.

Question 3.5: Is the composition of the lower mantle different from that of the upper mantle?

There are basically two methods to approach the problem of determining lower mantle composition, and both require making a priori assumptions about upper mantle composition. One method involves experimental determinations of the phase equilibrium diagram for the important mantle assemblages over the pressure and temperature range of the 660 km seismic discontinuity, leading to the determination of which composition has the phase transformation properties that best explain the observed depth and structure of the seismic discontinuity. The other method is to subject assumed upper mantle compositions to the pressures and temperatures of the lower mantle, and determine if any such compositions are consistent with lower mantle seismic properties over the wide pressure range of the lower mantle. Both approaches have been tried, but only recently have there been enough mineral property data to make them meaningful. Previously, models of lower mantle mineralogy were heavily influenced by Birch's "mixed oxide" proposal, in which stishovite SiO_2 and magnesiowüstite ($\text{Mg}, \text{Fe}\text{O}$) were presumed to be the dominant phases. It was found that the lower mantle is a few percent denser than an oxide mixture that is isochemical with pyrolite (Ringwood, 1970; Davies and Dziewonski, 1975). This difference was interpreted as being due to iron enrichment in the lower mantle relative to the upper mantle (Anderson, 1970).

The situation changed with the discovery by Liu (1974) of a high-density silicate perovskite structure for MgSiO_3 . Since then, it has been shown that nearly all mantle silicates transform to the perovskite structure at lower transition zone pressures. Since the density of MgSiO_3 -perovskite is 3–5% higher than the isochemical oxide mixture, the presence of silicate perovskites below the 660 km seismic discontinuity removes the requirement for a large increase in lower mantle iron content in order to reconcile upper mantle composition with lower mantle seismic properties. However, there is still room for a small difference between the iron and silica contents of the upper and lower mantle.

Experimental work on the high-pressure phase diagram of mantle silicates and their transformation to perovskite structures involves diamond anvil pressure devices and, particularly in Japan, large-volume split-anvil pressure devices. Figure 3.16 shows phase diagrams for the olivine system in the pressure range 22–26 GPa, at 1,373 K and 1,873 K, as determined by Ito and Takahashi (1989). γ spinel with an upper mantle composition $X_{\text{Mg}} \simeq 89$ transforms to a mixture of magnesium perovskite and magnesiowüstite over a very small pressure interval, less than 0.15 GPa, which corresponds to 4 km or less in depth. Unlike the exothermic olivine–spinel reaction, this reaction is endothermic and has a negative Clapeyron slope, $dp/dT \simeq -2.5 \text{ MPa K}^{-1}$ (Ito and Takahashi, 1989; Bina and Helffrich, 1994). The reaction

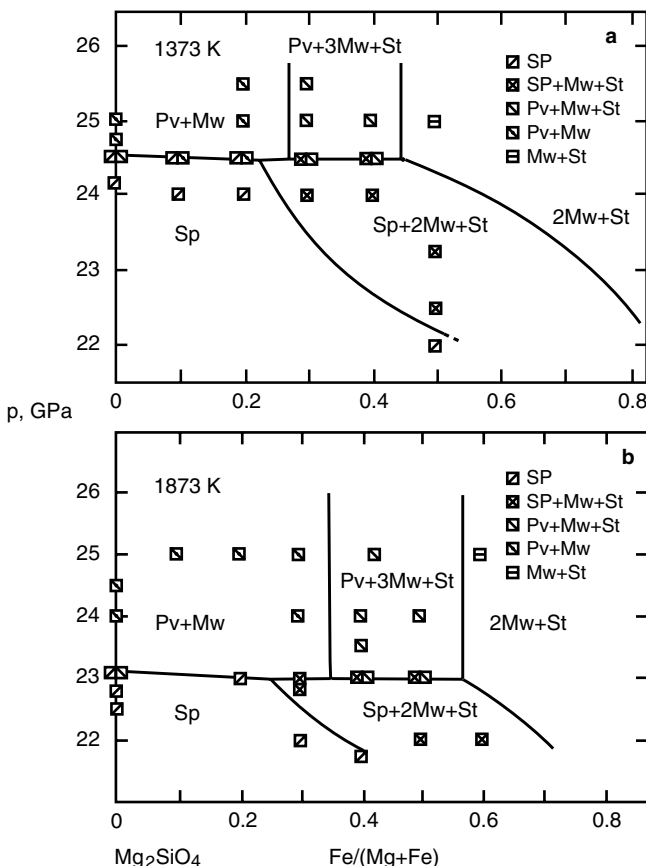


Figure 3.16. Phase diagram for the system $(\text{Mg}, \text{Fe})_2\text{SiO}_4$ between 22 and 26 GPa at (a) 1,373 K and (b) 1,873 K, determined by Ito and Takahashi (1989). Sp = spinel, Pv = perovskite structures, Mw = magnesiowüstite, St = stishovite.

pressure is nearly independent of iron content for $100 > X_{\text{Mg}} > 80$, the full range of possible mantle compositions. At 1,873 K, a reasonable estimate for the average temperature of that region of the mantle, the phase change occurs at 23.1 GPa, almost precisely at a depth of 660 km. At 1,373 K, more representative of temperatures in a subducting slab, the reaction occurs at 24.5 GPa, approximately 40 km deeper. This variation is nearly equal to the seismically observed variation of depths to the seismic discontinuity. Shearer and Masters (1992) and Flanagan and Shearer (1998a) have mapped the large-scale topography of the discontinuity (Figure 3.17), and find nearly 30 km of relief with the greatest depressions located beneath subduction zones. Detailed seismic studies of the depth of the 660 km seismic discontinuity beneath the Tonga (Richards and Wicks, 1990; Niu and Kawakatsu, 1995) and Izu-Bonin (Vidale and Benz, 1992; Wicks and Richards, 1993; Castle and Creager, 1997) slabs indicate depressions of the discontinuity up to 50–60 km below its nominal depth. These results offer a compelling argument that the 660 km seismic discontinuity marks the transformation of γ spinel to magnesium perovskite and magnesiowüstite in the olivine system. They argue strongly against the association of a major chemical compositional change with the 660 km seismic discontinuity since a chemical discontinuity should be locally dynamically

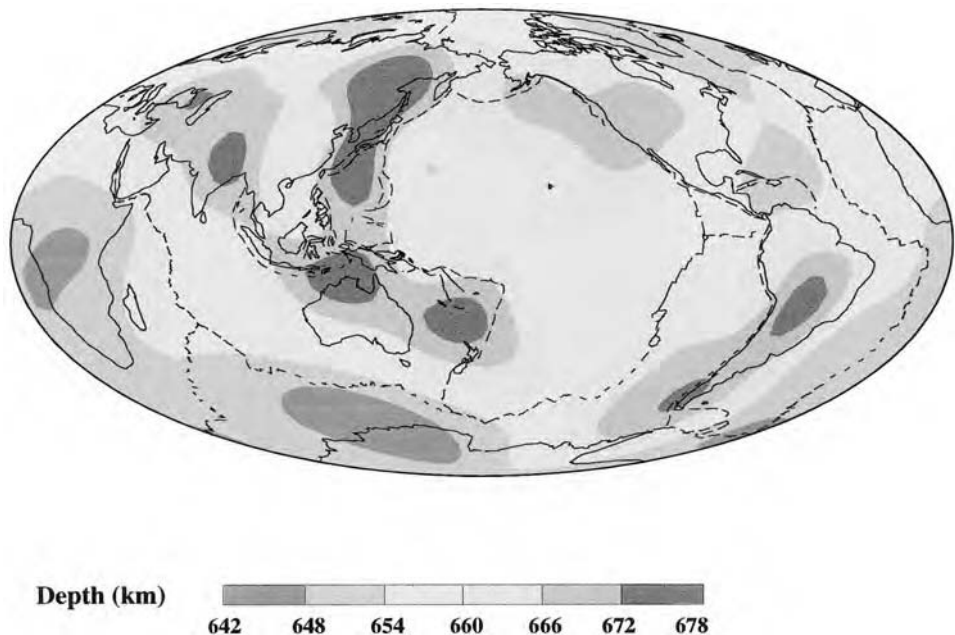


Figure 3.17. Depth of the 660 km seismic discontinuity. After Flanagan and Shearer (1998a).

For a color version of this figure, see plate section.

depressed by 100–300 km in subduction zones (Christensen and Yuen, 1984; Kincaid and Olson, 1987).

Perovskite-forming reactions also occur in the more silica-rich pyroxene system, but as is found for α olivine \rightarrow β -modified spinel reactions, the presence of Ca and Al tends to spread these reactions over a wider pressure interval. The reaction of greatest interest is garnet dissociating to MgSiO_3 and CaMgSiO_3 perovskites plus Al_2O_3 . This transformation begins at approximately the same pressure as in the olivine system, but it occurs over a broad pressure range, about 2–3 GPa (Irfune and Ringwood, 1987; Ito, 1989), and consequently it is spread out over a 50–100 km depth interval in the mantle below the 660 km seismic discontinuity. We conclude that the combination of perovskite-forming reactions in olivine and pyroxene systems can account for most of the fine structure in the lower portion of the transition zone contained in seismic Earth models such as PREM. The olivine reaction produces the reflecting discontinuity at 660 km depth, and the pyroxene reactions produce the region of high velocity gradients extending down to about 750 km depth, as shown in Figure 3.3.

While it is possible to explain the 660 km seismic discontinuity by perovskite-forming reactions, there is evidence for subtle compositional variations located somewhere within the transition zone. Over most of the pressure range of the lower mantle, from about 30 to 110 GPa, the Adams–Williamson condition (3.2.9) is satisfied to within 1% (Shankland and Brown, 1985) and the assumptions of homogeneity and adiabaticity are valid to a good approximation. It is therefore possible to determine if particular models of upper mantle composition, subjected to lower mantle pressures and temperatures, match the profiles of seismic velocity and density through the lower mantle. In order to make this comparison, it

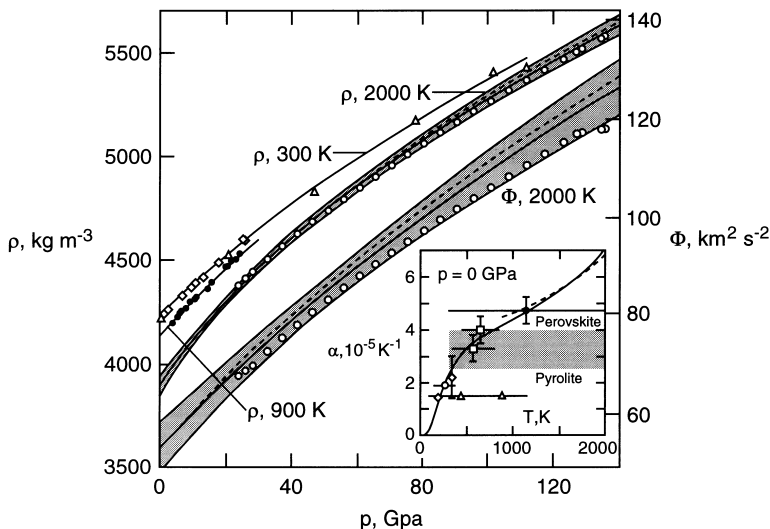


Figure 3.18. Comparison of density ρ and seismic parameter Φ in $(\text{Mg}_{0.9}\text{Fe}_{0.1})\text{SiO}_3$ perovskite with ρ and Φ in the lower mantle (modified from Stixrude et al., 1992). Perovskite density measurements at room temperature (300 K) are shown as open diamonds and triangles; measurements at 900 K are shown as solid circles. Solid and dashed lines represent extrapolations using equations of state fits to the data for various temperatures. Open circles represent Earth model PREM – the upper set is ρ , the lower set is Φ . There is relatively good agreement between the data and the extrapolated values for perovskite at the 2,000 K adiabat. The inset shows the zero-pressure dependence of thermal expansion on temperature used in the extrapolation. The shaded region separates values consistent with a perovskite lower mantle from those that are consistent with a pyrolyte lower mantle. These results suggest that silicate perovskite is the dominant lower mantle phase.

is necessary to have an accurate equation of state for silicate perovskite and magnesiowüstite at high pressures, including a thermal expansion correction for the higher temperatures in the lower mantle.

Knittle et al. (1986) inferred a large thermal expansivity for the perovskite structure in the lower mantle, in the neighborhood of $4 \times 10^{-5} \text{ K}^{-1}$, based on extrapolations of measurements made at low pressures and temperatures. With this value, Jeanloz and Knittle (1989) concluded that the pyrolyte model of upper mantle composition matches the PREM density profile in the lower mantle only if the temperature is low, in the neighborhood of 1,500 K. More likely temperatures, in excess of 2,000 K, imply that the pyrolyte model composition is less dense than the lower mantle, by about $4 \pm 2\%$, according to their analyses. This interpretation is far from certain, however, in part because pressure acts to reduce the thermal expansivity of perovskite, making it difficult to distinguish between it and magnesiowüstite on the basis of density alone (Chopelas and Boehler, 1992).

A more complete comparison of magnesioperovskite with lower mantle density and seismic velocity is shown in Figure 3.18, from Stixrude et al. (1992). This comparison demonstrates that a pure perovskite composition matches both the density and the bulk sound velocity of the lower mantle, at realistic lower mantle temperatures. In contrast, Stixrude et al. (1992) find that a pyrolyte (olivine-rich) upper mantle composition does not fit the seismically observed profiles as well. The implication is that the lower mantle may be mostly perovskite ($\text{Mg}, \text{Fe}\text{SiO}_3$), and therefore enriched in silica with respect to the dominantly olivine ($\text{Mg}, \text{Fe}\text{SiO}_4$) upper mantle.

These types of comparisons depend critically on mineral properties such as thermal expansivity and on the temperature in the transition zone, which is also uncertain. In addition, they do not determine where in the mantle the compositional change occurs. They do, however, constrain the range of possible density increases due to compositional stratification to lie within the limits 0–4%. Unfortunately, even this narrow range encompasses a wide spectrum of dynamical behaviors. If the stratification is low, corresponding to a density increase of 2% or less, compositional stratification is not likely to prevent subducting slabs from sinking into the lower mantle. At the upper limit, where the density increase due to composition is 4%, the stabilizing effect of chemical buoyancy is as great or greater than the destabilizing effect of thermal buoyancy, and subducted slabs would not sink deep into the lower mantle. In the intermediate range, it might be possible for some slabs to sink into the lower mantle, while others might be deflected in the transition zone. The evidence from seismic tomography discussed later in this chapter indicates that some slabs do sink into the lower mantle, while others appear to be deflected. This highlights why a precise knowledge of phase and compositional changes through the transition zone is so critical in determining the structure of mantle convection.

Better resolution of the seismic discontinuities and other fine structure in the transition zone continues to be an important goal of seismology. In addition to the seismic discontinuities at 410 and 660 km depth already discussed, there is evidence for another near 520 km depth. The 520 km seismic discontinuity is seen in topside reflections following P and S (Shearer, 1990, 1991), in underside reflections preceding SS (Shearer, 1991, 1996), and in ScS reverberations (Revenaugh and Jordan, 1991). However, the 520 km seismic discontinuity has not been detected in refraction studies. All of the seismic data are consistent with a global 520 km seismic discontinuity if the feature is spread out over a depth interval of 10–50 km and has changes in seismic velocities small enough to have avoided detection in routine seismic refraction studies (Shearer, 1996). The observations of the 520 km seismic discontinuity constrain the change in seismic impedance (product of seismic velocity and density) across the discontinuity to lie between about 2 and 4%. Most of the impedance change must occur in density rather than seismic velocity to account for the lack of detection of the 520 km seismic discontinuity in refraction studies. Shearer (1996) suggests that the known properties of the β -modified spinel \rightarrow γ spinel phase change are consistent with the seismic observations of the 520 km discontinuity.

The global topography of the 520 km discontinuity has been determined by Flanagan and Shearer (1998a); though subject to considerable uncertainty, the discontinuity appears to be elevated in the north and south central Pacific and depressed in the mid-Pacific. Flanagan and Shearer (1998a, 1999) also report on the large-scale topography of the 410 km seismic discontinuity which is lower in amplitude and largely uncorrelated with the topography in the 660 km discontinuity. In the vicinity of subduction zones there is little change from the average depth of the 410 km discontinuity, though depth variations perpendicular to the strike of the Tonga slab are as large as about 30 km and consistent with the elevation of the olivine– β -modified spinel phase boundary in cold regions (Flanagan and Shearer, 1998b).

3.6 The Lower Mantle

The lower mantle is 70% of the mass of the solid Earth and nearly half of the mass of the entire Earth. It is marked by a smooth variation in seismic properties with depth, a fact that was instrumental in the success of early spherical Earth models. Beneath the transition zone

and extending to within 300 km of the core–mantle boundary (CMB), a degree of uniformity prevails that is found nowhere else in the mantle. Early seismic array studies (Johnson, 1967) suggested small departures from isentropic conditions, in the form of subtle higher-order discontinuities. The trend of recent spherical models, however, is toward ever more homogeneity in the lower mantle, with the important exception of the layer D'' just above the core. As an illustration, Figure 3.19 shows the difference between the Bullen inhomogeneity parameter η and unity for three spherical Earth models (see also Brown and Shankland, 1981). The Bullen inhomogeneity parameter η is defined as

$$\eta \equiv \frac{K_a}{\rho} \frac{d\rho}{dp} = \Phi \frac{d\rho}{dp} \quad (3.6.1)$$

From (3.2.7) it is seen that $\eta = 1$ for isentropic conditions. Equation (3.6.1) can be rewritten using the hydrostatic relation (3.2.8) as

$$\eta = \frac{-K_a}{\rho^2 g} \frac{d\rho}{dr} = \frac{-\Phi}{\rho g} \frac{d\rho}{dr} \quad (3.6.2)$$

If we consider ρ as a function of temperature T and pressure and write

$$\frac{d\rho}{dr} = \left(\frac{\partial \rho}{\partial T} \right)_p \frac{dT}{dr} + \left(\frac{\partial \rho}{\partial p} \right)_T \frac{dp}{dr} \quad (3.6.3)$$

then (3.6.2) can be further transformed using (3.6.3), (3.2.5), (3.2.8), and thermodynamic relations from Chapter 6 ((6.6.2), (6.6.3), (6.6.33), (6.6.34), (6.7.19)) into

$$\eta - 1 = \frac{\alpha \Phi}{g} \left\{ \frac{dT}{dr} - \left(\frac{dT}{dr} \right)_a \right\} \quad (3.6.4)$$

where α is the thermal expansivity and $(dT/dr)_a$ is the adiabatic temperature gradient. For isentropic conditions it is again seen from (3.6.4) that $\eta = 1$. The quantity $\eta - 1$ is zero in a homogeneous isentropic region, it exceeds zero in regions with subadiabatic or stabilizing temperature gradients (since dT/dr is normally negative in the mantle and dT_a/dr is negative, subadiabaticity means $-dT/dr < -(dT/dr)_a$ or $dT/dr > (dT/dr)_a$ and $\eta - 1 > 0$), and it is less than zero in regions with destabilizing or superadiabatic temperature gradients (superadiabaticity means $-dT/dr > -(dT/dr)_a$ or $dT/dr < (dT/dr)_a$ and $\eta - 1 < 0$). From (3.2.6) and (3.6.1) the quantity $\eta - 1$ can also be written:

$$\eta - 1 = \frac{d\rho}{d\rho_a} - 1 \quad (3.6.5)$$

where $d\rho_a$ is the adiabatic or isentropic density change in the radius interval dr . If non-isentropic conditions are due to compositional density gradients, then stable compositional stratification requires $-d\rho > -d\rho_a$ (since $d\rho/dr$ is normally negative in the mantle and $d\rho_a/dr$ is negative) or $d\rho_a > d\rho$ and $\eta - 1 > 0$. Unstable compositional stratification requires $-d\rho < -d\rho_a$ and $\eta - 1 < 0$. Whether due to temperature or composition, $\eta - 1 > 0$ means stability against overturning and $\eta - 1 < 0$ means instability. Seismic Earth models such as PREM closely approximate the homogeneous, isentropic limit $\eta = 1$, from 800 km depth down to the D'' layer (Figure 3.19). Within the limits of seismic resolution, the spherically averaged lower mantle is essentially homogeneous and isentropic.

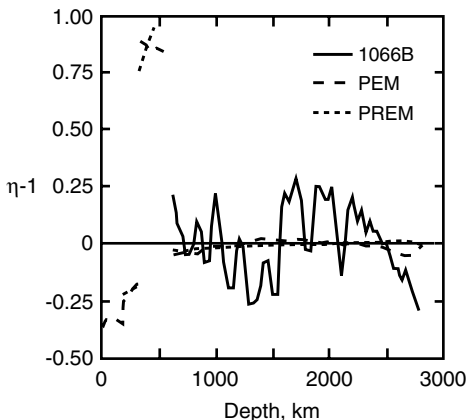


Figure 3.19. The difference between the Bullen inhomogeneity parameter η and unity through the mantle from three seismic Earth models (Shankland and Brown, 1985). The quantity $\eta - 1 = 0$ corresponds to a homogeneous, isentropic (well-mixed) state.

Why does the lower mantle appear so homogeneous in spherical Earth models? Part of the answer is the apparent absence of additional phase transformations at pressures higher than those in the transition zone. So, a mixture of silicate perovskite and magnesiowüstite can explain nearly all of the radial structure of the lower mantle. Ironically, this implies that magnesium silicate perovskite, a mineral unknown in the crust or mantle xenoliths, is the Earth's single most abundant mineral! The fact that Bullen's homogeneity index (Figure 3.19) is nearly unity through the lower mantle (apart from the D'' layer) indicates one of two possible states. The simplest state assumes uniform composition, and implies that the lower mantle has been homogenized by convective mixing. This assumption is implicit in the standard, whole mantle convection model.

The other possible state assumes that the lower mantle is nonuniform in both composition and temperature, but that their individual effects on Bullen's homogeneity index tend to cancel each other. In this state the lower mantle would appear to be grossly homogeneous, even though it is stratified. Convection that results from a close balance between thermal and chemical buoyancy forces in a fluid is called thermochemical convection. A model for large-scale thermochemical convection in the lower mantle due to chemical stratification has been proposed by Kellogg et al. (1999), as a way of reconciling the evidence of deep slab penetration discussed in this chapter with the need for long-lasting mantle isotopic reservoirs discussed in Chapter 12. Some dynamical implications of thermochemical mantle convection are discussed in Chapters 9 and 10.

3.7 The D'' Layer and the Core–Mantle Boundary

Question 3.6: Is the D'' layer a purely thermal boundary layer or does it have a compositional component?

A portion of the lower mantle that is definitely not homogeneous is the 300 km above the CMB, the so-called D'' layer. One of the most critical regions in the Earth in terms of geodynamical processes, it governs the interaction between the core and the mantle; it may also be the source of deep mantle plumes, a zone of active chemical reactions, and an

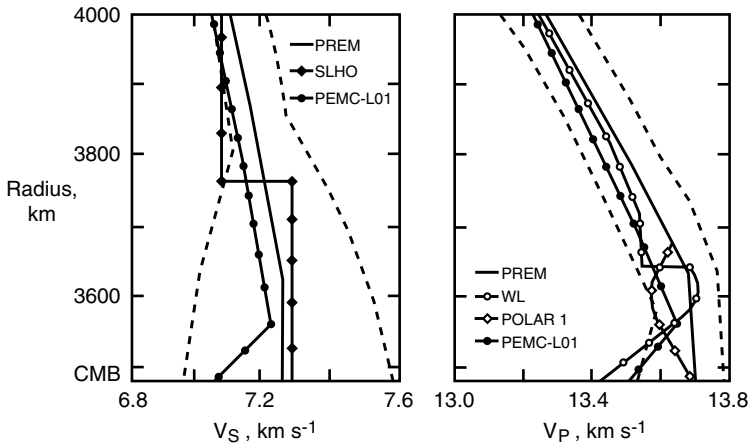


Figure 3.20. Profiles of V_S and V_P through the D'' region, including models PREM (Dziewonski and Anderson, 1981), SLHO and WL (Young and Lay, 1987), PEMC-L01 (Doornbos and Mondt, 1979), and POLAR 1 (Ruff and Helmberger, 1982). The dashed lines delineate an approximate envelope of the V_S and V_P profiles. After Lay (1989).

important geochemical reservoir (Loper and Lay, 1995). The D'' layer is now considered to contain the hot, basal thermal boundary layer of mantle convection, and seismological evidence indicates it may also be compositionally distinct from the rest of the lower mantle.

It is remarkable how much is known about the core–mantle boundary region from seismology (see Wysession et al., 1998, for a review). The early Earth models of Jeffreys, Bullen, and Gutenberg included a region 100–200 km thick above the CMB with negative P- and S-wave velocity gradients. These structures seemed to be demanded by observations of waves diffracted along the CMB. Subsequent investigations using high-frequency diffracted body waves (Doornbos and Mondt, 1979) yielded models with a slightly negative velocity gradient through the 75–100 km interval just above the CMB, as shown in Figure 3.20. More recent seismic studies (Garnero and Helmberger, 1996) have provided additional resolution of this region, and indicate the presence of a laterally variable ultra-low velocity zone (ULVZ) immediately above the CMB, with a velocity reduction of about 10% relative to the overlying mantle and a thickness of 40 km or less. The ULVZ is present beneath the central Pacific but appears to be either vanishingly thin or missing in other regions, such as beneath the Americas. Its large, negative velocity anomaly and the apparent correlation between its thickness variations and the three-dimensional structure of the lower mantle as imaged by global seismic tomography (see Figure 3.32) has led to the interpretation that this zone represents accumulation of partial melts, and is perhaps the source of deep mantle plumes (Williams and Garnero, 1996). Vidale and Hedlin (1998) have reported unusually large amplitude precursors to PKP due to scattering from a 60 km thick layer at the CMB north of Tonga. This scattering patch of the CMB lies in the “Equatorial Pacific Plume Group” structure distinguished by low S-wave velocities in the bottom few hundred kilometers of the mantle (Su et al., 1994). It is also near very low P wave velocities just at the base of the mantle (Garnero and Helmberger, 1996) which have been interpreted as due to partial melt (Williams and Garnero, 1996). Accordingly, Vidale and Hedlin (1998) explain the strong scattering at this patch as due to partial melt and suggest accompanying vigorous small-scale convection. The existence of partial melt at the base of the mantle is consistent

with data on the melting of lower mantle material; Holland and Ahrens (1997) used shock compression measurements of a perovskite and magnesiowüstite assemblage to place an upper bound on the solidus temperature of the assemblage of $4,300 \pm 270$ K at 130 ± 3 GPa (approximately the pressure at the CMB).

Question 3.7: Is there partial melt at the base of the mantle?

But D'' contains more than just a low-velocity zone. Evidence for additional structure in D'' first came from a set of seismic phases intermediate between the phases S and SKS, which has been identified in several regional studies by Lay and others (Lay and Helmberger, 1983; Young and Lay, 1987, 1990; Weber, 1993) and interpreted as refractions from a seismic discontinuity with a 2–3% shear velocity increase located 250–300 km above the CMB. Figure 3.21 is a compilation by Nataf and Houard (1993) indicating that this discontinuity has since been delineated over large portions of the CMB. Figure 3.20 shows that the velocity profiles inferred for D'' have either a negative gradient or a reduced positive gradient relative to the spherical Earth model PREM. In order to match absolute travel times, models with this discontinuity often contain another layer with reduced shear velocity gradient above the discontinuity.

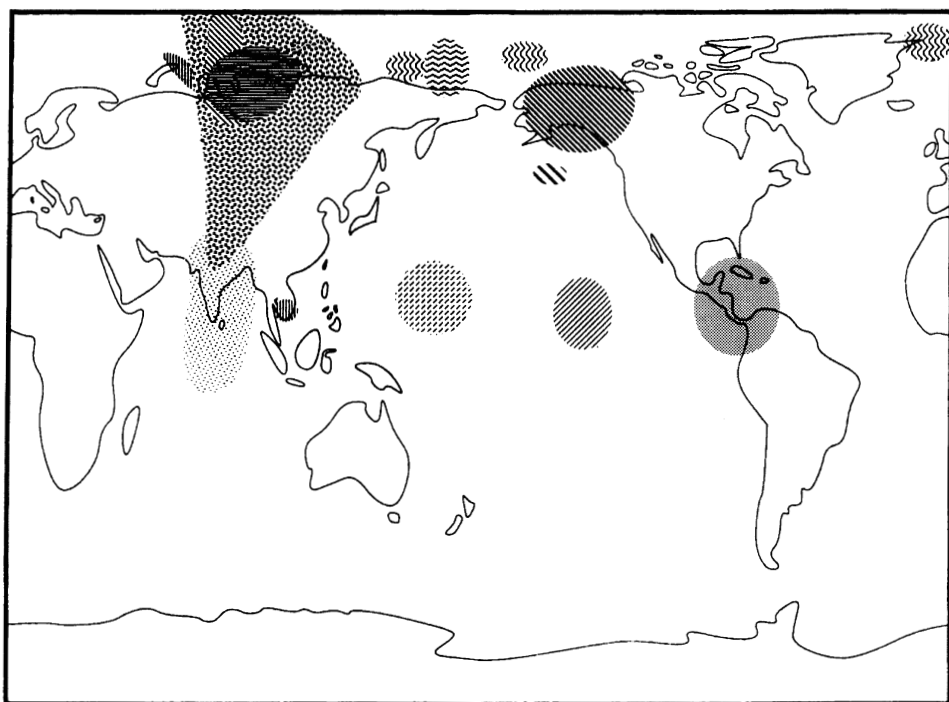


Figure 3.21. Composite map showing the different regions where a seismic discontinuity with a velocity increase has been detected at the top of D'' . Lightly shaded regions indicate small seismic velocity anomalies in D'' and darkly shaded regions indicate large seismic velocity anomalies. From Nataf and Houard (1993).

The seismic observations suggest a composite structure for D'', consisting of a sharp velocity increase located 150–300 km above the CMB, a layer with reduced velocity gradients just beneath, and the ULVZ just above the CMB. Reduced or even negative radial seismic velocity gradients are likely to be the result of the strongly superadiabatic temperature distribution in D''. This interpretation is supported by evidence for high seismic attenuation in D'' relative to the rest of the lower mantle (Shore, 1984). Low seismic velocities and high attenuation indicate that D'' is analogous to the LID–LVZ structure – a region with steep thermal gradients and perhaps partial melting. D'' and the LID–LVZ are, respectively, hot and cold thermal boundary layers produced by large-scale mantle convection (Verhoogen, 1973; Jones, 1977; Elsasser et al., 1979). However, some of the structure in D'' is likely to be compositional in origin (Loper and Lay, 1995). The discontinuity at the top of D'' might indicate a change in bulk composition, or alternatively it might represent an as yet unexplained pressure-induced phase change.

Global-scale variations in the thickness of the D'' layer are evident from the comparison of regional studies shown in Figure 3.20. In addition, there is also seismic evidence for heterogeneities in D'' distributed over shorter length scales. Scattering of high-frequency P waves indicates the presence of either roughness on the CMB or small-scale heterogeneities distributed within D'' (Haddon, 1982; Haddon and Buchbinder, 1987; Bataille and Flatté, 1988). The estimated wavelengths of the scatterers are in the range 20–200 km.

In addition to fine-scale heterogeneity in D'', long-wavelength topographic undulations of the CMB and variations of the thickness of D'' are expected. Broad-scale undulations of D'' and the CMB probably represent dynamic topography supported by stresses in the mantle that drive the convective motion. Dynamic calculations predict that mantle convection supports variations of several kilometers on the CMB (Hager and Richards, 1989; Forte et al., 1993). There have been numerous attempts to map dynamic topography on the CMB using the techniques of seismic tomography; these will be discussed later in this chapter.

The significance of the broad spectrum of heterogeneity in D'' and CMB topography derives from the fact that these cannot be static features. They must be dynamically supported by nonhydrostatic stresses in the lower mantle. Unsupported CMB topography would be expected to relax on a short time scale considering the rheology at the high temperatures in D''. Since the lifetime of unsupported topography is short, such topography must be supported dynamically and this implies a close connection between the pattern and amplitude of CMB and D'' undulations and the pattern of flow in the lower mantle, both at short and long wavelengths. The fact that heterogeneity is present on many scales indicates that the dynamical processes in D'' are multi-scale in character, and involve both thermal and compositional effects.

3.8 The Core

Seismic evidence for the outer core was first provided by Oldham (1906), who interpreted the shadow zone between epicentral angles 100° and 120° as a low-velocity shell from the Earth's center out to about 3,000 km radius. Gutenberg (1913) estimated the core radius at 3,471 km, within 0.5% of the presently accepted value $3,485 \pm 3$ km (Engdahl and Johnson, 1974). The inner core was discovered by Lehmann (1936), who recognized that seismic compressional waves traversing the inner core, the phase PKIKP, require a discontinuous increase in V_P near 1,220 km radius. Bullen (1946) interpreted this increase as the effect of finite rigidity, implying that the inner core is solid. The mean radius of the inner core is currently estimated at $1,216 \pm 3$ km (Souriau and Souriau, 1989).

Liquidity of the outer core was first established using solid Earth tide amplitudes and the period of the Chandler wobble (Jeffreys, 1929) and has been substantiated by the complete lack of evidence for shear wave transmission. However, the direct demonstration of inner core rigidity – an observation of shear wave propagation through the inner core via the phase PKJKP – is still controversial. The inner core rigidity indicated by the nonzero V_S in Figure 3.2 is inferred from normal mode frequencies that are particularly sensitive to core structure. It is interesting that the modern estimate for the inner core seismic shear velocity is within 10% of Bullen's (1946) original estimate. Poisson's ratio is evidently about 0.4 in the inner core, which is quite large in comparison with 0.24–0.26 found elsewhere in the solid Earth. For an ideal solid, with $V_P = V_S\sqrt{3}$, Poisson's ratio is 0.25, and is 0.5 in the liquid outer core. Metals typically have large Poisson ratios at high pressure, another indication of the metallic nature of the core.

Within the resolution of spherical Earth models, both the outer core and the inner core appear radially homogeneous, except perhaps in the neighborhood of the inner core boundary (ICB), where the inhomogeneity parameter η deviates from unity. Both of the core boundaries appear to be sharp. The CMB is no wider than 10 km (Engdahl et al., 1974) and the ICB is even sharper – probably 3 km or less. The density jump at the ICB, of great significance for core composition and for powering the geodynamo, has been estimated by Masters and Shearer (1990) to be $550 \pm 150 \text{ kg m}^{-3}$.

At seismic frequencies, the outer core shows practically no damping. Qamar and Eisenberg (1974) have estimated $Q \simeq 5,000$ from P waves multiply reflected off the underside of the CMB, while Cormier and Richards (1976) argue for an even larger value. The inner core is quite different in that respect. Doornbos (1974) obtained a Q profile from 1 Hz P waves that increases from 200 just beneath the ICB to near 2,000 at the Earth's center. Attenuation of radial normal modes requires a Q of about 200 near the ICB, rising to near 1,000 at the Earth's center (Masters and Shearer, 1990). The inner core is also seismically anisotropic, and this property has led to a discovery with important implications for the operation of the geodynamo. Seismic waves propagating through the inner core travel a few percent faster along the north–south direction than along paths through the equator (Poupine et al., 1983; Souriau and Romanowicz, 1997). When this difference was first recognized, the initial interpretation was that the inner core is transversely anisotropic, with a seismically fast axis aligned with the Earth's rotation axis (Morelli et al., 1986; Shearer et al., 1988; Creager, 1992; Song and Helmberger, 1993). Subsequently, Su and Dziewonski (1995) showed that a better fit to the data is obtained by allowing the axis of anisotropy to be inclined to the rotation axis by about 10° , although Souriau et al. (1997) question the reliability of the tilt determination. Explanations for the cause of inner core anisotropy include crystal alignment due to freezing controlled by the magnetic field (Karato, 1993), a simple large-scale inner core convection pattern (Romanowicz et al., 1996), or stress-induced texture accompanying heterogeneous growth (Yoshida et al., 1996).

The small deviation of the seismically fast axis from rotational alignment provides an explanation for reports of secular variation in travel times of seismic waves traversing the inner core (Song and Richards, 1996). Rotation of the inner core relative to the crust and mantle would change the inner core velocity structure along a given ray path, so that the travel times of waves from earthquakes originating from the same focal region and recorded at the same station would change with time. On this basis, Song and Richards (1996) inferred a 1° yr^{-1} prograde (eastward) anomalous rotation of the inner core and Su et al. (1996) inferred an even larger inner core prograde rotation, nearly 3° yr^{-1} . However, re-examination of the problem by Souriau et al. (1997) and by Laske

and Masters (1999) suggests caution in accepting the reality of inner core differential rotation.

The possibility that the inner core might rotate at a slightly different rate than the crust and mantle was first pointed out by Gubbins (1981), who argued that the low viscosity of the outer core fluid decouples the inner core from the silicate portion of the Earth, and that electromagnetic torques applied to the inner core can easily support anomalous rotation. One of the striking features of the convective dynamo simulations of Glatzmaier and Roberts (1995, 1996) is a prediction of anomalous prograde inner core rotation, at approximately one degree per year. In the Glatzmaier–Roberts dynamo simulations, strong prograde (eastward) flow occurs in the outer core fluid adjacent to the ICB, driven by large-scale density variations. The inner core responds to flow in the outer core through electromagnetic coupling (Aurnou et al., 1996) and also responds to mantle heterogeneity through gravitational coupling (Buffett and Glatzmaier, 2000). Thus, the inner core motion is a sensitive indicator of the torque balance near the Earth’s center.

Recent analyses of PKP phases traveling along east–west paths have revealed more detail about seismic heterogeneity and anisotropy in the inner core (Tanaka and Hamaguchi, 1997). P-wave velocities in the outermost 100–500 km of the inner core show a degree 1 heterogeneity with relatively fast velocities in an “eastern” hemisphere and slow velocities in a “western” hemisphere. Analysis of PKP phases traveling nearly parallel to the Earth’s spin axis revealed significant anisotropy only in the “western” hemisphere. The east–west hemispheric asymmetry in P-wave velocity and seismic anisotropy may be related to core dynamics, i.e., patterns of convection in the outer core, during inner core solidification (Tanaka and Hamaguchi, 1997). Hemispheric differences in the seismic structure of the inner core were also found by Shearer and Toy (1991) and Creager (1992).

The average density in the core, approximately $11,000 \text{ kg m}^{-3}$, greatly exceeds the average mantle density, $4,500 \text{ kg m}^{-3}$, making it implausible that the core could be a high-pressure phase of the mantle. Yet it was not until 1963 that Birch (1963), using velocity–density systematics to show that the mean atomic weight of the core is only slightly less than the atomic weight of iron, demonstrated the core and mantle to be compositionally distinct.

The outer core is certainly an alloy of iron and lighter compounds. The inner core is richer in iron than the outer core, although it probably contains lighter alloys as well. Nickel has nearly the same physical properties as iron at high pressures (Mao et al., 1990), and consequently we have no way of determining the nickel content of the core. For purposes of discussion, we use the term “iron” to mean an iron-rich, nickel–iron alloy.

Lighter elements that could be abundant in the core include oxygen, silicon, and sulfur (Knittle and Jeanloz, 1986; Poirier, 1994a). Amounts of these elements that would individually satisfy the core density are 7, 21, and 11%, respectively. Silicon is the least likely among these, because in elemental form it is so far out of equilibrium with magnesiowüstite that it should have been absorbed into the lower mantle during core formation. The possibility of MgO solubility in liquid iron at core conditions was suggested by Alder (1966) but has not been pursued further. Thus, by the process of elimination, only oxygen and sulfur are now considered probable candidates. The likely compounds, in addition to iron–nickel, are FeO, FeS, and perhaps FeS₂.

Question 3.8: What is the composition of the core? What is the major light element in the core?

The energetics of the core and the consequences for mantle convection are described by Verhoogen (1980). As discussed in Chapter 13, all portions of the Earth, including the core, cool as the radioactive elements within the mantle decay. The ICB is associated with the liquid–solid phase transition for iron with the appropriate alloying elements. As the core cools, the pressure at which the liquid–solid phase change takes place decreases. Thus the ICB moves outwards and liquid iron in the outer core freezes and becomes part of the inner core. The liquid-to-solid phase change is exothermic so that heat is generated upon freezing. For each degree Kelvin of cooling the heat liberated by the phase change is approximately equal to the loss of heat associated with the cooling (Loper, 1978a; Stevenson, 1981). The rate of crystallization is about 10^6 kg s^{-1} if one assumes the inner core has grown steadily to its present size in 4 Gyr.

Braginsky (1963) was the first to emphasize how the release of potential energy accompanying inner core freezing could provide a power source for the geodynamo. As iron-rich material freezes onto the inner core, the rejected liquid is enriched in light components, and is buoyant with respect to the outer core liquid. Accordingly, it must rise and mix with the outer core. This motion, called thermochemical convection, is likely to be a dominant source of kinetic energy powering the dynamo. It has been shown theoretically that thermochemical convection is more efficient at dynamo action than purely thermal convection, in the sense that it requires a smaller heat loss from the core to produce the same amount of magnetic field energy (Loper, 1978a; Verhoogen, 1980). It is estimated that only about 5 TW of core heat loss is needed to sustain the dynamo by thermochemical convection and that compositional buoyancy provides 2–4 times more power to the dynamo than does thermal buoyancy (Cardin and Olson, 1992; Lister and Buffett, 1995).

The relative importance of thermal to compositional convection in the core depends on the magnitude of the density increase at the ICB that is due to the change in composition. The part of the density increase due to the phase change from liquid to solid was estimated by Verhoogen (1961) to be less than 300 kg m^{-3} , but this value is highly uncertain. The remainder, $250 \pm 150 \text{ kg m}^{-3}$, is evidently due to iron enrichment. This latter part is available to drive compositional convection.

Question 3.9: What is the relative importance of thermal and compositional convection in powering the geodynamo?

Direct information on the composition of the inner core and the outer core has come from high-pressure equation of state measurements on iron compounds at core pressures. Figure 3.22 shows the 300 K density of solid iron in the ε (hexagonal) phase versus pressure, as determined by Mao et al. (1990) from both static (diamond cell) and dynamic (shock wave) measurements. Also shown are density versus pressure curves for the Earth model PREM. Inner core density is less than the density of solid ε -iron at 300 K, and it is still less than the PREM density when the thermal expansion correction is applied. The most plausible explanation for the discrepancy is that the inner core also contains some of the light alloy present in the outer core. Jephcoat and Olson (1987) concluded that about 5% sulfur in the inner core and 10–12% in the outer core matches the PREM density profile. Alternatively, an inner core with about 3% oxygen and an outer core with 7–8% oxygen matches the PREM density equally well (Poirier, 1994a).

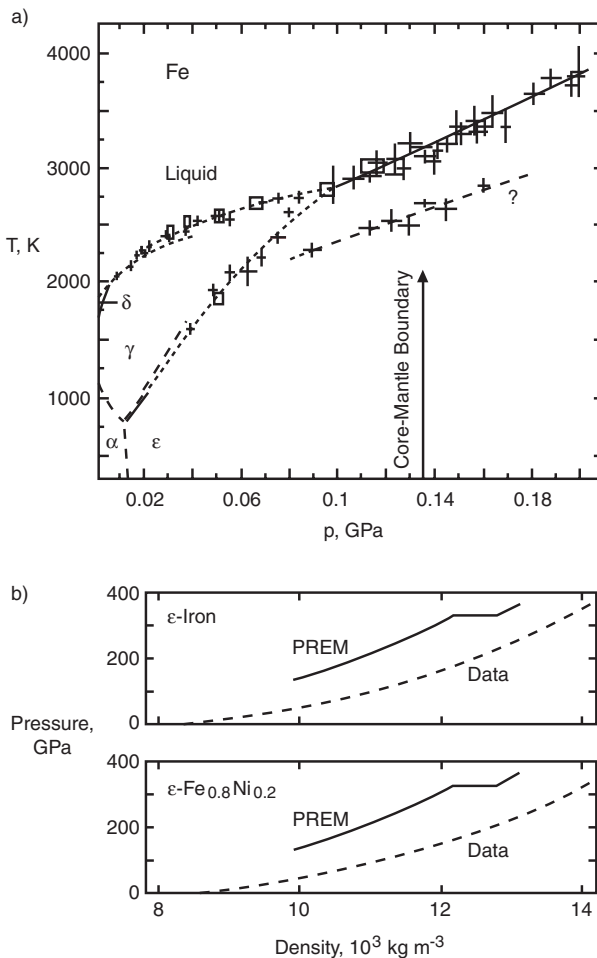


Figure 3.22. Equation of state data on iron at high temperature and pressure. (a) Experimentally determined phase diagram of iron, from Boehler (1993). The ϵ phase (hcp) appears to be the stable solid phase at core pressures. (b) Extrapolation of experimental pressure–density data for ϵ -iron and an iron–nickel alloy compared with Earth model PREM through the core, from Mao et al. (1990). Both the outer core and the inner core are systematically less dense than either metal. This discrepancy exists even after temperature corrections are applied, indicating that the core contains some lighter compounds.

3.9 Three-dimensional Structure of the Mantle

Until rather recently, global seismology was concerned almost entirely with the Earth’s radial structure. Lateral variations in seismic properties were recognized, but except for the upper 200 km or so, there was no systematic effort to resolve them on a global scale. Above 200 km depth there is a good correlation between seismic structure and large-scale tectonics, which is generally associated with variations in the structure of the lithosphere. For example, the LID is thickest beneath shields and platforms on continents and is practically nonexistent beneath spreading centers and continental regions with active extensional tectonics. The oceanic LID thickness varies with the square root of crustal age, as predicted by thermal boundary layer models of lithospheric cooling. All of this structure was anticipated on the basis of models

derived from other geophysical observations. Seismologists have now gone beyond this stage, and have provided three-dimensional images of the whole mantle. These images are obtained by a variety of techniques, collectively referred to as seismic tomography.

Lateral variations in seismic wave speeds must be related to the pattern of flow in the mantle. Horizontal (isobaric) differences in V_P and V_S result from differences in the elastic constants and density. These differences can be related to the horizontal gradients in density that drive mantle flows. In principle, well-resolved three-dimensional seismic images can provide important constraints on the body forces driving mantle convection. In practice, most of the interpretation of seismic tomographic images is qualitative and consists of a search for correlations with geological structure and other geophysical observables. Quantitative uses of seismic tomographic results have been made in some instances (see the discussion of mantle rheology in Chapter 5), but a number of simplifying assumptions must be made, and the validity of these assumptions has not been fully established.

The first limitation of seismic tomography is spatial resolution. Consider, for example, the problem of resolving the structure of subducted slabs located deep in the mantle, certainly one of the primary goals of this technique. The current resolution in global tomographic models is typically 500 km horizontally and 100 km vertically. Thus, velocity anomalies associated with deep slabs are likely to be smeared out.

Limits in lateral resolution affect the identification of structures directly related to the convection process. We know from the structure of subducted slabs that much of the lateral temperature heterogeneity in the upper mantle, and perhaps everywhere in the mantle, is concentrated in zones typically 100 km wide, the characteristic thickness of the oceanic lithosphere from which slabs are derived. Clearly, narrow slab structures are at the lower limit of what can be accurately resolved by global tomography. The situation for subducted slabs is improved somewhat by the fact that the earthquake density is high in the seismogenic part of slabs so that the resolution of fine structure around the Wadati–Benioff zones is better than for the mantle as a whole (van der Hilst et al., 1991). Still, some of the structures that are important in mantle dynamics may be missing from global tomographic models.

Another difficulty in interpreting seismic tomographic images is due to the fact that isobaric variations in seismic velocity are not simply related to density variations. Instead, they are sensitive to differences in composition and temperature, and to changes in phase (both solid–solid and solid–liquid), which are themselves dependent on composition and temperature. The problem is compounded when seismic velocity anomalies at different depths are compared, because of the sensitivity of V_P and V_S to changes in pressure. In short, quantitative applications of tomographic images involve uncertainties. However, this does not diminish the importance of the qualitative interpretation of tomographic images. Indeed, they are now one of the most compelling lines of evidence for the internal structure of mantle convection.

The data used in global seismic tomography include body wave travel times and waveforms, surface wave dispersion, and normal mode frequencies. The current generation of three-dimensional models has at its disposal several million travel times plus surface wave dispersion and waveform data over several thousand paths. Two different discretizations of the mantle are used. One divides the mantle into three-dimensional elements (boxes), and within each element, the perturbation of V_P or V_S from a spherical Earth model is calculated, based on the anomalous travel time or amplitudes along rays passing through the element. This technique was first used by Clayton and Comer (1983) and is the basis of the high-resolution models by Grand (1987, 1994) and by van der Hilst et al. (1991, 1997). The approach has also been used by Vasco and Johnson (1998), who employ arrival

times of 10 compressional and shear phases and two sets of differential times to infer the three-dimensional seismic velocity structure of the whole Earth from crust to inner core.

Alternatively, the anomalous seismic velocity distribution can be expressed as a truncated sum of spherical harmonics and orthogonal radial functions, as developed by Dziewonski (1984) and Woodhouse and Dziewonski (1984). The inversion procedure consists of solving for the coefficients of the radial functions for each spherical harmonic. This approach has been used to construct numerous global models of the entire mantle (Tanimoto, 1990; Su et al., 1994; Li and Romanowicz, 1996; Masters et al., 1996, among others).

Each approach has its merits and drawbacks. The element method computes the model only where there are sufficient data; however, the model is generally not complete and smooth. Truncated spherical harmonic representations result in a smooth and continuous model, but the model reliability is variable, particularly where the data are sparse. Normal modes have been used in two ways. Normal modes are split into $2l + 1$ separate frequencies (singlets) at each spherical harmonic degree l . The splitting is partly due to the Earth's rotation, through the Coriolis acceleration and the ellipticity. These effects can be calculated and their contribution removed from the data, leaving the splitting due to lateral structure. Only for the lowest degree modes has the splitting been measured, but they are a particularly useful data set because they are unbiased by baseline (timing) errors or uneven coverage (Dziewonski and Woodhouse, 1987). At larger spherical harmonic degrees splitting cannot be resolved, but there is a frequency shift relative to the frequency expected from a radially symmetric Earth model. Masters et al. (1982) used measurements of the frequency shift from fundamental mode Rayleigh wave spectra to deduce the presence of degree $l = 2$ heterogeneity.

Finally, long period surface and body wave data can be used in the time domain, by comparing seismograms from earthquakes with known source mechanisms to synthetic seismograms computed using radially symmetric Earth models. This is called the waveform method. None of these methods resolve the structure uniformly throughout the mantle. P-wave travel time anomalies are less useful for global studies of the upper mantle, and conversely, surface waves do not sample the lower mantle. Normal mode inversions discard the phase information and recover only the structure at even spherical harmonic degrees. Shear waves have proven to be particularly well suited to image the lower mantle, since their travel time anomalies are large.

Reviews of results of mantle tomography have been given by Woodhouse and Dziewonski (1989), Masters (1989), Hager and Clayton (1989), Romanowicz (1991), Montagner (1994), Ritzwoller and Lavelle (1995), and Kennett and van der Hilst (1998). Su and Dziewonski (1991) argue that long-wavelength heterogeneities are dominant in the mantle.

3.9.1 Upper Mantle Seismic Heterogeneity and Anisotropy

Figure 3.23 shows the perturbation in shear wave velocity at a depth of 210 km, relative to the spherical model PREM, obtained by Su et al. (1994). The range of velocity perturbations is quite large, $\pm 3\%$. The correlation of low shear wave velocity with the worldwide ridge system and the correlation of high shear wave velocity with continental shield and platform areas are both excellent. High shear wave velocities also occur beneath the oldest portions of the ocean basins. The depth extent of high-velocity roots beneath stable continental interiors and the extent of low-velocity roots beneath spreading centers can be inferred from the sequence of images at different upper mantle depths shown in Figure 3.24, from the S-wave model of Li and Romanowicz (1996). High shear wave velocity beneath the

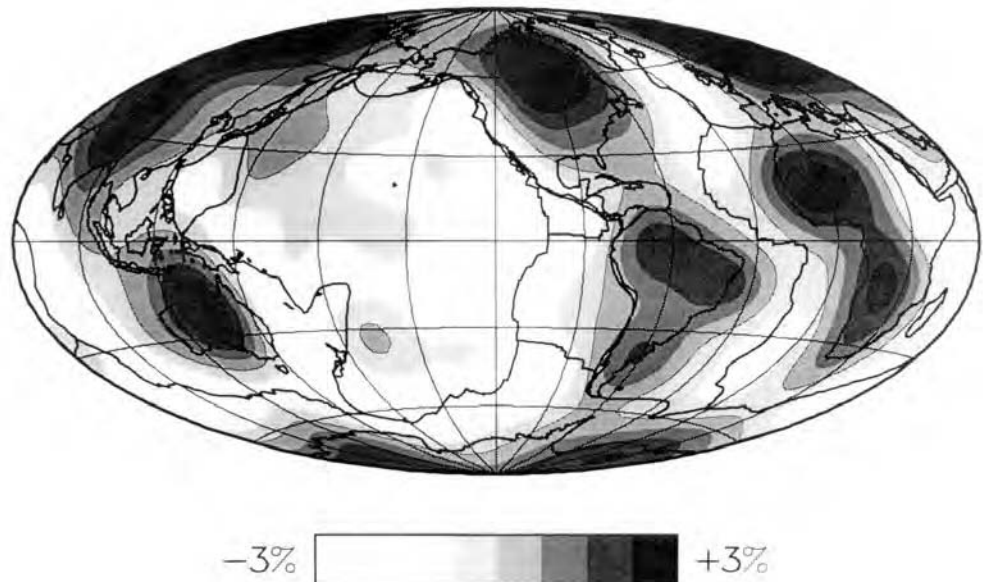


Figure 3.23. Perturbations in shear wave velocity V_s relative to the spherical Earth model PREM at a depth of 210 km complete to spherical harmonic degree 12, from the tomography model of Su et al. (1994).

Canadian shield and other continental shields is recognizable to 350 km depth. Low shear wave velocity beneath the global mid-ocean ridge system is nearly universal to 250 km depth and beneath the East Pacific, mid-Atlantic, and Antarctic ridges it appears to extend to 350 km depth.

The most important general finding from upper mantle seismic tomography is that the structure beneath the lithosphere is entirely compatible with a pattern of flow in the upper mantle constrained by plate motions. This establishes a direct connection between plate tectonics and the pattern of mantle convection. Ridges are associated with seismically slow mantle to a depth of at least several hundred kilometers. Seismic velocities beneath ridges are probably too low to be explained by excess temperature alone. More likely, there is a contribution from partial melting. The depth extent of the seismically slow region is not consistent with the upwelling of a completely adiabatic mantle. Some excess mantle temperature in the ridge root is required. However, the seismically slow region does not extend to great depths.

Question 3.10: How deep do the upwellings beneath mid-ocean ridges extend into the mantle? What are the implications for the passivity of mid-ocean ridges?

The high seismic velocities beneath stable continental interiors evident in Figures 3.23 and 3.24 offer a partial confirmation of Jordan's (1975, 1981) tectosphere concept. If these high-velocity roots also have high strength compared to other parts of the mantle at the same depth, they imply a relatively thick continental lithosphere. The global system of subduction zones, where positive shear wave velocity anomalies of 4% are known to exist, is not well resolved in Figure 3.24. Structures with lateral dimensions of the order of 100 km or less are

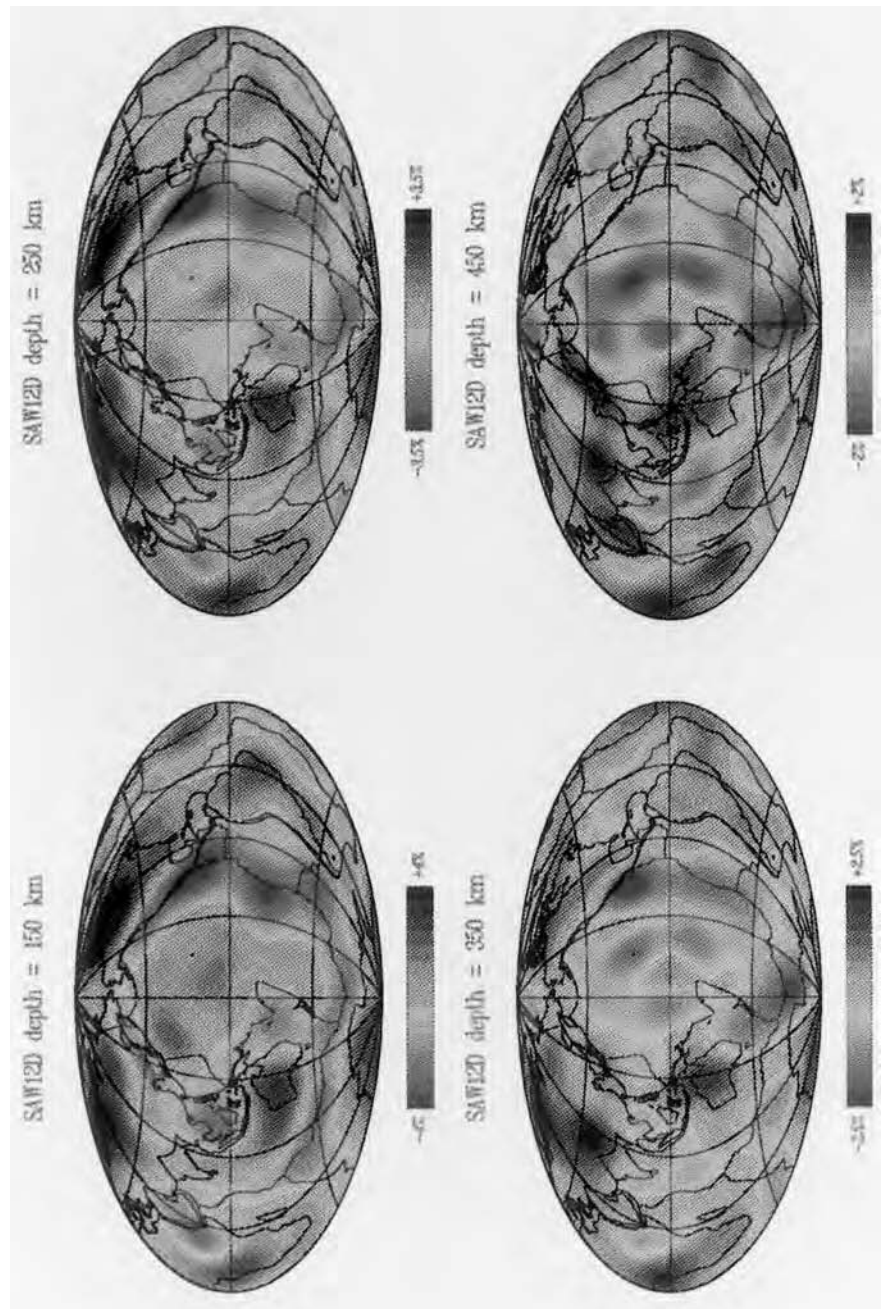


Figure 3.24. Perturbations in shear wave velocity V_s relative to the spherical Earth model PREM at various upper mantle depths from the model of Li and Romanowicz (1996).

For a color version of this figure, see plate section.

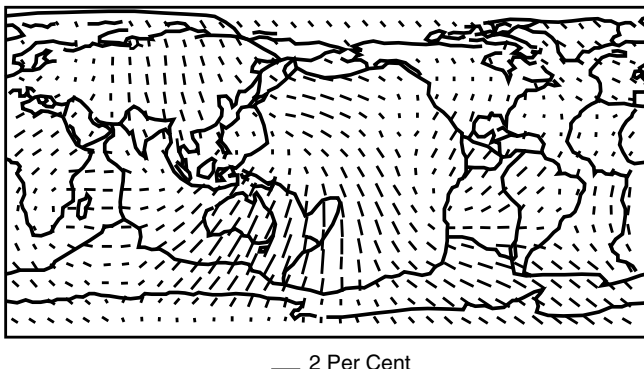


Figure 3.25. Directions of fastest principal axes beneath the lithosphere in azimuthally anisotropic Rayleigh wave propagation at 200 s period (Tanimoto and Anderson, 1985).

not resolved in global models, even if the associated seismic velocity anomalies are large. In subduction zone environments high-velocity slabs are in close proximity to low velocities in the back-arc region. This compounds the difficulty of resolving slabs with the spherical harmonic approach.

Seismic anisotropy exists in the upper mantle at about the 2% level, as discussed earlier in this chapter, and it provides information on the large-scale pattern of deformation. Lithospheric seismic anisotropy records the fossil spreading direction, whereas asthenospheric seismic anisotropy is thought to indicate the present direction of horizontal velocity, with vertical shear providing the mechanism for olivine grain alignment. Global inversions of long period surface wave data (Tanimoto and Anderson, 1985; Nataf et al., 1986) reveal a large-scale pattern of seismic anisotropy beneath the lithosphere that is generally consistent with the motion constrained by the plates (Figure 3.25). The largest seismic anisotropy occurs beneath the fastest moving plates, and there is an indication in the overall pattern of seismic anisotropy of divergence beneath the East Pacific Rise and convergence beneath the trenches in the western Pacific.

3.9.2 Extensions of Subducted Slabs into the Lower Mantle

Question 3.11: Do subducted slabs penetrate into the lower mantle?

The ultimate fate of the subducted lithosphere, and its trajectory beyond the seismicity cutoff, is one of the most important unsolved problems in mantle convection. The traditional interpretation of the pattern of deep seismicity is that slabs remain in the upper mantle. Early studies of focal depths indicated there are no earthquakes deeper than 700 km depth (Isacks et al., 1968; Isacks and Molnar, 1971). More recent focal depth determinations have confirmed this, and indeed the maximum depth is now judged to be 670–680 km (Stark and Frohlich, 1985). Focal mechanisms of very deep earthquakes, those just above the seismicity cutoff, mostly show down-dip compression, an indication that slabs encounter increased resistance at that depth. Evidence in support of this interpretation has been presented by Giardini and Woodhouse (1984), who detect a kink in the Tonga slab just above the 660 km seismic discontinuity. The increased resistance to subduction in the transition zone could be

due to compositional buoyancy or phase-change buoyancy associated with the endothermic phase transition. A significant increase in mantle viscosity associated with the 660 km phase change (see Chapter 5) would also result in resistance to subduction. The important difference between these explanations is that increased viscosity would deform slabs, but would not prevent them from sinking into the lower mantle, whereas compositional or phase-change buoyancy might.

Low slab temperatures result in seismic wave velocities 5–10% higher than in the surrounding mantle. Seismologists have long used this property to detect the presence of slab-related heterogeneities. An early study by Engdahl and Gubbins (1987) demonstrated that the Aleutian slab anomaly extends below the deepest seismicity, and Spakman (1986) showed that the same is true for the Hellenic slab.

Extensive evidence for aseismic extensions of slabs deeper than the 660 km seismic discontinuity in the western Pacific was assembled by Jordan (1977) and Creager and Jordan (1984, 1986a) using travel time residuals from deep focus slab earthquakes. Slab extensions below the deepest earthquakes produce a characteristic pattern of travel time anomalies. Creager and Jordan (1984, 1986a) concluded that the pattern of these travel time anomalies from deep earthquakes in the western Pacific could be explained by slab-shaped regions of high-velocity material extending to 1,400 km depth or more, with the same strike as the Wadati–Benioff zone from which the earthquakes originated. They argued that these residual sphere patterns indicate thermal anomalies from subducted lithospheric slabs extending below the transition zone and into the lower mantle. This interpretation was questioned, however, on the grounds that the effects of seismic anisotropy were not included (Anderson, 1987a) and that the travel time anomalies from deep earthquakes are contaminated by seismic heterogeneity unrelated to slabs (Zhou and Anderson, 1989).

There have been a growing number of high-resolution seismic tomographic studies attempting to answer the critical question of how slabs are affected by the 660 km seismic discontinuity and whether lithospheric material penetrates into the lower mantle (van der Hilst et al., 1991; Fukao et al., 1992; Spakman et al., 1993; Grand, 1994; van der Hilst, 1995; Grand et al., 1997; van der Hilst et al., 1997). In general, two different modes of slab interaction with the 660 km seismic discontinuity are inferred. In some cases the slab appears to descend into the lower mantle without significant change in dip angle. Examples of this behavior include the northern Kurile, Mariana, Kermadec, and Indonesia slabs. In other cases the slab appears to be bent at the 660 km seismic discontinuity. Some of the bent slabs appear to be deflected nearly into the horizontal, so they seem to be reclined on the 660 km seismic discontinuity. Examples of this behavior include the Izu–Bonin, southern Kurile, and Japan slabs. For other bent slabs the 660 km seismic discontinuity simply appears to kink the slab but not prevent it from sinking into the lower mantle. The central portion of the Tonga slab is an example of this behavior.

Regional-scale seismic tomography is particularly well suited for imaging slabs. Figure 3.26 shows a cross-section through the upper mantle beneath the Hellenic arc with the S-wave velocity structure determined by Spakman et al. (1993). The image contains a high-velocity, dipping tabular anomaly, extending to a 660 km depth beneath the arc, with low velocities in the overlying wedge. The structure is consistent with low temperatures in the subducting slab adjacent to a high-temperature back-arc region. There is a subhorizontal portion of the high-velocity anomaly located just above the 660 km discontinuity, suggesting that a kink exists in the slab at that depth. But there is also high velocity beneath the kink, an indication that the slab material continues beneath the transition zone into the lower mantle. Further evidence of this behavior is shown in Figure 3.27, from a tomographic study of

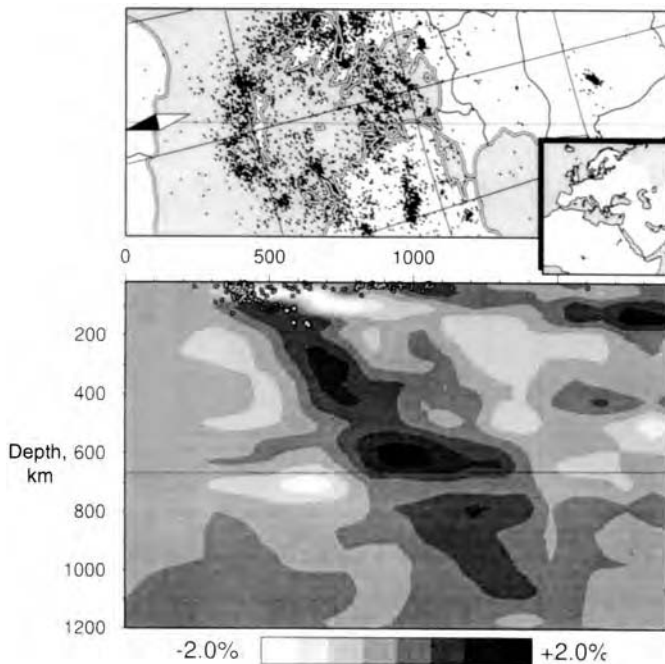


Figure 3.26. Perturbations in shear wave velocity V_S relative to the Jeffreys–Bullen spherical Earth model on a great circle cross-section through the Aegean upper mantle to a depth of 1,200 km as determined by Spakman et al. (1993). The upper panel is a reference map showing seismicity and the location of the cross-section. The horizontal dimension in the lower panel is distance in kilometers.

the mantle around the Tonga–Kermadec subduction zone by van der Hilst (1995). These images indicate along-strike variation in deep subduction, in which the slab in the northern cross-sections is deflected at 660 km depth while in the southern cross-section it appears to penetrate into the lower mantle with little change in dip angle.

Only recently has it become possible to construct global maps of mantle heterogeneity beneath the transition zone with sufficient spatial resolution to test the slab penetration hypothesis worldwide. Figure 3.28 shows a high-resolution block model P-wave tomographic image at 1,300 km depth by Widiyantoro and van der Hilst (1996) with about 90% spatial coverage. Prominent, linear high-velocity belts are present beneath the southern Asia convergence zone, west of the present-day location of the Tonga trench, and the Americas. All three of these belts coincide with the location of major convergent plate boundary regions active in the last 100 Myr (see Chapter 2). This correlation offers compelling evidence that the belts of high-velocity anomalies at 1,300 km depth represent remanents of subducted oceanic lithosphere. Additional evidence in support of this interpretation is found from the high-resolution studies by Grand (1987, 1994) of the seismic anomaly structure beneath the Americas, particularly the so-called Caribbean anomaly. Figure 3.29 shows the shear wave velocity structure beneath the Americas at 1,300–1,450 km depth determined by Grand (1994), compared with the location of the subduction zone off the west coast of North America between 60 and 90 Myr ago, as inferred from plate reconstructions by Engebretson et al. (1992). The shape and location of the Caribbean anomaly correlates well with the expected shape and location of slab material sinking in the lower mantle at $10\text{--}20 \text{ mm yr}^{-1}$.

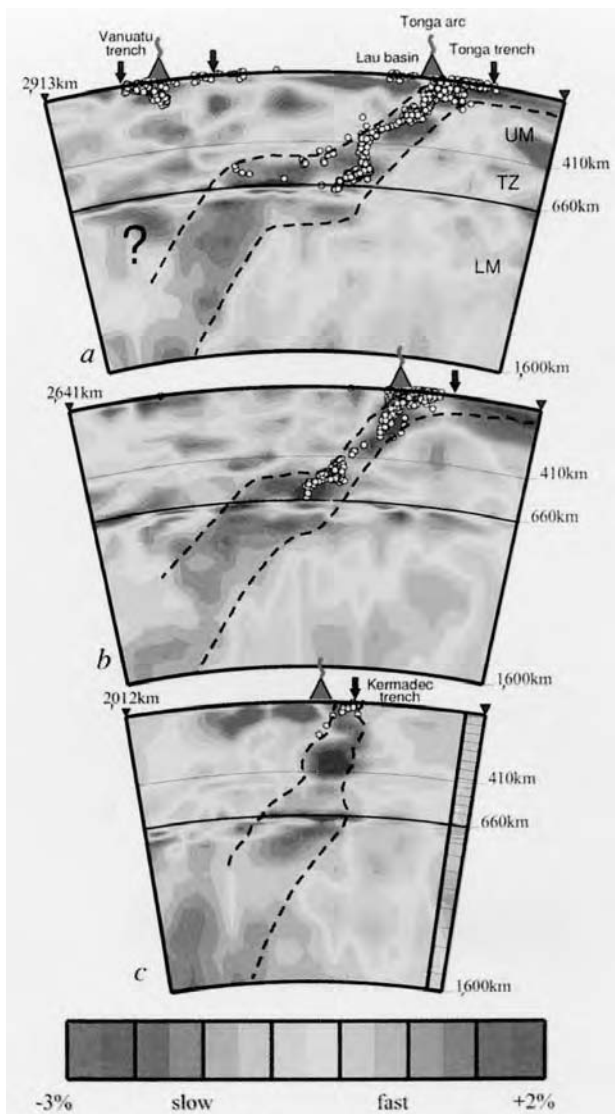


Figure 3.27. Tomographic images of seismic wave velocity V_p variations in the mantle beneath (a) the northern portion of the Tonga trench, (b) central Tonga, and (c) the Kermadec trench. Dots indicate earthquake foci. From van der Hilst (1995).

For a color version of this figure, see plate section.

The linear high seismic velocity anomalies in Figures 3.28 and 3.29 extend even deeper into the lower mantle as seen in Figure 3.30, which compares high-resolution P- and S-wave seismic tomographic models at a number of depths through the lower mantle (Grand et al., 1997). The linear anomalies beneath North and Central America and southern Asia are apparent even at 1,800 km depth. The generally good agreement between the P- and S-wave models argues convincingly for the reality of the linear high seismic velocity anomalies and their interpretation as subducted slabs.

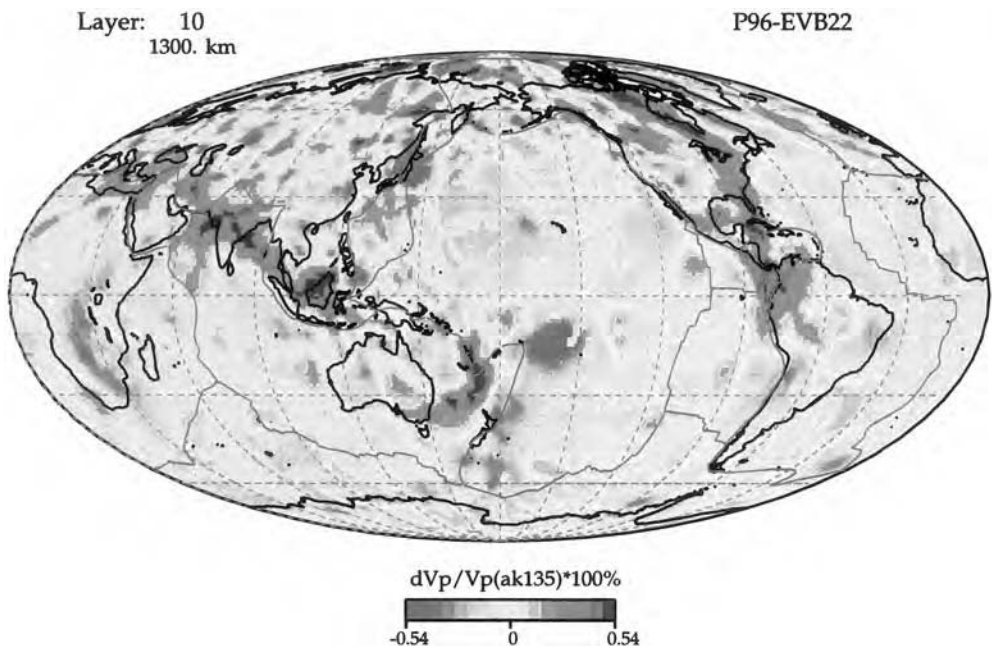


Figure 3.28. Perturbations in compressional wave velocity V_p relative to the spherical Earth model PREM at a depth of 1,300 km from the tomography model of Widjiantoro and van der Hilst (1996).

For a color version of this figure, see plate section.

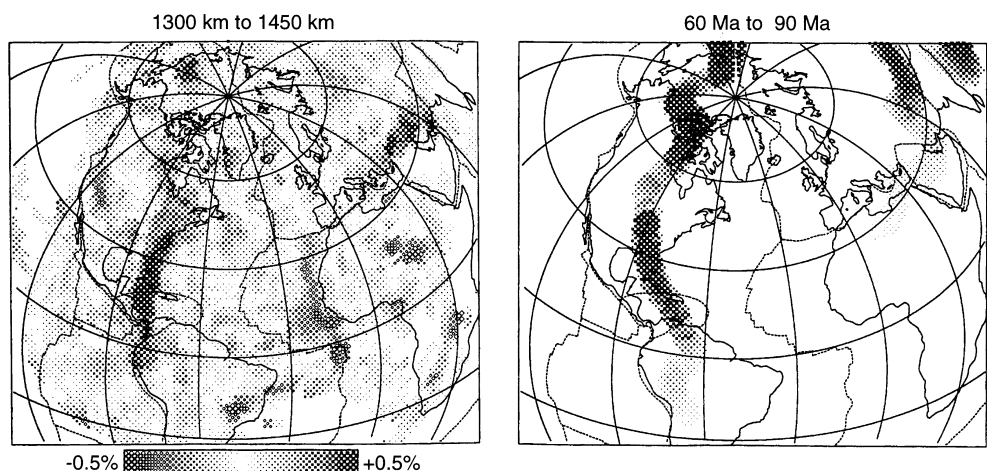


Figure 3.29. Perturbations in shear wave velocity V_s between 1,300 and 1,450 km depth beneath North America, determined by Grand (1994) (left), compared with the location of subduction zones between 60 and 90 Ma inferred by Engebretson et al. (1992) (right).

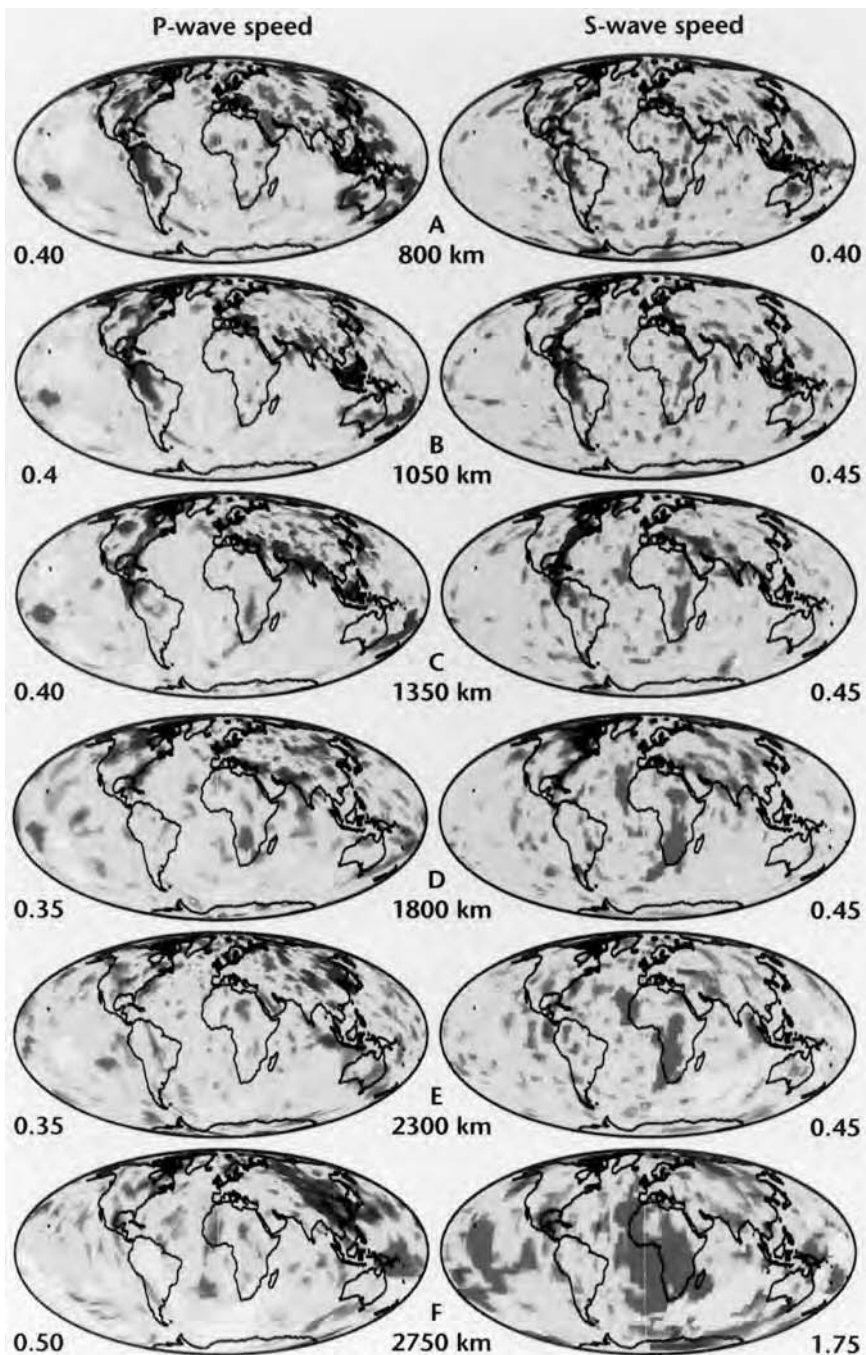


Figure 3.30. High-resolution P-wave and S-wave tomographic models of the lower mantle. Numbers at the sides of the images are the maximum anomaly in terms of percentage difference from the mean velocity. Blues are faster than average speed, reds are slower. White regions have no significant data sampling. After Grand et al. (1997).

For a color version of this figure, see plate section.

In summary, the three-dimensional images of the mantle derived from seismic tomography strongly support the hypothesis that at least some slabs penetrate through the transition zone and sink into the lower mantle. Although it is uncertain if every subduction zone has a lower mantle extension, there is now good evidence that large quantities of slab material are present in the lower mantle. What is still uncertain is whether some subducted slabs sink all the way to the core–mantle boundary or are assimilated into the lower mantle before reaching the CMB.

Question 3.12: *Do some subducted slabs sink all the way to the core–mantle boundary?*

Figure 3.31 provides evidence that at least some slabs sink all the way to the CMB. The figure shows cross-sections of mantle P-wave (A) and S-wave (B) velocity

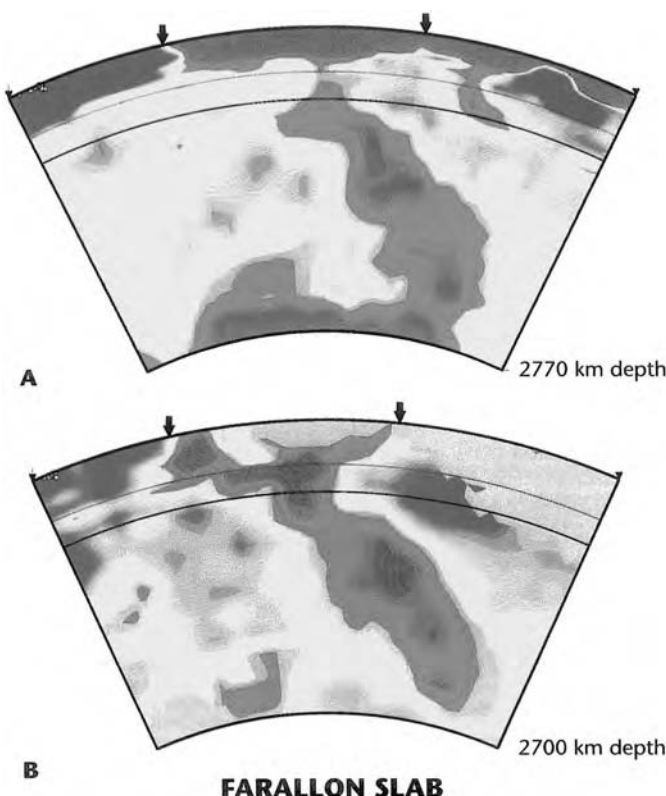


Figure 3.31. P- (A) and S- (B) wave velocity anomalies (relative to the global mean) at depths from the surface to the CMB in an approximately E–W cross-section of the mantle through the southern U.S. Reds indicate slow velocities, blues fast velocities. Differences in structure between the P-wave and S-wave models in the transition zone and near the CMB may be due to different data sampling in the two studies. The thin black lines are at depths of 410 and 660 km. After Grand et al. (1997).

For a color version of this figure, see plate section.

variations in an approximately east–west cross-section through the southern United States (Grand et al., 1997). The large slab-like fast seismic anomaly is probably the descending Farallon plate that subducted over the past approximately 100 Myr. The anomaly, and by implication the Farallon plate, extends all the way from the surface, through the depth of the 660 km seismic discontinuity and through the entire lower mantle to the CMB.

While there is evidence that at least some slabs sink all the way to the CMB, the shape of the slabs must change between about 1,800 km depth and the CMB since the long narrow structures seen in the tomographic images in the mid-mantle are replaced by broad large-scale features just above the CMB (Figure 3.30, van der Hilst et al., 1997). We will see in Chapter 10 that a change in the morphology of mantle downwellings from sheet-like to cylindrical with increasing depth is in accord with some numerical simulations of three-dimensional mantle convection (Bercovici et al., 1989a).

3.9.3 Lower Mantle Seismic Heterogeneity

Globally distributed seismic heterogeneity in the lower mantle was first investigated by Julian and Sengupta (1973) and by Dziewonski et al. (1977), both using P-wave travel time anomalies. The first global models of lower mantle structure were constructed using P-wave travel time residuals (Dziewonski, 1984). Although P waves continue to be used for lower mantle seismic tomography, there is an increasing number of lower mantle seismic tomography models based on S-wave travel times and waveforms. Su and Dziewonski (1997) have carried out simultaneous three-dimensional inversions of the seismic shear and bulk velocities in the mantle and find that the variations in these velocities are uncorrelated in the lower mantle.

Figure 3.32 shows a three-dimensional seismic shear wave velocity model of the mantle complete to spherical harmonic degree 16 by Masters et al. (1996) at different depths, contoured uniformly to permit comparison among the depths. Uniform contouring emphasizes the fact that large-scale mantle seismic heterogeneity is concentrated in the upper mantle above 300 km depth and near the base of the mantle, within 300 km of the CMB. Large-scale seismic heterogeneity is weakest from the base of the transition zone to about 2,200 km depth. This behavior is summarized in Figure 3.33, which shows the rms amplitude of the seismic heterogeneity from the model in Figure 3.32 as a function of depth. The shape of the profile of rms heterogeneity agrees qualitatively with the shape expected for whole mantle convection, with heterogeneity maxima in the surface and basal boundary layers separated by a broad heterogeneity minimum in the interior. The interior minimum corresponds to the region of the mantle where heterogeneity is reduced by the mixing action of convection. It is significant that the model does not exhibit an interior heterogeneity maximum at the boundary between the upper and the lower mantle, as would be expected if mantle convection were separated into two layers.

Although this and other similar tomographic models of the lower mantle contain structure that varies irregularly with depth, the largest-scale structure in these models is nearly independent of depth and is common to nearly all P-wave and S-wave models. As shown in the comparison of different models in Figure 3.34, the largest-scale structure in the lower mantle consists of a ring of high seismic velocity around the Pacific basin, separating two broad circular regions of lower than average seismic velocity, one centered in the south central Pacific and the other beneath Africa. The slow seismic anomaly centered beneath southern Africa is particularly well revealed in the S-wave model of Figure 3.31 where it extends from the base of the mantle to near 1,000 km depth. The high seismic velocity ring is

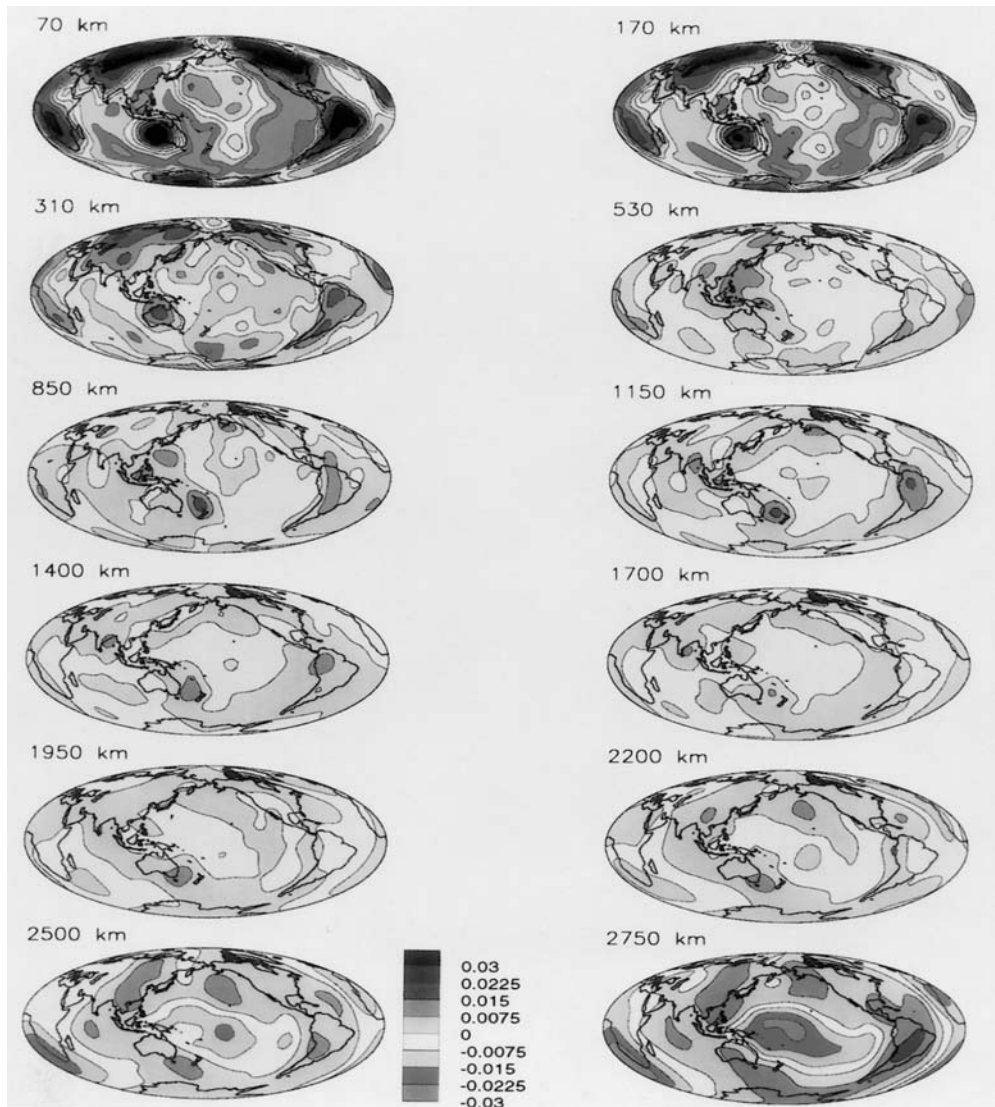


Figure 3.32. Perturbations in shear wave velocity V_S through the whole mantle at 12 depth slices, complete to spherical harmonic degree 16 determined by Masters et al. (1996).

For a color version of this figure, see plate section.

nearly a great circle, so the heterogeneity is approximately a spherical harmonic P_2^2 pattern. The ring of high seismic velocity corresponds roughly to the global system of Mesozoic and early Cenozoic subduction zones. If we interpret high seismic velocities as the result of low temperatures, then this structure indicates a ring of descending flow throughout the lower mantle, located approximately beneath long-lived convergent plate boundary regions. The broad columnar regions with lower than average seismic velocity beneath the Pacific and African plates then correspond to hotter than average mantle with upwelling velocity. The spherical harmonic degree 2 pattern of seismic velocities in the lower mantle, inferred

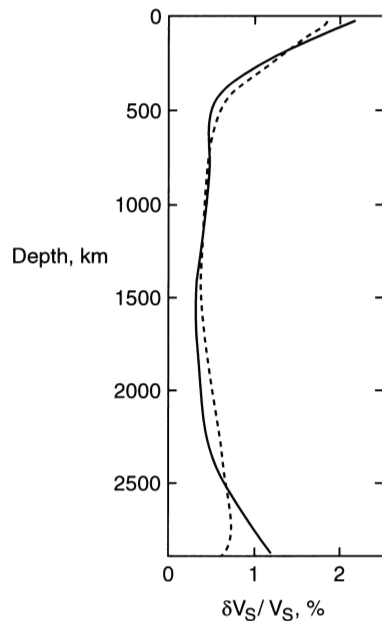


Figure 3.33. The perturbations in shear wave velocity V_S as a function of depth (solid curve) through the whole mantle from the tomography model of Masters et al. (1996) shown in Figure 3.32. The dashed curve is from the seismic tomography model of Su et al. (1994) for comparison.

to be the major pattern of upwellings and downwellings (Figure 3.34), is one of the most important results from mantle seismic tomography.

In the global tomography models, the level of heterogeneity in the layer D'' is higher than elsewhere in the lower mantle, although the large-scale pattern in D'' is similar to that in the rest of the lower mantle, as shown in Figure 3.34. We have already discussed the evidence for a seismic discontinuity at the top of D'', several hundred kilometers above the CMB. Variations in the height of the discontinuity, relative to the pattern of large-scale seismic heterogeneity in the rest of the lower mantle, provide a clue to the nature and origin of D''.

The existing evidence indicates a positive correlation between D'' layer thickness, measured by the depth of the velocity increase, and lower mantle seismic velocity variations, as shown in Figure 3.35 from Kendall and Shearer (1994). The D'' layer is well developed around the margins of the Pacific where Figure 3.35 indicates that the lower mantle is anomalously fast. In the central Pacific, where global seismic tomographic images indicate slow lower mantle seismic velocities, the D'' layer discontinuity is not so well defined (Garnero et al., 1988). This correlation suggests that the discontinuity at the top of D'' is best developed beneath lower mantle downwellings. This is not the expected behavior if the D'' layer is an ancient, highly dense reservoir, because in that case, it should be best developed beneath upwellings. However, it is possible to explain this correlation if D'' consists of material accumulating at the base of downwellings in the lower mantle. Such a distribution implies continual influx of new material from above, and that D'' is an open system (Olson and Kincaid, 1991). The most likely source of dense material is former lithospheric slabs subducted into the lower mantle, which has obvious implications for the degree of mass transfer between upper and lower mantle. It is important to emphasize that the correlations on which these arguments are based are poorly established, and therefore any models based on them are highly speculative. A more secure interpretation requires further exploration of D'' and its spatial variations as well as improved resolution of lower mantle structure.

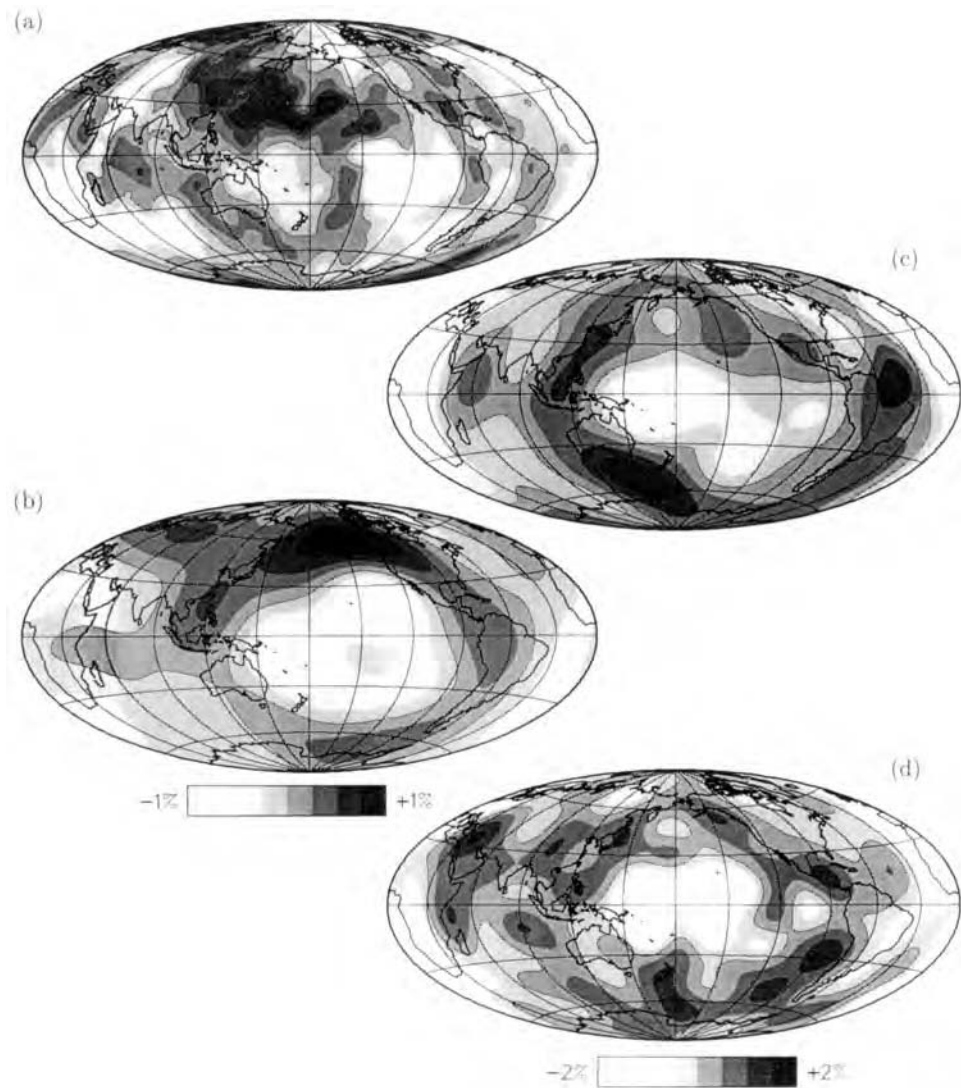


Figure 3.34. Comparison of four seismic tomography models of three-dimensional lower mantle structure. The $\pm 1\%$ scale applies to images (a) and (b); the $\pm 2\%$ scale applies to images (c) and (d). Image (a) is P-wave velocity variations at 2,566–2,900 km depth by Inoue et al. (1990); image (b) is S-wave velocity variations at 2,630–2,891 km depth by Tanimoto (1990); image (c) is S-wave velocity variations at 2,630–2,891 km depth by Masters et al. (1996); image (d) is S-wave velocity variations at 2,850 km depth by Su et al. (1994) for comparison.

3.9.4 Topography of the Core–Mantle Boundary

Question 3.13: What is the topography of the core–mantle boundary?

Another source of seismic heterogeneity that is directly coupled to the pattern of lower mantle convection is the shape of the core–mantle boundary. We have already mentioned the

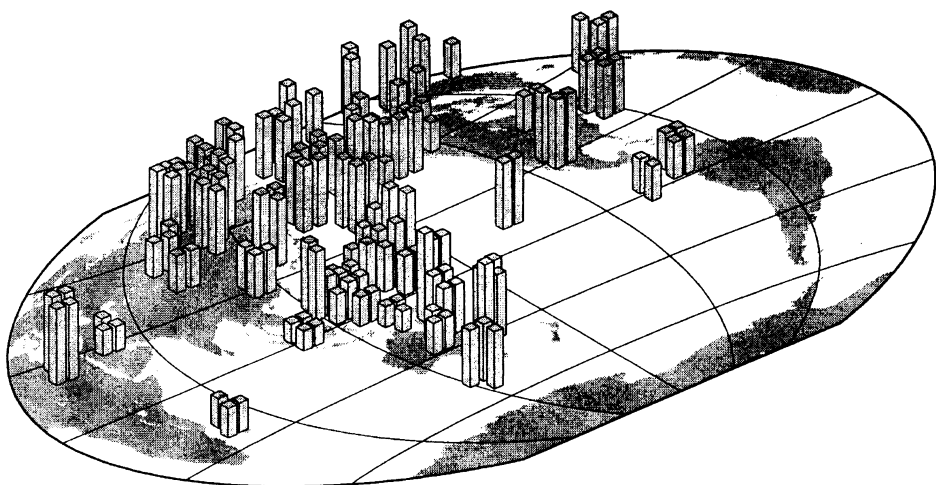


Figure 3.35. Lateral variations of the height of the top of the D'' layer compiled by Kendall and Shearer (1994).

observations of high-frequency P-wave scattering, from either the CMB, implying a rough CMB, or from small-scale heterogeneities distributed within D''.

Long-wavelength undulations of the CMB are an important constraint on the structure of flow in the lower mantle, since they are expected to be highly correlated with vertical motion. Unfortunately, long-wavelength CMB topography remains a controversial subject. Several investigators have used the travel times of transmitted and reflected core phases to map long-wavelength CMB heterogeneity, but there is little consistency among the results (see the review by Morelli, 1993). Using transmitted phases only, Creager and Jordan (1986b) interpreted travel time residuals as being due to either “inverse continents” – accumulations of heavy mantle material or “slag” – or light core material. However, the pattern of seismic heterogeneity they found is quite different from the results of Morelli and Dziewonski (1987), who used both reflections (PcP) and transmitted waves (PKP). In principle, a comparison of the travel time anomalies from these two phases can distinguish between CMB topography and heterogeneities in D'', because they are positively correlated for heterogeneities in D'' and negatively correlated for CMB topography. Furthermore, if the heterogeneity were due to core slag, then PcP should not show a travel time anomaly at all. Morelli and Dziewonski (1987) found negative correlation, indicating CMB topography as the source, and inferred a maximum range of ± 6 km. This result has been questioned, because Earth rotation data constrain the P_2^0 and P_2^1 spherical harmonic components of the topography to be small (see below). An analysis of travel time anomalies by Doornbos and Hilton (1989), including bottom side CMB reflections (PKKP) in addition to the other phases, resulted in a model with relatively little CMB topography (1.5 km^2 variance, versus 20 km^2 from the previous studies), and with most of the heterogeneous structure located in D''.

The only firm evidence for anomalous topography on the CMB comes from observations of luni-solar nutations and solid earth tides (Gwinn et al., 1986) which indicate that the CMB departs from hydrostatic shape at spherical harmonic degree 2 by 0.5–0.9 km (Wahr and de Vries, 1989). Although the issue remains open, it seems that there may be only a small amount of CMB topography (Rodgers and Wahr, 1993; Vasco and Johnson, 1998), and the problem of delineating it is aggravated by lateral variations in the D'' layer.

4

Mantle Temperatures and Thermodynamic Properties

4.1 Heat Conduction and the Age of the Earth

4.1.1 Cooling of an Isothermal Earth

Determinations of the temperature distribution within the Earth have long been a major focus of the physical sciences. Early in the nineteenth century it was recognized from temperature measurements in mines, that the temperature T increased with depth y at a rate $dT/dy = 20\text{--}30 \text{ K km}^{-1}$, the geothermal gradient. At that time, the heat flow at the Earth's surface implied by the geothermal gradient was attributed to the secular cooling of the planet, an inference that, as it turns out, was partially correct.

William Thompson (later Lord Kelvin) (Figure 4.1) used this assumption as the basis for his estimate of the age of the Earth (Burchfield, 1975). Thompson assumed that the Earth was conductively cooling from a hot initial state. He applied solutions for the cooling of a



Figure 4.1. Photograph of William Thompson (Lord Kelvin).

semi-infinite half-space to determine the time required to establish the present geothermal gradient. The distribution of temperature T at shallow depths can be modeled as one-dimensional, time-dependent heat conduction in the absence of heat sources (see Chapter 6):

$$\rho c \frac{\partial T}{\partial t} = k \frac{\partial^2 T}{\partial y^2} \quad (4.1.1)$$

In this heat conduction equation, ρ is the density, c is the specific heat, k is the thermal conductivity, y is the depth, and t is time. We consider a semi-infinite half-space defined by $y > 0$ which is initially at a temperature T_1 . At $t = 0$, the surface $y = 0$ is instantaneously subjected to the temperature T_0 and the surface temperature is held at T_0 for $t > 0$.

The solution to this problem, which serves as the basic thermal model of the oceanic lithosphere, is best obtained by introducing the nondimensional similarity variables

$$\theta = \frac{T_1 - T}{T_1 - T_0} \quad (4.1.2)$$

$$\eta = \frac{y}{2(\kappa t)^{1/2}} \quad (4.1.3)$$

where $\kappa = k/\rho c$ is the thermal diffusivity. The solutions at different times are “similar” to each other in the sense that the spatial dependence at one time can be obtained from the spatial dependence at a different time by stretching the coordinate y by the square root of the ratio of the times.

Derivatives with respect to the variables t and y transform to derivatives with respect to the variable η using the chain rule as follows:

$$\frac{\partial \theta}{\partial t} = \frac{d\theta}{d\eta} \frac{\partial \eta}{\partial t} = \frac{d\theta}{d\eta} \left(-\frac{1}{4} \frac{y}{\sqrt{\kappa t}} \frac{1}{t} \right) = \frac{d\theta}{d\eta} \left(-\frac{1}{2} \frac{\eta}{t} \right) \quad (4.1.4)$$

$$\frac{\partial \theta}{\partial y} = \frac{d\theta}{d\eta} \frac{\partial \eta}{\partial y} = \frac{d\theta}{d\eta} \frac{1}{2\sqrt{\kappa t}} \quad (4.1.5)$$

$$\frac{\partial^2 \theta}{\partial y^2} = \frac{1}{2\sqrt{\kappa t}} \frac{d^2 \theta}{d\eta^2} \frac{\partial \eta}{\partial y} = \frac{1}{4} \frac{1}{\kappa t} \frac{d^2 \theta}{d\eta^2} \quad (4.1.6)$$

Substitution of (4.1.2) to (4.1.6) into (4.1.1) gives

$$-\eta \frac{d\theta}{d\eta} = \frac{1}{2} \frac{d^2 \theta}{d\eta^2} \quad (4.1.7)$$

with the boundary conditions

$$\theta = 1 \text{ at } \eta = 0 \quad (4.1.8)$$

$$\theta = 0 \text{ as } \eta \rightarrow \infty \quad (4.1.9)$$

The introduction of the similarity variable reduces the partial differential equation (4.1.1) to an ordinary differential equation (4.1.7) in the variable η . This is appropriate as long as the similarity solution satisfies the required boundary conditions expressed as (4.1.8) and (4.1.9) in terms of the similarity variables.

Equation (4.1.7) can be integrated by letting

$$\phi = \frac{d\theta}{d\eta} \quad (4.1.10)$$

Upon rewriting (4.1.7) we obtain

$$-\eta d\eta = \frac{1}{2} \frac{d\phi}{\phi} \quad (4.1.11)$$

Integration is straightforward with the result

$$-\eta^2 = \ln \phi - \ln c_1 \quad (4.1.12)$$

where $-\ln c_1$ is the constant of integration. It follows that

$$\phi = c_1 e^{-\eta^2} = \frac{d\theta}{d\eta} \quad (4.1.13)$$

Upon integration we obtain

$$\theta = c_1 \int_0^\eta e^{-\eta'^2} d\eta' + 1 \quad (4.1.14)$$

where η' is a dummy variable of integration and the condition $\theta(0) = 1$ was used to evaluate the second constant of integration. Since $\theta(\infty) = 0$, we must have

$$0 = c_1 \int_0^\infty e^{-\eta'^2} d\eta' + 1 \quad (4.1.15)$$

The definite integral is

$$\int_0^\infty e^{-\eta'^2} d\eta' = \frac{\sqrt{\pi}}{2} \quad (4.1.16)$$

Thus the constant $c_1 = -2/\sqrt{\pi}$ and

$$\theta = 1 - \frac{2}{\sqrt{\pi}} \int_0^\eta e^{-\eta'^2} d\eta' \quad (4.1.17)$$

The definite integral is the definition of the error function

$$\text{erf}(\eta) \equiv \frac{2}{\sqrt{\pi}} \int_0^\eta e^{-\eta'^2} d\eta' \quad (4.1.18)$$

Thus we can rewrite θ as

$$\theta = 1 - \text{erf}(\eta) = \text{erfc}(\eta) \quad (4.1.19)$$

where $\text{erfc}(\eta)$ is the complementary error function. Values of the error function and the complementary error function are listed in Table 4.1; the functions are also shown in Figure 4.2.

The solution for the temperature as a function of time t and depth y is (4.1.19). It can be written in terms of the original variables as

$$\frac{T_1 - T}{T_1 - T_0} = \text{erfc}\left(\frac{y}{2\sqrt{kt}}\right) \quad (4.1.20)$$

Table 4.1. The Error Function and the Complementary Error Function

η	$\text{erf } \eta$	$\text{erfc } \eta$
0	0	1.0
0.02	0.022565	0.977435
0.04	0.045111	0.954889
0.06	0.067622	0.932378
0.08	0.090078	0.909922
0.10	0.112463	0.887537
0.15	0.167996	0.832004
0.20	0.222703	0.777297
0.25	0.276326	0.723674
0.30	0.328627	0.671373
0.35	0.379382	0.620618
0.40	0.428392	0.571608
0.45	0.475482	0.524518
0.50	0.520500	0.479500
0.55	0.563323	0.436677
0.60	0.603856	0.396144
0.65	0.642029	0.357971
0.70	0.677801	0.322199
0.75	0.711156	0.288844
0.80	0.742101	0.257899
0.85	0.770668	0.229332
0.90	0.796908	0.203092
0.95	0.820891	0.179109
1.0	0.842701	0.157299
1.1	0.880205	0.119795
1.2	0.910314	0.089686
1.3	0.934008	0.065992
1.4	0.952285	0.047715
1.5	0.966105	0.033895
1.6	0.976348	0.023652
1.7	0.983790	0.016210
1.8	0.989091	0.010909
1.9	0.992790	0.007210
2.0	0.995322	0.004678
2.2	0.998137	0.001863
2.4	0.999311	0.000689
2.6	0.999764	0.000236
2.8	0.999925	0.000075
3.0	0.999978	0.000022

At $y = 0$, the complementary error function is 1 and $T = T_0$. As $y \rightarrow \infty$ or $t = 0$, erfc is 0 and $T = T_1$. The general solution for θ or $(T_1 - T)/(T_1 - T_0)$ is shown as $\text{erfc } (\eta)$ in Figure 4.2.

Regions in the Earth in which heat diffusion is an important heat transfer mechanism are usually referred to as thermal boundary layers. In this case the thickness of the thermal boundary layer requires an arbitrary definition, since the temperature T approaches the initial

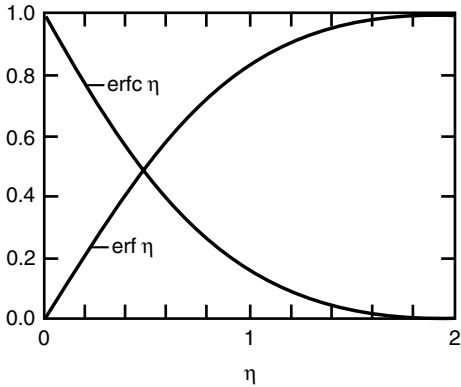


Figure 4.2. The error function $\text{erf } \eta$ and the complementary error function $\text{erfc } \eta$ as a function of η .

temperature T_1 asymptotically. We define the thickness of the boundary layer y_T as the value of y where $\theta = 0.1$. This thickness increases with time as the half-space cools. However, the condition $\theta = 0.1$ defines a unique value of the similarity variable η_T . From (4.1.19) and Table 4.1 we obtain

$$\eta_T = \text{erfc}^{-1}(0.1) = 1.16 \quad (4.1.21)$$

and from (4.1.3) we get

$$y_T = 2\eta_T \sqrt{\kappa t} = 2.32\sqrt{\kappa t} \quad (4.1.22)$$

The thickness of the thermal boundary layer is 2.32 times the characteristic thermal diffusion distance $\sqrt{\kappa t}$.

The heat flux q_0 at the surface $y = 0$ is given by differentiating (4.1.20) according to Fourier's law of heat conduction and evaluating the result at $y = 0$:

$$\begin{aligned} q_0 &= k \left(\frac{\partial T}{\partial y} \right)_{y=0} = \frac{k(T_1 - T_0)}{2\sqrt{\kappa t}} \frac{d}{d\eta} (\text{erf } \eta)_{\eta=0} \\ &= \frac{k(T_1 - T_0)}{\sqrt{\pi \kappa t}} \end{aligned} \quad (4.1.23)$$

Equation (4.1.23) shows that the surface heat flux is proportional to the product of conductivity k and the temperature difference $(T_1 - T_0)$ and inversely proportional to the thermal boundary layer thickness. With the standard definition $q = -k(\partial T / \partial y)$, the upward heat loss would be negative. Since the Earth's surface heat flow is always taken to be a positive quantity, the minus sign is not included in (4.1.23).

On the basis of (4.1.23), Thompson proposed that the age of the Earth t_0 is given by

$$t_0 = \frac{(T_1 - T_0)^2}{\pi \kappa (\partial T / \partial y)_0^2} \quad (4.1.24)$$

where $(\partial T / \partial y)_0$ is the present geothermal gradient. With $(\partial T / \partial y)_0 = 25 \text{ K km}^{-1}$, $T_1 - T_0 = 2,000 \text{ K}$, and $\kappa = 1 \text{ mm}^2 \text{s}^{-1}$, the age of the Earth from (4.1.24) is $t_0 = 65 \text{ Myr}$. Thompson arrived at this age using the geothermal gradient measured in mines. The values of the temperature difference and the thermal diffusivity used were also reasonable. Based on the

laws of physics known at that time, the mid-nineteenth century, the age given by Thompson was reasonable. We now recognize, however, that the continental crust has a near-steady-state heat balance due to the heat generated by the heat-producing isotopes within the crust and the mantle heat flux from below. Ironically, had Thompson known to apply the model to the oceanic lithosphere, he would have obtained very nearly its correct mean age.

4.1.2 Cooling of a Molten Earth

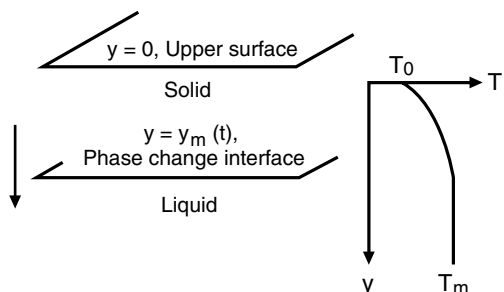
Thompson later modified the conductive cooling model of the Earth to include the hypothesis that its interior was initially molten. The existence of many surface volcanoes suggested to him that the Earth was cooling from an initially molten state. In order to model the solidification problem he considered the instantaneous cooling of a semi-infinite fluid half-space initially at the solidification temperature. The solution to this problem had been given by Stefan (1891).

The solidification problem is illustrated in Figure 4.3. The melt has solidified to the depth $y = y_m(t)$. We assume that there is molten material of uniform temperature T_m everywhere below the growing solid surface layer. The fact that the molten region does not extend infinitely far below the surface is of no consequence for the solution. We solve the heat conduction equation (4.1.1) in the interval $0 \leq y \leq y_m(t)$ subject to the conditions $T = T_0$ at $y = 0$, $T = T_m$ at $y = y_m(t)$, and $y_m = 0$ at $t = 0$. The position of the solidification boundary is a priori an unknown function of time. As in the case of the sudden cooling of a semi-infinite half-space, there is no length scale in this problem. For this reason, we once again introduce the dimensionless coordinate $\eta = y/2\sqrt{\kappa t}$ as in (4.1.3); it is also convenient to introduce the dimensionless temperature $\theta = (T - T_0)/(T_m - T_0)$ similar to (4.1.2).

The dimensionless coordinate η is obtained by scaling the depth with the thermal diffusion length $\sqrt{\kappa t}$ since there is no other length scale in the problem. Similarly, the depth of the solidification interface y_m must also scale with the thermal diffusion length in such a way that $y_m/\sqrt{\kappa t}$ is a constant. In other words, the depth of the solidification boundary increases with time proportionately with the square root of time. We have used dimensional arguments to determine the functional form of the dependence of y_m on t , a nontrivial result. Since $\eta = y/2\sqrt{\kappa t}$ and y_m is proportional to $\sqrt{\kappa t}$, the solidification boundary corresponds to a constant value $\eta_m = y_m/2\sqrt{\kappa t}$ of the similarity coordinate η . We denote this constant value by $\eta_m = \lambda$. Thus we have

$$y_m = 2\lambda\sqrt{\kappa t} \quad (4.1.25)$$

Figure 4.3. Growth of a solid layer at the surface of a solidifying magma. The surface $y = 0$ is maintained at $T = T_0$. Initially the half-space $y > 0$ contains a magma at its melt temperature T_m . The lower boundary of the solid layer $y = y_m(t)$ is shown.



With our definitions of θ and η it is clear that the heat conduction equation for $\theta(\eta)$ is identical with (4.1.7), whose solution we already know to be proportional to $\text{erf}(\eta)$. This form of solution automatically satisfies the condition $\theta = 0(T = T_0)$ on $\eta = 0(y = 0)$. To satisfy the remaining condition that $\theta = 1(T = T_m)$ at $\eta = \eta_m(y = y_m) = \lambda$, we need simply choose the constant of proportionality appropriately. The solution is

$$\theta = \frac{\text{erf}(\eta)}{\text{erf}(\lambda)} \quad (4.1.26)$$

which gives the temperature in the solidified layer $0 \leq y \leq y_m$. In the molten region $y > y_m$, $T = T_m$.

The constant λ is determined by requiring that the latent heat liberated at the solidification boundary be conducted vertically upward, away from the interface. In time δt , the interface moves downward a distance $(dy_m/dt)\delta t$. In so doing, a mass per unit area $\rho(dy_m/dt)\delta t$ is solidified, thus releasing an amount of latent heat $\rho L(dy_m/dt)\delta t$ per unit area (L is the latent heat liberated upon solidification per unit mass). Conservation of energy requires that this heat release be conducted away from the boundary at precisely the rate at which it is liberated. The heat cannot be conducted downward because the magma is at a constant temperature. Fourier's law of heat conduction gives the rate of upward heat conduction per unit time and per unit area at $y = y_m$ as $k(\partial T/\partial y)_{y=y_m}$. Multiplication of this by δt and equating it to $\rho L(dy_m/dt)\delta t$ gives the equation for finding λ :

$$\rho L \frac{dy_m}{dt} = k \left(\frac{\partial T}{\partial y} \right)_{y=y_m} \quad (4.1.27)$$

From (4.1.25) the speed of the solidification boundary is

$$\frac{dy_m}{dt} = \frac{\lambda \sqrt{\kappa}}{\sqrt{t}} \quad (4.1.28)$$

and the temperature gradient at $y = y_m$ is

$$\begin{aligned} \left(\frac{\partial T}{\partial y} \right)_{y=y_m} &= \left(\frac{d\theta}{d\eta} \right)_{\eta=\eta_m=\lambda} \left(\frac{\partial \eta}{\partial y} \right) (T_m - T_0) \\ &= \frac{(T_m - T_0)}{2\sqrt{\kappa t}} \frac{2}{\sqrt{\pi}} e^{-\lambda^2} \frac{1}{\text{erf}(\lambda)} \end{aligned} \quad (4.1.29)$$

Substitution of (4.1.28) and (4.1.29) into (4.1.27) gives

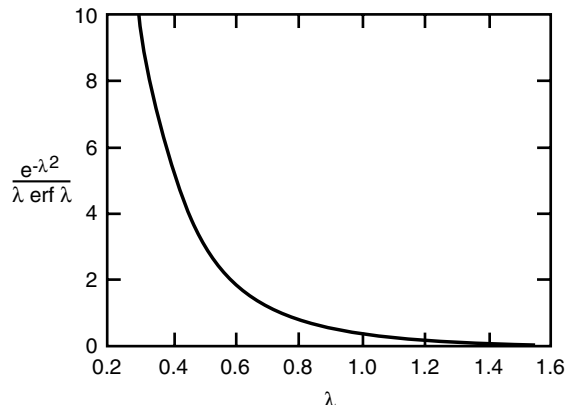
$$\frac{L\sqrt{\pi}}{c(T_m - T_0)} = \frac{e^{-\lambda^2}}{\lambda \text{erf}(\lambda)} \quad (4.1.30)$$

a transcendental equation for determining λ . Given a numerical value of the left side of (4.1.30), λ can be found by iteratively calculating the right side of the equation until agreement is found. Alternatively, the right side of (4.1.30) can be plotted as a function of λ , as in Figure 4.4, and the solution for a particular value of the left side of the equation can be found graphically.

On the basis of the solution to the solidification problem, the age of the Earth is given by

$$t_0 = \frac{(T_m - T_0)^2}{\pi \kappa (\partial T/\partial y)_0^2 \text{erf}^2(\lambda)} \quad (4.1.31)$$

Figure 4.4. The right side of the transcendental equation (4.1.30) for determining the growth of a solid layer at the surface of a solidifying magma as a function of λ .



By comparing (4.1.31) and (4.1.24) we see that solidification increases the estimate of the age of the Earth by the factor $1/\operatorname{erf}^2(\lambda)$. For $L = 400 \text{ kJ kg}^{-1}$, $c = 1 \text{ kJ kg}^{-1} \text{ K}^{-1}$, and $T_m - T_0 = 2,000 \text{ K}$, we find from (4.1.30) that $\lambda = 1.06$ and $\operatorname{erf}(\lambda) = 0.865$. Thus, including solidification increases the estimate of the age of the Earth by a factor of 4/3.

The calculations made by William Thompson were front page news in the London papers of the time and a debate raged over the age of the Earth. On one side were the clergy of the Church of England led by Bishop Wilburforce, who interpreted the Bible as giving an age of the Earth of some 4,000 yr. On the other side were the noted geologists of the day led by James Hutton, who argued that the sedimentary and fossil records required a much greater age for the Earth. However, they could not place quantitative limits on their estimates and much of the scientific establishment of the day accepted Thompson's estimate of the Earth's age, 50–100 Myr, as more reliable since it was based on seemingly reasonable theoretical arguments.

It was only with the discovery of radioactive elements and the implications for heat sources distributed within the Earth that a new approach to the thermal structure of the Earth was taken. Holmes (1915a, b, 1916) not only suggested that the decay of radioactive elements heated the interior of the Earth, but he also used their decay constants to suggest that the age of the Earth was billions of years.

4.1.3 Conductive Cooling with Heat Generation

The concept of secular cooling was subsequently replaced by the concept of a steady-state heat balance. The heat flux from the interior of the Earth was thought to be balanced with the heat generated by the decay of the radioactive elements. The most popular model involved a near-surface layer of thickness y_1 with a uniform rate of heat production per unit mass H overlying an interior totally depleted in the heat-producing elements. Again it was assumed that heat transport was by conduction.

On the assumption that heat is transported (conducted) only in the vertical direction and that there are no time variations, the heat conduction equation with heat sources can be written as

$$0 = k \frac{d^2 T}{dy^2} + \rho H \quad (4.1.32)$$

For the boundary conditions $T = T_0$ at $y = 0$ and $dT/dy = 0$ at $y = y_1$, (4.1.32) can be integrated to give

$$T = T_0 + \frac{\rho H}{k} \left(y_1 y - \frac{y^2}{2} \right) \quad (4.1.33)$$

If, in addition, the temperature at the base of the layer is prescribed to be the mantle temperature T_1 , we have

$$H y_1^2 = \frac{2k(T_1 - T_0)}{\rho} \quad (4.1.34)$$

Since the surface thermal gradient $(dT/dy)_0$ can also be prescribed, we find

$$y_1 = \frac{2(T_1 - T_0)}{(dT/dy)_0} \quad (4.1.35)$$

$$H = \frac{k}{2\rho(T_1 - T_0)} \left(\frac{dT}{dy} \right)_0^2 \quad (4.1.36)$$

$$T = T_0 + y \left(\frac{dT}{dy} \right)_0 \left[1 - \frac{y}{4(T_1 - T_0)} \left(\frac{dT}{dy} \right)_0 \right] \quad (4.1.37)$$

For $T_1 - T_0 = 1,300\text{ K}$ and $(dT/dy)_0 = 25\text{ K km}^{-1}$, (4.1.35) gives $y_1 = 104\text{ km}$. Further, for $\rho = 3,300\text{ kg m}^{-3}$ and $k = 3.3\text{ W m}^{-1}\text{ K}^{-1}$, (4.1.36) gives $H = 2.40 \times 10^{-10}\text{ W kg}^{-1}$. The resulting temperature profile is given in Figure 4.5. The thickness of the layer is about a factor of 3 larger than the thickness of the continental crust, but the concentration of heat-producing elements is very nearly that of typical continental rocks.

The basic hypothesis of an upward concentration of heat-producing elements with steady-state heat conduction was the generally accepted explanation for the temperature distribution in the Earth's interior from about 1920 to the late 1960s. It provided an explanation for the

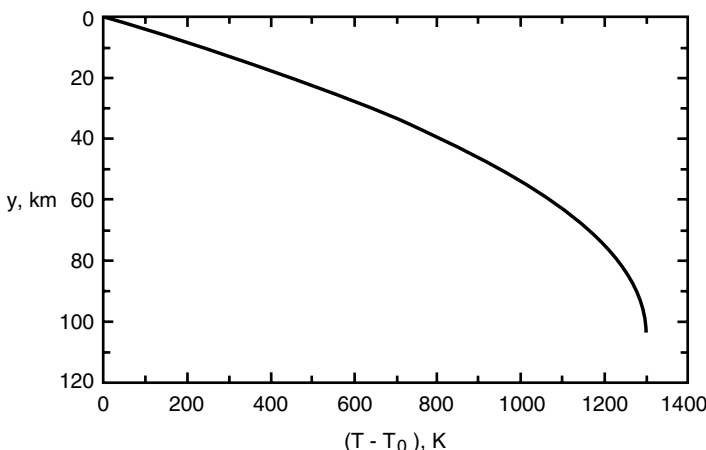


Figure 4.5. Near-surface temperature distribution in the Earth assuming a conduction profile with the heat-producing elements uniformly distributed in the region $0 < y < y_1$. On the assumption that $dT/dy = 0$ at $y = y_1$ and for $(dT/dy)_0 = 25\text{ K km}^{-1}$, $T_1 - T_0 = 1,300\text{ K}$, we have $y_1 = 104\text{ km}$ and $H = 2.4 \times 10^{-10}\text{ W kg}^{-1}$.

temperature gradient in the continental crust, but allowed for the solid upper mantle required by seismic studies.

The hypothesis that the heat-producing elements were strongly concentrated in the crust led to the prediction that the surface heat flow in the oceans, where the crust was known to be thin, would be considerably lower than the surface heat flow in the continents. Measurements by Revelle and Maxwell (1952) in the Pacific and by Bullard (1954) in the Atlantic showed that oceanic heat flow was very nearly equal to continental heat flow, so the prediction was not valid. Bullard et al. (1956) attributed this equality of heat flow to mantle convection. Nevertheless it took another 15 years before the model with an upward concentration of heat sources and steady-state heat conduction was discarded.

4.1.4 Mantle Convection and Mantle Temperatures

The acceptance of mantle convection in the late 1960s provided a natural explanation for the high thermal gradients near the Earth's surface; they are a consequence of thermal boundary layers associated with mantle convection. Beneath the boundary layers heat transport is primarily by convection and the thermal gradient at depth is nearly adiabatic.

Three distinct thermal regimes thus occur within the mantle–crust system (Jeanloz and Morris, 1986). First, there are nearly adiabatic regions, where advective heat transport by vertical motion dominates all other heat transfer mechanisms. Most of the lower mantle appears to be in this category, as are the upper mantle beneath the lithosphere and portions of the transition zone – roughly 90% of the mantle (Ito and Katsura, 1989). Practically all of the outer core is in this category as well. These regions are characterized by nearly isentropic (adiabatic) radial variations of temperature. Second, there are regions where heat transfer by advection is roughly equal to heat transport by conduction. These are the thermal boundary layers described in the previous section. Included in this category are oceanic lithosphere, part of the D'' layer at the base of the mantle, and part of the subcrustal lithosphere beneath continents. There also may be interfacial thermal boundary layers within the transition zone. Finally, there are regions where conductive heat transport dominates, called conduction layers. The continental crust and the upper mantle attached to it are the most important examples of this group. Altogether, conductive layers comprise less than 2% of the volume of the Earth.

Mantle convection can account for virtually all of the known temperature structure in the nearly adiabatic advective regions and thermal boundary layers. Taking into consideration the near-surface concentration of radioactive heat sources, it is possible to explain temperatures in the continental crust as well. This is certainly one of the major successes of convection theory.

The precision with which temperatures are known degrades with depth, and reflects the increased uncertainty in composition and thermodynamic parameters in the deep mantle and core. At the present time, lithospheric temperatures can be estimated to within about $\pm 10\%$. The uncertainty increases with depth, and in the lower mantle and the core reaches perhaps $\pm 30\%$, or about $\pm 1,000$ K. Unlike seismic structure, lateral variations in temperature are not small perturbations to the spherically averaged geotherm. In the upper mantle, lateral temperature variations approach $\pm 50\%$ of the spherical average temperature. The three-dimensional thermal structure of the mantle is closely connected to the pattern of mantle convection. Anomalously high temperatures are associated with regions of ascending flow, while anomalously low temperatures characterize regions with descending flow, such as subduction zones.

In addition to temperature, an understanding of mantle convection requires a knowledge of other thermodynamic parameters and properties, including density ρ , pressure p , specific heats c_p and c_v , thermal expansivity α , thermal conductivity k , thermal diffusivity κ , and the Grüneisen parameter γ . The thermodynamic properties of mantle phase transformations, including solid–solid and solid–liquid reactions, are also important. Some of these parameters are reasonably well constrained for the upper mantle by laboratory measurements and inferences drawn from geophysical data. At greater depths, however, the situation changes. Some properties, such as density, are known from seismology, while others, such as the specific heats, are well constrained by solid-state theory. Others, such as thermal conductivity, are poorly known.

4.1.5 Surface Heat Flow and Internal Heat Sources

Heat escaping from the Earth's interior is, in large part, brought to the surface by mantle convection. The Earth's surface heat loss is therefore a directly observable measure of its internal convective activity and thermal structure. The total heat flow from the interior of the Earth Q is given by

$$Q = \bar{q}_c A_c + \bar{q}_o A_o \quad (4.1.38)$$

where \bar{q}_c is the mean continental heat flux, A_c is the area of the continents, \bar{q}_o is the mean oceanic heat flux, and A_o is the area of the oceans. The distribution of the Earth's surface heat flux has been shown in Figure 2.8; values of \bar{q}_c and \bar{q}_o have been given by Pollack et al. (1993). The area of the continents, including the continental margins, is $A_c = 2 \times 10^8 \text{ km}^2$. Multiplication of this by $\bar{q}_c = 65 \text{ mW m}^{-2}$ gives the total heat flow from the continents $Q_c = 1.30 \times 10^{13} \text{ W}$. The area of the oceans, including the marginal basins, is $A_o = 3.1 \times 10^8 \text{ km}^2$. Multiplication of this by $\bar{q}_o = 101 \text{ mW m}^{-2}$ gives the total heat flow from the oceans $Q_o = 3.13 \times 10^{13} \text{ W}$. With $Q = Q_o + Q_c$, we find Q equal to $4.43 \times 10^{13} \text{ W}$. Accordingly, the mean surface heat flow for the Earth \bar{q}_s is given by $4.43 \times 10^{13} \text{ W}$ divided by the Earth's surface area of $5.1 \times 10^8 \text{ km}^2$, or $\bar{q}_s = 87 \text{ mW m}^{-2}$.

A substantial part of the heat lost through the Earth's surface originates in the interior of the Earth by the decay of the radioactive elements uranium, thorium, and potassium. Some part of the surface heat loss must also come from the overall cooling of the Earth through geologic time. An upper limit to the concentration of radioactive elements in the Earth can be derived by attributing all the surface heat loss to the radioactive heat generation. The upper bound to the mean heat generation per unit mass H is then given by

$$H = \frac{Q}{M} \quad (4.1.39)$$

where M is the mass of the heat-producing material in the Earth. If we assume that the entire mass of the Earth, $5.97 \times 10^{24} \text{ kg}$, is involved in radiogenic heat generation and take $Q = 4.43 \times 10^{13} \text{ W}$, we find an upper bound of $H = 7.42 \times 10^{-12} \text{ W kg}^{-1}$. However, on the basis of geochemical studies, it can be argued that the core cannot contain a significant fraction of the heat-producing elements in the Earth. In this case, the mass in (4.1.39) should be the mass of the mantle, $4.0 \times 10^{24} \text{ kg}$, and the upper bound becomes $H = 11.1 \times 10^{-12} \text{ W kg}^{-1}$.

A reduction must be made in the value of H appropriate to the mantle, since a substantial fraction of the heat lost from the continents originates in the highly concentrated radioactive isotopes of the continental crust. We estimate that of the mean continental heat flux of 65 mW m^{-2} , 28 mW m^{-2} can be attributed to the mantle and 37 mW m^{-2} to radioactive isotopes in the crust. This crustal contribution corresponds to a total heat flow of $7.4 \times 10^{12} \text{ W}$, or 17% of the total surface heat flow. Reduction of the mantle heat production by this amount gives $H = 9.22 \times 10^{-12} \text{ W kg}^{-1}$ as an upper bound to the mean heat generation rate per unit mass of the mantle.

Only a fraction of the Earth's present surface heat flow can be attributed to the decay of radioactive isotopes presently in the mantle. Since the radioactive isotopes decay into stable isotopes, heat production due to radioactive decay decreases with time. For example, we show below that the heat production three billion years ago was about twice as great as it is today. Because less heat is being generated in the Earth through time, less heat is also being convected to the surface. Thus, the vigor of mantle convection decreases with the age of the Earth. Since the strength of convection is dependent on viscosity, and the viscosity of the mantle is a sensitive function of its temperature, a decrease in the heat flux with time leads to a decrease in the mean mantle temperature. This cooling of the Earth in turn contributes to the surface heat flow. We consider this problem in detail in Chapter 13, and estimate that about 80% of the present surface heat flow can be attributed to the decay of radioactive isotopes presently in the Earth while about 20% comes from the cooling of the Earth. If we reduce the above upper bound to the present mantle heat production rate accordingly, we obtain $H = 7.38 \times 10^{-12} \text{ W kg}^{-1}$ as an estimate of the actual present mean rate of radiogenic heat production per unit mass in the mantle.

Radioactive heating of the mantle and crust is attributed to the decay of the uranium isotopes ^{235}U and ^{238}U , the thorium isotope ^{232}Th , and the potassium isotope ^{40}K . The rates of heat production and the half-lives $\tau_{1/2}$ of these isotopes are given in Table 4.2. At the present time natural uranium is composed of 99.28% by weight ^{238}U and 0.71% ^{235}U . Natural thorium is 100% ^{232}Th . Natural potassium is composed of 0.0119% ^{40}K . The present rates of heat production of natural uranium and potassium are also given in Table 4.2.

The ratios of potassium to uranium and thorium to uranium are nearly constant in a wide range of terrestrial rocks. Based on these observed ratios we take $C_0^{\text{K}}/C_0^{\text{U}} = 10^4$ and $C_0^{\text{Th}}/C_0^{\text{U}} = 4$, where C_0^{K} , C_0^{Th} , and C_0^{U} are the present mass concentrations of potassium, thorium, and uranium, respectively. The total present heat production rate per unit mass H_0

Table 4.2. Rates of Heat Release H and Half-lives $\tau_{1/2}$ of the Important Radioactive Isotopes in the Earth's Interior^a

Isotope	H (W kg^{-1})	$\tau_{1/2}$ (yr)	Concentration, C (kg kg^{-1})
^{238}U	9.46×10^{-5}	4.47×10^9	30.8×10^{-9}
^{235}U	5.69×10^{-4}	7.04×10^8	0.22×10^{-9}
U	9.81×10^{-5}		31.0×10^{-9}
^{232}Th	2.64×10^{-5}	1.40×10^{10}	124×10^{-9}
^{40}K	2.92×10^{-5}	1.25×10^9	36.9×10^{-9}
K	3.48×10^{-9}		31.0×10^{-5}

^a Heat release is based on the present mean mantle concentrations of the heat-producing elements.

is related to the heat generation rates of the individual radioactive elements by

$$H_0 = C_0^U \left(H^U + \frac{C_0^{\text{Th}}}{C_0^U} H^{\text{Th}} + \frac{C_0^K}{C_0^U} H^K \right) \quad (4.1.40)$$

With $H_0 = 7.38 \times 10^{-12} \text{ W kg}^{-1}$ and the other parameters as given above and in Table 4.2, we find that $C_0^U = 3.1 \times 10^{-8} \text{ kg kg}^{-1}$ or 31 ppb (parts per billion by weight). These preferred values for the mean mantle concentrations of heat-producing elements are also given in Table 4.2.

The mean heat production rate of the mantle in the past can be related to the present heat production rate using the half-lives of the radioactive isotopes – see Section 12.4.1. The concentration C of a radioactive isotope at time t measured backward from the present is related to the present concentration C_0 and the half-life of the isotope $\tau_{1/2}$ by

$$C = C_0 \exp\left(\frac{t \ln 2}{\tau_{1/2}}\right) \quad (4.1.41)$$

Thus, the past mean mantle heat production rate is given by

$$\begin{aligned} H &= 0.9927 C_0^U H^{238\text{U}} \exp\left(\frac{t \ln 2}{\tau_{238\text{U}}}\right) \\ &\quad + 0.0072 C_0^U H^{235\text{U}} \exp\left(\frac{t \ln 2}{\tau_{235\text{U}}}\right) \\ &\quad + C_0^{\text{Th}} H^{\text{Th}} \exp\left(\frac{t \ln 2}{\tau_{\text{Th}}}\right) \\ &\quad + 1.28 \times 10^{-4} C_0^K H^{40\text{K}} \exp\left(\frac{t \ln 2}{\tau_{40\text{K}}}\right) \end{aligned} \quad (4.1.42)$$

The rate of mean heat production based on (4.1.42) and parameter values in Table 4.2 is plotted as a function of time before the present in Figure 4.6. The past contributions of the individual radioactive elements are also shown. It can be seen that the rate of heat production 3 Gyr ago was about twice the present value. At the present time heat is produced primarily by ^{238}U and ^{232}Th , but in the distant past ^{235}U and ^{40}K were the dominant isotopes because of their shorter half-lives.

The concentrations of the heat-producing elements in surface rocks vary considerably. Some typical values are given in Table 4.3. The mantle values from Table 4.2 are included for reference. Partial melting at ocean ridges depletes mantle rock of incompatible elements such as uranium, thorium, and potassium. These incompatible elements are concentrated in the basaltic partial melt fraction. As a result, the oceanic crust (tholeiitic basalt) is enriched in these elements by about a factor of 4 relative to the undepleted mantle. Peridotites that have been depleted in the incompatible elements are sometimes found on the surface of the Earth. A typical example of the small concentrations of the heat-producing elements in a “depleted” peridotite is given in Table 4.3. Processes that lead to the formation of the continental crust, such as the volcanism associated with ocean trenches, further differentiate the incompatible elements. The concentrations of the heat-producing elements in a typical continental rock

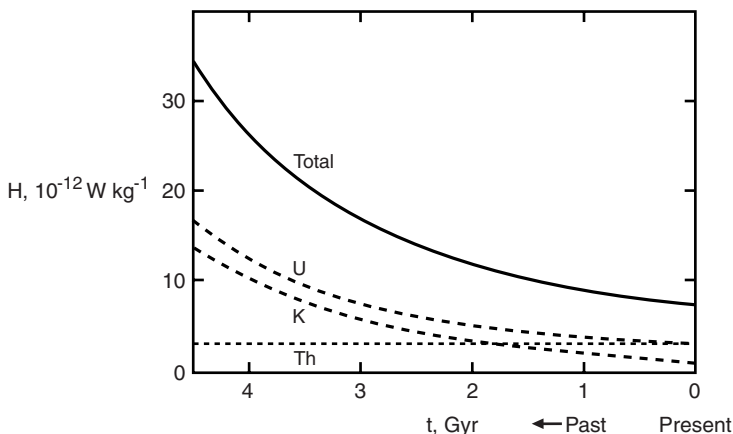


Figure 4.6. Mean mantle heat production rates due to the decay of the radioactive isotopes ^{238}U , ^{235}U , ^{232}Th , and ^{40}K as functions of time measured back from the present.

Table 4.3. Typical Concentrations of the Heat-producing Elements in Several Rock Types and the Average Concentrations in Chondritic Meteorites

Rock Type	Concentration		
	U (ppm)	Th (ppm)	K (%)
Reference undepleted mantle	0.031	0.124	0.031
“Depleted” peridotites	0.001	0.004	0.003
Tholeiitic basalt	0.9	2.7	0.83
Granite	4.7	20	4.2
Shale	3.7	12	2.7
Average continental crust	1.42	5.6	1.43
Chondritic meteorites	0.012	0.042	0.085

such as a granite are quite variable, but in general they are an order of magnitude greater than in tholeiitic basalts. Representative values of concentrations in granite are given in Table 4.3.

It is generally accepted that the chondritic class of meteorites is representative of primitive mantle material. The average concentrations of the heat-producing elements in chondritic meteorites are listed in Table 4.3. The concentrations of uranium and thorium are about a factor of 2 less than our mean mantle values, and the concentration of potassium is about a factor of 3 larger. The factor of 6 difference in the ratio $C_0^{\text{K}}/C_0^{\text{U}}$ is believed to represent a fundamental difference in elemental abundances between the Earth’s mantle and chondritic meteorites.

In the next two sections we will consider the structure of the upper thermal boundary layer comprising the oceanic and continental lithospheres. These boundary layers are relatively thin with thickness between 0 and about 200 km. In determining these thermal structures we will neglect adiabatic changes in temperature. Since the adiabatic gradient is only about 0.4 K km^{-1} this is a reasonable approximation. A systematic treatment of this approximation will be given in Chapter 6.

4.2 Thermal Regime of the Oceanic Lithosphere

The oceanic lithosphere is the upper thermal boundary layer of the convecting mantle. It is formed at accretional plate margins by the cooling of hot mantle rock. The oceanic lithosphere is convected away from ridge crests at the spreading rate deduced from the pattern of magnetic anomalies on the seafloor (see Chapter 2). The oceanic lithosphere thickens with time as the upper mantle cools by conduction and by hydrothermal heat loss to the oceans. The resulting thermal contraction produces an increase in seafloor depth with crustal age in the direction of seafloor spreading. Accompanying the increase in seafloor depth with crustal age are decreases in surface heat flow and a decreasing geoid height with age. It has been established that these trends do not continue unbroken onto the oldest oceanic lithosphere. Instead, there is a gradual transition in the vicinity of 70–100 Myr crustal ages, which appears to separate two different thermal boundary layer regimes. For crustal ages less than 70 Myr, the statistical variation in seafloor depth can be explained by a cooling half-space model. In this model, the depth of the water column, relative to its depth at the ridge crest, increases with the square root of the crustal age. The actual seafloor topography approximates this behavior at young ages (Parsons and Sclater, 1977). At greater ages, seafloor depth increases more slowly, on average. A similar trend is observed in geoid heights. The geoid height decreases linearly with crustal age to about 50 Myr in the North and South Atlantic and in the Indian Ocean (Sandwell and Schubert, 1980).

Interpretations of surface heat flow are more complex. Heat flow on the ocean floor is obtained from many thousands of point measurements and is subject to large variability. Variability in heat flow can be reduced by the careful selection of measurement sites and appropriate averaging (Sclater et al., 1980). For crustal ages between about 10 and 80 Myr the heat flow is inversely proportional to the square root of the crustal age, in agreement with the half-space cooling model.

Significant departures occur on young crust, presumably because of additional heat loss by hydrothermal circulation systems (Lister, 1980). There is also a significant departure from the predictions of the cooling half-space model for old ocean crust. Densely spaced heat flow measurements in the Pacific by Von Herzen et al. (1989) have suggested that the average heat flow on older ocean crust may also be higher than the heat flow predicted by the cooling half-space model, and this is substantiated in the data compiled by Stein and Stein (1992) (see also Stein and Stein, 1996).

4.2.1 Half-space Cooling Model

We first demonstrate that the temperature distribution in the oceanic lithosphere as determined using the cooling half-space model described in the previous section provides an adequate first-order model for ages less than about 80 Myr. The geometry is illustrated in Figure 4.7. Because of its low temperature, the lithosphere behaves as a rigid moving plate. The temperature in the plate is governed by the convection–conduction equation (see Chapter 6)

$$u_0 \frac{\partial T}{\partial x} = \kappa \left(\frac{\partial^2 T}{\partial x^2} + \frac{\partial^2 T}{\partial y^2} \right) \quad (4.2.1)$$

where u_0 is the velocity of seafloor spreading. The Peclét number for the oceanic lithosphere is defined by $Pe \equiv u_0 L / \kappa$, where L is a typical distance from the ocean ridge. With $u_0 = 50 \text{ mm yr}^{-1}$, $L = 1,000 \text{ km}$, and $\kappa = 1 \text{ mm}^2 \text{s}^{-1}$ as typical values, we find $Pe = 1,600$.

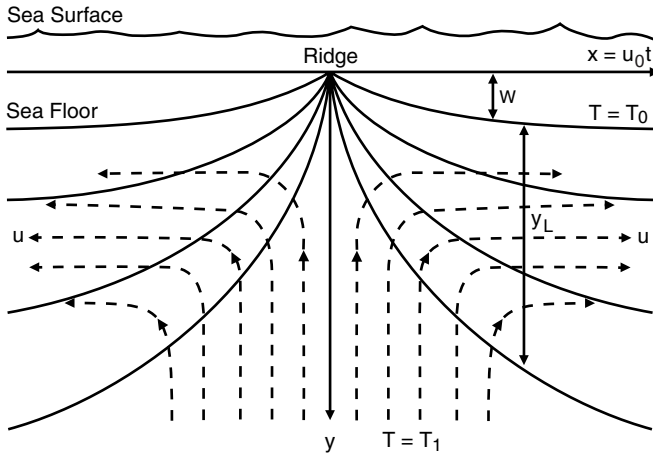


Figure 4.7. A sketch showing the model of oceanic lithosphere formation by seafloor spreading from a mid-ocean ridge used to derive the thermal boundary layer cooling curves. Solid contours are isotherms; dashed contours are streamlines. The depth to the subsiding seafloor w and the thickness of the lithosphere y_L are shown.

For a large Peclét number it is appropriate to make the boundary layer approximation and neglect horizontal heat conduction compared with vertical heat conduction, and (4.2.1) becomes

$$u_0 \frac{\partial T}{\partial x} = \kappa \frac{\partial^2 T}{\partial y^2} \quad (4.2.2)$$

Since $t = x/u_0$ we can rewrite (4.2.2) as

$$\frac{\partial T}{\partial t} = \kappa \frac{\partial^2 T}{\partial y^2} \quad (4.2.3)$$

which is identical to (4.1.1). The required initial and boundary conditions are $T = T_1$ at $t = 0$, $T = T_0$ at $y = 0$, and $T \rightarrow T_1$ as $y \rightarrow \infty$. Thus, the solution given in (4.1.20) is valid and the temperature distribution in the oceanic lithosphere is

$$\frac{T_1 - T}{T_1 - T_0} = \operatorname{erfc}\left(\frac{y}{2(\kappa t)^{1/2}}\right) \quad (4.2.4)$$

Isotherms as a function of depth and age are given in Figure 4.8 for $T_1 - T_0 = 1,300$ K and $\kappa = 1 \text{ mm}^2 \text{ s}^{-1}$.

From (4.1.23), the surface heat flow q_0 as a function of age t is given by

$$q_0 = \frac{k(T_1 - T_0)}{(\pi \kappa t)^{1/2}} \quad (4.2.5)$$

For $k = 3.3 \text{ W m}^{-1} \text{ K}^{-1}$ and other values as above, the surface heat flow is related to the age of the seafloor t by

$$q_0 = \frac{431}{\sqrt{t}} \quad (4.2.6)$$

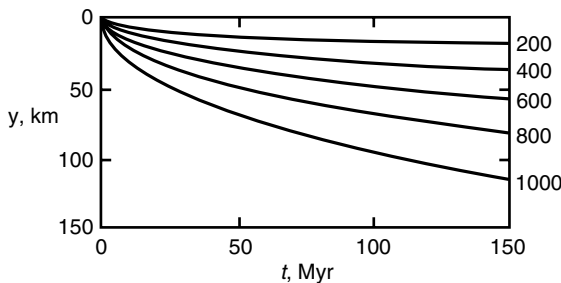


Figure 4.8. Isotherms as a function of depth and age in the oceanic lithosphere from (4.2.4) taking $T_1 - T_0 = 1,300\text{ K}$ and $\kappa = 1\text{ mm}^2\text{ s}^{-1}$. The isotherms are values of $T - T_0$ in K.

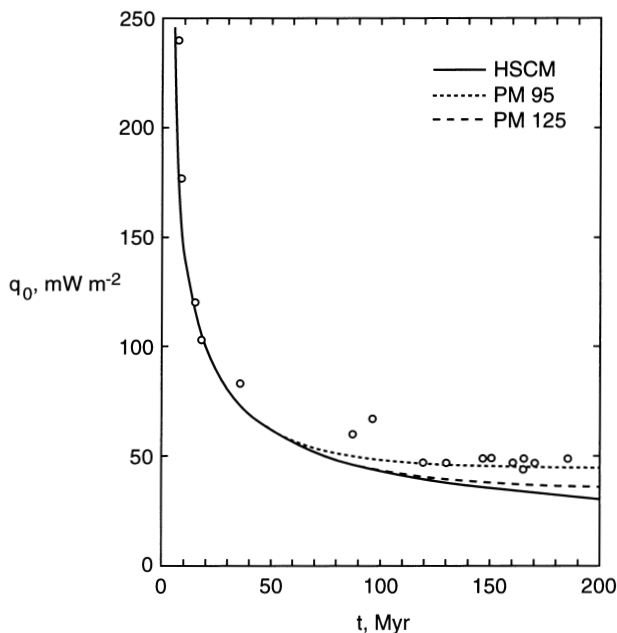


Figure 4.9. Heat flow as a function of the age of the ocean floor. The data points are from sediment-covered regions of the Atlantic and Pacific Oceans (Lister et al., 1990). Comparisons are made with the half-space cooling model (HSCM) from (4.2.6) and the plate model from (4.2.29) with $y_{L0} = 95\text{ km}$ (PM95) and with $y_{L0} = 125\text{ km}$ (PM125).

with t in Myr and q in mW m^{-2} . This result is compared with measurements of heat flow compiled by Lister et al. (1990) in Figure 4.9. Many measurements of the heat flow through the ocean floor have been carried out and, in general, they have a great deal of scatter (Stein and Stein, 1992, 1996). A major cause of this scatter is hydrothermal circulation through the oceanic crust. The heat loss associated with these circulations causes observed heat flows to be systematically low. Because of this problem, Lister et al. (1990) considered only measured values in thick sedimentary cover that would inhibit hydrothermal circulations. The heat flow predicted by the half-space cooling model is in reasonable agreement with the data, but it is somewhat less than the measured values.

The thickness of the oceanic lithosphere from (4.1.22) is

$$y_L = 2.32 (\kappa t)^{1/2} \quad (4.2.7)$$

For our nominal value of $\kappa = 1 \text{ mm}^2 \text{ s}^{-1}$, the thickness of the lithosphere in km is related to the seafloor age in Myr by

$$y_L = 13\sqrt{t} \quad (4.2.8)$$

With $t = 10 \text{ Myr}$ we have $y_L = 41 \text{ km}$ and with $t = 100 \text{ Myr}$ we have $y_L = 130 \text{ km}$. It should be emphasized that the thickness given in (4.2.7) is arbitrary in that it corresponds to $(T_1 - T)/(T_1 - T_0) = 0.9$.

The temperature distribution in the oceanic lithosphere can also be used to predict the morphology of oceanic ridges. As the oceanic lithosphere thickens, its temperature decreases and its density increases due to thermal contraction. The heavier lithosphere sags downward, thus deepening the oceans with increasing distance from the ridge. The depth of the ocean as a function of crustal age can be found by the application of the principle of isostasy, based on an assumed hydrostatic equilibrium. The principle of isostasy states that there is the same mass per unit area between the surface and some depth of compensation for any vertical column of material. This is equivalent to the assumption that the lithostatic pressure at some depth is horizontally homogeneous.

The mass per unit area in a column of any age is

$$\int_0^{y_L} \rho dy + w\rho_w$$

where y_L is the thickness of the lithosphere, ρ_w is the density of water, and w is the depth of the ocean floor below the ridge crest. At the ridge crest, $\rho = \rho_1$ the deep mantle density, and the mass of a column of vertical height $w + y_L$ is $\rho_1(w + y_L)$. Hydrostatic equilibrium requires that

$$w(\rho_w - \rho_1) + \int_0^{y_L} (\rho - \rho_1) dy = 0 \quad (4.2.9)$$

The first term in (4.2.9) represents a negative mass because water with density ρ_w is less dense than the mantle rock it has replaced because of the subsidence of the seafloor a distance w . The second term in the equation represents a positive mass because thermal contraction in the cooling lithosphere causes the density ρ to be higher than the reference hot mantle rock density ρ_1 . Introduction of the volume coefficient of thermal expansion α allows us to write

$$\rho - \rho_1 = \rho_1\alpha(T_1 - T) \quad (4.2.10)$$

Upon substitution of the temperature profile from (4.2.4) into (4.2.10) and further substitution of the result into (4.2.9), we obtain

$$w(\rho_1 - \rho_w) = \rho_1\alpha(T_1 - T_0) \int_0^\infty \operatorname{erfc}\left[\frac{y}{2\sqrt{\kappa t}}\right] dy \quad (4.2.11)$$

Since $\rho \rightarrow \rho_1$ and $T \rightarrow T_1$ at the base of the lithosphere, the limit on the integral has been changed from $y = y_L$ to $y = \infty$. We can rewrite (4.2.11) using (4.1.3) with the result

$$w = \frac{2\rho_1\alpha(T_1 - T_0)}{(\rho_1 - \rho_w)} (\kappa t)^{1/2} \int_0^\infty \operatorname{erfc}(\eta) d\eta \quad (4.2.12)$$

The definite integral has the value

$$\int_0^\infty \operatorname{erfc}(\eta) d\eta = \frac{1}{\sqrt{\pi}} \quad (4.2.13)$$

so that

$$w = \frac{2\rho_1\alpha(T_1 - T_0)}{(\rho_1 - \rho_w)} \left(\frac{\kappa t}{\pi} \right)^{1/2} \quad (4.2.14)$$

Equation (4.2.14) predicts that the depth of the ocean increases with the square root of the age of the ocean floor. For $\rho_1 = 3,300 \text{ kg m}^{-3}$, $\rho_w = 1,000 \text{ kg m}^{-3}$, $\kappa = 1 \text{ mm}^2 \text{ s}^{-1}$, $T_1 - T_0 = 1,300 \text{ K}$, and $\alpha = 3 \times 10^{-5} \text{ K}^{-1}$, the ocean subsidence w in km is related to the seafloor age in Myr by

$$w = 0.35\sqrt{t} \quad (4.2.15)$$

With $t = 10 \text{ Myr}$ we have $w = 1.1 \text{ km}$ and with $t = 100 \text{ Myr}$ we have $w = 3.5 \text{ km}$. This result with a ridge depth of 2.5 km is compared with seafloor depths in the oceans in Figure 4.10. For this comparison we have chosen the depths given by Johnson and Carlson (1992) obtained from DSDP (Deep Sea Drilling Program) and ODP (Ocean Drilling Program) drill sites. Corrections have been made for sediment thickness, and “normal” crust in the Atlantic, Pacific, and Indian Oceans is considered. Other comprehensive compilations of ocean depth data have been given by Renkin and Sclater (1988) and by Kido and Seno (1994) with similar results.

For seafloor ages of less than about 80 Myr the data correlate well with the half-space cooling model result given in (4.2.15). At ages greater than about 80 Myr the seafloor is

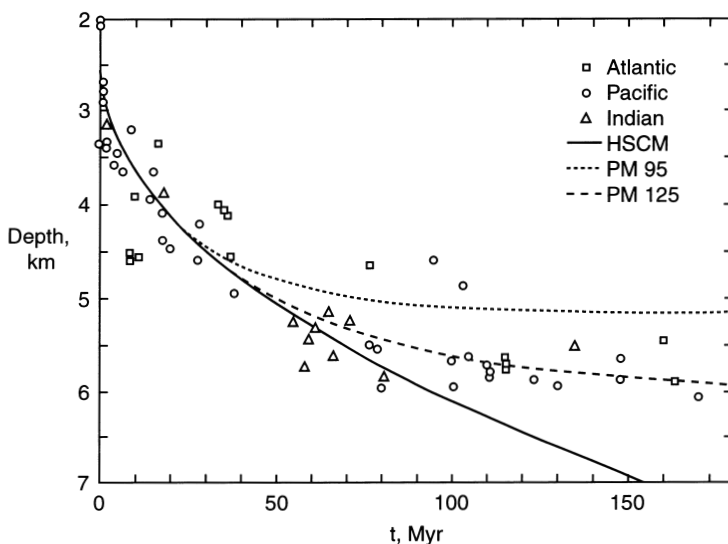


Figure 4.10. Seafloor depth as a function of age in the Atlantic, Pacific, and Indian Oceans. Data are from DSDP and ODP drill sites on normal ocean crust and depths have been corrected for sediment cover (Johnson and Carlson, 1992). Comparisons are made with the half-space cooling model (HSCM) from (4.2.15) and the plate model from (4.2.32) with $y_{L0} = 95 \text{ km}$ (PM95) and with $y_{L0} = 125 \text{ km}$ (PM125).

systematically shallower than the half-space cooling model prediction. The topography data in Figure 4.10 have much less scatter than the heat flow data in Figure 4.9, perhaps because the topography is an integral measure of the entire thermal structure of the lithosphere rather than the near-surface thermal gradient contaminated by hydrothermal effects.

We next consider a third independent measure of the thermal structure of the oceanic lithosphere. The Earth's gravitational field is a measure of the density distribution within the Earth. As discussed above in connection with seafloor subsidence, it is appropriate to assume isostatic equilibrium for the oceanic lithosphere. Haxby and Turcotte (1978) showed that the surface gravitational potential anomaly ΔU due to a shallow, long-wavelength isostatic density distribution is proportional to the dipole moment of the density distribution beneath the point of measurement:

$$\Delta U = 2\pi G \int_0^h y \Delta\rho(y) dy \quad (4.2.16)$$

where G is the gravitational constant, h is the depth of compensation, and $\Delta\rho(y)$ is the difference between the density $\rho(y)$ and a reference density.

The gravitational potential anomaly can be related directly to the geoid anomaly ΔN by

$$\Delta U = -g \Delta N \quad (4.2.17)$$

The geoid anomaly is the vertical distance between the actual equipotential surface of the Earth and the reference spheroid. Substitution of (4.2.17) into (4.2.16) gives

$$\Delta N = -\frac{2\pi G}{g} \int_0^h y \Delta\rho(y) dy \quad (4.2.18)$$

With the mantle density beneath the oceanic ridge taken as the reference density ($\Delta\rho = \rho - \rho_1$), the geoid anomaly associated with the subsiding, thermally compensated oceanic lithosphere can be written as

$$\Delta N = \frac{-2\pi G}{g} \left\{ \int_{-w}^0 y (\rho_w - \rho_1) dy + \int_0^\infty y (\rho - \rho_1) dy \right\} \quad (4.2.19)$$

The first term on the right side of (4.2.19) can be integrated directly and the second term can be rewritten using (4.2.10) relating density to temperature. The result is

$$\Delta N = \frac{-2\pi G}{g} \left\{ \frac{(\rho_1 - \rho_w) w^2}{2} + \alpha \rho_1 \int_0^\infty y (T_1 - T) dy \right\} \quad (4.2.20)$$

By using (4.2.14) for the ocean floor depth w and (4.2.4) for the temperature distribution in the lithosphere, we can obtain the following simple formula for the geoid anomaly over a spreading ridge:

$$\Delta N = -\frac{2\pi G \rho_1 \alpha \kappa (T_1 - T_0)}{g} \left\{ 1 + \frac{2\rho_1 \alpha (T_1 - T_0)}{\pi (\rho_1 - \rho_w)} \right\} t \quad (4.2.21)$$

This geoid anomaly is a linear function of the age of the seafloor. For $\rho_1 = 3,300 \text{ kg m}^{-3}$, $\kappa = 1 \text{ mm}^2 \text{s}^{-1}$, $T_1 - T_0 = 1,300 \text{ K}$, and $\alpha = 3 \times 10^{-5} \text{ K}^{-1}$, we find that the geoid anomaly ΔN in m is related to the age t in Myr by

$$\Delta N = -0.18t \quad (4.2.22)$$

With $t = 10 \text{ Myr}$ the geoid anomaly is $\Delta N = -1.8 \text{ m}$ and with $t = 100 \text{ Myr}$ the geoid anomaly is $\Delta N = -18 \text{ m}$.

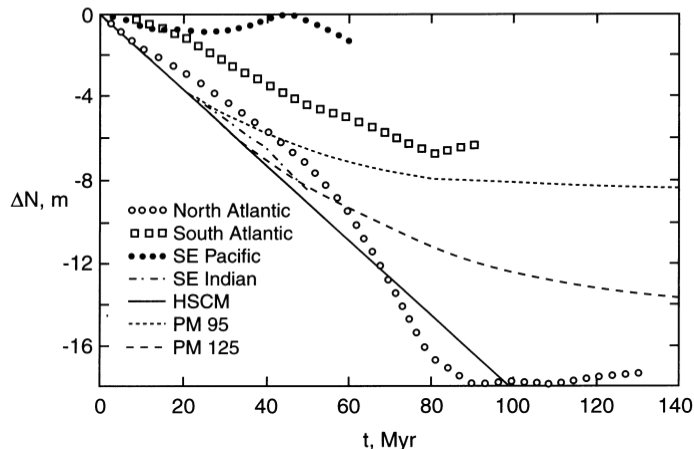


Figure 4.11. Geoid anomalies relative to ridge crests are given as a function of seafloor age for the North Atlantic, South Atlantic, SE Pacific, and SE Indian Oceans (Sandwell and Schubert, 1980). Comparisons are made with the half-space cooling model (HSCM) from (4.2.22) and the plate cooling model from (4.2.35) with $y_{L0} = 95$ km (PM95) and with $y_{L0} = 125$ km (PM125).

Over the oceans the sea surface represents an equipotential surface to a first approximation. Deviations are due to tides, ocean currents, and storms. Laser altimeter measurements of the sea surface from satellites define the geoid over the oceans and provide maps of geoid anomalies. Geoid anomalies as a function of seafloor age for several oceans are given in Figure 4.11 (Sandwell and Schubert, 1980). Also included in the figure is the linear prediction from (4.2.22). Reasonably good agreement is found between theory and the data for the Southeast Indian and North Atlantic Oceans, but there is considerably more scatter than with the topography data. This scatter can be attributed to the geoid anomalies caused by deeper density anomalies in the mantle. This problem has also been considered in detail by Richardson et al. (1995).

The oceanic lithosphere on the two sides of a fracture zone ideally has a constant age difference $t_2 - t_1$. Associated with this age difference is an offset in the geoid. If the half-space cooling model is valid, then the offset in the geoid $\Delta N_2 - \Delta N_1$ is related to the age difference across the fracture zone $t_2 - t_1$ by (4.2.22) with the result

$$\frac{\Delta N_2 - \Delta N_1}{t_2 - t_1} = -0.18 \text{ m Myr}^{-1} \quad (4.2.23)$$

The ratio of geoid offset to the age difference across a fracture zone is predicted to be a constant (Detrick, 1981; Sandwell and Schubert, 1982; Cazenave et al., 1983; Cazenave, 1984; Driscoll and Parsons, 1988; Marty et al., 1988; Freedman and Parsons, 1990). Ratios of geoid offset to age difference, $(\Delta N_2 - \Delta N_1) / (t_2 - t_1)$, for the Mendocino fracture zone are given in Figure 4.12 as a function of the mean age of the crust at the fracture zone, $\bar{t} = (t_1 + t_2)/2$. The data are from Sandwell and Schubert (1982) and from Marty et al. (1988). Although there is considerable scatter, the magnitude of the geoid offset-age difference ratio appears to systematically decrease from the value predicted by (4.2.23) at older ages.

Observations of surface heat flow, bathymetry, and geoid are all in quite good agreement with the half-space cooling model for ages less than about 80 Myr. The bathymetry data

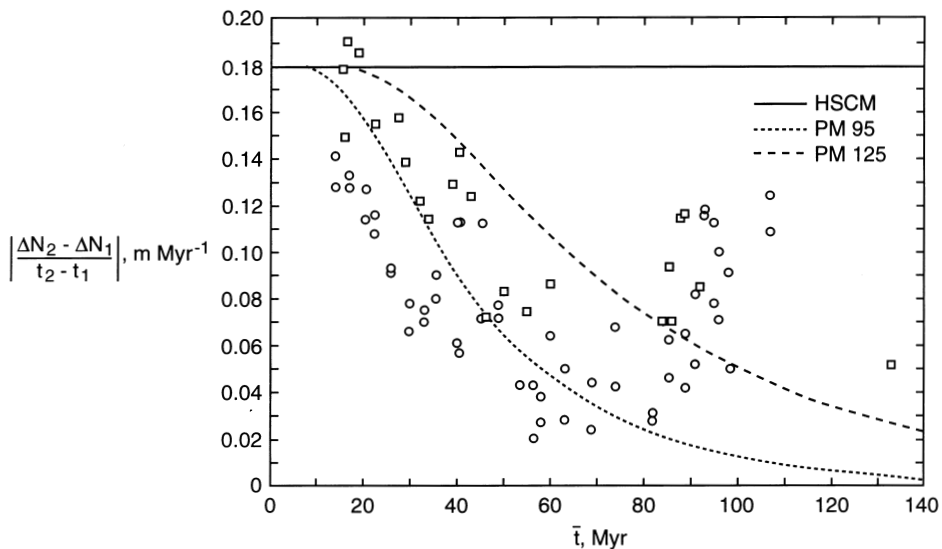


Figure 4.12. Magnitude of the ratio of the geoid offset $\Delta N_2 - \Delta N_1$ to the age difference $t_2 - t_1$ across the Mendocino fracture zone as a function of the mean age of the seafloor $\bar{t} = (t_1 + t_2)/2$. The squares are the data of Sandwell and Schubert (1982) and the circles are the data of Marty et al. (1988). Comparisons are made with the half-space cooling model (HSCM) from (4.2.23) and with the plate cooling model from (4.2.36) with $y_{L0} = 95$ km (PM95) and with $y_{L0} = 125$ km (PM125).

show the least scatter and show a clear flattening of the bathymetry versus age curves at greater ages.

Question 4.1: Why are there deviations from the half-space cooling model for the oceanic lithosphere at seafloor ages greater than about 80 Myr?

4.2.2 Plate Cooling Model

As discussed above, observational evidence indicates that the oceanic lithosphere does not continue to thicken with age at ages greater than 60–100 Myr as predicted by the half-space cooling model. The physical explanation is that basal heating of the oceanic lithosphere occurs either due to the impingement of plumes or due to secondary convection. A model for this process is provided by the cooling of a finite thickness plate (McKenzie, 1967).

The constant thickness of the plate is prescribed to be y_{L0} , the thickness of the lithosphere at large times. At the surface of the plate the temperature is the water temperature T_0 ($T = T_0$ at $y = 0$); at the base of the plate the temperature is the mantle temperature T_1 ($T = T_1$ at $y = y_{L0}$). Initially at the ridge, $x = t = 0$, the temperature is the mantle temperature ($T = T_1$ at $t = 0$). We require the solution of the heat conduction equation (4.2.3) that satisfies these boundary conditions. Carslaw and Jaeger (1984, p. 100) have given the appropriate solution in the form of an infinite series

$$T = T_0 + (T_1 - T_0) \left[\frac{y}{y_{L0}} + \frac{2}{\pi} \sum_{n=1}^{\infty} \frac{1}{n} \exp\left(-\frac{\kappa n^2 \pi^2 t}{y_{L0}^2}\right) \sin\left(\frac{n\pi y}{y_{L0}}\right) \right] \quad (4.2.24)$$

At large times, $t \gg y_{L0}^2/\kappa$, an equilibrium linear temperature profile is established:

$$T = T_0 + (T_1 - T_0) \frac{y}{y_{L0}} \quad (4.2.25)$$

At small times, $t \ll y_{L0}^2/\kappa$, the half-space cooling solution given above is recovered. The deviations from the half-space cooling solution are well approximated if only the first two terms of the expansion given in (4.2.24) are retained, with the result

$$\begin{aligned} T = T_0 + (T_1 - T_0) & \left[\frac{y}{y_{L0}} + \frac{2}{\pi} \exp\left(-\frac{\kappa\pi^2 t}{y_{L0}^2}\right) \sin\left(\frac{\pi y}{y_{L0}}\right) \right. \\ & \left. + \frac{1}{\pi} \exp\left(-\frac{4\kappa\pi^2 t}{y_{L0}^2}\right) \sin\left(\frac{2\pi y}{y_{L0}}\right) \right] \end{aligned} \quad (4.2.26)$$

We will use this approximation to derive a flattening of heat flow, bathymetry, and geoid.

From (4.1.23) and (4.2.24) the surface heat flow q_0 as a function of age t is given by

$$q_0 = \frac{k(T_1 - T_0)}{y_{L0}} \left[1 + 2 \sum_{n=1}^{\infty} \exp\left(-\frac{\kappa n^2 \pi^2 t}{y_{L0}^2}\right) \right] \quad (4.2.27)$$

For large times, $t \gg y_{L0}^2/\kappa$, the equilibrium value of the surface heat flow is

$$q_{0e} = \frac{k(T_1 - T_0)}{y_{L0}} \quad (4.2.28)$$

We can approximate the deviations of the surface heat flow from the half-space cooling result given in (4.2.5) by retaining the first two terms of the expansion given in (4.2.27) with the result

$$q_0 = \frac{k(T_1 - T_0)}{y_{L0}} \left[1 + 2 \exp\left(-\frac{\kappa\pi^2 t}{y_{L0}^2}\right) + 2 \exp\left(-\frac{4\kappa\pi^2 t}{y_{L0}^2}\right) \right] \quad (4.2.29)$$

For large times $t \rightarrow \infty$, the heat flow from (4.2.29) approaches the equilibrium heat flow given in (4.2.28).

We next compare the predictions of the plate model with the heat flow compilation as a function of seafloor age given in Figure 4.9. We take $k = 3.3 \text{ W m}^{-1} \text{ K}^{-1}$, $T_1 - T_0 = 1,300 \text{ K}$, $\kappa = 1 \text{ mm}^2 \text{ s}^{-1}$, and give results for $y_{L0} = 95$ and 125 km . For $y_{L0} = 95 \text{ km}$ the equilibrium $t \rightarrow \infty$ heat flow from (4.2.28) is $q_{0e} = 45 \text{ mW m}^{-2}$ and for $y_{L0} = 125 \text{ km}$ we have $q_{0e} = 34 \text{ mW m}^{-2}$. The plate model with $y_{L0} = 95 \text{ km}$ (PM95) is in somewhat better agreement with heat flow through old seafloor than is the plate model with $y_{L0} = 125 \text{ km}$ (PM125). This is the primary basis on which Stein and Stein (1992, 1996) proposed that $y_{L0} = 95 \text{ km}$. We will return to this issue when we consider the seafloor depth data.

We next obtain the depth of the ocean floor beneath the ridge crest w as a function of seafloor age t predicted by the plate model. Substitution of the temperature profile from (4.2.24) into (4.2.10) and further substitution into (4.2.9) gives

$$w = \frac{\rho_1 \alpha (T_1 - T_0) y_{L0}}{\rho_1 - \rho_w} \left[\frac{1}{2} - \frac{4}{\pi^2} \sum_{m=0}^{\infty} \frac{1}{(1+2m)^2} \exp\left[-\frac{\kappa(1+2m)^2 \pi^2 t}{y_{L0}^2}\right] \right] \quad (4.2.30)$$

Only the terms with $n = 1, 3, 5, \dots$ in (4.2.24) are included since the terms with $n = 2, 4, 6, \dots$ integrate to zero. For large times, $t \gg y_{L0}^2/\kappa$, the equilibrium depth w_e is given by

$$w_e = \frac{\rho_1 \alpha (T_1 - T_0) y_{L0}}{2(\rho_1 - \rho_w)} \quad (4.2.31)$$

This is the equilibrium depth of the old ocean basins beneath the ridge crests. This relation provides a constraint on the thickness of the plate in the plate cooling model. In comparing the predictions of this model with observations, we will consider plate thicknesses $y_{L0} = 95$ and 125 km. With $\rho_1 = 3,300 \text{ kg m}^{-3}$, $\rho_w = 1,000 \text{ kg m}^{-3}$, $T_1 - T_0 = 1,300 \text{ K}$, and $\alpha = 3 \times 10^{-5} \text{ K}^{-1}$, we find from (4.2.31) that $w_e = 2.7 \text{ km}$ for $y_{L0} = 95 \text{ km}$ and $w_e = 3.5 \text{ km}$ for $y_{L0} = 125 \text{ km}$. With the depth of ocean ridges equal to 2.5 km , the corresponding equilibrium depths of ocean basins are 5.2 km and 6 km , respectively.

We can approximate the deviations of bathymetry from the half-space cooling result given in (4.2.14) by retaining the first term of the expansion given in (4.2.30), with the result

$$w = \frac{\rho_1 \alpha (T_1 - T_0) y_{L0}}{\rho_1 - \rho_w} \left[\frac{1}{2} - \frac{4}{\pi^2} \exp\left(-\frac{\kappa \pi^2 t}{y_{L0}^2}\right) \right] \quad (4.2.32)$$

The $n = 2$ term in the temperature distribution (4.2.24) does not contribute to the bathymetry. Seafloor subsidence predicted by the plate cooling model is compared with observations and the half-space cooling model in Figure 4.10 for plate thicknesses of $y_{L0} = 95 \text{ km}$ (PM95) and $y_{L0} = 125 \text{ km}$ (PM125). The results for a plate thickness $y_{L0} = 125 \text{ km}$ appear to be in excellent agreement with the data. This agreement was first pointed out by Parsons and Sclater (1977) and confirmed by Renkin and Sclater (1988). While a thickness of $y_{L0} = 95 \text{ km}$ appears to be in good agreement with the heat flow data as shown in Figure 4.9, a thickness of $y_{L0} = 125 \text{ km}$ appears to be in good agreement with the subsidence data as shown in Figure 4.10. Because there is generally less scatter in seafloor bathymetry than in heat flow, we prefer the value $y_{L0} = 125 \text{ km}$ although we recognize there is considerable uncertainty in the choice.

Finally, we determine the geoid anomaly associated with the subsiding, thermally compensated oceanic lithosphere as predicted by the plate model. Substitution of the temperature profile from (4.2.24) into (4.2.20) and integration give

$$\begin{aligned} \Delta N = -\frac{2\pi G}{g} & \left\{ \frac{(\rho_1 - \rho_w) w^2}{2} + \alpha \rho_1 (T_1 - T_0) y_{L0}^2 \right. \\ & \left. \times \left[\frac{1}{6} + \frac{2}{\pi^2} \sum_{n=1}^{\infty} \frac{(-1)^n}{n^2} \exp\left(-\frac{\kappa n^2 \pi^2 t}{y_{L0}^2}\right) \right] \right\} \end{aligned} \quad (4.2.33)$$

with w given by (4.2.30). For large times, $t \gg y_{L0}^2/\kappa$, the equilibrium value of the geoid ΔN_e is given by

$$\Delta N_e = -\frac{2\pi G \alpha \rho_1 (T_1 - T_0) y_{L0}^2}{g} \left[\frac{1}{6} + \frac{\alpha \rho_1 (T_1 - T_0)}{8(\rho_1 - \rho_w)} \right] \quad (4.2.34)$$

This is the predicted difference in the geoid between ocean ridges and ocean basins. For the parameter values used above and $y_{L0} = 95 \text{ km}$, we find $\Delta N_e = -8.63 \text{ m}$ and with $y_{L0} = 125 \text{ km}$ we find $\Delta N_e = -14.9 \text{ m}$.

Again, we approximate the deviation of the geoid from the equilibrium value by retaining the first terms of the expansions given in (4.2.30) and (4.2.33), with the result

$$\Delta N = - \frac{2\pi G\rho_1\alpha(T_1 - T_0)y_{L0}^2}{g} \times \left\{ \left[\frac{1}{6} + \frac{\alpha\rho_1(T_1 - T_0)}{8(\rho_1 - \rho_w)} \right] - \frac{2}{\pi^2} \left[1 + \frac{\rho_1\alpha(T_1 - T_0)}{\rho_1 - \rho_w} \right] \exp\left(-\frac{\kappa\pi^2t}{y_{L0}^2}\right) + \frac{8\rho_1\alpha(T_1 - T_0)}{\pi^4(\rho_1 - \rho_w)} \exp\left(-\frac{2\kappa\pi^2t}{y_{L0}^2}\right) + \frac{1}{2\pi^2} \exp\left(-\frac{4\kappa\pi^2t}{y_{L0}^2}\right) \right\} \quad (4.2.35)$$

The values given by this relation are compared with the data and the half-space cooling model in Figure 4.11.

It is also of interest to apply the geoid predictions of the plate model to the geoid offsets across fracture zones given in Figure 4.12. As an approximation for the ratio of geoid offset to age difference across a fracture zone, we take the time derivative of the approximate result given in (4.2.35). This gives

$$\frac{d\Delta N}{dt} = - \frac{4\pi G\rho_1\alpha(T_1 - T_0)\kappa}{g} \left\{ \left[1 + \frac{\rho_1\alpha(T_1 - T_0)}{\rho_1 - \rho_w} \right] \exp\left(-\frac{\kappa\pi^2t}{y_{L0}^2}\right) - \frac{8\rho_1\alpha(T_1 - T_0)}{\pi^2(\rho_1 - \rho_w)} \exp\left(-\frac{2\kappa\pi^2t}{y_{L0}^2}\right) - \exp\left(-\frac{4\kappa\pi^2t}{y_{L0}^2}\right) \right\} \quad (4.2.36)$$

The values given by this relation are compared with the data and the half-space cooling model in Figure 4.12. The geoid offset data clearly show a divergence from the half-space cooling model, but the considerable scatter in the data does not constrain the plate thickness.

Question 4.2: How thick is old oceanic lithosphere?

The plate model is clearly an idealization of the oceanic lithosphere. There is no well-defined “lower plate boundary” in the mantle. The flattening of the cooling curves can be attributed to “basal heating” of the oceanic lithosphere. There are two competing hypotheses for this basal heating. The first is heat transfer from mantle plumes impinging on the base of the lithosphere, and the second is secondary convection in the lower lithosphere and underlying asthenosphere.

If basal heating of the oceanic lithosphere is caused by impinging mantle plumes, then a first approximation would be to assume that the heat flux to the base of the lithosphere is a constant. Doin and Fleitout (1996) have proposed a model for Constant Heat flow Applied to the Bottom Lithospheric ISotherm (CHABLIS model). In this model 40% of the surface heat flow is attributed to this basal heating and 60% to the subduction of the thickened oceanic lithosphere. It is generally accepted that mantle plumes are a source of basal heating so that the only question is the magnitude of the heating and whether secondary convection also contributes. Mantle plumes will be discussed in detail in Chapter 11.

Secondary convection as an explanation for the flattening of the cooling curves was proposed by Richter and Parsons (1975), Parsons and McKenzie (1978), and Fleitout and

Yuen (1984). In a fluid with constant viscosity, the entire thermal boundary layer will become unstable and separate from the boundary. For the oceanic lithosphere, the cold thermal boundary layer in mantle convection, this instability is the subduction of the lithosphere at an ocean trench. In terms of the strongly temperature-dependent rheology associated with the lithosphere, the secondary scale of convection is associated with an instability within the lithosphere rather than the instability of the entire lithosphere. In this sense it is a form of delamination of the lithosphere. As the oceanic or continental lithosphere ages, the lower part of the lithosphere, a few tens of kilometers thick, has a sufficiently low viscosity to develop an internal convective flow. Yuen and Fleitout (1984), Jaupart and Parsons (1985), and Davaille and Jaupart (1994) have carried out quantitative studies of this instability. Davaille and Jaupart (1994) find that an asthenospheric viscosity between 3×10^{18} and 4×10^{17} Pa s is required for secondary convection. As we will see in Chapter 5, these values are several orders of magnitude lower than most estimates. Many authors have argued both for and against the role of secondary convection in influencing the basal heat flux. These arguments have been summarized by Davaille and Jaupart (1994). Buck (1985) and Buck and Parmentier (1986) have carried out numerical calculations of secondary convection.

Analyses show that this secondary scale of convection will consist of convective cells aligned with the direction of seafloor spreading. Haxby and Weissel (1986) pointed out that there are systematic variations in the oceanic geoid that are aligned with the direction of seafloor spreading and attributed these anomalies to secondary mantle convection. Cazenave et al. (1995) and Wessel et al. (1996) have also discussed this association. Sleep (1994a) has argued that lithospheric thinning by mantle plumes provides an adequate explanation for the basal heating without secondary convection. Yuen et al. (1981) have also provided arguments against a second scale of convection in the upper mantle.

In summary, the temperature structure of oceanic lithosphere can be accounted for by heat transfer in a thermal boundary layer. Oceanic lithosphere evolves primarily by conductive cooling at young crustal ages and approaches thermal equilibrium at greater ages, a result of heat addition to the lithosphere by convective transfer from the mantle. For our preferred plate model with $y_{L0} = 125$ km, the contribution of basal heating to the oceanic heat flux is $q_{0e} = 34 \text{ mW m}^{-2}$. This is to be compared with the mean oceanic heat flow \bar{q}_o of $101 \pm 2.2 \text{ mW m}^{-2}$ (Pollack et al., 1993).

4.3 Temperatures in the Continental Lithosphere

Unlike the oceanic lithosphere, much of the continental lithosphere appears to be in a state of near-thermal equilibrium. There is little time dependence. The steady-state thermal structure is governed by heat conduction and radiogenic heat production. The radiogenic heat production is concentrated within the upper crust. The thermal structure at the base of the continental lithosphere is more uncertain and is likely to have significant time dependence. Because the adiabatic mantle is well mixed, it is expected that the temperatures beneath the oceanic and continental lithospheres will equilibrate at some depth. As discussed in Chapter 3, this depth remains a subject of considerable uncertainty. Seismological evidence indicates that continent–ocean differences persist to depths of nearly 300 km beneath some continental shields (Su et al., 1994; Li and Romanowicz, 1996).

Question 4.3: How thick is the continental lithosphere?

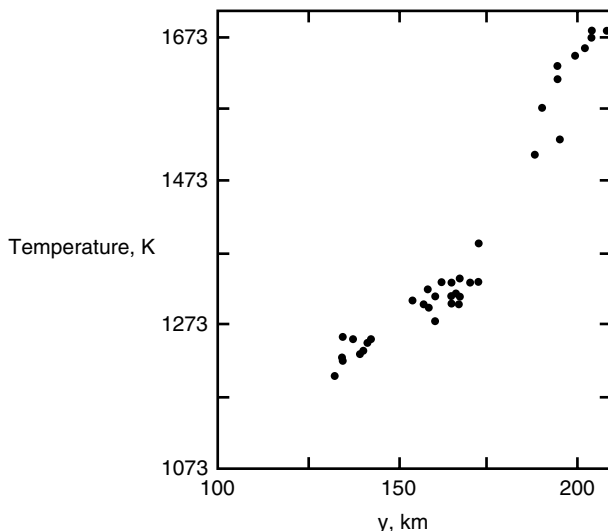


Figure 4.13. Equilibrium temperature and depth (pressure) combinations derived from geothermometry and geobarometry applied to garnet peridotite xenoliths from southern Africa (Finnerty and Boyd, 1987).

Continental crust and mantle temperatures are constrained by measurements of surface heat flow and by the heat production from radioactive decay in crustal rocks. Additional constraints on temperature in the continental lithosphere come from the petrology of mantle rocks. Phase equilibrium temperatures and pressures can be calculated for mineral assemblages found in mantle xenoliths. Figure 4.13 shows temperature–depth combinations from a number of such calculations for the southern African craton. These are usually interpreted as bounds on the actual temperature prevailing at that depth (Boyd, 1973; Boyd et al., 1985; Finnerty and Boyd, 1987).

One of the more important findings regarding continental geotherms is the correlation between surface heat flow and heat production in surface crystalline rocks from the same province. Four examples are given in Figure 4.14. These include the Sierra Nevada in California, the eastern United States (Lachenbruch, 1970), Norway and Sweden (Pinet and Jaupart, 1987), and the eastern Canadian shield (Pinet et al., 1991). In each case the data are in quite good agreement with a linear correlation between surface heat production and surface heat flow. This result is consistent with a heat production rate per unit mass H that decreases exponentially with depth y :

$$H = H_0 e^{-y/h_r} \quad (4.3.1)$$

In (4.3.1), H_0 is the surface ($y = 0$) radiogenic heat production rate per unit mass and h_r is a length scale for the decrease in H with depth. At the depth $y = h_r$, H is $1/e$ of its surface value. Substitution of (4.3.1) into the heat equation (4.1.32) yields the following equation governing the profile of temperature in the continental crust:

$$0 = k \frac{d^2 T}{dy^2} + \rho H_0 e^{-y/h_r} \quad (4.3.2)$$

Beneath the near-surface layer of heat-producing elements we assume that the upward heat flow at depth is q_r , i.e., $q \rightarrow -q_r$ as $y \rightarrow \infty$. The heat flow q_r is known as the reduced heat flow.

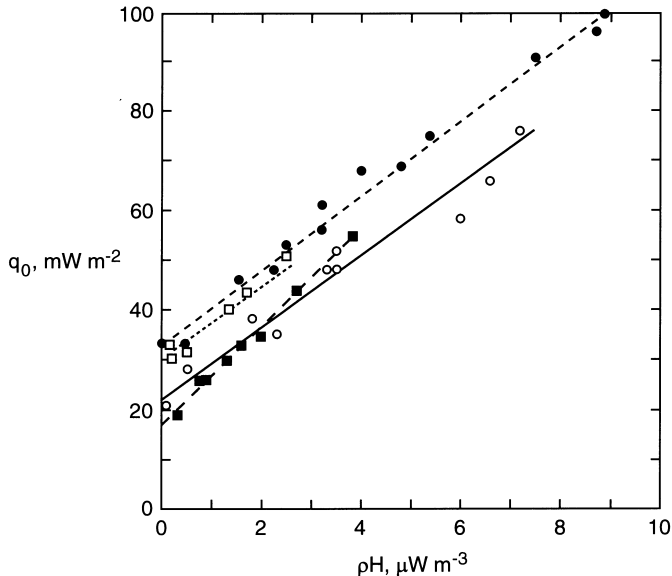


Figure 4.14. Dependence of surface heat flow q_0 on the radiogenic heat production per unit volume in surface rock ρH_0 in selected geological provinces. In each case the data are fit with the linear relationship (4.3.6). Solid squares and very long dashed line: Sierra Nevada; solid circles and intermediate dashed line: eastern U.S.; open circles and solid line: Norway and Sweden; open squares and short dashed line: eastern Canadian shield.

An integration of (4.3.2) yields

$$c_1 = k \frac{dT}{dy} - \rho H_0 h_r e^{-y/h_r} = -q - \rho H_0 h_r e^{-y/h_r} \quad (4.3.3)$$

The constant of integration c_1 can be determined from the boundary condition on the heat flux at great depth, i.e., from the mantle heat flux to the base of the lithosphere:

$$c_1 = q_r \quad (4.3.4)$$

Thus the heat flux at any depth is

$$q = -q_r - \rho H_0 h_r e^{-y/h_r} \quad (4.3.5)$$

The surface heat flow $q_0 = -q(y = 0)$ is obtained by setting $y = 0$ with the result

$$q_0 = q_r + \rho h_r H_0 \quad (4.3.6)$$

With an exponential depth dependence of radioactivity, the surface heat flow q_0 is a linear function of the surface radiogenic heat production rate per unit volume ρH_0 . Moreover, this linear surface heat flow–surface radiogenic heat production correlation is preserved under differential erosion.

The linear correlation (4.3.6) is fit to each of the four data sets given in Figure 4.14. For the Sierra Nevada data we find $q_r = 17 \text{ mW m}^{-2}$ and $h_r = 10 \text{ km}$; for the eastern United States data we find $q_r = 33 \text{ mW m}^{-2}$ and $h_r = 7.5 \text{ km}$; for the Norway and Sweden data we obtain

$q_r = 22 \pm 2 \text{ mW m}^{-2}$ and $h_r = 7.2 \pm 0.7 \text{ km}$; and for the eastern Canadian shield data we get $q_r = 30.5 \pm 1.8 \text{ mW m}^{-2}$ and $h_r = 7.1 \pm 1.7 \text{ km}$. In each case the thickness of the radiogenic layer is small compared to the thickness of the continental crust. Other authors have obtained similar results. Wright et al. (1980) found $q_r = 40 \pm 3 \text{ mW m}^{-2}$ and $h_r = 10 \pm 2 \text{ km}$ for the Canadian Appalachians, and Jaupart et al. (1982) found $q_r = 33 \pm 3 \text{ mW m}^{-2}$ and $h_r = 8.1 \pm 1.3 \text{ km}$ for the Appalachians in the eastern United States. Although a positive correlation between surface heat flow and surface heat generation is accepted, the general validity of the linear correlation (4.3.6) has been questioned (Drury, 1989).

No generally accepted mechanism for producing an exponential dependence of radiogenic heat production on depth in the continental crust has been proposed. It has been suggested that hydrothermal circulations are responsible (Turcotte and Oxburgh, 1972a). Magmatic and metamorphic fluid circulations can also play an important role (Jaupart et al., 1981). In many regions the linear correlation between q_0 and H_0 is only a crude approximation and in others it is not applicable. Jaupart (1983) has shown that horizontal variations in radiogenic heating significantly affect the q_0 versus H_0 relation. For example, the value of h_r inferred from the data will be smaller than the actual value of h_r if the exponentially depth-dependent radiogenic heating is confined to an isolated pluton of finite radius (see also England et al., 1980). The value of h_r inferred from the data will also be smaller than the actual value of h_r if the exponentially depth-dependent radiogenic heating also varies sinusoidally with horizontal distance. Surface heat flow integrates the variations of radiogenic heat production over depth and over large horizontal distances, and the smoothing can lead to an approximately linear relation between observed values of q_0 and measured values of H_0 .

Jaupart et al. (1981) have argued that the depth dependences of heating from the radioactive decay of uranium, thorium, and potassium have different length scales. The largest depth scale is associated with potassium and reflects the primary differentiation of the crust. The smallest depth scale is associated with thorium and is controlled by magmatic or metamorphic fluid circulation. Uranium has an intermediate depth scale that is set by the late effects of alteration due to meteoritic water. While caution is the word of the day in interpreting the linear q_0-H_0 relation in terms of h_r and q_r of a single exponentially depth-dependent radiogenic heating distribution, the simple interpretation is a useful first-order approach especially for q_r ; it represents a large-scale (hundreds of kilometers) average of the heat flow which is free of near-surface radioactivity variations and allows the calculation of representative geotherms (Jaupart, 1983; Jaupart et al., 1998).

The distribution of heat-producing elements in the continental crust has important implications for the thermal structure and thickness of the continental lithosphere. A detailed study of this problem has been carried out by Rudnick and Fountain (1995). These authors consider an upper continental crust with a thickness $h_{uc} = 12 \text{ km}$ and an average volumetric heat generation rate $\rho_{uc} H_{uc} = 1.8 \mu\text{W m}^{-3}$, a middle crust with $h_{mc} = 12 \text{ km}$ and $\rho_{mc} H_{mc} = 1.02 \mu\text{W m}^{-3}$, and a lower crust with $h_{lc} = 16 \text{ km}$ and $\rho_{lc} H_{lc} = 0.18 \mu\text{W m}^{-3}$. The whole crust has an average thickness $h_c = 40 \text{ km}$; the mean volumetric heat generation for the entire crust is $\rho_c H_c = 0.93 \mu\text{W m}^{-3}$, and the heat flow out of the crust due to radiogenic heat generation in all of the crust is $q_{cr} = 37 \text{ mW m}^{-2}$. Other authors have given a range of values for the radiogenic heat flow out of the crust. Weaver and Tarney (1984) gave $q_{cr} = 37 \text{ mW m}^{-2}$, Taylor and McLennan (1985) gave $q_{cr} = 23 \text{ mW m}^{-2}$, Shaw et al. (1986) gave $q_{cr} = 52 \text{ mW m}^{-2}$, and Wedepohl (1994) gave $q_{cr} = 50 \text{ mW m}^{-2}$. Pinet et al. (1991) suggest that the lower continental crust has an average volumetric heat generation rate of $\rho_{lc} H_{lc} = 0.4 \mu\text{W m}^{-3}$. We will assume $q_{cr} = 37 \text{ mW m}^{-2}$. Since the mean surface

heat flow in the continents is $\bar{q}_c = 65 \pm 1.6 \text{ mW m}^{-2}$ (Pollack et al., 1993), the basal heat input to the continental crust is $q_m = 28 \text{ mW m}^{-2}$.

The thermal structure of the continental lithosphere below the crust remains a subject of considerable debate. A limiting hypothesis is that the half-space cooling model given in Section 4.2.1 is applicable to the continental lithosphere. If this were the case, the thermal structure as a function of age t would be given by (4.2.4). The lithospheric thickness of 2-Gyr-old continents from (4.2.8) would be $y_L = 581 \text{ km}$. The corresponding mantle heat flow from (4.2.6) is $q_m = 9.6 \text{ mW m}^{-2}$. This is considerably less than the lowest estimates of the mantle heat flow q_m given above and suggests that the boundary layer analysis is not valid for the subcontinental lithosphere. The failure of boundary layer theory to predict the thermal structure of old continental lithosphere is not surprising since the theory also fails to predict the thermal structure of old oceanic lithosphere. Both are subject to basal heating, presumably from mantle plumes and/or secondary mantle convection.

An alternative model for the thermal structure of the continental lithosphere is the plate cooling model given in Section 4.2.2. If the analysis applied to the oceanic lithosphere is also applicable to the continental lithosphere, then the equilibrium thickness of the continental lithosphere can be obtained from (4.2.28) once the heat flow is specified. For $q_{0e} = q_m = 28 \text{ mW m}^{-2}$, as discussed above, $k = 3.3 \text{ W m}^{-1} \text{ K}^{-1}$, and $T_1 - T_0 = 1,300 \text{ K}$, we find from (4.2.28) that $y_{L0} = 153 \text{ km}$.

It was suggested by Sleep (1971) that thermal subsidence has occurred in many sedimentary basins. Thermal subsidence of sedimentary basins is attributed to the increase in density due to the cooling associated with a thickening thermal boundary layer (lithosphere), in direct analogy with the subsidence of the aging seafloor. Both the half-space cooling model for subsidence given in (4.2.14) and the plate cooling model for subsidence given in (4.2.32) can be applied to the free subsidence of sedimentary basins if the water density ρ_w is replaced by the sediment density ρ_s . However, the subsidence of many sedimentary basins is restricted by the flexural rigidity of the continental lithosphere. Thus, it is appropriate to consider the ratio of the depth w_s of a sedimentary layer deposited at a time t after the initiation of subsidence to the depth w_{s0} of the oldest sediments associated with the thermal subsidence episode. This ratio w_s/w_{s0} is related to the subsidence of a thermal boundary layer by (Turcotte, 1980a)

$$\frac{w_s}{w_{s0}} = 1 - \frac{w}{w_{L0}} \quad (4.3.7)$$

The values of w_s/w_{s0} obtained using the plate cooling model of Section 4.2.2 are given in Figure 4.15 for $\kappa = 1 \text{ mm}^2 \text{ s}^{-1}$ and $y_{L0} = 125 \text{ km}$. Also included in Figure 4.15 are the data given by Sleep (1971) for the subsidence of the Michigan, Appalachian, Gulf Coast, and Atlantic Coast basins of the United States. Each data point is the result of averaging a large number of wells. There is excellent agreement between the data and the model. The data points which lie below the curve can be attributed to periods when the basins were starved of sediments. It is clear from Figure 4.15 that the subsidence of many sedimentary basins ceases after about 100 Myr. The lack of further subsidence may again be attributed to the basal heating of the continental lithosphere by mantle plumes or other mechanisms. These results are clear evidence that the thickness of the continental lithosphere is close to 150 km.

As in the case of the oceanic lithosphere, geoid anomalies provide a further constraint on the thermal structure of the continental lithosphere (Turcotte and McAdoo, 1979; Doin et al., 1996). To apply this constraint we assume a thermal and crustal structure model of the continental lithosphere as follows. The surface of stable continental regions is assumed

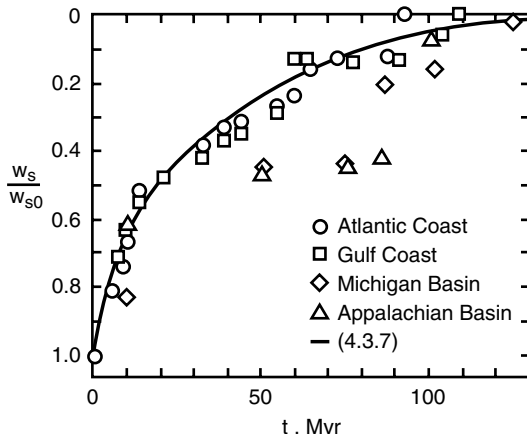


Figure 4.15. The ratio of the depth w_s of a sedimentary layer deposited at time t after the initiation of subsidence to the depth w_{s0} of the oldest sediments associated with the thermal subsidence episode for several sedimentary basins (after Sleep, 1971). The solid line is the theoretical subsidence from (4.3.7) for the plate model with $y_{L0} = 125$ km.

to lie at sea level. The continental crust is divided into two parts; the upper crust is assumed to have a thickness d_{uc} of 20 km, and the lower crust a thickness d_{lc} of 15 km. The upper crust is assumed to have a density $\rho_{uc} = 2,700 \text{ kg m}^{-3}$ at the reference mantle temperature. The lower crust has an unspecified density ρ_{lc} . This density distribution is illustrated in Figure 4.16. For the temperature distribution beneath the surface layer with internal heat generation (crust), it is appropriate to assume a linear temperature profile for old continental lithosphere:

$$T_L = T_0 + (T_1 - T_0) \left(\frac{y}{y_L} \right) \quad (4.3.8)$$

The model described above has two unknown parameters, ρ_{lc} and y_L . The condition of isostasy provides one equation relating the density of the lower crust and the thickness of the continental lithosphere. The difference in geoid height between ocean basins and continental cratons will be used to provide a second equation relating the lower crustal density and the thickness of the continental lithosphere. Isostasy (4.2.9) is applied to the

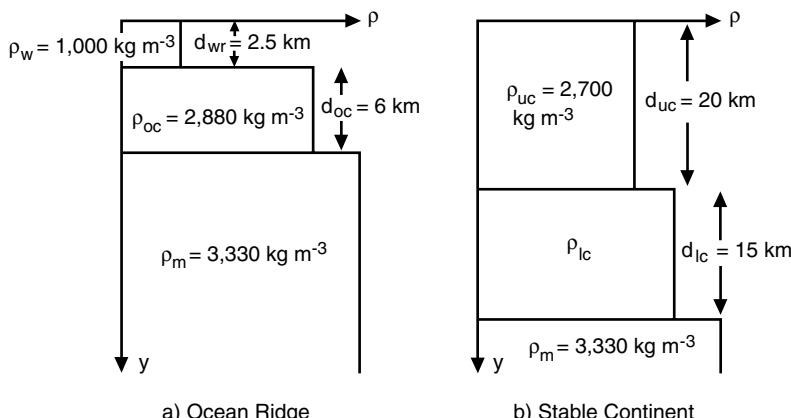


Figure 4.16. Illustration of the crustal density distributions (not to scale). (a) Ocean ridges. (b) Stable continental regions. The densities are evaluated at $T_m = 1,570$ K.

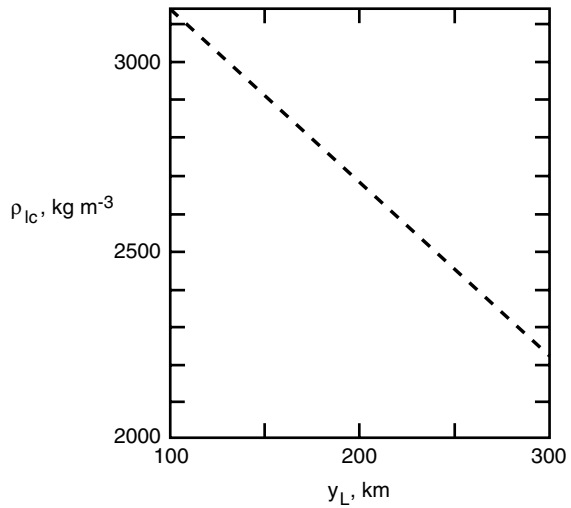


Figure 4.17. Dependence of the density of the lower continental crust on the thickness of the continental lithosphere based on the condition of isostasy given in (4.3.9).

continental lithosphere relative to the ocean ridge. For the assumed density distribution given in Figure 4.16 and the linear temperature profile given in (4.3.8), isostasy requires

$$\begin{aligned} &(\rho_{uc} - \rho_w) d_{wr} - (\rho_{oc} - \rho_{uc}) d_{oc} - (\rho_m - \rho_{uc}) (d_{uc} - d_{wr} - d_{oc}) \\ &- (\rho_m - \rho_{lc}) d_{lc} + \frac{1}{2} \rho_m \alpha (T_1 - T_0) y_L = 0 \end{aligned} \quad (4.3.9)$$

In (4.3.9) d_{wr} is the depth of the oceanic ridge, ρ_{oc} is the density of oceanic crust, d_{oc} is the thickness of oceanic crust, and d_{lc} is the thickness of the lower continental crust. The dependence of the lower continental crustal density on lithospheric thickness from (4.3.9) and parameter values given above and in Figure 4.16 is shown in Figure 4.17.

The value of the continental geoid height relative to the ocean ridge geoid height, obtained using (4.3.9) and (4.2.14), is

$$\begin{aligned} \Delta N = & - \left(\frac{2\pi G}{g} \right) \left\{ \frac{1}{2} (\rho_{uc} - \rho_w) d_{wr}^2 - \frac{1}{2} (\rho_{oc} - \rho_{uc}) [(d_{wr} + d_{oc})^2 - d_{wr}^2] \right. \\ & - \frac{1}{2} (\rho_m - \rho_{uc}) [d_{uc}^2 - (d_{wr} + d_{oc})^2] - \frac{1}{2} (\rho_m - \rho_{lc}) [(d_{uc} + d_{lc})^2 - d_{uc}^2] \\ & \left. + \frac{1}{6} \alpha \rho_m (T_1 - T_0) y_L^2 \right\} \end{aligned} \quad (4.3.10)$$

This result, (4.3.10), and the difference between the ocean basin geoid height and the ocean ridge geoid height (approximately -14 m, see Chapter 2) can be combined to yield the difference between the continental geoid height and the ocean basin geoid height as a function of the thickness of the continental lithosphere; the result is shown in Figure 4.18.

It is clear from Figure 4.18 that a thick continental lithosphere would be expected to result in sizable geoid anomalies over the continents. If the mean lithospheric thickness beneath the continents were 300 km, geoid anomalies greater than 50 m would be expected. In fact, geoid heights over the continents and ocean basins are equal within the variability. The decrease in geoid height due to the compensated continental crust is approximately equal to the increase in geoid height due to a somewhat thicker lithosphere. From Figure 4.18 it is concluded that the lithosphere thickness is $y_L = 180 \pm 20$ km. From Figure 4.17 the

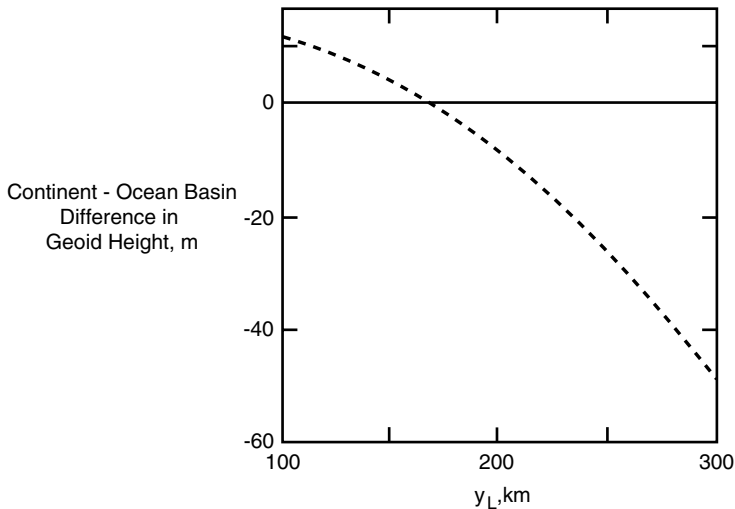


Figure 4.18. Dependence of the difference in geoid height between stable continents and ocean basins on the thickness of the continental lithosphere for the error function and linear temperature profiles.

corresponding density of the lower continental crust is $\rho_{lc} = 2,780 \pm 100 \text{ kg m}^{-3}$ referenced to the mantle reference temperature $T_m = 1,580 \text{ K}$. Rudnick and Fountain (1995) suggest that the density of the lower continental crust is $\rho_{lc} = 2,800\text{--}3,000 \text{ kg m}^{-3}$ (see also Smithson and Decker, 1974). To obtain larger values for the density of the lower crust, a thicker lower crust is required. For $k = 3.3 \text{ W m}^{-1} \text{ K}^{-1}$, the mantle heat flow from (4.3.8) with $y_L = 180 \text{ km}$ is $q_m = 24 \pm 3 \text{ mW m}^{-2}$. This is near the lower limit of acceptable values. The corresponding mantle geotherm is given in Figure 4.19. A continental lithospheric thickness of $175 \pm 25 \text{ km}$ is generally consistent with thermal considerations (Slater et al., 1980, 1981) but seismic velocity anomalies have been interpreted to give a thicker continental lithosphere

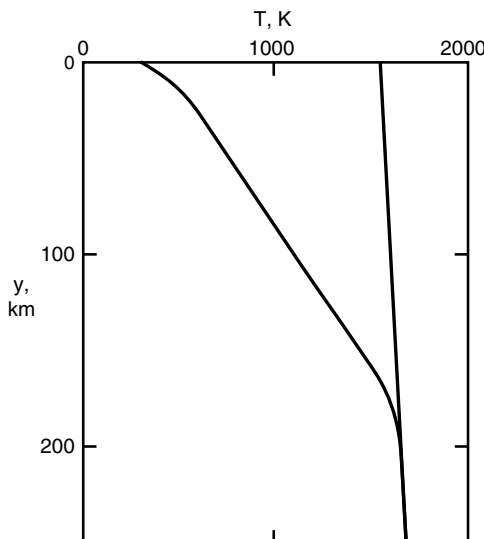


Figure 4.19. Continental geotherm based on thermal and geoid constraints.

as discussed in Chapter 3. A thicker continental lithosphere can be made consistent with the geoid observation if the continental lithosphere contains less dense, more depleted mantle rock than old oceanic lithosphere.

When the iron-rich basaltic component is removed from “fertile” mantle rock, the resulting depleted mantle rock is significantly less dense and is thus buoyant (Oxburgh and Parmentier, 1977). There is also observational evidence from studies of mantle xenoliths that the mantle lithosphere in continental cratons is at least partially made up of these depleted mantle rocks (Boyd, 1989). The role of the buoyant depleted mantle rock is a fundamental question in mantle dynamics. In many cases it must be mixed back into the near-homogeneous mantle, but in other cases it may remain isolated in the rigid continental lithosphere.

Question 4.4: *What is the fate of buoyant depleted mantle material created together with the continental crust?*

Evidence that the continental lithosphere beneath Archean shields must be at least 150 km thick comes from isotopic studies of diamond inclusions. These studies (Richardson et al., 1984; Boyd et al., 1985) suggest that the ambient temperature in the depth range 150–200 km has been 1,200–1,500 K for the last 3 Gyr.

Question 4.5: *What mechanism provides heat to the base of the continental lithosphere?*

Although the thickness of the continental lithosphere is uncertain, there is no question that old continental lithosphere is in a state of thermal equilibrium. The heat loss at the surface is balanced by the internal heat generation and basal heating. The half-space cooling model is not applicable to the continental lithosphere. If it were, the lithosphere would be subsiding and a thickening sedimentary veneer would be observed. This subsidence and sediment deposition are not occurring, so there must be basal heating. This basal heating is also consistent with the flattening of topography of the ocean basins.

There are two mechanisms proposed for the basal heating of the continental lithosphere and old oceanic lithosphere. These are plumes impinging on the base of the lithosphere and secondary convection beneath the lithosphere. An extensive discussion of these mechanisms was given in Section 4.2.2 with regard to the oceanic lithosphere. This discussion is also directly applicable to the continental lithosphere.

4.4 Partial Melting and the Low-velocity Zone

The best seismic indicator of the base of the lithosphere is the reversal in the velocities V_P and V_S at the boundary between the LID and the LVZ. As pointed out in Chapter 3, the LVZ (low-velocity zone) is present beneath much of the oceanic lithosphere, although the problem of resolving its depth is complicated by the presence of seismic anisotropy. Beneath stable continental interiors, the LVZ is either missing, or, if present, it occurs at depths greater than found beneath the oceans. The LVZ is usually better defined for shear waves than for compressional waves. Likewise, anomalous attenuation is observed for shear waves, while it is not so evident for compressional waves. The variation in LID depth with

crustal age is similar to the variation in thermal boundary layer thickness, and indicates that the LID–LVZ structure is tied to the geotherm.

Question 4.6: *What causes the seismic LVZ beneath the oceanic lithosphere?*

There are two plausible explanations for the LVZ. First, it could be due to steep thermal gradients. In a layer with uniform composition, the temperature gradient required to produce a particular gradient in shear wave velocity is given by

$$\frac{dT}{dy} = \left(\frac{\partial V_S}{\partial T} \right)_p^{-1} \left(\frac{dV_S}{dy} - \rho g \left(\frac{\partial V_S}{\partial p} \right)_T \right) \quad (4.4.1)$$

For the values of the pressure and temperature derivatives of V_S in peridotite from Table 4.4, we find that the shear wave velocity gradient vanishes at a geothermal gradient of $3.2 \pm 0.5 \text{ K km}^{-1}$. Among the geotherms in Figure 4.8, this critical gradient occurs at about 70 km beneath 30-Myr-old ocean crust, and may not occur at all beneath older ocean crust or beneath continental areas with low mantle heat flow.

Another explanation for the LVZ is that it is due to small concentrations of partial melt, distributed through the crystalline matrix in the form of intergranular films and small droplets. Turcotte (1982) has reviewed the evidence for partial melts in the LVZ and the geodynamic consequences. Extensive partial melting is an important constraint on the geotherm, since it requires temperatures in the LVZ to be at or above the solidus of the lowest melting point constituent.

The solidus temperature depends on both pressure and composition, but it is not very sensitive to variations in composition among the peridotites likely to be abundant in the upper mantle. At standard pressure, peridotites melt at about 1,400 K in the absence of water and other volatiles (Takahashi and Kushiro, 1983), and the solidus increases with pressure to around 1,700 K at 100 km depth. However, the situation is quite different if even low concentrations of H₂O are present. An H₂O content of just 0.1% lowers the standard pressure melting point to about 1,340 K, and it actually decreases with pressure, reaching a minimum near 1,270 K at about 3 GPa. Then, at higher pressures, it increases at a rate similar to the dry solidus. Higher water content reduces the fusion point even further (Wyllie, 1971). At

Table 4.4. Temperature and Pressure Coefficients of Seismic Velocity

Coefficient	Value ^a
$\left(\frac{\partial V_P}{\partial p} \right)_T$	$10 \pm 2 \times 10^{-8} \text{ ms}^{-1} \text{ Pa}^{-1}$
$\left(\frac{\partial V_S}{\partial p} \right)_T$	$3 \pm 1 \times 10^{-8} \text{ ms}^{-1} \text{ Pa}^{-1}$
$\left(\frac{\partial V_P}{\partial T} \right)_p$	$-0.4 \pm 0.1 \text{ ms}^{-1} \text{ K}^{-1}$
$\left(\frac{\partial V_S}{\partial T} \right)_p$	$-0.3 \pm 0.1 \text{ ms}^{-1} \text{ K}^{-1}$

^a For upper mantle peridotites, from Anderson et al. (1968).

the depth of the LVZ, differences in water content can alter the melting point by 300–400 K. Similarly, the presence of CO₂ reduces the melting point.

Unfortunately, the question of how much water and carbon dioxide are present in the mantle remains open (see Chapter 11). Most basaltic lavas erupt at temperatures around 1,525 K (Basaltic Volcanism Study Project, 1981). Extrapolation of this temperature along an adiabat gives 1,625 K at the depth of the LVZ, somewhere between the wet and dry solidus at that depth, suggesting that the true upper mantle solidus is between these extremes. If the dry peridotite solidus were the relevant fusion curve, there would be very little partial melt in the upper mantle and the worldwide LVZ could not be explained this way.

4.5 Temperatures, Partial Melting, and Melt Migration Beneath Spreading Centers

By far the greatest amount of partial melting in the Earth occurs beneath spreading centers. The present-day rate of plate creation is accompanied by at least 18 km³ yr⁻¹ of MORB production, resulting in the 6 km thick oceanic crust. The fact that oceanic crust averages this thickness at all active ridges, independent of their spreading rates, is an important constraint on temperature and on the processes of melt production and melt transfer in the mantle beneath divergent plate boundaries.

It is known that the neovolcanic zone, the region where MORB reaches the seafloor, is only a few kilometers wide (McClain et al., 1985; Lin et al., 1990). Crustal seismic reflection studies on the East Pacific Rise indicate that there may be small axial magma chambers, 3 km wide or less, located about 1 km below the ridge crest (Detrick et al., 1987; Harding et al., 1989; Sinton and Detrick, 1992; Calvert, 1995).

The petrology of MORB and the abyssal peridotites also provides important constraints. The chemistry of both abyssal peridotites (Dick, 1989) and MORB (Klein and Langmuir, 1987) indicates that the crustal thickness, as well as the depth and degree of partial melting, correlate with temperature variations in the upwelling mantle. The degree of partial melting, or melt fraction, needed to produce the standard 6 km of MORB is estimated to be 10–20% (Basaltic Volcanism Study Project, 1981). In addition, phase equilibria indicate that MORB melts are produced several tens of kilometers below the base of the crust (Stolper, 1980).

The basic mechanism for the generation of magmas beneath ocean ridges is reasonably well understood. In regions of mantle convection the thermal gradient in the mantle is near the adiabatic value. At relatively shallow depths (50–100 km) the adiabatic increase with depth in the mantle temperature is near 0.3 K km⁻¹. However, the solidus temperature of fertile mantle rock has a much larger increase with depth; in this depth range it is about 4 K km⁻¹. When hot mantle rock ascends beneath a spreading center it crosses the rock liquidus and partial melting results.

As the seafloor spreads at an ocean ridge the mantle rock beneath must ascend to fill the gap. The structure of a mid-ocean ridge is generally consistent with the concept of passive spreading, that plate divergence drives the upwelling and the partial melting of the underlying upper mantle, producing a near-uniform 6 km thick oceanic crust with a basaltic composition. Regions of anomalously thick oceanic crust (shallow bathymetry) associated with hot spots such as Iceland and the Azores result from the interaction of ascending mantle plumes with seafloor spreading centers. Additional melting results from the combination of two effects: the higher mantle temperature in the plumes and the higher ascent velocity associated with plume material. These are clearly not passive.

It is convenient to specify the temperature of the source region for MORB in terms of a potential temperature. This is the temperature the source rock would have if it were brought adiabatically to 1 atm pressure without melting. McKenzie and O’Nions (1991) have given potential temperatures of 1,470 K for N-type MORB and 1,700 K for E-type MORB. N-type MORB refers to a normal depleted distribution of rare earth elements, whereas E-type MORB refers to an “enriched” distribution of rare earth elements. E-type MORB is restricted to regions of anomalously thick oceanic crust and is a plume “signature.” Formation of MORB by melting in adiabatic decompression has also been considered by McKenzie and Bickle (1988), Forsyth (1993), and Iwamori et al. (1995).

4.5.1 Melt Migration by Porous Flow

Melt in the mantle is originally produced along grain boundaries, but it segregates and ascends through the residual solid matrix due to its differential buoyancy to form the oceanic crust. A number of mechanisms have been suggested for melt migration. Initially the melt probably ascends by a porous flow mechanism. Thus melt ascent can be modeled using Darcy’s law for flow in a porous medium (Frank, 1968b; Sleep, 1974; Turcotte and Ahern, 1978; Walker et al., 1978; Ahern and Turcotte, 1979; Stolper et al., 1981). As melt accumulates on grain boundaries it will form a network of channels. If the channels are interconnected, as illustrated in Figure 4.20, and if the solid matrix can compact, the melt can migrate through the solid matrix.

We model these channels as a cubic network of circular channels (see Figure 4.20). The side length b of the cubic structure is equivalent to the grain size. The diameter δ of the channels can be combined with b to yield an expression for the porosity $\phi - \phi_0$, where ϕ is the total porosity and ϕ_0 is the volume fraction of isolated pockets of liquid that do not contribute to the permeability:

$$\phi - \phi_0 = \frac{3\pi\delta^2}{4b^2} \quad (4.5.1)$$

The permeability k_p is a measure of the flow resistance in a porous medium. For the model considered, the permeability is (Bear, 1972, p. 163)

$$k_p = \frac{(\phi - \phi_0)\delta^2}{96} \quad (4.5.2)$$

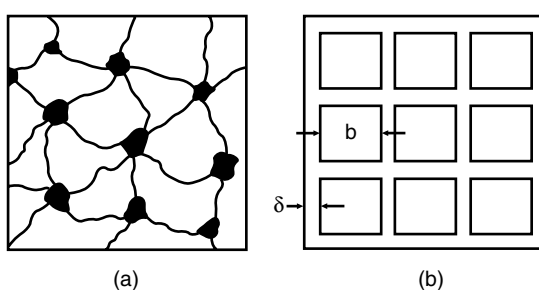


Figure 4.20. (a) Illustration of the formation of magma channels on grain intersections. (b) Diagram of the cubic matrix model of magma migration.

The combination of (4.5.1) and (4.5.2) gives the permeability as a function of grain size and connected porosity:

$$k_p = \frac{b^2 (\phi - \phi_0)^2}{72\pi} \quad (4.5.3)$$

We will use the standard theory for flow in porous media to specify how this permeability allows magma to migrate. Darcy's law for porous flow can be used if it is assumed that the pressure gradient driving flow is the differential buoyancy between the solid matrix and liquid magma $(\rho_s - \rho_l)g$, where ρ_s is the matrix density, ρ_l is the magma density, and g is the acceleration of gravity. Darcy's law gives the differential ascending pore velocity of the magma through the matrix as

$$\frac{1}{3} (\phi - \phi_0) (v_l - V) = \frac{k_p}{\mu_l} (\rho_s - \rho_l) g \quad (4.5.4)$$

where v_l is the magma vertical velocity, V is the vertical velocity of the matrix, and μ_l is the magma viscosity. The left side of (4.5.4) is the vertical fluid flux (Darcy velocity). In writing (4.5.4) we assume that the differential buoyancy between the magma and the solid is balanced by the viscous pressure drop due to the flow of the magma through the small vertical channels. Implicit in this formulation of the problem is the ability of the matrix to deform as the liquid escapes upward.

We assume a steady vertical flow of the mantle rock. Within the melt zone the upward flux of mass must be equal to the flux of mass into the melt zone, which leads to the following continuity relation

$$\rho_s v_0 = \frac{1}{3} (\phi - \phi_0) \rho_l v_l + \left(\frac{2}{3} \phi + \frac{1}{3} \phi_0 \right) \rho_l V + (1 - \phi) \rho_s V \quad (4.5.5)$$

where v_0 is the mantle ascent velocity below the melt zone. In addition, the degree of partial melting f at any point in the melt zone is related to the magma flux at that point by

$$f \rho_s v_0 = \frac{1}{3} (\phi - \phi_0) \rho_l v_l + \left(\frac{1}{3} \phi_0 + \frac{2}{3} \phi \right) \rho_l V \quad (4.5.6)$$

The magma-filled porosity ϕ can be determined in terms of the degree of partial melting f by combining (4.5.3)–(4.5.6) to yield

$$\phi^3 + C_1 \phi^2 + C_2 \phi + C_3 = 0 \quad (4.5.7)$$

where

$$C_1 = -(1 + 2\phi_0) \quad (4.5.8)$$

$$C_2 = \frac{2\phi_0 + \phi_0^2 + v_0(f - 1)}{\beta} - \frac{\rho_s f v_0}{\rho_l \beta} \quad (4.5.9)$$

$$C_3 = \frac{\rho_s v_0 f}{\rho_l \beta} - \phi_0^2 \quad (4.5.10)$$

$$\beta = \frac{-b^2 (\rho_s - \rho_l) g}{72\pi \mu_l} \quad (4.5.11)$$

The temperature T within the melt zone must satisfy the steady-state energy equation

$$\rho_s v_0 c_p \frac{dT}{dy} = k \frac{d^2 T}{dy^2} - Q_f \quad (4.5.12)$$

where k is the thermal conductivity, c_p is the specific heat at constant pressure (in (4.5.6) it is assumed that the specific heats of the liquid and solid are equal), and Q_f is the heat loss due to melting. The adiabatic temperature change has been neglected.

We assume that 25% of the mantle rock consists of a low melting temperature basaltic component. We also assume that the solidus temperature of the remaining 75% is never reached, thereby limiting partial melting to 25%. The dependence of the partial melt fraction f on temperature and depth in a mantle with 0.01% water (Ringwood, 1975) is illustrated in Figure 4.21. We approximate the equilibrium dependence of the partial melt fraction on depth (pressure) and temperature by

$$f = A \{ \exp [B(T - Cy - D)] - 1 \} \quad (4.5.13)$$

where A , B , C , and D are constants, and depth is given by $-y$ (in this section on melt migration we take the y -coordinate as positive upward so that upward magma migration velocities are positive). Equation (4.5.13) is also plotted in Figure 4.21. The approximation for large degrees of partial melt is quite good, but there is considerable deviation for low degrees of partial melt between the depths of 75 and 150 km. If included in our model, a small amount of melting would occur at depth but, as will be seen, no significant upward migration of magma would result.

The heat loss due to partial melting Q_f is given by

$$Q_f = L\rho_s v_0 \frac{df}{dy} \quad (4.5.14)$$

where L is the latent heat of fusion. Since melting is caused by both changes in pressure and temperature

$$\frac{df}{dy} = \frac{\partial f}{\partial y} + \frac{\partial f}{\partial T} \frac{dT}{dy} \quad (4.5.15)$$

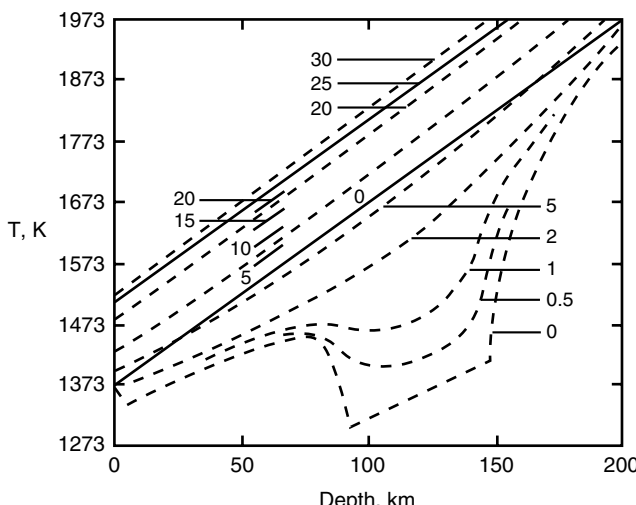


Figure 4.21. Dependence of partial melt fraction f of undepleted mantle (in percent) on temperature and depth. The dashed lines are values based on laboratory studies with 0.01% water, and solid lines are from (4.5.13) with $A = 0.4$, $B = 3.65 \times 10^{-3} \text{ K}^{-1}$, $C = 3 \times 10^{-3} \text{ Km}^{-1}$, and $D = 1,100 \text{ K}$.

and we can combine (4.5.13)–(4.5.15) to get

$$Q_f = ABL\rho_s v_0 \exp[B(T - Cy - D)] \left[\frac{dT}{dy} - C \right] \quad (4.5.16)$$

Substitution of (4.5.16) into (4.5.12) yields

$$\rho_s v_0 c_p \frac{dT}{dy} = k \frac{d^2 T}{dy^2} - ABL\rho_s v_0 \exp[B(T - Cy - D)] \left[\frac{dT}{dy} - C \right] \quad (4.5.17)$$

The solution within the melting zone requires the combined solution of (4.5.7), (4.5.13), and (4.5.17).

In the region of vertical flow beneath the melting zone $f = 0$. In this case (4.5.17) reduces to

$$v_0 \frac{dT}{dy} = \kappa \frac{d^2 T}{dy^2} \quad (4.5.18)$$

The temperature of the ascending rocks at great depth is T_m so we require $T \rightarrow T_m$ as $y \rightarrow -\infty$. Also, the temperature and temperature gradient must be continuous at the base of the melt zone. The solution of (4.5.18) which satisfies continuity of temperature is

$$T = T_m + (D + Cy_0 - T_m) \exp \left[\frac{v_0}{\kappa(y - y_0)} \right] \quad (4.5.19)$$

where y_0 is the base of the melt zone. There is an upstream temperature precursor below the melt zone.

In the region above the melt zone the magma produced within the melt zone migrates upward. In general, the solution for the migration velocity and magma-filled porosity in this zone would require the solution of (4.5.7). However, in most cases of interest the magma migration velocity v_l is large compared with the mantle velocity v_0 , i.e., $v_l \gg v_0$, and (4.5.3) and (4.5.4) can then be combined to give

$$v_l = \frac{(\rho_s - \rho_l) g b^2 (\phi - \phi_0)}{24\pi\mu_l} \quad (4.5.20)$$

Also in this limit it follows from (4.5.6) that

$$\frac{1}{3}(\phi - \phi_0)\rho_l v_l = f_0 \rho_s v_0 \quad (4.5.21)$$

where f_0 is the total degree of partial melting in the melt zone. The combination of (4.5.20) and (4.5.21) gives

$$\phi - \phi_0 = \frac{6}{b} \left[\frac{2\pi\mu_l f_0 \rho_0 v_0}{(\rho_s - \rho_l) g \rho_l} \right]^{1/2} \quad (4.5.22)$$

$$v_l = \frac{b}{2} \left[\frac{(\rho_s - \rho_l) g f_0 \rho_s v_0}{2\pi\mu_l \rho_l} \right]^{1/2} \quad (4.5.23)$$

for the magma-filled porosity and migration velocity above the melt zone.

We obtain numerical solutions for the structure of the melt zone by integration of (4.5.7), (4.5.13), and (4.5.17) for ϕ , f , and T . Integration proceeds from the base of the melt zone

Table 4.5. Parameters for Model of Melt Zone

Parameter	Value	Description	Source
k	$41.84 \text{ W m}^{-1} \text{ K}^{-1}$	Thermal conductivity	Clark (1966), pp. 459–82
c_p	$1.046 \text{ kJ kg}^{-1} \text{ K}^{-1}$	Specific heat	Clark (1966), pp. 459–82
L	$334.72 \text{ kJ kg}^{-1}$	Latent heat of fusion	Bottinga and Allègre (1978)
A	0.4	Constant in (4.5.13)	Ringwood (1975)
B	$3.65 \times 10^{-3} \text{ K}^{-1}$	Constant in (4.5.13)	Ringwood (1975)
C	$3.0 \times 10^{-3} \text{ Km}^{-1}$	Constant in (4.5.13)	Ringwood (1975)
D	1,373 K	Constant in (4.5.13)	Ringwood (1975)
ρ_s	$3,300 \text{ kg m}^{-3}$	Density of solid	
ρ_l	$2,600 \text{ kg m}^{-3}$	Density of liquid	
g	10 m s^{-2}	Gravitational acceleration	
b	2 mm	Grain size (capillary spacing)	Mercier et al. (1977)
ϕ_0	0.02	Unconnected porosity	Daines and Richter (1988)
μ_l	1 Pas; 10 Pas	Viscosity of liquid	Kushiro et al. (1976)
v_0	$10 \text{ mm yr}^{-1}; 50 \text{ mm yr}^{-1}$	Mantle ascent velocity	
μ_s	$10^{15}\text{--}10^{18} \text{ Pas}$	Shear viscosity of matrix	McKenzie (1984b)
ζ_s	$10^{15}\text{--}10^{18} \text{ Pas}$	Bulk viscosity of matrix	McKenzie (1984b)

upward. The temperature and temperature gradient given by (4.5.19) must be continuous at the base of the melt zone. The unknown position of the base y_0 is obtained by iteration. The values of the parameters used in our calculations are given in Table 4.5. The temperature of the ascending mantle rock is $T_m = 1,573$ K. Results are obtained for a magma viscosity of 10 Pa s (Ryan and Blevins, 1987). Mantle ascent velocities of 10 and 50 mm yr $^{-1}$ are considered. These represent the range of observed seafloor spreading velocities. The maximum ascent velocities beneath a ridge crest will be of the order of the seafloor spreading velocities.

Temperature as a function of depth is shown in Figure 4.22. Also included is the dependence of the degree of partial melting on temperature and depth from (4.5.13). As the degree of partial melting increases, the temperature decreases because the latent heat of fusion is

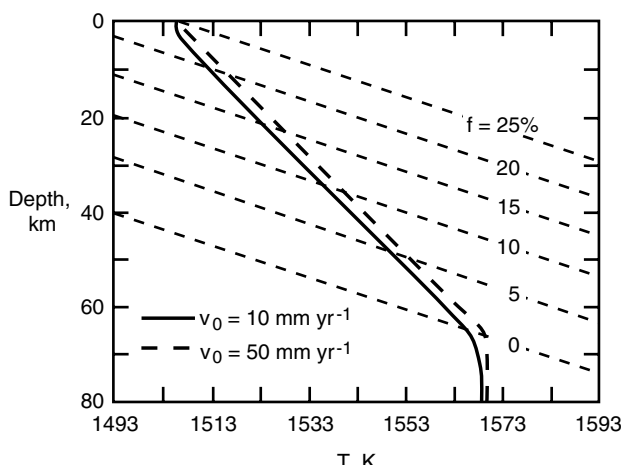


Figure 4.22. Dependence of temperature on depth for mantle rock ascending beneath an ocean ridge at velocities of 10 and 50 mm yr^{-1} . The degree of partial melting from (4.5.13) is also shown.

being extracted from the internal energy. If the temperature of the ascending mantle rock T_m was taken to be higher, the melting zone would be displaced downward. The degree of partial melting throughout the melt region is given in Figure 4.23. The degree of partial melting increases upward nearly linearly through the zone.

The partial melt volume fraction (porosity) is given as a function of depth in the melt zone in Figure 4.24. Without melt migration, ϕ equals f and the results in Figure 4.24 would be identical with the results in Figure 4.23. When the pores become connected to form a permeable matrix, f exceeds ϕ , meaning that the excess magma is squeezed out. In all cases the porosity is less than 1% greater than the assumed 2% unconnected porosity ($\phi_0 = 0.02$). The lower-viscosity magma flows more freely so the connected porosity $\phi - \phi_0$ is small. The slower ascent velocity gives more time for magma migration so that again the connected porosity is small.

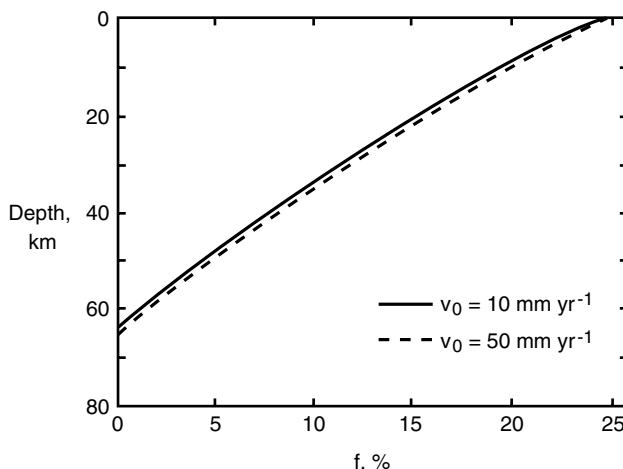


Figure 4.23. Dependence of degree of partial melting f on depth through the melt zone.

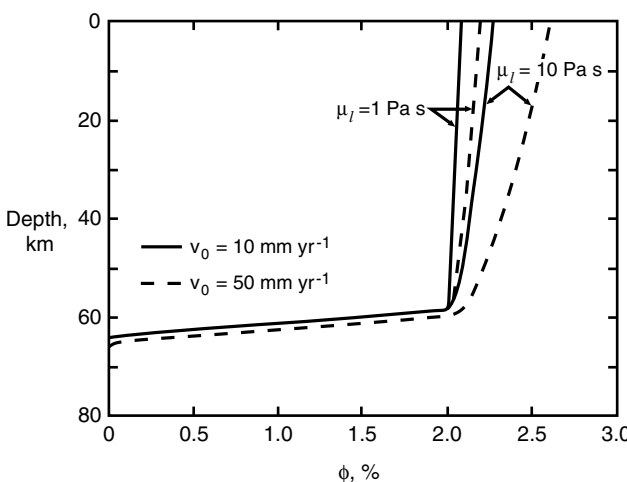


Figure 4.24. Dependence of the partial melt volume fraction ϕ on depth through the melt zone.

The dependence of the magma migration velocity v_l on depth in the melt zone is given in Figure 4.25. The maximum migration velocity in each case is two to three orders of magnitude greater than the mantle ascent velocity. Higher mantle ascent velocities also result in larger magma migration velocities.

The general structure of an oceanic ridge is illustrated in Figure 4.26. Loss of heat to the surface creates a cold rigid lithosphere. The cooling results in a freezing front which is defined by the solidus temperature of the magma. The degree of partial melting of the ascending mantle rock is also shown. In order to form the oceanic crust in the immediate vicinity of the oceanic ridge, considerable lateral migration of magma must occur. Insufficient magma is produced immediately below the ridge crest.

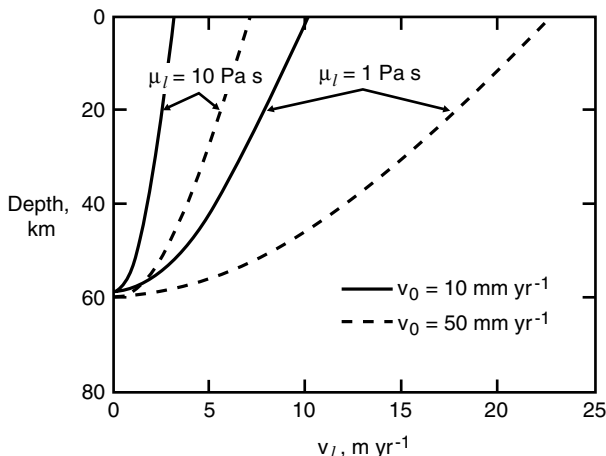


Figure 4.25. Dependence of the magma migration velocity v_l on depth through the melt zone.

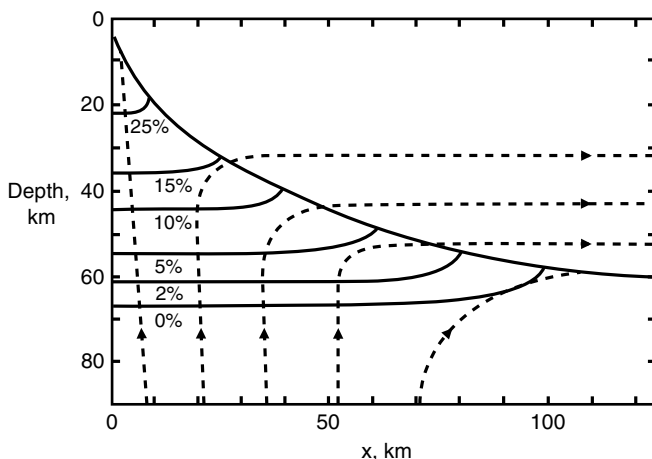


Figure 4.26. Idealized ridge structure. Dashed lines show the motion of the matrix. Degrees of partial melting are also shown. The solid line is the base of lithosphere as determined by the solidus. The coordinate x is the distance from the ridge crest.

An important conclusion of this model for magma migration is that large partial melt fractions cannot remain in the asthenosphere. The percentage partial melt present is only slightly greater than that necessary for the development of interconnected permeability. The excess magma flows rapidly upward to the upper boundary of the melt zone.

The first partial melt fraction produced at the greatest depths migrates upward and mixes with the later partial melt fractions produced at shallower depths. The uniformity of this mixing will strongly influence the composition of the surface volcanic rocks. Heterogeneity of ridge basalts will result if off-axis, low melt fraction magma reaches the surface and is erupted without mixing with near-axis, high melt fraction magma.

Although Ahern and Turcotte (1979) used an order of magnitude calculation to show that matrix compaction would occur beneath an ocean ridge, McKenzie (1984b) and Richter and McKenzie (1984) questioned the assumption. McKenzie (1984b) developed the full equations for the viscous collapse of the matrix with Darcy flow of a low-viscosity, immiscible fluid. Matrix compaction is important for transient problems and it leads to the generation of solitary waves or “magmons” (Scott and Stevenson, 1984, 1986; Barcilon and Richter, 1986; Barcilon and Lovera, 1989; Spiegelman, 1993a, b, c). Watson and Spiegelman (1994) and Spiegelman (1994) have studied the geochemical implications of magmons.

Ribe (1985a, b) studied compaction for the ascending flow beneath ocean ridges, and showed that unrestricted compaction would be expected and the results given above are valid. Following Ribe (1985a, b) we consider the problem illustrated in Figure 4.27. Again a simple one-dimensional model is considered in which mantle material ascends at constant speed v_0 and reaches its solidus at $y = 0$, where a fixed volume fraction f_0 melts. Above $y = 0$, the melt occupies a volume fraction (porosity) ϕ (we assume $\phi_0 = 0$ in this analysis) and migrates upward at a velocity v_l , and the unmelted residue (matrix) ascends at a velocity V . Although localized melting is unlikely to occur in the Earth’s mantle, the model illustrates the essential physics of compaction.

The governing equations for the model (McKenzie, 1984b) are conservation of mass for the fluid component

$$f_0 \rho_s v_0 = \phi \rho_l v_l \quad (4.5.24)$$

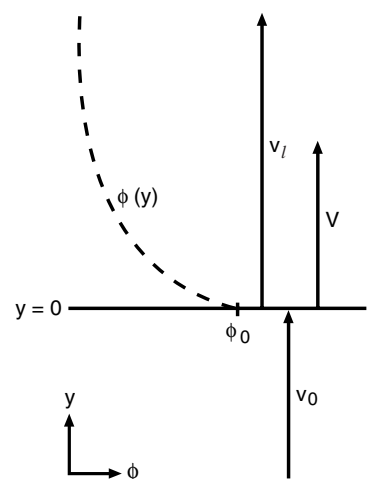


Figure 4.27. Schematic diagram of one-dimensional compaction model with localized melting. Material rises at velocity v_0 and volume fraction ϕ_0 and melts at $y = 0$. Above this level, melt and matrix ascend at velocities v_l and V , respectively. Porosity ϕ decreases upward due to effects of compaction.

conservation of mass

$$\phi \rho_l v_l + (1 - \phi) \rho_s V = \rho_s v_0 \quad (4.5.25)$$

force balance for the melt

$$0 = -\phi \rho_l g - \frac{\mu_l \phi^2}{k_p} (v_l - V) - \phi \frac{dp}{dy} \quad (4.5.26)$$

force balance for the matrix

$$0 = -(1 - \phi) \rho_s g + \frac{\mu_l \phi^2}{k_p} (v_l - V) - (1 - \phi) \frac{dp}{dy} + \left(\zeta_s + \frac{4}{3} \mu_s \right) \frac{d^2 V}{dy^2} \quad (4.5.27)$$

The dependent variables in (4.5.24)–(4.5.27) are the upward melt velocity v_l , the upward matrix velocity V , the porosity ϕ , and the melt pressure p ; μ_s is the dynamic viscosity of the matrix (viscosity in shear) and ζ_s is the bulk viscosity of the matrix. Equation (4.5.26) is the strict form of Darcy's law, which states that the velocity of the melt relative to the matrix is proportional to the effective pressure gradient. The last term in (4.5.27) is the "compaction" term, which describes the deformation of the matrix. For simplicity the viscosities ζ_s and μ_s have been assumed constant.

Equations (4.5.26) and (4.5.27) can be combined by eliminating dp/dy to yield

$$0 = -(1 - \phi) g \Delta \rho + \frac{\mu_l \phi}{k_p} (v_l - V) + \left(\zeta_s + \frac{4}{3} \mu_s \right) \frac{d^2 V}{dy^2} \quad (4.5.28)$$

where $\Delta \rho = \rho_s - \rho_l$. Equation (4.5.28) shows that melt segregation is governed by a balance of three forces: the differential buoyancy of the melt, the resistance to flow of melt through the matrix (Darcy resistance), and the resistance of the matrix to deformation (compaction term). If the compaction term can be ignored the flow is determined by a balance between differential buoyancy and Darcy resistance.

To complete the formulation we assume that the dependence of matrix permeability k_p on porosity ϕ is given by (4.5.3). Substitution of (4.5.3), (4.5.24), and (4.5.25) into (4.5.28) gives

$$0 = -(1 - \phi) g \Delta \rho + \frac{72 \pi \mu_l v_0}{\phi b^2} \left(\frac{f_0 \rho_s}{\phi \rho_l} - \frac{1 - f_0}{1 - \phi} \right) + (1 - f_0) v_0 \left(\zeta_s + \frac{4}{3} \mu_s \right) \frac{d^2}{dy^2} \left(\frac{1}{1 - \phi} \right) \quad (4.5.29)$$

In order to further simplify the problem we assume that $f_0 \ll 1$ and $\phi \ll 1$ and that $\rho_s = \rho_l = \rho$ everywhere except in the first term of (4.5.29) (the Boussinesq approximation). Equation (4.5.29) then becomes

$$0 = -g \Delta \rho + \frac{72 \pi \mu_l v_0}{b^2 \phi^2} (f_0 - \phi) + v_0 (\zeta_s + 4\mu_s/3) \frac{d^2 \phi}{dy^2} \quad (4.5.30)$$

This is a differential equation for the dependence of ϕ on depth.

The problem can be simplified even more by introducing the nondimensional quantities

$$\phi' = \frac{\phi}{f_0} \quad (4.5.31)$$

$$y' = \frac{y}{\delta_c} \quad (4.5.32)$$

where

$$\delta_c = \left[\frac{\mu_l}{k_0 (\zeta_s + \frac{4}{3} \mu_s)} \right]^{1/2} \quad (4.5.33)$$

is the compaction length with

$$k_0 = \frac{b^2 f_0^2}{72\pi} \quad (4.5.34)$$

Substitution of (4.5.31)–(4.5.34) into (4.5.30) gives

$$\frac{d^2 \phi'}{dy'^2} + \frac{1 - \phi'}{\phi'^2} = R \quad (4.5.35)$$

where

$$R = \frac{k_0 g \Delta \rho}{f_0 v_0 \mu_l} \quad (4.5.36)$$

is a dimensionless buoyancy.

The appropriate boundary conditions for (4.5.35) can be determined as follows. The viscosity of the matrix is finite, so compaction of a material element of the matrix occurs gradually as it ascends above $y' = 0$. At $y' = 0$, no compaction has yet occurred, so $\phi = f_0$ and $\phi' = 1$. As $y' \rightarrow \infty$, however, compaction nears completion, and ϕ is determined by a balance of the first two terms of (4.5.30) (Darcy's law). The dimensionless boundary conditions for (4.5.35) are therefore

$$\phi'(0) = 1 \quad (4.5.37)$$

$$\frac{1 - \phi'(\infty)}{\phi'^2(\infty)} = R \quad (4.5.38)$$

Equation (4.5.35) can be solved by introducing $F \equiv d\phi'/dy'$ and rewriting the equation in the form

$$F \frac{dF}{d\phi'} = R + \frac{\phi' - 1}{\phi'^2} \quad (4.5.39)$$

Integration of (4.5.39) gives

$$F = \left[2 \left\{ R (\phi' - \phi'_\infty) + \ln \left(\frac{\phi'}{\phi'_\infty} \right) + \frac{1}{\phi'} - \frac{1}{\phi'_\infty} \right\} \right]^{1/2} \quad (4.5.40)$$

Substitution of $d\phi'/dy'$ for F and integration give

$$y' = \frac{1}{\sqrt{2}} \int_{\phi'_\infty}^{\phi'} \left[R (\phi'' - \phi'_\infty) + \ln \left(\frac{\phi''}{\phi'_\infty} \right) + \frac{1}{\phi''} - \frac{1}{\phi'_\infty} \right]^{-1/2} d\phi'' \quad (4.5.41)$$

Numerical evaluation of (4.5.41) gives y' as a function of ϕ' in the partially molten zone. The results are shown for several values of the buoyancy parameter R in Figure 4.28. Compaction is confined to a boundary layer (compaction layer) whose thickness decreases with

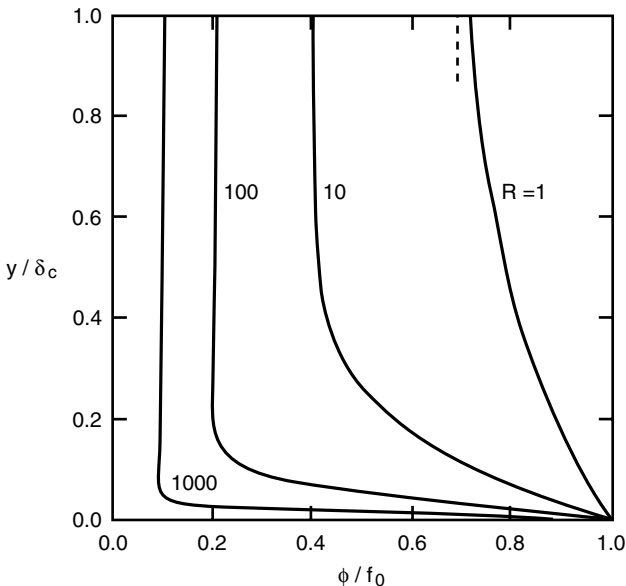


Figure 4.28. Porosity profiles for the localized melting model. Compaction is confined to a boundary layer (“compaction layer”) of thickness $\delta_R = R^{-1/2} \delta_c$. The dashed line shows $\phi(\infty)/f_0$ for $R = 1$, $\phi(\infty) \sim \phi(y = \delta_c)$ for other values of R .

increasing R . Above this layer, the porosity ϕ' has a constant value ϕ'_∞ as defined by (4.5.38). This state is known as uniform fluidization, and corresponds to a balance of buoyancy and Darcy resistance such that the porosity is constant. The approximate (dimensional) thickness of the compaction layer is therefore given by the reduced compaction length

$$\delta_R = R^{-1/2} \delta_c = \left[\frac{f_0 v_0 (\zeta_s + 4\mu_s/3)}{g \Delta \rho} \right]^{1/2} \quad (4.5.42)$$

Substitution of the appropriate parameter values from Table 4.5 shows that $\delta_R \approx 10\text{--}100\text{ m}$. This range of values is consistent with the estimate given by Ahern and Turcotte (1979) that a partially molten column exceeding about 80 m in height will collapse under its own weight. Note that the values used for ζ_s and μ_s ($10^{15}\text{--}10^{18}\text{ Pa s}$) are much less than the usual value of 10^{21} Pa s for the subsolidus viscosity of the mantle. This is because partial melting reduces the effective viscosity of the crystalline matrix as a whole (not the individual grains) by orders of magnitude; for a discussion see McKenzie (1984b). Other studies have been carried out by Khodakovskii et al. (1998) and Richardson (1998).

The upward drainage of magma through the solid matrix has a number of implications. Magma erupting at the surface or forming intrusive bodies comes from a variety of depths and a variety of source regions (Kenyon and Turcotte, 1987). There can be chemical interchange between the migrating fluid and the solid matrix (Korenaga and Kelemen, 1998). This can be particularly important in terms of incompatible trace elements such as the rare earths. The effect is similar to that in a chromatographic column (McKenzie, 1985, 1989; Ribe, 1985b; Richter, 1986; Navon and Stolper, 1987). There is considerable evidence for nonequilibrium behavior in the chemistry of mid-ocean ridge basalts (Salters and Hart, 1989). Spiegelman and Kenyon (1992) suggest that magma flow channels are separated by about 10 cm in order to explain the observed chemical disequilibrium during magma migration (Kenyon, 1998).

Spiegelman (1996) has considered some of the consequences of trace element partitioning. Beneath the mid-ocean ridge crest the asthenosphere reaches the base of the crust. Thus it is easy to envision how magma can migrate through the asthenosphere by the porous-flow mechanism to form a magma chamber. However, there are several problems with this mechanism. One of the major problems is the necessity of focusing the magma so that it reaches the immediate vicinity of the ridge axis. Volcanism is largely localized to within a few kilometers of the ridge crest and the oceanic crust appears to reach its normal thickness of about 6 km in this region. As illustrated in Figure 4.26, pressure-release melting beneath a passive spreading center necessarily occurs over a much broader region, of the order of 80 km on either side of the crest. There must be a mechanism which causes the magma to be focused into a much narrower region.

Question 4.7: How is magma focused into a narrow region in the vicinity of a ridge crest?

Buoyancy alone cannot accomplish this focusing, since it produces only vertical migration of magma. Spiegelman and McKenzie (1987) suggested that the viscous forces associated with mantle convection could provide the focusing, since they are of the same order as the buoyancy force in mantle convection. The parameter that governs this effect is $\Gamma_1 = 4\mu_s U / (\rho_s - \rho_l) g L^2$, where U and L are characteristic velocity and length scales associated with the mantle flow and μ_s is the mantle viscosity. With $\mu_s = 2 \times 10^{19}$ Pa s, $U = 0.05 \text{ m yr}^{-1}$, $\rho_s - \rho_l = 500 \text{ kg m}^{-3}$, $g = 10 \text{ m s}^{-2}$, and $L = 100 \text{ km}$, we find $\Gamma_1 = 3 \times 10^{-3}$. It does not appear that mantle viscosity is sufficiently large for the viscous stresses to influence magma migration.

Rabinowicz et al. (1987), Scott (1988), Buck and Su (1989), Scott and Stevenson (1989), and Su and Buck (1993) have suggested that the buoyancy of the magma itself can lead to a focusing of the melt flow. A parameter that relates the partial melt buoyancy to the thermal expansion buoyancy is given by $\Gamma_2 = \phi_r(\rho_s - \rho_l)/\rho_s \alpha_s \Delta T$, where ϕ_r is a reference magma porosity, α_s is the coefficient of thermal expansion of the solid, and ΔT is the temperature difference associated with mantle convection. With $\phi_r = 0.01$, $\alpha = 3 \times 10^{-5} \text{ K}^{-1}$, $\Delta T = 1,000 \text{ K}$, and the densities given above, we find $\Gamma_2 = 0.05$. Again, the effect is relatively small and requires large magma porosities to be effective. Kelemen and Dick (1995) and Kelemen et al. (1995a,b) showed that magma is focused in dunite shear zones. Sparks and Parmentier (1991), Ribe (1986, 1988), and Phipps Morgan (1987) have also considered problems associated with magma focusing. Phipps Morgan (1987) investigated the role of layered heterogeneities in focusing magma migration.

An additional problem with the porous-flow model is the observational evidence that melt segregates in the asthenosphere to form veins (Nicolas, 1986, 1990). Models for this have been proposed by Sleep (1988a) and Stevenson (1989a). Daines and Kohlstedt (1994) have proposed a transition from porous to channelized flow due to melt/rock reaction during melt migration. Aharonov et al. (1995) have also proposed a channeling instability. These authors basically argue that melt migration behaves like river networks. When channels of magma on grain boundary intersections merge, they widen channels like small streams merging to form rivers. Hart (1993) has provided geochemical arguments for a fractal tree channelization approach to magma migration. The problem of magma migration below ocean ridges has

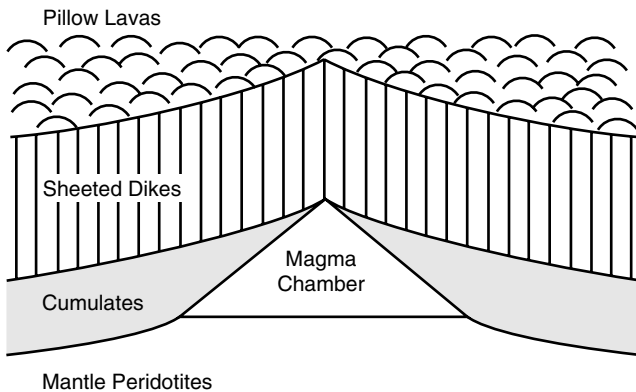


Figure 4.29. Illustration (not to scale) of the oceanic crust at a spreading center.

been reviewed by Ribe (1987), Stevenson and Scott (1991), Turcotte and Phipps Morgan (1992), and Kelemen et al. (1997).

4.5.2 Melt Migration in Fractures

We now turn to the problem of the migration of magma through the oceanic lithosphere at the ridge crest. There is considerable observational evidence that magma collects in a magma chamber at the base of the oceanic crust. Studies in Iceland and in ophiolites show that sheeted dike complexes are an essential feature of the generation of oceanic crust at spreading centers (Cann, 1974; Kidd, 1977). A schematic representation of this process is given in Figure 4.29. Magma is stored in a magma chamber at the base of the sheeted dike complex until the tensional stresses associated with seafloor spreading are sufficiently large that an upward propagating fluid-driven fracture initiates at the top of the magma chamber. This fracture creates a channel that allows the magma chamber to be fully or partially drained. Magma extruded at the surface forms pillow basalts. When flow ceases, the magma in the dike solidifies forming the youngest member of the sheeted dike complex.

Question 4.8: How does magma rise through the lithosphere?

Magma-driven fracture propagation is the only mechanism that has been proposed for the transport of magma through the lithosphere. The basic theory describing this phenomenon has been developed for hydraulically driven fracture propagation by Geertsma and DeKlerk (1969) and Geertsma and Haakens (1979). Solutions must simultaneously account for the fluid flow through the crack, the elastic deformation of surrounding rock, and the propagation of the fracture. Similarity solutions for laminar, pressure-driven, two-dimensional fluid fractures have been given by Spence and Turcotte (1985), with additional mathematical details in Spence and Sharp (1985). Similarity solutions for turbulent flow have been presented by Emerman et al. (1986). Applications of these solutions to the mechanics of dike injection have been given by Turcotte et al. (1987). Spera (1987) and Turcotte (1990) have provided an extended discussion of magma fracture.

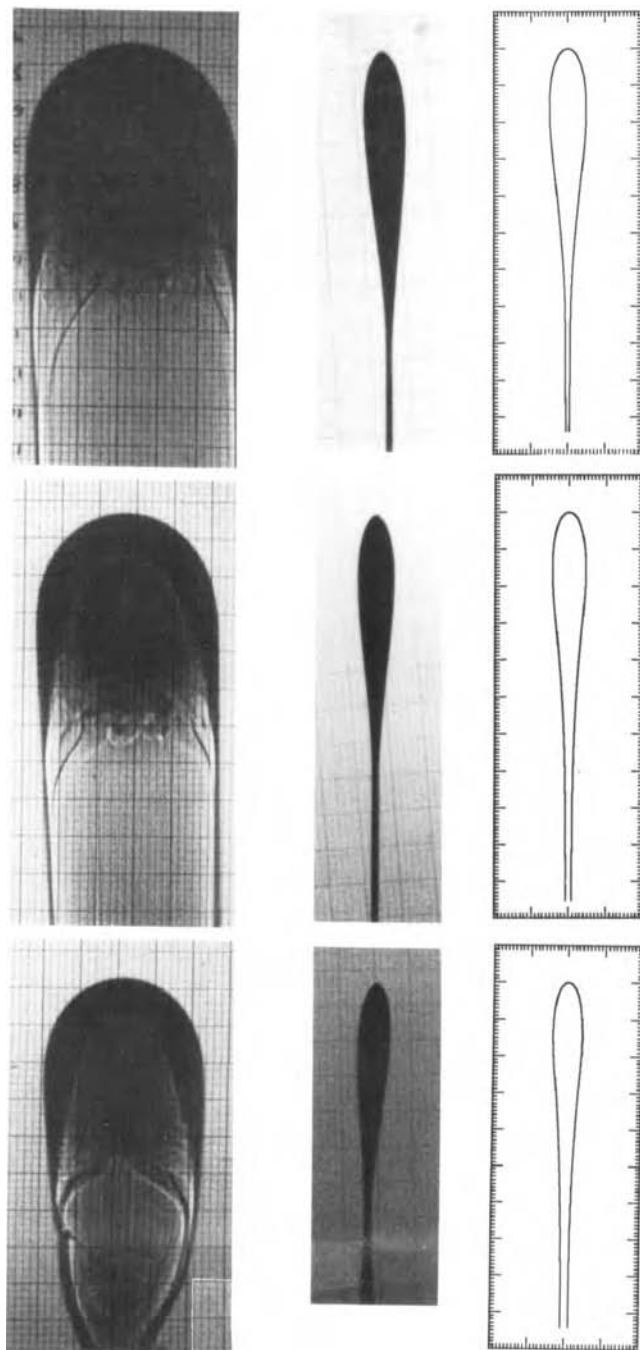


Figure 4.30. Experimentally determined geometry of a buoyancy-driven, liquid-filled fracture with constant source flux, propagating in an elastic medium, compared with theoretical equilibrium shapes. From left to right: in-plane, cross-section, and theoretical cross-section views. From Heimpel and Olson (1994).

Buoyancy-driven fracture propagation as a mechanism for magma migration through the lithosphere has been studied by Weertman (1971), Secor and Pollard (1975), Anderson and Grew (1977), and Davies (1999). A solution for the steady upward propagation of a two-dimensional fluid fracture driven by buoyancy has been given by Spence et al. (1987) for a single value of the stress intensity factor. Lister (1990a,b, 1991) and Lister and Kerr (1991) have extended this to obtain solutions for any value of the stress intensity factor. In these solutions the elastic deformation is important only in the vicinity of the crack tip; below the crack tip the width and flow velocity are determined by a simple balance between the buoyancy force and the viscous force, and either laminar or turbulent flow results. Spence and Turcotte (1990) have obtained a solution for a transient buoyancy-driven fracture neglecting the elastic tip effects. Heimpel and Olson (1994) have investigated this phenomenon experimentally, and compared the predictions of the laminar and viscous flow models with the shape and propagation speed of buoyant, fluid-filled cracks in several elastic media. Some of their results are shown in Figure 4.30. Other studies have been carried out by Meriaux and Jaupart (1998) and Meriaux et al. (1999).

It is instructive to solve a simplified set of equations in order to illustrate the interaction between the fluid flow and the crack propagation. A number of assumptions are made. The fracture is embedded in a uniform, impermeable medium with a shear modulus μ and Poisson's ratio ν . The magma is assumed to be a Newtonian fluid with a constant viscosity μ_l . A solution is obtained for the two-dimensional case illustrated in Figure 4.31. Fluid is injected at $x = y = 0$ and the two-sided crack propagates in the $+x$ and $-x$ directions. Various conditions on the injection rate or injection pressure can be applied; here we assume that the volumetric rate of injection per unit depth A is constant.

The length of the crack is $2l(t)$ and its width is $2h(x, t)$ with $h \ll l$. The rate of magma supply is related to the width and mean velocity at the origin by

$$A = 2h(0)\bar{u}(0) \quad (4.5.43)$$

where \bar{u} is the mean flow velocity in the x -direction. The volume of the crack is related to the volume of fluid injected by

$$At = 2 \int_{-l}^l h(x, t) dx \quad (4.5.44)$$

where A is taken to be a constant. In most cases it is appropriate to make the lubrication approximation whereby the inertia terms are neglected and the applied pressure gradient is balanced by the shear stress. In laminar flow this balance gives (Hirs, 1974)

$$\bar{u} = -\frac{1}{3} \frac{h^2}{\mu_l} \frac{\partial p}{\partial x} \quad (4.5.45)$$

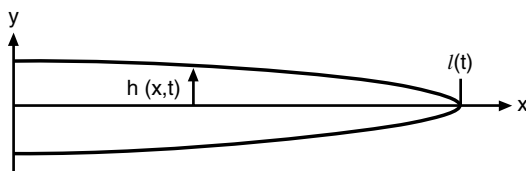


Figure 4.31. Geometry of propagating fluid-filled dike used in the analysis.

and for turbulent flow

$$\bar{u} = \left[\frac{2^{5/4} 15 h^{5/4}}{\rho^{3/4} \mu_l^{1/4}} \left(-\frac{\partial p}{\partial x} \right) \right]^{4/7} \quad (4.5.46)$$

The Reynolds number Re at the entrance to the crack is

$$Re = \frac{\rho A}{\mu_l} \quad (4.5.47)$$

It can be assumed that the flow is laminar if $Re < 10^3$ and turbulent if $Re > 10^3$.

The elastic deformation of the medium is given by (Barenblatt, 1962)

$$p(x, t) = -\frac{\mu}{\pi(1-\nu)} \int_{-l}^l \frac{\partial h(s, t)}{\partial s} \frac{ds}{(s-x)} \quad (4.5.48)$$

In the lubrication approximation the shear stress on the walls of the crack can be neglected in comparison with the fluid pressure. In the elastic theory for the propagation of cracks a stress singularity occurs at the crack tip. The strength of this singularity is related to the fracture resistance of the elastic material. Thus, it is appropriate to introduce the stress intensity factor K defined by (Irwin, 1957)

$$K = \frac{2l^{1/2}}{\pi} \int_0^l \frac{p(x, t) dx}{(l^2 - x^2)^{1/2}} \quad (4.5.49)$$

This is a particularly difficult set of equations to solve because of the singular behavior of the elastic deformation equation (4.5.48). However, reasonably accurate approximate solutions can be obtained. A simplified elastic strain equation can be written

$$p(0) = \frac{\mu}{(1-\nu)} \frac{h(0)}{l} \quad (4.5.50)$$

and this replaces (4.5.48). The flow equation (4.5.44) is replaced with

$$At = 2lh(0) \quad (4.5.51)$$

The shear flow equations (4.5.45) and (4.5.46) are approximated by

$$\bar{u}(0) = \frac{1}{3} \frac{h(0)^2 p(0)}{\mu_l l} \quad (4.5.52)$$

for laminar flow and

$$\bar{u}(0) = \left[\frac{2^{5/4} 15 h(0)^{5/4} p(0)}{\rho^{3/4} \mu_l^{1/4} l} \right]^{4/7} \quad (4.5.53)$$

for turbulent flow.

We first consider laminar flow in the limit that the fracture resistance is negligible compared with the viscous resistance to flow. A combination of (4.5.43), (4.5.50), (4.5.51), and

(4.5.52) gives

$$l = C_1 A^{1/2} \left[\frac{\mu}{(1-\nu)\mu_l} \right]^{1/6} t^{2/3} \quad (4.5.54)$$

$$2h(0) = C_2 A^{1/2} \left[\frac{\mu_l(1-\nu)}{\mu} \right]^{1/6} t^{1/3} \quad (4.5.55)$$

$$p(0) = C_3 \left(\frac{\mu}{1-\nu} \right)^{2/3} \left(\frac{\mu_l}{t} \right)^{1/3} \quad (4.5.56)$$

with $C_1 = 0.589$, $C_2 = 1.698$, and $C_3 = 1.44$. A numerical solution of the complete equations also yields (4.5.54)–(4.5.56) with $C_1 = 0.4636$, $C_2 = 1.49$, and $C_3 = 1.7279$ (Spence and Sharp, 1985). Geertsma and Haakens (1979) also found (4.5.54) and (4.5.55) with approximate solutions that gave $C_1 = 0.68$ and $C_2 = 1.87$.

We next consider turbulent flow in the limit that the fracture resistance is negligible compared with the viscous resistance to flow. Consideration of (4.5.43), (4.5.50), (4.5.51), and (4.5.53) gives

$$l = C_4 \frac{A^{3/8} \mu^{1/6} t^{2/3}}{\rho^{1/8} \mu_l^{1/24} (1-\nu)^{1/6}} \quad (4.5.57)$$

$$2h(0) = C_5 \frac{A^{5/8} \rho^{1/8} \mu_l^{1/24} (1-\nu)^{1/6} t^{1/3}}{\mu^{1/6}} \quad (4.5.58)$$

$$p(0) = C_6 \frac{A^{1/4} \rho^{1/4} \mu_l^{1/24} \mu^{2/3}}{(1-\nu)^{2/3} t^{1/3}} \quad (4.5.59)$$

with $C_4 = 1.40$, $C_5 = 0.714$, and $C_6 = 0.255$. By solving the complete equations, Emerman et al. (1986) also obtained (4.5.57)–(4.5.59) with $C_4 = 1.4183$, $C_5 = 0.5121$, and $C_6 = 0.2593$.

For laminar flow the condition under which the stress-intensity factor can be neglected is

$$\gamma = \frac{(1-\nu)^{3/4} K}{A^{1/4} \mu_l^{1/4} \mu^{3/4}} \ll 1 \quad (4.5.60)$$

and for turbulent flow the condition is

$$\gamma = \frac{(1-\nu)^{3/4} K}{A^{7/16} \mu_l^{1/16} \rho^{3/16} \mu^{3/4}} \ll 1 \quad (4.5.61)$$

If these inequalities are satisfied then the results given in (4.5.54)–(4.5.59) are valid.

The shape of the laminar dike is

$$\frac{h}{h(0)} = \left[1 - \left(\frac{x}{l} \right)^2 \right]^{2/3} \quad (4.5.62)$$

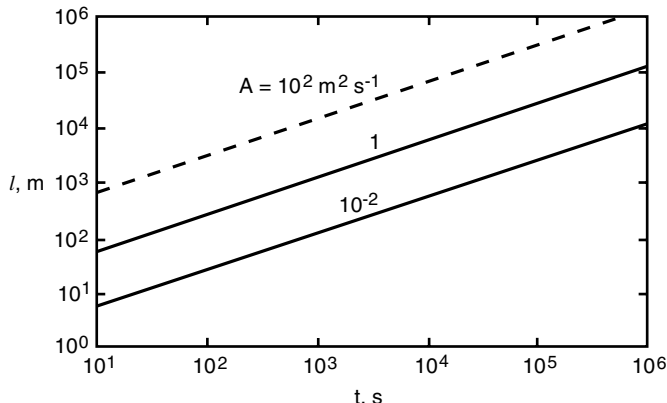


Figure 4.32. The half-length l of two-dimensional fluid-driven dikes as a function of injection time t for several values of the injection rate A . The solid lines are for laminar flow and the dashed line is for turbulent flow, $\mu_l = 10^2$ Pa s.

and the shape of the turbulent dike is

$$\frac{h}{h(0)} = \left[1 - \left(\frac{x}{l} \right)^2 \right]^{8/9} \quad (4.5.63)$$

(Emerman et al., 1986).

We now give some examples for basaltic dikes and consider first the role of the stress-intensity factor. Measured values of the critical stress-intensity factor have been summarized by Atkinson (1984). As a typical value we take $K = 3$ MN m $^{-3/2}$. Representative parameter values for dike injection are $A = 1$ m 2 s $^{-1}$, $\mu = 2 \times 10^{10}$ Pa, $\nu = 0.25$, $\mu_l = 10^2$ Pa s, and $\rho = 2,700$ kg m $^{-3}$. From (4.5.60) we find $\gamma = 0.0109$ for laminar flow, and from (4.5.61) we find $\gamma = 0.0192$ for turbulent flow. In most cases of dike injection it is appropriate to assume $\gamma \ll 1$. This is equivalent to neglecting the fracture resistance of the elastic medium compared to the flow resistance in the crack.

The half-length $l(t)$ of a propagating dike as a function of time is shown in Figure 4.32 for parameter values given above and for the additional magma injection rates $A = 10^{-2}$ and 10^2 m 2 s $^{-1}$. In obtaining Figure 4.32 it was also assumed that the transition to turbulent flow occurs for $Re = A\rho/\mu_l = 10^3$, and either (4.5.54) with $C_1 = 0.4636$ or (4.5.57) with $C_4 = 1.4183$ was used. The solid lines indicate laminar flow and the dashed line is for turbulent flow. The velocity of dike propagation is obtained by taking the time derivative of either (4.5.54) or (4.5.57). The dependence of the propagation velocity on time is shown in Figure 4.33. The maximum half-width $h(0)$ is obtained either from (4.5.55) with $C_2 = 1.495$ or from (4.5.58) with $C_5 = 0.5121$, and the results are given in Figure 4.34.

An important question for dike propagation is whether significant solidification will occur on the walls of the dike during magma injection. An estimate of the time required to solidify a crack of width $2h(0)$ has been given by Spence and Turcotte (1985). The solidification time is shown by the short dashed line SL in Figure 4.34 which was calculated for the latent heat of fusion $L = 400$ kJ kg $^{-1}$, the specific heat $c = 1$ kJ kg $^{-1}$, the temperature difference between the wall rock and the magma $T_m - T_0 = 800$ K, and the thermal diffusivity $\kappa = 0.5$ mm 2 s $^{-1}$. A dike would not be expected to propagate below this line. Dike closure rates due to solidification have also been investigated by Bruce and Huppert (1989).

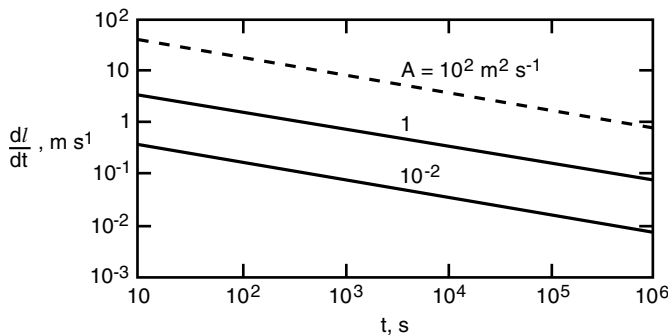


Figure 4.33. Propagation velocities dl/dt as a function of the injection time t for several values of the injection rate A . The solid lines are for laminar flow and the dashed line is for turbulent flow, $\mu_l = 10^2$ Pa s.

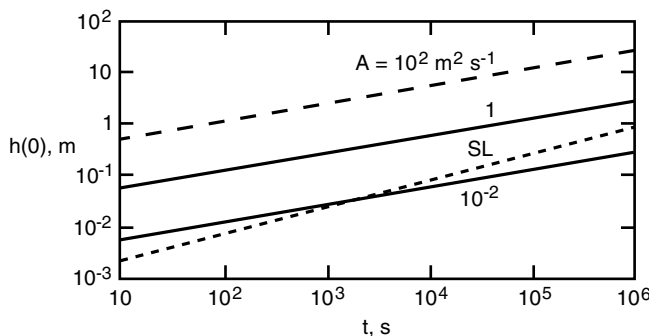


Figure 4.34. Maximum half-widths $h(0)$ as a function of the injection time t for several values of the injection rate A . The solid lines are for laminar flow and the dashed line is for turbulent flow, $\mu_l = 10^2$ Pa s. Dikes would be expected to solidify beneath the short dashed line denoted by SL.

We next consider the example of a dike on a sheeted dike complex at a mid-ocean ridge. For $l = 7.5$ km, $\mu_l = 10^2$ Pa s, $A = 10^2 \text{ m}^2 \text{ s}^{-1}$ and other properties as above, we find from Figure 4.32 that the required injection time is 400 s (about 7 min). The velocity of propagation from Figure 4.33 is 10 m s^{-1} and the maximum half-width from Figure 4.34 is $h(0) = 2$ m. This is in excellent agreement with typical observed widths in Iceland and in ophiolites (Delaney and Pollard, 1982).

The model given above is appropriate for a dike as it propagates upwards from a magma chamber to the surface. Once it reaches the surface, a dike behaves as an open channel for the ascending magma until the magma chamber is drained. Under these circumstances it is a reasonable approximation to treat the buoyancy-driven flow in a dike as a flow in a channel with buoyancy forces balanced by viscous forces. Extensive studies of buoyancy-driven flows of magma in pipes and channels have been given by Wilson and Head (1981). The conditions under which viscous dissipation coupled with a strongly temperature dependent viscosity can lead to a thermal instability have been given by Fujii and Uyeda (1974). Further studies of the role of viscous dissipation have been given by Hardee and Larson (1977) and by Hardee (1986).

As discussed above, one-dimensional channel flow is often a good approximation for the flow in a magma-driven fracture. The model is illustrated in Figure 4.35. For laminar flow

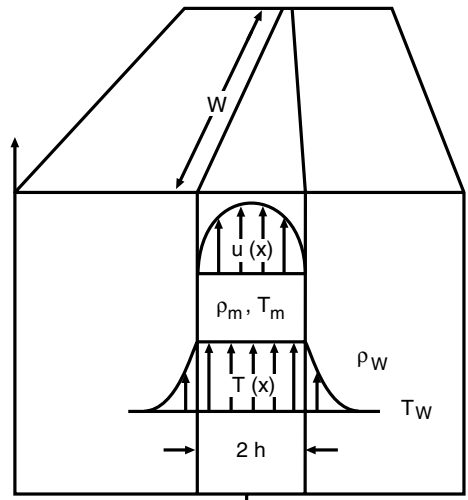


Figure 4.35. Illustration of the channel-flow model.

with a buoyancy drive the vertical flow rate Q in a channel of width $2h$ is (Hirs, 1974)

$$Q = \frac{2(\rho_s - \rho_l)gh^3}{3\mu_l} \quad (4.5.64)$$

The corresponding mean velocity \bar{u} in the channel is

$$\bar{u} = \frac{(\rho_s - \rho_l)gh^2}{3\mu_l} \quad (4.5.65)$$

Laminar flow applies if $Re < 10^3$. At higher values of the Reynolds number, the flow is turbulent, the vertical flow rate Q is (Hirs, 1974)

$$Q = \frac{2(30[\rho_s - \rho_l]g)^{4/7} h^{12/7}}{\rho_s^{3/7}} \left(\frac{2}{\mu_l}\right)^{1/7} \quad (4.5.66)$$

and the corresponding mean velocity is

$$\bar{u} = \frac{(30[\rho_s - \rho_l]g)^{4/7} h^{5/7}}{\rho_s^{3/7}} \left(\frac{2}{\mu_l}\right)^{1/7} \quad (4.5.67)$$

As an example we consider the ascent of a basaltic magma through the mantle and take $\mu_l = 100 \text{ Pa s}$ (Ryan and Blevins, 1987), $\rho_l = 2,800 \text{ kg m}^{-3}$, $\rho_s = 3,300 \text{ kg m}^{-3}$, and $g = 10 \text{ m s}^{-2}$. From (4.5.64) and (4.5.65) the transition from laminar to turbulent flow is found to occur for a dike width of $2h = 2 \text{ m}$ and $\bar{u} = 16.7 \text{ m s}^{-1}$. The dependence of the mean magma velocity on channel width is given in Figure 4.36.

If the crack is approximated by a constant width $2h$ and a length w , then the aspect ratio is $\alpha = w/2h$. In terms of the aspect ratio, the total flow volume V_m as a function of time is given by

$$V_m = \frac{4(\rho_s - \rho_l)g\alpha h^4 t}{3\mu_l} \quad (4.5.68)$$

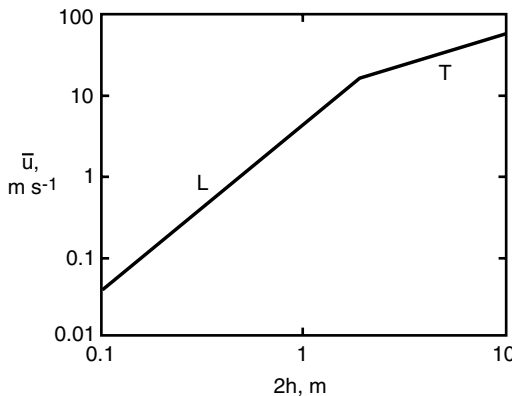


Figure 4.36. Dependence of the mean velocity \bar{u} in the dike on the dike width $2h$ for laminar L and turbulent T flows.

for laminar flow and

$$V_m = \frac{4(30[\rho_s - \rho_l]g)^{4/7} \alpha h^{19/7} t}{\rho_s^{3/7}} \left(\frac{2}{\mu_l}\right)^{1/7} \quad (4.5.69)$$

for turbulent flow. The flow volume is given as a function of time in Figure 4.37 for several channel widths and an aspect ratio $\alpha = 10^3$.

We now discuss thermal effects on the flow of magma through a channel. Because the wall rock has a temperature considerably below the solidus of the magma, it would be expected that solidification of the magma would occur on the boundaries of the flow channel. However, two effects tend to prevent solidification. The first is dissipative (frictional) heating in the magma and the second is the decrease in the melt temperature T_m of the magma as it ascends.

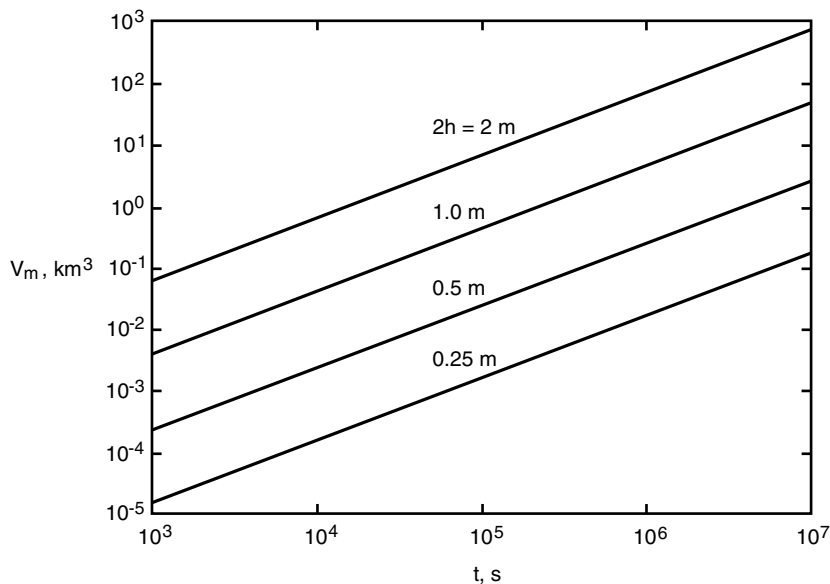


Figure 4.37. Dependence of the flow volume V_m on time t for several dike widths $2h$.

For laminar flow this balance is given by (Turcotte and Schubert, 1982)

$$\rho_s L \frac{dh'}{dt} = \frac{(\rho_s - \rho_l)^2 g^2 h^3}{3\mu_l} - \frac{\rho_l(\rho_s - \rho_l)gh^3 c}{3\mu_l} \frac{dT_m}{dy} - \frac{k_s(T_m - T_s)}{(\pi\kappa_s t)^{1/2}} \quad (4.5.70)$$

where dh'/dt is the rate of melting of the wall rock on one side of the dike (if dh'/dt is negative, it is the rate of solidification of the magma on one side). For simplicity we assume that the magma has a well-defined melt temperature T_m and the width of the channel $2h$ remains approximately constant. The first term on the right side of (4.5.70) represents dissipative heating, the second term the decrease in melt temperature with depth, and the third term the loss of heat to the wall rock. Integration of (4.5.70) gives

$$h' = \frac{(\rho_s - \rho_l)^2 g^2 h^3 t}{3\mu_l \rho_s L} \left[1 - \frac{\rho_l c}{(\rho_s - \rho_l)g} \frac{dT_m}{dt} \right] - \frac{2k_s(T_m - T_s)}{\rho_s L} \left(\frac{t}{\pi\kappa_s} \right)^{1/2} \quad (4.5.71)$$

The thermal balance for turbulent flow is

$$\begin{aligned} \rho_s L \frac{dh'}{dt} &= \frac{(30)^{4/7} [(\rho_s - \rho_l)g]^{11/7} h^{12/7}}{\rho_l^{3/7}} \left(\frac{2}{\mu_l} \right)^{1/7} \\ &\times \left[1 - \frac{\rho_l c}{(\rho_s - \rho_l)g} \frac{dT_m}{dy} \right] - \frac{k_s(T_l - T_s)}{(\pi\kappa_s t)^{1/2}} \end{aligned} \quad (4.5.72)$$

and integration gives

$$\begin{aligned} h' &= \frac{(30)^{4/7} [(\rho_s - \rho_l)g]^{11/7} h^{12/7}}{\rho_l^{3/7} \rho_s L} \left(\frac{2}{\mu_l} \right)^{1/7} t \left[1 - \frac{\rho_l c}{(\rho_s - \rho_l)g} \frac{dT_m}{dy} \right] \\ &- \frac{2k_s(T_m - T_s)}{\rho_s L} \left(\frac{t}{\pi\kappa_s} \right)^{1/2} \end{aligned} \quad (4.5.73)$$

We can now determine the width h' of the solidified or melted zone on the margins of a dike. In addition to the parameter values given above, we take $\rho L = 1.12 \times 10^9 \text{ J m}^{-3}$, $k_s = 2 \text{ W m}^{-1} \text{ K}^{-1}$, $T_m - T_s = 500 \text{ K}$, $\kappa_s = 0.7 \text{ mm}^2 \text{ s}^{-1}$, $c = 10^3 \text{ J kg}^{-1} \text{ K}^{-1}$, $dT_m/dy = -2 \text{ K km}^{-1}$. The dependence of h' on time is given in Figure 4.38 for several channel widths. It is seen that substantial melting of the wall rock can occur. This implies significant contamination of the primary magma.

The influence of viscous dissipation in preventing magma solidification in dikes has been investigated numerically by Carrigan et al. (1992), who modeled the flow of magma through long narrow channels with length to width ratios of 1,000:1 and larger. Their models not only incorporated dissipative heating but also included the strong dependence of magma viscosity on temperature (Shaw, 1969; Murase and McBirney, 1973; Ryan and Blevins, 1987; Ryerson et al., 1988). The results show that viscous heating can offset significant rates of heat loss to the surrounding rock provided that there is a sufficiently large pressure head to drive rapid flow through the dike (for a 1 m wide basaltic dike, a flow of about 2.7 m s^{-1} driven by a pressure gradient of 1.7 MPa km^{-1} is required). Such a pressure gradient can be provided by the exsolution of volatiles from the magma (a 7% void fraction will suffice). The ease of producing this pressure gradient by reducing the density of the magmatic column with addition of a gas phase makes it likely that flows of basaltic magma could be maintained in dikes tens of kilometers long. The presence of a gas phase may be important not only in

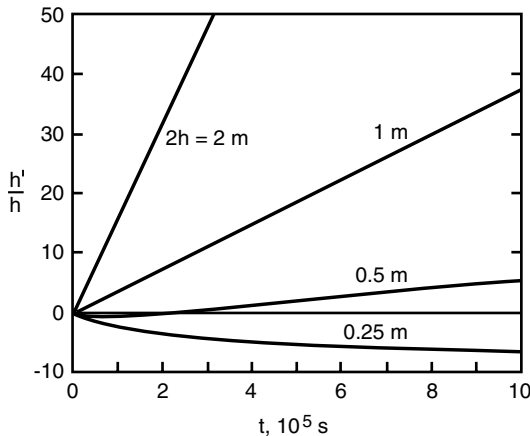


Figure 4.38. Dependence of the ratio of the thickness of melt solidified on the channel wall h' to the channel half-width h as a function of time t for several channel widths $2h$.

dike propagation but also in propagation of the fracture prior to initial injection of magma during dike emplacement (Anderson, 1978; Spera, 1984; Wilshire and Kirby, 1989; Carrigan et al., 1992). Vapor-propagated fracture is not subject to the pressure losses associated with the high viscosity of the magma or its weight (Carrigan et al., 1992).

The numerical calculations of Carrigan et al. (1992) also show how magma solidification in dike propagation is significantly delayed by a small amount of transverse flow (flow toward or away from the dike walls). Such transverse flow can be induced by rising bubbles, boundary roughness, or turbulence. Minor amounts of transverse flow must certainly occur in real dikes making estimates of magma solidification from idealized laminar flow models (Bruce and Huppert, 1989) overly conservative.

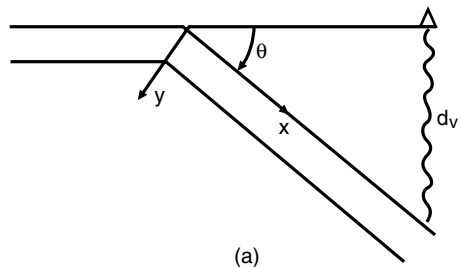
It is difficult to prevent solidification of magmas more viscous than basaltic magmas (silicic magmas) through the effects of viscous dissipation because of the large flow velocities and pressure gradients required (Carrigan et al., 1992). Carrigan and Eichelberger (1990) and Carrigan et al. (1992) suggest that andesitic or rhyolitic flows in a dike can be facilitated by an encapsulation effect in which a high-viscosity core of magma is surrounded by a lower-viscosity magma which is in contact with the dike walls. The low-viscosity magma may be of a different composition or it may have a different crystal or water content (magma viscosity increases with crystal content and increases with dryness). Larger dike widths are apparently required to accommodate the flow of more viscous magmas (Wada, 1994; Clemens, 1998).

4.6 Temperatures in Subducting Slabs

The greatest lateral variations in mantle temperatures occur within subducted lithosphere. Subduction of cold oceanic lithosphere is the major heat loss mechanism for the deep interior of the Earth, and it is also the most important component of the driving force for mantle convection.

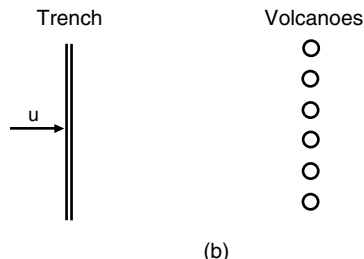
4.6.1 Frictional Heating on the Slip Zone

The thermal structure of the descending lithosphere can be modeled in an idealized way by considering the simplified geometry illustrated in Figure 4.39. The plate approaches the trench with a velocity u normal to the trench and descends into the mantle at an angle θ to the horizontal. This is equivalent to the transformation of a cold thermal boundary layer



(a)

Figure 4.39. Geometry of the descending plate. (a) Side view. (b) Vertical view.



(b)

into a cold descending plume in the boundary layer theory for thermal convection (see Chapter 8). On the basis of the boundary layer model, one would expect that these regions would have below-average surface heat flow. However, it is observed that high heat flow and volcanism occur behind ocean trenches. It was suggested independently by Oxburgh and Turcotte (1968) and by McKenzie and Sclater (1968) that frictional heating on the slip zone between the descending plate and the overriding mantle was responsible for the high heat flow and surface volcanism. To evaluate this idea a number of authors have calculated the temperature distribution in the descending plate. These include Turcotte and Oxburgh (1968) and McKenzie (1969), who assumed a constant-temperature boundary condition at the slip zone; McKenzie (1970) and Griggs (1972), who assumed a slip zone temperature equal to an undisturbed mantle temperature; and Oxburgh and Turcotte (1970), who assumed a shear stress on the slip zone that decreased with depth.

Subduction zone volcanism places an important constraint on the thermal structure of the descending slab. Geochemical studies have provided conclusive evidence that melting of subducted sediments is required to produce island arc volcanics. Thus it is reasonable to assume that melting of the descending oceanic crust takes place at a point on the slip zone beneath the volcanic arc. This hypothesis assumes that magmas produced on the slip zone rise nearly vertically to the surface. Clearly, the force bringing the magmas to the surface is the buoyancy force due to the low density of the magmas. At the depths at which the magmas are produced (100–200 km) the hydrostatic pressure is more than an order of magnitude greater than the ultimate strength of the rock. Therefore it is expected that the magmas will move through the rock owing to plastic deformation of the rock rather than through a conduit or fracture. Such movement is likely to be vertical in the direction of the body force, since there is no other preferred direction. With this hypothesis, the location of the volcanoes gives the point on the slip zone where the melting temperature is reached, and therefore provides specific evidence for studying the thermal structure of the descending plate.

We present a simplified model illustrating how frictional heating influences the thermal structure of the descending slab. A constant shear stress along the slip zone will be assumed

until at some depth the basalt solidus temperature is reached. At greater depths the temperature on the slip zone is assumed to be buffered at the basalt solidus. The linear chain of active volcanoes is assumed to lie a distance d_v above the slip zone. An x , y coordinate system is set up in the descending plate as illustrated in Figure 4.39. The temperature distribution in the oceanic lithosphere as it begins to subduct is assumed to be given by (4.2.4) with t the age of the subducted lithosphere. It is assumed that this is the initial temperature profile in the descending plate. The evolution of this initial profile is neglected, since it will take place on a time scale longer than that of interest here.

Since the conduction of heat in a solid is a linear phenomenon, the temperature increase due to heat conduction from the slip zone can be added to the initial temperature profile. The component of heat flux in the plate and normal to the slip zone q satisfies

$$u \frac{\partial q}{\partial x} = \kappa \frac{\partial^2 q}{\partial y^2} \quad (4.6.1)$$

The conduction of heat along the plate has been ignored here; the Peclét number of the flow ux/κ is large.

We will specify the heat entering the descending plate from the slip zone to the point on the slip zone where the basalt solidus is reached (i.e., for $x < x_v$). Since (4.6.1) is parabolic, the slip zone boundary condition for $x > x_v$ will not affect the solution for $x < x_v$. We assume that the heat flow per unit area entering the descending plate at the slip zone ($y = 0$) is related to the shear stress τ on the slip zone by

$$q = u\tau \quad (4.6.2)$$

In writing this relation, the energy radiated in seismic waves has been neglected in comparison with the energy dissipated by frictional heating on the slip zone. Use of (4.6.2) as a boundary condition on the heat flow entering the descending plate neglects both the heat conducted to the slip zone owing to the initial temperature distribution in the descending plate and the heat conducted upward through the overlying mantle. Fortunately these contributions tend to cancel.

The temperature in the descending plate due to the heat added at the slip zone is obtained from the heat flux by using the relation

$$T' = \frac{1}{k} \int_y^\infty q dy \quad (4.6.3)$$

The actual temperature in the descending plate is obtained by adding T' to the initial temperature profile from (4.2.4).

Before the temperature distribution in the descending plate can be obtained, it is necessary to prescribe the dependence of the shear stress on depth. Very little is known about this dependence; in fact, even the mechanism for motion across the slip zone is open to question. At shallow depths there is undoubtedly a well-defined fault zone with stick-slip behavior. However, at depths greater than about 20 km, where the hydrostatic pressure is large in comparison with the yield strength of the rock, some type of plastic flow is likely to occur. This plastic flow is expected to be a complicated function of pressure and temperature. We assume that the shear stress is a constant τ_0 independent of depth. The appropriate boundary

conditions for (4.6.1) are

$$\begin{aligned} q &= 0, & x = 0 \\ q &= u\tau_0, & y = 0 \\ q &= 0, & y \rightarrow \infty \end{aligned} \quad (4.6.4)$$

A similarity solution to this problem can be obtained by introducing

$$\eta = \frac{y}{2} \left(\frac{u}{\kappa x} \right)^{1/2} \quad (4.6.5)$$

Substitution of (4.6.5) into (4.6.1) gives

$$\left(\frac{d^2 q}{d\eta^2} \right) + 2\eta \left(\frac{dq}{d\eta} \right) = 0 \quad (4.6.6)$$

with the boundary conditions

$$\begin{aligned} q &= u\tau_0, & \eta = 0 \\ q &= 0, & \eta \rightarrow \infty \end{aligned} \quad (4.6.7)$$

The solution of (4.6.6) that satisfies the boundary conditions (4.6.7) is

$$q = u\tau_0 \operatorname{erfc} \left[\frac{y}{2} \left(\frac{u}{\kappa x} \right)^{1/2} \right] \quad (4.6.8)$$

The temperature T' from (4.6.3) and (4.6.8) is

$$T' = 2 \left(\frac{\kappa x}{u} \right)^{1/2} \frac{u\tau_0}{k} i^1 \operatorname{erfc} \left[\frac{y}{2} \left(\frac{u}{\kappa x} \right)^{1/2} \right] \quad (4.6.9)$$

where $i^n \operatorname{erfc}(\eta)$ is the n th integral of the error function (error function integrals are tabulated in Abramowitz and Stegun, 1964). For $x < x_m$, where x_m is the distance along the slip zone where melting first occurs, the temperature in the descending plate is obtained by adding (4.6.9) and (4.2.4).

The temperature on the slip zone for $x < x_m$ is given by

$$T_{sz} = 2 \left(\frac{\kappa x}{\pi u} \right)^{1/2} \frac{u\tau_0}{k} + T_0 \quad (4.6.10)$$

where T_0 is the surface temperature. We now assume that $T_{sz} = T_m$, the solidus temperature of basalt, when $x = x_m$ and $d_m = x_m \sin \theta$. Since the surface volcanism is assumed to mark the first occurrence of melting on the slip zone, $d_m = d_v$ and $x_m = x_v$. The constant shear stress on the slip zone is given by

$$\tau_0 = \frac{k(T_m - T_0)}{2} \left(\frac{\pi \sin \theta}{u d_v \kappa} \right)^{1/2} \quad (4.6.11)$$

From the solidus temperature, the velocity and geometry of the descending plate, the thermal properties of the plate, and the depth to the plate beneath the volcanoes, the shear stress on the slip zone can be determined.

A typical temperature distribution is given in Figure 4.40. The angle of dip is taken to be $\theta = 45^\circ$ and the velocity of the plate approaching the trench is 80 mm yr^{-1} . Within the slab we assume $k = 3.3 \text{ W m}^{-1} \text{ K}^{-1}$ and $\kappa = 1 \text{ mm}^2 \text{ s}^{-1}$. It is further assumed that $T_m - T_0 = 1,000 \text{ K}$ and $d_v = 150 \text{ km}$. From (4.6.11) the required shear stress on the slip zone is 126 MPa.

The Sea of Japan is an example of a region of anomalously high heat flow and high seismic attenuation that is often observed behind a volcanic line. We assume that this region extends 200 km beyond the volcanic line and that the temperature on the slip zone is buffered at the melt temperature beneath this region, i.e., to a depth of 325 km. The isotherms above the descending slab in this region are estimated and shown by the dashed lines in Figure 4.40. Convective transport of heat by magmas may occur in this region, or a secondary flow process in the mantle may dominate.

The ability of frictional heating to produce partial melting of the subducted oceanic crust and lithosphere remains a subject of controversy, as discussed in Section 2.5.5. Yuen et al. (1978) studied frictional heating on slip zones using thermally activated creep laws for the deformation. Since the rock becomes weak as the solidus is approached, they concluded that the maximum temperatures associated with frictional heating are always less than those required for partial melting. It is widely believed that release of volatiles by the heating of the descending crust plays an essential role in subduction zone magmatism by lowering the melting point of crustal rocks and rocks in the overlying mantle wedge (Anderson et al., 1976; Ringwood, 1977a; Bird, 1978a). However, as pointed out in Section 2.5.5, the precise roles of volatiles and frictional heating on the slip zone in producing magmas at subduction zones are not completely understood. Question 2.7 is worth repeating.

Question 4.9: What causes volcanism at subduction zones?

4.6.2 Phase Changes in the Descending Slab

Figure 4.40 shows the positions of the olivine–spinel and spinel–perovskite phase changes in a descending slab that penetrates the phase transitions. The thermal structure in the slab depends on the locations of the phase changes. It is seen that the phase changes are displaced from their equilibrium depths; the displacement is upward for the olivine–spinel phase change and downward for the spinel–perovskite phase change. The displacements of the phase boundaries result in buoyancy forces that strongly affect the sinking of the slab. It is important therefore to understand the physics involved in moving relatively cold (or hot) material through a phase change.

The opposite displacement of the two phase changes is due to their different character. The olivine–spinel phase change is exothermic, i.e., heat is released when the less dense olivine transforms to the more dense spinel. The spinel–perovskite + magnesiowüstite phase change is endothermic, i.e., heat must be added to transform the less dense spinel into the more dense perovskite and magnesiowüstite. The exothermic olivine–spinel phase change has a positive Clapeyron slope Γ , where Γ is the slope of the boundary separating the light and heavy phases in a p – T diagram (Figure 4.41) given by

$$\Gamma \equiv \frac{dp}{dT} = \frac{L_H \rho_l \rho_h}{T(\rho_h - \rho_l)} \quad (4.6.12)$$

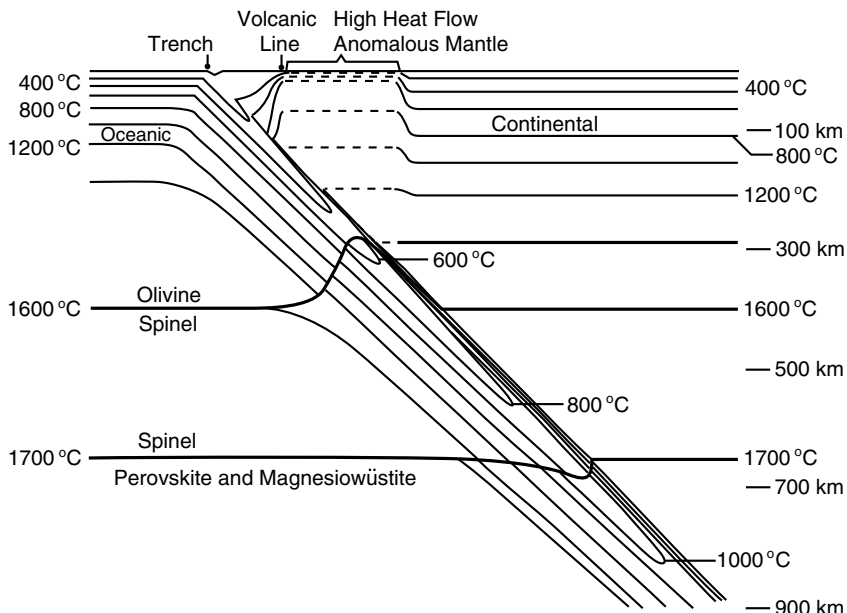


Figure 4.40. Thermal structure of the descending lithosphere including the effects of frictional heating on the slip zone and the olivine–spinel and spinel–perovskite transitions. The thin lines denote the isotherms and the heavy lines represent the equilibrium positions of the phase changes. The velocity of the plate approaching the trench is 80 mm yr^{-1} . Other parameter values are given in the text. The relatively large elevation of the olivine–spinel phase change and the relatively small depression of the spinel–perovskite transition in the slab are a consequence of the Clapeyron slopes assumed in the calculation, 4 MPa K^{-1} for the olivine–spinel phase change and -1.3 MPa K^{-1} for the spinel–perovskite phase change. More recent estimates of the Clapeyron slope of the spinel–perovskite phase change are even more negative, resulting in a larger downward deflection of this phase transition in the slab. After Schubert et al. (1975).

(ρ_l and ρ_h are the densities of the light and heavy phases, respectively, T is the temperature at which the phase transition occurs, and L_H is the latent heat of the phase change, positive when heat is released in transforming from the light phase to the heavy phase).

The upward displacement of the olivine–spinel phase boundary in the descending slab can be understood with reference to Figure 4.41a. The slab is colder than the surrounding mantle, and as a result it encounters the Clapeyron curve of the exothermic phase change at a lower pressure than the ambient mantle. The cold thermal anomaly of the descending slab distorts the olivine–spinel phase boundary upwards in the slab. However, as can be seen in Figure 4.41b, the relatively cold slab encounters the Clapeyron curve of the endothermic phase change at a higher pressure than the ambient mantle. The cold thermal anomaly of the descending slab distorts the spinel–perovskite phase boundary downwards in the slab. The downward depression of the spinel–perovskite phase boundary in the descending slab beneath the Izu-Bonin subduction zone has been quantified using seismic data by Castle and Creager (1998).

The wedge of dense spinel beneath the upwarped olivine–spinel phase boundary in the slab represents a positive density anomaly relative to the less dense olivine at the same depth in adjacent mantle. The positive density anomaly provides a downward body force that promotes the sinking of the slab. The wedge of spinel above the downwarped spinel–perovskite phase boundary in the slab represents a negative density anomaly relative to the

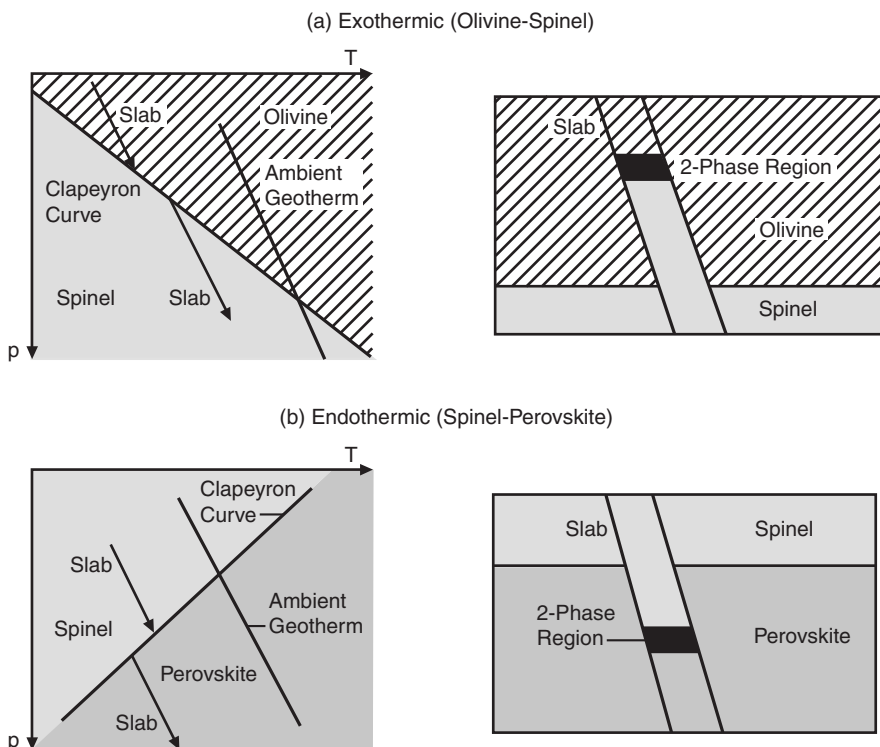


Figure 4.41. Sketch of equilibrium phase boundary displacement in a cold slab descending through (a) the exothermic olivine–spinel phase change and (b) the endothermic spinel–perovskite phase change. Motion through the phase transitions results in narrow two-phase regions in the slab. The positive Clapeyron slope of the exothermic phase change elevates the phase boundary in the slab while the negative Clapeyron slope of the endothermic phase change lowers the phase boundary in the slab. The p – T diagrams on the left show the path of the descending slab and the Clapeyron curves separating the phases. Univariant phase transitions are assumed.

more dense perovskite at the same depth in the surrounding mantle. The negative density anomaly provides an upward body force that opposes the sinking of the slab. The tendency of a thermally induced endothermic phase boundary distortion to oppose slab sinking has enormous significance for the dynamics of the mantle that is explored in considerable detail in Chapters 9 and 10. The effect is underestimated in Figure 4.40 by the small amount of distortion of the 660 km phase change in the slab. The magnitude of the Clapeyron slope of the 660 km phase change assumed in constructing Figure 4.40 is at least a factor of 2 smaller than currently accepted values of the Clapeyron slope magnitude, and the amplitude of thermally induced phase boundary distortion is directly proportional to the magnitude of Γ .

Thermally induced phase boundary distortions occur in response to any mantle thermal anomaly such as the positive thermal anomaly associated with mantle plumes. Figure 4.42 illustrates the distortion of the olivine–spinel and spinel–perovskite phase boundaries due to the upward motion of a hot mantle plume. The olivine–spinel phase boundary is displaced downward in the hot plume while the spinel–perovskite phase boundary is moved upward. The downward distortion of the olivine–spinel phase change makes the plume lighter than its surroundings, thereby promoting plume upwelling. The upward distortion

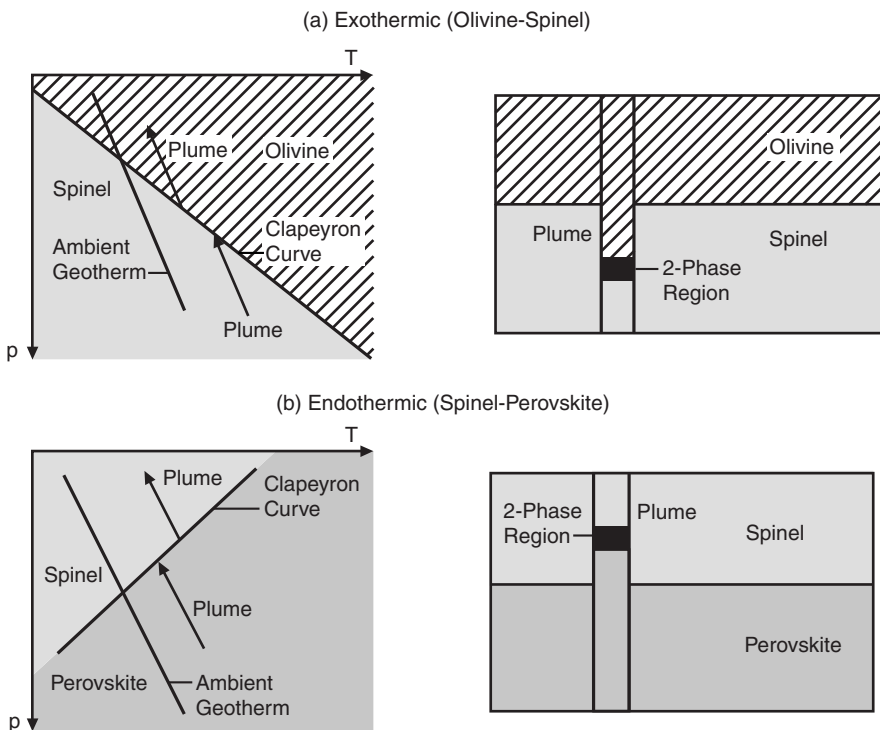


Figure 4.42. Similar to Figure 4.41 but for a hot plume rising through the phase transitions. The olivine–spinel phase boundary is displaced downward in the plume while the spinel–perovskite phase boundary moves upward in the plume.

of the spinel–perovskite phase change makes the plume heavier than its surroundings and tends to retard plume upwelling.

Latent heat release or absorption during slab descent through the major phase changes also affects the thermal state of the slab. Coupled with thermal expansivity and phase boundary distortion, it affects the net body force on the slab as well. Latent heat is released during the slab’s downward motion through the exothermic olivine–spinel phase change. The heat release tends to warm the slab. As a result of thermal expansion, the induced positive thermal anomaly exerts an upward body force on the slab, tending to retard its downward motion; the positive thermal anomaly also moves the phase boundary downward, contributing further to the body force resisting slab sinking. Latent heat release by the olivine–spinel phase transition leads to body forces opposing the downward motion of the descending slab.

Latent heat is absorbed during the slab’s downward motion through the endothermic spinel–perovskite phase change. The heat absorption tends to cool the slab. As a result of thermal contraction, the induced negative thermal anomaly exerts a downward body force on the slab, tending to assist its downward motion; the negative thermal anomaly also moves the phase boundary downward, providing an upward body force that resists slab sinking. Latent heat absorption by the spinel–perovskite phase transition both promotes and retards the downward motion of the descending slab.

Latent heat release and absorption also influences mantle plumes moving upward through the transition zone. Latent heat is released when an upwelling plume moves through the

Table 4.6. Summary of Dynamical Effects of Mantle Phase Changes

Phase Change	Phase Boundary Distortion by Advection of Thermal Anomalies	Phase Boundary Distortion Due to Release or Absorption of Latent Heat	Expansion or Contraction Due to Release or Absorption of Latent Heat
Exothermic (olivine–spinel)	Enhances hot upwelling and cold downflow	Retards	Retards
Endothermic (spinel–perovskite)	Retards hot upwelling and cold downflow	Retards	Enhances

spinel–perovskite phase change. The warming contributes to plume buoyancy through thermal expansion but it also tends to upwarp the phase boundary which tends to retard plume upwelling. Latent heat is absorbed when a plume rises through the olivine–spinel phase change which tends to cool the plume and retard its upflow. The cooling also tends to upwarp the phase boundary which adds to the negative buoyancy opposing plume upwelling. The phase change effects on mantle thermal anomalies and associated upflows and downflows are summarized in Table 4.6.

Two important assumptions are implicit in the above discussion of phase change effects in descending slabs (and plumes). We have treated the mantle phase changes as univariant, although in reality they are divariant. Univariant phase changes occur at a single value of temperature and pressure at the intersection of a geotherm and the Clapeyron curve. Divariant phase changes occur over a range of temperature and pressure and have associated two-phase regions (see the discussion of mantle phase transitions in Chapter 3). Because the olivine–spinel and spinel–perovskite phase transitions in the mantle occur over relatively narrow intervals of depth, the divariant nature of the phase changes does not have important dynamical consequences. Motion through a univariant phase change can also produce a two-phase region (Turcotte and Schubert, 1971) as depicted in Figures 4.41 and 4.42 and discussed in Section 4.8. Motion through a divariant phase change is discussed in more detail in Section 4.8.

The second major assumption implicit in the above discussion is that of thermodynamic equilibrium. This implies that a phase change will occur when the p – T curve of a rising or descending flow intersects the Clapeyron curve. However, solid–solid phase changes involve the rearrangement of mineral structures and they proceed at finite rates. If the rate of phase transformation is slow enough, as could occur at the low temperatures inside slabs, one phase could persist into the stability field of another phase, and completely alter the location of the phase boundary. Metastability is not regarded as important in plumes or at the depth of 660 km in slabs because temperatures are considered high enough for phase change reactions to proceed rapidly and equilibrium should prevail. However, metastability could affect the occurrence of the olivine–spinel phase change in the slab. Under equilibrium conditions, the olivine–spinel phase change in the slab occurs above the depth of 410 km (Figure 4.39) where temperatures in the slab could still be low enough to delay the onset of the phase transformation. We will see in the next section that metastability of the olivine–spinel phase transition could fundamentally change the thermal structure of the slab and modify its negative buoyancy.

4.6.3 Metastability of the Olivine–Spinel Phase Change in the Descending Slab

The depth of the olivine–spinel phase transformation in descending slabs determines the buoyancy force on the slab which could either drive or oppose subduction depending on whether the phase boundary is shallower or deeper than it is in the surrounding mantle (Schubert et al., 1975; Sung and Burns, 1976). It also determines the rheology of the slab (Riedel and Karato, 1997) and the stresses in the slab (Goto et al., 1987; Bina, 1996). As discussed above, the rate of transformation of olivine to spinel in a cold descending slab could be slow enough for a wedge of metastable olivine to form in the slab, in which case the phase boundary would be deeper than in the surrounding mantle and the associated body force would oppose subduction (Sung and Burns, 1976; Rubie and Ross, 1994; Daessler and Yuen, 1996; Marton et al., 1999; Schmeling et al., 1999). The presence of a metastable olivine wedge in the descending slab could be related to the occurrence of deep earthquakes, a phenomenon possibly related to the phase transformation (Green and Houston, 1995; Kirby et al., 1996).

Devaux et al. (1997) have presented a thermal model of a descending slab in which the transformation of olivine to spinel is controlled by pressure- and temperature-dependent reaction kinetics. They solve the two-dimensional, time-dependent heat conduction equation in the descending slab and include the latent heat of phase transformation, heat conduction parallel to the dip of the slab, and adiabatic heating. The model follows the formation of the metastable olivine wedge through time during the descent of the slab.

The calculations yield the representative slab structures shown in Figure 4.43. The parameter T_p is the thermal parameter of a slab (Kirby et al., 1996) given by

$$T_p = vt \sin \delta \quad (4.6.13)$$

where v is the down-dip descent velocity of the slab, t is the age of the slab entering the trench, and δ is the dip of the slab ($v \sin \delta$ is the vertical velocity of slab sinking). Old, cold slabs have large thermal parameters. The thermal parameter of a slab facilitates the description of its thermal structure and the length of the metastable olivine wedge. The

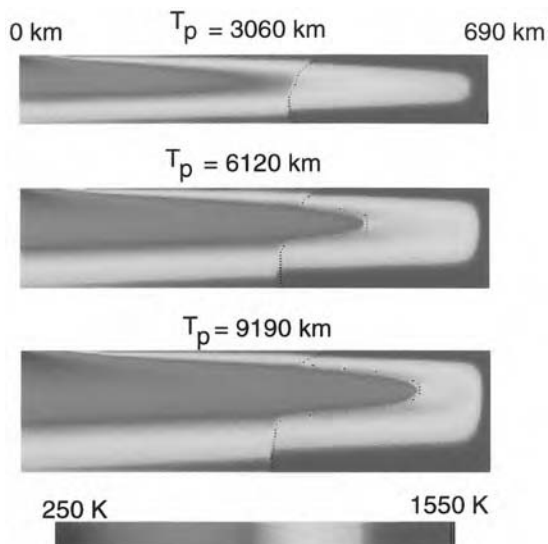


Figure 4.43. Temperature fields of three slabs with reaction rate-dependent olivine–spinel transformation. The slabs are shown horizontal but they dip 50° into the mantle. The horizontal coordinate is distance along the slab. The values of the thermal parameter T_p correspond to ages of 50, 100, and 150 Myr with $v = 80 \text{ mm yr}^{-1}$. The dotted lines mark the isocontour corresponding to 99% completion of the phase change. After Devaux et al. (1997).

For a color version of this figure, see plate section.

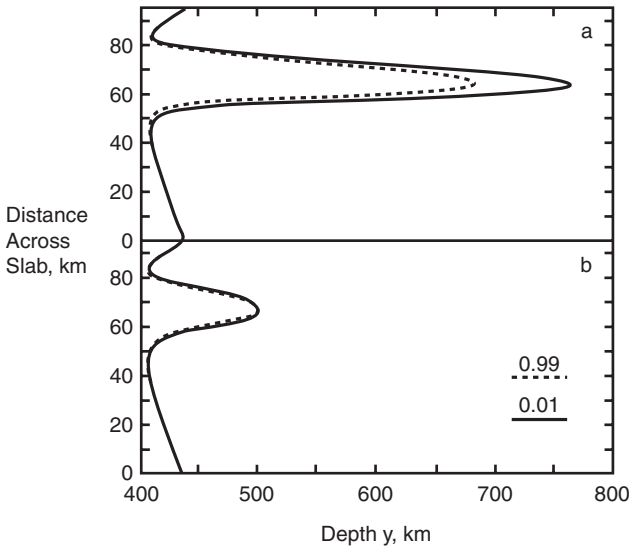


Figure 4.44. Olivine–spinel phase boundaries for a 100 Myr old slab with $v = 140 \text{ mm yr}^{-1}$ and $\delta = 70^\circ$. In (a) the calculation does not account for latent heat release while in (b) it does include the latent heat. The transformation is 1% complete along the dashed line and 99% complete along the solid line. After Devaux et al. (1997).

oldest slab depicted in Figure 4.43 ($T_p = 9,190 \text{ km}$) has a large metastable olivine wedge, while the youngest slab ($T_p = 3,060 \text{ km}$) has essentially no metastable olivine.

Latent heat release acts to reduce the size of the metastable olivine wedge as shown in Figure 4.44. In the top panel of the figure latent heat is not accounted for in the calculation, and the result is a large metastable olivine wedge and a wide two-phase region. In the bottom panel latent heat is included in the calculation, and the metastable wedge is small and has a very narrow two-phase region. Release of latent heat inside the slab warms it and speeds up the reaction kinetics, resulting in a short metastable olivine wedge.

Wedge lengths for a large number of calculations are shown in Figure 4.45 as a function of T_p . Two different reaction kinetics formulations are used in the calculations. In case 1 the reaction occurs over the temperature interval 773–788 K, while in case 2 it goes to completion in the temperature range 833–923 K (at pressures of about 15 GPa). For a value of T_p less than a certain value T_{pc} , which depends on the reaction kinetics case, the temperature inside the slab does not allow the formation of metastable olivine and there is no metastable olivine wedge. When $T_p > T_{pc}$, the slab is cold enough for a metastable olivine wedge to form. The length of the wedge increases approximately linearly with $T_p - T_{pc}$. The value of T_{pc} is about 7,000 km and 4,000 km for reaction kinetics cases 1 and 2, respectively. These values are consistent with the results of Kirby et al. (1996), who found from seismological observations that deep earthquakes occur only for $T_p > 5,000 \text{ km}$. Figure 4.45 shows that the length of the metastable olivine wedge in a descending slab is very sensitive to the assumed values of reaction kinetics parameters. The difference in wedge length could reach 130 km for the same T_p . Wedge length in slabs is thus difficult to estimate due to uncertainties in our knowledge of reaction kinetics.

The calculations of Devaux et al. (1997) raise problems for the association of deep earthquakes with the transformation of metastable olivine to spinel. The major difficulty is illustrated in Table 4.7, which compares calculated depths of the tips of the metastable

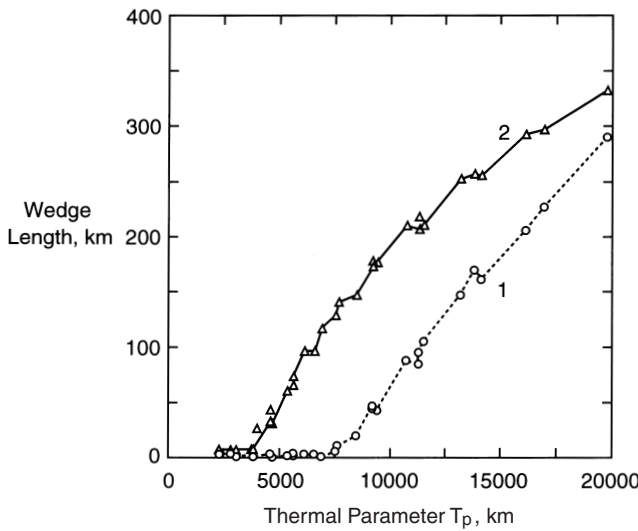


Figure 4.45. Length of metastable olivine wedge versus thermal parameter T_p for two reaction kinetics parameterizations described in the text. After Devaux et al. (1997).

olivine wedge with the depths of the deepest earthquakes in a number of slabs. In all cases except the Tonga slab, the maximum depths of the model metastable olivine wedges fail to reach the depths of the deepest earthquakes. Either the deep earthquakes are not associated with the transformation of metastable olivine to spinel or the reaction kinetics formulation of the model is in need of revision. Figure 4.45 shows that reaction kinetics case 1, which only allows formulation of a metastable olivine wedge at temperatures below about 773 K, predicts much smaller wedges than case 2 and no wedge at all for T_p between about 5,000 and 8,000 km. Yet Table 4.7 shows deep earthquakes in several slabs with T_p in this range. If

Table 4.7. Comparison Between the Depth of the Deepest Observed Earthquake and the Calculated Depth of the Metastable Olivine Wedge Tip^a

Slab	T_p ^b (km)	Depth ^c (km)	Wedge Tip Depth ^d (km)
Tonga	14,500	700	700
Eastern Java (125°E)	10,400	700	630
Kurile-Kamchatka	7,350	660	560
Izu-Bonin	7,350	580	550
Japan	6,100	600	530
Western Java (105°E)	6,000	620	520
South America (North)	5,000	660	480
South America (South)	5,000	640	480

^a After Devaux et al. (1997). ^b Thermal parameter calculated from Jarrard (1986). ^c Depth of the deepest observed earthquake from Kirby et al. (1996). ^d Calculated depth of the tip of the metastable olivine wedge with reaction kinetics case 2 from Devaux et al. (1997).

there is some association of deep earthquakes with olivine metastability, the reaction kinetics case 1 cannot be relevant to real mantle slabs.

Question 4.10: Is there a wedge of metastable olivine in old descending slabs?

Question 4.11: Is the olivine–spinel phase boundary in descending slabs shallower or deeper than it is in the surrounding mantle?

Question 4.12: What is the cause of deep earthquakes?

4.7 The Adiabatic Mantle

Throughout nearly 90% of the mantle the increase of temperature with depth closely approximates the condition of uniform entropy, usually referred to as adiabatic. Most of the upper mantle beneath the LVZ and practically all of the lower mantle, except the D'' layer, fall within this category. The approach to adiabaticity in these regions is a consequence of vigorous thermal convection, with advection by vertical motions dominating all other heat transfer mechanisms. With a typical vertical velocity w from subduction and slab length L as velocity and length scales, and the superadiabatic temperature increase across the lithosphere ΔT as the scale for temperature and entropy, the entropy equation (see Chapter 6 for a derivation of the entropy equation) in dimensionless form becomes

$$T \frac{Ds}{Dt} = \frac{1}{Pe} \nabla^2 T + H^* \quad (4.7.1)$$

where

$$Pe = wL/\kappa \quad (4.7.2)$$

is the Péclet number and $H^* = HL/\rho_m c_p \Delta T w$ is the dimensionless heat source strength. The slab Péclet number is $Pe \simeq 1,500$, and $H^* \simeq 0.01$. Consequently, $Ds/Dt \simeq 0$ and entropy is very nearly conserved in regions of the mantle with substantial vertical velocity.

In chemically homogeneous single-phase regions the temperature variation at constant entropy is given by (see Chapter 6)

$$\left(\frac{dT}{dy} \right)_s = \frac{\alpha g T}{c_p} = \frac{T}{H_T} \quad (4.7.3)$$

where

$$H_T = c_p/\alpha g \quad (4.7.4)$$

is the adiabatic temperature scale height, i.e., the depth over which the temperature increases by a factor of e due to adiabatic compression. Because thermal expansivity is difficult to determine in the deep mantle, (4.7.3) is usually expressed in terms of the Grüneisen parameter γ :

$$\gamma = \frac{\alpha K_T}{\rho c_v} = \frac{\alpha K_S}{\rho c_p} = \frac{\phi}{g H_T} \quad (4.7.5)$$

where ϕ is the seismic parameter defined in Chapter 3. A combination of (4.7.3) and (4.7.5) yields

$$\left(\frac{dT}{dy} \right)_s = \frac{\gamma g T}{\phi} \quad (4.7.6)$$

Since g and ϕ are known rather precisely from spherical Earth models, the problem of determining the adiabatic gradient reduces to finding the variation in γ with depth. Birch (1952) proposed $\gamma\rho \simeq \text{constant}$ through the lower mantle, a special case of the more general power-law formula

$$\frac{\gamma}{\gamma_0} = \left(\frac{\rho_0}{\rho} \right)^n \quad (4.7.7)$$

which is now commonly used. Mantle properties are given in Tables 4.8–4.11. These data indicate STP values for γ_0 of 1.2–1.8 for the abundant upper mantle minerals.

Table 4.8. Density and Elasticity of Mantle Minerals^a

Mineral	ρ (kg m^{-3})	$\delta\rho$ (Fe) (kg m^{-3})	K (GPa)	μ (GPa)
α olivine	3,220	1,180	129	82
β spinel	3,472	1,250	174	114
γ spinel	3,548	1,300	184	119
Orthopyroxene	3,205	800	104	77
Garnet	3,560	760	175	90
Majorite	3,520	975	175	150
Perovskite	4,105	1,080	274	153
Magnesiowüstite	3,583	2,280	162	130
Ilmenite	3,810	1,100	212	133
Stishovite	4,290	–	316	220

^a STP values; ρ indicates Mg end member; $\delta\rho$ (Fe) is density correction for Fe end member. From Weidner (1986); Jeanloz and Thompson (1983).

Table 4.9. Density and Seismic Velocities of Mantle Minerals^a

Mineral	ρ (kg m^{-3})	V_P (km s^{-1})	V_S (km s^{-1})
Olivine ($X_{\text{Mg}} = 90$)	3,350	8.3	4.8
β spinel ($X_{\text{Mg}} = 90$)	3,610	9.4	5.5
γ spinel ($X_{\text{Mg}} = 90$)	3,700	9.53	5.55
Orthopyroxene ($X_{\text{Mg}} = 90$)	3,280	7.9	4.7
Garnet	3,630	9.0	5.0
Majorite ($X_{\text{Mg}} = 90$)	3,600	9.1	5.1
Perovskite ($X_{\text{Mg}} = 100$)	4,105	10.2	5.7
Magnesiowüstite ($X_{\text{Mg}} = 90$)	3,810	8.6	5.0
Ilmenite ($X_{\text{Mg}} = 90$)	3,920	9.9	5.8
Stishovite	4,290	11.9	7.15

^a From Weidner (1986); Jeanloz and Thompson (1983).

Table 4.10. Density and Seismic Wave Velocities of Mantle Rocks^a

Rock Type	Density (kg m ⁻³)	V_P (km s ⁻¹)	V_S (km s ⁻¹)
Peridotites	3,310–3,530	8.2–8.35	4.7–4.9
Dunite	3,250–3,350	8.0–8.4	4.5–4.9
Eclogite	3,450–3,650	8.2–8.7	4.6–4.9

^a From Clark (1966); Manghnani et al. (1974).

Table 4.11. Thermodynamic Properties of Mantle Minerals^a

Mineral	ρ (kg m ⁻³)	c_p (J kg ⁻¹ K ⁻¹)	α ($\times 10^{-6}$ K ⁻¹)	k (W m ⁻¹ K ⁻¹)	γ
Olivine	3,220	838	25	3.1	1.18
Orthopyroxene	3,200	780	48	3.2	1.9
Garnet	3,630	760	20	3.2	1.1
Magnesiowüstite	3,580	925	32		1.5
Perovskite	4,105	733	22	5.1–1.4	

^a For $X_{\text{Mg}} = 100$ compositions at STP.

In the upper mantle and transition zone, the $n = 1$ version of (4.7.7) is often used, yielding adiabatic gradients in the range 0.3–0.45 K km⁻¹ (Stacey, 1977a). Accordingly, the adiabatic temperature increase amounts to 130–170 K and 90–150 K through the upper mantle and transition zone, respectively. Temperature changes across phase transformations are not included in these figures; they will be estimated later in this chapter.

In the lower mantle, γ is less certain. By relating the acoustical Grüneisen parameter, which can be obtained from seismic velocities, to the thermodynamic Grüneisen parameter (4.7.5), it is possible to estimate the adiabatic temperature scale height H_T in (4.7.5). Many variations of this method have been applied (Verhoogen, 1951, 1954; Stacey, 1977a; Anderson, 1979; Anderson, 1987b), and the results generally indicate $0.5 \leq n \leq 1$ and $1.2 \leq \gamma_0 \leq 1.5$. These give lower mantle adiabatic gradients in the range 0.25–0.4 K km⁻¹, implying adiabatic temperature increases of 550–900 K from 660 km to the CMB. All of these estimates are summarized in Table 4.12. The essential point is that we can estimate the total adiabatic temperature rise throughout the mantle beneath the lithosphere to be 800–1,300 K without phase transformation effects. The increase in the adiabatic temperature with depth associated with various values of the Grüneisen parameter is given in Figure 4.46. The results are given for a potential (zero-pressure) temperature of 1,600 K. We will demonstrate that this range changes very little when phase transformations are included. In contrast, the rise in absolute temperature between the Earth's surface and the CMB is probably in excess of 3,000 K. Pressure-induced temperature increases the geotherm by less than 40% in the silicate portion of the Earth. The rest of the increase occurs within thermal boundary layers. We have already discussed the arguments for a 1,300 K increase through the lithosphere. There must be other diffusive layers in the deep mantle, and the apparent adiabaticity through most of the lower mantle leaves only two regions where these thermal boundary layers can be – in the transition zone and in the D'' layer.

Table 4.12. Summary of Core and Mantle Temperatures

Region	Temperature Change (K)	Temperature (K)
Surface	–	273
Lithosphere	$1,300 \pm 100$	–
Base of lithosphere	–	$1,600 \pm 100$
Upper mantle adiabat	150 ± 20	–
Olivine → spinel	90 ± 30	–
410 km seismic discontinuity	–	$1,800 \pm 200$
Transition zone adiabat	120 ± 30	–
Spinel → perovskite	-70 ± 30	$2,000 \pm 250$
Transition zone TBL(s)	500 ± 500	–
Transition zone base	–	$1,900-2,900$
Lower mantle adiabat	700 ± 200	–
D'' TBL(s)	800 ± 700	–
Core–mantle boundary	–	$3,900 \pm 600$
Outer core adiabat	$1,000 \pm 400$	–
Inner–outer core boundary	–	$4,900 \pm 900$
Earth's center	–	$5,000 \pm 1,000$

TBL: thermal boundary layer.

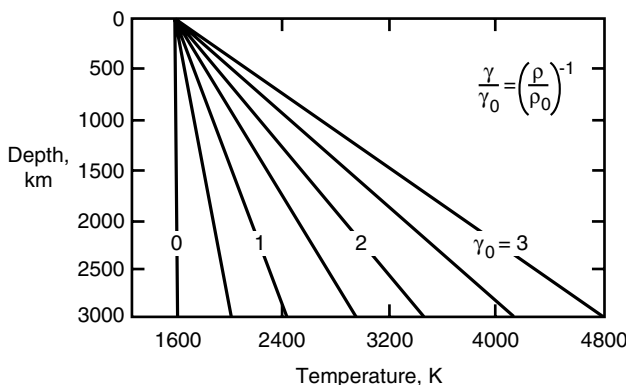


Figure 4.46. Adiabatic temperature variation with depth implied by various values of the Grüneisen parameter at zero pressure γ_0 , calculated assuming an inverse dependence of γ on density ρ . Preferred values for the mantle are in the range $1 < \gamma_0 < 2$. The results are given for a potential (zero-pressure) temperature of 1,600 K.

4.8 Solid-state Phase Transformations and the Geotherm

In the course of convective flow, mantle material is transported across the stability boundaries of phase transformations. We have already discussed how convection results in partial melting beneath spreading centers, the most important solid → liquid reaction produced by mantle convection. There is also flow across solid → solid phase transformations, particularly the olivine–spinel and spinel–perovskite plus magnesiowüstite transformations in the transition zone. Examples of this flow include the descent of slabs and the rise of plumes through the transition zone as discussed in Section 4.6. Because latent heat is released or absorbed as material passes through the phase boundaries, the geotherm is modified in the neighborhood

of the transformations as indicated schematically in Figures 4.41 and 4.42. Consequently, the depth and sharpness of mantle phase boundaries depend on the presence or absence of convective flow. In principle, this behavior can be used to map vertical flows in the transition zone. Since the olivine \rightarrow spinel reaction is exothermic, its mixed-phase region is deflected upward in cold, sinking regions and downward in hot, rising regions, adding to the thermal buoyancy force driving the motion (Figures 4.41 and 4.42 and Section 4.6). Perovskite-forming reactions, on the other hand, are endothermic, and therefore have the opposite effect (Figures 4.41 and 4.42 and Section 4.6).

As illustrated in Figures 4.47 and 4.48, the deflection of the geotherm at a phase transformation consists of two parts: a precursor thermal boundary layer on the upstream side of the mixed-phase region, and a high-gradient segment within the mixed-phase region itself. The refraction of the geotherm through the phase transformation can produce temperature differences of $\pm 100\text{ K}$ across discontinuities in the transition zone. This is called the Verhoogen effect. The influence of flow on the structure of mantle phase changes has been treated from many points of view (Verhoogen, 1965; Schubert and Turcotte, 1971; Turcotte and Schubert, 1971; Schubert et al., 1975; Olson and Yuen, 1982; Christensen,

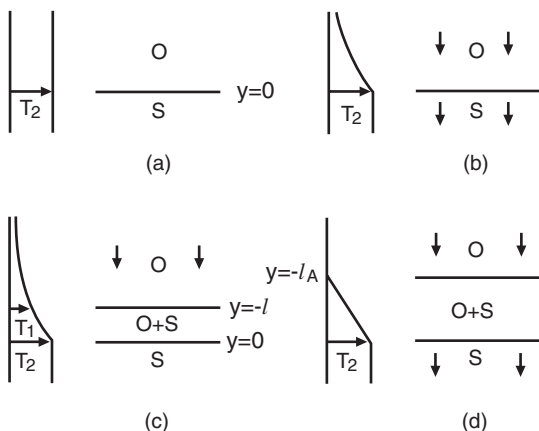


Figure 4.47. Dependence of temperature on depth and the structure of the phase change for downward flow through a univariant model of the olivine (O)-spinel (S) phase transition. (a) No flow, (b) slow flow with a phase discontinuity, (c) higher flow speed with a two-phase region, (d) isentropic flow (large flow speed). In this model olivine and spinel are representative of the light and heavy phases of any univariant phase change.

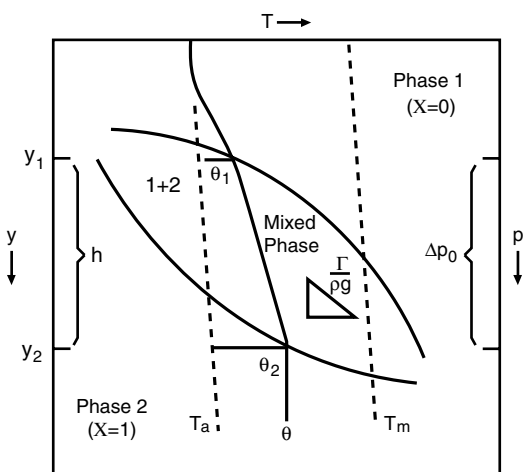


Figure 4.48. Sketch of the geometry used in the model of the thermal structure of a divariant solid-solid phase transformation in the presence of descending mantle flow. Temperature increases to the right; pressure and depth increase downward. The curve T_m is the normal upper mantle adiabat extrapolated through the phase change; T_a is an adiabat appropriate to a subducted slab in the upper mantle, extrapolated through the phase change. The curve θ is the geotherm refracted by downward flow through the phase change.

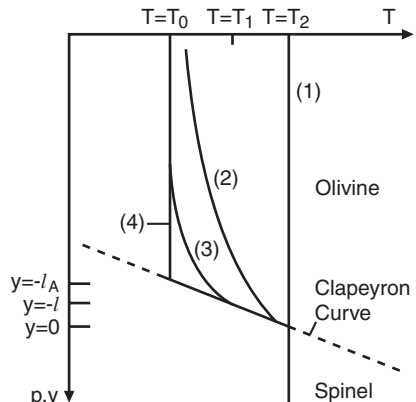


Figure 4.49. Depth profiles of temperature for downward flow through a univariant exothermic phase change typified by the olivine–spinel transformation. Curve (1) represents no flow and is a constant temperature. Curve (2) is for slow flow with a sharp phase discontinuity. Curve (3) is for a higher flow speed with a two-phase region. Curve (4) is for very fast flow and corresponds to the isentropic case.

1987). Here we first consider the effect of a uniform downward flow on a univariant phase transition. We then consider how a uniform downward flow modifies the structure of a divariant phase change. A divariant phase change is a more realistic model for either the 410 km or the 660 km seismic discontinuity.

Figure 4.47 shows how a uniform downward flow modifies the thermal structure of a univariant phase change. The analysis to follow will show that a precursor thermal boundary layer extends upstream of the phase boundary. If the velocity of the downflow is slow enough the phase change occurs at a discontinuity (as might be expected for a univariant phase change), but if the velocity is larger than a critical value a two-phase region develops. The width of the two-phase region increases with increasing downward flow speed and approaches a maximum value as flow speed becomes large.

The model of uniform downward flow through a univariant phase transition assumes a constant temperature far above and far below the phase change. The model neglects adiabatic compression. In the limit of no flow the phase boundary is at $y = 0$ (y is depth) and the temperature distribution is the isotherm labeled (1) in Figure 4.49. The transition from the light phase (referred to as olivine) to the deeper heavy phase (referred to as spinel) occurs discontinuously. In the limit of isentropic flow (large downward flow speed) (curve (4) in Figure 4.49), the temperature is $T = T_0$ upstream of the phase change and the phase change starts at the intersection of the $T = T_0$ isotherm with the Clapeyron curve at $y = -l_A$ (see also Figure 4.47d). The temperature distribution in this case continues along the Clapeyron curve until the phase transition to spinel is complete at $y = 0$ (where $T = T_2$). Between $y = -l_A$ and $y = 0$ there is a mixed-phase region in which the fraction of light phase (olivine) decreases with depth from 100% to 0% and the fraction of heavy phase (spinel) increases from 0% to 100%.

For an arbitrary downward flow velocity v , the temperature distribution is obtained from a solution of the energy equation (Chapter 6). Even in the case of a univariant phase transition, we must consider a two-phase region and write the energy equation as

$$\frac{DT}{Dt} - \frac{T \Delta s}{c_p} \frac{DX}{Dt} = \kappa \nabla^2 T \quad (4.8.1)$$

where X is the mass fraction of the dense phase (spinel), $1 - X$ is the mass fraction of the light phase (olivine), Δs is the entropy change of the phase transformation (positive for an exothermic reaction), κ is the thermal diffusivity, and c_p is the specific heat at constant

pressure. With the neglect of adiabatic compression and with the assumption that Δs is independent of temperature, thermodynamics requires that the two phases have the same specific heat so that, in practice, c_p can be regarded as the average value of the specific heats of the two phases (Turcotte and Schubert, 1972). For steady, one-dimensional downward flow, (4.8.1) becomes

$$\frac{dT}{dy} - \frac{T \Delta s}{c_p} \frac{dX}{dy} = \frac{\kappa}{v} \frac{d^2 T}{dy^2} \quad (4.8.2)$$

In single-phase regions, (4.8.2) becomes

$$\frac{dT}{dy} = \frac{\kappa}{v} \frac{d^2 T}{dy^2} \quad (4.8.3)$$

which gives, upon integration with the boundary conditions $T = T_2$ as $y \rightarrow \infty$ and $T = T_0$ as $y \rightarrow -\infty$,

$$T = T_2, \quad y > 0 \quad (4.8.4)$$

$$T = T_0 + (T_2 - T_0)e^{vy/\kappa}, \quad y < 0 \quad (4.8.5)$$

The temperature is constant on the downstream side of the phase change and there is a temperature precursor upstream of the phase change with a length scale κ/v . This temperature distribution corresponds to curve (2) in Figure 4.49 with the phase change occurring discontinuously at $y = 0$ (Figure 4.47b). The latent heat released as material moves through the phase change must be conducted upward from the phase change interface

$$k \left(\frac{dT}{dy} \right)_{y=0-} = \rho v T_2 \Delta s = k(T_2 - T_0) \frac{v}{\kappa} \quad (4.8.6)$$

or

$$T_2 - T_0 = T_2 \Delta s / c_p \quad (4.8.7)$$

From (4.8.7) it is seen that the temperature difference $T_2 - T_0$ is simply $T_2 \Delta s / c_p$ and is independent of v . From (4.8.6) the temperature gradient on the upstream side of the phase discontinuity is

$$\left(\frac{dT}{dy} \right)_{y=0-} = \frac{v T_2 \Delta s}{\kappa c_p} = \frac{v \rho T_2 \Delta s}{k} \quad (4.8.8)$$

The temperature gradient increases with v until curve (2) is tangent to the Clapeyron curve at $y = 0$ at a critical value of the downward velocity v_{crit} given by

$$\left(\frac{dT}{dy} \right)_{y=0-} = \frac{dT}{dp} \frac{dp}{dy} = \frac{1}{\Gamma} \rho g = \frac{v_{\text{crit}} \rho T_2 \Delta s}{k} \quad (4.8.9)$$

or

$$v_{\text{crit}} = \frac{k g}{\Gamma T_2 \Delta s} \quad (4.8.10)$$

As long as $v \leq v_{\text{crit}}$ the situation corresponding to curve (2) in Figure 4.49 is valid and there is no two-phase region. At low velocities, a two-phase region cannot exist because the two-phase region must lie on the Clapeyron curve, and the temperature gradient associated with the Clapeyron curve gives a heat flux that is too large to match the latent heat release at the phase change ($T_2 \Delta s$ is the latent heat release). When v exceeds v_{crit} , however, a two-phase region exists as shown in curves (3) and (4) of Figure 4.49 and in panels (c) and (d) of Figure 4.47.

The two-phase region that exists when $v > v_{\text{crit}}$ starts at $y = -l$ and ends at $y = 0$. The temperature at $y = -l$ is $T = T_1$. The temperature upstream of the two-phase region is obtained by integrating (4.8.3) with the boundary conditions $T = T_0$ as $y \rightarrow -\infty$ and $T = T_1$ at $y = -l$:

$$T = (T_1 - T_0) \exp \left\{ \frac{v}{\kappa} (y + l) \right\} + T_0, \quad y < -l \quad (4.8.11)$$

Again, there is a temperature precursor upstream of the phase change. Within the two-phase region $-l < y < 0$ the temperature must lie on the Clapeyron curve and $T = T_2$ at $y = 0$:

$$T = T_2 + \frac{\rho g}{\Gamma} y, \quad -l < y < 0 \quad (4.8.12)$$

Since (4.8.12) provides the temperature in the two-phase region, the energy equation becomes an equation for X :

$$\frac{\rho g}{\Gamma} - \frac{T \Delta s}{c_p} \frac{dX}{dy} = \frac{\rho g}{\Gamma} - \frac{\Delta s}{c_p} \left\{ T_2 + \frac{\rho g}{\Gamma} y \right\} \frac{dX}{dy} = 0 \quad (4.8.13)$$

where (4.8.13) has been obtained by substitution of (4.8.12) into (4.8.2). Integration of (4.8.13) gives

$$X = \frac{c_p}{\Delta s} \ln \left\{ \frac{\Gamma T_2}{\rho g} + y \right\} + c_1 \quad (4.8.14)$$

where c_1 is a constant of integration. The constant of integration can be evaluated by observing that there can be no discontinuity in the concentration X at the upstream phase boundary, i.e., $X = 0$ at $y = -l$. If there were a discontinuity in X at $y = -l$ then latent heat would be liberated at $y = -l$ and that heat would have to be conducted upwards. The slope of the temperature curve just above $y = -l$ would then have to exceed the slope of the Clapeyron curve (the slope of the temperature curve just below $y = -l$) and this is not possible (see Figure 4.49). Application of $X = 0$ at $y = -l$ to (4.8.14) gives

$$X = \frac{c_p}{\Delta s} \ln \frac{(\Gamma T_2 / \rho g + y)}{(\Gamma T_2 / \rho g - l)} \quad (4.8.15)$$

There is a discontinuity in concentration at $y = 0$, however, where an energy balance similar to (4.8.6) gives

$$k \left(\frac{dT}{dy} \right)_{y=0-} = \frac{k \rho g}{\Gamma} = \rho v (1 - X(y=0-)) T_2 \Delta s \quad (4.8.16)$$

or

$$X(y=0-) = 1 - \frac{kg}{v \Gamma T_2 \Delta s} \quad (4.8.17)$$

When $v = v_{\text{crit}}$, substitution of (4.8.10) into (4.8.17) gives $X(y = 0-) = 0$ and the two-phase region collapses into a discontinuity (curve (2) in Figure 4.49 applies). As $v \rightarrow \infty$, $X(y = 0-) \rightarrow 1$, the discontinuity vanishes, and the isentropic case is recovered (curve (4) in Figure 4.49 applies). Evaluation of (4.8.15) at $y = 0$ and substitution into (4.8.17) give

$$l = \frac{\Gamma T_2}{\rho g} \left[1 - \exp \left\{ \frac{-\Delta s}{c_p} \left(1 - \frac{v_{\text{crit}}}{v} \right) \right\} \right] \quad (4.8.18)$$

In the limit $v \rightarrow \infty$, $l \rightarrow l_A$ the thickness of the two-phase region in the isentropic limit and (4.8.18) gives

$$l_A = \frac{\Gamma T_2}{\rho g} \left\{ 1 - e^{-\Delta s/c_p} \right\} \quad (4.8.19)$$

The temperature T_1 can be determined by evaluating (4.8.12) at $y = -l$:

$$T_1 = T_2 - \frac{\rho g l}{\Gamma} \quad (4.8.20)$$

Substitution of (4.8.18) into (4.8.20) gives

$$T_1 = T_2 \exp \left\{ \frac{-\Delta s}{c_p} \left(1 - \frac{v_{\text{crit}}}{v} \right) \right\} \quad (4.8.21)$$

For the olivine–spinel phase transition $\Delta s/c_p \approx 0.07$ (Turcotte and Schubert, 1971) and the above formulas can be simplified by making the approximation $\Delta s/c_p \ll 1$. In this case we obtain the results

$$l \approx \frac{\Gamma T_2}{\rho g} \left\{ \frac{\Delta s}{c_p} \left(1 - \frac{v_{\text{crit}}}{v} \right) \right\} = \frac{\Gamma L_H}{\rho g c_p} \left(1 - \frac{v_{\text{crit}}}{v} \right) \quad (4.8.22)$$

$$l \approx \frac{\Gamma T_2 \Delta s}{\rho g c_p} = \frac{\Gamma L_H}{\rho g c_p} \quad (4.8.23)$$

$$T_1 \approx T_2 \left(1 - \frac{\Delta s}{c_p} \right) = T_2 - \frac{L_H}{c_p} \quad (4.8.24)$$

where we have identified $T_2 \Delta s$ as the latent heat of transformation L_H in the approximate formulas.

For the analysis of downward flow through the divariant phase change (Figure 4.48), we account for the mantle adiabat and write the energy equation in the form

$$\frac{D\theta}{Dt} - \frac{L_H}{c_p} \frac{DX}{Dt} = \kappa \nabla^2 \theta \quad (4.8.25)$$

where $\theta = T - T_a$ is the temperature departure from the normal mantle adiabat T_a , $T \Delta s$ is the latent heat L_H of the phase transformation (positive for an exothermic reaction), and c_p denotes the average value of the specific heat at constant pressure for both phases. In this discussion we regard L_H as a constant. For one-dimensional, steady-state motion, (4.8.25) is

$$\frac{d\theta}{dy} - \frac{L_H}{c_p} \frac{dX}{dy} = \frac{\kappa}{v} \frac{d^2\theta}{dy^2} \quad (4.8.26)$$

where y is depth. Outside of the mixed-phase region, X is constant and (4.8.26) reduces to the steady heat transport equation. Above the mixed-phase region, $X = 0$ and the solution to (4.8.26) consists of a precursor thermal boundary layer as in (4.8.5) and (4.8.11):

$$\theta = \theta_1 \exp\left(\frac{v(y - y_1)}{\kappa}\right) \quad (4.8.27)$$

where y_1 is the depth at the top of the mixed-phase region and θ_1 is the perturbation to the geotherm at y_1 . Below the two-phase region, the solution to (4.8.26) is just

$$\theta = \theta_2 \quad (4.8.28)$$

Within the mixed-phase region, the concentration of dense phase varies according to

$$\frac{dX}{dy} = \left(\frac{\partial X}{\partial p}\right)_T \frac{dp}{dy} + \left(\frac{\partial X}{\partial T}\right)_p \frac{dT}{dy} \quad (4.8.29)$$

In the divariant case there is a two-phase region even in the absence of flow. We approximate the coefficients using

$$\left(\frac{\partial X}{\partial p}\right)_T \simeq \frac{1}{\Delta p_0} \quad (4.8.30)$$

and

$$\left(\frac{\partial X}{\partial T}\right)_p \simeq -\frac{\Gamma}{\Delta p_0} \quad (4.8.31)$$

where Δp_0 is the pressure interval of the two-phase region at constant temperature, and

$$\Gamma = \frac{dp}{dT} \quad (4.8.32)$$

is the effective Clapeyron slope, shown in Figure 4.48. Substitution of (4.8.29)–(4.8.32) into (4.8.26) results in

$$(1 + \epsilon) \frac{d\theta}{dy} - \frac{\epsilon \rho g}{\Gamma} = \frac{\kappa}{v} \frac{d^2\theta}{dy^2} \quad (4.8.33)$$

with the dimensionless parameter

$$\epsilon = \frac{L_H \Gamma}{c_p \Delta p_0} \quad (4.8.34)$$

The temperature profile in the mixed-phase region must be continuous with both temperature and heat flux in the single-phase regions 1 and 2. These four continuity conditions determine both constants of integration in the solution to (4.8.33), as well as the thickness of the two-phase region, $h = y_2 - y_1$, and the temperature at y_1 , θ_1 . The solution to (4.8.33) in the two-phase region is

$$\theta = \theta_2 - \frac{\epsilon}{(1 + \epsilon)} \frac{\rho g}{\Gamma} \left(y_2 - y - \delta + \delta \exp\left(\frac{y - y_2}{\delta}\right) \right) \quad (4.8.35)$$

where $\delta = \kappa/(1 + \epsilon)v$. Analytical expressions for the thickness of the two-phase region can be obtained for limiting cases of fast and slow flow, corresponding to large and small values of h/δ .

For slow flow, continuity of heat flux yields

$$h = \frac{\Delta p_0}{\rho g} \quad (4.8.36)$$

and

$$\theta_1 \simeq \theta_2 \quad (4.8.37)$$

In this limit, the phase change thickness equals the static value, and practically all of the superadiabatic temperature rise occurs outside of the two-phase region, in the precursor thermal boundary layer.

For fast flow, continuity of heat flux yields

$$h = y_2 - y_1 = \frac{(1 + \epsilon)}{\epsilon} \frac{\Delta p_0}{\rho g} \quad (4.8.38)$$

and

$$\theta_1 = \frac{\kappa}{vh} \frac{L_H}{c_p} \quad (4.8.39)$$

In this limit, the phase change is thicker by the factor $\epsilon/(1 + \epsilon)$ than it is in the static case. Also, θ_1 is small, the precursor thermal boundary layer is negligible, and practically all the refraction of the geotherm occurs within the mixed-phase region.

Application of this divariant model to mantle reactions indicates that the olivine–spinel transformation is somewhat more sensitive to flow than are spinel–perovskite, garnet–perovskite or ilmenite–perovskite transformations, although there is some uncertainty in this conclusion because the critical thermodynamic parameters are poorly constrained. For the olivine– β -spinel reaction, the data in Tables 4.13 and 4.14 indicate that the geotherm is refracted by $L_H/c_p \simeq 90$ K and the dimensionless parameter $\epsilon \simeq 1$. The fast flow regime occurs where the vertical velocity exceeds 2.3 mm yr^{-1} and so is expected to occur in subduction zones. The mixed-phase region is about 8 km thick in static or slowly convecting regions and increases to a maximum thickness of 16 km in regions with large vertical velocities. The Clapeyron slope given in Table 4.14 predicts that depth anomalies in the 410 km seismic discontinuity are positively correlated with thermal anomalies, with a sensitivity of about 40 m K^{-1} . Consequently, variations in the depth of the 410 km seismic discontinuity indicate the direction of vertical flow, and variations in the thickness of the discontinuity can, in principle, determine the flow speed.

The above conclusions are based on the assumption of local thermodynamic equilibrium in the mixed-phase region. If equilibrium conditions do not prevail, for example if the phase change were metastable, then reaction kinetics would determine the phase boundary deflections as discussed in Section 4.6.3 in connection with the transformation of olivine to β spinel in the descending slab.

The same interpretation in terms of equilibrium thermodynamics can be given to variations in the 660 km seismic discontinuity, although uncertainties in physical properties are greater for this phase change. In addition, there is a very important difference between the reactions

Table 4.13. Density Change in Mantle Phase Transformations

Reaction	Depth (km)	$\Delta\rho/\rho$ (%)
α Olivine \rightarrow β spinel	410	7
β Spinel \rightarrow γ spinel	500–600	3
Orthopyroxene \rightarrow majorite	400–500	9
Ilmenite \rightarrow perovskite	660–750	5
γ spinel \rightarrow perovskite	660	10
Garnet–majorite \rightarrow ilmenite	500	5
Garnet–majorite \rightarrow ilmenite	500	5
Basalt \rightarrow eclogite	40–80	15
Spinel \rightarrow garnet peridotite	50–70	3
Peridotite \rightarrow peridotite + 10% melt	10–100	−20

Table 4.14. Clapeyron Slopes of Mantle Phase Transformations

Reaction	Depth (km)	dp/dT (MPa K $^{-1}$)
Olivine \rightarrow β spinel	410	1.6
β spinel \rightarrow γ spinel	500	4.3
γ spinel \rightarrow perovskite	660	−2.5
Peridotite solidus (dry)	0–200	10
Peridotite solidus (dry)	200–400	3
Peridotite solidus (wet)	0–200	−40
γ -spinel solidus	500–660	
Perovskite solidus	700–1,200	100
Perovskite solidus	1,200–2,900	40

near 660 km and those near 410 km. The perovskite-forming reactions are endothermic, and as discussed in Section 4.6.2, depth anomalies of the 660 km seismic discontinuity are expected to have negative correlation with lateral temperature anomalies. With the data in Tables 4.13 and 4.14, a temperature decrease of magnitude $|L_H|/c_p \simeq 70$ K for downward flow is predicted from the Verhoogen effect. The Clapeyron slope given in Table 4.14 predicts a temperature–depth sensitivity of 60 m K $^{-1}$.

As discussed in Chapter 3, the mixed-phase region for olivine compositions occupies a very narrow pressure interval, about 0.15 GPa under static conditions. The Péclet number exceeds one for this transformation where the vertical velocity exceeds 5 mm yr $^{-1}$. The transition thickness varies from about 4 km in the static limit to about 7 km where large vertical motions are present. In general, the phase transformations near 660 km are less sensitive indicators of mantle flow than the transformations near 410 km.

The main contribution from phase transformations to the driving force for mantle convection comes from depth variations of the two-phase regions. Since the olivine–spinel reaction is exothermic and the spinel–perovskite reaction is endothermic, their contributions to the total buoyancy tend to cancel. Consider the net effect on density from phase boundary deflections in the transition zone accompanying a temperature anomaly ΔT in a vertical

slab, as shown in Figure 4.40. The change in mass per unit slab area from phase boundary displacement is

$$\frac{\Delta\rho_{\alpha-\beta}\Gamma_{\alpha-\beta}\Delta T}{\rho_m g} + \frac{\Delta\rho_{\beta-\gamma}\Gamma_{\beta-\gamma}\Delta T}{\rho_m g} + \frac{\Delta\rho_{\gamma-pv}\Gamma_{\gamma-pv}\Delta T}{\rho_m g} \quad (4.8.40)$$

while the change in density due to the thermal anomaly $\Delta\rho_T$ is

$$\rho\alpha\Delta TD \quad (4.8.41)$$

where D is the slab length. The ratio of these density changes is

$$\frac{\Delta\rho_{\alpha-pv}}{\Delta\rho_T} = \frac{\Delta\rho_{\alpha-\beta}\Gamma_{\alpha-\beta} + \Delta\rho_{\beta-\gamma}\Gamma_{\beta-\gamma} + \Delta\rho_{\gamma-pv}\Gamma_{\gamma-pv}}{\rho_m^2 g \alpha D} \quad (4.8.42)$$

Terms in the numerator have opposite signs and tend to cancel. According to the data in Tables 4.13 and 4.14, the exothermic olivine \rightarrow β -spinel and β -spinel \rightarrow γ -spinel reactions dominate the endothermic γ -spinel \rightarrow perovskite reaction. The ratio in (4.8.42) is about +0.1 for a 700 km long slab. Thus, the integrated effect of transition zone phase changes may be to assist mantle convection. However, because the two major phase changes affect convection in opposite ways, it is possible that they act differentially, with the olivine–spinel reaction assisting convection in the upper mantle, while the spinel–perovskite reaction inhibits convective exchange between the upper and the lower mantle. This subject is treated more fully in Chapters 9 and 10.

Question 4.13: How do the major phase transitions between 410 and 660 km depth influence the style of mantle convection?

4.9 Temperatures in the Core and the D'' Layer

The fact that the Earth has a liquid outer core is an important constraint on temperatures in the solid mantle. At the CMB, solid mantle coexists with liquid core material. This is the simplest interpretation of the seismic structure in that region although, as discussed in Chapter 3, it is possible that conditions at the CMB are more complex. For example, it has been suggested that there might be partial melts in the mantle just above the CMB (Lay et al., 1998). Similarly there might be solidified “slag” material on the core side of the boundary. However, the evidence for either of these possibilities is not yet conclusive.

There is another constraint on temperature in the core, implied by the conditions at the inner core boundary (ICB). The character of the ICB is fully consistent with its being a solid–liquid phase transformation, implying that the temperature there equals the melting temperature of the outer core material. These two constraints, together with experimental determinations of the melting points of core and lower mantle compounds, indicate that the outer core and the lower mantle do not lie on the same adiabat. Specifically, the outer core adiabat is significantly above the adiabat which characterizes the adiabatic portion of the lower mantle, as shown in Figure 4.50.

One consequence of the difference between core and mantle adiabats is that the heat conducted from the core to the mantle across the CMB is larger than the heat conducted

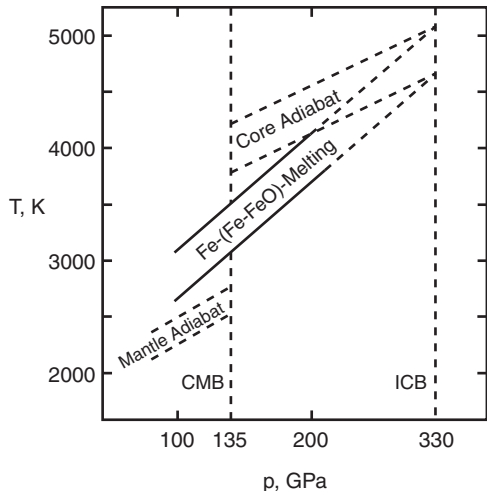


Figure 4.50. Sketch of melting and adiabatic relations in the outer core and lower mantle, adapted from Boehler (1993).

down the mantle adiabat. Heat flow from the core is an important energy source for convection in the lower mantle. It is probably responsible for much of the complexity in the structure of the D'' layer discussed in Chapter 3. In addition, core heat is thought to provide the energy for initiation of deep mantle thermal plumes, as we shall describe in Chapter 11.

Question 4.14: What is the heat flow from the core?

The total heat flow at the CMB is uncertain, but it can be constrained between maximum and minimum values using the following arguments. A reasonable upper limit comes from thermal history calculations for the whole Earth, which indicate that all but about 10 TW of the 40 TW surface heat flow can be accounted for by mantle sources (see Chapter 13). A reasonable lower limit comes from the heat transport at hot spots, on the assumption that hot spots are the surface expression of mantle plumes originating near the CMB (see Chapter 11). This gives about 4 TW for the heat flow at the CMB.

The larger figure of 10 TW corresponds to an average heat flow of 66 mW m^{-2} on the CMB, while 4 TW corresponds to an average of 26 mW m^{-2} . With $k = 12 \text{ W m}^{-1} \text{ K}^{-1}$ for the lower mantle thermal conductivity, the thermal gradient in the mantle at the CMB is 5.5 and 2.2 K km^{-1} for 10 and 4 TW, respectively. If this gradient extends over the entire thickness of the D'' layer (about 200 km), it corresponds to a temperature change of 1,100 K or 440 K for the two heat flows. The precise temperature change across D'' is uncertain because critical thermodynamic parameters, particularly thermal conductivity, are poorly constrained. Even so, the case for a thermal boundary layer of some sort in D'' is compelling (Zharkov et al., 1985; Loper and Lay, 1995; Lay et al., 1998).

Although melting relations in iron-rich compounds offer constraints on temperatures in the core–mantle boundary region, there is some ambiguity about which melting curves to use. A major difficulty in estimating core temperatures from the melting curves is that the melting temperatures of iron alloys depend on composition as well as pressure. For example, the presence of sulfur strongly depresses the melting point of iron at low pressures, while the

presence of oxygen does not. At low pressures, melting in the Fe–FeS system has a strong eutectic melting point (Usselman, 1975), whereas Fe–FeO melts consist of two immiscible liquids, one nearly pure Fe and the other nearly pure FeO (Verhoogen, 1980). High-pressure experimental evidence indicates that the immiscibility between Fe and FeO vanishes at core pressures (Ohtani and Ringwood, 1984; Knittle and Jeanloz, 1986). At higher pressures, both FeO and FeS may depress the iron melting curve, but by uncertain amounts. The effects of other possible light elements such as carbon and hydrogen are even more uncertain (Poirier, 1994a). Accordingly, the temperature at the ICB, which is presumed to be at the melting point, depends on what the light element composition of the core actually is.

Even without light elements, it is difficult to determine the melting temperature of pure iron at core pressures. Melting temperatures of iron at lower mantle pressures were measured in diamond cells by Boehler (1986) and Williams et al. (1987). These two studies arrived at widely different results, with Williams et al. (1987) finding melting temperatures near 100 GPa more than 1,000 K above those found by Boehler (1986). Subsequent improvements in experimental techniques have partially resolved this difference, in favor of the lower melting temperatures. Figure 4.51 shows the phase diagram of iron from diamond cell measurements by several investigators. Note the triple point between HCP- ε , FCC- γ , and liquid at around 100 GPa and 2,800 K. In Figure 4.51 there are implied boundaries between ε iron and the phases labeled α' and θ at high pressures. These phase changes have been inferred from weak changes in optical properties and have also been proposed on thermodynamic grounds (Matsui and Anderson, 1997).

A linear extrapolation of the melting curve in Figure 4.51 to the 330 GPa pressure of the inner core boundary leads to an iron melting temperature of about 4,850 K (Boehler, 1996). A Lindemann law extrapolation by Anderson and Duba (1997) yields a higher value, nearly

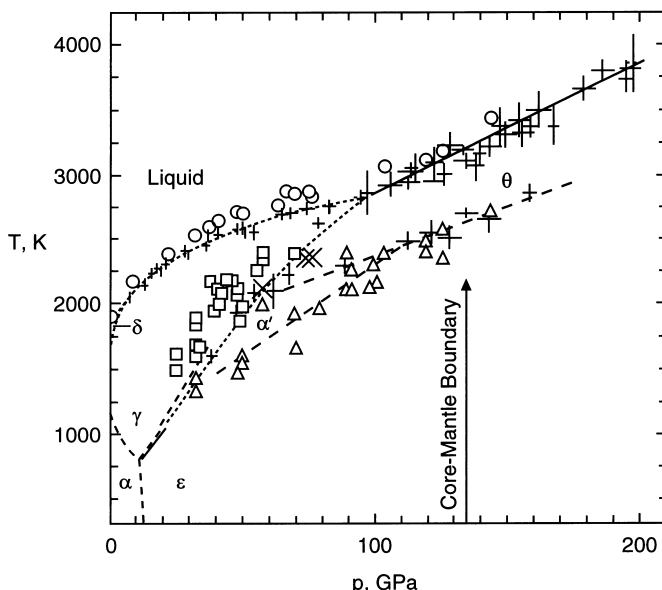


Figure 4.51. Experimental phase diagram of iron adapted from Boehler (1996). Crosses are from Boehler (1993). Open symbols (circles are melting; squares, triangles and crosses are solid–solid phase boundaries) are from Saxena et al. (1994).

6,000 K. From these temperatures it is possible to estimate the temperature at the CMB by extrapolating downward in pressure along a core adiabat. This procedure involves a number of critical assumptions, including the outer core being well mixed (adiabatic stratification), and light elements not affecting the melting of outer core material very much.

The question of how much light elements affect the core melting curve is not fully answered, as discussed above. At low pressures, it is well known that the addition of even small amounts of light elements, particularly sulfur, depresses the melting point of iron several hundred degrees because of eutectic behavior (Verhoogen, 1980). At high pressure the situation is less clear-cut. Measurements by Usselman (1975) and Urakawa et al. (1987) find substantial melting point depression to 15 GPa. However, melting point determinations of FeO and FeS to 50 GPa by Boehler (1992) and of FeO to 150 GPa by Boehler (1993) show diminished sensitivity to composition at high pressures, as indicated in Figure 4.52.

The other assumption necessary for the extrapolation is adiabatic stratification in the outer core. Then, the temperature drop through the outer core can be calculated from

$$\frac{dT}{dr} = -\frac{T}{H_T} \quad (4.9.1)$$

where $H_T = c_p/\alpha g$ is the adiabatic scale height. With $\alpha = 0.6 \text{ K}^{-1}$ and $c_p \simeq 3R$, (4.9.1) gives $\Delta T_{ad} \simeq 1,000 \text{ K}$ through the outer core; as indicated in Table 4.12, the exact value of the adiabatic temperature drop through the outer core depends on the assumed temperature at the ICB. We thus arrive at an estimated temperature of nearly 4,000 K at the CMB, with an uncertainty that is difficult to calculate but is surely $\pm 600 \text{ K}$.

As indicated in Figure 4.50, the estimated 4,000 K temperature at the CMB is well above the core melting curve at that pressure (by almost 1,000 K), but it is also far above the expected lower mantle adiabat extrapolated downward to the CMB. In order for the mantle and core temperature profiles to be continuous at the CMB, a strongly superadiabatic temperature

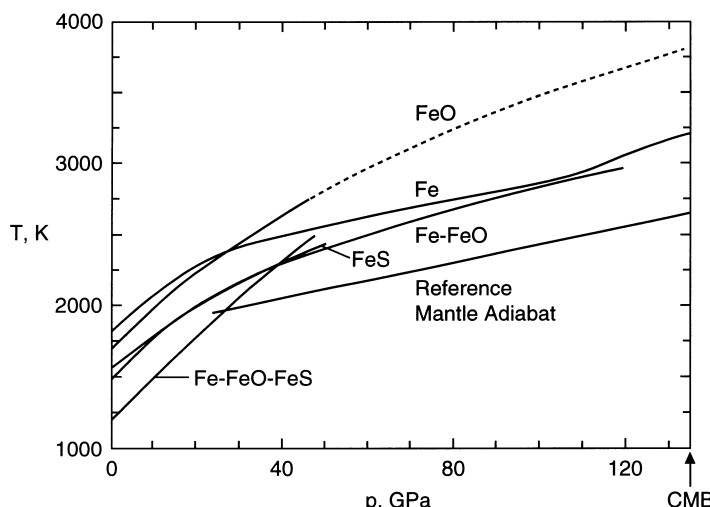


Figure 4.52. Summary of experimental melting temperatures in the system Fe–FeO–FeS from Boehler (1996), showing a tendency for high-pressure convergence.

gradient must be present in D'' (the liquid core cannot support such a large temperature drop on its side of the CMB). This is another argument in favor of a thermal boundary layer in the D'' region of the mantle. The existence of a thermal boundary layer in D'' was first proposed by Verhoogen (1973). The significance of this layer for the concept of whole-mantle convection was recognized in many early papers (Jones, 1977; Elsasser et al., 1979; Jeanloz and Richter, 1979; Stevenson, 1981; Loper, 1984a) and it continues to be the subject of much debate (Lay et al., 1998). One of the unresolved issues is the actual change in temperature across the D'' layer. Based on the heat flow constraints, the minimum value is in the 200 K range for each 100 km of D''. A superadiabatic temperature increase of this magnitude could easily be accommodated in a single thermal boundary layer just above the CMB.

According to Figure 4.50, however, the temperature change could be as large as 1,500 K. Such a large temperature increase would probably make the D'' layer strongly unstable, if it were isochemical with respect to the lower mantle. To counter the destabilizing effect of a strongly superadiabatic thermal boundary layer, the presence of some compositional heterogeneity in the D'' layer, with a stabilizing density gradient, would then be required. In Chapter 11, we examine the dynamical interaction between thermal and compositional buoyancy in the D'' layer.

Question 4.15: *What is the temperature change across the thermal boundary layer at the base of the mantle?*

4.10 Temperatures in the Transition Zone and Lower Mantle

Just as there is evidence that the lower mantle and the outer core are not on the same adiabat, there is also the possibility that the upper and lower mantle adiabats are significantly different. The presence of superadiabatic temperature increases through the transition zone is of great consequence for mantle convection. The model of whole-mantle convection predicts no large departures from isotropy in the transition zone, whereas the partially layered convection model predicts that there is one or more internal or interfacial thermal boundary layers between the upper mantle and the lower mantle. Delineation of interfacial diffusive thermal layers in the transition zone is among the outstanding problems in geothermometry.

Question 4.16: *Are there internal thermal boundary layers in the transition zone?*

At the present time about all we can say is that uncertainty in the geotherm allows for an interfacial layer somewhere beneath the 660 km seismic discontinuity. An upper bound on the possible superadiabatic temperature rise across such a layer is about 1,000 K. There could also be other smaller interfacial layers within the transition zone itself, but these would be even more difficult to detect. Figures 4.53 and 4.54 illustrate the primary constraints on the geotherm near the top of the lower mantle. If we identify the 410 and 660 km seismic discontinuities with the olivine \rightarrow β -spinel and γ -spinel \rightarrow perovskite plus magnesiowüstite reactions, then temperature at these depths is constrained to be approximately $1,750 \pm 100$ K and $1,900 \pm 150$ K, respectively (Ito and Takahashi, 1989).

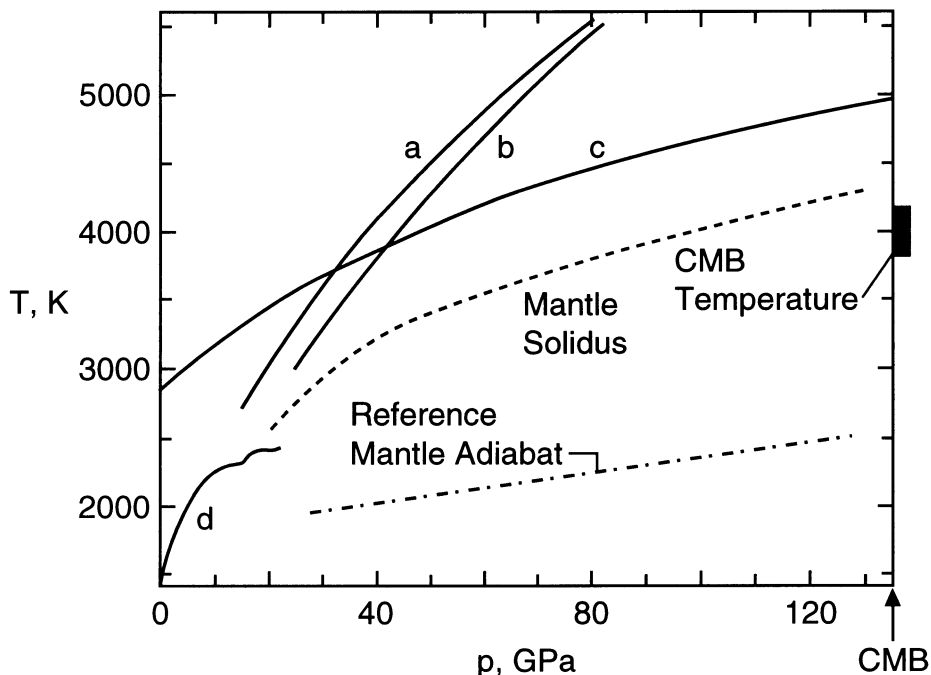


Figure 4.53. Summary of experimentally determined melting curves of transition zone lower mantle phases (solid curves) and a lower mantle solidus of pyrolite-like composition (dashed curve), adapted from Zerr et al. (1998). Solid melting curves correspond to (a) calcium perovskite, (b) magnesium perovskite, (c) magnesiowüstite, and (d) olivine–spinel. The dashed melting curve is for pyrolite and olivine compositions.

In the lower mantle, the geotherm is constrained to lie below the melting curve everywhere except perhaps at its base, just above the CMB. However, measured melting points for individual mantle phases are so high that, taken individually, they offer only weak constraints on the lower mantle temperatures. For example, melting of silicate perovskite, the most abundant phase in the lower mantle, has been measured at about 3,000 K for pressures corresponding to the region just below the transition zone (Heinz and Jeanloz, 1987). The increase in its melting temperature with pressure is quite steep (Zerr and Boehler, 1993; Shen and Lazor, 1995). Extrapolation of the silicate perovskite melting data to the pressure of the CMB would indicate a melting temperature in excess of 5,000 K there, as shown in Figure 4.53. If this were the appropriate melting curve for the lower mantle, partial melting at the base of the mantle would be extremely unlikely. The situation is essentially the same for melting of magnesiowüstite (Zerr and Boehler, 1994). As shown in Figure 4.53, its extrapolated melting point is also about 5,000 K at the CMB.

However, both shock wave (Holland and Ahrens, 1997) and diamond cell measurements (Zerr et al., 1998) indicate that assemblages with compositions similar to the upper mantle (olivine-like or pyrolite, see Chapter 3) melt at temperatures well below the melting temperatures of the individual phases. This is illustrated in Figure 4.53, which shows melting data and a solidus for a pyrolite composition derived from both diamond cell and shock wave data. The solidus temperature extrapolated to the CMB is about 4,300 K, in the range of possible temperatures for the CMB, as given in Table 4.12. Thus, it is at least possible that partial melting could occur at the CMB. This is of obvious importance if seismically

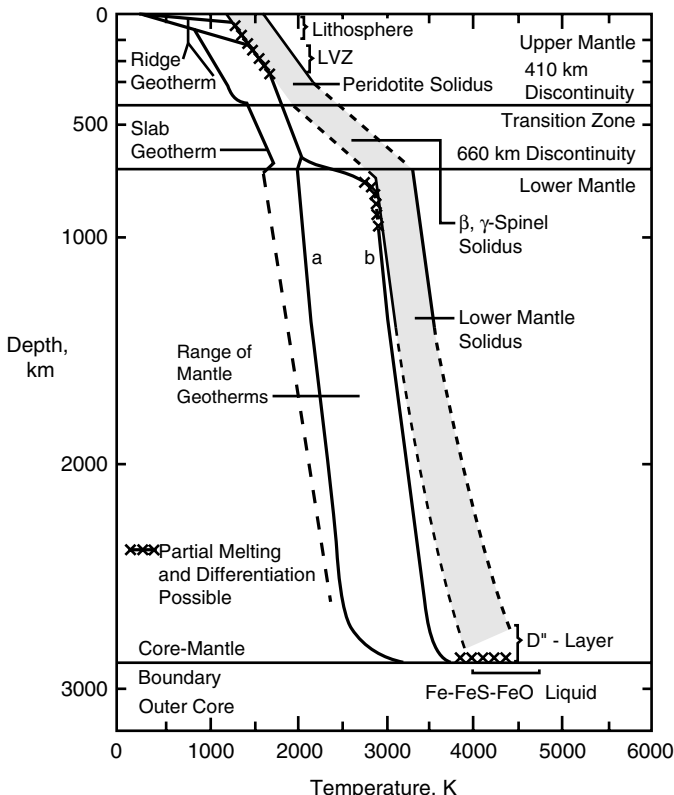


Figure 4.54. Summary of the range of mantle geotherms. Geotherms labeled a and b correspond to average whole mantle and partially layered convection, respectively. Regions where partial melting is possible are indicated.

observed ultra-low velocity zones at the CMB are to be interpreted as regions of partial melting at the base of the mantle (Garnero and Helmberger, 1995; Mori and Helmberger, 1995; Williams and Garnero, 1996; Revenaugh and Meyer, 1997; Vidale and Hedlin, 1998; Garnero et al., 1998).

In view of the uncertainties in transition zone and D'' structure and also because of the large lateral heterogeneities implied by seismic tomography, it is not possible to construct a unique geotherm for the whole mantle. For example, the adiabat near the top of the lower mantle could be anywhere from about 1,900 K to as high as 3,000 K, without violating the experimental constraints. We illustrate a range of mantle geotherms in Figure 4.54. In one end-member case (labeled a) the upper mantle and the lower mantle are on essentially the same adiabat; in another end-member case (labeled b) the lower mantle adiabat is 800 K higher than the upper mantle adiabat. The first smooth geotherm has a relatively low-temperature lower mantle and implies whole-mantle convection. The geotherm containing the interfacial boundary layer has a relatively hot lower mantle and would indicate layered or partially layered convection. Almost any geotherm lying between these two is also consistent with the data.

Table 4.12 summarizes the various contributions to the geotherm we have discussed. Much of the uncertainty in the geotherm is related to uncertainties in the composition of the mantle and core and to our incomplete knowledge of mantle and core thermodynamic parameters.

4.11 Thermodynamic Parameters

4.11.1 Thermal Expansion

The volume thermal expansion coefficient or thermal expansivity is defined by (see also Chapter 6)

$$\alpha = -\frac{1}{\rho} \left(\frac{\partial \rho}{\partial T} \right)_p \quad (4.11.1)$$

Since the magnitude of the driving force for thermal convection is linearly proportional to thermal expansivity, it is important to know the distribution of α through the mantle. We have already pointed out in Chapter 3 the significance of the thermal expansion of lower mantle phases in detecting compositional changes between upper and lower mantle.

Thermal expansion of most of the important mantle minerals has been measured at STP conditions. Some of the values are given in Table 4.11. It is difficult to predict accurately the variation of α with temperature and pressure using theoretical considerations alone. Theory does indicate the general trends, however. The thermal expansion coefficient increases approximately linearly with temperature when T/T_D is small, where T_D is the Debye temperature of the material. Above the Debye temperature, α increases with increasing temperature, although much more slowly. Since T_D is less than 1,100 K for all mantle silicates, the high temperature variation is relevant in the mantle. The change in thermal expansion coefficient with pressure was first investigated for mantle silicates by Birch (1939, 1952, 1968), who proposed that the product αK , where K is the bulk modulus, is independent of pressure. This law predicts that α should decrease by a factor of about 1/1.5 through the upper mantle, and by a factor of about 1/2 through the lower mantle, due to the increase in pressure.

Inferences drawn from geophysical data and laboratory measurements provide more definitive values of α for the upper mantle. We have already shown that the value $\alpha = 34 \times 10^{-6} \text{ K}^{-1}$ can be inferred for the oceanic lithosphere from the variation in seafloor depth, heat flow, and geoid height with crustal age on the flanks of mid-ocean ridges. Assuming α varies inversely with bulk modulus, one would predict $\alpha \simeq 20 \times 10^{-6} \text{ K}^{-1}$ at 400 km depth.

High-pressure phases often have smaller thermal expansion coefficients than low-pressure phases, and this appears to be true of mantle transition zone phases. However, it happens that the dominant lower mantle phases have anomalously large values of α .

At STP, silicate perovskite with a mantle-like composition ($\text{Mg}_{0.9}, \text{Fe}_{0.1}\text{SiO}_3$) has a thermal expansivity $\alpha_0 = 19-22 \times 10^{-6} \text{ K}^{-1}$ (Knittle et al., 1986; Parise et al., 1990). In general, thermal expansivity increases with temperature. At 800 K and standard pressure, for example, magnesiowüstite and magnesium perovskite have $\alpha = 45 \times 10^{-6} \text{ K}^{-1}$ and $\alpha = 42 \times 10^{-6} \text{ K}^{-1}$, respectively (Knittle and Jeanloz, 1986). Pressure dependence for these phases is just the opposite of temperature, and in the lower mantle this likely leads to a substantial decrease in α with depth (Chopelas and Boehler, 1989).

The variation of α through the lower mantle can be described with the use of the Anderson–Grüneisen parameter δ_T (Anderson, 1967; Birch, 1968):

$$\delta_T \equiv \left(\frac{\partial \ln \alpha}{\partial \ln \frac{1}{\rho}} \right)_T = - \left(\frac{\partial \ln \alpha}{\partial \ln \rho} \right)_T = \frac{-\rho}{\alpha} \left(\frac{\partial \alpha}{\partial \rho} \right)_T \quad (4.11.2)$$

The Anderson–Grüneisen parameter can also be written in terms of K_T , the isothermal bulk modulus (see Section 6.8), as follows. By considering $\rho = \rho(p, T)$, and using the

definitions of K_T and α , we can write the differential $d\rho$ as

$$\frac{d\rho}{K_T} dp - \rho\alpha dT \quad (4.11.3)$$

Cross-differentiation of the coefficients of dp and dT on the right of (4.11.3) yields

$$\frac{\partial}{\partial T} \left(\frac{\rho}{K_T} \right)_p = \frac{\partial}{\partial p} (-\rho\alpha)_T \quad (4.11.4)$$

which further simplifies to

$$\frac{1}{K_T^2} \left(\frac{\partial K_T}{\partial T} \right)_p = \left(\frac{\partial \alpha}{\partial p} \right)_T \quad (4.11.5)$$

The right side of (4.11.5) can be recast in the form

$$\left(\frac{\partial \alpha}{\partial p} \right)_T = \left(\frac{\partial \alpha}{\partial \rho} \right)_T \left(\frac{\partial \rho}{\partial p} \right)_T = \left(\frac{\partial \alpha}{\partial \rho} \right)_T \frac{\rho}{K_T} \quad (4.11.6)$$

Substitution of (4.11.6) into (4.11.5) yields

$$\rho \left(\frac{\partial \alpha}{\partial \rho} \right)_T = \frac{1}{K_T} \left(\frac{\partial K_T}{\partial T} \right)_p \quad (4.11.7)$$

and further substitution of (4.11.7) into (4.11.2) gives

$$\delta_T = -\frac{1}{\alpha K_T} \left(\frac{\partial K_T}{\partial T} \right)_p \quad (4.11.8)$$

Anderson et al. (1992) show that at constant temperature it is possible to approximate the dependence of δ_T on ρ by

$$\delta_T = \delta_{T_0} \left(\frac{\rho_0}{\rho} \right)^b \quad (4.11.9)$$

where δ_{T_0} is the value of δ_T at $p = 0$ when $\rho = \rho_0$ and b is a constant whose value is about 1.4. Substitution of (4.11.9) into (4.11.2) and integration along an isotherm gives

$$\frac{\alpha}{\alpha_0} = \exp \left\{ -\frac{\delta_{T_0}}{b} \left(1 - \left(\frac{\rho_0}{\rho} \right)^b \right) \right\} \quad (4.11.10)$$

where α_0 is the value of α when $\rho = \rho_0$ at the temperature for which (4.11.10) applies. It is clear from (4.11.10) that α decreases with increasing compression (increasing ρ) along an isotherm.

Although δ_T is not independent of (ρ_0/ρ) , the assumption that it has been made in the literature. Given that assumption, (4.11.2) can be integrated directly with the result

$$\frac{\alpha}{\alpha_0} = \left(\frac{\rho_0}{\rho} \right)^{\delta_T} \quad (4.11.11)$$

(Anderson, 1967; Barron, 1979; Anderson et al., 1990; Hemley and Cohen, 1992). Equation (4.11.11) also follows from (4.11.10) in the limit $b \rightarrow 0$. Equation of state measurements on silicate perovskites indicate that $\delta_T \simeq 6$ (Chopelas and Boehler, 1989; Mao et al., 1991), which, according to the approximation (4.11.11), leads to a decrease in α from $25\text{--}30 \times 10^{-6} \text{ K}^{-1}$ at 25 GPa and 2,000 K to about $10\text{--}15 \times 10^{-6} \text{ K}^{-1}$ just above the CMB (Chopelas and Boehler, 1989). As emphasized above, the parameter δ_T is not a constant but decreases somewhat with depth throughout the lower mantle (Chopelas and Boehler, 1992; Anderson et al., 1992) and (4.11.10) should be used to determine α . Nevertheless, the estimate $\alpha \approx 10 \times 10^{-6} \text{ K}^{-1}$ at the base of the lower mantle is a robust one. Wang and Reeber (1995) have obtained an estimate of about $9.4 \times 10^{-6} \text{ K}^{-1}$ for the thermal expansivity of periclase MgO, a possible lower mantle constituent, at the core-mantle boundary. The expected increase in temperature in the D'' layer may offset part of the pressure reduction, but nevertheless a substantial reduction in buoyancy is expected in the lower mantle with attendant consequences for mantle dynamics (Hansen et al., 1991, 1993).

Fei (1995) has presented a detailed compilation of thermal expansion data on many mantle-related minerals.

4.11.2 Specific Heat

Specific heats at constant pressure c_p and at constant volume c_v are defined by (see Chapter 6)

$$c_p = \left(\frac{\partial h}{\partial T} \right)_v \quad (4.11.12)$$

$$c_v = \left(\frac{\partial e}{\partial T} \right)_v \quad (4.11.13)$$

where e and h are the internal energy and enthalpy, respectively. Specific heats do not vary strongly with pressure or with temperature if the temperature is high, and for purposes of modeling mantle dynamics, they are usually represented as constants. STP values of c_p for a number of mantle minerals are given in Table 4.11. Below the Debye temperature T_D , both c_v and c_p increase with temperature, while above T_D , c_v approaches $25.1 \text{ J mol}^{-1} \text{ K}^{-1}$. Since the molecular weight of most mantle compounds is around 21, c_v is approximately $1,250 \text{ J kg}^{-1} \text{ K}^{-1}$. c_p is only a few percent larger than this. The variation in c_p with pressure is expected to be small on thermodynamic grounds, less than 10% through the pressure range of the mantle. Accordingly, we shall regard c_p as a constant in the range $1,200\text{--}1,300 \text{ J kg}^{-1} \text{ K}^{-1}$ in discussions of mantle dynamics. Heat capacities and related thermodynamic properties of minerals are tabulated and discussed by Navrotsky (1995).

4.11.3 Adiabatic Temperature Scale Height

The influence of compressibility on mantle convection depends on the magnitude of two dimensionless parameters. One of these is the Grüneisen parameter γ . We have already discussed in this chapter the variation of γ through the mantle. The second parameter is the dissipation number Di , the ratio of the depth of the convecting region D to a representative value of the adiabatic scale height H_T (see also Chapter 6):

$$Di = \frac{D}{H_T} \quad (4.11.14)$$

The adiabatic scale height varies with depth through the mantle, principally because of variations in the thermal expansion coefficient. Representative values are $H_T \simeq 4 \times 10^6$ m in the upper mantle and $H_T \simeq 6 \times 10^6$ m for the lower mantle. In a 660 km deep layer, the dissipation number is only about 0.16. Consequently, compressibility is not very important for flow confined to the upper mantle. For flow extending through the whole mantle, $Di \simeq 0.5$ and compressibility is more significant. Effects of compressibility on mantle convection are discussed in Chapter 10.

4.11.4 Thermal Conductivity and Thermal Diffusivity

Thermal conductivity is the proportionality factor in Fourier's law of heat conduction. For isotropic materials, it is defined by the relation

$$\mathbf{q} = -k\nabla T \quad (4.11.15)$$

where \mathbf{q} is the conductive heat flux vector (see Chapter 6). As indicated in Table 4.11, the thermal conductivity of upper mantle minerals is in the range $3.0\text{--}3.3 \text{ W m}^{-1} \text{ K}^{-1}$ at STP conditions. We also infer a value of $3.3 \text{ W m}^{-1} \text{ K}^{-1}$ for the oceanic lithosphere from the variation in seafloor depth, heat flow, and geoid height with crustal age. Clauser and Huenges (1995) have provided a detailed discussion of the thermal conductivity of rocks and minerals and compilations of data.

Predictions of k for the transition zone and the lower mantle based on theoretical considerations are difficult, because at high temperature and pressure the total conductivity is the sum of conductivities from several independent mechanisms. First, there is the ordinary lattice or phonon contribution, from thermal vibrations of the crystal lattice. This is the dominant contributor at low temperatures. At high temperature and pressure, two additional mechanisms are potentially important in the mantle. These are radiative conduction, which contributes if mantle minerals are slightly transparent at infrared frequencies, and thermal conduction through energy transport by excitons. The efficiency of each of these processes is highly uncertain in real mantle rocks, particularly at elevated temperature and pressure.

One traditional approach to estimating mantle conductivities is to establish correlations between thermal conductivity and other, better known mantle properties. Horai and Simmons (1970) and Schatz and Simmons (1972) demonstrated a linear correlation in minerals important in the upper mantle between seismic velocity and thermal conductivity measured at STP conditions of the form

$$k = 2.5 \times V_P - 15 \quad (4.11.16)$$

where V_P is in km s^{-1} . A similar result was also found for V_S . This law gives the canonical value of $3.3 \text{ W m}^{-1} \text{ K}^{-1}$ in the upper mantle, consistent with the conductivity inferred from the structure of the oceanic lithosphere. The same law predicts that k approaches $20 \text{ W m}^{-1} \text{ K}^{-1}$ in the lower mantle. Kieffer (1976) estimated the lattice contribution to thermal conductivity throughout the mantle by relating the pressure dependence of k to the volume dependence of the Grüneisen parameter.

In the theory of mantle convection, the thermal transport parameter which directly enters the equations of motion is the thermal diffusivity κ :

$$\kappa = \frac{k}{\rho c_p} \quad (4.11.17)$$

We have already inferred a value for κ of $0.8 \text{ mm}^2 \text{ s}^{-1}$ for the oceanic lithosphere; (4.11.17) predicts κ may increase to nearly $3 \text{ mm}^2 \text{ s}^{-1}$ in the lower mantle. Katsura (1995) has measured κ in olivine $(\text{Mg}_{0.89}\text{Fe}_{0.11})_2\text{SiO}_4$ under upper mantle conditions (to 9 GPa and 1,700 K). He finds that lattice thermal diffusivity increases with increasing pressure at the relatively small rate of 4.6% per 1 GPa, but that radiative thermal diffusivity may decrease with increasing pressure. According to the measurements of Katsura (1995), κ in the upper mantle has an almost constant value of $0.7\text{--}0.8 \text{ mm}^2 \text{ s}^{-1}$.

Empirical considerations such as the law above suggest k may increase substantially in the lower mantle. There are several lines of evidence supporting this point of view. Measurements by Osako and Ito (1991) of thermal diffusivity of MgSiO_3 -perovskite give $\kappa = 1.7 \text{ mm}^2 \text{ s}^{-1}$ at 340 K, which corresponds to a thermal conductivity $k = 5.1 \text{ W m}^{-1} \text{ K}^{-1}$. Their extrapolation predicts $k \simeq 12 \text{ W m}^{-1} \text{ K}^{-1}$ for the lattice conductivity in the temperature and pressure regime at the base of the mantle. Manga and Jeanloz (1997) have developed a model for the temperature and pressure dependence of k for MgO and find $k = 5\text{--}12 \text{ W m}^{-1} \text{ K}^{-1}$ under lower mantle conditions. According to their model k is nearly constant along an adiabat in the lower mantle.

Hofmeister (1999) has constructed a model of k for the mantle based on phonon lifetimes obtained from infrared reflectivity measurements. The $k(T, p)$ in her model depends on the geotherm $T(p)$, and a range of k values is obtained for different assumptions about the geotherm. Hofmeister (1999) finds that k decreases with depth near the surface, reaching a minimum of $2\text{--}3 \text{ W m}^{-1} \text{ K}^{-1}$ at the base of the upper thermal boundary layer. Thermal conductivity then increases with depth throughout most of the mantle except for a decrease in k that occurs in the lower thermal boundary layer at the base of the mantle (the D'' layer). Thermal conductivity in Hofmeister's (1999) model can change discontinuously at transition zone phase changes depending on the mineralogy. At the top of the D'' layer, Hofmeister's (1999) model yields values of k between about 5.8 and $6.7 \text{ W m}^{-1} \text{ K}^{-1}$. At the core–mantle boundary, her model gives a k of about $4.8 \text{ W m}^{-1} \text{ K}^{-1}$. Lattice thermal conductivity dominates radiative thermal conductivity throughout the mantle in this model, and the decrease in k with proximity to the core inside the D'' layer is due to the increase in temperature with depth across the layer.

Thermal conductivity in the D'' layer may be increased by the presence of metallic phases, a possibility discussed in Chapter 3. Manga and Jeanloz (1996) have analyzed the influence of metallic phases in D'' on transport properties. They find that the incorporation of 10–30% iron from the core would explain the reduced seismic velocities at the base of the mantle and could produce a 50% increase in thermal conductivity relative to pure perovskite, offsetting the decrease in thermal conductivity in the D'' layer predicted by the Hofmeister (1999) model. Knowledge of the thermal conductivity in the D'' layer would enable us to estimate the magnitude of the heat transfer from the core into the mantle.

5

Viscosity of the Mantle

5.1 Introduction

5.1.1 Isostasy and Flow

By the end of the nineteenth century, it was generally accepted that the Earth's solid interior behaved like a fluid on geologic time scales. The simple fact that the sea surface (geoid) and the solid surface of the Earth approximately coincide implies that the Earth's interior is nearly in hydrostatic equilibrium, a condition which can be maintained only by flow. This behavior was further confirmed by the isostatic state of mountain belts, a consequence of the low-density crustal roots beneath the mountains. Thus, the crust appears to float on a fluid mantle like blocks of wood float in water. This fluid behavior of the mantle on long time scales contrasts with the elastic behavior of the mantle on short time scales; the latter behavior is responsible for the elastic propagation of seismic waves through the mantle with relatively little attenuation. This combination of rheological behaviors may at first seem implausible, but there are many other examples in Nature, such as the ice in glaciers. Ice can transmit elastic waves on time scales of seconds, but ice is seen to flow on time scales of years.

5.1.2 Viscoelasticity

We first consider a simple model for a material that behaves as an elastic solid on short time scales and as a fluid on long time scales. For the elastic behavior we assume a linear relation between the elastic strain e_e and the stress τ :

$$e_e = \frac{\tau}{E} \quad (5.1.1)$$

where E is Young's modulus. For the fluid behavior we assume a linear Newtonian viscous relation between the fluid strain e_f and the stress τ :

$$\frac{de_f}{dt} = \frac{\tau}{2\mu} \quad (5.1.2)$$

where μ is the viscosity of the fluid. The Maxwell model for a viscoelastic material assumes that the material rate of strain de/dt is the linear superposition of the elastic rate of strain de_e/dt and the fluid rate of strain de_f/dt with the result

$$\frac{de}{dt} = \frac{de_e}{dt} + \frac{de_f}{dt} = \frac{1}{E} \frac{d\tau}{dt} + \frac{1}{2\mu} \tau \quad (5.1.3)$$

This is the fundamental rheological law relating strain rate, stress, and time rate of change of stress for a Maxwell viscoelastic material.

Consider the behavior of the viscoelastic material if a strain e_0 is suddenly applied at $t = 0$ and remains constant for $t > 0$. During the very rapid application of strain the time derivative terms in (5.1.3) dominate and the material behaves elastically. Therefore, the initial stress τ_0 at $t = 0+$ is

$$\tau_0 = Ee_0 \quad (5.1.4)$$

Subsequently, there is no change in the strain, $de/dt = 0$, and (5.1.3) reduces to

$$0 = \frac{\tau}{2\mu} + \frac{1}{E} \frac{d\tau}{dt} \quad (5.1.5)$$

This equation is integrated with the initial condition $\tau = \tau_0$ at $t = 0$ to give

$$\tau = \tau_0 \exp\left(-\frac{Et}{2\mu}\right) \quad (5.1.6)$$

The stress relaxes to $1/e$ of its original value in a time $2\mu/E$. The viscoelastic relaxation time t_{ve} is defined to be

$$t_{ve} \equiv \frac{\mu}{E} \quad (5.1.7)$$

On time scales short compared with t_{ve} the material behaves elastically, and on time scales long compared with t_{ve} the material behaves as a Newtonian viscous fluid. For the Earth's mantle it is appropriate to take $E = 70$ GPa and $\mu = 10^{21}$ Pas, and from (5.1.7) the viscoelastic relaxation time for the mantle is $t_{ve} = 450$ yr. This model provides the explanation for why seismic waves (time scales of 1–100 s) propagate elastically and why mantle convection (time scales of 1–100 Myr) occurs in a fluid-like manner.

Although the fluid behavior of the mantle is well established, this does not require that the mantle behave as a Newtonian viscous fluid as defined in (5.1.2). In general, a fluid can have any functional relationship between strain rate and stress. In fact, most fluids are well approximated by a power-law relation

$$\frac{de}{dt} = A\tau^n \quad (5.1.8)$$

where A is a rheological constant.

If $n = 1$ the fluid is Newtonian viscous and the rate of strain is linearly related to the stress. Alternative mechanisms for the fluid behavior of crystalline solids give either linear or power-law behavior with $n \approx 3$.

5.1.3 Postglacial Rebound

There are basically two approaches to the quantification of the fluid behavior of the mantle. The first involves observations of the mantle's response to loads and the second involves laboratory studies of the deformation of mantle minerals.

During glaciations large ice loads are applied to the Earth's surface. These loads deform the mantle on the same spatial scales and at the same rates as mantle convection, and can

be viewed as natural viscometric experiments, from which the viscosity of the mantle can be inferred. For example, the glacial loading of the Greenland ice sheet has depressed the land surface beneath the ice sheet well below sea level. During the last ice age large parts of North America, Europe, and Asia were covered by vast ice sheets. This ice age ended quite abruptly some 10,000 years ago and the removal of the ice load led to a transient rebound of the Earth's surface in these regions. This postglacial rebound has been quantified by studies of elevated shorelines (Figure 5.1). The inversion of postglacial rebound data to give the radial distribution of mantle viscosity has been the primary source of information on the fluid behavior of the mantle.

It should be emphasized that although it is common practice to give values of mantle viscosity, it is not established that the mantle behaves as a linear viscous medium. Following standard practice, we will generally describe the fluid behavior of the mantle in terms of its "viscosity," but it must be recognized that this may be an approximation to a more complex fluid rheology. The fluid-like behavior of the solid mantle on long time scales is often termed subsolidus flow or subsolidus creep and the viscosity of the mantle is often described as its creep viscosity.



Figure 5.1. Elevated shorelines on Östergransholm, Eastern Gotland, Sweden. Photographer and copyright holder, Arne Philip, Visby, Sweden; courtesy IGCP Project Ecostratigraphy.

It is also important to note that the strain associated with postglacial rebound is much smaller in magnitude than the strain associated with mantle convection. As a result of the large difference in strain, it is possible that postglacial rebound represents a transient creep of the mantle, while mantle convection is controlled by the long-term viscosity of the mantle. In general, viscosity associated with transient creep is smaller than steady-state creep viscosity, so the viscosity inferred from postglacial rebound may give only a lower bound for the long-term viscosity of the mantle (Karato, 1998).

5.1.4 Mantle Viscosity and the Geoid

A second source of data on the fluid behavior of the mantle comes from the gravity or geoid anomalies associated with mantle density anomalies. Mantle density anomalies contribute to the gravity field in two ways. A local mass excess or deficit affects the gravity field directly. It also forces a flow in the mantle which distorts the surface, the core–mantle boundary and any internal density interfaces due to phase changes or compositional changes. These boundary and interface distortions establish additional mass anomalies that also contribute to the gravity field. Since the induced mantle flow and boundary distortion depend on mantle viscosity, comparison of observed gravity or geoid anomalies with those inferred from mantle density anomalies constrains the viscosity of the mantle. The distribution of mass due to the subduction of oceanic lithosphere can be estimated reasonably accurately, and the associated gravity and geoid anomalies above subduction zones can be used to deduce mantle viscosity. Similarly, the distribution of mass anomalies in the mantle can be inferred from mantle seismic tomography and global variations in gravity deduced therefrom. Comparison of the inferred and observed gravity anomalies and geoid can be used to deduce the radial profile of mantle viscosity.

5.1.5 Mantle Viscosity and Earth Rotation

A third source of data on the fluid behavior of the mantle comes from measurements of the Earth's rotation. Redistribution of mass on the Earth's surface due to glaciation or deglaciation changes the Earth's moment of inertia. Since the Earth's angular momentum is conserved in this process, its angular velocity of rotation must change to compensate the change in moment of inertia (angular momentum is the product of moment of inertia and angular velocity). Redistribution of mass on the Earth's surface leads to flow and further mass redistribution in the mantle, additional changes in the Earth's moment of inertia, and further adjustments in the Earth's spin. Measurement of the Earth's rotation rate (length of day) in response to these mass redistributions in the Earth measures mantle viscosity since the mass adjustments are accomplished by flows controlled by mantle viscosity.

5.1.6 Laboratory Experiments

The strain rates typically associated with mantle convection are of the order of 10^{-15} to 10^{-14} s^{-1} . While in principle it is possible to achieve such small strain rates in the laboratory, the total strain will be extremely small. For example, even in a laboratory experiment with a length scale of 10 m and a time scale of 1 yr, the strain is just 3×10^{-7} to 3×10^{-6} m. When strains are so small it is not possible to guarantee that deformation is steady state. Steady-state creep occurs only at relatively large strains ($\geq 10^{-2}$), so laboratory experiments

interested in the measurement of steady-state creep properties must be carried out at much higher strain rates than occur in the mantle. Fortunately, mantle deformation mechanisms are thermally activated so that they have a strong exponential dependence on the inverse absolute temperature. Therefore, mantle rocks can be deformed in the laboratory at elevated temperatures and at high strain rates, but the results must be extrapolated down to mantle strain rates.

5.2 Global Isostatic Adjustment

Over the past two million years the Earth's surface has been subject to repeated cycles of glaciation and deglaciation. These cycles involve large shifts in the distribution of water and ice, on time scales of 10^4 – 10^5 yr. The solid Earth responds to the time variable loading that accompanies the shifting masses by internal deformations that change the shape of the surface. The time rate of change in the shape of the Earth is controlled by the distribution and time history of the load, and by the viscosity of the mantle.

Estimates of the viscosity of the mantle derived from loading phenomena require knowledge of the applied load, and observations of the spatial and temporal distribution of the Earth's response. In the case of glacial isostatic adjustment, the most important data are curves of relative local sea level over the past 15,000 years. These records contain information on both the change in seawater volume and the change in elevation due to deformation of the surface that accompanied the most recent melting event, which began about 18,000 years ago and ended about 6,000 years ago. In the northern hemisphere there were two major ice sheets, the Laurentide ice sheet centered over Hudson's Bay and the Fennoscandian ice sheet centered over Scandinavia (Figure 5.2). The uplift history of the Fennoscandian ice sheet was first established by Nansen (1928) using the elevations of raised beaches in the Gulf of Bothnia. (Fjridorf Nansen, polar explorer and oceanographer, is best known for his attempts to reach the North Pole, his discovery of the Ekman circulation, and his work on behalf of World War I refugees which earned him the Nobel peace prize. He was also a pioneer in glacial geomorphology.) It was immediately recognized that the time constant for uplift is proportional to mantle viscosity (Daly, 1934), and two alternative models, whose relative merits remain to this day a focus for debate, were proposed. Haskell (1935, 1937) determined the response of a uniform viscous half-space to surface loading, and applied this model to Nansen's uplift data from the center of the Fennoscandian ice sheet to obtain a mantle viscosity $\mu = 10^{21}$ Pas. This number has survived five decades and numerous later studies; it remains the canonical value for the viscosity of the mantle as a whole.

Van Bemmelen and Berlage (1935) presented an alternative approach to the rebound problem. They assumed that flow could be confined to a thin asthenospheric channel. This model implies that the viscosity varies substantially with depth through the mantle and, furthermore, is low in the region below the lithosphere, the asthenosphere. Within the interior of the loaded region this model reproduces observations as well as the half-space model. However, at the margins of the load the two models give very different rebound records and the half-space model is in much better agreement with observations (Cathles, 1980).

The problem of inferring mantle viscosity from observations of postglacial rebound has an extensive literature. Comprehensive reviews of this problem can be found in Walcott (1973), Cathles (1975), Peltier (1974, 1989), and Lambeck and Johnston (1998). Here we present the essential elements of the whole mantle and channel response models, and discuss how the predictions of each compare with the observations.

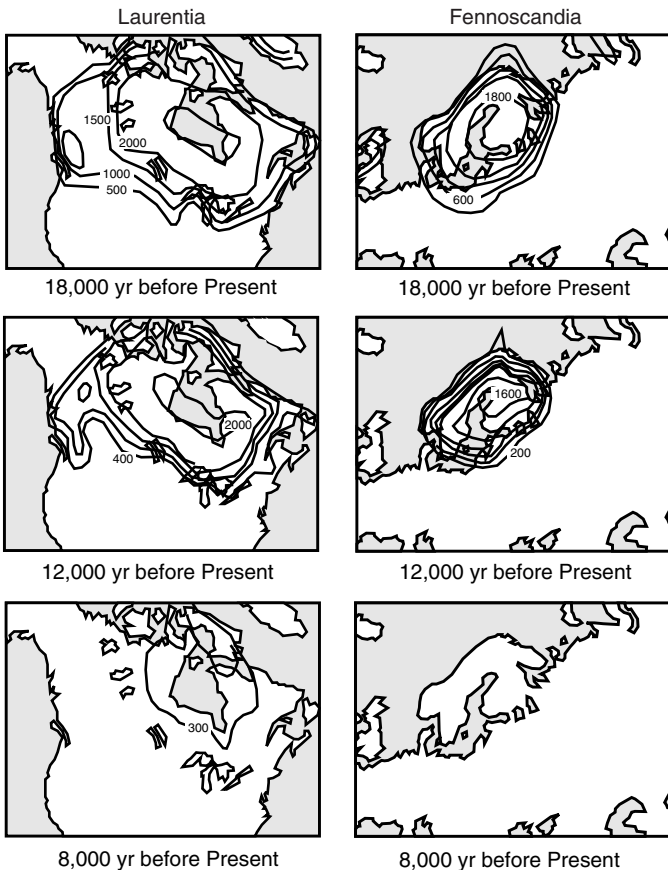


Figure 5.2. Deglaciation chronology for Laurentia (left) and Fennoscandia (right) from Wu and Peltier (1983).

5.2.1 Deformation of the Whole Mantle by a Surface Load

5.2.1.1 Half-space Model

We first consider the deformation of a mantle with a constant viscosity μ . If the horizontal scale of the glacial load is small compared with the radius of the Earth, it is appropriate to consider the flow in a semi-infinite, viscous fluid half-space ($y > 0$). The process of subsidence and rebound under the loading and unloading of an ice sheet is illustrated in Figure 5.3. In this approximate solution we assume that the load is removed instantaneously at $t = 0$ and that the initial displacement of the surface w_m is a periodic function of the horizontal coordinate x given by

$$w_m = w_{m0} \cos 2\pi x/\lambda \quad (5.2.1)$$

where λ is the wavelength and $w_m \ll \lambda$. The displacement of the surface w leads to a horizontal pressure gradient due to the hydrostatic load. When the surface is displaced upward (negative w), the pressure is positive. This corresponds to a positive load, and fluid is driven away from this region as the displacement decreases. When the surface is displaced

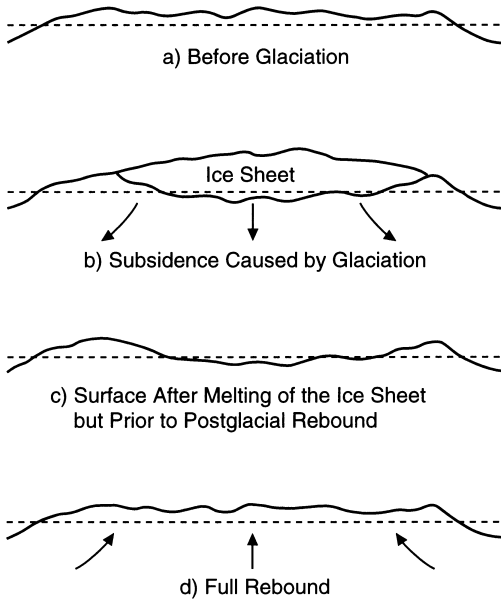


Figure 5.3. Subsidence due to glaciation and the subsequent postglacial rebound.

downward (positive w), the pressure is negative. This corresponds to the case when a load has been removed and fluid is driven into this region as the displacement decreases.

The return of the surface to an undeformed ($w = 0$) state is governed by the viscous flow in the half-space. For a very viscous, incompressible fluid, inertia can be neglected and the governing equations for a two-dimensional flow are

$$\frac{\partial u_x}{\partial x} + \frac{\partial u_y}{\partial y} = 0 \quad (5.2.2)$$

$$0 = -\frac{\partial p}{\partial x} + \mu \left(\frac{\partial^2 u_x}{\partial x^2} + \frac{\partial^2 u_x}{\partial y^2} \right) \quad (5.2.3)$$

$$0 = -\frac{\partial p}{\partial y} + \mu \left(\frac{\partial^2 u_y}{\partial x^2} + \frac{\partial^2 u_y}{\partial y^2} \right) \quad (5.2.4)$$

where p is pressure and u_x and u_y are the horizontal and vertical components of velocity, respectively. A full derivation of these equations is given in Chapter 6 (see (6.2.6) and (6.5.9)). With the introduction of the stream function (6.3.2)

$$u_x = \frac{\partial \psi}{\partial y}, \quad u_y = -\frac{\partial \psi}{\partial x} \quad (5.2.5)$$

so that (5.2.2) is automatically satisfied, the pressure can be eliminated from (5.2.3) and (5.2.4), resulting in a single equation, the biharmonic equation, for the stream function

$$0 = \frac{\partial^4 \psi}{\partial x^4} + 2 \frac{\partial^4 \psi}{\partial x^2 \partial y^2} + \frac{\partial^4 \psi}{\partial y^4} = \nabla^4 \psi \quad (5.2.6)$$

Since the initial surface displacement is of the form $\cos 2\pi x/\lambda$, it is reasonable to anticipate that ψ must also vary periodically with x in a similar fashion. However, since ψ and w are not simply related, it is a priori uncertain whether ψ varies as $\cos \pi x/\lambda$, $\sin 2\pi x/\lambda$, or some combination thereof. It turns out that ψ is directly proportional to $\sin 2\pi x/\lambda$; we assume this at the outset to simplify the discussion. However, it would only require some additional algebra to carry through the solution assuming that ψ is an arbitrary combination of $\sin 2\pi x/\lambda$ and $\cos 2\pi x/\lambda$. Thus we apply the method of separation of variables and take

$$\psi = \sin \frac{2\pi x}{\lambda} Y(y) \quad (5.2.7)$$

where $Y(y)$ is to be determined. By substituting this form of ψ into the biharmonic equation (5.2.6), we obtain

$$\frac{d^4 Y}{dy^4} - 2 \left(\frac{2\pi}{\lambda} \right)^2 \frac{d^2 Y}{dy^2} + \left(\frac{2\pi}{\lambda} \right)^4 Y = 0 \quad (5.2.8)$$

Solutions of the constant coefficient linear differential equation for Y are of the form

$$Y \propto \exp(my) \quad (5.2.9)$$

If this function is substituted for Y in (5.2.8), one finds that m is a solution of

$$m^4 - 2 \left(\frac{2\pi}{\lambda} \right)^2 m^2 + \left(\frac{2\pi}{\lambda} \right)^4 = \left(m^2 - \left(\frac{2\pi}{\lambda} \right)^2 \right)^2 = 0 \quad (5.2.10)$$

or

$$m = \pm \frac{2\pi}{\lambda} \quad (5.2.11)$$

These two values of m provide two possible solutions for Y :

$$\exp\left(\frac{2\pi y}{\lambda}\right) \quad \text{and} \quad \exp\left(-\frac{2\pi y}{\lambda}\right)$$

Since the differential equation for Y is of fourth order, the two solutions above are incomplete. Two additional solutions are required. It can be verified by direct substitution that

$$y \exp\left(\frac{2\pi y}{\lambda}\right) \quad \text{and} \quad y \exp\left(-\frac{2\pi y}{\lambda}\right)$$

also satisfy (5.2.8). The general solution for Y is the sum of these four solutions; it can be written as

$$\psi = \sin \frac{2\pi x}{\lambda} (A e^{-2\pi y/\lambda} + B y e^{-2\pi y/\lambda} + C e^{2\pi y/\lambda} + D y e^{2\pi y/\lambda}) \quad (5.2.12)$$

where the four arbitrary constants A, B, C, D are determined by the appropriate boundary conditions.

We first require the solution to be finite as $y \rightarrow \infty$ so that $C = D = 0$. The formula for the stream function simplifies to

$$\psi = \sin \frac{2\pi x}{\lambda} e^{-2\pi y/\lambda} (A + B y) \quad (5.2.13)$$

The velocity components u_x and u_y can be obtained by differentiating ψ according to (5.2.5). We find

$$u_x = \sin \frac{2\pi x}{\lambda} e^{-2\pi y/\lambda} \left\{ \frac{2\pi}{\lambda} (A + By) - B \right\} \quad (5.2.14)$$

and

$$u_y = \frac{2\pi}{\lambda} \cos \frac{2\pi x}{\lambda} e^{-2\pi y/\lambda} (A + By) \quad (5.2.15)$$

Since the part of the mantle that behaves like a fluid is overlain with a rigid lithosphere, we force the horizontal component of the velocity to be zero at $y = w$; that is, we apply the no-slip condition at the upper boundary of the fluid half-space. However, because the vertical displacement of this boundary is small, $w \ll \lambda$, it is appropriate to apply this condition at $y = 0$. By setting $u_x = 0$ at $y = 0$ in (5.2.14), we find that

$$B = \frac{2\pi A}{\lambda} \quad (5.2.16)$$

and

$$\psi = A \sin \frac{2\pi x}{\lambda} e^{-2\pi y/\lambda} \left(1 + \frac{2\pi y}{\lambda} \right) \quad (5.2.17)$$

$$u_x = A \left(\frac{2\pi}{\lambda} \right)^2 y e^{-2\pi y/\lambda} \sin \frac{2\pi x}{\lambda} \quad (5.2.18)$$

$$u_y = A \frac{2\pi}{\lambda} \cos \frac{2\pi x}{\lambda} e^{-2\pi y/\lambda} \left(1 + \frac{2\pi y}{\lambda} \right) \quad (5.2.19)$$

In order to evaluate the final constant A , it is necessary to equate the hydrostatic pressure head associated with the topography w to the normal stress at the upper boundary of the fluid half-space. The former quantity is $-\rho g w$, and the latter, from (6.15.2), is $p - 2\mu (\partial u_y / \partial y)$. Because the surface displacement is small, it is appropriate to equate these stresses at $y = 0$:

$$-\rho g w = p - 2\mu \frac{\partial u_y}{\partial y} \quad \text{at } y = 0 \quad (5.2.20)$$

To apply condition (5.2.20) we must first calculate the pressure and the displacement at $y = 0$.

The pressure can be found by inserting (5.2.18) for u_x into the horizontal force balance (5.2.3). One obtains

$$\frac{\partial p}{\partial x} = -2\mu A \left(\frac{2\pi}{\lambda} \right)^3 \sin \frac{2\pi x}{\lambda} \quad (5.2.21)$$

on $y = 0$. This can be integrated with respect to x to give

$$p = 2\mu A \left(\frac{2\pi}{\lambda} \right)^2 \cos \frac{2\pi x}{\lambda} \quad (5.2.22)$$

on $y = 0$. We also need $(\partial u_y / \partial y)$ on $y = 0$ for (5.2.20). This is easily found by differentiating (5.2.19) with respect to y and then evaluating the result on $y = 0$. We get

$$\left(\frac{\partial u_y}{\partial y} \right)_{y=0} = 0 \quad (5.2.23)$$

Condition (5.2.20) thus simplifies to

$$w_{y=0} = \frac{-2\mu A}{\rho g} \left(\frac{2\pi}{\lambda} \right)^2 \cos \frac{2\pi x}{\lambda} \quad (5.2.24)$$

The surface displacement w is related to the velocity field by the fact that the time derivative of w is just the vertical component of the surface velocity

$$\left(\frac{\partial w}{\partial t} \right)_{y=w} = u_y(y=w) \quad (5.2.25)$$

Again, since the vertical displacement of the surface is small ($w \ll \lambda$), we can write

$$\left(\frac{\partial w}{\partial t} \right)_{y=0} = u_y(y=0) \quad (5.2.26)$$

From (5.2.19) we have

$$u_y(y=0) = A \frac{2\pi}{\lambda} \cos \frac{2\pi x}{\lambda} \quad (5.2.27)$$

so that

$$\left(\frac{\partial w}{\partial t} \right)_{y=0} = A \frac{2\pi}{\lambda} \cos \frac{2\pi x}{\lambda} \quad (5.2.28)$$

By combining (5.2.24) and (5.2.28), we find that w at $y = 0$ satisfies

$$\frac{\partial w}{\partial t} = -w \frac{\lambda \rho g}{4\pi \mu} = -w \frac{\lambda g}{4\pi \nu} \quad (5.2.29)$$

This can be integrated, with the initial condition $w = w_m$ at $t = 0$, to give

$$w = w_m \exp \left(\frac{-\lambda \rho g t}{4\pi \mu} \right) = w_m \exp \left(\frac{-\lambda g t}{4\pi \nu} \right) \quad (5.2.30)$$

The surface displacement decreases exponentially with time as fluid flows from regions of elevated topography to regions of depressed topography. Equation (5.2.30) can be rewritten as

$$w = w_m e^{-t/\tau_r} \quad (5.2.31)$$

where τ_r , the characteristic time for the exponential relaxation of the initial displacement, is given by

$$\tau_r = \frac{4\pi \mu}{\rho g \lambda} = \frac{4\pi \nu}{g \lambda} \quad (5.2.32)$$

The viscosity of the mantle can be estimated from (5.2.32) once the relaxation time for postglacial rebound has been determined.

5.2.1.2 Spherical Shell Model

An analytic solution to the postglacial rebound problem is also possible for a spherical shell of incompressible, constant viscosity fluid. With the neglect of buoyancy forces, we can transform the equation of motion (see Chapter 6)

$$-\frac{\partial p}{\partial x_i} + \frac{\partial \tau_{ij}}{\partial x_j} = 0 \quad (5.2.33)$$

into a global energy balance by multiplying each term by the fluid velocity u_i and integrating over the shell. The result is

$$\begin{aligned} \int_{A_c} u_i p dA_i - \int_{A_s} u_i p dA_i + \int_{A_s} u_i \tau_{ij} dA_j \\ - \int_{A_c} u_i \tau_{ij} dA_j - \int_V \dot{e}_{ij} \tau_{ij} dV = 0 \end{aligned} \quad (5.2.34)$$

where V is the shell volume, A is the area of a bounding surface, τ_{ij} and \dot{e}_{ij} are stress and strain rate tensors, respectively, p is pressure, and the subscripts c and s refer to inner (core) and outer (surface) boundaries. For zero horizontal motion on the upper surface, as is appropriate for the lithosphere, and for an unperturbed inner surface, only the second and last terms in (5.2.34) contribute. The last term is the negative of the viscous dissipation function Φ (see Chapter 6). Further, we can write the surface vertical velocity u_r in terms of the change in surface elevation h and the pressure on the reference outer surface $r = r_s$ as

$$u_r(r_s) = \frac{\partial h}{\partial t} \quad (5.2.35)$$

and

$$p(r_s) = \rho_m g h + \sigma_s \quad (5.2.36)$$

where σ_s is the surface normal load, ρ_m is the mantle density, and g is the acceleration of gravity. Then (5.2.34) becomes

$$\int_{A_s} \left(\frac{\rho_m g}{2} \frac{\partial h^2}{\partial t} + \sigma_s \frac{\partial h}{\partial t} \right) dA = -\Phi \quad (5.2.37)$$

Here it is convenient to introduce spherical harmonic components. For each spherical harmonic of degree l , the terms in (5.2.37) are approximately

$$\int_{A_s} \frac{\rho_m g}{2} \left(\frac{\partial h^2}{\partial t} \right) dA \simeq \frac{\rho_m g r_s^2}{2} Y_l \frac{dh_l^2}{dt} \quad (5.2.38)$$

and

$$\Phi_l \simeq \mu l(l+1)(r_s - r_c) Y_l \left(\frac{dh_l}{dt} \right)^2 \quad (5.2.39)$$

where r_c is the core radius and Y_l is a spherical harmonic of degree l . Substitution of (5.2.38) and (5.2.39) into (5.2.37) yields

$$\frac{dh_l}{dt} + \frac{h_l}{\tau_l} = 0 \quad (5.2.40)$$

for the case of postglacial rebound where $\sigma_s = 0$ and

$$\tau_l \equiv \frac{\mu l(l+1)(r_s - r_c)}{\rho_m g r_s^2} \quad (5.2.41)$$

The rebound is evidently exponential for each spherical harmonic of the initial loading, with τ_l the relaxation time constant. Equation (5.2.41) is the spherical shell analogue of (5.2.32) with $l(l+1)(r_s - r_c)/r_s^2$ playing the role of $4\pi/\lambda$. Either (5.2.32) or (5.2.41) can be inverted to give mantle viscosity once τ_r or τ_l is determined from observations of postglacial rebound.

5.2.1.3 Postglacial Relaxation Time and Inferred Mantle Viscosity

Quantitative information on the rate of postglacial rebound can be obtained from elevated beach terraces (Table 5.1). Wave action over a period of time erodes a beach to sea level. If sea level drops or if the land surface is elevated, a fossil beach terrace is created. The age of a fossil beach can be obtained by radioactive dating using carbon 14 in shells and driftwood. The elevations of a series of dated beach terraces at the mouth of the Angerman River in Sweden are given in Figure 5.4. The elevations of these beach terraces are attributed to the postglacial rebound of Scandinavia since the melting of the ice sheet. The elevations have been corrected for changes in sea level. The uplift of the beach terraces is compared with the exponential time dependence given in (5.2.31). We assume that the uplift began 10,000 yr ago so that t is measured forward from that time to the present. We also assume that $w_{m0} = 300$ m with 30 m of uplift to occur in the future; that is, we take $w = 30$ m at $t = 10^4$ yr, the present. The solid line in Figure 5.4 is obtained with $t_r = 4,400$ yr. Except for the earliest times, there is quite good agreement with the data.

This value of the relaxation time can be used to obtain a viscosity for the mantle using (5.2.32). For the glaciation of Fennoscandia, a reasonable value for the wavelength is $\lambda = 3,000$ km. With $p = 3,300$ kg m $^{-3}$ and $g = 10$ m s $^{-2}$ along with $t_r = 4,400$ yr, we find that $\mu = 1.1 \times 10^{21}$ Pa s. A similar result would be obtained using (5.2.41) if spherical harmonic degree $l = 7$ is associated with the Fennoscandian ice sheet. Haskell (1935, 1936, 1937) originally obtained 10^{21} Pa s for the viscosity of the mantle using postglacial uplift data for Fennoscandia.

The above simple models are obviously only crude approximations of the actual recovery process, because they ignore the effects of mantle structure and the details of the ice loading. Nevertheless they are rather robust estimates. Since the problem is linear, solutions can be superimposed in order to consider other distributions of surface displacement. Later in this

Table 5.1. Postglacial Rebound Data

Quantity	Laurentide	Fennoscandia
Length (km)	4,000	2,250
Width (km)	2,500	1,350
Harmonic degree, l	6	8
Melting begins, 10^3 yr before the present	18	18
Melting ends, 10^3 yr before the present	6.5	8.5
Present central uplift rate, mm yr $^{-1}$	3–10	9
Relaxation time, 10^3 yr	2.6	4.4

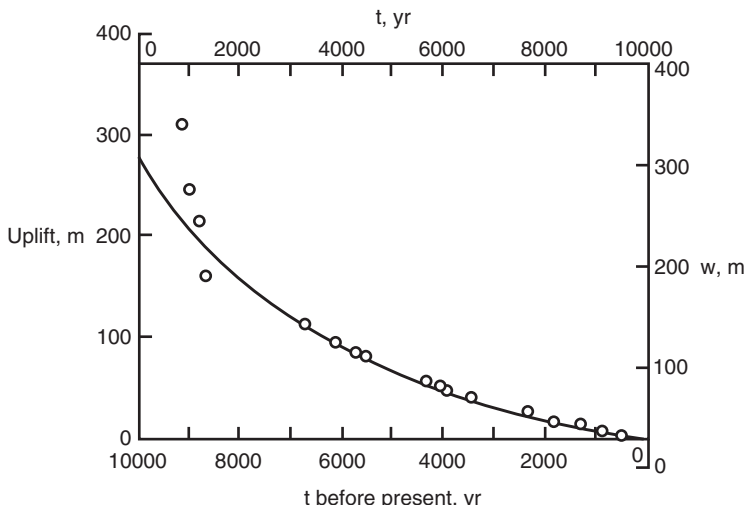


Figure 5.4. Uplift of the mouth of the Angerman River, Sweden, as a function of time before the present compared with the exponential relaxation model (5.2.31) for $w_{m0} = 300$ m less 30 m of uplift yet to occur, $\tau_r = 4,400$ yr, and an initiation of the uplift 10,000 yr ago.

section we review the modern analyses of this problem, which are based on essentially the same model, but include compressibility, elasticity, and the cyclical redistribution of load from ice to seawater and back to ice. These also yield $\mu \simeq 1-2 \times 10^{21}$ Pas for the global average mantle viscosity.

5.2.2 Ice Load Histories and Postglacial Sea Levels

The ice loads associated with glaciations have complex histories in terms of both thickness and spatial extent. Figures 5.2 and 5.5 show the pattern of the latest retreat of the margins of the Fennoscandian and Laurentian ice sheets, the two largest Pleistocene ice sheets in the northern hemisphere. It has been estimated that the Laurentian ice mass reached about 2×10^{19} kg at the height of glaciation, at about 18,000 yr ago, and the Fennoscandian ice mass reached 0.6×10^{19} kg at approximately the same time (Walcott, 1972a, b, 1973). Smaller ice sheets were present at that time along the northern margin of Eurasia. In the southern hemisphere, it is thought that the West Antarctic ice sheet was larger at that time than it is today, perhaps by as much as 0.6×10^{19} kg. The ice thickness is thought to have reached 2 km in Canada and about 1 km in Scandinavia. Instantaneous melting of all of these ice sheets would add about 130 m to the ocean depth. The change in relative sea level at a particular site after deglaciation depends on its position relative to the melting ice masses. Figure 5.6 shows some data on relative sea level versus time from coastal sites in North and South America. At locations within the sheet, there is only uplift (emergence); the sea level curve is essentially an exponential function of time since the removal of the load. At locations near the margin of the ice load, the history consists of an initial emergence, followed by submergence. At locations far removed from the load, sea level history consists of a sudden submergence, followed by a slow emergence.

The behavior at sites within the perimeter of the ice load and at sites very distant from it are easy to interpret in terms of the viscous adjustment of the mantle to ice melting. Within

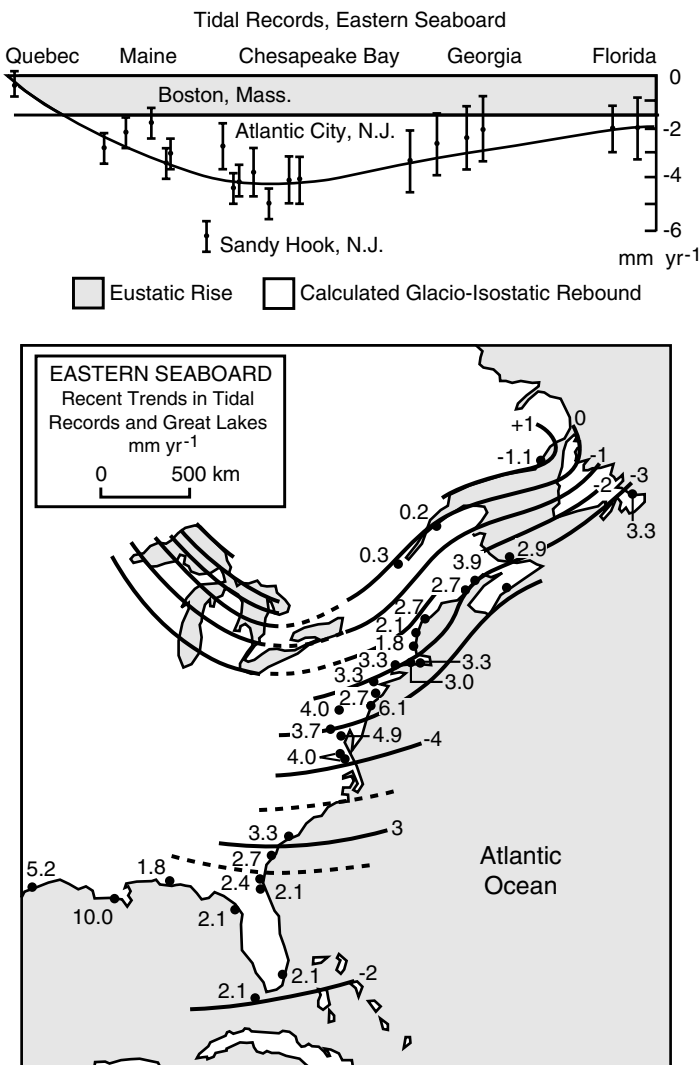


Figure 5.5. Present-day rates of submergence and emergence along the east coast of North America as inferred by Walcott (1972a). Contours are smoothed fits to data points.

the ice perimeter, removal of the surface load creates low pressure in the underlying mantle; the surface uplifts in response to converging flow in the mantle. Far from the ice loads, the increase in seawater volume first causes submergence; later, the redistribution of the load from ocean to continent results in a gradual emergence.

Sites close to the ice margin have a more complex history, which depends on both the ice load history and on radial variations in mantle viscosity. The sensitivity to mantle viscosity structure is illustrated in Figure 5.7 (Cathles, 1975). For the half-space (deep flow) model, long-wavelength anomalies relax more rapidly than short-wavelength anomalies. There is rapid uplift at the center of the low and the boundaries relax slowly. For the channel flow model, short-wavelength anomalies relax more rapidly than long-wavelength anomalies.

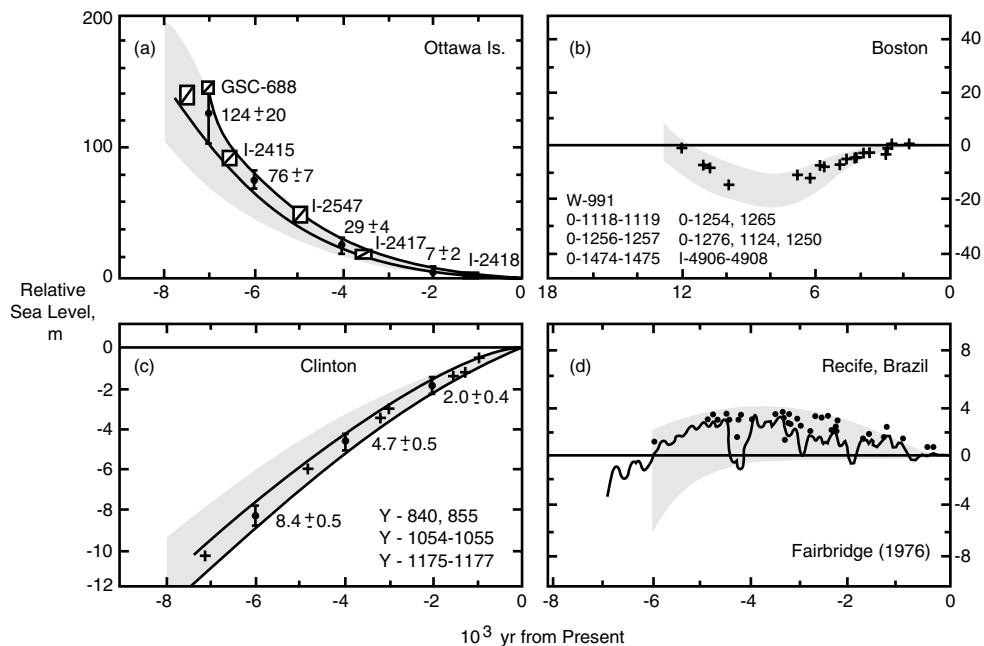


Figure 5.6. Relative sea level curves at three sites affected by the Laurentide ice mass. (a) Within the ice dome, (b) at the ice margin, (c) just beyond the ice margin, (d) far from the ice margin. From Peltier (1989).

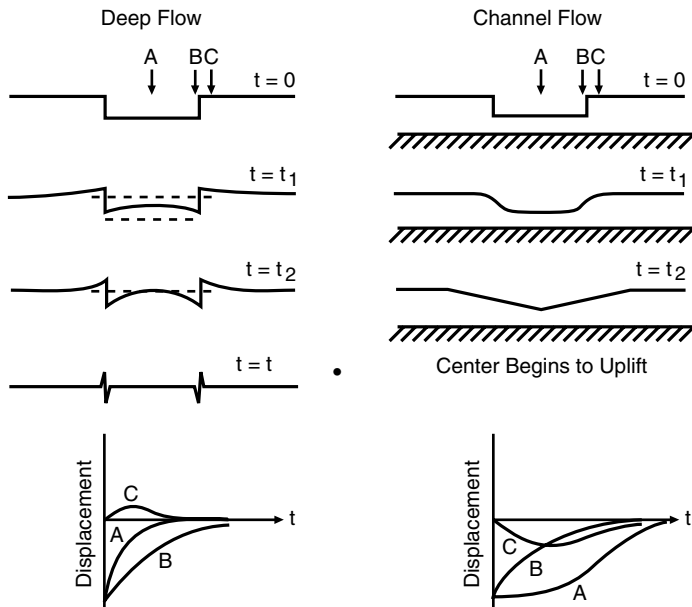


Figure 5.7. Schematic diagrams illustrating surface response to deglaciation in two models of mantle viscosity structure as a function of time from the initial melting (top) through the final recovery (bottom). Left: Response of a uniform viscous half-space (deep flow model). Right: Response of a low-viscosity asthenosphere channel above a more viscous half-space (shallow flow model). The time histories of uplift and subsidence at three locations are shown below each model. From Cathles (1975).

The margins relax rapidly and the central rebound is slow. The behavior at the margin C is quite different for the two models. For the deep flow model there is uplift, and for the channel flow model there is subsidence. Studies using a non-Newtonian viscosity give results that are similar to the channel flow models.

5.2.3 Evidence for a Low-viscosity Asthenosphere Channel

If there exists a low-viscosity channel or asthenosphere below which the viscosity is much larger, then in certain cases the isostatic adjustment to changes in the pattern of surface loads can be confined to within the channel. This leads to a rather different surface uplift pattern compared to the predictions of the isoviscous mantle model.

The classical channel model assumes that flow is confined to a horizontal channel with a thickness S which is confined between no-slip parallel boundaries, representing the lithosphere above and the more viscous mantle below. For simplicity, we allow uplift of the lithosphere but no uplift of the lower boundary. With the assumption that flow in the asthenosphere is entirely driven by horizontal pressure gradients associated with gradients in surface elevation and the applied surface load, the volume flux in the asthenosphere \underline{q} can be written as

$$\underline{q} = -\frac{\rho_m g S^3}{12\mu} \nabla_H \left(h + \frac{\sigma_s}{\rho_m g} \right) \quad (5.2.42)$$

where the subscript H refers to horizontal coordinates. Here we have taken the asthenosphere viscosity μ as constant. The conservation of mass equation (see Chapter 6) integrated across the channel is

$$\frac{\partial h}{\partial t} = -\nabla_H \cdot \underline{q} \quad (5.2.43)$$

Elimination of the volume flux from (5.2.42) and (5.2.43) results in a diffusion equation for the relative elevation

$$\frac{\partial h}{\partial t} - D \nabla_H^2 h = D \nabla_H^2 \left(\frac{\sigma_s}{\rho_m g} \right) \quad (5.2.44)$$

where

$$D = \frac{\rho_m g S^3}{12\mu} \quad (5.2.45)$$

is the viscous diffusion coefficient of the asthenosphere channel. In this model, the depression left by the melting ice diffuses with a time constant $t_D = (k^2 D)^{-1}$, where k is the wave number of the ice load.

Figure 5.7 illustrates the difference in uplift predicted for the whole mantle (deep flow) and the asthenosphere (channel flow) rebound models. In the whole mantle rebound model, the rate of uplift varies inversely with the wave number of the load for the half-space geometry or inversely with the square of the spherical harmonic degree for the spherical shell geometry; thus, the rebound occurs fastest on the largest scales. In contrast, the response of a thin channel is diffusive, with the highest wave numbers (smallest scales) decaying fastest ($t_D \propto k^{-2}$ so that $t_D \rightarrow 0$ as $k \rightarrow \infty$).

Another difference between the two models occurs near the margin of the ice load. In the thin channel model, unloading produces a noticeable peripheral trough, the result of spatially variable horizontal flow in the channel, whereas unloading in the whole mantle model results in primarily vertical flow beneath the depressed region, horizontal flow at great depth, and only a very small peripheral bulge. Despite the fact that sea level data did not show much evidence of the peripheral trough, the channel flow model was quite popular, because it predicted that 200 m of uplift remained near the center of the Fennoscandian ice load, seemingly consistent with the observed negative gravity anomalies over that region. In contrast, the whole mantle response model analyzed by Haskell (1935) predicted that only about 20 m of uplift remained for Fennoscandia. However, these figures are based on the assumption that complete isostatic equilibrium was in place at the time the ice caps began to melt. We now know that this was not the case, and consequently any estimate of the remaining uplift must take into account several cycles of glacial loading and unloading, not just the last half cycle. When several cycles are included, the amount of remaining uplift is reduced in all models, compared with the amount deduced from assuming initial isostatic equilibrium.

Despite the fact that postglacial rebound of the two major ice caps in the northern hemisphere can be explained by the response of an isoviscous mantle, there is evidence from other aspects of the postglacial adjustment phenomenon for the presence of a low-viscosity asthenosphere. One example is the rebound around Lake Bonneville, the Holocene lake of which the present Great Salt Lake is a remnant. The removal of the relatively confined Lake Bonneville load (only a few hundred kilometers in diameter) resulted in flow confined to the upper few hundred kilometers of the mantle. Uplift rates there indicate an elastic lid with a thickness of 23 ± 2 km and an asthenosphere viscosity of only about 10^{20} Pa s or less to a depth of at least 300 km (Crittenden, 1963; Cathles, 1975, 1980; Nakiboglu and Lambeck, 1983; Bills and May, 1987; Bills et al., 1994). As pointed out by Bills et al. (1994), fossil shorelines associated with Lake Bonneville were first recognized by Gilbert (1890), who correctly interpreted their elevations as due to rebound following the removal of the load supplied by the lake. Gilbert (1890) used the shoreline elevations to calculate the thickness of an elastic plate under Lake Bonneville (he obtained 50 km for the thickness) and also considered the possibility of inelastic material behavior beneath the plate, though he did not attempt a quantitative description of it.

Another indication of an asthenosphere channel comes from differential uplift detected at sites far from the ice load. Differential uplift is an edge effect, most evident along continental margins. Figure 5.8 illustrates differential uplift between two continental sites, one directly on the coast, the other some distance up a coastal inlet. Loading of the ocean by meltwater drives a flow from the suboceanic mantle to the subcontinental mantle; if this flow is confined to an asthenospheric channel, the response will not be simultaneous at the two sites, and the phase lag between the uplift at the two sites provides a measure of the channel diffusion coefficient.

The phase lag expected for a uniform asthenosphere channel can be calculated analytically from (5.2.44) for an infinitely long, straight coastline, as shown in Figure 5.8. If a layer of meltwater with thickness Δw is added to the ocean at time $t = 0$, the surface loading in (5.2.44) can be expressed as

$$\sigma_s = \rho_w g \Delta w H(x) \quad (5.2.46)$$

where ρ_w is the water density and $H(x)$ is the Heaviside step function with x denoting horizontal distance. The solution of (5.2.44) and (5.2.46) when $h = h_0$ prior to loading is

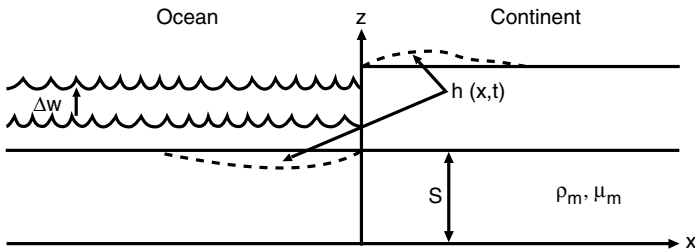


Figure 5.8. Diagram illustrating the surface response to sea level rise accompanying continental deglaciation along a continental margin far from the glaciated region.

given by

$$\Delta h = h(x, t) - h_0 = -\frac{\rho_w \Delta w}{\rho_m} \left(\frac{x}{\sqrt{\pi D t}} \exp\left(\frac{-x^2}{4 D t}\right) + \frac{1}{2} \operatorname{erfc}\left(\frac{x}{2\sqrt{D t}}\right) \right) \quad (5.2.47)$$

The first term is a transient; the second term contains the isostatic sea level changes

$$\Delta h \rightarrow \pm \frac{\rho_w \Delta w}{2 \rho_m} \quad (5.2.48)$$

for the ocean and continent, respectively. According to (5.2.47), the peripheral bulge diffuses into the continental interior at a rate

$$\frac{dx}{dt} = \sqrt{\frac{D}{t}} \quad (5.2.49)$$

Nakada and Lambeck (1989) and Lambeck and Nakada (1990) have used observations of differential uplift on the margin of Australia and beneath ocean islands to infer the existence of an asthenosphere channel with a rather low viscosity. They obtain a viscosity $\mu = 10^{20}$ Pa s for the upper mantle beneath ocean islands and $\mu = 2 \times 10^{20}$ Pa s in the upper mantle beneath continental margins far from the ice load. In either case, the inferred upper mantle viscosity is below the canonical value estimated for the whole mantle from rebound beneath and adjacent to ice loads.

There are other indications, not involving surface rebound after load removal, that asthenospheric material with viscosity 10^{20} Pa s or less exists in some locations beneath the lithosphere. One of these is the mantle upwelling that occurs at plate boundaries known as leaky transforms. Some predominantly transform boundaries such as the Dead Sea and Salton Trough–Gulf of California transforms have limited amounts of plate separation along strike. These transforms are leaky since new area forms along them. On the surface this produces prominent transform valleys or depressions that are associated with strike-slip faults and rhomb-shaped pull-apart basins. At depth the small lateral plate separation forms a vertical crack through the lithosphere. The crack must be filled by rising asthenosphere as rapidly as it opens. This places an upper limit on the viscosity of the infilling material because too viscous asthenosphere could not keep pace with geologically documented gap opening rates. Schubert and Garfunkel (1984) used a lubrication theory model of the rise of a viscous fluid into a slowly widening crack to place an upper limit on the viscosity μ of the material given by

$$\mu \leq \frac{g \rho_m H^2 t_S}{24l} \quad (5.2.50)$$

where g is the acceleration of gravity, ρ_m is the density of asthenospheric material, H is the full or present crack opening, t_S is the total time in which the opening occurred, and l is the height of material in the crack above the base of the adjacent plates (isostasy requires $l = \rho_l L / \rho_m$, where ρ_l is the density of the lithosphere and L is plate thickness). Application of (5.2.50) to the leaky sections of the Dead Sea transform ($H = 7$ km, $t_S = 5$ Myr) constrains the viscosity of the asthenosphere beneath this region to be less than about 1.5×10^{20} Pa s (Schubert and Garfunkel, 1984).

Schubert and Hey (1986) used the theory for the rise of asthenospheric material into a slowly widening lithospheric crack to estimate the viscosity of the asthenosphere beneath the propagating tip of the Galapagos rift system at 95.5°W . Rift propagation involves both extension of the rift in the axial direction and opening of the rift perpendicular to its strike. The widening crack near the rift tip must be filled by mantle material upwelling from the asthenosphere. The rift cannot extend or widen faster than mantle material can flow to occupy the crack. Accordingly, the rate of extension and widening near the rift tip is controlled by the viscosity of upwelling mantle material, and the history of rift propagation and opening can be used to constrain asthenosphere viscosity. Detailed geophysical surveys in the vicinity of the Galapagos 95.5°W propagating rift tip have established the opening history of the rift and its velocity of propagation. These data have been applied to (5.2.50) with the result that asthenospheric viscosity beneath the rift tip must be less than about $10^{17}\text{--}10^{18}$ Pa s (Schubert and Hey, 1986). Indeed, rift propagation would probably cease if the rift runs into asthenosphere much more viscous than $10^{18}\text{--}10^{19}$ Pa s. The temporal evolution of some plate boundaries requires there to be a very low viscosity asthenosphere beneath them.

Question 5.1: Is there a low-viscosity asthenosphere beneath some plates? What is the viscosity of the asthenospheric material?

5.3 Changes in the Length of Day

Sudden melting of the polar ice caps and the simultaneous rise in sea level increases the moment of inertia of the Earth by about one part in 10^{11} per meter of sea level rise (Munk and MacDonald, 1960). Over time the mantle adjusts by viscous flow due to the increased surface load from the added seawater, and the change in moment of inertia brought about by Holocene melting is gradually being reduced. Accompanying this slow reduction in moment of inertia is an increase in the Earth's spin rate, called the secular acceleration. The secular acceleration gives the time constant for isostatic adjustment to a spherical harmonic degree 2 surface load, and so provides an independent measure of mantle viscosity on the largest scale.

With isostatic adjustment included, the secular acceleration (denoted by subscript s) is related to changes in relative sea level h through

$$\frac{1}{\Omega} \left(\frac{d\Omega}{dt} \right)_s = -a \frac{dh^*}{dt} \quad (5.3.1)$$

$$\frac{dh^*}{dt} + \frac{h^*}{t_2} = \frac{dh}{dt} \quad (5.3.2)$$

where Ω is the Earth's spin rate, $a \simeq 10^{-11} \text{ m}^{-1}$ is a factor of proportionality in (5.3.1), t_2 is the spherical harmonic degree $l = 2$ relaxation time constant, and h^* is the sea level increase multiplied by a factor equal to the fractional departure from isostatic equilibrium at time t . Given the relative sea level history $h(t)$ and the secular acceleration $(d\Omega/dt)_s$, the solution to (5.3.1) and (5.3.2) can be inverted for t_2 . Dicke (1969) applied this method to estimates of the secular acceleration derived from historical eclipse data and inferred a time constant $t_2 \simeq 1,000 \text{ yr}$, consistent with a relatively low value for the average mantle viscosity in the neighborhood of 10^{21} Pa s . More recently, the secular acceleration has been inferred directly from the time rate of change of the $l = 2$ spherical harmonic coefficient of the Earth's gravitational potential, the so-called j_2 . Yoder et al. (1983) have obtained $j_2 = -0.35 \pm 0.03 \times 10^{-10} \text{ yr}^{-1}$ while Rubincam (1984) found $j_2 = -0.26 \pm 0.05 \times 10^{-10} \text{ yr}^{-1}$ from lunar laser ranging data. Devoti et al. (1997) have derived $j_2 = -0.25 \pm 0.07 \times 10^{-10} \text{ yr}^{-1}$ from satellite laser ranging to LAGEOS I and LAGEOS II for the time interval 1985–1996. j_2 is related to secular acceleration by

$$\left(\frac{d\Omega}{dt} \right)_s = -\frac{2\Omega Ma^2}{3C} j_2 \quad (5.3.3)$$

where M and a are Earth's mass and equatorial radius, and C is Earth's moment of inertia about its rotation axis (Lambeck, 1988, p. 640).

The above formulas can be generalized to include additional mantle structure, including the effects of a purely elastic lithosphere, density interfaces, and several layers of differing viscosity in the mantle. These changes result in a relaxation spectrum with several relaxation time constants. Yuen et al. (1982), Yuen and Sabadini (1984), and Sabadini and Yuen (1989) have performed numerous sensitivity analyses of layered models of mantle viscosity to determine the constraints on viscosity structure implied by the present value of j_2 . Interestingly, they find that two general classes of viscosity structure are consistent with j_2 being the result of glacial unloading at 6,000 yr before the present. One class consists of models with essentially constant viscosity, in which the lower mantle viscosity is approximately equal to the upper mantle viscosity of 10^{21} Pas , similar to the canonical value derived from sea level data from glaciated regions. The other class consists of models with lower mantle viscosities higher than this value, by a factor 10–100. Yuen and Sabadini (1984) show that the resolving power of j_2 , which was generally thought to extend through the whole mantle, is in fact limited to the region above 2,000 km depth.

More recently, Vermeersen et al. (1997) used a multilayered, incompressible, viscoelastic Earth model based on PREM to infer mantle viscosity from j_2 and true polar wander data (see below). They find that the mantle above about 1,400 km depth has an average viscosity of 10^{21} Pa s while the mantle below that depth has a somewhat larger viscosity. However, if the upper mantle and lower mantle are assigned separate viscosities, their model requires the upper mantle viscosity to be only $1.5 \times 10^{20} \text{ Pa s}$ and the lower mantle viscosity to be a factor of 25 times larger. In other words, the average mantle viscosity of 10^{21} Pa s determined by Haskell (1935) pertains not just to the upper mantle, but to the upper approximately 1,400 km of the mantle (Cathles, 1975; Mitrovica, 1996).

5.4 True Polar Wander

Redistribution of water on the Earth's surface by glaciation and deglaciation leads not only to adjustments in the Earth's spin rate, as discussed in the previous section, but also to changes



Figure 5.9. Schematic illustrating the direction of present true polar wander in relation to the Laurentide and Fennoscandia ice sheets. After Vermeersen et al. (1997).

in the orientation of the Earth's rotation axis, so-called polar wander. While Earth's angular momentum vector remains fixed in inertial space during internal mass readjustments, its rotation vector moves to accommodate changes in its inertia tensor brought about by the mass redistributions. Motion of the pole of rotation relative to the mantle (represented by the hot spot coordinate system) is referred to as true polar wander (TPW) to distinguish it from apparent polar wander, the motion of the pole relative to surface features that could result from movements of the plates. TPW is a direct result of motions in the mantle induced by shifting loads at the Earth's surface.

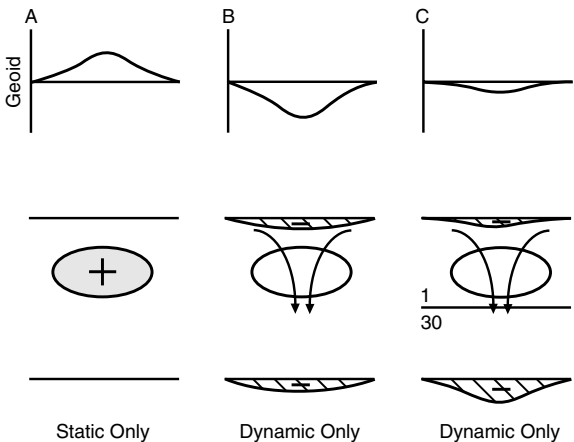
TPW can occur on a variety of time scales, from millions of years or longer to thousands of years or less. TPW on the longer time scales can result from a myriad of changes to the plates or the mantle (Ricard et al., 1992; Vermeersen and Vlaar, 1993; Vermeersen et al., 1994; Spada et al., 1996; Richards et al., 1997; Steinberger and O'Connell, 1997). On the shorter time scale, it is generally assumed that present TPW results from Pleistocene deglaciation. However, there is uncertainty as to what fraction of present TPW might be due to longer time scale mantle convection processes or even still shorter time scale processes associated with present ice sheets (James and Ivins, 1997). This, of course, contributes to the difficulty of inferring mantle viscosity from TPW data. Figure 5.9 shows that the direction of present TPW, toward the Laurentian and Fennoscandian ice sheets, is consistent with Pleistocene deglaciation as the cause of the motion.

Vermeersen et al. (1997) have used the TPW data of Dickman (1977) and McCarthy and Luzum (1996) to infer the viscosity of the mantle. The theory and Earth model are identical to those used in estimating mantle viscosity from \dot{J}_2 . TPW and \dot{J}_2 data can be used together or separately to infer mantle viscosity. The inferences about mantle viscosity reached by Vermeersen et al. (1997) (summarized in the previous section) are based on a joint application of the TPW and \dot{J}_2 data.

5.5 Response to Internal Loads

Another method for inferring mantle viscosity structure comes from the interpretation of the nonhydrostatic geoid in terms of the response of the Earth to internal density heterogeneity within the mantle. With the advent of the first global models of seismic tomography, it was

Figure 5.10. Illustration of the geoid anomaly above a positive density anomaly in the mantle. Left: Positive geoid anomaly from density anomaly in a static (undeforming) layer with zero dynamic topography. Center: Large negative geoid anomaly and dynamic topography in a uniform viscous layer. Right: Reduced negative geoid anomaly and dynamic topography due to a factor of 30 viscosity increase at mid-layer. From King (1995a).



noticed that long-wavelength geoid lows correlate with seismically fast and therefore presumably cold and heavy regions of the lower mantle, and, conversely, long-wavelength geoid highs correlate with seismically slow and light lower mantle (Dziewonski et al., 1977). This is the reverse of what would be expected in an undeformable Earth, where the geoid would exhibit a positive correlation with internal density anomalies. The resolution of this apparent paradox was given in an early paper by Pekeris (1935). The modern version of the theory has been developed and applied to mantle viscosity structure using seismic tomography by Hager and co-workers (Hager et al., 1985; Hager and Richards, 1989; Hager, 1991).

In order to calculate correctly the geoid due to mantle heterogeneity, it is necessary to consider contributions from both the internal density anomaly itself and the boundary deformations associated with flow induced by the anomaly. In the viscous mantle, stresses induced by density heterogeneity deform all compositional interfaces in the mantle, most importantly the surface (crust) and the core–mantle boundary. The net effect of internal sources and boundary deformation on the geoid is shown schematically in Figure 5.10 from King (1995). Whereas the geoid is positive over a dense anomaly in a hypothetically rigid mantle, it is strongly negative over a mantle with uniform viscosity, because the large negative surface topography induced over the load dominates the geoid signal. In fact, this situation results in too large a negatively correlated geoid. The simplest way to preserve the negative correlation between density anomalies and geoid and at the same time correctly model the observed geoid amplitude is to invoke a high-viscosity lower mantle, so that the boundary deformation is concentrated at the core–mantle boundary, rather than at the surface. This conclusion was reached by Hager (1984), Richards and Hager (1984), Ricard and Vigny (1989), and Thoraval and Richards (1997) who inferred a factor of 30 increase in viscosity from the upper mantle to the lower mantle. Subsequent studies using basically the same techniques have generally supported this conclusion (Ricard et al., 1989). For example, Figure 5.11 compares the observed low degree geoid and the geoid calculated for a two-layer model of the mantle using seismic heterogeneity. The two are in close agreement.

The geoid anomaly δV_l^m from internal loads is calculated at each spherical harmonic degree l and order m according to

$$\delta V_l^m = \frac{4\pi G r_e}{(2l+1)} \int_{r_c}^{r_e} K(r, \mu) \delta\rho(r)_l^m dr \quad (5.5.1)$$

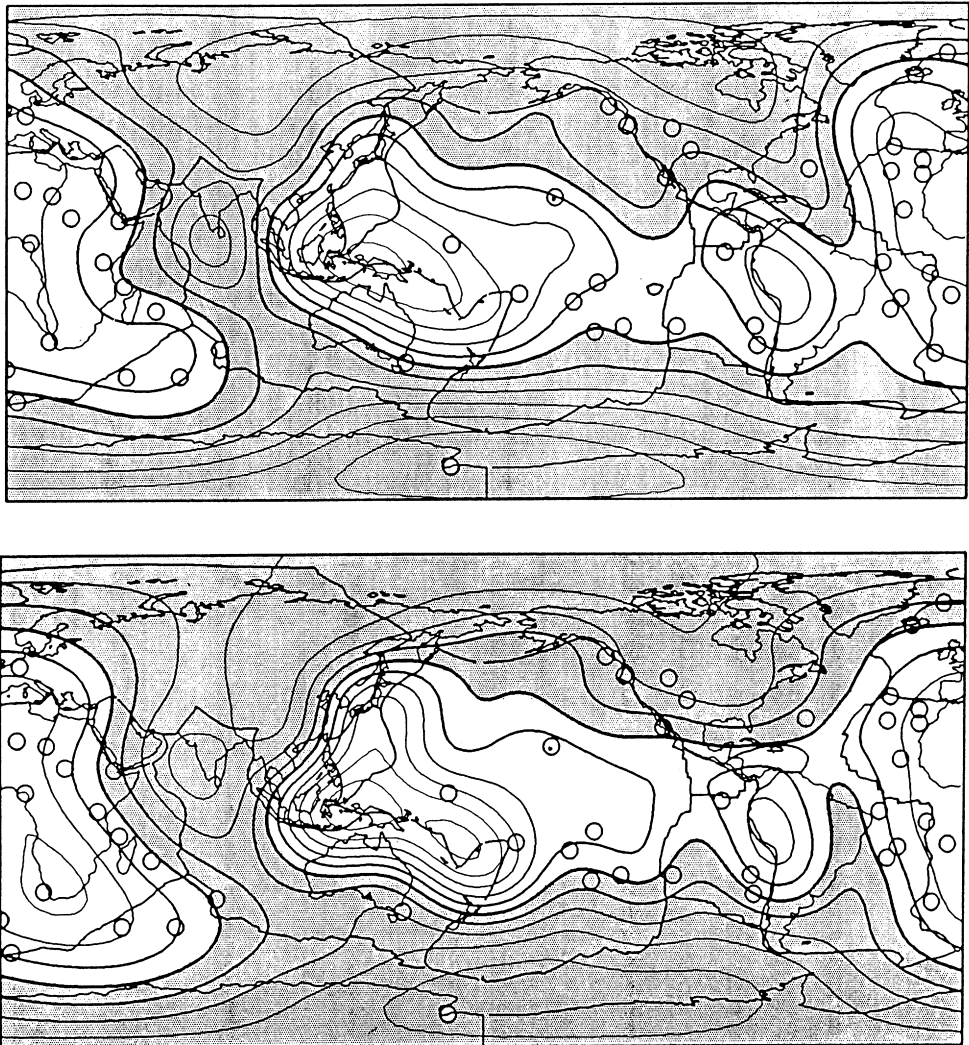


Figure 5.11. Comparison of nonhydrostatic geoid (top) and geoid computed from lower mantle seismic heterogeneity and dynamic topography in a two-layer mantle model with a factor 30 increase in viscosity at 660 km depth (bottom). Shaded regions are negative; unshaded regions are positive relative to the hydrostatic geoid. From Hager and Richards (1989).

where G is the gravitational constant, r_e is the Earth's radius, r_c is the radius of the Earth's core, $\delta\rho(r)_l^m$ is the density anomaly at each spherical harmonic degree and order, and K is the geoid response kernel, calculated from the deformation produced by viscous flow due to a surface density distribution at radius r , including the boundary deformation contributions. To use this method, it is necessary to convert seismic heterogeneity to density heterogeneity. The standard approach is to assume a linear relationship of the form

$$\delta\rho(r)_l^m = \frac{\delta\rho}{\delta v} \delta v_l^m \quad (5.5.2)$$

where v is seismic velocity. The ratio $\delta\rho/\delta v$ can be estimated as part of the modeling procedure, or it can be derived from mineral physics data. Typically, these two approaches yield different values for the ratio. A rationalization of this difference is an important geophysical objective, since it would remove a source of uncertainty in viscosity profile estimation as well as provide an additional constraint on the mineralogy of the lower mantle.

Question 5.2: *What is the relationship between density anomalies and seismic velocity anomalies in the mantle?*

There are two additional important points concerning the application of this technique for mantle viscosity estimation. First, it yields information only on viscosity variations through the mantle, not on absolute values of viscosity. Second, successful models that include a highly viscous lower mantle also predict significant dynamic topography at the surface, of the order of 2 km variations (Richards and Hager, 1984; Ricard et al., 1989). No such dynamical topography has been unequivocally identified despite several attempts. Lack of observable dynamical topography at long wavelengths is a critical problem, since the physical basis of the model is a direct cause-and-effect relationship between surface topography and geoid anomalies.

Question 5.3: *What is the dynamical topography associated with mantle convection?*

Aspects of the above approach can be simply illustrated for an internal mass load in a two-dimensional half-space. As in Section 5.2.1.1 we take y as the depth coordinate with $y = 0$ at the surface. The horizontal coordinate is x and we assume an internal mass load of the form $\sigma_d \cos kx$ at depth $y = d$, where σ_d is mass per unit area and $k = 2\pi/\lambda$ is the horizontal wave number of the load. The internal load causes flow in the half-space and topography at the surface, i.e., boundary deformation. The geoid anomaly arises from both the internal mass load and the boundary deformation. Aside from the mass load at $y = d$, the half-space has uniform density ρ and uniform viscosity.

Quantities of interest, such as surface deformation, can be determined by solving for the flow using the methods of Section 5.2.1.1. For this problem, the solution is algebraically complex and will not be carried out in detail here. For example, the flow field must be determined in the regions $0 < y < d$ and $y > d$. The stream function in the region $0 < y < d$ is of the form (5.2.12) and involves four constants. The stream function in the region $y > d$ is of the form (5.2.13) and involves two additional constants. There are a total of six constants to be determined by applying appropriate boundary conditions at the surface and matching conditions at $y = d$. Richards and Hager (1984) have determined the surface deformation to be

$$w = \frac{\sigma_d}{\rho} \cos kx (1 + kd) e^{-kd} (1 - e^{-t/\tau_r}) \quad (5.5.3)$$

where τ_r is the relaxation time given in (5.2.32). Initially, the surface is undeformed. At long times, $t \gg \tau_r$, there is steady-state surface deformation given by

$$w(t \rightarrow \infty) = \frac{\sigma_d}{\rho} \cos kx (1 + kd) e^{-kd} \quad (5.5.4)$$

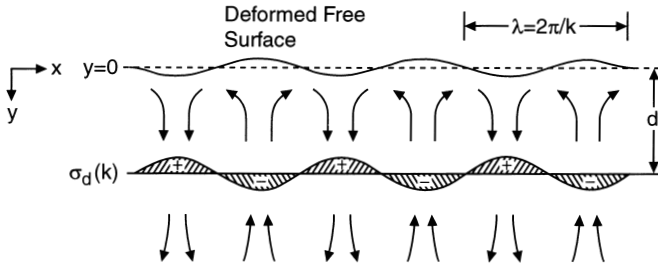


Figure 5.12. Sketch of the flow and surface deformation in a viscous half-space due to an internal load with areal mass density $\sigma_d \cos kx$ at depth $y = d$. Where the internal mass load is positive, the surface is deflected downward, creating a negative mass anomaly at the surface. Modified from Hager and Richards (1989).

The time scale for approach to the steady-state surface deformation is the viscous relaxation time τ_r of the half-space. Where the internal mass load is positive ($\sigma_d \cos kx > 0$), w is positive and the surface is deflected downward as seen in Figure 5.12. The “hole” at the surface represents a negative mass anomaly that lies directly above the positive mass anomaly of the internal load at $y = d$. Surface deflection is directly proportional to the internal loading and decreases in amplitude as the depth of the loading increases.

The geoid anomalies due to the mass anomalies at the surface and at $y = d$ can be obtained from the equation for the gravity anomaly δg_y due to a sheet mass of areal density $\sigma_0 \cos kx$ at $y = 0$:

$$\delta g_y = 2\pi G \sigma_0 \cos kx e^{ky} \quad (5.5.5)$$

where G is the gravitational constant (Turcotte and Schubert, 1982, p. 220). The gravity anomaly decays exponentially with vertical distance ($-y$) above the mass sheet. The length scale for the decay is k^{-1} . The gravity anomaly is related to the geoid anomaly δV by

$$\delta g_y = -\frac{\partial}{\partial y} \delta V \quad (5.5.6)$$

Integration of (5.5.6) after substitution of (5.5.5) gives

$$\delta V = \frac{-2\pi G \sigma_0}{k} \cos kx e^{ky} \quad (5.5.7)$$

The geoid anomaly at the surface due to the surface loading given by (5.5.4) is, according to (5.5.7),

$$\delta V_{\text{load}}(\text{surface}, y=0) = \frac{2\pi G \sigma_d}{k} \cos kx (1 + kd) e^{-kd} \quad (5.5.8)$$

(the areal mass density at $y = 0$ due to surface deformation is $-\rho w$ ($t \rightarrow \infty$)). The geoid anomaly at the surface ($y = 0$) due to the internal mass load at $y = d$ is, from (5.5.7),

$$\delta V_{\text{internal}}(\text{load}, y=0) = \frac{-2\pi G \sigma_d}{k} \cos kx e^{-kd} \quad (5.5.9)$$

(a shift in coordinates is required in using (5.5.7)). The total geoid anomaly is the sum of (5.5.8) and (5.5.9):

$$\delta V = \frac{2\pi G}{k} (kd) \sigma_d \cos kx e^{-kd} \quad (5.5.10)$$

The net contribution to the geoid anomaly comes from the negative mass anomaly at the surface induced by the internal load. The negative mass anomaly at the surface more than cancels the positive mass load at depth in contributing to the geoid anomaly. The geoid anomaly approaches zero as the load approaches the surface ($d \rightarrow 0$). The viscosity of the half-space has no effect on the geoid anomaly, which is basically why the technique discussed above for mantle viscosity determination measures only viscosity variations with depth. The viscosity in this problem determines only the relaxation time scale on which the internal load establishes the long-term surface deflection.

5.6 Incorporation of Surface Plate Motion

The two-layer viscosity structure obtained from applications of seismic tomography to the nonhydrostatic geoid is at variance with most published models of viscosity structure derived from postglacial rebound. The former approach yields a relatively high viscosity lower mantle separated at 660–1,200 km depth from a relatively low viscosity upper mantle, while the latter procedure gives a more uniform viscosity structure (see Table 5.2). In principle, additional constraints on mantle viscosity come from a consideration of horizontal forces, in particular the tractions on the base of the lithosphere that govern plate motions. It is theoretically possible to deduce the absolute viscosity of the mantle by modeling plate motions, since the velocities of plates are a result of the balance between density heterogeneity driving forces and viscous stresses resisting motion.

Several different procedures have been used to incorporate plate motion, but the basic principle behind all of them is the linear superposition of results from two viscous flow calculations, one with a rigid upper boundary condition that uses the observed distribution of subducted slabs and mantle seismic heterogeneity as the driving density heterogeneity, and another flow driven solely by the observed plate motions. By adjustment of the radial viscosity structure, solutions can be found that yield, to some approximation, zero net torque on each lithospheric plate. Ricard and Vigny (1989) and Forte et al. (1991) have explored this method and find that the coupling between plate motions and lower mantle heterogeneity is rather weak; plates are primarily driven by slabs and resisted by upper mantle viscous forces, whereas the long-wavelength geoid is mostly sensitive to lower mantle density heterogeneity and viscosity. In addition, there is a large uncertainty in the upper mantle viscosity derived from modeling plate motions, stemming from the

Table 5.2. Two-layer Mantle Viscosity Models

Data	Lithosphere Thickness (km)	Upper Mantle Viscosity (Pas)	Lower Mantle Viscosity (Pas)
Postglacial rebound ¹	120	1×10^{21}	4.5×10^{21}
Geoid ²	100	2×10^{19}	6×10^{21}
Geoid and plate velocities ³	100	2.6×10^{20}	1.3×10^{22}
Continental margins ⁴	75	2×10^{20}	7.5×10^{21}
Ocean Islands ⁵	50	1×10^{20}	1×10^{22}

¹Mitrovica and Peltier (1991), ²Hager and Richards (1989), ³Ricard and Vigny (1989),

⁴Lambeck and Nakada (1990), ⁵Nakada and Lambeck (1989).

numerous simplifying assumptions that are invoked in order to simulate plates with a viscous fluid model. These include neglect of edge forces such as fault resistance and neglect of lateral variations in viscosity, which are especially significant near plate margins. Nevertheless, consideration of plate motions seems to constrain the upper mantle viscosity to a value near 10^{20} Pas, in reasonable agreement with the results of postglacial rebound studies.

5.7 Application of Inverse Methods

Most studies of mantle viscosity yield viscosity structures that agree within about an order of magnitude. The principal disagreement concerns the difference in viscosity between the upper mantle and the lower mantle. A number of these studies are summarized in Table 5.2. Arguments favoring a near-uniform viscosity mantle based on deglaciation studies have been given by Tushingham and Peltier (1992), who suggest $\mu = 10^{21}$ Pas in the upper mantle and $\mu = 2 \times 10^{21}$ Pas in the lower mantle. Arguments favoring an order of magnitude difference in viscosity between the upper mantle and the lower mantle, also based on glaciation studies, have been given by Lambeck et al. (1990), who suggest $\mu = 3\text{--}5 \times 10^{20}$ Pas in the upper mantle and $\mu = 2\text{--}7 \times 10^{21}$ Pas in the lower mantle. Again, based on glaciation studies, it is concluded that the viscosity of the mantle falls in the range $0.65\text{--}1.10 \times 10^{21}$ Pas from the base of the lithosphere to a depth of 1,400 km; Mitrovica and Peltier (1995) argue that the lower mantle viscosity is in the range $0.5\text{--}3 \times 10^{21}$ Pas, and Peltier and Jiang (1996) suggest that the deepest part of the mantle has a factor of 10 higher viscosity than the upper part of the lower mantle. Peltier (1996a) and Lambeck and Johnston (1998) have reviewed many of these results.

Motivated by the disparities among mantle viscosity models, a number of authors have attempted to use the formalism of inverse theory to establish some reliable bounds on the class of acceptable viscosity structures. King (1995a) has organized the main results of inversions that rely primarily on data from plate motions, postglacial rebound, and the geoid. These are summarized in Figures 5.13–5.15.

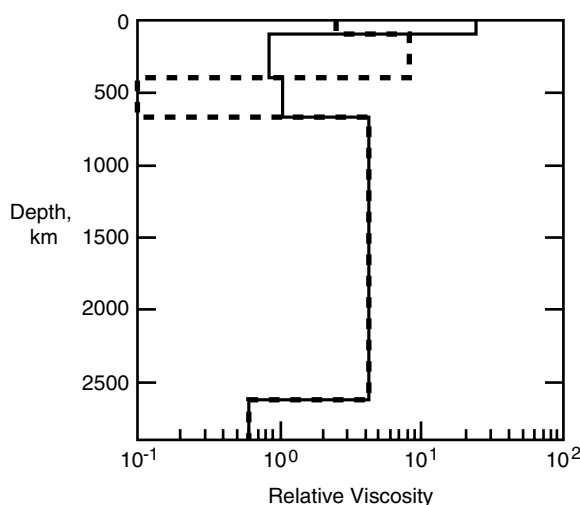


Figure 5.13. Suite of five-layer mantle viscosity profiles obtained by Forte et al. (1991) using mantle heterogeneity from seismic tomography and plate velocities. The preferred model is shown by the dashed line. The viscosity scale factor is 10^{21} Pas.

Figure 5.13 shows viscosity profiles obtained by Forte et al. (1991) from plate motion data, using the method of Bayesian inference. The profiles are based on a five-layer parameterization, and the heavy dashed line represents the preferred model. Note the presence of a low-viscosity channel at transition zone depths, as well as low-viscosity in the D'' layer. Figure 5.14 shows the result of a three-layer parameterized model obtained by Ricard et al. (1989) using Monte Carlo inversion of geoid and plate velocity data. This inversion produced two distinct classes of acceptable solutions, one with a low-viscosity transition zone, the other with high viscosity in the transition zone and relatively low-viscosity in the lower mantle. Finally, Figure 5.15 shows the results of an inversion by King and Masters (1992) using mantle S-wave velocity structure, the geoid, and an 11-layer parameterization. The examples of acceptable models are rather similar in this study, and all exhibit a low-viscosity transition zone and viscosity increases in the depth range 660–1,200 km.

Figure 5.14. Suite of three-layer mantle viscosity profiles obtained by Ricard et al. (1989) using mantle heterogeneity from seismic tomography, plate velocities, and the geoid in a Monte Carlo inversion. The preferred model is shown by the heavy dashed line. The viscosity scale factor is 10^{21} Pa s.

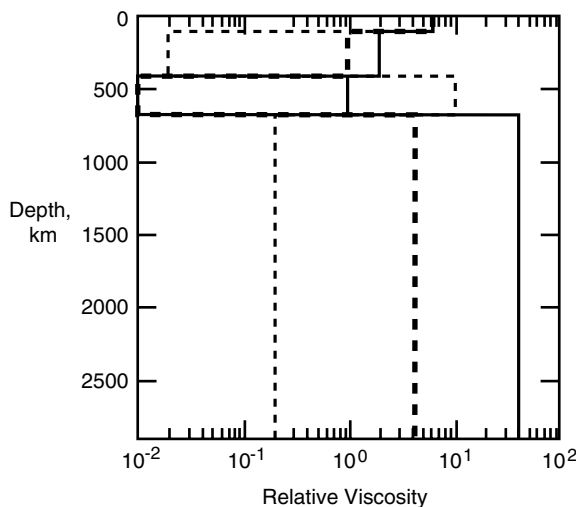
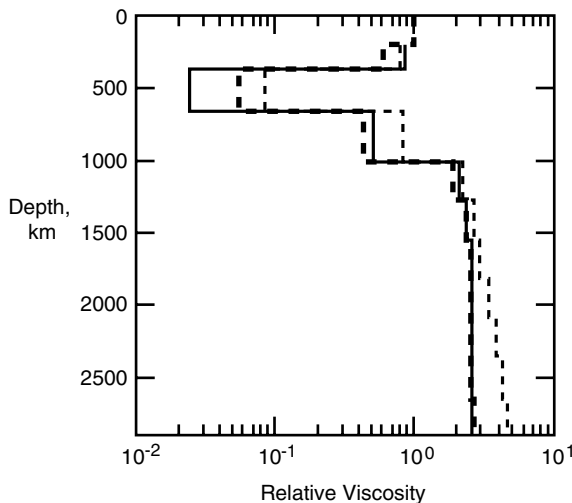


Figure 5.15. Suite of 11-layer mantle viscosity profiles obtained by King and Masters (1992) using mantle heterogeneity from S-wave tomography and the geoid. The preferred model is shown by the heavy dashed line. The viscosity scale factor is 10^{21} Pa s.



5.8 Summary of Radial Viscosity Structure

The differences among the various viscosity models in Table 5.2 and in Figures 5.13–5.15 reflect inconsistencies among the methods of inferring viscosity, lack of resolving power in the data and, in addition, the possibility of large lateral viscosity variations in the mantle. Even with these complications, it is possible to draw some general conclusions. First, the upper mantle is less viscous than the lower mantle, on average. The difference in average viscosity may only be a factor of 3, or alternatively it may be as much as 30. In either case the difference is substantial for mantle convection processes. The region where this increase occurs is at least as deep as the 660 km discontinuity and may be as deep as 1,200 km. The average viscosity of the upper mantle (beneath the lithosphere) is less than the canonical value of $\mu = 10^{21}$ Pa s, and the average viscosity for the lower mantle is higher than this value. In some regions there is unambiguous evidence for a low-viscosity asthenosphere, especially beneath the oceanic lithosphere, with viscosities in the range 10^{19} – 10^{20} Pa s. In all likelihood, lateral variations in viscosity in this region are large, making global average characterizations both difficult to define and misleading to use (D'Agostino et al., 1997; Giunchi et al., 1997). There is an indication of a low-viscosity region at the base of the transition zone, although this feature awaits further delineation and confirmation. There is no compelling evidence for a huge viscosity increase through the lower mantle, as might result from a strong pressure effect.

Question 5.4: What is the difference between the viscosity of the upper mantle and the viscosity of the lower mantle?

5.9 Physics of Mantle Creep

At temperatures that are a substantial fraction of their melting temperatures, crystalline solids deform “slowly” like a fluid. This creep deformation occurs under an applied stress due to thermally activated motion of atoms and ions associated with crystalline defects such as dislocations and atomic vacancies. The principal deformation mechanisms associated with mantle convection are atom/ion migration (known as diffusion or Herring-Nabarro creep if the migration occurs within grains and Coble creep if it occurs along grain boundaries) and dislocation migration (dislocation creep). The applicability of these processes to the deformation of the mantle was first proposed by Gordon (1967).

We first consider diffusion creep. Vacancies are empty sites in the crystalline lattice (Figure 5.16). At any nonzero temperature there is an equilibrium concentration of vacancies that is temperature dependent. Atoms migrate by the movement of adjacent vacancies (Figure 5.17); this is basically a diffusion process and it results in deformation or creep (Figure 5.18). Diffusion of atoms in a crystalline solid is a thermally activated process. The relevant diffusion coefficient D is given by the Arrhenius relation

$$D = D_0 \exp\left[-\frac{(E^* + pV^*)}{RT}\right] \quad (5.9.1)$$

where E^* is the activation energy per mole, V^* is the activation volume per mole, R is the universal gas constant, and D_0 is the frequency factor. The activation energy is the sum of the energy of formation of a vacancy and the energy barrier preventing the migration of an

Figure 5.16. Point defects in a crystal lattice. (a) An interstitial or extra atom, (b) a vacancy. The lattice tends to distort around the defect. After Twiss and Moores (1992).

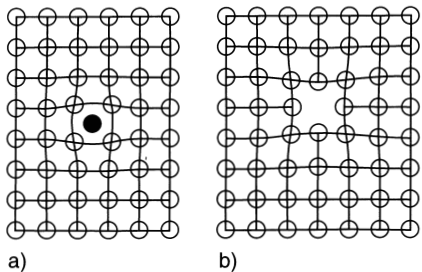


Figure 5.17. Illustration of the motion of a vacancy (v) from one lattice site to an adjacent one by the opposite motion of an atom (solid circle). Matter and vacancies diffuse in opposite directions. After Twiss and Moores (1992).

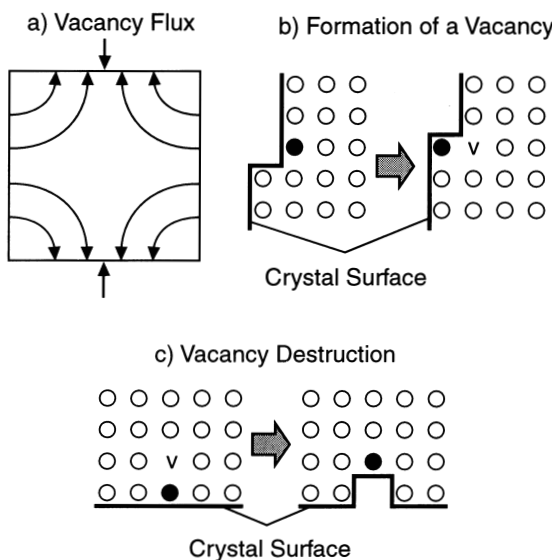
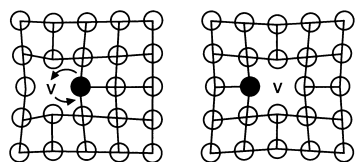


Figure 5.18. Diffusion creep or Herring-Nabarro creep due to vacancy diffusion in a crystal under uniaxial compression. (a) Vacancies diffuse toward the surface of highest normal (compressive) stress along the indicated paths. Atoms diffuse in the opposite direction. (b) Creation of a vacancy at a surface of minimum compressive stress. The solid lines mark the crystal surface. The solid circle marks the ion whose position changes to create the vacancy (v). The surface gradually builds out, lengthening the crystal normal to the compressive stress. Vacancies diffuse toward a surface of high compressive stress. (c) Destruction of a vacancy at a surface of maximum compressive stress. Removal of atoms from the surface and destruction of vacancies gradually shortens the crystal parallel to the maximum compressive stress. After Twiss and Moores (1992).

atom into an adjacent vacancy site, and the term pV^* takes account of the effect of pressure in reducing the number of vacancies and increasing the energy barrier. The exponential temperature dependence follows directly from the Maxwell–Boltzmann distribution of atomic energies. It gives the fraction of atoms that have sufficient energy to overcome the energy

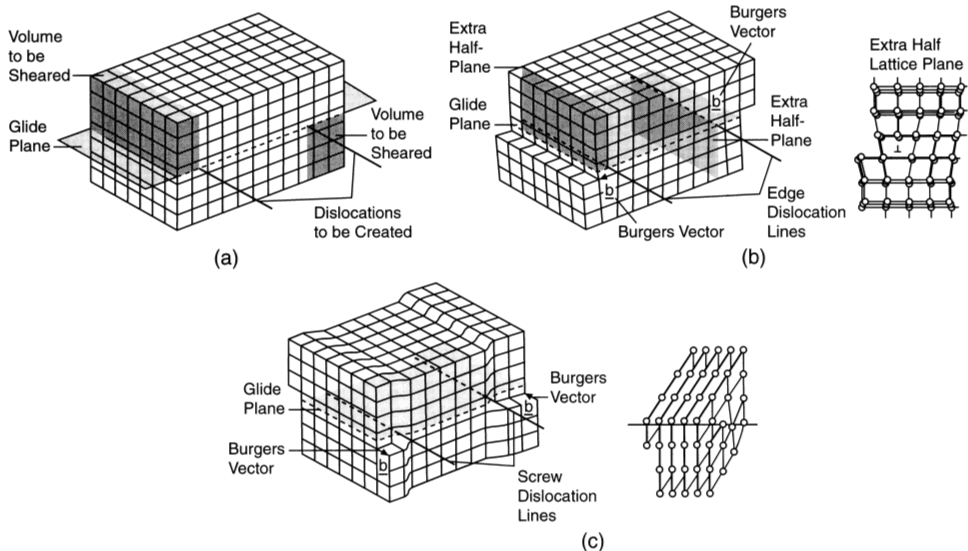


Figure 5.19. Geometry of edge and screw dislocations. The two examples of each type of dislocation in lattice blocks of (b) and (c) are dislocations of opposite sign. b is the Burgers vector. (a) A perfect crystal lattice into which dislocations are introduced in (b) and (c). (b) Edge dislocations of opposite sign produced by shearing the shaded volumes in (a) in a direction perpendicular to its interior edge. Each dislocation is at the edge of an extra half-plane of lattice points. The diagram to the right is a view down the edge dislocation line. The inverted T symbol stands for an edge dislocation. (c) Screw dislocations of opposite sign produced by shearing the shaded volumes in (a) one lattice dimension in a direction parallel to its interior edge. The diagram to the right shows that the crystal lattice planes form a continuous helical surface around the dislocation line. After Twiss and Moores (1992).

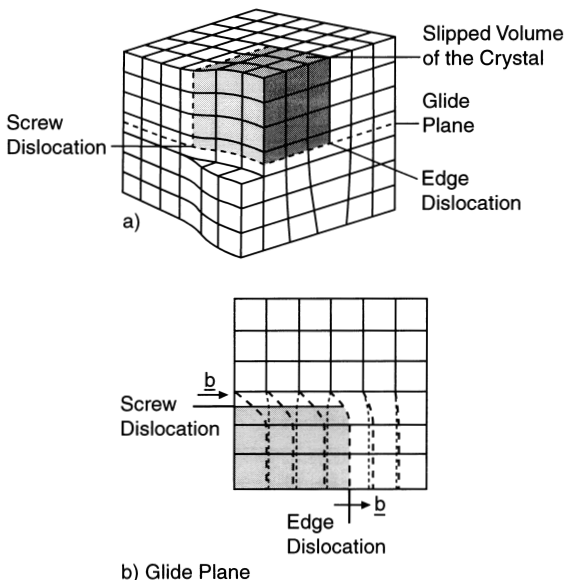
barrier between lattice sites and can thus jump into a vacancy as well as the fraction of lattice sites that are vacancies. It is also possible to account for both the temperature and pressure dependences of the diffusion coefficient using the relation

$$D = D_0 \exp\left(-\frac{aT_m}{T}\right) \quad (5.9.2)$$

where T_m is the melting temperature of the crystalline solid. The ratio T/T_m is referred to as the homologous temperature. The pressure dependence of the diffusion coefficient is accounted for by the pressure dependence of the melting temperature. Diffusion coefficients in silicate minerals have been reviewed by Freer (1981).

We now turn to dislocation creep. Dislocations are line or one-dimensional imperfections in the crystalline lattice (Figure 5.19). A dislocation is defined in terms of the Burgers vector b which is a measure of the relative atomic motion (slip) that occurs when a dislocation line passes through a lattice (Figure 5.19). The surface that traces the motion of a dislocation line is the glide surface, and such surfaces are usually planar (Figure 5.19). Specification of the Burgers vector and the line direction fully defines a dislocation. If the dislocation line is parallel to the Burgers vector, it is a screw dislocation (Figure 5.19). If the dislocation line is perpendicular to the Burgers vector, it is an edge dislocation (Figure 5.19). Most dislocations have both edge and screw components (Figure 5.20).

Figure 5.20. Boundaries of slipped portions of a crystal lattice. (a) The shaded volume of the crystal has slipped relative to the unshaded part. The boundaries of the glide plane are an edge and a screw dislocation. (b) View of the glide plane. The shaded area is the area over which slip has occurred. The boundary is an edge dislocation where b is normal to the boundary. The boundary is a screw dislocation where b is parallel to the boundary. Dotted and dashed lines show planes below and above the glide plane, respectively. After Twiss and Moores (1992).



The two principal ways in which dislocations can contribute to creep are by dislocation slip or glide and dislocation climb. In dislocation slip, the dislocation line moves through the lattice breaking interatomic bonds as it moves (Figure 5.21). This motion conserves mass because it does not require the addition or removal of atoms. Edge dislocations (or the edge components of mixed dislocations) also move by dislocation climb (Figure 5.22). In dislocation climb, the dislocation line moves by the addition of atoms. This is not mass conserving because it requires the diffusion of atoms from elsewhere in the lattice. Dislocation creep can also be thermally activated at relatively low stress levels. Again, the Maxwell–Boltzmann distribution gives the number of atoms that have sufficient energy to overcome the interatomic bonds restricting the motion of a dislocation.

Experiments and theory indicate that a general form of the relationship between strain rate $\dot{\epsilon}$ and deviatoric stress τ valid for both diffusion and dislocation creep is given by

$$\dot{\epsilon} = A \left(\frac{\tau}{\mu} \right)^n \left(\frac{b}{d} \right)^m \exp \left[-\frac{(E^* + pV^*)}{RT} \right] \quad (5.9.3)$$

where A is the pre-exponential factor, μ is the shear modulus, d is the grain size, and b is the magnitude of the Burgers vector. Typical values of n and m are $n = 1$ and $m = 2.5$ for diffusion creep and $n = 3.5$ and $m = 0$ for dislocation creep. For diffusion creep, the relation between strain rate $\dot{\epsilon}$ and deviatoric stress τ is linear, resulting in a Newtonian viscosity. For dislocation creep, the relation between strain rate $\dot{\epsilon}$ and deviatoric stress τ is strongly nonlinear, resulting in a nonlinear viscous rheology. Another difference between these mechanisms is the dependence on grain size. The diffusion creep viscosity decreases strongly with decreasing grain size d , while dislocation creep is insensitive to changes in grain size.

Grain boundaries are two-dimensional defects separating adjacent crystals with different lattice orientations. Grain size is controlled by grain growth and, in the dislocation creep regime, by dynamic recrystallization (De Bresser et al., 1998). Grain growth is a process that

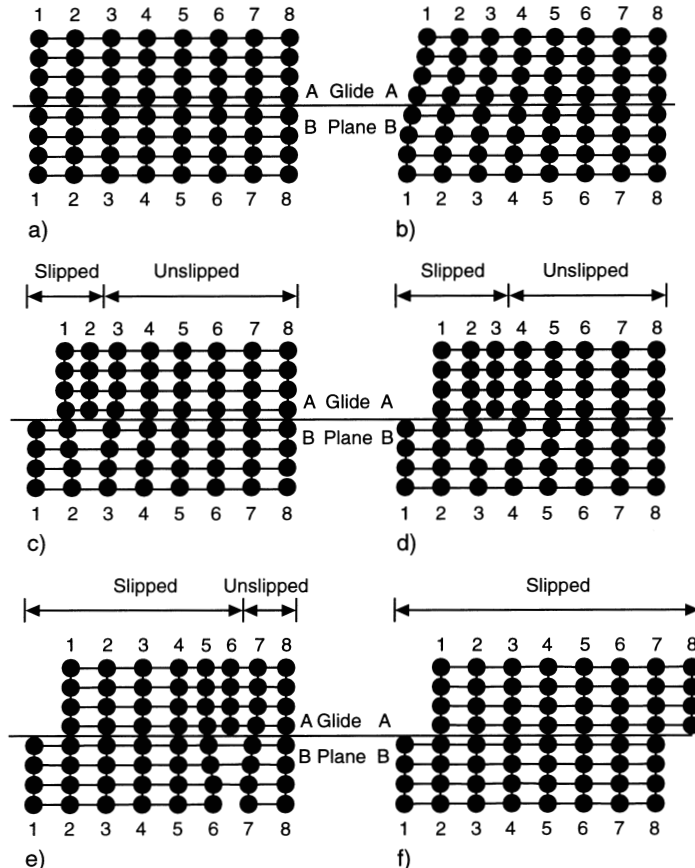


Figure 5.21. The glide or slip of a dislocation through a crystal lattice is accomplished by switching bonds of neighboring atoms across the glide plane. (a) through (f) illustrate the process of forming an edge dislocation and moving it through the crystal to produce one Burgers vector offset in the crystal. Crystallographic planes in the undeformed crystal are numbered 1 through 8. The letters A and B refer to parts of the crystal above and below the slip plane. After Twiss and Moores (1992).

reduces total energy by decreasing the grain boundary area per unit volume. Grain growth is the only process to control the size of grains in the diffusion creep regime. Clearly, grain growth would increase the size of grains with time until grain size was large enough to result in dislocation creep. However, the presence of other phases limits grain growth (Zener pinning) and stabilizes grain size. Therefore, grain size can be small and diffusion creep could be occurring in the mantle.

Creation and migration of new grain boundaries in a stressed crystal can reduce the strain energy. This is dynamic recrystallization which can occur only under dislocation creep. The higher the applied stress, the smaller the recrystallization grain size. In a monomineralic rock the steady-state grain size d in the dislocation creep regime is related to the applied deviatoric stress τ by

$$d = K b \left(\frac{\tau}{\mu} \right)^{-q} \quad (5.9.4)$$

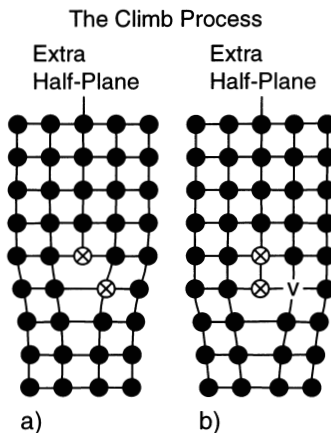


Figure 5.22. Schematic showing the climb of an edge dislocation. The dislocation climbs downward if an atom from a neighboring site jumps on to the extra half-plane (a to b) leaving a vacancy (*v*) behind which can then diffuse away. The dislocation climbs upward if a vacancy diffuses to a neighboring site and then jumps onto the extra half-plane (b to a). After Twiss and Moores (1992).

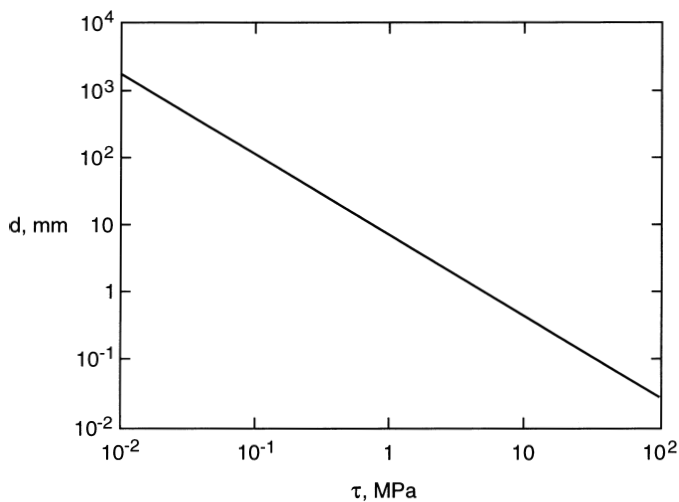


Figure 5.23. Dependence of grain size d on the deviatoric stress τ from (5.9.4).

where b is the magnitude of the Burgers vector, μ is the shear modulus, and K and q are nondimensional constants. The dependence of d on τ is given in Figure 5.23 for $K = 19$, $q = 1.2$, $b = 0.5$ nm, and $\mu = 80$ GPa, values appropriate for typical upper mantle minerals. The prediction of (5.9.4) is that grains can grow to meter size or larger with considerable reduction in deviatoric stress. This clearly cannot happen in the polycrystalline mantle of the Earth. The dependence of grain size on stress in the Earth's mantle remains controversial. Extensive discussions of creep processes applicable to mantle convection have been given by Weertman (1970), Ashby and Verrall (1977), Poirier (1985, 1995), Ranalli (1995), Evans and Kohlstedt (1995), and Drury and Fitz Gerald (1998).

Question 5.5: What is the dependence of grain size on deviatoric stress in the mantle?

The major minerals in the upper mantle are olivine, orthopyroxene, clinopyroxene, and garnets (see Chapter 3). One mineral can control the rheology of a rock if its volume fraction is greater than 20–30%, if it is significantly weaker than the other minerals, and if it forms an interconnected matrix. Olivine is the most abundant mineral and it is also probably the weakest, so that its rheology is likely to be dominant.

Laboratory experiments provide a direct means of determining the creep properties of mantle minerals (Goetze and Kohlstedt, 1973; Kohlstedt and Goetze, 1974). However, this approach does have serious difficulties, as noted in Section 5.1.6. In order to achieve steady-state deformation on reasonable (laboratory) time scales, the measurements must be carried out at much higher strain rates or higher temperatures than those associated with mantle convection. The laboratory results must then be extrapolated over many orders of magnitude in strain rate for application to the mantle. Also, laboratory experiments are generally carried out at much lower pressures than encountered in the mantle, again requiring a large extrapolation of results to mantle conditions.

Many laboratory measurements of olivine deformation have been carried out. These have been reviewed by Tsenn and Carter (1987), Karato and Wu (1993), Evans and Kohlstedt (1995), Kohlstedt et al. (1995), and Drury and Fitz Gerald (1998). The parameters for diffusion creep and dislocation creep in a dry upper mantle, as summarized by Karato and Wu (1993), are given in Table 5.3. An important question is whether diffusion creep is the applicable deformation mechanism in the upper mantle. The transition between dislocation creep and diffusion creep occurs when, for a given stress, the strain rates given by the two mechanisms are equal. In general, for a given stress, the deformation mechanism with the larger strain rate prevails. One way to delineate the regimes of applicability of rival deformation mechanisms is to use a deformation map (Frost and Ashby, 1982). A deformation map generally gives the stress as a function of temperature for several values of the strain rate. A deformation map for a dry upper mantle with $p = 0$, based on (5.9.3) and the parameter values in Table 5.3, is given in Figure 5.24. The diffusion creep values are based on a grain size $d = 3$ mm. This is a typical value for mantle rocks found in diatremes and in ophiolites. Dislocation creep is the applicable deformation mechanism for high stress levels and high

Table 5.3. Parameter Values for Diffusion Creep and Dislocation Creep in a Dry Upper Mantle^a

Quantity	Diffusion Creep	Dislocation Creep
Pre-exponential factor A (s^{-1})	8.7×10^{15}	3.5×10^{22}
Stress exponent n	1	3.5
Grain size exponent m	3	0
Activation energy E^* (kJ mol^{-1})	300	540
Activation volume V^* ($\text{m}^3 \text{mol}^{-1}$)	6×10^{-6}	2×10^{-5}

^a After Karato and Wu (1993). Other relevant parameter values are $\mu_{\text{shear}} = 80 \text{ GPa}$, modulus $b = 0.55 \text{ nm}$, and $R = 8.3144 \text{ J K}^{-1} \text{ mol}^{-1}$.

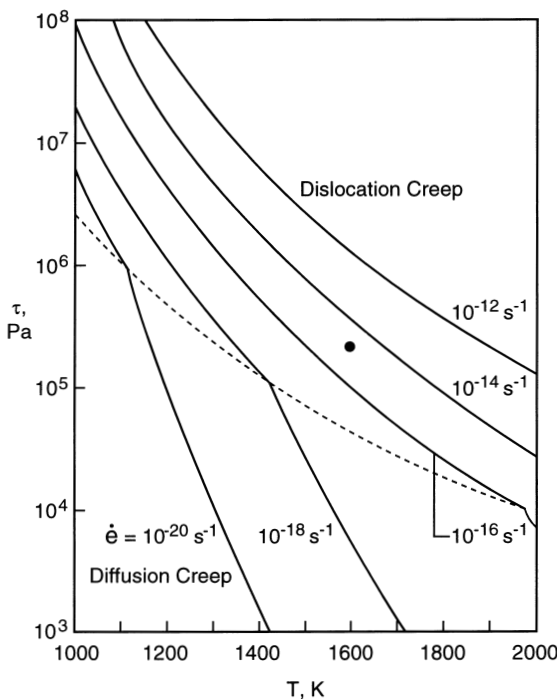


Figure 5.24. Deformation map for a dry upper mantle. The deviatoric stress τ is given as a function of temperature T for several strain rates $\dot{\epsilon}$. The dashed line separates the dislocation creep regime from the diffusion creep regime. The solid circle represents a typical condition for mantle convection.

temperatures, while diffusion creep is dominant for low stress levels and low temperatures. Uncertainties in flow law parameters lead to uncertainties of about an order of magnitude in deformation maps.

Typical values of $\dot{\epsilon}$ and T for mantle convection are $\dot{\epsilon} = 10^{-15} \text{ s}^{-1}$ and $T = 1,600 \text{ K}$; these values locate the large solid circle in Figure 5.24 and correspond to $\tau = 0.5 \text{ MPa}$. This point clearly falls in the dislocation creep field of the upper mantle deformation map. If (5.9.4) had been used to obtain grain sizes instead of assuming $d = 3 \text{ mm}$, the grain sizes would have been considerably larger and dislocation creep would have been applicable over the entire upper mantle deformation map given in Figure 5.24. Most authors who have published laboratory studies of mantle deformation have concluded that dislocation creep is the applicable deformation mechanism in the upper mantle. This conclusion is not consistent with almost all studies of postglacial rebound that favor a Newtonian viscosity for the mantle. In assessing whether dislocation creep or diffusion creep is dominant in the upper mantle, it must be emphasized that Figure 5.24 is for $p = 0$. Effects of pressure can change the dominant mechanism from dislocation creep in the shallow upper mantle to diffusion creep in the deeper upper mantle (Karato and Wu, 1993). Karato and Wu (1993) and Karato et al. (1995a) have argued that significant seismic anisotropy in the shallow upper mantle is evidence for dislocation creep at these depths, while weak seismic anisotropy in the lower mantle is evidence for diffusion creep at great depths. The nature of mantle deformation may well be a function of depth with dislocation creep occurring only in the shallow upper mantle.

Question 5.6: Is dislocation creep or diffusion creep the dominant deformation mechanism associated with mantle convection?

Question 5.7: Does the mantle behave like a Newtonian or a non-Newtonian fluid on geological time scales?

There are yet other factors contributing to our uncertainty about the viscosity of the mantle. One of these is the role of water (Hirth and Kohlstedt, 1996). Chopra and Paterson (1984) showed that trace amounts of water as low as 200–300 ppm by weight could significantly weaken olivine. Estimates of the water content of the mantle have been given by Bell and Rossman (1992). Kohlstedt et al. (1995) suggest that a dry rheology is applicable to the oceanic lithosphere and a wet rheology is applicable to the continental lithosphere. However, a high degree of depletion by melting in the continental upper mantle could mean that continental lithosphere as a whole is drier than oceanic lithosphere (Karato, 1999).

Partial melting can also influence mantle rheology (Hirth and Kohlstedt, 1995a, b; Kohlstedt and Zimmerman, 1996). Laboratory studies indicate that 1–3% melt can reduce the diffusion creep viscosity by a factor of 2–5. For dislocation creep, melt can also have a significant influence on the rheology.

The above discussion of mantle rheology has dealt mainly with the upper mantle where olivine is the principal mineral constituent. An important question is whether there will be a significant change in rheology across the 410 and 660 km seismic discontinuities. Between 410 and 660 km depth the dominant mineral will be spinel, and below 660 km depth the minerals (Mg, Fe)SiO₃ perovskite and magnesiowüstite will be dominant. This problem has been considered in some detail by Karato et al. (1995b). They suggest that there will be a small increase in viscosity at a depth of 410 km and a small decrease in viscosity at a depth of 660 km. Below 660 km depth the viscosity is predicted to increase with depth (pressure) so that the average lower mantle viscosity would be one to two orders of magnitude greater than the average upper mantle viscosity. The rheology of the lower mantle has been reviewed by Karato (1997).

Question 5.8: Are there changes in viscosity associated with the solid–solid phase changes in the transition zone?

5.10 Viscosity Functions

The scalar relationship between strain rate $\dot{\epsilon}$ and deviatoric stress τ given in (5.9.3) can be generalized to a full constitutive relation between the strain rate and deviatoric stress tensors. The generalized strain rate–deviatoric stress relation is (Christensen, 1989a)

$$\dot{\epsilon}_{ij} = \frac{1}{B} \left(\frac{\tau_2}{\mu} \right)^{n-1} \exp \left[- \left(\frac{E^* + pV^*}{RT} \right) \right] \tau_{ij} \quad (5.10.1)$$

$$B = \left(\frac{A}{\mu} \right)^{-1} \left(\frac{b}{d} \right)^{-m} \quad (5.10.2)$$

where τ_2 is the square root of the second invariant of the deviatoric stress tensor, and the coefficient B includes dependence on both rigidity and grain size. From (5.10.1) and the relation

$$\dot{e}_{ij} = \frac{1}{2\mu} \tau_{ij} \quad (5.10.3)$$

where μ is viscosity, we can identify the viscosity function as

$$\mu = \frac{B}{2} \left(\frac{\tau_2}{\mu_{\text{shear modulus}}} \right)^{1-n} \exp \left\{ \frac{E^* + pV^*}{RT} \right\} \quad (5.10.4)$$

On the right side of (5.10.4) we have written $\mu_{\text{shear modulus}}$ for the shear modulus to avoid confusion with the viscosity function μ . For diffusion creep with $n = 1$, (5.10.4) becomes

$$\mu_{\text{diff creep}} = \frac{1}{2} B_{\text{diff creep}} \exp \left[\frac{(E_{\text{diff creep}}^* + pV_{\text{diff creep}}^*)}{RT} \right] \quad (5.10.5)$$

For a grain size $d = 3$ mm and $\mu_{\text{shear modulus}} = 80$ GPa we have, from (5.9.3) and Table 5.3, $B_{\text{diff creep}} = 8.1 \times 10^{11}$ Pa s. For dislocation creep with $n = 3.5$ the viscosity function is given by

$$\mu_{\text{disloc creep}} = \frac{1}{2} B_{\text{disloc}} \left(\frac{\mu_{\text{shear modulus}}}{\tau_2} \right)^{2.5} \exp \left[\frac{(E_{\text{disloc creep}}^* + pV_{\text{disloc creep}}^*)}{RT} \right] \quad (5.10.6)$$

With $\mu_{\text{shear modulus}} = 80$ GPa we have, from (5.9.3) and Table 5.3, $B_{\text{disloc creep}} = 2.29 \times 10^{-12}$ Pa s. Figure 5.25 shows the dependence of the viscosity functions on temperature for shallow upper mantle conditions ($p = 0$) from (5.10.5) and (5.10.6) with parameter values given in Table 5.3. The result for diffusion creep (solid line) is independent of stress, and results for dislocation creep (dashed lines) are given for $\tau = 10^5$ and 10^6 Pa. For $\tau = 10^6$ Pa deformation is due to dislocation creep for the entire range of temperatures considered. For $\tau = 10^5$ Pa deformation is due to dislocation creep for $T > 1,415$ K and to diffusion creep for $T < 1,415$ K. For $\tau = 10^4$ Pa deformation is due to diffusion creep for the entire range of temperatures considered. Typical upper mantle viscosity and temperature values are $\mu = 3 \times 10^{20}$ Pa s and $T = 1,600$ K; this condition (large filled circle in Figure 5.25) lies in the dislocation creep field with $\tau = 10^5$ Pa.

It is generally concluded that laboratory studies favor dislocation creep as the dominant deformation mechanism for the shallow upper mantle. If dislocation creep also characterized the entire mantle, it would imply a strongly nonlinear rheology for the mantle with $\mu \sim \tau^{-2.5}$ as shown in (5.10.4). However, studies of mantle rheology based on postglacial rebound show that the adjustment of the mantle to shifts in surface loads is adequately described by a linear Newtonian behavior. A rationalization of these conclusions is possible if the flow associated with postglacial rebound is superimposed on a convecting mantle. If the deviatoric stresses associated with rebound are less than the deviatoric stresses associated with mantle convection, a linear behavior would be expected for rebound even in a non-Newtonian mantle (Weertman and Weertman, 1975; Wu, 1995). Another interpretation is

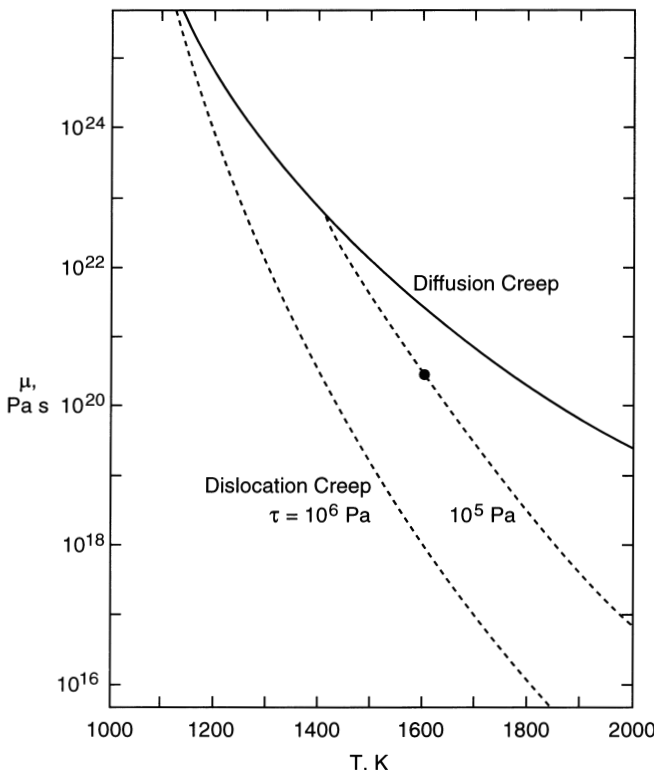


Figure 5.25. The dependence of the viscosity of a dry upper mantle on temperature is given for several stress levels. The solid line is for diffusion creep; the viscosity is not dependent on stress level. The dashed lines are for dislocation creep illustrating the dependence on the stress level. The solid circle represents a typical condition for mantle convection.

that diffusion creep characterizes all of the mantle except its shallowest depths and much of the deformation causing postglacial rebound indeed occurs in the linear Newtonian regime.

In the upper mantle, temperature variations control the behavior of the viscosity function (5.10.4), while in the lower mantle it is likely that pressure variations are equally important. Since temperature increases rapidly with increasing depth through the lithosphere, the effective viscosity drops rapidly from very high values through the lithosphere, reaching the observationally constrained range of $10^{19\text{--}21}$ Pa s in the asthenosphere. In the lower mantle, the influence of increasing temperature and increasing pressure act in opposite directions, so the inference of either a uniform viscosity throughout most of the lower mantle or a viscosity increasing with depth in the lower mantle is reasonable from a mineral physics perspective, although neither behavior is required.

The complete viscosity formula (5.10.4) is cumbersome to use in numerical modeling and accordingly it is often simplified. One common simplification, the exponential dependence of viscosity on temperature

$$\mu = \mu_0 \exp(-\gamma T) \quad (5.10.7)$$

is an adequate approximation over restricted temperature intervals, and it is used in applications where the pressure dependence can be neglected.

6

Basic Equations

6.1 Background

The defining property of fluids is their ability to deform. In the case of nearly incompressible fluids such as water, the deformation is associated with relatively small changes in density. For gases, on the other hand, changes in density are generally quite important. A fluid is treated as a continuum if the length scales of changes in fluid properties such as velocity are large compared with the atomic or molecular scale. In order to solve problems in fluid mechanics, it is necessary to solve the applicable continuum partial differential equations. For details of the derivations of the basic equations the reader is referred to Batchelor (1967).

Many solutions of these equations have been obtained and have been compared with observations. These solutions generally describe flows that are smooth or laminar. In fact, many observed flows are highly oscillatory in a random or statistical way. These flows are generally described as being turbulent. A fundamental understanding of turbulence does not exist; it is one of the major unsolved problems in physics. Under many circumstances laminar flows are unstable; small disturbances grow exponentially. These instabilities lead to turbulence.

Some sets of nonlinear differential equations give chaotic solutions, i.e., the solutions evolve in a nondeterministic manner. Infinitesimal disturbances can lead to first-order differences in flows. These solutions are associated with turbulence. However, true turbulence is so complex that not even the largest computers can resolve its structure. Three-dimensional disturbances exist on all scales from the molecular to those of the boundary conditions. In studies of mantle convection and other fluid problems in the Earth Sciences, the role of turbulent flow must always be kept in mind.

We next discuss the basic equations applicable to mantle convection. We must consider the conservation of mass, momentum, and energy for a fluid continuum, since the solid rocks of the mantle deform as a fluid on geological time scales. In addition, these conservation equations must be supplemented by an equation of state. The transport coefficients, viscosity and thermal conductivity, must also be specified.

6.2 Conservation of Mass

Conservation of mass for an infinitesimal volume element requires that

$$\frac{\partial \rho}{\partial t} + \frac{\partial}{\partial x_i} (\rho u_i) = 0 \quad (6.2.1)$$

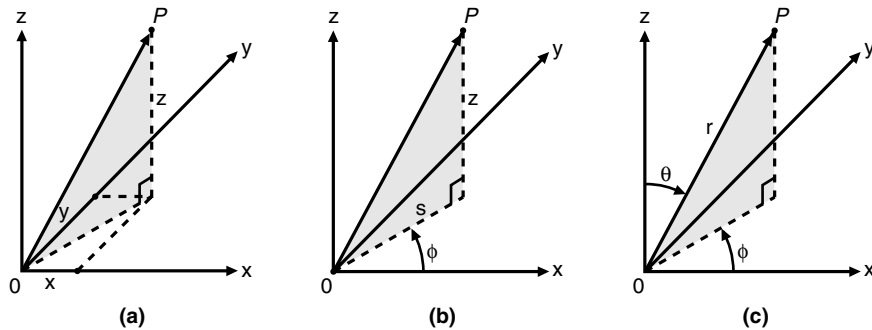


Figure 6.1. Cartesian (a), cylindrical (b), and spherical polar (c) coordinate systems.

where x_i is the position vector, t is time, ρ is the density of the fluid, and u_i is the fluid velocity. In writing (6.2.1) Cartesian tensor notation has been used. In this notation the appearance of a repeated subscript such as i in the second term of (6.2.1) implies a summation over the three directions ($i = 1, 2, 3$). Thus, when written explicitly in Cartesian (x, y, z) coordinates (Figure 6.1), (6.2.1) becomes

$$\frac{\partial \rho}{\partial t} + \frac{\partial}{\partial x} (\rho u_x) + \frac{\partial}{\partial y} (\rho u_y) + \frac{\partial}{\partial z} (\rho u_z) = 0 \quad (6.2.2)$$

The first term in (6.2.1) represents the change of mass in an elemental volume while the second term represents the net flux of mass into or out of the volume.

It is convenient to introduce the total derivative

$$\frac{D}{Dt} = \frac{\partial}{\partial t} + u_i \frac{\partial}{\partial x_i} \quad (6.2.3)$$

The operator D/Dt is the time derivative following the motion of an element of fluid. Since

$$\frac{\partial(\rho u_i)}{\partial x_i} = \rho \frac{\partial u_i}{\partial x_i} + u_i \frac{\partial \rho}{\partial x_i} \quad (6.2.4)$$

(6.2.1) can be rewritten in terms of the total derivative (6.2.3) as

$$\frac{1}{\rho} \frac{D\rho}{Dt} + \frac{\partial u_i}{\partial x_i} = 0 \quad (6.2.5)$$

In this form the equation for conservation of mass can be interpreted in terms of the change in volume of a fixed mass of fluid. This represents a Lagrangian rather than an Eulerian formulation of mass conservation. For the special case of an incompressible fluid, $D\rho/Dt \equiv 0$, (6.2.5) reduces to

$$\frac{\partial u_i}{\partial x_i} = 0 \quad (6.2.6)$$

The velocity u_i of an incompressible fluid is solenoidal or has zero divergence.

In spherical polar coordinates (r, θ, ϕ) (r is radius, θ is colatitude, and ϕ is longitude, Figure 6.1), the conservation of mass or continuity equation takes the form

$$\frac{\partial \rho}{\partial t} + \frac{1}{r^2} \frac{\partial}{\partial r} (r^2 \rho u_r) + \frac{1}{r \sin \theta} \frac{\partial}{\partial \theta} (\rho \sin \theta u_\theta) + \frac{1}{r \sin \theta} \frac{\partial}{\partial \phi} (\rho u_\phi) = 0 \quad (6.2.7)$$

where (u_r, u_θ, u_ϕ) are the velocity components in the (r, θ, ϕ) directions.

In cylindrical coordinates (s, z, ϕ) (s is the radius in a plane perpendicular to the cylindrical axis, z is the distance parallel to the cylindrical axis, and ϕ is longitude, Figure 6.1), mass conservation can be written as

$$\frac{\partial \rho}{\partial t} + \frac{\partial}{\partial z} (\rho u_z) + \frac{1}{s} \frac{\partial}{\partial s} (\rho u_s) + \frac{1}{s} \frac{\partial}{\partial \phi} (\rho u_\phi) = 0 \quad (6.2.8)$$

where (u_s, u_z, u_ϕ) are the components of velocity in the (s, z, ϕ) directions.

6.3 Stream Functions and Streamlines

For the special case of two-dimensional (x, y) incompressible flows, (6.2.6) becomes

$$\frac{\partial u_x}{\partial x} + \frac{\partial u_y}{\partial y} = 0 \quad (6.3.1)$$

For this case, it is convenient to define the stream function $\psi(x, y)$ by

$$u_x \equiv \frac{\partial \psi}{\partial y}, \quad u_y \equiv -\frac{\partial \psi}{\partial x} \quad (6.3.2)$$

so that (6.3.1) is automatically satisfied. It follows from the definition (6.3.2) that a line of constant ψ ($d\psi = 0$) is everywhere parallel to the velocity vector (u_x, u_y) ; such a line is known as a streamline. For example, if the flow is in the x -direction, $u_y = 0$, and from (6.3.2) ψ is a function only of y ; thus the streamlines (lines of constant ψ) are horizontal. If the flow is steady ($\partial/\partial t = 0$), streamlines are identical to particle paths; however, this is not the case for time-dependent or unsteady incompressible flows. It can be shown that the difference in stream function values between two streamlines measures the volumetric flow rate between the streamlines per unit distance perpendicular to the plane of the flow.

Stream functions can also be defined for incompressible axisymmetric ($\partial/\partial\phi = 0$) flows. In cylindrical coordinates the conservation of mass reduces to

$$\frac{\partial u_z}{\partial z} + \frac{1}{s} \frac{\partial}{\partial s} (su_s) = 0 \quad (6.3.3)$$

and the stream function is defined by

$$u_s \equiv -\frac{1}{s} \frac{\partial \psi}{\partial z}, \quad u_z \equiv \frac{1}{s} \frac{\partial \psi}{\partial s} \quad (6.3.4)$$

In spherical coordinates the incompressible conservation of mass equation for axisymmetric ($\partial/\partial\phi = 0$) flow is

$$\frac{\partial}{\partial r} (r^2 u_r) + \frac{r}{\sin \theta} \frac{\partial}{\partial \theta} (\sin \theta u_\theta) = 0 \quad (6.3.5)$$

and the stream function is defined by

$$u_r \equiv \frac{1}{r^2 \sin \theta} \frac{\partial \psi}{\partial \theta}, \quad u_\theta \equiv -\frac{1}{r \sin \theta} \frac{\partial \psi}{\partial r} \quad (6.3.6)$$

Other flows are also amenable to the introduction of a stream function. Steady compressible flows that are either two-dimensional or axisymmetric possess stream functions whose definitions are similar to the above with the components of the mass flux vector ρu_i written in place of the velocity u_i components.

6.4 Conservation of Momentum

The force balance on an elemental parcel of fluid leads to the equation for conservation of momentum. According to Newton's second law of motion, any imbalance of forces on the fluid parcel results in an acceleration of the elemental parcel. The governing equation is

$$\rho \frac{Du_i}{Dt} = -\frac{\partial p}{\partial x_i} + \frac{\partial \tau_{ij}}{\partial x_j} + \rho g_i \quad (6.4.1)$$

The term on the left of (6.4.1) is the product of the mass of an elemental fluid parcel and its acceleration Du_i/Dt , per unit volume of the parcel. The first two terms on the right of (6.4.1) comprise the net surface forces per unit volume on the elemental parcel and the third term is the net body force per unit volume. Surface forces in a fluid are those forces that act on the bounding surfaces of elemental fluid parcels, while volume forces are those forces that act on the fluid parcel throughout its volume. Surface forces have a magnitude proportional to the area of the surface on which they act, while body forces have a magnitude proportional to the volume of fluid on which they act. We consider gravity to be the only body force; the acceleration of gravity is g_i . Other examples of body forces include electrostatic, electromagnetic, centrifugal, and coriolis forces. Although coriolis forces due to the rotation of the Earth are important in meteorology, in oceanography, and in the Earth's liquid outer core, they are negligibly small in the Earth's mantle; the centrifugal force due to the Earth's rotation is included in the acceleration of gravity.

The net surface force is divided into two parts, one associated with the fluid pressure p and the other with deviatoric stresses described by the deviatoric stress tensor τ_{ij} . The surface forces acting on an infinitesimal two-dimensional rectangular fluid parcel are illustrated in Figure 6.2. The pressure force is isotropic, i.e., it has the same magnitude per unit area independent of the orientation of the infinitesimal surface on which it acts at a point. The pressure force is perpendicular to the surface on which it acts; for an infinitesimal surface area dA_i the pressure force is $-pdA_i$. In the absence of flow, the only surface force is the pressure force. With flow, additional deviatoric forces act on the surface of an elemental

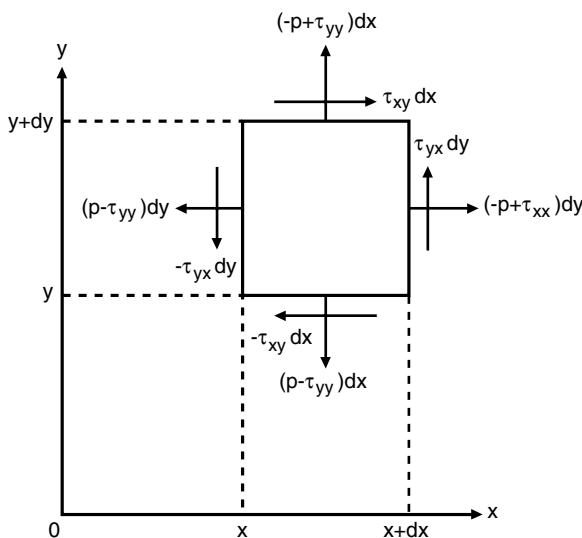


Figure 6.2. Illustration of the surface forces operating in the x - y plane.

parcel, both perpendicular and parallel to the surface. These deviatoric surface forces are caused by velocity gradients in the fluid and the property of the fluid known as viscosity. The deviatoric stress components are forces per unit area; the deviatoric stresses acting parallel to a surface are known as shear stresses. In Figure 6.2 deviatoric normal stresses are τ_{xx} and τ_{yy} and deviatoric shear stresses are τ_{xy} and τ_{yx} . It can be shown that the deviatoric stress components τ_{ij} comprise a tensor; the deviatoric surface force acting on any infinitesimal surface area dA_j is $\tau_{ij} dA_j$.

A torque balance on an elemental fluid parcel shows that the deviatoric stress tensor is symmetric, i.e.,

$$\tau_{ij} = \tau_{ji} \quad (6.4.2)$$

In two dimensions, the stress tensor has three independent components and in three dimensions there are six independent components.

For two dimensions the x - and y -components of the momentum equation (6.4.1) are

$$\rho \left(\frac{\partial u_x}{\partial t} + u_x \frac{\partial u_x}{\partial x} + u_y \frac{\partial u_x}{\partial y} \right) = -\frac{\partial p}{\partial x} + \frac{\partial \tau_{xx}}{\partial x} + \frac{\partial \tau_{xy}}{\partial y} \quad (6.4.3)$$

$$\rho \left(\frac{\partial u_y}{\partial t} + u_x \frac{\partial u_y}{\partial x} + u_y \frac{\partial u_y}{\partial y} \right) = -\frac{\partial p}{\partial y} + \frac{\partial \tau_{yy}}{\partial y} + \frac{\partial \tau_{xy}}{\partial x} + \rho g \quad (6.4.4)$$

assuming gravity acts in the positive y -direction. Explicit forms of the momentum equation in three dimensions and in Cartesian, cylindrical, and spherical coordinates are given in Section 6.14.

6.5 Navier–Stokes Equations

The relative velocity field in the infinitesimal neighborhood of a point in a fluid consists of a rigid body rotation with angular velocity $(1/2) e_{ijk} (\partial u_k / \partial x_j)$ (one half the curl of the velocity) and a nonrigid rate of deformation described by the strain rate tensor e_{ij} . The symbol e_{ijk} is known as the permutation symbol (it is a tensor of rank 3); it has the numerical value of +1 when i, j, k are distinct and in the order 123123 . . . , -1 when i, j, k are distinct and in the order 132132 . . . , and 0 when any of i, j, k are identical. The permutation symbol enables the vector cross product or curl of a vector to be carried out in Cartesian tensor formalism. The curl of the fluid velocity, equal to twice the local spin angular velocity of an infinitesimal fluid parcel, is known in fluid dynamics as the vorticity ζ_i . Local rigid body rotation about a point in a fluid does not produce deviatoric stress at that point.

The strain rate tensor e_{ij} of a fluid is given by

$$e_{ij} \equiv \frac{1}{2} \left(\frac{\partial u_i}{\partial x_j} + \frac{\partial u_j}{\partial x_i} \right) \quad (6.5.1)$$

The trace of this tensor $e_{ii} = \partial u_i / \partial x_i$ is the rate of change of volume per unit volume of an elemental fluid parcel (the dilatation rate). The off-diagonal components of e_{ij} account for rates of shear deformation of elemental fluid parcels; shear deformation alters the angles between lines of fluid parcels.

Nonzero rates of strain generate deviatoric stresses and for many fluids the dependence of τ_{ij} on e_{ij} is a linear one. Such fluids are said to be Newtonian, and if they are also isotropic

(the constants of proportionality in the deviatoric stress-strain rate relation are independent of the orientation of coordinate system axes), then the relation between τ_{ij} and e_{ij} is

$$\tau_{ij} = 2\mu e_{ij} + \lambda e_{kk} \delta_{ij} \quad (6.5.2)$$

where the Kronecker delta δ_{ij} is 0 if $i \neq j$ and 1 if $i = j$, μ is the dynamic viscosity, and λ is the second viscosity.

The average of the normal deviatoric stresses on three mutually perpendicular planes at a point in the fluid is $\tau_{ii}/3$ and from (6.5.2) this is given by

$$\frac{\tau_{ii}}{3} = e_{ii} \left(\lambda + \frac{2}{3} \mu \right) \equiv k_B e_{ii} \quad (6.5.3)$$

where k_B is the bulk viscosity, a measure of dissipation under compression or expansion. Combination of (6.5.2) and (6.5.3) gives

$$\tau_{ij} = 2\mu e_{ij} + \left(k_B - \frac{2}{3} \mu \right) e_{kk} \delta_{ij} = \mu \left(\frac{\partial u_i}{\partial x_j} + \frac{\partial u_j}{\partial x_i} \right) + \left(k_B - \frac{2}{3} \mu \right) \frac{\partial u_k}{\partial x_k} \delta_{ij} \quad (6.5.4)$$

Substitution of (6.5.4) into (6.4.1) gives

$$\rho \frac{D u_i}{D t} = - \frac{\partial p}{\partial x_i} + \frac{\partial}{\partial x_j} \left[\mu \left(\frac{\partial u_i}{\partial x_j} + \frac{\partial u_j}{\partial x_i} \right) + \left(k_B - \frac{2}{3} \mu \right) \delta_{ij} \frac{\partial u_k}{\partial x_k} \right] + \rho g_i \quad (6.5.5)$$

For many fluids k_B is very small and is often taken to be zero, an assumption known as the Stokes assumption; in a Newtonian-Stokesian fluid, the average of the total normal stresses on three mutually perpendicular planes at a point in the fluid equals the negative of the hydrostatic pressure. With $k_B = 0$, the constitutive or rheological law connecting deviatoric stress and strain rate (6.5.2) becomes

$$\tau_{ij} = 2\mu e_{ij} - \frac{2}{3} \mu e_{kk} \delta_{ij} = \mu \left(\frac{\partial u_i}{\partial x_j} + \frac{\partial u_j}{\partial x_i} - \frac{2}{3} \delta_{ij} \frac{\partial u_k}{\partial x_k} \right) \quad (6.5.6)$$

Substitution of (6.5.6) into (6.4.1) gives the Navier-Stokes equation

$$\rho \frac{D u_i}{D t} = - \frac{\partial p}{\partial x_i} + \frac{\partial}{\partial x_j} \left[\mu \left(\frac{\partial u_i}{\partial x_j} + \frac{\partial u_j}{\partial x_i} - \frac{2}{3} \delta_{ij} \frac{\partial u_k}{\partial x_k} \right) \right] + \rho g_i \quad (6.5.7)$$

For incompressible flow $\partial u_k / \partial x_k = 0$ from (6.2.6), and both (6.5.5) and (6.5.7) simplify to

$$\rho \frac{D u_i}{D t} = - \frac{\partial p}{\partial x_i} + \frac{\partial}{\partial x_j} \left[\mu \left(\frac{\partial u_i}{\partial x_j} + \frac{\partial u_j}{\partial x_i} \right) \right] + \rho g_i \quad (6.5.8)$$

If the dynamic viscosity is a constant, (6.5.8) further simplifies to

$$\rho \frac{D u_i}{D t} = - \frac{\partial p}{\partial x_i} + \mu \frac{\partial^2 u_i}{\partial x_j^2} + \rho g_i \quad (6.5.9)$$

This equation represents a balance between inertial forces, pressure forces, viscous forces, and the body force due to gravity. Explicit and more general forms of the Navier-Stokes equations for three-dimensional flows in Cartesian, cylindrical, and spherical polar coordinates are given in Section 6.15.

6.6 Vorticity Equation

In general, vorticity in the mantle is broadly distributed, but it is concentrated at plate boundaries such as strike-slip faults and transform faults. An equation for the vorticity can be obtained by taking the curl of ρ^{-1} times the momentum equation. Upon dividing the Navier-Stokes equation (6.5.7) by ρ and taking the curl ($e_{kli} \partial/\partial x_l$) we obtain

$$\begin{aligned} \frac{D\zeta_k}{Dt} = & \zeta_j \frac{\partial u_k}{\partial x_j} - \zeta_k \frac{\partial u_j}{\partial x_j} - e_{kli} \left(\frac{\partial}{\partial x_l} \frac{1}{\rho} \right) \frac{\partial p}{\partial x_i} + \frac{\mu}{\rho} \frac{\partial^2 \zeta_k}{\partial x_j^2} \\ & + e_{kli} \left(\frac{\partial}{\partial x_l} \frac{1}{\rho} \right) \frac{\partial \mu}{\partial x_j} \left(\frac{\partial u_i}{\partial x_j} + \frac{\partial u_j}{\partial x_i} \right) + \mu e_{kli} \left(\frac{\partial}{\partial x_l} \frac{1}{\rho} \right) \left(\frac{\partial^2 u_i}{\partial x_j^2} + \frac{\partial^2 u_j}{\partial x_i \partial x_j} \right) \\ & + \frac{1}{\rho} e_{kli} \frac{\partial^2 \mu}{\partial x_l \partial x_j} \left(\frac{\partial u_i}{\partial x_j} + \frac{\partial u_j}{\partial x_i} \right) + \frac{1}{\rho} \frac{\partial \mu}{\partial x_j} \left(\frac{\partial \zeta_k}{\partial x_j} + e_{kli} \frac{\partial^2 u_j}{\partial x_l \partial x_i} \right) \\ & + \frac{1}{\rho} e_{kli} \frac{\partial \mu}{\partial x_l} \left(\frac{\partial^2 u_i}{\partial x_j^2} + \frac{\partial^2 u_j}{\partial x_i \partial x_j} \right) - \frac{2}{3} e_{kli} \left(\frac{\partial}{\partial x_l} \frac{1}{\rho} \right) \frac{\partial \mu}{\partial x_i} \frac{\partial u_j}{\partial x_j} \\ & - \frac{2}{3} \mu e_{kli} \left(\frac{\partial}{\partial x_l} \frac{1}{\rho} \right) \frac{\partial^2 u_j}{\partial x_i \partial x_j} - \frac{2}{3} e_{kli} \frac{1}{\rho} \frac{\partial^2 \mu}{\partial x_l \partial x_i} \frac{\partial u_j}{\partial x_j} \end{aligned} \quad (6.6.1)$$

In deriving (6.6.1) we use the fact that the gravitational field is a potential field and $\text{curl } g_i$ is zero. The first term on the right side of (6.6.1) represents the contribution of vortex line stretching to the time rate of change of vorticity. The second term on the right side of (6.6.1) is the contribution of volume changes to the time rate of change of vorticity. The third term on the right side of (6.6.1) is the negative cross product of the gradient of ρ^{-1} and the gradient of p ; it is nonzero if isodensity and isobaric surfaces are distinct. It is an important generator of vorticity in the atmosphere and oceans and is referred to as the baroclinic term. The fourth term on the right side of (6.6.1) is the viscous diffusion of vorticity. All the remaining terms in (6.6.1) are nonzero only if there are nonzero gradients in density or viscosity.

For incompressible flow, (6.6.1) simplifies to

$$\begin{aligned} \frac{D\zeta_k}{Dt} = & \zeta_j \frac{\partial u_k}{\partial x_j} - e_{kli} \left(\frac{\partial}{\partial x_l} \frac{1}{\rho} \right) \frac{\partial p}{\partial x_i} + \frac{\mu}{\rho} \frac{\partial^2 \zeta_k}{\partial x_j^2} + e_{kli} \left(\frac{\partial}{\partial x_l} \frac{1}{\rho} \right) \frac{\partial \mu}{\partial x_j} \left(\frac{\partial u_i}{\partial x_j} + \frac{\partial u_j}{\partial x_i} \right) \\ & + \mu e_{kli} \left(\frac{\partial}{\partial x_l} \frac{1}{\rho} \right) \frac{\partial^2 u_i}{\partial x_j^2} + \frac{1}{\rho} e_{kli} \frac{\partial^2 \mu}{\partial x_l \partial x_j} \left(\frac{\partial u_i}{\partial x_j} + \frac{\partial u_j}{\partial x_i} \right) \\ & + \frac{1}{\rho} \frac{\partial \mu}{\partial x_j} \left(\frac{\partial \zeta_k}{\partial x_j} + e_{kli} \frac{\partial^2 u_j}{\partial x_l \partial x_i} \right) + \frac{1}{\rho} e_{kli} \frac{\partial \mu}{\partial x_l} \frac{\partial^2 u_i}{\partial x_j^2} \end{aligned} \quad (6.6.2)$$

If the dynamic viscosity μ is also a constant, (6.6.2) further simplifies to

$$\frac{D\zeta_k}{Dt} = \zeta_j \frac{\partial u_k}{\partial x_j} - e_{kli} \left(\frac{\partial}{\partial x_l} \frac{1}{\rho} \right) \frac{\partial p}{\partial x_i} + \frac{\mu}{\rho} \frac{\partial^2 \zeta_k}{\partial x_j^2} + \mu e_{kli} \left(\frac{\partial}{\partial x_l} \frac{1}{\rho} \right) \left(\frac{\partial^2 u_i}{\partial x_j^2} \right) \quad (6.6.3)$$

6.7 Stream Function Equation

In cases where there exists a stream function, it is useful to rewrite the momentum equation in terms of the stream function. As an example, we consider two-dimensional, incompressible

flow for which the stream function is given by (6.3.2). In this case, the Navier–Stokes equation (6.5.8) can be written as

$$\begin{aligned} & \rho \frac{\partial \psi_y}{\partial t} + \rho (\psi_y \psi_{xy} - \psi_x \psi_{yy}) \\ &= -\frac{\partial p}{\partial x} + \frac{\partial}{\partial x} \{2\mu \psi_{xy}\} + \frac{\partial}{\partial y} \{\mu(\psi_{yy} - \psi_{xx})\} + \rho g_x \end{aligned} \quad (6.7.1)$$

$$\begin{aligned} & -\rho \frac{\partial \psi_x}{\partial t} + \rho (-\psi_y \psi_{xx} + \psi_x \psi_{xy}) \\ &= -\frac{\partial p}{\partial y} + \frac{\partial}{\partial x} \{\mu(\psi_{yy} - \psi_{xx})\} - \frac{\partial}{\partial y} \{2\mu \psi_{xy}\} + \rho g_y \end{aligned} \quad (6.7.2)$$

where x and y subscripts on ψ indicate partial derivatives of ψ with respect to x and y , respectively. The pressure p can be eliminated from these equations by differentiating (6.7.1) with respect to y and subtracting the derivative of (6.7.2) with respect to x , with the result

$$\begin{aligned} & \frac{\partial \rho}{\partial y} \left\{ \frac{\partial \psi_y}{\partial t} + \psi_y \psi_{xy} - \psi_x \psi_{yy} \right\} + \frac{\partial \rho}{\partial x} \left\{ \frac{\partial \psi_x}{\partial t} + \psi_y \psi_{xx} - \psi_x \psi_{xy} \right\} \\ &+ \rho \left\{ \frac{\partial}{\partial t} \nabla^2 \psi + \left(\psi_y \frac{\partial}{\partial x} - \psi_x \frac{\partial}{\partial y} \right) \nabla^2 \psi \right\} \\ &= \left(\frac{\partial^2}{\partial y^2} - \frac{\partial^2}{\partial x^2} \right) \{\mu(\psi_{yy} - \psi_{xx})\} + \frac{\partial^2}{\partial x \partial y} (4\mu \psi_{xy}) + g_x \frac{\partial \rho}{\partial y} - g_y \frac{\partial \rho}{\partial x} \end{aligned} \quad (6.7.3)$$

Equation (6.7.3) is a single partial differential equation for the stream function of the flow. If viscosity and density can be considered constant, (6.7.3) simplifies to

$$\begin{aligned} & \rho \frac{\partial}{\partial t} \nabla^2 \psi + \rho \left(\psi_y \frac{\partial}{\partial x} - \psi_x \frac{\partial}{\partial y} \right) \nabla^2 \psi \\ &= \mu \left(\frac{\partial^2}{\partial y^2} - \frac{\partial^2}{\partial x^2} \right) (\psi_{yy} - \psi_{xx}) + 4\mu \psi_{xyyy} \end{aligned} \quad (6.7.4)$$

In two-dimensional incompressible flow the stream function is related to the z -component of the vorticity ζ_z by

$$\zeta_z = -\nabla^2 \psi \quad (6.7.5)$$

We can use (6.7.5) to rewrite (6.7.3) in the form

$$\begin{aligned} & \frac{\partial \rho}{\partial y} \left\{ \frac{\partial \psi_y}{\partial t} + \psi_y \psi_{xy} - \psi_x \psi_{yy} \right\} + \frac{\partial \rho}{\partial x} \left\{ \frac{\partial \psi_x}{\partial t} + \psi_y \psi_{xx} - \psi_x \psi_{xy} \right\} \\ & - \rho \left\{ \frac{\partial \zeta_z}{\partial t} + \psi_y \frac{\partial \zeta_z}{\partial x} - \psi_x \frac{\partial \zeta_z}{\partial y} \right\} \\ &= -\nabla^2 (\mu \zeta_z) - 2 \frac{\partial^2 \mu}{\partial x^2} \psi_{yy} - 2 \frac{\partial^2 \mu}{\partial y^2} \psi_{xx} + 4 \frac{\partial^2 \mu}{\partial x \partial y} \psi_{xy} + g_x \frac{\partial \rho}{\partial y} - g_y \frac{\partial \rho}{\partial x} \end{aligned} \quad (6.7.6)$$

6.8 Thermodynamics

Before explicitly considering conservation of energy, it is necessary to introduce some concepts from thermodynamics. The equilibrium thermodynamic state of any material can be constrained if any two state variables are specified. Examples of state variables include the pressure p and specific volume $v = 1/\rho$, as well as the temperature T . The equation of state is defined as the general relationship between these three variables:

$$f(p, v, T) = 0 \quad (6.8.1)$$

Every material has an equation of state.

It is often useful to introduce the coefficient of thermal expansion or thermal expansivity of a material defined by

$$\alpha = \frac{1}{v} \left(\frac{\partial v}{\partial T} \right)_p = -\frac{1}{\rho} \left(\frac{\partial \rho}{\partial T} \right)_p \quad (6.8.2)$$

This is the percentage increase in volume of a material per degree of temperature increase; the subscript p means that the pressure is held fixed. Similarly, the isothermal compressibility of a material is defined by

$$\chi_T = -\frac{1}{v} \left(\frac{\partial v}{\partial p} \right)_T = \frac{1}{\rho} \left(\frac{\partial \rho}{\partial p} \right)_T \quad (6.8.3)$$

This is the percentage increase in density per unit change in pressure at constant temperature. Both the coefficient of thermal expansion and the isothermal compressibility can be obtained from the equation of state.

Another important state variable is the specific internal energy e (internal energy per unit mass). The first law of thermodynamics states that the incremental change in internal energy δe is equal to the difference between the incremental heat added to the system δq and the incremental work done by the system δw :

$$\delta e = \delta q - \delta w \quad (6.8.4)$$

If work is carried out by compression, and if the process is reversible, we can write

$$dw = p dv \quad (6.8.5)$$

The word reversible implies that the change is carried out so slowly that the material passes through a succession of equilibrium states. Thus the incremental quantity δw can be replaced with the mathematical derivative dw .

The specific heat of a material is defined as the ratio of the increment of heat added to the material δq to the change in temperature δT . The specific heat is not defined uniquely unless the process is specified. The specific heat at constant volume is defined by

$$c_v = \left(\frac{\delta q}{\delta T} \right)_v \quad (6.8.6)$$

and the specific heat at constant pressure is defined by

$$c_p = \left(\frac{\delta q}{\delta T} \right)_p \quad (6.8.7)$$

The subscripts indicate that the state variable is held constant.

The second law of thermodynamics states that, for a reversible process,

$$dq = T ds \quad (6.8.8)$$

where the specific entropy s (entropy per unit mass) is a state variable. A process without heat addition is known as an adiabatic process. If, in addition, the process is reversible it is known as an isentropic process. For an isentropic process, the entropy is a constant. The second law of thermodynamics requires that the entropy increase for an irreversible adiabatic process. From (6.8.8) and the definitions of the specific heats, (6.8.6) and (6.8.7) can be written as

$$c_v = T \left(\frac{\partial s}{\partial T} \right)_v \quad (6.8.9)$$

and

$$c_p = T \left(\frac{\partial s}{\partial T} \right)_p \quad (6.8.10)$$

for reversible processes.

Several other state variables are commonly used. Flow equations are often expressed in terms of the specific enthalpy defined by

$$h \equiv e + pv \quad (6.8.11)$$

For systems with phase changes, it is often convenient to use the specific Helmholtz free energy

$$f \equiv e - Ts \quad (6.8.12)$$

or the specific Gibbs free energy

$$g \equiv h - Ts = e + pv - Ts \quad (6.8.13)$$

The state of a material is defined by any two of its state variables.

The combination of (6.8.4), (6.8.5), and (6.8.8) gives

$$de = T ds - p dv \quad (6.8.14)$$

Equivalent expressions for the enthalpy and free energies can be derived using (6.8.11)–(6.8.13):

$$dh = T ds + v dp \quad (6.8.15)$$

$$df = -s dT - p dv \quad (6.8.16)$$

$$dg = -s dT + v dp \quad (6.8.17)$$

It is possible to write the change of one state variable in terms of changes in any two other state variables using partial derivatives, for example

$$de = \left(\frac{\partial e}{\partial T} \right)_v dT + \left(\frac{\partial e}{\partial v} \right)_T dv \quad (6.8.18)$$

From (6.8.4), (6.8.5), the definition of c_v (6.8.6), and (6.8.18) we obtain

$$c_v = \left(\frac{\partial e}{\partial T} \right)_v \quad (6.8.19)$$

From (6.8.8), (6.8.15), the definition of c_p (6.8.7), and an expression for h similar to (6.8.18) it is found that

$$c_p = \left(\frac{\partial h}{\partial T} \right)_p \quad (6.8.20)$$

Another expression for de is

$$de = \left(\frac{\partial e}{\partial s} \right)_v ds + \left(\frac{\partial e}{\partial v} \right)_s dv \quad (6.8.21)$$

The combination of (6.8.14) and (6.8.21) gives

$$\left(\frac{\partial e}{\partial s} \right)_v = T, \quad \left(\frac{\partial e}{\partial v} \right)_s = -p \quad (6.8.22)$$

Similar results obtained from (6.8.15)–(6.8.17) are

$$\left(\frac{\partial h}{\partial s} \right)_p = T, \quad \left(\frac{\partial h}{\partial p} \right)_s = v \quad (6.8.23)$$

$$\left(\frac{\partial f}{\partial T} \right)_v = -s, \quad \left(\frac{\partial f}{\partial v} \right)_T = -p \quad (6.8.24)$$

$$\left(\frac{\partial g}{\partial T} \right)_p = -s, \quad \left(\frac{\partial g}{\partial p} \right)_T = v \quad (6.8.25)$$

The second partial derivatives of u , h , f , and g with respect to any pair of variables are independent of the order of differentiation. It then follows from (6.8.22)–(6.8.25) that

$$\left(\frac{\partial s}{\partial p} \right)_v = - \left(\frac{\partial v}{\partial T} \right)_s \quad (6.8.26)$$

$$\left(\frac{\partial s}{\partial v} \right)_p = \left(\frac{\partial p}{\partial T} \right)_s \quad (6.8.27)$$

$$\left(\frac{\partial s}{\partial v} \right)_T = \left(\frac{\partial p}{\partial T} \right)_v \quad (6.8.28)$$

$$\left(\frac{\partial s}{\partial p} \right)_T = - \left(\frac{\partial v}{\partial T} \right)_p \quad (6.8.29)$$

These are known as the Maxwell relations.

A useful thermodynamic variable introduced in Chapter 3 is the adiabatic compressibility χ_a , the percentage increase in density per unit change in pressure at constant entropy. It is given by

$$\chi_a \equiv -\frac{1}{v} \left(\frac{\partial v}{\partial p} \right)_s = \frac{1}{\rho} \left(\frac{\partial \rho}{\partial p} \right)_s \quad (6.8.30)$$

The reciprocal of the adiabatic compressibility is the adiabatic bulk modulus K_a , also introduced in Chapter 3:

$$K_a \equiv \frac{1}{\chi_a} \quad (6.8.31)$$

Similarly, the isothermal bulk modulus K_T is the reciprocal of χ_T :

$$K_T \equiv \frac{1}{\chi_T} \quad (6.8.32)$$

It is straightforward to show from the thermodynamic relations above that

$$\frac{\chi_T}{\chi_a} = \frac{c_p}{c_v} \quad (6.8.33)$$

In addition, it can be shown that

$$c_p = c_v + \frac{\alpha^2 T K_T}{\rho} \quad (6.8.34)$$

6.9 Conservation of Energy

We can now apply the second law of thermodynamics (6.8.8) to an elemental parcel of fluid in order to derive an equation for the conservation of energy. The thermal energy equation is

$$\rho T \frac{Ds}{Dt} = \tau_{ij} \frac{\partial u_i}{\partial x_j} + \frac{\partial}{\partial x_i} \left(k \frac{\partial T}{\partial x_i} \right) + \rho H \quad (6.9.1)$$

where k is the thermal conductivity and H is the rate of internal heat production per unit mass. The terms on the right side of (6.9.1) are, respectively, volumetric heat production rates due to viscous dissipation, thermal conduction, and internal heat generation. In writing (6.9.1) it is assumed that Fourier's law of heat conduction for an isotropic medium is applicable:

$$q_i = -k \frac{\partial T}{\partial x_i} \quad (6.9.2)$$

where q_i is the heat flux vector.

The viscous dissipation term in (6.9.1) is often denoted by Φ , the dissipation function:

$$\Phi \equiv \tau_{ij} \frac{\partial u_i}{\partial x_j} \quad (6.9.3)$$

We can evaluate the dissipation function for a Newtonian fluid by substituting (6.5.4) in (6.9.3) to obtain

$$\Phi = k_B \left(\frac{\partial u_i}{\partial x_i} \right)^2 + 2\mu \left\{ \frac{1}{2} \left(\frac{\partial u_i}{\partial x_j} + \frac{\partial u_j}{\partial x_i} \right) - \frac{1}{3} \left(\frac{\partial u_k}{\partial x_k} \right) \delta_{ij} \right\}^2 \quad (6.9.4)$$

where k_B is the bulk viscosity $\lambda + \frac{2}{3}\mu$ given in (6.5.3). The bulk viscosity leads to dissipation due to volume changes in a deforming fluid. The dynamic viscosity μ leads to dissipation through shear; there are no volume changes associated with the tensor $e_{ij} - \delta_{ij} (\partial u_k / \partial x_k) / 3$

in the second term on the right side of (6.9.4). Both bulk viscosity and dynamic viscosity are positive quantities and the heat generated by viscous dissipation is always positive, as can be seen from (6.9.4). For a Stokesian fluid, $k_B = 0$ and there is no viscous dissipation associated with compression and expansion.

The thermal energy equation (6.9.1) can be written in a number of alternate forms. We can express the time rate of change of the specific entropy following an elemental fluid parcel Ds/Dt by

$$\frac{Ds}{Dt} = \left(\frac{\partial s}{\partial T} \right)_p \frac{DT}{Dt} + \left(\frac{\partial s}{\partial p} \right)_T \frac{Dp}{Dt} \quad (6.9.5)$$

The partial derivatives appearing in (6.9.5) can be written in terms of well-known thermodynamic quantities using (6.8.2), (6.8.10), and (6.8.29) with the result

$$\frac{Ds}{Dt} = \frac{c_p}{T} \frac{DT}{Dt} - \frac{\alpha}{\rho} \frac{Dp}{Dt} \quad (6.9.6)$$

Substitution of (6.9.6) into (6.9.1) yields a new form of the thermal energy equation given by

$$\rho c_p \frac{DT}{Dt} - \alpha T \frac{Dp}{Dt} = \frac{\partial}{\partial x_i} \left(k \frac{\partial T}{\partial x_i} \right) + \Phi + \rho H \quad (6.9.7)$$

Other forms of the thermal energy equation listed below can be obtained by similar manipulations of the thermodynamic relationships

$$\rho \frac{De}{Dt} + p \frac{\partial u_i}{\partial x_i} = \frac{\partial}{\partial x_i} \left(k \frac{\partial T}{\partial x_i} \right) + \Phi + \rho H \quad (6.9.8)$$

$$\rho \frac{Dh}{Dt} - \frac{Dp}{Dt} = \frac{\partial}{\partial x_i} \left(k \frac{\partial T}{\partial x_i} \right) + \Phi + \rho H \quad (6.9.9)$$

$$\rho c_v \frac{DT}{Dt} - \frac{\alpha T}{\chi_T \rho^2} \frac{D\rho}{Dt} = \frac{\partial}{\partial x_i} \left(k \frac{\partial T}{\partial x_i} \right) + \Phi + \rho H \quad (6.9.10)$$

$$c_v T \frac{D}{Dt} (\ln T \rho^{-\gamma}) = \frac{\partial}{\partial x_i} \left(k \frac{\partial T}{\partial x_i} \right) + \Phi + \rho H \quad (6.9.11)$$

In (6.9.11) the quantity γ is the Grüneisen ratio defined by

$$\gamma \equiv \frac{\alpha}{\rho c_v \chi_T} = \frac{\alpha}{\rho c_p \chi_a} \quad (6.9.12)$$

For an incompressible fluid $D\rho/Dt = 0$, and the thermal energy equation takes the simple form (obtained from (6.9.10))

$$\rho c_v \frac{DT}{Dt} = \frac{\partial}{\partial x_i} \left(k \frac{\partial T}{\partial x_i} \right) + \Phi + \rho H \quad (6.9.13)$$

If the fluid is Newtonian as well as incompressible, Φ in (6.9.13) simplifies to (from (6.9.4) with $\partial u_i / \partial x_i = 0$)

$$\Phi = \frac{\mu}{2} \left(\frac{\partial u_i}{\partial x_j} + \frac{\partial u_j}{\partial x_i} \right)^2 \quad (6.9.14)$$

For a compressible fluid, the left side of (6.9.7) has an interesting interpretation; it can be written as

$$\rho c_p \left(\frac{DT}{Dt} - \frac{\alpha T}{\rho c_p} \frac{Dp}{Dt} \right)$$

From (6.8.2), (6.8.10), and (6.8.27) we can derive

$$\frac{\alpha T}{\rho c_p} = \left(\frac{\partial T}{\partial p} \right)_s \quad (6.9.15)$$

so that the thermal energy equation (6.9.7) can be rewritten as

$$\rho c_p \left(\frac{DT}{Dt} - \left(\frac{\partial T}{\partial p} \right)_s \frac{Dp}{Dt} \right) = \frac{\partial}{\partial x_i} \left(k \frac{\partial T}{\partial x_i} \right) + \Phi + \rho H \quad (6.9.16)$$

The thermodynamic quantity $(\partial T / \partial p)_s$ is the adiabatic derivative of temperature with respect to pressure, and the quantity in parentheses on the left of (6.9.16) is the time rate of change of a fluid element's temperature relative to the time rate of change of the temperature due to adiabatic compression or expansion. In the absence of other sources of heat, a fluid element would undergo changes in temperature by cooling adiabatically upon a decrease in pressure or heating adiabatically upon an increase in pressure according to

$$\left(\frac{DT}{Dt} \right)_s = \left(\frac{\partial T}{\partial p} \right)_s \frac{Dp}{Dt} = \frac{\alpha T}{\rho c_p} \frac{Dp}{Dt} \quad (6.9.17)$$

The energy for heating the fluid element upon compression derives from the work done by pressure forces on decreasing the element's volume. Similarly, the pressure work an element does against its surroundings on increasing its volume derives from the element's internal energy and the element cools.

The adiabatic temperature gradient can be obtained by combining (6.9.17) and the hydrostatic relation

$$\frac{\partial p}{\partial x_i} = \rho g_i \quad (6.9.18)$$

with the result

$$\left(\frac{\partial T}{\partial x_i} \right)_s = \frac{\alpha T g_i}{c_p} \quad (6.9.19)$$

It is sometimes useful to calculate how the kinetic energy ($u^2/2$ per unit mass) of an element of fluid changes with time. This can be done from the so-called mechanical energy equation, i.e., the scalar product of the conservation of momentum equation (6.4.1) with the velocity vector

$$\rho \frac{Du^2/2}{Dt} = -u_i \frac{\partial p}{\partial x_i} + \rho u_i g_i + u_i \frac{\partial \tau_{ij}}{\partial x_j} \quad (6.9.20)$$

The work done by the body force and the work done by the net surface force acting on a fluid element go directly into changing the kinetic energy of an element. From (6.9.8) it is seen that reversible $p \, dv$ work, heat conduction, viscous dissipation, and internal heating go directly into changing the internal thermal energy of a fluid element. The mechanical energy equation (6.9.20) does not represent an independent energy equation since it is derived from conservation of momentum. Section 6.16 gives the forms of the energy equation in Cartesian, cylindrical, and spherical polar coordinates.

6.10 Approximate Equations

With the exception of simplifications associated with rheology (e.g., Newtonian viscous behavior), the equations of the previous sections are completely general. However, when the equations are applied to thermal convection in the Earth's mantle, they can be considerably simplified. In this section we derive the approximate forms of the equations for conservation of momentum and energy appropriate to mantle convection.

A major source of simplification of the basic equations derives from the equation of state of mantle rocks. The density of the mantle is mainly a function of temperature and pressure $\rho = \rho(T, p)$, although there are significant density changes associated with phase transitions such as olivine–spinel and spinel–perovskite plus magnesiowüstite. There may also be important changes in mantle density due to variations in chemical composition, though the existence of compositional density changes in the mantle is uncertain. Here, we consider ρ only to be a function of T and p .

Most of the density change in the mantle is due to hydrostatic compression. The mantle density increases by approximately 65% between the surface and the core–mantle boundary. Density changes associated with the temperature and pressure variations accompanying convection are small compared to the spherically averaged density of the mantle. It is therefore appropriate to assume a linearized equation of state for mantle density of the form

$$\begin{aligned}\rho &= \bar{\rho}(\bar{T}, \bar{p}) + \rho' \\ &= \bar{\rho}(\bar{T}, \bar{p}) + \overline{\left(\frac{\partial \rho}{\partial p}\right)}_T p' + \overline{\left(\frac{\partial \rho}{\partial T}\right)}_p T' \\ &= \bar{\rho}(\bar{T}, \bar{p}) + \bar{\rho} \bar{\chi}_T p' - \bar{\alpha} \bar{\rho} T'\end{aligned}\quad (6.10.1)$$

where the overbar refers to a reference state and the primes to departures from it:

$$T = \bar{T} + T', \quad p = \bar{p} + p' \quad (6.10.2)$$

Note that the departures, the primed quantities, are not necessarily small.

It is convenient to take the reference state as motionless and steady. For simplicity, it is also generally assumed that the reference state varies with only one spatial variable, e.g., radius r in spherical models or depth in Cartesian models. The reference state pressure thus satisfies the static form of (6.4.1):

$$0 = -\frac{\partial \bar{p}}{\partial x_i} + \bar{\rho} \bar{g}_i \quad (6.10.3)$$

In (6.10.3), the acceleration of gravity \bar{g}_i in the reference state may be a function of position.

Because the bulk of a vigorously convecting system is approximately adiabatic, it is convenient to choose the reference state temperature to be adiabatic. The determination of the reference state requires the integration of (6.10.3), the hydrostatic equation, and (6.9.19), the equation for the adiabatic temperature gradient, and specification of the reference state equation of state $\bar{\rho} = \bar{\rho}(\bar{T}, \bar{p})$. For the moment, we bypass the details of the calculation of the reference state but offer a few additional comments.

The reference state is a mathematical device that facilitates the consideration of the basic equations. It need not actually exist. Specification of the reference state needs to be done with considerable care, especially when account is taken of mantle compressibility. Not only must the equation of state $\rho = \rho(p, T)$ be specified, but all the necessary thermodynamic

variables such as α , c_p , γ , χ_T , etc., must also be given (or determined) in a thermodynamically self-consistent way. There are instances in the literature when this is not done carefully enough. For example, thermodynamic variables are often indiscriminately assumed to be constants, ignoring thermodynamic constraints that preclude such assumptions. One of these constraints, derivable from (6.8.32), (6.8.34) and (6.9.12), is

$$\frac{c_p}{c_v} = 1 + \alpha\gamma T \quad (6.10.4)$$

It is therefore thermodynamically inconsistent to take the specific heats, α and the Grüneisen parameter γ , as constants in a reference state or a convecting state with varying temperature. Other thermodynamic constraints, obtainable by considering the differential relations $d\rho = (\rho/K_T) dp - \alpha\rho dT$ and $d\rho = -(\alpha T\rho/c_p) ds + \rho\chi_a dp$, are

$$\frac{1}{K_T^2} \left(\frac{\partial K_T}{\partial T} \right)_p = \left(\frac{\partial \alpha}{\partial p} \right)_T \quad (6.10.5)$$

$$\frac{\alpha^2}{\rho c_p} = \frac{\alpha}{c_p} \left(\frac{\partial c_p}{\partial p} \right)_s - \left(\frac{\partial \alpha}{\partial p} \right)_s - \frac{c_p}{T} \left(\frac{\partial \chi_a}{\partial s} \right)_p \quad (6.10.6)$$

Relations such as (6.10.5) and (6.10.6) and others place constraints on assumptions that can be made about the constancy or p , T dependences of thermodynamic variables.

With these words of caution about the reference state in mind, we return to the simplifications that occur when the basic equations are applied to mantle convection. The simplifications can be most readily demonstrated if scaling factors are introduced to nondimensionalize the equations. We first consider the linearized equation of state for the density in the convecting state (6.10.1) and nondimensionalize the equation with the scaling factors ρ_r (a representative density in the convecting state), ΔT_r (a characteristic temperature difference driving thermal convection), and χ_{T_r} and α_r (representative values of χ_T and α). We also need a scale for the dynamic pressure variations p' which we obtain by assuming comparability of pressure and viscous forces; if u_r is a velocity scale, then the scale for p' is $p_r = \mu_r u_r / b$, where μ_r is a representative viscosity and b is the depth of the convecting region. For a velocity scale we choose $u_r = k_r / \rho_r c_{p_r} b$, where k_r and c_{p_r} are characteristic values of k and c_p . Thus the pressure scale is $p_r = \mu_r k_r / \rho_r c_{p_r} b^2$. With these scaling factors, we introduce the dimensionless variables (denoted with an asterisk) $T'^* = T' / \Delta T_r$, $\rho^* = \rho / \rho_r$, $p'^* = (p' b^2 \rho_r c_{p_r}) / (\mu_r k_r)$, $u_i^* = (u_i b \rho_r c_{p_r}) / k_r$, $x_i^* = x_i / b$, $t^* = (t k_r) / (b^2 \rho_r c_{p_r})$, $\bar{\chi}_T^* = \chi_{T_r} / \chi_{T_r}$, $\bar{\alpha}^* = \bar{\alpha} / \alpha_r$.

In terms of these variables we rewrite (6.10.1) as

$$\frac{\rho^*}{\bar{\rho}^*} = 1 + \bar{\chi}_T^* p'^* M^2 Pr - \bar{\alpha}^* T'^* \epsilon \quad (6.10.7)$$

where

$$M^2 = \frac{k_r \chi_{T_r}}{\rho_r c_{p_r}^2 b^2}, \quad Pr = \frac{\mu_r c_{p_r}}{k_r}, \quad \epsilon = \alpha_r \Delta T_r \quad (6.10.8)$$

The dimensionless parameter Pr is the Prandtl number or the ratio of momentum diffusivity $\nu_r = \mu_r / \rho_r$ (ν_r is the kinematic viscosity) to thermal diffusivity $\kappa_r = k_r / \rho_r c_{p_r}$. For the mantle, μ_r is about 10^{21} Pa s, k_r is about $4 \text{ W m}^{-1} \text{ K}^{-1}$, and c_{p_r} is approximately

$1 \text{ kJ kg}^{-1} \text{ K}^{-1}$; these combine to give $Pr \approx 2.5 \times 10^{23}$. The Prandtl number of the Earth's mantle is essentially infinite. The dimensionless parameter ϵ is the fractional density change of mantle rocks due to temperature variations typical of those driving convection. The adiabatic increase of temperature with depth in the mantle does not contribute to the thermal drive for convection; only nonadiabatic temperature variations comprise ΔT_r . The magnitude of ΔT_r is 10^3 K ; it is determined in part by the rate of internal heating H , but it is also dependent on the heating of the mantle from below (from the core) and other properties of the mantle (e.g., viscosity) that fix the thermal regime of the convecting state. With α about equal to $3 \times 10^{-5} \text{ K}^{-1}$, ϵ is 3×10^{-2} . The dimensionless parameter M^2 measures the influence of compressibility; it is the ratio of the square of the characteristic velocity $k_r^2/\rho_r^2 c_{p_r}^2 b^2$ to the square of the mantle sound speed $1/\rho_r \chi_{a_r}$ (aside from the order unity factor χ_{T_r}/χ_{a_r}). In gas dynamics the ratio of the characteristic velocity to the sound speed is known as the Mach number. For the mantle, $\rho_r \approx 4,000 \text{ kg m}^{-3}$, $b \approx 3 \times 10^6 \text{ m}$, and χ_{T_r} is about $3 \times 10^{-12} \text{ Pa}^{-1}$. The value of M^2 for the mantle is thus about 10^{-33} and $M^2 Pr$ is 2×10^{-10} . Even if a typical mantle convective velocity of 10 mm yr^{-1} is used to estimate M^2 according to $(\text{mantle velocity})^2 \rho_r \chi_{T_r}$, M^2 is still so small that $M^2 Pr \ll 1$.

If the dimensionless quantities $\bar{\chi}_T^*$, $\bar{\alpha}^*$, p'^* , and T'^* in (6.10.7) are order unity or smaller, then density perturbations due to mantle convection are small compared to the reference hydrostatic density of the mantle, i.e., $\rho'/\bar{\rho} \ll 1$ because both ϵ and $M^2 Pr$ are much less than unity.

The conservation of mass equation (6.2.1) can be scaled and put in dimensionless form for application to the mantle by using the dimensionless linearized equation of state (6.10.7) and the dimensionless variables introduced above. The dimensionless conservation of mass equation becomes

$$\begin{aligned} & \bar{\rho}^* \bar{\chi}_T^* M^2 Pr \frac{\partial p'^*}{\partial t^*} - \bar{\alpha}^* \bar{\rho}^* \epsilon \frac{\partial T'^*}{\partial t^*} \\ & + \frac{\partial}{\partial x_i^*} \left[\{ \bar{\rho}^* + \bar{\rho}^* \bar{\chi}_T^* p'^* M^2 Pr - \bar{\rho}^* \bar{\alpha}^* \epsilon T'^* \} u_i^* \right] = 0 \end{aligned} \quad (6.10.9)$$

In the limit $\epsilon \rightarrow 0$ and $M^2 Pr \rightarrow 0$, (6.10.9) reduces to

$$\frac{\partial}{\partial x_i^*} (\bar{\rho}^* u_i^*) = 0 \quad (6.10.10)$$

Equation (6.10.10) is known as the anelastic conservation of mass equation (Ogura and Phillips, 1962; Gough, 1969). It is the appropriate form of mass conservation for mantle convection. The neglect of the term $\partial \rho'/\partial t$ in the anelastic mass conservation equation eliminates seismic waves from the set of equations governing mantle convection. Dynamically, phenomena in seismology and mantle convection do not overlap; they occur on vastly different time scales (seconds or minutes compared with millions of years and longer). The validity of the anelastic mass conservation equation requires

$$\epsilon \ll 1, \quad M^2 Pr \ll 1 \quad (6.10.11)$$

In dimensional form the anelastic mass conservation equation is

$$\frac{\partial}{\partial x_i} (\bar{\rho} u_i) = 0 \quad (6.10.12)$$

The anelastic approximation (6.10.11) has also been referred to as the liquid anelastic approximation by Jarvis and McKenzie (1980). The scaling factors adopted above implicitly assume that we are dealing with a liquid and not a gas.

For a model of the mantle in which $\bar{\rho}$ does not change appreciably with depth (recall that $\bar{\rho}$ increases by about 65% with depth across the mantle), the mass conservation equation appropriate to the model is the incompressible continuity equation $\partial u_i / \partial x_i = 0$. This incompressible form of the mass conservation equation is adopted in the Boussinesq approximation (Spiegel and Veronis, 1960; Mihaljan, 1962) of mantle convection discussed more fully below.

The condition necessary for the anelastic mass conservation equation to reduce to the incompressible continuity equation can be obtained by considering the change in $\bar{\rho}$ with depth in an adiabatic model of the mantle. The gradient of density in such a model $\partial \bar{\rho} / \partial x_i$ is given by $(d\rho/dp)_s \partial \bar{p} / \partial x_i$. From (6.8.30) this is $(\bar{\rho} \bar{\chi}_a) \partial \bar{\rho} / \partial x_i$. With the help of the hydrostatic relation (6.10.3) the gradient of the reference state density equals

$$\frac{\partial \bar{\rho}}{\partial x_i} = \bar{\rho}^2 \bar{\chi}_a \bar{g}_i \quad (6.10.13)$$

The length scale characterizing the increase of reference state density with depth is the local density scale height \bar{h}_d defined by

$$\bar{h}_d \equiv \left\{ \frac{1}{\bar{\rho}} \left| \frac{\partial \bar{\rho}}{\partial x_i} \right| \right\}^{-1} \quad (6.10.14)$$

From (6.10.13) and (6.9.12) \bar{h}_d is found to be

$$\bar{h}_d = (\bar{\rho} \bar{\chi}_a \bar{g})^{-1} = \frac{\bar{\gamma} \bar{c}_p}{\bar{\alpha} \bar{g}} \quad (6.10.15)$$

The change in $\bar{\rho}$ across the model mantle will be small if

$$\frac{b}{\bar{h}_d} = \frac{\bar{\alpha}^* \bar{g}^*}{\bar{\gamma}^* \bar{c}_p^*} \left(\frac{a_r g_r b}{\gamma_r c_{p_r}} \right) \ll 1 \quad (6.10.16)$$

On the assumption that the scaled quantities are order unity, b/\bar{h}_d is small if

$$\frac{1}{\gamma_r} \frac{\alpha_r g_r b}{c_{p_r}} \ll 1 \quad (6.10.17)$$

The quantity $\alpha_r g_r b / c_{p_r}$ is known as the dissipation number D :

$$D \equiv \frac{\alpha_r g_r b}{c_{p_r}} \quad (6.10.18)$$

From (6.10.16), the dissipation number divided by the Grüneisen parameter is thus the ratio of the thickness of the model mantle to the density scale height of the mantle (ignoring depth variations in \bar{h}_d).

The validity of the incompressible mass conservation equation requires $D/\gamma_r \ll 1$ in addition to (6.10.11). For the whole mantle, D is about 0.5, the Grüneisen parameter is about 1, and the incompressible mass conservation equation is only approximately valid in

studies of mantle convection. Nevertheless, because of its simplicity, and because effects of compressibility are not dramatic in mantle convection, the incompressible mass conservation equation is often adopted.

The dimensionless and scaled Navier–Stokes equation, from (6.5.7) and (6.10.7), is

$$\begin{aligned} \frac{1}{Pr} \left\{ \bar{\rho}^* + \bar{\rho}^* \bar{\chi}_T^* M^2 P r p'^* - \bar{\rho}^* \bar{\alpha}^* \epsilon T'^* \right\} \frac{D u_i^*}{D t^*} = & - \frac{\partial p'^*}{\partial x_i^*} + \bar{g}_i^* \bar{\rho}^* \bar{\chi}_T^* p'^* \frac{D c_{p_r}}{\gamma_r c_{v_r}} \\ & - \bar{g}_i^* \bar{\rho}^* \bar{\alpha}^* T'^* Ra + \frac{\partial}{\partial x_j^*} \left\{ \mu^* \left(\frac{\partial u_i^*}{\partial x_j^*} + \frac{\partial u_j^*}{\partial x_i^*} - \frac{2}{3} \delta_{ij} \frac{\partial u_k^*}{\partial x_k^*} \right) \right\} \end{aligned} \quad (6.10.19)$$

The variations in the acceleration of gravity due to convection have been assumed to be negligible. The reference state pressure gradient has been eliminated from (6.10.19) with the aid of the hydrostatic equation (6.10.3). In (6.10.19), the dimensionless parameter Ra is the Rayleigh number, defined by

$$Ra \equiv \frac{\alpha_r \Delta T_r \rho_r^2 g_r b^3 c_{p_r}}{\mu_r k_r} \quad (6.10.20)$$

The Rayleigh number multiplies the buoyancy force term in (6.10.19) associated with temperature variations, the major driving force for thermal convection; accordingly, Ra is the principal dimensionless parameter controlling the vigor of convection.

The left side of (6.10.19) is inversely proportional to the Prandtl number whose value for the mantle we have estimated to be about 10^{23} . It is therefore justified to neglect the inertial force in the Navier–Stokes equation for the mantle. In the anelastic approximation, the Navier–Stokes equation takes the dimensionless form

$$\begin{aligned} 0 = & - \frac{\partial p'^*}{\partial x_i^*} + g_i^* \bar{\rho}^* \bar{\chi}_T^* p'^* \frac{D c_{p_r}}{\gamma_r c_{v_r}} - \bar{g}_i^* \bar{\rho}^* \bar{\alpha}^* T'^* Ra \\ & + \frac{\partial}{\partial x_j^*} \left\{ \mu^* \left(\frac{\partial u_i^*}{\partial x_j^*} + \frac{\partial u_j^*}{\partial x_i^*} - \frac{2}{3} \delta_{ij} \frac{\partial u_k^*}{\partial x_k^*} \right) \right\} \end{aligned} \quad (6.10.21)$$

and the dimensional form

$$0 = - \frac{\partial p'}{\partial x_i} + \bar{\rho} \bar{g}_i (\bar{\chi}_T p' - \bar{\alpha} T') + \frac{\partial}{\partial x_j} \left\{ \mu \left(\frac{\partial u_i}{\partial x_j} + \frac{\partial u_j}{\partial x_i} - \frac{2}{3} \delta_{ij} \frac{\partial u_k}{\partial x_k} \right) \right\} \quad (6.10.22)$$

We have seen that the validity of the incompressible mass conservation equation adopted in the Boussinesq approximation requires $D/\gamma_r \rightarrow 0$. If we take this limit in (6.10.21) and use $\partial u_k^*/\partial x_k^* = 0$ and $\bar{\rho}^* = \bar{\alpha}^* = 1$ we get the dimensionless form of the Navier–Stokes equation in the Boussinesq approximation

$$0 = - \frac{\partial p'^*}{\partial x_i^*} - \bar{g}_i^* T'^* Ra + \frac{\partial}{\partial x_j^*} \left\{ \mu^* \left(\frac{\partial u_i^*}{\partial x_j^*} + \frac{\partial u_j^*}{\partial x_i^*} \right) \right\} \quad (6.10.23)$$

The dimensional form of (6.10.23) is

$$0 = - \frac{\partial p'}{\partial x_i} - \bar{\rho} \bar{g}_i \bar{\alpha} T' + \frac{\partial}{\partial x_j} \left\{ \mu \left(\frac{\partial u_i}{\partial x_j} + \frac{\partial u_j}{\partial x_i} \right) \right\} \quad (6.10.24)$$

with $\bar{\rho}$ and $\bar{\alpha}$ constant. In the Boussinesq approximation the buoyancy force term arises only from the density variations due to temperature variations. In the anelastic approximation there is also a buoyancy force term associated with pressure-induced density variations.

The scaled and nondimensional energy equation (6.9.7) is

$$\begin{aligned} & \left\{ \bar{\rho}^* + \bar{\rho}^* \bar{\chi}_T^* M^2 Pr p'^* - \bar{\rho}^* \bar{\alpha}^* \epsilon T'^* \right\} (\bar{c}_p^*) \frac{D}{Dt^*} (\bar{T}^* + T'^*) \\ & - \bar{\alpha}^* (\bar{T}^* + T'^*) \frac{Dp'^*}{Dt^*} \frac{\epsilon D}{Ra} - \bar{\alpha}^* (\bar{T}^* + T'^*) \bar{g}_i^* u_i^* \bar{\rho}^* D \\ & = \frac{\partial}{\partial x_i^*} \left\{ \bar{k}^* \frac{\partial}{\partial x_i^*} (\bar{T}^* + T'^*) \right\} + \Phi^* \frac{D}{Ra} \\ & + (\bar{\rho}^* + \bar{\rho}^* \bar{\chi}_T^* M^2 Pr p'^* - \bar{\rho}^* \bar{\alpha}^* \epsilon T'^*) H^* \left(\frac{b^2 H_r \rho_r}{k_r \Delta T_r} \right) \end{aligned} \quad (6.10.25)$$

In deriving (6.10.25) a representative internal heating rate H_r has been introduced. The quantity $b^2 H_r \rho_r / k_r \Delta T_r$ that appears in the last term of (6.10.25) is the ratio of a characteristic temperature difference associated with internal heat production $b^2 H_r \rho_r / k_r$ to the applied temperature difference ΔT_r . If the Rayleigh number in (6.10.20) is multiplied by $b^2 H_r \rho_r / k_r \Delta T_r$, one obtains an internal heating Rayleigh number Ra_H given by

$$Ra_H = \frac{\alpha_r \rho_r^3 g_r b^5 c_{p_r} H_r}{\mu_r k_r^2} \quad (6.10.26)$$

The internal heating Rayleigh number measures the contribution of internal heat production to the determination of convective vigor.

To obtain the anelastic form of the energy equation we take the limit $M^2 Pr \rightarrow 0$ and $\epsilon \rightarrow 0$. Equation (6.10.25) becomes

$$\begin{aligned} & \bar{\rho}^* \bar{c}_p^* \frac{D}{Dt^*} (\bar{T}^* + T'^*) - \bar{\alpha}^* (\bar{T}^* + T'^*) \bar{g}_i^* u_i^* \bar{\rho}^* D \\ & = \frac{\partial}{\partial x_i^*} \left\{ \bar{k}^* \frac{\partial}{\partial x_i^*} (\bar{T}^* + T'^*) \right\} + \Phi^* \frac{D}{Ra} + \bar{\rho}^* H^* \left(\frac{b^2 H_r \rho_r}{k_r \Delta T_r} \right) \end{aligned} \quad (6.10.27)$$

Equation (6.10.27) can be simplified further using

$$\bar{\rho}^* \bar{c}_p^* \frac{D\bar{T}^*}{Dt^*} = \bar{\rho}^* \bar{c}_p^* u_i^* \frac{\partial \bar{T}^*}{\partial x_i^*} = \bar{\rho}^* \bar{\alpha}^* \bar{T}^* D \bar{g}_i^* u_i^* \quad (6.10.28)$$

In deriving the dimensionless equation (6.10.28) use is made of the fact that \bar{T} is independent of time and is assumed to be an adiabat. The adiabatic temperature gradient in dimensionless form ($\partial \bar{T}^* / \partial x_i^*$ in (6.10.27)) is $\bar{\alpha}^* \bar{T}^* D \bar{g}_i^* / \bar{c}_p^*$. The anelastic form of the energy equation becomes

$$\begin{aligned} & \bar{\rho}^* \bar{c}_p^* \frac{DT'^*}{Dt^*} - T'^* \bar{\alpha}^* \bar{g}_i^* u_i^* \bar{\rho}^* D = \frac{\partial}{\partial x_i^*} \left\{ \bar{k}^* \frac{\partial}{\partial x_i^*} (\bar{T}^* + T'^*) \right\} \\ & + \Phi^* \frac{D}{Ra} + \bar{\rho}^* H^* \left(\frac{b^2 H_r \rho_r}{k_r \Delta T_r} \right) \end{aligned} \quad (6.10.29)$$

The dimensional form of the anelastic energy equation is

$$\bar{\rho} \bar{c}_p \frac{DT'}{Dt} - T' \bar{\alpha} \bar{g}_i u_i \bar{\rho} = \frac{\partial}{\partial x_i} \left\{ \bar{k} \frac{\partial}{\partial x_i} (\bar{T} + T') \right\} + \Phi + \bar{\rho} H \quad (6.10.30)$$

If \bar{k}^* , $\bar{\alpha}^*$, \bar{c}_p^* , and \bar{g}_i^* are constants, then the terms on the right sides of (6.10.29) and (6.10.30) representing heat conduction along the adiabat $\partial/\partial x_i^* (\bar{k}^* \partial \bar{T}^* / \partial x_i^*)$ and $\partial/\partial x_i (\bar{k} \partial \bar{T} / \partial x_i)$ become, respectively,

$$\frac{\partial}{\partial x_i^*} \left(\bar{k}^* \frac{\partial \bar{T}^*}{\partial x_i^*} \right) = \frac{\bar{k}^*}{\bar{c}_p^{*2}} \bar{\alpha}^{*2} D^2 \bar{g}_i^* \bar{g}_i^* \bar{T}^* \quad (6.10.31)$$

$$\frac{\partial}{\partial x_i} \left(k \frac{\partial T}{\partial x_i} \right) = \frac{\bar{k} \bar{\alpha}^2 \bar{g}^2}{\bar{c}_p^2} T \quad (6.10.32)$$

The formula for the adiabatic temperature gradient $\partial \bar{T}^* / \partial x_i^* = \bar{\alpha}^* \bar{T}^* D \bar{g}_i^* / \bar{c}_p^*$ has been used in deriving (6.10.31) and (6.10.32).

To obtain the form of the energy equation appropriate to the Boussinesq approximation, we need to take the limit of (6.10.29) as $D \rightarrow 0$. In this approximation the reference state density and specific heat are constants. The nondimensional form of the energy equation in the Boussinesq approximation is therefore

$$\bar{\rho}^* \bar{c}_p^* \frac{DT'^*}{Dt^*} = \frac{\partial}{\partial x_i^*} \left(\bar{k}^* \frac{\partial T'^*}{\partial x_i^*} \right) + \bar{\rho}^* H^* \left(\frac{b^2 H_r \rho_r}{k_r \Delta T_r} \right) \quad (6.10.33)$$

The term representing heat conduction along the adiabat in the anelastic energy equation is directly proportional to D^2 (see (6.10.31)) and in the limit $D \rightarrow 0$ vanishes from the Boussinesq approximation. In dimensional form, the energy equation in the Boussinesq approximation is

$$\bar{\rho} \bar{c}_p \frac{DT'}{Dt} = \frac{\partial}{\partial x_i} \left(\bar{k} \frac{\partial T'}{\partial x_i} \right) + \bar{\rho} H \quad (6.10.34)$$

with $\bar{\rho}$ and \bar{c}_p constant and with $\bar{T} = \text{constant}$ (since the reference state adiabat is a constant in this approximation).

In summary, the anelastic approximation requires $\epsilon \rightarrow 0$ and $M^2 Pr \rightarrow 0$. The basic equations for this approximation are given by (6.10.10) or (6.10.12), (6.10.21) or (6.10.22), and (6.10.29) or (6.10.30). The Boussinesq approximation requires $\epsilon \rightarrow 0$, $M^2 Pr \rightarrow 0$, and $D \rightarrow 0$. The basic equations for the Boussinesq approximation are (6.2.6), (6.10.23) or (6.10.24), and (6.10.33) or (6.10.34). Both approximations neglect inertial forces in the momentum equation appropriate to the limit $Pr \rightarrow \infty$. In the Boussinesq approximation, all thermodynamic variables including density are assumed constant, but a buoyancy force term due to temperature variations is included in the vertical force balance equation. Neither the anelastic approximation nor the Boussinesq approximation require the viscosity or the thermal conductivity to be constant. For convenience, we summarize the equations and dimensionless parameters below.

A. General Equations (Dimensional)

Conservation of Mass

$$\frac{1}{\rho} \frac{D\rho}{Dt} + \frac{\partial u_i}{\partial x_i} = 0 \quad (6.10.35)$$

Conservation of Momentum (Navier–Stokes Equation)

$$\rho \frac{Du_i}{Dt} = -\frac{\partial p}{\partial x_i} + \frac{\partial}{\partial x_j} \left[\mu \left(\frac{\partial u_i}{\partial x_j} + \frac{\partial u_j}{\partial x_i} - \frac{2}{3} \delta_{ij} \frac{\partial u_k}{\partial x_k} \right) \right] + \rho g_i \quad (6.10.36)$$

Conservation of Energy

$$\rho c_p \frac{DT}{Dt} - \alpha T \frac{Dp}{Dt} = \frac{\partial}{\partial x_i} \left(k \frac{\partial T}{\partial x_i} \right) + \Phi + \rho H \quad (6.10.37)$$

B. Anelastic, Infinite Prandtl Number Equations ($\epsilon \ll 1, M^2 Pr \ll 1$)

Conservation of Mass

$$\frac{\partial}{\partial x_i^*} (\bar{\rho}^* u_i^*) = 0 \quad (6.10.38)$$

$$\frac{\partial}{\partial x_i} (\bar{\rho} u_i) = 0 \quad (6.10.39)$$

Conservation of Momentum (Navier–Stokes Equation)

$$0 = -\frac{\partial p'^*}{\partial x_i^*} + g_i^* \bar{\rho}^* \bar{\chi}_T p'^* \frac{D}{\gamma_r} \frac{c_{p_r}}{c_{v_r}} - \bar{g}_i^* \bar{\rho}^* \bar{\alpha}^* T'^* Ra \\ + \frac{\partial}{\partial x_j^*} \left\{ \mu^* \left(\frac{\partial u_i^*}{\partial x_j^*} + \frac{\partial u_j^*}{\partial x_i^*} - \frac{2}{3} \delta_{ij} \frac{\partial u_k^*}{\partial x_k^*} \right) \right\} \quad (6.10.40)$$

$$0 = -\frac{\partial p'}{\partial x_i} + \bar{\rho} \bar{g}_i (\bar{\chi}_T p' - \bar{\alpha} T') + \frac{\partial}{\partial x_j} \left\{ \mu \left(\frac{\partial u_i}{\partial x_j} + \frac{\partial u_j}{\partial x_i} - \frac{2}{3} \delta_{ij} \frac{\partial u_k}{\partial x_k} \right) \right\} \quad (6.10.41)$$

Conservation of Energy

$$\bar{\rho}^* \bar{c}_p^* \frac{DT'^*}{Dt^*} - T'^* \bar{\alpha}^* \bar{g}_i^* u_i^* \bar{\rho}^* D = \frac{\partial}{\partial x_i^*} \left\{ \bar{k}^* \frac{\partial}{\partial x_i^*} (\bar{T}^* + T'^*) \right\} \\ + \Phi^* \frac{D}{Ra} + \bar{\rho}^* H^* \left(\frac{b^2 H_r \rho_r}{k_r \Delta T_r} \right) \quad (6.10.42)$$

$$\bar{\rho} \bar{c}_p \frac{DT'}{Dt} - T' \bar{\alpha} \bar{g}_i u_i \bar{\rho} = \frac{\partial}{\partial x_i} \left\{ \bar{k} \frac{\partial}{\partial x_i} (\bar{T} + T') \right\} + \Phi + \bar{\rho} H \quad (6.10.43)$$

Reference State

Motionless, steady, hydrostatic, and adiabatic

C. Boussinesq, Infinite Prandtl Number Equations ($\epsilon \ll 1, M^2 Pr \ll 1, D \ll 1$)

Conservation of Mass

$$\frac{\partial u_i^*}{\partial x_i^*} = 0 \quad (6.10.44)$$

$$\frac{\partial u_i}{\partial x_i} = 0 \quad (6.10.45)$$

Conservation of Momentum (Navier–Stokes Equation)

$$0 = -\frac{\partial p'^*}{\partial x_i^*} - \bar{g}_i^* T'^* Ra + \frac{\partial}{\partial x_j^*} \left\{ \mu^* \left(\frac{\partial u_i^*}{\partial x_j^*} + \frac{\partial u_j^*}{\partial x_i^*} \right) \right\} \quad (6.10.46)$$

$$0 = -\frac{\partial p'}{\partial x_i} - \bar{\rho} \bar{g}_i \bar{\alpha} T' + \frac{\partial}{\partial x_j} \left\{ \mu \left(\frac{\partial u_i}{\partial x_j} + \frac{\partial u_j}{\partial x_i} \right) \right\} \quad (6.10.47)$$

Conservation of Energy

$$\bar{\rho}^* \bar{c}_p^* \frac{DT'^*}{Dt^*} = \frac{\partial}{\partial x_i^*} \left(\bar{k}^* \frac{\partial T'^*}{\partial x_i^*} \right) + \bar{\rho}^* H^* \left(\frac{b^2 H_r \rho_r}{k_r \Delta T_r} \right) \quad (6.10.48)$$

$$\bar{\rho} \bar{c}_p \frac{DT'}{Dt} = \frac{\partial}{\partial x_i} \left(\bar{k} \frac{\partial T'}{\partial x_i} \right) + \bar{\rho} H \quad (6.10.49)$$

Reference State

$\bar{\rho}, \bar{c}_p, \bar{\alpha}$ are constants

D. Dimensionless Parameters

$$Pr = \text{Prandtl number} = \frac{\mu_r c_{p_r}}{k_r} \quad (6.10.50)$$

$$\epsilon = \alpha_r \Delta T_r \quad (6.10.51)$$

$$M^2 = \frac{k_r^2 \chi_{T_r}}{\rho_r c_{p_r}^2 b^2} \quad (6.10.52)$$

$$D = \text{dissipation number} = \frac{\alpha_r g_r b}{c_{p_r}} \quad (6.10.53)$$

$$Ra = \text{Rayleigh number} = \frac{\alpha_r \Delta T_r \rho_r^2 g_r b^3 c_{p_r}}{\mu_r k_r} \quad (6.10.54)$$

$$Ra_H = \text{internal heating Rayleigh number} = \frac{\alpha_r \rho_r^3 g_r b^5 c_{p_r} H_r}{\mu_r k_r^2} \quad (6.10.55)$$

6.11 Two-Dimensional (Cartesian), Boussinesq, Infinite Prandtl Number Equations

Since the incompressible mass conservation equation (6.10.45) is valid in the two-dimensional, Boussinesq, infinite Prandtl number approximation, there exists a stream function ψ as defined in (6.3.2). In addition, the stream function is related to the vorticity ζ_z by (6.7.5). The equation for the stream function can be obtained from (6.7.6) by neglecting the inertial terms on the left side of the equation. We assume that gravity points downward, in the positive y -direction, and take $g_x = 0$ and $g_y = g$ in (6.7.6). Further, in accord with (6.10.7), we replace ρg_y in (6.7.2) with $-\bar{\rho} \bar{\alpha} g T'$. Equation (6.7.6) then yields

$$0 = \nabla^2 (\mu \zeta_z) + 2 \frac{\partial^2 \mu}{\partial x^2} \psi_{yy} + 2 \frac{\partial^2 \mu}{\partial y^2} \psi_{xx} - 4 \frac{\partial^2 \mu}{\partial x \partial y} \psi_{xy} - \bar{\rho} \bar{\alpha} g \frac{\partial T'}{\partial x} \quad (6.11.1)$$

with

$$\zeta_z = -\nabla^2 \psi \quad (6.11.2)$$

Equations (6.11.1) and (6.11.2) need to be supplemented by the energy equation (6.10.49) for T' .

6.12 Reference State

In models of mantle convection based on the Boussinesq approximation, the reference state is simple to specify. The density is a constant ($\bar{\rho} = \text{constant}$) and the pressure \bar{p} can be found by integrating the hydrostatic equation (6.10.3). For a Cartesian model in which gravity points downward (the positive y -direction, with y the depth, and $y = 0$ the surface) and is constant, $\bar{g} = \bar{\rho} \bar{g} y$ (it has been assumed that the surface pressure is zero). For a spherical shell model of the mantle in which the mantle of density ρ_m surrounds a core of radius c and density ρ_c , the acceleration of gravity points radially inward and is given by

$$\begin{aligned} \bar{g}(r) &= \frac{G \bar{M}(r)}{r^2} \\ &= \frac{4}{3} \pi \rho_c G r, \quad 0 \leq r \leq c \end{aligned} \quad (6.12.1)$$

$$= \frac{4}{3} \pi G \left[r \rho_m + \frac{c^3}{r^2} (\rho_c - \rho_m) \right], \quad c \leq r \leq a \quad (6.12.2)$$

where G is the gravitational constant, r is radius (positive outward), a is the outer radius of the mantle shell, and $\bar{M}(r)$ is the mass internal to radius r (Turcotte and Schubert, 1982, p. 86). Integration of the hydrostatic equation

$$\frac{d\bar{p}}{dr} = -\bar{\rho} \bar{g}(r) \quad (6.12.3)$$

gives

$$\begin{aligned}\bar{p}(r) &= \frac{4}{3}\pi\rho_m Gc^3(\rho_c - \rho_m)\left(\frac{1}{r} - \frac{1}{a}\right) + \frac{2}{3}\pi G\rho_m^2(a^2 - r^2), \quad c \leq r \leq a \\ &= \frac{2}{3}\pi G\rho_c^2(c^2 - r^2) + \frac{2}{3}\pi G\rho_m^2(a^2 - c^2) \\ &\quad + \frac{4}{3}\pi\rho_m Gc^3(\rho_c - \rho_m)\left(\frac{1}{c} - \frac{1}{a}\right), \quad 0 \leq r \leq c\end{aligned}\quad (6.12.4)$$

where it has been assumed that $\bar{p}(a) = 0$. If the core radius is zero, (6.12.2) and (6.12.4) become

$$\bar{g}(r) = \frac{4}{3}\pi Gr\rho_m \quad (6.12.5)$$

$$\bar{p}(r) = \frac{2}{3}\pi G\rho_m^2(a^2 - r^2) \quad (6.12.6)$$

Pressure is a quadratic function of radius and the acceleration of gravity is a linear function of radius in a small constant density planet.

Since the adiabatic temperature in the Boussinesq approximation is simply a constant, it is often convenient to define a different reference state temperature in this approximation. One choice of the reference state temperature in the Boussinesq approximation is the solution of the steady heat conduction equation

$$0 = \frac{\partial}{\partial x_i} \left(\bar{k} \frac{\partial \bar{T}}{\partial x_i} \right) + \bar{\rho}H \quad (6.12.7)$$

Equation (6.12.7) follows from (6.9.7) since $\bar{u}_i = 0$, $\Phi = 0$, and $\partial/\partial t = 0$ in the reference state. For a Cartesian model with y the depth, (6.12.7) is

$$0 = \frac{d}{dy} \left(\bar{k} \frac{d\bar{T}}{dy} \right) + \bar{\rho}H \quad (6.12.8)$$

and for a spherical model with r the radius (6.12.7) is

$$0 = \frac{1}{r^2} \frac{d}{dr} \left(r^2 \bar{k} \frac{d\bar{T}}{dr} \right) + \bar{\rho}H \quad (6.12.9)$$

Equations (6.12.8) and (6.12.9) are straightforward to integrate once the dependences of \bar{k} and H on y or r are given. If \bar{k} and H are constant, integration of these equations results in

$$\bar{T} = -\frac{\bar{\rho}Hy^2}{2\bar{k}} + c_1y + c_2 \quad (6.12.10)$$

$$\bar{T} = -\frac{\bar{\rho}Hr^2}{6\bar{k}} + \frac{c_1}{r} + c_2 \quad (6.12.11)$$

where c_1 and c_2 are constants of integration determined by boundary conditions.

Reference states for fully compressible or anelastic models of mantle convection are more difficult to determine. A few relatively simple reference states are commonly assumed, but care is required in their use since they are not thermodynamically self-consistent nor are they realistic representations of the average mantle in all essential respects. In one reference state model, appropriate for Cartesian coordinates, \bar{g} , \bar{c}_p , $\bar{\alpha}$, and $\bar{\gamma}$ are taken as constants and the reference state is assumed to be adiabatic. Under these assumptions, and with y again denoting depth, the reference state is obtained by integrating (i) the hydrostatic equation

$$\frac{d\bar{p}}{dy} = \bar{\rho}\bar{g} \quad (6.12.12)$$

(ii) the adiabatic relation between temperature and pressure (6.9.5)

$$\frac{dT}{d\bar{p}} = \frac{\bar{\alpha}\bar{T}}{\bar{\rho}\bar{c}_p} \quad (6.12.13)$$

and (iii) the thermodynamic relation defining adiabatic compressibility (6.8.30)

$$\frac{1}{\bar{\rho}} \frac{d\bar{\rho}}{d\bar{p}} = \bar{\chi}_a \quad (6.12.14)$$

The combination of (6.10.15), (6.12.12), and (6.12.14) gives the Adams–Williamson relation

$$\frac{1}{\bar{\rho}} \frac{d\bar{\rho}}{dy} = \bar{\rho}\bar{g}\bar{\chi}_a = \frac{\bar{g}\bar{\alpha}}{\bar{c}_p\bar{\gamma}} \quad (6.12.15)$$

with the integral

$$\bar{\rho} = \bar{\rho}(y=0) e^{(y\bar{g}\bar{\alpha})/(\bar{c}_p\bar{\gamma})} = \bar{\rho}(y=0) e^{y/\bar{h}_d} \quad (6.12.16)$$

where \bar{h}_d is the reference state density scale height defined in (6.10.14). If b is the maximum depth of the reference state, (6.12.16) can also be written as

$$\bar{\rho} = \bar{\rho}(y=0) e^{(y/b)(\bar{D}/\bar{\gamma})} \quad (6.12.17)$$

where \bar{D} is the dissipation number of the basic state

$$\bar{D} = \frac{\bar{\alpha}\bar{g}b}{\bar{c}_p} \quad (6.12.18)$$

(see 6.10.18). The hydrostatic equation (6.12.12) with $\bar{\rho}$ given by (6.12.16) can now be integrated to give

$$\bar{p} = \bar{\rho}(y=0)\bar{g}\bar{h}_d \left(e^{y/\bar{h}_d} - 1 \right) \quad (6.12.19)$$

where $\bar{\rho}(y=0)$ has been taken to be zero.

The equation for temperature (6.12.13) can be combined with (6.12.12) to give

$$\frac{1}{\bar{T}} \frac{dT}{dy} = \frac{\bar{\alpha}\bar{g}}{\bar{c}_p} \quad (6.12.20)$$

and integrated to yield

$$\bar{T} = \bar{T}(y=0) e^{(y\bar{\alpha}\bar{g})/\bar{c}_p} = \bar{T}(y=0) e^{\bar{\gamma}(y/\bar{h}_d)} = \bar{T}(y=0) e^{y(\bar{D}/b)} \quad (6.12.21)$$

The scale height for pressure and density are the same, i.e., \bar{h}_d , but the scale height for temperature is $\bar{h}_d/\gamma = b/D$. The adiabatic temperature gradient in the reference state increases exponentially with depth according to

$$\left(\frac{d\bar{T}}{dy} \right)_a = \frac{\bar{\alpha}\bar{g}}{\bar{c}_p} \bar{T} = \frac{\bar{\alpha}\bar{g}\bar{T}(y=0)}{\bar{c}_p} e^{\bar{\gamma}(y/\bar{h}_d)} = \left(\frac{dT}{dy} \right)_a (y=0) e^{\bar{\gamma}(y/\bar{h}_d)} \quad (6.12.22)$$

This has the tendency of stabilizing the deep reference state against convection. The adiabatic temperature gradient in the Earth's deep mantle does not increase exponentially with depth; indeed, it may decrease with depth since $\bar{\alpha}$ decreases with depth in the mantle (Chapter 4). Thus, the strong stabilization of the deep reference state is not applicable to the mantle and caution is necessary in interpreting convection models using this reference state in terms of the real mantle. A similar reference state can be defined for a spherical model. Since (6.12.12)–(6.12.14) apply to a spherical model (with the same assumptions about the constancy of \bar{g} , \bar{c}_p , $\bar{\alpha}$, and $\bar{\gamma}$) with $-r$ replacing y , similar integral relations are obtained for $\bar{T}(r)$, $\bar{\rho}(r)$, and $\bar{\rho}(r)$.

A second reference state applicable to anelastic models of convection is the adiabatic, hydrostatic, polytropic state used by Glatzmaier (1988), Bercovici et al. (1989a), and Glatzmaier et al. (1990).

In this reference state the Grüneisen parameter $\bar{\gamma}$ is assumed constant and the combination of (6.9.12), (6.12.13), and (6.12.14) gives

$$\frac{d\bar{T}}{d\bar{\rho}} = \bar{\gamma} \frac{\bar{T}}{\bar{\rho}} \quad (6.12.23)$$

Integration of (6.12.23) for a spherical model yields

$$\frac{\bar{T}(r)}{\bar{T}(c)} = \left\{ \frac{\bar{\rho}(r)}{\bar{\rho}(c)} \right\}^{\bar{\gamma}} \quad (6.12.24)$$

where $r = c$ is the radius of the lower boundary of the reference state shell. Equation (6.12.24) applies to any spherical, adiabatic reference state with $\bar{\gamma}$ constant and also applies to a Cartesian reference state with $\bar{T}(y)$ and $\bar{\rho}(y)$ replacing $\bar{T}(r)$ and $\bar{\rho}(r)$. It is clear that (6.12.17) and (6.12.21) also satisfy (6.12.24). The polytropic reference state employs the Murnaghan equation (Murnaghan, 1951)

$$\bar{K}_a = \bar{K}_{a0} + \bar{K}'_{a0}\bar{\rho} \quad (6.12.25)$$

to approximate the adiabatic bulk modulus ($K_a = \chi_a^{-1}$ (6.8.31)) as a linear function of pressure (\bar{K}_{a0} and \bar{K}'_{a0} are constants). From (6.8.30), (6.8.31), and (6.12.25) we obtain

$$\bar{\rho} \frac{d\bar{P}}{d\bar{\rho}} = \bar{K}_{a0} + \bar{K}'_{a0}\bar{\rho} \quad (6.12.26)$$

which can be integrated to give

$$\bar{P} = \frac{\bar{K}_{a0}}{\bar{K}'_{a0}} \bar{\rho}_0 - \bar{K}'_{a0} \left\{ \bar{\rho} \bar{K}'_{a0} - \bar{\rho}_0 \bar{K}'_{a0} \right\} \quad (6.12.27)$$

where $\bar{\rho}_0$ is the reference state density at $\bar{p} = 0$. The equation relating \bar{p} and $\bar{\rho}$ can be put in the form of a polytropic equation by introducing the polytropic index n given by

$$n \equiv \left(\frac{\bar{K}'_{a0}}{\bar{K}_{a0}} - 1 \right)^{-1} \quad (6.12.28)$$

so that (6.12.27) becomes

$$\bar{p} = \frac{\bar{K}_{a0}}{\bar{K}'_{a0}} \bar{\rho}_0^{-\bar{K}'_{a0}} \left\{ \bar{\rho}^{(n+1)/n} - \bar{\rho}_0^{(n+1)/n} \right\} \quad (6.12.29)$$

With reference state temperature and pressure known in terms of the density through (6.12.24) and (6.12.29), it is only necessary to determine $\bar{\rho}(r)$ to complete the specification of the reference state. We can find $\bar{\rho}(r)$ by integrating the hydrostatic equation (6.12.3). Substitution of (6.12.29) into (6.12.3) and use of (6.12.1) to specify $\bar{g}(r)$ give

$$\bar{K}_{a0} \bar{\rho}_0^{-\bar{K}'_{a0}} \bar{\rho}^{(1/n)-1} \frac{d\bar{\rho}}{dr} = -\frac{4\pi G}{r^2} \int_0^r \bar{\rho}(r') r'^2 dr' \quad (6.12.30)$$

After multiplication of (6.12.30) by r^2 and differentiation of the result with respect to r , we obtain a second-order differential equation for $\bar{\rho}(r)$:

$$\frac{\bar{K}_{a0}}{\bar{K}'_{a0}} \bar{\rho}_0^{-\bar{K}'_{a0}} \frac{(n+1)}{4\pi G} \frac{d}{dr} \left(r^2 \frac{d}{dr} \bar{\rho}^{1/n} \right) = -\bar{\rho} r^2 \quad (6.12.31)$$

Integration of (6.12.31) subject to appropriate conditions gives $\bar{\rho}(r)$. Equation (6.12.31) is known as the Lane-Emden equation in the astrophysical literature (Cox and Giuli, 1968). The two conditions required for the integration of (6.12.31) are

$$\bar{\rho} = \bar{\rho}_0 \text{ at } r = a \text{ and } \bar{M}(r = a) = 4\pi \int_c^a \bar{\rho}(r') r'^2 dr' \quad (6.12.32)$$

where $r = a$ is the outer radius of the reference state shell (the Earth's radius) and $\bar{M}(r = a)$ is the total prescribed mass of the shell (the mass of the Earth's mantle). The integration of (6.12.31) and (6.12.32) must be done numerically.

A thermodynamically self-consistent formulation of the reference state and the thermodynamic parameters required for the description of the convective state can be obtained from an equation of state of the form

$$\bar{\rho}(\bar{p}, \bar{T}) = \bar{\rho}_0(\bar{T}) \left\{ \frac{\bar{K}'_{0T} \bar{p}}{\bar{K}_{0T}(\bar{T})} \right\}^{1/\bar{K}'_{0T}} \quad (6.12.33)$$

where $\bar{\rho}_0(\bar{T})$ is the zero-pressure density as a function of temperature and $\bar{K}_{0T}(\bar{T})$ is the zero-pressure isothermal bulk modulus as a function of temperature. The functions $\bar{\rho}_0(\bar{T})$ and $\bar{K}_{0T}(\bar{T})$ are assumed known, e.g., from laboratory measurements, and the constant \bar{K}'_{0T} is also assumed given. From (6.12.33), (6.8.3), and (6.8.32) we can obtain

$$\bar{K}_T(\bar{T}, \bar{p}) = \bar{K}_{0T} + \bar{K}'_{0T} \bar{p} \quad (6.12.34)$$

From (6.12.33) and (6.8.2) we can determine $\bar{\alpha}$:

$$\bar{\alpha}(\bar{T}, \bar{p}) = \bar{\alpha}_0(\bar{T}) + \frac{\bar{p}}{\bar{K}_T(\bar{T}, \bar{p})} \frac{1}{\bar{K}_{0T}(\bar{T})} \frac{d\bar{K}_{0T}(\bar{T})}{d\bar{T}} \quad (6.12.35)$$

where

$$\bar{\alpha}_0(\bar{T}) \equiv -\frac{1}{\bar{\rho}_0(\bar{T})} \frac{d\bar{\rho}_0(\bar{T})}{d\bar{T}} \quad (6.12.36)$$

The function $\bar{\alpha}_0(\bar{T})$ is the zero-pressure coefficient of thermal expansion. We can also calculate \bar{c}_v if we assume \bar{c}_p (a constant) is known and use

$$\bar{c}_v(\bar{T}, \bar{p}) = \bar{c}_p - \frac{\bar{\alpha}^2(\bar{T}, \bar{p}) \bar{T} \bar{K}_T(\bar{T}, \bar{p})}{\bar{\rho}(\bar{T}, \bar{p})} \quad (6.12.37)$$

As in previous examples, the reference state can be obtained by integrating (6.12.12) or (6.12.3) using (6.12.33) to relate \bar{p} and $\bar{\rho}$ and (6.12.1) to obtain $\bar{g}(r)$ (or assuming $\bar{g} = \text{constant}$). The temperature must be determined by the simultaneous integration of (6.12.13) (it is assumed that the reference state is adiabatic) with $\bar{\alpha}$ obtained from (6.12.35) and (6.12.36). The linearized equation of state for the convection calculations (6.10.1) involves $\bar{\rho}$, \bar{X}_T , $(\bar{K}_T)^{-1}$ and $\bar{\alpha}$ which can all be determined from the reference state solution (6.12.33) and (6.12.34) and (6.12.35). The input quantities in this approach are the constants \bar{c}_p and \bar{K}'_{0T} . All other thermodynamic variables $\bar{\rho}$, \bar{p} , \bar{T} , $\bar{\alpha}$, \bar{c}_v , etc., are calculable from relations given above.

6.13 Gravitational Potential and the Poisson Equation

In writing the equations of the preceding sections we have implicitly assumed that the acceleration of gravity g_i does not depend on the density perturbations of the flow. While this is a good approximation in mantle convection, it is often of interest to calculate the variations in the gravitational potential V or the geoid due to variations in mantle density associated with convection for comparison with observations of the Earth's geoid. Such a comparison constrains models of the mantle as discussed in Chapter 5. Calculation of the geoid in a mantle convection model is facilitated by including the gravitational potential in the set of equations to be solved.

The equation for the gravitational potential V is the Poisson equation

$$\nabla^2 V = -4\pi G\rho \quad (6.13.1)$$

where V is related to the acceleration of gravity g_i by

$$g_i = \frac{\partial V}{\partial x_i} \quad (6.13.2)$$

With ρ represented as the sum of a reference state density $\bar{\rho}$ and a perturbation density ρ' as in (6.10.1), and V and g similarly separated into reference state and perturbation parts

$$V = \bar{V} + V' \quad (6.13.3)$$

$$g_i = \bar{g}_i + g'_i \quad (6.13.4)$$

we can write

$$\nabla^2 \bar{V} = -4\pi G \bar{\rho} \quad (6.13.5)$$

$$\bar{g}_i = \frac{\partial \bar{V}}{\partial x_i} \quad (6.13.6)$$

$$\nabla^2 V' = -4\pi G \rho' \quad (6.13.7)$$

$$g'_i = \frac{\partial V'}{\partial x_i} \quad (6.13.8)$$

The gravitational body force in the momentum equation for the perturbation state is the sum of two terms $\rho' \bar{g}_i + \bar{\rho} g'_i = \rho' \bar{g}_i + \bar{\rho} (\partial V' / \partial x_i)$ (the nonlinear term $\rho' (\partial V' / \partial x_i)$ is neglected). Only the first of these terms has been included in the momentum equations of the previous sections. The simultaneous solution for convection and the gravitational potential requires the addition of (6.13.7) to the equation set and the inclusion of the term $\bar{\rho} (\partial V' / \partial x_i)$ in the momentum equation.

6.14 Conservation of Momentum Equations in Cartesian, Cylindrical, and Spherical Polar Coordinates

The dimensional forms of the conservation of mass equation in Cartesian, cylindrical, and spherical polar coordinates have been given in (6.2.2), (6.2.7), and (6.2.8), respectively. Here we give the dimensional forms of the conservation of momentum equations in Cartesian, cylindrical, and spherical polar coordinates.

Cartesian Coordinates (x, y, z)

$$\begin{aligned} & \rho \left(\frac{\partial u_x}{\partial t} + u_x \frac{\partial u_x}{\partial x} + u_y \frac{\partial u_x}{\partial y} + u_z \frac{\partial u_x}{\partial z} \right) \\ &= -\frac{\partial p}{\partial x} + \frac{\partial \tau_{xx}}{\partial x} + \frac{\partial \tau_{xy}}{\partial y} + \frac{\partial \tau_{xz}}{\partial z} + \rho g_x \end{aligned} \quad (6.14.1)$$

$$\begin{aligned} & \rho \left(\frac{\partial u_y}{\partial t} + u_x \frac{\partial u_y}{\partial x} + u_y \frac{\partial u_y}{\partial y} + u_z \frac{\partial u_y}{\partial z} \right) \\ &= -\frac{\partial p}{\partial y} + \frac{\partial \tau_{yx}}{\partial x} + \frac{\partial \tau_{yy}}{\partial y} + \frac{\partial \tau_{yz}}{\partial z} + \rho g_y \end{aligned} \quad (6.14.2)$$

$$\begin{aligned} & \rho \left(\frac{\partial u_z}{\partial t} + u_x \frac{\partial u_z}{\partial x} + u_y \frac{\partial u_z}{\partial y} + u_z \frac{\partial u_z}{\partial z} \right) \\ &= -\frac{\partial p}{\partial z} + \frac{\partial \tau_{zx}}{\partial x} + \frac{\partial \tau_{zy}}{\partial y} + \frac{\partial \tau_{zz}}{\partial z} + \rho g_z \end{aligned} \quad (6.14.3)$$

where (g_x, g_y, g_z) is the acceleration of gravity.

Cylindrical Coordinates (s, z, ϕ)

$$\begin{aligned} & \rho \left(\frac{\partial u_s}{\partial t} + u_s \frac{\partial u_s}{\partial s} + \frac{u_\phi}{s} \frac{\partial u_s}{\partial \phi} + u_z \frac{\partial u_s}{\partial z} - \frac{u_\phi^2}{s} \right) \\ &= -\frac{1}{\rho} \frac{\partial p}{\partial s} + \frac{\partial \tau_{zs}}{\partial z} + \frac{\partial \tau_{ss}}{\partial s} + \frac{1}{s} \frac{\partial \tau_{\phi s}}{\partial \phi} + \frac{\tau_{ss} - \tau_{\phi \phi}}{s} + \rho g_s \end{aligned} \quad (6.14.4)$$

$$\begin{aligned} & \rho \left(\frac{\partial u_z}{\partial t} + u_s \frac{\partial u_z}{\partial s} + \frac{u_\phi}{s} \frac{\partial u_z}{\partial \phi} + u_z \frac{\partial u_z}{\partial z} \right) \\ &= -\frac{1}{\rho} \frac{\partial p}{\partial z} + \frac{\partial \tau_{zz}}{\partial z} + \frac{\partial \tau_{sz}}{\partial s} + \frac{1}{s} \frac{\partial \tau_{\phi z}}{\partial \phi} + \frac{\tau_{sz}}{s} + \rho g_z \end{aligned} \quad (6.14.5)$$

$$\begin{aligned} & \rho \left(\frac{\partial u_\phi}{\partial t} + u_s \frac{\partial u_\phi}{\partial s} + \frac{u_\phi}{s} \frac{\partial u_\phi}{\partial \phi} + u_z \frac{\partial u_\phi}{\partial z} + \frac{u_\phi u_s}{s} \right) \\ &= -\frac{1}{\rho} \frac{1}{s} \frac{\partial p}{\partial \phi} + \frac{\partial \tau_{z\phi}}{\partial z} + \frac{\partial \tau_{s\phi}}{\partial s} + \frac{1}{s} \frac{\partial \tau_{\phi\phi}}{\partial \phi} + \frac{\tau_{s\phi} + \tau_{\phi s}}{s} + \rho g_\phi \end{aligned} \quad (6.14.6)$$

where (g_s, g_z, g_ϕ) is the acceleration of gravity.

Spherical Polar Coordinates (r, θ, ϕ)

$$\begin{aligned} & \rho \left(\frac{\partial u_r}{\partial t} + u_r \frac{\partial u_r}{\partial r} + \frac{u_\theta}{r} \frac{\partial u_r}{\partial \theta} + \frac{u_\phi}{r \sin \theta} \frac{\partial u_r}{\partial \phi} - \frac{(u_\theta^2 + u_\phi^2)}{r} \right) \\ &= -\frac{\partial p}{\partial r} + \rho g_r + \frac{\partial \tau_{rr}}{\partial r} + \frac{1}{r} \frac{\partial \tau_{r\theta}}{\partial \theta} + \frac{1}{r \sin \theta} \frac{\partial \tau_{r\phi}}{\partial \phi} + \frac{1}{r} (2\tau_{rr} - \tau_{\theta\theta} - \tau_{\phi\phi} + \tau_{r\theta} \cot \theta) \end{aligned} \quad (6.14.7)$$

$$\begin{aligned} & \rho \left(\frac{\partial u_\theta}{\partial t} + u_r \frac{\partial u_\theta}{\partial r} + \frac{u_\theta}{r} \frac{\partial u_\theta}{\partial \theta} + \frac{u_\phi}{r \sin \theta} \frac{\partial u_\theta}{\partial \phi} - \frac{u_r u_\theta}{r} - \frac{u_\phi^2 \cot \theta}{r} \right) \\ &= -\frac{1}{r} \frac{\partial p}{\partial \theta} + \rho g_\theta + \frac{\partial \tau_{r\theta}}{\partial r} + \frac{1}{r} \frac{\partial \tau_{\theta\theta}}{\partial \theta} + \frac{1}{r \sin \theta} \frac{\partial \tau_{\theta\phi}}{\partial \phi} + \frac{1}{r} (\tau_{\theta\theta} \cot \theta - \tau_{\phi\phi} \cot \theta + 3\tau_{r\theta}) \end{aligned} \quad (6.14.8)$$

$$\begin{aligned} & \rho \left(\frac{\partial u_\phi}{\partial t} + u_r \frac{\partial u_\phi}{\partial r} + \frac{u_\theta}{r} \frac{\partial u_\phi}{\partial \theta} + \frac{u_\phi}{r \sin \theta} \frac{\partial u_\phi}{\partial \phi} + \frac{u_\phi u_r}{r} + \frac{u_\theta u_\phi \cot \theta}{r} \right) \\ &= -\frac{1}{r \sin \theta} \frac{\partial p}{\partial \phi} + \rho g_\phi + \frac{\partial \tau_{r\phi}}{\partial r} + \frac{1}{r} \frac{\partial \tau_{\theta\phi}}{\partial \theta} + \frac{1}{r \sin \theta} \frac{\partial \tau_{\phi\phi}}{\partial \phi} + \frac{1}{r} (3\tau_{r\phi} + 2\tau_{\theta\phi} \cot \theta) \end{aligned} \quad (6.14.9)$$

where (g_r, g_θ, g_ϕ) is the acceleration of gravity.

6.15 Navier–Stokes Equations in Cartesian, Cylindrical, and Spherical Polar Coordinates

Section 6.14 gives general forms of the inertial, pressure, and gravity force terms of the Navier–Stokes equations in Cartesian, cylindrical, and spherical polar coordinates. Here, we

focus on only the forms of the deviatoric stress contributions to the Navier–Stokes equations. We first give explicit formulas for the components of the deviatoric stress tensor and the strain rate tensor.

Cartesian Coordinates (x, y, z)

$$\tau_{xx} = 2\mu e_{xx} - \frac{2}{3}\mu(e_{xx} + e_{yy} + e_{zz}) = 2\mu \frac{\partial u_x}{\partial x} - \frac{2}{3}\mu \left(\frac{\partial u_x}{\partial x} + \frac{\partial u_y}{\partial y} + \frac{\partial u_z}{\partial z} \right) \quad (6.15.1)$$

$$\tau_{yy} = 2\mu e_{yy} - \frac{2}{3}\mu(e_{xx} + e_{yy} + e_{zz}) = 2\mu \frac{\partial u_y}{\partial y} - \frac{2}{3}\mu \left(\frac{\partial u_x}{\partial x} + \frac{\partial u_y}{\partial y} + \frac{\partial u_z}{\partial z} \right) \quad (6.15.2)$$

$$\tau_{zz} = 2\mu e_{zz} - \frac{2}{3}\mu(e_{xx} + e_{yy} + e_{zz}) = 2\mu \frac{\partial u_z}{\partial z} - \frac{2}{3}\mu \left(\frac{\partial u_x}{\partial x} + \frac{\partial u_y}{\partial y} + \frac{\partial u_z}{\partial z} \right) \quad (6.15.3)$$

$$\tau_{xy} = \tau_{yx} = 2\mu e_{xy} = 2\mu e_{yx} = \mu \left(\frac{\partial u_y}{\partial x} + \frac{\partial u_x}{\partial y} \right) \quad (6.15.4)$$

$$\tau_{xz} = \tau_{zx} = 2\mu e_{xz} = 2\mu e_{zx} = \mu \left(\frac{\partial u_x}{\partial z} + \frac{\partial u_z}{\partial x} \right) \quad (6.15.5)$$

$$\tau_{yz} = \tau_{zy} = 2\mu e_{yz} = 2\mu e_{zy} = \mu \left(\frac{\partial u_z}{\partial y} + \frac{\partial u_y}{\partial z} \right) \quad (6.15.6)$$

Cylindrical Coordinates (s, z, ϕ)

$$\begin{aligned} \tau_{ss} &= 2\mu e_{ss} - \frac{2}{3}\mu(e_{ss} + e_{zz} + e_{\phi\phi}) \\ &= 2\mu \frac{\partial u_s}{\partial s} - \frac{2}{3}\mu \left(\frac{1}{s} \frac{\partial}{\partial s}(su_s) + \frac{\partial u_z}{\partial z} + \frac{1}{s} \frac{\partial u_\phi}{\partial \phi} \right) \end{aligned} \quad (6.15.7)$$

$$\begin{aligned} \tau_{zz} &= 2\mu e_{zz} - \frac{2}{3}\mu(e_{ss} + e_{zz} + e_{\phi\phi}) \\ &= 2\mu \frac{\partial u_z}{\partial z} - \frac{2}{3}\mu \left(\frac{1}{s} \frac{\partial}{\partial s}(su_s) + \frac{\partial u_z}{\partial z} + \frac{1}{s} \frac{\partial u_\phi}{\partial \phi} \right) \end{aligned} \quad (6.15.8)$$

$$\begin{aligned} \tau_{\phi\phi} &= 2\mu e_{\phi\phi} - \frac{2}{3}\mu(e_{ss} + e_{zz} + e_{\phi\phi}) \\ &= 2\mu \left(\frac{1}{s} \frac{\partial u_\phi}{\partial \phi} + \frac{u_s}{s} \right) - \frac{2}{3}\mu \left(\frac{1}{s} \frac{\partial}{\partial s}(su_s) + \frac{\partial u_z}{\partial z} + \frac{1}{s} \frac{\partial u_\phi}{\partial \phi} \right) \end{aligned} \quad (6.15.9)$$

$$\tau_{s\phi} = \tau_{\phi s} = 2\mu e_{s\phi} = 2\mu e_{\phi s} = \mu \left(\frac{1}{s} \frac{\partial u_s}{\partial \phi} + \frac{\partial u_\phi}{\partial s} - \frac{u_\phi}{s} \right) \quad (6.15.10)$$

$$\tau_{sz} = \tau_{zs} = 2\mu e_{sz} = 2\mu e_{zs} = \mu \left(\frac{\partial u_s}{\partial z} + \frac{\partial u_z}{\partial s} \right) \quad (6.15.11)$$

$$\tau_{\phi z} = \tau_{z\phi} = 2\mu e_{\phi z} = 2\mu e_{z\phi} = \mu \left(\frac{1}{s} \frac{\partial u_z}{\partial \phi} + \frac{\partial u_\phi}{\partial z} \right) \quad (6.15.12)$$

$$e_{ss} = \frac{\partial u_s}{\partial s}, \quad e_{zz} = \frac{\partial u_z}{\partial z}, \quad e_{\phi\phi} = \frac{1}{s} \frac{\partial u_\phi}{\partial \phi} + \frac{u_s}{s} \quad (6.15.13)$$

Spherical Polar Coordinates (r, θ, ϕ)

$$\begin{aligned}\tau_{rr} &= 2\mu e_{rr} - \frac{2}{3}\mu(e_{rr} + e_{\theta\theta} + e_{\phi\phi}) = 2\mu \frac{\partial u_r}{\partial r} \\ &\quad - \frac{2}{3}\mu \left(\frac{1}{r^2} \frac{\partial}{\partial r}(r^2 u_r) + \frac{1}{r \sin \theta} \frac{\partial}{\partial \theta}(u_\theta \sin \theta) + \frac{1}{r \sin \theta} \frac{\partial u_\phi}{\partial \phi} \right)\end{aligned}\quad (6.15.14)$$

$$\begin{aligned}\tau_{\theta\theta} &= 2\mu e_{\theta\theta} - \frac{2}{3}\mu(e_{rr} + e_{\theta\theta} + e_{\phi\phi}) = 2\mu \left(\frac{1}{r} \frac{\partial u_\theta}{\partial \theta} + \frac{u_r}{r} \right) \\ &\quad - \frac{2}{3}\mu \left(\frac{1}{r^2} \frac{\partial}{\partial r}(r^2 u_r) + \frac{1}{r \sin \theta} \frac{\partial}{\partial \theta}(u_\theta \sin \theta) + \frac{1}{r \sin \theta} \frac{\partial u_\phi}{\partial \phi} \right)\end{aligned}\quad (6.15.15)$$

$$\begin{aligned}\tau_{\phi\phi} &= 2\mu e_{\phi\phi} - \frac{2}{3}\mu(e_{rr} + e_{\theta\theta} + e_{\phi\phi}) = 2\mu \left(\frac{1}{r \sin \theta} \frac{\partial u_\phi}{\partial \phi} + \frac{u_r}{r} + \frac{u_\theta \cot \theta}{r} \right) \\ &\quad - \frac{2}{3}\mu \left(\frac{1}{r^2} \frac{\partial}{\partial r}(r^2 u_r) + \frac{1}{r \sin \theta} \frac{\partial}{\partial \theta}(u_\theta \sin \theta) + \frac{1}{r \sin \theta} \frac{\partial u_\phi}{\partial \phi} \right)\end{aligned}\quad (6.15.16)$$

$$\tau_{r\theta} = \tau_{\theta r} = 2\mu e_{r\theta} = 2\mu e_{\theta r} = \mu \left\{ r \frac{\partial}{\partial r} \left(\frac{u_\theta}{r} \right) + \frac{1}{r} \frac{\partial u_r}{\partial \theta} \right\}\quad (6.15.17)$$

$$\tau_{r\phi} = \tau_{\phi r} = 2\mu e_{r\phi} = 2\mu e_{\phi r} = \mu \left\{ \frac{1}{r \sin \theta} \frac{\partial u_r}{\partial \phi} + r \frac{\partial}{\partial r} \left(\frac{u_\phi}{r} \right) \right\}\quad (6.15.18)$$

$$\tau_{\theta\phi} = \tau_{\phi\theta} = 2\mu e_{\theta\phi} = 2\mu e_{\phi\theta} = \mu \left\{ \frac{\sin \theta}{r} \frac{\partial}{\partial \theta} \left(\frac{u_\phi}{\sin \theta} \right) + \frac{1}{r \sin \theta} \frac{\partial u_\theta}{\partial \phi} \right\}\quad (6.15.19)$$

$$e_{rr} = \frac{\partial u_r}{\partial r}, \quad e_{\theta\theta} = \frac{1}{r} \frac{\partial u_\theta}{\partial \theta} + \frac{u_r}{r}, \quad e_{\phi\phi} = \frac{1}{r \sin \theta} \frac{\partial u_\phi}{\partial \phi} + \frac{u_r}{r} + \frac{u_\theta \cot \theta}{r}\quad (6.15.20)$$

The deviatoric stress contributions to the Navier–Stokes equations for constant viscosity μ are given in the following expressions which take the form

$$\rho \frac{Du_i}{Dt} = -\frac{\partial p}{\partial x_i} + \rho g_i + \text{deviatoric stress contributions}\quad (6.15.21)$$

Deviatoric stress contributions in Cartesian coordinates (x, y, z)

x-component

$$\mu \nabla^2 u_x + \frac{\mu}{3} \frac{\partial}{\partial x} \left(\frac{\partial u_x}{\partial x} + \frac{\partial u_y}{\partial y} + \frac{\partial u_z}{\partial z} \right)$$

y-component

$$\mu \nabla^2 u_y + \frac{\mu}{3} \frac{\partial}{\partial y} \left(\frac{\partial u_x}{\partial x} + \frac{\partial u_y}{\partial y} + \frac{\partial u_z}{\partial z} \right)$$

z-component

$$\mu \nabla^2 u_z + \frac{\mu}{3} \frac{\partial}{\partial z} \left(\frac{\partial u_x}{\partial x} + \frac{\partial u_y}{\partial y} + \frac{\partial u_z}{\partial z} \right)$$

$$\nabla^2 = \frac{\partial^2}{\partial x^2} + \frac{\partial^2}{\partial y^2} + \frac{\partial^2}{\partial z^2}\quad (6.15.22)$$

Deviatoric stress contributions in cylindrical coordinates (s, z, ϕ)
 s -component

$$\mu \left\{ \nabla^2 u_s - \frac{u_s}{s^2} - \frac{2}{s^2} \frac{\partial u_\phi}{\partial \phi} \right\} + \frac{\mu}{3} \frac{\partial}{\partial s} \left\{ \frac{1}{s} \frac{\partial}{\partial s} (su_s) + \frac{1}{s} \frac{\partial u_\phi}{\partial \phi} + \frac{\partial u_z}{\partial z} \right\}$$

z -component

$$\mu \nabla^2 u_z + \frac{\mu}{3} \frac{\partial}{\partial z} \left\{ \frac{1}{s} \frac{\partial}{\partial s} (su_s) + \frac{1}{s} \frac{\partial u_\phi}{\partial \phi} + \frac{\partial u_z}{\partial z} \right\}$$

ϕ -component

$$\mu \left\{ \nabla^2 u_\phi + \frac{2}{s^2} \frac{\partial u_s}{\partial \phi} - \frac{u_\phi}{s^2} \right\} + \frac{\mu}{3} \frac{1}{s} \frac{\partial}{\partial \phi} \left\{ \frac{1}{s} \frac{\partial}{\partial s} (su_s) + \frac{1}{s} \frac{\partial u_\phi}{\partial \phi} + \frac{\partial u_z}{\partial z} \right\}$$

$$\nabla^2 = \frac{\partial^2}{\partial s^2} + \frac{1}{s} \frac{\partial}{\partial s} + \frac{1}{s^2} \frac{\partial^2}{\partial \phi^2} + \frac{\partial^2}{\partial z^2} \quad (6.15.23)$$

Deviatoric stress contributions in spherical polar coordinates (r, θ, ϕ)
 r -component

$$\begin{aligned} & \mu \left\{ \nabla^2 u_r - \frac{2u_r}{r^2} - \frac{2}{r^2} \frac{\partial u_\theta}{\partial \theta} - \frac{2u_\theta \cot \theta}{r^2} - \frac{2}{r^2 \sin \theta} \frac{\partial u_\phi}{\partial \phi} \right\} \\ & + \frac{\mu}{3} \frac{\partial}{\partial r} \left\{ \frac{1}{r^2} \frac{\partial}{\partial r} (r^2 u_r) + \frac{1}{r \sin \theta} \frac{\partial}{\partial \theta} (u_\theta \sin \theta) + \frac{1}{r \sin \theta} \frac{\partial u_\phi}{\partial \phi} \right\} \end{aligned}$$

θ -component

$$\begin{aligned} & \mu \left\{ \nabla^2 u_\theta + \frac{2}{r^2} \frac{\partial u_r}{\partial \theta} - \frac{u_\theta}{r^2 \sin^2 \theta} - \frac{2 \cos \theta}{r^2 \sin^2 \theta} \frac{\partial u_\phi}{\partial \phi} \right\} \\ & + \frac{\mu}{3} \frac{1}{r} \frac{\partial}{\partial \theta} \left\{ \frac{1}{r^2} \frac{\partial}{\partial r} (r^2 u_r) + \frac{1}{r \sin \theta} \frac{\partial}{\partial \theta} (u_\theta \sin \theta) + \frac{1}{r \sin \theta} \frac{\partial u_\phi}{\partial \phi} \right\} \end{aligned}$$

ϕ -component

$$\begin{aligned} & \mu \left\{ \nabla^2 u_\phi - \frac{u_\phi}{r^2 \sin^2 \theta} + \frac{2}{r^2 \sin^2 \theta} \frac{\partial u_r}{\partial \phi} + \frac{2 \cos \theta}{r^2 \sin^2 \theta} \frac{\partial u_\theta}{\partial \phi} \right\} \\ & + \frac{\mu}{3} \frac{1}{r \sin \theta} \frac{\partial}{\partial \phi} \left\{ \frac{1}{r^2} \frac{\partial}{\partial r} (r^2 u_r) + \frac{1}{r \sin \theta} \frac{\partial}{\partial \theta} (u_\theta \sin \theta) + \frac{1}{r \sin \theta} \frac{\partial u_\phi}{\partial \phi} \right\} \end{aligned}$$

$$\nabla^2 = \frac{1}{r^2} \frac{\partial}{\partial r} \left(r^2 \frac{\partial}{\partial r} \right) + \frac{1}{r^2 \sin \theta} \frac{\partial}{\partial \theta} \left(\sin \theta \frac{\partial}{\partial \theta} \right) + \frac{1}{r^2 \sin^2 \theta} \frac{\partial^2}{\partial \phi^2} \quad (6.15.24)$$

If the viscosity is not constant, the following terms must be added to the deviatoric contributions to the Navier–Stokes equations given above.

Cartesian Coordinates (x, y, z)

x-component

$$-\frac{2}{3} \frac{\partial u_i}{\partial x_i} \frac{\partial \mu}{\partial x} + \frac{\partial \mu}{\partial x_i} \left(\frac{\partial u_i}{\partial x} + \frac{\partial u_x}{\partial x_i} \right)$$

y-component

$$-\frac{2}{3} \frac{\partial u_i}{\partial x_i} \frac{\partial \mu}{\partial y} + \frac{\partial \mu}{\partial x_i} \left(\frac{\partial u_i}{\partial y} + \frac{\partial u_y}{\partial x_i} \right)$$

z-component

$$-\frac{2}{3} \frac{\partial u_i}{\partial x_i} \frac{\partial \mu}{\partial z} + \frac{\partial \mu}{\partial x_i} \left(\frac{\partial u_i}{\partial z} + \frac{\partial u_z}{\partial x_i} \right)$$

Cylindrical Coordinates (s, z, φ)

s-component

$$-\frac{2}{3} (\nabla \cdot \underline{u}) \frac{\partial \mu}{\partial s} + 2 \frac{\partial \mu}{\partial s} \frac{\partial u_s}{\partial s} + \frac{\partial \mu}{\partial z} \left(\frac{\partial u_z}{\partial s} + \frac{\partial u_s}{\partial z} \right) + \frac{1}{s} \frac{\partial \mu}{\partial \phi} \left\{ s \frac{\partial}{\partial s} \left(\frac{u_\phi}{s} \right) + \frac{1}{s} \frac{\partial u_s}{\partial \phi} \right\}$$

z-component

$$-\frac{2}{3} (\nabla \cdot \underline{u}) \frac{\partial \mu}{\partial z} + 2 \frac{\partial \mu}{\partial z} \frac{\partial u_z}{\partial z} + \frac{\partial \mu}{\partial s} \left\{ \frac{\partial u_z}{\partial s} + \frac{\partial u_s}{\partial z} \right\} + \frac{1}{s} \frac{\partial \mu}{\partial \phi} \left\{ \frac{\partial u_\phi}{\partial z} + \frac{1}{s} \frac{\partial u_z}{\partial \phi} \right\}$$

φ-component

$$\begin{aligned} & -\frac{2}{3} (\nabla \cdot \underline{u}) \frac{1}{s} \frac{\partial \mu}{\partial \phi} + \frac{2}{s} \frac{\partial \mu}{\partial \phi} \left(\frac{1}{s} \frac{\partial u_\phi}{\partial \phi} + \frac{u_s}{s} \right) \\ & + \frac{\partial \mu}{\partial s} \left\{ s \frac{\partial}{\partial s} \left(\frac{u_\phi}{s} \right) + \frac{1}{s} \frac{\partial u_s}{\partial \phi} \right\} + \frac{\partial \mu}{\partial z} \left\{ \frac{\partial u_\phi}{\partial z} + \frac{1}{s} \frac{\partial u_z}{\partial \phi} \right\} \end{aligned}$$

$$\nabla \cdot \underline{u} = \frac{1}{s} \frac{\partial}{\partial s} (s u_s) + \frac{1}{s} \frac{\partial u_\phi}{\partial \phi} + \frac{\partial u_z}{\partial z} \quad (6.15.25)$$

Spherical Polar Coordinates (r, θ, φ)

r-component

$$\begin{aligned} & -\frac{2}{3} (\nabla \cdot \underline{u}) \frac{\partial \mu}{\partial r} + 2 \frac{\partial \mu}{\partial r} \frac{\partial u_r}{\partial r} + \frac{1}{r} \frac{\partial \mu}{\partial \theta} \left\{ \frac{1}{r} \frac{\partial u_r}{\partial \theta} + r \frac{\partial}{\partial r} (u_\theta r) \right\} \\ & + \frac{1}{r \sin \theta} \frac{\partial \mu}{\partial \phi} \left[\frac{1}{r \sin \theta} \frac{\partial u_r}{\partial \phi} + r \frac{\partial}{\partial r} \left(\frac{u_\phi}{r} \right) \right] \end{aligned}$$

θ-component

$$\begin{aligned} & -\frac{2}{3} (\nabla \cdot \underline{u}) \frac{1}{r} \frac{\partial \mu}{\partial \theta} + \frac{2}{r} \frac{\partial \mu}{\partial \theta} \left[\frac{1}{r} \frac{\partial u_\theta}{\partial \theta} + \frac{u_r}{r} \right] \\ & + \frac{\partial \mu}{\partial r} \left[\frac{1}{r} \frac{\partial u_r}{\partial \theta} + r \frac{\partial}{\partial r} \left(\frac{u_\theta}{r} \right) \right] + \frac{1}{r \sin \theta} \frac{\partial \mu}{\partial \phi} \left\{ \frac{1}{r \sin \theta} \frac{\partial u_\theta}{\partial \phi} + \frac{\sin \theta}{r} \frac{\partial}{\partial \theta} \left(\frac{u_\phi}{\sin \theta} \right) \right\} \end{aligned}$$

ϕ -component

$$\begin{aligned}
 & -\frac{2}{3}(\nabla \cdot \underline{u}) \frac{1}{r \sin \theta} \frac{\partial \mu}{\partial \phi} + \frac{2}{r \sin \theta} \frac{\partial \mu}{\partial \phi} \left\{ \frac{1}{r \sin \theta} \frac{\partial u_\phi}{\partial \phi} + \frac{u_r}{r} + \frac{u_\theta \cot \theta}{r} \right\} \\
 & + \frac{\partial \mu}{\partial r} \left\{ \frac{1}{r \sin \theta} \frac{\partial u_r}{\partial \phi} + r \frac{\partial}{\partial r} \left(\frac{u_\phi}{r} \right) \right\} + \frac{1}{r} \frac{\partial \mu}{\partial \theta} \left\{ \frac{1}{r \sin \theta} \frac{\partial u_\theta}{\partial \phi} + \frac{\sin \theta}{r} \frac{\partial}{\partial \theta} \left(\frac{u_\phi}{\sin \theta} \right) \right\} \\
 \nabla \cdot \underline{u} &= \frac{1}{r^2} \frac{\partial}{\partial r} (r^2 u_r) + \frac{1}{r \sin \theta} \frac{\partial}{\partial \theta} (\sin \theta u_\theta) + \frac{1}{r \sin \theta} \frac{\partial u_\phi}{\partial \phi} \tag{6.15.26}
 \end{aligned}$$

6.16 Conservation of Energy Equation in Cartesian, Cylindrical, and Spherical Polar Coordinates

In this section we provide expressions for writing the energy equation in the major coordinate systems. Since the energy equation can be written in a variety of useful forms, we do not explicitly write all variations of the energy equation but instead provide necessary equations for quantities entering any form of the conservation of thermal energy.

Cartesian Coordinates (x, y, z)

$$\frac{D}{Dt} = \frac{\partial}{\partial t} + u_x \frac{\partial}{\partial x} + u_y \frac{\partial}{\partial y} + u_z \frac{\partial}{\partial z} \tag{6.16.1}$$

$$\nabla \cdot (k \nabla T) = \frac{\partial}{\partial x} \left(k \frac{\partial T}{\partial x} \right) + \frac{\partial}{\partial y} \left(k \frac{\partial T}{\partial y} \right) + \frac{\partial}{\partial z} \left(k \frac{\partial T}{\partial z} \right) \tag{6.16.2}$$

$$\begin{aligned}
 \Phi &= 2\mu \left\{ \left(\frac{\partial u_x}{\partial x} \right)^2 + \left(\frac{\partial u_y}{\partial y} \right)^2 + \left(\frac{\partial u_z}{\partial z} \right)^2 + \frac{1}{2} \left(\frac{\partial u_x}{\partial y} + \frac{\partial u_y}{\partial x} \right)^2 + \frac{1}{2} \left(\frac{\partial u_y}{\partial z} + \frac{\partial u_z}{\partial y} \right)^2 \right. \\
 &\quad \left. + \frac{1}{2} \left(\frac{\partial u_z}{\partial x} + \frac{\partial u_x}{\partial z} \right)^2 \right\} + \lambda \left(\frac{\partial u_x}{\partial x} + \frac{\partial u_y}{\partial y} + \frac{\partial u_z}{\partial z} \right)^2 \tag{6.16.3}
 \end{aligned}$$

Cylindrical Coordinates (s, z, ϕ)

$$\frac{D}{Dt} = \frac{\partial}{\partial t} + u_s \frac{\partial}{\partial s} + \frac{u_\phi}{s} \frac{\partial}{\partial \phi} + u_z \frac{\partial}{\partial z} \tag{6.16.4}$$

$$\nabla \cdot (k \nabla T) = \frac{1}{s} \frac{\partial}{\partial s} \left\{ ks \frac{\partial T}{\partial s} \right\} + \frac{1}{s} \frac{\partial}{\partial \phi} \left\{ \frac{k}{s} \frac{\partial T}{\partial \phi} \right\} + \frac{\partial}{\partial z} \left\{ k \frac{\partial T}{\partial z} \right\} \tag{6.16.5}$$

$$\begin{aligned}
 \Phi &= \mu \left[2 \left\{ \left(\frac{\partial u_s}{\partial s} \right)^2 + \left(\frac{1}{s} \frac{\partial u_\phi}{\partial \phi} + \frac{u_s}{s} \right)^2 + \left(\frac{\partial u_z}{\partial z} \right)^2 \right\} + \left(\frac{1}{s} \frac{\partial u_z}{\partial \phi} + \frac{\partial u_\phi}{\partial z} \right)^2 \right. \\
 &\quad \left. + \left(\frac{\partial u_s}{\partial z} + \frac{\partial u_z}{\partial s} \right)^2 + \left(\frac{1}{s} \frac{\partial u_s}{\partial \phi} + \frac{\partial u_\phi}{\partial s} - \frac{u_\phi}{s} \right)^2 \right] + \lambda \left\{ \frac{\partial u_s}{\partial s} + \frac{1}{s} \frac{\partial u_\phi}{\partial \phi} + \frac{u_s}{s} + \frac{\partial u_z}{\partial z} \right\}^2 \tag{6.16.6}
 \end{aligned}$$

Spherical Polar Coordinates (r, θ, ϕ)

$$\frac{D}{Dt} = \frac{\partial}{\partial t} + u_r \frac{\partial}{\partial r} + \frac{u_\theta}{r} \frac{\partial}{\partial \theta} + \frac{u_\phi}{r \sin \theta} \frac{\partial}{\partial \phi} \quad (6.16.7)$$

$$\begin{aligned} \nabla \cdot (k \nabla T) &= \frac{1}{r^2} \frac{\partial}{\partial r} \left\{ kr^2 \frac{\partial T}{\partial r} \right\} + \frac{1}{r^2 \sin \theta} \frac{\partial}{\partial \theta} \left(k \sin \theta \frac{\partial T}{\partial \theta} \right) \\ &\quad + \frac{1}{r^2 \sin^2 \theta} \frac{\partial}{\partial \phi} \left(k \frac{\partial T}{\partial \phi} \right) \end{aligned} \quad (6.16.8)$$

$$\begin{aligned} \Phi &= \mu \left[2 \left\{ \left(\frac{\partial u_r}{\partial r} \right)^2 + \left(\frac{1}{r} \frac{\partial u_\theta}{\partial \theta} + \frac{u_r}{r} \right)^2 + \left(\frac{1}{r \sin \theta} \frac{\partial u_\phi}{\partial \phi} + \frac{u_r}{r} + \frac{u_\theta \cot \theta}{r} \right)^2 \right\} \right. \\ &\quad + \left\{ \frac{1}{r \sin \theta} \frac{\partial u_\theta}{\partial \phi} + \frac{\sin \theta}{r} \frac{\partial}{\partial \theta} \left(\frac{u_\phi}{\sin \theta} \right) \right\}^2 + \left\{ \frac{1}{r \sin \theta} \frac{\partial u_r}{\partial \phi} + r \frac{\partial}{\partial r} \left(\frac{u_\phi}{r} \right) \right\}^2 \\ &\quad \left. + \left\{ r \frac{\partial}{\partial r} \left(\frac{u_\theta}{r} \right) + \frac{1}{r} \frac{\partial u_r}{\partial \theta} \right\}^2 \right] \\ &\quad + \lambda \left[\frac{\partial u_r}{\partial r} + \frac{1}{r} \frac{\partial u_\theta}{\partial \theta} + \frac{2u_r}{r} + \frac{1}{r \sin \theta} \frac{\partial u_\phi}{\partial \phi} + \frac{u_\theta \cot \theta}{r} \right]^2 \end{aligned} \quad (6.16.9)$$

Linear Stability

7.1 Introduction

In this chapter we will be concerned with the onset of thermal convection when the fluid is heated just enough that weak convective motions begin to take over from conduction or radiation and transfer some of the heat. We will assume that the onset of convection occurs as a bifurcation from a motionless conductive state. We treat the onset of convection as a problem in the stability of the basic motionless state, i.e., we subject the basic state to perturbations of temperature and velocity and determine conditions under which the perturbations decay or amplify. The onset of convection corresponds to the state in which perturbations have zero growth rate.

If perturbations have a negative growth rate, i.e., if they decay, the basic motionless state is stable and heat is transported conductively. If perturbations have a positive growth rate, they amplify and establish a state of motion in which heat is partly transported convectively. We subject the basic state to perturbations of infinitesimal amplitude. In this case the stability problem can be linearized in the sense that quadratic and higher order products of perturbation quantities can be neglected compared to linear order perturbation quantities.

The linear stability or onset of convection problem is a classic problem with a large literature (see, e.g. Chandrasekhar, 1961). Although mantle convection is a highly nonlinear phenomenon, the linearized stability problem is relevant because it is amenable to analytical description and it contains much of the physics of the nonlinear convective state.

7.2 Summary of Basic Equations

The basic equations governing the onset of thermal convection are the conservation equations of mass, momentum, and energy discussed in Chapter 6. We adopt the Boussinesq approximation discussed in Chapter 6; the incompressible continuity equation is then the appropriate form of mass conservation

$$\frac{\partial u_i'^*}{\partial x_i^*} = 0 \quad (7.2.1)$$

where $u_i'^*$ is the dimensionless fluid velocity in the perturbed state. We assume $Pr = \infty$ as appropriate to the mantle and use (6.10.23) as the form of momentum conservation for a

Boussinesq fluid

$$0 = \frac{-\partial p'^*}{\partial x_i^*} - g_i^* T'^* Ra + \frac{\partial^2 u_i'^*}{\partial x_j^*} \quad (7.2.2)$$

In writing (7.2.2) we have simplified (6.10.23) by assuming constant dynamic viscosity ($\mu^* = 1$) and we have used (7.2.1) to eliminate one of the viscous terms. All nondimensional quantities (denoted by asterisks) are scaled as in Chapter 6. The Rayleigh number Ra is defined in (6.10.20). Primes refer to perturbation quantities as defined in Chapter 6. With the assumptions enumerated above, the relevant energy equation is (6.10.33)

$$\frac{DT'^*}{Dt^*} = \frac{\partial T'^*}{\partial t^*} + u_i'^* \frac{\partial T'^*}{\partial x_i^*} = \frac{\partial^2 T'^*}{\partial x_i^{*2}} + H^* \left(\frac{b^2 H_r \rho_r}{k_r \Delta T_r} \right) \quad (7.2.3)$$

where density, specific heat at constant pressure, and thermal conductivity have all been taken as constant ($\bar{\rho}^* = 1$, $\bar{c}_p^* = 1$, $\bar{k}^* = 1$).

The perturbation quantities in (7.2.1)–(7.2.3) are changes from a motionless adiabatic reference state (see Chapter 6). However, while the adiabatic state is an appropriate reference state for a vigorously convecting fluid, it is not a particularly good choice of a reference state for the onset of convection problem. The basic state at the onset of convective instability has a conductive temperature profile, not an adiabatic temperature profile. Since the adiabatic temperature of a Boussinesq fluid is a constant, T'^* is essentially the total temperature of the fluid; T'^* is not a perturbation quantity at all, in the sense that perturbation quantities have infinitesimal amplitude at the onset of convection. Instead T'^* is the sum of the motionless basic state steady conduction temperature profile T_c^* and a small amplitude departure θ'^* :

$$\theta'^* \equiv T'^* - T_c^* \quad (7.2.4)$$

The quantity θ'^* is a true perturbation quantity and is dynamically induced.

Similarly, p'^* as defined in Chapter 6 is not a true perturbation quantity. The variable p'^* is the pressure perturbation relative to a hydrostatic pressure computed using the adiabatic density (Chapter 6); the adiabatic density of a Boussinesq fluid is a constant. In the basic state at the onset of convection there is a density variation associated with the conductive temperature profile; the density variation modifies the hydrostatic pressure at convective onset and p'^* includes this effect. In the motionless conductive state, $u_i^* = 0$, $T'^* = T_c^*$ and (7.2.2) becomes

$$\frac{\partial p'^*}{\partial x_i^*} = -g_i^* T_c^* Ra \quad (7.2.5)$$

We denote the solution to this contribution to the hydrostatic pressure as p_c^* and define a true perturbation pressure Π'^* as

$$\Pi'^* \equiv p'^* - p_c^* \quad (7.2.6)$$

The quantity Π'^* is dynamically induced.

The equations for the onset of instability problem are obtained from (7.2.1)–(7.2.3) by substituting for T'^* from (7.2.4) and for p'^* from (7.2.6):

$$\frac{\partial u_i^*}{\partial x_i^*} = 0 \quad (7.2.7)$$

$$0 = \frac{-\partial \Pi'^*}{\partial x_i^*} - g_i^* \theta'^* Ra + \frac{\partial^2 u_i^*}{\partial x_j^{*2}} \quad (7.2.8)$$

$$\frac{\partial \theta'^*}{\partial t} + u_i^* \frac{dT_c^*}{dx_i^*} = \frac{\partial^2 \theta'^*}{\partial x_i^{*2}} \quad (7.2.9)$$

In arriving at (7.2.9) we neglected the nonlinear advective heat transport term $u_i^* \partial \theta'^* / \partial x_i^*$ on the left side of (7.2.9) since this term is quadratic in the small-amplitude perturbations u_i^* and θ'^* (u_i^* as defined in Chapter 6 is a true perturbation quantity in the convective onset problems since the reference state in Chapter 6 is motionless as is the basic state at convection onset). In addition, to get (7.2.9) we used the equation satisfied by the basic state heat conduction temperature (see 6.12.7 and 6.10.8) with $\bar{k}^* = 1$ and $\bar{\rho}^* = 1$:

$$0 = \frac{\partial^2 T_c^*}{\partial x_i^{*2}} + H^* \left(\frac{b^2 H_r \rho_r}{k_r \Delta T_r} \right) \quad (7.2.10)$$

Finally, we simplify (7.2.9) by setting $\partial \theta'^* / \partial t^* = 0$. This is partly justified by the fact that the onset of convection is defined by perturbations with zero growth rate. Additionally, the validity of $\partial \theta'^* / \partial t^* = 0$ requires that the perturbations at the onset of convection are not oscillatory in time. The absence of time dependence at the onset of convection is known as the principle of exchange of stabilities (Chandrasekhar, 1961); in the remainder of this chapter we consider only those convective instability problems for which the principle is valid and we replace (7.2.9) by

$$u_i^* \frac{dT_c^*}{dx_i^*} = \frac{\partial^2 \theta'^*}{\partial x_i^{*2}} \quad (7.2.11)$$

The equations for the analysis of the linearized stability of conductive motionless states against convection are (7.2.7), (7.2.8), and (7.2.11). In the following sections we solve these equations for a number of different heating modes, boundary conditions, and geometries.

7.3 Plane Layer Heated from Below

We first consider the onset of thermal convection in an infinite horizontal fluid layer of thickness b heated from below (Lord Rayleigh, 1916). The problem is illustrated in Figure 7.1. The upper surface at $y = 0$ is maintained at temperature T_0 and the lower surface at $y = b$ is maintained at temperature T_1 ; $T_1 > T_0$. The temperature scaling factor ΔT_r (see Chapter 6) is taken as $T_1 - T_0$. The gravitational field acts in the $+y$ -direction and the acceleration of gravity g is assumed constant. Thermally driven convection is expected because the fluid near the upper boundary is cooler and more dense than the fluid near the lower boundary; the fluid near the lower boundary will tend to rise and the fluid near the upper boundary will tend to sink.

In the absence of convection, heat will be conducted from the lower boundary to the upper boundary. With a constant thermal conductivity, the dimensionless conductive temperature T_c^* is a solution of (7.2.10) with $H^* = 0$. With the boundary conditions given above, T_c^* can only depend on y , and integration of (7.2.10) gives the linear temperature profile

$$T_c^* = \frac{T_0}{T_1 - T_0} + y^* \quad (7.3.1)$$

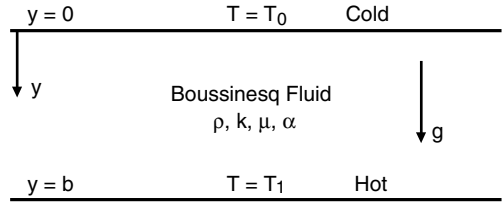


Figure 7.1. Sketch of a plane fluid layer heated from below for the problem of the onset of thermal convection.

where $y^* = y/b$. The corresponding heat flux is

$$q_c^* = \frac{q_c}{k(T_1 - T_0)/b} = \frac{-kdT_c/dy}{k(T_1 - T_0)/b} = \frac{-dT_c^*/dy^*}{dy^*} = -1 \quad (7.3.2)$$

or

$$q_c = \frac{-k(T_1 - T_0)}{b} \quad (7.3.3)$$

The pressure in the motionless conductive basic state p is given by (6.10.2) as

$$p = \bar{p} + p' \quad (7.3.4)$$

where \bar{p} is the hydrostatic pressure associated with the adiabatic reference state density (see 6.10.3). This adiabatic density ρ is a constant in the Boussinesq fluid layer and (6.10.3) becomes

$$\frac{d\bar{p}}{dy} = \rho g \quad (7.3.5)$$

or

$$\bar{p} = \rho gy + p_0 \quad (7.3.6)$$

where p_0 is the surface pressure. In the motionless state, $p' = p_c$, the hydrostatic pressure associated with the variation in the conductive temperature T_c . From (7.2.5) and (7.3.1) we can write

$$\frac{dp_c^*}{dy^*} = - \left\{ \left(\frac{T_0}{T_1 - T_0} \right) + y^* \right\} Ra \quad (7.3.7)$$

which integrates to

$$p_c^* = -Ra \left\{ \frac{T_0 y^*}{T_1 - T_0} + \frac{y^{*2}}{2} \right\} \quad (7.3.8)$$

(the constant of integration is zero). We can convert (7.3.8) to dimensional form using the scaling of Chapter 6 and the definition of the Rayleigh number in (6.10.20):

$$p_c = -\rho g \alpha \left\{ T_0 y + \frac{1}{2} \left(\frac{T_1 - T_0}{b} \right) y^2 \right\} \quad (7.3.9)$$

The combination of (7.3.4), (7.3.6), and (7.3.9) gives the pressure in the motionless basic state as

$$p = p_0 + \rho gy - \rho g\alpha \left\{ T_0 y + \frac{1}{2} \left(\frac{T_1 - T_0}{b} \right) y^2 \right\} \quad (7.3.10)$$

The equations for the dynamically induced infinitesimal perturbations u^*, π'^*, θ'^* are (7.2.7), (7.2.8), and (7.2.11). We limit the perturbation problem to two dimensions (x^*, y^*) with x^* the horizontal coordinate, i.e., there are no spatial variations in the horizontal direction orthogonal to x^* and there are only two nonzero perturbation velocity components (u^*, v^*) in the (x^*, y^*) directions. We rewrite these equations as

$$\frac{\partial u^*}{\partial x^*} + \frac{\partial v^*}{\partial y^*} = 0 \quad (7.3.11)$$

$$\frac{\partial \Pi'^*}{\partial x^*} = \left(\frac{\partial^2}{\partial x^{*2}} + \frac{\partial^2}{\partial y^{*2}} \right) u^* \quad (7.3.12)$$

$$\frac{\partial \Pi'^*}{\partial y^*} = -\theta'^* Ra + \left(\frac{\partial^2}{\partial x^{*2}} + \frac{\partial^2}{\partial y^{*2}} \right) v^* \quad (7.3.13)$$

$$v^* = \left(\frac{\partial^2}{\partial x^{*2}} + \frac{\partial^2}{\partial y^{*2}} \right) \theta'^* \quad (7.3.14)$$

The boundary conditions required for the solution of (7.3.11)–(7.3.14) comprise conditions on the temperature at the upper ($y^* = 0$) and lower ($y^* = 1$) surfaces and conditions on both velocity components (u^*, v^*) at both surfaces. It is possible to consider a large variety of such conditions. For the moment we focus on boundaries that are isothermal, impermeable, and shear stress free; these conditions are expressed mathematically as

$$v^* = \theta'^* = 0 \quad \text{at } y^* = 0, 1 \quad (7.3.15)$$

$$\frac{\partial u^*}{\partial y^*} = 0 \quad \text{at } y^* = 0, 1 \quad (7.3.16)$$

The number of equations can be reduced by introduction of the stream function ψ^* (6.3.2)

$$u^* = \frac{\partial \psi^*}{\partial y^*}, \quad v^* = \frac{-\partial \psi^*}{\partial x^*} \quad (7.3.17)$$

and by elimination of the pressure perturbation (differentiate (7.3.12) with respect to y^* and (7.3.13) with respect to x^* and subtract); (7.3.11)–(7.3.14) then become

$$0 = \nabla^{*4} \psi^* + Ra \frac{\partial \theta'^*}{\partial x^*} = \frac{\partial^4 \psi^*}{\partial x^{*4}} + 2 \frac{\partial^4 \psi^*}{\partial x^{*2} \partial y^{*2}} + \frac{\partial^4 \psi^*}{\partial y^{*4}} + Ra \frac{\partial \theta'^*}{\partial x^*} \quad (7.3.18)$$

$$0 = \nabla^{*2} \theta'^* + \frac{\partial \psi^*}{\partial x^*} = \left(\frac{\partial^2}{\partial x^{*2}} + \frac{\partial^2}{\partial y^{*2}} \right) \theta'^* + \frac{\partial \psi^*}{\partial x^*} \quad (7.3.19)$$

(see also 6.11.1 and 6.11.2). By differentiating (7.3.18) with respect to x^* and substituting for $\partial\psi^*/\partial x^*$ from (7.3.19), we arrive at a single partial differential for θ'^* :

$$\begin{aligned} 0 &= \nabla^{*6}\theta'^* - Ra \frac{\partial^2\theta'^*}{\partial x^{*2}} \\ &= \frac{\partial^6\theta'^*}{\partial x^{*6}} + 3 \frac{\partial^6\theta'^*}{\partial x^{*4}\partial y^{*2}} + 3 \frac{\partial^6\theta'^*}{\partial x^{*2}\partial y^{*4}} + \frac{\partial^6\theta'^*}{\partial y^{*6}} - Ra \frac{\partial^2\theta'^*}{\partial x^{*2}} \end{aligned} \quad (7.3.20)$$

The boundary conditions for (7.3.20) follow from a combination of (7.3.15)–(7.3.19) and are

$$\theta'^* = \frac{\partial^2\theta'^*}{\partial y^{*2}} = \frac{\partial^4\theta'^*}{\partial y^{*4}} = 0 \quad \text{on } y^* = 0, 1 \quad (7.3.21)$$

Equation (7.3.20) is a linear partial differential equation with constant coefficients; the equation and the boundary conditions (7.3.21) are homogeneous. With $\Delta T_r = T_1 - T_0$, the Rayleigh number, defined in (6.10.20), can be written as

$$Ra = \frac{\alpha g (T_1 - T_0) b^3}{\nu \kappa} \quad (7.3.22)$$

where κ is the thermal diffusivity and ν is the kinematic viscosity.

The solution of (7.3.20) and (7.3.21) can be obtained by considering temperature perturbations that are periodic in the horizontal coordinate x^* :

$$\theta'^* = \hat{\theta}'^*(y^*) \sin\left(\frac{2\pi x^*}{\lambda^*}\right) \quad (7.3.23)$$

where $\lambda^* = \lambda/b$ is the a priori unknown dimensionless horizontal wavelength of the temperature perturbation. This approach is equivalent to a Fourier expansion of θ'^* in the horizontal coordinate. Substitution of (7.3.23) into (7.3.20) yields a sixth-order ordinary differential equation for $\hat{\theta}'^*(y^*)$:

$$\left(\frac{d^2}{dy^{*2}} - \frac{4\pi^2}{\lambda^{*2}}\right)^3 \hat{\theta}'^*(y^*) = \frac{-4\pi^2 Ra}{\lambda^{*2}} \hat{\theta}'^*(y) \quad (7.3.24)$$

The solution of this constant coefficient ordinary differential equation subject to the boundary conditions (from (7.3.21))

$$\hat{\theta}'^* = \frac{d^2\hat{\theta}'^*}{dy^{*2}} = \frac{d^4\hat{\theta}'^*}{dy^{*4}} = 0 \quad \text{on } y^* = 0, 1 \quad (7.3.25)$$

is

$$\hat{\theta}'^* = \hat{\theta}_0' \sin \pi y^* \quad (7.3.26)$$

provided

$$\left(\pi^2 + \frac{4\pi^2}{\lambda^{*2}}\right)^3 = \frac{4\pi^2 Ra}{\lambda^{*2}} \quad (7.3.27)$$

or

$$Ra = Ra_{cr} = \frac{(\pi^2 + 4\pi^2/\lambda^{*2})^3}{4\pi^2/\lambda^{*2}} = \frac{\pi^4}{4\lambda^{*4}} (4 + \lambda^{*2})^3 \quad (7.3.28)$$

where Ra_{cr} is the critical Rayleigh number for the onset of convection.

The solution obtained for the temperature perturbation exists only for values of Ra given by (7.3.28). A plot of Ra_{cr} versus $2\pi/\lambda^*$ according to (7.3.28) is shown in Figure 7.2. It is seen that Ra_{cr} has a minimum value $Ra_{cr}(\min)$ given by solving

$$\frac{\partial Ra_{cr}}{\partial (2\pi/\lambda^*)} = \frac{\partial}{\partial (2\pi/\lambda^*)} \frac{(\pi^2 + 4\pi^2/\lambda^{*2})^3}{4\pi^2/\lambda^{*2}} = 0 \quad (7.3.29)$$

The value of $Ra_{cr}(\min)$, the minimum critical Rayleigh number for the onset of convection, occurs at $\lambda^* = \lambda_{cr}^*$; from (7.3.29) and (7.3.28), the values of λ_{cr}^* and $Ra_{cr}(\min)$ are

$$\lambda_{cr}^* = 2\sqrt{2} = 2.828, \quad Ra_{cr}(\min) = \frac{27\pi^4}{4} = 657.5 \quad (7.3.30)$$

The value $Ra_{cr}(\min)$ is the smallest value of the Rayleigh number at which convection could occur in the infinite plane fluid layer. If Ra is smaller than $Ra_{cr}(\min)$ the conductive fluid layer is stable and no convection can occur. If Ra is greater than $Ra_{cr}(\min)$, the fluid layer is unstable and convection can occur within a range of wavelengths corresponding to $Ra \geq Ra_{cr}$ (see 7.3.28 and Figure 7.2). The solution to this problem was first obtained by Lord Rayleigh (1916).

With the temperature perturbation given by a combination of (7.3.23) and (7.3.26)

$$\theta'^* = \hat{\theta}_0'^* \sin \pi y^* \sin \frac{2\pi x^*}{\lambda^*} \quad (7.3.31)$$

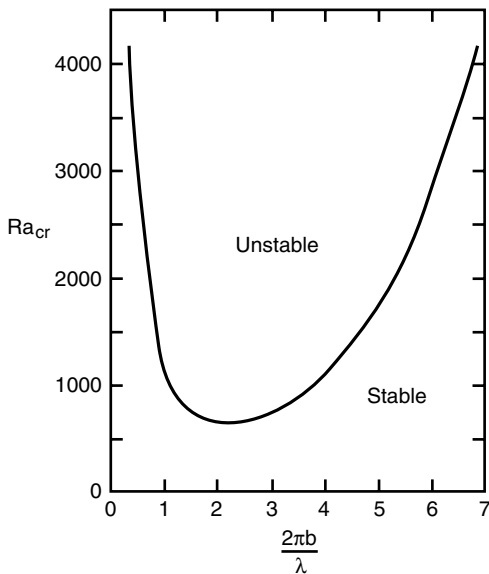


Figure 7.2. Critical Rayleigh number Ra_{cr} for the onset of thermal convection in a fluid layer heated from below with stress free boundaries as a function of dimensionless wave number $2\pi b/\lambda$.

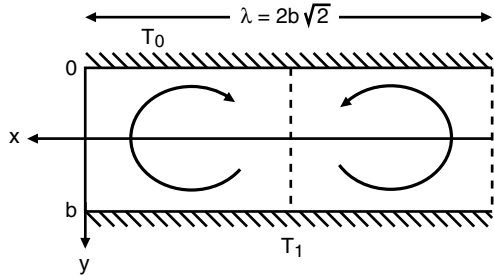


Figure 7.3. Sketch of two-dimensional counterrotating cells at the onset of convection in a fluid layer heated from below.

one can determine ψ^* from (7.3.19) as

$$\psi^* = - \left(\frac{\lambda^*}{2\pi} \right) \left(\frac{4\pi^2}{\lambda^{*2}} + \pi^2 \right) \hat{\theta}'_0 \sin \pi y^* \cos \frac{2\pi x^*}{\lambda^*} \quad (7.3.32)$$

From (7.3.17) and (7.3.32) the velocity components are

$$u^* = - \left(\frac{\lambda^*}{2} \right) \left(\frac{4\pi^2}{\lambda^{*2}} + \pi^2 \right) \hat{\theta}'_0 \cos \pi y^* \cos \frac{2\pi x^*}{\lambda^*} \quad (7.3.33)$$

$$v^* = - \left(\frac{4\pi^2}{\lambda^{*2}} + \pi^2 \right) \hat{\theta}'_0 \sin \pi y^* \sin \frac{2\pi x^*}{\lambda^*} \quad (7.3.34)$$

The solution takes the form of counterrotating cells as illustrated in Figure 7.3. The width of each cell is $b\lambda^*/2$; for $\lambda_{cr}^* = 2\sqrt{2}$ this width is $b\sqrt{2}$. The aspect ratio of the cell at $\lambda = \lambda_{cr}^*$ is the ratio of cell width to height or $\sqrt{2}$. Because the system of equations and boundary conditions is linear and homogeneous, the stability analysis does not predict the amplitude of the convection, i.e., $\hat{\theta}'_0$ is arbitrary.

Holmes (1931) applied this stability analysis to the Earth's mantle. He concluded that the minimum critical thermal gradient for whole mantle convection is 3 K km^{-1} ($Ra_{cr}(\text{min})$) can be converted into a minimum critical thermal gradient for the onset of convection by setting $Ra = Ra_{cr}(\text{min})$ in (7.3.22) and solving for $(T_1 - T_0)/b^*$). Since the near-surface thermal gradient is an order of magnitude larger than this value, he concluded that convection currents are required in the mantle and that these convection currents are responsible for continental drift. It took another 40 years before this revolutionary assertion became generally accepted.

For fixed-surface boundary conditions, i.e., $u^* = 0$ on $y^* = 0, 1$ instead of the condition used above on $\partial u^* / \partial y^*$ (7.3.16), a numerical solution is required for the linear stability problem (Pellew and Southwell, 1940). For this case the minimum critical Rayleigh number is $Ra_{cr}(\text{min}) = 1,707.8$ and the corresponding dimensionless wavelength of the convective rolls is $\lambda_{cr}^* = 2.016$. For a shear stress free upper boundary and a fixed lower boundary, $Ra_{cr}(\text{min}) = 1,100.7$ and $\lambda_{cr}^* = 2.344$. Different velocity boundary conditions have about a factor of 2 effect on the value of the minimum critical Rayleigh number. As expected, fixed surface boundary conditions are stabilizing relative to free surface boundary conditions, i.e., the value of $Ra_{cr}(\text{min})$ is higher with fixed boundaries. Table 7.1 summarizes these values of $Ra_{cr}(\text{min})$ and λ_{cr}^* .

An alternative thermal boundary condition of relevance to mantle convection involves specification of the upward heat flux q_b at the lower boundary instead of the temperature.

Table 7.1. Values of the Minimum Critical Rayleigh Number and Associated Dimensionless Horizontal Wavelength for the Onset of Convection in Plane Fluid Layers with Different Surface Boundary Conditions and Modes of Heating

Surface Boundary Conditions and Mode of Heating	Ra_{cr} (min)	λ_{cr}^*
Both boundaries shear stress free and isothermal, no internal heating. $H^* = 0$.	657.5	$2\sqrt{2} = 2.828$
Both boundaries fixed and isothermal. $H^* = 0$.	1,707.8	2.016
Shear stress free upper boundary, fixed lower boundary, both boundaries isothermal. $H^* = 0$.	1,100.7	2.344
Both boundaries shear stress free, upper boundary isothermal, lower boundary specified heat flux. $H^* = 0$.	384.7	3.57
Both boundaries fixed, upper boundary isothermal, lower boundary specified heat flux. $H^* = 0$.	1,295.8	2.46
Upper boundary shear stress free and isothermal, lower boundary fixed and heat flux prescribed. $H^* = 0$.	816.7	2.84

In this case the thermal boundary conditions are

$$\theta'^* = 0 \quad \text{on } y^* = 0 \quad \text{and} \quad \frac{\partial \theta'^*}{\partial y^*} = 0 \quad \text{on } y^* = 1 \quad (7.3.35)$$

The velocity conditions on the boundaries can be taken as impermeable and either fixed (no-slip) or shear stress free. To obtain a temperature scale for these thermal boundary conditions we calculate the temperature drop across the fluid layer in the conduction state (the conduction temperature profile is linear in y , as in the case of isothermal boundaries):

$$\Delta T_r = \frac{qb}{k} \quad (7.3.36)$$

Substitution of (7.3.36) into (6.10.20) yields the form of the Rayleigh number for the heat flux lower boundary condition:

$$Ra_q = \frac{\alpha g q_b b^4}{k \kappa \nu} \quad (7.3.37)$$

Solutions to this stability problem have been obtained by Sparrow et al. (1964). For shear stress free surface boundary conditions $Ra_{q,cr}(\text{min}) = 384.7$ and $\lambda_{cr}^* = 3.57$, for fixed surface boundary conditions $Ra_{q,cr}(\text{min}) = 1,295.8$ and $\lambda_{cr}^* = 2.46$, and for a shear stress free upper boundary and a fixed lower boundary $Ra_{q,cr}(\text{min}) = 816.7$ and $\lambda_{cr}^* = 2.84$. The values of the minimum critical Rayleigh numbers for prescribed lower boundary heat flux are somewhat smaller than those for the isothermal boundaries and the horizontal widths of the cells are larger. These results are summarized in Table 7.1.

If mantle convection is layered, then it would be appropriate to calculate the heat flow Rayleigh number for the upper mantle, since the upper mantle could be regarded as a separately convecting layer with a given heat flux at its base. To calculate Ra_q for the upper mantle we require the mean heat flux q_m through the upper mantle. The total heat flow from the interior of the Earth Q can be obtained by the multiplication of the area of the continents by the mean continental heat flux and adding the product of the oceanic area and the mean oceanic heat flow. The continents, including the continental margins, have an

area $A_c = 2 \times 10^8 \text{ km}^2$. Multiplication of this by the mean observed continental heat flux of 65 mW m^{-2} gives the total heat flow from the continents as $Q_c = 1.30 \times 10^{13} \text{ W}$. The oceans, including the marginal basins, have an area $A_o = 3.1 \times 10^8 \text{ km}^2$. Multiplication of this by the mean oceanic heat flux of 101 mW m^{-2} yields the total heat flow from the oceans as $Q_o = 3.13 \times 10^{13} \text{ W}$. By adding the heat flow from the continents and the oceans, we find that the total surface heat flow is $Q = 4.43 \times 10^{13} \text{ W}$. Division by the surface area $A = 5.1 \times 10^8 \text{ km}^2$ gives the mean surface heat flux of 87 mW m^{-2} (see Section 4.1.5).

A substantial fraction of the heat lost from the continents originates within the continental crust. This must be removed in order to obtain the mean heat flux through the upper mantle. We estimate that 37 mW m^{-2} of the continental heat flux is due to internal heat generation from radioactive elements in the crust. Thus the mantle contribution to the continental heat flux is 28 mW m^{-2} . When this is multiplied by the area of the continents, including the margins, and added to the oceanic contribution, we find that the total heat flow from the mantle is $Q_m = 3.69 \times 10^{13} \text{ W}$. Thus the mean heat flux through the upper mantle is $q_m = 72.4 \text{ mW m}^{-2}$ (see Section 4.1.5).

In order to complete the specification of the Rayleigh number Ra_q for upper mantle convection we take $\rho = 3.6 \times 10^3 \text{ kg m}^{-3}$, $g = 10 \text{ m s}^{-2}$, $\alpha = 3 \times 10^{-5} \text{ K}^{-1}$, $b = 700 \text{ km}$, $k = 4 \text{ W m}^{-1} \text{ K}^{-1}$, $\kappa = 1 \text{ mm}^2 \text{ s}^{-1}$, and $\mu = 10^{21} \text{ Pas}$. Substitution of these values into (7.3.37) gives $Ra_q = 4.8 \times 10^6$. Thus the ratio of the Rayleigh number Ra_q to the minimum critical Rayleigh number for upper mantle convection $Ra_{q,cr}(\min)$ is between $r = Ra_q/Ra_{q,cr}(\min) = 3.6 \times 10^3$ and 1.2×10^4 , depending upon the applicable velocity boundary conditions.

7.4 Plane Layer with a Univariant Phase Transition Heated from Below

As discussed in Chapter 4, and as will be emphasized in Chapters 9 and 10, the major mantle phase transitions at depths of 410 km and 660 km have a significant influence on temperature and flow in the mantle. In (4.6.2) we discussed how phase boundary distortion and release or absorption of latent heat tend to enhance or retard material transport through a phase transition; the different effects are summarized in Table 4.6 and illustrated in Figures 4.41 and 4.42. The ability of thermal convection to occur in a fluid layer containing a phase change is strongly affected by the flow enhancement and retardation effects associated with the phase change. A linear stability analysis for the onset of thermal convection in a fluid layer with a phase change both reveals these effects and quantifies them. The basic physics of how the olivine–spinel and spinel–perovskite phase changes influence mantle convection is contained in the phase change instability problem. The onset of thermal convection in a fluid layer with a univariant phase transition heated from below has been studied by Schubert et al. (1970), Schubert and Turcotte (1971), and Busse and Schubert (1971). The linear stability problem for a fluid layer with a divariant phase change has been discussed by Schubert et al. (1975).

We consider a situation similar to that of Section 7.3 except that the fluid layer has a univariant phase change at its midpoint $y = b/2$. The fluid is assumed to be in thermodynamic equilibrium both in the unperturbed reference state and in the perturbed state at the onset of thermal convection. The location of the phase boundary is thus determined by the intersection of the Clapeyron curve with the pressure–temperature curve for the fluid layer. In the perturbed state the phase boundary will be distorted from its initial position

at $y = b/2$. The slope of the Clapeyron curve Γ is given by (4.6.12)

$$\Gamma = \left(\frac{dp}{dT} \right)_c = \frac{L_H \rho_l \rho_h}{T (\rho_h - \rho_l)} \quad (7.4.1)$$

In the cases of the olivine–spinel and spinel–perovskite+magnesiowüstite phase changes, the light phase lies above the heavy phase, which is implicit in writing (7.4.1). The olivine–spinel phase change is exothermic, L_H is positive, and Γ is positive. The spinel–perovskite phase change is endothermic, L_H is negative, and Γ is negative.

We assume that $\rho_h - \rho_l \ll \rho_l, \rho_h$, and that both phases have the same values of dynamic viscosity μ , thermal conductivity k , specific heat at constant pressure c_p , thermal diffusivity κ , and kinematic viscosity ν (μ, k, c_p, κ , and ν are constants). Each phase is assumed to be a Boussinesq fluid, i.e., the density of each phase is regarded as constant except insofar as the thermal expansion of the fluid provides a force of buoyancy. The value of the coefficient of thermal expansion α is assumed to be constant and the same for both phases. The difference in density between the two phases is taken into account in determining the distortion of the phase change boundary and in the pressure boundary condition at the phase change interface. Two instability mechanisms are present in this model, the ordinary Rayleigh instability associated with the thermal expansion of the fluid and a phase change instability driven by the density difference between the phases.

In the undisturbed state there is a constant temperature gradient of magnitude β :

$$\beta = \frac{T_1 - T_0}{b} \quad (7.4.2)$$

(see Section 7.3). There are also pressure gradients $\rho_l g$ and $\rho_h g$ in the upper and lower phases, respectively (see 7.3.5). Since the less dense phase lies above the more dense phase, $\rho g / \beta > \Gamma$.

The solution to this linear stability problem can be obtained by writing equations similar to those in Section 7.3 for each of the two phases. The temperature perturbations in each of the phases $\hat{\theta}'^*_l$ and $\hat{\theta}'^*_h$ are solutions of (7.3.24) subject to the boundary conditions (7.3.25). The solutions to (7.3.24) involve 6 a priori unknown constants in each of the phases for a total of 12 unknowns to be determined as part of the solution. Boundary conditions (7.3.25) provide 6 equations for the 12 unknowns, leaving 6 unknowns still to be determined. The additional conditions follow from appropriate matching of $\hat{\theta}'^*_l$ and $\hat{\theta}'^*_h$ at the phase change interface. At the phase change boundary, mass flow, temperature, tangential stress, and tangential velocity must be continuous. In the linear stability analysis these continuity conditions can be applied at the undisturbed position $y = b/2$ of the phase change. Continuity of temperature is simply

$$\theta'_l{}^* = \theta'_h{}^* \quad \text{at} \quad y^* = \frac{1}{2} \quad (7.4.3)$$

Continuity of mass flux can be simplified, by using (7.3.19) and neglecting the difference between ρ_l and ρ_h , to yield

$$\left(\frac{\partial^2}{\partial x^{*2}} + \frac{\partial^2}{\partial y^{*2}} \right) \theta'_l{}^* = \left(\frac{\partial^2}{\partial x^{*2}} + \frac{\partial^2}{\partial y^{*2}} \right) \theta'_h{}^* \quad \text{at} \quad y^* = \frac{1}{2} \quad (7.4.4)$$

Continuity of tangential stress can be written, with the aid of (6.15.4), (7.3.11), and (7.3.14), in the form

$$\frac{\partial^2}{\partial y^{*2}} \nabla^{*2} \theta'_l{}^* = \frac{\partial^2}{\partial y^{*2}} \nabla^{*2} \theta'_h{}^* \quad \text{at} \quad y^* = \frac{1}{2} \quad (7.4.5)$$

where $\nabla^{*2} = \partial^2/\partial x^{*2} + \partial^2/\partial y^{*2}$. Continuity of tangential velocity, with the aid of (7.3.11) and (7.3.14), becomes

$$\frac{\partial}{\partial y^*} \nabla^{*2} \theta_l'^* = \frac{\partial}{\partial y^*} \nabla^{*2} \theta_h'^* \quad \text{at } y^* = \frac{1}{2} \quad (7.4.6)$$

There are two more conditions to be satisfied at the phase change interface. One of these is a result of the mass flux across the phase boundary, which causes energy to be released or absorbed depending on the direction of the phase change. At the phase boundary an amount of energy $\rho v L_H$ is absorbed or released per unit time and per unit area. The energy absorbed or released at the interface must be balanced by the difference in the perturbation heat flux into and out of the phase boundary. This linearized condition is

$$\frac{v^* L_H}{c_p(T_1 - T_0)} = \frac{\partial \theta_l'^*}{\partial y^*} - \frac{\partial \theta_h'^*}{\partial y^*} \quad \text{at } y^* = \frac{1}{2} \quad (7.4.7)$$

or, using (7.3.14),

$$\frac{L_H}{c_p(T_1 - T_0)} \nabla^{*2} \theta'^* = \frac{\partial \theta_l'^*}{\partial y^*} - \frac{\partial \theta_h'^*}{\partial y^*} \quad \text{at } y^* = \frac{1}{2} \quad (7.4.8)$$

Finally, the normal stress must be continuous at the phase boundary. Because of the nonzero pressure gradient in the unperturbed state, the linearization of this condition requires introduction of the vertical displacement η of the distorted phase boundary. Continuity of normal stress at the phase boundary can be written as

$$\Pi_l'^* - \Pi_h'^* = \frac{-gb^3(\rho_h - \rho_l)}{\mu\kappa} \eta^* \quad (7.4.9)$$

In (7.4.9) the difference in perturbation pressure between the two phases is equated to the hydrostatic head generated by the density difference between the phases and the displacement of the phase boundary. This pressure difference forces the flow that can result in a phase change driven instability.

Since the condition (7.4.9) introduces an additional unknown, the phase change interface displacement, yet another equation must be used to complete the solution. This is simply the requirement that the boundary between the phases must lie on the Clapeyron curve. The phase boundary displacement can thus be related to the temperature and pressure perturbations by

$$\eta^* = \frac{\Pi_l'^* - \theta_l'^*(\Gamma b^2 (T_1 - T_0)/\mu\kappa)}{(b^3/\mu\kappa)(g\rho_l - \Gamma\beta)} = \frac{\Pi_h'^* - \theta_h'^*(\Gamma b^2 (T_1 - T_0)/\mu\kappa)}{(b^3/\mu\kappa)(g\rho_h - \Gamma\beta)} \quad (7.4.10)$$

The temperature and pressure perturbations in (7.4.10) are evaluated at $y^* = 1/2$. The remaining details of the solution can be found in Schubert and Turcotte (1971). Here we proceed to discuss the results.

The solution to the above system of equations depends on the following four dimensionless parameters:

$$S = \frac{(\rho_h - \rho_l)/\rho}{\alpha b (\rho g / \Gamma - \beta)} \quad (7.4.11)$$

$$Ra_{L_H} = \frac{\alpha g b^3 L_H / c_p}{\nu \kappa} \quad (7.4.12)$$

λ^* (the dimensionless horizontal wavelength), and Ra as given by (7.3.22). In writing S in (7.4.11) the small difference between ρ_h and ρ_l has been neglected, except insofar as S is proportional to $(\rho_h - \rho_l)$. The interpretation of S is facilitated by rewriting (7.4.11) in the form

$$S = P \left(1 - \frac{\beta \Gamma}{\rho g} \right)^{-1} \quad (7.4.13)$$

where

$$P = \frac{\Gamma (\rho_h - \rho_l)}{\alpha \rho^2 g b} = \frac{(\Gamma (T_1 - T_0) / \rho g) (\rho_h - \rho_l)}{\alpha \rho b (T_1 - T_0)} \quad (7.4.14)$$

(see also Section 10.4). The parameter P is known as the phase buoyancy parameter (Christensen and Yuen, 1985) and it is essentially identical to S since the factor $(1 - \beta \Gamma / \rho g)^{-1}$ is near unity for the olivine–spinel and spinel–perovskite phase transitions. By examination of the far right side of (7.4.14) it can be seen that P is the ratio of the mass per unit area due to phase boundary distortion caused by the temperature difference across the layer ($T_1 - T_0$) to the mass per unit area associated with thermal expansion and $(T_1 - T_0)$. Thus, P or S measures the relative importance to convection of forces associated with phase boundary distortion and thermal expansion. The parameter Ra_{L_H} is a Rayleigh number based on the temperature difference L_H / c_p . It measures the stabilizing influence of the latent heat in the olivine–spinel phase transition and the destabilizing influence of the latent heat in the spinel–perovskite phase transition (see Table 4.6). The definition of Ra in (7.3.22) can be generalized to refer to the superadiabatic temperature difference across the layer, i.e., (7.3.22) can be rewritten as

$$Ra = \frac{\alpha g b^4 (T_1 - T_0)}{\nu \kappa b} = \frac{\alpha g b^4 \beta}{\nu \kappa} \quad (7.4.15)$$

and $\beta - \beta_{ad}$ can be substituted for β in (7.4.15) to yield

$$Ra = \frac{\alpha g b^4 (\beta - \beta_{ad})}{\nu \kappa} \quad (7.4.16)$$

where β_{ad} is the magnitude of the adiabatic temperature gradient given by (4.7.3). The generalization from (7.4.15) to (7.4.16) can be made since it is only the superadiabatic temperature difference across a fluid layer that is effective in driving convection and in the Boussinesq case of this section β_{ad} is approximated as zero.

The limiting cases $\alpha \rightarrow 0$ and $\beta \rightarrow \beta_{ad}$, $\alpha \rightarrow 0$ and $\beta \neq \beta_{ad}$, $\alpha \neq 0$ and $\beta \rightarrow \beta_{ad}$ have been studied in detail by Busse and Schubert (1971). The results of the analysis for the case $\alpha \rightarrow 0$, $\beta \neq \beta_{ad}$ have been applied to mantle phase changes by Schubert et al. (1970). This case is of particular interest since for $\alpha = 0$ the ordinary Rayleigh instability is not present, and one may focus on the phase change as the source of instability. For the olivine–spinel phase change, the inflow of relatively cold material from above the phase change boundary (due to the zero-order temperature gradient) forces the interface to a region of lower hydrostatic pressure, i.e., upward. With the interface displaced upward, the heavier material below the interface gives a hydrostatic pressure head tending to drive the flow

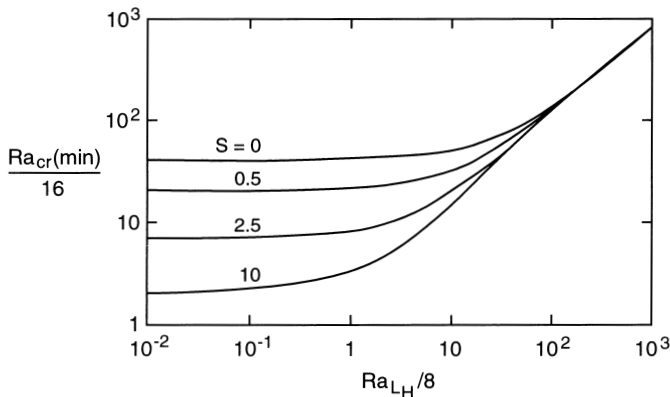


Figure 7.4. The minimum critical Rayleigh number $Ra_{cr}(\min)$ for the onset of thermal convection in a plane fluid layer with an exothermic univariant phase change in the middle of the layer as a function of Ra_{LH} for various values of S . After Schubert and Turcotte (1971).

downward, leading to instability. However, the downward flow of fluid through the interface releases heat, thus tending to warm the fluid and return the phase boundary to its unperturbed location. The inflow of cold material tends to promote instability, whereas release of heat by the phase change promotes stability. In regions of downward flow the phase boundary is displaced upward and in regions of upward flow the phase boundary is moved downward (see Section 4.6.2).

Figure 7.4 gives the minimum (over all possible perturbation horizontal wavelengths) critical Rayleigh number $Ra_{cr}(\min)$ for the onset of thermal convection in a fluid layer with a univariant phase change at its midpoint as a function of Ra_{LH} for various positive values of S corresponding to an exothermic phase change like that of olivine to spinel. For $Ra_{LH} = S = 0$ there is no phase change, and the results are in agreement with those of the previous section which give $Ra_{cr}(\min) = 27\pi^4/4 = 657.5$. In the limit $\alpha \rightarrow 0$, Ra and $Ra_{LH} \rightarrow 0$, $S \rightarrow \infty$, and the appropriate Rayleigh number for the phase change density difference $RaS \rightarrow 327.384$ for $Ra_{LH}/Ra = 0$ (Schubert et al., 1970; Busse and Schubert, 1971). In the ordinary Rayleigh instability, the density change due to thermal expansion is spread throughout the fluid layer. In the phase change instability of a fluid with $\alpha = 0$, the density change occurs at a single position in the fluid. The Rayleigh number for the former problem can be found analytically, whereas for the latter the determination of the Rayleigh number requires the numerical evaluation of a transcendental expression.

Since, in the exothermic case, Ra_{LH} represents the stabilizing effect of latent heat release at the phase change interface, it is clear from Figure 7.4 that $Ra_{cr}(\min)$ increases with increasing Ra_{LH} at a fixed value of S . As can be seen from Figure 7.4, for sufficiently large Ra_{LH} the minimum critical Rayleigh number becomes insensitive to the value of S . Also, for sufficiently large Ra_{LH} the critical Rayleigh number for symmetric convection (Figure 7.4) exceeds the critical Rayleigh number for antisymmetric convection 657.5 (Chandrasekhar, 1961). We find from Figure 7.4 that $Ra_{cr}(\min)$ decreases as S increases for fixed Ra_{LH} . This reflects the fact that as S increases the fractional density change associated with the exothermic phase transition becomes increasingly significant as compared with the density change associated with thermal expansion, and the phase change plays a more important role in driving the instability, thus reducing the critical Rayleigh number. For a wide range

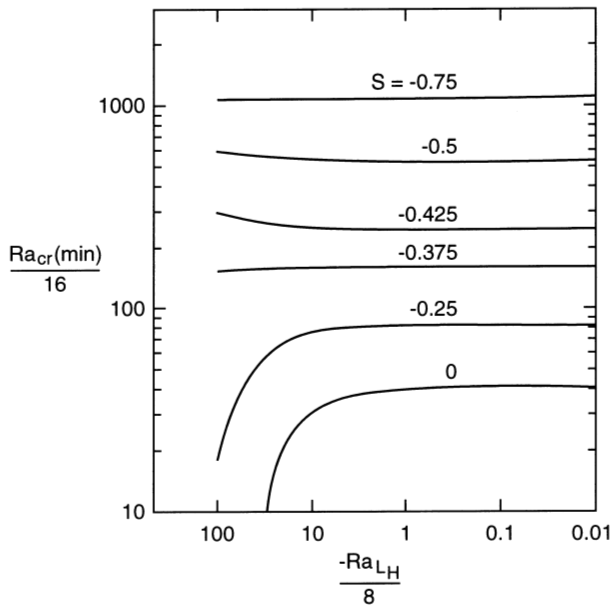


Figure 7.5. The minimum critical Rayleigh number $Ra_{cr}(\text{min})$ for the onset of thermal convection in a plane fluid layer with an endothermic univariant phase change in the middle of the layer as a function of Ra_{LH} for various values of S . After Schubert et al. (1975).

of values of Ra_{LH} and S , the critical Rayleigh number for symmetric convection through a phase change is lower than the critical Rayleigh number for a single-phase fluid.

Figure 7.5 gives the minimum critical Rayleigh number for the onset of thermal convection in a fluid layer with a univariant phase change at its midpoint as a function of Ra_{LH} for various negative values of S corresponding to an endothermic phase change like that of spinel to perovskite. For the endothermic phase change both Ra_{LH} and S are negative. Comparison of Figures 7.5 and 7.4 shows that the effects of $|S|$ and $|Ra_{LH}|$ on layer instability are opposite in the endothermic case compared with the exothermic case. As $|S|$ increases in Figure 7.5, phase boundary distortion becomes more important and the layer becomes more stable. For the case $S = 0$, there is no phase boundary distortion and the latent heat effect is seen in Figure 7.5 to be a destabilizing influence (see Table 4.6).

Values of the phase change instability parameters P (or S) and Ra_{LH} for the olivine–spinel and spinel–perovskite + magnesiowüstite phase changes can be estimated as follows. The Clapeyron slope for the olivine–spinel phase change is between 1.5 and 2.5 MPa K $^{-1}$ (Akaogi et al., 1989; Katsura and Ito, 1989) while Γ for the spinel–perovskite phase transition is -2 to -4 MPa K $^{-1}$ (see Section 10.4). Bina and Helffrich (1994) suggest $\Gamma_{410} = 3$ MPa K $^{-1}$ and $\Gamma_{660} = -2.5$ MPa K $^{-1}$. For $(\rho_h - \rho_l)/\rho$ we take 0.05 for olivine–spinel and 0.010 for spinel–perovskite. We evaluate L_H for both phase changes from (7.4.1) with $T = 2,000$ K. In addition we take $\alpha = 3 \times 10^{-5}$ K $^{-1}$, $v = 2.5 \times 10^{17}$ m 2 s $^{-1}$, $\rho = 4,000$ kg m $^{-3}$, $g = 10$ ms $^{-2}$, $b = 10^3$ km, and $k = 4$ W m $^{-1}$ K $^{-1}$. We find $P_{440} \approx 0.1$ and $P_{660} \approx -0.25$. For the olivine–spinel transition we obtain $Ra_{LH} \approx 6 \times 10^4$ and for the spinel–perovskite transition we get $Ra_{LH} \approx -1.8 \times 10^5$. The maximum values of $|Ra_{LH}|$ in Figures 7.4 and 7.5 are somewhat smaller than these estimates of Ra_{LH} for the olivine–spinel and spinel–perovskite phase changes in the mantle.

The question of whether the transition zone phase changes hinder or enhance mantle convection is best discussed using results from two-dimensional and three-dimensional numerical models of finite-amplitude thermal convection with phase changes. These results are presented in Chapters 9 and 10. The linear stability problem of this section is of value in that it brings out much of the physics that is important in how phase changes influence mantle convection.

Question 7.1: What is the influence of the olivine–spinel and spinel–perovskite + magnesiowüstite phase changes on mantle convection?

Peltier et al. (1989) presented a stability analysis for a spherical shell with a univariant phase transition.

7.5 Plane Layer Heated from Within

In this section we consider the onset of thermal convection in an infinite horizontal fluid layer heated internally and cooled from above. The entire mantle can be approximated by such a layer in that the mantle is heated primarily by the decay of radiogenic elements distributed throughout its interior; only a relatively small amount ($\approx 10\%$) of the surface heat flow enters the mantle from below at the core–mantle boundary. The geometry is identical to that of Section 7.3. However, in this case the lower boundary is assumed to be insulating so that no heat flux enters the layer from below. The internal heat sources are assumed to be distributed uniformly throughout the layer with H = heat generation rate per unit mass of fluid = constant. The upper boundary is taken to be isothermal at temperature T_0 . Again, either shear stress free or fixed surface boundaries can be considered. The scale for nondimensionalization of the temperature ΔT_r is the characteristic conductive temperature difference across the fluid layer due to the internal heat production:

$$\Delta T_r = \frac{b^2 H \rho}{k} \quad (7.5.1)$$

Length is dimensionless with respect to layer thickness b and the scale for the internal heat generation rate is $H_r = H$ so that $H^* = 1$.

The dimensionless conduction temperature in this case is a solution of (7.2.10) subject to the above boundary conditions:

$$T_c^* = \frac{T_0}{(b^2 H \rho / k)} + y^* - \frac{y^{*2}}{2} \quad (7.5.2)$$

The nondimensional conductive heat flux in the vertically downward direction q_c^* is given by

$$q_c^* = \frac{q_c}{b H \rho} = -\frac{k(dT_c/dy)}{b H \rho} = -\frac{dT_c^*}{dy^*} \quad (7.5.3)$$

From the above two expressions we can write

$$q_c^* = -(1 - y^*) \quad (7.5.4)$$

At the bottom of the layer, $y^* = 1$, q_c^* is zero, while at the top, $y^* = 0$, q_c^* is -1 ; in between, q_c^* varies linearly with depth. The conductive heat flux is negative since heat flows upward. A simple energy balance requires that at any position in the layer, the upward conductive heat flux is the product of the volumetric heat production rate ρH and the thickness of the underlying layer ($b - y$).

The pressure in the motionless conductive basic state is the sum of \bar{p} given by (7.3.6) and p_c , the hydrostatic pressure associated with the variation in T_c with y . The equation for $p_c^* = p_c [\mu_r/b)(k_r/\rho_r c_p r_b)]^{-1}$ is (7.2.5) or

$$\frac{dp_c^*}{dy^*} = -Ra_H T_c^* \quad (7.5.5)$$

where Ra_H is the internal heating Rayleigh number which, from (6.10.20) and (7.5.1), is

$$Ra_H = \frac{\alpha g \rho H b^5}{k \kappa \nu} \quad (7.5.6)$$

With T_c^* given by (7.5.2), (7.5.5) becomes

$$\frac{dp_c^*}{dy^*} = -Ra_H \left\{ \frac{T_0}{b^2 H \rho / k} + y^* - \frac{y^{*2}}{2} \right\} \quad (7.5.7)$$

which integrates to

$$p_c^* = -Ra_H \left\{ \frac{T_0}{b^2 H \rho / k} y^* + \frac{y^{*2}}{2} - \frac{y^{*3}}{6} \right\} \quad (7.5.8)$$

(the constant of integration is zero). The dimensional form of (7.5.8) is

$$p_c = -\alpha \rho g \left\{ T_0 y + \frac{1}{2} \left(\frac{\rho H b}{k} \right) y^2 - \frac{1}{6} \left(\frac{\rho H}{k} \right) y^3 \right\} \quad (7.5.9)$$

The equations for the dynamically induced perturbations u^* , v^* , Π'^* , and θ'^* are (7.3.11)–(7.3.13) and (7.2.11) which, from (7.5.3), can be written as

$$(1 - y^*) v^* = \left(\frac{\partial^2}{\partial x^{*2}} + \frac{\partial^2}{\partial y^{*2}} \right) \theta'^* \quad (7.5.10)$$

As was the case for the stability of the plane layer heated from below, we limit ourselves here to the two-dimensional stability of the internally heated plane layer.

For shear stress free and impermeable surfaces the velocity boundary conditions are

$$v^* = \frac{\partial u^*}{\partial y^*} = 0 \quad \text{on } y^* = 0, 1 \quad (7.5.11)$$

while for rigid and impermeable surfaces the velocity boundary conditions are

$$v^* = u^* = 0 \quad \text{on } y^* = 0, 1 \quad (7.5.12)$$

With the upper surface isothermal and the lower surface insulating, the temperature boundary conditions are

$$\theta'^* = 0 \quad \text{on } y^* = 0 \quad \text{and} \quad \frac{\partial \theta'^*}{\partial y^*} = 0 \quad \text{on } y^* = 1 \quad (7.5.13)$$

The solution to this stability problem can be obtained using the approach of Section 7.3 (7.3.17–7.3.21). Equation (7.3.18) is still valid (with Ra replaced by Ra_H), while (7.3.19) is replaced by (7.5.10) or

$$0 = \nabla^{*2}\theta'^* + \frac{\partial\psi^*}{\partial x^*}(1 - y^*) \quad (7.5.14)$$

By differentiating (7.5.14) with respect to x^* , taking the Laplacian of (7.3.18), and combining the two results, we obtain a single partial differential equation for ψ^* :

$$0 = \nabla^{*6}\psi^* - Ra_H(1 - y^*)\frac{\partial^2\psi^*}{\partial x^{*2}} \quad (7.5.15)$$

For shear stress free surfaces the boundary conditions in terms of ψ^* follow from (7.3.17), (7.3.18), (7.5.11), and (7.5.13):

$$\frac{\partial\psi^*}{\partial x^*} = \frac{\partial^2\psi^*}{\partial y^{*2}} = 0 \quad \text{on } y^* = 0, 1 \quad (7.5.16)$$

$$\frac{\partial^4\psi^*}{\partial y^{*4}} = 0 \quad \text{on } y^* = 0 \quad \text{and} \quad \nabla^{*4}\frac{\partial\psi^*}{\partial y^*} = 0 \quad \text{on } y^* = 1 \quad (7.5.17)$$

For rigid surfaces, the conditions on $\partial^2\psi^*/\partial y^{*2}$ in (7.5.16) are replaced by

$$\frac{\partial\psi^*}{\partial y^*} = 0 \quad \text{on } y^* = 0, 1 \quad (7.5.18)$$

and (7.5.17) is replaced by

$$\nabla^{*4}\psi^* = 0 \quad \text{on } y^* = 0, \quad \nabla^{*4}\frac{\partial\psi^*}{\partial y^*} = 0 \quad \text{on } y^* = 1 \quad (7.5.19)$$

As in the preceding section, we can assume ψ^* is periodic in the horizontal coordinate x^* :

$$\psi^* = \hat{\psi}^*(y^*) \sin \frac{2\pi x^*}{\lambda^*} \quad (7.5.20)$$

where λ^* is the a priori unknown dimensionless horizontal wavelength of the perturbation stream function. Substitution of (7.5.20) into (7.5.15)–(7.5.19) yields

$$\left(\frac{d^2}{dy^{*2}} - \frac{4\pi^2}{\lambda^{*2}} \right)^3 \hat{\psi}^*(y^*) = -Ra_H(1 - y^*) \frac{4\pi^2}{\lambda^{*2}} \hat{\psi}^*(y^*) \quad (7.5.21)$$

$$\hat{\psi}^* = \frac{d^2\hat{\psi}^*}{dy^{*2}} = 0 \quad \text{on } y^* = 0, 1 \quad (\text{shear stress free surfaces}) \quad (7.5.22)$$

$$\frac{d^4 \hat{\psi}^*}{dy^{*4}} = 0 \quad \text{on } y^* = 0 \quad (\text{shear stress free surface})$$

$$\left(\frac{d^2}{dy^{*2}} - \frac{4\pi^2}{\lambda^{*2}} \right)^2 \frac{d\hat{\psi}^*}{dy^*} = 0 \quad \text{on } y^* = 1 \quad (\text{shear stress free surface}) \quad (7.5.23)$$

$$\hat{\psi}^* = \frac{d\hat{\psi}^*}{dy^*} = 0 \quad \text{on } y^* = 0, 1 \quad (\text{rigid surfaces}) \quad (7.5.24)$$

$$\left(\frac{d^2}{dy^{*2}} - \frac{4\pi^2}{\lambda^{*2}} \right)^2 \hat{\psi}^* = 0 \quad \text{on } y^* = 0 \quad (\text{rigid surface}) \quad (7.5.25)$$

$$\left(\frac{d^2}{dy^{*2}} - \frac{4\pi^2}{\lambda^{*2}} \right)^2 \frac{d\hat{\psi}^*}{dy^*} = 0 \quad \text{on } y^* = 1 \quad (\text{rigid surface})$$

A simple analytic solution of (7.5.21)–(7.5.25) is not possible because (7.5.21) is an ordinary differential equation with nonconstant coefficients. The analogous equation for the heated from below stability problem (7.3.24) is a constant coefficient ordinary differential equation. The source of the difficulty is the basic state conductive temperature gradient which is constant when heating is from below and a linear function of depth when heating is from within. Nevertheless, a rather straightforward numerical solution of this system of equations is obtainable by standard techniques.

A solution of this problem has been obtained by Roberts (1967). With an insulated (zero heat flux) lower boundary, an isothermal upper boundary, and free-surface boundary conditions the minimum critical value of this Rayleigh number is $Ra_{H,cr}(\min) = 867.8$ and the corresponding nondimensional wavelength is $\lambda_{cr}^* = 3.51$. For fixed surface boundary conditions $Ra_{H,cr}(\min) = 2,772$ and $\lambda_{cr}^* = 2.39$ and for a free upper boundary and fixed lower boundary $Ra_{H,cr}(\min) = 1,612.6$ and $\lambda_{cr}^* = 2.78$.

It is appropriate to apply the Rayleigh number based on internal heat generation to whole mantle convection. This neglects the flux of heat out of the core but this is estimated to be only about 10% of the surface heat flux. The heat generation in the mantle H can be estimated by dividing the total mantle heat flow $Q_m = 3.69 \times 10^{13}$ W obtained above by the mass of the mantle $M_m = 4.0 \times 10^{24}$ kg; the result is $H = 9.23 \times 10^{-12}$ W kg $^{-1}$. It will be shown in Chapter 13 that part of the equivalent heat generation is due to the secular cooling of the mantle and part is due to heat produced by the radioactive isotopes of uranium, thorium, and potassium.

In order to complete the specification of the Rayleigh number for whole mantle convection, we take $\rho = 4.6 \times 10^3$ kg m $^{-3}$, $b = 2,900$ km, and the other values used above for layered upper mantle convection. Substitution of these values into (7.5.6) gives $Ra_H = 3 \times 10^9$. Thus the ratio of the Rayleigh number Ra_H to the minimum critical Rayleigh number for whole mantle convection $Ra_{H,cr}(\min)$ is between $r = Ra_H/Ra_{H,cr}(\min) = 3.6 \times 10^6$ and 1.2×10^6 depending upon the applicable boundary conditions. A comparison of this result with that obtained in Section 7.3 shows that the value of r is about a factor of 100 larger for whole mantle convection than it is for layered mantle convection. The requirement that the Rayleigh number be greater than 10^9 for simulations of whole mantle convection provides an important constraint on numerical models of mantle convection, as we will discuss in later chapters.

Question 7.2: How supercritical is the mantle?**7.6 Semi-infinite Fluid with Depth-dependent Viscosity**

We next consider the onset of thermal convection in a semi-infinite fluid with a strongly depth-dependent viscosity. In the linear stability problem a depth-dependent viscosity can take account of any pressure and temperature dependence that the viscosity may have since the required viscosity is only a function of the zero-order temperature and pressure that in turn are only functions of depth. If it is assumed that the viscosity has an exponential depth dependence given by

$$\mu = \mu_s e^{y/h} \quad (7.6.1)$$

where μ_s is the surface viscosity at $y = 0$, y is measured downward, and h is the scale depth of the viscosity variation, then the appropriate Rayleigh number is

$$Ra_\mu = \frac{\rho g \alpha \beta h^4}{\kappa \mu_s} \quad (7.6.2)$$

where β is the temperature gradient in the semi-infinite fluid. The solution to this problem has been obtained by Schubert et al. (1969). For a free surface boundary condition $Ra_{\mu,cr}(\min) = 23$ and $\lambda_{cr}^* = 13.1$, and for a fixed surface boundary condition $Ra_{\mu,cr}(\min) = 30$ and $\lambda_{cr}^* = 12.3$. The critical Rayleigh numbers are small and the critical nondimensional wavelengths are large because the convective flow extends several scale depths into the fluid. The effects of small variations in fluid properties on the stability problem have been studied by Palm (1960), Segel and Stuart (1962), Palm and Øiann (1964), Segel (1965), Busse (1967), and Palm et al. (1967). These studies were primarily concerned with the form and direction of the flow, i.e., whether the flow takes the form of two-dimensional rolls or three-dimensional hexagons. McKenzie (1988) has examined the symmetries of convective transitions in space and time.

A related problem is the stability of a thickening thermal boundary layer in a semi-infinite fluid. If the semi-infinite fluid initially has a uniform temperature T , and the temperature of the upper surface is instantaneously reduced to T_0 , a thermal boundary layer develops. Its structure has been given in (4.1.20). In the presence of a gravitational field the cold, dense thermal boundary layer is unstable. The tendency of the dense thermal boundary layer to sink into the underlying less dense fluid can be analyzed as a linear stability problem for the onset of thermal convection. The thermal boundary layer thickens with time until it reaches a critical thickness when convection begins. The boundary layer thickness y_T has been defined in (4.1.22). The applicable Rayleigh number for this problem is defined in terms of the thickness of the thermal boundary layer rather than the thickness of the full layer:

$$Ra_{y_T} = \frac{\alpha g (T_1 - T_0) y_T^3}{\nu \kappa} \quad (7.6.3)$$

For free surface boundary conditions Jaupart and Parsons (1985) found that the minimum critical value of this Rayleigh number is $Ra_{y_T,cr}(\min) = 807$. Substitution of this value into (7.6.3) yields a formula for the thickness of the boundary layer at the onset of convection:

$$y_T = \left\{ \frac{807 \nu \kappa}{\alpha g (T_1 - T_0)} \right\}^{1/3} \quad (7.6.4)$$

With $\mu = 10^{21}$ Pa s, $\rho = 3,300$ kg m $^{-3}$, $\kappa = 1$ mm 2 s $^{-1}$, $\alpha = 3 \times 10^{-5}$ K $^{-1}$, $g = 10$ ms $^{-2}$, and $T_1 - T_0 = 1,300$ K, (7.6.4) gives $y_T = 85.6$ km corresponding, according to (4.2.8), to an age of 43.3 Myr. According to this constant viscosity theory, one would expect the onset of secondary convection beneath the oceanic lithosphere to set in at an age of about 43 Myr. In Chapter 8 we will utilize this boundary layer instability to derive approximate solutions for fully developed thermal convection.

Jaupart and Parsons (1985) have also considered this problem for a depth-dependent viscosity of the form

$$\mu = \mu_1 + (\mu_0 - \mu_1) e^{-y/h} \quad (7.6.5)$$

where μ_0 is the value of the viscosity at the surface $y = 0$ and μ_1 is the value of the viscosity at great depth $y \rightarrow \infty$. They found a bifurcation in the stability problem for intermediate values of the viscosity contrast μ_0/μ_1 . For $\mu_0/\mu_1 < 10^3$, the instability includes the entire thermal boundary layer, as in the constant viscosity case. For $\mu_0/\mu_1 > 10^3$ only the lower part of the thermal boundary layer becomes unstable and a “stagnant lid” develops (see the discussion of stagnant-lid convection in Chapters 13 and 14). The whole-layer instability is associated with subduction while the partial layer instability is associated with delamination or secondary convection. Laboratory experiments carried out by Davaille and Jaupart (1994) have verified this bifurcation. These authors concluded that the asthenosphere viscosity must be in the range $\mu = 3 \times 10^{18}$ to 4×10^{17} Pa s for secondary convection to develop beneath the oceanic lithosphere.

Yuen et al. (1981) also considered this problem for a depth-dependent viscosity. In their model, the dependence of viscosity on depth arose from the strong dependence of μ on temperature and the dependence of temperature on depth appropriate to the oceanic lithosphere given by (4.2.4). They also concluded that secondary convection beneath the oceanic lithosphere required the existence of a pronounced low-viscosity asthenosphere beneath the lithosphere.

In all the above linear stability problems wherein viscosity varies with depth, the relevant equation for the perturbation stream function can be easily obtained from (6.11.1) and (6.11.2). When $\mu = \mu(y)$, (6.11.1) can be written (with ζ_z eliminated using (6.11.2)) as

$$\nabla^4 \psi + \frac{2}{\mu} \frac{d\mu}{dy} \frac{\partial}{\partial y} \nabla^2 \psi = \frac{-\rho\alpha g}{\mu} \frac{\partial T'}{\partial x} + \frac{1}{\mu} \frac{d^2\mu}{dy^2} (\psi_{xx} - \psi_{yy}) \quad (7.6.6)$$

Question 7.3: Is there secondary or small-scale thermal convection in the oceanic asthenosphere due to gravitational instability of the lower part of the oceanic lithosphere?

7.7 Fluid Spheres and Spherical Shells

In this section we consider the onset of thermal convection in homogeneous fluid spheres and spherical shells. With the application to planets in mind, we take the force of gravity to be radially inward and let $\bar{g} = \bar{g}(r)$, where r is the radial coordinate. We adopt the Boussinesq approximation and consider $\bar{\rho} = \text{constant}$. The reference state for these models was discussed in Section 6.12. From (6.12.5) and (6.12.6) we can write $\bar{g}(r)$ and $\bar{p}(r)$ for a

sphere of radius a as

$$\bar{g}(r) = \frac{4}{3}\pi Gr\bar{\rho} \quad (7.7.1)$$

$$\bar{p}(r) = \frac{2}{3}\pi G\bar{\rho}^2(a^2 - r^2) \quad (7.7.2)$$

For a spherical shell of inner radius c , outer radius a , and constant density $\bar{\rho}$ surrounding a core of average density ρ_c , $\bar{g}(r)$ and $\bar{p}(r)$ are given by (6.12.2) and (6.12.4)

$$\bar{g}(r) = \frac{4}{3}\pi G \left\{ r\bar{\rho} + \frac{c^3}{r^2}(\rho_c - \bar{\rho}) \right\}, \quad c \leq r \leq a \quad (7.7.3)$$

$$\bar{p}(r) = \frac{4}{3}\pi\bar{\rho}Gc^3(\rho_c - \bar{\rho})\left(\frac{1}{r} - \frac{1}{a}\right) + \frac{2}{3}\pi G\bar{\rho}^2(a^2 - r^2), \quad c \leq r \leq a \quad (7.7.4)$$

and $\bar{p}(a)$ has been taken as zero.

The temperature in the reference state T_c is the conduction solution given by (6.12.11). For the uniformly heated sphere the constant c_1 is zero, and c_2 can be determined from the condition $T_c(r = a) = 0$ with the result

$$T_c = -\frac{\bar{\rho}H}{6k}(r^2 - a^2) \quad (7.7.5)$$

For the spherical shell with isothermal inner and outer boundaries maintained at temperatures $T_c(r = c) = T_1$ and $T_c(r = a) = 0$, (6.12.11) gives

$$T_c = -\frac{\bar{\rho}H}{6k}r^2 + \frac{1}{r} \left[\frac{T_1 - (\bar{\rho}H/6k)(a^2 - c^2)}{(1/c - 1/a)} \right] + \frac{\bar{\rho}H}{6k}(a^2 + c^2 + ac) - \frac{T_1c}{(a - c)}, \quad c \leq r \leq a \quad (7.7.6)$$

For the sphere, the radial temperature gradient β_c in the conductive reference state is

$$\beta_c(r) \equiv \frac{dT_c}{dr} = -\frac{\bar{\rho}H}{3k}r \quad (7.7.7)$$

while for the spherical shell β_c is

$$\beta_c = -\frac{\bar{\rho}H}{3k}r - \frac{1}{r^2} \left[\frac{T_1 - (\bar{\rho}H/6k)(a^2 - c^2)}{(1/c - 1/a)} \right], \quad c \leq r \leq a \quad (7.7.8)$$

The heat flux in the conductive reference state q_c is given by Fourier's law in the form

$$q_c = -k\beta_c \quad (7.7.9)$$

Clearly q_c is a function of r . At the outer surface $r = a$, q_c for the sphere is

$$q_c(r = a) = -k\beta_c(r = a) = \frac{\bar{\rho}Ha}{3} \quad (7.7.10)$$

and q_c for the spherical shell is

$$\begin{aligned} q_c(r = a) &= -k\beta_c(r = a) = \frac{\bar{\rho}Ha}{3} + \frac{1}{a^2} \left[kT_1 - \frac{(\bar{\rho}H/6)(a^2 - c^2)}{(1/c - 1/a)} \right] \\ &= \frac{\bar{\rho}Ha}{3} - \frac{\bar{\rho}Hac}{6}(a + c) + \frac{kT_1}{a^2} \end{aligned} \quad (7.7.11)$$

The spherical shell is heated partly from within and partly from below.

A complete specification of the reference state requires determination of the hydrostatic pressure p_c due to the variation in T_c . From (6.10.24) we can write

$$\frac{dp_c}{dr} = \bar{\rho} \bar{g}(r) \bar{\alpha} T_c(r) \quad (7.7.12)$$

In this Boussinesq model we treat the thermal expansivity $\bar{\alpha}$ as constant. Equation (7.7.12) can be integrated to give $p_c(r)$ by using the above expressions for $\bar{g}(r)$ and $T_c(r)$. For the uniformly heated sphere we obtain

$$p_c = -\frac{2\pi G}{9k} \bar{\alpha} \bar{\rho}^3 H \left(\frac{r^4}{4} - \frac{a^2 r^2}{2} \right) \quad (7.7.13)$$

(the constant of integration is zero). The total pressure in the motionless basic state for the sphere is the sum of (7.7.2) and (7.7.13):

$$p = \frac{2}{3} \pi G \bar{\rho}^2 \left\{ a^2 - r^2 - \frac{\bar{\alpha} \bar{\rho} H}{3k} \left(\frac{r^4}{4} - \frac{a^2 r^2}{2} \right) \right\} \quad (7.7.14)$$

For the spherical shell, integration of (7.7.12) gives

$$\begin{aligned} p_c = & \frac{4}{3} \pi G \bar{\alpha} \bar{\rho}^2 \left[-\frac{\bar{\rho} H}{6k} \left\{ \frac{r^4}{4} + \frac{r c^3 (\rho_c - \bar{\rho})}{\bar{\rho}} \right\} + \left\{ \frac{T_1 - (\bar{\rho} H / 6k)(a^2 - c^2)}{(1/c - 1/a)} \right\} \right. \\ & \times \left\{ r - \frac{c^3}{2r^2} \frac{(\rho_c - \bar{\rho})}{\bar{\rho}} \right\} + \left\{ \frac{\bar{\rho} H}{6k} (a^2 + c^2 + ac) - \frac{T_1 c}{(a - c)} \right\} \\ & \times \left. \left\{ \frac{r^2}{2} - \frac{c^3}{r} \frac{(\rho_c - \bar{\rho})}{\bar{\rho}} \right\} \right], \quad c \leq r \leq a \end{aligned} \quad (7.7.15)$$

The total pressure in the motionless basic state for the spherical shell is the sum of (7.7.4) and (7.7.15).

The linearized equations for the dynamically induced infinitesimal perturbations at convection onset \underline{u}' , Π' , and θ' are the dimensional versions of (7.2.7), (7.2.8), and (7.2.11):

$$\nabla \cdot \underline{u}' = 0 \quad (7.7.16)$$

$$0 = -\nabla \Pi' + \bar{\alpha} \bar{\rho} \bar{g}(r) \hat{r} \theta' + \mu \nabla^2 \underline{u}' \quad (7.7.17)$$

$$\underline{u}' \cdot \nabla T_c = \kappa \nabla^2 \theta' \quad (7.7.18)$$

where \hat{r} is the radial unit vector. The dynamically induced pressure perturbation Π' can be eliminated from the equations by taking the curl of (7.7.17) and using $\nabla \times \hat{r} = 0$:

$$0 = \bar{\alpha} \bar{\rho} \bar{g}(r) \nabla \theta' \times \hat{r} + \mu \nabla^2 \underline{\omega}' \quad (7.7.19)$$

where $\underline{\omega}'$ is the perturbation vorticity $\underline{\omega}' \equiv \nabla \times \underline{u}'$. The perturbation temperature equation (7.7.18) can be simplified by noting that $\nabla T_c = \beta_c(r) \hat{r}$:

$$u'_r \beta_c(r) = \kappa \nabla^2 \theta' \quad (7.7.20)$$

In Section 7.8 dealing with spherical harmonics, we discuss how any solenoidal vector field (a vector field with zero divergence) can be represented by the sum of poloidal and toroidal vector fields. The velocity field \underline{u}' is a solenoidal vector field by virtue of (7.7.16) and it is convenient for the solution of the present problem to represent \underline{u}' accordingly:

$$\underline{u}' \equiv \nabla \times (\nabla \times (\Phi \hat{\underline{r}})) + \nabla \times (\Psi \hat{\underline{r}}) \quad (7.7.21)$$

where Φ is the poloidal scalar and Ψ is the toroidal scalar (see Section 7.8). This representation of the perturbation velocity field automatically satisfies the continuity equation (7.7.16). The components of the perturbation velocity and vorticity fields can be written in terms of Φ and Ψ as

$$u'_r = \frac{1}{r^2} L^2 \Phi \quad (7.7.22)$$

$$u'_{\theta} = \frac{1}{r} \frac{\partial^2 \Phi}{\partial r \partial \theta} + \frac{1}{r \sin \theta} \frac{\partial \Psi}{\partial \phi} \quad (7.7.23)$$

$$u'_{\phi} = \frac{1}{r \sin \theta} \frac{\partial^2 \Phi}{\partial r \partial \phi} - \frac{1}{r} \frac{\partial \Psi}{\partial \theta} \quad (7.7.24)$$

$$\omega'_r = \frac{1}{r^2} L^2 \Psi \quad (7.7.25)$$

$$\omega'_{\theta} = \frac{1}{r} \frac{\partial^2 \Psi}{\partial r \partial \theta} - \frac{1}{\sin \theta} \frac{\partial}{\partial \phi} \left\{ \nabla^2 \left(\frac{\Phi}{r} \right) \right\} \quad (7.7.26)$$

$$\omega'_{\phi} = \frac{1}{r \sin \theta} \frac{\partial^2 \Psi}{\partial r \partial \phi} + \frac{\partial}{\partial \theta} \left\{ \nabla^2 \left(\frac{\Phi}{r} \right) \right\} \quad (7.7.27)$$

where (r, θ, ϕ) are spherical coordinates, and L is a horizontal differential operator defined in the next section.

Only the poloidal function Φ contributes to the radial component of the velocity while only the toroidal function Ψ contributes to the radial component of the vorticity. As a result, the temperature equation (7.7.20) does not involve the toroidal function Ψ . Inspection of the vorticity equation (7.7.19) shows that its radial component is independent of θ' and Φ . Therefore, the toroidal function Ψ is identically zero in this onset of convection problem, i.e., buoyancy forces only induce a poloidal velocity field through the coupling of θ' and Φ in (7.7.20) and in the horizontal components of (7.7.19).

The problem of onset of convective instability in the sphere or spherical shell reduces to the solution of (7.7.20) and (7.7.19) for θ' and Φ . The solution can be most readily obtained by an expansion of θ' and Φ in terms of spherical harmonics (see Section 7.8 for a discussion of these functions):

$$\theta' = \sum_{l=0}^{\infty} \sum_{m=-l}^l \theta'_{lm}(r) Y_l^m(\theta, \phi) \quad (7.7.28)$$

$$\Phi = \sum_{l=0}^{\infty} \sum_{m=-l}^l \Phi_{lm}(r) Y_l^m(\theta, \phi) \quad (7.7.29)$$

Substitution of (7.7.28) and (7.7.29) into (7.7.19) and (7.7.20) results in

$$\frac{\bar{\alpha} \bar{\rho} \bar{g}(r)}{\mu r} \theta'_{lm} = D_l^2 \left(\frac{\Phi_{lm}(r)}{r} \right) \quad (7.7.30)$$

$$\frac{\beta_c(r) l(l+1)}{r^2} \Phi_{lm}(r) = \kappa D_l (\theta'_{lm}(r)) \quad (7.7.31)$$

where D_l is the differential operator given in (7.8.17); the θ and ϕ components of (7.7.19) are redundant, both leading to (7.7.30).

Equations (7.7.30) and (7.7.31) are coupled ordinary differential equations in r for the spherical harmonic components of the perturbation temperature field and the perturbation poloidal velocity field at the onset of convection. A single differential equation for the dynamically induced temperature perturbation $\theta'_{lm}(r)$ can be obtained by solving (7.7.31) for $\Phi_{lm}(r)/r$ and substituting in (7.7.30) with the result

$$\frac{l(l+1)\bar{\alpha} \bar{\rho} \bar{g}(r)}{\kappa \mu r} \theta'_{lm}(r) = D_l^2 \left\{ \frac{r}{\beta_c(r)} D_l (\theta'_{lm}(r)) \right\} \quad (7.7.32)$$

For the internally heated sphere, $\bar{g}(r)$ is given by (7.7.1) and $\beta_c(r)$ is given by (7.7.7); substitution of these formulae into (7.7.32) gives

$$D_l^{*3}(\theta'_{lm}) = -\frac{4\pi}{9} l(l+1) Ra_{sp} \theta'_{lm} \quad (7.7.33)$$

where D_l^* is the dimensionless form of (7.8.17) with the radius of the sphere as the length scale, and Ra_{sp} is the appropriate Rayleigh number for the internally heated sphere given by

$$Ra_{sp} \equiv \frac{\bar{\alpha} \bar{\rho}^3 H G a^6}{k \kappa \mu} \quad (7.7.34)$$

For the spherical shell, $\bar{g}(r)$ is given by (7.7.3) and $\beta_c(r)$ is given by (7.7.8); substitution of these formulae into (7.7.32) yields

$$\begin{aligned} & D_l^{*2} \left\{ \left[1 + \frac{(a^3/2r^3) (6kT_1/\bar{\rho}Ha^2 - (1 - (c^2/a^2)))}{(a/c - 1)} \right]^{-1} D_l^*(\theta'_{lm}) \right\} \\ &= -\frac{4\pi}{9} l(l+1) Ra_{sp} \left\{ 1 + \frac{c^3}{r^3} \left(\frac{\rho_c}{\bar{\rho}} - 1 \right) \right\} \theta'_{lm} \end{aligned} \quad (7.7.35)$$

Equations (7.7.33) and (7.7.35) are solved subject to boundary conditions appropriate to isothermal, impermeable, and either rigid (no-slip) or shear stress free boundary conditions. For the internally heated sphere, these conditions are applied only at the outer boundary, with the additional requirement that the solution remains finite at the origin $r = 0$. Impermeability of a spherical surface requires $u_r = 0$ on the surface. From (7.7.22), (7.7.28), and $L^2 Y_l^m = l(l+1)Y_l^m$, we can write the impermeability condition for each spherical

harmonic as $\Phi_{lm} = 0$ on $r = a$ and on $r = c$ for the spherical shell. The condition of isothermality on the spherical surfaces is, from (7.7.28), $\theta'_{lm} = 0$ on $r = a$ and on $r = c$ for the shell. Equation (7.7.31) shows that the condition $\Phi_{lm} = 0$ is equivalent to $D_l \theta'_{lm} = 0$. If a bounding spherical surface is rigid, then the tangential velocity components u'_θ and u'_ϕ must vanish on the surface. From (7.7.23), (7.7.24), and (7.7.29) it is seen that $u'_\theta = u'_\phi = 0$ is equivalent to $d\Phi_{lm}/dr = 0$.

If a bounding spherical surface is shear stress free, then the viscous stresses $\tau'_{r\theta}$ and $\tau'_{r\phi}$ must vanish on the surface. The viscous shear stresses are given by (6.15.17) and (6.15.18); vanishing of these stresses on a spherical surface requires

$$r \frac{\partial}{\partial r} \left(\frac{u'_\theta}{r} \right) + \frac{1}{r} \frac{\partial u'_r}{\partial \theta} = 0 \quad (7.7.36)$$

and

$$\frac{1}{r \sin \theta} \frac{\partial u'_r}{\partial \phi} + r \frac{\partial}{\partial r} \left(\frac{u'_\phi}{r} \right) = 0 \quad (7.7.37)$$

on the surface. Since $u'_r = 0$ on the surface, $\partial u'_r / \partial \theta$ and $\partial u'_r / \partial \phi$ are also zero on the surface and (7.7.36) and (7.7.37) simplify to

$$\frac{\partial}{\partial r} \left(\frac{u'_\theta}{r} \right) = \frac{\partial u'_\theta}{\partial r} - \frac{1}{r} u'_\theta = 0 \quad (7.7.38)$$

$$\frac{\partial}{\partial r} \left(\frac{u'_\phi}{r} \right) = \frac{\partial u'_\phi}{\partial r} - \frac{1}{r} u'_\phi = 0 \quad (7.7.39)$$

on the spherical surface. From (7.7.23) and (7.7.24), these conditions are equivalent to

$$\frac{d}{dr} \left\{ \frac{1}{r^2} \frac{d\Phi_{lm}}{dr} \right\} = 0 \quad (7.7.40)$$

on the surface; since $\Phi_{lm} = 0$ on the spherical surface (7.7.40) is also equivalent to

$$\frac{d^2}{dr^2} \left(\frac{\Phi_{lm}}{r} \right) = 0 \quad (7.7.41)$$

on a shear stress free spherical surface.

7.7.1 The Internally Heated Sphere

The onset of thermal convection in a uniformly heated sphere occurs at a value of Ra_{sp} determined by the solution of (7.7.33) subject to the conditions

$$\theta'_{lm} = D_l^* \theta'_{lm} = 0 \quad \text{on } \frac{r}{a} = 1 \quad (7.7.42)$$

and either

$$\frac{d}{d(r/a)} D_l^* \theta'_{lm} = 0 \quad \text{on } \frac{r}{a} = 1 \quad (7.7.43)$$

for a rigid surface or

$$\frac{d^2}{d(r/a)^2} D_l^* \theta'_{lm} = 0 \quad \text{on} \quad \frac{r}{a} = 1 \quad (7.7.44)$$

for a shear stress free surface. Chandrasekhar (1961) proves the validity of the exchange of stabilities for this problem, an assumption we adopted at the beginning of our analysis with the neglect of the $\partial\theta'/\partial t$ term in (7.7.18). Though there is no simple analytic solution to this problem, a numerical solution of the ordinary differential equation (7.7.33) subject to (7.7.42) and either (7.7.43) or (7.7.44) is straightforward. The resulting values of Ra_{sp} , denoted by $Ra_{sp,cr}$, are given in Table 7.2 for both the rigid and shear stress free boundary conditions on the surface of the sphere. The values of $Ra_{sp,cr}$ in the table are from Chandrasekhar (1961); solutions of this linearized stability problem have also been obtained by Jeffreys and Bland (1951), Chandrasekhar (1952, 1953), Backus (1955), Roberts (1965a), and Zebib et al. (1983).

The critical Rayleigh numbers depend only on the value of l , i.e., for a given l , all convective modes with $-l \leq m \leq l$ have the same value of $Ra_{sp,cr}$ and are equally likely to occur at the onset of convection, according to linear theory. A nonlinear theory is required to determine the modes with preferred values of m when $Ra_{sp} > R_{sp,cr}(l)$. Convective modes with a given value of l cannot occur unless $Ra_{sp} \geq R_{sp,cr}(l)$; when the equality holds m can have any value between $-l$ and l , when the inequality holds there are preferred values of m that can be determined from a nonlinear analysis of the convective problem. As Table 7.2 shows, the minimum critical Rayleigh number for the free surface boundary condition is $Ra_{sp,cr}(\min) = 2,213.9$ and for the fixed surface boundary condition it is $Ra_{sp,cr}(\min) = 5,758.3$. In both cases the minimum critical Rayleigh number is associated with the $l = 1$ mode, a single convective cell. The pattern of the axisymmetric $l = 1$ mode of convection is shown by the isotherms and streamlines in a meridional cross-section in Figure 7.6. The value of Ra_{sp} for the case shown in the figure is 9,550, so convection is somewhat nonlinear and spherical harmonic modes with $l \neq 1$ are also present. Nevertheless, the flow is essentially similar to convection at the onset of instability. There is upwelling at one pole and downwelling at the other. The highest velocities occur near the outer boundary as fluid crosses the equatorial plane.

It is of interest to apply the above results to the Moon. We assume that the Moon has a rigid outer shell with a thickness of 300 km and therefore take $a = 1,400$ km.

Table 7.2. Values of the Critical Rayleigh Number $Ra_{sp,cr}$ for the Onset of Thermal Convection in a Uniformly Internally Heated, Self-gravitating Fluid Sphere

l	Shear Stress Free Outer Boundary	Rigid Outer Boundary
	$Ra_{sp,cr}$	$Ra_{sp,cr}$
1	2.2139×10^3	5.7583×10^3
2	3.7415×10^3	7.4406×10^3
3	6.2843×10^3	1.0818×10^4
4	1.0013×10^4	1.5727×10^4
5	1.5186×10^4	2.2373×10^4
6	2.2093×10^4	3.1041×10^4

Note: The minimum values of $Ra_{sp,cr}$ are printed in bold.

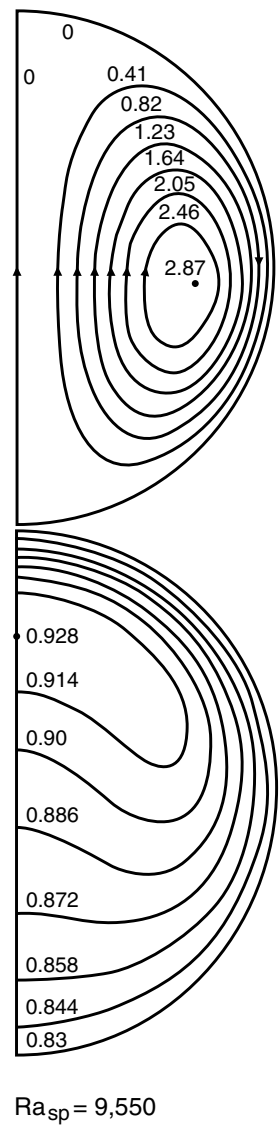


Figure 7.6. Single-cell convection in an internally heated sphere at $\text{Ra}_{\text{sp}} = 9,550$. Top: streamlines; bottom: isotherms. The highest temperature in the sphere lies along the axis of the upwelling nearer the surface than the center of the sphere. After Zebib et al. (1983).

We also take $H = 9 \times 10^{-12} \text{ W kg}^{-1}$ (by analogy with the Earth), $\bar{\rho} = 3,340 \text{ kg m}^{-3}$, $G = 6.67 \times 10^{-11} \text{ N m}^2 \text{ kg}^{-2}$, $\alpha = 3 \times 10^{-5} \text{ K}^{-1}$, $k = 4 \text{ W m}^{-1} \text{ K}^{-1}$, $\kappa = 1 \text{ mm}^2 \text{ s}^{-1}$, and $\text{Ra}_{\text{sp},\text{cr}} = 5,758$ corresponding to a rigid outer boundary. From the condition $\text{Ra}_{\text{sp}} > \text{Ra}_{\text{sp},\text{cr}}$ for convection to occur, we find that convection would be expected within the Moon for viscosities less than $\mu = 2 \times 10^{23} \text{ Pa s}$. This is about two orders of magnitude larger than the viscosity in the Earth's mantle. Thus convection would be expected within the lunar interior, at least until volcanism removed the radiogenic heat sources.

Question 7.4: Is there mantle convection in the lunar interior?

7.7.2 Spherical Shells Heated Both from Within and from Below

If we consider spherical shells for which

$$T_1 = \frac{\bar{\rho}H}{6k} (a^2 - c^2) \quad (7.7.45)$$

and $\rho_c = \bar{\rho}$, then from (7.7.8) we find

$$\beta_c = -\frac{\bar{\rho}H}{3k}r \quad (7.7.46)$$

and (7.7.11) gives

$$q_c(r = a) = \frac{1}{3}\bar{\rho}Ha \quad (7.7.47)$$

In addition, (7.7.3) reduces to

$$\bar{g}(r) = \frac{4}{3}\pi G\bar{\rho}r \quad (7.7.48)$$

In this special case, the spherical shell is similar to the full sphere in that the acceleration of gravity and the radial temperature gradient of the conductive state are the same in the shell and the sphere. The heat flux at the outer boundary is the same for the shell and the sphere. Equation (7.7.35) which governs the onset of convection in the spherical shell reduces to (7.7.33), the equation for the sphere, and Ra_{sp} is the only dimensionless parameter, other than the radius ratio of the shell, to control the onset of convective instability in the shell.

The onset of thermal convection in this particular case of a uniformly internally heated spherical shell occurs at a value of Ra_{sp} determined by the solution of (7.7.33) subject to appropriate boundary conditions. The conditions are (7.7.42) the isothermal, impermeable conditions, applied not only at the outer boundary $r/a = 1$, but also at the inner boundary, $r/a = c/a = \eta$, where we have introduced η to represent the radius ratio of the inner and outer boundaries. We also apply either (7.7.43) or (7.7.44) at both $r/a = 1$ and $r/a = \eta$ depending on whether the boundary is rigid or shear stress free. The principle of exchange of stabilities is valid in this special spherical shell problem just as it is for the sphere (Chandrasekhar, 1961). The values of Ra_{sp} at the onset of convection in the spherical shell are denoted by $Ra_{sp,cr}$ and are listed in Table 7.3 (after approximate results given in Chandrasekhar, 1961). The values depend on l , the size of the shell η , and the nature of the boundaries. The minimum values of $Ra_{sp,cr}$ tend to increase and tend to occur at larger values of l with increasing η . Thus, as the shell becomes thinner, the onset of convection tends to occur at larger spherical harmonic degrees or at shorter horizontal length scales. For a given η , the minimum values of $Ra_{sp,cr}$ are larger when boundaries are rigid than when they are shear stress free; for a given η , the minimum values of $Ra_{sp,cr}$ are also larger when $r/a = 1$ is rigid and $r/a = \eta$ is shear stress free than when the reverse is the case. The larger the fraction of the boundary surface that is rigid, the larger Ra_{sp} must be to initiate convection.

The initiation of convection in the internally heated and heated from below spherical shell with shear stress free boundaries has also been studied by Schubert and Zebib (1980) for the case $\eta = 0.5$, a value close to that of the Earth's mantle. Their results for $Ra_{sp,cr}$ given in Table 7.4 are in good agreement with those of Chandrasekhar (1961). The most unstable mode has $l = 3$. The axisymmetric form of the $l = 3$ convective mode is similar to the mode of convection illustrated later in this section when we discuss the instability of a base-heated spherical shell.

Table 7.3. Approximate Values of $Ra_{sp,cr}$ (After Chandrasekhar, 1961) for the Onset of Thermal Convection in a Uniformly Internally Heated Spherical Shell That is Also Heated at its Base;
 $\beta_c(r) = -\bar{\rho} Hr/3k$, $\bar{g}(r) = \frac{4}{3}\pi G \bar{\rho} r$

l/η	$Ra_{sp,cr}$					
	Both Boundaries Shear Stress Free					
0.2	0.3	0.4	0.5	0.6	0.8	
1	3.732×10^3	6.090×10^3	1.205×10^4	2.996×10^4	1.005×10^5	5.578×10^6
2	4.088×10^3	5.094×10^3	7.814×10^3	1.561×10^4	4.392×10^4	1.972×10^6
3	6.361×10^3	6.841×10^3	8.566×10^3	1.377×10^4	3.168×10^4	1.074×10^6
4	1.003×10^4	1.023×10^4	1.135×10^4	1.536×10^4	2.919×10^4	7.198×10^5
5	1.519×10^4	1.526×10^4	1.595×10^4	1.914×10^4	3.089×10^4	5.483×10^5 ^a

^a The smallest value of $Ra_{sp,cr}$ at $\eta = 0.8$ is 3.655×10^5 for $l = 10$.

l/η	$Ra_{sp,cr}$					
	$r/a = 1$ Shear Stress Free, $r/a = \eta$ Rigid					
0.2	0.3	0.4	0.5	0.6	0.8	
1	4.668×10^3	9.053×10^3	2.043×10^4	5.696×10^4	2.093×10^5	1.323×10^7
2	4.450×10^3	6.309×10^3	1.126×10^4	2.616×10^4	8.415×10^4	4.582×10^6
3	6.479×10^3	7.477×10^3	1.064×10^4	2.013×10^4	5.472×10^4	2.426×10^6
4	1.006×10^4	1.055×10^4	1.274×10^4	1.993×10^4	4.531×10^4	1.568×10^6
5	1.520×10^4	1.541×10^4	1.687×10^4	2.267×10^4	4.347×10^4	1.144×10^6 ^a

^a The smallest value of $Ra_{sp,cr}$ at $\eta = 0.8$ is 5.843×10^5 for $l = 12$.

l/η	$Ra_{sp,cr}$					
	$r/a = 1$ Rigid, $r/a = \eta$ Shear Stress Free					
0.2	0.3	0.4	0.5	0.6	0.8	
1	1.029×10^4	1.585×10^4	3.189×10^4	8.508×10^4	2.712×10^5	1.484×10^7
2	8.401×10^3	1.077×10^4	1.739×10^4	3.681×10^4	1.088×10^5	5.140×10^6
3	1.117×10^4	1.226×10^4	1.617×10^4	2.814×10^4	7.060×10^4	2.720×10^6
4	1.604×10^4	1.648×10^4	1.893×10^4	2.760×10^4	5.825×10^4	1.758×10^6
5	2.278×10^4	2.294×10^4	2.446×10^4	3.103×10^4	5.564×10^4	1.283×10^6 ^a

^a The minimum value of $Ra_{sp,cr}$ at $\eta = 0.8$ is 6.520×10^5 for $l = 12$.

l/η	$Ra_{sp,cr}$					
	Both Boundaries Rigid					
0.2	0.3	0.4	0.5	0.6	0.8	
1	1.270×10^4	2.189×10^4	4.871×10^4	1.329×10^5	4.783×10^5	2.883×10^7
2	9.146×10^3	1.316×10^4	2.402×10^4	5.682×10^4	1.841×10^5	9.891×10^6
3	1.141×10^4	1.347×10^4	2.003×10^4	3.982×10^4	1.128×10^5	5.167×10^6
4	1.609×10^4	1.705×10^4	2.141×10^4	3.571×10^4	8.702×10^4	3.282×10^6
5	2.279×10^4	2.318×10^4	2.601×10^4	3.709×10^4	7.749×10^4 ^a	2.345×10^6 ^b

^a The minimum value of $Ra_{sp,cr}$ at $\eta = 0.6$ is 7.599×10^4 for $l = 6$.

^b The minimum value of $Ra_{sp,cr}$ at $\eta = 0.8$ is 9.518×10^5 for $l = 13$.

Note: The minimum value of $Ra_{sp,cr}$ for a given η is printed in bold.

Table 7.4. Critical Rayleigh Numbers $Ra_{sp,cr}$ for the Onset of Convection in Spherical Shells with Combined Heating and Shear Stress Free Boundaries (After Schubert and Zebib, 1980; Zebib et al., 1983)

l/η	0.4	0.5	0.6
1	1.2020×10^4	2.9958×10^4	1.0041×10^5
2	7.7982×10^3	1.5604×10^4	4.3894×10^4
3	8.5536×10^3	1.3762×10^4	3.1667×10^4
4	1.1344×10^4	1.5356×10^4	2.9175×10^4
5	1.5943×10^4	1.9135×10^4	3.0873×10^4

Note: Minimum values of $Ra_{sp,cr}$ are printed in bold.

The onset of thermal convection in spherical shells heated both from within and from below and with shear stress free boundaries was also considered by Zebib et al. (1983) for $\eta = 0.4$ and 0.6. Their results for $Ra_{sp,cr}$ are summarized in Table 7.4 and are in generally good agreement with the values in Table 7.3 from Chandrasekhar (1961). As η changes from 0.4 to 0.5 to 0.6, the most unstable mode of convection changes from $l = 2$ to 3 to 4 (Table 7.4). The value of η for the Earth's mantle is close to 0.55, midway between the values of η at which the preferred mode of convection onset changes from $l = 3$ to $l = 4$. The $l = 3$ axisymmetric mode of convection, illustrated later, has three cells in a meridional cross-section. The $l = 4, m = 0$ mode has four cells in a meridional plane as shown in Figure 7.7. Since there is symmetry with respect to the equatorial plane, only one hemisphere is shown. The flow shown in Figure 7.7 is actually for a supercritical value of Ra_{sp} equal to 4.58×10^4 , but the convection pattern is essentially similar to that at the onset of convection. The shell size in Figure 7.7 is $\eta = 0.5$, and from Table 7.4 it is seen that the $l = 4, m = 0$ mode has the lowest critical Rayleigh number among the equatorially symmetric (even) modes.

7.7.3 Spherical Shell Heated from Within

The onset of convection in a spherical shell heated only from within has been investigated by Schubert and Zebib (1980) and Zebib et al. (1983). In this circumstance the shell has an adiabatic or insulating lower boundary and the conduction temperature profile can be determined by solving (7.7.8) for the value of T_1 that makes $\beta_c(r = c) = 0$ with the result

$$T_c = \frac{\bar{\rho}H}{3k} \left(-\frac{r^2}{2} - \frac{c^3}{r} + \frac{a^2}{2} + \frac{c^3}{a} \right) \quad (7.7.49)$$

Differentiation of (7.7.49) gives

$$\beta_c(r) = \frac{\bar{\rho}H}{3k} \left(-r + \frac{c^3}{r^2} \right) \quad (7.7.50)$$

The stability problem for the onset of convection involves the solution of (7.7.32) with $\beta_c(r)$ given by (7.7.50) and $\bar{g}(r)$ given by (7.7.48). Schubert and Zebib (1980) and Zebib et al. (1983) considered the boundaries to be impermeable and shear stress free with the upper boundary isothermal and the lower one insulating. Thus the boundary conditions are (7.7.42) and (7.7.44) on $r/a = 1$, (7.7.44) on $r/a = \eta$, $D_l^* \theta'_{lm} = 0$ on $r/a = \eta$, and $d\theta'_{lm}/d(r/a) = 0$ on $r/a = \eta$. The appropriate Rayleigh number for this problem is still

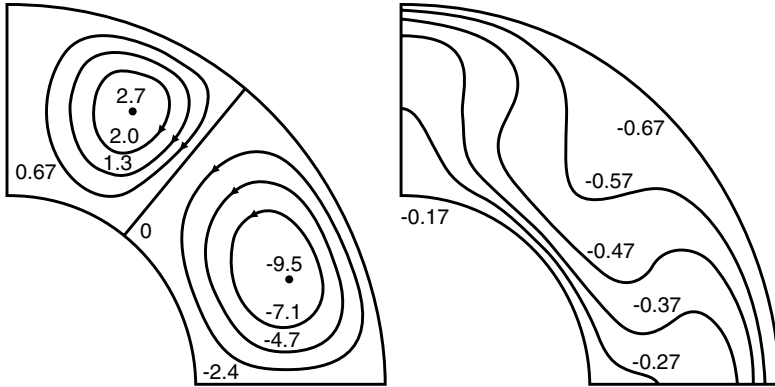


Figure 7.7. Isotherms (right) and streamlines (left) in a meridional plane for the $l = 4, m = 0$ mode at $Ra_{sp} = 4.58 \times 10^4$. Heating is both from below and from within and $\eta = 0.5$. Only one hemisphere is shown because of equatorial symmetry. There is one fast and one slow cell in each hemisphere. After Schubert and Zebib (1980).

Table 7.5. Critical Rayleigh Numbers $Ra_{sp,cr}^*$ for the Onset of Convection in a Sphere and in Spherical Shells Heated Only from Within

l/η	0	0.1	0.2	0.3	0.4	0.5	0.6	0.7
1	9,272.6	6,616.7	4,927.8	3,970.5	3,550.7	3,594.7	4,217.7	5,983.4
2	15,668.7	9,390.7	5,736.6	3,743.3	2,691.0	2,193.8	2,103.7	2,512.7
3	26,320.6	15,610.3	8,984.7	5,213.5	3,199.5	2,174.3	1,720.0	1,703.1
4	41,939.3	24,849.0	14,126.9	7,825.5	4,374.1	2,599.1	1,747.4	1,448.6
5	63,602.9	37,669.5	21,334.7	11,615.5	6,181.2	3,352.7	1,980.3	1,401.6
6	92,528.6	54,786.4	30,966.0	16,729.6	8,681.0	4,439.1	2,374.0	1,466.5

Note: The minimum values of $Ra_{sp,cr}^*$ for a given η are printed in bold.

Ra_{sp} given by (7.7.34). However, to facilitate comparison with the original references we introduce the Rayleigh number Ra_{sp}^* given by

$$Ra_{sp}^* = \frac{4}{3}\pi(1-\eta)^5 Ra_{sp} \quad (7.7.51)$$

The form of the spherical shell internal heating Rayleigh number given by Ra_{sp}^* is based on the value of \bar{g} at $r = a$ and the thickness of the shell as the length scale.

Values of Ra_{sp}^* necessary for the onset of convection, $Ra_{sp,cr}^*$, are given in Table 7.5 for modes of convection with spherical harmonic degree $l = 1\text{--}6$ in shells of various sizes including the sphere. The results are also presented in graphical form in Figure 7.8. The preferred form of axisymmetric convection, i.e., the convective mode with the minimum value of $Ra_{sp,cr}^*$, has one meridional cell ($l = 1$) for $0 \leq \eta \lesssim 0.275$, two meridional cells ($l = 2$) for $0.275 \lesssim \eta \leq 0.5$, and three meridional cells ($l = 3$) for $0.5 \lesssim \eta \lesssim 0.6$. Nonaxisymmetric modes of instability with $m \leq l$ are also possible; the preferred mode of convection from among the axisymmetric and nonaxisymmetric states must be determined from a nonlinear analysis. The shell sizes at which axisymmetric motions with odd and even numbers of meridional cells have the same values of $Ra_{sp,cr}^*$ offer particularly intriguing opportunities for finite-amplitude studies.

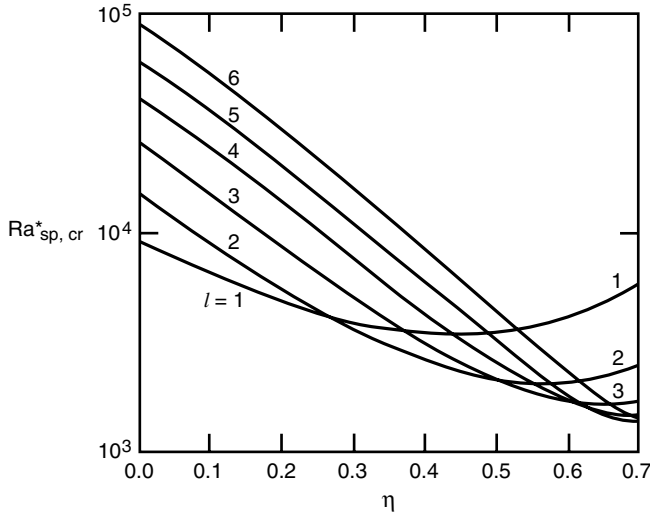


Figure 7.8. Critical Rayleigh number $Ra_{sp,cr}^*$ for the onset of convection as a function of the shell size parameter η for different values of the meridional wave number l (spherical harmonic degree) when heating is from within. After Zebib et al. (1983).

7.7.4 Spherical Shell Heated from Below

So far in our discussion of the onset of thermal convection in spherical shells, we have dealt with fluid shells that are internally heated. Here, we consider heating from below and set $H = 0$. We still consider the acceleration of gravity to be that appropriate to a homogeneous sphere, i.e., $\bar{g}(r)$ is given by (7.7.48). From (7.7.8) with $H = 0$ we can write

$$\beta_c(r) = -\frac{T_1}{r^2(1/c - 1/a)} = -\frac{a^2}{r^2} |\beta_c(r=a)| \quad (7.7.52)$$

The differential equation governing the onset of instability is (7.7.32) with $\bar{g}(r)$ and $\beta_c(r)$ given by (7.7.48) and (7.7.52), respectively. We can write this equation as

$$D_l^{*2} \left\{ \left(\frac{r}{a}\right)^3 D_l^* \left(\theta'_{lm} \left(\frac{r}{a} \right) \right) \right\} = -l(l+1) Ra_{sp,hb} \theta'_{lm} \left(\frac{r}{a} \right) \quad (7.7.53)$$

where, as before, D_l^* is the dimensionless operator and the appropriate Rayleigh number is

$$Ra_{sp,hb} \equiv \frac{\bar{\alpha} \bar{g}(r=a) |\beta_c(r=a)| a^4}{\kappa \nu} \quad (7.7.54)$$

Solutions of (7.7.53) for isothermal, impermeable, shear stress free boundaries (conditions (7.7.42) and (7.7.44) on $r/a = 1$ and $r/a = \eta$) are given in Chandrasekhar (1961) and Zebib et al. (1980, 1983). Table 7.6 summarizes the values of $Ra_{sp,hb,cr}^*$ from Zebib et al. (1983) for the onset of thermal convection in the shell. The results are also shown in Figure 7.9. Again, to facilitate comparison with the original reference we have introduced

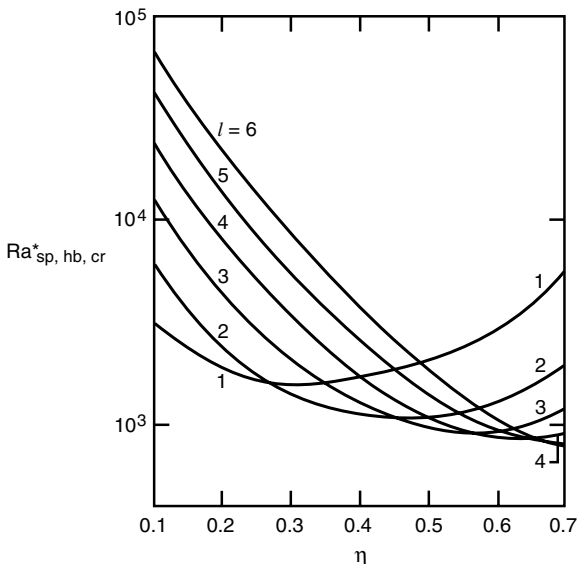
$$Ra_{sp,hb}^* = Ra_{sp,hb} \frac{(1-\eta)^4}{\eta} \quad (\eta \neq 0) \quad (7.7.55)$$

Table 7.6. Critical Rayleigh Numbers $Ra_{sp,hb,cr}^*$ for the Onset of Thermal Convection in a Spherical Shell Heated Only from Below (After Zebib et al., 1983); Boundaries are Shear Stress Free and Isothermal

l/η	0.1	0.2	0.3	0.4	0.5	0.6	0.7
1	3,248.0	1,907.2	1,630.2	1,706.1	2,086.5	2,966.6	5,047.2
2	6,288.8	2,423.0	1,450.8	1,133.1	1,095.7	1,300.1	1,941.7
3	13,687.3	4,485.8	2,119.9	1,286.0	978.5	941.6	1,189.6
4	26,303.1	8,287.6	3,489.4	1,780.9	1,109.6	871.9	917.9
5	45,643.5	14,270.5	5,727.7	2,630.8	1,410.2	928.5	816.1
6	73,544.2	22,962.6	9,054.0	3,915.6	1,885.0	1,072.7	797.2

Note: The minimum values of $Ra_{sp,hb,cr}^*$ for a given η are printed in bold.

Figure 7.9. Similar to Figure 7.8 but for spherical shells heated from below. The appropriate critical Rayleigh number is denoted by $Ra_{sp,hb,cr}^*$. After Zebib et al. (1983).



The Rayleigh number $Ra_{sp,hb}^*$ is based on the value of \bar{g} at $r = a$, the temperature difference across the shell, and the thickness of the shell as the length scale.

When heating is only from below there is one meridional cell ($l = 1$) at the onset of convection (with $m = 0$) for shells with $\eta \lesssim 0.275$; there are two meridional cells ($l = 2$ and $m = 0$) for $0.275 \lesssim \eta \lesssim 0.46$, three meridional cells ($l = 3$ and $m = 0$) for $0.46 \lesssim \eta \lesssim 0.575$, and four meridional cells ($l = 4$ and $m = 0$) for $0.575 \lesssim \eta \lesssim 0.63$, etc. There are special values of shell size indicated by the intersections of curves in Figure 7.9 for which modes with odd and even values of l have the same $Ra_{sp,hb,cr}^*$. Though we have seen an example of an $l = 1$ axisymmetric mode in the case of an internally heated sphere in Figure 7.6, we show another example of $l = 1$ dominated axisymmetric convection for a shell heated from below with $\eta = 0.2$ in Figure 7.10. This case is interesting because the convective cell is predominantly confined to the hemisphere in which there is upwelling at the pole. Though not at the onset of convection, the flow in Figure 7.10 is only slightly supercritical since $Ra_{sp,hb}^*$ is only 2,400.

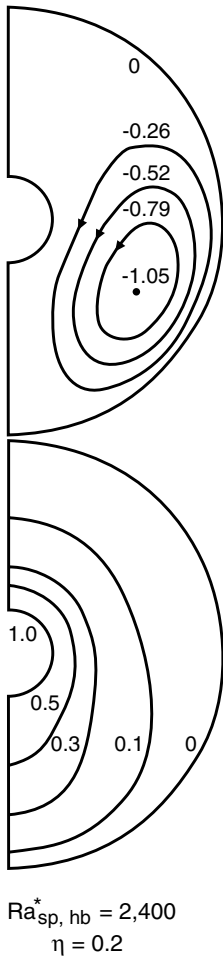
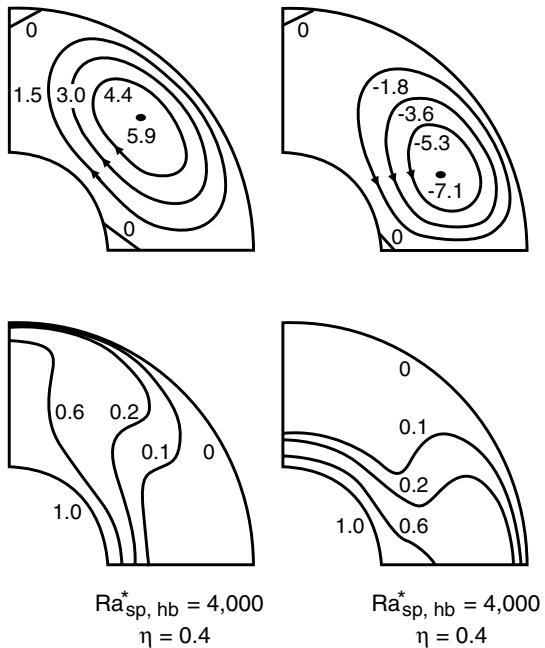


Figure 7.10. Streamlines (top) and isotherms (bottom) for convection heated from below in a shell with $\eta = 0.2$ and $\text{Ra}_{\text{sp}, \text{hb}}^* = 2,400$. The single-cell flow (predominantly $l = 1, m = 0$) is mainly confined to the hemisphere in which there is upwelling at the pole. After Zebib et al. (1983).

Since an $l = 4, m = 0$ mode of convection has already been shown in Figure 7.7 for a spherical shell with combined heating, we show here only two additional figures to illustrate the $l = 2, m = 0$ and $l = 3, m = 0$ modes of convection. The $l = 2, m = 0$ convection mode is shown in Figure 7.11 for heating from below, $\eta = 0.4$, and $\text{Ra}_{\text{sp}, \text{hb}}^* = 4,000$, a slightly supercritical state. Because of symmetry only one hemisphere is shown. Two distinct modes of convection are possible (as shown): one has upwelling at the pole and the other has polar downflow. Multiple convection states can occur even with the restriction to particular values of l and m .

Figure 7.12 illustrates the pattern of convection associated with the $l = 3$ axisymmetric mode for a slightly supercritical Rayleigh number $\text{Ra}_{\text{sp}, \text{hb}}^* = 1.6 \times 10^4$ in a shell heated from below with $\eta = 0.5$ (Zebib et al., 1980). Nonaxisymmetric modes with $l = 3$ are also unstable but are not illustrated here. As previously noted, linear stability theory cannot resolve the selection degeneracy among the axisymmetric ($m = 0$) and nonaxisymmetric ($m = 1, 2, 3$) modes with $l = 3$. The $l = 3$ axisymmetric mode has three cells in the meridional plane (Figure 7.12). The equatorial cell rotates more rapidly than do the polar cells. Upwelling occurs at one of the poles and at about 45° latitude in the opposite hemisphere. The pattern of convection is not symmetric about the equator.

Figure 7.11. Cellular structure of a pair of equatorially symmetric motions with either rising (left) or sinking (right) at the poles. Because of symmetry only one hemisphere is shown. Heating is from below, $\eta = 0.4$, and $Ra_{sp,hb}^* = 4,000$. Streamlines are at the top and isotherms are at the bottom. The flows are dominated by $l = 2, m = 0$ modes. After Zebib et al. (1983).



7.8 Spherical Harmonics

Spherical geometry is of obvious relevance to studies of mantle convection and it is therefore of importance to consider the representation and solution of the equations of mass, momentum, and energy in spherical coordinates. Geophysical observables of the structure and dynamics of the mantle, e.g., the gravity field, are also conveniently described in spherical coordinates.

Any function of position on a spherical surface can be represented by a complete set of basis functions known as spherical harmonics $Y_l^m(\theta, \phi)$ (θ is colatitude, ϕ is longitude):

$$Y_l^m(\theta, \phi) = \left(\frac{(2l+1)}{4\pi} \frac{(l-m)!}{(l+m)!} \right)^{1/2} P_l^m(\cos \theta) e^{im\phi} \quad (7.8.1)$$

In (7.8.1), l and m are integers, $l \geq 0$ and $-l \leq m \leq l$, and $P_l^m(\cos \theta)$ are associated Legendre functions defined in terms of the Legendre polynomials $P_l(\cos \theta) = P_l^0(\cos \theta)$ by

$$P_l^m(\cos \theta) = (-\sin \theta)^m \frac{d^m P_l(\cos \theta)}{d(\cos \theta)^m}, \quad 0 \leq m \leq l \quad (7.8.2)$$

and

$$P_l^{-m}(\cos \theta) = (-1)^m \frac{(l-m)!}{(l+m)!} P_l^m(\cos \theta) \quad (7.8.3)$$

(Hobson, 1955; Abramowitz and Stegun, 1964). The Legendre polynomials $P_l(\cos \theta)$ in (7.8.2) are given by

$$P_l(\cos \theta) = \frac{1}{2^l l!} \frac{d^l}{d(\cos \theta)^l} (\cos^2 \theta - 1)^l \quad (7.8.4)$$

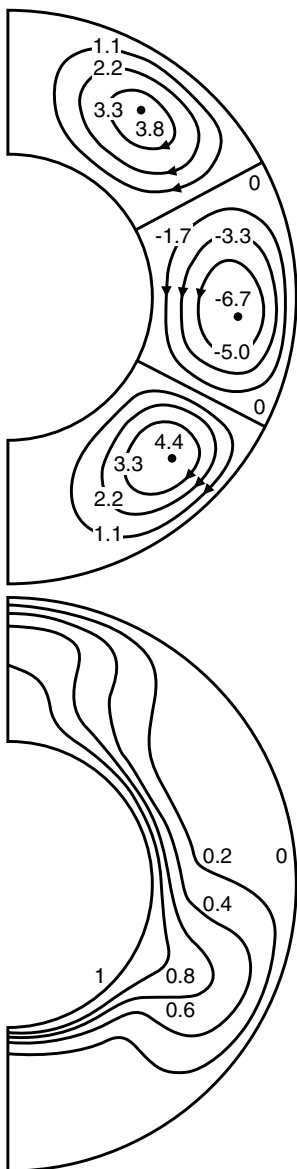


Figure 7.12. Streamlines (top) and isotherms (bottom) in a meridional plane for axisymmetric convection in a spherical shell with $\eta = 0.5$ and heating from below. The three-cell solution is dominated by the $l = 3$, $m = 0$ mode. The Rayleigh number $Ra_{sp,hb}^* = 1.6 \times 10^4$ is supercritical. After Zebib et al. (1980).

From (7.8.2) it is clear that $P_l^0(\cos \theta) = P_l(\cos \theta)$. Table 7.7 summarizes some useful formulas for the Legendre polynomials and associated Legendre functions. The functions $Y_l^0 = ((2l + 1)/4\pi)^{1/2} P_l(\cos \theta)$ are functions only of latitude and accordingly are known as zonal harmonics. More generally, when $m \neq 0$ the spherical harmonics are known as tesseral harmonics except for the case $m = l$ when they are known as sectoral harmonics.

The order m of the spherical harmonic gives the number of great circles passing through both poles on which Y_l^m is zero. The difference between the degree l of the spherical harmonic and its order m gives the number of small circles parallel to the equatorial plane on which Y_l^m is zero. The small circles of constant latitude and the great circles of constant longitude

Table 7.7. Formulae Involving Legendre Polynomials and Associated Legendre Functions

Legendre Polynomials
$\frac{dP_{l+1}}{d\cos\theta} - \frac{dP_{l-1}}{d\cos\theta} - (2l + 1)P_l = 0$
$(l + 1)P_{l+1} - (2l + 1)\cos\theta P_l + lP_{l-1} = 0$
$\frac{dP_{l+1}}{d\cos\theta} - \cos\theta \frac{dP_l}{d\cos\theta} - (l + 1)P_l = 0$
$(\cos^2\theta - 1)\frac{dP_l}{d\cos\theta} - l\cos\theta P_l + lP_{l-1} = 0$
$\frac{d^l P_l}{d\cos\theta^l} = \frac{(2l)!}{2^l l!}$
$P_l(0) = 0$ (l odd), $P_l(0) = (-1)^{\frac{l}{2}} \frac{1 \cdot 3 \cdot 5 \cdots (l-1)}{2 \cdot 4 \cdot 6 \cdots l}$ (l even)
$P_l(1) = 1$
$P_l(-\cos\theta) = (-1)^l P_l(\cos\theta)$
$\frac{dP_l}{d\cos\theta}(0) = -(l + 1)P_{l+1}(0)$
$\frac{dP_l}{d\cos\theta}(1) = \frac{l}{2}(l + 1)$
Associated Legendre Functions (Smythe, 1968 ^a)
$P_{l+1}^{m+1} = -(l + m + 1) \sin\theta P_l^m + \cos\theta P_l^{m+1}$
$P_{l+1}^{m+1} - P_{l-1}^{m+1} = -(2l + 1) \sin\theta P_l^m$
$P_{l-1}^{m+1} = -(m - l) \sin\theta P_l^m + \cos\theta P_l^{m+1}$
$P_l^{m+1} + 2m \frac{\cos\theta}{\sin\theta} P_l^m + (m + l)(l - m + 1) P_l^{m-1} = 0$
$(m - l - 1)P_{l+1}^m + (2l + 1) \cos\theta P_l^m - (m + l)P_{l-1}^m = 0$
$-\frac{2m}{\sin\theta} P_l^m = P_{l-1}^{m+1} + (m + l - 1)(m + l) P_{l-1}^{m+1}$
$-\sin\theta \frac{dP_l^m}{d\cos\theta} = +m \frac{\cos\theta}{\sin\theta} P_l^m + P_l^{m+1}$
$= -\frac{1}{2}(m + l)(l - m + 1) P_l^{m-1} + \frac{1}{2} P_l^{m+1}$
$= -m \frac{\cos\theta}{\sin\theta} P_l^m - (m + l)(l - m + 1) P_l^{m-1}$
$\sin^2\theta \frac{dP_l^m}{d\cos\theta} = m \cos\theta P_l^m - (m + l)(l - m + 1)(2l + 1)^{-1} (P_{l+1}^m - P_{l-1}^m)$
$= (l + 1) \cos\theta P_l^m - (l - m + 1) P_{l+1}^m$
$= (2l + 1)^{-1} [(m - l - 1)l P_{l+1}^m + (l + 1)(m + l) P_{l-1}^m]$
$= -l \cos\theta P_l^m + (m + l) P_{l-1}^m$
$P_l^m(0) = 0$ ($l + m$ odd)
$P_m^m(\cos\theta) = (-1)^m (2m - 1)!! \sin^m\theta$

^a The associated Legendre function defined by Smythe (1968) differs from the definition here by a minus sign when m is odd.

on which Y_l^m are zero are the nodal lines of Y_l^m . The latitudinal nodal lines are symmetric about the equator and the longitudinal nodal lines are separated by the angle π/m ($m \neq 0$). The total number of nodal lines, both small and great circles, equals the degree l of the spherical harmonic. When $m = 0$, the nodal lines of Y_l^0 divide the spherical surface into latitudinal zones (hence the name zonal harmonics). When $m = l$, Y_l^m is proportional to $\sin^l\theta$ (since $P_l(\cos\theta)$ is a polynomial in $\cos\theta$ of maximum degree l , $d^l P_l(\cos\theta)/d(\cos\theta)^l$ is a constant, and from (7.8.2) $Y_l^m \propto \sin^l\theta$), and there are no small circle nodal lines; there are great circle nodal lines of constant longitude that divide the spherical surface into sectors (hence the name sectoral harmonics). Figure 7.13 shows the nodal lines of several low degree and order spherical harmonics. Table 7.8 gives the functional forms of several low degree

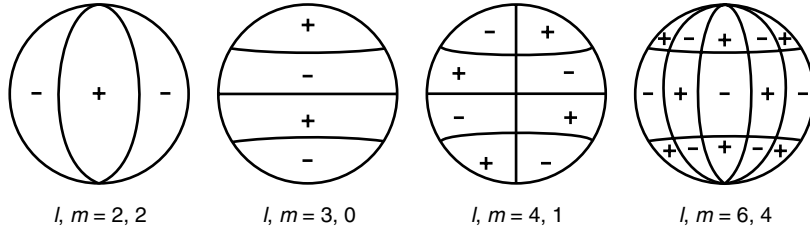


Figure 7.13. Nodal lines of some spherical harmonics. After Stacey (1992).

and order spherical harmonics. Inspection of Table 7.8 illustrates that

$$Y_l^{-m}(\theta, \phi) = (-1)^m Y_l^m(\theta, \phi)^* \quad (7.8.5)$$

a result that can be obtained by combining (7.8.1) and (7.8.3) (the asterisk signifies the complex conjugate).

The spherical harmonic basis functions are orthonormal over the surface of a sphere

$$\int_0^{2\pi} d\phi \int_0^\pi d\theta \sin \theta Y_l^m(\theta, \phi) Y_{l'}^{m'}(\theta, \phi)^* = \delta_{ll'} \delta_{mm'} \quad (7.8.6)$$

where $\delta_{ll'}$ is zero unless $l = l'$ and $\delta_{mm'} = 0$ unless $m = m'$. Accordingly, any function $f(r, \theta, \phi)$ (r is radius) can be expanded according to

$$f(r, \theta, \phi) = \sum_{l=0}^{\infty} \sum_{m=-l}^l f_{lm}(r) Y_l^m(\theta, \phi) \quad (7.8.7)$$

where

$$f_{lm}(r) = \int_0^{2\pi} d\phi \int_0^\pi d\theta \sin \theta f(r, \theta, \phi) Y_l^m(\theta, \phi)^* \quad (7.8.8)$$

In addition to being a convenient set of basis functions for the surface of a sphere, spherical harmonics are the functions that arise when separable solutions of Laplace's equation are sought in spherical coordinates. Indeed, this is the fundamental mathematical approach for the derivation of the spherical harmonics. From (6.15.24) it can be verified that if V is of the form

$$V = c \left(r^{-l-1}, r^l \right) Y_l^m(\theta, \phi) \quad (c = \text{constant}) \quad (7.8.9)$$

then

$$\begin{aligned} \nabla^2 V &= c \left\{ \frac{(2l+1)}{4\pi} \frac{(l-m)!}{(l+m)!} \right\}^{1/2} e^{im\phi} \left(r^{-l-3}, r^{l-2} \right) \\ &\times \left\{ \frac{d^2 P_l^m}{d\theta^2} + \frac{\cos \theta}{\sin \theta} \frac{d P_l^m}{d\theta} + \left(l(l+1) - \frac{m^2}{\sin^2 \theta} \right) P_l^m \right\} \end{aligned} \quad (7.8.10)$$

Table 7.8. Spherical Harmonics $l \leq 3$ and $-l \leq m \leq l$

l	P_l	P_l^m	Y_l^m
0	1	$P_0^0 = 1$	$Y_0^0 = \frac{1}{\sqrt{4\pi}}$
1	$\cos \theta$	$P_1^{-1} = \frac{1}{2} \sin \theta$	$Y_1^{-1} = \frac{1}{2} \sqrt{\frac{3}{2\pi}} \sin \theta e^{-i\phi}$
		$P_1^0 = \cos \theta$	$Y_1^0 = \sqrt{\frac{3}{4\pi}} \cos \theta$
		$P_1^1 = -\sin \theta$	$Y_1^1 = -\sqrt{\frac{3}{8\pi}} \sin \theta e^{i\phi}$
2	$\frac{1}{2} (3 \cos^2 \theta - 1)$	$P_2^{-2} = \frac{1}{8} \sin^2 \theta$	$Y_2^{-2} = \frac{1}{8} \sqrt{\frac{30}{\pi}} \sin^2 \theta e^{-2i\phi}$
		$P_2^{-1} = \frac{1}{2} \sin \theta \cos \theta$	$Y_2^{-1} = \frac{1}{2} \sqrt{\frac{15}{2\pi}} \sin \theta \cos \theta e^{-i\phi}$
		$P_2^0 = \frac{1}{2} (3 \cos^2 \theta - 1)$	$Y_2^0 = \frac{1}{2} \sqrt{\frac{5}{4\pi}} (3 \cos^2 \theta - 1)$
		$P_2^1 = -3 \sin \theta \cos \theta$	$Y_2^1 = -\frac{1}{2} \sqrt{\frac{15}{2\pi}} \sin \theta \cos \theta e^{i\phi}$
		$P_2^2 = 3 \sin^2 \theta$	$Y_2^2 = \frac{1}{8} \sqrt{\frac{30}{\pi}} \sin^2 \theta e^{2i\phi}$
3	$\frac{1}{2} (5 \cos^3 \theta - 3 \cos \theta)$	$P_3^{-3} = \frac{\sin^3 \theta}{48}$	$Y_3^{-3} = \frac{1}{8} \sqrt{\frac{35}{\pi}} \sin^3 \theta e^{-3i\phi}$
		$P_3^{-2} = \frac{1}{8} \sin^2 \theta \cos \theta$	$Y_3^{-2} = \frac{1}{8} \sqrt{\frac{210}{\pi}} \sin^2 \theta \cos \theta e^{-2i\phi}$
		$P_3^{-1} = \frac{1}{8} \sin \theta (5 \cos^2 \theta - 1)$	$Y_3^{-1} = \frac{1}{8} \sqrt{\frac{21}{\pi}} \sin \theta (5 \cos^2 \theta - 1) e^{-i\phi}$
		$P_3^0 = \frac{1}{2} (5 \cos^3 \theta - 3 \cos \theta)$	$Y_3^0 = \frac{1}{2} \sqrt{\frac{7}{4\pi}} (5 \cos^3 \theta - 3 \cos \theta)$
		$P_3^1 = -\frac{3}{2} (5 \cos^2 \theta - 1) \sin \theta$	$Y_3^1 = -\frac{3}{8} \sqrt{\frac{7}{3\pi}} (5 \cos^2 \theta - 1) \sin \theta e^{i\phi}$
		$P_3^2 = 15 \cos \theta \sin^2 \theta$	$Y_3^2 = \frac{1}{4} \sqrt{\frac{105}{2\pi}} \cos \theta \sin^2 \theta e^{2i\phi}$
		$P_3^3 = -15 \sin^3 \theta$	$Y_3^3 = -\frac{1}{8} \sqrt{\frac{35}{\pi}} \sin^3 \theta e^{3i\phi}$

The last quantity in curly brackets in (7.8.10) is identically zero and (7.8.10) is Laplace's equation

$$\nabla^2 V = 0 \quad (7.8.11)$$

i.e., the associated Legendre functions $P_l^m(\cos \theta)$ are the latitudinal functions that lead to separable solutions of Laplace's equation in spherical coordinates. The associated Legendre

functions are solutions of

$$\frac{d^2 P_l^m}{d\theta^2} + \frac{\cos \theta}{\sin \theta} \frac{dP_l^m}{d\theta} + \left\{ l(l+1) - \frac{m^2}{\sin^2 \theta} \right\} P_l^m = 0 \quad (7.8.12)$$

The restriction of l to positive integers ≥ 0 and m to $-l \leq m \leq l$ insures that P_l^m is finite at the poles and single-valued in ϕ .

It is useful to write the Laplacian in terms of derivatives with respect to r and a differential operator L^2 involving only θ and ϕ :

$$\nabla^2 = \frac{\partial^2}{\partial r^2} + \frac{2}{r} \frac{\partial}{\partial r} - \frac{1}{r^2} L^2 \quad (7.8.13)$$

where

$$L^2 \equiv -\frac{1}{\sin \theta} \frac{\partial}{\partial \theta} \left(\sin \theta \frac{\partial}{\partial \theta} \right) - \frac{1}{\sin^2 \theta} \frac{\partial^2}{\partial \phi^2} \quad (7.8.14)$$

It is straightforward to show that

$$L^2 Y_l^m(\theta, \phi) = l(l+1) Y_l^m(\theta, \phi) \quad (7.8.15)$$

from which it follows, together with (7.8.13), that

$$\nabla^2 f(r) Y_l^m(\theta, \phi) = Y_l^m(\theta, \phi) D_l f(r) \quad (7.8.16)$$

where

$$D_l \equiv \frac{d^2}{dr^2} + \frac{2}{r} \frac{d}{dr} - \frac{l(l+1)}{r^2} \quad (7.8.17)$$

We conclude this section by discussing the representation of solenoidal vector fields in terms of their toroidal and poloidal components and of the role of spherical harmonics therein. The velocity field \underline{u} of an incompressible flow is solenoidal as is the vorticity field $\underline{\omega} \equiv \nabla \times \underline{u}$. Any solenoidal vector field can be written as the sum of a poloidal vector field \underline{S}

$$\underline{S} \equiv \nabla \times \left(\nabla \times \left(\frac{\Phi}{r} \underline{r} \right) \right) = \nabla \times \left(\nabla \left(\frac{\Phi}{r} \right) \times \underline{r} \right) \quad (7.8.18)$$

and a toroidal vector field \underline{T}

$$\underline{T} \equiv \nabla \times \left(\frac{\Psi}{r} \underline{r} \right) = \nabla \left(\frac{\Psi}{r} \right) \times \underline{r} \quad (7.8.19)$$

(Chandrasekhar, 1961). The components of \underline{S} and \underline{T} in spherical coordinates (r, θ, ϕ components) are

$$\underline{S} = \left(\frac{1}{r^2} L^2 \Phi, \frac{1}{r} \frac{\partial^2 \Phi}{\partial r \partial \theta}, \frac{1}{r \sin \theta} \frac{\partial^2 \Phi}{\partial r \partial \phi} \right) \quad (7.8.20)$$

$$\underline{T} = \left(0, \frac{1}{r \sin \theta} \frac{\partial \Psi}{\partial \phi}, -\frac{1}{r} \frac{\partial \Psi}{\partial \theta} \right) \quad (7.8.21)$$

The toroidal vector field has no radial component. If Φ and Ψ are expanded in terms of spherical harmonics according to (7.8.7) with radially dependent coefficients $\Phi_{lm}(r)$ and $\Psi_{lm}(r)$, then each spherical harmonic contribution to \underline{S} and \underline{T} is, respectively,

$$\underline{S}_{lm} \equiv \left(\frac{l(l+1)}{r^2} \Phi_{lm}(r) Y_l^m, \frac{1}{r} \frac{d\Phi_{lm}}{dr} \frac{\partial Y_l^m}{\partial \theta}, \frac{1}{r \sin \theta} \frac{d\Phi_{lm}}{dr} \frac{\partial Y_l^m}{\partial \phi} \right) \quad (7.8.22)$$

$$\underline{T}_{lm} \equiv \left(0, \frac{\Psi_{lm}(r)}{r \sin \theta} \frac{\partial Y_l^m}{\partial \phi} - \frac{\Psi_{lm}(r)}{r} \frac{\partial Y_l^m}{\partial \theta} \right) \quad (7.8.23)$$

These vector spherical harmonic fields have the following properties (Chandrasekhar, 1961). \underline{S}_{lm} and \underline{T}_{lm} are solenoidal and orthogonal to each other, i.e.,

$$\int_0^{2\pi} d\phi \int_0^\pi d\theta \sin \theta \underline{S}_{lm} \cdot \underline{T}_{lm} = 0 \quad (7.8.24)$$

In addition, if \underline{S}_{lm} (\underline{T}_{lm}) and $\underline{S}'_{l'm'}(\underline{T}'_{l'm'})$ are derived from different spherical harmonics they are orthogonal in the sense of (7.8.24). If \underline{S}_{lm} (\underline{T}_{lm}) and \underline{S}'_{lm} (\underline{T}'_{lm}) are derived from the same spherical harmonics

$$\begin{aligned} & r^2 \int_0^{2\pi} d\phi \int_0^\pi d\theta \sin \theta \underline{S}_{lm} \cdot \underline{S}'_{lm} \\ &= l(l+1) \left\{ \frac{l(l+1)}{r^2} \Phi_{lm}(r) \Phi'_{lm}(r) + \frac{d\Phi_{lm}}{dr} \frac{d\Phi'_{lm}}{dr} \right\} \end{aligned} \quad (7.8.25)$$

$$r^2 \int_0^{2\pi} d\phi \int_0^\pi d\theta \sin \theta \underline{T}_{lm} \cdot \underline{T}'_{lm} = l(l+1) \Psi_{lm}(r) \Psi'_{lm}(r) \quad (7.8.26)$$

8

Approximate Solutions

8.1 Introduction

The linear stability analysis presented in the last chapter gives the critical Rayleigh number for the onset of thermal convection under a variety of conditions. However, because the governing equations have been linearized, the solutions cannot predict the magnitude of finite-amplitude convective flows. In order to do this it is necessary to retain nonlinear terms in the governing equations.

Even in the simplest thermal convection problems the governing equations are sufficiently complex that analytical solutions cannot be found. There are basically two methods for obtaining nonlinear solutions. The first is to make approximations and the second is to obtain fully numerical solutions. We will address the former method in this chapter and the latter method in the subsequent two chapters.

In this chapter we will consider four approximations used to obtain a better understanding of thermal convection. We first consider an eigenmode expansion of the basic equations. This approach provides one of the methods used to obtain fully numerical solutions. However, in this chapter we consider only severe truncations of the full set of eigenmode equations. Retention of only the lowest-order nonlinear terms leads to the Lorenz (1963) equations. This set of equations is of great interest because its solution was the first demonstration of deterministic chaos. In this approximate approach we address the question:

Question 8.1: Is mantle convection chaotic?

This question leads directly to a second question:

Question 8.2: Is mantle convection turbulent?

The second approximate approach we consider is boundary layer theory. This approach reproduces the basic structure of thermal convection cells at high Rayleigh numbers. The third approach is the mean field approximation. We conclude by considering weakly nonlinear stability theory, an extension of the linear stability theory to slightly nonlinear convection.

8.2 Eigenmode Expansions

In this section we will consider only the simplest thermal convection problem. We will obtain two-dimensional solutions for the flow in a fluid layer heated from below with shear stress free boundary conditions. We will assume that the Boussinesq approximation is applicable and that all fluid properties are constant. Initially, we will consider finite values of the Prandtl number and retain the time-dependent terms in the momentum equation.

From (6.10.19), (7.2.7)–(7.2.9), and (7.3.1) the applicable nondimensional equations are

$$\frac{\partial u^*}{\partial x^*} + \frac{\partial v^*}{\partial y^*} = 0 \quad (8.2.1)$$

$$\frac{1}{Pr} \left(\frac{\partial u^*}{\partial t^*} + u^* \frac{\partial u^*}{\partial x^*} + v^* \frac{\partial u^*}{\partial y^*} \right) = - \frac{\partial \Pi^*}{\partial x^*} + \left(\frac{\partial^2}{\partial x^{*2}} + \frac{\partial^2}{\partial y^{*2}} \right) u^* \quad (8.2.2)$$

$$\frac{1}{Pr} \left(\frac{\partial v^*}{\partial t^*} + u^* \frac{\partial v^*}{\partial x^*} + v^* \frac{\partial v^*}{\partial y^*} \right) = - \frac{\partial \Pi^*}{\partial y^*} - Ra \theta^* + \left(\frac{\partial^2}{\partial x^{*2}} + \frac{\partial^2}{\partial y^{*2}} \right) v^* \quad (8.2.3)$$

$$\frac{\partial \theta^*}{\partial t} + v^* + u^* \frac{\partial \theta^*}{\partial x^*} + v^* \frac{\partial \theta^*}{\partial y^*} = \left(\frac{\partial^2}{\partial x^{*2}} + \frac{\partial^2}{\partial y^{*2}} \right) \theta^* \quad (8.2.4)$$

With $Pr \rightarrow \infty$ and upon linearization, this set reduces to the stability equations given in (7.3.11)–(7.3.14). The boundary conditions (7.3.15) and (7.3.16) remain applicable.

Introduction of the stream function through (7.3.17) and elimination of the pressure perturbation Π^* leads to

$$\begin{aligned} \frac{1}{Pr} & \left[\left(\frac{\partial^2}{\partial x^{*2}} + \frac{\partial^2}{\partial y^{*2}} \right) \frac{\partial \psi^*}{\partial t^*} + \frac{\partial \psi^*}{\partial y^*} \left(\frac{\partial^2}{\partial x^{*2}} + \frac{\partial^2}{\partial y^{*2}} \right) \frac{\partial \psi^*}{\partial x^*} \right. \\ & \left. - \frac{\partial \psi^*}{\partial x^*} \left(\frac{\partial^2}{\partial x^{*2}} + \frac{\partial^2}{\partial y^{*2}} \right) \frac{\partial \psi^*}{\partial y^*} \right] = \frac{\partial^4 \psi^*}{\partial x^{*4}} + 2 \frac{\partial^4 \psi^*}{\partial x^{*2} \partial y^{*2}} + \frac{\partial^4 \psi^*}{\partial y^{*4}} + Ra \frac{\partial \theta^*}{\partial x^*} \end{aligned} \quad (8.2.5)$$

$$\frac{\partial \theta^*}{\partial t^*} + \frac{\partial \psi^*}{\partial y^*} \frac{\partial \theta^*}{\partial x^*} - \frac{\partial \psi^*}{\partial x^*} \frac{\partial \theta^*}{\partial y^*} = \left(\frac{\partial^2}{\partial x^{*2}} + \frac{\partial^2}{\partial y^{*2}} \right) \theta^* + \frac{\partial \psi^*}{\partial x^*} \quad (8.2.6)$$

The boundary conditions from (7.3.15) and (7.3.16) take the form $\theta^* = \partial \psi^* / \partial x^* = \partial^2 \psi^* / \partial y^{*2} = 0$ on $y^* = 0, 1$. We require solutions of this pair of partial, nonlinear differential equations. The convective terms on the left sides of the two equations introduce the nonlinearities.

Based on the cellular form of the linear stability solutions obtained in Section 7.3, a logical approach to obtaining the solutions of (8.2.5) and (8.2.6) is to expand the solutions for ψ^* and θ^* in a Fourier series with a fundamental nondimensional wavelength λ^* . This is known as an eigenmode expansion and, following Saltzman (1962), we write

$$\psi^*(x^*, y^*, t^*) = \sum_{m=-\infty}^{\infty} \sum_{n=-\infty}^{\infty} \psi_{m,n}(t^*) \cos \frac{2\pi mx^*}{\lambda^*} \sin n\pi y^* \quad (8.2.7)$$

$$\theta^* = \sum_{m=-\infty}^{\infty} \sum_{n=-\infty}^{\infty} \theta_{m,n}^*(t^*) \sin \frac{2\pi mx^*}{\lambda^*} \sin n\pi y^* \quad (8.2.8)$$

The expansions satisfy the boundary conditions (7.3.15) and (7.3.16), as restated above, on a term by term basis. Substitution of (8.2.7) and (8.2.8) into (8.2.5) and (8.2.6) gives

$$\begin{aligned} \frac{d\psi_{m,n}^*}{dt^*} = & \sum_{p=-\infty}^{\infty} \sum_{q=-\infty}^{\infty} \frac{2\pi^2}{\lambda^*} (mq - np) \psi_{p,q}^* \psi_{m-p,n-q}^* \\ & - Ra Pr \left(\frac{2\pi m}{\lambda^*} \right) \left[\pi^2 \left(\frac{4m^2}{\lambda^{*2}} + n^2 \right) \right]^{-1} \theta_{m,n}^* + Pr(\pi^2) \left(\frac{4m^2}{\lambda^{*2}} + n^2 \right) \psi_{m,n}^* \end{aligned} \quad (8.2.9)$$

$$\begin{aligned} \frac{d\theta_{m,n}^*}{dt^*} = & \sum_{p=-\infty}^{\infty} \sum_{q=-\infty}^{\infty} \frac{2\pi^2}{\lambda^*} (mq - np) \psi_{p,q}^* \theta_{m-p,n-q}^* \\ & - \left(\frac{2\pi m}{\lambda^*} \right) \psi_{m,n}^* - \pi^2 \left(\frac{4m^2}{\lambda^{*2}} + n^2 \right) \theta_{m,n}^* \end{aligned} \quad (8.2.10)$$

These equations constitute an infinite set of total differential equations for the $\psi_{m,n}^*$ and $\theta_{m,n}^*$. The nonlinear terms couple modes of all orders. The retention and solution of a large number of these equations constitutes one approach to the numerical solution of the thermal convection equations. In this chapter, however, we are concerned with low-order truncations of this equation set.

8.3 Lorenz Equations

Lorenz (1963) strongly truncated the eigenmode expansions of ψ^* and θ^* and kept the smallest number of terms that would consistently retain nonlinear interactions. With the introduction of three time-dependent coefficients $A(\tau)$, $B(\tau)$, and $C(\tau)$, his truncations took the form

$$\psi^* = \frac{1}{2^{1/2}\lambda^*} (4 + \lambda^{*2}) A(\tau) \sin \left(\frac{2\pi x^*}{\lambda^*} \right) \sin \pi y^* \quad (8.3.1)$$

$$\theta^* = \frac{1}{\pi r} \left[C(\tau) \sin 2\pi y^* - 2^{1/2} B(\tau) \cos \left(\frac{2\pi x^*}{\lambda^*} \right) \sin \pi y^* \right] \quad (8.3.2)$$

where

$$\tau = \pi^2 \left[1 + \left(\frac{2}{\lambda^*} \right)^2 \right] t^* \quad (8.3.3)$$

$$r = \frac{Ra}{Ra_{cr}} \quad (8.3.4)$$

with Ra_{cr} given by (7.3.28). These equations satisfy the same set of boundary conditions as (8.2.9) and (8.2.10).

Since only one term in the stream function expansion is retained, we require only the $m = n = 1$ equation from the set given in (8.2.9). In terms of the quantities introduced in (8.3.1) and (8.3.2) this can be written as

$$\frac{dA}{d\tau} = Pr(B - A) \quad (8.3.5)$$

No nonlinear terms are retained in the stream function equation. Since two terms are retained in the energy equation we require both the $m = 0, n = 2$ and the $m = n = 1$ equations from the set given in (8.2.10). In terms of the quantities introduced in (8.3.1) and (8.3.2) these can be written as

$$\frac{dB}{d\tau} = rA - B - AC \quad (8.3.6)$$

$$\frac{dC}{d\tau} = -bC + AB \quad (8.3.7)$$

where

$$b = \frac{4}{[1 + (2/\lambda^*)^2]} \quad (8.3.8)$$

The three first-order differential equations (8.3.5)–(8.3.7) are the Lorenz equations. These equations would be expected to give accurate solutions of the full equations when the Rayleigh number is slightly supercritical, but large errors would be expected for strong convection because of the extreme truncation.

Solutions of the Lorenz equations represent cellular, two-dimensional convection. Because only one term is retained in the expansion of the stream function, the particle paths are closed and represent streamlines even when the flow is unsteady. The coefficient B represents temperature variations associated with the stream function mode A . The coefficient C represents a horizontally averaged temperature mode. A detailed discussion of the behavior of the Lorenz equations has been given by Sparrow (1982).

In order to examine the behavior of the Lorenz equations we first determine the allowed steady-state solutions. Obviously the steady-state solution $A = B = C = 0$ corresponds to heat conduction without flow. An additional pair of allowed solutions is

$$A = B = \pm [b(r - 1)]^{1/2} \quad (8.3.9)$$

$$C = r - 1 \quad (8.3.10)$$

These solutions correspond to cellular rolls either rotating clockwise or counterclockwise. A stability analysis for the conduction solution shows that it is stable for $r < 1$ and unstable for $r > 1$. The Lorenz equations have the same stability limit for the onset of convection as the full equations with the same boundary conditions!

For $0 < r < 1$ the only steady solution is the conduction solution $A = B = C = 0$ and it is stable. For $r > 1$ there are the two solutions given by (8.3.9) and (8.3.10) which are stable and the unstable conduction solution. For obvious reasons the transition at $r = 1$ is known as a pitchfork bifurcation.

The stability of the steady solution given in (8.3.9) and (8.3.10) can also be examined. Expansion about this solution with

$$A = \pm [b(r - 1)]^{1/2} + A_1 e^{\lambda\tau} \quad (8.3.11)$$

$$B = \pm [b(r - 1)]^{1/2} + B_1 e^{\lambda\tau} \quad (8.3.12)$$

$$C = r - 1 + C_1 e^{\lambda\tau} \quad (8.3.13)$$

and substitution into (8.3.5)–(8.3.7) with linearization gives the characteristic equation

$$\lambda^3 + (Pr + b + 1)\lambda^2 + (r + Pr)b\lambda + 2bPr(r - 1) = 0 \quad (8.3.14)$$

This equation has one real negative root and two complex conjugate roots when $r > 1$. If the product of the coefficients of λ^2 and λ equals the constant term, we obtain

$$r = \frac{Pr(Pr + b + 3)}{Pr - b - 1} \quad (8.3.15)$$

At this value of r the complex roots of (8.3.14) have a transition from negative to positive real parts. This is the critical value of r for the instability of steady convection and represents a subcritical Hopf bifurcation. If $Pr > b + 1$ the steady solutions given by (8.3.9) and (8.3.10) are unstable for Rayleigh numbers larger than that given by (8.3.15).

To further examine the behavior of the Lorenz equations it is necessary to carry out numerical solutions. Following Lorenz (1963) we consider $\lambda^* = 8^{1/2}$, the critical value from (7.3.30), so that b , from (8.3.8), equals $8/3$. For these values the steady-state solution given by (8.3.1), (8.3.2), (8.3.9), and (8.3.10) becomes

$$\psi^* = \pm [24(r - 1)]^{1/2} \sin\left(\frac{\pi x^*}{2^{1/2}}\right) \sin \pi y^* \quad (8.3.16)$$

$$\theta^* = \frac{1}{\pi r} \left\{ (r - 1) \sin 2\pi y^* \mp \left[\frac{16}{3}(r - 1) \right]^{1/2} \cos\left(\frac{\pi x^*}{2^{1/2}}\right) \sin \pi y^* \right\} \quad (8.3.17)$$

The Nusselt number Nu is a measure of the efficiency of convective heat transfer across the layer; it is the ratio of the heat transferred by convection to the conductive heat transfer without convection. In terms of nondimensional variables it is given by

$$Nu = 1 + \left\langle \frac{\partial \theta^*}{\partial y^*} \right\rangle_S \quad (8.3.18)$$

where $\langle \rangle_S$ indicates an average across either the upper or lower surface. Substitution of (8.3.17) into (8.3.18) gives

$$Nu = 1 + \frac{2(r - 1)}{r} \quad (8.3.19)$$

This relation is not in good agreement with experiment when r is significantly larger than unity. This is clearly due to the extreme truncation which is only expected to be valid near the stability limit $r = 1$. Nevertheless, it is of interest to explore the behavior of the Lorenz equations for larger values of r .

From (8.3.15), the critical Rayleigh number for stability of the steady-state solutions is $r = 24.74$ for $Pr = 10$, $\lambda^* = 8^{1/2}$ and $b = 8/3$. For values of r greater than this value unsteady solutions are expected. A numerical solution of the Lorenz equations for $r = 28$, $Pr = 10$ and $b = 8/3$ is given in Figure 8.1. The figure shows the temporal evolution of the solution in the three-dimensional A , B , C phase space with the nondimensional time τ as the parameter. The projection of the evolving numerical solution onto the A , B plane is given in Figure 8.1a and the projection onto the C , B plane is given in Figure 8.1b. These are known as phase portraits. The dependence of the variable B on time τ is shown in Figure 8.1c. The solution randomly oscillates between cellular rolls with clockwise rotation, $B > 0$, and counterclockwise rotation, $B < 0$. The unstable fixed points from (8.3.9) and (8.3.10), $A = B = \pm 72^{1/2}$, $C = 27$, are the crosses in Figures 8.1a and b.

This solution is chaotic in that adjacent solutions diverge exponentially in time. The solution oscillates about a fixed point with growing amplitude until it flips into the other quadrant

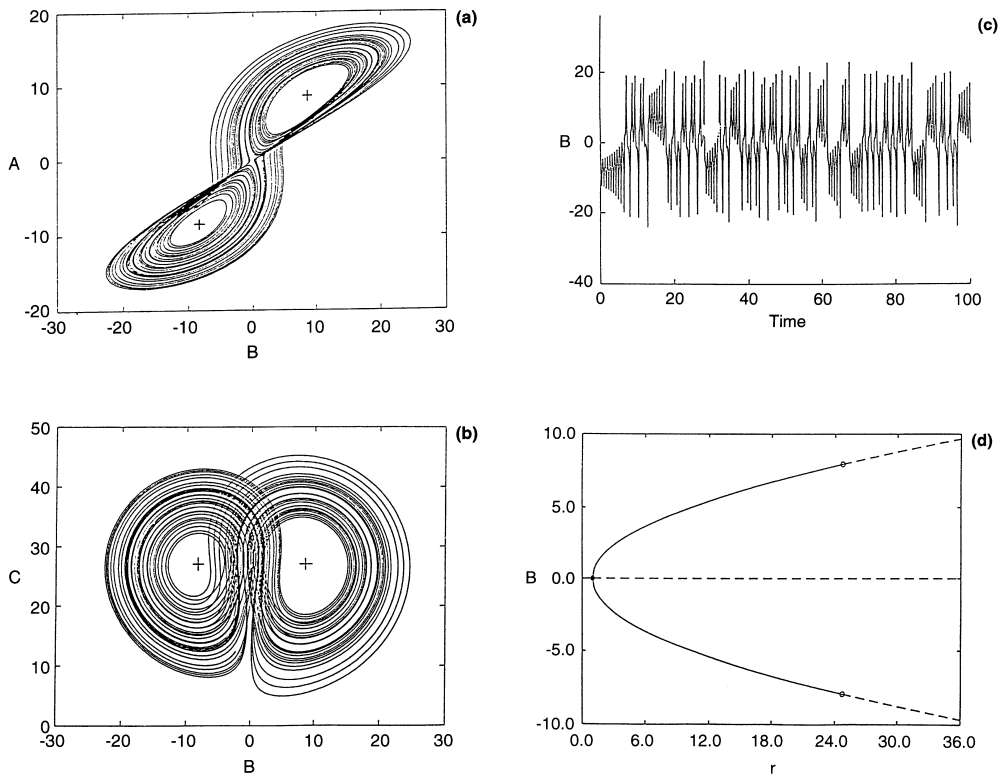


Figure 8.1. A numerical solution of the Lorenz equations (8.3.5), (8.3.6), and (8.3.7) with $Pr = 10$, $b = 8/3$, $r = 28$. Solution in the A , B , C phase space projected (a) on the A , B , plane and (b) on the C , B plane. (c) Time dependence of the coefficient B . (d) Bifurcation diagram giving the loci of the fixed points projected onto the B , r plane. The solid lines represent stable fixed points, and the dashed lines represent unstable fixed points; the solid circle is a pitchfork bifurcation, and the open circles are Hopf bifurcations.

where it oscillates about the other fixed point. The cellular flow oscillates in amplitude until the amplitude goes to zero. Then cells previously rotating in the clockwise direction rotate in the counterclockwise direction. The fixed points behave as “strange attractors.” In Figure 8.1d the fixed points are projected on the B , r plane. This is known as a bifurcation diagram. The solid lines represent stable fixed points and the dashed lines represent unstable fixed points; the solid circle is a pitchfork bifurcation and the open circles are Hopf bifurcations.

An essential feature of the solution is that the value of C is always positive and oscillates aperiodically around a positive value. It is the C term that gives an approximation to a boundary layer structure. The growth and decay of C around a positive value is an approximation to the growth and separation of the thermal boundary layers at the top and bottom of the convection cell. Physically and mathematically, the aperiodic oscillations of this boundary layer are coupled with and drive the growth and reversal of the convective roll, represented by the aperiodic oscillations of A and B . This is illustrated in Figure 8.1b. The direction of the trajectory near $B = 0$ is always toward $C = 0$. The direction of the trajectory along the outer wings of the attractor is always in the positive C direction. When C is at its highest point, the boundary layer is thin and the flow velocities are decreasing. This

quiescence of the convective motion allows the boundary layer to grow, B remains small, and C decreases. At some point the boundary layer becomes unstable and convection resumes, either as a clockwise roll or a counterclockwise roll. As the convective motion increases, the boundary layer thins and the value of C grows. The amplitude of the convective motion consequently slows down and the absolute values of A and B once again move toward zero. Once convective motion has slowed enough, the boundary layer can grow again. Every time the convective motion stops to let the thermal boundary layer grow, the cell is presented with a choice of whether to convect in a clockwise or a counterclockwise direction. This choice is made after each turnover. It is this freedom of choice in a completely deterministic system that produces the chaotic, aperiodic behavior of the Lorenz attractor.

The essential feature of the solution of the Lorenz equations in this parameter range is deterministic chaos. One consequence of the deterministic chaos of the Lorenz equations is that solutions that begin a small distance apart in phase space diverge exponentially. With essentially infinite sensitivity to initial conditions, the zero-order behavior of a solution is not predictable.

It should be emphasized that the numerical solution of the Lorenz equations given above is not a valid solution for thermal convection in a fluid layer. The Rayleigh number is outside the range of validity of the Lorenz truncation. Nevertheless, this solution has a great significance in that it was the first solution to exhibit the mathematical conditions for chaotic behavior. But the significance goes beyond this. Experimental studies and numerical simulations of thermal convection in a fluid layer heated from below at high Rayleigh numbers and intermediate values of Prandtl number are generally unsteady and “turbulent.”

The Rayleigh number for mantle convection depends strongly upon whether the mantle convects as a single layer or as two layers separated by the 660 km seismic discontinuity. The generally accepted range for the Rayleigh number corresponding to these two cases lies between 10^7 and 10^9 (see Chapter 7). Because the Prandtl number for the mantle is so large, the momentum terms on the left side of the stream function equation (8.2.5) can be neglected. Thus, the only nonlinear terms are in the energy equation (8.2.6). The question is whether these terms can generate chaotic behavior and thermal turbulence.

This question is first addressed by determining whether the Lorenz equations yield chaotic solutions in the limit $Pr \rightarrow \infty$. In this limit (8.3.5) requires

$$A = B \quad (8.3.20)$$

and the substitution of this result into (8.3.6) and (8.3.7) gives

$$\frac{dB}{d\tau} = (r - 1)B - BC \quad (8.3.21)$$

$$\frac{dC}{d\tau} = -bC + B^2 \quad (8.3.22)$$

Again, these equations have the steady-state ($d/d\tau = 0$) solution $A = B = C = 0$ corresponding to the conduction solution. These equations also have the same fixed points as the Lorenz equations as given in (8.3.9) and (8.3.10) corresponding to cellular rolls rotating either in the clockwise or counterclockwise direction. A stability analysis again shows that the conduction solution is stable for $r < 1$ and unstable for $r > 1$. However, the steady solution consisting of cellular rolls is now stable for the entire range $r > 1$. In the limit of infinite Prandtl number the Lorenz equations do not yield chaotic solutions. This result has been used to argue that mantle convection is not chaotic. However, we will show in the next

section that a higher-order truncation yields chaotic solutions at infinite Prandtl number. Also, numerical solutions of the full equations of motion and temperature for infinite Pr are chaotic at high Ra , suggesting that mantle convection is also chaotic.

8.4 Higher-order Truncations

We next consider higher-order truncations of the Saltzman equations given in (8.2.9) and (8.2.10). Only the limit $Pr \rightarrow \infty$ applicable to mantle convection will be considered. In this limit the Fourier coefficients of the stream function $\psi_{m,n}^*$ can be related to the Fourier coefficients of the temperature $\theta_{m,n}^*$ using (8.2.9) with the result

$$\psi_{m,n}^* = -Ra \left(\frac{2\pi m}{\lambda^*} \right) \frac{\theta_{m,n}^*}{(4\pi^2 m^2/\lambda^{*2} + \pi^2 n^2)^2} \quad (8.4.1)$$

This formula is then substituted into (8.2.10). The lowest consistent order of truncation beyond that used by Lorenz is $m = 2$ for the expansion in x^* ($m = 1, 2$) and $n = 4$ for the expansion in y^* ($n = 1, 2, 3, 4$). This truncation yields a set of 12 ordinary differential equations for the time dependence of the temperature coefficients:

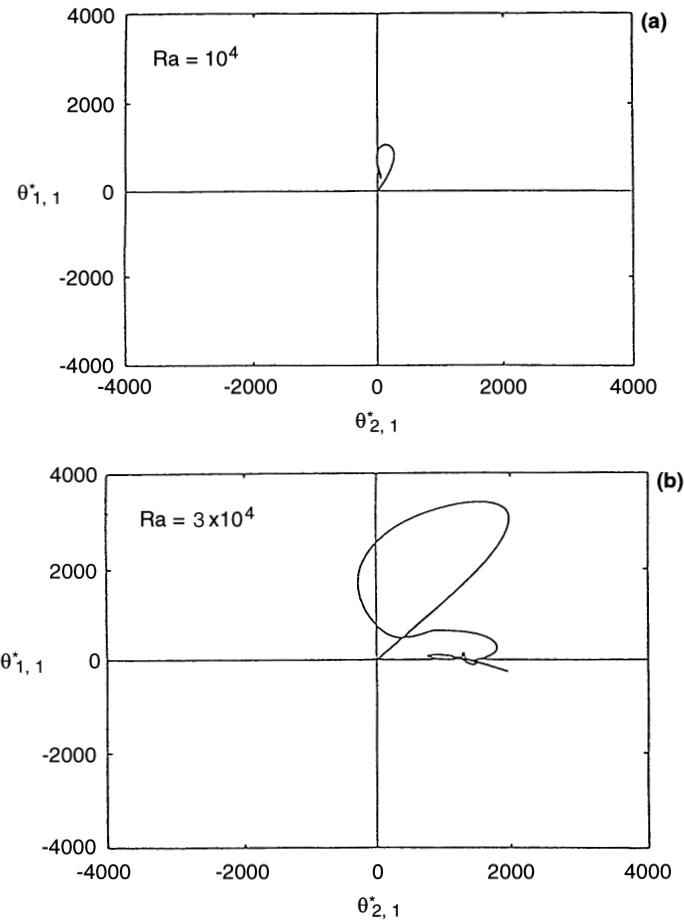
$$\begin{aligned} \frac{d\theta_{m,n}^*}{dt^*} = & - \sum_{p=-2}^2 \sum_{q=-4}^4 \frac{2\pi^2}{\lambda^*} (mq - np) \left(\frac{2\pi p}{\lambda^*} \right) \frac{\theta_{p,q}^* \theta_{m-p,n-q}^*}{[(4\pi^2 p^2/\lambda^{*2}) + \pi^2 q^2]^2} \\ & + Ra \left(\frac{2\pi m}{\lambda^*} \right)^2 \frac{\theta_{m,n}^*}{[(4\pi^2 m^2/\lambda^{*2}) + \pi^2 n^2]^2} - \pi^2 \left(\frac{4m^2}{\lambda^{*2}} + n^2 \right) \theta_{m,n}^* \end{aligned} \quad (8.4.2)$$

It is necessary to take twice the resolution in the vertical direction compared to the horizontal direction in order to resolve the $u^* \partial \theta^* / \partial x^*$ term in the energy equation.

The time evolution of the 12 coefficients $\theta_{0,1}^*, \theta_{0,2}^*, \theta_{0,3}^*, \theta_{0,4}^*, \theta_{1,1}^*, \theta_{1,2}^*, \theta_{1,3}^*, \theta_{1,4}^*, \theta_{2,1}^*, \theta_{2,2}^*, \theta_{2,3}^*, \theta_{2,4}^*$ is found by numerically integrating the 12 equations given by (8.4.2) (Stewart and Turcotte, 1989). The time evolution can be thought of as trajectories in a 12-dimensional phase space. It is convenient to project the 12-dimensional trajectories onto the two-dimensional phase space consisting of $\theta_{1,1}^*$ and $\theta_{2,1}^*$. These correspond to the fundamental mode and the first subharmonic. There are two parameters in this problem, the Rayleigh number, Ra or r , and the wavelength. In this discussion solutions are given only for the critical value of the wavelength $\lambda^* = 2^{3/2}$.

At the subcritical Rayleigh numbers $0 < r < 1$ ($0 < Ra < 657.512$) the only fixed point of the solution is at the origin and it is stable; there is no flow. For higher Rayleigh numbers, the two fixed points corresponding to clockwise and counterclockwise rotations in the fundamental mode $\theta_{1,1}^*$ become stable. The steady-state solution for $Ra = 10^4$ ($r = 15.21$) is given in Table 8.1. It is seen that only 6 of the 12 coefficients are nonzero: $\theta_{0,2}^*, \theta_{0,4}^*, \theta_{1,1}^*, \theta_{1,3}^*, \theta_{2,2}^*$, and $\theta_{2,4}^*$. This solution was obtained by specifying an initial condition near the origin and studying the time evolution of the 12 coefficients using (8.4.2). This time evolution projected onto the $\theta_{1,1}^*, \theta_{2,1}^*$ plane is given in Figure 8.2a. Although the subharmonic coefficient $\theta_{2,1}^*$ is zero at the fixed point, it is nonzero during the time evolution.

The steady-state solution for $Ra = 3 \times 10^4$ ($r = 45.62$) is also given in Table 8.1. It is seen that only 4 of the 12 coefficients are nonzero: $\theta_{0,2}^*, \theta_{0,4}^*, \theta_{2,1}^*$, and $\theta_{2,3}^*$. At this Rayleigh number the fundamental mode and its associated harmonics $\theta_{1,1}^*, \theta_{1,3}^*, \theta_{2,2}^*$, and $\theta_{2,4}^*$ are zero at the stable fixed point. The time evolution of the solution projected onto the $\theta_{1,1}^*, \theta_{2,1}^*$ plane



is given in Figure 8.2b. Finally, the steady-state solution for $Ra = 4.3 \times 10^4$ ($r = 65.39$) is given in Table 8.1. It is seen that 8 of the 12 coefficients are nonzero: $\theta_{0,1}^*$, $\theta_{0,2}^*$, $\theta_{0,3}^*$, $\theta_{0,4}^*$, $\theta_{2,1}^*$, $\theta_{2,2}^*$, $\theta_{2,3}^*$, and $\theta_{2,4}^*$. All of the $\theta_{1,n}^*$ coefficients are zero including the fundamental mode $\theta_{1,1}^*$. The time evolution of the solution projected onto the $\theta_{2,1}^*$, $\theta_{1,1}^*$ plane is given in Figure 8.2c. It is seen that the evolution prior to entering the stable fixed point is much more complex; the solution oscillates in the positive $\theta_{2,1}^*$, $\theta_{1,1}^*$ quadrants before entering the negative quadrants.

The time evolution of the solution for $Ra = 4.5 \times 10^4$ ($r = 68.44$) is given in Figure 8.2d; it is fully chaotic and no fixed points are stable. The flow alternates between aperiodic oscillations about the two fundamental modes (clockwise and counterclockwise) and the two subharmonic modes (clockwise and counterclockwise). All 12 coefficients are nonzero and are time-dependent. The time dependence of the $\theta_{2,1}^*$ and $\theta_{1,1}^*$ coefficients is shown in Figure 8.3. The resemblance with the time behavior of the Lorenz attractor illustrated in

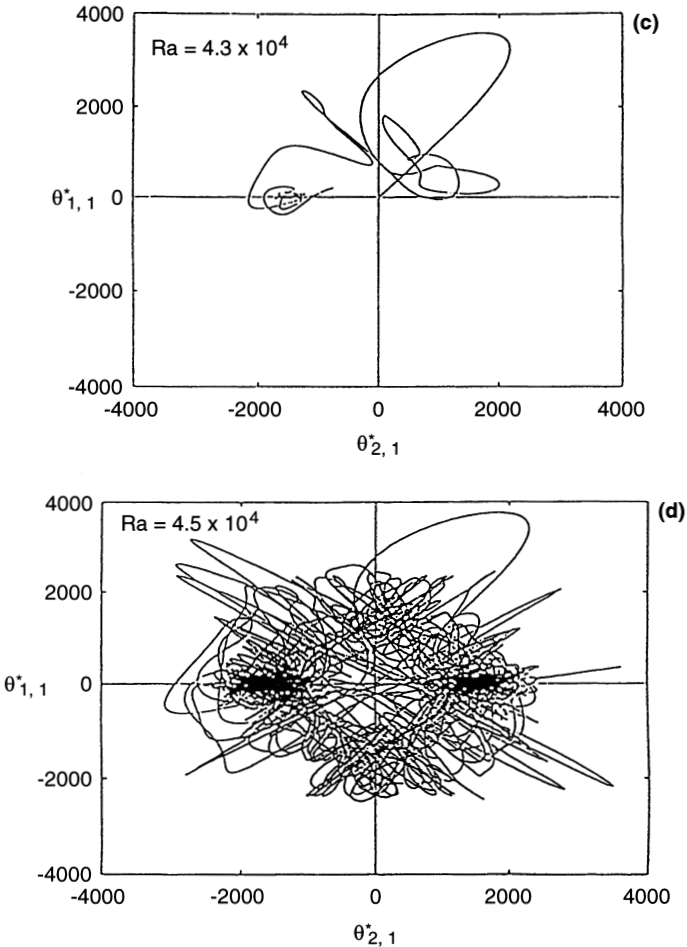


Figure 8.2. Numerical solutions of the 12-mode infinite Prandtl number equations projected onto the $\theta_{1,1}^*$, $\theta_{2,1}^*$ plane of the 12-dimensional phase space. (a) $Ra = 10^4$ ($r = 15.21$), (b) $Ra = 3 \times 10^4$ ($r = 45.62$), (c) $Ra = 4.3 \times 10^4$ ($r = 65.39$), (d) $Ra = 4.5 \times 10^4$ ($r = 68.44$).

Figure 8.1c is striking. The oscillatory behavior of the $\theta_{2,1}^*$ mode amplifies until the flow undergoes a turbulent burst in the fundamental $\theta_{1,1}^*$ mode, where it is briefly trapped before flipping into the $\theta_{2,1}^*$ mode with the opposite sense of rotation.

In order to better understand the transitions in the behavior of the time-dependent solutions, we show in Figure 8.4 two projections of the loci of fixed points as a function of the Rayleigh number of the system. The solid lines denote stable fixed points, the dashed lines unstable fixed points, and the open circles Hopf bifurcations. Figure 8.4a shows a projection on the $\theta_{1,1}^*$, Ra plane. The solution $\theta_{1,1}^* = 0$, representing the conduction solution, becomes unstable and bifurcates at $Ra = 657.512$ giving two stable symmetric solutions which do not contain the $\theta_{2,1}^*$ mode. One branch of this solution appears in the positive quadrant and is labeled “ $\theta_{1,1}^*$ pure” in Figure 8.4a to distinguish it from the mixed-mode solution, which contains a contribution from the $\theta_{2,1}^*$ mode. Each branch becomes unstable and undergoes a subcritical pitchfork bifurcation at $Ra = 3.802 \times 10^4$, producing four unstable mixed-mode

Table 8.1. Numerical Values of Fourier Coefficients of the Fixed Points of the 12-mode Equations (8.4.2)

$r = Ra/R_{cr}$	Ra		
	10^4	3×10^4	4.3×10^4
	15.21	45.62	65.39
$\theta_{0,1}^*$	0.000	0.000	-2120.222
$\theta_{0,2}^*$	-1506.097	-4571.719	-6663.231
$\theta_{0,3}^*$	0.000	0.000	-366.705
$\theta_{0,4}^*$	-286.133	-2191.940	-3355.777
$\theta_{1,1}^*$	506.978	0.000	0.000
$\theta_{1,2}^*$	0.000	0.000	0.000
$\theta_{1,3}^*$	66.170	0.000	0.000
$\theta_{1,4}^*$	0.000	0.000	0.000
$\theta_{2,1}^*$	0.000	1117.832	-1415.752
$\theta_{2,2}^*$	426.445	0.000	-398.378
$\theta_{2,3}^*$	0.000	509.313	-623.561
$\theta_{2,4}^*$	105.531	0.000	-490.614

solutions, labeled “ $\theta_{1,1}^*$ mixed”. Each $\theta_{1,1}^*$ mixed-mode branch sweeps back to a saddle bifurcation at $Ra = 1.909 \times 10^4$. This type of bifurcation configuration (subcritical pitchfork plus two saddles) typically produces hysteresis effects when the saddle has one stable branch and one unstable branch. Here the “ $\theta_{1,1}^*$ mixed” solution has one unstable manifold (out of 12) on one side of the saddle, and two unstable manifolds on the other.

The second bifurcation of the conduction solution is at $Ra = 1,315.023$, where two unstable symmetric fixed points dominant in the subharmonic $\theta_{2,1}^*$ mode appear. Since these fixed points contain no component in the $\theta_{1,1}^*$ mode, we call these “ $\theta_{2,1}^*$ pure” unstable solution branches. Each of these branches becomes stable and undergoes a pitchfork bifurcation at $Ra = 2,041.918$, resulting in the solution branches labeled “ $\theta_{2,1}^*$ mixed” in Figures 8.4a and b. The $\theta_{2,1}^*$ mixed-mode branches nearly connect with the $\theta_{1,1}^*$ mixed-mode branches.

Both the fundamental and the subharmonic pure-mode solutions are stable between $Ra = 2,369$ and $Ra = 3.802 \times 10^4$. The trajectories in Figures 8.2a and b have the same initial condition, yet in Figure 8.2a they converge to the fundamental subharmonic stable fixed point. Presumably this is because the unstable mixed-mode branches disrupt the separatrix between the basin of the attraction of the fundamental and subharmonic pure-mode solutions. Note that the transition from Figure 8.2a to Figure 8.2b occurs at a Rayleigh number above the stability limit of the fundamental mode.

The third bifurcation of the conduction solution is at $Ra = 4.140 \times 10^4$, where two unstable symmetric solutions in the fundamental mode $\theta_{1,1}^*$ appear. These are labeled “new $\theta_{1,1}^*$ pure” in Figure 8.4a. Each of these undergo Hopf bifurcations at $Ra = 5.23 \times 10^4$ and $Ra = 5.53 \times 10^4$. At no point does the origin itself undergo a Hopf bifurcation, nor does the conduction solution bifurcate to mixed-mode solutions.

There are no Hopf bifurcations for the conduction or fundamental harmonic solutions; however, the stable subharmonic branch undergoes two Hopf bifurcations (Figure 8.4b), one at $Ra = 4.37 \times 10^4$ and one at $Ra = 6.36 \times 10^4$. Each mixed-mode saddle ($\theta_{1,1}^*$ mixed) undergoes two Hopf bifurcations, at $Ra = 4.491 \times 10^4$ and $Ra = 5.039 \times 10^4$. Each mixed-mode saddle ($\theta_{2,1}^*$ mixed) undergoes six Hopf bifurcations. Each of these Hopf

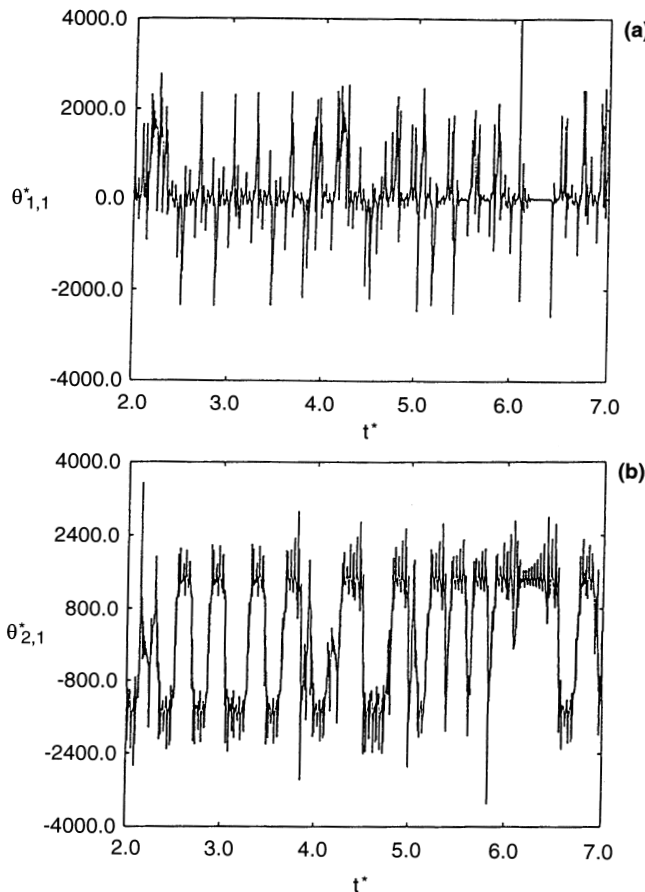


Figure 8.3. Time dependence of the coefficients (a) $\theta_{1,1}^*$ and (b) $\theta_{2,1}^*$ for the solution given in Figure 8.2d, $Ra = 4.5 \times 10^4$.

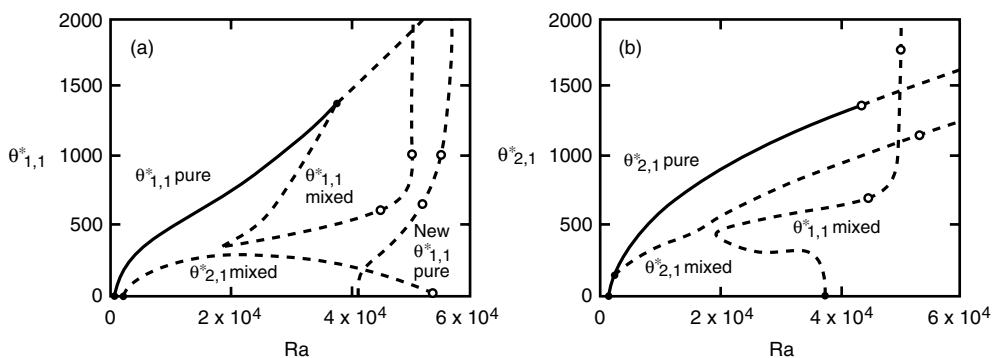


Figure 8.4. Bifurcation diagrams for the 12-mode infinite Prandtl number equations. The fixed points of (8.4.2) are projected onto the (a) $\theta_{1,1}^*$, Ra plane and (b) the $\theta_{2,1}^*$, Ra plane. Stable branches are shown as solid lines, unstable branches as dashed lines, pitchfork bifurcations as solid circles, and Hopf bifurcations as open circles.

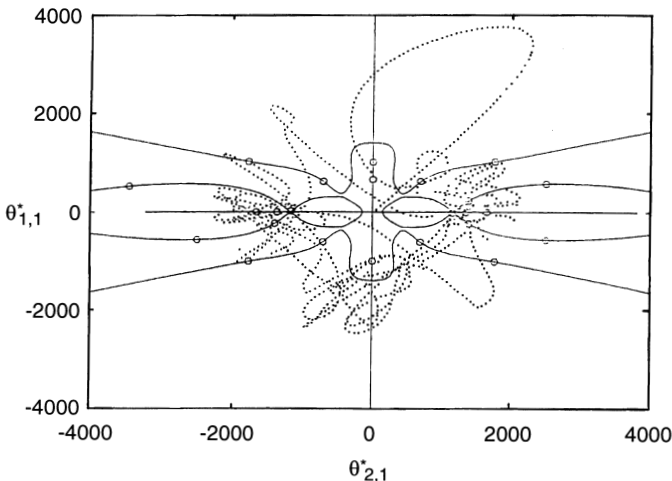


Figure 8.5. Loci of the fixed points from Figure 8.4 projected onto the $\theta_{1,1}^*, \theta_{2,1}^*$ plane. Superimposed as a dotted line is the time evolution of the chaotic solution from Figure 8.2d.

bifurcations sheds stable or unstable periodic orbits which are responsible for the oscillations of the trajectory at $Ra = 4.5 \times 10^4$ shown in Figure 8.2d. In Figure 8.5, the first 7,000 points of the trajectory at $Ra = 4.5 \times 10^4$ are projected onto the $\theta_{1,1}^*, \theta_{2,1}^*$ plane (dotted line) superimposed on the central portion of the branches of the fixed points (solid lines). Note that the trajectory weaves aperiodically around several Hopf bifurcations (circles).

Physically, infinite Prandtl number, high Rayleigh number convection becomes time-dependent through boundary layer instabilities that generate thermal plumes. In terms of spectral expansions, these instabilities result from the nonlinear coupling in the convective terms of the heat equation.

The 12-mode expansion gives solutions that are clearly chaotic. A valid question is whether higher-order expansions also yield chaotic solutions. In order to examine this question 24- and 40-mode expansions have been considered. At $Ra = 10^4$, both models converge to fixed points, and the energy distribution among the Fourier modes is qualitatively correct; modes which should be nearly zero are almost zero, while large-amplitude modes have comparable amplitudes, within 10%. At $Ra = 5 \times 10^4$, however, the temporal behavior of the 24-mode model and the 40-mode model diverge significantly: the 40-mode model goes to a fixed point while the 24-mode model goes to a periodic orbit. At higher Rayleigh numbers, this relationship inverts, the 24-mode model going to a stable fixed point and the 40-mode model to a periodic orbit. Therefore, it is not always true that adding more modes in the expansion will always reduce the time-dependent behavior of the solutions – or the dimension of the attractor – in the infinite Prandtl number case; sometimes the opposite is true.

In Figure 8.6 we show the periodic orbit of the 40-mode system projected onto the $\theta_{1,1}^*, \theta_{2,1}^*$ plane at Rayleigh number $Ra = 1.9 \times 10^5$. Because the system is symmetric under the transformation $\theta_{m,n}^* \rightarrow -\theta_{m,n}^*$ this periodic orbit also occurs in the other quadrants of the system. Figure 8.7 shows the periodic orbit after bifurcation to

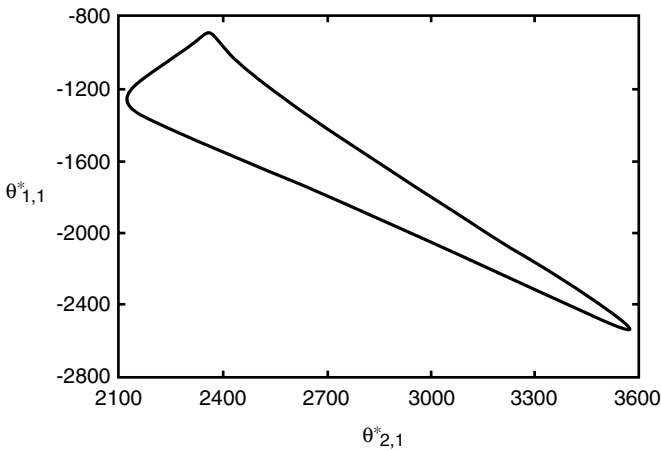


Figure 8.6. Periodic orbit of the 40-mode system at $Ra = 1.9 \times 10^5$.

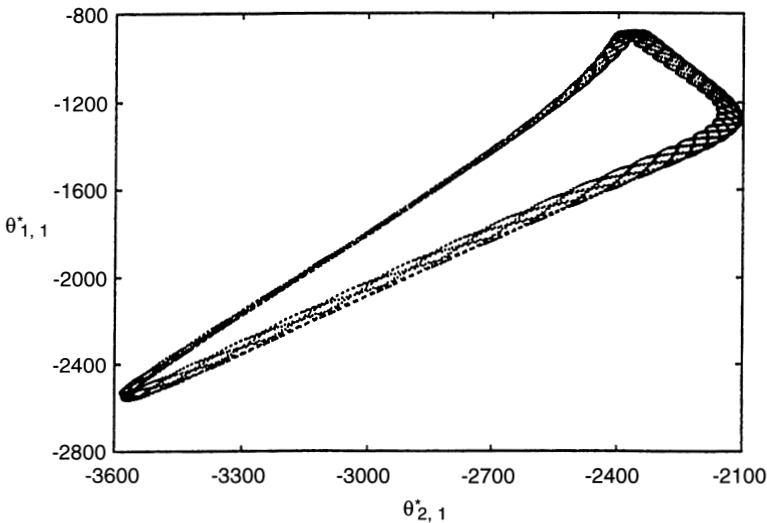


Figure 8.7. Periodic orbit after the transition to a two-torus in the 40-mode system at $Ra = 1.9 \times 10^5$.

a two-torus. This occurs near Rayleigh number $Ra = 1.95 \times 10^5$. A second temporal frequency has been introduced that causes the periodic orbit to wind around in two dimensions, remaining on the surface of a torus. The ratio between the two frequencies is approximately 50.

The study of thermal convection at infinite Prandtl number may be the best way to relate low-order chaotic systems to high-order turbulent systems. At infinite Prandtl number, viscous damping occurs in the same wavelength band as the buoyancy input. Flows have relatively little short-wavelength energy. The 40-mode expansion considered here approaches the resolution of some numerical calculations that exhibit fluid turbulence.

8.5 Chaotic Mantle Mixing

Question 8.3: Is the subducted oceanic lithosphere mixed and homogenized in the mantle?

One of the important questions in mantle dynamics is the fate of the subducted oceanic lithosphere. There are two limiting hypotheses. The first is that the layered oceanic lithosphere is mixed and homogenized into the reservoir into which it is subducted, the upper mantle for layered mantle convection or the whole mantle for whole mantle convection. Mixing and homogenization take place in two steps. The first step is to kinematically stretch and thin heterogeneities in the mantle flow. The final homogenization is accomplished by diffusion processes. The second limiting hypothesis is that components in the layered oceanic lithosphere are separately segregated into mantle layers.

Before discussing the dynamics of mantle mixing we consider the mass balance associated with mantle heterogeneities. The primary heterogeneity is the creation of the layered oceanic lithosphere at oceanic ridges. A basaltic oceanic crust with a thickness of about 6 km overlies a complementary zone of depleted mantle rock. These layers are estimated to have a combined thickness of about 60 km. The present rate at which seafloor is being created is approximately $2.8 \text{ km}^2 \text{ yr}^{-1}$. With a processing depth of 60 km and a mean density of $3,200 \text{ kg m}^{-3}$, the current rate at which mantle is being processed at oceanic ridges is $\dot{M}_0 = 5.4 \times 10^{14} \text{ kg yr}^{-1}$. If this rate was also applicable in the past then a mantle processing time t_p can be defined by

$$t_p = \frac{M_m}{\dot{M}_0} \quad (8.5.1)$$

where M_m is the mass of the complementary mantle reservoir. For layered mantle convection $M_m = 1.05 \times 10^{24} \text{ kg}$ (the mass of the upper mantle) and $t_p = 1.94 \text{ Gyr}$. For whole mantle convection $M_m = 4.06 \times 10^{24} \text{ kg}$ and $t_p = 7.52 \text{ Gyr}$.

Because the heat generation by radioactive isotopes was larger in the past, it is likely that the rate of seafloor spreading was also higher in the past. With the assumption that the mass flux processed at mid-ocean ridges \dot{M} scales with the rate of heat generation in the mantle, we write

$$\dot{M} = \frac{M_m}{t_p} \exp\left(\frac{t_e - t}{t_R}\right) \quad (8.5.2)$$

where t_e is the age of the Earth, t is time measured forward from the creation of the Earth, and t_R is the characteristic time for the decay of heat-producing elements in the Earth.

We denote the mass of the mantle that has been processed in the interval $t_i < t < t_e$ by M_R ; this is the mass of the mantle that is younger than $t_e - t_i$. The mass of the mantle that is older than $t_e - t_i$ is given by $M_{ti} = M_m - M_R$. The rate of production of M_R is only a fraction of the mass flux processed at mid-ocean ridges because of reprocessing. Only the fraction M_{ti}/M_m of \dot{M} is newly added to M_R . The rate of production of M_R is therefore given by

$$\frac{dM_R}{dt} = \dot{M} \left(1 - \frac{M_R}{M_m}\right) = \frac{M_m}{t_p} \left(1 - \frac{M_R}{M_m}\right) \exp\left(\frac{t_e - t}{t_R}\right) \quad (8.5.3)$$

Integration of (8.5.3) with the condition $M_R = 0$ at $t = t_i$ gives

$$M_R = M_m \left\{ 1 - \exp \left[\frac{t_R}{t_p} \left(1 - \exp \left(\frac{t_e - t_i}{t_R} \right) \right) \right] \right\} \quad (8.5.4)$$

$$M_{ti} = M_m - M_R = M_m \exp \left\{ \frac{t_R}{t_p} \left[1 - \exp \left(\frac{t_e - t_i}{t_R} \right) \right] \right\} \quad (8.5.5)$$

The dependence of M_{ti}/M_m on t_i is given in Figure 8.8 for $t_R = 3.6$ Gyr. It is seen that half of the mantle reservoir has been processed in the last 1.6 Gyr for layered mantle convection and in the last 3.25 Gyr for whole mantle convection.

Equation (8.5.5) gives the mass of the mantle reservoir that was either processed prior to t_i or was never processed. The amount of primitive mantle that remains M_p is obtained by setting $t_i = 0$ in (8.5.5) with the result

$$M_p = M_m \exp \left\{ \frac{t_R}{t_p} \left[1 - \exp \left(\frac{t_e}{t_R} \right) \right] \right\} \quad (8.5.6)$$

For layered mantle convection we find that $M_p/M_m = 0.01$ and for whole mantle convection $M_p/M_m = 0.30$. Thus we conclude that 30% of the mantle is primitive for whole mantle convection while only 1% of the upper mantle is primitive for layered mantle convection. It should be emphasized that these are only estimates because some of the assumptions made above are open to question. For example, the rate of processing in the past could have been higher than that given by (8.5.2). Also, we have assumed complete homogenization of the mantle reservoir.

The conclusion from the above is that a substantial fraction of the mantle reservoir has been processed through the oceanic lithosphere in the relatively recent past. Subduction introduces major heterogeneities into the mantle on the scale of 10 km. In order to determine the fate of these heterogeneities we consider the time scale on which mantle mixing occurs. Mixing is accomplished by convective strains that thin heterogeneous regions until diffusion can complete the homogenization. These processes have been studied extensively by workers in the field of polymer chemistry who denote the convective thinning process

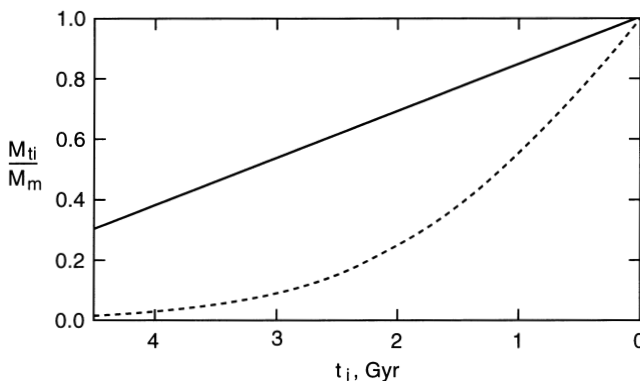


Figure 8.8. The dependence of M_{ti}/M_m on t_i from (8.5.5) for layered mantle convection (dashed curve) and whole mantle convection (solid curve). Parameter values are $t_R = 3.6$ Gyr, $t_e = 4.6$ Gyr, $t_p = 1.94$ Gyr (layered mantle convection) or 7.52 Gyr (whole mantle convection).

as “stirring” and the diffusive homogenization as “mixing” (Ottino, 1989, 1990). In the mantle, chemical diffusion acts on the scale of centimeters or less (Kellogg and Turcotte, 1987, 1990) and is ineffective in homogenizing larger-scale heterogeneities. The “mixing time” for chemical heterogeneities in the mantle is therefore the time required for stirring to deform heterogeneities to the centimeter scale on which diffusion acts.

A number of papers have considered convective mixing as it applies to the mantle. Richter and Ribe (1979) considered an idealized, two-dimensional model of Rayleigh-Bénard convection and calculated the thinning of heterogeneities with time. From laboratory and numerical experiments, Richter et al. (1982) showed that time-dependent convection is more effective in thinning heterogeneities than steady convection. Olson et al. (1984a,b) pointed out the relative importance of pure and simple shear on mixing rates. Numerical calculations of convective stirring by Hoffman and McKenzie (1985) indicate that the thinning is accomplished primarily by pure shear. Heterogeneities may experience continuous stretching accompanied by rapid deformation, or they may experience periods of rapid mixing interspersed with periods of quiescence in which mixing is slow. Thus, a distribution of thicknesses of heterogeneities will develop after convective mixing begins. Gurnis (1986a,b) and Gurnis and Davies (1986a,b) argue that some heterogeneities persist in regions where convective mixing is ineffective. The work on convective mixing in the mantle has been reviewed by Kellogg (1992, 1993).

The evolution of infinitesimal elliptical strain markers in the flow can be used to quantify rates of mixing. McKenzie (1979) calculated the evolution of markers in steady thermal flows; Hoffman and McKenzie (1985) used the same methods to study the evolution of large-scale heterogeneities in unsteady flows. The cumulative strain of a strain marker can be determined by summing the incremental strain at each position along the particle path. Assume that the strain marker is elliptical and infinitesimal, with a semi-major axis a and semi-minor axis b . The evolution of a strain marker is defined by its position, its aspect ratio, $\epsilon \equiv a/b$, and its orientation θ with respect to a fixed ξ -axis. The position is obtained by integrating the velocity components. The deformation of an infinitesimal strain marker in a two-dimensional, time-dependent flow is governed by

$$\frac{d\epsilon}{dt^*} = 2\epsilon(\alpha^* \cos 2\theta + \beta^* \sin 2\theta) \quad (8.5.7)$$

and

$$\frac{d\theta}{dt^*} = \left(\frac{\epsilon^2 + 1}{\epsilon^2 - 1} \right) (-\alpha^* \sin 2\theta + \beta^* \cos 2\theta) + \omega^* \quad (8.5.8)$$

where α^* , β^* , and ω^* are components of the nondimensional strain-rate tensor and are given by

$$\alpha^* = \frac{\partial u^*}{\partial \xi^*} \quad (8.5.9)$$

$$\beta^* = \frac{1}{2} \left(\frac{\partial u^*}{\partial \eta^*} + \frac{\partial v^*}{\partial \xi^*} \right) \quad (8.5.10)$$

$$\omega^* = \frac{1}{2} \left(\frac{\partial u^*}{\partial \eta^*} - \frac{\partial v^*}{\partial \xi^*} \right) \quad (8.5.11)$$

with u^* , v^* the velocity components in the directions of the ξ^* , η^* axes, respectively.

Since the deformation history of any particle is a function of its trajectory, which is unique in the flow, overall mixing is best characterized by the strains of a large number of particles equivalent to a distribution of particle sizes after a given time. Such a distribution is a characteristic of all flows and arises from the fact that some particles undergo periods of quiescence with little deformation, while others are deformed rapidly in a short time. The distribution of strains enables us to obtain a quantitative measure of the mixing accomplished in the flow by providing an effective strain rate. Ten et al. (1998) have introduced the particle and line method to quantify mixing.

Mixing is relatively inefficient for steady cellular flows. Efficient mixing requires a time-dependent flow. Kellogg and Turcotte (1990) considered mixing in a flow generated by the Lorenz attractor. Here we show the results of a mixing calculation by Kellogg and Stewart (1991) for the flow illustrated in Figure 8.3. This fully chaotic flow was determined from the 12-mode truncation of the infinite Prandtl number thermal convection equations described in the previous section at $Ra = 4.5 \times 10^4$. Christensen (1989b), Christensen and Hofmann (1994), and Dupeyrat et al. (1995) have also carried out similar mixing calculations using numerical solutions of two-dimensional mantle convection. Numerical solutions of three-dimensional mixing have been carried out by Schmalzl et al. (1995, 1996). Ferrachat and Ricard (1998) have compared chaotic mixing with nonchaotic mixing.

The effectiveness of the chaotic flow of Figure 8.3 at mixing heterogeneities is revealed in Figure 8.9 by the scattering of a cluster of passive markers placed in the box. The streamlines illustrate “snapshots” of the flow which tends to be dominated by two cells in the horizontal and one or two in the vertical. Because the flow is time dependent, streamlines are not particle paths. The flow is “space-filling” in that a cluster of particles disperses to fill the box. The rate at which a marker deforms depends on its path, which depends on its initial position. A statistical description of mixing is obtained by distributing a large number of markers evenly throughout the box, and then tracking their evolution. The distribution of strains which results is characteristic of the flow. The distribution obtained with 900 particles is shown in Figure 8.10 for times from $t^* = 0.1$ to $t^* = 0.9$. The fraction f of markers which have been stretched to a length greater than a/a_0 is plotted against a/a_0 .

Strain is accomplished primarily by pure shear (exponential elongation). This is illustrated in Figure 8.11, in which the strain attained by half the particles ($f = 0.50$) is plotted as a

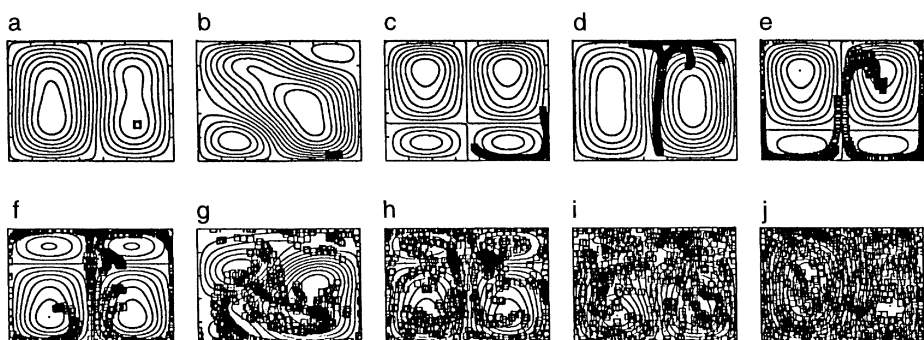


Figure 8.9. Cluster of particles scattered by the chaotic flow of Figure 8.2d. Nine hundred particles were placed in a box of dimensions 0.01×0.01 (a), and their positions tracked and plotted after increments of $t^* = 0.1$. Instantaneous streamlines are also shown.

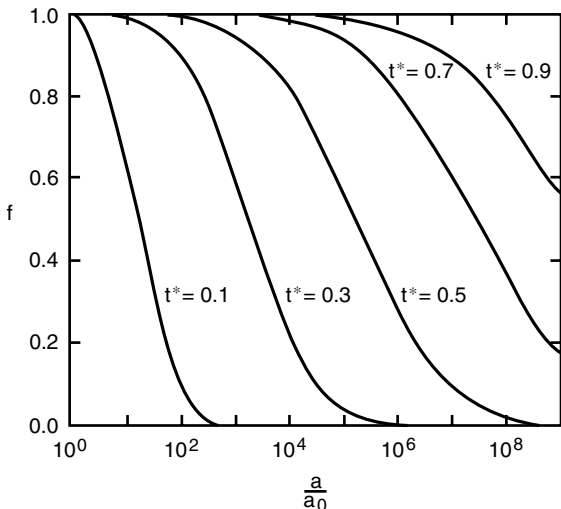


Figure 8.10. Distribution of strains in the chaotic flow of Figure 8.2d. The fraction f of particles which have reached an elongation of a/a_0 or larger is plotted against a/a_0 . The curves are the distributions achieved at times t^* ranging from $t^* = 0.1$ to $t^* = 0.9$.

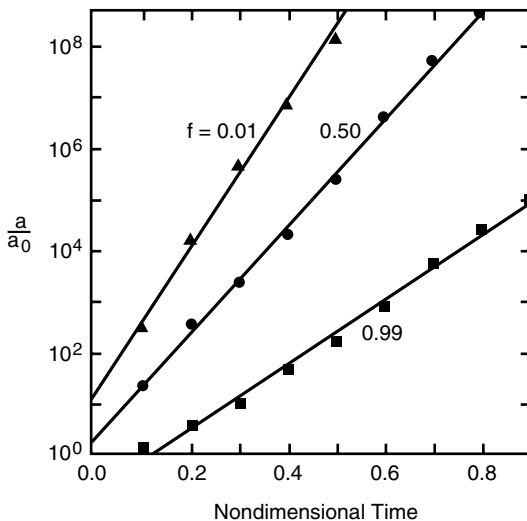


Figure 8.11. Strain evolution paths in the chaotic flow of Figure 8.2d. The strain a/a_0 reached by a fraction of the particles f is plotted as a function of the nondimensional time t^* for $f = 0.01$, $f = 0.50$, and $f = 0.99$.

function of time. The strain evolution has the form

$$a = a_0 e^{2\alpha t^*} \quad (8.5.12)$$

where α is the strain rate. We define an effective strain rate of the flow α_e as the minimum strain rate acting on half the strain markers in the fluid, and we obtain $\alpha_e = 10.3$ for this flow from the numerical results. Since the strain measures the separation of two points (the extremes of the semi-major axis of the ellipse), this is equivalent to estimating the maximum Lyapunov exponent $\lambda_1 = \alpha_e / \ln 2$ for the physical flow. Because the flow is incompressible and conserves area, there is an equivalent minimum exponent $\lambda_2 = -\lambda_1$.

Figure 8.11 also contains a plot of the minimum strain attained by 99% of particles ($f = 0.99$) and the minimum strain attained by the most deformed 1% of particles

($f = 0.01$). The latter curve provides an estimate of the maximum strain accomplished by the flow. The particles which are least deformed are also deformed primarily by pure shear, although the effective strain rate is low for these markers.

Chemical diffusion acts on the scale of centimeters to destroy heterogeneities in the mantle (Kellogg and Turcotte, 1987). An effective mixing time for mantle convection is the time required to stretch a 10 km heterogeneity to a width of 1 cm. From Figure 8.10, $t^* = 1$ is the dimensionless mixing time for the mantle. To determine the mixing time in years, we calculate the dimensionless mean surface velocity and scale this to a plate velocity of 100 mm yr^{-1} . The mixing time is 500 Myr if the mantle convects as a single layer, and 120 Myr if the mantle convects in two layers with a barrier to convection at 660 km.

The first question which arises in discussing the geological implications of the mixing hypothesis is whether there is direct observational evidence for an imperfectly mixed mantle. Allègre and Turcotte (1986) argue that the “marble cake structure” associated with imperfect mixing can be seen in high-temperature peridotites, which represent samples of the Earth’s mantle. Typical locations include Beni Bousera, Rhonda, and Lherz. These rocks consist primarily of depleted lherzolite. Embedded in this matrix are bands of pyroxenite comprising a few percent of the massif. Trace element studies of these bands indicate that they were originally basaltic in composition (Loubet and Allègre, 1982). In places where pyroxenite bands are not found, the peridotite has the fertile composition required to produce basalts on partial melting. Isotope studies of the Rhonda and Beni Bousera peridotites show that the pyroxenite bands have a wide range of values of Sr, Nd, and Pb isotopes. The isotope ratios cover the entire range seen in oceanic basalts, but they do not form a distinct isochron indicating an emplacement age (Polve and Allègre, 1980; Zindler et al., 1983; Hamelin and Allègre, 1988). These characteristics led Allègre and Turcotte (1986) to postulate that the bands are samples of former oceanic crust which have been subducted and deformed by convective shear before emplacement into their current locations. Some of the bands may originate later as dikes (Boudier, 1978; Nicolas and Jackson, 1982). The bands range in thickness from a few meters to a few centimeters and some have been extensively folded. According to this hypothesis, they have undergone five to six orders of magnitude of thinning from an initial thickness of 6 km. The distinctive isotopic signature of the bands is destroyed by diffusive homogenization on the scale of centimeters.

Further evidence for the marble cake structure of the mantle comes from eclogitic xenoliths associated with basaltic volcanism and kimberlites. MacGregor and Manton (1986) suggest that the Roberts Victor eclogites are ancient oceanic crust. In some kimberlites, diamonds are found in the eclogite nodules. These “eclogitic” diamonds have been found to have carbon isotope ratios characteristic of sediments (Harris, 1987). A number of authors have suggested that subducted carbonates are one source of diamonds (Frank, 1967; Sharp, 1974; Helmstaedt and Gurney, 1984; Meyer, 1987; Jacob et al., 1994; Daniels et al., 1996). Pearson et al. (1989) found graphitized diamonds in the pyroxenite bands of the Beni Bousera high-temperature peridotite in Morocco. These observations are consistent with the above interpretation. Sediments are entrained in the subducted oceanic crust. During convective mixing in the deep interior some carbonate sediments are transformed to diamonds as the oceanic crust in which they are embedded is stretched and thinned.

Most mid-ocean ridge basalts (MORB) have remarkably uniform isotope ratios of long-lived systems such as Nd, Sr, and Pb on a worldwide basis. The values of these signatures indicate that the subducted oceanic crust has been stirred into the MORB source region. Deviations about the mean MORB values do exist, however; these deviations can be measured on all scales along mid-ocean ridges (Gurnis, 1986b, c). We interpret this variety as the

influence of incompletely mixed subducted ancient oceanic crust. Melting under ocean ridges randomly samples the mantle source of MORB, and thus the chemistry of MORB reflects variations in the upper mantle. In regions where there is little variation in the underlying source or where heterogeneities are small, MORB will exhibit little small-scale variation. Likewise, where melting occurs over a wide region under the ridge, rapid mixing of the magma will lead to very uniform isotope signatures. Elsewhere, MORB may exhibit a wider range of chemical signatures. Large-scale variations in isotope signatures, such as the Dupal anomaly, may reflect past large-scale variations in the nature or quantity of subducted material. One mechanism for this would be spatial or temporal variability in the subduction of continental sediments. It is possible to completely homogenize the fluid on the scale of individual convection cells while not completely homogenizing across cells. Thus large-scale heterogeneities may persist longer than small-scale heterogeneities.

Oceanic island basalts (OIB) exhibit a wide range of isotope chemistry (White, 1985; Allègre and Turcotte, 1986). Observed isotopic anomalies require 1.5–2.5 Gyr to develop. In addition, the excesses of ^3He in some ocean island basalts indicate that the source region also contains a component of primordial material. White (1985) suggested that the presence of subducted sediments is a possible source for the range of isotope chemistry. Hofmann et al. (1986) suggested that all heterogeneities seen in oceanic basalts result from the influence of incompletely homogenized subducted oceanic crust. Davies (1984) argues that mantle mixing is inefficient, so that these anomalies can develop in the mantle. This hypothesis is not consistent with the results discussed here. For example, in the case of whole mantle convection we find that 99% of the mantle is homogenized in 1.8 Gyr. Instead, we favor the hypothesis for the origin of OIB proposed by Allègre and Turcotte (1985). These authors suggest that the isotopic heterogeneities develop in the isolated reservoir of the continental crust and lithosphere, and that the anomalous isotopic signatures of OIB come from recently subducted continental sediments and recently delaminated continental lithosphere that has not been homogenized by mantle mixing.

8.6 Boundary Layer Theory

8.6.1 Boundary Layer Stability Analysis

Another approximate approach to the study of finite-amplitude thermal convection is a boundary layer analysis. For large values of the Rayleigh number it is expected that changes in temperature will be restricted to thin thermal boundary layers adjacent to the boundaries of the convecting region. We will first consider a boundary layer stability approach. We again consider a fluid layer heated from below in the Boussinesq approximation with constant properties. The stability of a thickening thermal boundary layer was considered in Section 7.6. It was shown that instability occurred when a Rayleigh number based on the thickness of the thermal boundary layer reached a critical value. In the boundary layer stability approach it is assumed that the thermal boundary layer separates from the boundary when the stability criterion is satisfied. This technique was developed by Howard (1966). It has been used to study mantle convection by Parsons and McKenzie (1978) and by Kenyon and Turcotte (1983).

It is assumed that thermal gradients are restricted to thin thermal boundary layers on the upper and lower boundaries of the layer. The core or interior of the fluid layer is assumed to be isothermal; by symmetry, the core or interior temperature T_c is given by

$$T_c = T_0 + \frac{1}{2} (T_1 - T_0) \quad (8.6.1)$$

where T_0 is the temperature of the upper boundary and T_1 is the temperature of the lower boundary ($T_1 > T_0$). The two thermal boundary layers are assumed to be transient so that the one-dimensional heat conduction analysis given in Section 4.1.1 is applicable. Initially, at $t = 0$, the core fluid with temperature T_c is assumed to be in contact with the boundaries. Subsequently there is conductive heat loss to the surface and thin thermal boundary layers develop. Because of the symmetry we consider only the development of the cold thermal boundary layer adjacent to the upper boundary. The results can also be directly applied to the hot thermal boundary layer adjacent to the lower boundary. The temperature distribution in the cold thermal boundary layer as a function of time is, from (4.1.20),

$$\frac{T_c - T}{T_c - T_0} = \operatorname{erfc} \frac{y}{2\sqrt{\kappa t}} \quad (8.6.2)$$

A similar expression can be written for the thickening hot boundary layer on the lower boundary.

The thickness of the thermal boundary layer from (4.1.22) is

$$y_T = 2.32 (\kappa t)^{1/2} \quad (8.6.3)$$

The thickness of the boundary layer increases with the square root of the time since the layer was established. The basic assumption in this analysis is that a linear stability criterion can be applied to the boundary layers. It is assumed that the boundary layers thicken until the stability criterion is satisfied, at which time they break away from the boundary surfaces and are replaced by isothermal core fluid; the process then repeats. The breakaway criterion is assumed to be given by the boundary layer stability criterion developed in Section 7.6. The applicable Rayleigh number, given in (7.6.3), is based on the boundary layer thickness. The critical value of the Rayleigh number $Ra_{y_T,cr}$ gives a critical value for the boundary layer thickness $y_{T,cr}$:

$$Ra_{y_T,cr} = \frac{\alpha g(T_1 - T_0)y_{T,cr}^3}{2\nu\kappa} \quad (8.6.4)$$

The factor of 2 in the denominator on the right side of (8.6.4) arises because the temperature difference in (7.6.3) is $T_c - T_0$ in the notation of this section and from (8.6.1) $T_c - T_0 = (1/2)(T_1 - T_0)$. The critical value of this Rayleigh number for free-surface boundary conditions is $Ra_{y_T,cr} = 807$ (see Section 7.6).

From (8.6.3) and (8.6.4) the time at which boundary layer breakaway occurs t_c is given by

$$t_c = \frac{1}{5.38\kappa} \left[\frac{2\nu\kappa Ra_{y_T,cr}}{\alpha g(T_1 - T_0)} \right]^{2/3} \quad (8.6.5)$$

The mean heat flow \bar{q} across the layer in the time t_c is, from (4.1.23),

$$\bar{q} = \frac{2k(T_c - T_0)}{(\pi\kappa t_c)^{1/2}} = \frac{k(T_1 - T_0)}{(\pi\kappa t_c)^{1/2}} \quad (8.6.6)$$

The factor of 2 on the right side of (8.6.6) occurs because it is necessary to integrate (4.1.23) to give mean surface heat flow. The combination of (8.6.5) and (8.6.6) gives

$$\bar{q} = 1.31k(T_1 - T_0) \left[\frac{\alpha g(T_1 - T_0)}{2\nu\kappa Ra_{y_T,cr}} \right]^{1/3} \quad (8.6.7)$$

The nondimensional measure of the heat flux across the layer is the Nusselt number Nu introduced in (8.3.18); with (8.6.7) we obtain

$$Nu = \frac{\bar{q}b}{k(T_1 - T_0)} = 1.04 \left(\frac{Ra}{Ra_{y_T,cr}} \right)^{1/3} = 1.04r^{1/3} \quad (8.6.8)$$

where Ra is the Rayleigh number based on the layer thickness and $r = Ra/Ra_{y_T,cr}$. We find that the Nusselt number is proportional to the Rayleigh number to the one-third power. For $Ra_{y_T,cr} = 807$ we obtain

$$Nu = 0.112 Ra^{1/3} \quad (8.6.9)$$

This result will be compared with results from other approximate methods and from experiments later in this chapter.

The boundary layer stability criterion can also be applied to the case in which the mean heat flow across the layer is given. In this case the heat flow \bar{q} in (8.6.7) is specified and the required temperature difference $T_1 - T_0$ is determined. A nondimensional measure of the temperature difference across the layer is the ratio Θ of the temperature difference with convection to the temperature difference without convection; from (8.6.7) we obtain

$$\Theta = \frac{k(T_1 - T_0)}{b\bar{q}} = 0.971 \left(\frac{Ra_{y_T,cr}}{Ra_{\bar{q}}} \right)^{1/4} = 0.971 r_{\bar{q}}^{-1/4} \quad (8.6.10)$$

where, in accordance with (7.3.37),

$$Ra_{\bar{q}} = \frac{\alpha g \bar{q} b^4}{\kappa \nu} \quad (8.6.11)$$

is the Rayleigh number based on the layer thickness b and the mean heat flux \bar{q} and $r_{\bar{q}} = Ra_{\bar{q}}/Ra_{y_T,cr}$. The nondimensional temperature Θ is inversely proportional to the Rayleigh number $Ra_{\bar{q}}$ to the one-quarter power. For $Ra_{y_T,cr} = 807$, we find

$$\Theta = 5.18 Ra_{\bar{q}}^{-1/4} \quad (8.6.12)$$

As a final example of a boundary layer stability analysis we consider a fluid layer heated from within. In this case there is only one thermal boundary layer on the upper boundary and the isothermal interior or core temperature is T_1 . The stability criterion for this single boundary layer is

$$Ra_{y_T,cr} = \frac{\alpha g (T_1 - T_0) y_{T,cr}^3}{\kappa \nu} \quad (8.6.13)$$

From (8.6.3) and (8.6.13), the time at which boundary layer breakup occurs t_c is given by

$$t_c = \frac{1}{5.38\kappa} \left[\frac{\nu \kappa Ra_{y_T,cr}}{\alpha g (T_1 - T_0)} \right]^{2/3} \quad (8.6.14)$$

The mean heat flow out of the upper boundary is, from (8.6.6),

$$\bar{q} = \frac{2k(T_1 - T_0)}{(\pi \kappa t_c)^{1/2}} \quad (8.6.15)$$

The substitution of (8.6.14) into (8.6.15) gives

$$\bar{q} = 2.61k(T_1 - T_0) \left[\frac{\alpha g (T_1 - T_0)}{\nu \kappa Ra_{y_T,cr}} \right]^{1/3} \quad (8.6.16)$$

The mean heat flow out of the upper boundary \bar{q} is related to the heat generation rate per unit mass in the layer H by

$$\bar{q} = \rho H b \quad (8.6.17)$$

The temperature difference across the single boundary layer $T_1 - T_0$ is obtained from (8.6.16) and (8.6.17) with the result

$$T_1 - T_0 = \left(\frac{\rho H b}{2.61k} \right)^{3/4} \left(\frac{\nu \kappa Ra_{y_T,cr}}{\alpha g} \right)^{1/4} \quad (8.6.18)$$

With the introduction of the characteristic temperature for a fluid layer heated from within given by (7.5.1), the nondimensional core temperature from (8.6.18) is given by

$$\Theta = \frac{k(T_1 - T_0)}{\rho H b^2} = 0.487 \left(\frac{Ra_{y_T,cr}}{Ra_H} \right)^{1/4} = 0.487 r^{-1/4} \quad (8.6.19)$$

where the Rayleigh number for a fluid layer heated from within Ra_H has been defined in (7.5.6). Again, for $Ra_{y_T,cr} = 807$ we find

$$\Theta = 2.60 Ra_H^{-1/4} \quad (8.6.20)$$

We have now obtained solutions using the boundary layer stability analysis for three thermal convection problems. For a fluid layer with prescribed boundary temperatures we have parameterized the heat flow across the layer (the Nusselt number) in terms of the Rayleigh number. For fluid layers with either a specified heat flux or specified internal heating rate we have parameterized the temperature difference across the layer in terms of the Rayleigh number.

In the next section we will obtain similar parameterizations using an alternative boundary layer model. The results for the two methods will be compared with each other and with numerical calculations. In Chapters 13 and 14 parameterized thermal convection will be used to study the thermal evolution of the Earth and the planets.

In terms of thermal convection within the planets, the analysis presented in this section would be analogous to episodic subduction events. We will see in Chapter 14 that episodic subduction on Venus has been proposed as the mechanism for heat loss from the interior of that planet.

8.6.2 Boundary Layer Analysis of Cellular Convection

We will now develop a boundary layer analysis of steady cellular thermal convection (Turcotte and Oxburgh, 1967; Roberts, 1979; Olson and Corcos, 1980; Mitrovica and Jarvis, 1987). We will limit our considerations to very large Prandtl numbers so that the inertia terms in the momentum equations can be neglected. Again we consider a fluid layer of thickness b heated from below and cooled from above. The upper boundary is maintained at a temperature T_0 and the lower boundary at a temperature T_1 . The boundary layer structure and

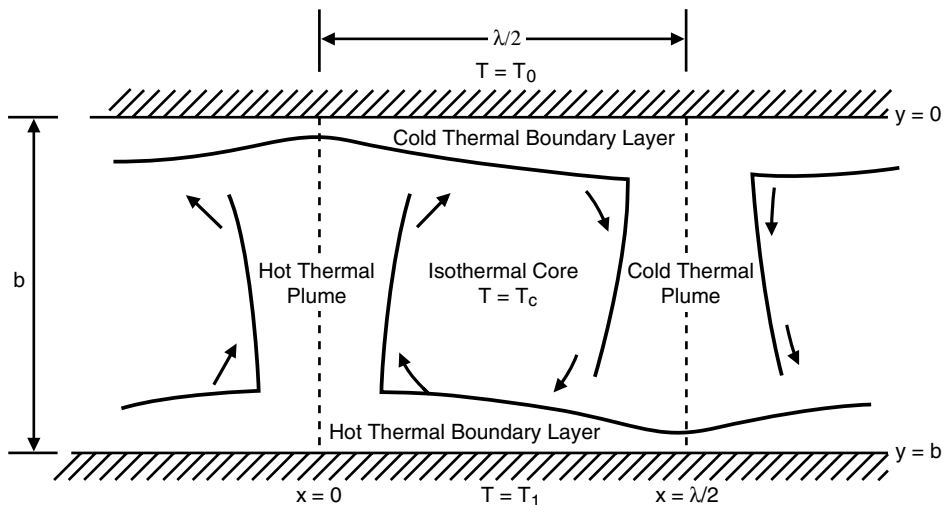


Figure 8.12. Boundary layer structure of two-dimensional thermal convection cells in a fluid layer heated from below.

coordinates are illustrated in Figure 8.12. The flow is divided into cellular two-dimensional rolls of width $\lambda/2$; alternate rolls rotate in opposite directions. We assume that the width of a cell corresponds to the linear stability value given by (7.3.30) and take $\lambda = 8^{1/2}b$. The entire flow field is highly viscous. On the cold upper boundary a thin cold thermal boundary layer forms. When the two cold boundary layers of adjacent cells meet, they separate from the boundary and form a cold descending sheet (plume). Similarly, a hot thermal boundary layer forms on the lower boundary of the cell. When two hot boundary layers from adjacent cells meet, they form a hot ascending sheet (plume). The buoyancy forces in the ascending and descending sheets drive the flow. The core or interior of each cell is nearly isothermal.

There are striking similarities and important differences between this simple model and mantle convection. To a good approximation the cold thermal boundary layers are the lithospheric plates of plate tectonics. The boundaries between cells where hot material ascends and the cold thermal boundary layers form are analogous to mid-ocean ridges. The boundaries between cells where the cold boundary layers meet, separate from the boundary, and form cold descending sheets are analogous to subduction zones. An important difference between the model and the mantle is that subduction in the simple boundary layer model is symmetric while subduction in the Earth is invariably asymmetric. The hot ascending sheets formed from the hot lower thermal boundary layers are two-dimensional analogues of the nearly axisymmetric mantle plumes associated with hot spots such as Hawaii and Iceland. In the model, the ascending sheets lie immediately below the zones of divergent surface flow. In the Earth, this is sometimes the case, e.g., Iceland and the Azores, but often it is not, e.g., Hawaii. The ascending sheets of the two-dimensional boundary layer model are not analogues of the shallow, passive, sheet-like upflow that occurs beneath mid-ocean ridges in the mantle. Instead, as just noted, they must be regarded as analogues of the active forms of upflow in the deep mantle, i.e., the approximately axisymmetric plumes. Two-dimensional models are not very good analogues of some of the morphological elements of fully three-dimensional mantle convection. In particular, the active upflow sheets of the

two-dimensional boundary layer model are not like the active upflow quasi-axisymmetric plumes of the mantle or of three-dimensional convection. Finally, in the model, strong temperature gradients are restricted to horizontal thermal boundary layers and vertical ascending and descending structures as is also likely the case for the Earth's mantle.

The two-dimensional boundary layer model can be quantified. Although an exact solution for the boundary layer model requires numerical methods, we can obtain an analytic solution by making a number of approximations. We first obtain the structure of the cold thermal boundary layer adjacent to the upper cooled boundary. The coordinate y is measured downward from this boundary and the coordinate x is measured horizontally from the point of diverging flows as illustrated in Figure 8.12. We assume that the horizontal velocity boundary condition at $y = 0$ is $u = \text{constant} = u_0$. For a fluid with free-surface boundary conditions the horizontal velocity would be zero at $x = 0, \lambda/2$ and a maximum near $x = \lambda/4$. But our assumption of constant velocity is a good approximation for mantle convection since the rigidity of the lithosphere results in a near-constant surface velocity.

Again, we assume symmetry between the cold thermal boundary layer adjacent to the upper boundary of the cell and the hot thermal boundary layer adjacent to the lower boundary so that the temperature of the isothermal core of the cell is given by (8.6.1). The thermal structure of the cold thermal boundary layer has been found in Section 4.2. The temperature distribution in the cold thermal boundary layer can be obtained from (4.2.4) with the result

$$\frac{T_c - T}{T_c - T_0} = \operatorname{erfc} \left[\frac{y}{2} \left(\frac{u_0}{\kappa x} \right)^{1/2} \right] \quad (8.6.21)$$

where t in (4.2.4) has been identified with x/u_0 . By symmetry this result can also be used to give the temperature in the hot thermal boundary layer.

The surface heat flow from (4.2.5) is given by

$$q_s = k(T_c - T_0) \left(\frac{u_0}{\pi \kappa x} \right)^{1/2} \quad (8.6.22)$$

Over the width of the cell $0 < x < 2^{1/2}b$, the total heat flow Q is

$$Q = \int_0^{2^{1/2}b} q dx = 2k(T_c - T_0) \left(\frac{2^{1/2}bu_0}{\pi \kappa} \right)^{1/2} \quad (8.6.23)$$

It is necessary to determine u_0 before the actual flux across a convecting layer can be determined.

At the boundary between two cells where the flows converge, the cold thermal boundary layers from two adjacent cells turn through 90° to form a cold, symmetric descending thermal sheet. Since little heat conduction will occur during the transition from a downflow thermal boundary layer to a downflow thermal sheet, the distribution of temperature in the newly formed sheet is the same as in the boundary layer. As in the case of the horizontal velocity in the cold boundary layer, we assume that the vertical velocity v in the cold descending sheet is a constant equal to v_0 . However the velocity v_0 may differ from the velocity u_0 . Since the heat convected by the descending sheet just after its formation must equal the heat convected by the cold thermal boundary layer just before formation of the sheet, the thickness of the plume relative to the boundary layer must be in the ratio u_0/v_0 . Therefore, the temperature distribution in the plume just as it is formed is given by

$$\frac{T_c - T}{T_c - T_0} = \operatorname{erfc} \left[\frac{v_0}{2u_0} \left(\frac{2^{1/2}b}{2} - x \right) \left(\frac{2u_0}{2^{1/2}b\kappa} \right)^{1/2} \right] \quad (8.6.24)$$

with a similar expression for the other half of the symmetrical sheet formed from the adjacent cell.

As the cold sheet descends it broadens and its minimum temperature decreases, but its heat content remains the same. Thus, the negative buoyancy of the plume also remains the same and it can be determined from the initial temperature. The downward buoyancy force on the cold plume is given by

$$F_b = 2\rho_0 g \alpha b \int_{\lambda/2}^{-\infty} (T_c - T) dx \quad (8.6.25)$$

This is the total force per unit depth on the cold downflow sheet. It is appropriate to replace the integral across the finite width of the sheet with the infinite integral since $T \rightarrow T_c$ at the edge of the sheet. Substitution of (8.6.24) into (8.6.25) and integration with $x' = b/2^{1/2} - x$ gives

$$\begin{aligned} F_b &= 2\rho_0 g \alpha (T_c - T_0) b \int_0^{\infty} \operatorname{erfc} \left\{ \frac{v_0 x'}{2u_0} \left(\frac{u_0}{2^{1/2} b \kappa} \right)^{1/2} \right\} dx' \\ &= 4\rho_0 g \alpha (T_c - T_0) b \frac{u_0}{v_0} \left(\frac{2^{1/2} b \kappa}{u_0} \right)^{1/2} \int_0^{\infty} \operatorname{erfc} z dz \\ &= 4\rho_0 g \alpha (T_c - T_0) b \frac{u_0}{v_0} \left(\frac{2^{1/2} b \kappa}{\pi u_0} \right)^{1/2} \end{aligned} \quad (8.6.26)$$

Since the problem is entirely symmetrical, the lower hot thermal boundary layer and hot upflow sheet are identical to their cold counterparts when $T_c - T_0$ is replaced by $T_c - T_1$. The total upward buoyancy force on the hot ascending sheet is equal to the downward force on the cold sheet.

Determination of the viscous flow in the isothermal core requires a solution of the biharmonic equation. However, an analytic solution cannot be obtained for the boundary conditions of this problem. Therefore, we approximate the core flow with the linear velocity profiles shown in Figure 8.13, i.e., we take

$$u = u_0 \left(1 - 2 \frac{y}{b} \right) \quad (8.6.27)$$

$$v = -v_0 \left(1 - 2^{1/2} \frac{x}{b} \right) \quad (8.6.28)$$

In order to conserve fluid we require

$$2^{1/2} v_0 = u_0 \quad (8.6.29)$$

The velocity distribution given in (8.6.27) and (8.6.28) can be derived from the stream function

$$\psi = u_0 \left[y \left(\frac{y}{b} - 1 \right) + x \left(\frac{x}{2b} - \frac{1}{2^{1/2}} \right) \right] \quad (8.6.30)$$

Thus this flow satisfies the biharmonic equation. However, it must be emphasized that the flow does not satisfy the required boundary conditions. For example, the condition $v = 0$ at $y = 0, b$ is not satisfied. Nevertheless, the assumed profiles are reasonable approximations to the actual flow near the center of the cell.

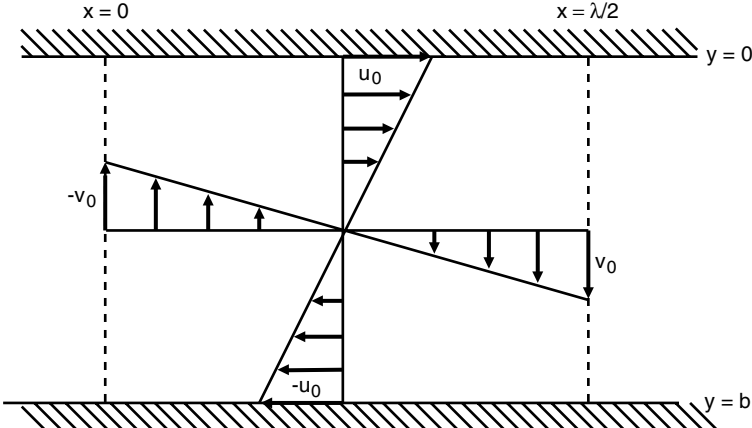


Figure 8.13. Linear velocity profiles used to model the core flow in a convection cell. The areas under the triangles are equal to conserve fluid.

The shear stress τ_v on the vertical boundaries of the core flow is given by

$$\tau_v = \mu \frac{\partial v}{\partial x} = \frac{2^{1/2} v_0 \mu}{b} = \frac{u_0 \mu}{b} \quad (8.6.31)$$

and the shear stress τ_h on the horizontal boundaries is given by

$$\tau_h = \mu \frac{\partial u}{\partial y} = \frac{2 u_0 \mu}{b} \quad (8.6.32)$$

The rate at which work is done on each vertical boundary by the shear stress is $b\tau_v v_0$ and the rate at which work is done on each horizontal boundary is $2^{1/2} b\tau_h u_0$. The rate at which the buoyancy force does work on each plume is $F_b v_0$. The rate at which work is done on the vertical sheets by the gravitational body force must equal the rate at which work is done on the boundaries by the shear stresses, with the result

$$F_b v_0 = 2b\tau_v v_0 + 2^{3/2} b\tau_h u_0 \quad (8.6.33)$$

Substitution of (8.6.29), (8.6.31), and (8.6.32) reduces this to

$$F_b = 10\mu u_0 \quad (8.6.34)$$

Further substitution of (8.6.26) into (8.6.34) gives

$$u_0 = \frac{\kappa}{b} \frac{2^{1/2}}{5^{2/3} \pi^{1/3}} Ra^{2/3} = 0.330 \frac{\kappa}{b} Ra^{2/3} \quad (8.6.35)$$

where the Rayleigh number for a fluid layer heated from below (7.3.22) has been introduced.

With the mean velocity along the upper boundary of the cell now determined, the total heat flux through the cell can be found from (8.6.23), which gives

$$Q = k(T_1 - T_0) \frac{2^{1/2}}{5^{1/3} \pi^{2/3}} Ra^{1/3} = 0.386 k(T_1 - T_0) Ra^{1/3} \quad (8.6.36)$$

The heat flux across the layer by conduction in the absence of convection is given by

$$Q_c = 2^{1/2}k(T_1 - T_0) \quad (8.6.37)$$

The Nusselt number is the ratio of (8.6.36) to (8.6.37) or

$$Nu = \frac{Q}{Q_c} = 0.273 Ra^{1/3} \quad (8.6.38)$$

This result can be written in terms of $r = Ra/Ra_{cr}$ using the applicable value of the critical Rayleigh number $Ra_{cr} = 657$:

$$Nu = 2.37r^{1/3} \quad (8.6.39)$$

These results, (8.6.38) and (8.6.39), can be compared with the results obtained using the boundary layer stability analysis given in (8.6.8) and (8.6.9). The two approaches give the same power-law dependence of Nusselt number on Rayleigh number. However the coefficients differ by about a factor of 2.5.

Extensive numerical studies of two-dimensional thermal convection in a fluid layer heated from below have been carried out by Moore and Weiss (1973) (see Chapter 9). Their results correlate well with the power-law relation

$$Nu = 2.24r^{0.318} \quad (8.6.40)$$

This numerical result is in quite good agreement with the boundary layer result given in (8.6.39). For $r = 100$, the boundary layer analysis (8.6.39) gives $Nu = 11.0$ and the numerical solution (8.6.40) gives $Nu = 9.69$. Considering the many approximations that have been made, this agreement is quite good.

The boundary layer analysis can also be applied if the mean heat flux \bar{q} across the layer is prescribed. The Rayleigh number based on \bar{q} , $Ra_{\bar{q}}$, is defined in (7.3.37). The mean heat flux \bar{q} is given by

$$\bar{q} = \frac{1}{b\sqrt{2}} \int_0^{b\sqrt{2}} q_s(x) dx \quad (8.6.41)$$

Substitution of (8.6.22) into (8.6.41) yields

$$\bar{q} = 2k(T_c - T_0) \left(\frac{u_0}{2^{1/2}b\pi\kappa} \right)^{1/2} \quad (8.6.42)$$

Elimination of $(T_c - T_0)$ between (8.6.26) and (8.6.42) and use of (8.6.29) give

$$F_b = \frac{4\rho_0 g \alpha \bar{q} b^2 \kappa}{k u_0} \quad (8.6.43)$$

Elimination of F_b from (8.6.34) and (8.6.43) yields

$$u_0 = \frac{\kappa}{b} \left(\frac{2}{5} \right)^{1/2} Ra_{\bar{q}}^{1/2} = 0.632 \frac{\kappa}{b} Ra_{\bar{q}}^{1/2} \quad (8.6.44)$$

where $Ra_{\bar{q}}$ has been defined in (7.3.37). Substitution of (8.6.44) into (8.6.42) and use of $T_1 - T_0 = 2(T_c - T_0)$ give the temperature difference across the layer

$$T_1 - T_0 = \frac{\bar{q}b}{k} 5^{1/4} \pi^{1/2} Ra_{\bar{q}}^{-1/4} = \frac{\bar{q}b}{k} 2.65 Ra_{\bar{q}}^{-1/4} \quad (8.6.45)$$

The temperature difference decreases as the Rayleigh number gets larger. Introduction of the nondimensional temperature Θ as in (8.6.10) and use of $r = Ra_{\bar{q}}/Ra_{\bar{q},cr}$ with $Ra_{\bar{q},cr} = 807$ give

$$\Theta = 2.65 Ra_{\bar{q}}^{-1/4} = 0.50 r_{\bar{q}}^{-1/4} \quad (8.6.46)$$

Again, these results can be compared with the results of the boundary layer stability analysis in (8.6.10) and (8.6.12). The same power-law dependence is found, i.e., $\Theta \sim Ra_{\bar{q}}^{-1/4}$, but the coefficient differs by about a factor of 2.

We now apply this boundary layer analysis to layered mantle convection. In Section 7.3 we concluded that the applicable Rayleigh number is $Ra_{\bar{q}} = 4.8 \times 10^6$. With $\kappa = 1 \text{ mm}^2 \text{s}^{-1}$ and $b = 700 \text{ km}$ we find from (8.6.44) that $u_0 = 1.8 \times 10^{-9} \text{ m s}^{-1}$ (57 mm yr^{-1}), which is quite close to the mean velocity of the surface plates. With $\bar{q} = 60.6 \text{ mW m}^{-2}$ and $k = 4 \text{ W m}^{-1} \text{ K}^{-1}$, we find from (8.6.45) that $T_1 - T_0 = 630 \text{ K}$. This is about one-half the expected value.

Boundary layer theory can also be applied to a fluid layer that is heated from within and cooled from above. Again, the flow is divided into counterrotating two-dimensional cells with dimensions b and $1.75b$ based on the linear stability analysis with shear stress-free boundary conditions ($\lambda_{cr}^* = 3.51$, Section 7.5). A cold thermal boundary layer forms on the upper boundary of each cell. When the two cold boundary layers from adjacent cells meet, they separate from the upper boundary to form a cold descending sheet. For the fluid layer heated from within there is no heat flux through the lower boundary and no hot boundary layers or upflow sheets develop. The problem is illustrated in Figure 8.14.

The heat flow out of the upper boundary layer is given by (8.6.23) modified for the appropriate aspect ratio. The total heat production in the cell (per unit width) is $1.75\rho H b^2$. Since we assume a steady-state heat balance we can write, using (8.6.23),

$$1.75\rho H b^2 = 2k(T_c - T_0) \left(\frac{1.75u_0b}{\pi\kappa} \right)^{1/2} \quad (8.6.47)$$

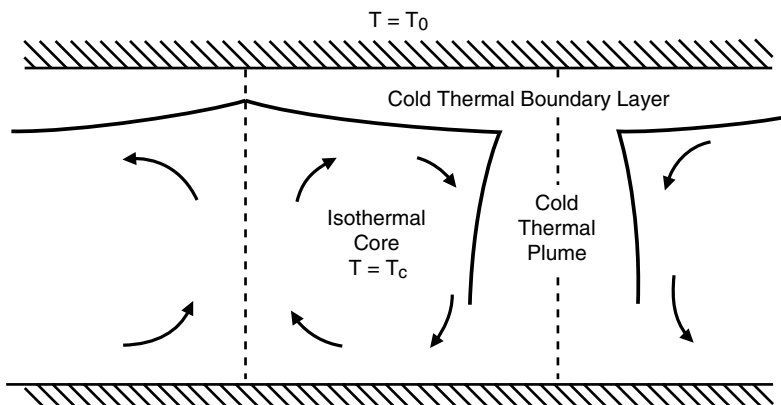


Figure 8.14. The boundary layer structure of two-dimensional thermal convection cells in a fluid layer heated from within and cooled from above.

In this case there is only one-half of a single cold downflow sheet associated with each convection cell. Thus we replace (8.6.33) with

$$\frac{1}{2}F_b v_0 = 2b\tau_v v_0 + 3.5b\tau_h u_0 \quad (8.6.48)$$

In addition, we require

$$1.75v_0 = u_0 \quad (8.6.49)$$

in place of (8.6.29) and

$$\tau_v = \frac{2v_0\mu}{1.75b} = \frac{2u_0\mu}{1.75^2 b} \quad (8.6.50)$$

in place of (8.6.31). Substitution of (8.6.32), (8.6.49), and (8.6.50) into (8.6.48) gives

$$F_b = 27.1u_0\mu \quad (8.6.51)$$

For this problem the buoyancy force on a descending sheet is given by

$$F_b = 4\rho_0 g \alpha (T_c - T_0) 1.75b \left(\frac{1.75b\kappa}{\pi u_0} \right)^{1/2} \quad (8.6.52)$$

in place of (8.6.26). The combination of (8.6.47), (8.6.51), and (8.6.52) gives

$$u_0 = 0.475 \frac{\kappa}{b} Ra_H^{1/2} \quad (8.6.53)$$

where Ra_H has been defined in (7.5.6). Substitution of (8.6.53) into (8.6.47) gives the core or interior temperature

$$T_c - T_0 = 1.70 \frac{\rho H b^2}{k} Ra_H^{-1/4} \quad (8.6.54)$$

The core temperature decreases with increasing Rayleigh number. With the introduction of the nondimensional temperature, as in (8.6.19), and $r_H = Ra_H/Ra_{H,cr}$ with $Ra_{H,cr} = 868$, we obtain

$$\Theta = \frac{k(T_c - T_0)}{\rho H b^2} = 1.70 Ra_H^{-1/4} = 0.31 r_H^{-1/4} \quad (8.6.55)$$

This result can be compared with the boundary layer stability analysis given in (8.6.20). The same power-law dependence is found, $\Theta \sim Ra_H^{-1/4}$, but the coefficient differs by about a factor of 1.5.

We now apply this boundary layer analysis to whole mantle convection. In Section 7.5 we concluded that the Rayleigh number based on internal heat generation for whole mantle convection is $Ra_H = 3 \times 10^9$. With $\kappa = 1 \text{ mm}^2 \text{ s}^{-1}$ and $b = 2,900 \text{ km}$, we find from (8.6.53) that $u_0 = 9 \times 10^{-9} \text{ m s}^{-1}$ (250 mm yr^{-1}), which is about 4 times larger than the value deduced above for layered mantle convection and is also about the same factor larger than observations. With $\rho = 4.6 \times 10^3 \text{ kg m}^{-3}$, $H = 9.23 \times 10^{-12} \text{ W kg}^{-1}$, and $k = 4 \text{ W m}^{-1} \text{ K}^{-1}$, we find from (8.6.54) that $T_c - T_0 = 650 \text{ K}$. Again, this is about one-half the expected value.

The boundary layer methods introduced in this section approximate the thermal boundary layer structure of finite-amplitude thermal convection. The general structure of a thermal boundary layer that thickens in time and space and then becomes gravitationally unstable forming descending sheets closely resembles the creation and subduction of the oceanic lithosphere in plate tectonics. Morris and Canright (1984) have given a boundary layer analysis for a fluid layer with a strongly temperature dependent viscosity.

8.7 Single-mode Mean Field Approximation

Another approximate method for solving the equations of thermal convection is the single-mode mean field theory. In this approach, pioneered by Herring (1963, 1964) and Roberts (1965b), the horizontal structure of convection is coarsely represented by a single mode, e.g. a trigonometric function of specified wavelength in two-dimensional flow, while the vertical structure of convection is determined more accurately by solving approximate forms of the momentum and energy equations. The Lorenz equations, like the mean field equations, also use a single mode to represent the horizontal structure of convection. However, unlike the mean field equations, which allow a ‘complete’ representation of the vertical structure of convection, the Lorenz equations represent the vertical structure with only two eigenmodes, (8.3.1) and (8.3.2).

In order to illustrate the single-mode mean field approach we again consider the steady two-dimensional convection of a Boussinesq fluid in a layer heated from below. The relevant nondimensional equations are (6.10.44), (6.10.46), and (6.10.48), which we write for steady convection with infinite Prandtl number and constant fluid properties as

$$\frac{\partial u^*}{\partial x^*} + \frac{\partial v^*}{\partial y^*} = 0 \quad (8.7.1)$$

$$0 = -\frac{\partial p^*}{\partial x^*} + \left(\frac{\partial^2}{\partial x^{*2}} + \frac{\partial^2}{\partial y^{*2}} \right) u^* \quad (8.7.2)$$

$$0 = -\frac{\partial p^*}{\partial y^*} - T^* Ra + \left(\frac{\partial^2}{\partial x^{*2}} + \frac{\partial^2}{\partial y^{*2}} \right) v^* \quad (8.7.3)$$

$$u^* \frac{\partial T^*}{\partial x^*} + v^* \frac{\partial T^*}{\partial y^*} = \left(\frac{\partial^2}{\partial x^{*2}} + \frac{\partial^2}{\partial y^{*2}} \right) T^* \quad (8.7.4)$$

and the y -coordinate points downward. We represent the temperature field as the sum of a horizontally averaged part (T^*) and a horizontally variable part $T^{*'}:$

$$T^* = \langle T^* \rangle(y^*) + T^{*'}(x^*, y^*) \quad (8.7.5)$$

with $\langle T^{*'} \rangle = 0$. The velocity components are assumed to be horizontally varying with zero horizontal average $\langle u^* \rangle = 0$. We eliminate the pressure by taking the curl of (8.7.2) and (8.7.3) with the result

$$0 = Ra \frac{\partial T^*}{\partial x^*} + \left(\frac{\partial^2}{\partial x^{*2}} + \frac{\partial^2}{\partial y^{*2}} \right) \left(\frac{\partial u^*}{\partial y^*} - \frac{\partial v^*}{\partial x^*} \right) \quad (8.7.6)$$

(see also (6.11.1) and (6.11.2) for $\mu = \text{constant}$). The horizontal averages of (8.7.1) and (8.7.6) provide no information. The horizontal average of the energy equation (8.7.4) is

$$\left\langle u^* \frac{\partial T^{*'}}{\partial x^*} + v^* \frac{\partial T^{*'}}{\partial y^*} \right\rangle = \left(\frac{\partial^2}{\partial x^{*2}} + \frac{\partial^2}{\partial y^{*2}} \right) \langle T^* \rangle \quad (8.7.7)$$

Subtraction of (8.7.7) from (8.7.4) gives

$$\begin{aligned} u^* \frac{\partial T^{*'}}{\partial x^*} + v^* \frac{\partial T^{*'}}{\partial y^*} - \left\langle u^* \frac{\partial T^{*'}}{\partial x^*} + v^* \frac{\partial T^{*'}}{\partial y^*} \right\rangle &+ \left(u^* \frac{\partial}{\partial x^*} + v^* \frac{\partial}{\partial y^*} \right) \langle T^* \rangle \\ &= \left(\frac{\partial^2}{\partial x^{*2}} + \frac{\partial^2}{\partial y^{*2}} \right) T^{*'} \end{aligned} \quad (8.7.8)$$

The standard procedure in mean field theory is to make the so-called “weak coupling” approximation by assuming

$$\left(u^* \frac{\partial}{\partial x^*} + v^* \frac{\partial}{\partial y^*} \right) T^{*'} = \left\langle u^* \frac{\partial T^{*'}}{\partial x^*} + v^* \frac{\partial T^{*'}}{\partial y^*} \right\rangle \quad (8.7.9)$$

With this assumption (8.7.8) becomes

$$\left(u^* \frac{\partial}{\partial x^*} + v^* \frac{\partial}{\partial y^*} \right) \langle T^* \rangle = \left(\frac{\partial^2}{\partial x^{*2}} + \frac{\partial^2}{\partial y^{*2}} \right) T^{*'} \quad (8.7.10)$$

The unknowns in the single-mode mean field theory are $u^*(x^*, y^*)$, $v^*(x^*, y^*)$, $\langle T^* \rangle(y^*)$, and $T^{*'}(x^*, y^*)$. The equations are (8.7.1), (8.7.6), (8.7.7), and (8.7.10).

Exact analyses of thermal convection show that the “weak coupling” approximation is not completely justifiable. It leads to a simplified system of equations within what is already a nonrigorous approximation (the single-mode mean field theory) of the full equations of convection. Its effect is to smear large temperature gradients such as those associated with thermal plumes and to isolate the top and bottom thermal boundary layers (Olson, 1981).

We represent the horizontal variations in temperature and velocity with trigonometric functions and take

$$T^{*'}(x^*, y^*) = \hat{T}^*(y^*) \sin \left(\frac{2\pi x^*}{\lambda^*} \right) \quad (8.7.11)$$

$$u^*(x^*, y^*) = \hat{u}^*(y^*) \cos \left(\frac{2\pi x^*}{\lambda^*} \right) \quad (8.7.12)$$

$$v^*(x^*, y^*) = \hat{v}^*(y^*) \sin \left(\frac{2\pi x^*}{\lambda^*} \right) \quad (8.7.13)$$

Substitution into (8.7.1), (8.7.6), (8.7.7), and (8.7.10) yields

$$\hat{u}^* = \frac{\lambda^*}{2\pi} \frac{d\hat{v}^*}{dy^*} \quad (8.7.14)$$

$$\hat{v}^* \frac{d\langle T^* \rangle}{dy^*} = \frac{d^2 \hat{T}^*}{dy^{*2}} - \hat{T}^* \left(\frac{2\pi}{\lambda^*} \right)^2 \quad (8.7.15)$$

$$0 = Ra \left(\frac{2\pi}{\lambda^*} \right) \hat{T}^* + \left\{ \frac{d^2}{dy^{*2}} - \left(\frac{2\pi}{\lambda^*} \right)^2 \right\} \left\{ \hat{v}^* \left(\frac{2\pi}{\lambda^*} \right) - \frac{d\hat{u}^*}{dy^*} \right\} \quad (8.7.16)$$

$$\frac{2\pi \hat{u}^* \hat{T}^*}{\lambda^*} + \hat{v}^* \frac{d\hat{T}^*}{dy^*} = 2 \frac{d^2 \langle T^* \rangle}{dy^{*2}} \quad (8.7.17)$$

The horizontal velocity \hat{u}^* can be eliminated from the system of equations by substituting (8.7.14) into (8.7.16) and (8.7.17) with the result

$$0 = Ra \hat{T}^* + \left\{ \frac{d^2}{dy^{*2}} - \left(\frac{2\pi}{\lambda^*} \right)^2 \right\} \left\{ \hat{v}^* - \left(\frac{\lambda^*}{2\pi} \right)^2 \frac{d^2 \hat{v}^*}{dy^{*2}} \right\} \quad (8.7.18)$$

$$\frac{d}{dy^*} \left\{ \hat{v}^* \hat{T}^* \right\} = 2 \frac{d^2 \langle T^* \rangle}{dy^{*2}} \quad (8.7.19)$$

Equation (8.7.18) can be integrated to give (after multiplication by \hat{v}^*)

$$\hat{v}^* \frac{d\langle T^* \rangle}{dy^*} = \frac{1}{2} \hat{v}^{*2} \hat{T}^* - c_1 \hat{v}^* \quad (8.7.20)$$

where c_1 is a constant of integration whose value is determined from the boundary conditions. The right sides of (8.7.15) and (8.7.20) can be equated to give

$$\frac{1}{2} \hat{v}^{*2} \hat{T}^* - c_1 \hat{v}^* = \frac{d^2 \hat{T}^*}{dy^{*2}} - \hat{T}^* \left(\frac{2\pi}{\lambda^*} \right)^2 \quad (8.7.21)$$

Equations (8.7.18) and (8.7.21) constitute two ordinary differential equations in the two unknowns \hat{T}^* and \hat{v}^* . Equation (8.7.21) is nonlinear and a numerical integration of the equations subject to appropriate boundary conditions is required.

Figure 8.15 shows solutions of (8.7.18), (8.7.20), and (8.7.21) obtained by Quarenii and Yuen (1984) for the case of isothermal, impermeable and stress-free boundaries for which

$$\hat{v}^* = \frac{d^2 \hat{v}^*}{dy^{*2}} = \hat{T}^* = 0 \quad \text{on } y^* = 0, 1 \quad (8.7.22)$$

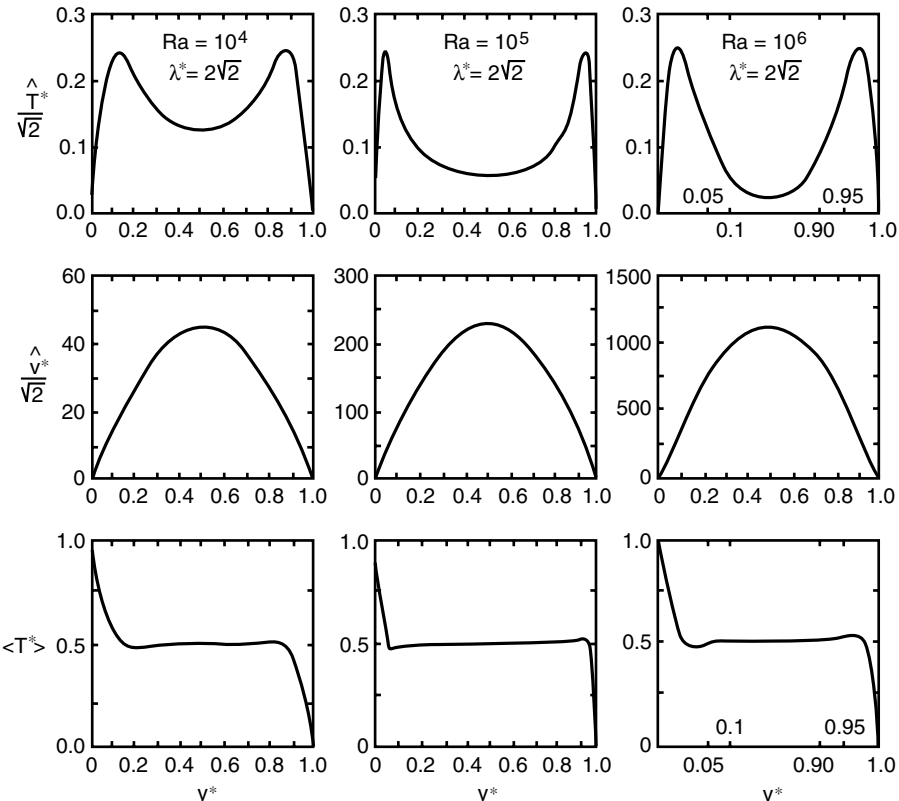


Figure 8.15. The amplitude of the horizontally varying part of the temperature, the amplitude of the horizontally varying vertical velocity, and the horizontally averaged part of the temperature as a function of y^* from a solution of the single-mode mean field equations (Quarenii and Yuen, 1984) for isothermal, impermeable, and stress-free boundaries at $Ra = 10^4$, 10^5 , and 10^6 .

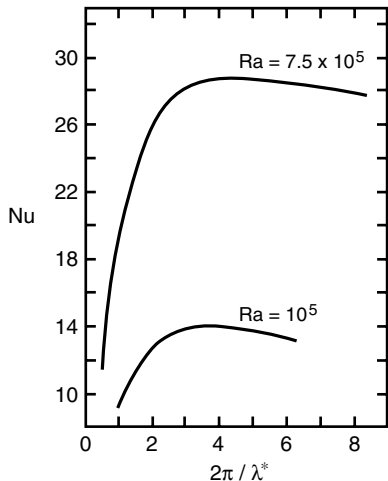


Figure 8.16. Nusselt number versus horizontal wavelength for solutions similar to those shown in Figure 8.15 and for $Ra = 10^5$ and $Ra = 7.5 \times 10^5$ (after Quarenii and Yuen, 1984).

In addition, the horizontally averaged temperature satisfies

$$\langle T^* \rangle = 1 \quad \text{on } y^* = 0 \quad \text{and} \quad \langle T^* \rangle = 0 \quad \text{on } y^* = 1 \quad (8.7.23)$$

The solutions are for $Ra = 10^4, 10^5, 10^6$ and for $\lambda^* = 2\sqrt{2}$ corresponding to two-dimensional convective rolls with aspect ratio $\sqrt{2}$. Thermal boundary layers are prominent in the solutions for \hat{T}^* and $\langle T^* \rangle$; the boundary layers thin with increasing Ra (note the scale change for $Ra = 10^6$). An isothermal “core” is apparent in the plot of horizontally averaged temperature.

The Nusselt number Nu for solutions similar to those shown in Figure 8.15 is seen in Figure 8.16 to depend on the wavelength of the convective cells. The horizontally averaged heat transfer at a given Ra maximizes at a particular value of λ^* . For $Ra \geq 10^4$ the maximum Nu is found to be proportional to $Ra^{0.36}$ (Quarenii and Yuen, 1984), in good agreement with results from asymptotic analyses and numerical solutions to the complete equations.

Single-mode mean field theory can also be applied to the study of convection in spherical shells (Olson, 1981). The nondimensional equations for an infinite Prandtl number, Boussinesq fluid with constant properties are (8.7.1)–(8.7.4), written in vector form to facilitate application to spherical geometry

$$\nabla^* \cdot \underline{u}^* = 0 \quad (8.7.24)$$

$$0 = -\nabla^* p^* + \hat{r}^* T^* Ra + \nabla^{*2} \underline{u}^* \quad (8.7.25)$$

$$\underline{u}^* \cdot \nabla^* T^* = \nabla^{*2} T^* \quad (8.7.26)$$

where \hat{r}^* is the unit vector in the radial direction and the length scale in the definition of the Rayleigh number is taken as the outer radius of the spherical shell. By analogy to (8.7.5) we write

$$T^* = \langle T^* \rangle(r^*) + T^{*'}(r^*, \theta, \phi) \quad (8.7.27)$$

where r^* , θ , and ϕ are spherical coordinates.

The horizontal average of the temperature equation (8.7.26) is

$$\langle \underline{u}^* \cdot \nabla T^* \rangle = \nabla^{*2} \langle T^* \rangle \quad (8.7.28)$$

Upon subtraction of (8.7.28) from (8.7.26) we obtain

$$\underline{u}^* \cdot \nabla^* T^{*'} - \langle \underline{u}^* \cdot \nabla^* T^{*'} \rangle + \underline{u}^* \nabla^* \langle T^* \rangle = \nabla^{*2} T^{*'} \quad (8.7.29)$$

We again adopt the “weak coupling” approximation by assuming

$$\underline{u}^* \cdot \nabla^* T^{*'} = \langle \underline{u}^* \cdot \nabla^* T^{*'} \rangle \quad (8.7.30)$$

The temperature equation for the horizontally varying part of T^* becomes

$$\underline{u}^* \cdot \nabla^* \langle T^* \rangle = \nabla^{*2} T^{*'} \quad (8.7.31)$$

which is equivalent to (8.7.10) but written in vector notation. The curl of the momentum equation is

$$0 = Ra \nabla^* T^{*'} \times \hat{\underline{r}}^* + \nabla^{*2} \nabla^* \times \underline{u}^* \quad (8.7.32)$$

which is equivalent to (8.7.6) but written in vector notation.

The solution of (8.7.24), (8.7.28), (8.7.31), and (8.7.32) can be obtained by representing the velocity field by a purely poloidal vector according to

$$\underline{u}^* = \nabla^* \times \left\{ \nabla^* \left(\frac{\Phi^*}{r^*} \right) \times \underline{r}^* \right\} \quad (8.7.33)$$

(see Section 7.8). The single-mode convective structure can be written as

$$\Phi^* = \Phi_l^{*m}(r^*) Y_l^m(\theta, \phi) \quad (8.7.34)$$

$$T^{*'} = T_l^{*'} Y_l^m(\theta, \phi) \quad (8.7.35)$$

where a single mode now refers to a single value of the spherical harmonic degree l . Substitution of (8.7.33)–(8.7.35) into (8.7.28), (8.7.31) and (8.7.32) gives

$$D_l^{*2} \left(\frac{\Phi_l^{*m}}{r^*} \right) = \frac{T_l^{*'} m}{r^*} \quad (8.7.36)$$

$$D_l^* \left(T_l^{*'} \right) = \frac{l(l+1)}{r^{*2}} \Phi_l^{*m} \frac{d \langle T^* \rangle}{dr^*} \quad (8.7.37)$$

$$\Delta^{*2} \langle T^* \rangle = \frac{1}{r^{*2}} \frac{d}{dr^*} \left\{ l(l+1) \Phi_l^{*m} T_l^{*'} \right\} \quad (8.7.38)$$

where

$$D_l^* = \Delta^{*2} - \frac{l(l+1)}{r^{*2}} \quad \text{and} \quad \Delta^{*2} = \frac{1}{r^{*2}} \frac{d}{dr^*} \left(r^{*2} \frac{d}{dr^*} \right), \quad \text{see (7.8.17)} \quad (8.7.39)$$

Impermeable, isothermal, and shear stress-free boundary conditions require that

$$T_l^{*'} = \Phi_l^{*m} = \frac{d^2 (\Phi_l^{*m}/r^*)}{dr^{*2}} = 0 \quad \text{at} \quad r^* = 1, a^* \quad (8.7.40)$$

$$\langle T^* \rangle = 0, 1 \quad \text{at} \quad r^* = 1, a^* \quad (8.7.41)$$

where a^* is the ratio of the inner radius of the shell to its outer radius (the dimensionless inner radius).

Integration of (8.7.38) between the limits r^* and 1 yields

$$Nu_1 + r^{*2} \frac{d\langle T^* \rangle}{dr^*} = l(l+1) \Phi_l^{*m} T_l^{*m} \quad (8.7.42)$$

where Nu_1 is the Nusselt number at the outer surface. Evaluation of (8.7.42) at the inner surface $r^* = a^*$ gives $Nu_1 = a^{*2} Nu_{a^*}$, where Nu_{a^*} is the Nusselt number at the lower surface $r^* = a^*$. This is a simple consequence of energy conservation for steady convection in the absence of internal heating – the constancy of total heat flow with radius requires the heat flux to be inversely proportional to r^{*2} . Equations (8.7.36), (8.7.37), and (8.7.42) together with boundary conditions (8.7.40) and (8.7.41) give the single-mode mean field mathematical description of steady, heated from below convection in a spherical shell with isothermal and shear stress-free surfaces. The system requires numerical integration of the nonlinear ordinary differential equations for its solution.

Olson (1981) has discussed the solution in the limit of very large Ra . In this limit ($Ra \geq 10^6$), solutions to the mean field equations exhibit two distinct regimes – an interior one and boundary layers at the inner and outer surfaces. The interior region is characterized by convective heat transport and conduction is unimportant. In the thermal boundary layers, conductive and convective heat fluxes are in balance. It can be shown from the above equations that in the asymptotic limit of large Ra , Nu_1 is given by

$$Nu_1 = \frac{1}{4\pi} C_1(l, a^*) Ra^{1/3} \quad (8.7.43)$$

where C_1 is numerically determined and depends on the degree of the spherical harmonic mode and the dimensionless inner radius. As in (8.6.38) Nu_1 scales as $Ra^{1/3}$. The dimensionless rms average surface velocity u_1^* at the outer surface can also be shown to be given by

$$u_1^* = C_2(l, a^*) Ra^{2/3} \quad (8.7.44)$$

where C_2 is numerically determined and

$$u_1^* = \left| l(l+1) \frac{d\Phi_l^{*m}}{dr^*} (r^* = 1) \right| \quad (8.7.45)$$

for zonal modes and

$$u_1^* = \left| \frac{l(2l+1)}{2} \frac{d\Phi_l^{*m}}{dr^*} (r^* = 1) \right| \quad (8.7.46)$$

for sectoral modes. As in (8.6.35), u_1^* scales as $Ra^{2/3}$.

The utility of single-mode mean field theory is its relative computational simplicity which allows for investigations of convection in a great variety of circumstances. While our discussion of this theory has been limited to steady convection with heating from below and shear stress-free boundaries, mean field theory can be straightforwardly extended to include time dependence, internal heating, different boundary conditions, different flow geometries, e.g., layered convection, and temperature- and pressure-dependent rheological and thermal properties (Quarenghi and Yuen, 1988). Vincent and Yuen (1989) have used multi-mode mean field calculations to explore chaotic thermal convection.

8.8 Weakly Nonlinear Stability Theory

A formal expansion of the convection solution in powers of a small parameter ϵ recovers the linear stability problem and allows extension of the solution into the weakly nonlinear regime applicable when the Rayleigh number is only slightly supercritical. This approach was introduced in papers by Gor'kov (1958) and Malkus and Veronis (1958) and has been discussed in more recent review papers by Busse (1978, 1989).

8.8.1 Two-dimensional Convection

We consider the weakly nonlinear thermal convection of a plane layer of fluid heated from below. We adopt the Boussinesq approximation, assume constant fluid properties, and take the Prandtl number to be infinite. For simplicity, we first consider two-dimensional, steady convection in the form of rolls. The dimensionless coordinate x^* is horizontal, y^* is downward, $y^* = 0$ is the surface, and $y^* = 1$ is the base of the fluid layer. The nonlinear equations are given by (8.2.5) and (8.2.6) which we rewrite here as

$$\nabla^{*4}\psi^* = -Ra \frac{\partial\theta^*}{\partial x^*} \quad (8.8.1)$$

$$\nabla^{*2}\theta^* + \frac{\partial\psi^*}{\partial x^*} = \frac{\partial\psi^*}{\partial y^*} \frac{\partial\theta^*}{\partial x^*} - \frac{\partial\psi^*}{\partial x^*} \frac{\partial\theta^*}{\partial y^*} \quad (8.8.2)$$

The boundaries are assumed to be isothermal, impermeable, and shear stress free. The boundary conditions are given by (7.3.15) and (7.3.16):

$$\theta^* = v^* = \frac{\partial u^*}{\partial y^*} = 0 \quad \text{on } y^* = 0, 1 \quad (8.8.3)$$

or

$$\theta^* = \psi^* = \frac{\partial^2\psi^*}{\partial y^{*2}} = 0 \quad \text{on } y^* = 0, 1 \quad (8.8.4)$$

We expand the solution in powers of a small parameter ϵ ($\epsilon \ll 1$) according to

$$\theta^* = \epsilon\theta_1^* + \epsilon^2\theta_2^* + \epsilon^3\theta_3^* + \dots \quad (8.8.5)$$

$$\psi^* = \epsilon\psi_1^* + \epsilon^2\psi_2^* + \epsilon^3\psi_3^* + \dots \quad (8.8.6)$$

$$Ra = Ra_{cr} + \epsilon Ra_1 + \epsilon^2 Ra_2 + \dots \quad (8.8.7)$$

In writing the expansion of the Rayleigh number in powers of ϵ , we anticipate that the lowest-order term will be the critical Rayleigh number for the onset of convection found in the linear stability problem of Section 7.3 and given by (7.3.28).

Equations (8.8.5)–(8.8.7) are substituted into (8.8.1), (8.8.2) and (8.8.4) and equation sets are generated by grouping terms of $O(\epsilon)$, $O(\epsilon^2)$, $O(\epsilon^3)$, etc. The $O(\epsilon)$ equations are

$$\nabla^{*4}\psi_1^* = -Ra_{cr} \frac{\partial\theta_1^*}{\partial x^*} \quad (8.8.8)$$

$$\nabla^{*2}\theta_1^* + \frac{\partial\psi_1^*}{\partial x^*} = 0 \quad (8.8.9)$$

$$\theta_1^* = \psi_1^* = \frac{\partial^2\psi_1^*}{\partial y^{*2}} = 0 \quad \text{on } y^* = 0, 1 \quad (8.8.10)$$

Equations (8.8.8)–(8.8.10) define the linear stability problem considered in Section 7.3. From (7.3.23) and (7.3.26) we can write

$$\theta_1^* = \hat{\theta}_{1,0}^* \sin \pi y^* \sin \frac{2\pi x^*}{\lambda^*} \quad (8.8.11)$$

From (7.3.32) we have

$$\psi_1^* = -\frac{\lambda^*}{2\pi} \left(\pi^2 + \frac{4\pi^2}{\lambda^{*2}} \right) \hat{\theta}_{0,1}^* \sin \pi y^* \sin \frac{2\pi x^*}{\lambda^*} \quad (8.8.12)$$

From (7.3.28) we can write the critical Rayleigh number for the onset of convection as

$$Ra_{cr} = \frac{(\pi^2 + 4\pi^2/\lambda^{*2})^3}{4\pi^2/\lambda^{*2}} \quad (8.8.13)$$

The $O(\epsilon^2)$ equations are

$$\nabla^{*4} \psi_2 + Ra_{cr} \frac{\partial \theta_2^*}{\partial x^*} = -Ra_1 \frac{\partial \theta_1^*}{\partial x^*} \quad (8.8.14)$$

$$\nabla^{*2} \theta_2^* + \frac{\partial \psi_2^*}{\partial x^*} = \frac{\partial \psi_1^*}{\partial y^*} \frac{\partial \theta_1^*}{\partial x^*} - \frac{\partial \psi_1^*}{\partial x^*} \frac{\partial \theta_1^*}{\partial y^*} \quad (8.8.15)$$

$$\theta_2^* = \psi_2^* = \frac{\partial^2 \psi_2^*}{\partial y^{*2}} = 0 \quad \text{on } y^* = 0, 1 \quad (8.8.16)$$

Equations (8.8.14)–(8.8.16) comprise an inhomogeneous linear system of equations that is solvable if and only if the inhomogeneous part (the right sides of (8.8.14) and (8.8.15)) is orthogonal to all solutions of the adjoint homogeneous problem. This is known as the solvability condition. The homogeneous problem is identical to the linear stability problem and it is self-adjoint. The inhomogeneous terms on the right of (8.8.15) are proportional to $\sin 2\pi y^*$ which is antisymmetric about $y^* = 1/2$. The homogeneous solution is proportional to $\sin \pi y^*$ which is symmetric about $y^* = 1/2$. Thus the inhomogeneous terms on the right side of (8.8.15) are orthogonal to the solutions of the homogeneous or linear stability problem. However, the inhomogeneous term on the right of (8.8.14) is proportional to $\sin \pi y^*$ and it is not orthogonal to solutions of the homogeneous problem. The only way a solution to the inhomogeneous problem can exist is for $Ra_1 = 0$. In fact, the solvability condition requires $Ra_n = 0$ for all odd integers n because of the symmetry of the nonlinear advection terms in the temperature equation (Busse, 1978).

Substitution of (8.8.11) and (8.8.12) into (8.8.15) and use of $Ra_1 = 0$ yields the simplified $O(\epsilon^2)$ equations

$$\nabla^{*4} \psi_2^* + Ra_{cr} \frac{\partial \theta_2^*}{\partial x^*} = 0 \quad (8.8.17)$$

$$\nabla^{*2} \theta_2^* + \frac{\partial \psi_2^*}{\partial x^*} = -\frac{\pi}{2} \left(\pi^2 + \frac{4\pi^2}{\lambda^{*2}} \right) \hat{\theta}_{1,0}^* \sin 2\pi y^* \quad (8.8.18)$$

The solution of (8.8.16)–(8.8.18) is readily found to be

$$\psi_2^* = 0 \quad (8.8.19)$$

$$\theta_2^* = \frac{1}{8\pi} \left(\pi^2 + \frac{4\pi^2}{\lambda^{*2}} \right) \hat{\theta}_{1,0}^* \sin 2\pi y^* \quad (8.8.20)$$

The nonlinear contribution to the temperature given by (8.8.20) is independent of x^* and constitutes a modification by convection of the horizontally averaged temperature in the fluid layer.

The $O(\epsilon^3)$ equations are

$$\nabla^{*4} \psi_3^* + Ra_{cr} \frac{\partial \theta_3^*}{\partial x^*} = -Ra_2 \frac{\partial \theta_1^*}{\partial x^*} \quad (8.8.21)$$

$$\nabla^{*2} \theta_3^* + \frac{\partial \psi_3^*}{\partial x^*} = \frac{\partial \psi_1^*}{\partial y^*} \frac{\partial \theta_2^*}{\partial x^*} - \frac{\partial \psi_1^*}{\partial x^*} \frac{\partial \theta_2^*}{\partial y^*} \quad (8.8.22)$$

$$\theta_3^* = \psi_3^* = \frac{\partial^2 \psi_3^*}{\partial y^{*2}} = 0 \quad \text{on } y^* = 0, 1 \quad (8.8.23)$$

We are mainly interested in finding Ra_2 which, with (8.8.7), can be used to identify the expansion parameter ϵ as

$$\epsilon^2 = \frac{Ra - Ra_{cr}}{Ra_2} \quad (8.8.24)$$

It is not necessary to solve for θ_3^* and ψ_3^* to determine Ra_2 . It suffices to apply the solvability condition to (8.8.21) and (8.8.22). The nonlinear terms on the right side of (8.8.22) are proportional to $\sin \pi y^* \cos 2\pi y^*$ and are symmetric about $y^* = 1/2$ as is the term on the right side of (8.8.21) which is proportional to $\sin \pi y^*$. The solvability condition therefore requires Ra_2 to be nonzero and it can be determined as follows.

We rewrite (8.8.21) and (8.8.22) by substitution from (8.8.11), (8.8.12), and (8.8.20) and obtain

$$\nabla^{*4} \psi_3^* + Ra_{cr} \frac{\partial \theta_3^*}{\partial x^*} = -Ra_2 \frac{2\pi}{\lambda^*} \hat{\theta}_{1,0}^* \sin \pi y^* \cos \frac{2\pi x^*}{\lambda^*} \quad (8.8.25)$$

$$\nabla^{*2} \theta_3^* + \frac{\partial \psi_3^*}{\partial x^*} = -\frac{1}{4} \left(\pi^2 + \frac{4\pi^2}{\lambda^{*2}} \right)^2 \hat{\theta}_{1,0}^{*3} \sin \pi y^* \cos 2\pi y^* \sin \frac{2\pi x^*}{\lambda^*} \quad (8.8.26)$$

Equation (8.8.26) can be rewritten as

$$\nabla^{*2} \theta_3^* + \frac{\partial \psi_3^*}{\partial x^*} = -\frac{1}{8} \left(\pi^2 + \frac{4\pi^2}{\lambda^{*2}} \right)^2 \hat{\theta}_{1,0}^{*3} (\sin 3\pi y^* - \sin \pi y^*) \sin \frac{2\pi x^*}{\lambda^*} \quad (8.8.27)$$

From the viewpoint of solvability, it is only necessary to consider the terms on the right sides of (8.8.25) and (8.8.27) that are resonant with the homogeneous solution of these equations. These are the terms proportional to $\sin \pi y^*$ since the solution to the homogeneous equations is proportional to $\sin \pi y^*$. The resonant parts of (8.8.25) and (8.8.27) are

$$\nabla^{*4} \psi_3^* + Ra_{cr} \frac{\partial \theta_3^*}{\partial x^*} = -Ra_2 \frac{2\pi}{\lambda^*} \hat{\theta}_{1,0}^* \sin \pi y^* \cos \frac{2\pi x^*}{\lambda^*} \quad (8.8.28)$$

$$\nabla^{*2} \theta_3^* + \frac{\partial \psi_3^*}{\partial x^*} = \frac{1}{8} \left(\pi^2 + \frac{4\pi^2}{\lambda^{*2}} \right)^2 \hat{\theta}_{1,0}^{*3} \sin \pi y^* \sin \frac{2\pi x^*}{\lambda^*} \quad (8.8.29)$$

We eliminate ψ_3^* by taking $\partial/\partial x^*$ of (8.8.28) and ∇^{*4} of (8.8.29) and subtract to get

$$\nabla^{*6} \theta_3^* - Ra_{cr} \frac{\partial^2 \theta_3^*}{\partial x^{*2}} = \hat{\theta}_{1,0}^* \sin \pi y^* \sin \frac{2\pi x^*}{\lambda^*} \left\{ \frac{1}{8} \left(\pi^2 + \frac{4\pi^2}{\lambda^{*2}} \right)^4 \hat{\theta}_{1,0}^{*2} - \frac{4\pi^2}{\lambda^{*2}} Ra_2 \right\} \quad (8.8.30)$$

Elimination of the resonance requires that the right side of (8.8.30) is zero or

$$Ra_2 = \frac{\lambda^{*2}}{32\pi^2} \left(\pi^2 + \frac{4\pi^2}{\lambda^{*2}} \right)^4 \hat{\theta}_{1,0}^{*2} \quad (8.8.31)$$

$$= \frac{1}{8} \left(\pi^2 + \frac{4\pi^2}{\lambda^{*2}} \right) \hat{\theta}_{1,0}^{*2} Ra_{cr} \quad (8.8.32)$$

Substitution of (8.8.32) into (8.8.24) gives

$$\epsilon^2 = \left(\frac{Ra - Ra_{cr}}{Ra_{cr}} \right) \frac{8}{(\pi^2 + 4\pi^2/\lambda^{*2}) \hat{\theta}_{1,0}^{*2}} \quad (8.8.33)$$

If we take $\lambda^* = \lambda_{cr}^* = 2\sqrt{2}$ (see 7.3.30) then (8.8.32) and (8.8.33) become

$$Ra_2 = \frac{3\pi^2}{16} \hat{\theta}_{1,0}^{*2} Ra_{cr} \quad (8.8.34)$$

$$\epsilon^2 = \left(\frac{Ra - Ra_{cr}}{Ra_{cr}} \right) \frac{16}{3\pi^2 \hat{\theta}_{1,0}^{*2}} \quad (8.8.35)$$

We can determine the Nusselt number Nu using (8.3.18). Since $\partial\theta_1^*/\partial y^*$ has a zero horizontal average we can write

$$Nu = 1 + \left\langle \frac{\partial\theta^*}{\partial y^*} \right\rangle_S = 1 + \epsilon^2 \left\langle \frac{\partial\theta_2^*}{\partial y^*} \right\rangle_S \quad (8.8.36)$$

Substitution of (8.8.20) and (8.8.33) into (8.8.36) gives

$$Nu = 1 + 2 \left(\frac{Ra - Ra_{cr}}{Ra_{cr}} \right) \quad (8.8.37)$$

Equation (8.8.37) gives the Nusselt number–Rayleigh number relation for weakly nonlinear convection in the form of two-dimensional rolls. Busse (1989) presents results analogous to (8.8.37) for three-dimensional convection with square and hexagonal planforms (we consider hexagons below). These results were first obtained by Malkus and Veronis (1958). Rolls have a higher heat transport than squares, which in turn have a higher heat transport than hexagons. The Nusselt number given by (8.8.37) is identical to the value of Nu obtained from the Lorenz equations (see 8.3.19)!

8.8.2 Three-dimensional Convection, Hexagons

We consider the same situation as just above except for the planform of convection which we now take to be fully three dimensional in the form of hexagons. The following approach, due to Paul Roberts, is also similar to the one we followed in the two-dimensional case just above.

Since convection in this case is poloidal (we are considering infinite Prandtl number, see also Section 7.8) the velocity vector can be written as

$$\underline{u}^* = (u^*, v^*, w^*) = \left(-\frac{\partial^2 S^*}{\partial x^* \partial y^*}, \nabla_H^{*2} S^*, -\frac{\partial^2 S^*}{\partial z^* \partial y^*} \right) \quad (8.8.38)$$

where u^* , v^* , and w^* are Cartesian components of velocity in the x^* , y^* , z^* directions, y^* points vertically down, x^* and z^* are horizontal coordinates, and ∇_H^* is the horizontal gradient operator $(\partial/\partial x^*, 0, \partial/\partial z^*)$. If the Prandtl number is not infinite, nonlinear interactions generate toroidal flow at second order through the inertial terms. The velocity components given by (8.8.38) automatically satisfy the incompressible conservation of mass equation

$$\frac{\partial u^*}{\partial x^*} + \frac{\partial v^*}{\partial y^*} + \frac{\partial w^*}{\partial z^*} = 0 \quad (8.8.39)$$

The infinite Prandtl number momentum equations are readily obtainable by generalizing (8.2.2) and (8.2.3) to three dimensions:

$$0 = -\frac{\partial \Pi^*}{\partial x^*} + \nabla^{*2} u^* \quad (8.8.40)$$

$$0 = -\frac{\partial \Pi^*}{\partial y^*} - Ra \theta^* + \nabla^{*2} v^* \quad (8.8.41)$$

$$0 = -\frac{\partial \Pi^*}{\partial z^*} + \nabla^{*2} w^* \quad (8.8.42)$$

The pressure Π^* can be eliminated from these equations by differentiating (8.8.40) with respect to y^* and substituting for $\partial \Pi^*/\partial y^*$ from (8.8.41). Similarly, we can differentiate (8.8.42) with respect to y^* and substitute for $\partial \Pi^*/\partial y^*$ from (8.8.41). With the velocity components given by (8.8.38) these operations give

$$0 = \frac{\partial}{\partial x^*} (-Ra \theta^* + \nabla^{*4} S^*) \quad (8.8.43)$$

$$0 = \frac{\partial}{\partial z^*} (-Ra \theta^* + \nabla^{*4} S^*) \quad (8.8.44)$$

Thus, $-Ra \theta^* + \nabla^{*4} S^*$ is independent of the horizontal coordinates. Consistent with the boundary conditions, it suffices to take

$$\nabla^{*4} S^* - Ra \theta^* = 0 \quad (8.8.45)$$

The temperature equation is the generalization of (8.2.4) to three dimensions. For steady convection, and with the use of (8.8.38) for the velocity components, we can write

$$\nabla^{*2} \theta^* - \nabla_H^{*2} S^* = -\frac{\partial^2 S^*}{\partial x^* \partial y^*} \frac{\partial \theta^*}{\partial x^*} + \nabla_H^{*2} S^* \frac{\partial \theta^*}{\partial y^*} - \frac{\partial^2 S^*}{\partial z^* \partial y^*} \frac{\partial \theta^*}{\partial z^*} \quad (8.8.46)$$

Boundary conditions are those of the previous section.

We expand the solution in powers of a small parameter ϵ ($\epsilon \ll 1$) as in (8.8.5)–(8.8.7) with S^* replacing ψ^* in (8.8.6). The $O(\epsilon)$ equations are

$$\nabla^{*4} S_1^* - Ra_{cr} \theta_1^* = 0 \quad (8.8.47)$$

$$\nabla^{*2} \theta_1^* - \nabla_H^{*2} S_1^* = 0 \quad (8.8.48)$$

The $O(\epsilon^2)$ equations are

$$\nabla^{*4} S_2^* - Ra_{cr} \theta_1^* = Ra_1 \theta_1^* \quad (8.8.49)$$

$$\nabla^{*2}\theta_2^* - \nabla_H^{*2}S_2 = -\frac{\partial^2 S_1^*}{\partial x^* \partial y^*} \frac{\partial \theta_1^*}{\partial x^*} + \nabla_H^{*2}S_1^* \frac{\partial \theta_1^*}{\partial y^*} - \frac{\partial^2 S_1^*}{\partial z^* \partial y^*} \frac{\partial \theta_1^*}{\partial z^*} \quad (8.8.50)$$

The $O(\epsilon^3)$ equations are

$$\nabla^{*4}S_3^* - Ra_{cr}\theta_3^* = Ra_1\theta_2^* + Ra_2\theta_1^* \quad (8.8.51)$$

$$\begin{aligned} \nabla^{*2}\theta_3^* - \nabla_H^{*2}S_3^* = & -\frac{\partial^2 S_1^*}{\partial x^* \partial y^*} \frac{\partial \theta_2^*}{\partial x^*} - \frac{\partial^2 S_1^*}{\partial z^* \partial y^*} \frac{\partial \theta_2^*}{\partial z^*} + \nabla_H^{*2}S_1^* \frac{\partial \theta_2^*}{\partial y^*} + \nabla_H^{*2}S_2^* \frac{\partial \theta_1^*}{\partial y^*} \\ & - \frac{\partial^2 S_2^*}{\partial x^* \partial y^*} \frac{\partial \theta_1^*}{\partial x^*} - \frac{\partial^2 S_2^*}{\partial z^* \partial y^*} \frac{\partial \theta_1^*}{\partial z^*} \end{aligned} \quad (8.8.52)$$

The following planform functions are appropriate for the characterization of hexagonal convection cells at this order:

$$f_1(x^*, z^*) = \sqrt{\frac{2}{3}} \left\{ \cos a^* x^* + \cos a^* \left(\frac{x^*}{2} - \frac{\sqrt{3}}{2} z^* \right) + \cos a^* \left(\frac{x^*}{2} + \frac{\sqrt{3}}{2} z^* \right) \right\} \quad (8.8.53)$$

$$\begin{aligned} f_2(x^*, z^*) = & \sqrt{\frac{2}{3}} \left\{ \cos \sqrt{3}a^* z^* + \cos \sqrt{3}a^* \left(\frac{z^*}{2} + \frac{\sqrt{3}}{2} x^* \right) \right. \\ & \left. + \cos \sqrt{3}a^* \left(\frac{z^*}{2} - \frac{\sqrt{3}}{2} x^* \right) \right\} \end{aligned} \quad (8.8.54)$$

$$f_3(x^*, z^*) = \sqrt{\frac{2}{3}} \left\{ \cos 2a^* x^* + \cos 2a^* \left(\frac{x^*}{2} - \frac{\sqrt{3}}{2} z^* \right) + \cos 2a^* \left(\frac{x^*}{2} + \frac{\sqrt{3}}{2} z^* \right) \right\} \quad (8.8.55)$$

$$\begin{aligned} f_4(x^*, z^*) = & \sqrt{\frac{2}{3}} \left\{ \cos a^* (2x^* + \sqrt{3}z^*) + \cos a^* \left(\frac{x^*}{2} - \frac{3\sqrt{3}}{2} z^* \right) \right. \\ & \left. + \cos a^* \left(\frac{5}{2} x^* - \frac{\sqrt{3}}{2} z^* \right) \right\} \end{aligned} \quad (8.8.56)$$

$$\begin{aligned} f_5(x^*, z^*) = & \sqrt{\frac{2}{3}} \left\{ \cos a^* (2x^* - \sqrt{3}z^*) + \cos a^* \left(\frac{5}{2} x^* + \frac{\sqrt{3}}{2} z^* \right) \right. \\ & \left. + \cos a^* \left(\frac{x^*}{2} + \frac{3\sqrt{3}}{2} z^* \right) \right\} \end{aligned} \quad (8.8.57)$$

where $a^* = 2\pi/\lambda^*$ and $\langle f_i^2 \rangle = 1$, $i = 1, \dots, 5$ (brackets indicate a horizontal average).

Some useful results are

$$\nabla_H^{*2}f_1 = -a^{*2}f_1, \quad \nabla_H^{*2}f_2 = -3a^{*2}f_2, \quad \nabla_H^{*2}f_3 = -4a^{*2}f_3, \quad \nabla_H^{*2}f_{4,5} = -7a^{*2}f_{4,5} \quad (8.8.58)$$

$$f_1^2 = 1 + \sqrt{\frac{2}{3}} \left(f_1 + f_2 + \frac{1}{2} f_3 \right), \quad f_1 f_2 = \sqrt{\frac{2}{3}} \left(f_1 + f_3 + \frac{1}{2} (f_2 + f_4) \right) \quad (8.8.59)$$

$$\nabla_H^* f_1 \cdot \nabla_H^* f_1 = a^{*2} \left(1 + \frac{1}{\sqrt{6}} (f_1 - f_2 - f_3) \right) \quad (8.8.60)$$

$$\nabla_H^* f_1 \cdot \nabla_H^* f_2 = \sqrt{\frac{3}{2}} a^{*2} \left(f_1 - \frac{1}{2} (f_4 + f_5) \right) \quad (8.8.61)$$

The solution of the $O(\epsilon)$ system of equations and boundary conditions is

$$S_1^* = A \sin \pi y^* f_1 \quad (8.8.62)$$

$$\theta_1^* = \frac{a^{*2}}{(a^{*2} + \pi^2)} A \sin \pi y^* f_1 \quad (8.8.63)$$

$$Ra_{cr} = \frac{(a^{*2} + \pi^2)^3}{a^{*2}} \quad (8.8.64)$$

The critical Rayleigh number for the onset of hexagonal convection is identical to that given in (8.8.13).

The nonlinear terms on the right side of (8.8.50) in the $O(\epsilon^2)$ system can be written (after some algebra and use of (8.8.59) and (8.8.60)) as

$$\begin{aligned} & - \frac{\partial^2 S_1^*}{\partial x^* \partial y^*} \frac{\partial \theta_1^*}{\partial x^*} + \nabla_H^{*2} S_1^* \frac{\partial \theta_1^*}{\partial y^*} - \frac{\partial^2 S_1^*}{\partial z^* \partial y^*} \frac{\partial \theta_1^*}{\partial z^*} \\ &= - \frac{\pi a^{*4} A^2}{(a^{*2} + \pi^2)} \left(1 + \frac{1}{2\sqrt{6}} (3f_1 + f_2) \right) \sin 2\pi y^* \end{aligned} \quad (8.8.65)$$

The solvability of the $O(\epsilon^2)$ system therefore requires $Ra_1 = 0$. With $Ra_1 = 0$, we can eliminate S_2^* between (8.8.49) and (8.8.50) to obtain

$$\nabla^{*6} \theta_2^* - Ra_{cr} \nabla_H^{*2} \theta_2^* = -Ra_{cr} \frac{\pi a^{*4} A^2}{(\pi^2 + a^{*2})} \nabla^{*4} \left[\left(1 + \frac{1}{2\sqrt{6}} (3f_1 + f_2) \right) \sin 2\pi y^* \right] \quad (8.8.66)$$

The solution of (8.8.66) can therefore be written as

$$\theta_2^* = (A_0 + A_1 f_1 + A_2 f_2) \sin 2\pi y^* \quad (8.8.67)$$

To find A_0 , A_1 , and A_2 note that

$$(\nabla^{*6} - Ra_{cr} \nabla_H^{*2}) \sin 2\pi y^* = -(2\pi)^6 \sin 2\pi y^* \quad (8.8.68)$$

$$(\nabla^{*6} - Ra_{cr} \nabla_H^{*2}) f_1 \sin 2\pi y^* = - \left\{ (4\pi^2 + a^{*2})^3 - a^{*2} Ra_{cr} \right\} f_1 \sin 2\pi y^* \quad (8.8.69)$$

$$(\nabla^{*6} - Ra_{cr} \nabla_H^{*2}) f_2 \sin 2\pi y^* = - \left\{ (4\pi^2 + 3a^{*2})^3 - 3a^{*2} Ra_{cr} \right\} f_2 \sin 2\pi y^* \quad (8.8.70)$$

Equations (8.8.66)–(8.8.70) yield

$$A_0 = \frac{a^{*4} A^2}{4\pi (\pi^2 + a^{*2})} \quad (8.8.71)$$

$$A_1 = \frac{3\pi}{2\sqrt{6}} \frac{a^{*4} A^2}{(\pi^2 + a^{*2})} \frac{(4\pi^2 + a^{*2})^2}{\left\{ (4\pi^2 + a^{*2})^3 - a^{*2} Ra_{cr} \right\}} \quad (8.8.72)$$

$$A_2 = \frac{\pi a^{*4} A^2}{2\sqrt{6} (\pi^2 + a^{*2})} \frac{(4\pi^2 + 3a^{*2})^2}{\left[(4\pi^2 + 3a^{*2})^3 - 3a^{*2} Ra_{cr} \right]} \quad (8.8.73)$$

Substitution of the solution for θ_2^* into (8.8.50) gives

$$\begin{aligned} S_2^* &= \frac{\pi a^{*4} A^2 Ra_{cr}}{2\sqrt{6} (\pi^2 + a^{*2})} \\ &\times \left[\frac{3f_1}{(4\pi^2 + a^{*2})^3 - a^{*2} Ra_{cr}} + \frac{f_2}{(4\pi^2 + 3a^{*2})^3 - 3a^{*2} Ra_{cr}} \right] \sin 2\pi y^* \end{aligned} \quad (8.8.74)$$

To proceed further, we need to evaluate the nonlinear terms on the right side of (8.8.52). With S_1^* , θ_1^* , S_2^* , and θ_2^* now known, the evaluation is straightforward though algebraically lengthy. The nonlinear terms contain the resonant part

$$\mathcal{R} = \pi a^{*2} A f_1 \cos \pi y^* \left\{ A_0 + \frac{1}{2\sqrt{6}} (3A_1 + A_2) \right\} \quad (8.8.75)$$

which may, with the help of (8.8.71)–(8.8.73), be written as

$$\mathcal{R} = \frac{a^{*6} A^3}{2\Lambda (\pi^2 + a^{*2})} f_1 \cos \pi y^* \quad (8.8.76)$$

where

$$\Lambda = 2 \left\{ 1 + \frac{3\pi^2 (4\pi^2 + a^{*2})^2}{2 \left[(4\pi^2 + a^{*2})^3 - a^{*2} Ra_{cr} \right]} + \frac{\pi^2 (4\pi^2 + 3a^{*2})^2}{6 \left[(4\pi^2 + 3a^{*2})^3 - 3a^{*2} Ra_{cr} \right]} \right\}^{-1} \quad (8.8.77)$$

We keep only the resonant part of the nonlinear terms on the right side of (8.8.52), solve for θ_3^* from (8.8.51), and substitute into (8.8.52) to obtain, apart from nonresonant terms,

$$\nabla^* S_3^* - Ra_{cr} \nabla_H^* S_3^* = f_1 \cos \pi y^* \left\{ -a^{*2} Ra_2 A + Ra_{cr} \mathcal{R} \right\} \quad (8.8.78)$$

The solvability of the complete version of (8.8.78) requires that the resonant term on the right side of (8.8.78) be zero; this determines Ra_2 and gives

$$Ra_2 = Ra_{cr} \frac{a^{*4} A^2}{2\Lambda (\pi^2 + a^{*2})} \quad (8.8.79)$$

From (8.3.18), (8.8.67), and (8.8.71) we now have

$$Nu = 1 + 2\pi A_0 = 1 + \frac{a^{*4} A^2}{2 (\pi^2 + a^{*2})} = 1 + \Lambda \frac{Ra_2}{Ra_{cr}} \quad (8.8.80)$$

For the critical mode, for which $a^{*2} = \pi^2/2$ and $Ra_{cr} = 27\pi^4/4$, (8.8.77) gives

$$\Lambda = \frac{48,750}{33,599} \approx 1.450936 \quad (8.8.81)$$

which is less than 2, showing that the hexagon transfers less heat than the roll for the same supercritical Rayleigh number. An identical result has been obtained by Busse (1989).

9

Calculations of Convection in Two Dimensions

9.1 Introduction

Although approximate solutions, such as those considered in the previous chapter, provide important insights into mantle convection, numerical solutions are required for a full understanding of the phenomenon. Ideally, numerical models should be three dimensional because whenever convection occurs in Nature it is invariably a three-dimensional phenomenon and thermal convection in the Earth's mantle is no exception to this rule. The evidence from plate tectonics and seismic tomography clearly indicates that the flow pattern is three dimensional beneath the lithosphere. However, even the largest computers are not adequate to model all the relevant physics of fully three-dimensional mantle convection. Two-dimensional numerical models of convection have therefore proven to be extremely useful for exploring the basic fluid mechanics of mantle convection.

The eventual goal of numerical modeling is to provide a complete picture of the flow within the Earth's mantle. This would be analogous to the general circulation models (GCMs) used in weather forecasting and climate modeling. There are a number of difficulties associated with the development of a comprehensive mantle convection model:

(1) The appropriate equations must be specified. We know what the appropriate fluid equations are and these have been presented in Chapter 6. However, we do not know all the nonfluid rheological laws that are important in mantle convection. For example, we are uncertain about how to model subduction and other types of lithospheric deformation which directly interact with the fluid processes at depth. The introduction of fault-like behavior into flow models is at an early stage of development (see Chapter 10) and the efforts in this direction are, so far, incomplete.

Question 9.1: *What are the multi-rheological laws governing deformation of the crust and mantle?*

(2) The spatial resolution of three-dimensional numerical models is inadequate to simulate important small-scale features of mantle convection. The largest computers accommodate the practical usage of models with a grid resolution of about 10 million points or a spatial resolution in a Cartesian box of depth 2,900 km of about 10 km. Calculations in three-dimensional spherical geometry can presently achieve about 25 km global resolution. This is the characteristic scale of plumes and thermal boundary layers. While there are techniques

to improve resolution locally, it is not always possible to predict ahead where such resolution will be required in the flow domain.

(3) Mantle convection is almost certainly chaotic. Thus, forward modeling is inherently prone to errors even with the best resolution. This is the same problem faced by weather forecasters, i.e., the butterfly effect.

(4) There is a lack of data to constrain mantle convection models. The surface velocities of the plates, surface topography and bathymetry, surface heat flow, the surface gravity field (geoid), and the geochemical anomalies of rocks are data sets that provide constraints on mantle convection. However, velocities and density distributions at depth are poorly constrained. Mantle seismic tomography provides important information on internal density anomalies, as discussed in Chapter 3, but the spatial resolution, though improving all the time, remains relatively coarse, and there is also uncertainty in relating seismic velocity anomalies to anomalies in density caused by temperature, composition, and effects of melting.

Question 9.2: How are mantle seismic velocity heterogeneities partitioned among temperature, composition, and melting?

Although a global mantle convection model remains a viable goal, numerical calculations of mantle convection have provided a wealth of insights into fundamental mechanisms. Two-dimensional calculations are discussed in this chapter and three-dimensional calculations in the next chapter.

The great advantage of two-dimensional calculations is the high spatial resolution available. Today, it is possible to achieve a grid resolution better than 10 km in two-dimensional models. However, care must always be taken in extrapolating results obtained in two dimensions to three dimensions. We begin with the simplest problem relevant to the mantle, steady convection in a layer heated from below. Building from this basic model, we then consider some of the important effects which make mantle convection such a rich and complex process. These include time dependence, a temperature- and pressure-dependent rheology, a non-Newtonian rheology, compressibility and viscous dissipation, phase changes, density stratification, and continental rafts.

Since this chapter is based on numerical solutions, it is useful to set out at the beginning the equations of motion for two-dimensional convection in a variable viscosity fluid derived in Chapter 6. With the Boussinesq approximation (see Chapter 6) the conservation equations for vorticity, temperature, and phase (or composition) are, using the notation in Chapter 7,

$$\left(\frac{\partial^2}{\partial y^2} - \frac{\partial^2}{\partial x^2} \right) \mu^* \left(\frac{\partial^2}{\partial y^2} - \frac{\partial^2}{\partial x^2} \right) \psi + 4 \frac{\partial^2}{\partial x \partial y} \mu^* \frac{\partial^2}{\partial x \partial y} \psi = -Ra \frac{\partial T}{\partial x} + Rb \frac{\partial \Gamma}{\partial x} \quad (9.1.1)$$

$$\frac{\partial T}{\partial t} + u \frac{\partial T}{\partial x} + v \frac{\partial T}{\partial y} = \nabla^2 T + Q \quad (9.1.2)$$

$$\frac{\partial \Gamma}{\partial t} + u \frac{\partial \Gamma}{\partial x} + v \frac{\partial \Gamma}{\partial y} = 0 \quad (9.1.3)$$

and

$$(u, v) = \left(\frac{\partial \psi}{\partial y}, -\frac{\partial \psi}{\partial x} \right) \quad (9.1.4)$$

Here ψ , T and Γ are the dimensionless stream function, temperature and phase (or composition) field variables, μ^* is the nondimensional viscosity function, and Q is the dimensionless internal heat production. As in Chapters 6 and 7, the y -coordinate points downward. These equations use the layer depth b , the thermal diffusion time b^2/κ and the temperature difference across the layer ΔT as length, time, and temperature scales, respectively. A reference viscosity, μ_0 , often the value of the viscosity at the surface, is used in scaling μ^* .

The two Rayleigh numbers that appear explicitly are

$$Ra = \frac{\alpha g \Delta T b^3}{\kappa \mu_0} \quad (9.1.5)$$

and

$$Rb = \frac{\Delta \rho g b^3}{\kappa \mu_0} \quad (9.1.6)$$

The dimensionless heat source term

$$Q = \frac{b^2 \rho H}{k \Delta T} \quad (9.1.7)$$

is related to another Rayleigh number, the one based on internal heat production Ra_H and defined in Chapter 7:

$$Ra_H = Q Ra \quad (9.1.8)$$

In order to solve these equations it is necessary to discretize them. Three standard approaches are finite differences, finite elements, and spectral methods. There are many variations on these techniques and others which we will not consider here. The reader is referred to the original papers for the details of the numerical techniques. If considerable care is not taken, numerical artifacts may occur. Grid refinement is one standard approach to the elimination of numerical artifacts. The grid spacing is systematically reduced until there is no significant change in the results obtained. The best verification of the results, however, is agreement with computations carried out independently using different numerical techniques, or with experiments.

9.2 Steady Convection at Large Rayleigh Number

In Chapter 7 we concluded that the Rayleigh number for layered mantle convection is $Ra_q = 4.8 \times 10^6$ and the internal heating Rayleigh number for whole mantle convection is $Ra_H = 3 \times 10^9$. These Rayleigh numbers are, respectively, approximately 10^4 and 10^6 times the critical Rayleigh number for the onset of convection. The Rayleigh number Ra for whole mantle convection based on the superadiabatic temperature increase from the surface to the core–mantle boundary is of the order 10^7 , approximately 10^4 times critical. In the geologic past, particularly in the early Archean, Earth's Rayleigh number was presumably even higher, because the mantle was hotter and therefore less viscous than at present.

A useful starting model of mantle convection is therefore thermal convection in a fluid layer with uniform viscosity at a Rayleigh number well above the critical value. If the layer is heated from below, steady-state two-dimensional solutions exist and can be compared with the predictions of Chapter 8 derived from boundary layer theory. In terms of dimensionless variables, the steady-state versions of the vorticity and temperature equations (9.1.1) and (9.1.2) can be written as

$$\nabla^4 \psi = -Ra \frac{\partial T}{\partial x} \quad (9.2.1)$$

and

$$u \frac{\partial T}{\partial x} + v \frac{\partial T}{\partial y} = \nabla^2 T + Q \quad (9.2.2)$$

The usual boundary conditions are impermeable and stress-free upper and lower boundaries, and reflecting side walls, on which the heat flow, horizontal velocity and shear stress vanish. The upper boundary is usually taken to be isothermal, appropriate for the Earth's surface. The lower boundary condition is either isothermal, appropriate for the core–mantle boundary, or uniform heat flux, which is sometimes used to model the conduction of heat from the lower mantle under the assumption of two-layer convection.

One important goal in solving the simplified equations (9.2.1) and (9.2.2) is to obtain scaling laws for heat transport, fluid velocity, thermal boundary layer thickness and other parameters over a wide range of Rayleigh numbers. The horizontally averaged (denoted by brackets) Nusselt number introduced in (8.3.18)

$$\langle Nu \rangle = \left\langle \frac{\partial T}{\partial y} - vT \right\rangle \quad (9.2.3)$$

is a particularly important diagnostic, and its dependence on Ra (9.1.5–9.1.6) has been the subject of numerous investigations. It turns out that scaling laws obtained from steady isoviscous convection yield surprisingly realistic predictions for mantle observables such as average heat flow, thermal boundary layer thickness, and surface velocity.

There have been a number of systematic treatments of this problem, especially for the case of unit aspect ratio (square-shaped) cells (McKenzie et al., 1973, 1974; Hewitt et al., 1980; Jarvis, 1984; Schubert and Anderson, 1985; Olson, 1987; Christensen, 1989c). Figure 9.1 shows the arrangement of hot and cold thermal boundary layers and the hot and cold plumes appropriate for $Ra = 10^5$, and Figure 9.2 shows steady-state temperature contours from finite difference computations (Jarvis, 1984) over the range $10^{0.1} \leq Ra/Ra_{cr} \leq 10^5$, with $Ra_{cr} = 779.273$ the critical Rayleigh number for convection onset. At high Rayleigh number the temperature structure consists of thin thermal boundary layers surrounding an isothermal core region, as anticipated in the boundary layer analysis of Chapter 8. The core temperature is the mean of the boundary temperatures, as expected from symmetry. The streamline pattern in all cases shown in Figure 9.2 is very nearly the same as in Figure 9.1; to a good approximation, only the magnitude of the fluid velocity increases with Rayleigh number. Steady-state solutions of this type can be found to very high Rayleigh numbers. Christensen (1989c) has presented finite element solutions for this case up to $Ra = 10^9$.

Efficiency of heat transport is perhaps the most important result of these steady-state calculations. The parameterized models of mantle thermal history we describe in Chapters 13 and 14 are based on the heat transport law derived from steady-state calculations such as

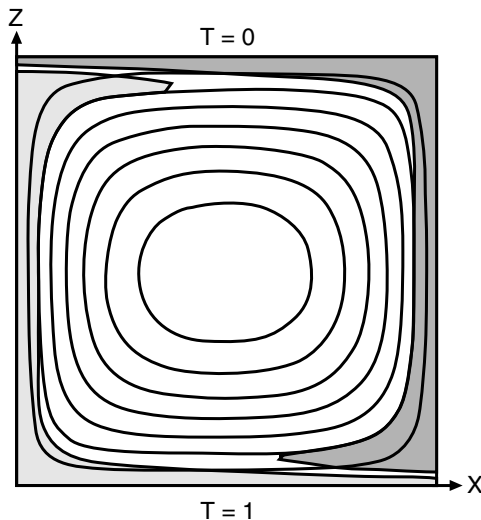


Figure 9.1. The structure of steady-state, two-dimensional, Rayleigh–Bénard convection at infinite Prandtl number, with streamlines of the motion (solid contours), hot thermal boundary layer and rising plume (light shading), and cold thermal boundary layer and sinking plume (dark shading).

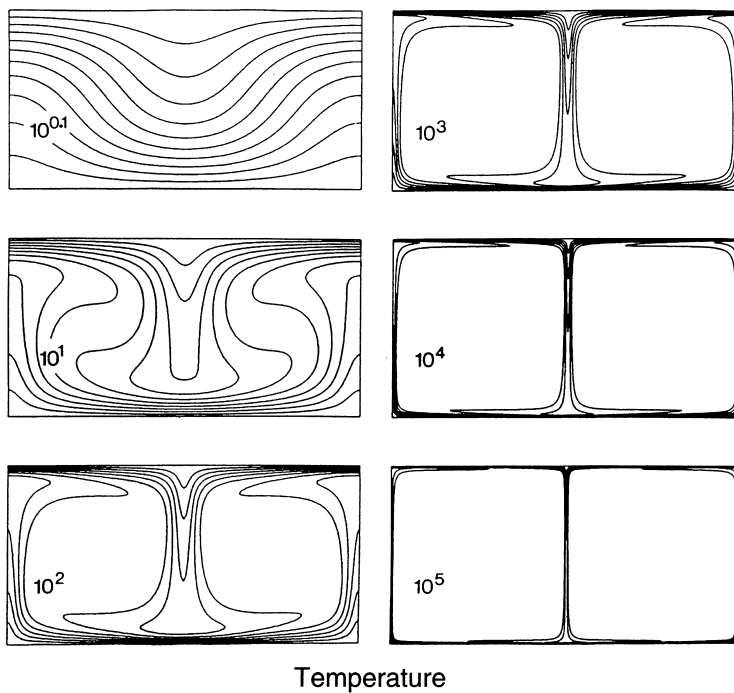


Figure 9.2. Contours of temperature for steady, two-dimensional, Rayleigh–Bénard convection in aspect ratio one cells heated from below (Jarvis, 1984), showing the development of thermal boundary layers with increasing Rayleigh number. Numbers indicate the ratio Ra/Ra_{cr} , with $Ra_{cr} = 779.27$.

these. The heat transport law is expressed in terms of the Nusselt number (9.2.3), usually as a power law of the form

$$Nu = cRa^\beta \quad (9.2.4)$$

The thickness of the thermal boundary layers varies with the reciprocal of Nu , while the fluid velocity typically scales as $u \simeq Ra^{2\beta}$. Boundary layer theory (Chapter 8) yields $\beta = 1/3$ with the coefficient c depending on the cell width. For square cells, calculations by Jarvis (1984) give $c = 0.29$, $\beta = 0.318$, while Schubert and Anderson (1985) obtain $c = 0.27$ and $\beta = 0.319$ for $10^2 \leq Ra/Ra_{cr} \leq 10^5$. Christensen (1989c) finds that no single power law fits the Nusselt number for all Ra values. Near $Ra = 10^6$, his results give

$$c = 0.27, \quad \beta = 0.3185 \quad (9.2.5)$$

and they slowly asymptote toward the $1/3$ power law at very large Ra . There is likewise a set of power-law formulas obtained for fluid velocities. For example, Jarvis and Peltier (1982) find

$$\langle u \rangle = 0.12Ra^{0.645} \simeq 0.12Ra^{2\beta} \quad (9.2.6)$$

for the dimensionless horizontally averaged free-surface velocity.

Calculations of high Rayleigh number steady asymmetric convection in a spherical shell heated from below with an inner to outer radius ratio of 0.5 yield a value for β equal to 0.28 (Zebib et al., 1985). The spherical asymmetric computations were carried out for Rayleigh numbers as large as 100 times the critical Ra for the onset of convection. There is only one stable axisymmetric pattern of convection in the spherical shell. This circulation is symmetric about the equator and has two meridional cells with rising motion at the poles. Thickening of the thermal boundary layer and plume at the pole is responsible for the decreased heat transfer compared with the boundary layer scaling. Nevertheless, axisymmetric spherical convection solutions give a Nu - Ra relation in good agreement with that of two-dimensional Cartesian solutions.

In addition to yielding geophysically reasonable values for thermal boundary layer thickness, heat flow and surface velocities for realistic Rayleigh numbers in the range $1-3 \times 10^7$, the simple model of two-dimensional, steady, basally heated convection has other strengths. For example, the basic structure of the flow – diffuse global motion driven by thin (regional scale) thermal anomalies – is consistent with the situation in mantle convection. The model also contains an active lower thermal boundary layer analogous to the D'' layer. To be sure, there are important elements missing from this simple model, and there are obvious deficiencies in the results, such as the absence of tectonic plates at the surface, mechanically strong subducted slabs, and concentrated thermal plume upwellings. Despite these shortcomings, the qualitative (and even semi-quantitative) agreement between this simplified model and some important observables provided early support for the application of convection theory to the mantle.

Using the model of steady convection in a homogeneous, isoviscous fluid as the starting point, we now consider some of the additional effects known to influence mantle convection. Among these are time dependence, internal heating, lithospheric plates, temperature-dependent and pressure-dependent viscosity, depth-dependent thermodynamic properties, and phase and compositional changes in the transition zone. It turns out that when some of these complications are added to models of thermal convection one at a time, the results

actually depart farther from the behavior of the mantle, leading to a less realistic model. Evidently a number of the complications listed above tend to cancel one another, so that a model without a proper combination of complicating effects may actually behave less satisfactorily than a simpler one.

9.3 Internal Heat Sources and Time Dependence

Most of the heat for mantle convection comes from the mantle itself, from a combination of radioactive decay of uranium and other heat-producing isotopes, plus secular cooling of the mantle. We argue in Chapters 3 and 13 that no more than about 10–20% of the mantle heat comes from the core. Accordingly, convection driven by internal heating is a closer approximation to mantle convection than the model of base-heated convection just described.

An important effect of internal heating is that convection invariably becomes time dependent. This can be understood by considering how the picture of steady convection in Figure 9.1 is modified by addition of uniformly distributed volumetric heat sources. If the flow pattern were steady, then the heat produced by radioactive decay in the core of the cell would have to be removed from that region by thermal conduction. This would require large thermal gradients in the cell interior, and the buoyancy associated with these gradients would soon destroy the steadiness of the flow.

Numerical calculations demonstrate how time dependence in the flow pattern acts to remove heat generated in the cell interior. Figure 9.3 shows an example of time-dependent convection from calculations by Jarvis (1984) in which a fraction $r = 0.1$ of the surface heat loss is produced internally and the rest by basal heating. In these calculations, a constant heat flux lower boundary condition was used, so that the appropriate form of the Rayleigh number is the one based on the bottom heat flux q_b (7.3.7):

$$Ra_f = \frac{\alpha g q_b b^4}{k \kappa v} \quad (9.3.1)$$

Time dependence occurs through repeated generation of thermal boundary layer instabilities. The parcel of relatively cold fluid labeled A was produced by a perturbation in the thermal boundary layer during the previous overturn. It becomes entrained in the general circulation and as it sinks beside the sidewall plume, it causes a large increase in the kinetic energy of the flow. As it approaches the lower boundary it perturbs the hot thermal boundary layer, producing a hot parcel B. As parcel A is swept into the ascending region its negative buoyancy partially stalls the upwelling, producing yet another perturbation labeled C, which will further disturb the flow. The time dependence of the motion is thus maintained through a process analogous to a self-excited oscillator, in which parcels of anomalous temperature fluid are repeatedly generated by perturbation of the thermal layers by the remanents of older parcels. In this regime, the global structure of the flow does not change much – it remains a single cell driven by fixed upwelling and downwelling plumes on its margins. The main source of time dependence are the thermal boundary layer instabilities. Hansen et al. (1990) and Yuen et al. (1993) have termed this behavior soft turbulence.

In convecting fluids driven wholly or in part by internal heat generation, the motion becomes increasingly time dependent as the Rayleigh number is increased. Figure 9.4 from Jarvis (1984) shows spatially chaotic, multi-cellular flow in an internally heated fluid with $Ra_f = 1.5 \times 10^9$ and $r = 0.2$. Here the volumetric heat generation is so intense that the flow pattern is forced to change continually in order to efficiently remove heat from the

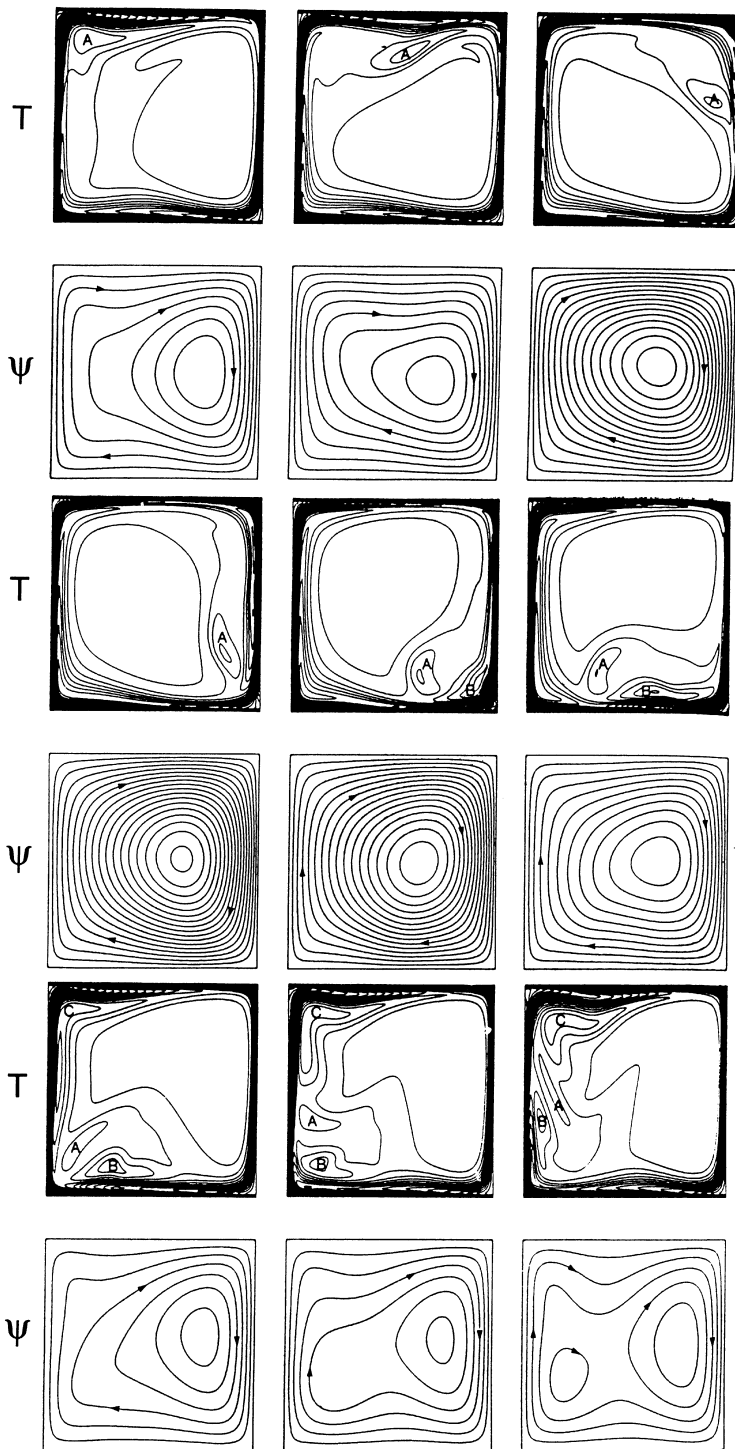


Figure 9.3. Snapshots of time-dependent convection at $Ra_q = 5 \times 10^8$ and $r = 0.1$, where Ra_q and r are the heat flow Rayleigh number and ratio of internal to basal heating, respectively, from calculations by Jarvis (1984). T is temperature and ψ is stream function. Time increases from left to right and top to bottom.

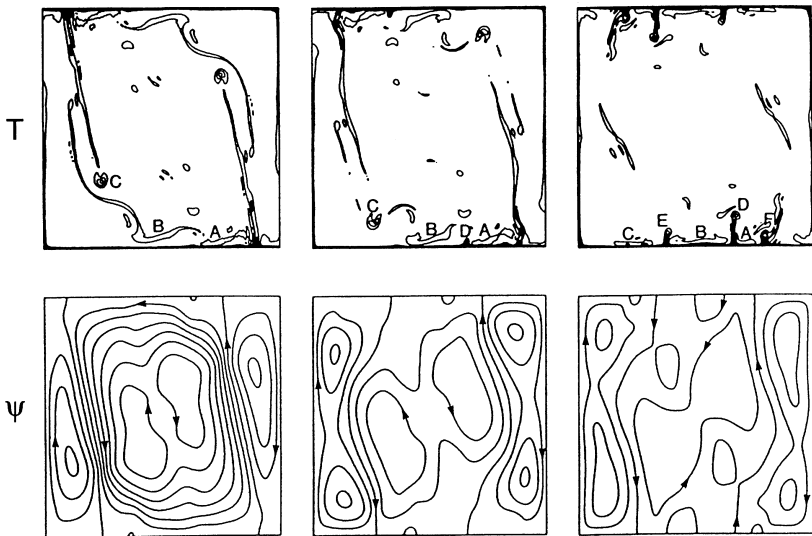


Figure 9.4. Snapshots of internally heated Rayleigh–Bénard convection at $Ra_q = 1.5 \times 10^9$ and $r = 0.2$ in the thermally turbulent regime, from calculations by Jarvis (1984). T is temperature and ψ is stream function. Time progresses from left to right.

interior. The motion is driven by the combined effects of many small transient plumes and their remnants.

Chaotic time dependence is easily excited in a volumetrically heated fluid because of the need to advect heat from the interior of cells. It also occurs in base-heated convection, when the Rayleigh number is extremely high. The transition from convection with chaotic time history but essentially stationary cell patterns (the so-called soft turbulent regime) to convection with an unorganized cell pattern (the so-called hard turbulent regime) has been shown to occur in infinite Prandtl number fluids heated entirely from below near $Ra = 10^7$, and at lower Rayleigh number if internal heat generation is present (Hansen et al., 1990, 1991; Yuen et al., 1993).

Travis and Olson (1994) have studied the time dependence of convection with internal heat sources in a two-dimensional cylindrical annulus; their results are summarized in Figures 9.5 and 9.6. The regime diagram in Figure 9.5 shows that the transitions from steady to oscillatory to soft turbulent (boundary layer instabilities) to hard turbulent (multi-cell turbulent) regimes all occur at lower Rayleigh number when internal heat sources are present. Figure 9.6 shows successive snapshots of the convection in the hard turbulent regime, which reveal that both the temperature and the flow structure reorganize on short time scales. Another example of the thermal structure in the hard turbulent regime is seen in Figure 9.7 from the base-heated, Cartesian calculations of Yuen et al. (1993).

The above flows are examples of so-called thermal turbulence, a form of turbulence in which the only nonlinearity is heat advection. Conditions in the mantle are such that some form of thermal turbulence, similar to the turbulence found in these calculations, is very likely present.

Question 9.3: Is mantle convection turbulent?

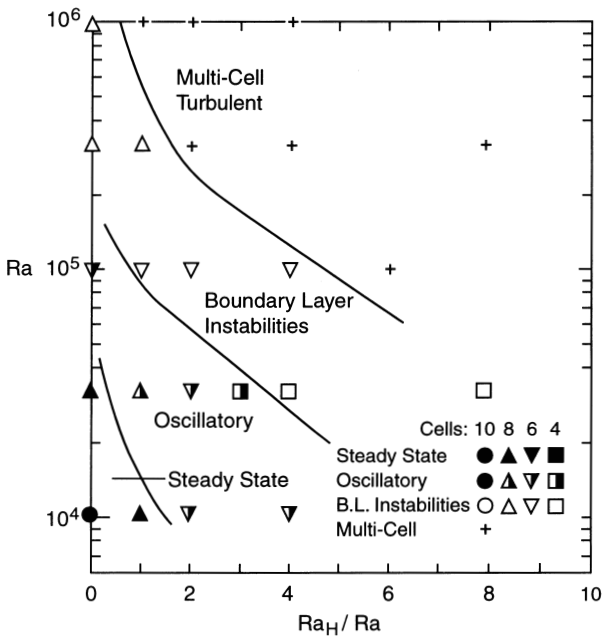


Figure 9.5. Regime diagram for two-dimensional thermal convection in an annulus with both basal and internal heating from calculations by Travis and Olson (1994). The dimensionless parameter for internal heat generation is $Q = \text{Ra}_H/\text{Ra}$.

9.4 Convection with Surface Plates

Question 9.4: How does the emergence of plates in mantle convection influence the nature of that convection?

Perhaps the most significant difference between mantle convection and thermal convection in an ordinary viscous fluid is the presence of the mobile lithospheric plates. As we have discussed in previous chapters, lithospheric plates place a set of constraints on mantle flow that make the surface motion pattern very different from that of a convecting viscous fluid. Ultimately, the theory of mantle convection should be capable of fully accounting for plate tectonic processes. That goal will be reached only when realistic models of lithospheric plate motion can be calculated directly from the equations of motion and the rheological laws governing rock deformation, without resorting to ad hoc prescriptions designed to make the surface behave in a plate-like fashion.

Short of that goal, it is still useful to examine simpler models of convection with mobile surface plates, in which either the plate geometry, the speed of plate motion, or both are imposed on the flow. These so-called intermediate models provide a tractable way to simulate some of the interactions between the lithosphere, which deforms primarily by brittle failure, and the underlying viscous mantle.

The simplest example of an intermediate model of convection with plates consists of imposing a uniform horizontal velocity boundary condition at the upper surface of a layer

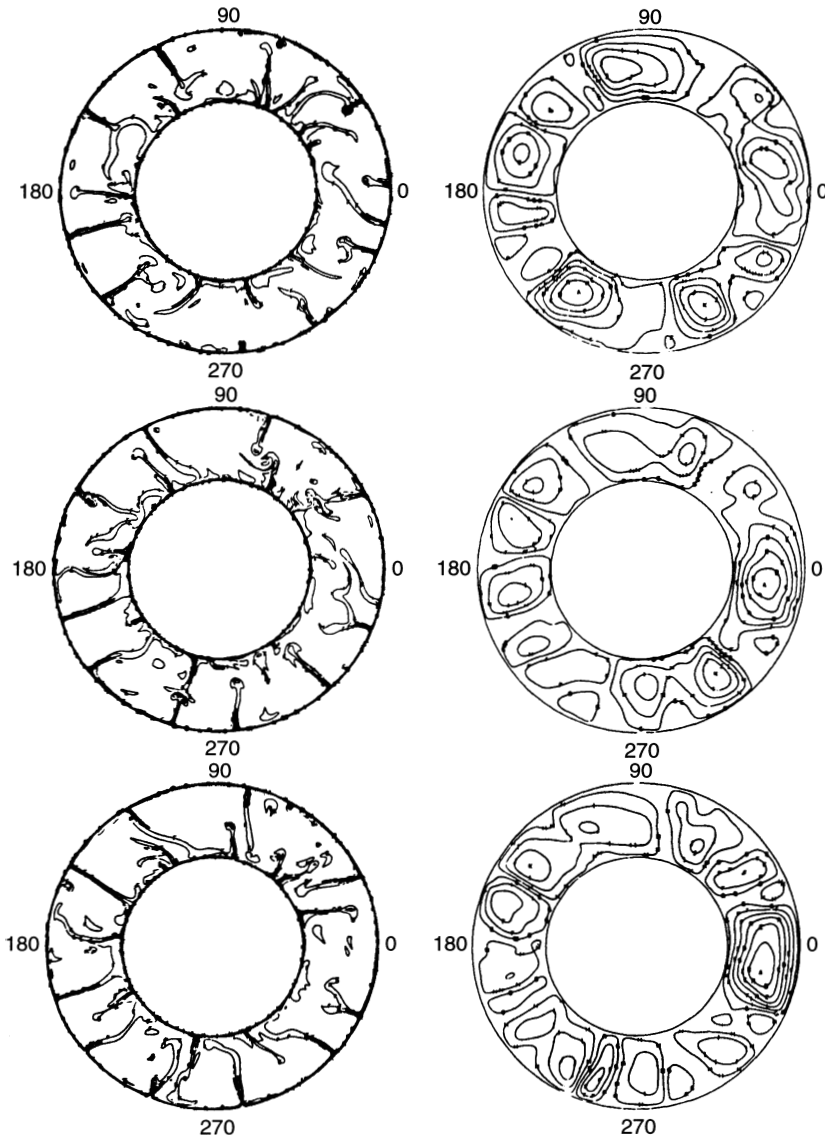


Figure 9.6. Three snapshots showing temperature (left) and stream function contours (right) for convection in a cylindrical annulus at $Ra = 10^7$ and $Ra_H = 24 \times 10^7$ ($Q = 24$), in the hard turbulent regime, from Travis and Olson (1994). The dimensionless time interval is 2×10^{-4} , corresponding to approximately 50 Myr in mantle convection. Time progresses from top to bottom.

of fluid undergoing Rayleigh–Bénard convection. Specification of the surface velocity adds another dimensionless parameter to the system, the Péclet number

$$Pe = \frac{Ub}{\kappa} \quad (9.4.1)$$

where U is the imposed surface speed. In whole mantle flow, $Pe \simeq 1–3 \times 10^3$.

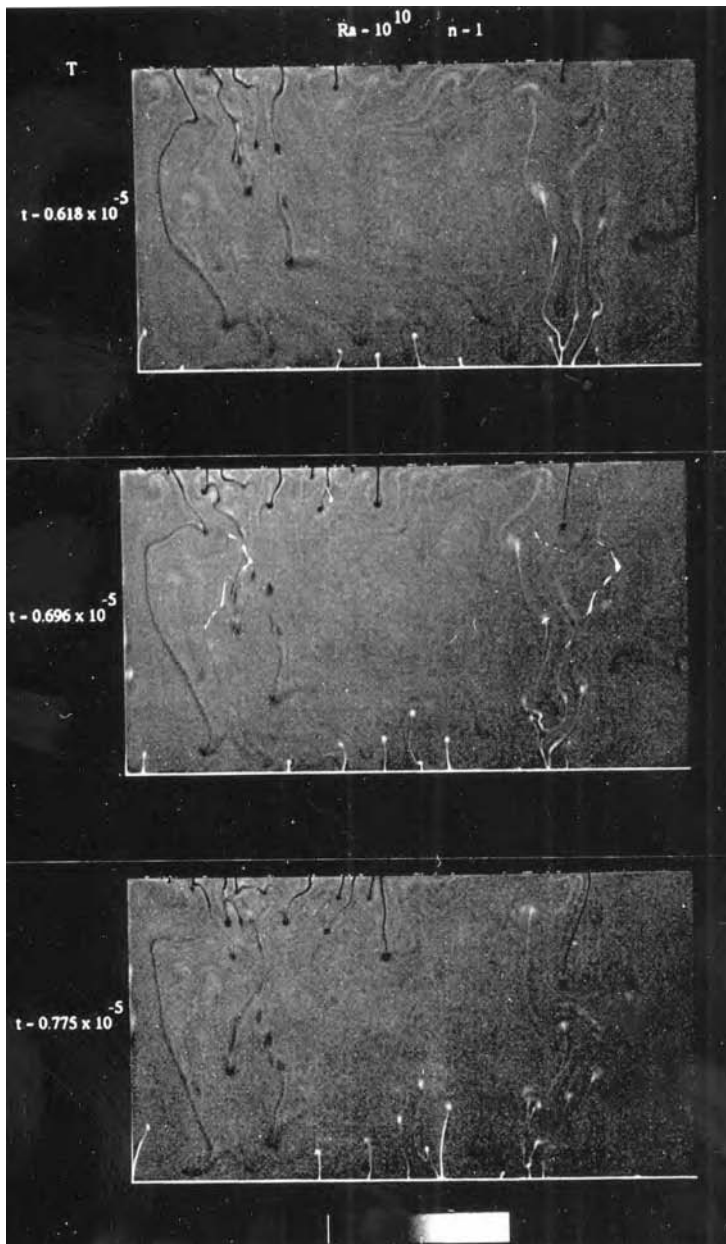


Figure 9.7. Snapshots, at three different times, of base-heated Rayleigh–Bénard convection at $Ra = 10^{10}$ in the regime of hard thermal turbulence from calculations by Yuen et al. (1993).

Figure 9.8 shows the various flow regimes as a function of Ra and Pe as determined from two-dimensional numerical models by Lux et al. (1979), and Figure 9.9 shows stream function and temperature fields for some of the cases. These figures show the transition from forced convection, in which the plate speed far exceeds the buoyancy-driven fluid velocity (high Pe), to the opposite extreme, in which the plate is essentially stationary and acts like a rigid lid (low Pe). In the forced convection limit the flow is entirely controlled by the moving

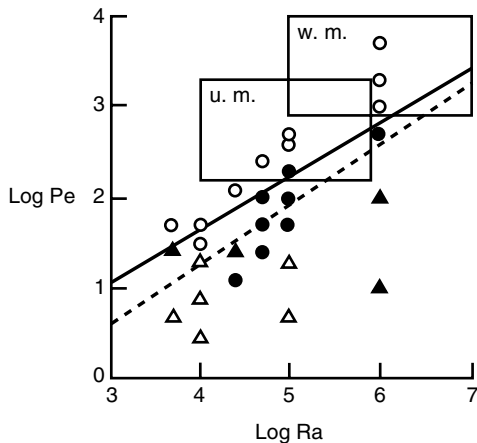


Figure 9.8. Regime diagram (log Péclet number versus log Rayleigh number) for two-dimensional Rayleigh–Bénard convection beneath a moving plate, from calculations by Lux et al. (1979). Open circles represent steady single cells; open triangles are steady multiple cells; closed circles and closed triangles are time-dependent single and multiple cells, respectively. Portions of the parameter space applicable to whole mantle (w.m.) and upper mantle (u.m.) convection are indicated by boxes.

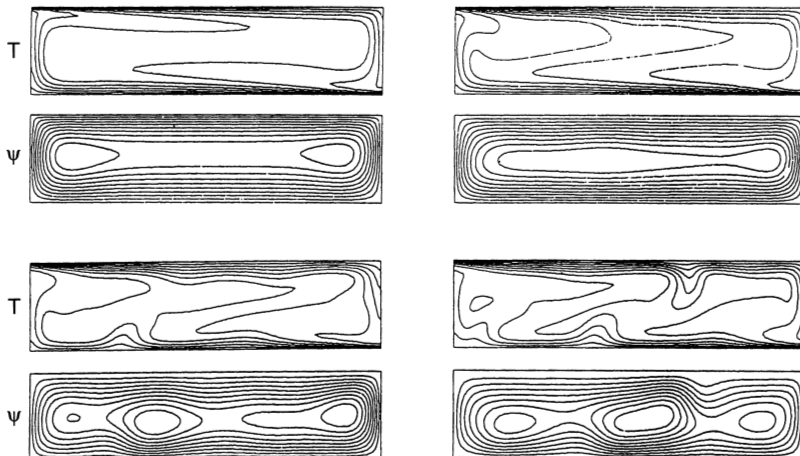


Figure 9.9. Snapshots of temperature T (top) and stream function ψ (bottom) contours from calculations of convection beneath a moving plate by Lux et al. (1979), showing the change in convective structure with decreasing plate speed. All calculations are made at $Ra = 10^5$, with the following values of dimensionless plate speed Pe : upper left, 500; upper right, 200; lower left, 100; lower right, 50.

plate and all upwellings and downwellings are located directly beneath plate boundaries. The interesting regime for the mantle is the transition between these limits, wherein the flow is time dependent and contains recurring boundary layer instabilities. In the transition regime, upwellings do not always correspond to divergent plate boundaries, but may also occur beneath plate interiors. The transition regime marks the change from net tension to net compression in the plate. Zero net force on the base of the plate corresponds to a freely drifting plate, the so-called raft condition. The balance of forces on plates presented in Chapter 2 suggests that there is some tendency for lithospheric plates to approximate this condition.

The imposition of plate velocity on two-dimensional convection is not a fully realistic model for mantle convection. Not only does it create an artificial separation between mantle

convection and plate motions, it also obscures the fact that convection beneath moving plates tends to become three dimensional (Richter and Parsons, 1975).

A somewhat more compliant way to introduce plate effects is to impose only the plate geometry as a boundary condition, and determine in the calculation the equilibrium between the convection and the plate speeds. This approach has been tried by a number of authors using various methods for achieving plate-like behavior on the top surface (Olson and Corcos, 1980; Davies, 1986, 1988a, 1989; Gurnis and Hager, 1988; Gable et al., 1991; Zhong and Gurnis, 1995a; Doin et al., 1997) and an intercomparison of a number of these calculations has been made by King et al. (1992). All these methods rely on producing weak plate boundaries and strong plate interiors, either by designating mechanically weak zones in the plate a priori or by using a nonlinear (power-law) viscosity in the plate. Figure 9.10 shows an example of a time-dependent calculation from Weinstein and Olson (1992) in which a thin surface sheet with a high power-law ($n = 11$) rheology is dynamically coupled to thermal convection in an isoviscous fluid layer. The pattern of motion in the non-Newtonian sheet consists of several segments with nearly constant velocity, separated by rather narrow zones of divergence and convergence.

Bercovici (1993) has made a careful study of how well various nonlinear viscosity laws mimic plate behavior, and finds that very strongly nonlinear viscosities, either stick-slip rheologies or power-law rheologies with power-law exponents $n > 11$, are needed to even approximate plate behavior. Since deformation experiments indicate power-law exponents $n < 5$ for mantle minerals (Chapter 5), it is clear that plate behavior is not due to power-law creep in the lithosphere alone. Rather, plate behavior results from a combination of brittle failure (faulting) and ductile creep processes that lead to localized flow at plate margins. In addition to power-law creep, other ductile flow mechanisms may be crucial to plate-like behavior. These include Peierls flow (strain rate has an exponential dependence on stress) which occurs at higher stresses than dislocation creep and a semi-brittle regime of flow (failure of the rock through distributed microcracks) which

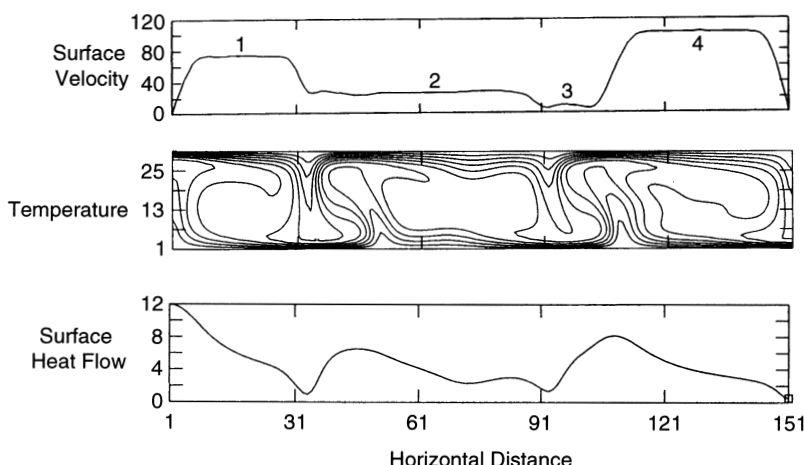


Figure 9.10. Snapshot of convection in a fluid layer at $Ra = 5 \times 10^5$ with a thin, non-Newtonian surface sheet, from Weinstein and Olson (1992). The central panel shows temperature contours, the top panel shows the surface velocity pattern (local Péclet number), and the bottom panel shows the surface heat flow pattern (local Nusselt number).

can be modeled as a ductile yield stress. Deformation in the ductile regime becomes history dependent at lithospheric temperatures because of dynamic recrystallization during creep coupled with the slowness of grain growth and annealing. These can lead to strain weakening and localization of deformation. Models based just on stress-dependent viscosity in the lithosphere provide only a crude representation of these phenomena, in part, because they do not correctly model the history-dependent weakening that fault motion and ductile creep processes provide. Later in this chapter we show some numerical calculations of subduction that incorporate motion on faults. Finally, it is important to note that two-dimensional numerical models of convection with plates do not include transverse plate boundaries (transform fault zones and oblique subduction zones) which are the primary locations of toroidal deformation in the mantle (Chapter 2). Future research on this problem will be directed toward including appropriate plate-like rheological descriptions of the lithosphere in fully three-dimensional convection models. Already there is some progress on this very challenging problem (Tackley, 1998a) as discussed in the next chapter.

9.5 Role of Phase and Chemical Changes

In Chapter 4 we showed how deflection of the equilibrium phase boundary of the exothermic olivine–spinel reaction adds buoyancy to thermal convection while deflection of the endothermic spinel–perovskite reaction reduces the buoyancy of thermal convection. The roles of exothermic and endothermic phase changes in mantle convection are also illustrated in the phase change instability problem discussed in Chapter 7. An early study by Christensen and Yuen (1985) demonstrated that the endothermic perovskite-forming reactions near 660 km depth could produce layering in mantle convection, provided the Clapeyron slope of the reaction is sufficiently steep, the critical value estimated then to be near -6 MPa K^{-1} .

The possibility of phase-change-induced layering in the mantle was taken up again several years later by a number of investigators using large-scale models of isoviscous convection at higher Rayleigh numbers (Machetel and Weber, 1991; Peltier and Solheim, 1992; Zhao et al., 1992; Solheim and Peltier, 1993, 1994a,b; Tackley et al., 1993; Weinstein, 1993). As summarized in the review by Christensen (1995), all of these studies show basically the same tendency toward layering in the presence of an endothermic phase change as the Rayleigh number of the convection is increased. Figure 9.11, from calculations by Zhao et al. (1992), shows the development of layered convection in the presence of both an exothermic phase change at 410 km depth and an endothermic phase change at 660 km depth. These same calculations indicate that the layered structure is invariably “leaky”; material occasionally crosses the phase boundary, sometimes in catastrophic “avalanches” occurring after a sufficiently large mass of negatively buoyant fluid has accumulated near the phase change (Machetel and Weber, 1991; Bercovici et al., 1993; Tackley et al., 1993; Solheim and Peltier, 1994a,b; King and Ita, 1995; Peltier, 1996b; Pysklywec and Mitrovica, 1997). One of the reasons that layering develops so readily in many of these calculations is that they assume an isoviscous mantle rheology. Cold, negatively buoyant sinking sheets are easily deflected at the endothermic phase boundary, since they have the same viscosity as the rest of the fluid. In mantle convection, most of the heat and buoyancy are transported in mechanically strong subducting slabs. Since slabs are capable of acting as stress guides and resist bending, they interact with the endothermic phase boundary differently than does an

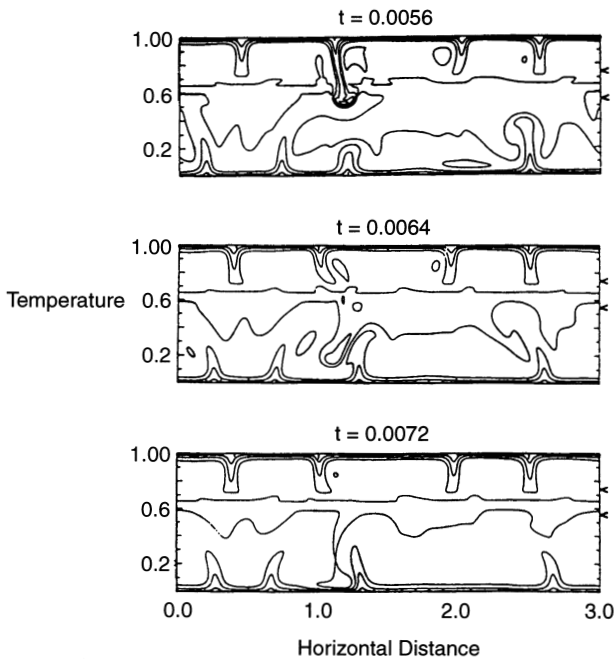


Figure 9.11. Snapshots at three successive times showing temperature contours of convection in a layer with an exothermic phase change (modeling the olivine–spinel transformation) and an endothermic phase change (modeling the spinel–perovskite phase change), from calculations by Zhao et al. (1992) with $Ra = 10^6$ and $Q = 10$. The location of the phase changes are indicated by arrows.

isoviscous sheet. We will discuss the role of the mechanical strength of subducting slabs in a later section.

The temporal behavior of phase-change-induced layering is strongly influenced, and inadequately simulated, by two-dimensional models (Cartesian or axisymmetric). Two-dimensional models with an endothermic phase change show much more episodic behavior, sometimes with oscillations between complete layering and no layering at all, than do three-dimensional models. In the fully three-dimensional model of Tackley et al. (1993) the spherical shell mantle is never totally layered; mantle avalanches occur somewhere in the shell at all times and while mass transfer across 660 km depth is decreased by local effects of retardation by the endothermic phase change, net mass flow across 660 km is never zero. In three-dimensional models with an endothermic phase change at 660 km depth there is always a whole mantle style of convection with localized cold upper mantle down-wellings temporarily stalled above the phase change leading to avalanches of material into the lower mantle. Three-dimensional models thus show a more continuous temporal behavior (in a global sense) than two-dimensional models. While two-dimensional models can appear to be completely layered at a particular instant of time, when averaged over a sufficiently long period of time, two-dimensional models show the same degree of layering as three-dimensional models (Tackley, 1997). When averaged over time, the 660 km phase change in both two-dimensional and three-dimensional models reduces the mass exchange between upper mantle and lower mantle by perhaps a factor of 2 compared to models with no phase change.

Earlier, we cautioned that two-dimensional models do not necessarily yield results that are in agreement with those of three-dimensional models. The overprediction of phase-change-induced episodicity by two-dimensional models is a prime example of this. There are several possible reasons for why two-dimensional models are more episodic than three-dimensional models (Tackley, 1997): (1) In three dimensions, downflows are cylindrical. In two dimensions they are linear (sheet-like). Cylindrical downflows penetrate the endothermic phase change more readily than linear downwellings and therefore they result in smaller, less vigorous, and more frequent avalanches (Bercovici et al., 1993). (2) Cylindrical avalanches last longer than linear avalanches and thus they have a greater chance of overlapping other avalanches in time. (3) There is a higher probability of temporal overlap of cylindrical avalanches compared with linear avalanches because it is possible to fit more simultaneous avalanches into the three-dimensional domain than the two-dimensional domain. The effects of phase changes on mantle convection in three dimensions are extensively discussed in the next chapter.

A change in bulk composition through the transition zone is another possible cause of mantle layering. In Chapter 3 we reviewed the evidence for differences in composition between the upper mantle and the lower mantle. The most important compositional difference for mantle dynamics is a possible increase in iron content with depth, which would make the mantle “bottom heavy” and tend to stabilize it against convective overturn. Silicate enrichment of the lower mantle would not have the same effect on density as iron enrichment, and its dynamical effects are more difficult to predict.

Early numerical experiments by Richter and McKenzie (1981) carried out at low Rayleigh numbers seemed to indicate that even very small compositional gradients – amounting to only 1% or so density increase from upper mantle to lower mantle – would divide mantle convection into layers. Subsequent calculations at more realistic Rayleigh numbers and including temperature-dependent viscosity (Christensen and Yuen, 1985) plus some laboratory experiments with temperature-dependent viscosity fluids (Olson, 1984) showed that a compositional density increase close to 3% is needed for layering. That amount is very near the threshold of resolution of mantle density differences (see Chapter 3) and so leaves open the question of dynamically significant differences in upper mantle versus lower mantle composition. There remains the possibility that a “phantom” change in bulk composition occurs below the 660 km discontinuity, augmenting the stabilizing effect of the spinel–perovskite phase change there. Weinstein (1992) has shown that thermal convection in a fluid with an endothermic phase change and an initially diffuse compositional gradient evolves toward a state with two homogeneous layers separated by a chemical discontinuity, with the average depth of the chemical discontinuity close to the average depth of the phase boundary. Perhaps there is an explanation in terms of convection dynamics for why compositional and phase change boundaries might coexist in the same depth range in the mantle.

Puster and Jordan (1997) have attempted to quantify the amount of layering or stratification in the Earth’s mid-mantle (600–1,500 km depth) by examining the radial correlation function of shear wave velocity anomalies in seismic tomography models. Their analysis yields a radial correlation length for shear wave velocity anomalies versus depth which is assumed to be representative of the radial correlation length of mantle temperature anomalies. The radial correlation length for temperature is used to construct a thermal stratification index which Puster and Jordan (1997) show is a good proxy for the vertical mass flux stratification index in numerical convection models with an endothermic phase change. Puster and Jordan (1997) conclude that the mid-mantle is only weakly stratified, if it is layered at all.

Question 9.5: Are there compositional changes as well as phase changes in the transition zone?

Question 9.6: To what extent is the mantle layered by the phase changes and possible compositional gradients of the transition zone?

9.6 Effects of Temperature- and Pressure-dependent Viscosity

As discussed in Chapter 5, solid-state creep processes in mantle minerals are activated by temperature and deactivated by pressure. Accordingly, mantle viscosity depends on both temperature and pressure. The temperature dependence is particularly strong, as indicated in Chapter 5.

Laboratory experiments have amply demonstrated how the temperature structure and the planform of thermal convection in oils and syrups are affected by temperature-dependent viscosity (Booker, 1976; Richter, 1978; Nataf and Richter, 1982; Richter et al., 1983; Weijermars, 1988a,b; White, 1988; Weinstein and Christensen, 1991; Davaille and Jaupart, 1993; Giannandrea and Christensen, 1993). Three basic regimes of convection are found to occur, depending on the variation in viscosity between the hot interior of the fluid and the cold surface thermal boundary layer. When this viscosity difference is relatively small, a viscosity ratio of less than about 100, the cold thermal boundary layer is mechanically similar to the rest of the fluid, and the convective planform and temperature structure are essentially the same as in isoviscous convection. For larger viscosity ratios, several thousand or less, the cold thermal boundary layer participates in the convection but deforms more slowly than the interior fluid and so controls the heat transfer and to a large extent the dissipation of kinetic energy. The planform with a stress-free upper boundary is typically large aspect ratio cells in this regime (Weinstein and Christensen, 1991; Tackley, 1993; Ratcliff et al., 1997). Finally, in experiments with still larger viscosity contrasts, the cold thermal boundary layer becomes effectively immobile (Nataf and Richter, 1982). As pointed out by Morris and Canright (1984) and by Nataf (1991), the flow in this regime resembles convection beneath a rigid or stagnant-lid. According to a scaling analysis by Solomatov (1995), the stagnant lid regime occurs when the viscosity contrast in the fluid exceeds approximately 3,000. Experimental determinations of heat transfer in fluids with temperature-dependent viscosity, although usually made with rigid boundary conditions, are generally consistent with this picture (Davaille and Jaupart, 1993; Giannandrea and Christensen, 1993).

There is always some arbitrariness in properly defining the Rayleigh number for variable viscosity convection. Two definitions have found common use. One is (9.1.5) with μ_0 the viscosity at the surface temperature, often denoted by Ra_0 . The other, usually denoted by $Ra_{(T)}$, is calculated using the viscosity of some appropriately defined average (i.e., representative) temperature. This parameter is not known a priori, and must be determined in the course of the calculation. In addition, there is a parameter characterizing the sensitivity of viscosity to temperature. A good choice for this parameter is the ratio of viscosities at the boundary temperatures $\mu(T = 0)/\mu(T = 1)$. For mantle creep this parameter is like a dimensionless activation energy. Often an exponential law is chosen to numerically approximate the activation energy formula for viscosity, in which case

the factor

$$\gamma = \ln \left(\frac{\mu(T=0)}{\mu(T=1)} \right) \quad (9.6.1)$$

is used.

Numerous authors have investigated convection with temperature-dependent viscosity as a model of mantle convection, beginning with the pioneering study by Houston and De Bremaecker (1975) and continuing with Parmentier et al. (1976), Daly (1980), Jacoby and Schmeling (1982), Tackley (1993), Christensen (1984a), Moresi and Solomatov (1995), and Ratcliff et al. (1997). Most of these authors have considered stress-free boundary conditions; Grasset and Parmentier (1998) have studied the problem using rigid boundary conditions. Figure 9.12 shows examples of calculations in the first and third convection regimes, the nearly isoviscous and the stagnant-lid regimes, respectively.

Figure 9.13 shows the variation of Nusselt number and average surface velocity as a function of Rayleigh number and viscosity ratio from Christensen's (1984a) stress-free

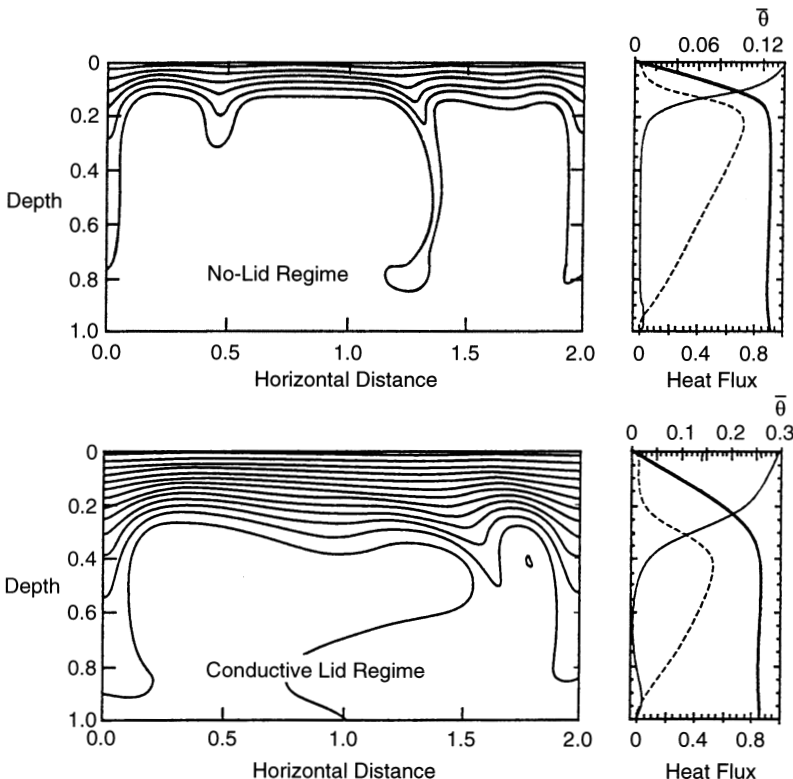


Figure 9.12. Temperature contours θ and horizontally averaged temperature profiles $\bar{\theta}$ for two-dimensional convection in an internally heated fluid with temperature-dependent viscosity, by Grasset and Parmentier (1998). Top panels show the case $Ra_0 = 10^5$ and $\gamma = 40$ in the regime of essentially isoviscous flow. Bottom panels show the case $Ra_0 = 10^4$ and $\gamma = 30$ in the stagnant (conductive) lid regime. The bold profile curve is horizontally averaged temperature $\bar{\theta}$; the dotted and solid curves are convective and conductive heat fluxes, respectively.

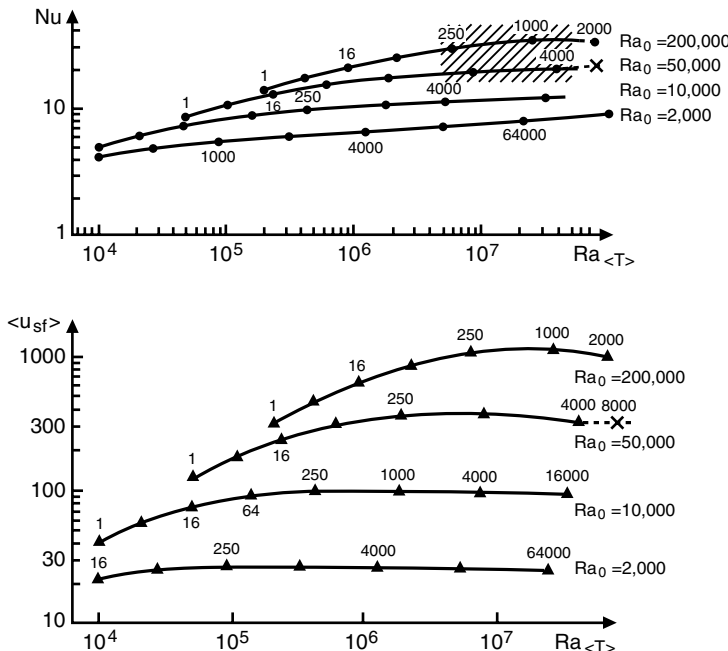


Figure 9.13. Heat transport and surface velocity in calculations of convection in a layer of fluid with temperature-dependent viscosity by Christensen (1984c). Top: Nusselt number versus Rayleigh number $Ra_{(T)}$ based on the average mid-depth temperature. The parameter Ra_0 is based on the surface viscosity and the small numbers are the surface-to-base viscosity ratio. Bottom: Dimensionless average surface speed ($\langle u_{sf} \rangle$ or Pe) for the same calculations. The shaded region is the portion of this parameter space appropriate for the mantle.

boundary calculations. The first two of the three flow regimes found experimentally are present in these results. The points labeled 1 correspond to isoviscous convection. Curves drawn through these points give a power law with exponent $\beta = 0.3185$ for the dependence of Nu on Rayleigh number and a power law with exponent approximately 2β for the Rayleigh number dependence of the average surface velocity. However, as the viscosity becomes increasingly sensitive to temperature, the slopes of the curves decrease and become almost independent of Rayleigh number. The physical interpretation is that convection in this regime is essentially controlled by the mechanical properties of the high-viscosity upper boundary layer, and is nearly independent of convection in the underlying low-viscosity fluid. In these calculations the pattern of surface motion is not plate-like. Surface velocity varies smoothly from zero at cell boundaries to a maximum near cell centers, as in isoviscous convection. But the speed of surface flow is limited by the rate of deformation in the boundary layer at the cell corners. In that respect these calculations are more similar to the mantle than are the isoviscous ones. The third regime, in which the cold thermal boundary layer is immobilized by its high viscosity, is not well represented in Figure 9.13. The stagnant-lid regime may have application to single-plate planets such as Venus, but it is not a good model for the Earth. Further discussion of these and other calculations of convection with temperature-dependent viscosity is given in Chapter 10. Still additional discussion and application to convection in the Earth and planets is given in Chapters 13 and 14.

Question 9.7: How is mantle convection influenced by the temperature and pressure dependence of rock viscosity?

9.7 Effects of Temperature-dependent Viscosity: Slab Strength

The addition of temperature-dependent viscosity allows numerical models to simulate the behavior of mechanically strong subducting slabs. Two-dimensional numerical models and laboratory experiments have proven to be very useful for addressing the important problems of how subduction initiates, and also how slabs interact with the 660 km discontinuity (Toth and Gurnis, 1998; Zhong et al., 1998).

The mechanism by which one plate begins to sink beneath another to form a subduction zone is crucial for understanding the connection between plate tectonics and convection processes at greater depths in the mantle. Figure 9.14 shows temperature and velocity fields at two stages during the initial development of a subduction zone from calculations by Toth and Gurnis (1998). In these calculations the convergence rate is specified and the model includes a pre-existing fault dipping at 30°. By varying the friction across the fault surface, a range of subduction styles is seen. The case of a weak fault is illustrated in Figure 9.14, which results in markedly one-sided subduction, a nearly stationary overriding plate, and clockwise circulation in the mantle wedge behind the trench – in agreement with the inferred structure at many subduction zones.

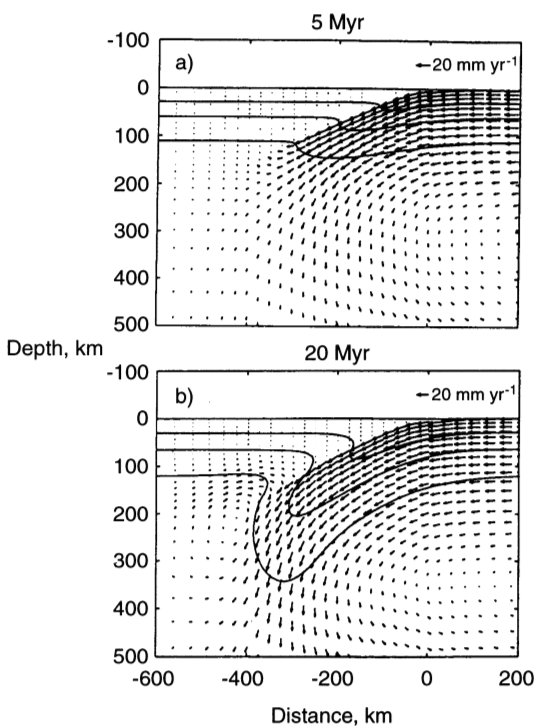


Figure 9.14. Temperature contours and velocity vectors at (a) 5 Myr and (b) 20 Myr in a two-dimensional converging flow with a pre-existing fault, from a numerical model of subduction zone initiation by Toth and Gurnis (1998).

Question 9.8: How does subduction initiate?

As noted in previous chapters, the ability of subducted lithosphere to apply a concentrated load on the 660 km discontinuity is a crucial element in the layering of the mantle and the amount of mass exchange between the upper mantle and lower mantle (Davies, 1995a; King and Ita, 1995). Indeed, the variety of morphologies among present-day slabs, as imaged by seismic tomography (see Chapter 3), suggests that the style of slab deformation varies from one subduction zone to the next, depending on variables such as subduction history, dip angle, plate age, and trench migration rate.

The amount of slab penetration into the lower mantle depends not only on the properties of the slab, but also on how the slab approaches the 660 km seismic discontinuity. Penetration is enhanced when the trench is stationary and the slab motion is entirely longitudinal, whereas penetration is reduced or eliminated when backward migration of the trench imparts a retrograde component to the slab motion (Kincaid and Olson, 1987).

Figures 9.15 and 9.16 show results of calculations by Christensen and Yuen (1984) on slab penetration through a chemical discontinuity and a nearly coincident endothermic phase

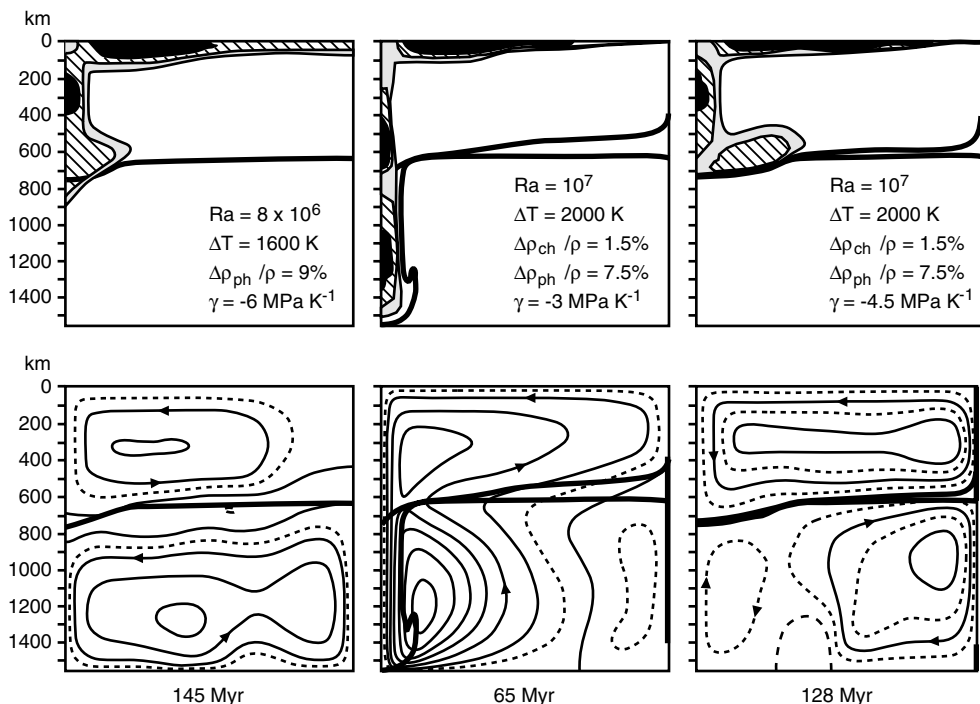


Figure 9.15. Examples of the three regimes of slab penetration across a model transition zone consisting of an endothermic phase change and a density increase due to a change in chemistry, from calculations by Christensen and Yuen (1984). Top panels show viscosity variations within the slab; bottom panels show streamlines. Dark curves are phase and chemical boundaries. Left: Leaky two-layer convection through a -6 MPa K^{-1} phase change. Center: Deep slab penetration through a -3 MPa K^{-1} phase change plus a 1.5% chemical density increase. Right: Slab deflection by a -4.5 MPa K^{-1} phase change plus a 1.5% chemical density increase.

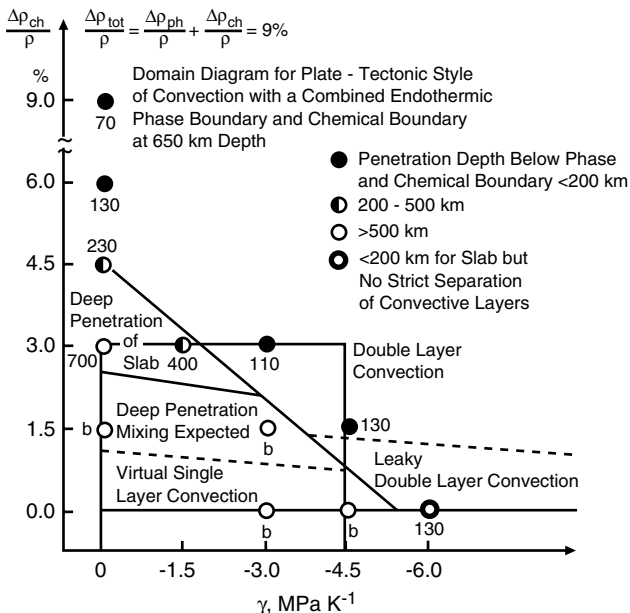


Figure 9.16. Regime diagram for slab penetration from calculations by Christensen and Yuen (1984). Axes represent increasing strengths of chemical (vertical axis) and phase change (horizontal axis) effects. The possible range of mantle parameters is indicated by the rectangular area.

boundary, for the case of a fixed trench. These calculations were made using a marker chain to represent a step in the phase function Γ in (9.1.3) to model both the chemical discontinuity and the phase change. Also, a power-law viscosity was used in the cold boundary layer to create mechanically weak zones in the upper corners of the cell, in order to obtain rapid subduction of the plate. Figure 9.15 shows three regimes of slab penetration for various combinations of the phase change Clapeyron slope and the density change due to chemistry. Figure 9.16 summarizes all the calculations in a regime diagram for depth of slab penetration below the discontinuity, and shows the range of possible models, given present uncertainties in the properties of the 660 km discontinuity. The three principal modes of slab penetration – double-layer convection, deep slab penetration with mixing, and single-layer convection – are all likely styles of slab behavior, given the present level of uncertainty in the spinel-perovskite Clapeyron slope and the possibility of a subtle change in chemical composition. The styles of slab interaction with the 660 km discontinuity due to a possible viscosity jump across the boundary (Kincaid and Olson, 1987) are similar to the modes of interaction associated with the phase change and possible chemical change properties of the transition. As a consequence of this, there will be ambiguity in attributing seismic observations of slab deformation in the transition zone to a specific property of the 660 km discontinuity.

When the retrograde motion of a trench is included, the range of possible slab deformation is even greater. Figure 9.17 shows a comparison of slab deformation styles obtained from two-dimensional numerical calculations by Christensen (1996) with laboratory experiments by Guillou-Frottier et al. (1995) for cases without and with trench motion. Without trench motion the slab penetrates the discontinuity, forming a large folded pile in the lower layer.

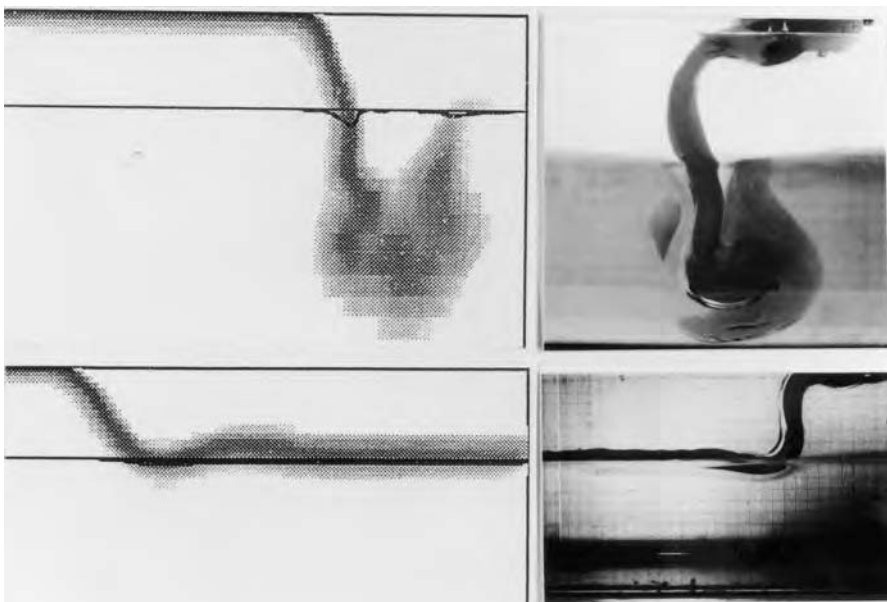


Figure 9.17. Comparison of slab deformation calculated by Christensen (1996; left) with laboratory experiments by Guillou-Frottier et al. (1995; right). Top panels show slab penetration across density and viscosity discontinuities without trench rollback. Bottom panels show slab deflection at the discontinuity with trench rollback.

The same slab subducted with trench rollback is deflected at the discontinuity and remains in the upper layer. Laboratory studies of slab descent with trench motion have also been carried out by Shemenda (1992, 1993) and Griffiths et al. (1995).

Yet another factor influencing slab behavior in the transition zone is chemical heterogeneity within the slab itself. Figure 9.18 compares deformation of a chemically homogeneous slab and a chemically differentiated slab with trench rollback at an endothermic phase boundary with a viscosity change from calculations by Christensen (1997). The homogeneous slab is partially deflected at the discontinuity, before finally penetrating the lower layer. The heterogeneous slab folds upon deflection, and by trapping low-density upper layer material within the folds, it resists penetration into the lower layer.

Seismic imaging of heterogeneity in the lower mantle beneath subduction zones indicates the presence of high-velocity structures that appear to be former oceanic lithosphere (see Chapter 3). However, the horizontal dimensions of this heterogeneity are typically greater than the nominal 100 km thickness of subducted slabs in the upper mantle. One way to account for this difference is to invoke slab buckling near the base of the transition zone as shown in Figure 9.18. Slab buckling is expected if the lower mantle is more viscous than the upper mantle as discussed in Chapter 5, because in that case the negative buoyancy of the slab is supported by contact with the lower mantle.

Figure 9.19 illustrates the influence on subduction of a 30-fold viscosity increase at mid-depth in a viscous fluid layer, from calculations by Gurnis and Hager (1988). Slabs entering the highly viscous lower layer decelerate under compressional stresses, fold into broad piles and slowly sink, forming a broad-scale downwelling that evolves on a much longer time scale than the more rapid fluctuations characteristic of the upper layer.

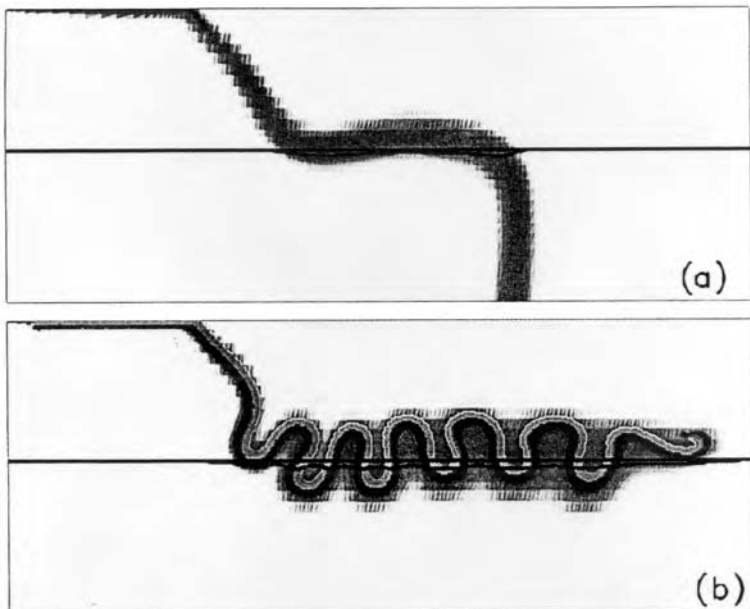


Figure 9.18. Comparison of slab deformation calculated by Christensen (1997) for (a) chemically homogeneous lithosphere and (b) chemically differentiated lithosphere interacting with an endothermic phase boundary.

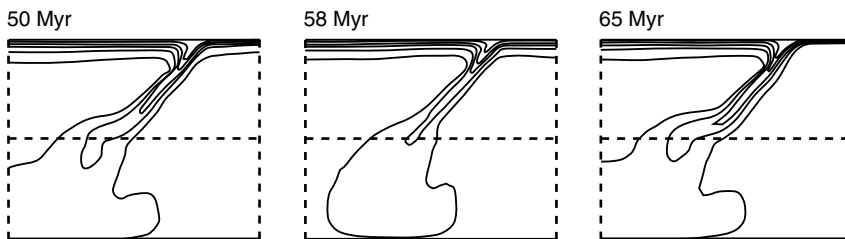


Figure 9.19. Three snapshots showing temperature contours of a slab folding on contact with a 30-fold viscosity increase, marked by dashed line, from calculations by Gurnis and Hager (1988).

Question 9.9: How do descending slabs interact with the spinel \rightarrow perovskite + magnesiowüstite phase change at a depth of 660 km?

King and Hager (1994) have studied the influence of slab strength on the geoid signal over subduction zones with a two-dimensional numerical model incorporating the temperature dependence of viscosity. Their calculations show that lateral variations of viscosity due to cold temperatures in a descending slab have only a minor effect on the long-wavelength (spherical harmonic degree 4–9) geoid which is most sensitive to radial viscosity variations.

9.8 Mantle Plume Interaction with an Endothermic Phase Change

Just as temperature-dependent viscosity has a strong influence on how slabs interact with the 660 km discontinuity, the strong temperature dependence of viscosity also affects how upwelling mantle plumes behave on encountering the endothermic phase change. As discussed in Chapter 4, a hot plume incident on an endothermic phase change causes an upward deflection of the phase change and a release of latent heat (Schubert et al., 1975). The extra amount of heavy material beneath the upwarped phase boundary relative to the undisturbed surroundings produces a downward body force opposing the upwelling of the plume. The latent heat release, on the other hand, contributes a positive buoyancy that promotes plume upwelling (Schubert et al., 1975). Phase boundary displacement is dominant in the dynamics, and the endothermic phase change acts to retard the plume; a sufficiently strong phase transition, i.e., one with a negative Clapeyron slope (dp/dT of the phase transition, where p is pressure and T is temperature) of large magnitude, could completely impede the upward progress of a mantle plume. Though the latent heat release does not play a central role in the dynamics of the plume interaction with the phase change, the additional heat supplied to a plume that rises through the phase change will substantially increase the temperature of the plume and its potential to modify the lithosphere.

The interaction of a mantle plume with an endothermic phase change has been studied by Nakakuki et al. (1994, 1997), Nakakuki and Fujimoto (1994), Steinbach and Yuen (1994a, 1995, 1997), Schubert et al. (1995), and Monnereau and Rabinowicz (1996). If the Clapeyron slope of the phase change is sufficiently negative, -3 to -4 MPa K^{-1} (Nakakuki et al., 1994; Schubert et al., 1995), the upward motion of a plume is completely impeded by the phase change. However, if the Clapeyron slope of the phase change is less negative, e.g., -2 MPa K^{-1} , a plume can penetrate the phase transition (Nakakuki et al., 1994; Schubert et al., 1995) (see Figure 10.41). The weakness of a plume (due to its low viscosity, in turn due to its higher temperature, all relative to its immediate surroundings) makes it more difficult to penetrate an endothermic phase change compared to a constant viscosity upwelling. This, of course, is opposite to the viscosity effect of descending slabs that encounter the phase change.

Plumes that reach the upper mantle after passage through the endothermic phase change are considerably hotter than plumes that rise in the absence of a phase change (see Figure 10.41). This is also seen in Figure 9.20, which shows plume centerline temperature as a function of depth in the mantle for axisymmetric and planar plumes incident on an endothermic phase change with different Clapeyron slopes (Schubert et al., 1995). In the lower mantle, temperature along the axis of the plume decreases with proximity to the phase change boundary in essentially the same way, independent of the Clapeyron slope of the phase change. The planar upflow cools much more rapidly with height above the lower boundary than does the axisymmetric plume because of the larger surface area for heat exchange with the ambient mantle in the planar case. The rate of temperature decrease with height above the lower boundary is approximately constant in the entire lower mantle for the axisymmetric plumes, but this rate decreases with proximity to the upper mantle for the planar upflows. In the absence of a phase change the plumes rise through the upper mantle with essentially no decrease in centerline temperature until very near the surface where temperature drops sharply across a thermal boundary layer to the value of the surface temperature. The plume centerline temperature in the upper mantle when there is no phase change is more than 50K hotter for the axisymmetric plume as compared with the planar upflow. When the Clapeyron slope has its most negative value and the plume is stopped from

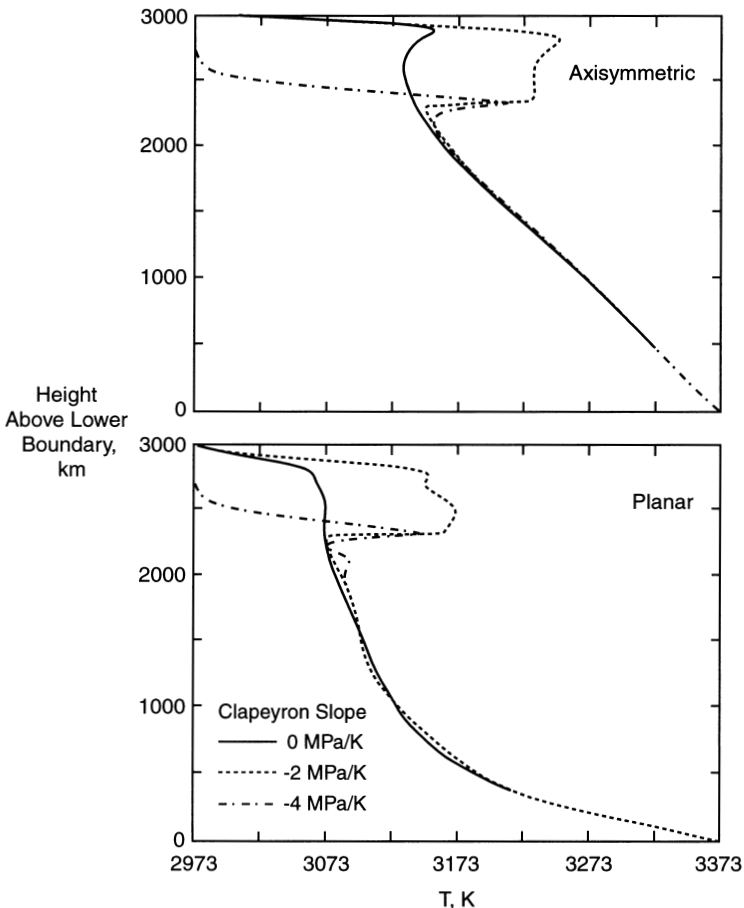


Figure 9.20. Plume centerline temperature as a function of height above the lower boundary in the numerical model of Schubert et al. (1995). Plumes encounter an endothermic phase change 660 km below the top boundary with Clapeyron slopes of 0, -2 , -4 MPa K^{-1} . The case of a Clapeyron slope of 0 MPa K^{-1} is equivalent to no phase change. For a Clapeyron slope of -2 MPa K^{-1} the plumes penetrate the phase change, but for a slope of -4 MPa K^{-1} they are stopped by the phase change. Passage through the phase change (-2 MPa K^{-1}) results in considerable heating of the plume (compare with 0 MPa K^{-1}). Axisymmetric plumes are hotter than planar plumes although both start out at the same temperature at the lower boundary.

entering the upper mantle by the phase change, there is an abrupt decrease of temperature in a thermal boundary layer at the phase change to an essentially isothermal upper mantle. In this case there is some heating of the plume by latent heat release in the vicinity of the phase boundary, and a temperature spike occurs at the boundary. When the Clapeyron slope allows plume penetration into the upper mantle, latent heat release upon crossing the phase change heats the plume considerably, and little cooling of the plume occurs in the traverse of the upper mantle until the temperature is forced to drop to the surface temperature across the surface thermal boundary layer. In the upper mantle the plumes are about 100 K hotter having passed through the phase change compared to the plumes that do not encounter a phase change. The axisymmetric plume that penetrates the phase change is about 75 K hotter in the upper mantle than its planar counterpart.

Because of plume heating through the liberation of latent heat by the endothermic phase change, plumes arriving at the base of the lithosphere have greater potential for thermally thinning the lithosphere and producing partial melts as a consequence of having passed through the phase change. Steinbach and Yuen (1994a, 1995, 1997) suggest that plume heating by the phase change could actually lead to melting in the transition zone.

The “extra” heating experienced by a plume in rising through the endothermic phase transition depends on the state of the plume surroundings. If a plume is part of a broader large-scale upwelling, then its surroundings would also be heated by passage through the phase transition and the thermal anomaly of the plume relative to its surroundings would be reduced. In the chaotic convective regime of the Earth’s mantle, it can be expected that plumes will impinge on the phase transition and enter into regions of the upper mantle that are both relatively hot and cold owing to previous episodes of upwelling and downwelling. Therefore the importance of plume heating by the endothermic phase change in determining the magmatic and volcanic consequences of a plume’s arrival near the surface will depend on the state of the upper mantle at the time. Stated differently, if the mantle in the vicinity of the phase transition were adiabatic, then the latent heat would be included in the adiabat, and a plume rising through the transition would not be heated more than its surroundings. However, owing to the accumulation of cold downflows above the phase transition and the episodic flushing of this material into the lower mantle, the mantle in the vicinity of the phase transition may be nonadiabatic.

The volumes of hot spot swells have been used to estimate the heat flux coming from the Earth’s core on the assumption that the heat content of mantle plumes (reflected in the swell volume) derives from the core (Davies, 1988b; Sleep, 1990; Davies and Richards, 1992). However, if a substantial fraction of the plume thermal content comes from the phase change heat pulse, then the inferred core heat flow would be an overestimate.

Axisymmetric structures are hotter upon reaching the upper mantle than their planar counterparts (Figure 9.20). Axisymmetric plumes are therefore more efficient than planar upwellings in bringing hot material from deep in the mantle to near the surface. This may account for the preference of plumes over planar upflows in three-dimensional models of spherical mantle convection (Bercovici et al., 1989a; Tackley et al., 1993, 1994). Some of these same models and the theoretical study of Bercovici et al. (1993) indicate that cylindrical structures penetrate the endothermic phase change more readily than planar ones.

Viscous dissipation as well as latent heat release can heat mantle plumes passing through the spinel–perovskite transition (Steinbach and Yuen, 1994a, 1995, 1997). The heating by viscous dissipation and latent heat release is enhanced by the nonlinear coupling due to temperature-dependent viscosity; the heating that occurs when plumes impinge on the 660 km phase change can also be enhanced by the depth variations of viscosity and thermal conductivity across the phase change and through the lower mantle which control the number and vigor of plumes rising from the core–mantle boundary. Plumes which stall at the 660 km phase change can spread hot material laterally and serve as a source of secondary plumes from the base of the upper mantle (Steinbach and Yuen, 1997). This phenomenon is essentially the inverse of the mantle avalanche. The heating that occurs when plumes impinge on the 660 km phase change can enhance the tendency toward layering in convection with phase changes through the coupling with temperature-dependent viscosity; basically, the heated transition zone becomes a low-viscosity region tending to separate the upper mantle from the lower mantle (Steinbach and Yuen, 1995).

Question 9.10: How do mantle plumes interact with the endothermic phase change at a depth of 660km?

9.9 Non-Newtonian Viscosity

The rheological formula used in Chapter 5 to fit experimental creep data on mantle minerals can be written in terms of the strain rate tensor $\dot{\epsilon}_{ij}$, the shear stress tensor τ_{ij} , and the effective shear stress τ (square root of the second invariant of the shear stress tensor $(\frac{1}{2}\tau_{ij}\tau_{ij})^{1/2}$) as

$$\dot{\epsilon}_{ij} = A\tau^{n-1} \exp\left(-\frac{H}{RT}\right) \tau_{ij} \quad (9.9.1)$$

where A is the pre-exponential factor, H is the activation enthalpy, R is the gas constant, T is the temperature, and n is the power-law index. $n = 1$ is found for diffusion-controlled creep and yields a Newtonian viscosity, while $3 \leq n \leq 5$ is found for dislocation creep. From this relation we can define the effective viscosity μ_{eff} as

$$\mu_{\text{eff}} = \frac{A^{-1/n}}{2\dot{\epsilon}^{(n-1)/n}} \exp\left(\frac{H}{nRT}\right) = \frac{1}{2} A^{-1} \tau^{1-n} \exp\left(\frac{H}{RT}\right) \quad (9.9.2)$$

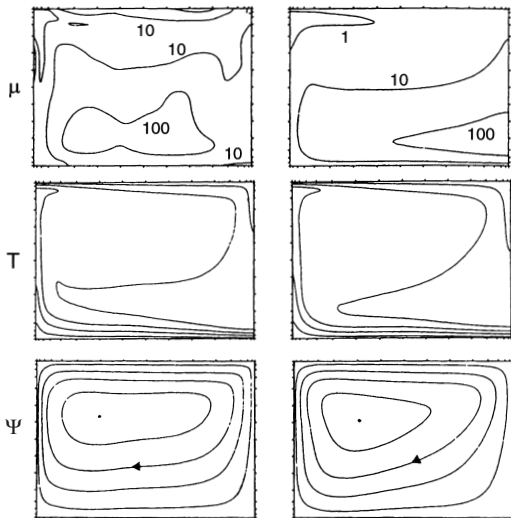
where $\dot{\epsilon}$ is the effective strain rate (square root of the second invariant of the strain rate tensor $(\frac{1}{2}\dot{\epsilon}_{ij}\dot{\epsilon}_{ij})^{1/2}$).

Systematic investigations of steady-state thermal convection using various versions of this formula for power-law viscosity have been made by Parmentier et al. (1976), Parmentier (1978), Parmentier and Morgan (1982), Cserepes (1982), and Christensen (1983a, 1984a, 1985a). The review by Christensen (1989a) summarizes the basic findings of steady-state calculations. Effects of non-Newtonian viscosity on time-dependent convection have been studied using numerical models by Christensen and Yuen (1989), Malevsky and Yuen (1992), and Larsen et al. (1996a). Van Keken et al. (1992) have investigated the nature of time dependence in convection with a Newtonian lower layer and a non-Newtonian upper layer, and as discussed earlier in this chapter, Weinstein and Olson (1992) have determined conditions for which power-law viscosity concentrated in a thin sheet above a convecting, Newtonian viscous fluid results in plate-like behavior of the upper surface.

The power-law index determined experimentally for dislocation creep, $3 \leq n \leq 5$, leads to a somewhat better approximation of plate-like behavior for the cold upper thermal boundary layer, compared to isoviscous models of thermal convection, and also has important effects on the structure of the flow, particularly when temperature and pressure dependence of the viscosity are included in the same model. The factor n appearing in the argument of the exponential term of the effective viscosity formula (9.9.2) means that the sensitivity of effective viscosity to temperature and pressure is weaker for a power-law rheology than it is for the purely temperature-dependent laws (the pressure dependence occurs through the activation enthalpy). Figure 9.21 is a comparison by Christensen (1984a) between temperature- and pressure-dependent viscosity convection with power-law exponent $n = 5$ and Newtonian viscosity ($n = 1$) convection with an activation enthalpy only one-third as large. The general similarity in flow structure is typical, and illustrates how power-law viscosity tends to modify the structure of thermoviscous convection in a way that makes it behave more like isoviscous convection.

When convection is highly time dependent, the effects of nonlinear viscosity are more dramatic. Figure 9.22 shows a sequence of snapshots of temperature and stream function

Figure 9.21. A comparison of variable viscosity convection calculations by Christensen (1984a). Left panels illustrate convection in a fluid with non-Newtonian viscosity (power-law exponent $n = 5$) and experimentally determined activation enthalpy for olivine. Right panels show convection in a fluid with Newtonian viscosity and activation enthalpy one-third of the experimentally determined value for olivine. μ is viscosity, T is temperature, and ψ is stream function. Note the logarithmic contour intervals on relative viscosity.



from a long box calculation by Malevsky and Yuen (1992) with power law $n = 3$, at an effective Rayleigh number about 1,000 times critical. The temperature field is dominated by narrow plumes and small thermals originating from thermal boundary layers, as in the case of Newtonian convection. However, the motion is highly irregular across the box, and consists at any instant of a few rapidly circulating, low-viscosity eddies, surrounded by nearly quiescent and highly viscous fluid. The vigorous eddies are driven by the most energetic plumes, which form and disappear in a transient manner, creating a shifting pattern in the flow. An interesting possible consequence of non-Newtonian convection in the mantle is large regional variations in flow velocities correlated inversely with large lateral variations in viscosity.

Examination of the behavior of localized structures in the flow reveals that the combination of temperature- and stress-dependent viscosity leads to even more radical departures from convection with uniform viscosity. With this rheology, the possibility exists for a positive feedback situation to develop in localized regions of the fluid, whereby rapid deformation and reduced viscosity couple together to produce small-scale high-velocity upwellings and downwellings (Larsen and Yuen, 1997a, b). An example is shown in Figure 9.23 from calculations by Larsen and Yuen (1997a), in which a localized instability from the basal hot thermal boundary layer ascends at speeds up to 1.5 m yr^{-1} , nearly 20 times the rms velocity of the fluid as a whole.

Question 9.11: How is mantle convection influenced by the power-law viscosity of rocks?

9.10 Depth-dependent Thermodynamic and Transport Properties

The increase in hydrostatic pressure with depth through the mantle affects both thermodynamic and transport properties, and so has a substantial effect on mantle convection, particularly where the flow extends over the whole mantle. The depth variation of three

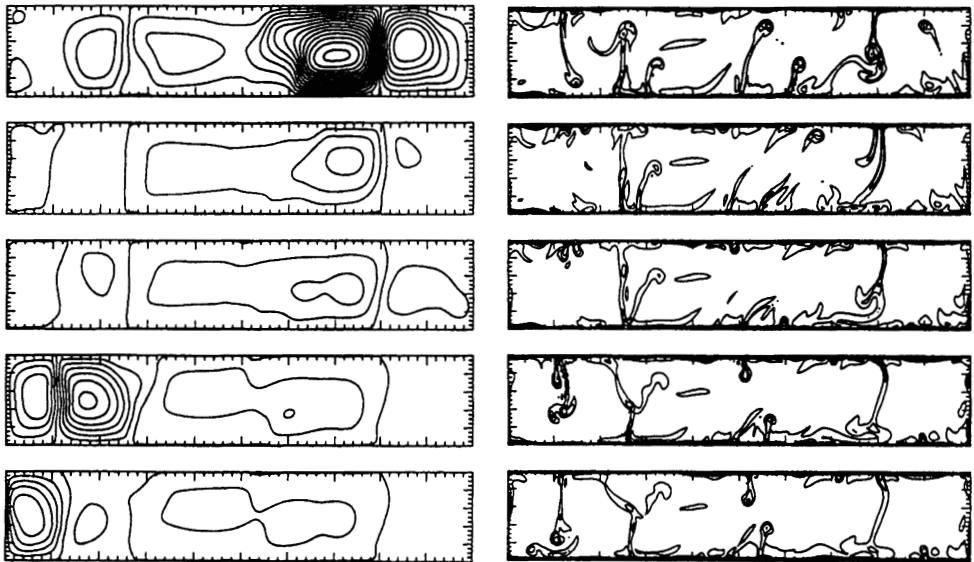


Figure 9.22. Time-dependent thermal convection in a power-law fluid with $n = 3$ by Malevsky and Yuen (1992). Shown are temperature contours (right) and stream function contours (left) at four snapshots in time (time progresses from top to bottom). Note the shifting centers of intense motion.

properties – viscosity, thermal expansivity, and thermal conductivity – are especially significant. As discussed in Chapter 5, there is mounting evidence in favor of a roughly 30-fold increase in viscosity in the region near the base of the transition zone. In addition to any step increases in viscosity at phase changes, we also expect a more gradual increase in viscosity with depth (pressure) because of the activation volume (assuming this effect overcomes the opposite effect of adiabatic temperature increase with depth) (see Chapter 5). In Chapter 4 we reviewed the evidence indicating a large decrease in thermal expansion coefficient at the pressures of the lower mantle, and we summarized the somewhat more speculative arguments for an increase in thermal conductivity at lower mantle pressures.

Considered jointly, the variation in these three properties amounts to a reduction with depth of the locally defined Rayleigh number, by a factor which may be as large as 100. This reduction implies that the characteristic time scales for flow in the lower mantle are considerably longer than for the upper mantle, so that, for example, slab material will decelerate as it enters the lower mantle. It also implies that the characteristic time scales for instability are longer in the lower mantle, so that dynamical structures originating in the lower mantle are expected to be more persistent than otherwise similar ones originating in the upper mantle.

Figure 9.24 illustrates the change in the structure of convection due to a decrease with depth of the thermal expansion coefficient α . The top panel shows temperature contours for convection at $Ra = 2 \times 10^7$ with uniform α ; the bottom panel displays temperature contours for convection with a factor 10 decrease in α with depth (Hansen et al., 1991). In the variable α calculation, Ra based on the value of α at the top surface is also 2×10^7 . Reduced buoyancy in the lower portion of the layer suppresses some boundary layer instabilities, resulting in fewer and more coherent rising plumes than in the uniform thermal expansivity case. The spatial and temporal scales of the motion tend to be larger at greater

$$Ra_{\text{eff}}=10^6, \Delta\mu(T)=600, \Delta\mu(\text{depth})=10, \Delta\alpha(\text{depth})=1/3, n=3$$

$$T_0=0.3, D_0=0.05, \text{ aspect ratio } 4$$

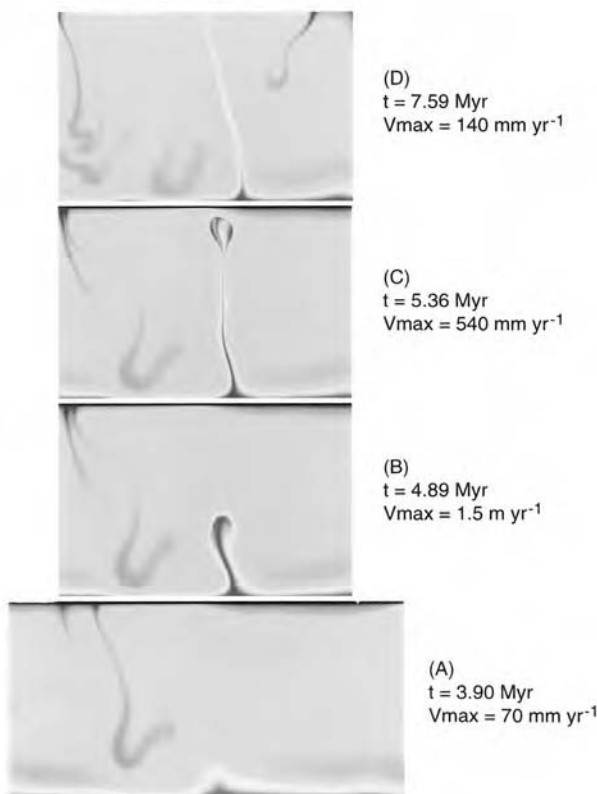


Figure 9.23. Snapshots of temperature showing development of a localized high-velocity upwelling in two-dimensional thermal convection with temperature- and stress-dependent viscosity, from calculations by Larsen and Yuen (1997a). Time increases from bottom to top at approximately 1 Myr intervals. Peak fluid velocities are 0.7, 1.5, 0.54 and 0.14 m yr⁻¹, respectively.

For a color version of this figure, see plate section.

depth. This effect has been advanced by Hansen and Yuen (1994) as a possible mechanism to explain the apparent stationarity of hot spots thought to originate in the lower mantle.

Depth-dependent properties also affect the behavior of mantle downwellings, particularly the behavior of subducted slabs. The combination of increased viscosity and decreased thermal expansivity broadens the cold thermal anomalies associated with sinking sheets, resulting in a more diffuse pattern of heterogeneity than is the case with uniform properties (Hansen et al., 1992a, 1993).

Question 9.12: How is mantle convection influenced by changes with depth in its thermodynamic and transport properties?

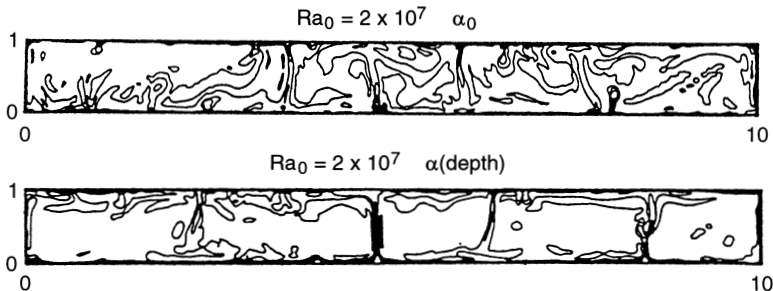


Figure 9.24. A comparison of thermal convection with uniform and depth-dependent thermal expansion coefficient α , showing snapshots of temperature contours from calculations by Hansen et al. (1991). Top panel is base-heated Rayleigh–Bénard convection with constant thermal expansion coefficient; bottom panel is similar except the thermal expansion coefficient decreases by a factor of 10 with depth. Ra_0 is based on the value of α at the top boundary.

9.11 Influence of Compressibility and Viscous Dissipation

As shown in Chapter 6 (6.10.18) the nondimensional dissipation number D determines the importance of both compressibility and viscous dissipation in thermal convection. Turcotte et al. (1974), Hewitt et al. (1975), and Jarvis and McKenzie (1980) have carried out numerical studies of the role of viscous dissipation and compressibility in thermal convection. For the Earth's mantle $D \approx 0.5$ and the influence of both compressibility and viscous dissipation on the form of global mantle convection is relatively minor. However, viscous heating can be important locally, especially in small-scale structures such as plumes and narrow downflows (van den Berg and Yuen, 1997) as we discuss in Chapter 10, where effects of compressibility and viscous dissipation are considered in greater detail in the context of three-dimensional convection.

Question 9.13: What are the effects of viscous heating on mantle dynamics?

9.12 Continents and Convection

The best delineated heterogeneity affecting mantle convection is the continental crust. Interaction between continents and mantle convection is controlled by the buoyancy of continental rocks with respect to mantle rocks which prevents large-scale subduction of continental crust. Instead of subduction, the convective history of continental crust involves repeated aggregation into supercontinents, instability of this configuration after several hundred million years, and subsequent episodes of dispersal, ultimately leading to the next aggregation. This is the so-called Wilson cycle discussed in Chapter 2.

The lower mantle structure may preserve some of the history of the Wilson cycle and provide a clue as to how it works. About 200 Myr ago, the supercontinent Pangea was located at the present-day position of the major African geoid high, presumably the site of a large-scale lower mantle upwelling. Since the breakup of Pangea most continents have drifted toward geoid lows. This behavior suggests that supercontinent breakup occurs over upwellings in the lower mantle, and during dispersal the continents drift toward lower mantle downwellings (Chase, 1979a; Anderson, 1982).

Numerical and laboratory models of the Wilson cycle explain this phenomenon in terms of the floating continental crust and lithosphere interacting dynamically with mantle convection (Gurnis, 1988; Zhong and Gurnis, 1993; Guillou and Jaupart, 1995; Lowman and Jarvis, 1995, 1996). In the dispersed state continents drift and converge toward downwellings where subduction zones tend to be concentrated. Continent–continent collisions occur at these sites, building supercontinents and terminating the subduction. Subsequently, new subduction zones form around the margins of the supercontinent, inducing upwellings beneath the supercontinent interior and leading to another episode of breakup and dispersal. According to this scenario the presence of large blocks of continental crust and lithosphere induces a long-term cycle in the structure of mantle convection in which periods of supercontinent formation alternate with episodes of continental drift.

Various parts of the Wilson cycle have been simulated with two-dimensional convection models. Figure 9.25 shows the breakup and subsequent drift of a raft on the surface of a convecting fluid layer, from calculations by Gurnis (1988). The raft is coupled to the viscous fluid and is assumed to break under tension at a specified yield stress. The raft is put into tension by the pattern of convection. An upwelling develops beneath the raft and downwellings develop along the margins of the raft, analogous to mantle plumes beneath the interior of a supercontinent and subduction zones around its perimeter. When the yield stress is reached the raft breaks and the segments begin to drift. Because of the cyclic boundary conditions, the segments collide to form another supercontinent structure and the cycle begins again.

The optimal convection pattern for breakup consists of an upwelling beneath the continent interior and downwelling beneath the margins. The central upwelling can result from thermal heterogeneity provided by the overlying continental crust, which has a higher thermal conductivity than the oceanic crust and upper mantle. The effect of this lateral heterogeneity is illustrated in Figure 9.26, which shows upwellings developing in a convecting fluid layer subject to heterogeneous thermal boundary conditions along the upper surface. To the left and the right of the tic marks, the upper boundary condition is isothermal, representing the

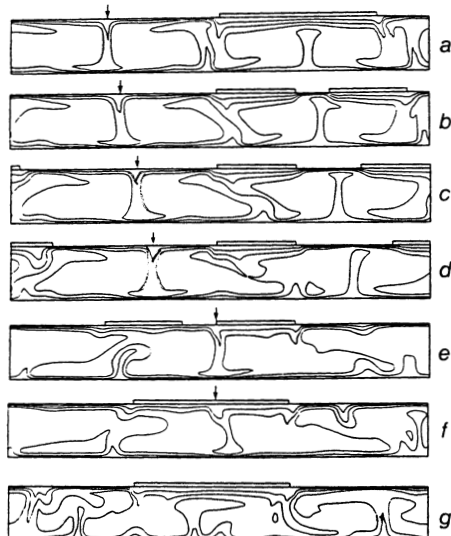


Figure 9.25. Snapshots of temperature contours illustrating the Wilson cycle in thermal convection at $Ra = 10^5$, from calculations by Gurnis (1988). A surface raft with finite yield stress, indicated by narrow strips on the upper surface, represents mobile continental crust. Arrows mark the downwelling toward which the continent segments converge. Time progresses from (a) to (g).

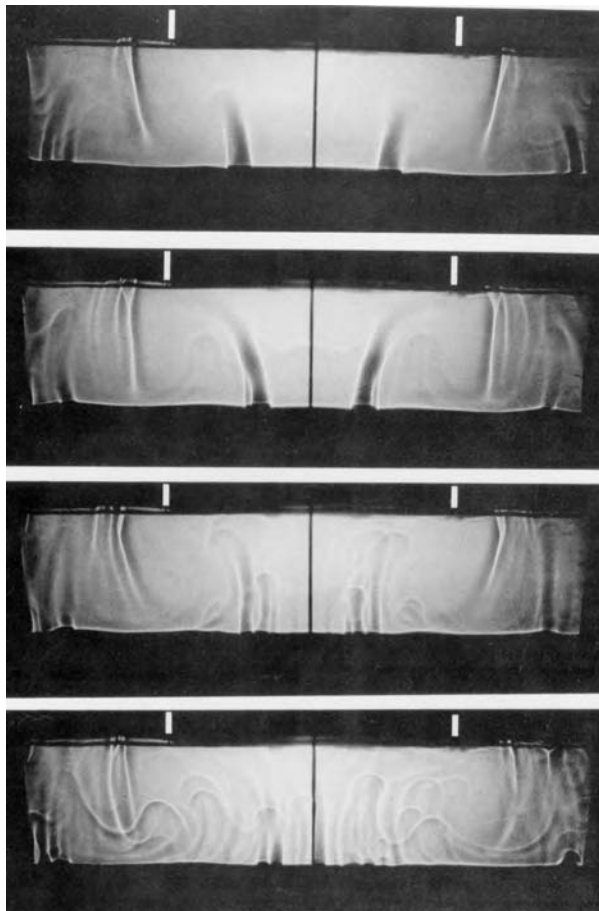


Figure 9.26. Shadowgraph images of cross-sectional temperature structure for thermal convection in a fluid layer with temperature-dependent viscosity and heterogeneous thermal boundary conditions, from experiments by Guillou and Jaupart (1995). Markers along the upper boundary indicate the extent of a high thermal conductivity strip with temperature fixed some distance above the fluid, representing continental lithosphere. Outside the markers the temperature is fixed at the fluid boundary, representing the oceanic lithosphere. Time progresses from top to bottom. Note upwelling plumes beneath the interior and descending sheets near the margins of the conducting strip.

oceanic crust situation. Within the tic marks is a thermally conducting strip with its temperature fixed at some distance above the fluid, representing the effect of the thicker continental lithosphere and the more thermally conductive continental crust. This form of boundary heterogeneity leads to slightly higher temperatures in the fluid beneath the conductive strip compared to the fluid beneath the fixed temperature regions at the same depth. Convective upwellings preferentially form beneath the conductive strip and convective downwellings preferentially form near the margins of the conductive strip.

But heterogeneity in thermal properties is not the only way to establish the optimal convection pattern for continental breakup. Heterogeneity in the mechanical condition at the surface is also able to induce an upwelling from the bottom boundary. Calculations in which continents are modeled as locally rigid patches with an otherwise free-slip boundary

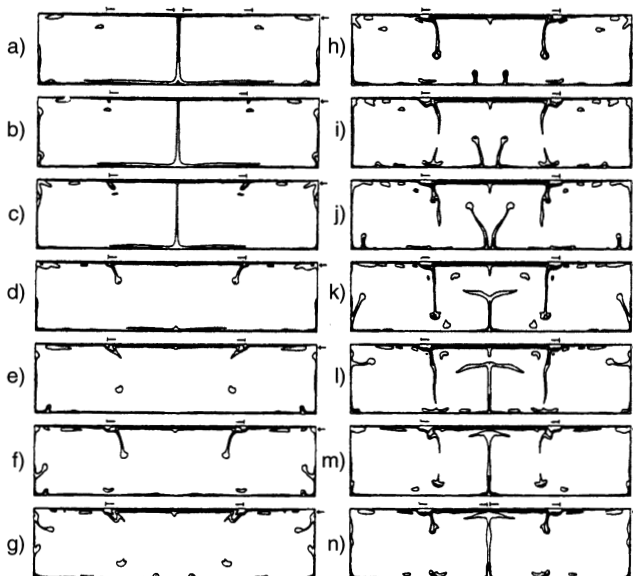


Figure 9.27. Snapshots of temperature contours illustrating the Wilson cycle in thermal convection at $Ra = 10^7$, from calculations by Lowman and Jarvis (1996). Thin surface rafts, with edges indicated by arrows along the upper surface, represent mobile continental crust. Note the flow reversal following collision. Time progresses from (a) to (n).

(mentioned above) also show a tendency for upwellings to form beneath continents, if they are wide enough. Downwellings at the edges of broad continents induce upwelling flow in between. The continental margins are preferred sites for the initiation of subduction, because the intrinsic buoyancy of the continental crust promotes formation of one-sided downwellings (Trubitsyn and Rykov, 1997). If the lateral dimension of the supercontinent approximately matches the preferred wavelength of the underlying convection, a central upwelling will naturally develop. This is illustrated in Figure 9.27 from Lowman and Jarvis (1996), which shows the evolution of convection in a two-dimensional layer with two mobile surface rafts. The rafts collide at a convergence, triggering a reversal in the flow pattern to one with marginal downwellings and a central upwelling. It therefore appears that the Wilson cycle can be explained, in the context of two-dimensional flow, by a relatively simple interaction between large rafts of continental lithosphere and mantle convection.

Not only do continental-like rafts provide an explanation for the Wilson cycle, but they also may contribute to the dominance of long wavelengths in the seismic heterogeneity spectrum of the mantle. Long-wavelength thermal structure is established by rafts in the cylindrical convection model of Zhong and Gurnis (1993). When a raft is relatively stationary, heat accumulates beneath it due to less efficient heat transfer through the raft and instabilities in the bottom thermal boundary layer. This effect establishes the large-scale thermal structure and resultant flow which enhances raft motion. Raft motion in turn diminishes the large-scale thermal structure and raft velocity decreases. The process is periodic in the model of Zhong and Gurnis (1993). Continent-ocean differences in the real Earth, like those in the model, can thus enforce large-scale structure on the mantle, as can other things such as radial viscosity variation and the endothermic phase change at 660 km depth.

Accumulations of continental crustal material can affect mantle convection in a number of other ways as brought out in a series of papers by Lenardic and Kaula (1995b, 1996), Lenardic (1997, 1998), and Moresi and Lenardic (1997). In these papers, thermal convection occurs in a chemically dense fluid below mobile, chemically light fluid that accumulates above downwellings. The chemically light fluid does not participate in the deep convection, but it is advected at the surface and forms continental crustal-like piles with thicknesses self-consistently maintained by the convective stresses applied to the base of the chemical boundary layer. In Lenardic and Kaula (1996) and Lenardic (1997) it is shown that the accumulations of crustal or chemically light material smooth out lateral variations in the heat flux supplied to the base of the chemically buoyant layer by the underlying convection; the result is a laterally near constant surface heat flux where chemically light material accumulates due to the finite thermal conductivity of the buoyant “crust.”

The thermal effect of chemically light or crustal material can be assessed by comparing the thermal resistance of the crust (thermal resistance is directly proportional to crustal thickness and inversely proportional to crustal thermal conductivity) to that of the mantle (mantle thermal resistance is directly proportional to the thickness of the upper thermal boundary layer and inversely proportional to mantle thermal conductivity). The ratio of these resistances (mantle/crust) is the Biot number. For a Biot number small compared with unity (crustal thermal resistance \gg mantle thermal resistance) a laterally near constant heat flux condition will pertain at the base of the crust, while for a Biot number large compared with unity (crustal thermal resistance \ll mantle thermal resistance) a laterally near constant temperature will pertain at the base of the crust. In the models of Lenardic and Kaula (1996) and Lenardic (1997), the Biot number is about unity, but the effect of crustal material is still to enforce the laterally near constant heat flux condition. For the Earth, the Biot number is ≥ 1 since the upper thermal boundary layer of mantle convection is several times thicker than the average continental crust and the thermal conductivities of crustal and mantle rocks are comparable.

Lenardic (1998) has used similar model calculations to show that heat loss through the oceans increases relative to heat loss through the continents as convection becomes more vigorous, i.e., as Rayleigh number increases. This provides an explanation for the so-called Archean paradox, i.e., that continental geotherms in the Archean were similar to those at present even though the Earth must have been hotter and the overall heat flow must have been larger in the Archean. Both these suppositions are reconcilable if the heat loss through the oceans was a larger fraction of the Earth’s total heat flow in the Archean compared to the present.

The effects of continental crustal material on mantle convection have been explored by Moresi and Lenardic (1997) in a three-dimensional Cartesian model similar to the two-dimensional models discussed above. As in the two-dimensional models, chemically light material accumulates in continent-like agglomerations above downwellings and, in the $1 \times 1 \times 1$ box calculations, modifies the overall planform of convection.

Doin et al. (1997) have used a two-dimensional numerical model to study how convective processes control the thicknesses of continental and oceanic lithospheres. Their model uses tracer particles to represent chemical heterogeneity and in some of their calculations chemical buoyancy is also included. Their model also includes a temperature- and pressure-dependent Newtonian viscosity; the pressure dependence of the viscosity is found to be important for the model to yield equilibrium thicknesses of about 100 km for old oceanic lithosphere. A periodic plate tectonic cycle is imposed on the model by the specification of surface velocity boundary conditions; a nonsubductible part of the surface associated with

a continent is enforced. The calculation self-consistently determines the thickness of the lithosphere beneath the continental and oceanic parts of the surface. This model is able to produce lithospheric thicknesses comparable to old oceanic lithosphere and thick cratonic lithosphere. However, convective instabilities associated with lateral density contrasts at the interface between thick continental lithosphere and thinner oceanic lithosphere gradually erode the continental lithospheric root. The convective erosion of the thick continental lithosphere is not prevented by inclusion of chemical buoyancy into the calculations. It is therefore suggested that long-term preservation of a thick continental root requires both chemical buoyancy and enhanced viscosity of the root material. The increased viscosity of the continental lithosphere must have a nonthermal origin. Devolatilization of the refractory rocks forming the continental root is one mechanism that can explain the higher viscosity of the root (Pollack, 1986).

Still other studies of how continent–ocean differences influence mantle convection have been carried out by Rabinowicz et al. (1980), Christensen (1983b), Mimouni and Rabinowicz (1988), and Walzer and Hendel (1997). These studies indicate that convection cells beneath continents can transfer heat laterally from the subcontinental mantle to adjacent oceanic regions.

Question 9.14: What are the consequences of continents for the nature of mantle convection?

9.13 Convection in the D'' Layer

The large temperature drop across the D'' layer can drive small-scale convection there (see Chapter 4). Vigorous convection in the D'' layer is enhanced by the strong temperature dependence of viscosity which can produce viscosity variations of many orders of magnitude in the layer. Olson et al. (1987) have simulated convection in the D'' layer using a two-dimensional numerical model that incorporates the temperature dependence of viscosity with an Arrhenius law. Figure 9.28 shows results from these calculations at three different times during the growth of convective instabilities in a hot lower thermal boundary layer across which temperature rises by 800 K and viscosity decreases by a factor of 10^4 . In the top panel of Figure 9.28, corresponding to a time of 47.6 Myr after diffusive thickening of the boundary layer began, convective instabilities appear in the form of quasi-periodic perturbations confined predominantly to the lowest 50 km. By 63.5 Myr (middle panel) the perturbations develop into a vigorously convecting array of hot, low-viscosity diapirs trapped within the D'' layer by overlying high-viscosity lower mantle material. Coalescence of diapirs occurs between this stage and 79.4 Myr (bottom panel), producing diapirs that eventually detach from the layer and give rise to mantle plumes. The rheology of the D'' layer controls the scale of boundary layer convection and dictates the number of diapirs that must merge in order to achieve the escape size. The initiation of mantle plumes as a thermal boundary layer instability is discussed in more detail in Chapter 11.

Convective activity in the D'' layer creates dynamic topography on the core–mantle boundary (CMB) as seen in Figure 9.28. The amplitude of CMB topography grows in step with the boundary layer instabilities and closely reflects, at each stage, the horizontal dimensions of the diapirs. At 63.5 Myr the amplitude is nearly 2 km with half-widths in the range 20–50 km. Small-scale convection in a D'' layer with a viscosity decrease of 10^4 or greater is able to produce CMB topography in accord with seismic scattering observations (Olson et al., 1987).

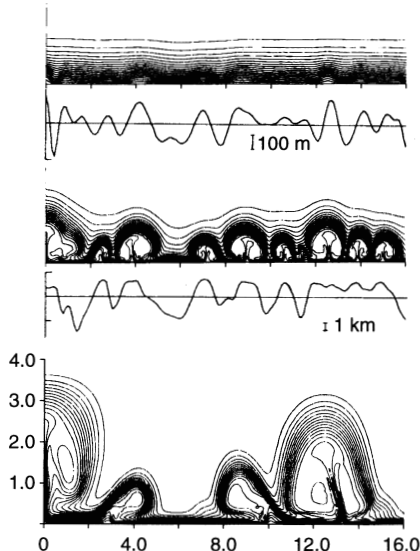


Figure 9.28. Temperature contours and core–mantle boundary topography in a two-dimensional numerical simulation of the growth of convective instabilities in the D'' thermal boundary layer with thermally activated viscosity. Vertical and horizontal axis units are 100 km and 200 km, respectively. The viscosity contrast across the thermal boundary layer is 10^4 and the three snapshots are at times 47.6, 63.5, and 79.4 Myr (top to bottom) after the imposition of an 800 K temperature increase at the lower boundary. The initial state is isothermal prior to the application of the bottom boundary increase in temperature. After Olson et al. (1987).

Regional differences in P-wave scattering may be a reflection of various stages of boundary layer and plume growth occurring simultaneously but at different locations on the CMB.

In the above model of small-scale convection in the D'' layer, the layer is assumed to be a thermal boundary layer. However, as discussed in Chapters 3 and 4, the D'' layer can be a compositional boundary layer as well as a thermal one. Compositional variations at the CMB would likely involve a layer of enhanced density at the base of the mantle. The denser material might be enriched in iron due to incomplete core formation or chemical reactions between the core and mantle (Knittle and Jeanloz, 1991). Other mechanisms for producing an extra dense layer at the CMB include segregation of the eclogite component of subducted slabs (Christensen and Hofmann, 1994) and partial melting of mantle material (Garnero and Helmberger, 1996; Williams and Garnero, 1996). If the chemically dense layer is enriched in metal it will conduct heat more efficiently than the overlying mantle (Manga and Jeanloz, 1996).

Numerical studies of how a chemically extra dense layer at the CMB affects convection in the D'' layer and overlying mantle have been carried out by Christensen (1984b), Davies and Gurnis (1986), Hansen and Yuen (1988, 1989), Farnetani (1997), Kellogg (1997), Montague et al. (1998), and Tackley (1998b). Sleep (1988b) developed an analytical model to investigate how extra dense material would be entrained into an overlying large-scale mantle circulation. Dense fluid can be entrained into an overlying convective system through cusps that form by the drag of overlying upwellings on the extra dense layer. High density in the layer retards entrainment. Sleep (1988b) estimated that a density contrast of 6% would be necessary for the extra dense layer to survive over geologic time. He noted that a dense chemical layer could convect internally and thereby entrain light material from above, further diluting the layer. Sleep's (1988b) estimate of a 6% density contrast may be an overestimate if the thermal expansivity in the D'' layer is more like $1 \times 10^{-5} \text{ K}^{-1}$ instead of the $2 \times 10^{-5} \text{ K}^{-1}$ value he assumed (see Chapter 4).

An extra dense layer at the CMB that could not mix readily with the overlying mantle would constitute an additional thermal resistance in the mantle and increase the temperature

at the CMB. Large lateral variations in heat flow from the core would occur if the extra dense material could be pushed aside by slabs arriving at the CMB. If extra dense material at the CMB could not be entrained in plumes, the hottest material would not be incorporated into plume heads, thus reducing the temperature and buoyancy of these structures (Farnetani, 1997).

Figure 9.29 shows how an extra dense basal layer influences convection in the two-dimensional numerical simulations of Montague et al. (1998). In these calculations the layer is heated from below and $Ra = 10^7$. Starting conditions included a compositionally distinct extra dense layer at the base of the rectangular box with dimensionless thickness 0.07 (equivalent to a thickness of 200 km). In Figure 9.29a, the buoyancy number B

$$B = \frac{\Delta\rho_c}{\rho\alpha\Delta T} \quad (9.13.1)$$

(ΔT is the temperature difference across the box and $\Delta\rho_c$ is the density difference due to composition), the ratio of thermal to chemical density differences, is unity. In this case the dense layer is almost flat. Upwellings in the overlying mantle cause a pile-up of dense material beneath them. Downwellings in the overlying mantle push dense material aside and depress the boundary of the chemical layer. When $B = 0.6$, Figure 9.29c, the chemical density contrast is smaller and the dense layer interacts more with the overlying convection. Downwellings push the dense material almost completely aside and upwellings form larger

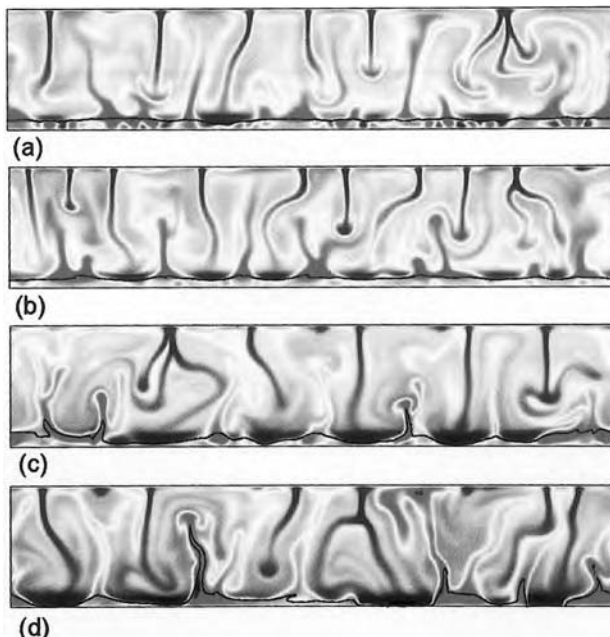


Figure 9.29. Snapshots of residual temperatures (relative to the horizontally averaged temperature) in two-dimensional, thermochemical convection with an initial dense basal layer. The thin solid line is the boundary between extra dense material and background material. (a) κ is constant and $B = 1$, (b) κ is increased by a factor of 2 in the extra dense material and $B = 1$, (c) κ is constant and $B = 0.6$, (d) κ is increased by a factor of 2 in the extra dense material and $B = 0.6$. After Montague et al. (1998).

For a color version of this figure, see plate section.

piles of dense material beneath them (compared with the case $B = 1$). When $B = 1$, Figure 9.29a, there is small-scale convection in the dense layer. There is little correlation between the small-scale convection in the dense layer and convection in the overlying region, suggesting that fine structure at the base of the mantle may not be well correlated with large-scale structure in the mantle (Montague et al., 1998). An increase in thermal diffusivity κ of the dense layer by a factor of 2, Figure 9.29b, destroys the small-scale convective motions in the dense layer. An increase in κ of the dense layer by a factor of 2 also modifies the flow considerably when $B = 0.6$, Figure 9.29d. With the more thermally conductive dense layer, plumes are hotter and entrain more dense material (compared to the case $B = 0.6$, $\kappa = \text{constant}$).

Question 9.15: Is the D'' layer a chemical boundary layer as well as a thermal boundary layer?

Question 9.16: Is there small-scale convection in the D'' layer?

10

Numerical Models of Three-dimensional Convection

10.1 Introduction

Numerical models of convection are solutions to the equations of continuity, motion, temperature and state obtained through a variety of approaches including finite difference, finite element, finite volume, Galerkin and spectral-transform techniques. Early numerical models of mantle convection were two dimensional, either planar or axisymmetric (e.g., Richter, 1973; Moore and Weiss, 1973; Houston and De Bremaecker, 1975; Parmentier and Turcotte, 1978; Lux et al., 1979; Schubert and Zebib, 1980). As discussed in Chapter 9, two-dimensional models provide insights into mantle convection and are useful to explore complex and nonlinear effects of material behavior. However, they cannot simulate the actual style of mantle convection, which is fully three dimensional. The main features of mantle convection, linear slabs, quasi-cylindrical plumes, and toroidal motion are fundamentally three dimensional in nature. In addition, two-dimensional modes of convection are often unstable to three-dimensional disturbances even at relatively low Rayleigh number (Busse, 1967; Richter, 1978; Travis et al., 1990a). Three-dimensional numerical models of thermal convection in rectangular (Cserepes et al., 1988; Houseman, 1988; Travis et al., 1990a, b; Cserepes and Christensen, 1990; Christensen and Harder, 1991; Ogawa et al., 1991) and spherical (Baumgardner, 1985, 1988; Machetel et al., 1986; Glatzmaier, 1988; Glatzmaier et al., 1990; Bercovici et al., 1989a, b, c, 1991, 1992; Schubert et al., 1990) geometries began to appear in the late 1980s and provided a more realistic picture of the form of convection in the mantle. At present, three-dimensional numerical models of mantle convection are widely carried out and ever-increasing computational power permits inclusion of increasingly realistic material properties and behavior into the models. In this chapter we discuss these solutions, progressing from simple to complex. All these solutions are based on the equations derived in Chapter 6 for the infinite Prandtl number limit.

Question 10.1: *What is the style of three-dimensional thermal convection in the mantle and how does it relate to the plates and the major structures of the mantle?*

10.2 Steady Symmetric Modes of Convection

10.2.1 Spherical Shell Convection

Although numerical models of steady, symmetric thermal convection are not directly relevant to the mantle, they are useful in gaining an understanding of the basic nature of three-dimensional convection and in validating numerical codes. Such simple modes of three-dimensional convection exist when fluid layers are heated either from below or from within and the Rayleigh number is not excessively large. Figure 10.1 shows the patterns of convection that occur in a bottom-heated spherical shell of Boussinesq fluid with constant gravity, constant viscosity, inner to outer radius ratio of 0.55, and isothermal, stress-free boundaries (Bercovici et al., 1989b). The figure shows two isothermal surfaces with dimensionless temperatures 0.2 and 0.5 at three values of the Rayleigh number (6.10.20) $Ra = 2,000, 14,000$, and $70,000$. The critical value of Ra for the onset of convection in this case is 712, so that steady, symmetric convection occurs for relatively large Ra , about 100 times the critical Ra for convection onset. The protrusions in the isotherm surfaces represent upwelling regions or plumes, and the apparent troughs are downwelling areas. If the upwellings are assumed to mark the apexes of a polyhedron, then the patterns in Figure 10.1 define two modes of convection, one associated with a tetrahedron and the other with an octahedron (the octahedron belongs to a family of polyhedrons with cubic symmetry). Modes of three-dimensional finite amplitude convection with tetrahedral and cubic symmetries exist because the critical Rayleigh numbers for convection onset Ra_{cr} with $l = 3$ and $l = 4$ (l is the degree or latitudinal wave number of a spherical harmonic mode) are almost equal ($Ra_{cr} = 712$ for $l = 3$ and $Ra_{cr} = 729$ for $l = 4$, Bercovici et al., 1989b). Nevertheless, it is rather remarkable that both these modes of steady, symmetric convection persist as far into the nonlinear regime as $Ra/Ra_{cr} = 100$. Both the cubic and tetrahedral patterns of three-dimensional convection were predicted by the perturbation analyses of Busse (1975) and Busse and Riahi (1982). The cubic pattern of convection has also been found numerically by Young (1974) and Machetel et al. (1986). Polygonal patterns of spherical convection are the analogues of hexagonal patterns of plane layer convection (Busse, 1978) which occur in plane layers without midplane symmetry (there is no midplane symmetry in the spherical shell).

The patterns of three-dimensional spherical convection shown in Figure 10.1 are further illustrated by the contours of radial velocity midway through the shell depicted in Figure 10.2. For both the tetrahedral and cubic patterns, the upwellings are cylindrical and are separated by a linear network of downwelling sheets. As Ra increases, the upwellings and downwellings become narrower and the virtually stagnant region between them widens. The maximum velocities and temperatures (not shown) occur in the upwelling plumes. In the solutions of Figures 10.1 and 10.2, the upwellings are in the form of cylindrical plumes at all depths in the shell, while the downwelling sheets break up into descending plume-like structures in the bottom of the shell (Bercovici et al., 1989b).

The vertical structure of the spherical solutions we have been discussing is illustrated by the radial profiles of spherically averaged nondimensional temperature shown in Figure 10.3 and by the isotherm distributions in cross-sectional planes shown in Figure 10.4 (Bercovici et al., 1989b). As Ra increases, a large central portion of the shell becomes more stably stratified, the upper and lower thermal boundary layers become thinner (Figure 10.3), and the upwelling and downwelling regions narrow (Figure 10.4). The thermal boundary layers at the top and bottom of the shell have essentially the same thickness (Figure 10.3, see also Zebib et al., 1980). The temperature change across the bottom thermal boundary layer

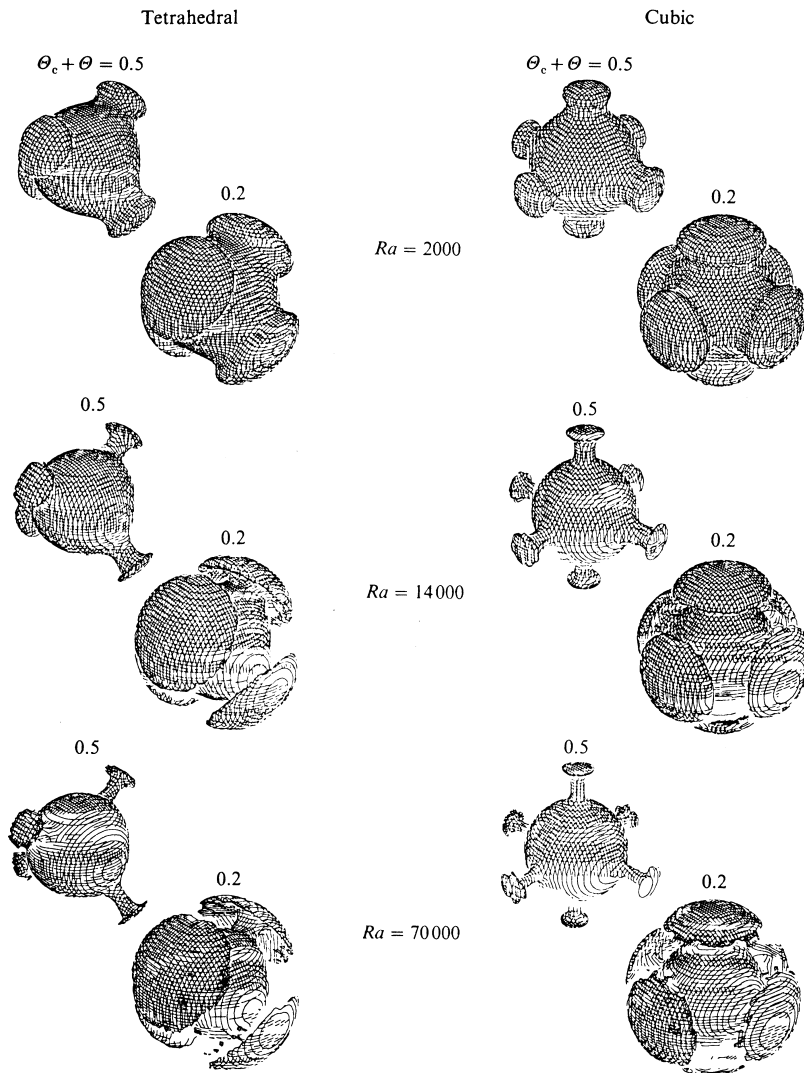


Figure 10.1. Three-dimensional isothermal surfaces for tetrahedral and cubic patterns of convection in a bottom-heated spherical shell of Boussinesq fluid with constant gravity and inner to outer radius ratio 0.55 at $Ra = 2,000$, $14,000$, and $70,000$. The shell has isothermal, stress-free boundaries. Two isotherms are shown for each case corresponding to dimensionless temperatures $\Theta_c + \Theta$ of 0.2 and 0.5, where Θ_c is the lower boundary temperature. After Bercovici et al. (1989b).

is about $(1/0.55)^2$ times the temperature change across the top thermal boundary layer (Figure 10.3), in accordance with energy conservation for these steady modes of convection which requires equality of heat flow into and out of the shell at the bottom and top boundaries, respectively.

The heat fluxes carried by the cubic and tetrahedral modes of convection are compared by the Nusselt number Nu versus Rayleigh number Ra curves in Figure 10.5 (Bercovici et al., 1989b; Iwase and Honda, 1997). The cubic mode of convection transports more heat than the tetrahedral mode, but it is not in any sense a preferred mode of convection. Initial

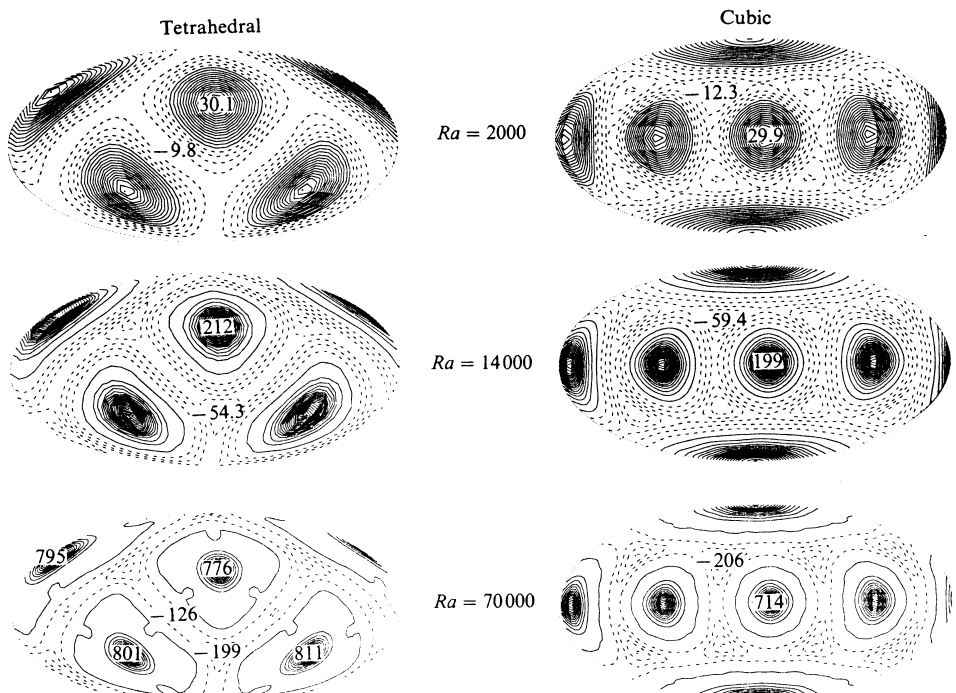


Figure 10.2. Radial velocity contours (in a Hammer-Aitoff equal-area projection) of the tetrahedral and cubic patterns of convection on a spherical surface midway through the shell for $Ra = 2,000$, $14,000$, and $70,000$. Dashed contours indicate downwelling and solid contours denote upwelling; the solid contour separating the negative velocity region from the positive one is the zero value contour. The numerical values are the maximum upwelling and downwelling nondimensional velocities; the other upwelling and downwelling areas have the same maximum velocities as those shown, unless otherwise indicated. After Bercovici et al. (1989b).

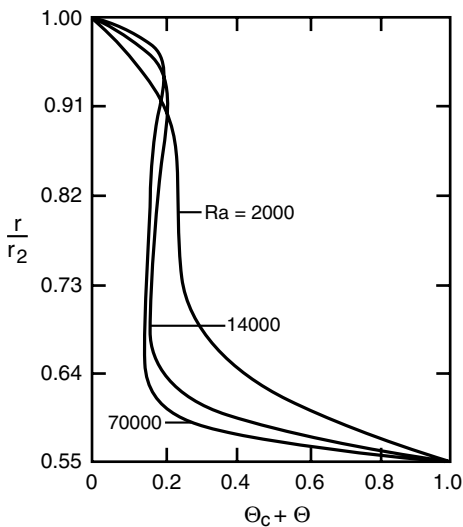


Figure 10.3. Spherically averaged radial profiles of nondimensional temperature $\Theta_c + \Theta$ at $Ra = 2,000$, $14,000$, and $70,000$ for the tetrahedral pattern of convection (the profiles of the cubic pattern of convection are essentially identical). r_2 is the outer radius of the spherical shell and r is the radial coordinate. After Bercovici et al. (1989b).

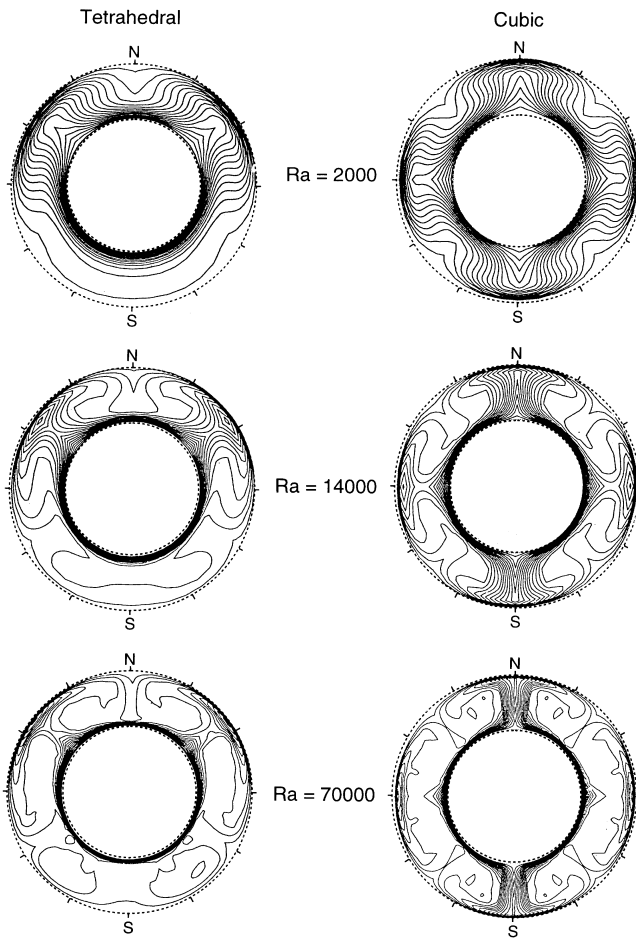


Figure 10.4. Isotherms in a cross-sectional plane for the tetrahedral and cubic convection patterns at $Ra = 2,000$, $14,000$, and $70,000$. After Bercovici et al. (1989b).

conditions determine which pattern of steady convection, cubic or tetrahedral, is realized in any numerical experiment. The maximum heat flow at a boundary occurs where vertically moving fluid impinges on the boundary (downwellings at the bottom, upwellings at the top) since the fluid increases the temperature contrast at the boundary and compresses the isotherms in the boundary layer; the minimum heat flow at a boundary occurs where fluid moves away from the boundary since the fluid has almost the same temperature as the boundary and its motion pulls the isotherms towards the middle of the shell (Figure 10.4).

Steady tetrahedral (degree $l = 3$ and order $m = 2$ dominant spherical harmonic signature) and cubic (degree $l = 4$ and orders $m = 0, 4$ dominant spherical harmonic signature) patterns of three-dimensional convection in a spherical shell also occur when the viscosity depends strongly on temperature. Ratcliff et al. (1996a) have systematically investigated these flows in a bottom-heated spherical shell with inner to outer radius ratio of 0.55 filled with a Boussinesq fluid whose viscosity μ is proportional to $\exp\{-E(T - T_{\text{ref}})\}$ (E is an activation parameter, T is temperature, and T_{ref} is a reference temperature). The shell

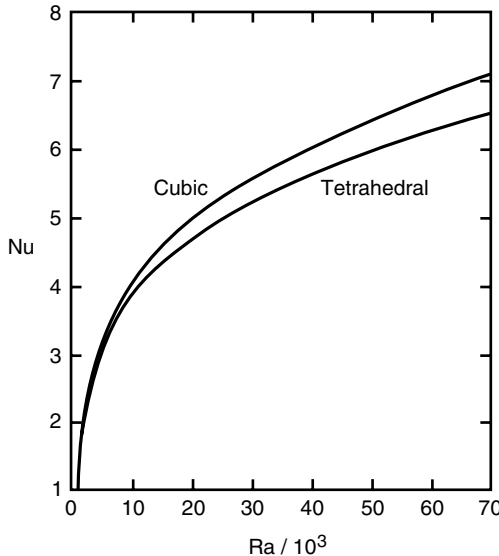


Figure 10.5. Nusselt number versus Rayleigh number for cubic and tetrahedral modes of convection in a bottom-heated spherical shell with inner to outer radius ratio of 0.55. After Bercovici et al. (1989b).

boundaries are impermeable, isothermal, and shear stress free. The solutions depend on two dimensionless parameters: the Rayleigh number Ra (with viscosity evaluated at the mean of the boundary temperatures) and r_μ the ratio of the maximum to the minimum viscosity (the ratio of viscosity evaluated at the upper cold boundary temperature to viscosity evaluated at the lower hot boundary temperature). Interpretation of the results is facilitated by knowledge of the spherical harmonic mode critical Rayleigh numbers for the onset of convection Ra_{cr} summarized in Table 10.1. It is seen that for $r_\mu \leq 100$, the minimum Ra_{cr} occurs for $l = 3$, while for larger values of r_μ up to 10^3 , the minimum Ra_{cr} occurs for $l = 2$. For tetrahedral convection $l = 3$ is the dominant mode while for cubic convection $l = 4$ is predominant.

The three-dimensional structure of the tetrahedral convection pattern can be seen in the temperature isosurfaces of Figure 10.6. These surfaces enclose all fluid with a nondimensional temperature larger than $T = 0.2$ (which is roughly the mean temperature

Table 10.1. Critical Values of Ra for Convection Onset in a Spherical Shell of Fluid with Strongly Temperature Dependent Viscosity

r_μ	$l = 1$	$l = 2$	$l = 3$	$l = 4$	$l = 5$	$l = 6$
1	1,864.34	888.84	(711.95)	729.38	851.31	1,063.95
3	2,010.85	967.48	(781.31)	805.06	943.04	1,181.35
10	2,136.65	1,085.05	(913.73)	963.07	1,135.81	1,418.09
20	2,193.76	1,172.09	(1,022.25)	1,095.56	1,296.29	1,610.44
25	2,210.50	1,203.92	(1,062.94)	1,145.28	1,356.00	1,681.00
30	2,223.80	1,231.46	(1,098.41)	1,188.52	1,407.66	1,741.61
40	2,260.40	1,316.96	(1,209.05)	1,322.58	1,566.04	1,924.74
100	2,313.49	1,456.04	(1,387.91)	1,535.20	1,811.01	2,199.60
500	2,511.45	(1,918.44)	1,945.51	2,153.50	2,471.15	2,880.75
700	2,578.46	(2,046.56)	2,088.10	2,299.43	2,614.08	3,014.69
1,000	2,663.98	(2,196.39)	2,248.43	2,457.29	2,762.52	3,147.63

Note: The minimum critical value Ra_{cr} for each viscosity ratio is shown in parentheses.
After Ratcliff et al. (1996a).

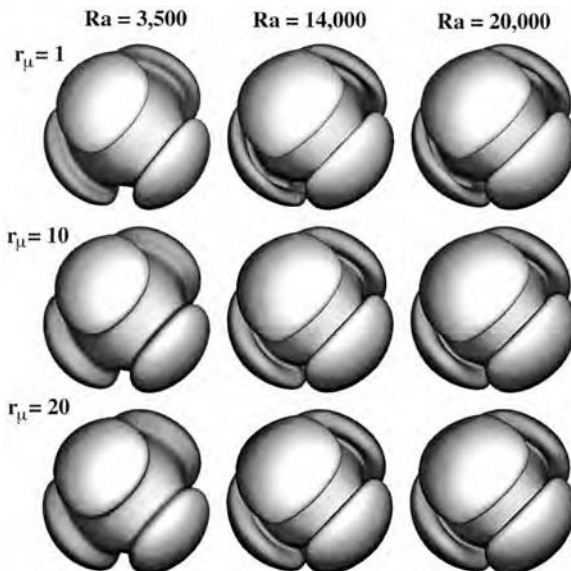


Figure 10.6. Temperature isosurfaces (nondimensional temperature = 0.2) for steady tetrahedral convection with strongly temperature dependent viscosity. Ra is based on the viscosity evaluated at the mean of the boundary temperatures. After Ratcliff et al. (1996a).

of the interior). Temperature isosurfaces for calculations at several values of Ra and r_μ are included in the figure. As convective vigor is increased (i.e., increasing Ra at fixed r_μ), more hot fluid is advected toward the surface, increasing the size of the upwelling plume heads. In addition, the thermal boundary layers become thinner, as evidenced by the narrowing of the plume conduits. The combination of a thinner upper boundary layer and larger plume heads forces the downwelling fluid into narrow, sheet-like structures near the surface. Where downwelling sheets intersect, flow is focused into cylindrical downwellings. Increasing the viscosity contrast at constant Rayleigh number has an opposite but less pronounced effect, tending to round the edges of the plume heads and slightly thicken the $T = 0.2$ isotherm of the plume conduits. Examination of the horizontally averaged radial profiles of temperature, flow speed, and viscosity leads to similar conclusions about the nature of the flows. Figure 10.7 compares radial profiles from the three calculations comprising the bottom row of isosurfaces in Figure 10.6; viscosity contrast is fixed at $r_\mu = 20$ and Ra varies from 3,500 to 20,000. The thinning of the thermal boundary layers with increasing Rayleigh number can be clearly seen in the temperature and viscosity profiles. Figure 10.8 shows similar radial profiles for cases with Ra fixed at 14,000 and r_μ varying from 1 to 20 (center column of isosurfaces in Figure 10.6). The temperature profiles show a slight thickening of the thermal boundary layers and a small increase in the temperature of the interior with increasing r_μ . The interior temperature increases with viscosity contrast, because as the viscosity of the cold upper boundary layer increases (Figure 10.8, right), the cold, viscous fluid is less able to participate in the convective motions and is thus less efficient at transferring heat from the interior to the surface.

Isosurfaces of constant temperature for the cubic solutions are shown in Figure 10.9. Because the cubic solutions are stable over a larger range of Rayleigh number and viscosity contrast compared to the tetrahedral solutions, differences between the temperature

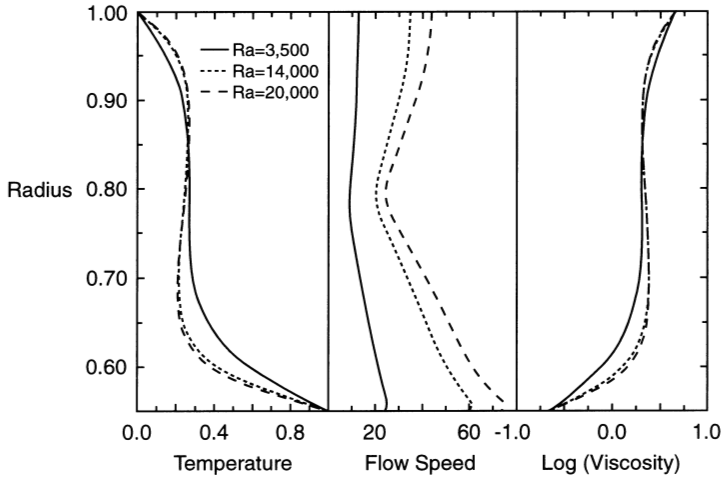


Figure 10.7. Horizontally averaged radial profiles of dimensionless temperature, flow speed, and viscosity at $r_\mu = 20$ for the tetrahedral solutions shown in the bottom row of Figure 10.6. After Ratcliff et al. (1996a).

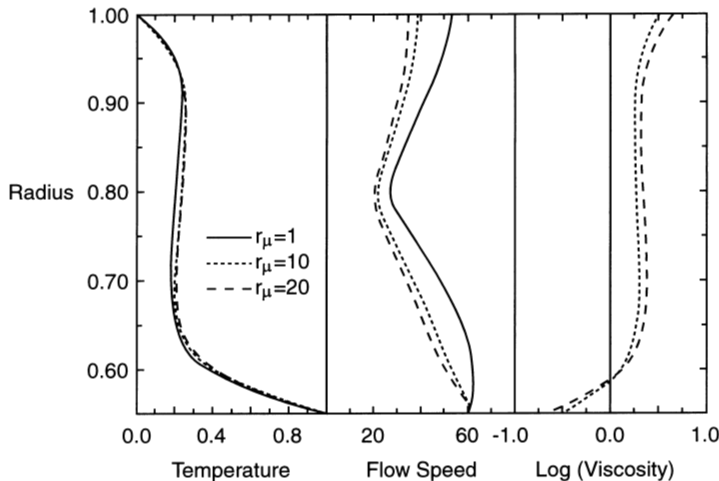


Figure 10.8. Horizontally averaged radial profiles of dimensionless temperature, flow speed, and viscosity at $Ra = 14,000$ for the tetrahedral solutions shown in the middle column of Figure 10.6. After Ratcliff et al. (1996a).

isosurfaces at different values of Ra and r_μ are more prominent in the cubic case than they are in the tetrahedral case. The effects of increasing Rayleigh number are particularly noticeable in the isoviscous calculations (top row of the figure) with the extreme narrowing of the plume conduits. Thickening and rounding of the plume heads is also more evident as viscosity contrast is increased. As a consequence of the plume head thickening, downwelling flow is able to maintain a sheet-like character to greater depths (notice the rightmost column of isosurfaces, for instance). Thermal boundary layer thinning with increasing Rayleigh number is also more distinct in the radial profiles of horizontally averaged temperature and viscosity

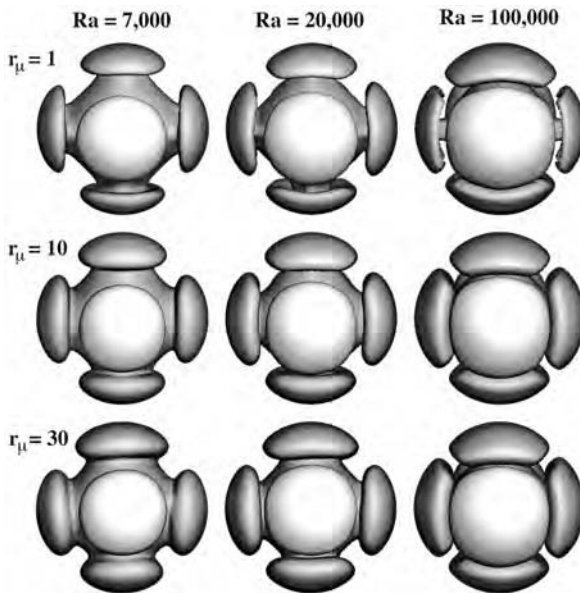


Figure 10.9. Temperature isosurfaces (nondimensional temperature = 0.2) for steady cubic convection in a spherical shell of fluid with strongly temperature dependent viscosity. Ra is based on the viscosity evaluated at the mean of the boundary temperatures. After Ratcliff et al. (1996a).

of the cubic cases in Figure 10.10 compared with the tetrahedral cases in Figure 10.7, since Ra varies over a greater range for the cubic solutions. The radial profiles of horizontally averaged temperature, flow speed, and viscosity in Figure 10.11 for different r_μ and fixed Ra display interior warming and sluggish-lid formation with increasing r_μ , similar to the tetrahedral cases.

The heat flux transported by these steady modes of convection with strongly temperature dependent viscosity is given by the Nu - Ra results summarized in Figure 10.12. The figure shows that if Ra is scaled by Ra_{cr} , then Nu does not depend explicitly on r_μ ; instead, the following simple relations pertain for $(Ra/Ra_{cr}) \gtrsim 10$:

$$Nu = 2.02 \left(\frac{Ra}{Ra_{cr}} \right)^{0.25} \quad (\text{steady tetrahedral convection}) \quad (10.2.1)$$

$$Nu = 2.12 \left(\frac{Ra}{Ra_{cr}} \right)^{0.26} \quad (\text{steady cubic convection}) \quad (10.2.2)$$

The Nu - (Ra/Ra_{cr}) relations in (10.2.1) and (10.2.2) are similar to each other and to the isoviscous results of Bercovici et al. (1989b), who obtained a power-law exponent of 0.26 for tetrahedral flows and 0.28 for cubic flows. This result suggests that the isoviscous Nu - Ra relation can be made relevant to planetary thermal history calculations that use the approach of parameterized convection and account for the strong temperature dependence of mantle viscosity by scaling Ra with Ra_{cr} , though it is not clear that this approach will work when viscosity variations are large enough to result in stagnant-lid convection (see Chapters 13 and 14).

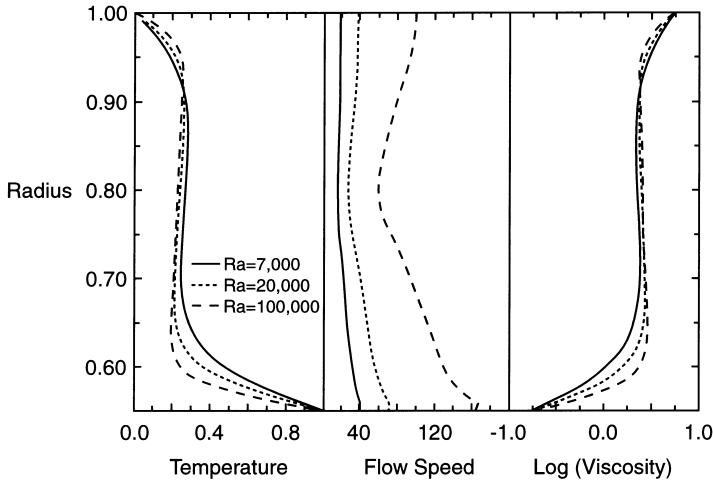


Figure 10.10. Horizontally averaged radial profiles of dimensionless temperature, flow speed, and viscosity at $r_\mu = 30$ for the cubic solutions shown in the bottom row of Figure 10.9. After Ratcliff et al. (1996a).

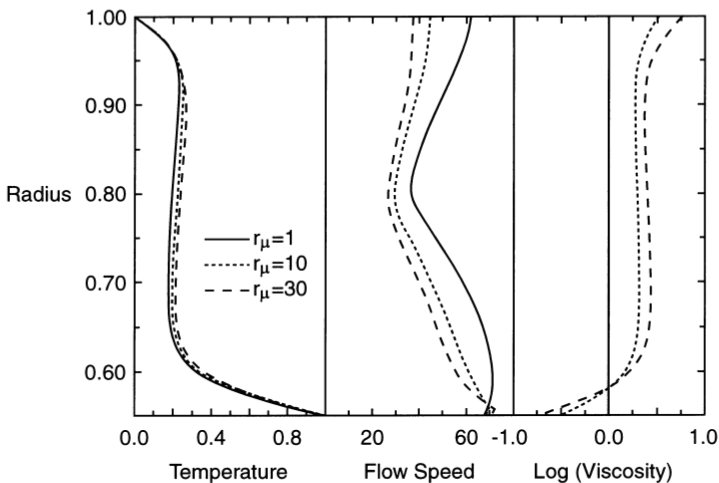


Figure 10.11. Horizontally averaged radial profiles of dimensionless temperature, flow speed, and viscosity at $Ra = 20,000$ for the cubic solutions shown in the middle column of Figure 10.9. After Ratcliff et al. (1996a).

Steady tetrahedral and cubic patterns of convection exist only for relatively small values of viscosity contrast $r_\mu \lesssim 30$, much less than values of r_μ that pertain to planetary interiors. At larger values of r_μ convection is nonsteady and convection planforms are generally more complex, without the simple symmetries of the tetrahedral and cubic patterns discussed here. The tetrahedral and cubic solutions presented above demonstrate the tendency of convection with strongly temperature dependent viscosity to form a sluggish lid as r_μ is increased (illustrated in the velocity profiles of Figures 10.8 and 10.11). The sluggish lid is a region of cold viscous fluid near the upper boundary that participates less strongly in the convective motions as viscosity contrast is increased. Indeed, as r_μ is increased to a value large enough, the sluggish lid becomes essentially immobile and a stagnant lid is formed. As discussed in

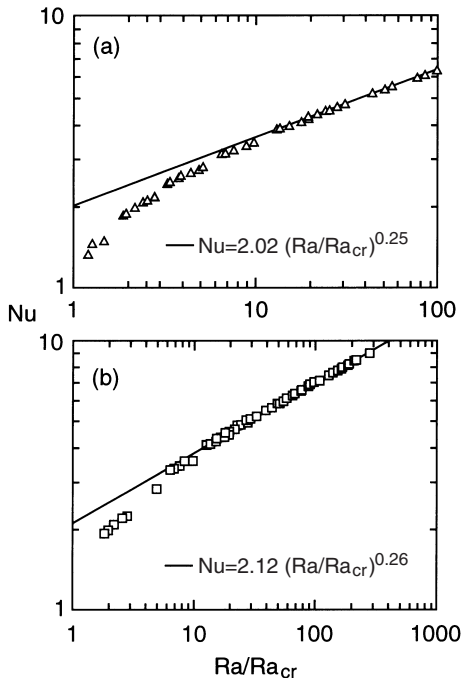


Figure 10.12. Nusselt number Nu versus Rayleigh number ratio Ra/Ra_{cr} (Ra based on the viscosity evaluated at the mean of the boundary temperatures) for the tetrahedral (a) and cubic (b) modes of steady convection with strongly temperature dependent viscosity. Numerical results for tetrahedral convection are shown by triangles in (a). Numerical results for cubic convection are shown by squares in (b). Least-squares power-law fits to the results at high Ra/Ra_{cr} are shown by the straight lines. After Ratcliff et al. (1996a).

more detail in Chapter 13, depending on Ra and r_μ there exist three modes of convection with strongly variable viscosity, a low-viscosity contrast regime, a sluggish-lid regime, and a stagnant-lid regime. These different modes of convection have very different planforms and heat transfer efficiencies.

For sufficiently small Rayleigh number there also exist steady modes of tetrahedral and cubic convection when fluid shells are heated from within (Busse and Riahi, 1982; Riahi et al., 1982; Schubert et al., 1993). Figure 10.13 shows the pattern of steady tetrahedral convection in an internally heated spherical shell with inner/outer radius ratio of 0.55 when the Rayleigh number Ra_Q

$$Ra_Q = \frac{\alpha g Q d^5}{k \kappa \nu} \quad (10.2.3)$$

(α is the thermal expansivity, g is the acceleration of gravity, Q is the volumetric density of the rate of internal heating, d is the shell thickness, k is thermal conductivity, κ is thermal diffusivity, and ν is kinematic viscosity) is 1.4×10^4 (the minimum critical Rayleigh number for convection onset is 1.449×10^3 and corresponds to $l = 3$). The basic modes of downflow in the spherical shell are isolated cylindrical plumes located at the vertices of a tetrahedron (Figure 10.13). The steady cubic mode of convection in this internally heated spherical shell (at the same Ra_Q of 1.4×10^4) shown in Figure 10.14 is also characterized by downwelling cylindrical plumes located at the faces of a cube (Schubert et al., 1993). The cold downflows in both solutions are surrounded by haloes of hot upflows which form an interconnected region containing circular plume-like concentrations of hot upwelling material. The hot upflow concentrations do not arise from instability of a hot lower thermal boundary layer since there is no such boundary layer in the internally heated case. Instead, the plume-like

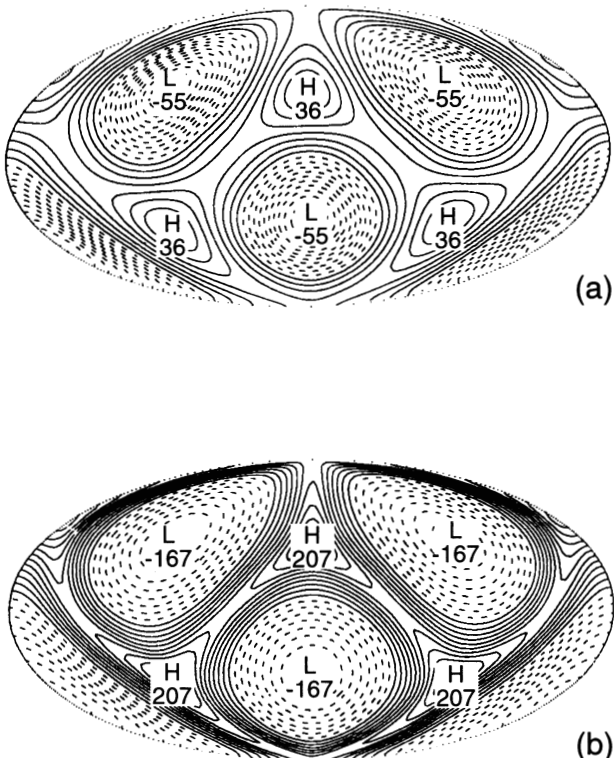


Figure 10.13. Isotherms relative to the spherically averaged temperature on two spherical surfaces at dimensionless radii 0.99 (a) (radius = 1 is the top) and 0.56 (b) (radius = 0.55 is the bottom) in steady, internally heated, spherical convection at $Ra_Q = 1.4 \times 10^4$. The isotherms are plotted on an equal-area projection showing the entire spherical surface at a given radius. The numbers are the maximum hot and minimum cold temperature anomalies. After Schubert et al. (1993).

concentrations of hot upflow are a return flow forced by mass conservation and the downflow plumes that sink onto the lower boundary, spread out, and squeeze the hot upflow into narrow haloes and circular concentrations.

10.2.2 Rectangular Box Convection

We noted above that hexagonal patterns of plane layer convection are analogues of the polygonal patterns of spherical convection. Hexagonal convection cells occur in plane fluid layers that lack midplane symmetry because of such effects as temperature-dependent viscosity (Oliver and Booker, 1983; White, 1988). It has been found that steady convection with hexagonal planforms also occurs in plane layers of Boussinesq fluid heated from below with isothermal, stress-free boundaries and constant properties (Travis et al., 1990a; Ogawa et al., 1991). Thus the absence of midplane symmetry is not a necessary condition for hexagonal convection. Hexagonal convection cells are illustrated in Figure 10.15, which shows a perspective view of two isothermal surfaces (with dimensionless temperatures 0.25 and 0.75) in a bottom-heated rectangular box of unit depth and square horizontal cross-section with side 3 times the depth at a Rayleigh number of 10^5 (Travis et al., 1990a). Only

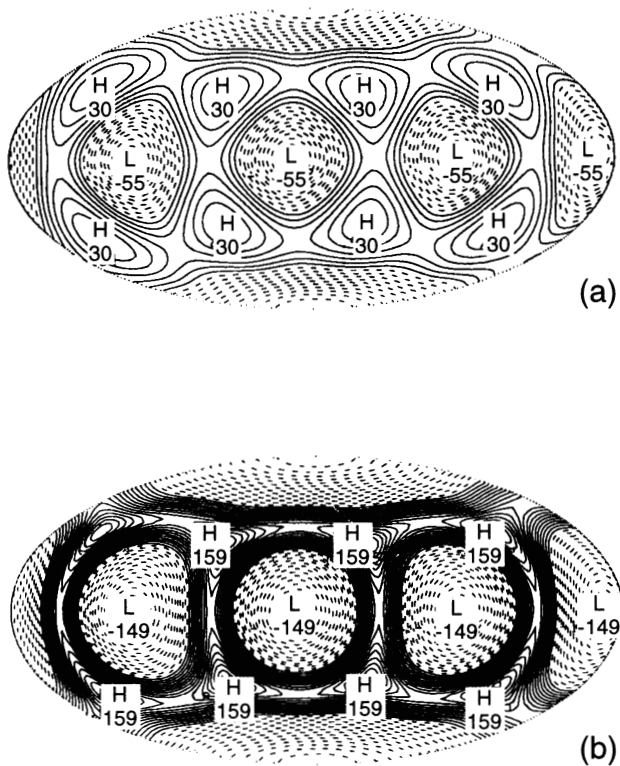


Figure 10.14. Steady cubic pattern of convection under identical conditions as the solution in Figure 10.13. After Schubert et al. (1993).

portions of adjacent hexagonal cells are outlined by the isotherms. Upwelling cylindrical plumes at the centers of the hexagonal cells are surrounded by descending sheets of fluid along the sides of the cells. The downflow sheets merge into descending plumes in the bottom of the layer. The hexagonal cell convection pattern of Figure 10.15 is further described by the midplane contours of temperature and vertical velocity and the upper surface horizontal velocity vectors in Figure 10.16. Upward flow is strongly concentrated in the hot central plume at the midplane, while downward flow is concentrated in cold thin sheets along the edges of the hexagons. Concentrations of downwelling exist within the sheets at the corners of the hexagons. Horizontal flow at the upper surface is outward from the center of a hexagon and into the boundaries. Horizontal flow into the cell boundaries has a velocity component parallel to the boundaries and directed toward the corners of the hexagon. This component of motion leads to the formation of downflow concentrations within the sheets at the hexagon's corners. Ogawa et al. (1991) have computed an equivalent steady hexagonal cell convection mode in a bottom-heated rectangular box with unit depth and rectangular cross-section (3×1.5) at $Ra = 10^5$.

A variety of other steady three-dimensional convection patterns occur in bottom-heated rectangular boxes (Busse et al., 1994). Figures 10.17 and 10.18 show rectangular cell convection in a $3 \times 3 \times 1$ box at $Ra = 10^5$. There is ascending motion in the center of the rectangle and descending flow along the four cell walls. Both hexagonal and rectangular

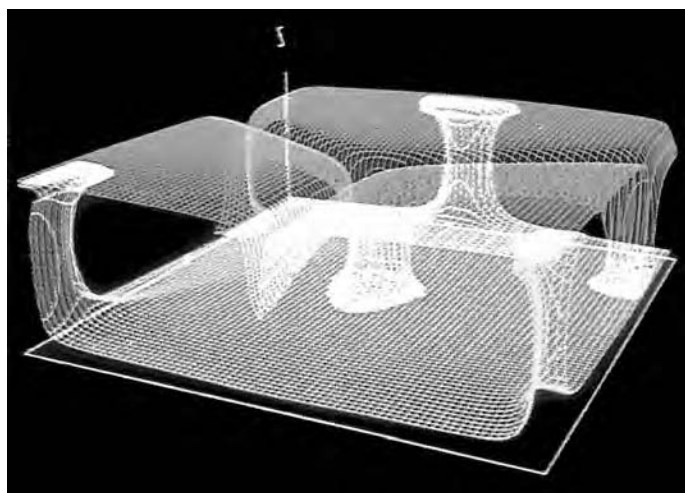


Figure 10.15. Constant temperature surfaces (dimensionless temperatures 0.25 and 0.75) in steady hexagonal cell convection at $Ra = 10^5$ in a bottom-heated rectangular box with dimensions $3 \times 3 \times 1$ (normalized by depth). After Travis et al. (1990a).

For a color version of this figure, see plate section.

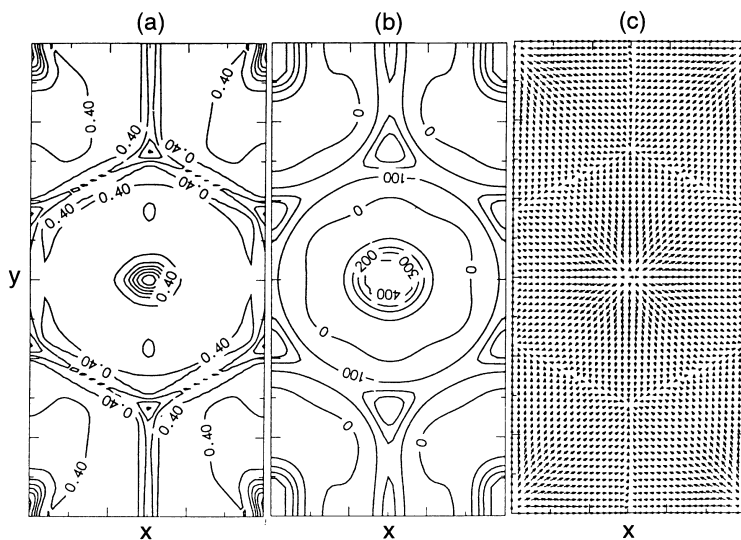


Figure 10.16. Midplane temperature (a) and vertical velocity contours (b), and horizontal velocity vectors at the upper surface (c) in hexagonal convection in a bottom-heated rectangular box ($3 \times 3 \times 1$) at $Ra = 10^5$. After Travis et al. (1990a).

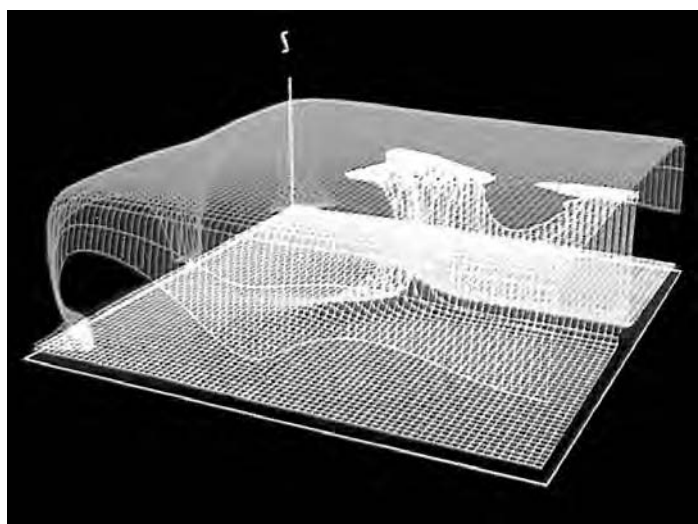


Figure 10.17. Constant temperature surfaces (dimensionless temperatures 0.25 and 0.75) in steady three-dimensional rectangular cell convection in a $3 \times 3 \times 1$ rectangular box heated from below at $Ra = 10^5$. After Travis et al. (1990a).

For a color version of this figure, see plate section.

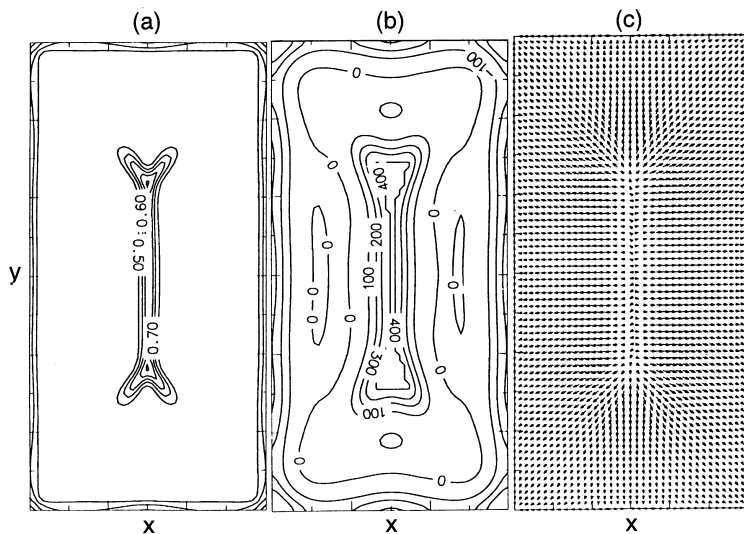


Figure 10.18. Midplane temperature (a) and vertical velocity contours (b), and horizontal velocity vectors at the upper surface (c) in the rectangular cell convection mode of Figure 10.17. After Travis et al. (1990a).

three-dimensional convection occur in identical rectangular boxes similarly heated. The different modes of convection are obtained through different initial conditions. Steady bimodal three-dimensional convection patterns have been found in bottom-heated rectangular boxes with horizontal cross-sections having sides less than twice the depth (Figures 10.19–10.22). The steady-state convection mode that is realized in numerical calculations of convection in bottom-heated rectangular boxes depends on Rayleigh number, size and shape of the horizontal cross-section of the box, and initial conditions. There is no preference among solutions obtained to maximize heat transfer. In fact, the sensitivity of heat transfer to planform variations at constant Ra is less than 10%. Curiously, the heat transfer relation

$$Nu = 0.268Ra^{0.319} \quad (10.2.4)$$

obtained from unit aspect ratio two-dimensional bottom-heated convection rolls (Schubert and Anderson, 1985) is also a good prediction of heat transfer in three-dimensional convection in bottom-heated rectangular boxes for Ra as large as 5×10^5 (Travis et al., 1990a).

Steady, symmetric three-dimensional convection patterns have also been found to occur in fluids with strongly temperature dependent viscosity (Christensen and Harder, 1991; Ogawa et al., 1991). The dependence of viscosity on temperature destroys the midplane symmetry of the plane layer solutions discussed above and results in three-dimensional convection patterns with hot upwelling plumes surrounded by sheets of cold sinking fluid. An example of this style of convection is provided in Figure 10.23, which shows rectangular cells with upflow plumes at the rectangle centers, downflow sheets along the four sides, and cold downwelling plume concentrations in the sheets (Ogawa et al., 1991). The convecting fluid in this case is contained in a rectangular box heated from below with dimensions $3 \times 1.5 \times 1$. The viscosity of the fluid μ depends exponentially on temperature T according to $\mu \propto \exp(-\text{constant} \times T)$, and the ratio of the viscosity at the top boundary to that at the bottom is 3.2×10^4 (the upper and lower surfaces of the box are isothermal and stress free); the Rayleigh number based on the viscosity at the top boundary is 32. Steady rectangular three-dimensional convection occurs beneath a cold, high-viscosity stagnant lid, as shown by the vertical profiles of horizontally averaged temperature, viscosity, and root mean square velocity in Figure 10.23. Motions are negligible in this high-viscosity lid which does not participate in the underlying convection. The average temperature rise across the whole layer occurs mostly within the stagnant lid and immediately below it in the underlying top thermal boundary layer, making the isothermal core of the convecting region nearly as hot as the lower boundary (the isothermal core of the convecting region is at 85% of the bottom temperature). Most of the average viscosity change across the layer occurs in the upper stagnant lid and in the fluid just below. Heat is transferred in the vertical direction only by conduction in the lid. Stagnant-lid convection is discussed in more detail in Chapters 13 and 14.

Ogawa et al. (1991) have found another mode of steady, three-dimensional convection in bottom-heated rectangular boxes with strongly temperature dependent viscosity. The style of convection, illustrated in Figure 10.24, is a three-dimensional bimodal pattern that involves all the fluid in the box, i.e., it is a whole-layer mode of convection without a stagnant lid. Whole-layer bimodal convection occurs for values of the viscosity ratio between the top and bottom of the layer that are smaller than the viscosity ratios in stagnant-lid rectangular convection (comparing cases with the same Ra based on the viscosity at the top boundary). The viscosity ratio that separates these modes of steady three-dimensional

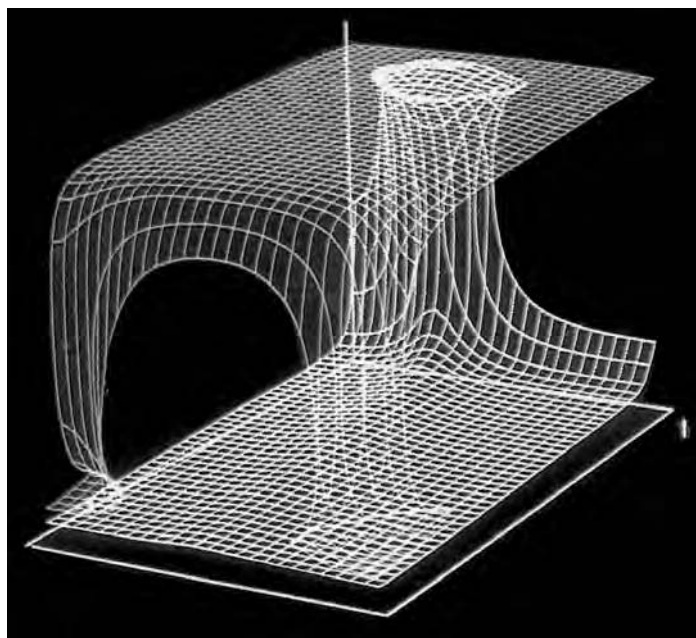


Figure 10.19. Isothermal surfaces (dimensionless temperatures 0.25 and 0.75) in three-dimensional bimodal convection in a bottom-heated rectangular box ($1.7 \times 1 \times 1$) at $Ra = 10^5$. The depth of the box is unity. After Travis et al. (1990a).

For a color version of this figure, see plate section.

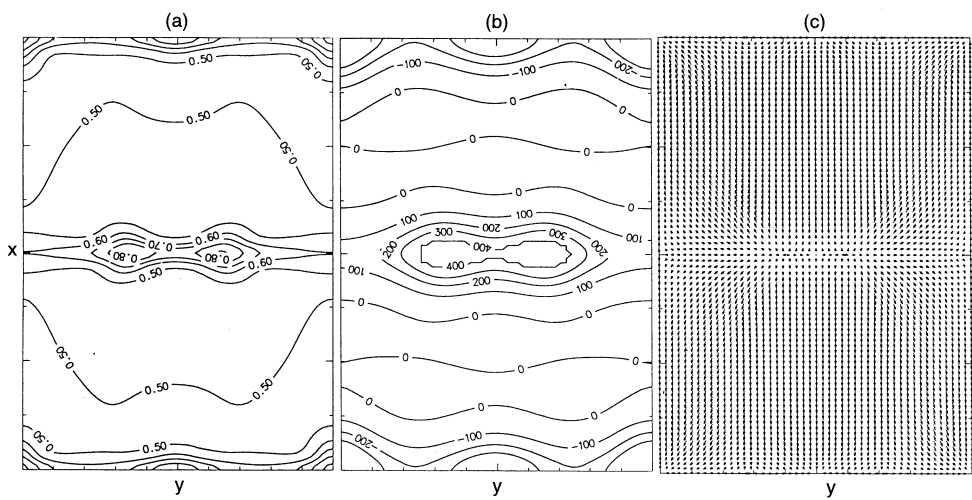


Figure 10.20. Midplane contours of temperature (a) and vertical velocity (b), and upper surface horizontal velocity vectors (c) for the steady bimodal convection mode of Figure 10.19. After Travis et al. (1990a).

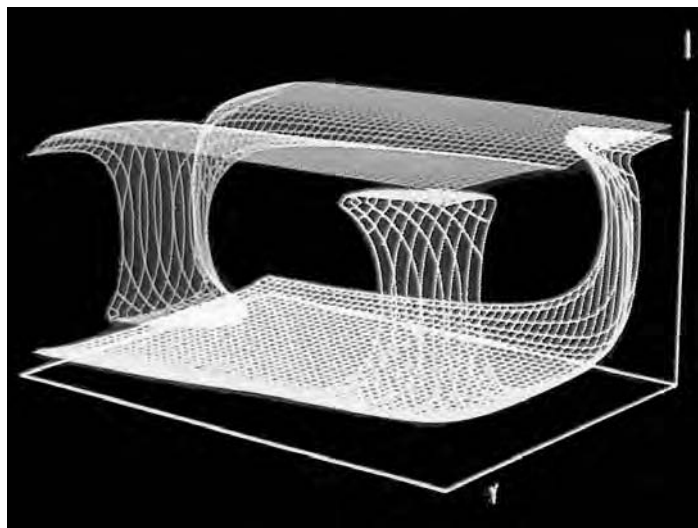


Figure 10.21. Isothermal surfaces (dimensionless temperatures 0.25 and 0.75) in steady bimodal convection in a bottom-heated rectangular box ($1.96 \times 1.41 \times 1$) at $Ra = 4 \times 10^4$. The depth of the box is unity. After Travis et al. (1990a).

For a color version of this figure, see plate section.

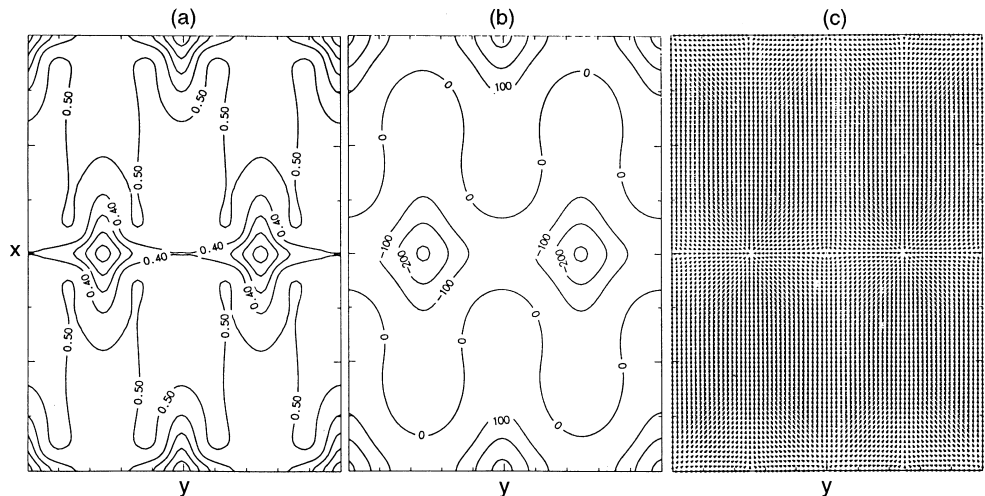


Figure 10.22. Midplane contours of temperature (a) and vertical velocity (b), and upper surface horizontal velocity vectors (c) for the steady bimodal convection mode of Figure 10.21. After Travis et al. (1990a).

convection increases with the top boundary Rayleigh number R_t (the critical ratio is given by $1.18 \times 10^3 R_t^{0.309}$, Ogawa et al., 1991) so that whole-layer bimodal convection can occur in layers with large viscosity ratios between top and bottom boundaries. The viscosity ratio between the top and bottom in Figure 10.24 is 10^3 and the Rayleigh number based on the viscosity at the top is 10^3 . The rectangular box has dimensions $3 \times 1.5 \times 1$. The horizontally averaged fluid velocity at the top boundary is seen to be nonzero in the figure (dashed curve marked by arrow in Figure 10.24), an indicator of whole-layer convection and the absence of a stagnant lid. The mode of convection is bimodal with rectangular

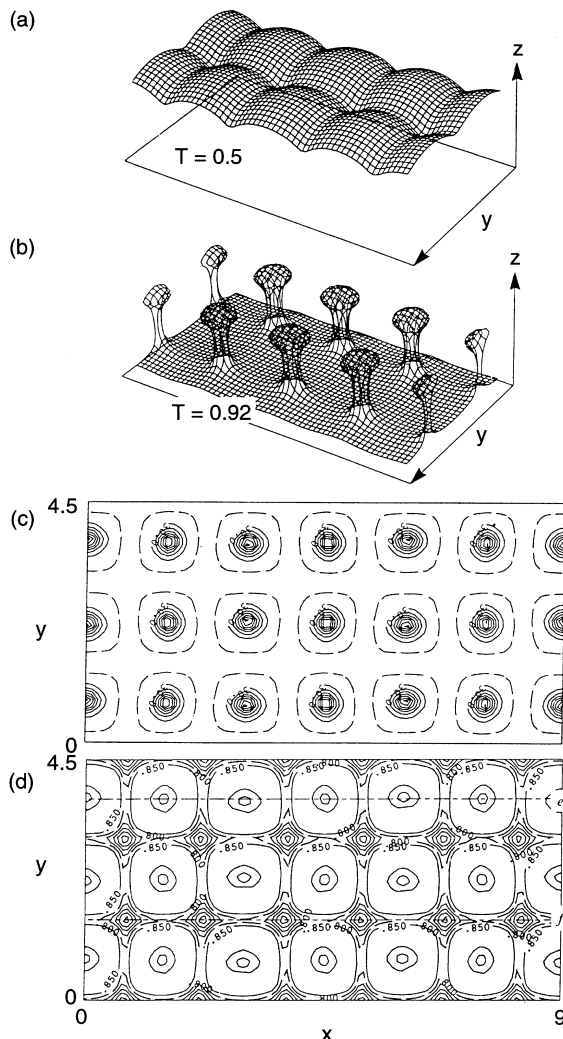


Figure 10.23. Rectangular cell three-dimensional convection in a bottom-heated rectangular box ($3 \times 1.5 \times 1$) with isothermal, stress-free top and bottom boundaries containing fluid whose viscosity is exponentially dependent on temperature. The ratio of the viscosity at the temperature of the top surface to that at the temperature of the bottom surface is 3.2×10^4 and the Rayleigh number based on the viscosity at the temperature of the top boundary is 32. (a) and (b) Isothermal surfaces (dimensionless temperatures 0.5 and 0.92). (c) Contours of vertical velocity on the midplane. (d) Midplane temperature contours. (Continued)

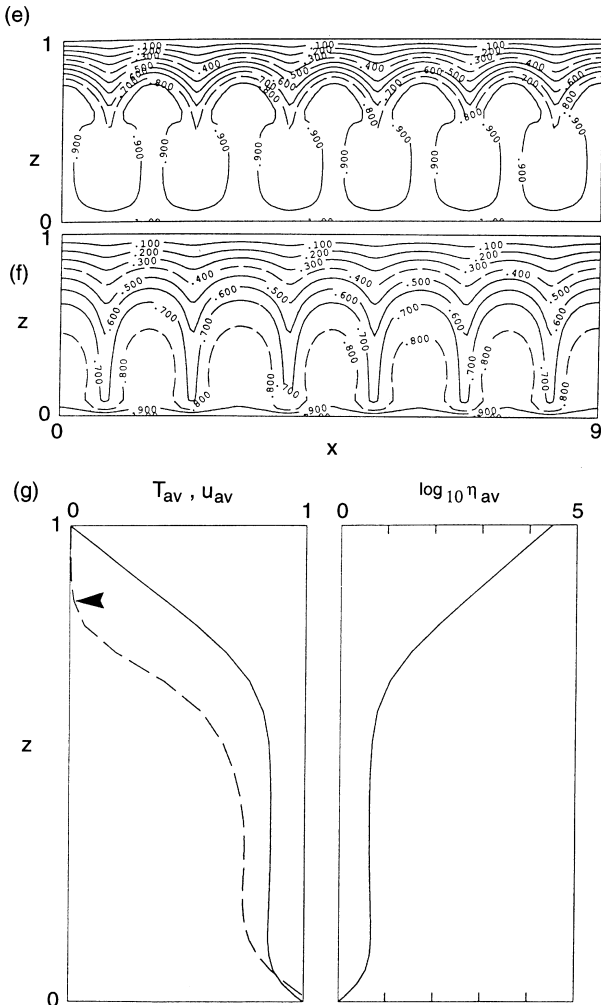


Figure 10.23. (e) and (f) Isotherms in the vertical sections along the cuts labeled e and f in (d). (g) Vertical profiles of horizontally averaged temperature (solid), root mean square velocity (dashed) and viscosity (solid). The arrow indicates the base of the stagnant lid. After Ogawa et al. (1991).

planform (Figures 10.24a–c). A hot upwelling plume occurs at the center of the cell and cold downwelling plumes form at the four corners of the cell. The cylindrical concentrations of the plumes become narrower as the top to bottom viscosity ratio increases, i.e., as the dependence of viscosity on the temperature becomes stronger. The vertical velocities in the cylindrical cores of the hot upwelling plumes are much larger than the upwelling velocities in the surrounding fluid, a contrast that does not apply to the downwelling velocities in the cold sinking plumes (Figure 10.24c). The low velocity in the cylindrical core of the cold downwelling plume is due to the high viscosity of this fluid.

The plumes have sheet-like extensions. The vertical velocity in the sheet-like extensions of the cold downwelling plumes is almost the same as the vertical velocity in the cylindrical cores of the plumes as can be seen from Figure 10.24. The sheet-like extensions of a cold

sinking plume become narrower and more elongated as the top to bottom viscosity ratio increases. The sheet-like extensions of hot upwelling plumes also become more elongated as this viscosity ratio increases. The locations of the hot upwelling plumes deviate slightly from a straight line (see the dash-dotted line e in Figure 10.24d); a similar observation applies to the cold downwelling plumes (dash-dotted line f in Figure 10.24d).

The isotherms in the vertical sections in Figures 10.24e and f are significantly distorted from horizontal even just beneath the top boundary, and the dependence of the

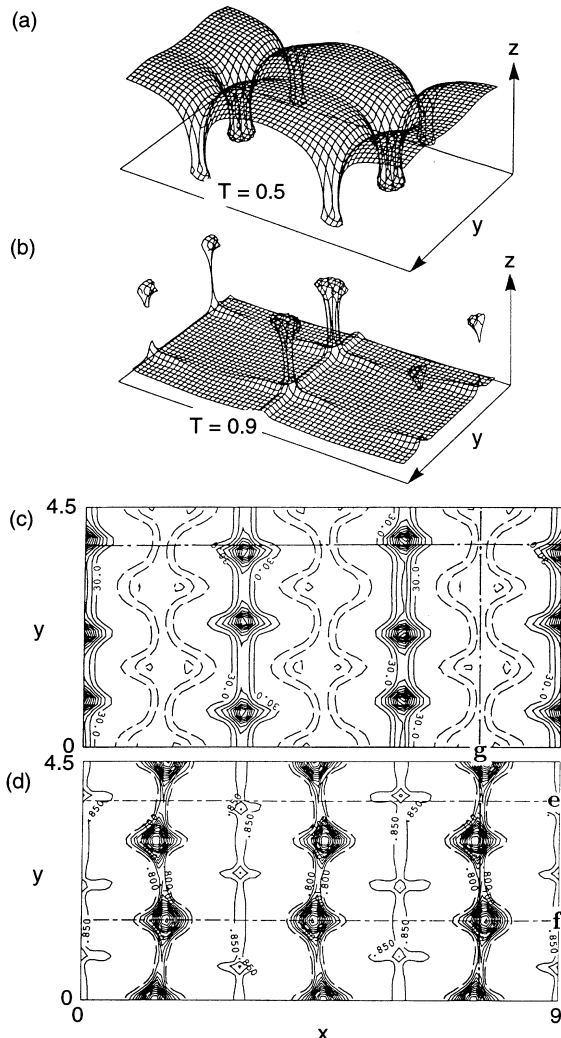


Figure 10.24. Rectangular bimodal whole-layer convection in a rectangular box ($3 \times 1.5 \times 1$) heated from below with isothermal stress-free top and bottom boundaries containing fluid whose viscosity is exponentially dependent on temperature. The ratio of the top viscosity to the bottom viscosity is 10^3 and the Rayleigh number based on the top viscosity is 10^3 . (a) and (b) Isothermal surfaces (dimensionless temperatures 0.5 and 0.9). (c) Midplane contours of constant vertical velocity (solid – upward, dashed – downward). (d) Isotherms in the midplane. (Continued)

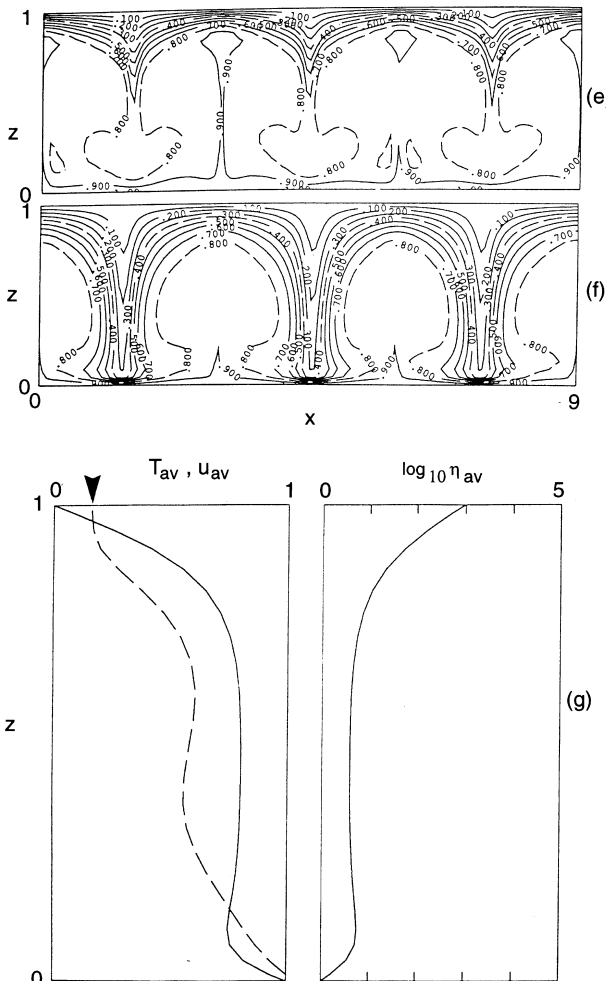


Figure 10.24. (e) and (f) Isotherms in the vertical sections marked e and f in (d). (g) Vertical profiles of horizontally averaged temperature (solid) and viscosity (solid) and root mean square velocity (dashed). After Ogawa et al. (1991).

horizontally averaged temperature on depth deviates significantly from linear in the top thermal boundary layer (Figure 10.24g). Accordingly, advection contributes importantly to vertical heat transport even just beneath the top surface. Chapter 13 contains additional discussion of the whole-layer mode of convection in fluids with strongly temperature dependent viscosity.

An important characteristic of three-dimensional convection with temperature-dependent viscosity is the vertical component of vorticity. In the case of mantle convection, the vertical vorticity component is comparable to the horizontal vorticity at the Earth's surface mainly due to the existence of strike-slip deformation along major transform faults. However, the vertical vorticity component is not significantly excited in a thermally convecting Newtonian fluid with strongly temperature dependent viscosity (Christensen and Harder, 1991; Ogawa et al., 1991). Flow with nonzero vertical vorticity is known as toroidal flow, as discussed

in Chapter 2. Significant toroidal flow is excited only by strongly nonlinear rheological behavior in narrow zones of deformation (Bercovici, 1995a).

Just as there exist steady symmetric modes of three-dimensional convection in internally heated spherical shells, there exist similar modes of convection in plane layers (Roberts, 1967; Tveitereid and Palm, 1976; Clever, 1977; Tveitereid, 1978) and in rectangular boxes of fluid heated from within (Schubert et al., 1993). Examples of such modes are shown in Figure 10.25 for internally heated convection in a $3 \times 3 \times 1$ rectangular box at a Rayleigh number of 1.4×10^4 (Ra_Q is defined as in (10.2.3) but d is the height of the box), the same value of Ra_Q used in the spherical shell solutions discussed earlier. The minimum critical Rayleigh number for the onset of convection in this situation is 862.3. The flows of Figure 10.25 all consist of downwelling cylindrical plumes in a broad background of upflow (downwellings also occur as cylindrical structures in internally heated steady spherical convection as discussed above). The different patterns correspond to different sites of plume downwelling. In Figure 10.25a downwellings are centered at the midpoints of opposite sides of the square horizontal cross-section. In Figure 10.25b centers of downwelling are at opposite corners of the square horizontal cross-section while in Figure 10.25c there are three downflows, two in adjacent corners of the square horizontal cross-section and one at the midpoint of the opposite side.

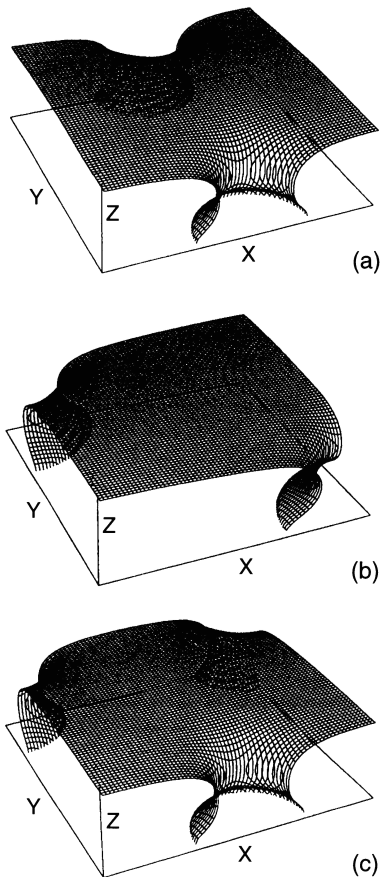


Figure 10.25. The dimensionless isotherm surface 0.1 in three different examples of steady, internally heated convection in a $3 \times 3 \times 1$ rectangular box at $Ra_Q = 1.4 \times 10^4$. The Nusselt numbers of the flows in (a), (b), and (c) are 3.390, 3.272, and 3.393, respectively. The dimensionless temperature of the isothermal top boundary is zero in all cases and the maximum dimensionless temperature in each case is around 0.15. After Schubert et al. (1993).

10.3 Unsteady, Asymmetric Modes of Convection

Three-dimensional convection at high Rayleigh number, especially with some amount of internal heating, is invariably time dependent and asymmetric. The steady symmetric modes of three-dimensional convection discussed in the previous section are atypical and associated with the relatively low Rayleigh numbers of most of the solutions presented. In Cartesian geometry, the steady modes discussed above may also be associated with relatively small box size, i.e., with boxes whose horizontal dimensions are comparable to their heights. Only in the case of pure bottom heating are steady symmetric three-dimensional solutions possible at Rayleigh numbers up to 100 times the critical Ra for convection onset. Heated from within convection becomes time dependent at very low supercritical Rayleigh numbers both in two dimensions (Schubert and Anderson, 1985) and in three dimensions (Schubert, 1992). Even when steady three-dimensional convection is possible, the realization of such steady convection for arbitrarily initialized states may not occur or may require very long integration times. In this section we discuss the unsteady, asymmetric three-dimensional solutions typical of high Rayleigh number convection in fluid layers.

Time dependence and loss of symmetry in bottom-heated three-dimensional convection occurs with increasing Rayleigh number and, in the case of convection in rectangular boxes, with the size and aspect ratio of the horizontal cross-section. Time dependence and asymmetry in heated from below convection are not as strong as they are in fluid layers with internal heating. Complexity in temporal and spatial variability generally increases with an increase in the fraction of vertical heat transport due to heating from within. Travis et al. (1990a) have reported time-dependent, three-dimensional solutions for convection in bottom-heated rectangular boxes that essentially maintain the basic spatial symmetries of the solutions discussed in the previous section. Figure 10.26 shows such a time-dependent, essentially hexagonal solution in a box with dimensions $3.5 \times 3.5 \times 1$ at $Ra = 10^5$. Recall that a steady hexagonal convection occurred at the same Rayleigh number but in a $3 \times 3 \times 1$ box. Figure 10.26 shows a time sequence of the 0.25 and 0.75 isothermal surfaces which reveal the periodic growth and decay of a downflow plume in part responsible for the time dependence of the flow. In Figure 10.26a the plume is fully extended, in Figure 10.26b it has weakened, in Figure 10.26c a new plume is developing, and in Figure 10.26d the plume is again fully developed. Traveling thermal ridge disturbances in the upper and lower thermal boundary layers also contribute to the time dependence of this flow.

Another example of time-dependent, three-dimensional bottom-heated convection in a rectangular box is shown in Figure 10.27. The computation of Figure 10.27 was carried out in a $3 \times 3 \times 1$ box with isothermal, no-slip conditions on the top and bottom boundaries and impermeable, reflecting sidewalls at $Ra = 1.5 \times 10^5$ (Travis et al., 1990b). The figure shows the isothermal surfaces with dimensionless temperatures 0.25 and 0.75, and contours of constant temperature on horizontal surfaces at dimensionless depths of 0.25 and 0.75. All of these representations of the temperature field are at a single instant of time. Unlike the previous example of time-dependent, base-heated convection with hexagonal planform, the convection pattern in Figure 10.27 has no spatial symmetry. The distorted quadrilaterals are characteristic of what is generally known as a spoke pattern of convection (Whitehead and Parsons, 1978). Rising and descending plumes are connected to the bottom and top thermal boundary layers by hot thermal ridges and cold thermal trenches, respectively. The ridges and trenches radiate from the plumes like the spokes from the hub of a wheel. Angles between adjacent spokes are usually about 90° . The pattern of cold descending flow is similar to the pattern of hot upwellings, except that it is shifted diagonally, so that upflows

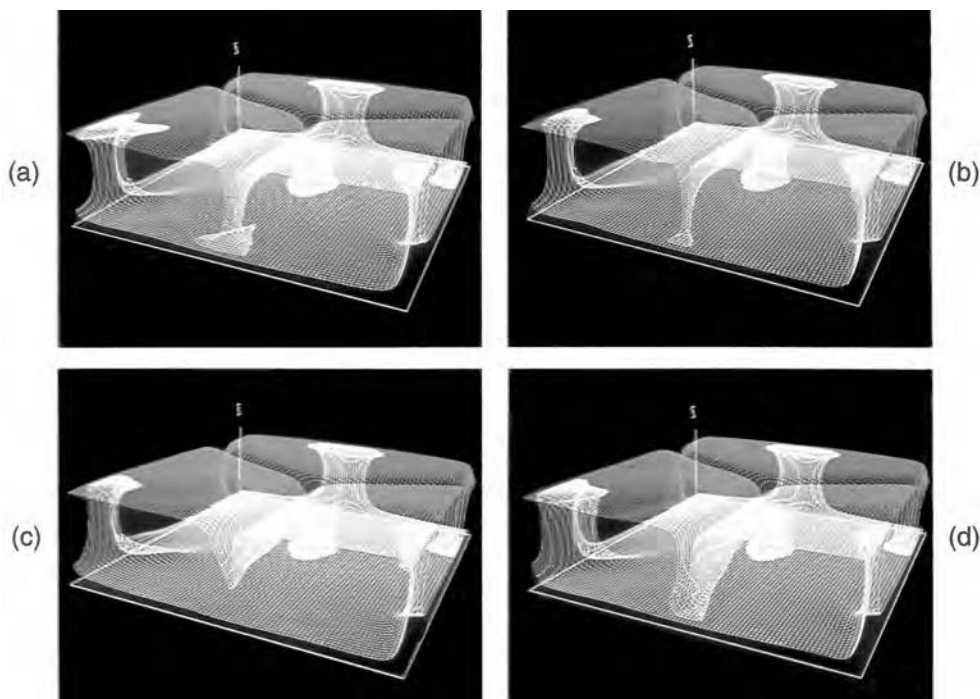


Figure 10.26. Unsteady hexagonal convection in a $3.5 \times 3.5 \times 1$ rectangular box with stress-free boundaries heated from below at $Ra = 10^5$. Isothermal surfaces (dimensionless temperatures 0.25 and 0.75) are shown at dimensionless times (a) $t = 0.5260$, (b) $t = 0.5277$, (c) $t = 0.5294$, and (d) $t = 0.5311$ during one cycle of a variable downflow plume. After Travis et al. (1990a).

For a color version of this figure, see plate section.

and downflows form offset, nearly orthogonal networks. The weak time dependence in this example is manifest in the slow drift of the spokes which reorganize the planform on a long time scale.

Another example of time-dependent, asymmetric, three-dimensional, base-heated thermal convection is shown in Figures 10.28 and 10.29. In this case, convection occurs in a spherical shell with inner to outer radius ratio of 0.55 (similar to the radius ratio of the Earth's mantle) and isothermal, stress-free boundaries at a Rayleigh number about 100 times the value of Ra for the onset of convection (Bercovici et al., 1989a,c). Unlike all the previous calculations discussed so far in this chapter, the fluid in this case is not a simple Boussinesq fluid; it is a compressible fluid with a basic state radial profile of density similar to that of the Earth's mantle and effects of viscous dissipation and adiabatic heating and cooling from compression and expansion are included in the model. Accordingly, the time dependence and asymmetry of the convection in Figures 10.28 and 10.29 could be due to non-Boussinesq effects, although different initial conditions could also account for these more complex convective states compared with the comparable Ra discussed in the previous section.

The convective pattern in Figure 10.28 is characterized by three cylindrical upwelling plumes surrounded by a network of downwelling sheets. The upwelling plumes are vividly

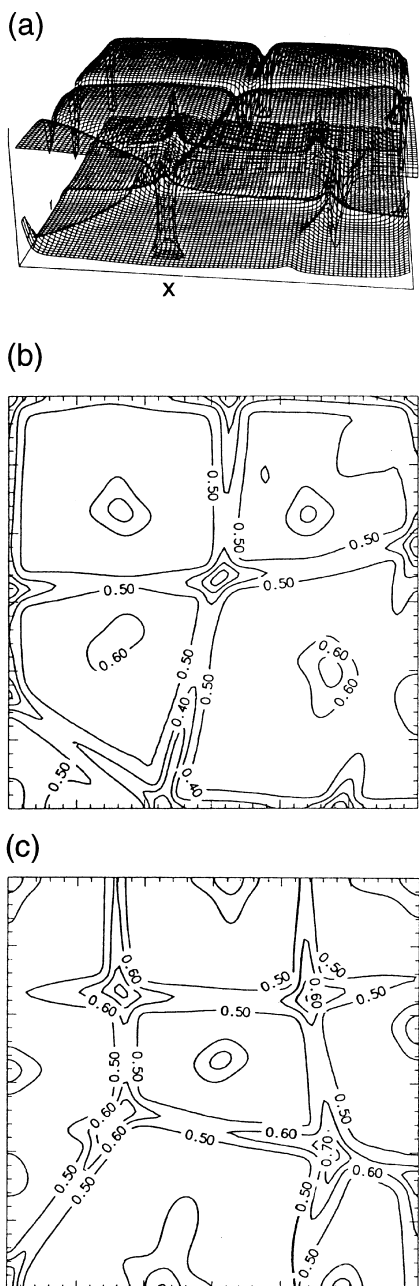


Figure 10.27. Dimensionless isotherms (a) 0.25 and 0.75, and contours of constant temperature on horizontal surfaces at dimensionless depth 0.75 (b) and 0.25 (c) in bottom-heated weakly time dependent spoke convection in a $3 \times 3 \times 1$ rectangular box at $Ra = 1.5 \times 10^5$ and at a dimensionless time 0.19. The top and bottom boundaries are isothermal and no-slip. After Travis et al. (1990b).

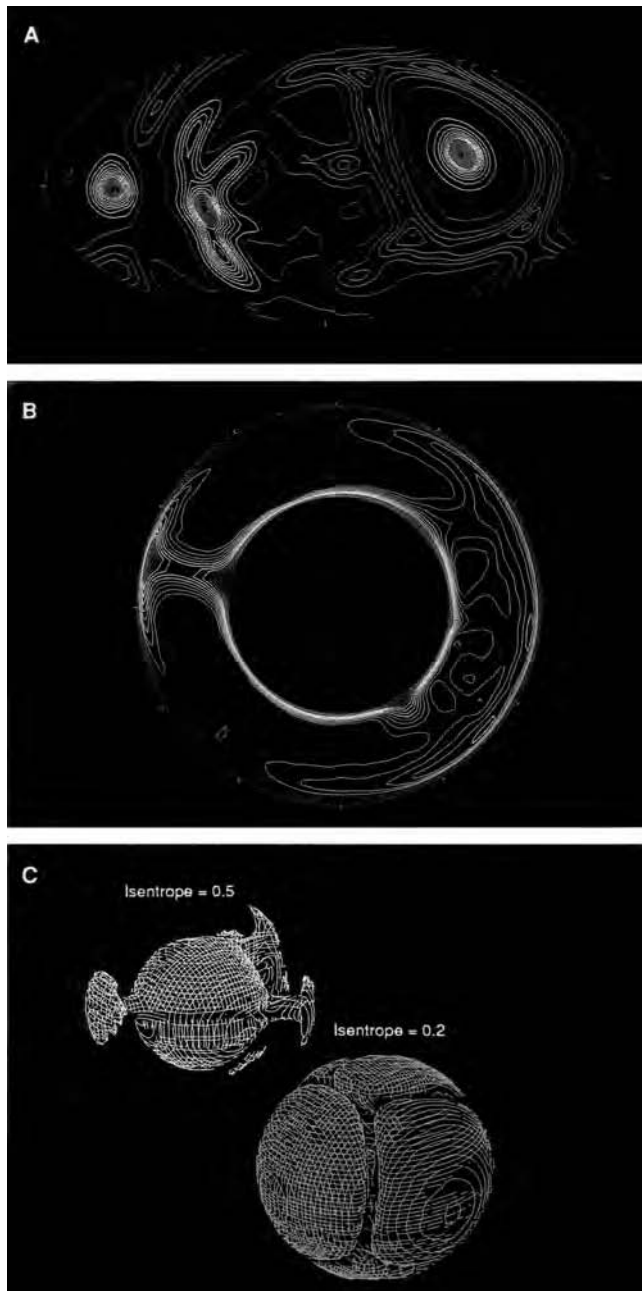


Figure 10.28. Time-dependent, asymmetric convection in a bottom-heated spherical shell with inner to outer radius ratio 0.55 and isothermal, stress-free boundaries at a Rayleigh number about 100 times the value of Ra for convective onset. The fluid in the shell is compressible with a radial basic state density profile comparable to that of the Earth's mantle. (a) Contours of radial velocity on a spherical surface midway through the shell in an equal-area projection, (b) contours of constant entropy in a meridional cross-section, and (c) three-dimensional isentropic surfaces with dimensionless entropy 0.2 and 0.5. Isentropic surfaces and contours in compressible convection are analogous to isotherms in Boussinesq convection. After Bercovici et al. (1989a).

For a color version of this figure, see plate section.

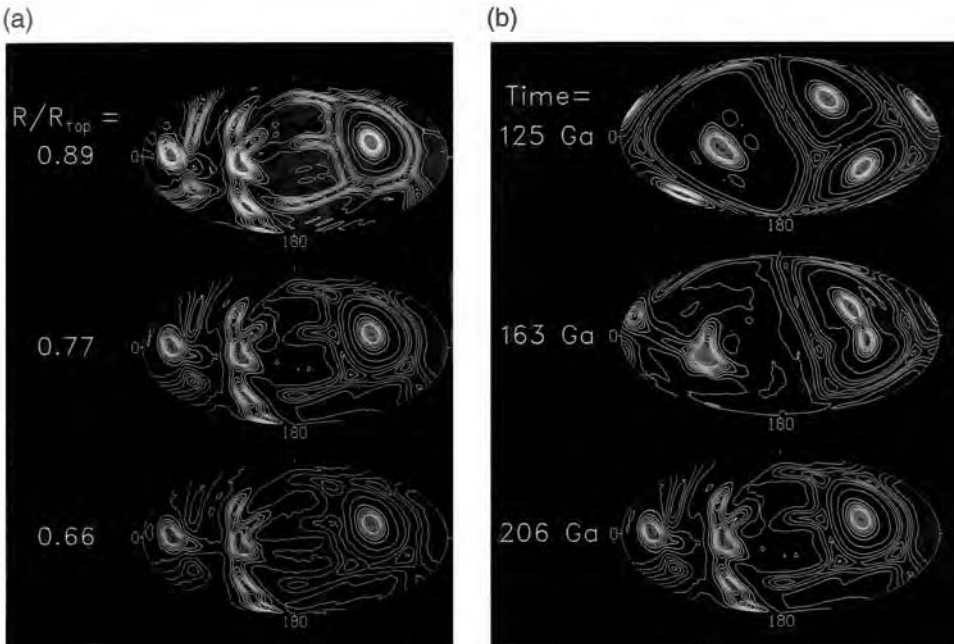


Figure 10.29. Contours of radial velocity in the calculation of Figure 10.28 for different depths at a given instant of time (a) and for different times at one depth (midway through the shell) (b). After Bercovici et al. (1989c).

For a color version of this figure, see plate section.

displayed in the mushroom-shaped protuberances on the isentropic surfaces and the downwelling sheets appear as linear troughs in these surfaces. Upflow plumes emanate from the hot thermal boundary layer at the base of the shell (see the meridional cross-section in Figure 10.28) and maintain a quasi-cylindrical structure with a concentrated hot thermal anomaly across almost the entire shell (Figure 10.29a). The weaker (lower velocity and less concentrated) downflow sheets that emanate from the top cold thermal boundary layer (meridional cross-section, Figure 10.28) are most sheet-like in the upper half of the shell and begin to broaden and disintegrate as they diverge into the bottom of the shell (Figure 10.29a). Though not shown in Figures 10.28 and 10.29, the thermal anomalies in the upwelling plumes are also stronger and more concentrated than they are in the downwelling sheets. The differences in radial velocity and temperature structure between the plumes and sheets is a consequence of the loss of midplane symmetry in spherical geometry. On average, the same net heat flow must leave the shell at the top surface as enter it at the bottom surface. Because of the different surface areas yet comparable boundary layer thicknesses, the horizontally averaged temperature drop across the bottom boundary layer exceeds that across the top boundary layer to provide equality of average heat flow through both surfaces. Thus, fluid rising in plumes from the base of the shell has greater thermal and buoyancy anomalies than fluid sinking in sheets from the top of the shell (Bercovici et al., 1989a).

The time dependence of the base-heated spherical convection in Figures 10.28 and 10.29 occurs early as a reduction in the number of upflow plumes (by fusion of plumes at their bases) (Figure 10.29b) and later, after three plumes are established, as an alternating attraction and

repulsion of the two closely spaced plumes (Figure 10.29b). The temporal evolution of the convection pattern is controlled by the slow drift of upwelling plumes.

The weak time dependence of the bottom-heated convective modes discussed above is in contrast to the generally strong time dependence that occurs with internal heating. Figure 10.30 shows temperature variations at different times in a $4 \times 4 \times 1$ rectangular box with stress-free upper and lower boundaries containing a constant viscosity Boussinesq fluid undergoing convection due entirely to internal heating at a Rayleigh number of nearly 6×10^5 (Houseman, 1988). The main features of the flow are cold downwelling sheets and cylindrical plumes immersed in a broad, relatively hot upwelling. The cold downflow sheets are prominent only at early times (Figure 10.30a) (due to initial conditions); they contract and break up with time (Figure 10.30b) leaving only cold downflow plumes as the dominant flow structures in a diffuse upward flow (Figures 10.30c and d). The flow is strongly time dependent. Individual downflow plumes drift horizontally and coalesce with neighbors creating temporarily elongated structures that subsequently contract or break up. New downwelling plumes form as a consequence of instability of the cold upper thermal boundary layer. The convective style is similar to that observed in laboratory experiments

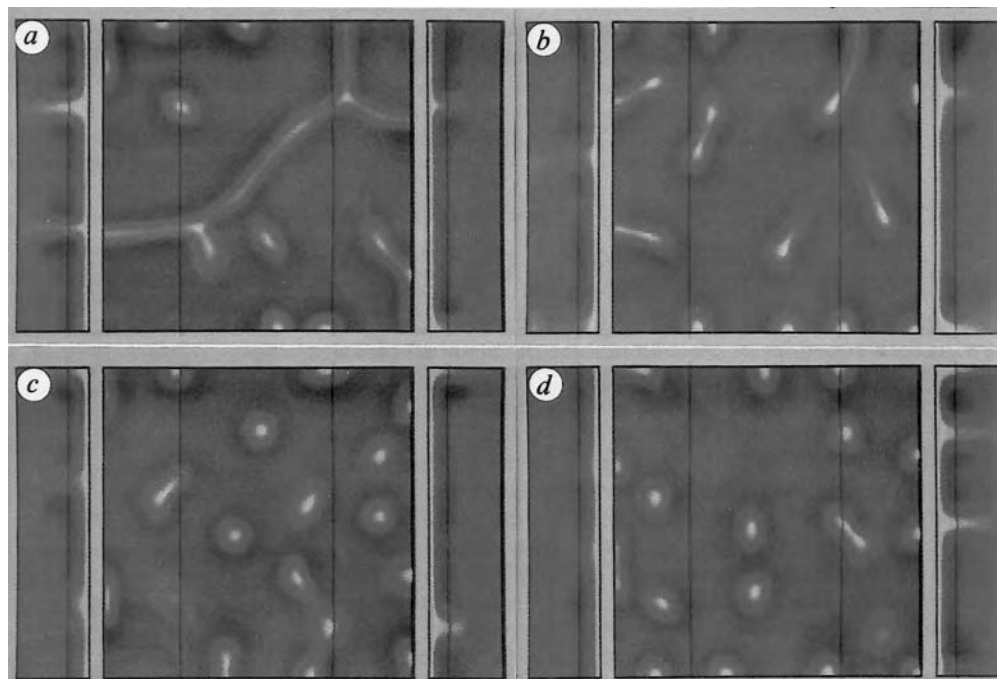


Figure 10.30. Temperature variations due to convection in a $4 \times 4 \times 1$ internally heated rectangular box of constant viscosity Boussinesq fluid. The upper and lower boundaries are stress free and the bottom surface is insulated. Color indicates temperatures: the average temperature of the box is red, grading to white for colder fluid and black for hotter fluid. The square horizontal section in the middle is at a depth of 0.25 and the vertical sections to either side are 0.25 from opposite sides of the box (up is inward for the vertical sections). The different panels correspond to different dimensionless times: (a) 0.0911, (b) 0.1327, (c) 0.1630, and (d) 0.1945. After Houseman (1988).

For a color version of this figure, see plate section.

with internally heated fluids (Figure 10.31) (Carrigan, 1982, 1985; Weinstein and Olson, 1990).

Internally heated convection in a spherical shell is illustrated in Figures 10.32 and 10.33 (Bercovici et al., 1989a,c). Except for the mode of heating, which is entirely from within, the circumstances of the calculation (e.g., shell size, degree of supercriticality, nature of the fluid, etc.) are the same as in the case of the heated from below spherical shell just discussed (the thermal boundary condition on the bottom is zero heat flux in accordance with the mode of heating). The main features of the flow are cylindrical and sheet-like downwellings and broad regions of upwelling, similar to the structures in the rectangular box calculation of Figure 10.30. The cylindrical downflows are transient structures while the sheet-like downflows are longer lived, unlike the downflow sheets of the rectangular box. The downflows in the spherical shell broaden with depth but otherwise maintain their structures (Figure 10.33). The largest temperature and velocity anomalies occur in the downwelling plumes and sheets. The similarity of downwelling structures in both spherical and Cartesian models of fully three dimensional internally heated convection suggest that sheet-like and cylindrical downflows are a fundamental feature of this style of convection independent of the geometry of the enclosure.

When heating is both from below and within, three-dimensional convection generally involves all the flow structures that are prominent in the end-member heating cases, i.e., principal upflows are cylindrical plumes while major downflows are sheets and cylinders. This style of convection is illustrated in Figures 10.34 and 10.35 for a spherical shell the size of the Earth's mantle containing a constant viscosity compressible fluid stratified in density similar to the mantle and heated mainly from within, also similar to the mantle (Glatzmaier et al., 1990). In the upper part of the spherical shell, cold dense fluid tends to converge and sink in long narrow sheets and isolated cylindrical downflows, the surface expressions of which are thin elongate arcuate concentrations of cold thermal anomalies and quasi-circular cold spots (Figure 10.34). The descending sheets and cylinders are fed by a cold upper thermal boundary layer (Figure 10.35). Convergent flow into the downwelling sheets is generally perpendicular to the strike of the elongate cold thermal anomalies although there are cylindrical-like concentrations of downflow and cold temperature near the ends of the elongate structures. The isolated cylindrical downwellings of cold fluid are fed by radially convergent inflows. Near the top of the spherical shell, the cold downwellings plunge into a background of generally diffuse weakly divergent upflow of warm buoyant fluid. There are some circular concentrations of relatively hot fluid on the upper spherical surface of Figure 10.34 representing the divergent outflow of hot upwelling cylindrical plumes. The relatively weak upwelling plume signatures are best revealed by sites of radially outward horizontal flow. The radial velocity structures are similar to, but broader than, the thermal anomalies.

As shown by the temperature anomalies and radial velocities on the middle and inner spherical surfaces of Figure 10.34, cylindrical downwellings tend to broaden, and thin downwelling sheets also tend to broaden and break up into cylindrical downflows with increasing depth. The radial velocity structures on the middle and inner surfaces in Figure 10.34 are more connected than are the temperature anomalies, showing that relatively warm fluid is sometimes swept downwards by strong descending flows. The lower spherical surfaces of Figure 10.34 also display concentrated hot thermal anomalies in the form of a connected network of circular spots representing hot upwelling cylindrical plumes. The upflow plumes emanate from a hot lower thermal boundary layer (Figure 10.35) and are marked by concentrations of hot thermal anomalies and radially inward horizontal flow. The plumes are forced

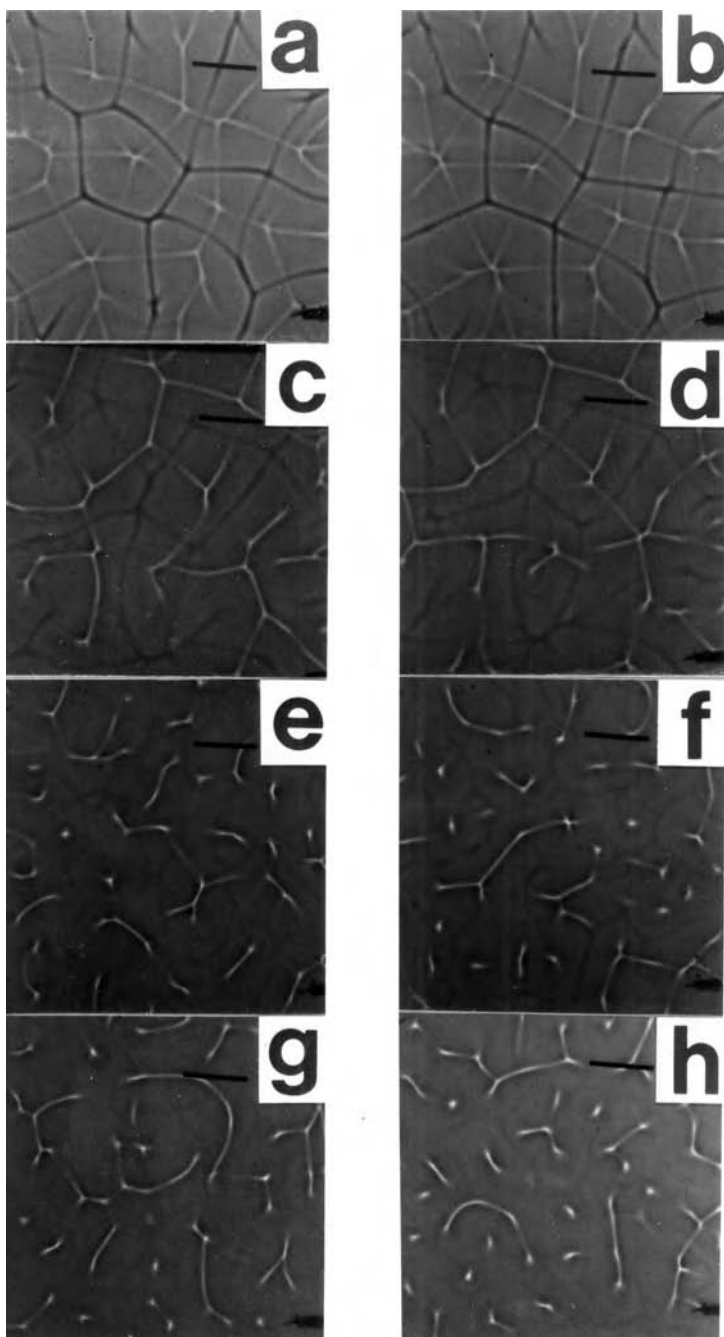


Figure 10.31. Shadowgraphs of the planform of internally heated convection in a laboratory experiment of Weinstein and Olson (1990). The Rayleigh number based on the imposed temperature difference is 1.5×10^5 . The Rayleigh number based on the amount of internal heat generation is 0 in (a) and (b), 9×10^5 in (c) and (d), 18×10^5 in (e) and (f), and 27×10^5 in (g) and (h). The left and right panels are separated by 8 min in time. The scale bar in the upper right corner of each panel represents the thickness of the fluid layer. The bright and dark lines in the shadowgraph show the locations of descending (cold) and ascending (hot) sheets of fluid, respectively. The planform is characteristic of the spoke pattern of convection.

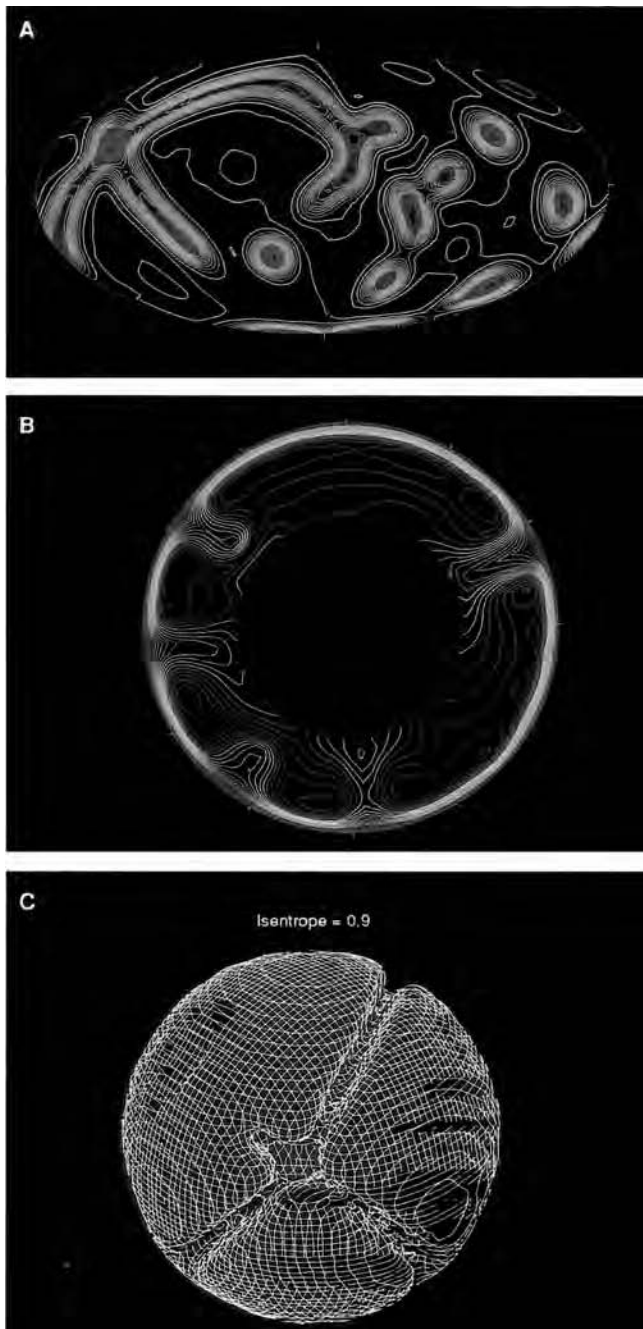


Figure 10.32. Strongly time dependent asymmetric thermal convection in a spherical shell heated entirely from within. The lower boundary is insulated and the Rayleigh number is about 100 times the value for the onset of convection. Other properties of the fluid shell are identical to those in the calculations of Figures 10.28 and 10.29. The format is similar to that of Figure 10.28 except for the isentropic surface in (c) which has dimensionless entropy 0.9. After Bercovici et al. (1989a).

For a color version of this figure, see plate section.

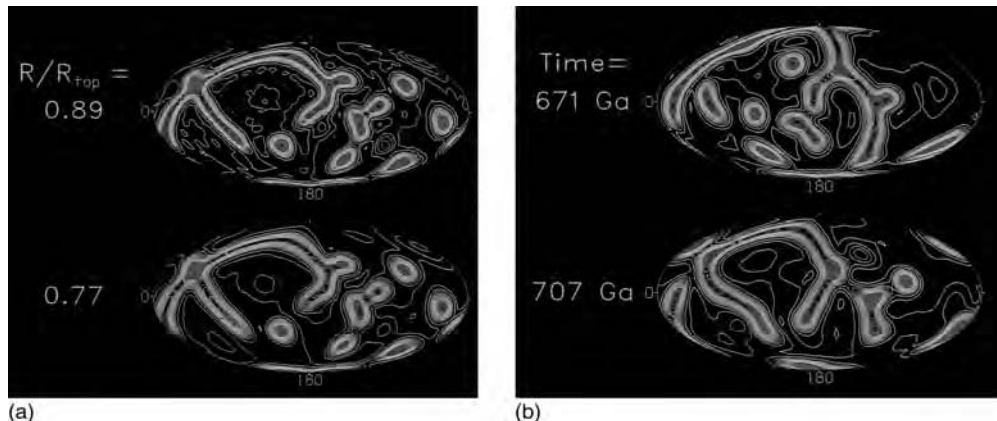


Figure 10.33. Contours of radial velocity in the calculation of Figure 10.32 for different depths at a given instant of time (a) and for different times midway through the shell (b). After Bercovici et al. (1989c).

For a color version of this figure, see plate section.

upward at vertices of a connected grid between the cold downwelling structures that sink onto and spread outward along the lower boundary of the shell. The plumes broaden as they rise into the upper half of the shell feeding the weak background of warm upwelling there. The hot thermal anomalies in the cores of the cylindrical upflows are strongly attenuated as the plumes near the upper surface. The style of convection illustrated in Figure 10.34 is similar to the spoke pattern of three-dimensional bottom-heated convection (Figure 10.27) in that upwelling plumes form at the intersections of warm linear thermals.

Equatorial cross-sections of the thermal anomalies and velocities in the flow of Figure 10.34 (and at an intermediate time step) are shown in Figure 10.35 (Glatzmaier et al., 1990). The cold and hot thermal boundary layers at the upper and lower surfaces, respectively, are clearly seen. Also obvious are the cold descending sheets and cylindrical structures which sink off the top boundary layer and broaden as they encounter the bottom boundary, and the hot upwelling cylindrical plumes which rise off the lower boundary layer and broaden as they encounter the top boundary.

The number and vigor of upwelling plumes in the three-dimensional convection of fluids heated both from below and within depends on the percentage of the total heat flow due to bottom heating. In the example discussed above (Figures 10.34 and 10.35) there are many plumes which are readily detectable near the bottom of the spherical shell, but which weaken and spread laterally in the top of the shell and become difficult to identify there. In a numerical calculation of convection in a predominantly internally heated Boussinesq fluid in a $3 \times 3 \times 1$ rectangular box (Travis et al., 1990b), no plumes occurred (in this calculation, the Rayleigh number based on the temperature difference between the bottom and top of the box was 1.5×10^5 while the Rayleigh number based on the volumetric heating rate was 1.8×10^6). As seen in Figure 10.36, the convective structures in this calculation are downwelling sheets and cylinders in a diffuse upflow, just as in strictly internally heated convection.

Bercovici et al. (1989c) studied the changes in the morphology of three-dimensional convection with the percentage of internal heating in combined heating cases. Figure 10.37 compares the convective styles of spherical shells heated 50% and 80% from within. There are more, but weaker, plumes with the larger percentage of internal heating. Plumes only

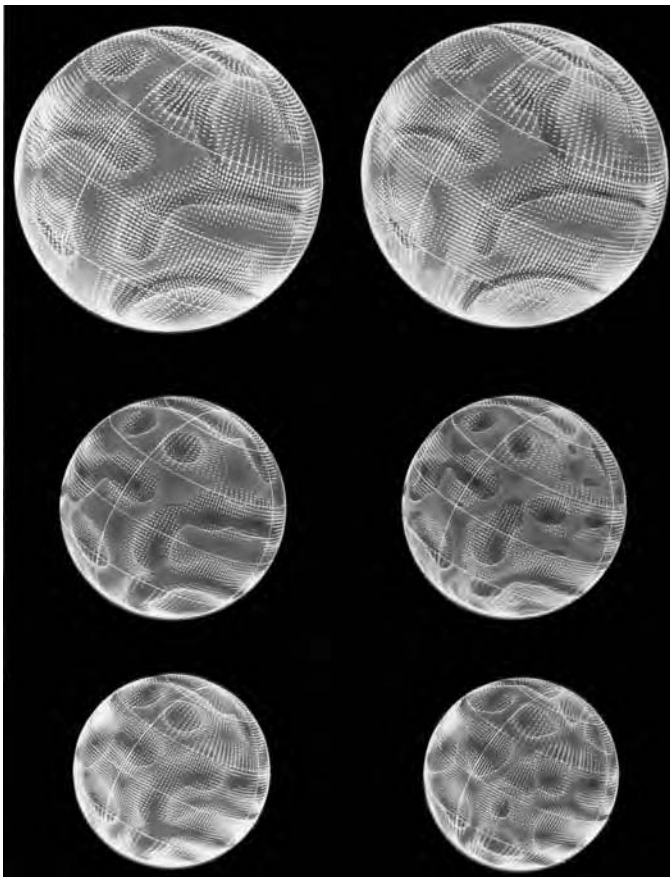
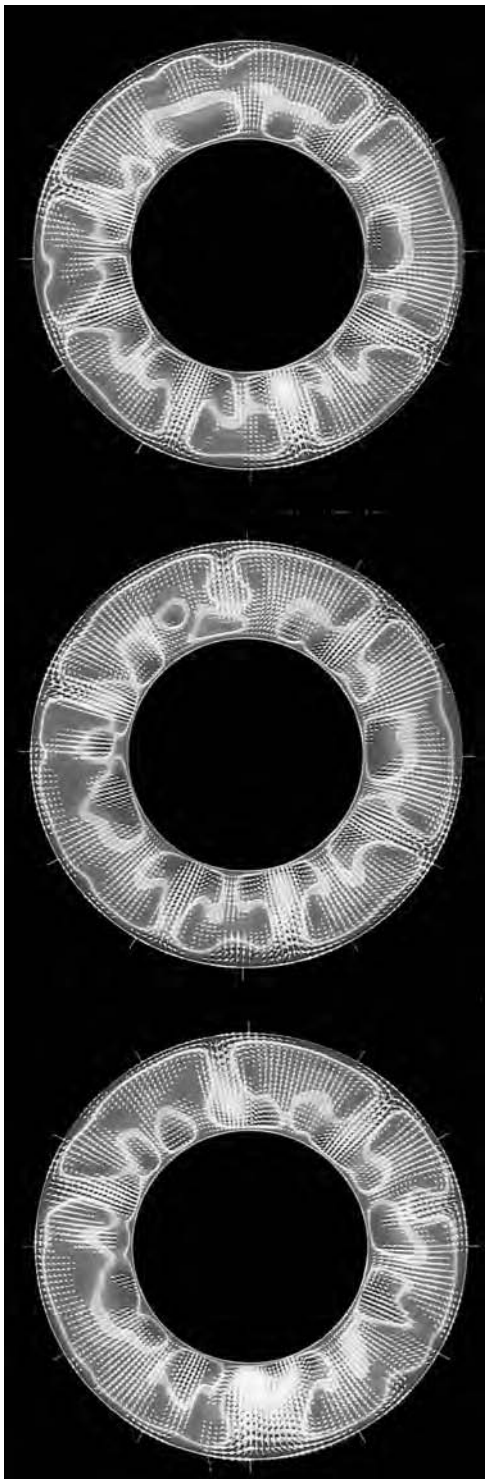


Figure 10.34. Convective velocities (left) and temperatures (right) at a single instant of time in three constant radius surfaces (5,940, 4,350, and 3,770 km) in a numerical model of fully three dimensional thermal convection in a spherical shell of compressible fluid with constant viscosity heated largely from within. The spherical surfaces are scaled according to their radii. The colors in the three plots on the left represent the radial component of velocity with a contour increment of 1.5 mm yr^{-1} . Reds and yellows represent upflow (maximum velocity 12 mm yr^{-1}). The colors on the right represent the temperature relative to the spherically averaged value at each radius with a contour increment of 50 K . Reds and yellows represent hot fluid (temperature anomaly maximum 400 K) and blues represent cold fluid (temperature anomaly minimum -650 K). The arrows represent the direction and amplitude of the horizontal velocity in these surfaces. All arrows are scaled in the same way (maximum velocity 20 mm yr^{-1} , velocities less than 2 mm yr^{-1} are not plotted). The top and bottom boundaries of the shell are isothermal and stress free. About 80% of the heat flow through the top surface is generated inside the shell whose inner and outer radii are 3,480 and 6,370 km. Parameters are identical to the case in Glatzmaier et al. (1990) (the uniform rate of internal heat generation is $10^{-11} \text{ W kg}^{-1}$, it is incorrectly given as $10^{-14} \text{ W kg}^{-1}$ in Glatzmaier et al., 1990). In physical space the grid contains 33 radial levels (more densely packed near the boundaries), 96 latitudinal points, and 192 longitudinal points. In spectral space, spherical harmonics up to degree and order 63 are retained. The integration time step in the calculation is 10^6 yr . The Grüneisen parameter, specific heat at constant pressure, thermal conductivity, and dynamic viscosity are constant with values 1.1 , $1.2 \text{ kJ K}^{-1} \text{ kg}^{-1}$, $23 \text{ W K}^{-1} \text{ m}^{-1}$, and $5.6 \times 10^{22} \text{ Pa s}$. The adiabatic reference state is a polytrope with index 0.4 , a zero-pressure bulk modulus of 115.15 GPa , a zero-pressure density of $3,500 \text{ kg m}^{-3}$, a density at the bottom of $5,570 \text{ kg m}^{-3}$, a temperature at the bottom of $3,000 \text{ K}$, and a temperature at the top of $1,800 \text{ K}$. The heat flux out of the top is about $5 \times 10^{13} \text{ W}$. The volume-averaged Rayleigh number due to both the superadiabatic temperature drop and the internal heating is 1.6×10^6 , about 200 times greater than the critical Rayleigh number required for the onset of convection. The bottom and top surfaces are held at $3,270$ and $1,070 \text{ K}$, respectively. After Glatzmaier et al. (1990).

For a color version of this figure, see plate section.

Figure 10.35. Equatorial cross-sections of convective velocities and thermal anomalies in the flow of Figure 10.34. Time increases from top to bottom (the time steps are at intervals of 200 Myr). The thermal anomalies are temperatures relative to the radially dependent adiabatic temperature profile with a contour increment of 50 K. Reds and yellows represent hot fluid (maximum 300 K) and blues represent cold fluid (minimum of -750 K). The arrows represent velocities in the cross-sectional plane and are scaled as in Figure 10.34. After Glatzmaier et al. (1990).

For a color version of this figure, see plate section.



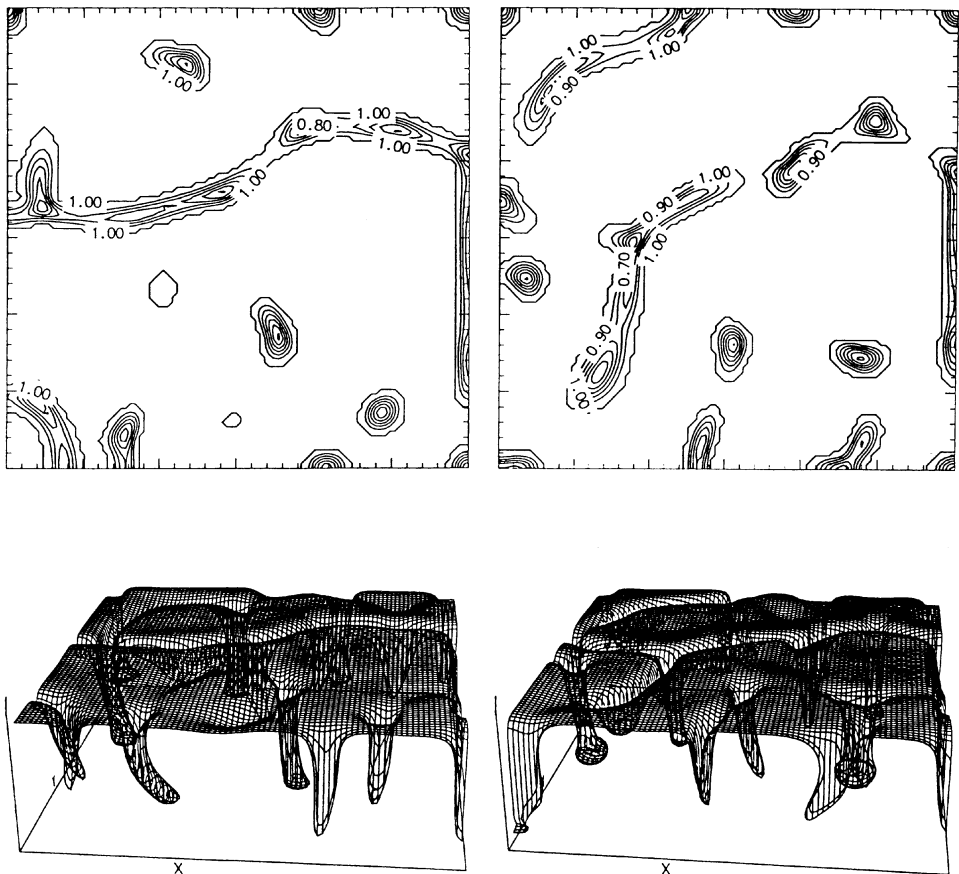


Figure 10.36. Three-dimensional planform of thermal convection in a predominantly internally heated Boussinesq fluid in a $3 \times 3 \times 1$ rectangular box with no-slip boundaries at the top and bottom. The top panels show temperature contours on a horizontal plane located at a fractional depth of 0.25 while the bottom panels are the 0.9 dimensionless isotherm surfaces. The left column is at a dimensionless time 0.01 earlier than the right column. After Travis et al. (1990b).

carry the heat entering the shell from below. Thus, the total heat transported by the 10 plumes of the 80% internally heated case is less than the heat transported by the 4 plumes of the 50% internally heated case. The temporal evolution of these cases shows that with less internal heating, plumes are able to coalesce with time into a smaller number of more vigorous plumes. The downwelling structures are more vigorous when there is more internal heating and they tend to prevent the coalescence of the weaker plumes.

It should be clear from Figures 10.34–10.37 that like the case of pure internal heating, predominantly heated from within convection is also strongly time dependent at high Rayleigh number. As in Figure 10.31, the patterns of convection change with time mainly through the evolution of the cold downflow structures. The long arcuate downwelling sheets drift horizontally, break up, and attach to other downflow sheets and cylinders. The downwelling cylinders also move laterally and attach to other downflow structures. New downwelling structures form sporadically at random sites through gravitational instability of the cold upper thermal boundary layer. Downflows cease when they drain the local boundary layer

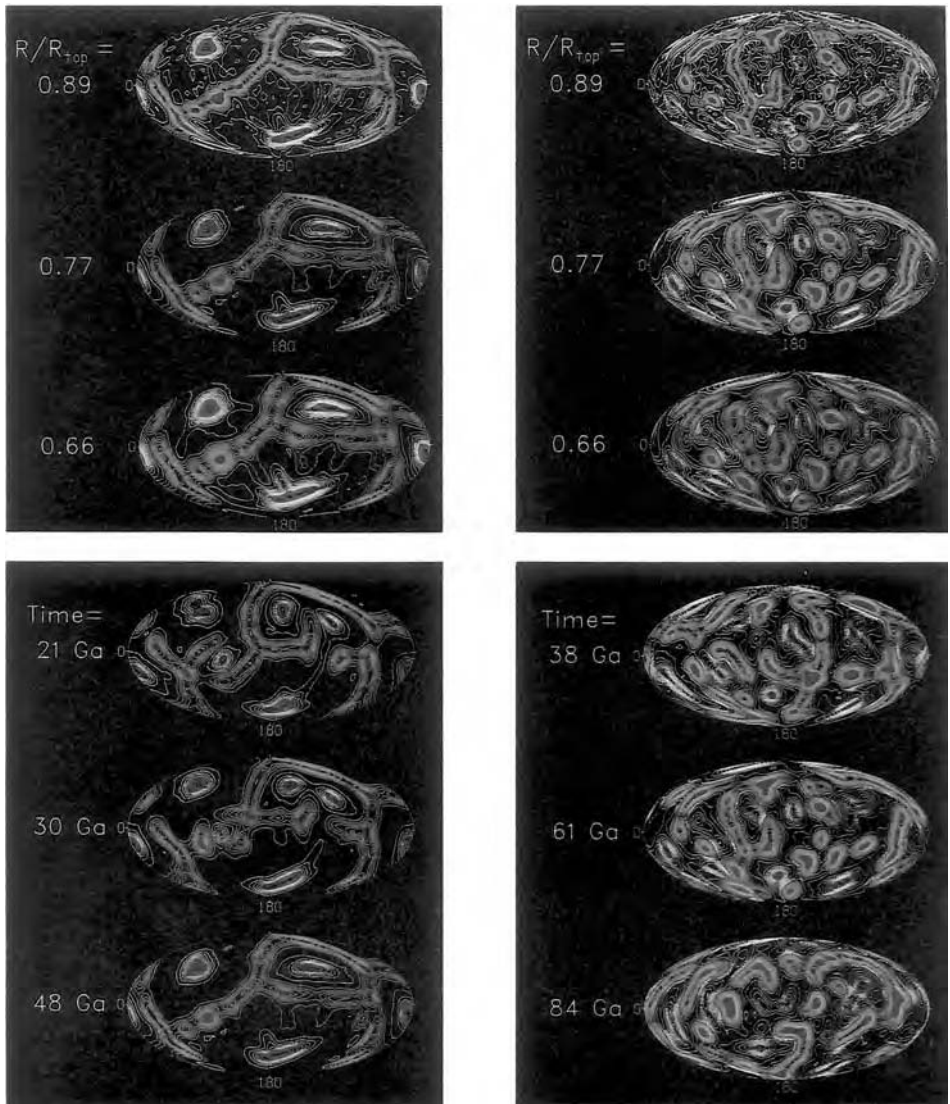


Figure 10.37. Styles of three-dimensional convection in a spherical shell of compressible fluid heated both from within and from below. The planforms on the left are for 50% internal heating, while those on the right are for 80% internal heating. The panels show radial velocity contours on an equal-area projection of a spherical surface at different depths for one time (top) and at different times for one depth ($r/r_{\text{top}} = 0.77$) (bottom). Colors represent equal intervals of velocity (reds and yellows are upflows, blues are downflows). The Rayleigh numbers in both cases are about 100 times the critical Ra for the onset of convection. After Bercovici et al. (1989c).

For a color version of this figure, see plate section.

of cold heavy material. Figure 10.35 shows different stages in the development of the cold heavy downwellings, from their origin as sinkers off the upper cold thermal boundary layer to their detachment as fully developed downflows. The different time frames in the rectangular box model of Figure 10.36 illustrate instances in the breakup of long arcuate downflow

sheets and in the attachment of long sheets to other sheets and isolated cylindrical downflows. Attachment can take place by the propagation or lengthening of sheets parallel to their long dimension or strike. Downwelling sheets reach out to other nearby downflows and take hold of them. If there is a concentration of downflow near the end of a sheet, the region of concentration can break away from the sheet and escape as an isolated downflow.

Through the processes of breakup of long downwelling sheets and attachment of downwelling sheets and cylindrical downflows and initiation of new downflows, the pattern of convection evolves continuously with time. While there are continual changes with time in the detailed pattern of downwelling, the overall nature of the convection, i.e., the manifestation of downwelling predominantly as long arcuate sheet-like structures, some connected and some isolated, and some cylindrical concentrations, is unchanging.

Hot upwelling plumes in the spherical shell models drift laterally, are initiated sporadically at random sites on the lower boundary, wax and wane in strength, and coalesce. The temporal evolution of the upwelling plumes is controlled by the falling of the cold heavy downflow structures onto the lower boundary. Upon encountering the lower boundary the downflows locally quench the hot thermal boundary layer either extinguishing an upflow plume or pushing it aside. Reheating of the cold material eventually reestablishes the hot thermal boundary layer as a potential source for an upwelling plume.

The total kinetic energy in the model of Figures 10.34 and 10.35 oscillates chaotically in time with amplitudes typically about 20% of the mean (Glatzmaier et al., 1990). The power spectrum of the kinetic energy time series has the broadband character indicative of a chaotic system. Chaotic thermal convection of an infinite Prandtl number fluid has also been found to occur in two-dimensional numerical models (Machetel and Yuen, 1987; Vincent and Yuen, 1988). In general, the temporal complexity of convective flows increases with the percentage of internal heating, other factors remaining the same (Bercovici et al., 1989c; Weinstein and Olson, 1990).

The morphological structures of three-dimensional thermal convection in realistic models of the Earth's mantle are strikingly similar to the main dynamical structures found in the mantle. The sheet-like downflows in the models are analogues of the descending slabs in the mantle, and the linear arcuate intersections of the downflow sheets with the surface in the models are analogues of arcuate subduction zones on the Earth's surface. The cylindrical upflows in the models are analogues of plumes believed to occur in the mantle beneath hot spots. The close match of model and real Earth dynamical upflow and downflow structures must be counted as a major success of thermal convection theory in explaining the movement of material in the mantle. Of course, the realistic models of the mantle discussed so far are not realistic enough to explain more detailed characteristics of mantle dynamical structures, but inclusion of other effects discussed in the following sections will bring the convection models even closer to the real Earth.

10.4 Mantle Avalanches

The numerical models discussed in the previous section have shown that the basic structures of mantle convection are arcuate cold downwelling sheets and quasi-cylindrical hot upwelling plumes. The flows in which these structures occur are strongly time dependent, even chaotic, and the structures evolve continuously with time through a variety of processes. While some of the models discussed in Section 10.3 have basic properties similar to that of the mantle, they lack certain elements of realism that strongly influence the nature

of mantle convection. In this and the following sections we explore the consequences of incorporating more realistic thermal, mechanical, and rheological properties of the mantle into three-dimensional numerical simulations of mantle convection. Here we discuss the strong influence of the major mantle phase transitions on the style of mantle convection, with emphasis on the effects of the transition from spinel to perovskite and magnesiowüstite that occurs at a depth of about 660 km in the mantle.

As suggested by the two-dimensional numerical simulations discussed in Chapter 9, the endothermic phase change at a depth of about 660 km in the mantle exerts a profound control on the style of mantle convection (Schubert and Tackley, 1995; Tackley, 1997). The thermophysical basis for the effects of the spinel–perovskite + magnesiowüstite phase transition on mantle convection has been discussed in Chapter 9. Here we explain how these effects are manifest in three-dimensional numerical simulations of mantle convection. These simulations have been carried out in Cartesian geometry by Honda et al. (1993a, b) and Yuen et al. (1994) and in a spherical shell by Tackley et al. (1993, 1994), Tackley (1996a, b), and Machetel et al. (1995).

The spherical shell model of Tackley et al. (1993) contains the endothermic spinel to perovskite+magnesiowüstite phase change (at a depth of 670 km in the model). The mantle is self-gravitating and compressible (the anelastic approximation is adopted). The Murnaghan equation of state is used with pressure p and density ρ related by $p \propto \rho^{1+(1/n)} - \rho_0^{1+(1/n)}$, where n is the polytropic index. A constant Grüneisen parameter of 1.0 and a polytropic index of 0.5 yields a model radial density profile in reasonable agreement with PREM. Thermal expansivity in the model varies from 3.0×10^{-5} at the surface to 2.2×10^{-5} at 670 km depth and 1.2×10^{-5} at the core–mantle boundary (CMB). Heat capacity is assumed constant at $1,250 \text{ J kg}^{-1} \text{ K}^{-1}$. Dynamic viscosity is a function of depth only, increasing roughly exponentially from $1.7 \times 10^{22} \text{ Pa s}$ at the surface to $1.9 \times 10^{22} \text{ Pa s}$ at 670 km depth to $2.1 \times 10^{23} \text{ Pa s}$ at the CMB. Thermal conductivity is $2.3 \text{ W m}^{-1} \text{ K}^{-1}$ at the surface and increases with depth as the fourth power of density, giving a lower mantle increase consistent with experiments (Osako and Ito, 1991) and theory (Anderson, 1987b). The surface and the CMB are isothermal and stress free; the surface temperature is fixed at 1,060 K and the CMB temperature is 3,450 K. The temperature rise across the mantle is comprised of 1,140 K due to adiabatic compression and 1,250 K due to superadiabaticity. The mantle is internally heated at the rate $2.75 \times 10^{-12} \text{ W kg}^{-1}$, about half the chondritic heating rate. The volume-averaged Rayleigh numbers resulting from internal heating and superadiabaticity are 1.8×10^7 and 1.2×10^6 , respectively. These values of Ra are more than an order of magnitude smaller than those for the real Earth. The model assumes a Clapeyron slope of -4 MPa K^{-1} (Ito and Takahashi, 1989; Ito et al., 1990), a high value that maximizes the influence of the phase change. The model results in a mean surface heat flow of $2 \times 10^{13} \text{ W}$, similar to that of the Earth, and convective velocities as large as about 40 mm yr^{-1} and typically 6 mm yr^{-1} at the surface, smaller than that of the Earth.

Figure 10.38 illustrates the shape of cold downflows in the model of Tackley et al. (1993). There is a network of interconnected sheets in the upper mantle and cylinders in the lower mantle. The sheet-like downflows do not extend below 670 km depth. Material in these sheets cannot penetrate the phase change; instead, this material flows laterally on top of the phase change and accumulates in quasi-cylindrical piles (with diameter about 1,000 km) at the intersections of the sheets. When enough cold and heavy material piles up to overcome the inhibitive force of the phase boundary, the pile breaks through the phase boundary and sinks into the lower mantle in an event described as an avalanche (Tackley et al., 1993).

The cylindrical avalanches in the lower mantle spread out like pancakes when they fall onto the lower or core–mantle boundary. The avalanches provide efficient conduits for rapidly flushing large quantities of cold material all the way to the core–mantle boundary where the spreading cold material effectively cools the core.

The picture of mantle convection provided by Figure 10.38 is a snapshot at one particular time. The scene changes dramatically in detail with time, the positions and numbers of upper mantle sheets and lower mantle cylinders change, but the overall character is unchanged. There are always upper mantle sheets and lower mantle cylinders. Avalanches occur sporadically in space and time. At any one time there are always several avalanches in progress.

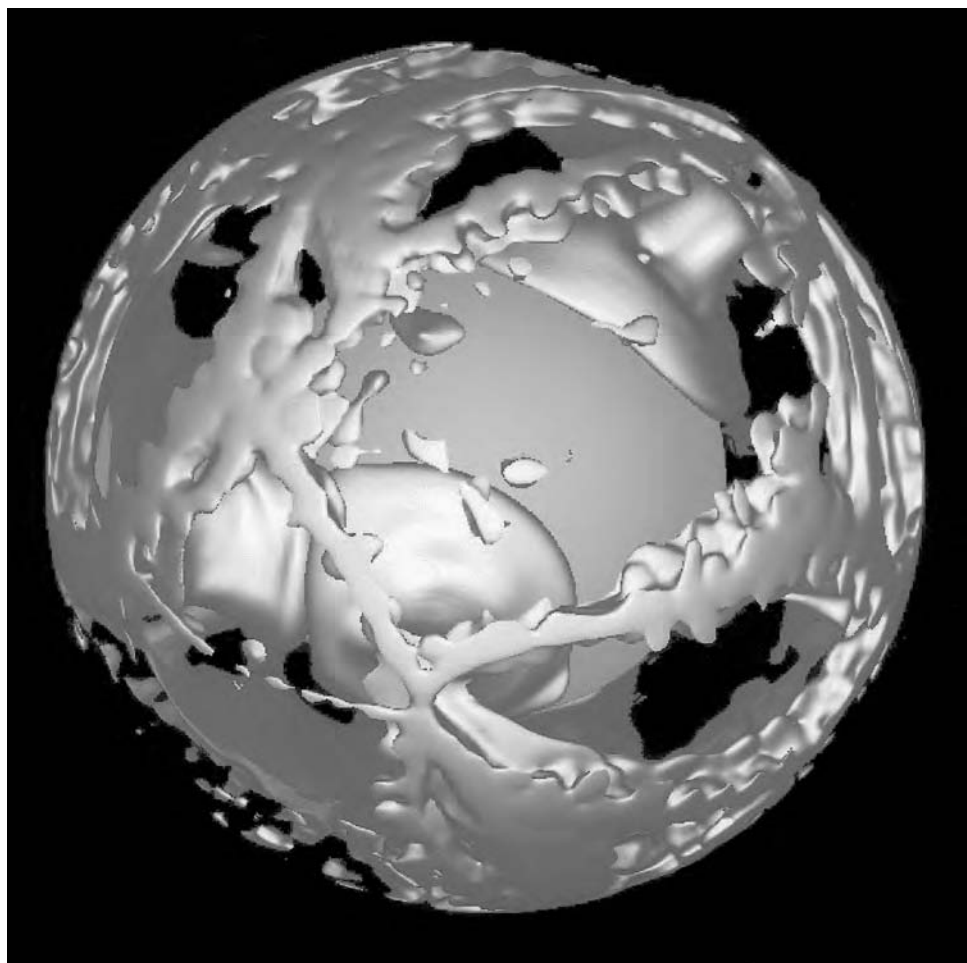


Figure 10.38. A snapshot of a cold isothermal surface in the model of Tackley et al. (1993). The blue surface is 110 K lower in temperature than the horizontally averaged temperature at every radius. The green surface is the lower boundary of the model (the core). A network of interconnected linear downflows is visible in the upper mantle with three large cylindrical downwellings in the lower mantle that spread out into pools of cold material above the core–mantle boundary.

For a color version of this figure, see plate section.

Convection is therefore of the whole-mantle type since there is always substantial mass exchange between the upper and lower mantles. Two-dimensional models (Machetel and Weber, 1991; Peltier and Solheim, 1992; Weinstein, 1993; Solheim and Peltier, 1994a, b; Ita and King, 1994), on the other hand, predict long periods of time in which the endothermic phase change cuts off any mass transfer across the transition, forcing the mantle into a two-layer mode of convection which is eventually terminated by a massive avalanche of material that has piled up on the phase boundary. Intermittent whole-layer and two-layer mantle convection on a global scale does not occur in three-dimensional models (see also the discussion in Section 9.5). Machetel et al. (1995) have reported a layered three-dimensional solution when the Clapeyron slope γ of the endothermic phase transition is -4 MPa K^{-1} . Their solution assumes that thermal expansivity $\alpha = 1.4 \times 10^{-5} \text{ K}^{-1}$ throughout the mantle; this value of α is appropriate for the lower mantle but it is too low for the transition zone (see Chapter 4). As will be seen below when we discuss the phase buoyancy parameter, the effectiveness of an endothermic phase transition in inhibiting flow is proportional to γ/α , so a value of α that is a factor of 2 too low is equivalent to a calculation with $\gamma = -8 \text{ MPa K}^{-1}$ and a realistic α . Such a large value of γ is unrealistic for the Earth's 660 km phase transition. By reducing thermal buoyancy to an unrealistic value in the transition zone, Machetel et al. (1995) enabled cold downflows to be stopped by the endothermic phase transition with $\gamma = -4 \text{ MPa K}^{-1}$.

The hot upwellings that are complementary to the cold downflows of Figure 10.38 are shown in Figure 10.39. There are broad hot regions in the upper mantle, hot ridges at the core–mantle boundary, and a single plume of hot material connecting the core–mantle boundary with one of the hot upper mantle regions. This picture is again a snapshot of a highly time variable situation. The hot ridges on the core–mantle boundary are swept around and form and re-form in response to the avalanches of cold material falling sporadically on the core–mantle boundary. Plumes of hot material erupt irregularly from ridge intersections. The number of plumes in this simulation is relatively small because of the thorough blanketing of the core by the cold avalanches. Most of the upflow occurs in a broad featureless rise of material characteristic of internally heated convection.

Both the cold downflows and hot upflows are simultaneously visible in the temperature cross-sections of Figure 10.40. There are horizontally broad regions of both hot and cold material in the upper mantle in addition to small-scale convection cells. The broad regions of cold material correspond to the pile-up of downflows on the endothermic phase change. Some of the broad hot regions are fed by hot material from mantle plumes. There is strong heterogeneity in the upper mantle at large horizontal dimensions as a consequence of the inhibitory effect of the phase change on the sheet downwellings. There is also broad horizontal structure at the core–mantle boundary which is almost surrounded by cold avalanche material. One of these avalanches connects the upper mantle to the core–mantle boundary. Another avalanche is in its earliest stages, before the sinking cold material has fallen onto the core–mantle boundary. A couple of well-developed mantle plumes are seen to emerge from the core–mantle thermal boundary layer; a few incipient plumes are also visible. Figure 10.40 also shows that the smaller downwellings of the model without the endothermic phase change slow down and broaden with depth in the lower mantle (due to increasing viscosity and decreasing thermal expansivity with depth). These downwellings are less efficient in blanketing the core with cold material than are the avalanches in the phase change model, with the result that there is enhanced plume formation at the lower boundary of the model without the phase change.

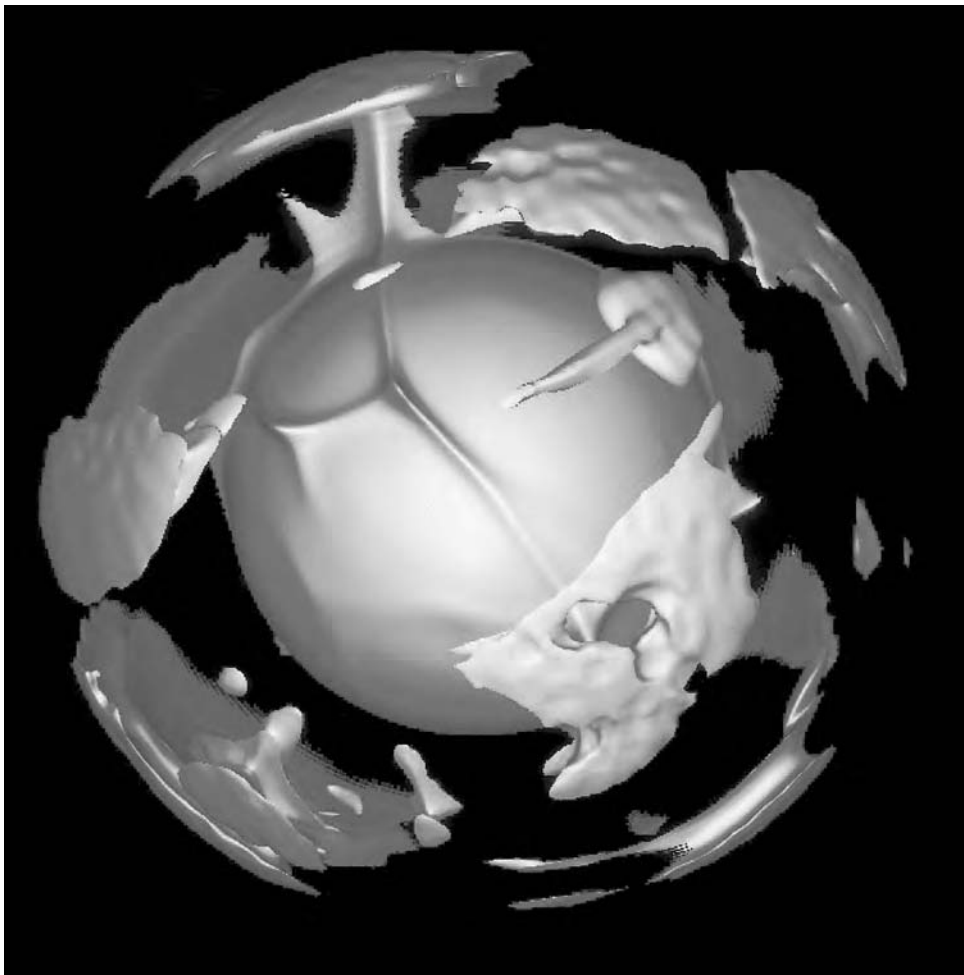


Figure 10.39. A hot isothermal surface in the model of Tackley et al. (1993) at the same instant of time as in Figure 10.38. The red surface shows where the temperature is 110 K higher than the reference state adiabat at all depths. A single plume from the core–mantle boundary supplies hot material to a region of the upper mantle. Most broad hot regions of the upper mantle are not directly linked to lower mantle structures.

For a color version of this figure, see plate section.

The above results emphasize the role of the endothermic phase change in producing avalanches and in controlling the dominant length scales in different regions of the mantle. The behavior of the phase change responsible for these results is the displacement of the phase boundary in response to changes in temperature. Though the latent heat of the phase change has less important dynamical effects, it is still significant for the thermal state of plume material reaching the upper mantle. Passage of a plume through the phase change heats the plume through the absorption of latent heat released by the endothermic phase change as more dense perovskite converts to less dense spinel (Schubert et al., 1995) (Figure 10.41). The additional plume heat has important consequences for the manifestation of a plume as a hot spot. A hotter plume can more effectively thin the lithosphere, produce partial melts due to pressure-release melting in the plume, and melt the rock of the lower lithosphere.

Heat release in regions of material upwelling through the endothermic phase change can also result in the formation of diapiric structures in the upper mantle (Liu et al., 1991).

Comparison of the above model results with seismic observations of the mantle shows that the spinel–perovskite phase change is a key to explaining the seismic data and understanding

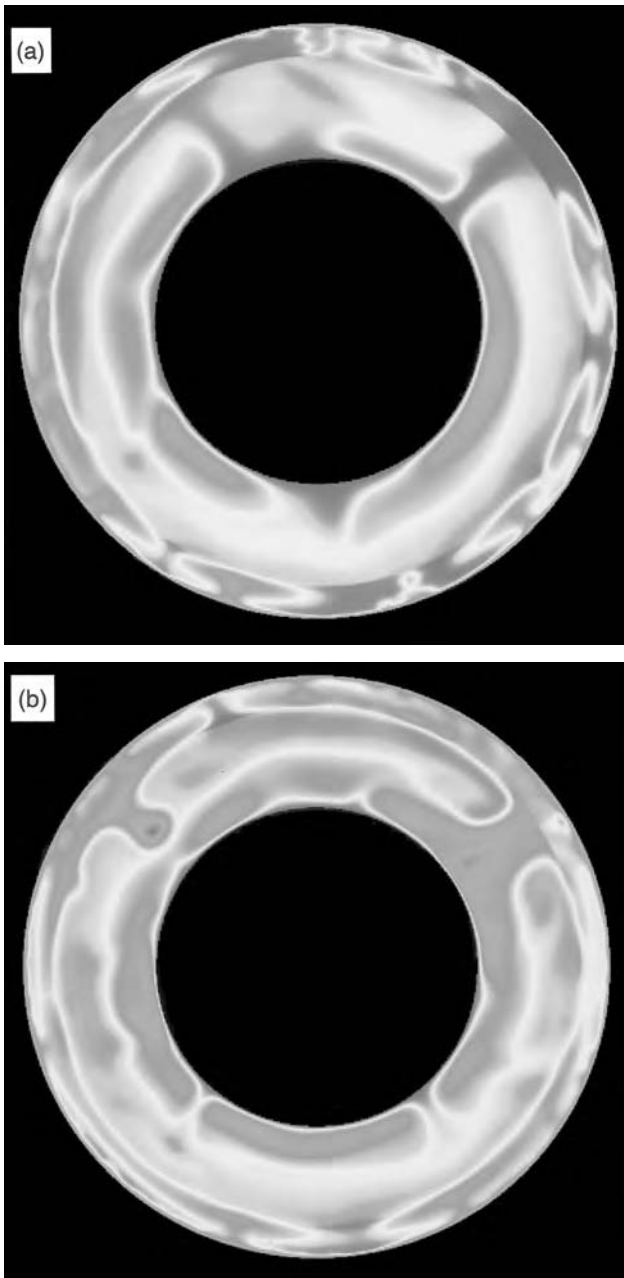


Figure 10.40. Different cross-sectional slices of the superadiabatic temperature field in the model of Tackley et al. (1993) at the same time as in Figures 10.38 and 10.39 (a) and (b). Red is hot and blue is cold with the temperature scale varying between +350 K and -1,050 K. (Continued)

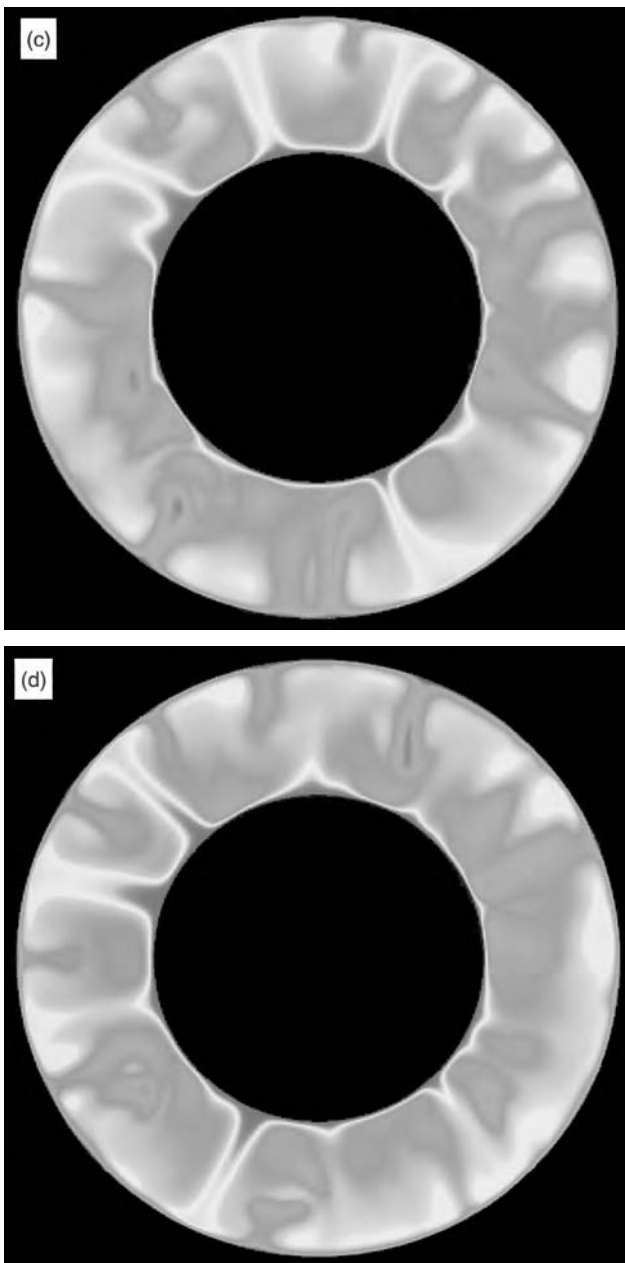


Figure 10.40. (c) and (d) show similar cross-sections of superadiabatic temperature for a numerical calculation that does not include the endothermic phase change (Tackley et al., 1993). The temperature scale in (c) and (d) ranges between +220 K and -780 K.

For a color version of this figure, see plate section.

mantle convection. The seismic tomographic images of van der Hilst et al. (1991) and Fukao et al. (1992) suggest that the slabs beneath the southern Kuril, Japan and Izu-Bonin arcs meet resistance at 660 km depth and tend to flatten and move horizontally at this depth, while the slabs beneath the Mariana and Kuril-Kamchatka arcs plunge through 660 km depth into the

Axisymmetric Model

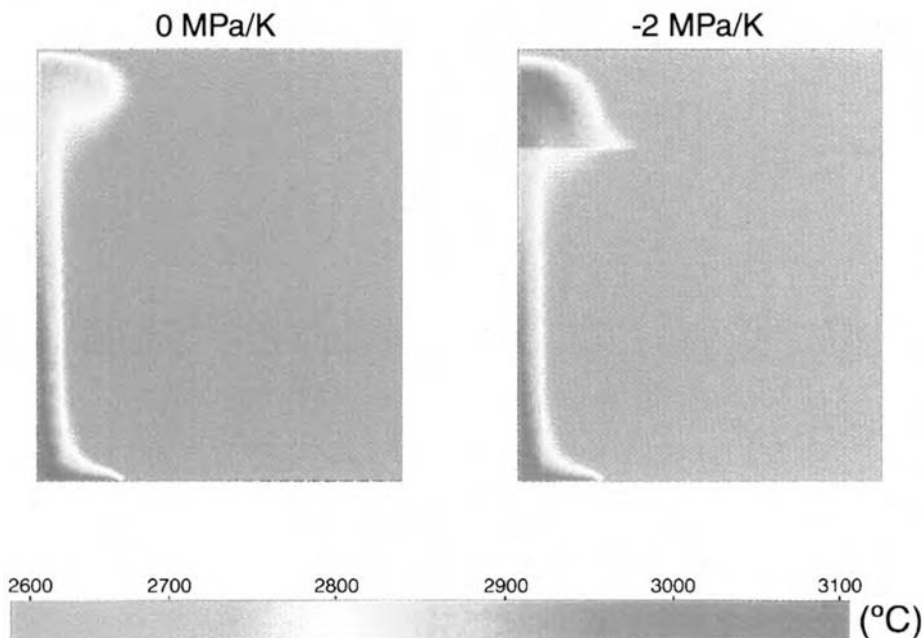


Figure 10.41. Temperature fields of two axisymmetric plumes, one that has passed through an endothermic phase change (right) and one that has not (left). The plume that went through the phase change is about 100 K hotter than the other plume. After Schubert et al. (1995).

For a color version of this figure, see plate section.

lower mantle. The flattening out of the slabs may be analogous to the pile-up of cold sheet-like downflows on the endothermic phase boundary in the model calculations, a consequence of the downward displacement of the phase change caused by the cold temperatures of the downwellings. Why some real slabs are able to penetrate the 660 km depth phase change while no model slabs are capable of this may be due to differences in the numerical models and the Earth, of which there are many. For example, real slabs are relatively rigid due to the strong dependence of mantle viscosity on temperature, while the three-dimensional spherical numerical models discussed above do not account for variable viscosity. The rigidity of real slabs may also affect how accumulations of slabs on the 660 km discontinuity might ultimately sink under their weight into the lower mantle because slab material is not able to flow horizontally along the strike of a slab as can the less viscous material in the model calculations. Cylindrical accumulations of material at slab intersections above the 660 km depth phase transition may not be able to form in the Earth, and avalanches, if they occur in the Earth, may be unlike those in the numerical models. Some real slabs may be able to penetrate the 660 km depth phase change because of the angle at which they impinge on the transition; in the numerical model the sheets fall vertically on the phase change, the most favorable angle for penetration.

Retrograde trench migration (Garfunkel et al., 1986) may also play a role in whether slabs are able to penetrate the 660 km phase change in the Earth (Yoshioka and Wortel, 1995; Christensen, 1996; Moresi and Gurnis, 1996). Laboratory experiments on subduction (Kincaid and Olson, 1987; Griffiths et al., 1995; Guillou-Frottier et al., 1995) show that

retrograde trench migration can cause a highly viscous slab to flatten out along an interface across which the viscosity and density increase abruptly from the upper layer to the lower layer. Similar behavior has been found in a numerical study of retrograde migrating slabs interacting with the 660 km endothermic phase transition (Christensen, 1996). In these numerical experiments, trench migration velocities in excess of $20\text{--}40 \text{ mm yr}^{-1}$ always resulted in slab flattening on the phase change. However, even flattened slabs eventually penetrated the phase transition. The same phenomenon could occur in the Earth for retrograde migrating slabs encountering the 660 km phase change with either the inhibitory effect of the phase change or a jump in viscosity at the phase change boundary providing resistance to slab penetration.

Question 10.2: Do the properties of the endothermic phase change at a depth of 660 km explain the seismically observed morphological diversity in slabs near the base of the upper mantle and the top of the lower mantle?

Global seismic tomography (Su et al., 1992; Su et al., 1994) has shown the structure of mantle heterogeneity to be characterized by relatively strong long wavelength variations in the upper mantle, relatively weak variations over a broad wavelength spectrum in the upper part of the lower mantle, and relatively strong long wavelength variations near the base of the mantle (Figure 10.42). The spectrum of thermal heterogeneity in the model calculations of Figures 10.38–10.40, also shown in Figure 10.42, bears a striking resemblance to the observed spectrum of seismic heterogeneity. There is a similar concentration of power at long wavelengths in the upper mantle and in the bottom of the lower mantle of the model. The endothermic phase change in the model is essential in establishing these predominant wavelengths in the different regions, although the match of the model heterogeneity spectrum to seismic observations is partly due to other factors such as the viscosity increase with depth and the percent basal heating. The piling up of cold downflows on the phase boundary creates the long-wavelength upper mantle heterogeneity, while the spreading of cold downflow avalanches on the core–mantle boundary creates the long-wavelength heterogeneity at the bottom of the lower mantle. Models that do not incorporate the endothermic phase change

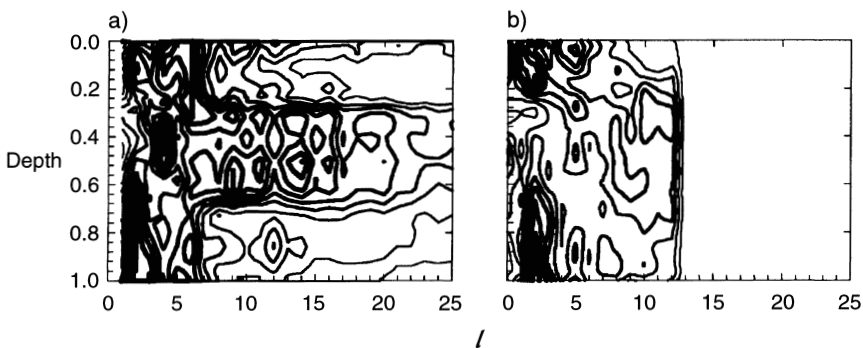


Figure 10.42. A spectral heterogeneity map for thermal anomalies in the calculation of Figures 10.38–10.40 (a) and seismic velocity in the seismic model SH12/WM13 of Su et al. (1992) (b) (see also Su et al., 1994). The plots are normalized by the total root mean square amplitude at each radius. The parameter l is the degree of the spherical harmonic. After Tackley et al. (1994). Redrawn from Schubert and Tackley (1995).

(Tackley et al., 1993, 1994) yield a spectrum of thermal heterogeneity unlike the observed spectrum of seismic heterogeneity (Su et al., 1992; Su et al., 1994).

Question 10.3: *Is the 660 km phase change responsible for imposing the long-wavelength spectral character of mantle seismic heterogeneity?*

Mantle avalanches, in addition to mantle plumes, can bring anomalously hot mantle material to the base of the lithosphere. When an avalanche takes place, a large amount of cold material that was piled up on the 660 km phase change is rapidly flushed into the lower mantle and is replaced by hotter mantle material from below. While anomalously cold upper mantle material sinks into the lower mantle during an avalanche, anomalously hot lower mantle material rises into the upper mantle to conserve mass. Though an avalanche is fundamentally a downflow phenomenon, its consequence for the upper mantle can be analogous to the arrival of a lower mantle plume, i.e., the inflow of anomalously hot material. Thus it is possible that major tectonothermal events normally associated with mantle plumes, e.g., the massive outpourings of continental flood basalts, could instead be caused by avalanche events in the mantle (Schubert and Tackley, 1995).

Question 10.4: *Do the avalanches that occur in mantle convection models also occur in the Earth's mantle?*

Mantle avalanches are affected by the exothermic olivine– β -modified spinel phase change at a depth of about 410 km in the mantle. In general, it would be expected that the 410 km phase change would mitigate against mantle avalanches because the exothermic 410 km phase change acts dynamically opposite to the endothermic 660 km phase change (Schubert et al., 1975). The net result of phase boundary distortion due to temperature and latent heat effects is to promote flow through the 410 km phase change whereas flow is impeded by the 660 km phase change (Schubert et al., 1975). While the 410 km phase change mitigates against the thermal and dynamical effects of the 660 km phase change, the 660 km phase change dominates the dynamics and thermics because the magnitudes of the Clapeyron slope and density change of the 660 km phase transition are larger than those of the shallower phase change. Numerical models of the combined effects of both phase transitions on mantle convection have been carried out by Steinbach and Yuen (1992), Zhao et al. (1992), Solheim and Peltier (1994a, b), and Tackley et al. (1994).

The relative influence of the olivine– β -modified spinel and spinel–perovskite+ magnesiowüstite phase transitions on mantle convection can be assessed by evaluating the phase buoyancy parameter P (Schubert and Turcotte, 1971; Schubert et al., 1975; Christensen and Yuen, 1985) (see Section 7.4)

$$P \equiv \frac{\gamma \Delta \rho}{\alpha \rho^2 g d} = \frac{(\gamma \Delta T / \rho g) \Delta \rho}{\rho \alpha \Delta T d} \quad (10.4.1)$$

where γ is the Clapeyron slope of the phase transition

$$\gamma = \left(\frac{dp}{dT} \right)_c = \frac{Q \rho_1 \rho_2}{T \Delta \rho} \quad (10.4.2)$$

Q is the latent heat required per unit mass to change material of phase 2 into that of phase 1, the upper phase is phase 1 and the lower phase is phase 2, $\Delta\rho = \rho_2 - \rho_1$, ρ is density, T is temperature, ΔT is the characteristic temperature difference (the superadiabatic temperature change across the convecting layer), p is pressure, α is thermal expansivity, g is the acceleration of gravity, and d is the thickness of the convecting region. The parameter P is the ratio of the mass per unit area due to phase boundary distortion caused by ΔT (the numerator in the far right side of 10.4.1) to the mass per unit area associated with thermal expansion and the temperature difference ΔT (the denominator in the far right side of 10.4.1). The parameter P is identical, to within the near-unity factor $(1 - \gamma\beta/\rho g)^{-1}$ (β is the magnitude of the temperature gradient), with the parameter S of Schubert and Turcotte (1971) and Schubert et al. (1975).

If we evaluate (10.4.1) for each of the phase transitions and assume $\alpha\rho gd$ has the same value for both phase changes, then we can write

$$\frac{P_{410}}{P_{660}} = \frac{(\gamma\Delta\rho/\rho)_{410}}{(\gamma\Delta\rho/\rho)_{660}} \quad (10.4.3)$$

The fractional density change for the 410 km discontinuity is about 5% and it is about 10% for the 660 km discontinuity. The Clapeyron slope for the 410 km phase change is between 1.5 MPa K^{-1} and 2.5 MPa K^{-1} (Akaogi et al., 1989; Katsura and Ito, 1989) and it is between about -2 MPa K^{-1} and -4 MPa K^{-1} for the 660 km phase change. Bina and Helffrich (1994) have reassessed the thermochemical data on the Clapeyron slopes of the 410 km and 660 km phase transitions and propose a value of about 3 MPa K^{-1} for γ_{410} and a value of about -2.5 MPa K^{-1} for γ_{660} . If we use $\gamma_{410} = 2 \text{ MPa K}^{-1}$ and $\gamma_{660} = -3 \text{ MPa K}^{-1}$ then the magnitude of P_{410}/P_{660} is 1/3 (if we use the Clapeyron slopes determined by Bina and Helffrich (1994) we get 0.6). The magnitude of P_{410}/P_{660} is even smaller since α actually decreases with depth between the depths of 410 km and 660 km (Anderson et al., 1992; Chopelas and Boehler, 1992). On this basis, the phase change at 660 km depth should dominate over the shallower phase change with regard to the influence of the phase changes on mantle convection. This conclusion is confirmed by the numerical models of Tackley et al. (1994) discussed below.

Tackley et al. (1994) have generalized their model described above to include the shallower phase change at a depth of 410 km in the mantle. The style of convection when both major mantle phase transitions are included is illustrated in Figure 10.43 (compare with Figures 10.38 and 10.39). For the model shown in Figure 10.43, Tackley et al. (1994) assumed $\gamma_{410} = -\gamma_{660} = 4 \text{ MPa K}^{-1}$ and $\Delta\rho_{410} = \Delta\rho_{660} = 400 \text{ kg m}^{-3}$ (a strong 410 km phase change). With both phase transitions included in the model, the convection is more complex compared with the model containing only the 660 km phase change. Avalanches display a wider range of morphologies and are generally smaller and more frequent. The 410 km phase change limits the amount of cold material that can pile up above the 660 km phase change; when accumulations become thick enough to straddle the 410 km phase transition, the additional negative buoyancy caused by the upward deflection of the 410 km phase change pushes the cold material through the 660 km phase transition, resulting in more frequent and smaller avalanches. The range of morphologies is greater because such breakthroughs may be forced before cold material is able to flow to triple junctions and accumulate into broad pools.

The hot isosurfaces in Figure 10.43 show several strong plume-like upwellings which readily penetrate the 660 km phase change. The smaller avalanches that occur when both

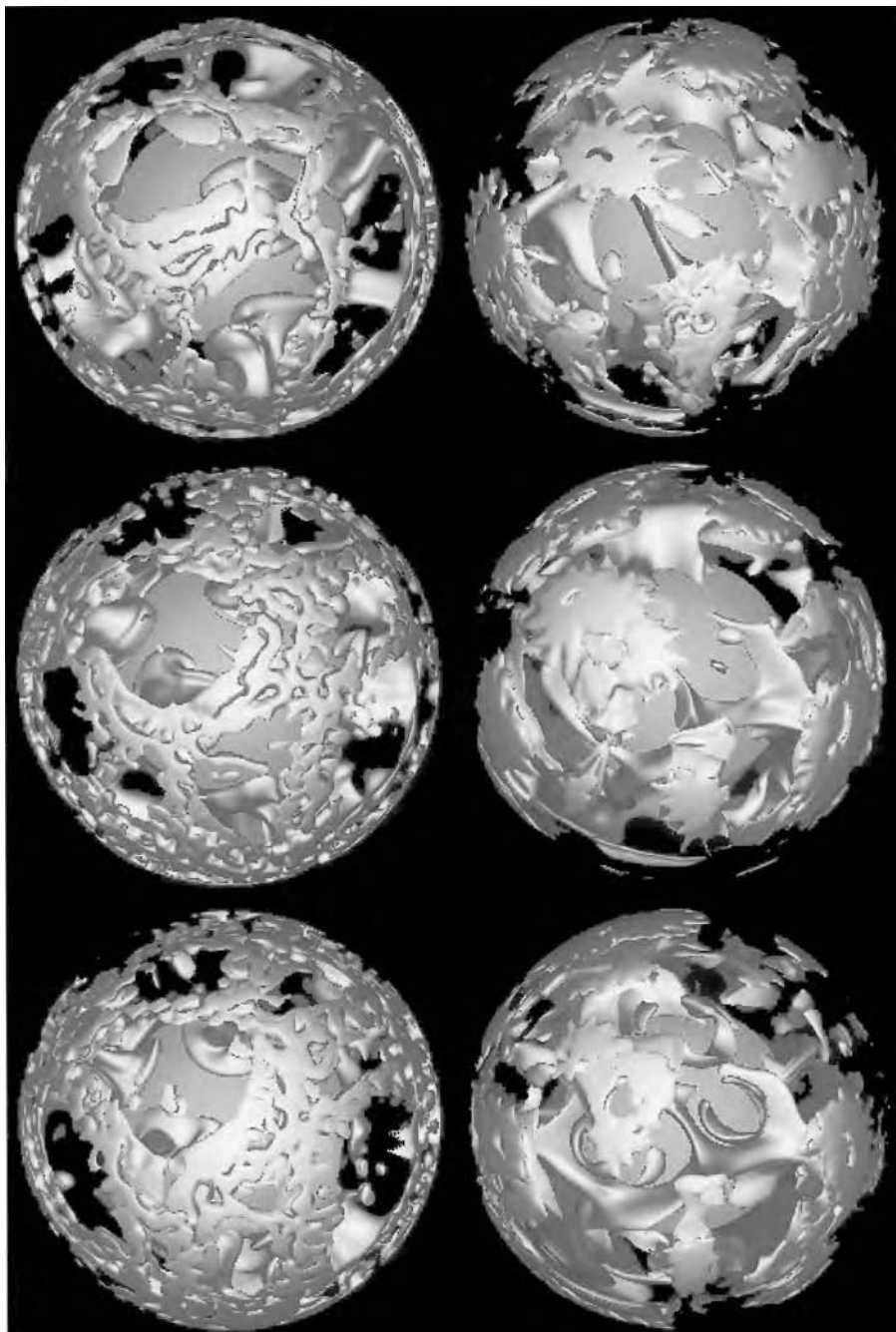


Figure 10.43. Cold downflows (left) and hot upflows at three times (at intervals of about 500 Myr) during the simulation of mantle convection by a model containing phase transitions at depths of 400 km and 670 km (Tackley et al., 1994). Cold and hot isosurfaces show where the temperature is 110 K lower and higher, respectively, than the horizontal average. The core–mantle boundary is shown in green. Time increases down the figure.

For a color version of this figure, see plate section.

phase transitions are present are less effective in surrounding the CMB with cold material and thus a larger fraction of the core heat loss is taken up in driving active upwellings.

Examination of Figure 10.43 and related results shows that three distinct regions of the mantle can be identified when both phase transitions govern the style of mantle convection: (1) the upper mantle, characterized by linear downwellings and pools of cold material above the 660 km phase change; (2) the mid-mantle characterized by large cylindrical downwelling plumes and weaker upwelling plumes; and (3) the deep mantle, characterized by pools of avalanched material surrounding the core and a network of interconnected hot ridges which sometimes break through the mid-mantle in the form of plumes to the upper mantle. The upper mantle can be further divided into a transition zone in which the pools of cold material accumulate and the shallow mantle which contains narrow linear downwellings and the upper thermal boundary layer. The phase change at a depth of 660 km is predominant in establishing this structure which is also apparent in the spectral heterogeneity map of Figure 10.42.

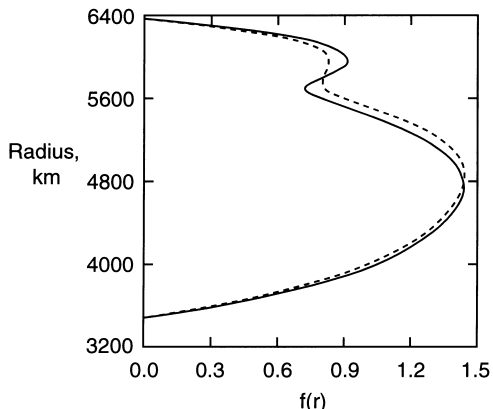
Tackley et al. (1994) calculated the geoid anomalies associated with the flow in Figure 10.43. A number of studies (Ricard et al., 1984; Richards and Hager, 1984; Hager and Clayton, 1989) have shown that the net geoid resulting, for example, from a cold temperature anomaly (a positive mass anomaly) is the small difference of two large terms, the geoid high associated with the anomaly itself and the geoid low associated with the dynamically induced negative topography at the surface and the CMB. The sign and amplitude of the observed geoid are sensitive to the radial viscosity structure and any chemical stratification that might exist. For the flow of Figure 10.43, a cold temperature anomaly (a positive mass anomaly) at the 660 km phase transition deflects the 660 km phase boundary downward, resulting in a negative mass anomaly. The geoid contributions of these opposite mass anomalies partially cancel, thereby reducing the geoid contribution from transition zone heterogeneity. In contrast, deflection of the 410 km phase boundary results in a geoid contribution of the same sense as from temperature anomalies in that region, enhancing the geoid contribution from the middle of the upper mantle. The geoid for the flow of Figure 10.43 is completely dominated by the structure in the upper mantle. The geoid signals over major downwellings in the flow of Figure 10.43 turn out to be geoid lows. The geoid signals over slab downwellings in the Earth are geoid highs (Figures 2.4–2.6). It is well known that Earth models give geoid highs over subduction zones only if they have a large increase of viscosity with depth at the 660 km phase boundary (Hager and Clayton, 1989; Davies and Richards, 1992; King and Masters, 1992; Forte et al., 1993). Indeed, the need to match subduction zone geoid highs in Earth models is the major observational constraint requiring a viscosity jump from the upper mantle to the lower mantle across the 660 km phase boundary. The model of Figure 10.43 does not include a viscosity jump at the depth of 660 km and accordingly it does not yield a geoid high over mantle downwellings.

The spherically averaged temperature in the flow of Figure 10.43 shows boundary layers at the surface, at 660 km depth and at the core–mantle boundary, and subadiabatic regions in both the upper mantle and lower mantle. Subadiabatic interior temperature gradients are expected in a mantle heated substantially from within (Schubert, 1992; Parmentier et al., 1994), but the avalanches strongly increase the subadiabaticity of the lower mantle by piling up cold material above the core–mantle boundary.

A measure of the degree of layering in the flows of Figures 10.38, 10.39, and 10.43 is provided by the radial mass flux diagnostic (Peltier and Solheim, 1992)

$$f(r) \equiv \frac{\langle \rho |u_r| \rangle}{(1/(r_{\text{surf}} - r_{\text{cmb}})) \int \langle \rho |u_r| \rangle dr} \quad (10.4.4)$$

Figure 10.44. Radial mass flux function $f(r)$ defined in (10.4.4) versus radius for flow with both exothermic and endothermic phase transitions (dashed curve) and for flow with only the endothermic phase change (solid curve). After Tackley et al. (1994).



which is shown in Figure 10.44 for both flows. The radial mass flux diagnostic measures the amount of mass transfer across a radius by calculating the average over a spherical surface of the absolute value of the radial mass flux $\langle \rho |u_r| \rangle$ at a radius r (the brackets indicate an average over the spherical surface and u_r is the radial velocity). An average of the absolute value of the mass flux determines the amount of mass transfer across the surface, whether inward or outward. The denominator in (10.4.3) normalizes $f(r)$ by integrating $\langle \rho |u_r| \rangle$ over radius. The tendency of the endothermic phase change to inhibit mass transfer across itself is shown by the local minimum in $f(r)$ in Figure 10.44. Comparison of $f(r)$ for the cases with and without the exothermic phase change shows that the presence of the 410 km phase change promotes mass exchange across the deeper phase transition – $f(r)$ for the case with the 410 km phase change (dashed curve) has a less pronounced minimum at the depth of the endothermic phase change than $f(r)$ for the flow with only the endothermic phase change. While the endothermic phase change does inhibit mass exchange across itself, the flow in this spherical model of the present Earth is never layered, i.e., mass transfer between the upper mantle and lower mantle always takes place.

Question 10.5: Is mantle convection in the Earth partially layered by effects of the 660 km phase change?

The radial mass flux function can be analyzed in terms of its spherical harmonic content. Such an analysis of the flows in Figures 10.38, 10.39, and 10.43 shows that long-wavelength components of the flow (spherical harmonic degree $l = 5$ and lower) are essentially unaffected by the 660 km phase change while short-wavelength components ($l = 10$ and higher) are increasingly inhibited (with increasing l) by the 660 km phase change (Tackley et al., 1994). Short-wavelength density anomalies are supported by the deflection of the 660 km phase change while long-wavelength density anomalies cannot be supported and result in mantle avalanches (Tackley et al., 1994).

Tackley (1995) has presented an analytic model that explains the wavelength dependence of the penetrability of the endothermic phase change observed in the numerical results. The model assumes a horizontal phase change interface at $y = 0$ with light material above and heavy material below. A sinusoidal temperature variation with horizontal wavelength λ is

applied at $y = 0$. The applied temperature variation creates a horizontally varying sheet mass anomaly at $y = 0$ due to thermal expansivity; it also creates another sheet mass anomaly (at $y = 0$) due to phase boundary distortion (see (10.4.1) for expressions for the mass per unit area in these sheets). The sheet mass anomalies drive flows in the viscous half-spaces above and below the mass sheets; the flow can be determined by solving the biharmonic equation for the stream function in the half-spaces and appropriately matching the solutions at $y = 0$. If the resulting expression for the vertical velocity is set to zero at $y = 0$ there results the condition for impenetrability of the endothermic phase change. The critical wavelength λ_{cr} below which flow will be inhibited by the phase change and above which flow will penetrate the phase change is given by

$$\lambda_{cr} = -\frac{\pi}{2} Pd \quad (10.4.5)$$

where d is the overall thickness of the region of flow and P is negative for an endothermic phase transition. Equation (10.4.5) demonstrates the inhibitory effect of an endothermic phase change on flows with short wavelength; since P is generally small compared with unity, λ_{cr} is seen to be a small fraction, $-\pi P/2$ of d . Long wavelengths ($\lambda > \lambda_{cr}$) penetrate the phase change while short wavelengths ($\lambda < \lambda_{cr}$) are inhibited from penetration. Alternatively, stronger phase changes (larger $-P$) are required to stop longer wavelength flows. Narrow upwellings and downwellings are deflected more easily by the phase change than are broader structures, providing an explanation for why higher Rayleigh number Ra flows show a greater propensity toward layering, since convective features narrow with increasing Ra (Tackley, 1995) (Figure 10.45).

In two-dimensional models of convection with an endothermic phase change (Machetel and Weber, 1991; Peltier and Solheim, 1992; Weinstein, 1993; Solheim and Peltier, 1994a, b), mantle avalanches are more violent and abrupt and terminate periods of fully layered convection. This does not occur in three-dimensional models of the present Earth; as discussed above, avalanches overlap in time and are always occurring at some location or other in the spherical shell. Tackley et al. (1994) have identified several explanations for these differences between the two-dimensional and three-dimensional flows. Cylindrical downflows penetrate the endothermic phase change more readily than linear downflows and thus result in smaller, less vigorous and more frequent avalanches (Bercovici et al., 1993). Cylindrical avalanches last longer, thereby increasing the chance for temporal overlap with other avalanches. This is because they take longer to exhaust their pool of feeding material than do linear avalanches as a consequence of the radial influx of material toward the center of the downflow. The synchronicity of avalanches in two-dimensional models is less likely in three-dimensional models because of the more rapid falloff in velocity with distance from a three-dimensional downflow. Temporal overlaps of avalanches are more likely in three dimensions because it is possible to fit more simultaneous avalanches into a sphere than fit into axisymmetric geometry (see Section 9.5 for additional discussion of the differences between two-dimensional and three-dimensional models of mantle convection with an endothermic phase change).

While the 660 km phase change in the Earth may be responsible for the flattening and buckling of some slabs (van der Hilst et al., 1991; Fukao et al., 1992; van der Hilst, 1995; Tajima and Grand, 1998), it is clear that this phase change does not preclude at least certain slabs from entering the lower mantle (Grand et al., 1997; van der Hilst et al., 1997, 1998; Kennett et al., 1998; van der Hilst and Kárason, 1999). The endothermic phase transition has not resulted in layered mantle convection in the present Earth. The inhibitory effect of the endothermic phase transition is directly proportional to the magnitude of its

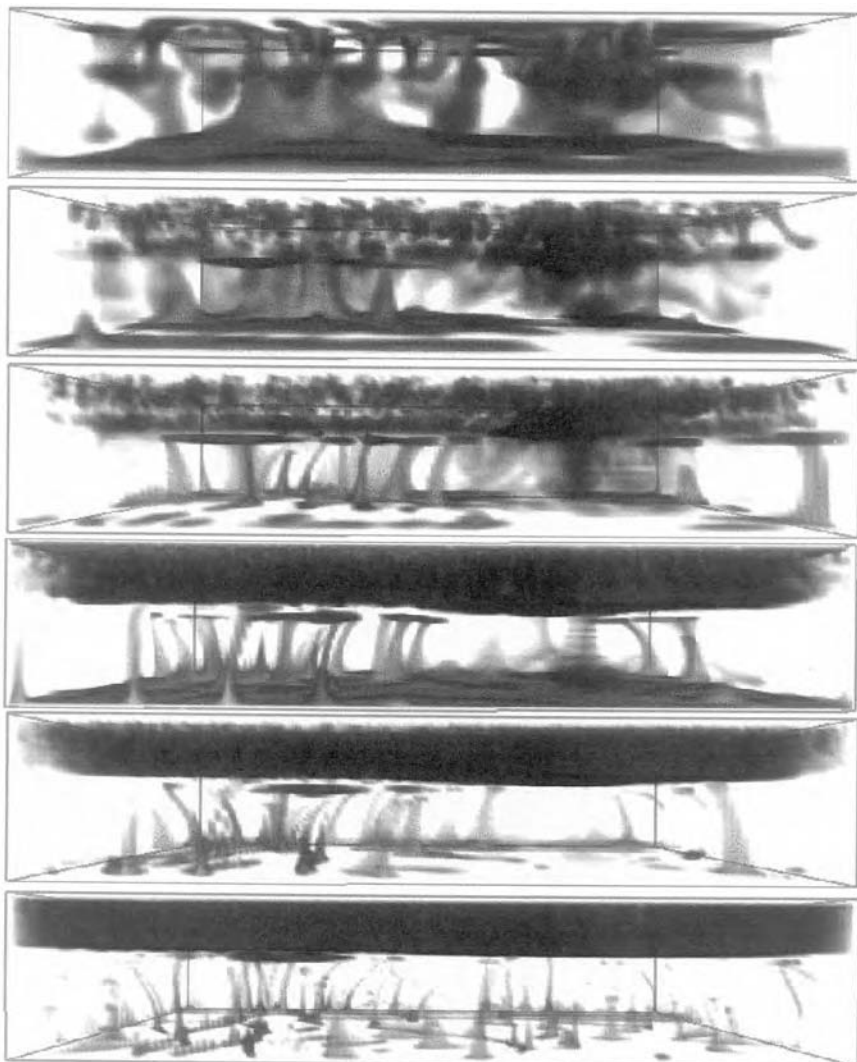


Figure 10.45. Simulations of three-dimensional convection with an endothermic phase change at different values of the Rayleigh number (Ra increases downward). At lower values of Ra the phase change does not significantly influence the whole-layer flow (top). At intermediate values of Ra (middle) partially layered, avalanche-modulated convection occurs. At the highest values of Ra (bottom) the phase change completely layers the flow and there are no mantle avalanches. After Yuen et al. (1994).

For a color version of this figure, see plate section.

Clapeyron slope. In the models of this section where the endothermic phase change produced such dramatic effects as mantle avalanches, the Clapeyron slope of the endothermic phase change was generally taken to be -4 MPa K^{-1} . However, the value of the Clapeyron slope for the 660 km phase change in the real Earth is still uncertain and it may be smaller in magnitude than 4 MPa K^{-1} (Bina and Helffrich, 1994; Chopelas et al., 1994). The dramatic effects of the endothermic phase change are not seen in model calculations that use $\gamma = -2 \text{ MPa K}^{-1}$, for example. Early papers on the effects of phase changes on mantle

convection (e.g., Schubert et al., 1975) did not identify the potentially dramatic effects of the 660 km phase transition in part because the Clapeyron slope of the phase change was poorly determined at the time (even its sign was debated) and its magnitude was believed to be much smaller than presently accepted values. Uncertainties in mantle phase relations still prevail and demand caution in applying results of convection modeling with phase changes to the real Earth (Bina and Liu, 1995). Liu (1994) has reported that the Clapeyron slope of the 660 km phase transition changes from negative to positive at temperatures between 1,700°C and 2,000°C. Thus, cold downwellings could be inhibited by the endothermic character of the 660 km phase transition at relatively low temperatures while hot upwellings (plumes) could be enhanced in their upward motion by the exothermic character of the same phase transition at relatively high temperatures. Another complexity that arises in assessing the effects of phase transitions on mantle convection in the real Earth is the uncertain contribution of the nonolivine components of the mantle which undergo their own phase transitions (Weidner and Wang, 1988). The effects of mantle phase transitions on real slabs in the Earth are also moderated by the high viscosity of the slabs (Zhong and Gurnis, 1994b; King and Ita, 1995).

Though the 660 km phase transition has not layered the present Earth, the early, hotter, more vigorously convecting Earth may have been layered by the phase change since the tendency toward phase change layering by an endothermic phase transition is greater at higher Rayleigh number (more vigorous convection) (Yuen et al., 1994) (Figure 10.45). (This would not be true if the nature of the phase change was altered by higher temperatures as proposed by Liu (1994).) The Earth's mantle could have started off layered and have undergone a transition to avalanche-style convection as the Earth cooled, resulting in major geologic events in the Earth's history (Steinbach et al., 1993; Honda and Yuen, 1994; Breuer and Spohn, 1995; Davies, 1995b; Yuen et al., 1995; Brunet and Machetel, 1998). These possibilities are discussed in greater detail in Chapter 13, which deals with Earth thermal evolution.

The olivine–spinel and spinel–perovskite phase changes may also play a significant role in determining the style of mantle convection in Venus and Mars as discussed in Chapter 14. Convection on Venus occurs beneath a sluggish or stagnant lid (no subduction) and numerical calculations show that phase-change-induced layering is stronger for this mode of convection than it is with plates and subduction (Schubert et al., 1997). The major mantle phase transitions occur at greater depths in Mars than in Earth, and as a result they may favor a mode of convection with one or two dominant plumes (see Chapter 14).

10.5 Depth-dependent Viscosity

One of the major successes of the mantle convection model with an endothermic phase change is its ability to produce dominant long-wavelength structure in the upper mantle and in the bottom of the lower mantle, in agreement with results from seismic tomography (Section 10.4) and the long-wavelength-dominated geoid.

Question 10.6: Is the 660 km phase change responsible for the dominance of long wavelengths in the Earth's nonhydrostatic geoid?

Nevertheless, there are other ways to possibly explain the predominantly long wavelength seismic heterogeneity and gravity signature of the mantle. Tectonic plates impose a long

wavelength on mantle convection (Davies, 1988a; Zhong and Gurnis, 1994b; Bunge and Richards, 1996) though one may then ask why the plates are so large.

Question 10.7: Why are tectonic plates so large?

The thermal insulation effect of continents (Gurnis and Zhong, 1991), the effect of temperature-dependent viscosity (Daly, 1980; Tackley, 1993), and effects of depth-dependent properties such as viscosity and thermal expansivity (Balachandar et al., 1992; Hansen et al., 1993; Zhang and Yuen, 1995; Bunge et al., 1996, 1997; Bunge and Richards, 1996), may all contribute to the predominance of large length scales in the mantle. In this section we discuss the spectral “reddening” effect of mantle convection models that assume an increase in viscosity in going from the upper mantle to the lower mantle. An increase in viscosity of the lower mantle by perhaps a factor of 30 or larger compared with the upper mantle is a feature of a number of Earth viscosity models based on geoid data (Hager and Richards, 1989; Ricard and Wuming, 1991; Corrieu et al., 1994), postglacial rebound observations (Nakada and Lambeck, 1989; Forte and Mitrovica, 1996; Mitrovica, 1996), and Earth rotation data (Yuen and Sabadini, 1985; Ricard et al., 1992; Ivins et al., 1993) (see Chapter 5 and reviews of mantle viscosity models by King, 1995a, b).

Figure 10.46 shows temperature variations in a model of three-dimensional convection in a spherical shell of internally heated, infinite Prandtl number, Boussinesq fluid (Bunge et al., 1996). The shell is the size of the Earth’s mantle. All thermal and mechanical properties are constant except for viscosity, which is a constant in the upper mantle and is also a constant, but 30 times larger, in the lower mantle. The upper surface is isothermal and the lower surface is insulated. Both upper and lower boundaries are free-slip. The internal heating Rayleigh number Ra_Q based on the viscosity of the upper mantle is 4×10^7 . By way of comparison, Figure 10.46 also shows the thermal field for a calculation with the same viscosity in the upper mantle and lower mantle. The Ra_Q for this constant viscosity calculation is 4.8×10^6 , very close to the “average” Ra_Q for the case with the higher-viscosity lower mantle.

The internally heated constant viscosity convection shown in Figure 10.46a is dominated by numerous quasi-cylindrical downflows spaced relatively close together. The downflows are surrounded by a broad and diffuse upwelling of hotter fluid. This is the same pattern of mantle convection found by Houseman (1988) in Cartesian geometry and by Bercovici et al. (1989a) in spherical geometry (see also Figures 10.30 and 10.32). However, when the lower mantle viscosity is 30 times higher than the upper mantle viscosity (Figure 10.46b) the pattern of convection is markedly different. It consists of long, sheet-like downwellings near the surface with relatively large spacing between the sheets. In the constant viscosity case the quasi-cylindrical downwellings persist all the way to the core–mantle boundary, but in the high-viscosity lower mantle case the sheet-like downwellings break up into large diffuse blobs as they enter and traverse the lower mantle. Thus we see numerous, relatively small, quasi-circular patches of cold material at the core–mantle boundary in Figure 10.46a, and large areas of cold fluid which have squeezed hot material into a network of narrow linear structures (hot ridges) on the core–mantle boundary in Figure 10.46b.

Evidently, the increased lower mantle viscosity in these models is responsible for changing the morphology of downwellings from quasi-cylindrical to the more Earth-like sheets. It is also responsible for reddening the spectrum of the thermal heterogeneities in accordance with the long-wavelength-dominated spectra of the Earth’s geoid (peak at spherical

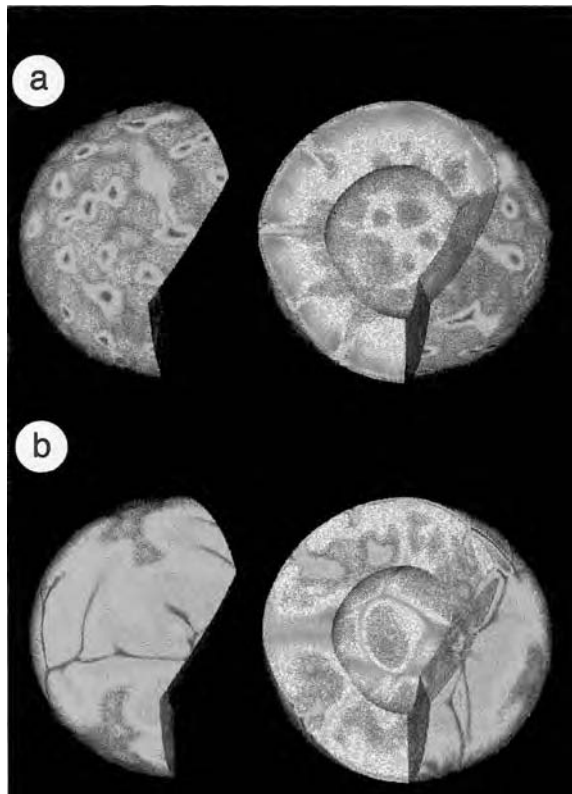


Figure 10.46. Temperature distribution in a model of internally heated convection with (a) constant viscosity and (b) lower mantle viscosity = 30 times upper mantle viscosity. The upper surface of the figure is 250 km below the isothermal surface of the model. Red is hot, blue is cold. After Bunge et al. (1996).

For a color version of this figure, see plate section.

harmonic degrees 2–3, Lerch et al., 1983) and seismic velocity heterogeneity (peak at spherical harmonic degree 2, Inoue et al., 1990; Su and Dziewonski, 1991) (Bunge et al., 1996). Bunge and Richards (1996) have obtained even better agreement between model thermal spectral heterogeneity maps and observed seismic velocity spectral heterogeneity maps by combining both an increase of viscosity with depth and the imposition of prescribed plate motion boundary conditions in a model of spherical three-dimensional mantle convection (see also Ray and Anderson, 1994).

Question 10.8: Is an increase of viscosity with depth responsible for the long-wavelength dominance of the Earth's geoid and mantle seismic velocity heterogeneity?

Tackley (1996a) has studied the relative effectiveness of a viscosity increase with depth and the 660 km phase transition in reddening the spectrum of thermal heterogeneity in mantle convection models. He has found that the relative importance of these effects depends strongly on Rayleigh number Ra . At relatively low Ra , a jump in viscosity from the upper mantle to the lower mantle is more effective at producing long-wavelength structure in mantle convection than is the 660 km phase change. However the reverse is true at relatively high Ra . The dominance of the 660 km phase change over viscosity increase with depth in reddening

the spectrum of thermal heterogeneity in mantle flows occurs at an internal heating Rayleigh number greater than about 10^8 (Tackley, 1996a). The increase in effectiveness of the 660 km phase change in reddening the flow that occurs with increasing Ra is tied to the occurrence of avalanches in the flow. At relatively low Ra , avalanches do not occur. As Ra is increased, weak avalanches form but they do not significantly affect the large-scale flow structure. As Ra is increased further, strong avalanches occur; these are sufficiently large to organize flow over a large area and impose long wavelengths on the flow. At still higher Ra , the 660 km phase change would completely layer the convection (Christensen and Yuen, 1985; Yuen et al., 1994) and dominant wavelengths would decrease as indicated by two-layer spherical calculations (Glatzmaier and Schubert, 1993).

Some models of mantle viscosity structure have indicated the possibility of a low-viscosity layer a few hundred kilometers thick (or less) at the depths of the 660 km seismic discontinuity (Mitrovica and Forte, 1997; Milne et al., 1998). Cserepes and Yuen (1997) have studied the effect of such a mid-mantle low-viscosity zone on three-dimensional convection with the influence of the 660 km phase change included. They found that a low-viscosity zone associated with the 660 km phase change enforces layered convection; mantle avalanches do not occur since the reduced viscosity facilitates the horizontal flow of material and eliminates the accumulation of material in pools at the phase change boundary.

A major reason for the variation of viscosity with depth in the mantle is the dependence of viscosity on temperature and pressure (Chapter 5). Mantle viscosity tends to decrease with increasing temperature and therefore this effect tends to decrease mantle viscosity with depth. However, mantle viscosity tends to increase with pressure, an effect which results in a tendency of mantle viscosity to increase with depth. The pressure effect can cancel the temperature effect or even dominate, producing a relatively high viscosity lower mantle and a relatively low viscosity upper mantle (with the exception of the lithosphere) (Sammis et al., 1977, 1981; Ellsworth et al., 1985; Ivins et al., 1993). The combined temperature and pressure effects on mantle viscosity can be represented by the proximity of the temperature to the melting or solidus temperature of the mantle (the homologous temperature, see Chapter 5). High melting temperatures for lower mantle materials (Zerr and Boehler, 1993, 1994; Shen and Lazor, 1995; Zerr et al., 1997, 1998) would suggest a relatively high lower mantle viscosity (van Keken et al., 1994; van Keken and Yuen, 1995). Mantle viscosity also depends on other effects such as stress, phase changes, and volatile content (Chapter 5). The overall dependence of mantle viscosity on depth is a net result of all these more fundamental causes of viscosity variation which also produce horizontal variations in viscosity. The net depth dependence of viscosity is a major factor influencing the dominant length scales in mantle convection. Tackley (1998b) has carried out three-dimensional numerical simulations of mantle convection including a thermochemical D'' layer.

There have been a number of numerical calculations of how the strong temperature dependence of mantle viscosity influences the nature of three-dimensional mantle convection. These will be discussed in Chapter 14.

10.6 Two-layer Convection

Prior to the development of higher resolution seismic tomography, it was argued by many authors that the seismic discontinuity at 660 km depth resulted in layered mantle convection. However, seismic tomography has provided convincing evidence that there is substantial transport of material across the 660 km seismic discontinuity at the present time

(see Chapter 3). However, we have discussed above how the 660 km phase change modifies mantle convection, and could have dynamically layered the mantle early in the Earth's evolution when the mantle was convecting more vigorously and its Rayleigh number was higher than at present. For these reasons we discuss two-layer spherical models of mantle convection in this section.

Question 10.9: *Was the Earth's mantle divided into separately convecting upper and lower layers early in the Earth's evolution?*

In addition to its possible relevance to convection in the early Earth, two-layer convection is of intrinsic interest as an end-member case in the spectrum of mantle convection models between whole-mantle convection and two-layer mantle convection. Two-dimensional models of layered mantle convection have been carried out by Christensen (1981), Busse (1981), Richter and McKenzie (1981), Cserepes and Rabinowicz (1985), and Ellsworth and Schubert (1988). The three-dimensional layered convection model we discuss here is by Glatzmaier and Schubert (1993).

The model of two-layer spherical convection computes flow in a spherical shell the size of the Earth's mantle. The nondeformable, impermeable boundary separating the shells coincides with the position of the upper mantle–lower mantle transition in the Earth. The upper and lower boundaries are impermeable, stress free, and isothermal. At the interface between the layers' horizontal velocity, horizontal shear stress, temperature, and radial heat flux are continuous and radial velocity is zero. The fluid is anelastic and has infinite Prandtl number. The reference state is an adiabatic, hydrostatic state that approximates the Earth's mantle. The fluid is heated both internally and from below with about 80% of the heating generated directly from within. The viscosity is constant and has the same value in both layers. The solutions yield a surface heat flow of about 5×10^{13} W, corresponding to vigorous, time-dependent convection.

Figure 10.47 compares the approximately time-independent spherically averaged temperature profile in the two-layer case with that of a whole-mantle convection model basically identical to the layered model but without the interface that forces the layering. The impermeable interface in the two-layer case produces a steep temperature gradient in the interface region in order to conduct the heat flux through the interface. This internal thermal boundary layer is a thermal resistance that raises the mean temperature in the lower shell by about 1,400 K compared to the whole-layer case. Both the two-layer and whole-layer calculations assume an isothermal lower boundary. The 1,400 K increase in the lower boundary temperature of the two-layer case was determined iteratively under the requirement that both two-layer and whole-layer cases transfer the same heat flux to the surface.

Figure 10.48 shows the structure of convection in the two-layer case. Convection in the upper shell is a complicated network of narrow convective rolls, unlike the pattern of linear, arcuate sheet-like downflows seen in whole-mantle models (Figures 10.28 and 10.34). The dominant length scale in the upper layer is relatively small, comparable to the thickness of the upper shell. The pattern of convection in the upper layer is similar to that seen in plane layer convection with the structure and amplitude of upflow very similar to that of downflow. The pattern of convection in the lower shell is similar to that in whole-layer models (Figure 10.34) with relatively large blobs of cold fluid covering the core–mantle boundary and pushing hot fluid into a linear network of interconnected ridges. Figure 10.47 also illustrates that the

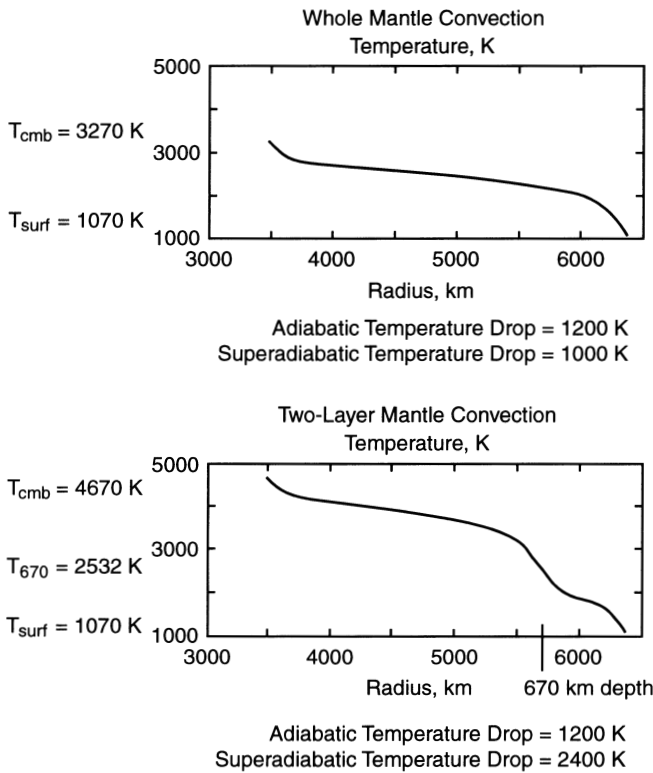


Figure 10.47. Spherically averaged radial profiles of temperature in similar whole-mantle and two-layer convection models. After Glatzmaier and Schubert (1993).

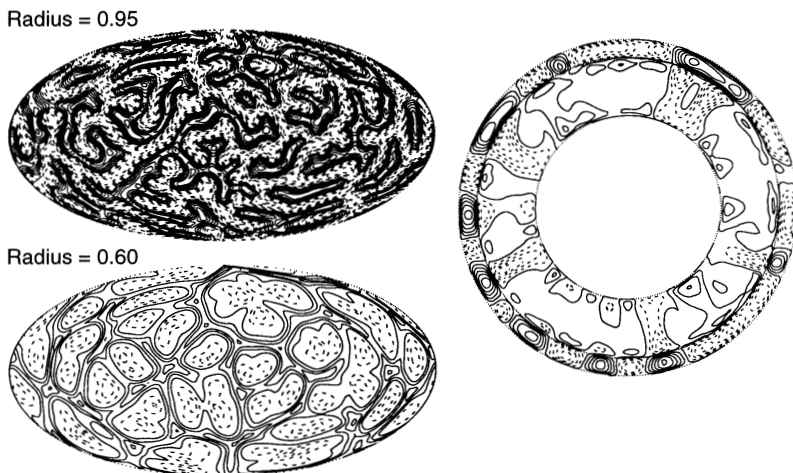


Figure 10.48. A snapshot of the temperature anomalies relative to the spherically averaged temperature in Figure 10.47. Isotherms are plotted in spherical surfaces (equal-area projections) at dimensionless radii of 0.95 and 0.60 (the outer boundary is at a dimensionless radius of 1.0 and the inner boundary is at 0.55) and on an equatorial cross-section. After Glatzmaier and Schubert (1993).

coupling between the upper layer and lower layer is viscous as opposed to thermal since continuous temperature perturbations tend to pass through zero and change sign near the interface. The viscous coupling between the shells is an attempt to compromise between the small horizontal scale preferred in the upper layer and the large horizontal scale preferred in the lower layer.

Glatzmaier and Schubert (1993) also modeled whole-layer and two-layer convection when the viscosity in the lower shell is 30 times larger than the viscosity in the upper shell. They found changes in the dominant length scales of the flows similar to those found in the later studies of Bunge et al. (1996). In both whole-layer and two-layer convection, the dominant length scale in the lower layer is larger than it is in the case of constant viscosity. In the two-layer case, the coupling between layers is less viscous and more thermal when the lower layer has a larger viscosity than the upper layer compared with the isoviscous case.

Radial correlation functions (Jordan et al., 1993) for the flows discussed in this section are shown in Figure 10.49. The correlation between two depths is proportional to the surface integral of the product of the temperature anomalies (relative to the spherical average) at the two depths. The function measures the correlation of a spherical heterogeneity in surfaces

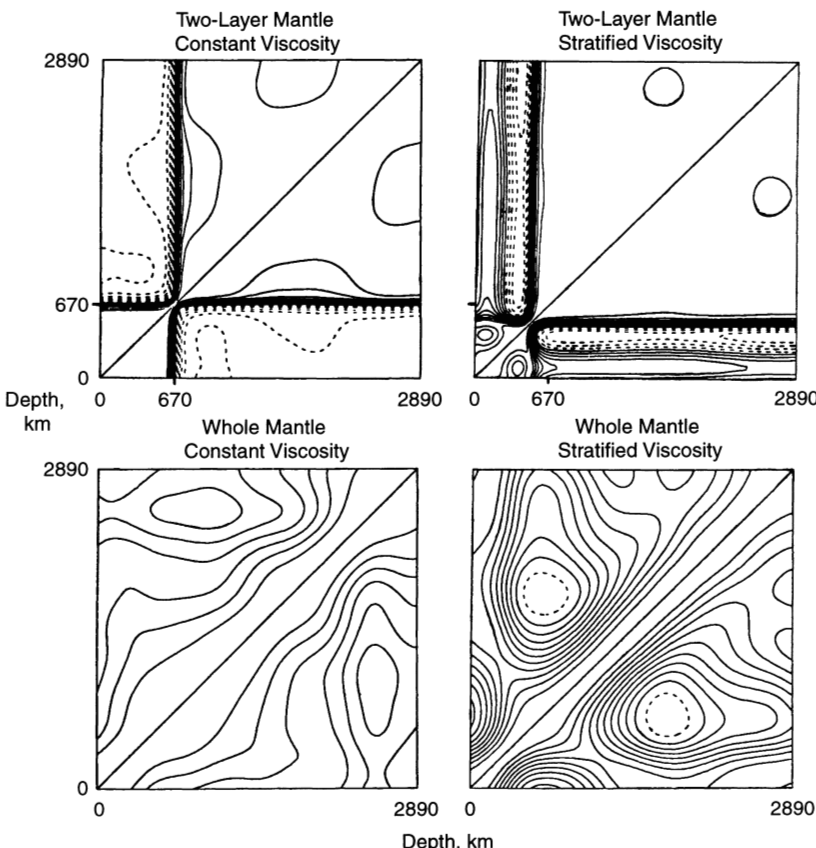


Figure 10.49. Radial correlation functions (Jordan et al., 1993) for four different convection models. The diagonal is unity. Solid contours are positive and dashed contours are negative. The contour interval is 0.1. After Glatzmaier and Schubert (1993).

at different depths. The depth of the imposed interface (670 km) is evident in the radial correlations of the two-layer models; the correlation is very high everywhere in the lower shells for the two-layer models. The correlations for the whole-layer models, especially for the stratified viscosity case (factor of 30 higher viscosity in the lower layer compared with the upper layer), are more like those obtained from seismic models of the Earth's mantle which show a slight decorrelation between 660 km depth and mid-mantle but no clear 660 km discontinuity.

The results of this section show that two-layer convection does not provide a good model for convection in the Earth's mantle. The long, arcuate surface expressions of downwelling sheets in the whole-layer convection model are strikingly similar to subduction zones on the Earth, whereas the short-wavelength, roll-like character of the upflows and downflows in the upper layer of the two-layer model has no counterpart in the global tectonic expression of mantle convection at the Earth's surface. The large horizontal scale of convection in the lower layer of the two-layer model does not impose itself on the scale of convection in the upper layer, which removes this effect as a possible explanation of the large scale of convection observed in the Earth's upper mantle.

10.7 Compressibility and Adiabatic and Viscous Heating

While a number of the three-dimensional numerical convection models discussed earlier in this chapter include some effects of compressibility, e.g., use of the anelastic conservation of mass equation, none of these papers systematically and self-consistently study compressibility and associated effects such as viscous heating. Investigations that focus on compressibility and viscous heating in three-dimensional convection have been carried out by Bercovici et al. (1992), Balachandar et al. (1992, 1993), and Zhang and Yuen (1995).

Question 10.10: How important is viscous heating in the Earth's mantle?

Question 10.11: Does compressibility in the Earth's mantle significantly affect the nature of mantle convection?

Bercovici et al. (1992) considered three-dimensional convection in a spherical shell the size of the Earth's mantle containing a compressible (anelastic) fluid. The model assumes a spherically symmetric adiabatic hydrostatic reference state based on the Murnaghan equation in which the bulk modulus is a linear function of the reference state pressure (6.12.25). The shell is heated entirely from below and viscosity, thermal conductivity, specific heat at constant pressure, and the Grüneisen ratio are taken as constants. The acceleration of gravity and the thermal expansivity vary with radius in the model mantle. The nondimensional parameters that govern convection in the shell of compressible fluid are:

- (i) K' , the coefficient of pressure in the linear expression for bulk modulus as a function of pressure. K' is taken as 3.5, characteristic of the Earth's mantle according to PREM (Dziewonski and Anderson, 1981). The polytropic index n is $(K' - 1)^{-1}$.
- (ii) γ , the Grüneisen parameter, held constant at 1.
- (iii) \overline{Di} , the radially averaged dissipation number.

- (iv) $g_{\text{bot}} (4\pi G \bar{\rho}_{\text{bot}} d)^{-1}$ which is held fixed at 1.26 (g_{bot} is the acceleration of gravity at the bottom of the shell, G is the gravitational constant, $\bar{\rho}_{\text{bot}}$ is the reference state density at the bottom of the shell, and d is the thickness of the shell).
- (v) $\bar{T}_{\text{bot}} (\Delta T_{sa})^{-1}$, where T_{bot} is the adiabatic reference temperature at the bottom of the shell and ΔT_{sa} is the superadiabatic temperature difference across the shell.
- (vi) $c_p \bar{T}_{\text{bot}} (g_{\text{bot}} d)^{-1}$ which is kept fixed at 0.12, where c_p is the constant specific heat.
- (vii) $r_{\text{bot}}/r_{\text{top}}$ which is fixed at 0.55 characteristic of the Earth's mantle, where r_{bot} is the inner radius of the shell and r_{top} is the outer radius of the shell.
- (viii) $\langle Ra \rangle$ the volume-averaged Rayleigh number = $\langle \alpha g d^3 \Delta T_{sa} / \nu \kappa \rangle$, where α is thermal expansivity, a function of radius r , g is acceleration of gravity, a function of r , ν is kinematic viscosity, a function of r through the dependence of density ρ on r , and κ is thermal diffusivity, a function of r through $\rho(r)$.

The shell boundaries are impermeable, stress free, and isothermal. Bercovici et al. (1992) vary \bar{Di} , $\bar{T}_{\text{bot}}/\Delta T_{sa}$, and $\langle Ra \rangle$ in their study of compressibility effects. The energy equation of the model includes the viscous dissipation term and adiabatic heating (cooling).

Bercovici et al. (1992) solve the linear problem for the onset of convection in the spherical shell and report the results summarized in Table 10.2. The minimum critical value of $\langle Ra \rangle$ occurs at spherical harmonic degree $l = 3$ for all the values of \bar{Di} and $\bar{T}_{\text{bot}}/\Delta T_{sa}$ considered. In order to understand the linear stability results and the finite amplitude solutions discussed below, it is essential to appreciate the stability characteristics of the basic state corresponding to different values of \bar{Di} and $\bar{T}_{\text{bot}}/\Delta T_{sa}$. These are shown in Figure 10.50. With increasing $\bar{T}_{\text{bot}}/\Delta T_{sa}$, the thickness of the upper stable part of the shell increases at the expense of the unstable lower part of the shell. The stability of fluid near the top of the shell leads to a penetrative convection opposite in character to that of the plane layer, constant dissipation number case of Jarvis and McKenzie (1980). In their plane layer model with g and α constant and $K' = 1$, the adiabatic temperature profile is an exponential function of height and the conductive temperature profile is linear; the upper part of the plane layer is unstable and the bottom part is stable. As a consequence, penetrative flow occurs at the base of the plane layer in contrast to the spherical shell case discussed above. The compressible spherical shell study of Machetel and Yuen (1989) also had penetrative convection at the bottom of the shell because of assumptions about the internal heating concentration and a constant dissipation. Clearly, care must be taken in comparing results of compressible convection studies, especially regarding the character of basic state stability.

Table 10.2. Critical Rayleigh Number $\langle Ra \rangle_{cr}$ for the Spherical Shell Anelastic Model

\bar{Di}	$\bar{T}_{\text{bot}}/\Delta T_{sa}$	$l = 1$	$l = 2$	$l = 3$	$l = 4$	$l = 5$
0	–	1,919	915	(733)	751	878
0.25	1	2,029	979	(795)	823	969
0.25	10	1,899	920	(750)	781	924
0.25	30	1,616	781	(633)	650	754
0.50	1	2,140	1,039	(847)	880	1,037
0.50	10	1,481	722	(591)	616	727
0.50	30	863	420	(342)	352	409

Note: $r_{\text{bot}}/r_{\text{top}} = 0.547$. The minimum $\langle Ra \rangle_{cr}$ (shown in parentheses) occurs at $l = 3$ in all cases. After Bercovici et al. (1992).

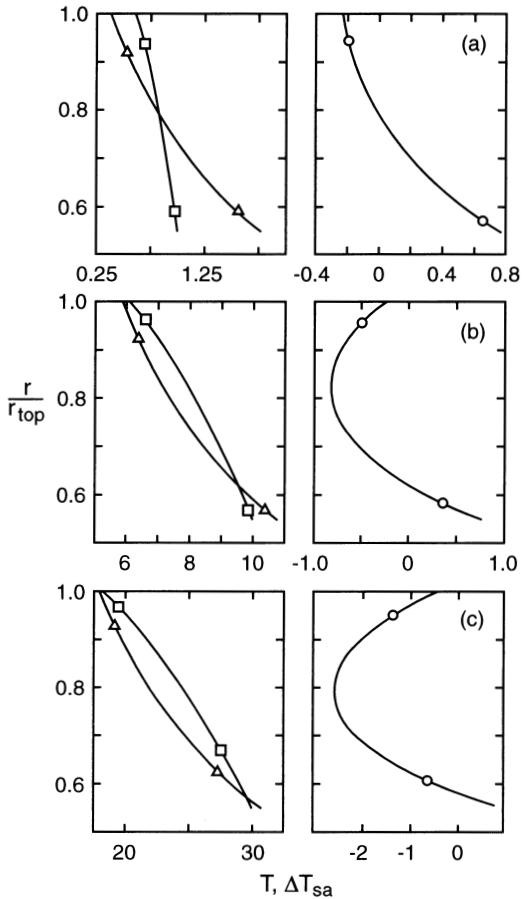


Figure 10.50. Basic state radial profiles of conduction temperature (triangles, left panels), radial profiles of adiabatic reference state temperature (squares, left panels), and radial profiles of superadiabatic temperature (circles, right panels) for $\bar{D}i = 0.5$ and (a) $\bar{T}_{\text{bot}}/\Delta T_{\text{sa}} = 1$, (b) 10, (c) 30. All temperatures are in units of ΔT_{sa} . After Bercovici et al. (1992).

The pattern of convection at a relatively low Rayleigh number ($\langle Ra \rangle \approx 10 \langle Ra \rangle_{cr}$) and for $\bar{D}i = 0.5$ in the spherical shell model of Bercovici et al. (1992) is shown in Figure 10.51. For $\bar{T}_{\text{bot}}/\Delta T_{\text{sa}} = 1$, convection has a dominant tetrahedral signature. As in the Boussinesq case (Bercovici et al., 1989b), upwellings in the form of cylindrical plumes are surrounded by an interconnected network of downwelling sheets (Figure 10.51a). As $\bar{T}_{\text{bot}}/\Delta T_{\text{sa}}$ increases from 1 to 10 the pattern of convection remains essentially the same (Figure 10.51b), but as $\bar{T}_{\text{bot}}/\Delta T_{\text{sa}}$ increases to 30, polyhedral symmetry is lost and upwelling occurs in many (about 10) narrow cylindrical plumes while downwelling is broad and featureless (Figure 10.51c). This is the opposite of what occurred in the plane layer, constant Di study (Jarvis and McKenzie, 1980) and the internally heated spherical shell study (Machetel and Yuen, 1989) wherein upwellings were essentially eliminated and downwellings became narrow (upwelling was broad and featureless). In these studies, the narrowing of downwelling was due to enhancement of the upper boundary layer and elimination of the lower one. In the Bercovici et al. (1992) model, as $\bar{T}_{\text{bot}}/\Delta T_{\text{sa}}$ increases, the unstable portion of the shell is confined to an ever thinner layer near the bottom leading to narrower and more numerous plumes that penetrate the upper stable and conductive part of the shell and cause a broad compensating downward mass flux. The solution at $\bar{T}_{\text{bot}}/\Delta T_{\text{sa}} = 30$ in

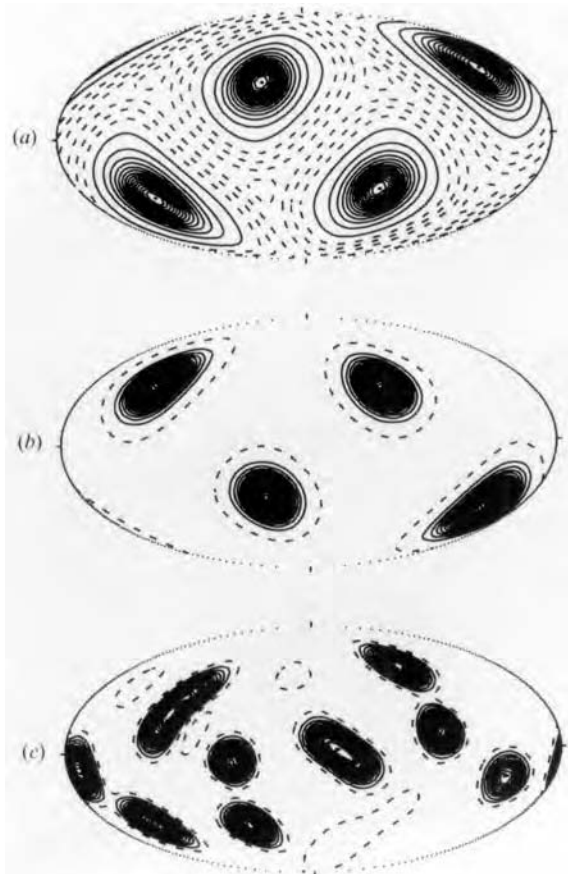


Figure 10.51. Contours of radial velocity on a spherical surface at $r/r_{\text{top}} = 0.77$ for $\bar{D}i = 0.5$ and $\langle Ra \rangle \approx 10 \langle Ra \rangle_{\text{cr}}$. (a) $\bar{T}_{\text{bot}}/\Delta T_{sa} = 1$, (b) 10, (c) 30. Solid contours denote positive or upward velocities and dashed contours denote negative velocities. After Bercovici et al. (1992).

Figure 10.51c is time dependent and characterized by the continuous formation and coalescence of plumes. All the solutions in Figure 10.51 have subadiabatic interiors (except for boundary layers).

Viscous heating in the compressible solutions of Figure 10.51 is of particular interest. It is between 1 and 10% of the other terms in the energy equation and is largest in the boundary layers and smallest in the middle of the shell. Figure 10.52 shows the spatial distribution of viscous heating. At mid-depth, $r/r_{\text{top}} = 0.77$, viscous heating is concentrated in and around the upwelling plumes. At the top and bottom of the shell, viscous heating is concentrated directly above or below upwelling and downwelling regions. The locations of maximum viscous heating are where the upwelling plumes meet the upper or lower boundary.

Compressibility effects in the previous solutions are most significant when the net superadiabatic temperature difference across the shell is small relative to the characteristic adiabatic temperature, i.e., when $\bar{T}_{\text{bot}}/\Delta T_{sa}$ is $O(10)$. For the Earth, ΔT_{sa} is of the same order as the temperature at the base of the mantle adiabat, i.e., $\bar{T}_{\text{bot}}/\Delta T_{sa}$ is $O(1)$. Thus, compressibility is probably not of great importance in determining the global spatial structure of mantle convection. However, compressibility does promote time dependence of the flow and viscous heating can be important locally as discussed further below. The

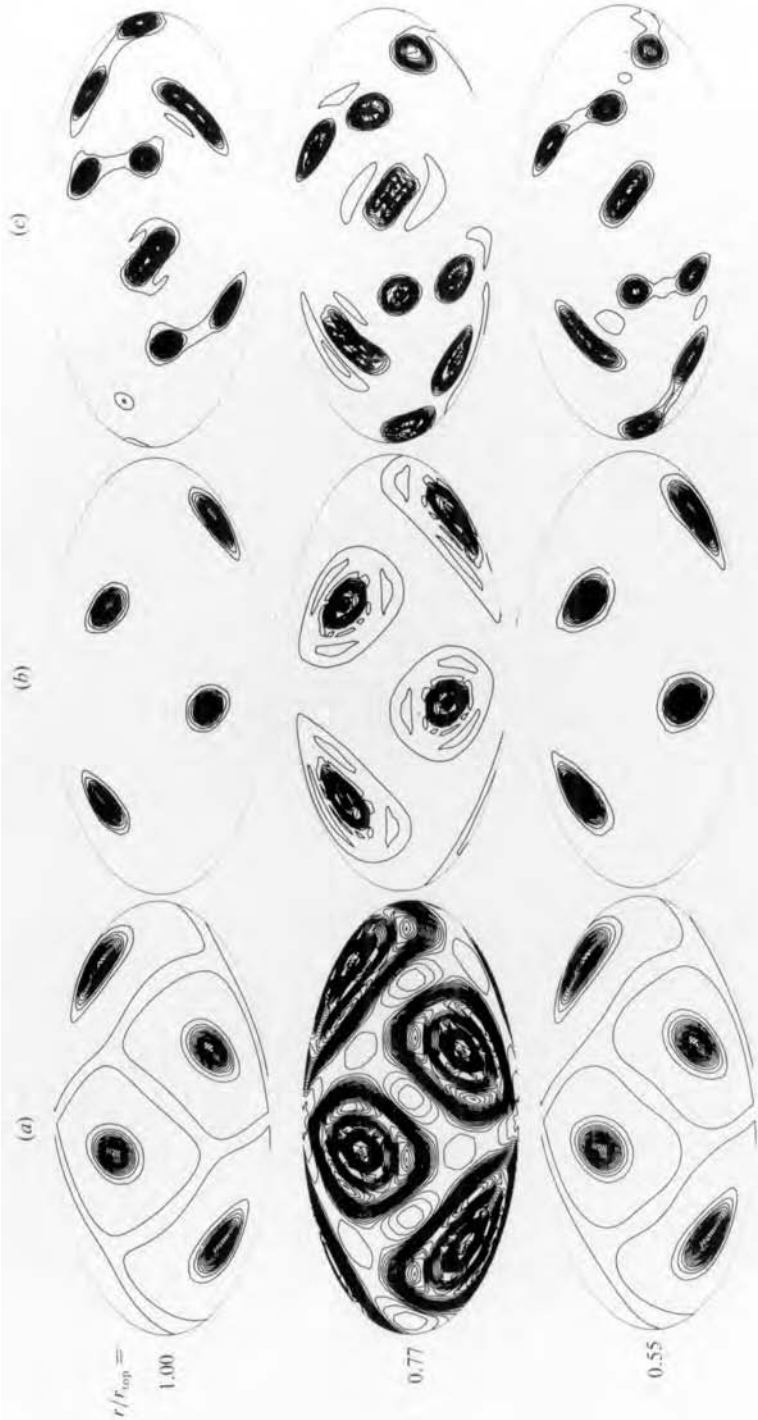


Figure 10.52. Contours of viscous heating at different depths for the solutions of Figure 10.51. (a) $\bar{T}_{\text{bot}}/\Delta T_{\text{sa}} = 1$, (b) 10, (c) 30. After Bercovici et al. (1992).

solutions of Bercovici et al. (1992) discussed above did not include internal heating which is important for the Earth's mantle. The main influence of internal heating is to cause penetrative convection near the base of the shell (Machetel and Yuen, 1989) because increased amounts of internal heating decrease the basal heat flow which eventually becomes smaller than the conductive heat flux along the adiabat at the core–mantle boundary (CMB). The conductive heat flow along the adiabat at the CMB is $k\alpha g T / c_p$ evaluated at the base of the mantle; this value is about 1 mW m^{-2} . Thus, the base of the mantle is highly superadiabatic and penetrative convection is unlikely to occur there. Stabilization of the lower portion of the mantle occurred in the compressible models of Jarvis and McKenzie (1980) and Machetel and Yuen (1989) because the assumption of constant Di in their models led to unrealistically large values of the magnitude of the adiabatic temperature gradient at the bottom of their models. Even with internal heating, penetrative convection near the base of the mantle does not occur in models of mantle convection with Earth-like adiabats (Solheim and Peltier, 1990).

In general, compressibility in mantle convection is important if the conductive heat flow along the adiabat is comparable with the total heat flow through the mantle (Bercovici et al., 1992). Both heat flows increase with the size of a planet. While a planet the size of Earth causes greater compression than a planet the size of Mars, it also cools more slowly. Therefore, while a large planet undergoes more compression, it is hotter and has a larger heat flow than a small planet which diminishes the significance of compressibility.

The compressible convection solutions of Bercovici et al. (1992) are for relatively low values of the Rayleigh number; higher values of Rayleigh number have been considered by Balachandar et al. (1992, 1993, 1995a,b), Balachandar and Yuen (1994), and Zhang and Yuen (1996a). The effects of compressibility in these solutions are difficult to isolate because the flows are affected by depth variations in other parameters such as mantle viscosity. Balachandar et al. (1992) consider compressible convection in a $5 \times 5 \times 1$ rectangular box for surface Rayleigh numbers as high as 5×10^6 . In their model the value of the dissipation number at the surface is 0.4 and viscosity increases by a factor of 10 between the top and bottom of their box; thermal expansivity α and thermal conductivity k are also depth dependent with α decreasing with depth and k increasing with depth. The adiabatic reference state density is determined by integrating the Adams–Williamson equation. Heating is from below and the top and bottom boundaries are impermeable, stress free, and isothermal. Figure 10.53 shows the style of time-dependent convection at a surface Rayleigh number of 5×10^6 . Convection consists of rising cylindrical plumes and descending sheets. Decreasing viscosity and increasing thermal expansivity with height strengthens the upwellings and focuses them into a few strong plumes. Increasing viscosity and decreasing thermal expansivity with depth slows down and weakens the descending sheets. The multiple plumes seen in the figure move along the bottom boundary and merge towards the center of the square cross-section to form a stronger plume in the middle of the square. Strong downwelling sheets occur at the edges of the square horizontal cross-section as well as smaller downflow sheets in the interior of the square that drift laterally and re-form. The solution in Figure 10.53 has a superadiabatic region in the lower 20% of the box. In Balachandar et al. (1993), solutions for this model were obtained at surface Rayleigh numbers up to 4×10^7 . The planform of convection at a Rayleigh number of 4×10^7 is similar to that in Figure 10.53. However, the flow is more chaotic near the top than it is at a Rayleigh number of 5×10^6 and there are more downflow instabilities and sinking blobs of fluid from the top boundary layer. Viscous heating in the flows at Rayleigh numbers of 5×10^6 and 4×10^7 is strongest near the top and bottom boundaries and it increases with increasing Rayleigh number; it is also larger at

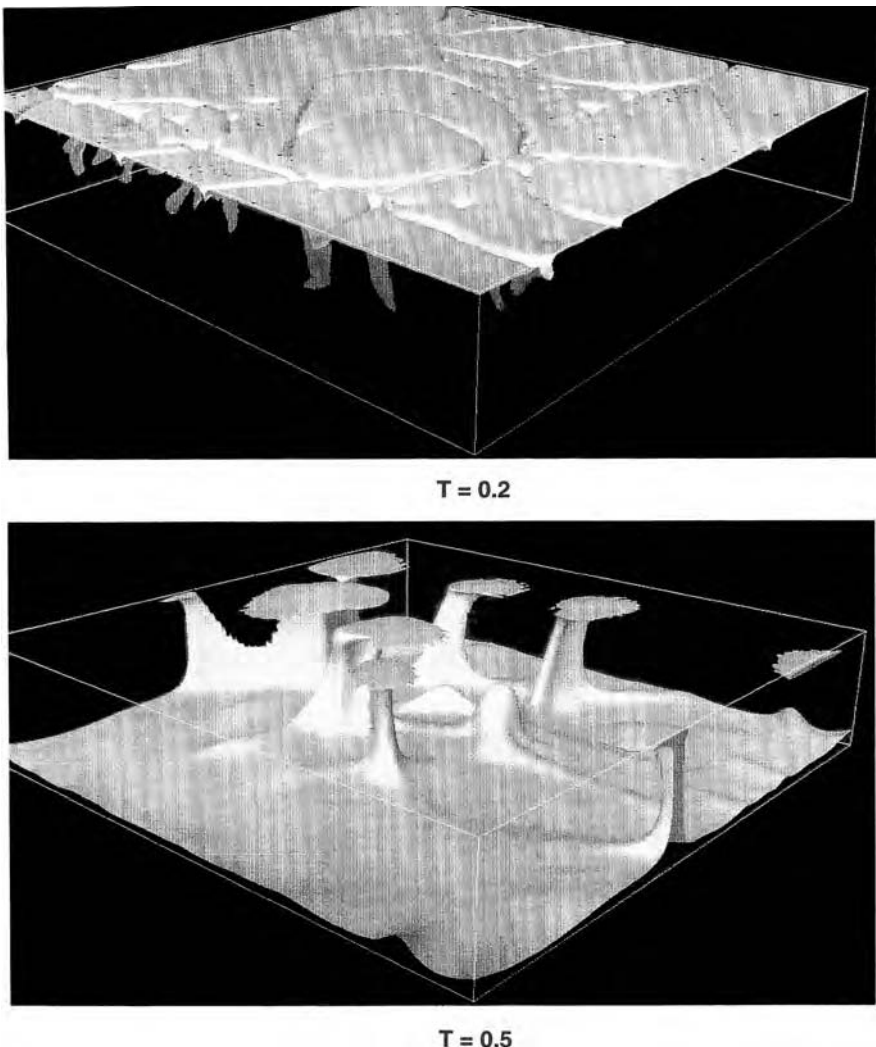


Figure 10.53. Isosurfaces of dimensionless temperature at a surface Rayleigh number of 5×10^6 in the three-dimensional compressible convection model of Balachandar et al. (1992, 1993). The $T = 0.2$ isosurface shows the descending sheets while the $T = 0.5$ isosurface reveals the upwelling cylindrical plumes.

For a color version of this figure, see plate section.

the top boundary than at the bottom boundary due to the higher velocities of the upwellings. Adiabatic cooling in these flows is zero at the boundaries and increases in the interior with a peak near the top boundary. Large viscous heating occurs in regions of strong plume activity.

Zhang and Yuen (1996a) have studied three-dimensional compressible convection in a spherical shell. They use the anelastic approximation and employ an adiabatic reference state based on the Adams–Williamson equation. The equations of their model are:

(1) Conservation of mass

$$\nabla \cdot (\rho_{\text{ref}} \underline{u}) = 0 \quad (10.7.1)$$

where ρ is the adiabatic reference state density and $\underline{u} = (u_r, u_\theta, u_\varphi)$ is velocity (u_r, u_θ, u_φ are velocity components in spherical coordinates).

(2) Conservation of momentum in nondimensional form

$$-\tilde{\nabla}\tilde{p} + \tilde{\nabla}\left(\tilde{\rho}_{\text{ref}}\tilde{\Psi}\right) + \tilde{\nabla}\cdot\tilde{\underline{\epsilon}} = \left(\tilde{\Psi}\frac{\tilde{d}\tilde{\rho}_{\text{ref}}}{d\tilde{r}} - Ra\tilde{\alpha}\tilde{\rho}_{\text{ref}}\Theta\right)\hat{\underline{\epsilon}} \quad (10.7.2)$$

where the curly overbar indicates dimensionless quantities, length is dimensionless with respect to the thickness d of the spherical shell, \tilde{r} is the dimensionless radial coordinate, $\tilde{p} = (p - p_{\text{ref}}) (d^2/\mu_0\kappa_0)$ is the nondimensional dynamic pressure, p_{ref} is the adiabatic hydrostatic reference state pressure, subscript zero denotes values at the outer surface of the shell, $\tilde{\rho}_{\text{ref}} = \rho_{\text{ref}}/\rho_{\text{ref},0}$, other physical properties are made dimensionless with their surface values, μ is viscosity, κ is thermal diffusivity, $Ra = \alpha_0\rho_{\text{ref},0}g_0d^3\Delta T_{sa}/\kappa_0\mu_0$, α is thermal diffusivity, g_0 is the acceleration of gravity at the surface, ΔT_{sa} is the superadiabatic temperature difference across the shell, $\Theta = (T - T_{\text{ref}})/\Delta T_{sa}$ is the nondimensional temperature in excess of the adiabatic reference state temperature T_{ref} , $\tilde{\Psi}$ is the dimensionless geopotential $= (d^2\rho_0/\mu_0\kappa_0)\Psi$, the nondimensional deviatoric stress tensor $\tilde{\underline{\epsilon}}$ is related to the nondimensional strain rate tensor $\underline{\epsilon}$ by $\underline{\epsilon} = \tilde{\mu}(\tilde{r})\tilde{\underline{\epsilon}}$, and $\tilde{\mu}(\tilde{r}) = \mu(r)/\mu_0$ is the dimensionless radially varying viscosity.

(3) Poisson equation

$$\tilde{\nabla}^2\tilde{\Psi} = \tilde{G}Ra\tilde{\alpha}\tilde{\rho}_{\text{ref}}\Theta \quad (10.7.3)$$

where $\tilde{G} = 4\pi G\rho_{\text{ref},0}d/g_0$ and G is the gravitational constant.

(4) Temperature equation

$$\begin{aligned} & \left\{ \frac{\partial\Theta}{\partial\tilde{t}} + \tilde{u}_r \frac{\partial\Theta}{\partial\tilde{r}} + \frac{\tilde{u}_\theta}{\tilde{r}} \frac{\partial\Theta}{\partial\theta} + \frac{\tilde{u}_\varphi}{\tilde{r}\sin\theta} \frac{\partial\Theta}{\partial\varphi} \right\} \\ &= \frac{\tilde{k}}{\tilde{\rho}_{\text{ref}}} \frac{1}{\tilde{r}^2} \frac{d}{d\tilde{r}} \left(\tilde{r}^2 \frac{d\tilde{T}_{\text{ref}}}{d\tilde{r}} \right) + \frac{1}{\tilde{\rho}_{\text{ref}}} \frac{d\tilde{k}}{d\tilde{r}} \left(\frac{\partial\Theta}{\partial\tilde{r}} + \frac{d\tilde{T}_{\text{ref}}}{d\tilde{r}} \right) + \tilde{H} \\ &+ \frac{\tilde{k}}{\tilde{\rho}_{\text{ref}}} \left\{ \frac{1}{\tilde{r}} \frac{\partial^2}{\partial\tilde{r}^2} \left(\tilde{r}^2 \frac{\partial\Theta}{\partial\tilde{r}} \right) + \frac{1}{\tilde{r}^2\sin\theta} \frac{\partial}{\partial\theta} \left(\sin\theta \frac{\partial\Theta}{\partial\theta} \right) + \frac{1}{\tilde{r}^2\sin\theta} \frac{\partial\Theta}{\partial\varphi} \right\} \\ &+ \frac{Di_0\tilde{\mu}}{\tilde{\rho}_{\text{ref}}Ra} \tilde{\Phi} - Di_0\tilde{u}_r\tilde{\alpha}\Theta \end{aligned} \quad (10.7.4)$$

where $\tilde{H} = Hd^2/\kappa_0c_{p0}\Delta T_{sa}$ is the nondimensional internal heating rate, \tilde{t} is nondimensional time scaled with κ_0/d^2 , Di_0 is the surface value of the dissipation number $= \alpha_0g_0d/c_{p0}$ (c_p , the specific heat at constant pressure, is assumed constant), $\tilde{\Phi}$ is the dimensionless viscous dissipation rate, and the last term in (10.7.4) represents adiabatic heating and cooling. The dissipative heating term is

$$\begin{aligned} \tilde{\Phi} = 2 & \left\{ \left(\frac{\partial\tilde{u}_r}{\partial\tilde{r}} \right)^2 + \left(\frac{1}{\tilde{r}} \frac{\partial\tilde{u}_\theta}{\partial\theta} + \frac{\tilde{u}_r}{\tilde{r}} \right)^2 + \left(\frac{1}{r\sin\theta} \frac{\partial\tilde{u}_\theta}{\partial\varphi} + \frac{\tilde{u}_r}{\tilde{r}} + \frac{\tilde{u}_\theta\cot\theta}{\tilde{r}} \right)^2 \right\} \\ &+ \left\{ \tilde{r} \frac{\partial}{\partial\tilde{r}} \left(\frac{\tilde{u}_\varphi}{\tilde{r}} \right) + \frac{1}{\tilde{r}\sin\theta} \frac{\partial\tilde{u}_r}{\partial\varphi} \right\}^2 + \left\{ \frac{\sin\theta}{\tilde{r}} \frac{\partial}{\partial\theta} \left(\frac{\tilde{u}_\varphi}{\sin\theta} \right) + \frac{1}{\tilde{r}\sin\theta} \frac{\partial\tilde{u}_\theta}{\partial\varphi} \right\}^2 \end{aligned}$$

$$+ \left\{ \tilde{r} \frac{\partial}{\partial \tilde{r}} \left(\frac{\tilde{u}_\varphi}{\tilde{r}} \right) + \frac{1}{\tilde{r}} \frac{\partial \tilde{u}_r}{\partial \theta} \right\}^2 + \left\{ \frac{\sin \theta}{\tilde{r}} \frac{\partial}{\partial \theta} \left(\frac{\tilde{u}_\varphi}{\sin \theta} \right) + \frac{1}{\tilde{r} \sin \theta} \frac{\partial \tilde{u}_\theta}{\partial \varphi} \right\}^2 - \frac{2}{3} \left(\tilde{\nabla} \cdot \tilde{u} \right)^2 \quad (10.7.5)$$

Equations (10.7.1)–(10.7.5) can be obtained from the basic equations in Chapter 6. It can be shown that the volume integral of the dissipative heating over the entire shell is balanced by the pressure work done in adiabatic heating (Turcotte et al., 1974):

$$\int_{\text{shell}} \frac{Di_0 \tilde{\mu} \tilde{\Phi}}{Ra} d^3 \tilde{V} = \int_{\text{shell}} Di_0 \tilde{\rho}_{\text{ref}} \tilde{u}_r \tilde{\alpha} \Theta d^3 \tilde{V} \quad (10.7.6)$$

For the adiabatic reference state Zhang and Yuen (1996a) use the Adams–Williamson equation and the assumption that $\tilde{\alpha}/\tilde{\gamma} = \tilde{\rho}_{\text{ref}}^{-2}$ (γ is the Grüneisen parameter) to derive

$$\frac{1}{\rho_{\text{ref}}} \frac{d\rho_{\text{ref}}}{d\tilde{r}} = \frac{-Di_0 \tilde{\alpha}}{\gamma_0 \tilde{\gamma}} = \frac{-Di_0}{\gamma_0} \left(\frac{\rho_{\text{ref},0}}{\rho_{\text{ref}}} \right)^2 \quad (10.7.7)$$

Integration of (10.7.7) gives

$$\tilde{\rho}_{\text{ref}} = \left\{ 1 + \frac{2Di_0}{\gamma_0} (\tilde{r}_0 - \tilde{r}) \right\}^{1/2} \quad (10.7.8)$$

(\tilde{r}_0 is the dimensionless outer radius of the shell, r_0/d) in qualitative agreement with seismic density models of the mantle. For $\tilde{\alpha}$, Zhang and Yuen (1996a) use

$$\tilde{\alpha} = \tilde{\rho}_{\text{ref}}^{-n} \quad (10.7.9)$$

with n a constant between 5 and 6 (Chopelas and Boehler, 1992) and for \tilde{k} they assume

$$\tilde{k} = \tilde{\rho}_{\text{ref}}^3 \quad (10.7.10)$$

(Anderson, 1987b). From the equation for the adiabatic temperature gradient

$$\frac{dT_{\text{ref}}}{d\tilde{r}} = \frac{-\alpha g dT_{\text{ref}}}{c_p} \quad (10.7.11)$$

the hydrostatic equation, and the definition of the Grüneisen parameter, we obtain

$$d(\ln T_{\text{ref}}) = \frac{\tilde{\alpha}}{2} \gamma_0 d\tilde{\rho}_{\text{ref}}^2 \quad (10.7.12)$$

which, with (10.7.9), can be integrated to give

$$\frac{T_{\text{ref}}}{T_{\text{ref},0}} = \exp \left\{ \frac{\gamma_0}{(n-2)} \left(1 - \tilde{\rho}_{\text{ref}}^{2-n} \right) \right\} \quad (10.7.13)$$

Radial profiles of $\tilde{\rho}_{\text{ref}}$, \tilde{k} , $\tilde{\alpha}$, and \tilde{T}_{ref} in the model of Zhang and Yuen (1996a) are shown in Figure 10.54. $\tilde{\alpha}$ decreases with depth, \tilde{T}_{ref} and $\tilde{\rho}_{\text{ref}}$ increase with depth, and \tilde{k} also increases with depth. Figure 10.54 also shows the radial variation in $\tilde{\mu}$ assumed by Zhang and Yuen

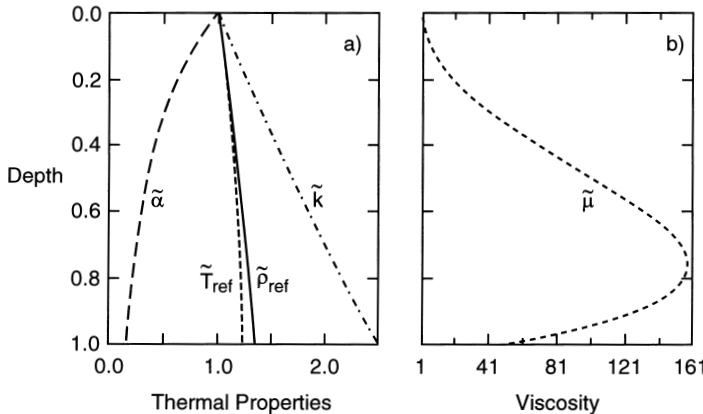


Figure 10.54. Radial profiles of (a) $\tilde{\rho}_{\text{ref}}$, \tilde{k} , $\tilde{\alpha}$, \tilde{T}_{ref} and (b) $\tilde{\mu}$ in the compressible, spherical convection model of Zhang and Yuen (1996a).

(1996a); their model has a viscosity maximum in the lower mantle above the core–mantle boundary.

The basic morphology of convection in the model of Zhang and Yuen (1996a) involves upwelling hot plumes and descending cold sheets. The number and strengths of the plumes and sheets is strongly influenced by the depth variation of viscosity in the model. We focus here on the nature of adiabatic heating and cooling and viscous heating in the flow. The viscous dissipation term ($Di_0 \tilde{\mu}/Ra$) $\tilde{\Phi}$ in (10.7.4) is shown in Figure 10.55 for two cases with and without internal heating. In both cases Ra is 3×10^6 and $Di_0 = 0.5$. Also, both cases employ impermeable, isothermal, and free-slip top and bottom boundaries. Viscous dissipation is relatively large near the upper and lower boundaries of the shell in both cases; local values of viscous dissipation far exceed the horizontally averaged values. The maximum viscous heating is larger in the case where internal heating is included than it is when $\tilde{H} = 0$. However, the opposite is true on average. According to Zhang and Yuen (1996a), the magnitude of the horizontally averaged viscous heating is generally comparable with radiogenic heating and the maximum values of viscous heating are locally an order of magnitude larger.

Adiabatic heating (and cooling), the term $-Di_0 \tilde{\alpha} \tilde{u}_r \Theta$ in (10.7.4), is shown in Figure 10.56 for the internally heated cases of Figure 10.55. Adiabatic cooling in the plumes (negative values in Figure 10.56a) is a maximum (in absolute value) in the upper part of the shell where the viscosity is relatively low; adiabatic heating in the sheet downflows (positive values in Figure 10.56a) is also a maximum in the upper part of the shell. The magnitude of the adiabatic cooling by plumes is much larger than the magnitude of the adiabatic heating in downflows because thermal anomalies in upflow plumes are larger in magnitude than they are in downflow sheets. The net horizontally averaged effect of adiabatic heating and cooling is to cool the interior (Figure 10.56b). The depth dependences of adiabatic heating and cooling and viscous dissipation have also been studied by Balachandar et al. (1993) and Tackley (1996b).

Figure 10.57 shows planforms of viscous heating and adiabatic heating in the internally heated case of Figure 10.55. The maximum values of viscous heating occur in the narrow downwelling regions; though not as large, viscous heating is also significant in the upwelling plumes. Adiabatic cooling is largest at plume centers while adiabatic heating is largest in the

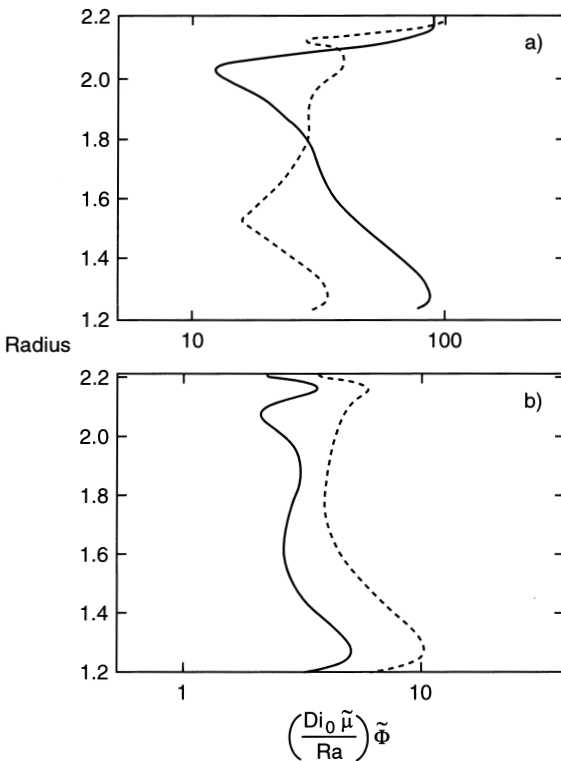


Figure 10.55. Maximum (a) and spherically averaged (b) values of viscous heating $(Di_0 \tilde{\mu}/Ra)\tilde{\Phi}$ as a function of radius in the spherical shell compressible convection model of Zhang and Yuen (1996a). The solid curves are for a case that includes internal heating ($\tilde{H} = 10$) while the dashed curves are for a case that is heated only from below ($\tilde{H} = 0$).

sheet-like downflows (Figure 10.57b). Adiabatic heating and viscous heating reinforce each other in warming the downflow sheets. In the upflow plumes however, adiabatic cooling acts opposite to viscous heating. This vertical asymmetry in the heating terms tends to increase the interior temperature of compressible convection.

Zhang and Yuen (1996b) have extended their model of compressible convection in a spherical shell to take into account temperature- and pressure-dependent viscosity. Aside from viscosity, the model is identical to the one just discussed (Zhang and Yuen, 1996a). The variable viscosity model has a maximum viscosity contrast of about 200 over depth and about 100 laterally. With strongly temperature dependent viscosity, upwelling plumes are faster and generate more viscous heating compared with constant viscosity or depth-dependent viscosity. Viscous heating is large at the top of plumes and where the plumes impinge on the upper boundary. Viscous heating in the plumes retards adiabatic cooling and maintains plume temperatures at a substantial fraction of the hot bottom boundary temperature.

With temperature-dependent viscosity there are large horizontal variations in viscosity which cause strong local toroidal motions in the neighborhood of fast upwelling plume heads, though on the basis of a horizontal average toroidal energy is only about 10% of poloidal energy (Zhang and Yuen, 1996b). Figure 10.58 shows the close correlation among toroidal velocities, plume heads and viscous heating. The strongest toroidal motions and the largest

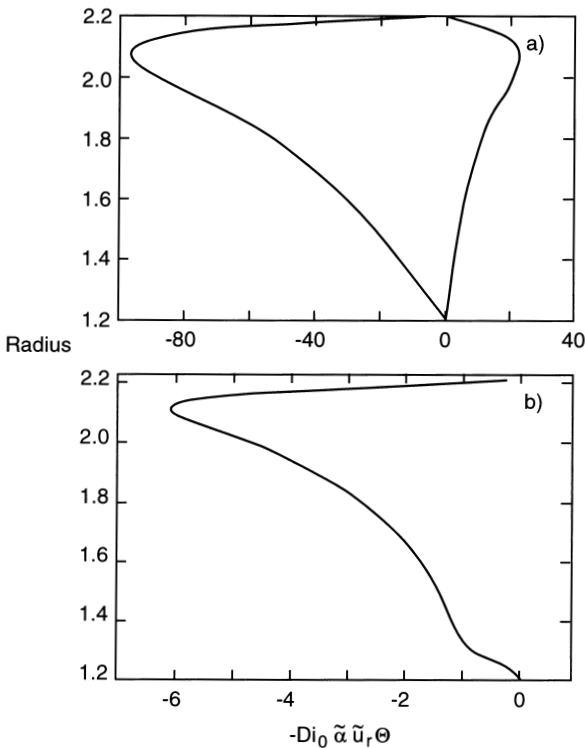


Figure 10.56. Radial variations in the adiabatic heating term $-Di_0 \tilde{\alpha} \tilde{u}_r \Theta$ for the internally heated case of Figure 10.55. (a) shows radial profiles of maximum and minimum values (cooling by rising plumes corresponds to negative values, heating by sinking sheets gives positive values). (b) shows the radial profile of the net horizontally averaged adiabatic heating (cooling) term which corresponds to cooling of the interior. After Zhang and Yuen (1996a).

viscous heating occur directly above or near plume heads. The positive feedback between viscous heating and temperature-dependent viscosity enhances the toroidal motions where the plumes impinge on the top boundary. Zhang and Yuen (1996b) speculate that this effect could explain microplate rotation in regions with hot spot activity such as Easter Island. The toroidal motions arising from compressible convection with temperature-dependent viscosity have also been studied by Balachandar et al. (1995a).

10.8 Plate-like Rheology

Question 10.12: What essential rheological behavior needs to be incorporated into models of mantle convection for plate tectonics to arise from the model in a natural, self-consistent way?

One of the major challenges in mantle convection modeling is the self-consistent, self-generation of plate-like behavior by the flow. Plate tectonics on the Earth is a product of the

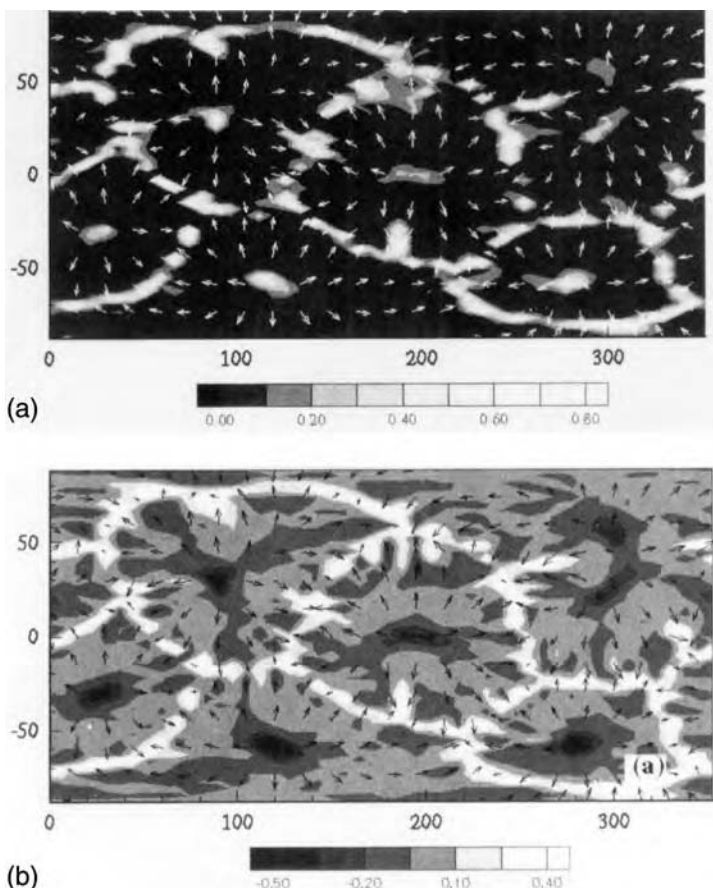


Figure 10.57. Planforms of near-surface viscous (a) and adiabatic (b) heating in the internally heated case of Figure 10.55. The adiabatic heating distribution is shown at a dimensionless depth of 0.1. Viscous and adiabatic heating are normalized by their maximum values. After Zhang and Yuen (1996a).

thermal convection of a multi-rheological fluid with both viscous and nonviscous characteristics (mantle and crustal rocks). Numerical and laboratory models of mantle convection have largely assumed viscous-like rheologies that are inherently incapable of producing a flow with the features of plate tectonics. Attempts to account for the influence of plates on mantle convection models have involved the a priori imposition of plate-like characteristics on the simulations including the specification of surface velocity or surface stress boundary conditions (Chase, 1979b; Hager and O'Connell, 1979, 1981; Olson and Corcos, 1980; Gable et al., 1991; Bunge and Richards, 1996), the introduction of weakened zones at the surface (Schmeling and Jacoby, 1981; Gurnis, 1988; Davies, 1989; King and Hager, 1990; King and Ita, 1995; Zhong and Gurnis, 1995b, 1996), and the incorporation of separate rheological layers at the surface (Ribe, 1992; Weinstein and Olson, 1992). Temperature-dependent viscosity, though an important element of realism in plate-like rheological behavior, is insufficient in itself to generate plates, instead producing sluggish and rigid lids atop convecting layers (Nataf and Richter, 1982; Stengel et al., 1982; Solomatov, 1995; Ratcliff et al., 1997; see Chapter 13 for additional discussion of convection with temperature-dependent viscosity). The plates also play an essential role in the partitioning of energy between toroidal

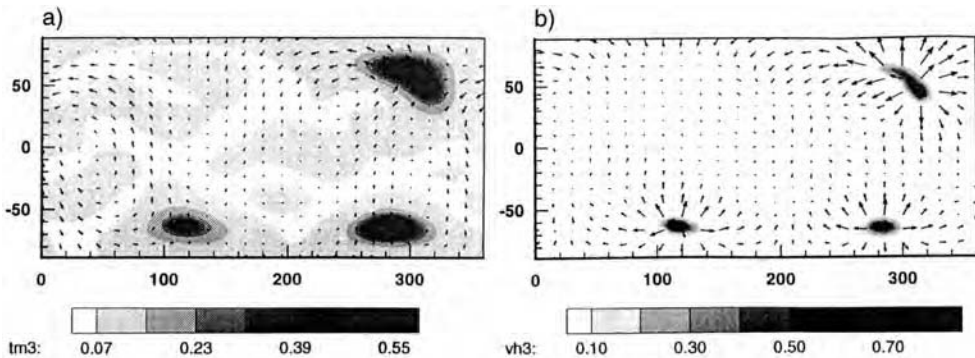


Figure 10.58. Toroidal velocity vectors and temperature (a) at a depth of 200 km in spherical shell compressible convection with temperature- and pressure-dependent viscosity at an average Rayleigh number of 10^6 . The distribution of viscous dissipation and total velocity vectors (b) in the same flow and at the same depth as in (a). In (a) the largest velocity vector is 0.124 cm yr^{-1} while in (b) it is 0.492 cm yr^{-1} . Viscous heating is normalized by its maximum value. After Zhang and Yuen (1996b).

and poloidal components (O'Connell et al., 1991; Čadek and Ricard, 1992; Hsui et al., 1995).

Plate-like behavior involves the localization of deformation to narrow zones. In the Earth this is achieved by faulting in the brittle and elastic upper part of the lithosphere and by ductile shear localization below this layer. Narrow shear zones can be produced by a number of processes that result in self-lubrication or strain weakening, i.e., the reduction in the stress required to maintain a given strain rate with increasing strain. Such processes could include: (1) grain size reduction by dynamic recrystallization, resulting in a transition from grain-size-insensitive dislocation creep to grain-size-sensitive diffusion creep with an accompanying strong reduction in effective viscosity (Karato et al., 1980, 1986; Drury et al., 1991; Vissers et al., 1995; Jaroslav et al., 1996; Kameyama et al., 1997; Jin et al., 1998), (2) void (pores and microcracks) generation and infilling with volatiles (Bercovici, 1998; Regenauer-Lieb, 1999), (3) the feedback between viscous dissipation and temperature-dependent viscosity (Yuen et al., 1978; Fleitout and Froidevaux, 1980; Obata and Karato, 1995), and damage or weakening by production of microcracks, for example (Lyakhovsky et al., 1997a,b).

All the above processes result in the creation of damage (used in a general sense to represent weakening by any of the mechanisms discussed), but damaged or weak zones in materials also heal or strengthen with time by annealing or diffusion resulting in the destruction of damage. A relationship for the evolution of damage with time can be derived by quantitative representations of the growth and destruction processes, and a rheological law can be obtained by supplementing the damage equation with a connection between damage and viscosity. Rheological laws for the viscous dissipation and void-volatile mechanisms have been derived by Bercovici (1998). Such rheological laws are characterized by strain rate weakening, i.e., stress initially increases with increasing strain rate, it reaches a maximum at some critical strain rate, and then it decreases with further increase in strain rate. Bercovici (1993, 1995b, 1996, 1998) has applied strain rate weakening rheologies due to "stick-slip" behavior, viscous dissipation feedback, and void-volatile self-lubrication to the problem of plate generation in a two-dimensional lithospheric sheet with deformation driven by specified sources and sinks of mass. His studies have shown that strain rate weakening rheology is

effective in producing self-localization of shear and narrow shear zones which give good approximations to transform faults.

Tackley (1998a) has constructed a generic strain rate weakening rheology and has incorporated it into a three-dimensional model with prescribed sources of buoyancy from a constant viscosity, three-dimensional convection solution. His rheological law is of the form

$$\underline{\underline{\sigma}} = \frac{2\sigma_{yield}^2 \mu}{\sigma_{yield}^2 + \mu^2 \dot{\underline{\underline{e}}}^2} \dot{\underline{\underline{e}}} \quad (10.8.1)$$

where $\underline{\underline{\sigma}}$ is the stress tensor, $\dot{\underline{\underline{e}}}$ is the strain rate tensor, σ_{yield} is a yield stress (maximum possible stress), μ is the viscosity of undamaged material, and $\dot{\underline{\underline{e}}}^2 = \dot{\underline{\underline{e}}} : \dot{\underline{\underline{e}}}$. Equation (10.8.1) is similar to the stress-strain rate equations derived by Bercovici for viscous dissipation (Bercovici, 1996) and void-volatile self-lubrication (Bercovici, 1998). It is seen from (10.8.1) that for small $\dot{\underline{\underline{e}}}$ the material behaves like a Newtonian viscous fluid with undamaged viscosity μ while for large $\dot{\underline{\underline{e}}}$ stress is inversely proportional to strain rate.

The model consists of a constant thickness surface layer about 100 km thick (lithosphere) with an undamaged viscosity 10^4 times larger than that of the underlying material (mantle), all in a rectangular box. The momentum equation is solved subject to a given three-dimensional distribution of buoyancy forces derived from a three-dimensional convection calculation with constant viscosity. The rheological law (10.8.1) is used in solving the momentum equation with the prescribed buoyancy forces. The full thermal convection problem for the strain rate weakening rheology is not solved. Parameters such as yield stress and undamaged viscosity are chosen to yield plate-like solutions in the upper layer. A shortcoming of the idealized strain rate weakening rheology and the arbitrary choice of rheological parameters is the lack of a direct connection between the model rheological parameters and the measured rheological properties of mantle rocks.

Figure 10.59 shows results for a $1 \times 1.4 \times 1$ box that is basally heated (Tackley, 1998a). The prescribed temperature field has an upwelling along one edge of the box and a downwelling at the diagonally opposite edge (Figure 10.59a). The viscosity/velocity solution for the prescribed thermal buoyancy field has two high-viscosity plate-like regions surrounded by weak zones (Figure 10.59b). The larger plate is moving diagonally across the box relative to the nearly stationary smaller plate; the two plates are separated by a weak shear zone. This localized weak shear zone, which does not lie above any upwelling or downwelling, is an important feature of the solution and is similar to a transform fault. There are also weak zones above upwellings and downwellings. The boundary between a weak zone and a plate in this solution is extremely sharp (one grid cell) and is characteristic of the strain rate weakening rheology. Horizontal divergence (Figure 10.59c) is focused at the upwelling and downwelling corners, while vertical vorticity, an indicator of strike-slip motion, is concentrated in a line coincident with the shear plate margin (Figure 10.59c). Both horizontal divergence and vertical vorticity are concentrated in the lithosphere.

Results for a similar calculation carried out in a wide $8 \times 8 \times 1$ box heated from below are shown in Figure 10.60 (Tackley, 1998a). The temperature field (Figure 10.60a) is typical of bottom-heated, constant property convection at modest Rayleigh number (10^5). The lithospheric viscosity and velocity fields (Figure 10.60b) have numerous small equi-dimensional strong plates separated by narrow weak zones. Weak zones occur above upwellings and downwellings and also connect the upflows and downflows together. Weak zones above upwellings and downwellings are comparable in size to the flow features and are associated with strong convergence and divergence; interconnecting weak zones localize down to a

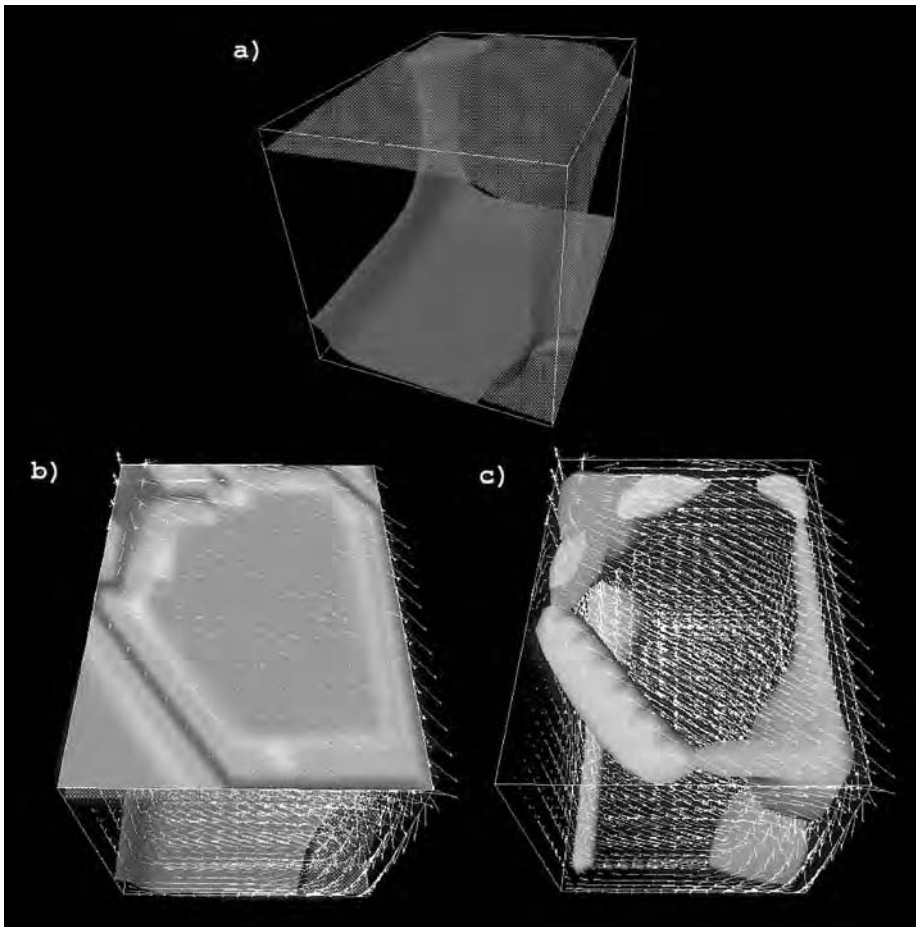


Figure 10.59. Model results for velocity, viscosity, horizontal divergence, and vorticity driven by a prescribed thermal buoyancy field in a rectangular box containing a high-viscosity lithosphere with strain rate weakening viscosity overlying an isoviscous mantle with Newtonian rheology. (a) Temperature isosurfaces (red is hot, blue is cold), (b) viscosity (orange is large, violet is small, viscosity varies between 10^{-1} and 10^4 times the mantle viscosity) and velocity vectors, and (c) horizontal divergence/convergence (light and dark purple) and vertical vorticity (green and blue). After Tackley (1998a).

For a color version of this figure, see plate section.

size limited by the viscosity underneath the lithosphere and are associated with high vertical vorticity (Figure 10.60c). A viscoplastic rheology (stress saturates beyond the yield point) is much less effective in producing plate-like characteristics (Figures 10.60d and e). While weak zones occur above upwellings and downwellings there are no weak zones analogous to transform faults.

The plate pattern produced by convection with internal heating is shown in Figure 10.61 (Tackley, 1998a). It is characterized by small, mobile plates surrounding cylindrical downwellings and embedded in a generally stagnant lid. The two plates near the lower left edge of Figure 10.61b are moving from passive spreading centers toward the elongated downwelling between them. These two plates have transform margins at their ends. The passive spreading

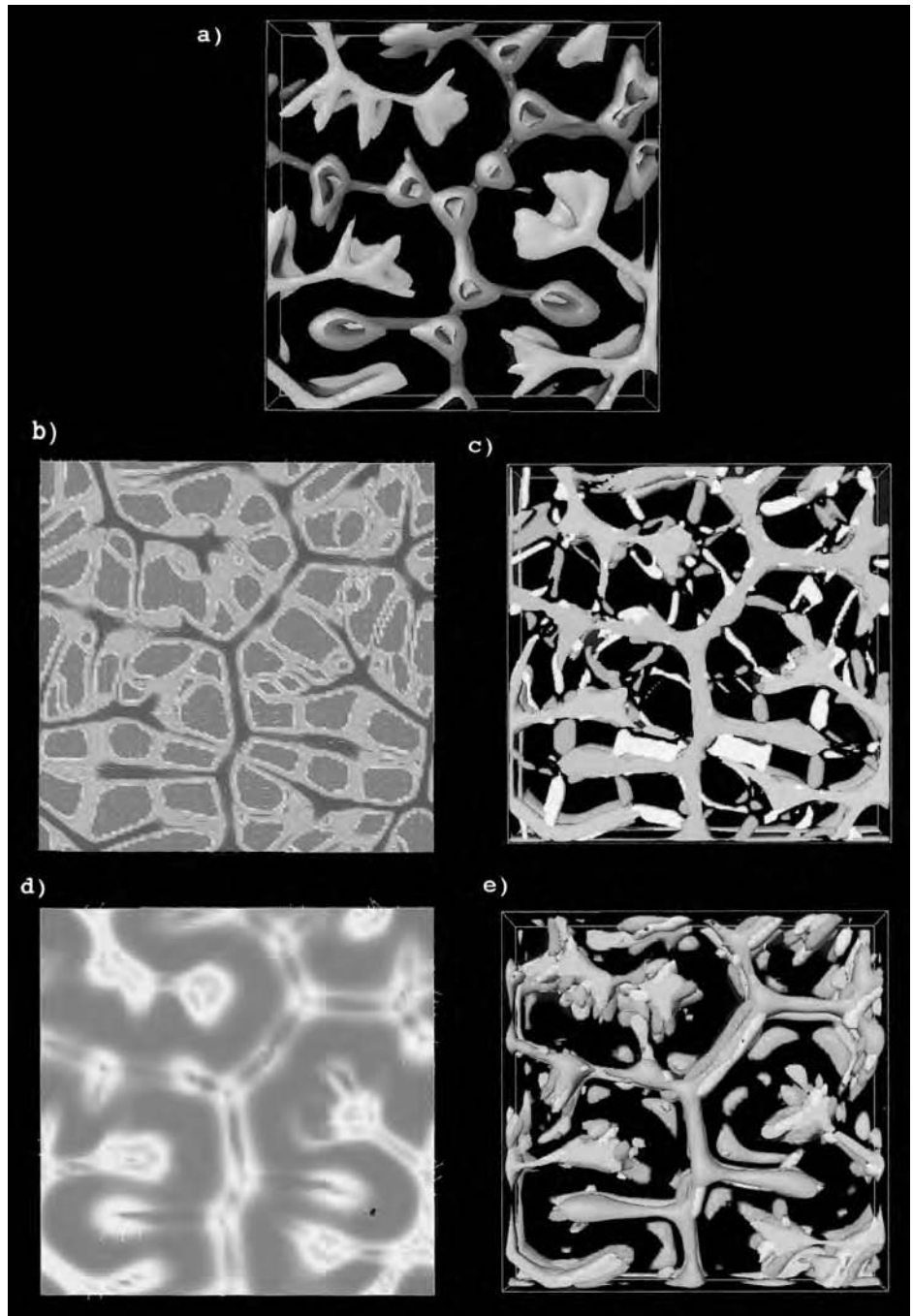


Figure 10.60. Similar to Figure 10.59 for a wide box of dimension $8 \times 8 \times 1$. The panels in (d) and (e) are similar to (b) and (c) but for a viscoplastic rheology. After Tackley (1998a).

For a color version of this figure, see plate section.

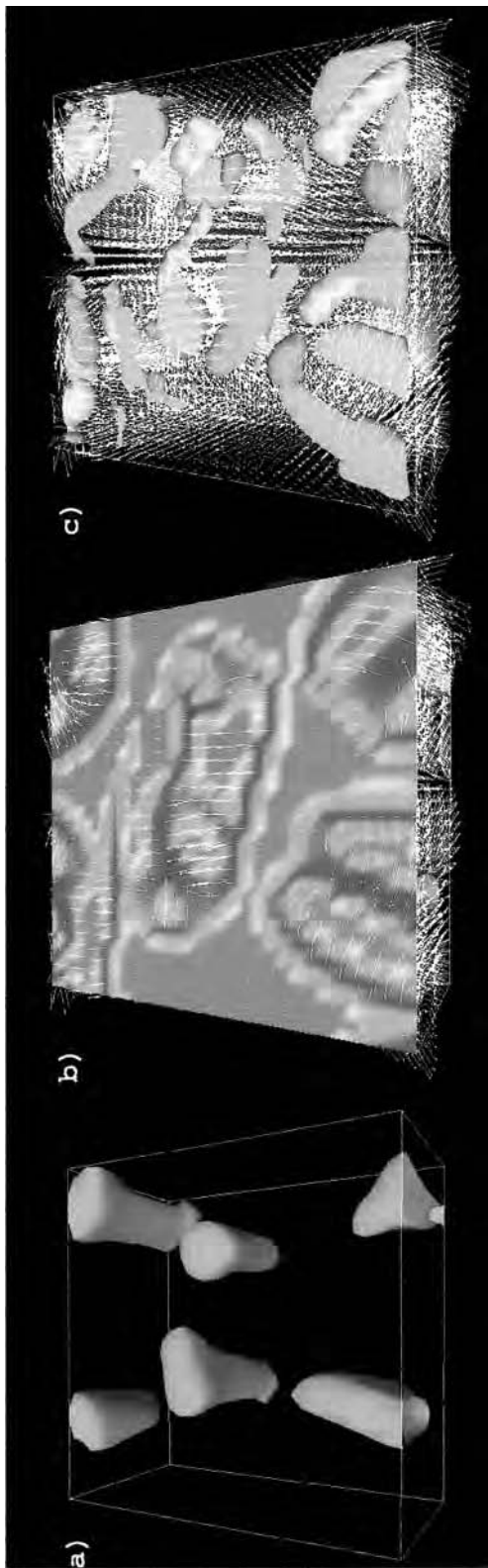


Figure 10.61. Similar to Figure 10.59 for flow driven by thermal buoyancy forces from a convection calculation with only internal heating. The residual temperature isosurface in (a) shows the pattern of downwelling – mainly cylindrical, but sometimes elongated (lower left). (b) Velocity vectors and lithospheric viscosity. (c) Horizontal divergence (green and blue) and vertical vorticity (yellow and mauve). After Tackley (1998a).

For a color version of this figure, see plate section.

centers generated in the model may be analogous to mid-ocean ridges on the Earth which are generally believed to be passive structures, i.e., they do not lie above deep-seated sheet-like upwellings in the mantle (Schubert, 1992).

The solution shown in Figure 10.62 (Tackley, 1998a) is for a more Earth-like, compressible model in a $4 \times 4 \times 1$ box. The thermal field has long linear downwellings and a broad megaplume upwelling in the center of the box. The main weak zones lie above the upflows and downflows, but narrow weak zones with high vorticity connect the weak zones above the upwellings and downwellings.

The strain rate weakening rheology is seen to account for several characteristics of plate-like behavior (Tackley, 1998a). It is able to produce high-viscosity plates separated by narrow low-viscosity or weak zones, with sharp transitions between the plates and the weak zones. Weak zones form above upflows and downflows with a width comparable to the underlying flows; these weak zones are associated with predominant convergence and divergence. Narrow weak zones also connect upwellings and downwellings; these weak zones have large vertical vorticity and strike-slip motion but also a significant amount of convergent/divergent motion. With internal heating, passive spreading centers form together with small plates surrounded by weak zones. The formation of narrow weak zones that resemble transform faults is a key step in producing plate tectonics from a buoyancy-driven flow. The toroidal motion associated with strike-slip faults on the Earth is a major part of plate velocities and derives from the nonviscous rheology of the lithosphere as illustrated here by the strain weakening rheology of the model lithosphere.

The strain weakening rheology does not reproduce all the attributes of plate tectonics. The plates in the model are too small compared with tectonic plates. There is no one-sided subduction as there is in the Earth and the distribution of plates and weak zones in the internally heated case is not very Earth-like; there are passive spreading margins in the model, but not a global interconnected system of passive spreading centers as in the mid-ocean ridge system on Earth. Clearly, the model strain weakening rheology does not account for all the important rheological and mechanical complexities of the Earth's lithosphere. Among the things not taken into account in the model are the contrasts between continental and oceanic crust and lithosphere and the memory of past deformation in the fault-ridden crust of the Earth.

Some plate-like features have also been produced in the three-dimensional convection model of Trompert and Hansen (1998). They employ a temperature and strain rate dependent rheology of the form

$$\mu = 2 \left(\frac{1}{\mu_T} + \frac{1}{\mu_e} \right)^{-1} \quad (10.8.2)$$

where

$$\mu_T = e^{-AT} \quad (10.8.3)$$

$$\mu_e = \mu^* + \sigma^* \left(\underline{\dot{\epsilon}} : \underline{\dot{\epsilon}} \right)^{-1/2} \quad (10.8.4)$$

μ is viscosity, A is a constant controlling the viscosity contrasts generated by temperature differences μ_T , μ_e is the strain rate dependent part of the viscosity, σ^* controls the stress level at which failure occurs, and μ^* is the effective viscosity at higher stresses. Unlike the model discussed above by Tackley (1998a), the model of Trompert and Hansen (1998)

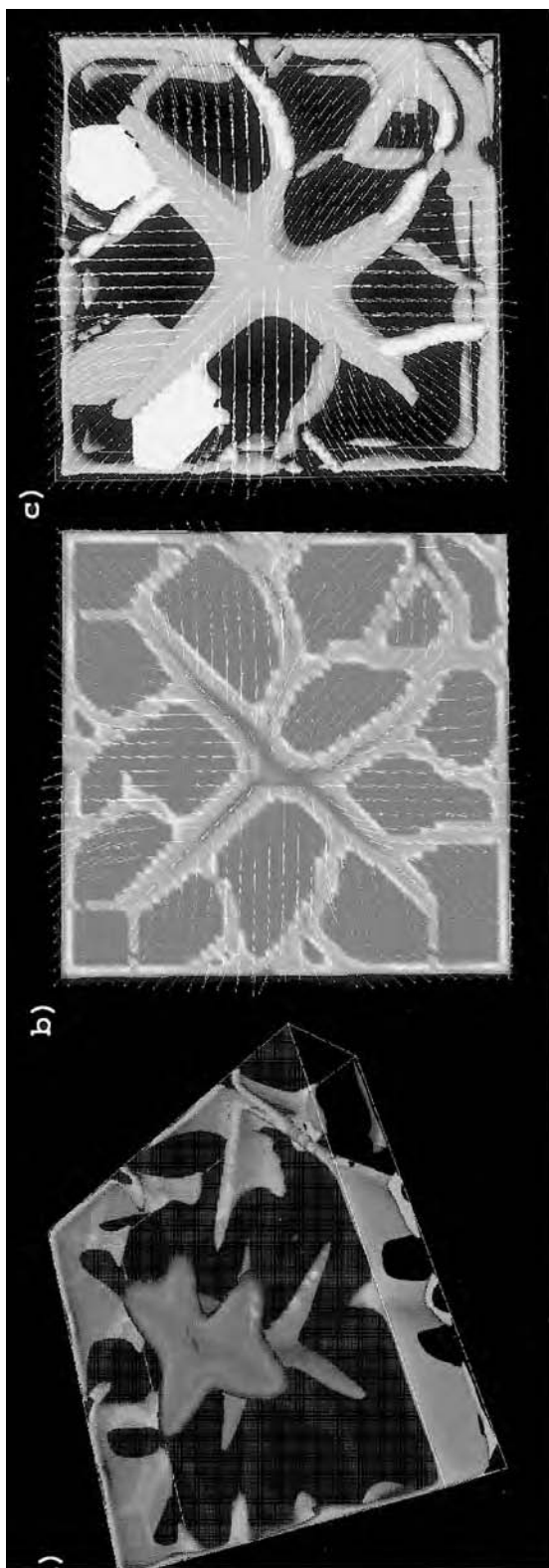


Figure 10.62. Similar to Figure 10.59 for a compressible, Earth-like, basally heated model in a $4 \times 4 \times 1$ box. After Tackley (1998a).

For a color version of this figure, see plate section.

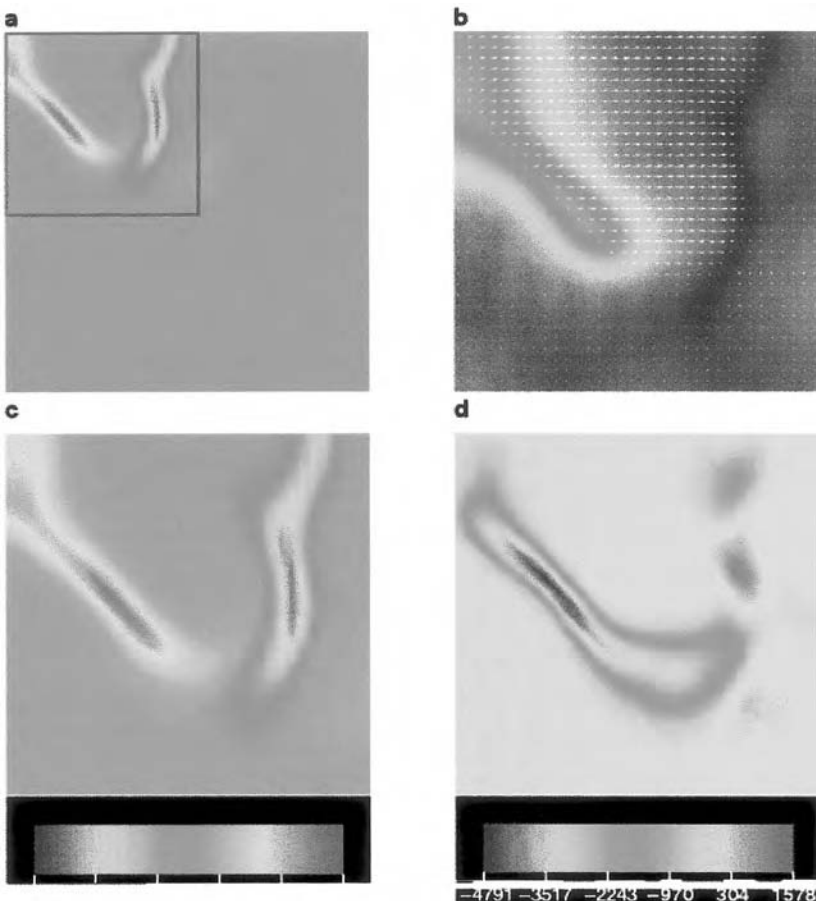


Figure 10.63. Plate-like behavior in the mantle convection model of Trompert and Hansen (1998). (a) Horizontal divergence (red) and convergence (blue). The entire top surface of the box is shown. Narrow zones of divergence and convergence are shown in the upper left corner. The red square outlines the region shown in more detail in (b), (c), and (d). (b) Velocity vectors and the temperature field slightly below the surface (blue is cold and green is warm). (c) Horizontal divergence. (d) Vertical vorticity.

For a color version of this figure, see plate section.

solves the full convection problem and generates a self-consistent thermal, mechanical, and rheological solution.

Trompert and Hansen (1998) present a solution for bottom-heated convection in a $4 \times 4 \times 1$ box with a surface Rayleigh number of 10^2 and a viscosity contrast across the box due to temperature of 10^5 . Convection in their model is strongly episodic. It consists of a long period of stagnant-lid convection (see Chapter 13) followed by a brief period of subduction of parts of the lid, followed by a long period of new lid formation where the old lid subducted, followed by a repetition of these events. During the brief period of subduction the system displays some plate-like behavior as shown in Figure 10.63. The figure shows narrow divergent and convergent zones in the upper left part of an otherwise stagnant lid (Figure 10.63a). The part of the lid between the ridge and subduction zone segments moves as a plate, i.e., it has almost constant velocity over the moving region and sharp velocity

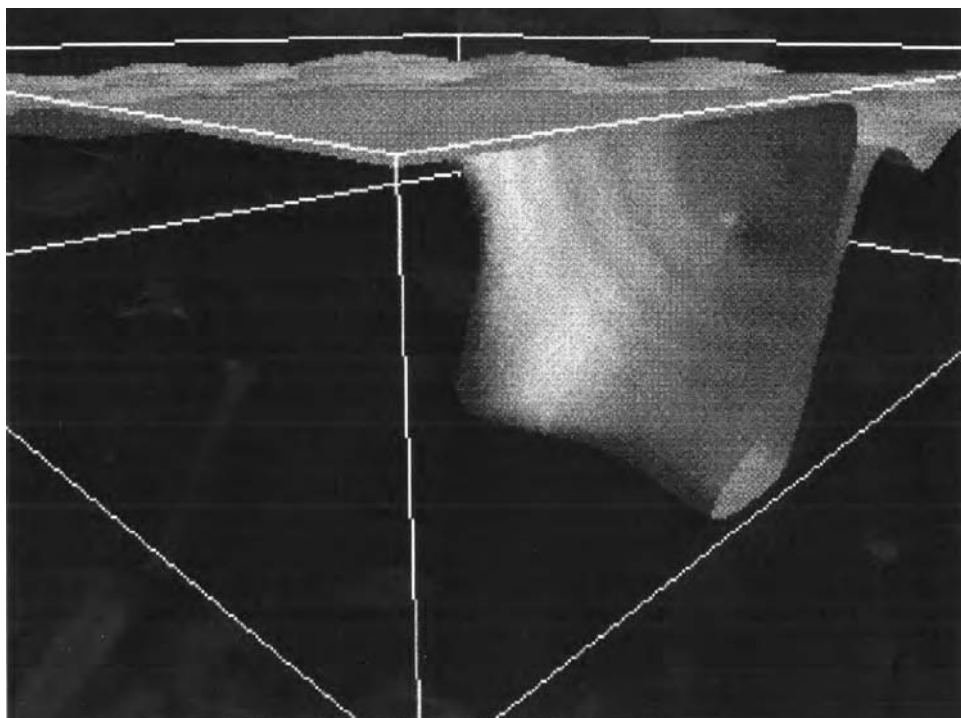


Figure 10.64. A temperature isosurface illustrating sheet-like downwelling during a brief period of lithosphere subduction in the model of Trompert and Hansen (1998).

changes near its boundaries (Figure 10.63b). There is transform-like motion over parts of the plate boundaries. In particular, a large amount of vertical vorticity coincides with part of the divergent margin. The part of the cold lid that subducts descends into the interior as a sheet-like downwelling (Figure 10.64) reminiscent of a descending slab. The downwelling sheet spreads horizontally over the bottom boundary and trench migration occurs at the surface.

The model of Trompert and Hansen (1998) displays several plate-like behaviors including plate-like regions with nearly constant velocity, fairly sharp changes in velocity at plate boundaries, sheet-like downflow, and trench migration. However, these behaviors occur only episodically and for short periods unlike plate tectonics on Earth. The behavior of the model may actually be more relevant to Venus, which is thought to undergo sluggish- or stagnant-lid convection and which experienced a global resurfacing event perhaps involving subduction of all or a large part of its lithosphere some 500 Myr ago (see the discussion of Venus in Chapter 14). The rheology used by Trompert and Hansen (1998) is not a strain rate weakening rheology and consequently it does not give continuous plate tectonic behavior.

10.9 Three-dimensional Models of Convection Beneath Ridges and Continents

Numerical calculations of three-dimensional convection beneath spreading centers have been carried out by Sparks and Parmentier (1993), Sparks et al. (1993) and Rabinowicz et al. (1993). Laboratory studies of this problem have been performed by Kincaid et al. (1996). Moresi and Lenardic (1997) have carried out three-dimensional numerical simulations of crustal deformation and subcontinental mantle convection.

11

Hot Spots and Mantle Plumes

11.1 Introduction

Hot spots are anomalous areas of surface volcanism that cannot be directly associated with plate tectonic processes. The term hot spot is used rather loosely. It is often applied to any long-lived volcanic center that is not part of the global network of mid-ocean ridges and island arcs. The classic example is Hawaii. Anomalous regions of thick crust on ocean ridges are also considered to be hot spots. The prototype example is Iceland.

There is little agreement on the total number of hot spots. Several hot spot lists have been published, and the number of volcanic centers included on these lists ranges from about 20 to more than 100. In one of his original papers associating hot spots with mantle plumes, Morgan (1972) listed 19 hot spots. Crough and Jurdy (1980) listed 42, Wilson (1973) listed 66, and Vogt (1981) listed 117. Table 11.1 gives the coordinates of 30 hot spots from the list of Crough and Jurdy (1980), and Figure 11.1 shows the locations of 20 prominent hot spots (see also Figure 2.23). In many cases hot spots have well-defined tracks associated with volcanic ridges or lines of volcanic edifices; these are also shown in Figure 11.1 and in Figure 2.23. A few hot spots and the tracks they have made appear on all lists, either because of high eruption rates in the recent past or because they have produced conspicuous traces. Among these are Hawaii, Iceland, Reunion, Cape Verde, and the Azores. Others, such as Bermuda, do not have an extensive volcanic history, but qualify as hot spots because they sit atop broad topographic rises or seafloor swells. Large continental volcanic centers, such as Yellowstone and some in East Africa, make most lists because of their similarity to oceanic hot spots.

The concept of stationary heat sources in the mantle was introduced by Wilson (1963c) as an explanation for the Hawaiian chain. Morgan (1971, 1972) was the first to advocate a global array of deep mantle plumes for the origin of hot spots. Morgan envisioned mantle plumes to be vertical conduits in which hot mantle material rises buoyantly from the lower mantle to the lithosphere at velocities as large as 1 m yr^{-1} . The plume concept has steadily gained acceptance in spite of the fact that the geological, geophysical, and geochemical evidence for plumes, while growing, is still largely indirect. There are also some critical observations that plume theory has never satisfactorily explained.

Table 11.1. *Hot Spot Locations^a*

Hot Spot	Overlying Plate	Latitude (degree)	Longitude (degree)
Hawaii	Pacific	20	-157
Samoa	Pacific	-13	-173
St. Helena	Africa	-14	-6
Bermuda	N. America	33	-67
Cape Verde	Africa	14	-20
Pitcairn	Pacific	-26	-132
MacDonald	Pacific	-30	-140
Marquesas	Pacific	-10	-138
Tahiti	Pacific	-17	-151
Easter	Pac-Naz	-27	-110
Reunion	Indian	-20	55
Yellowstone	N. America	43	-111
Galapagos	Nazca	0	-92
Juan Fernandez	Nazca	-34	-83
Ethiopia	Africa	8	37
Ascencion	S. Am-Afr	-8	-14
Afar	Africa	10	43
Azores	Eurasia	39	-28
Iceland	N. Am-Eur	65	-20
Madeira	Africa	32	-18
Canary	Africa	28	-17
Hoggar	Ind-Ant	-49	69
Bouvet	Afr-Ant	-54	2
Pr. Edward	Afr-Ant	-45	50
Eifel	Eurasia	48	8
San Felix	Nazca	-24	-82
Tibesti	Africa	18	22
Trinadade	S. America	-20	-30
Tristan	S. Am-Afr	-36	-13

^a After Crough and Jurdy (1980).

Question 11.1: *Do mantle plumes exist?*
Question 11.2: *Which “hot spots” are associated with mantle plumes?*

Although the direct evidence (e.g., Wolfe et al., 1997) for the existence of mantle plumes is sparse, their occurrence is consistent with our present understanding of mantle dynamics. We routinely associate the subducted lithosphere with the instability of the upper thermal boundary layer. We also expect a thermal boundary layer at the base of the convecting layer, the D'' layer at the bottom of the mantle or an internal thermal boundary layer for layered mantle convection. Instabilities of this basal thermal boundary layer would be expected to generate mantle plumes.

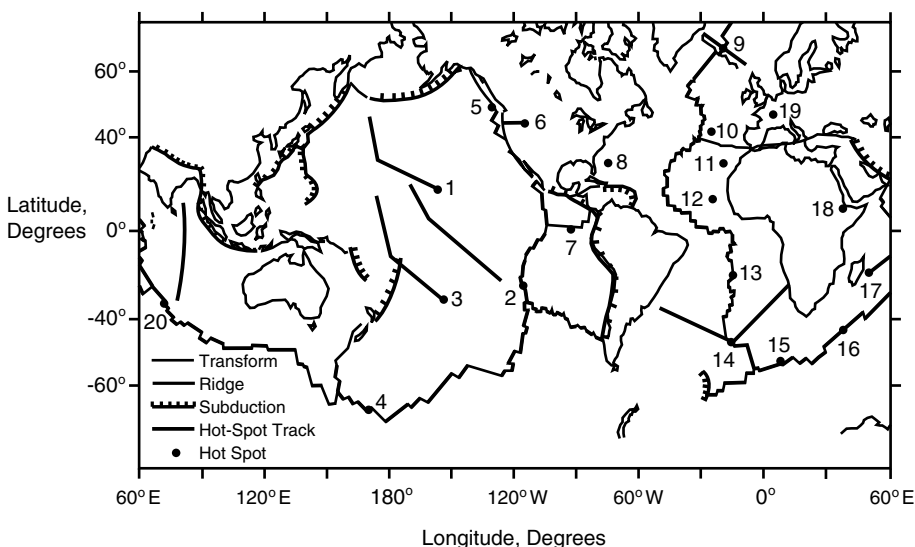


Figure 11.1. Hot spot and hot spot track locations: 1, Hawaii (Hawaiian-Emperor Seamount Chain); 2, Easter (Tuamoto-Line Island Chain); 3, MacDonald Seamount (Austral-Gilbert-Marshall Island Chain); 4, Bellany Island; 5, Cobb Seamount (Juan de Fuca Ridge); 6, Yellowstone (Snake River Plain-Columbia Plateau); 7, Galapagos Islands; 8, Bermuda; 9, Iceland; 10, Azores; 11, Canary Islands; 12, Cape Verde Islands; 13, St. Helena; 14, Tristan da Cunha (Rio Grande Ridge (w), Walvis Ridge (e)); 15, Bouvet Island; 16, Prince Edward Island; 17, Reunion Island (Mauritius Plateau, Chagos-Lacadive Ridge); 18, Afar; 19, Eifel; 20, Kerguelen Plateau (Ninety-East Ridge).

11.2 Hot Spot Tracks

The prototype of a hot spot track is the Hawaiian-Emperor chain of volcanic islands and seamounts (see Figure 2.24). The associated hot spot volcanism has resulted in a nearly continuous volcanic ridge that extends some 4,000 km from near the Aleutian Islands to the now very active Kilauea volcano on the big island of Hawaii, as illustrated in Figure 11.2a. The chain is composed of more than 100 individual volcanic shields. There is a remarkably uniform age progression, with the age of each volcanic shield increasing nearly linearly with distance from Kilauea. The average propagation rate of the track across the Pacific plate has been about 90 mm yr^{-1} over the past 40 Myr and the average time interval between formation of successive shields is about 0.7 Myr. This age progression is illustrated in Figure 11.2c.

A striking feature of this track is the bend that separates the near-linear track of the Emperor chain from the near-linear track of the Hawaiian chain. The bend in the track occurred at about 43 Myr ago when there was an abrupt shift in the position of the pole of rotation of the Pacific plate. This shift was part of a global reorientation of plate motions over a span of a few million years (Richards and Lithgow-Bertelloni, 1996) and has been associated with the continental collision between India and Asia. The rate of volcanism associated with the Hawaiian-Emperor chain has been variable, as illustrated in Figure 11.2d. Following the bend, volcanic activity was low for about 10 Myr; since then activity has generally increased with time.

Many hot spots are associated with linear tracks, as indicated in Figure 11.1. When the relative motions of the plates are removed, the hot spots appear to move together. This behavior led Morgan (1972) to conclude that hot spots are fixed with respect to the mantle.

Numerous analyses of hot spot track and plate motion directions have established that hot spots are indeed relatively stationary for time intervals of 50–100 Myr (Morgan, 1983; Jurdy and Gordon, 1984). However, they are certainly not precisely fixed. Their motion is, nevertheless, significantly slower than seafloor spreading rates. For example, Molnar and Atwater (1973) and Molnar and Stock (1987) detect relative motion between Hawaii and hot spots in the Atlantic and Indian Oceans amounting to a few mm yr^{-1} . A more recent study of hot spot fixity by Steinberger and O'Connell (1998) calculated the hot spot motion expected from the advection of mantle plumes by large-scale flow in the mantle driven by a combination of surface plate motions and lower mantle density heterogeneity, and found relative velocity between hot spots up to 10 mm yr^{-1} . It is important to emphasize that this relative stationarity is not an accurate description of every hot spot. Many hot spots are variable, and these produce either segmented tracks or, in some cases, a short pulse of activity. Other hot spots have simultaneously active volcanism at several places along the track. For these, the concept of approximate stationarity is less meaningful. Even the Hawaiian hot spot, which has persisted for 110 Myr, has exhibited large variations in its strength, as evidenced by variations in the rates of melt production and swell formation (Davies, 1992).

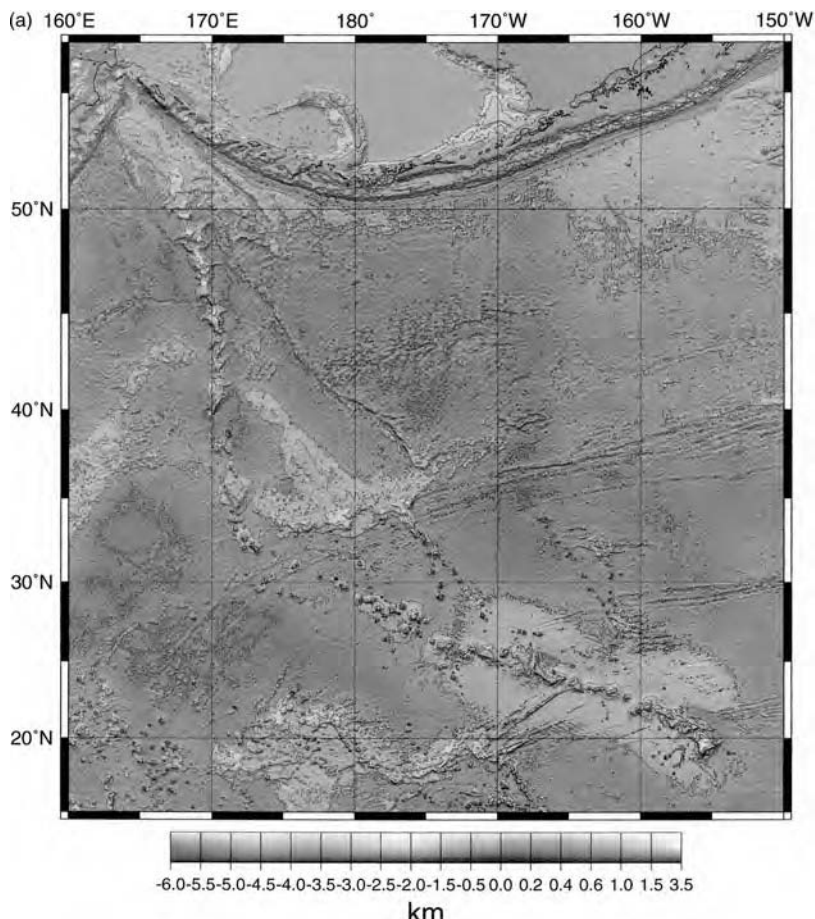


Figure 11.2. (a) Seafloor topography in the region around the Hawaiian-Emperor chain, after Smith and Sandwell (1997). (Continued)

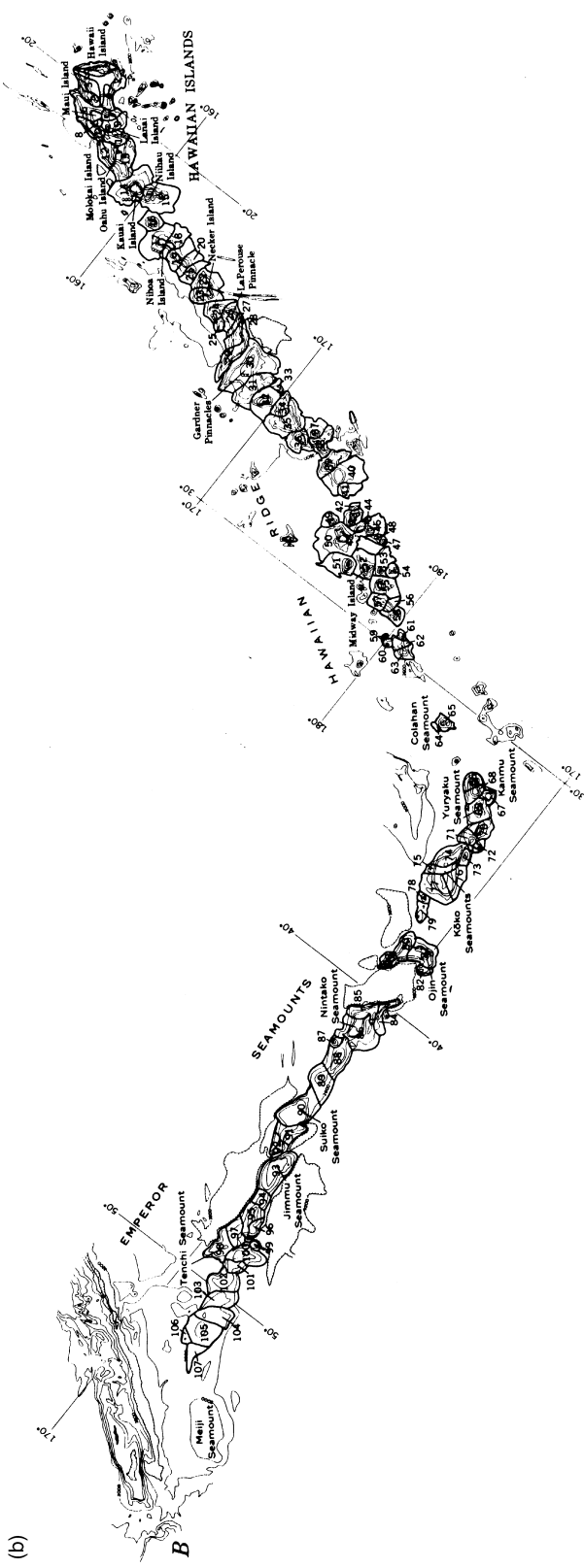


Figure 11.2. (b) Volcanic centers in the Hawaiian-Emperor chain, from Bargar and Jackson (1974). (Continued)

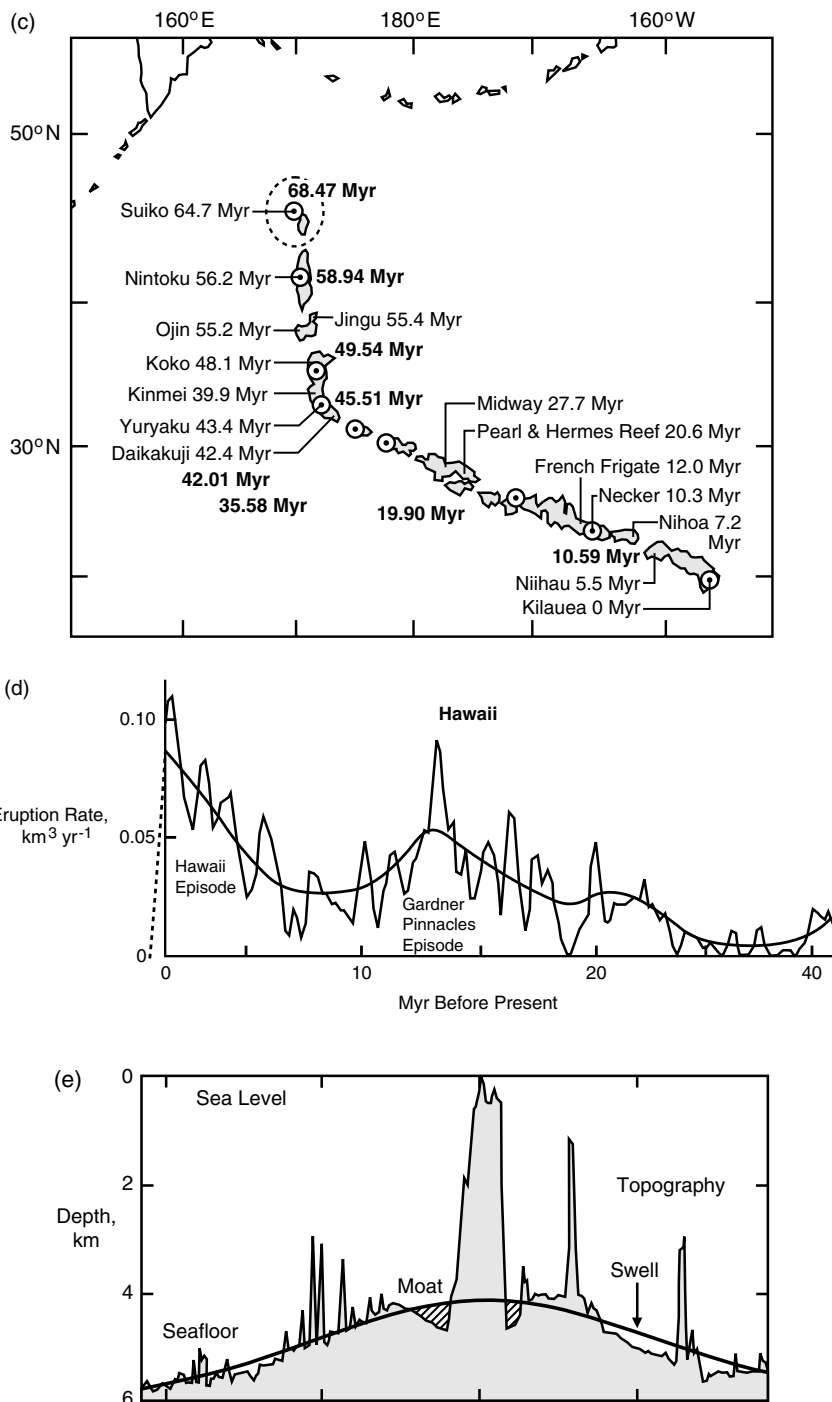


Figure 11.2. (c) Age progression along the chain, from Molnar and Stock (1987). (d) Estimated eruption rates versus time along the chain, from Vogt (1979). (e) Bathymetric and gravity profiles across the Hawaiian ridge at Oahu, from Watts (1976).

For a color version of part (a), see plate section.

Hot spots appear to be better defined in the ocean basins than in the continents. Certainly not all the volcanism of the western United States can be associated with a series of hot spots. The volcanism at Yellowstone with the associated track along the Snake River Plain appears to fit most definitions of a hot spot. But other volcanism in the western United States is probably due to a thin weak lithosphere and a near surface source rather than deep-seated plumes.

11.3 Hot Spot Swells

Most hot spots are associated with topographic swells. Hot spot swells are regional topographic highs with widths of about 1,000 km and up to 3 km of anomalous elevation. The swell associated with the Hawaiian hot spot is illustrated in Figure 11.2e. The swell is roughly parabolic in planform and it extends upstream of the active hot spot, i.e., toward the spreading center of the East Pacific Rise. The excess elevation associated with the swell decays rather slowly down the track of the hot spot.

There is considerable observational evidence that the topography of hot spot swells is directly associated with a geoid anomaly (Haxby and Turcotte, 1978). This correspondence is strong evidence that the excess topography and mass of the swell are compensated at depth by anomalously light, possibly hot mantle rock. One model for isostatic compensation assumes horizontal variations in density over a prescribed depth W , the so-called Pratt compensation. The variable density ρ_p is related to the elevation h above the adjacent ocean basins by

$$\rho_p = \frac{\rho_0 W + \rho_w h}{W + h} \quad (11.3.1)$$

where ρ_0 is the reference density corresponding to zero elevation, ρ_w is seawater density, and W is referred to as the depth of compensation. With the ocean basin as reference, the geoid anomaly ΔN associated with the compensated topography is

$$\Delta N = -\frac{2\pi G}{g} \left[\int_{-h}^0 (\rho_p - \rho_w) y dy + \int_0^W (\rho_p - \rho_0) y dy \right] = \frac{\pi G (\rho_0 - \rho_w)}{g} h W \quad (11.3.2)$$

The geoid anomaly is linearly dependent on the topography so that the local geoid to topography ratio GTR should be a constant for each swell.

The dependence of the observed geoid anomalies on bathymetry across the Hawaiian and Bermuda swells is given in Figure 11.3. Also included are the predicted geoid anomalies from (11.3.2) for $\rho_0 = 3,300 \text{ kg m}^{-3}$, $\rho_w = 1,000 \text{ kg m}^{-3}$, and several values of W . Within the scatter of the data, good agreement is obtained for Pratt compensation with a depth of compensation W of about 100 km. Geoid topography ratios for a variety of oceanic swells have been compiled by Sandwell and MacKenzie (1989). Their results are given in Figure 11.4. It is significant that none of the hot spot geoid anomalies shows evidence of very deep compensation.

The cause of hot spot swells and how the topography is compensated remain subjects of some controversy (Sleep, 1992). Several theories have been proposed for the origin of hot spot swells. Crough (1978, 1983) and Detrick and Crough (1978) proposed a thermal rejuvenation hypothesis associated with a thinning of the lithosphere. They proposed that the flow associated with an impinging plume thinned the thermal lithosphere in the vicinity of the active hot spot and supported this argument by comparing the decay of the swell downstream

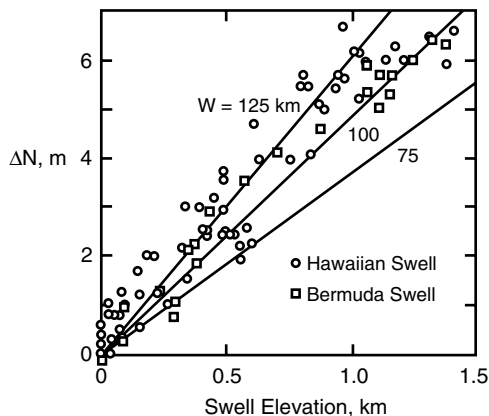


Figure 11.3. Dependence of the observed geoid anomalies ΔN on bathymetry across the Hawaiian and Bermuda Swells (Crough, 1978; Haxby and Turcotte, 1978) compared with the theoretical prediction (11.3.2) of Pratt compensation models with various depths of compensation W .

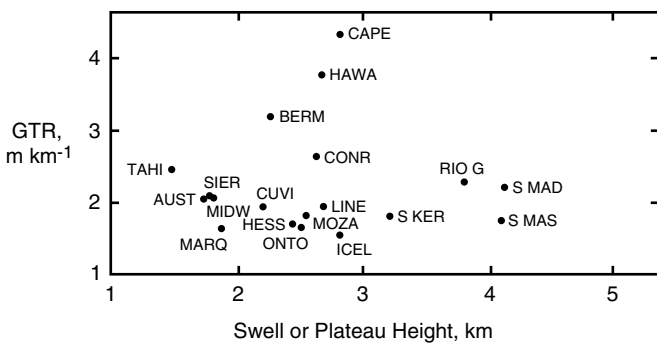


Figure 11.4. Dependence of the geoid to topography ratio (GTR) on maximum topography for various oceanic swells (Sandwell and MacKenzie, 1989). Cape Verde Rise (CAPE), Hawaiian Swell (HAWA), Bermuda Swell (BERM), Conrad Rise (CONR), Tahiti Swell (TAHI), Austral Swell (AUST), Sierra Leone Rise (SIER), Midway Swell (MIDW), Marquesas Swell (MARQ), Cuver and Wallaby Plateaus (CUVI), Hess Rise (HESS), Ontong-Java Plateau (ONTO), Mozambique Plateau (MOZA), Line Swell (LINE), Iceland (ICEL), South Kerguelen Plateau (S KER), Rio Grande Rise (RIO G), South Mascarene Plateau (S MAS), South Madagascar Ridge (S MAD).

of the Hawaiian hot spot with the cooling of a reheated lithospheric plate. Related numerical calculations have also been carried out by Sandwell (1982), Sleep (1987), and Liu and Chase (1989). Moore and Schubert (1997a) argue that the sign of the curvature of the observed geoid-topography relation favors the lithospheric thinning hypothesis.

Nevertheless, there are a number of uncertainties with lithospheric thinning as the cause of hot spot swells. On one hand, Emerman and Turcotte (1983), Monnereau et al. (1993), and Davies (1994) argued that thermal erosion by a plume is an inefficient means of thinning the lithosphere. Their thermomechanical models produced rates of thinning that are about an order of magnitude too slow to provide thermal rejuvenation. On the other hand, more recent, fully three dimensional numerical calculations of plume-lithosphere interactions incorporating strongly temperature-dependent viscosity show that the impingement of plumes at the base of the lithosphere leads to gravitational instability and sinking of parts of the lower lithosphere above the plume, a process that rapidly thins the lithosphere (Moore et al., 1998b, 1999).

A second argument against the lithospheric thinning hypothesis comes from heat flow measurements along hot spot tracks. If hot spots erode the lithosphere and reset the thickness of the plate to a value appropriate to a younger age, then greater heat flow and rate of subsidence would be observed, as compared to undisturbed lithosphere with the same age (Crough, 1978). From the cooling half-space model presented in Chapter 4, the relationship between rate of subsidence of the swell $d(h_\infty - h)/dt$ and anomalous surface heat flow $q - q_\infty$ is

$$\frac{d(h_\infty - h)}{dt} = \frac{\alpha(q - q_\infty)}{c_p(\rho_m - \rho_w)} \quad (11.3.3)$$

where α is thermal expansivity, $\rho_m - \rho_w$ is the mantle–seawater density contrast, c_p is specific heat, and the subscript ∞ refers to values on the seafloor far from the swell. Small heat flow anomalies, of about $5\text{--}10 \text{ mW m}^{-2}$, have been measured on the flanks of some oceanic hot spot swells (Detrick et al., 1981, 1986; Von Herzen et al., 1982; Bonneville et al., 1997). However, heat flow determinations by Von Herzen et al. (1989) indicate that the excess oceanic heat flow over the Hawaiian swell is too small by nearly an order of magnitude for consistency with the thinned lithosphere required to produce the observed swell topography, according to (11.3.3). Of course, the lithosphere could be thinned at a hot spot swell before a new steady conductive thermal state is established in the thinner lithosphere. In this event, an excess heat flow would not be measured at the surface above the swell.

A second class of models for hot spot swells involves dynamic support by viscous plume flow without any lithosphere thinning. When the hot plume flow reaches the base of the lithosphere it must flow radially outward along the bottom of the lithosphere. A mushroom-shaped cap forms at the top of the plume as it is deflected by the lithosphere (Olson et al., 1988) (see Figure 11.18a). The result of the lateral plume deflection is a horizontal pressure gradient with the highest pressure at the center of the plume. This pressure results in uplift of the lithosphere and a hot spot swell.

Another source of support for hot spot swells is the buoyancy of the hot plume material in the asthenosphere. The anomalously hot plume material that spreads out beneath the lithosphere has a thermal buoyancy that can produce uplift. Beneath a moving plate, the plume cap is advected in the direction of plate motion and spreads by viscous flow in the transverse direction, as shown in three-dimensional plume calculations (Ribe and Christensen, 1994; Moore et al., 1998b). This effect, coupled with the time variability in source strength at hot spots (Davies, 1992), can explain the evolution of hot spot swells without the need to invoke lithospheric thinning. Based on a series of numerical calculations, Robinson et al. (1987) and Robinson and Parsons (1988) have argued that a low viscosity asthenosphere beneath a swell can give geoid–topography correlations for dynamic support that are indistinguishable from those of lithospheric thinning models.

A variation on the thermal buoyancy model has been proposed by Phipps Morgan et al. (1995), who argue that compositional buoyancy associated with depleted mantle rock is responsible for the uplift of a hot spot swell. However, Moore and Schubert (1997a) showed that the sign of the curvature in the observed geoid–topography relation for the Hawaiian swell is opposite to what would be expected for chemical compositional buoyancy.

Question 11.3: What mechanism is responsible for the formation of hot spot swells?

11.4 Hot Spot Basalts and Excess Temperature

A large fraction of the volcanic rocks associated with hot spots have a basaltic composition with a major element chemistry very similar to that of mid-ocean ridge basalt (MORB). However, there are significant differences in both trace element composition and isotope ratios. These differences are discussed in detail in Chapter 12.

Whereas MORB forms by partial melting of mantle peridotites previously depleted in incompatible trace elements such as K, Rb, U, and Th, ocean island basalt (OIB) produced at hot spots often lacks this depletion in trace elements, indicating that OIB comes from a distinct parent material. Isotopic compositions indicate that OIB is derived from a mixture of sources, including the depleted MORB source, possibly a more primitive mantle component, and one or more enriched sources (possibly recycled continental crust or subcontinental lithosphere).

MORB is a result of pressure-release melting within large-scale upwellings beneath actively spreading ridges. As discussed in Chapter 3, seismic evidence indicates that these upwellings generally do not extend through the transition zone, and in many cases may be even shallower. If this is true, then most of the material in the upwellings beneath spreading centers comes from the upper mantle.

In contrast, there are various lines of evidence indicating that the source for hot spots lies deeper in the mantle and is associated with upwellings that are several hundred degrees hotter than beneath normal spreading centers. Ridge-centered hot spots such as Iceland produce much thicker crust than do the ridges on which they lie (White, 1993). We have shown in Chapter 4 that the amount of basalt melt produced in an upwelling depends primarily on the depth at which the rising material intersects the solidus, which in turn depends on the potential (zero pressure) temperature of the adiabat on which the ascending material lies. Greater crustal thickness at ridge-centered hot spots indicates higher mantle temperatures at the hot spot, compared with other parts of the ridge. The calculations of pressure-release partial melting in Chapter 4 indicate that the extra crustal thickness at hot spots requires the temperature in hot spot upwellings to be 200–300 K above the potential temperature (1,600 K) of a normal mantle adiabat. Because subsolidus upwellings in the mantle are nearly isentropic, the excess temperature beneath hot spots must be derived from a region of the mantle with higher potential temperature than the normal upper mantle which forms the ridges. The higher upwelling temperatures therefore indicate an origin deeper than normally tapped by a spreading center. White and McKenzie (1989, 1995) estimate that melting begins at depths of 110 km or greater and extends to depths of 70–30 km. Watson and McKenzie (1991) have carried out a detailed study of melt generation at Hawaii. They estimate that the maximum mantle adiabat has a potential temperature of 1,830 K, that the degree of partial melting is 6.9%, and that the depth range of melting is 127–72 km.

Chemical differences in basalts along the mid-ocean ridges also indicate excess temperature beneath hot spots. Klein and Langmuir (1987) used variations in crustal Na₂O content and its correlation with ridge crest topography to infer excess potential temperatures of about 250 K for ridge-centered hot spots. Schilling (1991) used variations in trace element concentrations along the mid-Atlantic ridge to infer excess potential temperatures near 200 K for Atlantic hot spots. High upwelling temperatures at hot spots in continental regions also suggest a deep source of melting. Crough et al. (1980) have argued that kimberlites, which are known to come from below 100 km depth, are associated with hot spot tracks on continental cratons.

The geometry of hot spot track–ridge intersections also supports the interpretation that the source of hot spots lies deeper in the mantle than the region affected by spreading centers. There are numerous instances where ridges have migrated over hot spots, and in all of these cases, passage of the ridge has left the hot spot intact (Morgan, 1981). Figure 11.5 illustrates this effect for the Reunion hot spot. When a ridge passes over a hot spot, the hot spot track is affected, but the hot spot itself is not. Hot spot activity simply jumps from one plate to the other and the track becomes discontinuous, but the hot spot is not excavated by the migrating spreading center. If the hot spot source were shallower than the depth of upwelling beneath the spreading center, we would expect that the hot spot source would be excavated by the upwelling and incorporated into the accreting plates. Since this is not observed, it follows that the hot spot source lies below the depth of upwelling beneath a spreading center.

A strong correlation between hot spots and ultra-low seismic velocity zones (ULVZ) at the base of the mantle (Williams et al., 1998) provides additional support for a deep source of mantle plumes, a source located in the D'' layer at the bottom of the mantle. Helmberger et al. (1998) used the time delay and amplification of the seismic phase SKPdS relative to SKS to infer the existence of a 40 km thick ULVZ at the core–mantle boundary (CMB) beneath Iceland; they hypothesize that this is the source of the mantle plume beneath Iceland.

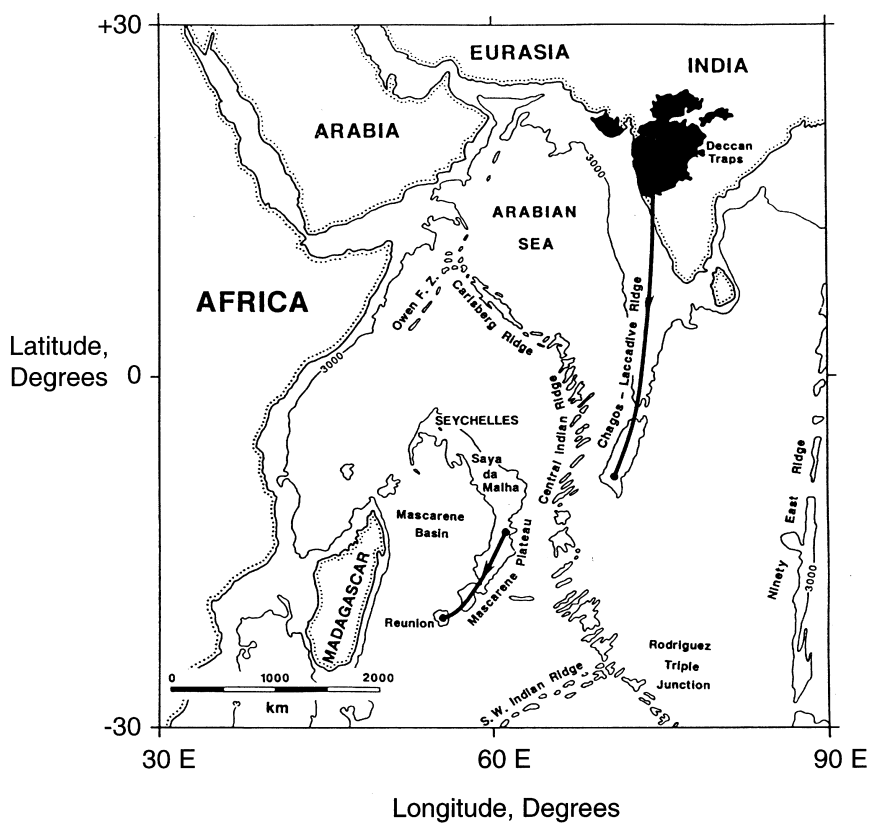


Figure 11.5. The relationship between the Reunion hot spot track and the Deccan Flood Basalts, from White and McKenzie (1989).

(The seismic phase SKPdS is diffracted along the CMB and samples the ULVZ along its length compared with SKS which travels approximately vertically and spends less time in the ULVZ. The ULVZ is a 5–40 km thick layer at the base of the mantle with P- and S-wave velocity anomalies of 10% or larger, indicative of partial melting.) Tomographic evidence for a narrow whole mantle plume beneath Iceland has been given by Bijwaard and Spakman (1999). Russell et al. (1998) have studied the anisotropy of ScS seismic phases which changes from SH normally ahead of SV to the opposite for waves traversing a localized region of the CMB beneath Hawaii. They attribute the earlier SV arrival to a vertical fabric established by plume upwelling at the CMB beneath Hawaii and identify this part of the CMB as the source of the mantle plume beneath Hawaii. A lower mantle source for the Iceland plume is also suggested by the broadband seismic experiment of Shen et al. (1998) discussed in Section 11.6.

Question 11.4: What is the depth of the source of mantle plumes?

11.5 Hot Spot Energetics

Question 11.5: How much heat is transported by mantle plumes?

There are several methods for measuring the strength of a hot spot. The most straightforward method is to measure the rate of production of volcanic rocks at the hot spot. This can be inferred from the volumes of the volcanic edifices and the volcanic ridge and its age progression. The rate of production for the Hawaiian hot spot has been given in Figure 11.2d; the present rate is about $Q_B = 0.1 \text{ km}^3 \text{ yr}^{-1}$. If the basaltic volcanism at Hawaii represents a mean degree of melting of 5%, the required plume flux would be $Q_V = 2 \text{ km}^3 \text{ yr}^{-1}$.

An alternative method for determining the strength of a hot spot is to consider the rate of swell formation. If it is assumed that the excess mass of a swell is compensated by an equal mass deficit at depth, then the rate at which hot (light) plume material forms the swell can be determined. The rate of swell formation is given by

$$\dot{M}_{ps} = (\rho_m - \rho_w) A_{ps} u_m \quad (11.5.1)$$

where \dot{M}_{ps} is the mass flux of a plume hot spot swell, u_m is the plate speed relative to the “fixed” hot spot, ρ_m and ρ_w are mantle and seawater densities, respectively, and A_{ps} is the cross-sectional area of the swell in a vertical plane normal to the hot spot track. The cross-sectional area of the swell is calculated from

$$A_{ps} = \int_{-\infty}^{\infty} h_{ps} dx \quad (11.5.2)$$

where x is a horizontal coordinate in the vertical plane normal to the hot spot track and h_{ps} is the elevation of the plume swell relative to the surrounding seafloor. The quantity \dot{M}_{ps} is also called the plume buoyancy flux. Sleep (1990) gives values of \dot{M}_{ps} for 37 plumes and Davies (1988b) gives values of \dot{M}_{ps} for 26 plumes. The values given by Sleep (1990) are listed in Table 11.2.

Table 11.2. Hot Spot Energetics

Hot Spot	Buoyancy Flux ^a	Volume Flux	Heat Transport
	\dot{M}_{ps} (kg s^{-1})	Q_V ($\text{km}^3 \text{yr}^{-1}$)	Q (GW)
Afar	1,200	1.9	50
Australia, East	900	1.4	38
Azores	1,100	1.7	46
Baja	300	0.5	12
Bermuda	1,100	1.7	46
Bouvet	400	0.6	17
Bowie	300	0.5	12
Canary	1,000	1.5	42
Cape Verde	1,600	2.5	67
Caroline	1,600	2.5	67
Crozet	500	0.8	21
Discovery	500	0.8	21
Easter	3,300	5.1	138
Fernando	500	0.8	21
Galapagos	1,000	1.5	42
Great Meteor	500	0.8	21
Hawaii	8,700	13.7	363
Hoggar	900	1.4	38
Iceland	1,400	2.2	58
Juan de Fuca	300	0.5	12
Juan Fernandez	1,600	2.5	67
Kerguelen	500	0.8	21
Louisville	900	1.4	38
MacDonald	3,300	5.1	138
Marquesas	3,300	5.1	138
Martin	500	0.8	21
Meteor	500	0.8	21
Pitcairn	3,300	5.1	138
Reunion	1,900	2.9	79
St. Helena	500	0.8	21
Samoa	1,600	2.5	67
San Felix	1,600	2.5	67
Tahiti	3,300	5.1	138
Tasman, Central	900	1.4	38
Tasman, East	900	1.4	38
Tristan	1,700	2.6	71
Yellowstone	1,500	2.3	62
Total	54,900	85	2,288

^a After Sleep (1990).

Isostatic compensation implies that mass addition to a swell is balanced by an equal addition of light material at depth. We hypothesize that this is the flux of light buoyant material in the plume that forms the hot spot. If Q_V denotes the plume volume flux, and $\Delta\rho = \rho_m - \rho_p$ is the mean plume density deficit relative to the upper mantle, then

$$\dot{M}_{ps} = Q_V \Delta\rho \quad (11.5.3)$$

If the density anomaly is assumed to be due to thermal expansion and variations in composition are neglected, then we can write

$$\Delta\rho = \rho_m\alpha\Delta T \quad (11.5.4)$$

where ΔT is the mean temperature excess in the plume. From the discussion of hot spot excess temperatures in the previous section, we take $\Delta T = 200$ K. Different hot spots may have a higher or lower ΔT , and the uncertainties are considerable. Other estimates of plume parameters are given in Table 11.3. Substitution of these parameter values into (11.5.4) gives $\Delta\rho = 20 \text{ kg m}^{-3}$. With this value and (11.5.3) we calculate the volume fluxes of the 37 plumes listed in Table 11.2. The values of Q_V are also given in the table.

The total heat transport Q in a plume is related to the plume volume flux by

$$Q = \rho_m c_p Q_V \Delta T \quad (11.5.5)$$

The combination of (11.5.3)–(11.5.5) gives a relationship between the heat flux Q and the mass flux \dot{M}_{ps} :

$$Q = \frac{c_p \dot{M}_{ps}}{\alpha} \quad (11.5.6)$$

Parameter values from Table 11.3 are used with (11.5.6) to calculate the heat fluxes for the 37 plumes listed in Table 11.3. Values of Q are also given in Table 11.2.

Hawaii, with a heat flow $Q = 363$ GW, is the most energetic hot spot by about a factor of 2.5. It alone represents about 16% of the global hot spot heat transport of about 2,300 GW. The global hot spot heat flow in turn represents about 5% of the total global heat flow of 4.4×10^{13} W (Pollack et al., 1993). From Table 11.2 the volume flux associated with the Hawaiian plume is $Q_V = 13.7 \text{ km}^3 \text{ yr}^{-1}$. This is almost an order of magnitude greater than the flux deduced above from the rate of production of volcanic rocks, $Q_c = 2 \text{ km}^3 \text{ yr}^{-1}$. By inference, the ratio of plume mass flux to magma production is relatively inefficient at the Hawaiian hot spot, in comparison with the ratio at mid-ocean ridges. The same calculation

Table 11.3. Mantle Plume Parameters

Parameter	Symbol	Value	Units
Thermal anomaly	ΔT	200	K
Thermal expansivity	α	3×10^{-5}	K^{-1}
Gravity	g	9.8	m s^{-2}
Buoyancy	g'	0.06	m s^{-2}
Density	ρ_m	3,400	kg m^{-3}
Mantle viscosity	μ_m	10^{21}	Pas
Source viscosity	μ_p	10^{19}	Pas
Rheological parameter	γ	6	—
Specific heat at constant pressure	c_p	1,250	$\text{J}(\text{kg K})^{-1}$
Thermal conductivity	k	3.3	$\text{W}(\text{m K})^{-1}$
Thermal diffusivity	κ	0.8×10^{-6}	$\text{m}^2 \text{ s}^{-1}$
Heat transport	Q	≤ 360	GW
Volume flux	Q_V	≤ 440	$\text{m}^3 \text{ s}^{-1}$
Plume density deficit	$\Delta\rho$	20	kg m^{-3}

applied to other hot spots indicates that crust production at mid-plate hot spots is generally inefficient in comparison with ridges. This is consistent with the model of partial melting by pressure release given in Chapter 4.

It must be emphasized that the use of thermal buoyancy flux is independent of any lithospheric thinning by heat transfer from the hot plume material. Heating of the lower lithosphere is balanced by a cooling of the plume material so that the net thermal buoyancy remains unaffected.

It is not universally accepted that the thermal buoyancy flux is the primary compensation mechanism for hot spot swells. Phipps Morgan et al. (1995) argue that the compositional buoyancy associated with depleted mantle rock is the primary compensation mechanism. The compositional buoyancy flux \dot{M}_{pc} is given by

$$\dot{M}_{pc} = Q_D \Delta\rho_c \quad (11.5.7)$$

where Q_D is the volume flux of depleted plume material and $\Delta\rho_c$ is the density difference between fertile (undepleted) and depleted mantle rock. With the assumption that the volume flux of volcanics is Q_B and that the mean degree of partial melting is f , the volume flux of depleted rock is given by

$$Q_D = \left(\frac{1-f}{f} \right) Q_B \quad (11.5.8)$$

By combining (11.5.7) and (11.5.8) we obtain

$$\dot{M}_{pc} = \left(\frac{1-f}{f} \right) Q_B \Delta\rho_c \quad (11.5.9)$$

For Hawaii we take $f = 0.05$, $Q_B = 0.1 \text{ km}^3 \text{ yr}^{-1}$, and $\Delta\rho_c = 15 \text{ kg m}^{-3}$ and find that $\dot{M}_{pc} = 905 \text{ kg s}^{-1}$. This represents about 10% of the thermal buoyancy flux for Hawaii ($M_{ps} = 8,700 \text{ kg s}^{-1}$) given in Table 11.2. We conclude that the thermal buoyancy flux dominates over the compositional buoyancy flux.

Just as hot spot heat transfer is secondary to the heat transport by large-scale plate motions, hot spots represent a secondary source of magmatism, compared to the global mid-ocean ridge system. At the present time, basaltic crust is produced at a rate of $18 \text{ km}^3 \text{ yr}^{-1}$ at spreading centers (Basaltic Volcanism Study Project, 1981), and probably less than about $1 \text{ km}^3 \text{ yr}^{-1}$ is produced on average at hot spots (Table 11.4). However, the relative strength of the two sources, as implied by present-day heat flow and eruption rates, is somewhat biased, because there is good evidence that hot-spot-related magmatism is strongly variable in time. Extremely high rates of magmatic activity are associated with initiation of new hot spots, and with the resurgence of pre-existing ones.

Table 11.4. Sources of Basaltic Volcanism

Source	Eruption Rate ($\text{km}^3 \text{ yr}^{-1}$)
Seafloor spreading	18
All hot spots	≤ 1
Hawaii (current)	$\simeq 0.1$
Flood basalt eruptions (transient)	1–5

11.6 Evidence for Mantle Plumes from Seismology and the Geoid

The hot spot locations listed in Table 11.1 reveal that hot spots are not regularly distributed on the Earth's surface. However, they are not randomly distributed either. Indeed Jurdy and Stefanick (1990) have argued that the hot spot distribution is self-similar (fractal). Most hot spots occur within two major clusters, one centered on the African plate, the other in the South Pacific. These clusters roughly coincide with highs in the long-wavelength geoid. The association between hot spot clusters and geoid highs is best seen by comparing hot spot locations with a residual geoid, one in which the effects of subducting slabs is removed. Figure 11.6 shows this correlation, as determined by Crough and Jurdy (1980). The geoid highs over Africa and the Pacific are part of the spherical harmonic degree 2 pattern that dominates the residual geoid. Although the clusters of hot spot swells contribute to these two residual geoid highs, they are not the primary cause. Instead, these geoid highs appear to be supported by large-scale density heterogeneity located in the lower mantle. In Chapter 5 we present the arguments for a lower mantle source for the degree 2 residual geoid, the most important geophysical evidence being the correlation with the pattern of large-scale seismic heterogeneity in the lower mantle (Silver et al., 1988). In addition, the South Pacific geoid high corresponds roughly to the location of the so-called DUPAL isotopic anomaly in OIBs (Castillo, 1988). Further, and as discussed in Section 11.4, hot spots are highly correlated with ULVZs at the base of the mantle that may mark the sources of mantle plumes (Helmberger et al., 1998; Williams et al., 1998).

McNutt and Fischer (1987) associate the cluster of hot spots in the South Pacific with a "superswell". Hot spots included are Caroline, Samoa, Pitcairn, Marquesas, MacDonald, Easter, Juan Fernandez, and San Felix. The superswell is a broad region of anomalously elevated seafloor with an excess elevation of a few hundred meters. Detailed discussions of this

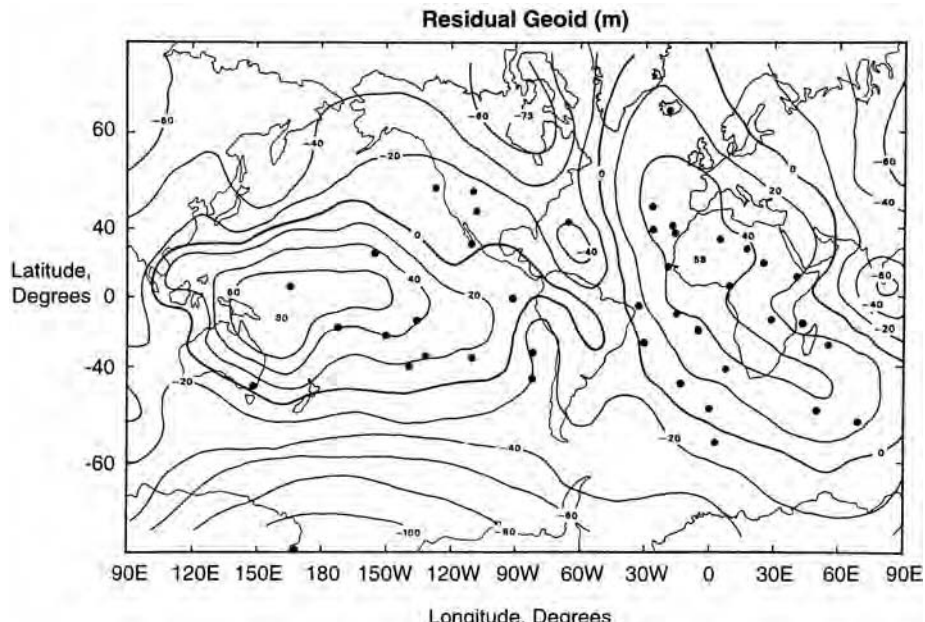


Figure 11.6. The relationship between the residual geoid after removal of subducted slab effects (contours in meters) and hot spot locations (dots) from Crough and Jurdy (1980).

proposed superswell have been given by Sichoix et al. (1998) and by McNutt (1998). However, the existence of the superswell has been questioned by Levitt and Sandwell (1996), although there is no question that there are many seamounts and extensive volcanic edifices throughout the region. Larson (1991) associates this region with the remnants of a mid-Cretaceous (120–80 Ma) superplume. Ebinger and Sleep (1998) attribute the extensive Cenozoic volcanism throughout east Africa to the impingement of a massive plume.

Although these correlations offer support for the concept that mantle plumes are the cause of hot spots, they do not, by themselves, verify the existence of deep mantle plumes. Indeed, there are very few unambiguous observational constraints on the structure of mantle plumes. The linear distribution and age progression of shield volcanoes along hot spot tracks indicates that mantle plumes cannot be tabular, like crustal dikes, but instead must be nearly circular in cross-section. The sharp bend in the Hawaiian and other hot spot tracks at the time of the change in the direction of the Pacific Plate motion indicates that the trajectory of the plume material through the mantle must be primarily radial.

Seismic imaging of narrow, conduit-like structures beneath hot spots would constitute a direct verification of the plume theory, and would provide a means for determining their source region in the mantle. At present, however, the seismic evidence for mantle plumes is largely confined to possible plume structures in the upper mantle.

Images of upper mantle heterogeneity beneath ocean basins obtained using seismic surface wave tomography indicate the existence of anomalous regional-scale structure that may be associated with some hot spots. Figure 11.7 shows cross-sections of seismic shear wave velocity structure beneath four hot spot locations, as determined by Zhang and Tanimoto (1989, 1992, 1993). The images show a 1,000 km diameter region of anomalously seismically slow mantle upstream of Hawaii, extending to approximately 200 km depth. Regions

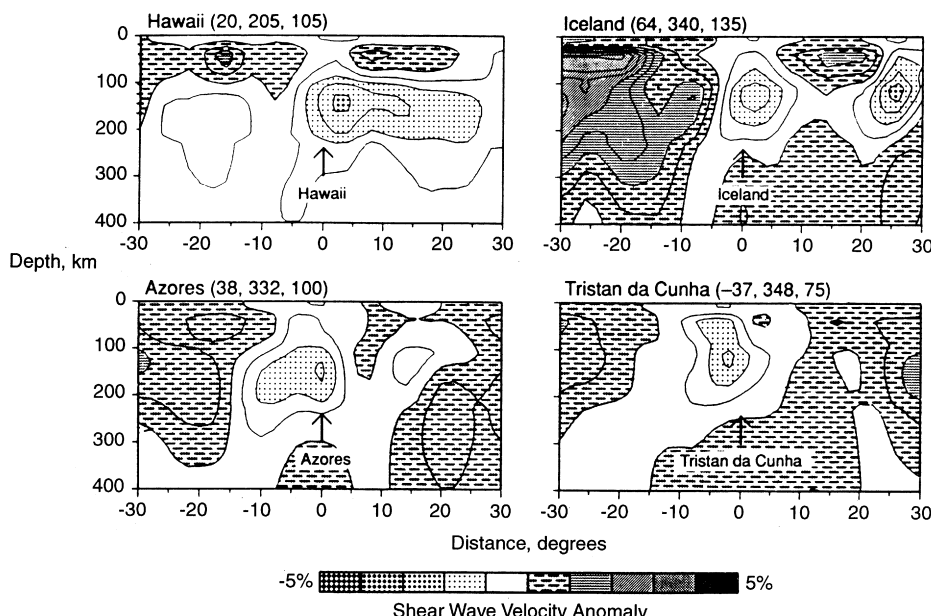


Figure 11.7. Cross-sections of upper mantle seismic shear wave velocity structure (percent variations) at four hot spot locations, determined by Zhang and Tanimoto (1992). Horizontal scale is great circle degrees; hot spot latitude, longitude, and cross-section azimuth are given in parentheses.

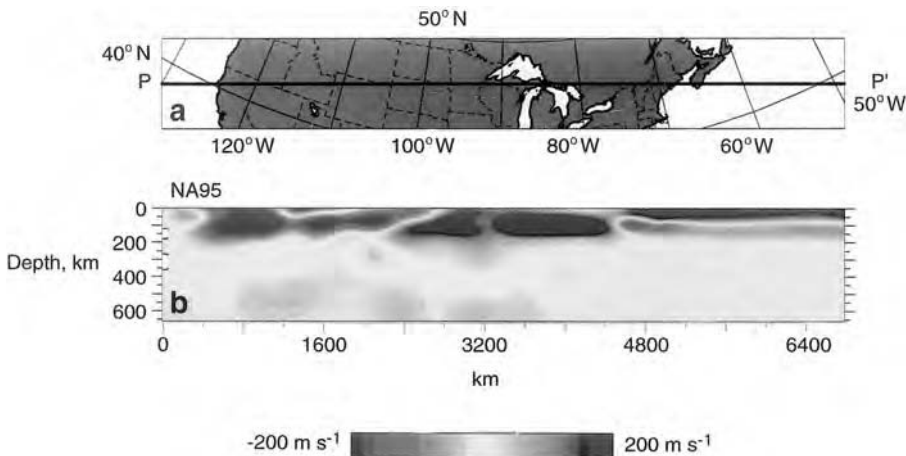


Figure 11.8. Cross-section of upper mantle seismic shear wave velocity variations beneath North America along PP', determined by van der Lee and Nolet (1997).

For a color version of this figure, see plate section.

with anomalously slow seismic velocity several hundred kilometers in radius and extending to about 200 km depth are also indicated beneath the Iceland, Azores, and Tristan hot spots. If these structures are in fact related to mantle plumes, then it is clear that mantle plumes are not simply narrow conduit structures. Seismic surface waves do not resolve the narrow structure predicted by the theory for mantle plume conduits (see Section 11.9). Instead, these images suggest that hot (and hence seismically slow) plume material spreads out beneath the lithosphere, over dimensions comparable to the hot spot swells. In Section 11.11 we present a dynamical model for plume–lithosphere interaction which relates the spatial and temporal evolution of the hot spot swell to the spread of the plume material beneath the plate.

Additional seismic evidence on the question of mantle plume structure scales has come from regional-scale tomographic studies around three hot spots in particular: Yellowstone, Iceland, and the Bowie hot spot in the northeast Pacific. Beneath Yellowstone, a 100 km wide zone of low P-wave velocity is present to 100 km depth beneath the current hot spot location and extends westward, roughly parallel to the hot spot track, reaching about 200 km depth beneath the Snake River Plain, as shown in Figure 11.8 from van der Lee and Nolet (1997). The extremely low seismic velocities in this region have long been attributed to partial melting in the upper mantle (Iyer, 1979, 1984), although the geometry of the Yellowstone track anomaly indicates a strongly tilted, subhorizontal conduit if it is indeed due to plume activity (Humphreys and Dueker, 1994).

Beneath the Iceland hot spot, regional seismic tomography has detected a cylindrical zone of low P- and S-wave velocities that extends from 100 km depth to at least 400 km depth (Wolfe et al., 1997). As shown in Figure 11.9, this seismic velocity anomaly has a radius of about 150 km. The magnitude of the P-wave velocity anomaly is about 2% and the magnitude of the S-wave velocity anomaly is about 4%. The relationship between this fine-scale structure and the broader-scale anomaly shown in Figure 11.7 is unclear. The conduit model in Section 11.9 predicts that the radius of the thermal halo surrounding a vertical mantle plume conduit with the flux of the Iceland hot spot lies in the range 100–170 km, consistent with the seismic tomography. However, the results in Section 11.11 indicate that

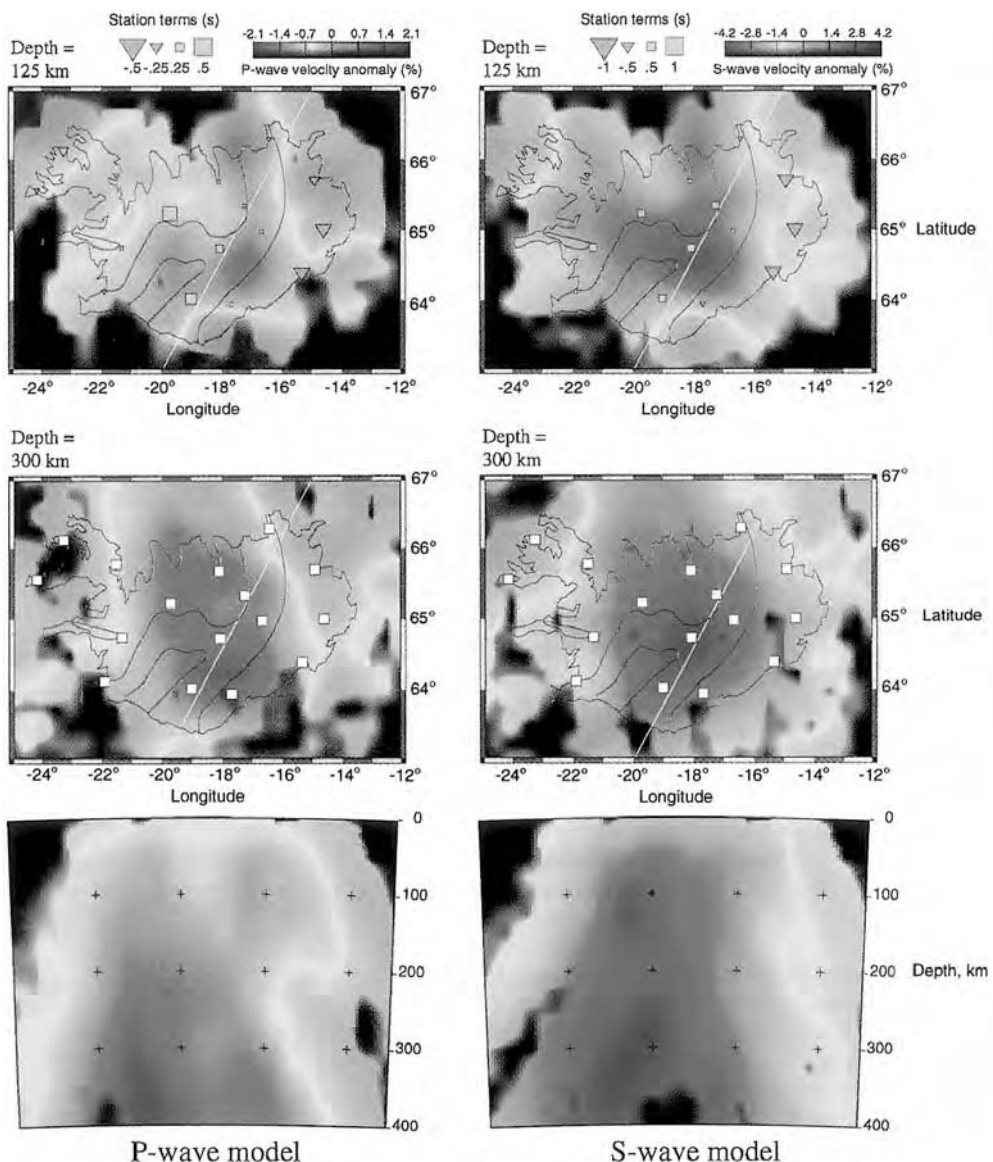


Figure 11.9. Upper mantle compressional wave velocity (left) and shear wave velocity (right) variations beneath Iceland determined by Wolfe et al. (1997). Variations at 125 km depth (top row), 300 km depth (middle row), and in cross-section (bottom row).

For a color version of this figure, see plate section.

mantle plumes are expected to spread out beneath the lithosphere, and should therefore be significantly wider than the observed 150 km at sublithospheric depths. Perhaps this discrepancy can be explained by channeling of the plume by the spreading center, a subject we discuss later in this chapter.

The Iceland plume structure has been “traced” down through the transition zone by Shen et al. (1998) who detect a thinning of the transition zone (the radial distance between the phase

transitions at depths of 410 km and 660 km) by 20 km over a circular region of radius 200 km beneath central and southern Iceland. The thinning of the transition zone beneath Iceland compared to the thickness of the transition zone in surrounding areas is consistent with the downward displacement of the 410 km phase transition and the upward displacement of the 610 km phase change by a mantle plume originating in the lower mantle, as discussed in Section 4.6 and illustrated in Figure 4.41. In the study of Shen et al. (1998), the transition zone thickness is determined from P410s and P660s (P-wave to S-wave conversions from phase transitions at depths of 410 km and 660 km, respectively) differential travel times. These differential times are insensitive to seismic heterogeneities shallower than 410 km depth.

Nataf and VanDecar (1993) have reported imaging the plume structure deep beneath the relatively weak Bowie hot spot. Using seismic waveforms they inferred the existence of a localized anomaly with roughly 150 km radius and a reduced wave velocity equivalent to roughly 300 K excess temperature in the transition zone beneath the hot spot, the first suggestion of a possible deep mantle plume structure.

Unambiguous detection of lower mantle plumes by seismology remains an elusive goal. However, there are seismic techniques available that could be used to prospect for deep mantle plumes, in addition to the ones already in use. It has been argued theoretically that mantle conduits might possibly be the cause of unexplained frequency splitting among normal modes (Lognonne and Romanowicz, 1990). The concentrated shear flow in a mantle plume conduit would induce seismic anisotropy through alignment of the seismically fast *a*-axis of olivine. Deployments of ocean-bottom seismometers around energetic hot spots such as Hawaii could provide the necessary coverage to resolve plume structure through the upper mantle and perhaps into the lower mantle. Indeed, as discussed in Section 11.4, Russell et al. (1998) have detected a seismic velocity anisotropy in a localized region of the CMB beneath Hawaii which could mark the source of the plume beneath the Hawaiian hot spot.

While the above seismic observations do not resolve the full depth extent of hot spot sources, they do identify cylindrical, plume-like structures beneath hot spots to considerable depths. Moreover, the seismic CMB observations and their correlation with hot spot locations provide strong support for the CMB as the source of many hot spots.

11.7 Plume Generation

Question 11.6: *What is the physical mechanism for the generation of mantle plumes?*

Although some hot spots appear to last for more than 100 Myr, they are nonetheless transient features. One of the attractive aspects of plume theory is that it can account for the transient character of hot spots. As discussed in Chapters 8–10, the Rayleigh number of mantle convection is in the range 5×10^6 to 5×10^7 . This value of Ra is sufficiently supercritical to insure that mantle convection is intrinsically time dependent. The numerical calculations discussed in Chapters 9 and 10 reveal that one of the important elements in time-dependent convection is the repeated generation of instabilities in the thermal boundary layers. In fully developed time-dependent convection these instabilities of hot boundary layers develop into thermal plumes. Plumes emerge repeatedly from the boundary layers, sometimes becoming

integral components of the convective motion, sometimes as short-lived transients. Ultimately, plumes are destroyed by the shifting pattern of flow and new plumes form to take their place.

Thermal plumes in the Earth's mantle can be attributed to instabilities in hot thermal boundary layers. This places important constraints on possible source regions for plumes in the mantle. In Chapter 4 we argued that there are only two regions in the mantle where hot thermal boundary layers may exist. One region is the layer D'', just above the CMB. On theoretical grounds, plumes originating from a thermal boundary layer in D'' are an expected component of lower mantle convection (Stacey and Loper, 1983). The geophysical evidence for a thermal boundary layer at the bottom of the mantle includes the seismologically detected ultra-low velocity zone just above the CMB discussed in Chapter 3 and the apparent mismatch between lower mantle and core adiabats, indicating a 300–1,000 K superadiabatic temperature rise across D''.

The other region where plume formation is possible is the base of the transition zone. Uncertainty in the lower mantle geotherm allows for the existence of a superadiabatic interfacial thermal layer between the upper mantle and the lower mantle, with a temperature increase that could be as large as 800 K. An interfacial thermal layer near the base of the transition zone is expected if mantle convection is strongly inhibited at the transition zone.

Without conclusive evidence for the source of mantle plumes there is no compelling reason to reject either source region, although the seismic observations discussed above strongly favor the D'' layer as the source. Indeed, plumes may originate from both regions. Alternatively, lower mantle plumes may be so altered by the transition zone that they appear to originate from within it. Fortunately, the mechanics of boundary layer instability are, for the most part, governed by local conditions, and it is not necessary to be specific about the depth of the thermal boundary layer in constructing a model for the early stages of plume development.

Certain dynamical conditions must be met before instabilities in a thermal boundary layer are possible. Furthermore, if these instabilities are to develop into plumes, they must grow to a critical size in a time which is shorter than the mean residence time of material in the boundary layer. The following rudimentary model provides estimates of the time scales involved in each of these two steps, for the case of plume formation in a chemically homogeneous thermal boundary layer.

In high Rayleigh number thermal convection, each new plume can be viewed as a transient instability of the time-dependent thermal boundary layers. A tractable model for the initial stage of plume formation can be derived by considering the time development of instabilities in a deep layer of viscous fluid heated from below. For the moment, we ignore other motions in the fluid. Later, we can compare the time scales predicted by this model with the residence time for material in the thermal boundary layer to determine if the instabilities are influenced by the presence of large-scale flow.

In a deep fluid layer heated from below, the criterion for the onset of localized thermal instability depends primarily on the boundary layer Rayleigh number Ra_δ defined as

$$Ra_\delta = \frac{\alpha g \Delta T (\delta(t))^3}{\kappa \nu} \quad (11.7.1)$$

where α is thermal expansivity, g is the acceleration of gravity, ΔT is the superadiabatic temperature rise across the thermal boundary layer, $\delta(t)$ is the local boundary layer thickness which depends on the time t since heating is first applied, κ is thermal diffusivity and ν is kinematic viscosity, here assumed constant. We suppose that the time-dependent conditions

can be represented by a sequence of transient episodes, each leading to the formation of a new plume. We further assume that at the beginning of each episode the boundary layer initially grows by diffusion according to

$$\delta(t) = (\pi \kappa t)^{1/2} \quad (11.7.2)$$

Howard (1966) proposed that instability occurs when the local Rayleigh number reaches a critical value Ra_{cr} . The condition for instability is then

$$Ra_\delta = Ra_{cr} \quad (11.7.3)$$

where $Ra_{cr} \simeq 3 \times 10^3$. The combination of (11.7.1)–(11.7.3) yields the onset time t_{cr} for boundary layer instability:

$$t_{cr} = \frac{1}{\pi \kappa^{1/3}} \left(\frac{\nu R a_{cr}}{\alpha g \Delta T} \right)^{2/3} \quad (11.7.4)$$

This expression predicts rather fast onset times for instabilities in hot thermal boundary layers in the mantle. The numerical values in Table 11.3 for mantle thermodynamic and transport properties give $t_{cr} = 30$ Myr, assuming a low viscosity in the source region. This is short compared to the time scale of large-scale convective overturn in the lower mantle. According to this analysis, the conditions are met for producing localized instabilities near the base of the mantle provided that region has low viscosity.

The presence of growing perturbations in a thermal boundary layer which is otherwise at rest does not automatically insure plume formation in a convecting fluid because the larger-scale motion can suppress the finite-amplitude development of the instabilities. In order for plumes to develop from thermal instabilities, the instability growth rate must also be larger than the transport rate within the thermal boundary layer. Generally, the growth rate of an instability depends inversely on the local viscosity, so that a strong temperature dependence of viscosity promotes the growth of instabilities in hot thermal boundary layers. Numerical simulations indicate that instabilities can grow into starting plumes in the D'' layer on 50–100 Myr time scales provided the viscosity in the boundary layer is several orders of magnitude less than the lower mantle average (Olson et al., 1987). The growth mechanism involves coalescence of numerous small perturbations to form a disturbance large enough to separate from the thermal boundary layer.

Figure 11.10 shows the results of a two-dimensional numerical calculation of plume formation in a hot thermal boundary layer at the base of a fluid with a strongly temperature dependent viscosity. For comparison, Figure 11.11 shows plume formation via the Rayleigh–Taylor instability mechanism, from an experiment by Bercovici and Kelly (1997). The incipient plumes form as diapirs, growing by the influx of buoyant, low-viscosity fluid. In Figures 11.10 and 11.11, the fluid is initially at rest and motion is entirely due to the instabilities themselves.

According to linear theory for Rayleigh–Taylor instability, the initial length scale R of an incipient diapir formed this way depends on the buoyant layer thickness at the time of instability δ_c , its viscosity ν_p , and the viscosity of the overlying mantle layer ν_m

$$R \simeq \left(\frac{\nu_m}{\nu_p} \right)^{1/3} \delta_c \quad (11.7.5)$$

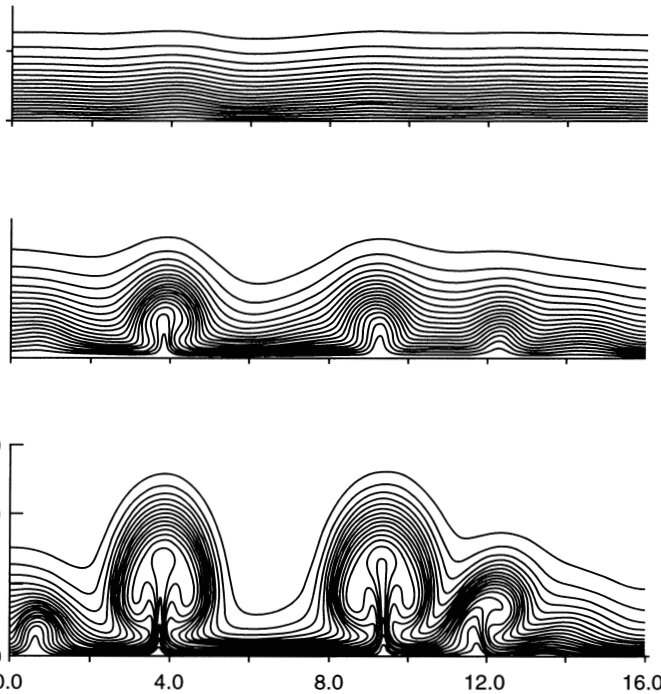


Figure 11.10. Two-dimensional numerical calculation of thermal boundary layer instability and plume formation (for details see Olson et al., 1987). For this simulation the contour intervals are $\Delta T = 40$ K, the viscosity contrast is 10^3 , the vertical and horizontal axis units are 100 and 200 km, respectively, and temperature distributions are given at 64, 83, and 93 Myr (top to bottom).

and the diapir spacing is proportional to the same factor, with a larger coefficient (Loper and Eltayeb, 1986; Ribe and de Valpine, 1994).

Diapirs begin to separate from the thermal boundary layer when their speed of buoyant ascent exceeds their growth rate. The conditions for separation can be obtained from the following model (Whitehead and Luther, 1975). We assume that the diapir has a spherical shape with radius R and that its volume V increases with time due to the influx of hot fluid at the volumetric rate Q_V :

$$\frac{dV}{dt} = Q_V \quad (11.7.6)$$

The diapir radius grows according to

$$\frac{dR}{dt} = \frac{Q_V}{4\pi R^2} \quad (11.7.7)$$

The ascent speed of the spherical diapir can be approximated by the Stokes velocity U_∞ of a buoyant fluid sphere in an infinite, more viscous fluid:

$$U_\infty = \frac{g' R^2}{3\nu_m} \quad (11.7.8)$$

where $g' = g\Delta\rho/\rho$ is the diapir buoyancy and ν_m is the kinematic viscosity of the exterior fluid. Here, $\Delta\rho = \rho_m - \rho_p$ is the density difference between the exterior mantle and the

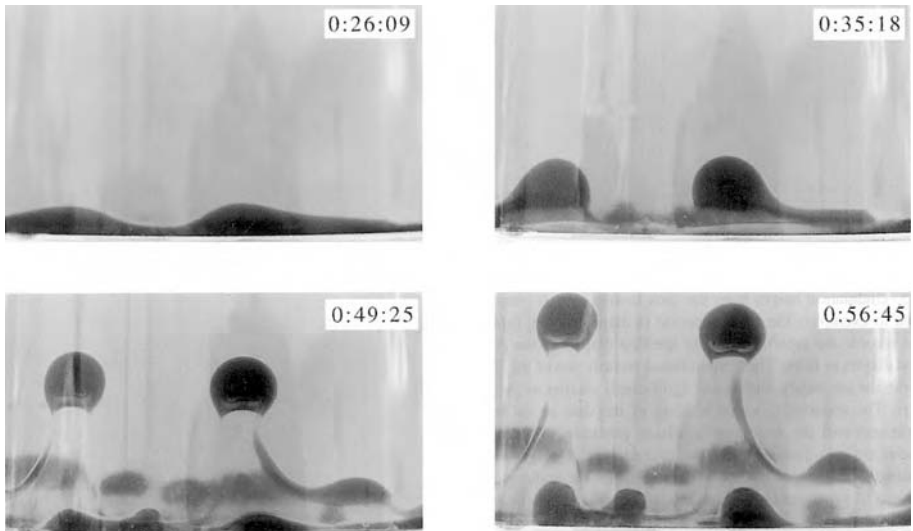


Figure 11.11. Photographs from a laboratory experiment showing plume initiation by instability of a thin, low-density, low-viscosity glucose fluid layer beneath a deep, high-density, high-viscosity glucose fluid layer. Times and depth scale are indicated. From Bercovici and Kelly (1997).

For a color version of this figure, see plate section.

diapir, and is assumed constant in this derivation. Separation is estimated to occur when U_∞ exceeds the inflation rate dR/dt . With (11.7.7) and (11.7.8), this condition yields

$$R_s = \left(\frac{3\nu_m Q_V}{4\pi g'} \right)^{1/4} \quad (11.7.9)$$

and

$$t_s = \left(\frac{4\pi}{3Q_V} \right)^{1/4} \left(\frac{\nu_m}{g'} \right)^{3/4} \quad (11.7.10)$$

where R_s is the radius at separation and t_s is the time required to grow to that size.

This simple model prescribes the conditions at separation in terms of an assumed constant volume flux into the growing diapir. However, both numerical calculations (Olson et al., 1987) and laboratory experiments (Bercovici and Kelly, 1997) indicate that the process is more complex than this, because the growing diapir tends to exhaust the boundary layer during its inflation, which delays the time of separation compared to (11.7.4). Bercovici and Kelly (1997) obtain an alternate expression for the radius at separation:

$$R_s \simeq \left(\frac{\nu_m}{\nu_p} \right)^{2/9} \delta_c \quad (11.7.11)$$

However, the geophysical implications of both models are the same: because of the large viscosity of the lower mantle, starting plumes require large diapirs for separation from a lower mantle thermal boundary layer. A numerical estimate demonstrates this point. Table 11.2 gives the estimated volume flux for the Hawaiian hot spot, $Q_V = 13.7 \text{ km}^3 \text{ yr}^{-1}$. With this value and values of other mantle parameters from Table 11.3, (11.7.9) and (11.7.10)

predict a separation radius $R_s \simeq 150$ km and $t_s \simeq 2.4$ Myr. Alternatively, if we assume an initial diapir radius $R_i \simeq 150$ km we can use (11.7.10) to estimate the separation time. The parameters from Table 11.3 then give $t_s \simeq 3$ Myr. These are very approximate estimates, which depend critically on uncertain parameters, most notably the lower mantle viscosity. However, they do indicate some of the important attributes of lower mantle plumes. First, buoyant plumes originating from the deep mantle necessarily have large volumes. Second, the time required for separation, once a plume diapir begins to form in the thermal boundary layer, is generally shorter than the time required for the initial instability to develop. Third, the entire process of plume formation can occur at the basal boundary layer in D'' within 50 Myr.

The analysis above is based on the assumption that only thermal buoyancy effects are important in mantle plume formation. This may not be the case. As discussed in Chapter 3, there is a variety of evidence that chemical heterogeneity is responsible for much of the seismic heterogeneity in the D'' layer. If plumes indeed originate near the base of the mantle, then chemically induced buoyancy may play a significant role in their formation and development. The same comments apply to plume formation in the transition zone, if chemical stratification controls the dynamics in that region.

One interpretation of the seismic structure of D'' is a thick thermal boundary layer that includes a step increase in density due to composition at about 200 km above the CMB. The fluid dynamical behavior of such a thermochemical boundary layer has been investigated using a variety of approaches, including numerical experiments (Christensen, 1984b; Hansen and Yuen, 1988, 1990; Kellogg, 1997), theory Sleep (1988b), and laboratory experiments (Olson and Kincaid, 1991). All of these studies find that the structure and the long-term survival of a chemically dense layer requires that the stabilizing buoyancy due to chemistry must equal or exceed the destabilizing thermal buoyancy. This condition is usually expressed in terms of the dimensionless parameter B , the ratio of stabilizing chemical density variation to destabilizing thermal density variation across the layer. Generally, it is found that $B \geq 1$ is needed to maintain a chemical layer in the presence of thermal plumes. Since the fractional density decrease due to the adverse temperature gradient in D'' may be 2%, a fairly large density increase from compositional stratification is needed if the layer is to survive.

Figure 11.12 from Kellogg (1997) illustrates the three principal flow regimes in this system. In cases with $B < 1$, where the stabilizing buoyancy from compositional stratification is small compared to the destabilizing thermal buoyancy, the developing thermal diapirs entrain some of the dense material, resulting in thermochemical plumes. Once these plumes form, they remove most of the dense material by entrainment, as shown in the $B = 0$ case in Figure 11.12. In the opposite extreme where $B > 1$, plume formation is retarded by the stable chemical layer but not prevented. For plumes to develop, the thermal boundary layer must grow until it is large enough to overcome the stabilizing effect of the dense material. This can happen in one of two ways. If the heavy layer is thin, the thermal boundary layer grows by diffusion until it is thicker than the chemical layer, and thermal plumes form above the chemical layer, as shown in the $B = 10$ case in Figure 11.12. If the dense layer is thick, it can undergo internal convective instability and the whole system can convect in two layers, as discussed in Chapter 9. The most interesting situation occurs when $B \simeq 1$. As shown in Figure 11.12, in this case the dense material is swept into piles beneath the rising plumes, and an internal circulation develops in the layer, driven by the exterior flow. This results in a persistent layer with large amplitude thickness variations on several scales. The wide spectrum of seismically inferred heterogeneity in D'' may be explained by thermochemical convection in this regime.

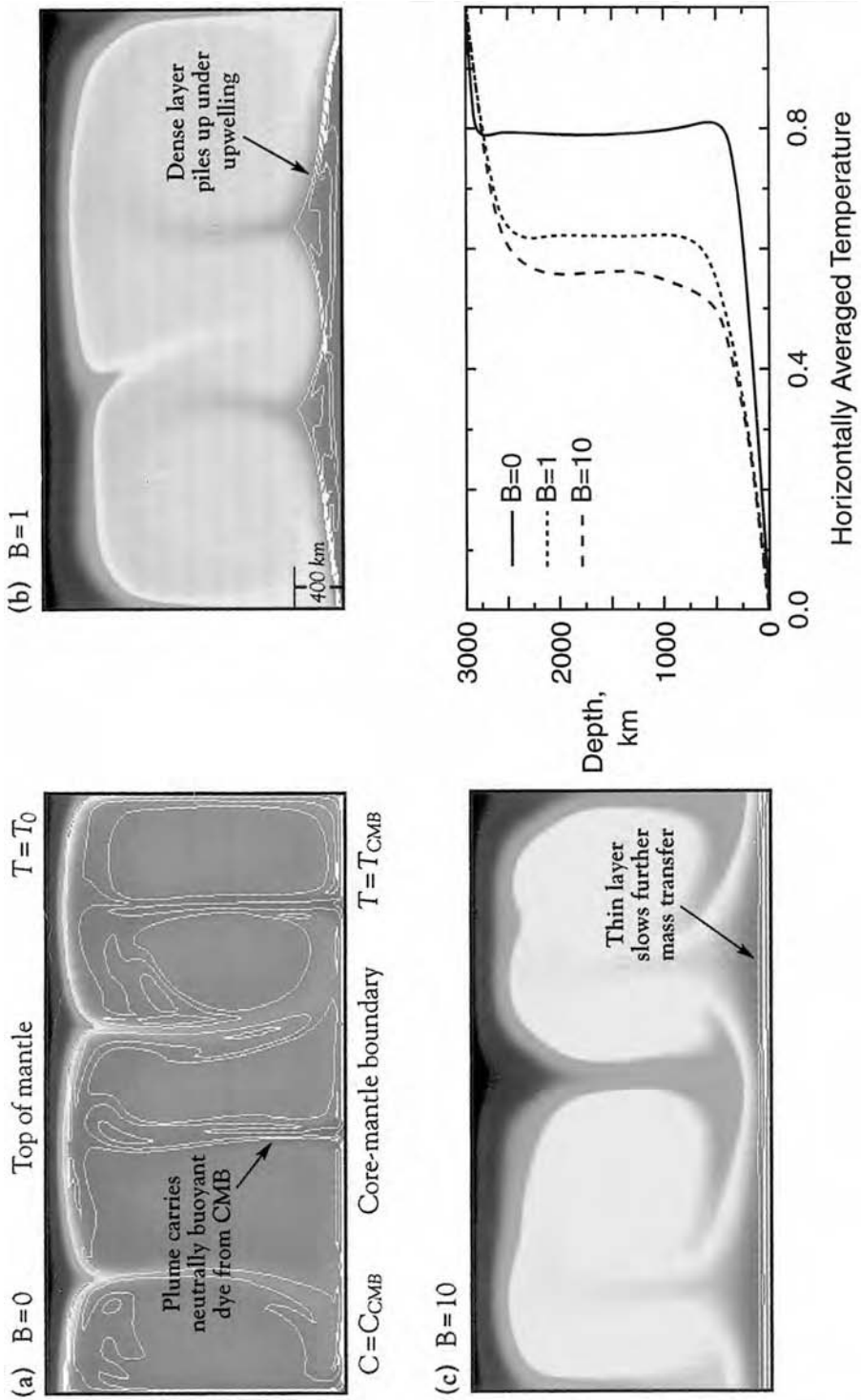


Figure 11.12. (a–c) Variation of temperature (shades) and composition (contours) in two-dimensional numerical calculations by Kellogg (1997) of thermochemical convection in the D''-layer for different values of B , the ratio of compositional to thermal buoyancy. (d) Laterally averaged temperature profiles for cases a–c.

For a color version of this figure, see plate section.

11.8 Plume Heads and Massive Eruptions

Question 11.7: What causes massive flood basalt eruptions?

Numerical and laboratory studies on the initial ascent of a low-viscosity buoyant plume through a high-viscosity fluid provide important insights into the process of hot spot formation (Whitehead and Luther, 1975; Whitehead, 1982; Olson and Singer, 1985; Griffiths, 1986; Griffiths and Campbell, 1990; Couillette and Loper, 1995; Bercovici and Mahoney, 1994; van Keken, 1997; Weinberg, 1997). In general, these studies have shown that the plume consists of a leading diapir or plume head followed by a thin conduit connecting the diapir with the source region. An example from a laboratory experiment is given in Figure 11.13. In this case, the stationary background fluid was a glucose syrup. The plume fluid consisted of a mixture of the glucose syrup with water that resulted in a lower density and a lower viscosity. The experiments of Griffiths (1986) produced similar results using hot polybutene oil injected into cold (heavy, viscous) oil of the same composition. An example of a starting plume from a numerical experiment by van Keken (1997) is shown in Figure 11.14.

The basic mechanics of starting mantle plumes can be understood using a simple model proposed by Whitehead and Luther (1975) for the ascent of a plume head through a viscous fluid. This is an extension of the analysis previously given in (11.7.6)–(11.7.10). The plume head is again modeled as a spherical diapir whose ascent velocity is given by (11.7.8). For a steady state in which the plume head neither gains nor loses fluid, the mean velocity of flow through the conduit is also U_∞ . Thus, the volume flux of fluid through the trailing conduit is given by

$$Q_V = AU_\infty \quad (11.8.1)$$

where A is the cross-sectional area of the conduit. By assuming laminar, parabolic, buoyantly driven Poiseuille flow through the circular conduit, we can write

$$A = \left(\frac{8\pi\nu_p Q_V}{g'} \right)^{1/2} \quad (11.8.2)$$

where ν_p is the plume kinematic viscosity. The combination of (11.8.1) and (11.8.2) gives

$$U_\infty = \left(\frac{g'Q_V}{8\pi\nu_p} \right)^{1/2} \quad (11.8.3)$$

for the terminal ascent speed. Equations (11.7.8) and (11.8.3) give

$$V_\infty = \frac{4\pi}{3} (3\nu_m)^{3/2} \left(\frac{Q_V}{8\pi g' \nu_p} \right)^{3/4} \quad (11.8.4)$$

for the steady state or terminal volume V_∞ of the plume head.

Following an early suggestion by Morgan (1981), both White and McKenzie (1989) and Richards et al. (1989) have proposed that massive flood basalt eruptions are the result of extrusion of melt from the plume head as it intrudes the lithosphere from below. According to this model, flood basalt eruptions mark the initiation of a hot spot track (Duncan and Richards, 1991). Richards et al. (1989) argue that four continental flood basalt provinces in particular



Figure 11.13. Photograph of a low-density, low-viscosity glucose fluid plume ascending in a high-density, high-viscosity glucose fluid (from Olson and Singer, 1985).

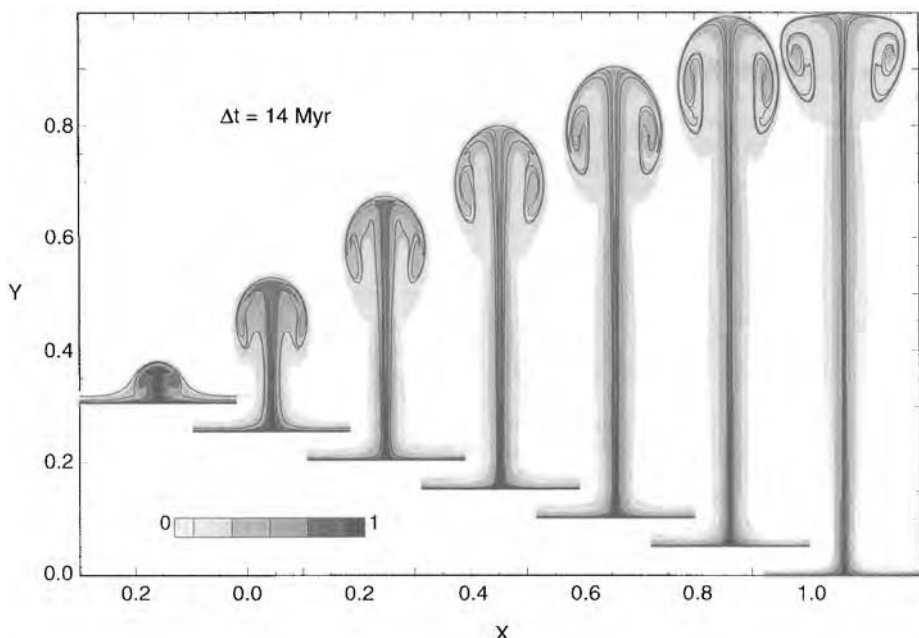


Figure 11.14. Growth of an axisymmetric mantle plume with strongly temperature dependent viscosity from a calculation by van Keken (1997) shown at 14 Myr intervals. Scale bar indicates relative temperatures.

Table 11.5. Flood Basalts and Hot Spot Eruption Rates^a

Flood Basalt	Age (Myr)	Eruption Volume (10^6 km^3)	Duration (Myr)	Hot Spot	Eruption Rate ($\text{km}^3 \text{ yr}^{-1}$)
Deccan	67 ± 1	1.5	1	Reunion	0.04
N. Atlantic	60 ± 1	2.0	2	Iceland	0.02
Parana	125 ± 5	1.5	2	Tristan	0.03
Karoo	195 ± 5	2	2	Pr. Edward	0.02

^a From Richards et al. (1989).

(Deccan, Tertiary North Atlantic, Parana, and Karoo) represent the onset of currently active hot spots (Reunion, Iceland, Tristan da Cunha, Prince Edward), and that in each case nearly $2 \times 10^6 \text{ km}^3$ of magma was extruded within a few million years of hot spot initiation as the plume head reached the base of the lithosphere. Campbell et al. (1989), Hill (1991), Griffiths and Campbell (1991a), and Hill et al. (1992) have discussed the implications of plume head interaction with the lithosphere in terms of surface volcanism and tectonics. They associate many features of Archean geology with plume head–lithosphere interactions. Basaltic flows are associated with plume heads and komatiitic flows are associated with plume tails in the Archean. The interaction of plumes and plume heads with the lithosphere has also been studied by Bercovici and Lin (1996), Sleep (1996, 1997), Moore et al. (1998b, 1999), Ratcliff et al. (1998), and Leitch et al. (1998).

Most of the major continental flood basalt provinces younger than 250 Myr are located at the beginning of a hot spot track. Table 11.5 lists some of these provinces, the hot spots that emerge from them, plus estimates of the magmatic volume during the flood basalt eruption and the present hot spot eruption rate. Figure 11.5 illustrates the relationship between the Reunion hot spot track and the Deccan Traps. The Reunion hot spot evidently began with a massive flood basalt event, with an eruption volume in excess of $1.5 \times 10^6 \text{ km}^3$ in a time interval less than 1 Myr. Since then, Reunion hot spot activity has been nearly continuous for 60 Myr, but with an average eruption rate of only about $0.02 \text{ km}^3 \text{ yr}^{-1}$. It is significant that the volume erupted during the very brief hot spot initiation episode exceeds the total volume erupted along the remainder of the track. This is typical of the behavior of newly formed hot spots (see Table 11.5).

From Table 11.2, the volume flux beneath the Reunion hot spot is $Q_V = 2.9 \text{ km}^3 \text{ yr}^{-1}$. Using parameters given in Table 11.3, we find from (11.8.3) that $U_\infty = 0.27 \text{ myr}^{-1}$. From (11.8.1), the cross-sectional area of the plume conduit is $A = 10^4 \text{ km}^2$, so that the radius of the conduit is $r_{pc} = 58 \text{ km}$. This radius is sufficiently large to explain the horizontal extent of volcanism at hot spots and sufficiently small to explain the difficulty of detecting plumes using seismic tomography. From (11.8.4), the volume of the plume head is $V_\infty = 2 \times 10^8 \text{ km}^3$, so that the radius of the plume head is $r_{ph} = 350 \text{ km}$. From Table 11.5, the volume of erupted volcanics in the Deccan Traps is estimated to be $V_V = 1.5 \times 10^6 \text{ km}^3$. If the basaltic volcanism of the Deccan Traps represents a mean degree of melting of 5%, the required plume head volume would be $V_\infty = 3 \times 10^7 \text{ km}^3$. Thus, the efficiency of magma generation is similar to that obtained in Section 11.5 for the present volcanism at the Hawaiian hot spot. With the ascent velocity given above, the ascent time from D'' to the base of the lithosphere, a distance of about 2,800 km, is about 10 Myr.

One expected consequence of plume ascent through the mantle is entrainment of mantle material into the leading diapir and into the trailing conduit. Material entering the thermal boundary layer surrounding a thermal diapir becomes heated and therefore buoyant and

less viscous. As a result, a portion of this material is incorporated into the diapir. It has been demonstrated experimentally that some entrainment occurs in thermal diapirs by this mechanism (Griffiths, 1986) and also in plume conduits that are tilted by an external shear flow (Richards and Griffiths, 1989). As a consequence of entrainment, mantle plumes likely consist of a mixture of material from the source region and material encountered along the ascent path (Campbell and Griffiths, 1990; Griffiths and Campbell, 1991b). The amount of entrainment is subject to debate. Griffiths and Campbell (1990) proposed that entrainment increases plume mass transport several fold; however, numerical simulations of starting plumes generally find less than 30% increase (van Keken, 1997; Farnetani, 1997).

Another puzzling characteristic of hot spot behavior that the plume model seems to account for is resurgence. Perhaps the most dramatic example of hot spot resurgence is found in the record of flood basalts, which often show evidence for two distinct episodes of eruptive activity, separated in time by 20–40 Myr. Bercovici and Mahoney (1994) proposed that this is due to the separation of the initial plume head from the tail structure during ascent through the mantle, and the subsequent development of a second plume head, which arrives at the lithosphere after the first diapir. The phenomenon of separation of the plume head from the trailing conduit occurs in situations where the conduit is very narrow, owing to a large contrast in viscosity between the plume material and its surroundings. Figure 11.15 from van Keken (1997) illustrates this effect in a numerical calculation of a starting plume in a medium with stress-dependent rheology. Concentrated shear stresses reduce the viscosity in the conduit, causing a pinch from which the leading diapir separates. The second diapir forms in the low-viscosity wake of the first diapir, and it travels at relatively high velocity up the low-resistance path provided by the first. In the extreme case where the viscosity in the wake of the first diapir is very low, the second diapir ascends as a solitary wave, as discussed in Section 11.10.

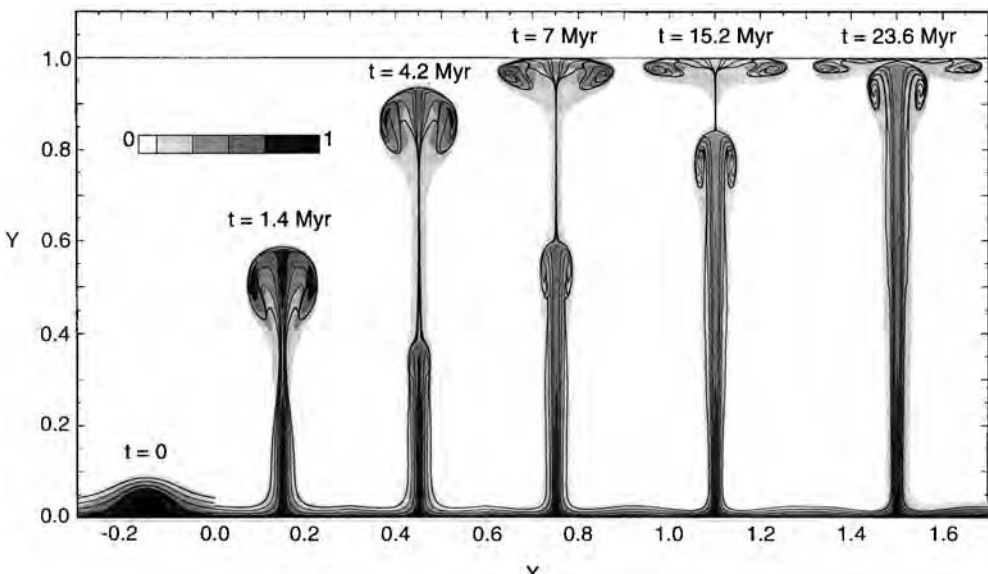


Figure 11.15. Growth of an axisymmetric mantle plume with strongly temperature dependent and stress-dependent viscosity from a calculation by van Keken (1997). Times are shown. The scale bar indicates relative temperatures. The horizontal line marks the upper boundary.

Interaction of a plume with the endothermic phase transition at 660 km depth may also cause the triggering of a second plume head (Bercovici and Mahoney, 1994). Schubert et al. (1995) suggest that there is a significant increase in mantle plume temperature associated with the upward passage of a plume through the spinel–perovskite phase change (see Chapter 9).

11.9 Plume Conduits and Halos

Question 11.8: What is the structure of a mantle plume?

Numerical and analytic models of thermal plume structure have added support to Morgan's original proposal that subsolidus buoyantly driven flow is possible in narrow mantle conduits. For example, Parmentier et al. (1975) obtained numerical solutions for axisymmetric plumes in a 700 km deep layer with olivine rheology as a model for plumes in the upper mantle. They found that strongly temperature dependent viscosity and basal heating were both necessary for establishing a narrow conduit. Yuen and Schubert (1976) derived similarity solutions for steady-state two-dimensional plumes with thermally activated rheology, and verified that concentrated, high-velocity flows occur in plumes with mantle-like rheology. The plume structures obtained by Yuen and Schubert (1976) are only approximations to real plumes, because the solutions assumed constant temperature, rather than zero temperature gradient along the plume axis. Loper and Stacey (1983), Loper (1984b), and Hauri et al. (1994) have derived analytical solutions for steady-state axisymmetric plumes in an unbounded fluid with exponentially temperature dependent viscosity in the asymptotic limit of large viscosity variations. In this limit, the steady-state plume structure consists of a narrow high-velocity core, or conduit, imbedded within a broader thermal halo. High-resolution numerical calculations (Olson et al., 1993; Albers and Christensen, 1996) demonstrate that this arrangement is also the basic plume structure for mantle rheology based on thermally activated creep. Larsen and Yuen (1997a) have carried out a detailed numerical calculation of plume structure in a fluid with a temperature dependent and non-Newtonian rheology.

Figure 11.16 shows the steady-state axisymmetric plume structure from a numerical calculation by Olson et al. (1993). In this calculation, the plume forms above a circular region on the lower boundary which is maintained at a higher temperature than the surrounding fluid. The viscosity at the boundary temperature is 10^{-4} times the ambient fluid viscosity. The steady-state heat transport is about 370 GW, similar to the estimated heat transport beneath the Hawaiian hot spot.

A simplified but illustrative analytical model for a steady-state axisymmetric mantle plume can be derived by assuming a thin vertical conduit along which the structure changes slowly in the vertical direction. Following Loper and Stacey (1983), we consider plumes with exponential rheology of the form

$$\mu = \mu_m \exp\left(-\frac{\gamma(T - T_m)}{\Delta T}\right) \quad (11.9.1)$$

where μ is dynamic viscosity, T is temperature, and $\Delta T = T_s - T_m$. The subscript m refers to mantle values far from the plume, and the subscript s refers to the temperature in the source region of the plume. The exponential rheological law (11.9.1) approximates the thermally activated creep of mantle rocks for $\gamma \simeq 4\text{--}10$.

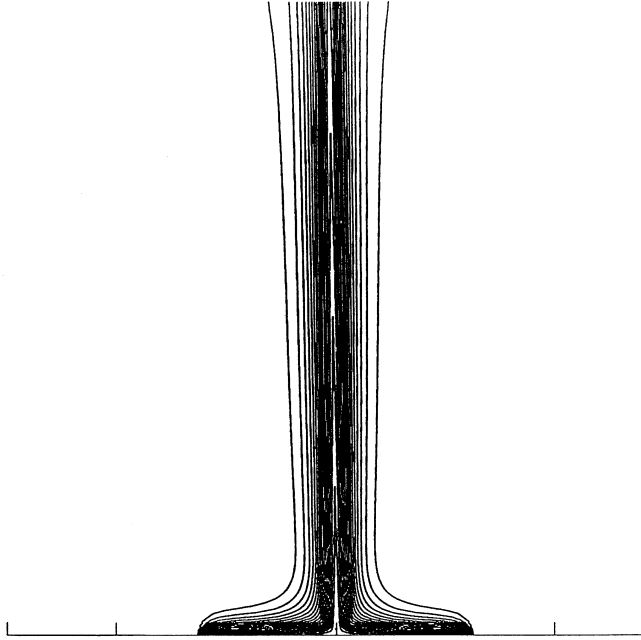


Figure 11.16. Detailed thermal structure (shown by temperature contours) of a steady-state, axisymmetric thermal plume above a heated circular region at the base of a fluid half-space with strongly temperature dependent viscosity, from a numerical calculation of Olson et al. (1993).

As Morris (1982) has demonstrated, whenever the rheological parameter γ is large, the high-temperature, low-viscosity regions of the fluid contain deformation layers where flow is concentrated. In an axisymmetric plume, the deformation layer is the conduit. The high-velocity conduit, with radius δ_c , is surrounded by the broader thermal halo, which extends to a radius δ_T . Within the conduit, the motion is buoyantly driven and primarily vertical. Within the halo, the motion is much slower and is primarily radial entrainment.

The equations of motion can be simplified by exploiting the fact that vertical gradients in the plume are much smaller than radial gradients. In this limit, the equations of continuity, vertical momentum, and heat for incompressible, axisymmetric, steady-state flow reduce to

$$\frac{1}{s} \frac{\partial(su_s)}{\partial s} + \frac{\partial u_z}{\partial z} = 0 \quad (11.9.2)$$

$$\rho_m \alpha g(T - T_m) + \frac{1}{s} \frac{\partial}{\partial s} \left(s \mu \frac{\partial u_z}{\partial s} \right) = 0 \quad (11.9.3)$$

$$u_s \frac{\partial T}{\partial s} + u_z \frac{\partial T}{\partial z} = \frac{\kappa}{s} \frac{\partial}{\partial s} \left(s \frac{\partial T}{\partial s} \right) \quad (11.9.4)$$

where s, z are cylindrical coordinates, $\underline{u} = (u_s \hat{s} + u_z \hat{z})$ is fluid velocity, \hat{s}, \hat{z} are unit vectors in the coordinate directions, ρ_m is mantle density, α is thermal expansivity, and κ is thermal

diffusivity. Equation (11.9.2) follows from (6.15.25). The axial momentum equation can be derived from expressions in (6.15.23) and (6.15.25) and the temperature equation follows from (6.16.4) and (6.16.5). Boundary conditions are

$$u_z \rightarrow 0, T \rightarrow T_m \quad \text{as } s \rightarrow \infty \quad (11.9.5)$$

$$\frac{\partial u_z}{\partial s} = \frac{\partial T}{\partial s} = 0 \quad \text{at } s = 0 \quad (11.9.6)$$

A full solution of this set of partial differential equations is quite complex. In order to obtain an approximate solution, the temperature distribution is taken to be

$$\theta = \frac{T - T_m}{\Delta T} = \theta_0(z) (1 - (s/\delta_T)^2) \quad (11.9.7)$$

where θ is the dimensionless plume temperature anomaly and the subscript 0 refers to the plume axis $s = 0$. The viscosity is assumed to be given by

$$\mu = \mu_0 \exp(\gamma \theta_0(s/\delta_T)^2) \quad (11.9.8)$$

with

$$\mu_0 = \mu_m \exp(-\gamma \theta_0) \quad (11.9.9)$$

The plume centerline viscosity, given by (11.9.9), increases exponentially as the centerline temperature anomaly decays. From (11.9.8), the viscosity falls exponentially as the square of the distance s from the centerline of the plume.

In order to determine the velocity profile in the plume we substitute (11.9.7)–(11.9.9) into (11.9.3). We further assume that the temperature variation can be neglected except for the exponential dependence through the viscosity and write

$$\rho_m \alpha g \theta_0 \Delta T + \frac{1}{s} \frac{\partial}{\partial s} [s \mu_0 \exp(\gamma \theta_0(s/\delta_T)^2)] = 0 \quad (11.9.10)$$

Equation (11.9.10) is then integrated twice to give

$$u_z = u_{z0} \exp(-\gamma \theta_0(s/\delta_T)^2) \quad (11.9.11)$$

where

$$u_{z0} = \frac{\rho_m \alpha g \delta_T^2 \Delta T}{4\gamma \mu_0} \quad (11.9.12)$$

To obtain an equation for the change in centerline temperature with height, we evaluate (11.9.4) at $s = 0$ and substitute (11.9.7) and (11.9.11), yielding

$$\frac{d\theta_0}{dz} = -\frac{4\kappa\theta_0}{\delta_T^2 u_{z0}} \quad (11.9.13)$$

A second relationship between θ_0 and u_{z0} comes from the requirement for constant heat flow Q in the conduit:

$$Q = 2\pi \rho_m c_p \Delta T \int_0^\infty s u_z \theta \, ds \simeq \frac{\pi \rho_m c_p \Delta T \delta_T^2 u_{z0}}{\gamma} \quad (11.9.14)$$

Elimination of $\delta_T^2 u_{z0}$ from (11.9.13) and (11.9.14) yields, after integration,

$$\theta_0(z) = \exp\left(-\frac{4\pi k \Delta T z}{\gamma Q}\right) \quad (11.9.15)$$

with the condition $\theta_0 = 1$ at $z = 0$. By eliminating u_{z0} from (11.9.12) and (11.9.14), we find that the halo radius is given by

$$\delta_T = \left(\frac{2\gamma}{\rho_m \Delta T}\right)^{1/2} \left(\frac{Q\mu_0}{\pi\alpha g c_p}\right)^{1/4} \quad (11.9.16)$$

The centerline velocity u_{z0} is then given by

$$u_{z0} = \left(\frac{Q\alpha g}{\pi\mu_0 c_p}\right)^{1/2} \quad (11.9.17)$$

From (11.9.11) the conduit radius δ_w is related to the halo radius δ_T by

$$\delta_w = \frac{\delta_T}{(\gamma\theta_0)^{1/2}} \quad (11.9.18)$$

This simple model allows us to address several important issues regarding conduits in the mantle. The first question is whether narrow conduits can extend across the whole mantle and not spread out by diffusive heat loss. A necessary condition is that temperatures in the conduit remain high, allowing the conduit viscosities to remain low. We will consider strong ($Q = 300$ GW), intermediate ($Q = 30$ GW), and weak ($Q = 3$ GW) plumes. Other parameter values are taken from Table 11.3. From (11.9.16), the radii of the thermal halos for the three cases are $\delta_T = 170$, 96, and 54 km. From (11.9.17), the centerline velocities are $u_{z0} = 1.5$, 0.5, and 0.15 m yr^{-1} .

On the assumption that the plume originates in the D'' layer we have $z = 2,900$ km. For a Hawaiian type plume ($Q = 300$ GW, $\dot{M}_{ps} \simeq 9,000 \text{ kg s}^{-1}$) we find from (11.9.15) that $\theta_0 = 0.99$ at the surface. Thus the drop in the plume centerline temperature anomaly is only 1%. For an intermediate strength plume ($Q = 30$ GW, $\dot{M}_{ps} \simeq 900 \text{ kg s}^{-1}$) we find $\theta_0 = 0.88$ at the surface, a drop in centerline temperature anomaly of 12%. For a weak plume ($Q = 3$ GW, $\dot{M}_{ps} \simeq 90 \text{ kg s}^{-1}$) we find $\theta_0 = 0.27$ at the surface so that 63% of its temperature excess is lost. For comparison, Figure 11.17 shows how the reduction in plume temperature with height scales with plume buoyancy flux in the numerical calculations of Albers and Christensen (1996).

Although the model of an isolated cylindrical plume in an unbounded fluid is highly simplified compared to the actual conditions in the mantle, these results do serve to point out some of the problems with the presumption that all hot spots are caused by plumes initiated near the CMB. First, very weak plumes with Q less than about 10 GW would not be expected to penetrate through the entire mantle, and so are unlikely to originate near the CMB. Weak plumes cool too much on ascent, and thus are expected to spread out (through increased conduit viscosity) and arrive at the base of the lithosphere with too little excess temperature to produce melting. This is consistent with the results given in Table 11.2 in which the weakest hot spots have $Q = 12$ GW.

In the opposite extreme, there is a problem to explain why the excess temperature in the strongest plumes is no more than a few hundred degrees, if they originate near the CMB. For example, calculations by Albers and Christensen (1996) predict large excess temperatures,

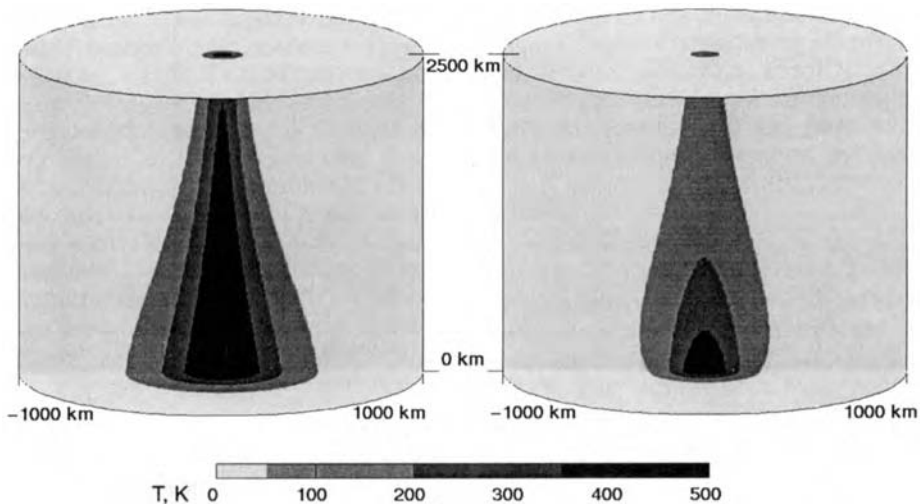


Figure 11.17. Potential temperature variations in steady axisymmetric mantle plumes with strongly temperature and stress dependent viscosity, from calculations by Albers and Christensen (1996). Left: strong thermal plume (buoyancy flux $4,100 \text{ kg s}^{-1}$); right: weak thermal plume (buoyancy flux 500 kg s^{-1}). Note the rapid temperature reduction with height along the axis of the weak plume.

500 K or more, for plumes with mass fluxes comparable to the Hawaiian hot spot originating from a thermal boundary layer with a temperature anomaly of 1,000 K. Since conditions near the CMB indicate a temperature increase of about that magnitude across D'' (see Chapter 4), the most energetic hot spots should exhibit a much larger excess temperature than melting data indicate. One possible explanation is that the D'' layer is chemically stratified, as discussed earlier in this chapter. In that case, the stratification would prevent plumes from forming with the entire D'' temperature anomaly. Calculations by Farnetani (1997) indicate that chemical stratification in D'' can indeed reduce excess temperatures in energetic plumes to more realistic values.

11.10 Instabilities and Waves

Steady-state axisymmetric plume conduits are possible if the plume source strength does not vary in time and if the conduit is not deformed by other motions in the fluid. It is unlikely that these conditions are met in the Earth's mantle. Mantle plumes coexist with larger-scale flows associated, for example, with plate motions, and these larger-scale motions are time dependent. Many hot spots, such as Hawaii, are located far from plate boundaries, in places where we expect the flow in the mantle to be predominantly horizontal. Fluid mechanical studies have demonstrated that a larger-scale horizontal motion of the fluid surrounding a plume readily deforms the narrow conduit, producing a variety of disturbances and instabilities including solitary waves and diapir chains. These may be significant elements in mantle plumes and may account for some of the characteristics of hot spots.

Figure 11.18a shows a low-viscosity plume intruding a cold, highly viscous thermomechanical boundary layer. A train of large amplitude waves is seen propagating up the conduit. Figure 11.18b shows a solitary conduit wave propagating up an otherwise uniform cylindrical conduit. These waves are generated in the source region or by disturbances in the flow

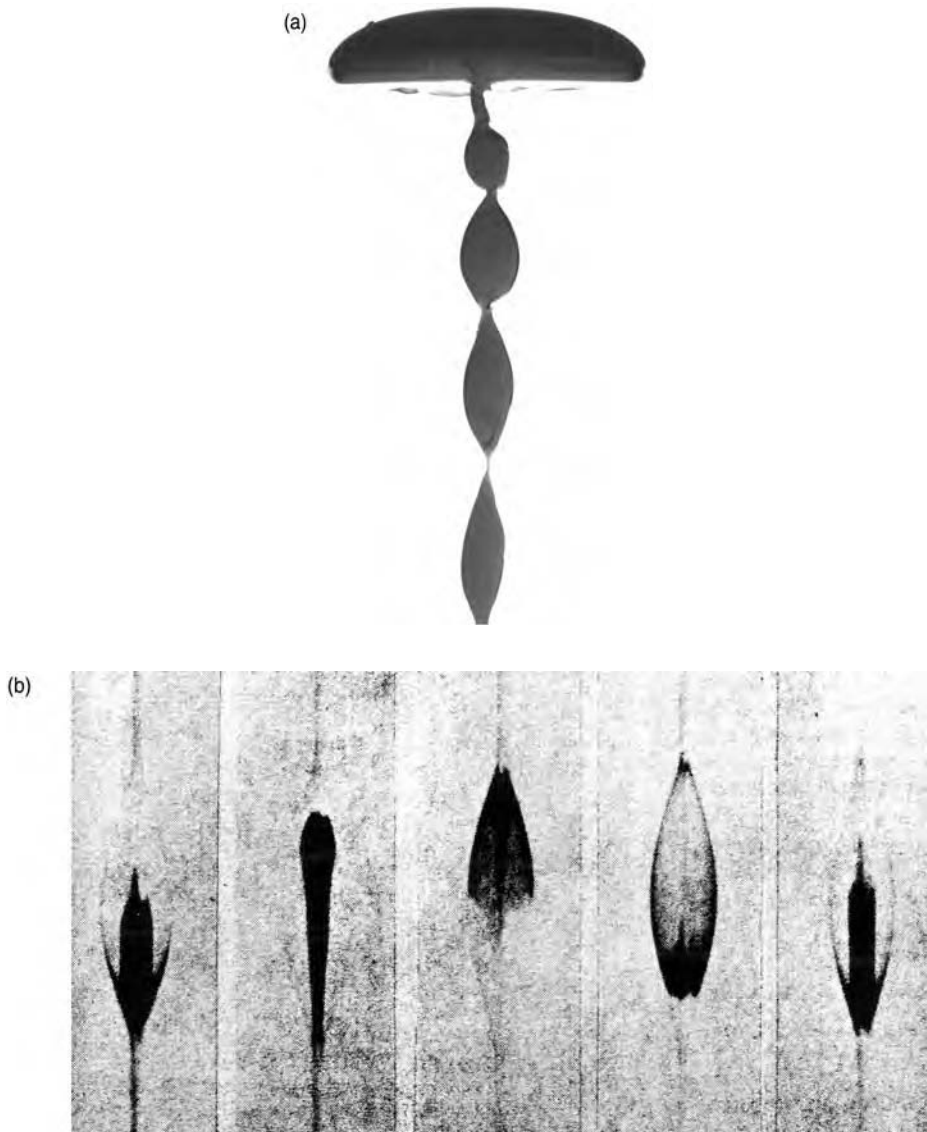


Figure 11.18. (a) Photograph of a low-viscosity plume with conduit waves spreading beneath a highly viscous cold thermal boundary layer from Olson (1990). (b) Photographs of dye tracer transport in a propagating conduit wave, from Whitehead and Helffrich (1988).

along the conduit, and propagate vertically upward, maintaining their shape, at speeds much higher than the fluid velocities in the undisturbed conduit. The waves are associated with increases in conduit flux; decreasing flux causes the conduit to collapse without producing waves (Olson and Christensen, 1986; Scott et al., 1986; Whitehead, 1987, 1988; Schubert et al., 1989a). Conduit waves represent a possible mechanism for flux variability in mantle plumes, as well as a means for rapid transport of material from the source boundary layer to the surface (Whitehead and Helffrich, 1988, 1990).

The properties of conduit waves can be understood by considering the mechanics of a low-density, low-viscosity, vertical, fluid-filled conduit with a circular cross-sectional

area $A(z)$ imbedded in an infinite, homogeneous, and more viscous matrix. The conduit is deformed by viscous normal forces exerted on the conduit wall by the flow of the exterior fluid, which contributes to the dynamic pressure within the conduit. The expression for the vertical pressure gradient within a deforming fluid conduit is

$$\frac{\partial p}{\partial z} = -\rho g' - \frac{\partial \sigma_n}{\partial z} \quad (11.10.1)$$

where σ_n is the normal stress exerted by the exterior fluid on the conduit wall. Flow in the conduit is assumed to obey Poiseuille's law (see 11.8.2)

$$Q_V = -\frac{A^2}{8\pi\rho v_p} \frac{\partial p}{\partial z} \quad (11.10.2)$$

To first order in the slope of the conduit wall, σ_n is proportional to the rate of contraction of the conduit, so that

$$\sigma_n = -\frac{\rho v_m}{A} \frac{\partial A}{\partial t} \quad (11.10.3)$$

where v_m is the kinematic viscosity of the material outside the plume. The model is closed by adding the continuity equation for the conduit, in the form

$$\frac{\partial A}{\partial t} = -\frac{\partial Q_V}{\partial z} \quad (11.10.4)$$

By writing (11.10.1)–(11.10.3) in terms of A and Q_V , we get

$$Q_V = \frac{A^2}{8\pi v_p} \left(g' + v_m \frac{\partial}{\partial z} \left(\frac{1}{A} \frac{\partial Q_V}{\partial z} \right) \right) \quad (11.10.5)$$

In the undisturbed portions of the conduit, where $A = A_0$, (11.10.5) reduces to the Poiseuille flow relation for buoyantly driven motion (11.8.2)

$$Q_{V_0} = \frac{g' A_0^2}{8\pi v_p} \quad (11.10.6)$$

with the subscript zero denoting the undisturbed state.

Analytical solutions to (11.10.4) and (11.10.5) have been obtained for isolated solitary waves by Scott and Stevenson (1984) in the context of porous medium flow, and by Olson and Christensen (1986) for waves in fluid conduits. Isolated solitary wave solutions have the form

$$A = A_0 + A_{\max} \exp \left(\frac{-4\zeta^2}{\lambda^2} \right) \quad (11.10.7)$$

where

$$\zeta = z - ct \quad (11.10.8)$$

c is the wave propagation speed, and the pulse length λ is

$$\lambda = \left(\frac{8cv_m}{g'} \right)^{1/2} \quad (11.10.9)$$

For a large disturbance, where $A_{\max} \gg A_0$, the propagation speed c is related to the amplitude by

$$c = c_0 \ln \left(\frac{A_{\max}}{A_0} \right) \quad (11.10.10)$$

in which $c_0 = 2QV_0/A_0$ is the average fluid velocity in the conduit. The effective duration of the wave pulse Δt is just

$$\Delta t = \frac{\lambda}{c} = \left(\frac{8v_m}{g'c} \right)^{1/2} \quad (11.10.11)$$

and V , the volume of material transported by the wave, is given by

$$V = \int_{-\infty}^{\infty} (A - A_0) d\xi = \left(\frac{2\pi cv_m}{g'} \right)^{1/2} A_{\max} \quad (11.10.12)$$

The dispersion relationship (11.10.10) has been verified experimentally by Olson and Christensen (1986) and Whitehead and Helffrich (1990). The images of a solitary conduit wave in Figure 11.18b from Whitehead and Helffrich (1990) confirm that large amplitude conduit wave shapes have Gaussian profiles, as given by (11.10.7).

Solitary waves provide a mechanism for rapid transport of buoyant material from deep in the mantle to the near-surface. As an example, assume that a surge in hot spot activity lasts 2 Myr, and during the surge, the hot spot heat transport is 360 GW, similar to the present day power of Hawaii. On the basis of (11.10.11) and the numerical values in Table 11.3, this surge would propagate through the mantle at 0.75 m yr^{-1} and have a wavelength $\lambda \simeq 1,000 \text{ km}$. The propagation speed is many times the ascent speed of a Stokes diapir with the same volume. At the height of the surge, the conduit would dilate to about 70 km radius, and according to (11.10.12), the total volume in the surge would amount to $2.2 \times 10^7 \text{ km}^3$. A wave with this magnitude could produce a continental flood basalt event or a large oceanic plateau with only 10% partial melting. Over the past 10 Myr, both Iceland and Hawaii have experienced surges in volcanic activity (Vogt, 1979). One explanation for hot spot surges is the multiple diapir mechanism of Bercovici and Mahoney (1994) discussed earlier in the context of double flood basalt eruptions. Another possible explanation is that these surges represent the arrival of large conduit waves. The flow within conduit waves consists mostly of recirculation along closed streamlines, as shown Figure 11.18b. Chemically distinct material, as well as heat, can be advected to the lithosphere within the waves, with less contamination than in undisturbed conduit flow. Consequently, the isotopic composition of the material in the surge should more closely reflect the source region composition.

Conduit waves also serve as the mechanism for plume instabilities due to background shear in the mantle. Figure 11.19 illustrates the formation of a diapir chain from a sheared conduit. In this case, the shear is produced by relative motion between the matrix fluid and the plume source. Whereas conduit waves propagate stably in a vertical plume, they are not stable when the plume is inclined beyond a critical angle, which is found experimentally to be approximately 60° (Whitehead, 1982). The component of the buoyancy force normal to the tilted conduit distorts the waves, and they become enlarged on the upward side of the conduit. This permits the waves to detach, forming separate diapirs above the trajectory of the conduit. The detachment process repeats itself in a continuously sheared conduit, producing a chain of diapirs as shown in Figure 11.19. Thus, a major effect of large-scale

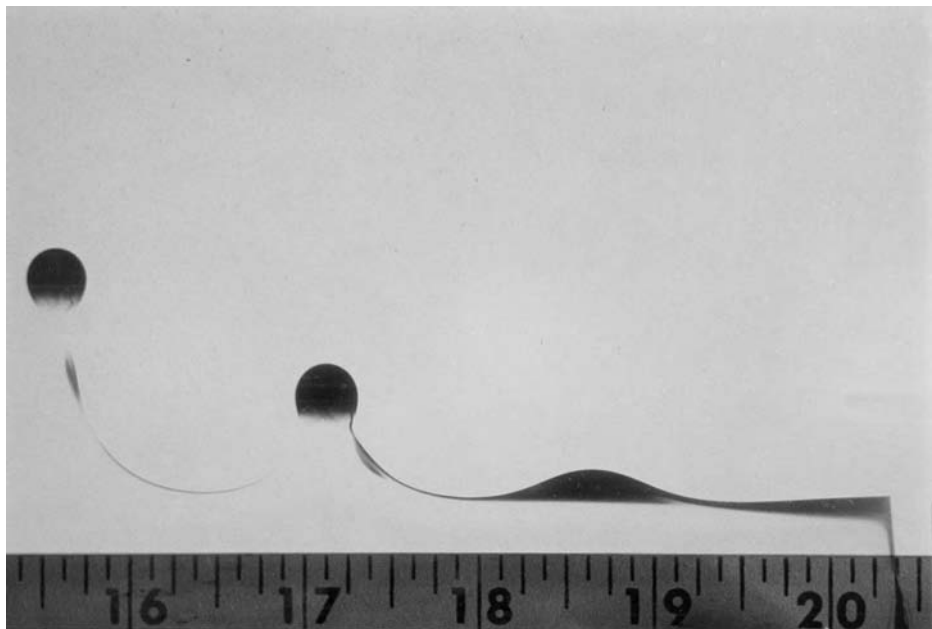


Figure 11.19. Photograph of a chain of diapirs formed by instability of a tilted conduit, from Olson and Singer (1985).

mantle convection on plumes is expected to be the formation of diapirs by the tilt-induced instability of conduit waves. Tilt instabilities might occur in the asthenosphere below the moving plate, provided the shear is sufficiently large. This is a possible explanation for why hot spot tracks are composed of discrete volcanic shields, rather than continuous ridges (Skilbeck and Whitehead, 1978).

Just as conduit waves evolve into discrete diapirs in a tilted conduit, isolated diapirs evolve into conduit waves if the diapirs come in contact with a conduit. This can occur even if the diapir intersects a fossil conduit, one formed by a previously active plume. This is illustrated in Figure 11.20, which shows a diapir intruding a fossil plume conduit and converting to a rapidly propagating conduit wave. It is conceivable that numerous fossil conduits persist in the mantle, providing high-velocity ascent paths from the deep mantle to the lithosphere.

Question 11.9: Do conduit waves occur in the Earth's mantle?

11.11 Dynamic Support of Hot Spot Swells

One of the major predictions of plume theory is the formation of seafloor swells around hot spots. As a mantle plume impinges on the lithosphere from below, its vertical velocity necessarily decreases and the buoyant plume material spreads laterally in the mantle near the base of the plate. The buoyancy of the plume material supports a topographic rise, the hot spot swell. If the plate is moving relative to the hot spot, plume material is expected to be dragged along, creating a hot spot swell elongated in the direction of plate motion.

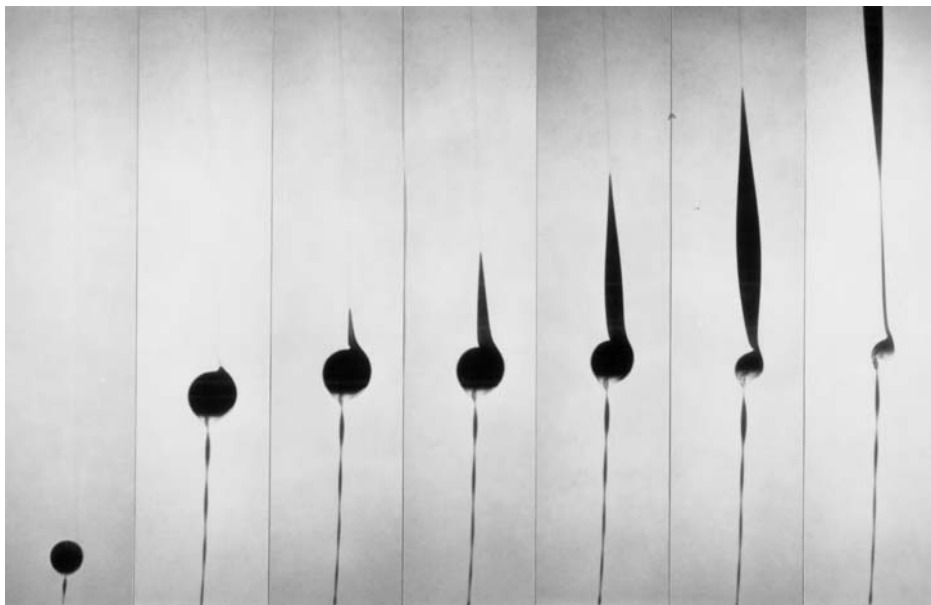


Figure 11.20. Photograph sequence, equally spaced in time, showing conversion of a diapir into a wave as it intrudes a fossil conduit, from Olson and Singer (1985).

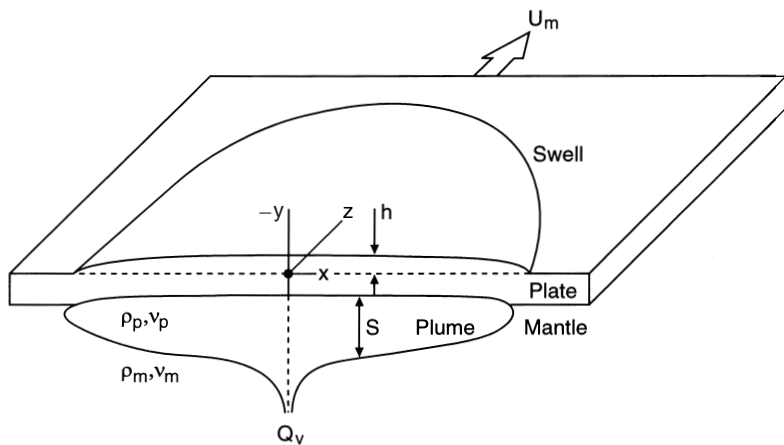


Figure 11.21. Sketch showing geometry of a plume spreading beneath a moving plate.

The evolution of a mantle plume spreading beneath moving lithosphere can be modeled in a simplified way by considering the flow of buoyant, viscous fluid from a point source located in a homogeneous, viscous asthenosphere beneath a rigidly moving plate (Figure 11.21). We assume that the rate of plume spreading is controlled entirely by the properties of the plume material. In addition, it is assumed, for the sake of simplicity, that the undisturbed asthenosphere moves together with the plate at a velocity u_m , that the buoyancy g' and

kinematic viscosity of the plume material ν_p are both constants, and that the plume material is injected beneath the plate at a fixed point \underline{x}_p , representing a narrow, vertical, and stationary conduit source. As the plume material spreads away from the conduit, its thickness S rapidly becomes small compared to its lateral dimensions, and the flow of the plume relative to the moving plate can be modeled using the approximations of lubrication theory, appropriate for flow in a thin channel.

With all of the above approximations, the horizontal velocity of the spreading plume material \underline{u}_p is governed by a channel flow equation of the form

$$\frac{\partial^2 \underline{u}_p}{\partial y^2} = \frac{g'}{\nu_p} \nabla_H S \quad (11.11.1)$$

where y is the depth coordinate and ∇_H is the gradient with respect to horizontal coordinates. Integration of (11.11.1) vertically across the intrusion, subject to the conditions that the asthenosphere below and the plate above the intrusion move with the same velocity \underline{u}_m , yields the following expression for the horizontal plume flux \underline{q} :

$$\underline{q} = \int_0^S \underline{u}_p dy = \underline{u}_m S - \frac{g'}{48\nu_p} \nabla_H S^4 \quad (11.11.2)$$

The continuity equation for intrusion from a point source at $\underline{x} = \underline{x}_p$ can be written as

$$\frac{\partial S}{\partial t} = -\nabla_H \cdot \underline{q} + Q_V \delta(\underline{x} - \underline{x}_p) \quad (11.11.3)$$

where Q_V is the volumetric transport rate of the plume and δ is the delta function. Substitution of (11.11.2) into (11.11.3) yields the lubrication equation for the evolution of the plume thickness

$$\frac{\partial S}{\partial t} + (\underline{u}_m \cdot \nabla_H) S = \sigma \nabla_H^2 S^4 + Q_V \delta(\underline{x} - \underline{x}_p) \quad (11.11.4)$$

where

$$\sigma = \frac{g'}{48\nu_p} \quad (11.11.5)$$

is a parameter which determines how fast the plume spreads laterally by buoyancy forces. Various forms of this basic equation have been used by Olson (1990), Ribe and Christensen (1994), and Phipps Morgan et al. (1995) to model the evolution of the Hawaiian and other hot spot swells.

The lubrication equation can be written in dimensionless form using \underline{u}_m and $(Q_V/2\pi\underline{u}_m)^{1/2}$ as velocity and length scales, respectively. We use asterisks for dimensionless variables and rewrite (11.11.4) as

$$\frac{\partial S^*}{\partial t^*} + (\hat{\underline{u}} \cdot \nabla_H^*) S^* = I \nabla_H^{*2} S^{*4} + \delta(\underline{x}^* - \underline{x}_p^*) \quad (11.11.6)$$

where I is a dimensionless number characterizing the swell shape

$$I = \frac{g' Q_V}{96\pi \nu_p \underline{u}_m^2} \quad (11.11.7)$$

and \hat{u} is the unit vector in the direction of plate motion. The parameter I can be related to the heat transport in a thermal plume using

$$I = \frac{Q}{96\pi\mu_p H_T u_m^2} \quad (11.11.8)$$

where $H_T = c_p/\alpha g$ is the adiabatic temperature scale height.

In a steady state, the shape of the spreading plume is entirely governed by the magnitude of I . For large values of I , corresponding to a large conduit discharge, low plume viscosity or slow plate motion, buoyant spreading dominates over plate advection, and the spreading plume and its topographic rise are nearly circular in planform. For small values of I , corresponding to either a weak plume, fast plate motion or high asthenosphere viscosity, advection dominates over spreading and the steady-state shape of the buoyant region and the topography it supports is highly elongated in the direction of plate motion. The isostatic topography above the spreading plume is just

$$h = \frac{\Delta\rho}{(\rho_m - \rho_w)} S \quad (11.11.9)$$

where $\Delta\rho = \rho_m\alpha\Delta T$ is the plume density deficit relative to the mantle and ρ_w is seawater density. The isostatic geoid height anomaly associated with the swell is given by

$$\Delta N = \frac{\pi G(\Delta\rho)LS}{g} \left(\frac{S}{L} + 2 \right) \quad (11.11.10)$$

where G is the gravitational constant and L is the plate thickness. The ratio of geoid height to topography, the GTR, is constant over most of the swell and is equal to

$$\text{GTR} = \frac{\Delta N}{h} \simeq \frac{2\pi G(\rho_m - \rho_w)L}{g} \quad (11.11.11)$$

where it has been assumed that $S/L \ll 1$. Since much of the hot spot swell topography is supported isostatically, the shape of the swell approximates the shape of the buoyant plume material. Thus, a first-order model for swells produced by a spreading plume is obtained by rescaling the solution to (11.11.4) or (11.11.6) according to (11.11.9), using an assumed plume density anomaly $\Delta\rho$. The model applies to both thermally buoyant and compositionally buoyant plumes, although the effects of heat diffusion ultimately play a role in the evolution of thermal plumes. It is important to emphasize that this is not a good model for swells in the immediate neighborhood of a plume conduit where the topography is influenced by the buoyant conduit and by flexure of the lithosphere, and the geoid is not isostatic.

Table 11.6 lists the estimated values of the parameter I of major oceanic hot spot swells, assuming $\mu_p = 10^{20}$ Pa s for the dynamic viscosity of the plume. The table also gives the speeds of the plates in which each hot spot is formed. While there is a range of values of I in Table 11.6, most values fall within one of two groups. Many of the swells have values of I less than one. This category includes all of the high power swells associated with Pacific hot spots. Hot spots within this group, for example Hawaii, tend to have well-defined, elongated tracks and ridge-shaped swells. The other extreme is represented by the Cape Verde and Ethiopian hot spots. These have values of I 10–100 times larger than the first group. The swells associated with these hot spots are more dome-like, as opposed to ridge-like.

Table 11.6. Hot Spot Swell Shape Parameter, I

Hot Spot	Plate Speed (mm yr ⁻¹)	I ^a
Hawaii	96	0.3
St. Helena	10	1.6
Bermuda	27	0.5
Cape Verde	5	21.4
Yellowstone	30	0.6
Easter ^b	105	0.12
MacDonald ^b	105	0.12
Marquesas ^b	105	0.12
Tahiti ^b	105	0.12
Pitcairn ^b	105	0.12
Reunion	15	2.8
Tristan	12	3.9
Afar	7	8.6
Azores	15	2.5
Canary	15	1.5
Kerguelen	6	3.1
Ethiopia	7	9.8
Ascension	40	2.7

^aBased on a plume viscosity of 10²⁰ Pas.

^bPacific Superswell group.

Figures 11.22 and 11.23 show results from three-dimensional numerical calculations by Ribe and Christensen (1994) of a stationary thermal plume impinging on a moving plate. The model parameters were chosen to represent the Hawaiian hot spot. As in the lubrication model, the buoyant plume material is advected by the plate motion and spreads in the lateral direction under its own buoyancy. Figure 11.23 shows cross-sections and plan views of the spreading plume and the topography and geoid anomalies it produces. Also shown are comparisons of the predictions from the lubrication model with the observed axial topographic anomaly along the Hawaiian Ridge, as determined by Crough (1978). Ribe and Christensen (1994) find that most of the swell topography is attributable to dynamic support by the plume material, although thermal expansion of the lithosphere does contribute.

The presence of plume material beneath the lithosphere can account for the evolution of hot spot swell topography. It also is consistent with the lack of a large heat flow anomaly, which would be expected if lithospheric heating were the main cause of the swell. However, there are some observations this model does not explain. The GTR predicted by this model is too large compared to GTRs measured over hot spot swells, by nearly a factor of 2. In addition, there is no clear seismic evidence for elongated thermal anomalies beneath swells, either within the lithosphere or at sublithospheric depths (Woods and Okal, 1996). The absence of both low seismic velocities and large heat flow anomalies along hot spot tracks has led Phipps Morgan et al. (1995) to propose that the buoyancy of the material underlying hot spot swells is primarily chemical rather than thermal in origin, and is the residue of partial melt extraction at the hot spot. Calculations of plume–lithosphere interaction by Manglik and Christensen (1997) which explicitly include melt depletion buoyancy indicate that the buoyant residue tends to rise to the base of the overlying plate and therefore might behave dynamically similar to a thermal plume. As noted previously, however, the curvature of

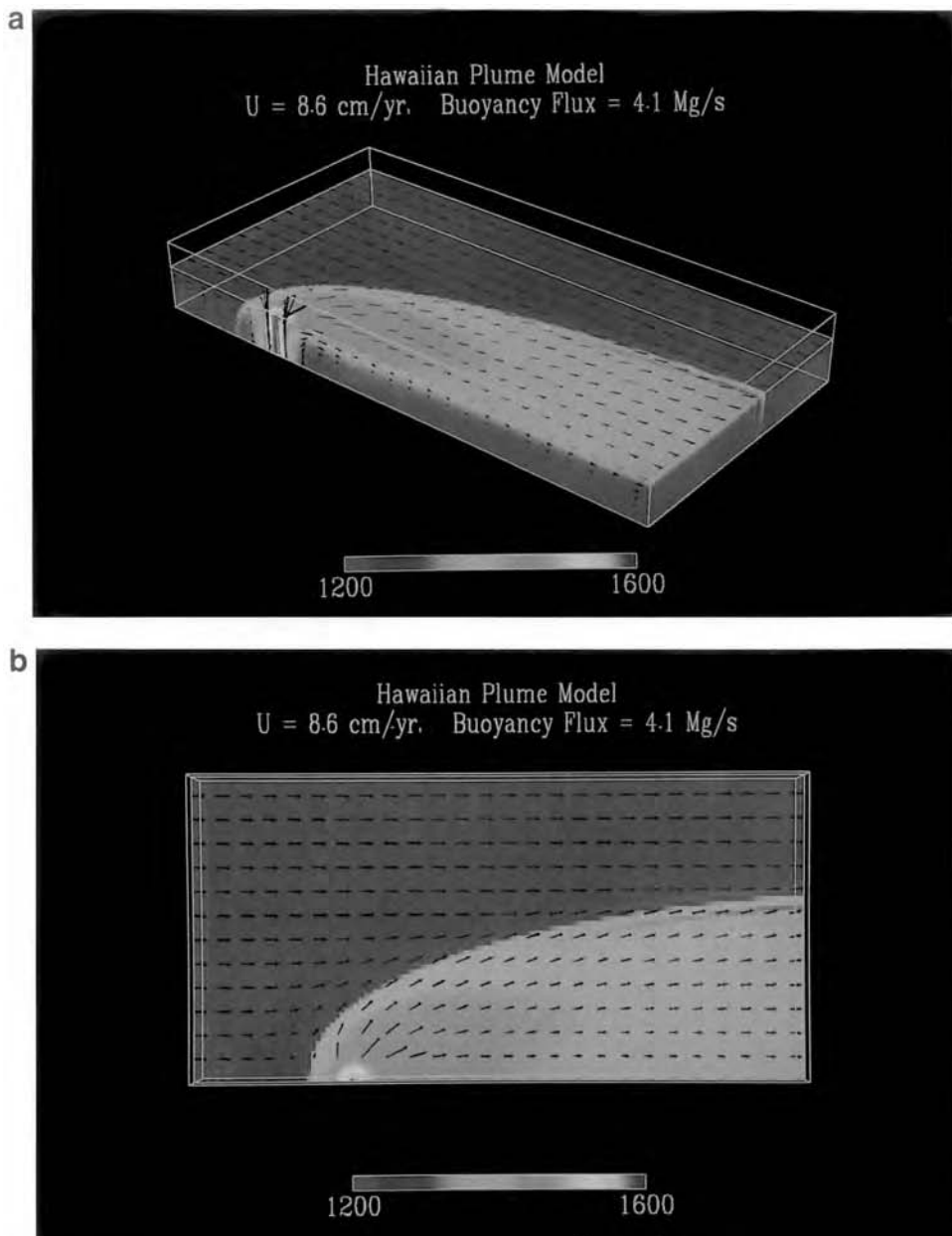


Figure 11.22. Results of a three-dimensional numerical calculation of a thermal plume beneath a moving plate, from Ribe and Christensen (1994). Arrows show fluid velocity; contours are temperatures in degree Celsius. Parameters are chosen for the Hawaiian hot spot. (a) Oblique side view; (b) top view. The surface displayed in (b) is at 150 km depth.

For a color version of this figure, see plate section.

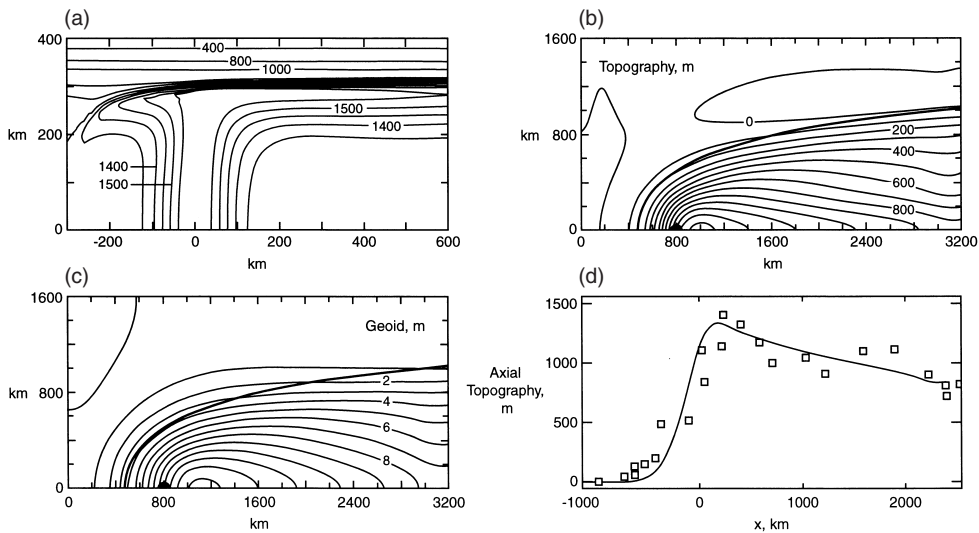


Figure 11.23. Temperature cross-section (a), topography (b), geoid (c), and axial topography compared with Hawaiian swell data (d) from the plume–lithosphere calculation shown in Figure 11.22. After Ribe and Christensen (1994).

the geoid–topography relation at the Hawaiian hot spot is not consistent with chemically buoyant support of the swell (Moore et al., 1998b).

11.12 Plume–Ridge Interaction

Hot spots are preferentially concentrated near mid-ocean ridges. Iceland is the best known example of a ridge-centered hot spot, and it produces symmetric tracks on both the North American and Eurasian plates. Other hot spots such as the Azores and Galapagos lie off the ridge axis because the ridge has migrated in time relative to the hot spot source.

The Iceland hot spot affects the seafloor topography and the trace element content of mid-ocean ridge basalts for several hundred kilometers along the ridge axis (Schilling, 1973), indicating that significant flow of plume material parallel to the ridge occurs there. Ridges near off-axis hot spots such as the Galapagos show evidence of plume contamination even in cases where the ridge has migrated 1,000 km or more from the hot spot location (Schilling, 1991). These observations have led to the concept that ridges act as migrating “sinks” for plume material, which is transported within subhorizontal conduits beneath the oceanic lithosphere from the hot spot to the spreading center (Schilling et al., 1985).

The dynamics of ridge-centered plumes has been investigated experimentally by Feighner and Richards (1995) and numerically by Feighner et al. (1995) and Ribe et al. (1995). Dynamical interaction between off-axis plumes and ridges has been investigated experimentally by Kincaid et al. (1995) and numerically by Ito et al. (1997).

The basic result of these studies is illustrated in Figure 11.24 from Ito et al. (1997), which shows planform views of tracers at three stages of plume interaction with a migrating spreading center. In the ridge-centered stage, the plume width as measured along the ridge W_0 reaches a steady-state value that depends primarily on the plume volume flux Q_V and

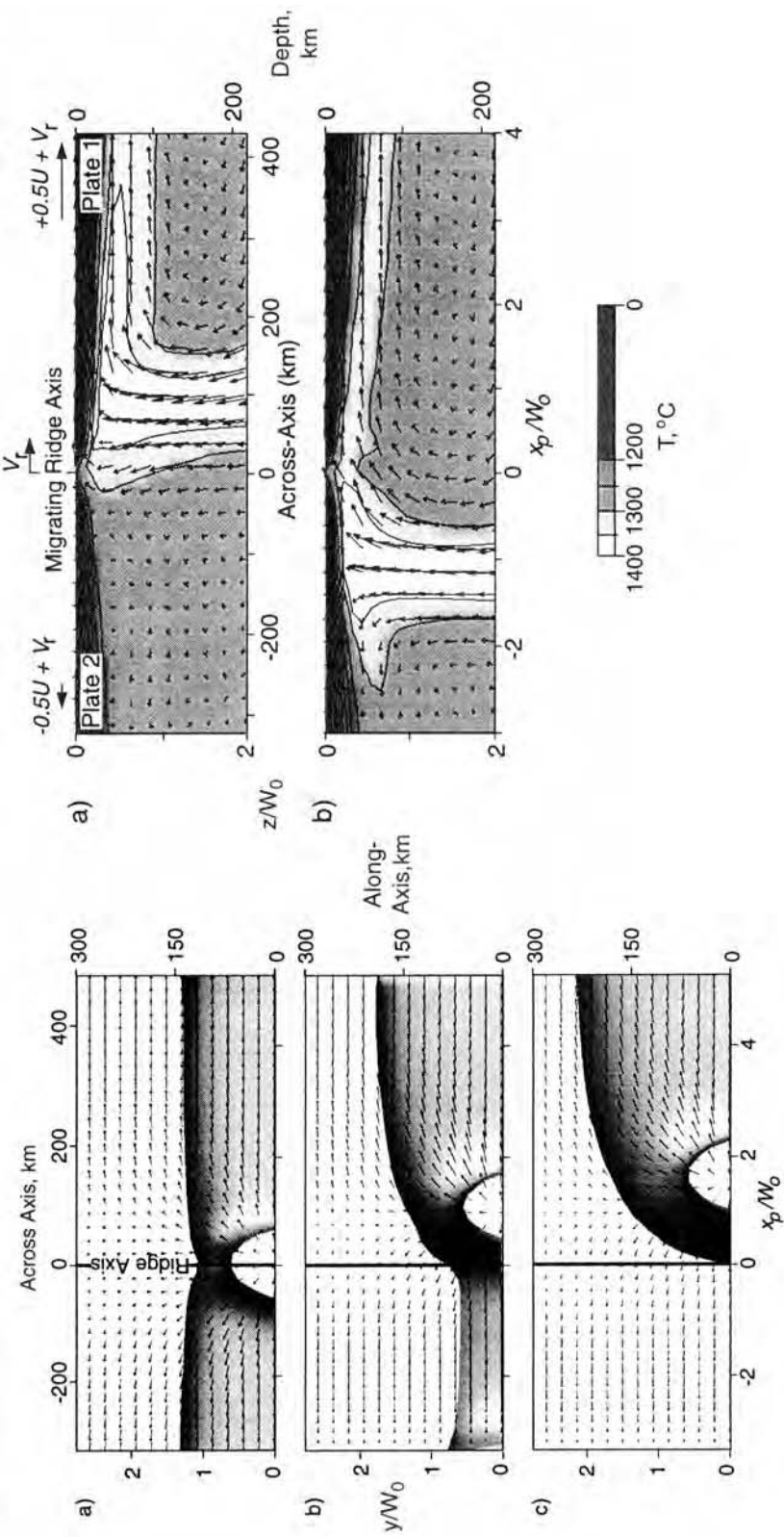


Figure 11.24. Results of a three-dimensional numerical calculation of a thermal plume beneath a migrating spreading center from Ito et al. (1997). Parameters are chosen for the Galapagos hot spot. Left column: Sequence in time showing evolution of plume planform as the ridge migrates relative to the plume. Arrows show fluid velocity at 64 km depth; shading indicates chemical tracer density. Time progresses from top to bottom. Right column: Cross-sections showing (a) a ridge migrating toward a plume and (b) ridge migrating away from a plume. Arrows show fluid velocity; shading denotes temperatures in degree Celsius.

the half-spreading rate of the plates U according to (Feighner and Richards, 1995)

$$W_0 = c \left(\frac{Q_V}{U} \right)^{1/2} \quad (11.12.1)$$

with the factor $c \simeq 1.5$, depending on other parameters of the system (Ribe et al., 1995; Ito et al., 1997). After the ridge migrates away from the hot spot, the plume approaches the shape of a mid-plate plume discussed in the previous section.

Unlike the case of a mid-plate hot spot, for which the observed swell topography can be matched with an excess temperature near 250 K and a conduit radius of 50–100 km, the observed ridge-centered swells can be matched only with models having excess temperatures less than 100 K and conduit radii near 300 km (Ribe et al., 1995; Ito et al., 1997). These numbers do not agree with the seismic tomographic results for Iceland discussed earlier in this chapter, indicating the need for further work on the structure of ridge-centered hot spots.

Another issue that remains unresolved is the deflection of mantle plumes toward spreading centers. The geochemical evidence indicates that such deflection is widespread. The experiments by Kincaid et al. (1995), which demonstrate that, under some circumstances, plume material can flow upstream along the base of a moving plate in low-viscosity channels, offer some dynamical support for the concept. However, the numerical calculations on plume–ridge interaction do not exhibit this effect. Perhaps this is because the formation of subhorizontal channels requires extremely low (that is, melt-like) viscosities.

11.13 Massive Eruptions and Global Change

Question 11.10: Are mass extinctions related to flood basalt events?

Numerous studies have suggested that continental flood basalt eruptions influence the Earth's climate enough to cause mass extinctions. In particular, Officer et al. (1987), McCartney and Loper (1989), and Courtillot (1994) present the arguments and the evidence in favor of this mechanism. These papers (and several recent books on the subject, including Officer and Page (1993) and Courtillot (1995)) point out that recent dating of the Deccan flood basalts place that event just before the period of massive extinctions at the Cretaceous–Tertiary (K/T) boundary, near 65 Myr ago. The widely accepted explanation for the K/T extinctions is the meteorite impact hypothesis, advanced by Alvarez et al. (1980, 1984) to account for the famous iridium anomaly often found in sediments at the K/T boundary. While this and other evidence can be explained by meteorite impact, the fact remains that volcanic eruptions are known to result in large, transient changes in global climate, and so it is of interest to determine whether there is a causal relationship between flood basalts and faunal change.

Cooling of the Earth's surface temperature by volcanic eruption is caused by increased aerosol concentrations in the stratosphere. The most important volcanically produced species for global cooling is probably SO₂, which has a residence time in the stratosphere of about a year (Pollack et al., 1976). Another effect of massive eruption on continents is the release of HCl and H₂SO₄, which could result in catastrophic acid rains, altering the pH of the upper ocean and possibly destroying the ozone layer (Officer et al., 1987). All of these effects are just speculations at the present time, because we do not know the quantities of volcanic gas released during flood basalt events.

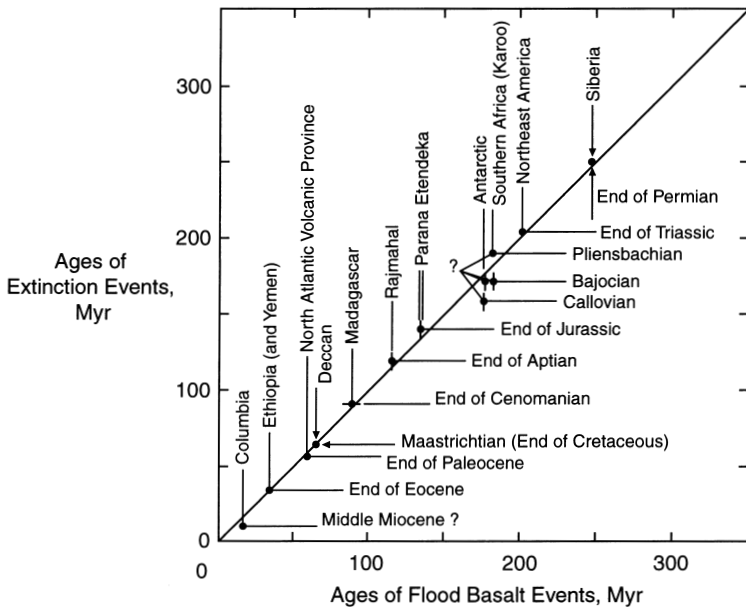


Figure 11.25. The correlation between ages of flood basalts and major mass extinction events, from Courtillot (1995).

However, from a purely empirical point of view, there is some support for the concept that extinctions are related to flood basalt events. Figure 11.25 from Courtillot (1995) shows the striking correlation between the dates of major flood basalt events from the past 300 Myr as determined by various workers, together with estimated dates for the major extinction events during the same time interval, according to Raup and Sepkoski (1986). Most of the mass extinctions appear to have occurred during flood basalt activity. Although this correlation is suggestive, the causal relationship between the two phenomena remains to be demonstrated. However, it does suggest some important tests. One test is to determine, with accurate dating, whether extinctions actually follow massive eruptions. Another test is to determine if flood basalt activity affects climate. Larson (1991) has argued that the Cretaceous greenhouse – when deep ocean temperatures were perhaps 10 K warmer than present – was the result of CO₂ released during particularly high levels of flood basalt activity in the mid-Cretaceous. More work is needed to substantiate these interesting possibilities.

Along these lines, Marzoli et al. (1999) have reported new ⁴⁰Ar/³⁹Ar data on extensive basaltic magmatism in Brazil that forms part of the continental flood basalt province known as the Central Atlantic Magmatic Province (CAMP). The CAMP basalts cover an enormous area of more than 7×10^6 km² (in parts of North America, Europe, Africa, and South America) and were emplaced in just a few million years with peak activity at 200 Ma. The magmatic event is associated with the breakup of Pangea and it overlaps closely in age with the Triassic–Jurassic (T–J) boundary. The T–J boundary marks the occurrence of a major mass extinction involving marine and terrestrial genera and families. The large spatial extent of CAMP and its brevity in time suggest a connection between the event and the T–J extinctions (Courtillot et al., 1996; Marzoli et al., 1999).

12

Chemical Geodynamics

12.1 Introduction

Much can be learned about the evolution of the Earth by considering the fluid dynamics of mantle convection and the associated thermal problems. However, chemical effects play a crucial role. Volcanism extracts some elements preferentially and can result in chemical buoyancy. Volcanic differentiation also preferentially extracts the radiogenic elements from the mantle into the continental crust.

In order to understand how volcanic processes influence mantle convection, it is necessary to have a general understanding of the major element petrology. However, both trace element studies and isotope studies provide important constraints. Partial melting of mantle rock concentrates incompatible elements into the resulting magma, but isotope ratios remain unaffected. Thus isotope systematics provide quantitative constraints on the long-term evolution of the mantle and processes such as the convective mixing of subducted lithosphere. In this chapter we will discuss some of these isotope families, observations of isotope ratios in rocks and in the atmosphere, and the implications for mantle convection. We will call this chemical geodynamics (Allègre, 1982, 1987). A general treatment of the use of isotopes in geology has been given by Faure (1986) and by Dickin (1995).

12.2 Geochemical Reservoirs

The primary geochemical cycle of the solid Earth is directly associated with plate tectonics and mantle convection; it is illustrated schematically in Figure 12.1. This is a box model in which the principal geochemical reservoirs are included. These are the core, the mantle, the oceanic crust, the continental crust, the oceans, and the atmosphere. In terms of the formation of the Earth, the mantle was the primary reservoir. The core was formed by the differentiation of the dense iron-rich components. The oceanic and continental crusts were formed by the differentiation of the light early melting silicic components. The origin of the oceans and atmosphere remains controversial. The relative contributions of internal degassing and extraterrestrial inputs are also uncertain.

The creation of the oceanic crust at mid-ocean ridges leads to the strong concentration of incompatible elements from the upper mantle into the basaltic oceanic crust through the partial melting process. Gases and fluids generated by this volcanism transfer incompatible and volatile elements to the oceans and atmosphere. Hydrothermal processes also exchange material between the oceanic crust and the oceans. The oceanic crust is coated with sediments that are primarily derived from the continents.

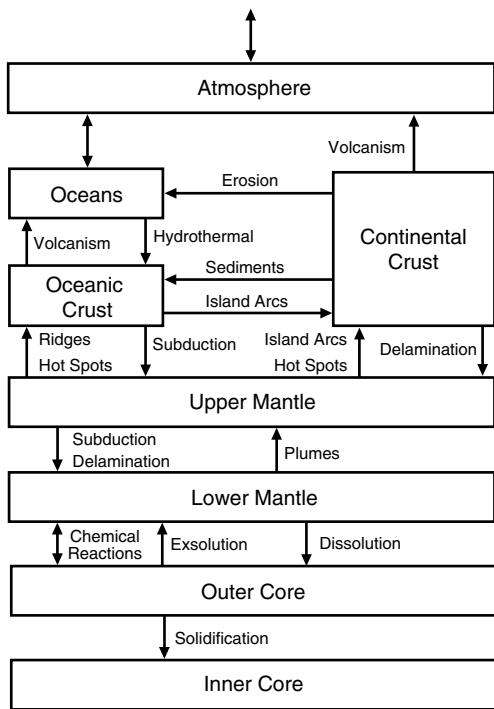


Figure 12.1. Schematic diagram of the geochemical reservoirs and interactions involved in the chemical geodynamic behavior of the Earth.

At ocean trenches the altered oceanic crust is cycled back into the Earth's interior. Along with the descending lithospheric plate, some continental material, including altered oceanic crust and entrained sediments, is recycled into the mantle at subduction zones. At a depth of about 100 km, the upper part of the oceanic crust melts and partial melting occurs in the overlying mantle wedge; these processes further concentrate incompatible elements and result in island arc volcanism. Island arc volcanism, together with continental flood basalt volcanism and hot spot volcanism, form new continental crust. However, all these sources have compositions that are considerably more mafic (basaltic) than the present silicic composition of the continental crust. Further differentiation of the continental crust is attributed to remelting events and delamination of the mafic lower continental crust (see Section 2.7). The magmas from the mantle associated with subduction zone volcanism, flood basalt volcanism, and hot spot volcanism intrude the continental crust and in the presence of water produce silicic (granitic) magmas. These magmas rise into the upper crust, making the upper crust more silicic and the lower crust more mafic. Subsequently the mafic dense rocks of the lower crust are returned to the mantle by delamination. The net result is that continental crust becomes more silicic with time, transforming into a reservoir for the incompatible elements, including the radiogenic elements U, Th, and K and the light rare earth elements.

Although the continental crust is small in volume, its enrichment in incompatible elements is so large that it constitutes a significant reservoir for these elements. The atmosphere constitutes an important reservoir for the radiogenic gases helium and argon. While the oceanic crust plays a critical role in chemical geodynamics, its volume is so small that it can be neglected in isotopic mass balances.

The mantle reservoir in Figure 12.1 is divided into two parts, an upper mantle reservoir and a lower mantle reservoir. Since the style of mantle convection still has uncertain aspects, we consider the mantle as both a two-layer system with limited transport between the layers and a single convecting layer. Even with two-layer mantle convection, substantial transport of material between the layers is likely to occur. Subducted lithosphere may penetrate into the lower layer while plumes generated in the lower layer may penetrate through the upper layer. Active convective processes in either layer may entrain material from the other layer.

The core reservoir in Figure 12.1 is also divided into two parts in accordance with our knowledge of the structure of the core. Cooling of the Earth through geologic time has resulted in the growth of a solid inner core. In this process, light alloying elements such as Si are concentrated into the liquid outer core which becomes progressively richer in the light elements with time. Of particular importance here are possible modes of interaction of the lower mantle and outer core including chemical reactions at the core–mantle boundary, exsolution of light elements from the outer core into the lower mantle, and dissolution of heavy elements from the lower mantle into the outer core. While there is much speculation about core–mantle mass exchange, there is no strong evidence for significant material transport between these reservoirs and in the following we assume such transport is negligible and neglect the core reservoir.

12.3 Oceanic Basalts and Their Mantle Reservoirs

Basalts formed at mid-ocean ridges (MORB) and at oceanic islands (OIB) generally have the same major element composition. Both are generated by pressure-release partial melting of mantle rock. But when considered in terms of trace element and isotopic compositions, MORB and OIB can be quite different.

Isotope ratios and the distributions of rare earth elements show that normal MORB are nearly uniformly depleted (Gast, 1968; Allègre et al., 1980; Bougault et al., 1980). Normal MORB is defined in this context as the oceanic crust of that portion of the ridge system with bathymetric depths greater than 2 km. This excludes, for example, crustal sections near Iceland and the Azores. Due to the kinematics of plate tectonics, the mid-ocean ridge system randomly migrates over the upper mantle. MORB is a random sample of the upper mantle reservoir; the near uniformity of normal MORB in terms of rare earth distributions and isotope ratios is evidence that the upper mantle is a nearly uniform depleted reservoir. This near uniformity of the MORB source reservoir is attributed to mixing due to convection in the reservoir. The subducted oceanic lithosphere will be heated in about 50 Myr and will become part of the convecting mantle reservoir. Convective mixing will string out the layered oceanic lithosphere until, after a few hundred million years, heterogeneities are reduced to a small scale.

The complementary nature of the continental crust and the MORB source reservoir requires that the material from which the crust has been extracted be mixed back into the MORB source reservoir. This is taken as conclusive evidence that the subducted oceanic lithosphere is mixed back into the upper mantle reservoir. The fate of the subducted oceanic lithosphere has long been a subject of controversy. Dickinson and Luth (1971) suggested that the subducted lithosphere lies at the base of the mantle; Oxburgh and Parmentier (1977) suggested that due to its buoyancy, it underplates the continental lithosphere. However, the chemical evidence is conclusive: a large fraction of the subducted lithosphere is mixed back into the upper mantle reservoir on a time scale of a few hundred million years.

Although normal MORB is nearly uniform in terms of both incompatible element concentrations and isotope ratios, OIB are not. Included in the OIB are anomalous segments of the mid-ocean ridge system such as Iceland and the Azores. In the cases of Iceland and Hawaii, the isotope data can be explained in terms of mixing between a depleted (MORB source) reservoir and a relatively pristine undepleted reservoir and other source regions (Sun and Hanson, 1975). The pristine reservoir can be associated with all or some fraction of the lower mantle beneath the 660 km seismic discontinuity. In the cases of other ocean islands such as Tristan, Gough, Kerguelen, St. Helena, Azores, and the Society Islands, the isotope signatures may result from the presence in the depleted mantle reservoir of incompletely homogenized subducted oceanic crust and entrained sediments (Chase, 1981; Hofmann and White, 1982; Zindler et al., 1982). These isotope signatures probably developed in the continental crust and lithosphere (Allègre and Turcotte, 1985), since chemical heterogeneities would not persist for a sufficient length of time in the convecting mantle to develop the observed isotopic variations.

O’Nions et al. (1979), Wasserburg and DePaolo (1979), Allègre et al. (1980), DePaolo (1980), Jacobsen and Wasserburg (1980a, b, 1981), Allègre (1982), and O’Nions (1987) have all discussed the implications of crustal extraction from the mantle for isotope systematics. Mass balance calculations were given and the depleted mantle reservoir was associated with the upper mantle. However, estimates of errors (Allègre et al., 1983a, b) cast some doubt on this conclusion.

Question 12.1: Do the isotope systematics of MORB require separate upper mantle and lower mantle reservoirs indicative of layered mantle convection?

In the discussion given above the reservoirs have been treated as homogeneous. Clearly this is only an approximation (Hart, 1988). As discussed in Chapter 8, it is necessary to mix the subducted lithosphere back into the mantle in order to achieve a depleted reservoir. The subducted lithosphere has strong chemical heterogeneities on the scale of tens of kilometers. We have previously discussed the two end-member consequences of this heterogeneity: (1) chemical segregation and (2) homogenization by kinematic mixing. The latter end member is clearly favored. Allègre and Turcotte (1986) discussed this mixing in terms of a marble cake mantle, support for which has come from studies of ophiolites (Hamelin and Allègre, 1988) and basalts on the East Pacific Rise (Prinzhofer et al., 1989).

Isotope heterogeneities are a primary feature of OIB, but, to a lesser degree, they are also associated with MORB. The OIB heterogeneities are directly associated with subducted (delaminated) material that has not been remixed into the mantle, and possibly with a pristine mantle reservoir. The isotope anomalies in OIB require ~ 2 Gyr to develop. If these develop in the mantle, the implication is that mantle mixing is incomplete on this time scale. The alternative is that the anomalies develop in isolated reservoirs such as the crust or core before the material is injected into the mantle reservoir(s).

Isotope heterogeneities are also associated with MORB. There is much larger scatter in the isotope values of MORB from the mid-Atlantic ridge than from the East Pacific Rise. The heterogeneities decrease systematically with increased spreading rate. The conclusion is that melting processes beneath ocean ridges homogenize the magmas by sampling larger source regions at higher spreading rates. Zindler et al. (1984) confirmed this conclusion by showing that there is much greater variability in the isotope values for young seamounts

adjacent to the East Pacific Rise. The local melting associated with the seamounts gives a better representation of the actual heterogeneities of the source region.

Variations in the composition of MORB are also observed on a much larger global scale. Dupre and Allègre (1983) pointed out that there is a systematic lead (Pb)-strontium (Sr) variation in Indian Ocean basalts. Hart (1984) called this the DUPAL anomaly and expanded on its significance. Staudigel et al. (1991) argued for a South Pacific isotopic and thermal anomaly referred to as the SOPITA and associated it with the subduction of old slabs. Staudigel and King (1992) associated these anomalies with variations in rates of subduction.

12.4 Simple Models of Geochemical Evolution

The interpretation of isotope ratios requires a model of the relevant geochemical reservoirs and the material exchange among the reservoirs. The model must also describe how the reservoirs and the exchange processes vary with geologic time. The interpretations of isotope ratios therefore depend in part on the models used to interpret them. We will present below some of the simpler models used in the interpretation of isotope ratios (Turcotte and Kellogg, 1986a).

The isotopic systems used in mantle geochemistry consist of a radioactive parent isotope with a mole density j (moles per unit mass), a radiogenic daughter isotope with a mole density i^* , and a nonradiogenic reference isotope with a mole density i . The isotope ratio α is defined by

$$\alpha = \frac{i^*}{i} \quad (12.4.1)$$

and is usually expressed by

$$\varepsilon = \left(\frac{\alpha}{\alpha_s} - 1 \right) \times 10^4 = \left[\left(\frac{i^*/i}{i_s^*/i_s} \right) - 1 \right] \times 10^4 \quad (12.4.2)$$

(DePaolo and Wasserburg, 1976), where the subscript s refers to the bulk silicate Earth. The composition ratio μ is defined by

$$\mu = \frac{j}{i} \quad (12.4.3)$$

and is usually expressed by the fractionation factor

$$f = \frac{\mu}{\mu_s} - 1 = \left(\frac{j/i}{j_s/i_s} \right) - 1 \quad (12.4.4)$$

(DePaolo and Wasserburg, 1976).

12.4.1 Radioactivity

The concentrations of the radioactive parent isotope j and the radiogenic daughter isotope i^* vary with time t according to the principle of radioactive decay:

$$\frac{dj}{dt} = -\lambda j \quad (12.4.5)$$

$$\frac{di^*}{dt} = \lambda j \quad (12.4.6)$$

where λ is the decay constant and time t is measured forward. The concentration of a radioactive parent isotope decreases at a rate proportional to the concentration of the parent isotope, while the concentration of the radiogenic daughter isotope increases at the same rate. The integrals of (12.4.5) and (12.4.6) are

$$j = j_0 e^{-\lambda t} \quad (12.4.7)$$

$$i^* = i_0^* + j_0 (1 - e^{-\lambda t}) \quad (12.4.8)$$

where subscript zero refers to the concentrations at $t = 0$. The half-life $t_{1/2}$ of a radioactive parent isotope is the time required for one-half of the atoms present at $t = 0$ to decay. By putting $j = j_0/2$ in (12.4.7) we obtain

$$0.5 = e^{-\lambda t_{1/2}} \quad (12.4.9)$$

or

$$t_{1/2} = \frac{\ln 2}{\lambda} = \frac{0.69315}{\lambda} \quad (12.4.10)$$

Table 12.1 lists some of the more widely studied isotopic systems together with their decay constants and half-lives (Blum, 1995).

The isotope and composition ratios can be related through (12.4.7) and (12.4.8) (with their definitions (12.4.1) and (12.4.4)) as

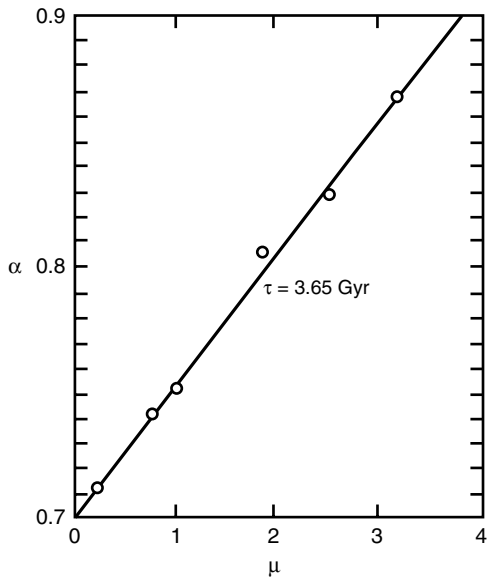
$$\alpha = \alpha_0 + \mu (e^{\lambda t} - 1) \quad (12.4.11)$$

where α_0 is the isotope ratio at $t = 0$. This relation may be used to determine the “age” of a rock. The age refers to the parent radionuclides and daughter products which became “frozen” into the rock. Thus a measured date may represent the time since the crystallization of the rock or the time since a metamorphic event when the rock was heated to sufficiently high temperatures for chemical changes to occur.

Table 12.1. Isotopic Systems Commonly Used in Mantle Geochemistry and Their Properties

Isotopic System	Radioactive Parent Isotope	Radiogenic Daughter Isotope	Stable Reference Isotope	Decay Constant of Radioactive Parent γ (Gyr $^{-1}$)	Half-life of Radioactive Parent $t_{1/2}$ (Gyr)
Rb-Sr	^{87}Rb	^{87}Sr	^{86}Sr	1.42×10^{-2}	48.8
Sm-Nd	^{147}Sm	^{143}Nd	^{144}Nd	6.54×10^{-3}	106
U-Pb	^{238}U	^{206}Pb	^{204}Pb	1.551×10^{-1}	4.469
U-Pb	^{235}U	^{207}Pb	^{204}Pb	9.848×10^{-1}	0.704
Th-Pb	^{232}Th	^{208}Pb	^{204}Pb	4.948×10^{-2}	14.01

Figure 12.2. Rb–Sr isochron for the Amitsoq gneiss from the Godthaab district of southwestern Greenland. This is one of the oldest terrestrial rocks. Data are from Moorbat et al. (1972). The correlation with (12.4.12) gives an age $\tau = 3.65$ Gyr.



For a number of isotopic systems it is a good approximation to assume that $\lambda t \ll 1$. When this approximation is applied to (12.4.11) we obtain

$$\alpha = \alpha_0 + \lambda t \mu \quad (12.4.12)$$

If it is appropriate to assume that α_0 is the same for different minerals in a rock at the time it became a closed system, then measurements of α versus μ for different minerals in the rock should lie on a straight line known as the whole-rock isochron. The age is proportional to the slope according to (12.4.12). An example of a whole rock rubidium–strontium isochron for one of the oldest terrestrial rocks from west Greenland is given in Figure 12.2 (properties of the Rb–Sr system are given in Table 12.2).

12.4.2 A Two-reservoir Model with Instantaneous Crustal Differentiation

The simplest model of geochemical evolution is a two-reservoir model consisting of continental crust of mass M_c that was instantaneously separated from a mantle reservoir of mass

Table 12.2. Present-day Parameter Values for Isotopic Systems (Jacobsen and Wasserburg, 1980b; Allègre et al., 1983b)

Isotopic System	Sm–Nd	Rb–Sr
Composition ratio, bulk silicate Earth μ_s	0.1967 ± 0.0030	0.8923 ± 0.00726
Isotope ratio, bulk silicate Earth α_s	0.512622 ± 0.0112	0.704755 ± 0.00445
Normalized isotope ratio ε_{mp}	10 ± 5	-29 ± 15
Enrichment factor D_{si}	29 ± 9	–
Q (Gyr $^{-1}$)	25.3 ± 0.2	17.7 ± 1.5
Mantle fractionation factor f_{mp}	0.12 ± 0.2	-0.78 ± 0.22
Crustal fractionation factor f_{cp}	-0.451 ± 0.06	–

M_m at a time τ_c before the present (τ_c is the age of crustal separation). The mass of the mantle source reservoir and the time of crustal separation can be constrained by the measured values of the isotope ratios (α or ε) and composition ratios (μ or f) (DePaolo, 1979, 1980; Jacobsen and Wasserburg, 1979, 1980a).

For comparison with observed values of isotopic ratios and fractionation factors, we need to develop expressions for the model quantities f_c , f_m , ε_c , and ε_m , where subscripts c and m refer to the crustal and mantle reservoirs, respectively. From the definitions of ε and f in (12.4.2) and (12.4.4), it is clear that we need to derive formulas for $i_c^*(t)$, $i_m^*(t)$, $i_s^*(t)$, $j_c(t)$, $j_m(t)$, and $j_s(t)$. This can be done using (12.4.7) and (12.4.8) provided we are careful to identify the amounts of the parent and daughter in the initial state of each reservoir and to measure time forward from the instant of creation of each reservoir. Prior to crustal separation all material evolves as bulk silicate Earth with an initial time $t = 0$, and the initial amounts of the parent and daughter are j_{s0} and i_{s0}^* . For the crustal and mantle source reservoirs, the initial time is $t_e - \tau_c$ (t_e is the age of the Earth) and the initial amounts of the parent and daughter are written $\langle i_c^* \rangle$, $\langle i_m^* \rangle$, $\langle j_c \rangle$ and $\langle j_m \rangle$, where the brackets indicate that a quantity is evaluated at $t = t_e - \tau_c$. The initial values of i^* and j in the crustal reservoir are represented by enrichment factors relative to the bulk silicate Earth at the time of separation:

$$D_{si} \equiv \frac{\langle i_c^* \rangle}{\langle i_s^* \rangle} = \frac{\langle i_c \rangle}{i_{s0}} \quad (12.4.13)$$

$$D_{sj} \equiv \frac{\langle j_c \rangle}{\langle j_s \rangle} \quad (12.4.14)$$

In writing (12.4.13) it has been assumed that the radiogenic and nonradiogenic isotopes have the same enrichment factors. The initial values of i^* and j in the mantle source reservoir can be related to D_{si} and D_{sj} by the application of mass conservation for the parent radionuclide and daughter species at the time of crustal separation:

$$\langle i_s^* \rangle (M_c + M_m) = \langle i_c^* \rangle M_c + \langle i_m^* \rangle M_m \quad (12.4.15)$$

$$\langle j_s \rangle (M_c + M_m) = \langle j_c \rangle M_c + \langle j_m \rangle M_m \quad (12.4.16)$$

A similar equation applies to the nonradiogenic isotope. Equations (12.4.15) and (12.4.16) can be arranged to give

$$\frac{\langle i_m^* \rangle}{\langle i_s^* \rangle} = \frac{\langle i_m \rangle}{\langle i_{s0} \rangle} = 1 - \frac{M_c}{M_m} (D_{si} - 1) \quad (12.4.17)$$

$$\frac{\langle j_m \rangle}{\langle j_s \rangle} = 1 - \frac{M_c}{M_m} (D_{sj} - 1) \quad (12.4.18)$$

where, consistent with (12.4.13), we have assumed the equality of the enrichment factors of the radiogenic and nonradiogenic isotopes in the mantle source reservoir at the time of crustal formation.

Application of (12.4.7) and (12.4.8) to the crustal and mantle reservoirs, use of the initial condition formulas (12.4.13), (12.4.14), (12.4.17), (12.4.18), and the use of the definitions of ε (12.4.2) and f (12.4.4) give the required formulas for the isotopic ratios and fractionation factors. The procedure is straightforward, but algebraically involved. The results can be

written as

$$f_c = \frac{D_{sj}}{D_{si}} - 1 \quad (12.4.19)$$

$$f_m = \left[\frac{1 - (M_c/M_m) \{D_{sj} - 1\}}{1 - (M_c/M_m) \{D_{si} - 1\}} \right] - 1 \quad (12.4.20)$$

$$\varepsilon_c = Q f_c (\tau_c - \tau) \quad (12.4.21)$$

$$\varepsilon_m = Q f_m (\tau_c - \tau) \quad (12.4.22)$$

where

$$Q = 10^4 \frac{j_{s0}}{i_{s0}^*} \lambda \quad (12.4.23)$$

and τ is the age

$$\tau \equiv t_e - t \quad (12.4.24)$$

In writing (12.4.19)–(12.4.22), a number of simplifying assumptions have been made. These mainly involve the approximation of exponential factors by linear functions of the exponents, e.g., $\exp[-\lambda(t_e - \tau)] \approx 1 - \lambda(t_e - \tau)$. Other approximations assume $(j_{s0}\lambda t_e / i_{s0}^*) \ll 1$; only the leading terms are retained in (12.4.19)–(12.4.22). Equations (12.4.19) and (12.4.20) neglect the loss of the parent due to radioactive decay since crustal formation (valid if $\lambda\tau_c \ll 1$).

By evaluating (12.4.19)–(12.4.22) at the present time $\tau = 0$ (subscript p will be used to indicate present-day values), expressions for τ_c and M_c/M_m can be obtained in terms of the measurable quantities ε_{mp} , f_{cp} , and f_{mp} :

$$\tau_c = \frac{\varepsilon_{mp}}{Q f_{mp}} \quad (12.4.25)$$

$$\frac{M_c}{M_m} = \left\{ D_{si} \left(1 - \frac{f_{cp}}{f_{mp}} \right) - 1 \right\}^{-1} \quad (12.4.26)$$

The results given in (12.4.25) and (12.4.26) are also valid for the gradual formation of the continental crust if τ_c is interpreted as the mean age at which the crust was extracted from the mantle reservoir, as will be shown later. We next evaluate these formulas for τ_c and M_c/M_m using data from the widely investigated samarium (Sm)–neodymium (Nd) and Rb–Sr systems.

12.4.3 Application of the Two-reservoir Model with Instantaneous Crustal Addition to the Sm–Nd and Rb–Sr Systems

In order to employ (12.4.25) and (12.4.26) to estimate τ_c and M_c/M_m , we first need to establish the numerical values of the composition ratios, isotope ratios, and other parameters that enter these equations. The values we need are summarized in Table 12.2. Reference values of the Sm–Nd system for the bulk silicate Earth are based on data from chondritic

meteorites (this is commonly known as a chondritic uniform reservoir, or CHUR) (Jacobsen and Wasserburg, 1980b; DePaolo, 1988). Meteorite data do not yield bulk silicate Earth values for the Rb–Sr system because the Earth is significantly depleted in these elements relative to chondritic meteorites. Allègre et al. (1983b) have specified values of μ_s and α_s for the Rb–Sr system on the basis of strontium (Sr)–neodymium (Nd) isotopic correlations. Values of $(f_{cp})_{\text{Sr}}$ and $(D_{si})_{\text{Sr}}$ cannot be estimated because of the variability of the concentrations of rubidium and strontium in the crust.

From (12.4.25) and Table 12.2 it is possible to obtain the mean age of the crustal reservoir. Substitution of the above values gives $\tau_c = 3.3$ Gyr for the Sm–Nd system and $\tau_c = 2.1$ Gyr for the Rb–Sr system. This difference in ages can be attributed either to uncertainties in the isotope parameters or to differential crustal recycling. The uncertainties in the isotope parameters, particularly $(f_{mp})_{\text{Nd}}$, are sufficiently large to explain the difference in ages. The values for mantle fractionation are somewhat better constrained for the Rb–Sr system since the degree of fractionation is larger. Thus the lower age of 2.1 Gyr is favored by most geochemists.

The above values can be compared with those given by other authors based on geological and geochemical constraints. Examples include $\tau_c = 3.5$ Gyr (Reymer and Schubert, 1984), 2.82 Gyr (Dewey and Windley, 1981), 2.70 Gyr (Allègre, 1982), 2.64 Gyr (O’Nions et al., 1979), 2.56 Gyr (McLennan and Taylor, 1982), 1.89 Gyr (Veizer and Jansen, 1979), and 1.38 Gyr (Hurley and Rand, 1969).

Assuming that $\tau_c = 2.1$ Gyr we will now determine the constraints on reservoir masses. If $\tau_c = 2.1$ Gyr and ε_{mp} (Nd) = 10 we find from (12.4.25) that $(f_{cp})_{\text{Nd}} = 0.188$, a value that is within the uncertainties given in Table 12.2. To obtain the ratio of the mass of the continental crust to the mass of the depleted mantle using (12.4.26), the Sm–Nd system must be used since $(f_{cp})_{\text{Sr}}$ is unknown. With the assumption $(f_{mp})_{\text{Nd}} = 0.188$ and the use of other values from Table 12.2, (12.4.26) gives $M_c/M_m = 0.010$. For comparison, the ratio of the mass of the crust to the mass of the entire mantle is 0.0050 ± 0.0005 and the ratio of the mass of the crust to the mass of the upper mantle (depths less than 660 km) is 0.0180 ± 0.002 . The calculated value for the mass of the mantle reservoir is intermediate between the mass of the entire mantle and the mass of the upper mantle; however, the uncertainties span both masses.

One of the major uncertainties involved in the calculation of the mass of the depleted reservoir is the value of $(D_{si})_{\text{Nd}}$. In determining this value Allègre et al. (1983b) took the mean crustal concentration of neodymium to be 29 ppm. Another point of view is given by Taylor and McLennan (1981), who argued that the lower crust is depleted in neodymium and gave a mean crustal concentration of 16 ppm. This corresponds to $(D_{si})_{\text{Nd}} = 16$ and, using this value with $(f_{cp})_{\text{Nd}} = -0.451$ and $(f_{mp})_{\text{Nd}} = 0.19$, one obtains $M_c/M_m = 0.019$. This is almost exactly the value required for layered mantle convection. Thus, generally accepted isotopic and concentration values are consistent with layered mantle convection. This correspondence is one of several results that has led many geochemists to favor layered mantle convection over whole mantle convection. The Sm–Nd and Rb–Sr results are summarized in Table 12.3.

12.4.4 A Two-reservoir Model with a Constant Rate of Crustal Growth

The instantaneous crustal growth model is clearly an oversimplification; a more realistic model considers a linear growth with time of the continental crust. In this model the mass

Table 12.3. Parameter Values (Assumed and Calculated) of the Two-reservoir Model Based on Assumed Values Given by Allègre et al. (1983b)

	Sm–Nd System	Rb–Sr System
ϵ_{mp}	10	−29
f_{mp}	0.188	−0.78
Q, Gyr^{-1}	25.3	17.7
D_{si}	16.6	20
f_{cp}	−0.451	1.42
ϵ_{cp}	−24.0	53
D_{sj}	9.1	48.4
D_{ci}	19.7	24.8
D_{cj}	9.9	114
D_{ri}	23.7	31.2
D_{rj}	10.9	376

Note: In all cases $\tau = 2.1 \text{ Gyr}$, and $M_c/M_m = 0.018$. Calculated values are italicized.

of the continental crust is given by

$$M_c = 0, \quad t_{c0} > t > 0, \quad t_e > \tau > \tau_{c0}$$

$$M_c = M_{c0} \left(\frac{t - t_{c0}}{\Delta t_c} \right), \quad t_{c0} + \Delta t_c > t > t_{c0}, \quad \tau_{c0} > \tau > \tau_{c0} - \Delta t_c \quad (12.4.27)$$

$$M_c = M_{c0}, \quad t_e > t > t_{c0} + \Delta t_c, \quad \tau_{c0} - \Delta t_c > \tau > 0$$

where t_{c0} is the time at which crustal growth began, corresponding to the age τ_{c0} ($\tau_{c0} = t_e - t_{c0}$), Δt_c is the time interval over which crustal growth occurred, and M_{c0} is the final mass of the continental crust. During the initial period $t_e > \tau > \tau_{c0}$ ($0 < t < t_{c0}$) when there is no crustal growth,

$$j_m = j_0, \quad i_m = i_0, \quad i^* = i_0^* + j_0 \lambda t \quad (12.4.28)$$

since to this order of approximation the loss of the parent isotope is negligible. During the period of crustal growth $\tau_{c0} > \tau > \tau_{c0} - \Delta t_c$ ($t_{c0} < t < t_{c0} + \Delta t_c$), the evolution of the stable isotope and the evolution of the parent and daughter isotopes in the mantle are given by

$$M_m \frac{dj_m}{dt} = -j_m \frac{M_{c0}}{\Delta t_c} D_{cj} \quad (12.4.29)$$

$$M_m \frac{di_m}{dt} = -i_m \frac{M_{c0}}{\Delta t_c} D_{ci} \quad (12.4.30)$$

$$M_m \frac{di_m^*}{dt} = -i_m^* \frac{M_{c0}}{\Delta t_c} D_{ci} + M_m j_m \lambda \quad (12.4.31)$$

In the crustal reservoir, the evolution is described by

$$M_{c0} \left(\frac{t - t_{c0}}{\Delta t_c} \right) \frac{dj_c}{dt} + \frac{M_{c0}}{\Delta t_c} j_c = D_{cj} \frac{M_{c0}}{\Delta t_c} j_m \quad (12.4.32)$$

$$M_{c0} \left(\frac{t - t_{c0}}{\Delta t_c} \right) \frac{di_c}{dt} + \frac{M_{c0}}{\Delta t_c} i_c = D_{ci} \frac{M_{c0}}{\Delta t_c} i_m \quad (12.4.33)$$

$$M_{c0} \left(\frac{t - t_{c0}}{\Delta t_c} \right) \frac{di_c^*}{dt} + \frac{M_{c0}}{\Delta t_c} i_c^* = D_{ci} \frac{M_{c0}}{\Delta t_c} i_m^* + M_{c0} \left(\frac{t - t_{c0}}{\Delta t_c} \right) \lambda j_c \quad (12.4.34)$$

The enrichment factors D_{cj} and D_{ci} used in (12.4.29)–(12.4.34) are defined by

$$D_{cj} \equiv \frac{j_c}{j_m}, \quad D_{ci} \equiv \frac{i_c}{i_m} \quad (12.4.35)$$

and it is also assumed that $i_c^*/i_m^* = D_{ci}$. The enrichment factors D_{cj} and D_{ci} are taken to be constants in time; thus, the mass added to the crust is enriched by a constant ratio relative to the mantle. Since the mantle becomes increasingly depleted with time, the concentrations in the material added to the crust decrease with time. The relationships between D_s of the previous section and D_c introduced here will be discussed below. In writing (12.4.29)–(12.4.31) the mass of the depleted mantle reservoir M_m is taken to be approximately constant in time.

Equations (12.4.29)–(12.4.34) can be integrated analytically. Though the integration is straightforward, the solutions are somewhat complicated algebraically and will not be written here. However, some simplified forms of the results will be discussed. The bulk silicate Earth enrichment factors introduced in (12.4.13) and (12.4.14) can be determined for the model of this section by evaluating the ratios at the time of completion of crustal formation $t_c + \Delta t_c$. The solution of (12.4.29)–(12.4.34) provides expressions for j_e , j_m , i_c , and i_m and the bulk silicate Earth values for i_s and j_s can be found from (12.4.15) and (12.4.16) evaluated at $t = t_c + \Delta t_c$. The result is

$$D_{ci} = -\frac{M_m}{M_{c0}} \ln \left\{ 1 - \frac{D_{si} M_{c0}}{M_m} \right\} \quad (12.4.36)$$

$$D_{cj} = -\frac{M_m}{M_{c0}} \ln \left\{ 1 - \frac{D_{sj} M_{c0}}{M_m} \right\} \quad (12.4.37)$$

where M_{c0} has been neglected in comparison with M_m . If $D_{ci} M_{c0}/M_m$ and $D_{cj} M_{c0}/M_m$ are both much less than unity, then the solution of (12.4.29)–(12.4.34) can be approximated by the formulas in Table 12.4.

12.4.5 Application of the Two-reservoir Model with Crustal Growth Linear in Time to the Sm–Nd System

We apply the results of the previous section to the Sm–Nd system using values obtained from Tables 12.2 and 12.3. The values of D_{ci} and D_{cj} calculated from (12.4.36) and (12.4.37) are given in Table 12.3. Three cases are considered: (1) $\tau_{c0} = 4.2$ Gyr and $\Delta t_c = 4.2$ Gyr, i.e., uniform growth of the continents since 4.2 Gyr before the present; (2) $\tau_{c0} = 3.1$ Gyr and $\Delta t_c = 2$ Gyr, i.e., uniform crustal growth between 3.1 Gyr and 1.1 Gyr before the present; and (3) the case considered earlier with instantaneous crustal growth at 2.1 Gyr before the

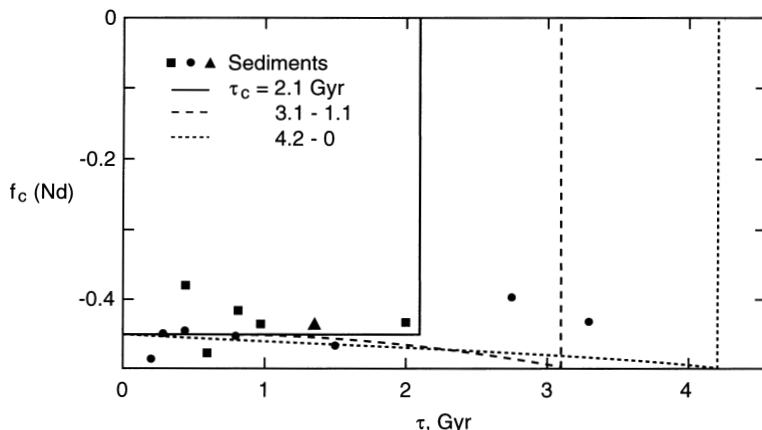


Figure 12.3. Fractionation factors (f_c)_{Nd} for the continental crust as a function of age for several models of uniform crustal growth: (1) instantaneous creation of the continental crust at $\tau_c = 2.1$ Gyr; (2) uniform accretion of the continental crust between $\tau_{c0} = 3.1$ and 1.1 Gyr; (3) uniform accretion of the continental crust between $\tau_{c0} = 4.2$ Gyr and the present. The solid circles are data for Australian shales of various ages (Allègre and Rousseau, 1984), the solid squares are British sediments (O'Nions et al., 1983), and the solid triangle is a Canadian sediment (Frost and O'Nions, 1984).

present. The dependence of the crustal fractionation factor f_c on time given in Figure 12.3 shows that f_c is nearly independent of the rate of crustal formation as predicted by the simplified formula in Table 12.4. The dependence of the mantle fractionation factor f_m on time plotted in Figure 12.4 shows that f_m increases nearly linearly during crustal formation as predicted by the simplified formula in Table 12.4. The dependence of the crustal isotope ratio ε_c on time is given in Figure 12.5. As predicted in Table 12.4, the growth of ε_c is nearly linear in time and has one-half the slope during crustal growth that it has after crustal growth is completed. The time dependence of the mantle isotope ratio ε_m is shown in Figure 12.6. The increase is nearly quadratic in time during crustal growth as predicted in Table 12.4. Since the mean age of the continents is 2.1 Gyr in each example, the present values of f_c , f_m , ε_c , and ε_m are the same as those given in Table 12.3.

The theoretical results in Figures 12.3, 12.5, and 12.6 can be compared with data on the isotope ratios and fractionation factors. Figure 12.3 includes data on continental

Table 12.4. Formulas for the Isotope Ratios and Fractionation Factors of the Two-reservoir Model with Continental Growth Linear in Time When $D_{ci} M_{c0}/M_m \ll 1$ and $D_{cj} M_{c0}/M_m \ll 1$

	$0 < t < t_{c0}$	$t_{c0} < t < t_{c0} + \Delta t_c$	$t_{c0} + \Delta t_c < t < t_e$
f_c	0	$\frac{D_{cj}}{D_{ci}} - 1$	$\frac{D_{cj}}{D_{ci}} - 1$
f_m	0	$(D_{ci} - D_{cj}) \frac{M_{c0}}{M_m} \left(\frac{t - t_{c0}}{\Delta t_c} \right)$	$(D_{ci} - D_{cj}) \frac{M_{c0}}{M_m}$
ε_c	0	$\frac{1}{2} f_c Q (t - t_{c0})$	$f_c Q (t - \frac{1}{2} \Delta t_c - t_{c0})$
ε_m	0	$\frac{1}{2} f_m Q (t - t_{c0})$	$f_m Q (t - \frac{1}{2} \Delta t_c - t_{c0})$

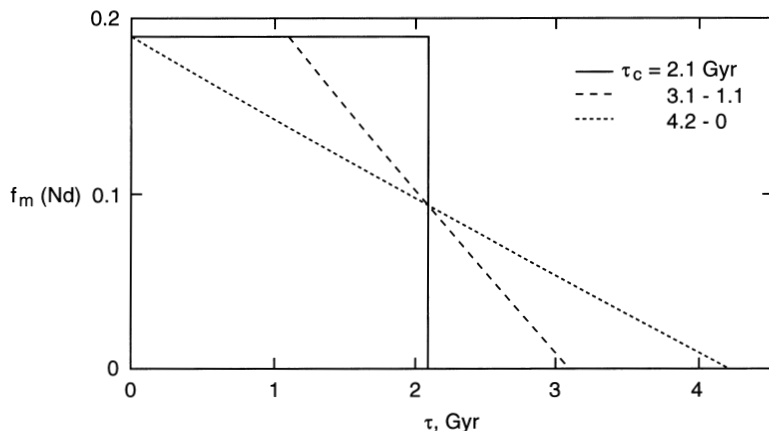


Figure 12.4. Fractionation factors (f_m)_{Nd} for the depleted mantle reservoir as a function of age for the models of uniform crustal growth given in Figure 12.3.

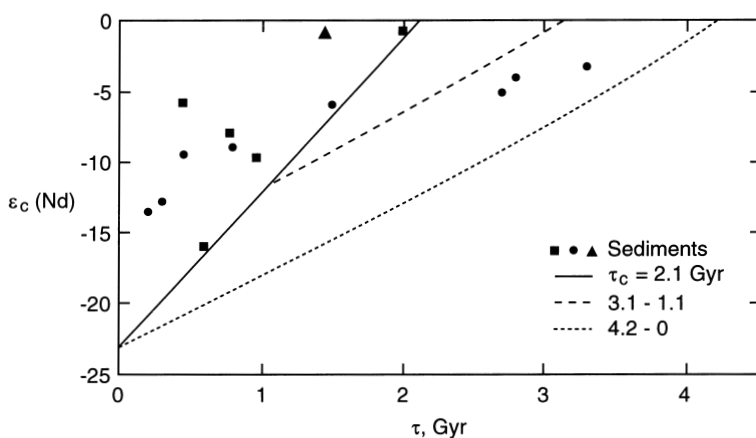


Figure 12.5. Isotopic ratios ε_c (Nd) for the continental crust as a function of age for the models of uniform crustal growth given in Figure 12.3. The solid circles, squares, and triangle represent data from the same sources as in Figure 12.3.

Sm–Nd fractionation factors for shales and sediments (Australian shales – Allègre and Rousseau, 1984; British sediments – O’Nions et al., 1983; a Canadian sediment – Frost and O’Nions, 1984). The data are consistent with (f_c) _{Nd} nearly constant in time as predicted by the theory.

Figure 12.5 includes data on Sm–Nd ε values for shales and sediments from the same sources as in Figure 12.3. Young shales have ε_c (Nd) values considerably less than the predicted value of -24 (Table 12.3), a likely consequence of erosion. Most erosion occurs in young orogenic belts; the rocks in these belts are systematically younger than average age rocks in the continental crust. Allègre and Rousseau (1984) suggested that the sedimentary ε should be corrected by a simple multiplicative factor. When this is done the linear trend of the data points in Figure 12.5 is in good agreement with the linear growth model for the continental crust.

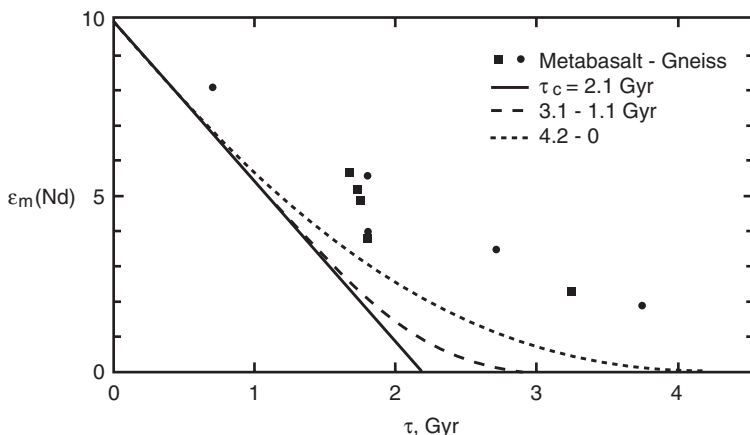


Figure 12.6. Isotopic ratios $\epsilon_m(\text{Nd})$ for the depleted mantle reservoir as a function of age for the models of uniform crustal growth given in Figure 12.3. The data are for a series of metabasalts and gneisses with various ages; the solid circles are from a compilation of data by DePaolo (1983) and the solid squares are data compiled by Nelson and DePaolo (1984).

DePaolo (1983) has argued that ϵ values for a series of metabasalts and gneisses of various ages are representative of the depleted mantle reservoir at the time they were erupted. These values and others compiled by Nelson and DePaolo (1984) are shown in Figure 12.6. The data lie significantly above the model curves for continuous growth of the continents. This is evidence that the early volume of the continents was significantly larger than any continuous growth model can give with the required mean age of 2.1 Gyr.

12.4.6 A Two-reservoir Model with Crustal Recycling

Isotope systematics can be substantially influenced if significant quantities of continental crust are recycled back into the mantle. Isotopic effects of crustal recycling have been considered by Armstrong (1968, 1969, 1981) and by Armstrong and Hein (1973). DePaolo (1983) has argued that Sm–Nd and lutetium (Lu)–hafnium (Hf) isotope systematics require substantial crustal recycling; however, this has been disputed by Patchett and Chauvel (1984). The term recycling refers to the transfer of crustal material into the depleted mantle reservoir at a subduction zone or by continental delamination.

If a significant fraction of the mass of the continents is recycled to the mantle, then recycling can reduce the mean age of the continental crust. Recycling may also influence isotopic systems even if the volume of crust recycled is small. If processes within the continental crust or in the creation of sediments or altered oceanic crust strongly concentrate either or both of the elements of the isotopic system, then significant quantities of these elements may be returned to the mantle even though the total mass recycled is small.

Crustal recycling can be accomplished by the entrainment of sediments in the subducted crust, by the erosion of the overlying continental crust during the subduction process, or by the inclusion of the lower continental crust in the delamination of the continental lithosphere. Quantitative estimates of these processes are difficult to carry out. This section presents a simplified model in which the recycled material has the mean crustal concentrations j_c , i_c^* , and i_c . Mass is added to the continental crust at the same rate that the crust is recycled into

the mantle so that the mass of the continental crust is a constant. The objective of this model is to illustrate the influence of crustal recycling.

For this purpose, recycling enrichment ratios D_{ri} and D_{rj} are introduced in such a way that

$$j_c = D_{rj} j_m \quad (12.4.38)$$

$$i_c = D_{ri} i_m \quad (12.4.39)$$

The continental crust is instantaneously created at time τ_c before the present (with concentrations i_c and j_c) and then recycled back into the mantle at a constant rate \dot{M}_c given by

$$\dot{M}_c = \frac{M_c}{\tau_r} \quad (12.4.40)$$

The recycling time τ_r is the time required to recycle the entire continental crust into the mantle. The mass of the crust M_c is held constant so that material is added to the continental crust at the same rate \dot{M}_c that it is recycled. In this model the material added to the continental crust has the concentrations of i_c and j_c . Consistent with previous approximations, the effects of isotopic decay on j are neglected. Thus the mass being added to the continents has the same concentrations of i and j as the recycled material. The concentrations j_m , j_c , i_m , and i_c are independent of time and follow from mass balances of the form $M_m j_m + M_c j_c = (M_m + M_c) j_s$:

$$j_m = \frac{j_s}{1 + (M_c D_{rj} / M_m)} \quad (12.4.41)$$

$$i_m = \frac{i_s}{1 + (M_c D_{ri} / M_m)} \quad (12.4.42)$$

$$j_c = \frac{D_{rj} j_s}{1 + (M_c D_{rj} / M_m)} \quad (12.4.43)$$

$$i_c = \frac{D_{ri} i_s}{1 + (M_c D_{ri} / M_m)} \quad (12.4.44)$$

where again M_c has been neglected compared with M_m . Comparison of (12.4.43) and (12.4.44) with (12.4.17) and (12.4.18) shows that the recycling enrichment factors can be related to the enrichment factors for instantaneous crustal extraction from the bulk silicate Earth by

$$D_{ri} = \frac{D_{si}}{1 - (M_c / M_m) D_{si}} \quad (12.4.45)$$

$$D_{rj} = \frac{D_{sj}}{1 - (M_c / M_m) D_{sj}} \quad (12.4.46)$$

The fractionation factors are also independent of time and are given by substitution of (12.4.41)–(12.4.44) into (12.4.3):

$$f_m = \frac{(M_c / M_m) (D_{ri} - D_{rj})}{1 + (M_c D_{rj} / M_m)} \quad (12.4.47)$$

$$f_c = \frac{(D_{rj} - D_{ri}) / D_{ri}}{1 + (M_c D_{rj} / M_m)} \quad (12.4.48)$$

Although the concentrations of the parent and reference isotopes are constant to the order of approximation considered, the concentrations of the daughter isotope are not. The equations that govern the evolution of the daughter isotope in the crustal and mantle reservoirs are, by analogy with (12.4.31) and (12.4.34),

$$M_m \frac{di_m^*}{dt} = -i_m^* D_{ri} \frac{M_c}{\tau_r} + i_c^* \frac{M_c}{\tau_r} + M_m \lambda j_m \quad (12.4.49)$$

$$M_c \frac{di_c^*}{dt} = i_m^* D_{ri} \frac{M_c}{\tau_r} - i_c^* \frac{M_c}{\tau_r} + M_c \lambda j_c \quad (12.4.50)$$

where it has been assumed that $i_c^* = D_{ri} i_m^*$. These equations include the transfer of the daughter isotope between the reservoirs and the production within the reservoirs. Analytic solutions of these equations are readily obtainable by integration after taking j_m and j_c from (12.4.41) and (12.4.43). If $D_{ri} M_c / M_m \ll 1$ and $D_{rj} M_c / M_m \ll 1$, the exact solutions simplify to

$$\varepsilon_m = Q \tau_r (D_{ri} - D_{rj}) \frac{M_c}{M_m} \left[1 - \exp\left(-\frac{(\tau_c - \tau)}{\tau_r}\right) \right] \quad (12.4.51)$$

$$\varepsilon_c = Q \tau_r \left(\frac{D_{rj}}{D_{ri}} - 1 \right) \left[1 - \exp\left(-\frac{(\tau_c - \tau)}{\tau_r}\right) \right] \quad (12.4.52)$$

12.4.7 Application of the Two-reservoir Model with Crustal Recycling to the Sm–Nd System

We apply the above recycling model to the Sm–Nd system. Relevant parameters are given in Table 12.3 which also lists the values for D_{ri} and D_{rj} obtained from (12.4.45) and (12.4.46). Two examples of recycling are considered: $\tau_c = 4.2$ Gyr and $\tau_r = 3.65$ Gyr, and $\tau_c = 3.15$ Gyr and $\tau_r = 5.00$ Gyr. The recycling times are chosen so that the mean age of the continents is 2.1 Gyr in each case. The case $\tau_c = 2.1$ Gyr and no recycling is considered for comparison. The dependence of ε_c and ε_m on time are shown in Figures 12.7 and 12.8, respectively. In all cases the present values are the same since the equivalent mean ages of the continental reservoir are the same, i.e., 2.1 Gyr. In all cases $f_c = -0.45$ and $f_m = 0.19$ are independent of time since the initial formation of the continental crust.

The data in Figure 12.7 are the same as the $\varepsilon_c(\text{Nd})$ data shown in Figure 12.5. It was noted in the discussion of Figure 12.5 that the data would be reconciled with a continuous crustal growth model if account were taken of erosion. Figure 12.7 shows that the addition of crustal recycling does nothing to improve the fit of models with data.

The $\varepsilon_m(\text{Nd})$ data of Figure 12.6 are also included in Figure 12.8. It was noted in the discussion of Figure 12.6 that the data implied an early continental crustal volume larger than could be reconciled with continuous crustal growth (with a mean $\tau_c = 2.1$ Gyr) and no recycling. Figure 12.8 shows that the data lie within the range predicted by these recycling models. Significant recycling is required to explain the high initial isotope ratios of the rocks. This is the same conclusion given by DePaolo (1983); however, this conclusion was strongly attacked by Patchett and Chauvel (1984) on the grounds that the same effect could be achieved by diluting the depleted mantle with undepleted mantle material.

The crustal fractionation factor f_c in the recycling model is nearly constant, as shown by (12.4.48). This is in agreement with the data in Figure 12.3; thus, the observations do not distinguish between the continuous growth and the recycling models. However, the

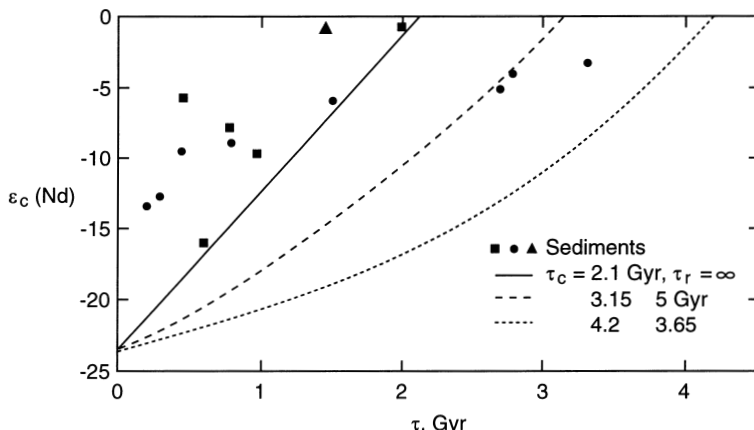


Figure 12.7. Isotopic ratios $\varepsilon_c(\text{Nd})$ for the continental crust as a function of age for several models of crustal recycling: (1) instantaneous creation of the continental crust at $\tau_c = 2.1 \text{ Gyr}$; (2) instantaneous creation of the continental crust at $\tau_c = 3.15 \text{ Gyr}$ followed by crustal recycling with a recycling time $\tau_r = 5.0 \text{ Gyr}$; (3) instantaneous creation of the continental crust at $\tau_c = 4.2 \text{ Gyr}$ followed by crustal recycling with a recycling time $\tau_r = 3.65 \text{ Gyr}$.

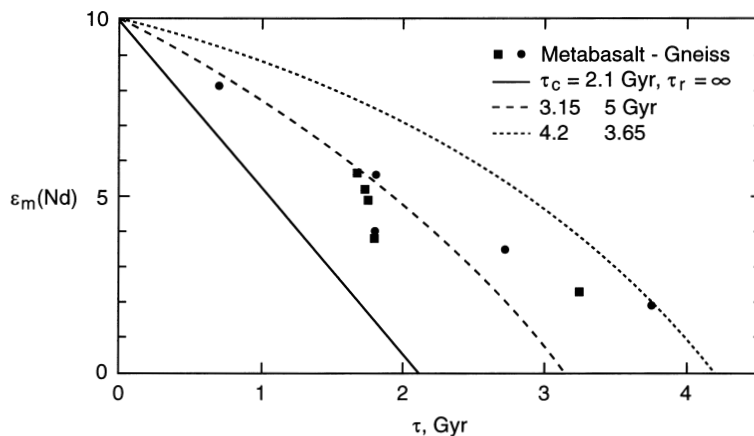


Figure 12.8. Isotopic ratios $\varepsilon_m(\text{Nd})$ for the depleted mantle reservoir as a function of age for the models of crustal recycling given in Figure 12.7. The data are from the sources given in Figure 12.6.

near constancy of the observations has two important implications. First, the processes leading to the enrichment of the continental crust were the same in the Archean as they are today. Second, the observations argue against recycling of significant amounts of continental crust with a different mean fractionation ratio than the current mean continental value. The mantle fractionation factor is significantly different for the two models (see (12.4.47) and Figure 12.4). However, as discussed earlier, the mantle Sm–Nd fractionation factor is so small that all data are suspect.

Phanerozoic rates of crustal growth and crustal recycling have been studied by Reymer and Schubert (1984). Their preferred volume rate for the addition of new continental crust

is $1.65 \text{ km}^3 \text{ yr}^{-1}$ and their preferred value for the rate of crustal recycling is $0.59 \text{ km}^3 \text{ yr}^{-1}$; these give a net crustal growth rate of about $1 \text{ km}^3 \text{ yr}^{-1}$; Kay (1980) used balance studies of K, Rb, Ba and other trace elements in arc magmas to estimate the current net rate of growth of the continents at $0.91 \text{ km}^3 \text{ yr}^{-1}$. This is roughly half the mean rate required to produce a continental crust with a mean age of 4.2 Gyr. He also pointed out that much of the continental material which is subducted at trenches may be cycled back to the crust via arc volcanism. The complex processes of erosion, subduction, and melting have been dominant features in the chemical evolution of the continental crust. The K mass balances suggest that the mechanisms for formation of the continents may have evolved through time.

The model presented in the previous section for linear crustal growth from $\tau = 4.2 \text{ Gyr}$ to the present requires a rate of crustal growth of $2.3 \text{ km}^3 \text{ yr}^{-1}$ (assuming $\rho_c = 2,750 \text{ kg m}^{-3}$), roughly double the growth rate estimates for the Phanerozoic and the present given above. The crustal recycling model with $\tau_c = 4.2 \text{ Gyr}$ and $\tau_r = 3.65 \text{ Gyr}$ requires that the rates of crustal addition and subtraction be $1.95 \text{ km}^3 \text{ yr}^{-1}$ (no crustal growth). These values compare to recycling rates of $2(\pm 1) \text{ km}^3 \text{ yr}^{-1}$ given by Armstrong (1981) and $2.5(\pm 1.2) \text{ km}^3 \text{ yr}^{-1}$ given by DePaolo (1983) which are significantly larger than the estimate of about $0.6 \text{ km}^3 \text{ yr}^{-1}$ given by Reymer and Schubert (1984). Studies of geochemical cycles and reservoirs clearly require large rates for crustal addition and possibly recycling during the last 2 Gyr.

12.5 Uranium, Thorium, Lead Systems

The uranium (U)-thorium (Th)-lead (Pb) isotope system also provides important constraints on the evolution of the Earth. This system has the advantage that two different uranium isotopes decay to two different lead isotopes with different decay constants (Table 12.1). The system has the disadvantage that the elements are active chemically and the parent and daughter elements behave quite differently. Some of the available data have been reviewed by Sun (1980).

12.5.1 Lead Isotope Systematics

For the U-Th-Pb isotopic system, the radioactive parent isotopes are ^{238}U , ^{235}U , and ^{232}Th with mole densities j , j' , and j'' . The radioactive daughter isotopes are ^{206}Pb , ^{207}Pb , and ^{208}Pb with mole densities i^* , i^{**} , and i^{***} . The nonradiogenic reference isotope is ^{204}Pb with a mole density i . The decay constants are denoted by λ , λ' , and λ'' .

The U-Th-Pb system is commonly discussed in terms of the composition ratios

$$\mu = \frac{j}{i}, \quad v = \frac{j'}{j}, \quad \kappa = \frac{j''}{j} \quad (12.5.1)$$

and the isotope ratios

$$\alpha = \frac{i^*}{i}, \quad \beta = \frac{i^{**}}{i}, \quad \gamma = \frac{i^{***}}{i} \quad (12.5.2)$$

The time evolution of a closed system is given by equations analogous to (12.4.7), (12.4.8), and (12.4.11):

$$\alpha = \mu_0 (1 - e^{-\lambda t}) + \alpha_0 \quad (12.5.3)$$

$$\beta = v_0 \mu_0 (1 - e^{-\lambda' t}) + \beta_0 \quad (12.5.4)$$

$$\gamma = \kappa_0 \mu_0 (1 - e^{-\lambda'' t}) + \gamma_0 \quad (12.5.5)$$

$$\mu = \mu_0 e^{-\lambda t} \quad (12.5.6)$$

$$v = v_0 e^{(\lambda - \lambda')t} \quad (12.5.7)$$

$$\kappa = \kappa_0 e^{(\lambda - \lambda'')t} \quad (12.5.8)$$

where α_0 , β_0 , and γ_0 are initial values of the isotope ratios and μ_0 , v_0 , and κ_0 are initial values of the composition ratios. It is not appropriate to use the linear approximation of the exponentials for the decay of the uranium isotopes because of the relatively large values of the decay constants (Table 12.1).

Initial values for the lead isotope ratios have been obtained from studies of iron meteorites (Tatsumoto et al., 1973). Virtually no uranium or thorium is present in these meteorites so that the measured values are taken to be primeval; these are $\alpha_0 = 9.307$, $\beta_0 = 10.294$, and $\gamma_0 = 29.476$. Initial values of the composition ratios μ_0 , v_0 , and κ_0 are related to the composition ratios of the present bulk silicate Earth μ_{sp} , v_{sp} , and κ_{sp} (assumed to have evolved as a closed system) by

$$\mu_{sp} = \mu_0 e^{-\lambda t_e} \quad (12.5.9)$$

$$v_{sp} = v_0 e^{(\lambda - \lambda')t_e} = \frac{1}{137.8} \quad (12.5.10)$$

$$\kappa_{sp} = \kappa_0 e^{(\lambda - \lambda'')t_e} \quad (12.5.11)$$

since the present uranium isotope ratio is $v_{sp} = j'_{sp}/j_{sp} = 1/137.8$ ($v_0 = 1/3.16$). The present lead isotope ratios for the bulk silicate Earth are

$$\alpha_{sp} = \mu_{sp} (e^{\lambda t_e} - 1) + 9.307 \quad (12.5.12)$$

$$\beta_{sp} = \frac{\mu_{sp}}{137.8} (e^{\lambda' t_e} - 1) + 10.294 \quad (12.5.13)$$

$$\gamma_{sp} = \mu_{sp} \kappa_{sp} (e^{\lambda'' t_e} - 1) + 29.476 \quad (12.5.14)$$

This is known as the Holmes–Houtermans model based on independent derivations by Holmes (1946) and Houtermans (1946).

Elimination of μ_{sp} from (12.5.12) and (12.5.13) gives

$$\frac{\beta_{sp} - 10.294}{\alpha_{sp} - 9.307} = \frac{1}{137.8} \left(\frac{e^{\lambda' t_e} - 1}{e^{\lambda t_e} - 1} \right) \quad (12.5.15)$$

Data for α_{sp} and β_{sp} from several meteorites (Patterson, 1956) are given in Figure 12.9. The data give an age $\tau_e = 4.55$ Gyr which is believed to represent the age of the solar system.

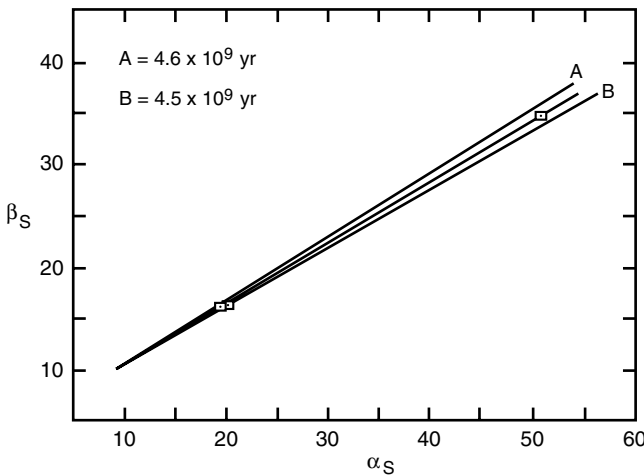


Figure 12.9. Lead isotope ratios for several iron and stony meteorites (Patterson, 1956). Three isochrons are given from (12.5.15); the best agreement is with 4.55 Gyr and this is taken to be the age of the solar system and is known as the geochron.

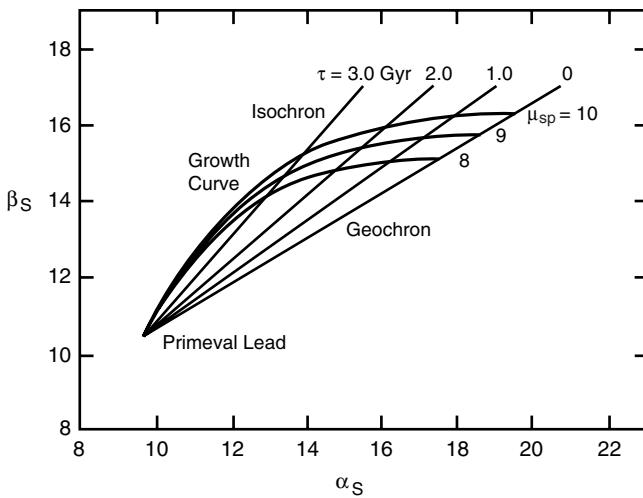


Figure 12.10. Growth curves for the lead isotopic ratios α and β are given for several values of the present U-Pb ratio μ_{sp} . Geochrons are shown for several ages τ .

The evolution of primeval lead in a closed system is illustrated in Figure 12.10. The isotope ratios β_S and α_S follow the growth curves given by (12.5.3) and (12.5.4); results are given for present uranium(U)-lead (Pb) ratios $\mu_{sp} = 8, 9, 10$. At the present time the growth curves of the closed system lie on the geochron, in the past the growth curves lay on the isochrons shown for $\tau = 1, 2, 3$ Gyr.

In order for lead to lie on a growth curve, it must have been a closed system for the age of the Earth. Some galena (PbS) deposits have been found that satisfy this condition. These deposits are associated with sediments and volcanics in greenstone belts and island arcs

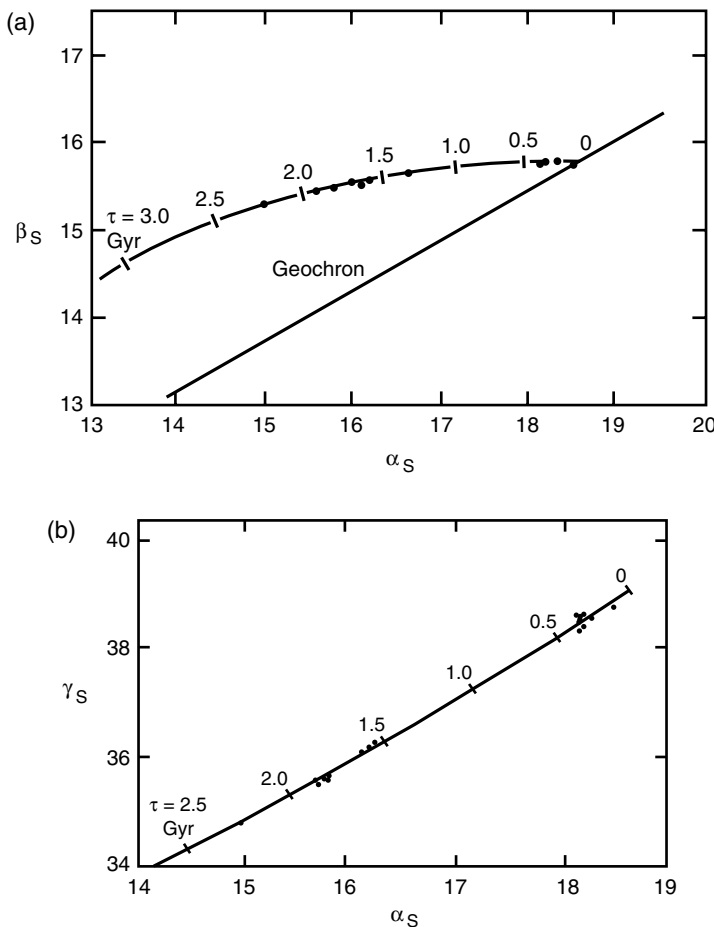


Figure 12.11. Lead isotope ratios α , β , and γ are given by the solid circles for several “conformable” lead deposits (Kanasewich, 1968). In (a) the uranium daughter isotopes correlate well with the growth curve corresponding to $\mu_{sp} = 9$. In (b) the thorium and uranium daughter isotopes correlate well with the growth curve taking $\kappa_{sp} = 4.21$ as well as $\mu_{sp} = 9$.

that are conformable with the host rocks (in contrast to cross-cutting veins). Thus, they are known as conformable lead deposits.

Lead isotope data for several “conformable” lead deposits are given in Figure 12.11 (Kanasewich, 1968). The β_S - α_S data in Figure 12.11a correlate well with the growth curve corresponding to $\mu_{sp} = 9$. The γ_S - β_S data in Figure 12.11b also correlate well with a growth curve taking $\kappa_{sp} = 4.21$ as well as $\mu_{sp} = 9$. It should be emphasized that “conformable” lead deposits are defined to be those that lie on a growth curve. Most lead deposits appear to have been derived from source regions which have generated excess radiogenic lead. This is also the case for the lead isotopes in both MORB and OIB as will be shown.

In studying U-Th-Pb systematics it is convenient to introduce the ratio of the radiogenic components of the daughter isotopes ^{208}Pb and ^{206}Pb defined by

$$\alpha^* \equiv \frac{\gamma - \gamma_0}{\alpha - \alpha_0} \quad (12.5.16)$$

From (12.5.12) and (12.5.14) we obtain

$$\alpha_{sp}^* = \kappa_{sp} \left(\frac{e^{\lambda'' t_e} - 1}{e^{\lambda t_e} - 1} \right) \quad (12.5.17)$$

We will now apply these results to our two-reservoir model.

12.5.2 Application to the Instantaneous Crustal Differentiation Model

The U–Th–Pb system can be studied in the context of the instantaneous crustal differentiation model. Similar extraction models have been considered by Armstrong (1968, 1969), Russell (1972), Cumming and Richards (1975), Stacey and Kramers (1975), and Zartman and Doe (1981).

At $t = t_e - \tau_c$, (12.5.3) – (12.5.8) give

$$\alpha_{sc} = \mu_0 \left(1 - e^{-\lambda(t_e - \tau_c)} \right) + \alpha_0 \quad (12.5.18)$$

$$\beta_{sc} = \mu_0 v_0 \left(1 - e^{-\lambda'(t_e - \tau_c)} \right) + \beta_0 \quad (12.5.19)$$

$$\gamma_{sc} = \mu_0 \kappa_0 \left(1 - e^{-\lambda''(t_e - \tau_c)} \right) + \gamma_0 \quad (12.5.20)$$

$$\mu_{sc} = \mu_0 e^{-\lambda(t_e - \tau_c)} \quad (12.5.21)$$

$$v_{sc} = v_0 e^{(\lambda - \lambda')(t_e - \tau_c)} \quad (12.5.22)$$

$$\kappa_{sc} = \kappa_0 e^{(\lambda - \lambda'')(t_e - \tau_c)} \quad (12.5.23)$$

Only the composition ratios μ and κ change when the crust is formed since α , β , γ , and v are isotope ratios. From (12.4.3) and (12.4.13), (12.4.14), and (12.4.20) the changes in μ and κ are related to the mean enrichment factors by

$$\frac{\mu_{c0}}{\mu_{sc}} = \frac{j_{c0} i_{sc}}{i_{c0} j_{sc}} = \frac{D_{sj}}{D_{si}} \quad (12.5.24)$$

$$\frac{\mu_{m0}}{\mu_{sc}} = \frac{1 - (M_c/M_m)(D_{sj} - 1)}{1 - (M_c/M_m)(D_{si} - 1)} \equiv \xi \quad (12.5.25)$$

$$\frac{\kappa_{c0}}{\kappa_{sc}} = \frac{j''_{c0} j_{sc}}{j_{c0} j''_{sc}} = \frac{D''_{sj}}{D_{sj}} \quad (12.5.26)$$

$$\frac{\kappa_{m0}}{\kappa_{sc}} = \frac{1 - (M_c/M_m)(D''_{sj} - 1)}{1 - (M_c/M_m)(D_{sj} - 1)} \equiv \frac{\xi''}{\xi} \quad (12.5.27)$$

where μ_{c0} , κ_{c0} , μ_{m0} , and κ_{m0} are the ratios for the enriched crust and depleted mantle, respectively, at the time of formation of the crust and D''_{sj} is defined similar to D_{sj} in (12.4.14). Formulas for the present lead isotope ratios of the crust and mantle can be found

by careful manipulation of the above equations

$$\alpha_{cp} = \mu_{sp} \left[e^{\lambda t_e} - e^{\lambda \tau_c} + \frac{D_{sj}}{D_{si}} (e^{\lambda \tau_c} - 1) \right] + \alpha_0 \quad (12.5.28)$$

$$\beta_{cp} = \frac{\mu_{sp}}{137.8} \left[e^{\lambda' t_e} - e^{\lambda' \tau_c} + \frac{D_{sj}}{D_{si}} (e^{\lambda' \tau_c} - 1) \right] + \beta_0 \quad (12.5.29)$$

$$\gamma_{cp} = \kappa_{sp} \mu_{sp} \left[e^{\lambda'' t_e} - e^{\lambda'' \tau_c} + \frac{D''_{sj}}{D_{si}} (e^{\lambda'' \tau_c} - 1) \right] + \gamma_0 \quad (12.5.30)$$

$$\alpha_{mp} = \mu_{sp} [e^{\lambda t_e} - e^{\lambda \tau_c} + \xi (e^{\lambda \tau_c} - 1)] + \alpha_0 \quad (12.5.31)$$

$$\beta_{mp} = \frac{\mu_{sp}}{137.8} [e^{\lambda' t_e} - e^{\lambda' \tau_c} + \xi (e^{\lambda' \tau_c} - 1)] + \beta_0 \quad (12.5.32)$$

$$\gamma_{mp} = \kappa_{sp} \mu_{sp} [e^{\lambda'' t_e} - e^{\lambda'' \tau_c} + \xi'' (e^{\lambda'' \tau_c} - 1)] + \gamma_0 \quad (12.5.33)$$

where (12.5.9)–(12.5.11) have been used to introduce present bulk silicate Earth values.

From (12.5.16), (12.5.28), (12.5.30), (12.5.31), and (12.5.33), the present crust and mantle values of α^* are given by

$$\alpha_{cp}^* = \kappa_{sp} \frac{e^{\lambda'' t_e} - e^{\lambda'' \tau_c} + (D''_{sj}/D_{si}) (e^{\lambda'' \tau_c} - 1)}{e^{\lambda t_e} - e^{\lambda \tau_c} + (D_{sj}/D_{si}) (e^{\lambda \tau_c} - 1)} \quad (12.5.34)$$

$$\alpha_{mp}^* = \kappa_{sp} \frac{e^{\lambda'' t_e} - e^{\lambda'' \tau_c} + \xi'' (e^{\lambda'' \tau_c} - 1)}{e^{\lambda t_e} - e^{\lambda \tau_c} + \xi (e^{\lambda \tau_c} - 1)} \quad (12.5.35)$$

These lead isotope results for instantaneous crustal differentiation are compared below with MORB data. The MORB isotope data are taken to be representative of the depleted mantle reservoir.

The envelope for the dependence of β_{mp} on α_{mp} for the lead isotope data from MORB (White, 1985) is shown in Figure 12.12. The geochron from (12.5.12) and (12.5.13) is shown for $t_e = 4.55$ Gyr. For the bulk silicate Earth, $\mu_{sp} = 8.05$ is a preferred value. The point on the geochron corresponding to this U–Pb ratio is illustrated in Figure 12.12. This model assumes that lead was preferentially segregated into the continental crust at a time τ_c ago. Thus ξ , defined by (12.5.25), is greater than 1 since D_{si} is larger than D_{sj} . The magnitude of ξ is a measure of the degree of preferential segregation.

The lead isotope data for MORB are assumed to reflect the isotopic state of the depleted mantle reservoir. The dependence of β_{mp} on α_{mp} for $\tau_c = 1, 2$, and 3 Gyr is given by the solid lines in Figure 12.12. The distance from the geochron increases as ξ increases. Values corresponding to $\xi = 1.5, 2.0$, and 2.5 are illustrated by the dotted lines. The MORB field can be explained by a crustal segregation age τ_c between about 1.5 and 2.0 Gyr and values of ξ_c between 1.0 and about 2.0. The mean age of the continental crust inferred from the model and the lead isotope data from MORB is about 1.7 Gyr. With $\xi = 1.5$, $D_{sj} = 32$ and $M_c/M_m = 0.018$, (12.5.25) gives $D_{si} = 71$; thus, lead must be strongly fractionated into the continental crust.

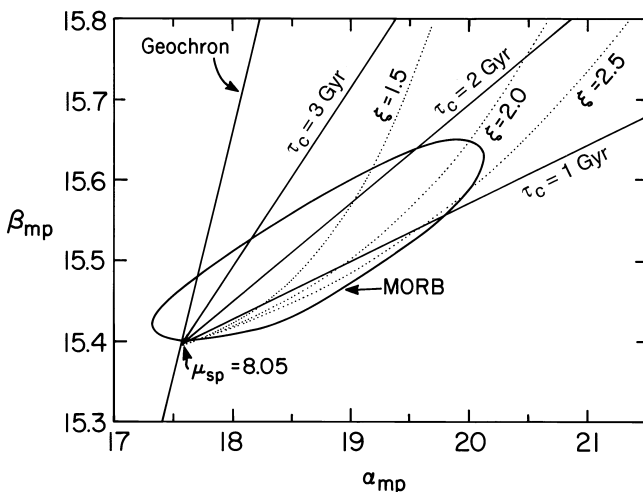


Figure 12.12. Predicted values of the lead isotope ratios for the depleted mantle based on a model of instantaneous crustal formation. The geochron for the present bulk silicate Earth from (12.5.12) and (12.5.13) is shown. The U-Pb composition ratio from the bulk silicate Earth is assumed to be $\mu_{sp} = 8.05$. The isotope ratios for the depleted mantle from (12.5.31) and (12.5.32) are given for various ages τ_c of crustal formation by the solid lines. The distance from the geochron increases with increased removal of lead from the mantle. The intersections of the dotted lines with the solid lines give the required values of ξ . The field for lead data obtained from MORB (White, 1985) is also included.

The model for MORB lead based on instantaneous crustal formation requires the removal of lead. The upper continental crust is not enriched in lead relative to uranium, however, and thus there is no direct evidence that the continental crust serves as the complementary lead-enriched reservoir. This lack of an obvious lead-enriched reservoir has become known as the missing lead paradox. The missing lead might reside in the lower continental crust (Doe and Zartman, 1979; O’Nions and Hamilton, 1981) or in the core (Vollmer, 1977). Since the mean age of extraction from the mantle of the missing lead is between 1.5 and 2 Gyr, and since the age of core formation is about 4.4 Gyr, the core is unlikely to be the reservoir of the missing lead. It has been suggested that there is excess lead in the lower crust, but this has not been established with any degree of confidence. The age of extraction of lead, ≈ 1.7 Gyr, is less than the age of extraction associated with the Rb-Sr system, ≈ 2.1 Gyr. As was discussed above, however, this difference can be accounted for by preferential recycling of either the parent or daughter elements.

Because of the relative fractionation of thorium and uranium into basalts, direct measurements of κ_p have been suspect. Data on the isotope ratio $^{230}\text{Th}/^{232}\text{Th}$ can be used to infer the value of κ_p in the source region for the basalts. Data obtained on MORB and OIB by Allègre et al. (1986) using this technique are shown in Figure 12.13. The geochron obtained from (12.5.12), (12.5.14), and (12.5.16) is also included in this figure. The OIB data fall between the MORB data and a point on the geochron; this trend can be interpreted as a mixing line with the OIB composed of a MORB component with $\kappa_{mp} = 2.5 \pm 0.2$ and a pristine component with $\kappa_{sp} = 4.2 \pm 0.2$. This mixing trend can be taken as further geochemical evidence for the existence of a nearly pristine (lower mantle) reservoir as well as a depleted (upper mantle) reservoir.

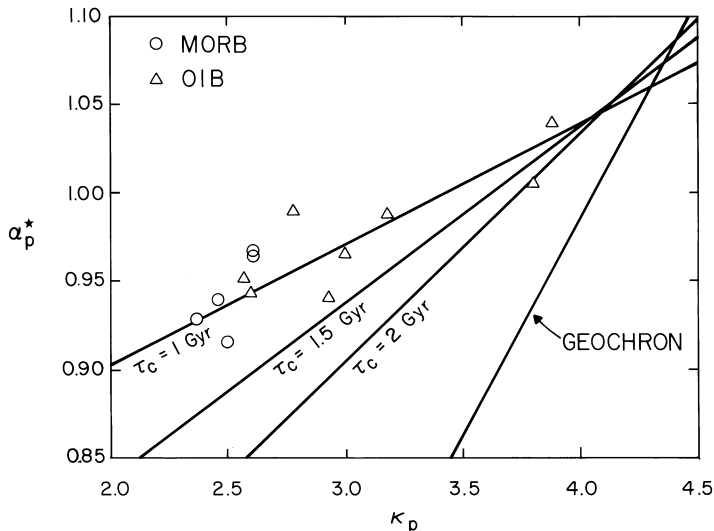


Figure 12.13. Predicted values of the lead isotope ratio α_p^* for MORB and OIB as a function of the present Th–U ratio κ_p based on a model of instantaneous crustal formation. The geochron for the bulk silicate Earth from (12.5.12), (12.5.14), and (12.5.16) is given. The modern Th–U ratio for the bulk silicate Earth is assumed to be $\kappa_{sp} = 4.2$. The isotope ratios for the depleted mantle from (12.5.35) are given for various ages of crustal formation τ_c by the solid lines. Calculations were made assuming $\xi = 1.5$. The distance from the geochron increases with increasing ξ'' . The data points for MORB and OIB are from Allègre et al. (1986).

Also given in Figure 12.13 are the results from the instantaneous crustal formation model, assuming that thorium was preferentially segregated into the continental crust at a time τ_c ago. Equation (12.5.35) gives the value of α_{mp}^* for $\tau_c = 1, 1.5$, and 2 Gyr. The value $\kappa_{sp} = 4.2$ is consistent with the mixing line trend of the data. The previous study of the uranium system gives $\xi = 1.5$. Various values of ξ'' correspond to the various values of κ_{mp} given by

$$\kappa_{mp} = \frac{\xi''}{\xi} \kappa_{sp} \quad (12.5.36)$$

With a crustal extraction age of 2 Gyr, the mantle cannot produce enough ^{208}Pb to reach the MORB values of α^* . Reasonably good agreement with the data is obtained if a crustal extraction age $\tau_c = 1$ Gyr is taken. Thus the thorium (Th)–uranium (U) system requires a much younger crustal extraction age than the isotope systems discussed previously.

Galer and O’Nions (1985, 1986) assumed that $\kappa_{sp} = 3.85$ and concluded that the residence time of thorium in the depleted mantle reservoir is less than 600 Myr. These authors attributed the short residence time to transport of thorium from the lower mantle to the upper mantle. An alternative explanation for the young age is the preferential recycling of either the parent or daughter elements from the crust to the depleted mantle reservoir. Collerson and Kamber (1999) have presented data on the time evolution of κ_m . They conclude that κ_m systematically decreases from a value $\kappa_m \approx 4$ at 3 Ga to the value $\kappa_{mp} \approx 2.5$ today. They attribute this decrease to the preferential recycling into the mantle of uranium relative to thorium at subduction zones. The preferential recycling is attributed to an oxidizing atmosphere and hydrosphere.

It has been established that the nearly homogeneous MORB source reservoir has a Th–U ratio $\kappa_{mp} = 2.5 \pm 0.2$. If this ratio is applicable to the whole mantle and if the bulk Earth Th–U ratio is $\kappa_{sp} \approx 4$, then the Th–U ratio for the continental crust must be $\kappa_{cp} \approx 12$. This is much higher than estimates of κ_{cp} which generally lie in the range $\kappa_{cp} = 4\text{--}5$. A uniform mantle value of κ_{mp} equal to 2.5 ± 0.2 leads to an extreme missing thorium paradox. Alternatives are to assume either that the mantle is vertically stratified in κ_{mp} or that there is a pristine lower mantle reservoir with $\kappa_m \approx 4$.

12.6 Noble Gas Systems

In this section we consider isotopic systems that produce the rare gases helium, argon, and xenon. As shown in Table 12.5, the heat producing decay of ^{238}U , ^{235}U , and ^{232}Th generates ^4He and the heat producing decay of ^{40}K generates ^{40}Ar . Thus, the rate of production of these rare gas isotopes can be related to the rates of heat generation in the mantle and crust. The rare gas systems have both advantages and disadvantages when used in reservoir modeling (Allègre et al., 1983c). The gases (particularly helium) have high diffusion rates in the mantle and therefore migrate readily. Thus, measured concentrations must be treated with considerable care; however, the high mobility leads to high rates of mantle degassing, and measurements on concentrations and fluxes in the oceans and the atmosphere can be interpreted to provide insights into rates of production and transport in the mantle. Care must also be taken with concentration measurements of the heavy rare gases, i.e., argon and xenon, because of atmospheric contamination. This is not such a serious problem with helium, however, because atmospheric concentrations are low.

Rare gas observations on MORB and OIB can also be interpreted in terms of a “primitive” signature. The Earth’s mantle (and presumably the core) was extensively outgassed during accretion. High concentrations of nonradiogenic rare gas isotopes ^3He , ^{36}Ar are taken as evidence for a primitive mantle (or core) reservoir that was less extensively outgassed. Many studies of these systems have been carried out for the Earth, e.g., Turekian (1959), Ozima (1975), O’Nions and Oxburgh (1983), Mamyrin and Tolstikhin (1984), Sarda et al. (1985), Allègre et al. (1987), Oxburgh and O’Nions (1987), Zhang and Zindler (1989), Porcelli and Wasserburg (1995), and Hanan and Graham (1996). Turcotte and Schubert (1988) studied the implications of radiogenic noble gases in planetary atmospheres. Rare gas systematics have been reviewed by Ozima (1994), Farley and Neroda (1998), and McDougall and Honda (1998).

Table 12.5. Isotope Decay Reactions That Produce Rare Gases and the Associated Decay Constants (Allègre et al., 1987)

Isotopic Reaction	Decay Constant λ (Gyr $^{-1}$)	Half-life
		$\tau_{1/2}$ (Gyr)
$^{238}\text{U} \rightarrow ^{206}\text{Pb} + ^4\text{He}$	1.551×10^{-1}	4.469
$^{235}\text{U} \rightarrow ^{207}\text{Pb} + ^4\text{He}$	9.849×10^{-1}	0.7038
$^{232}\text{Th} \rightarrow ^{208}\text{Pb} + ^4\text{He}$	4.948×10^{-2}	14.009
$^{40}\text{K} \rightarrow ^{40}\text{Ar}$	5.81×10^{-2}	11.93
$(^{40}\text{K} \rightarrow ^{40}\text{Ar}, ^{40}\text{Ca})$	(5.543×10^{-1})	(1.2505)
$^{129}\text{I} \rightarrow ^{129}\text{Xe}$	41	0.01691

12.6.1 Helium

The total content of ^{40}Ar in the atmosphere is attributed to volcanic degassing of the Earth's interior. While global balances of ^{40}Ar can be carried out, it is not possible to do the same for ^4He because of the relatively rapid loss of this light constituent from the atmosphere. Instead, studies of ^4He require determinations of the fluxes of ^4He among the mantle, ocean, and atmosphere reservoirs. Measurements of helium isotope ratios in the oceans have been used to estimate the flux of ^4He from the oceans to the atmosphere (Craig et al., 1975). If this flux is equated to the flux of ^4He from the upper mantle, it can be used to constrain the volume of the Earth that is being degassed. It is difficult to make flux balances for the helium content of the atmosphere because the loss of helium from the atmosphere is poorly constrained.

A review of many aspects of the helium system has been given by Mamyrin and Tolstikhin (1984). The isotope composition ratio (molal) of primordial helium from carbonaceous chondrites enriched in gases is $^4\text{He}/^3\text{He} = 1500\text{--}3500$. The present isotope ratio for the atmosphere is $^4\text{He}/^3\text{He} = 7.2 \times 10^5$. A large fraction of the ^4He in the atmosphere is attributed to the decay of ^{235}U , ^{238}U , and ^{232}Th in the mantle and crust (Table 12.5). This radiogenic helium plus primordial helium migrate from the mantle and crust to the oceans and atmosphere. A small amount of ^3He is also produced in the Earth's interior by nuclear reactions involving ^6Li .

The helium isotopes escape from the atmosphere because of their relatively low masses. The residence time of helium in the atmosphere is estimated to be 500,000 yr (Craig and Lupton, 1981). ^3He is also generated in the upper atmosphere by cosmic ray bombardment. Measurements of the $^4\text{He}/^3\text{He}$ ratio for gases trapped in MORB have relatively little scatter with a mean value of about $^4\text{He}/^3\text{He} = 86,000$. Thus it is appropriate to neglect the flux of primordial ^4He from the mantle compared with the mantle flux of radiogenic ^4He . Measurements of helium isotope ratios and concentrations have been carried out in the oceans. These measurements show that the water on the crest and flanks of the East Pacific Rise has a large ($\approx 30\%$) ^3He anomaly relative to atmospheric values. This anomaly is attributed to a large flux of helium from the oceanic crust to the oceans associated with volcanism and hydrothermal activity on the East Pacific Rise. The $^4\text{He}/^3\text{He}$ ratio in the atmosphere is about 8 times higher than the $^4\text{He}/^3\text{He}$ ratio from the upper mantle because the helium flux into the atmosphere from the continents is highly radiogenic.

Craig et al. (1975) have determined the helium flux from the oceans to the atmosphere. Using measured profiles of $^3\text{He}/^4\text{He}$ ratios in the oceans, they find that the mass flux of ^4He is $F_{^4\text{He}} = (3.2 \pm 1) \times 10^5 \text{ kg yr}^{-1}$. This can also be interpreted as the ^4He flux from the mantle. O'Nions and Oxburgh (1983) used this flux to determine the concentration of uranium and thorium in the depleted reservoir. To make this calculation, it is necessary to hypothesize that the production rate of ^4He in the depleted reservoir is equal to the loss at ocean ridges. Hydrothermal circulations must scavenge the oceanic crust of a large fraction of the He transported from the mantle in the basaltic magma.

With the assumption of a steady state, the mass flux of helium is related to the mass concentration of uranium in the depleted reservoir by (see Table 12.5)

$$F_{^4\text{He}} = \left[8\lambda + \frac{7\lambda'}{137.9} + 6\lambda''(1.033)R_{\text{Th/U}} \right] \frac{M_m C_{\text{U}}}{59.1} \quad (12.6.1)$$

where $R_{\text{Th/U}}$ is the mass concentration ratio of thorium to uranium, M_m is the mass of the

depleted mantle reservoir, and λ , λ' , and λ'' are the decay constants for ^{238}U , ^{235}U , and ^{232}Th , respectively. We first consider the production of ^4He in the continental crust and reinterpret (12.6.1) to apply to the crustal reservoir, i.e., we take M_m to be the mass of the continental crust and use crustal values of $R_{\text{Th}/\text{U}}$ and C_{U} . For the mean concentration of uranium we take $C_{\text{U}} = 0.91 \text{ ppm}$ (Taylor and McLennan, 1985, Table 3.5). With $R_{\text{Th}/\text{U}} = 4.5$ and the mass of the continental crust $M = 2.03 \times 10^{22} \text{ kg}$ we find from (12.6.1) that $F_{^4\text{He}} = 8.2 \times 10^5 \text{ kg yr}^{-1}$ ($7.7 \times 10^9 \text{ atoms m}^{-2}\text{s}^{-1}$). These values for the mean concentrations of the heat-producing elements in the continental crust give a heat flux $q = 24 \text{ mW m}^{-2}$, a reasonable fraction of the observed mean continental heat flux of 65 mW m^{-2} . The difference (41 mW m^{-2}) is the mantle contribution to the continental heat flow (see Section 4.3).

For the production of ^4He in the mantle, we consider the two alternative hypotheses of whole mantle and layered mantle convection. For whole mantle convection we extract the continental crust from the entire mantle. As assumed above, we take the average concentrations for the crust and mantle prior to the extraction of the crust to be $C_{\text{U}} = 25 \text{ ppb}$ and $C_{\text{Th}} = 95 \text{ ppb}$ for the depleted whole mantle reservoir ($R_{\text{Th}/\text{U}} = 3.8$). From (12.6.1) we find that the rate of production of ^4He in this reservoir is $F_{^4\text{He}} = 3.4 \times 10^6 \text{ kg yr}^{-1}$. This compares with the observed flux of $(3.2 \pm 1) \times 10^5 \text{ kg yr}^{-1}$. Thus, for whole mantle convection the efficiency of extraction of ^4He from the mantle is 9%. The ^4He flux and production balance for whole mantle convection are illustrated in Figure 12.14a.

For two-layer mantle convection the continental crust is extracted from the upper mantle. For the concentrations of uranium and thorium in the bulk silicate Earth and continental crust given above, the appropriate values for a depleted upper mantle are $C_{\text{U}} = 8 \text{ ppb}$ and $C_{\text{Th}} = 20 \text{ ppb}$. We have taken $R_{\text{Th}/\text{U}} = 2.5$ based on the work of Galer and O'Nions (1985) and Allègre et al. (1987), who concluded that this is the appropriate value for the depleted mantle reservoir from which MORB are derived. It does not appear possible to accommodate this inference in the whole mantle convection model since the resulting $R_{\text{Th}/\text{U}}$ value for the bulk silicate Earth would be much too low or the value for the continental crust would be much too high. The rate of production of ^4He in the depleted upper mantle reservoir from (12.6.1) is $M_{^4\text{He}} = F_{^4\text{He}} = 3.2 \times 10^5 \text{ kg yr}^{-1}$. This is equal to the observed mantle flux. With layered mantle convection, a steady-state balance of production and loss of ^4He appears to be possible; i.e., the flux of ^4He out of the depleted upper mantle reservoir is equal to the rate of production within it (O'Nions and Oxburgh, 1983).

As previously noted, the $^4\text{He}/^3\text{He}$ ratio for MORB is quite constant with a mean value of 88,000 (a factor of 8.4 lower than the atmospheric value) (Staudacher et al., 1994; Allègre et al., 1995). The ^3He component of the mantle flux is $F_{^3\text{He}} = 3.7 \text{ kg yr}^{-1}$ ($4.6 \times 10^4 \text{ atoms m}^{-2}\text{s}^{-1}$). This must be primordial and have been stored in the interior of the Earth for the last 4.55 Gyr. For steady-state degassing of the upper mantle reservoir, this must represent a flux of ^3He from the lower mantle to the upper mantle. Accordingly, there must also be a flux of ^4He from the lower mantle, but its magnitude will depend on the $^4\text{He}/^3\text{He}$ ratio for this reservoir. A minimum flux would correspond to the primordial ratio of 2,500 which gives $F_{^4\text{He}} = 9.2 \times 10^3 \text{ kg yr}^{-1}$ ($8.6 \times 10^4 \text{ atoms m}^{-2}\text{s}^{-1}$). A maximum flux estimate can be based on the $^4\text{He}/^3\text{He}$ ratio found for basalts from the Loihi seamount (Kurz and Jenkins, 1981, 1982; Kurz et al., 1982a,b, 1983; Rison and Craig, 1983; Allègre et al., 1983c). Samples from Loihi seamount give $^4\text{He}/^3\text{He} = 30,000 \pm 10,000$ with samples from other Hawaiian volcanoes giving somewhat lower values. The interpretation of the high ^3He values from the Hawaiian volcanoes is that these volcanoes are sampling a primitive reservoir. High ^3He values are also found in Iceland. The maximum values from Loihi can be interpreted as minimum values for a primitive lower mantle reservoir. With this

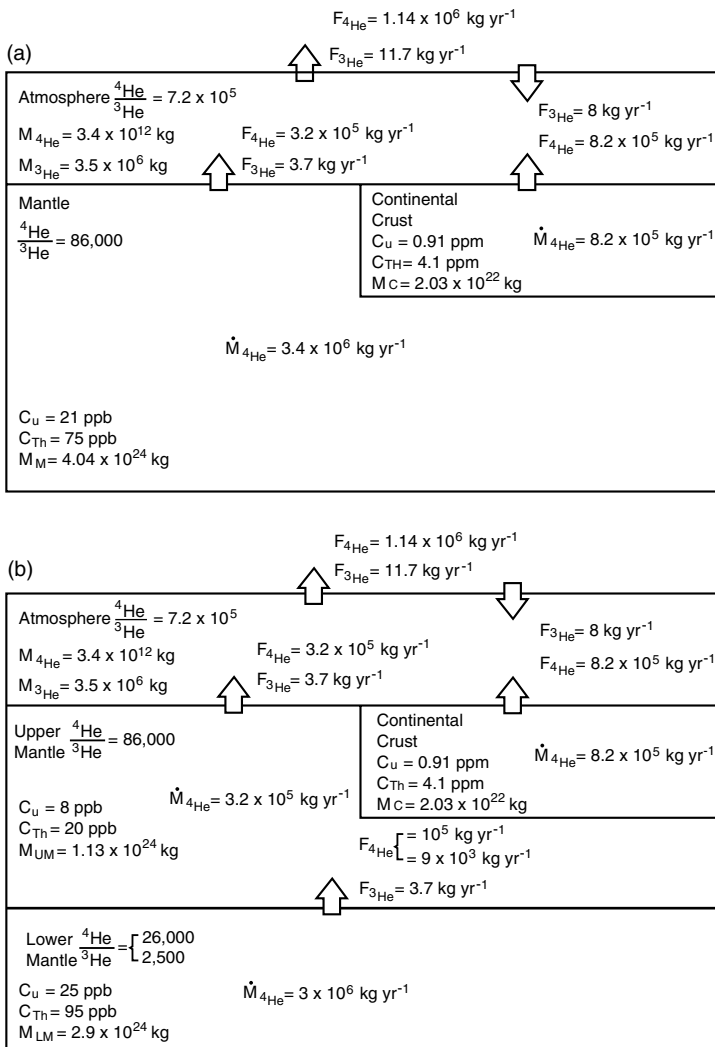


Figure 12.14. Alternative models for the transport of the helium isotopes through the mantle, crust, and atmosphere of the Earth. (a) Whole mantle convection. The ${}^4\text{He}$ flux to the atmosphere represents 9% of the ${}^4\text{He}$ produced in the mantle. (b) Layered mantle convection. The upper mantle is entirely outgassed.

hypothesis Allègre et al. (1987) have determined a minimum contamination from a primitive lower mantle reservoir to explain the ${}^3\text{He}$ in MORB samples.

A significant additional flux of ${}^3\text{He}$ into the atmosphere comes from the solar wind and interstellar gas. This contribution is estimated to be about $8 \text{ kg yr}^{-1} (10^5 \text{ atoms m}^{-2} \text{s}^{-1})$ (Holzer and Axford, 1971; Bühler et al., 1976). Thus we estimate that the total flux of ${}^3\text{He}$ through the atmosphere is about $F_{^3\text{He}} = 11.7 \text{ kg yr}^{-1} (14.6 \times 10^4 \text{ atoms m}^{-2} \text{s}^{-1})$ with very considerable uncertainty. With the mass of ${}^3\text{He}$ in the atmosphere $M_{^3\text{He}} = 3.5 \times 10^6 \text{ kg}$, the mean residence time for ${}^3\text{He}$ in the atmosphere is 300,000 yr. The total flux of ${}^4\text{He}$ through the atmosphere is $F_{^4\text{He}} = 1.14 \times 10^6 \text{ kg yr}^{-1} (1.07 \times 10^{10} \text{ atoms m}^{-2} \text{s}^{-1})$. With the mass of ${}^4\text{He}$ in the atmosphere $M_{^4\text{He}} = 3.4 \times 10^{12} \text{ kg}$, the mean residence time for ${}^4\text{He}$ in the

atmosphere is 3×10^6 yr. Although it is generally accepted that the escape rate for ${}^3\text{He}$ is considerably higher than the escape rate for ${}^4\text{He}$, many uncertainties remain (Pudovkin et al., 1981). The ${}^4\text{He}$ flux and production balance for the two-layer mantle model is summarized in Figure 12.14b.

Anderson (1993, 1998a,b) has argued that significant quantities of cosmogenic ${}^3\text{He}$ enter the sedimentary veneer on the oceanic crust and are subducted. Allègre et al. (1993), however, pointed out that the ${}^3\text{He}$ flux out of the mantle at oceanic ridges far exceeds the current flux of ${}^3\text{He}$ from space.

Question 12.2: Do the ${}^3\text{He}$ anomalies observed in some OIB indicate that there is a “primitive” mantle reservoir?

12.6.2 Argon

There is almost no primordial ${}^{40}\text{Ar}$ in the Earth; for practical purposes all ${}^{40}\text{Ar}$ found in the atmosphere is the result of the radioactive decay of ${}^{40}\text{K}$ within the Earth’s interior. The present isotope ratio for the atmosphere is ${}^{40}\text{Ar}/{}^{36}\text{Ar} = 295.5$. The mass of ${}^{40}\text{Ar}$ in the atmosphere is $M_{{}^{40}\text{Ar}} = 6.60 \times 10^{16}$ kg. Because of the heavy atomic mass of argon, significant quantities of the argon isotopes do not escape the atmosphere.

The ${}^{40}\text{Ar}$ in the Earth’s atmosphere must have been transported from the Earth’s interior to the atmosphere. Transport processes include volcanism, hydrothermal circulation through the continental and oceanic crusts, and erosion. The mass of ${}^{40}\text{Ar}$ produced over the age of the Earth $\tau_e = 4.55$ Gyr in a reservoir of mass M is related to the mean concentration of potassium in the reservoir C_K by

$$M_{{}^{40}\text{Ar}} = 1.28 \times 10^{-4} \frac{\lambda_{{}^{40}\text{Ar}}}{\lambda_{{}^{40}\text{K}}} [\exp(\lambda_{{}^{40}\text{K}} \tau_e) - 1] M C_K \quad (12.6.2)$$

With the mass of ${}^{40}\text{Ar}$ known we can either specify C_K and determine M or specify M and determine C_K .

Based on heat flow considerations and a variety of geochemical studies we will specify the mean concentration of potassium in the crust and mantle. The Urey number Ur is the ratio of the heat produced within the Earth by radioactive decay to the total surface heat flow; the difference from unity is due to the secular cooling of the Earth. Since the total surface heat flow is quite well known, the Urey number can be directly related to the mean concentration of potassium in the crust and mantle ($R_{\text{K/U}}$ and $R_{\text{Th/U}}$ are specified). For $R_{\text{Th/U}} = 3.8$ and $R_{\text{K/U}} = 12,700$, we find that a Urey number of unity, the case of no secular cooling, corresponds to average concentrations for the crust and mantle of $C_U = 35$ ppb, $C_{\text{Th}} = 133$ ppb, and $C_K = 450$ ppm. Based on a variety of studies (see Section 13.2) we take $Ur = 0.7$, which, with $R_{\text{Th/U}}$ and $R_{\text{K/U}}$ given above, results in $C_U = 25$ ppb, $C_{\text{Th}} = 95$ ppb, and $C_K = 450$ ppm. With the substitution of $M_{{}^{40}\text{Ar}} = 6.60 \times 10^{16}$ kg and $C_K = 320$ ppm into (12.6.2) we find that $M = 1.34 \times 10^{24}$ kg. For whole mantle convection the entire mantle would be expected to be well mixed. Since the mass of the entire mantle and crust is $M = 4.06 \times 10^{24}$ kg, outgassing of ${}^{40}\text{Ar}$ would be only 33% efficient if whole mantle convection were occurring. This assumes that both the crust and mantle are degassed equally. However, it is likely that the crust is more completely degassed than the mantle and we also consider the possibility that potassium currently in the crust has lost all its argon to

the atmosphere. By taking the mean concentration of potassium in the continental crust to be $C_K = 0.91\%$ (Taylor and McLennan, 1985, Table 3.5) and the mass of the continental crust to be $M_c = 2.03 \times 10^{22}$ kg, we find that 31% of the argon in the atmosphere could have been generated from the potassium presently in the Earth's continental crust. Attributing the remaining 69% to the whole mantle, we infer the efficiency of outgassing to be 23%. Thus, for whole mantle convection the required efficiency of argon extraction would be between 23 and 33% depending upon the role of the continental crust (Allègre et al., 1996).

For layered mantle convection we assume that the crust and upper mantle with mass $M = 1.15 \times 10^{24}$ kg is completely outgassed of ^{40}Ar . However, this does not account for all the ^{40}Ar in the atmosphere. In addition, about 7% of the ^{40}Ar generated in the lower mantle must also have been outgassed. This violates the basic assumption of the two-layer model that the upper and lower mantle reservoirs are isolated. Some hot spot volcanism, e.g., at Hawaii and Iceland, has lower mantle (primitive) affinities, indicative of the communication between these reservoirs. Measurements of $^{40}\text{Ar}/^{36}\text{Ar}$ ratios for MORB exhibit considerable scatter with a range of 10,000–40,000 (Allègre et al., 1983c; Sarda et al., 1999). This extreme range has been attributed to the recycling of atmospheric argon into the MORB source reservoir. At the other extreme, measurements of $^{40}\text{Ar}/^{36}\text{Ar}$ ratios from Loihi seamount give values in the range 400–4,000 (Hiyagon et al., 1992). These differences are taken as further evidence that a primitive reservoir is being sampled. The two alternative models for the ^{40}Ar mass balance are illustrated in Figure 12.15.

The above models of ^{40}Ar degassing rely on assumed values of $R_{\text{Th/U}}$, $R_{\text{K/U}}$, and Ur . With $R_{\text{Th/U}}$ and $R_{\text{K/U}}$ fixed, the reservoir mass required to account for all the atmospheric ^{40}Ar is inversely proportional to Ur . The generally accepted range of values for Ur is 0.5–0.7.

(a)		
Atmosphere	$M_{^{40}\text{Ar}} = 6.6 \times 10^{16}$ kg	
Mantle + Crust $C_K = 320$ ppm	$M_{^{40}\text{Ar}} = 13.4 \times 10^{16}$ kg (= 20×10^{16} kg)	
(b)		
Atmosphere	$M_{^{40}\text{Ar}} = 6.6 \times 10^{16}$ kg	
Upper Mantle + Crust	$C_K = 320$ ppm	$M_{^{40}\text{Ar}} = 0$ (5.6×10^{16} kg)
Lower Mantle	$C_K = 320$ ppm	$M_{^{40}\text{Ar}} = 13.4 \times 10^{16}$ kg (14.4×10^{16} kg)

Figure 12.15. Alternative models for ^{40}Ar degassing of the Earth. Masses of ^{40}Ar in the various reservoirs $M_{^{40}\text{Ar}}$ are given. The values in parentheses are the total masses of ^{40}Ar produced in the reservoirs in the last 4.55 Gyr. (a) Whole mantle convection. The atmospheric ^{40}Ar represents a 33% outgassing of the entire mantle. (b) Layered mantle convection. The atmospheric ^{40}Ar represents a total degassing of the upper mantle (above 660 km) and a 7% degassing of the lower mantle.

Accordingly, the efficiencies of ^{40}Ar degassing could be somewhat larger than the values given above. The balance assumes that there has been no significant loss of ^{40}Ar from the atmosphere. On the basis of ^4He and ^{40}Ar fluxes, O'Nions and Tolstikhin (1996) have argued that the flux of material between the upper mantle and lower mantle is only about 1/50th of the slab flux.

The escape of argon from the mantle to the oceans and atmosphere is a complex phenomenon. The degassing may be controlled by solubility in melts, i.e., by gas–melt partitioning. In this case argon would be expected to degas more rapidly than helium (Jambon et al., 1986; Lux, 1987). If degassing were controlled by solid–magma partitioning, helium would be expected to degas more rapidly (Hiyagon and Ozima, 1986; Lux, 1987). Solid-state diffusion may also play an important role. There is certainly a strong tendency for the noble gases to be concentrated in melts. The gases may escape when these melts solidify or by subsequent processes such as hydrothermal circulations.

The 9% efficiency of degassing of ^4He in the whole mantle model is considerably less than the 23–33% degassing efficiency obtained for ^{40}Ar . As discussed above, the efficiency of extraction for argon would be expected to be greater if solubility in a melt was the governing mechanism in degassing. However, there are considerable uncertainties in the determination of the helium flux which is a present value, while the inferred argon efficiency is an average over the entire age of the Earth. It is quite possible that the efficiency of extraction of ^{40}Ar was higher in the past when the Earth was hotter and there was more volcanism (McGovern and Schubert, 1989). Nevertheless, with whole mantle convection relatively small fractions of the radiogenic noble gases generated in the mantle escape to the Earth's atmosphere.

Not only is argon degassed from the mantle, but it can be recycled back into the mantle as well. Sarda et al. (1999) have demonstrated a correlation between maximum $^{40}\text{Ar}/^{36}\text{Ar}$ values with $^{206,207,208}\text{Pb}/^{204}\text{Pb}$ in MORB glass samples from the entire length of the mid-Atlantic ridge. High (low) $^{40}\text{Ar}/^{36}\text{Ar}$ values correlate with low (high) $^{206,207,208}\text{Pb}/^{204}\text{Pb}$ values. The correlation is interpreted as indicative of mixing between a degassed-depleted upper mantle component and a recycled component with high $^{206}\text{Pb}/^{204}\text{Pb}$ ratios (19–21) and low $^{40}\text{Ar}/^{36}\text{Ar}$ ratios (300–1,000). The data indicate that atmospheric rare gases are recycled to the mantle and that argon can serve as a tracer of mantle recycling and subduction.

12.6.3 Xenon

Studies of xenon isotopes in basalts also provide constraints on geochemical reservoirs. The isotope ^{129}Xe was produced by the radioactive decay of extinct ^{129}I which had a half-life of about 16 Myr (Table 12.5). Thus anomalies in $^{129}\text{Xe}/^{130}\text{Xe}$ must have developed very early in Earth history. The isotope ratio for the atmosphere is $^{129}\text{Xe}/^{130}\text{Xe} = 6.48$. Measurements of $^{129}\text{Xe}/^{130}\text{Xe}$ ratios for MORB consistently have higher values although there is considerable scatter (Staudacher and Allègre, 1982; Allègre et al., 1983c). The highest value is $^{129}\text{Xe}/^{130}\text{Xe} = 7.65$ (Kunz et al., 1998). The excess ^{129}Xe in MORB is taken as evidence that the depleted mantle reservoir was substantially outgassed during accretion. This outgassing was responsible for the formation of the atmosphere (Kunz et al., 1998). However, no ^{129}Xe anomalies (relative to atmospheric values) are found in OIB, including Hawaii. If Hawaii is sampling a primitive reservoir, this primitive reservoir does not have excess ^{129}Xe . One explanation is that the primitive reservoir was not totally degassed during accretion.

12.7 Isotope Systematics of Ocean Island Basalts

So far we have concentrated on the crustal and depleted mantle reservoirs. We now turn to the isotope systematics of ocean island basalts (OIB). Unlike MORB, the OIB have considerable isotopic variability. Interpretations of this variability require an identification of the sources of OIB. It is clear that OIB cannot come from the nearly homogeneous upper mantle reservoir that is the source of MORB. The ocean islands where OIB are found are hot spots that are attributed to partial melting in mantle plumes. The likely source of the mantle plumes is the instability of the hot thermal boundary layer at the base of the convecting part of the mantle which could lie at the core–mantle boundary or at the boundary between distinct upper and lower mantle reservoirs. Small-scale convective instability in the lower thermal boundary layer (Olson et al., 1987) feeds hot buoyant material into plumes or diapirs that rise upward through the mantle. If mantle convection is layered, then at least part of the signature can be attributed to a pristine or near-pristine lower mantle. Mantle material from the pristine layer can be entrained into the plume as it ascends from the boundary layer. Mantle material is also entrained into the plume as it rises through all depths. Pressure-release melting accompanies the upward transport of material and generates OIB.

Thus, the source of OIB is mantle plumes, but material can enter plumes from anywhere between the bottom thermal boundary layer and the surface. Even the subducted oceanic lithosphere and delaminated continental lithosphere can become entrained into mantle plumes. These units sink through the mantle, warming gradually by adiabatic compression and by conduction from anomalously hot material at depth. Upon warming, some of this material can become entrained in the general mantle circulation and eventually into upwelling plumes, or the sinking material can descend to the bottom of the convecting region, warm within the lower thermal boundary layer, and be swept into unstable diapirs or plumes rising from the boundary layer. As part of the ascending mantle plumes, the formerly subducted and delaminated material can contribute to the isotopic heterogeneity associated with OIB. Thus, some of the isotopic heterogeneity of OIB could have developed within the aging continental crust and lithosphere.

Both Allègre and Turcotte (1985) and White (1985) have proposed that OIB can be divided into four types based on the isotopic correlations shown in Figures 12.16–12.19 (Zindler et al., 1982; Hart, 1984; Zindler and Hart, 1986; Tatsumoto et al., 1987). The figures also show data from MORB. The four OIB classifications and MORB are characterized as follows.

MORB (I). In addition to normal mid-ocean ridge basalts (N-type MORB), this group includes a substantial fraction of the OIB from Iceland, the Galapagos, and Easter Island. The source is the well-mixed, depleted upper mantle reservoir, as discussed above. Mantle plumes probably contribute to the basaltic volcanism on Iceland, Galapagos and Easter Island, but these ocean islands are difficult to separate from adjacent ocean ridges. The Nd–Sr correlation for MORB from the East Pacific Rise in Figure 12.16 tightly clusters near the depleted mantle value, $\varepsilon_p(\text{Nd}) = 10$, $\varepsilon_p(\text{Sr}) = 29$. This can be attributed to the large quantities of basalt produced by this rapidly spreading ridge.

Hawaii (II). Hawaiian basalts appear to be a mixture between basalts from the depleted mantle reservoir and basalts from a relatively pristine reservoir. The positions of Hawaii in the isotope correlation plots of Figures 12.16–12.19 confirm this association. In particular, the Hawaiian basalts in the Nd–Sr correlation plot given in Figure 12.16 lie on a mixing line trend between the depleted mantle reservoir (DMR) and the bulk silicate Earth (BSE). Both Hawaii and Iceland have ${}^3\text{He}$ signatures indicative of a pristine component. Both can be

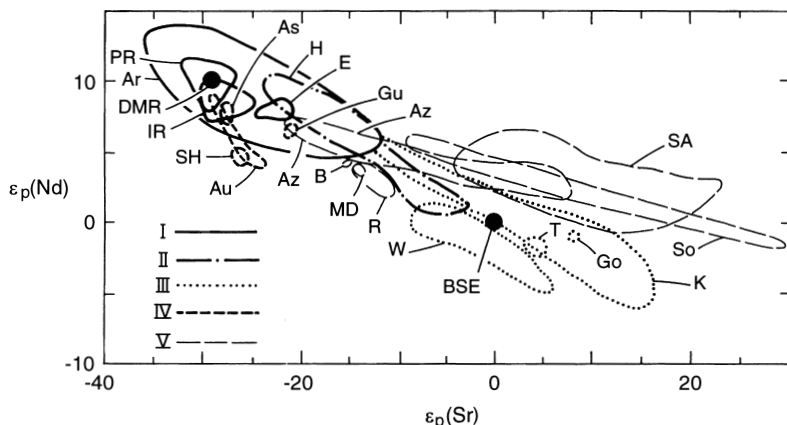


Figure 12.16. Nd–Sr isotope correlations for MORB and OIB. Data fields are from Zindler et al. (1982); Hart (1984); Allègre and Turcotte (1985); White (1985), and Tatsumoto et al. (1987). The data for basalts are divided into five groups: I. MORB. Included are data from the mid-Atlantic ridge (AR), East Pacific Rise (PR), the southwest section of the Indian Ridge (IR), and Easter Island (E). II. Hawaii (H). III. Kerguelen (K). Also included are data from Gough (GO), Tristan da Cunha (T), and the Walvis Ridge (W). IV. St. Helena (SH). Also included are data from Ascension (As), the Australs (Au), and Guadalupe (Gu). V. Society (So). Also included are data from Samoa (Sa), the Azores (Az), Rapa Ridge (R), MacDonald (MD), and Bouvet (B). Solid circles indicate bulk silicate Earth (BSE) values ($\varepsilon(\text{Nd}) = \varepsilon(\text{Sr}) = 0$) and depleted mantle reservoir (DMR) values ($\varepsilon(\text{Nd}) = 10, \varepsilon(\text{Sr}) = -29$).

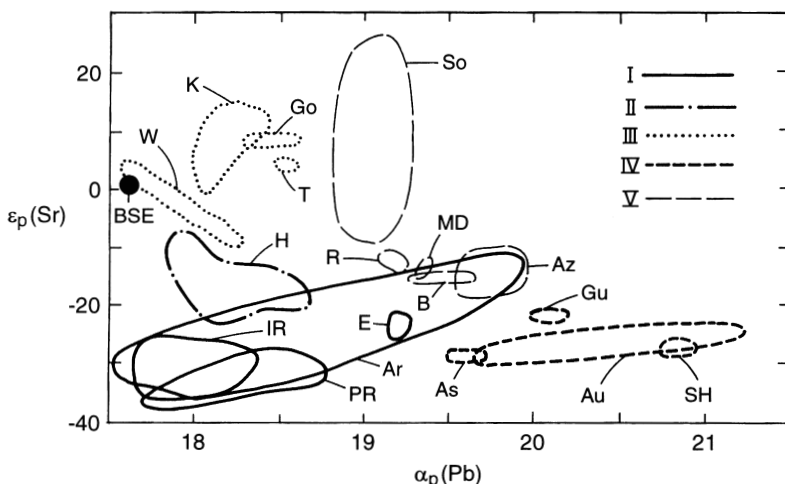


Figure 12.17. Sr–Pb isotope correlations for MORB and OIB. Data are from the sources given in Figure 12.16. The data for basalts are divided into the five groups described in Figure 12.16. The solid circle indicates BSE values ($\varepsilon(\text{Sr}) = 0, \alpha(\text{Pb}) = 17.6$).

associated with strong mantle plumes that entrain pristine lower mantle rock. These plumes rise from portions of the lower thermal boundary layer that do not contain recently subducted or delaminated lithospheres. The Hawaiian basalts present strong evidence that there is a mantle reservoir of nearly pristine mantle rock.

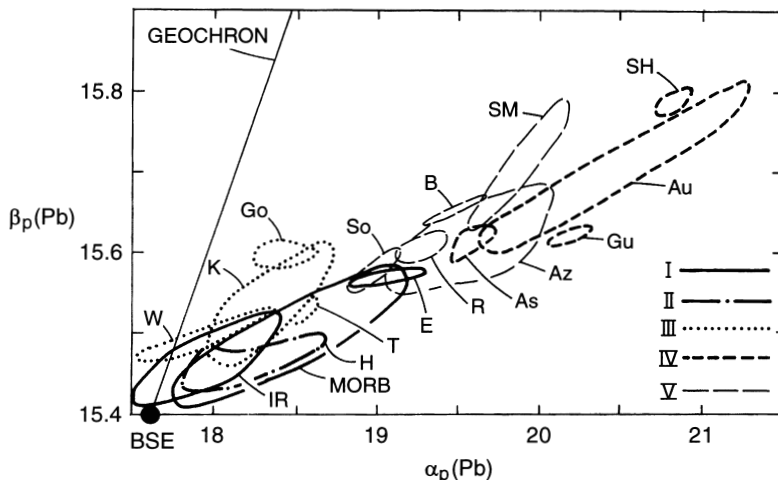


Figure 12.18. Pb–Pb isotope correlations for MORB and OIB. Data are from the sources given in Figure 12.16. The data for basalts are divided into five groups according to Figure 12.16. The solid circle indicates BSE values ($\alpha(\text{Pb}) = 17.6$, $\beta(\text{Pb}) = 15.4$).

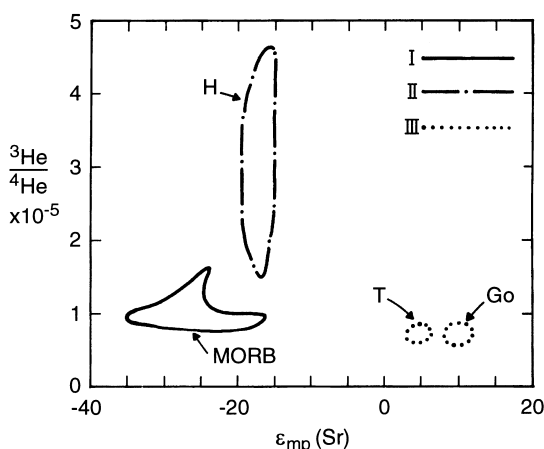


Figure 12.19. Helium (He)–strontium (Sr) isotope correlations for MORB and OIB. Data fields are from Allègre and Turcotte (1985). The data for basalts are divided into the same five groups as shown in Figure 12.16. Only three groups are shown here: I. MORB. II. Hawaii (H). III. Kerguelen (K), including data from Gough (Go) and Tristan da Cunha (T).

Kerguelen (III). The end member of this group is denoted as the enriched mantle member number one (EM1). The group also includes Gough, Tristan da Cunha, and the Walvis Ridge. These islands have a nearly pristine signature for Sr, Nd, and Pb but not for ${}^3\text{He}$. The pristine signature is particularly striking in the Sr–Pb correlation plot in Figure 12.17. The $\beta_p(\text{Pb})$ – $\alpha_p(\text{Pb})$ correlation in Figure 12.18 shows relatively little lead loss but an old model age. One interpretation is that the source is recently delaminated old continental lithosphere. Such a delamination would not be expected to include the radiogenic upper continental crust. Its Sr, Nd, and Pb isotope signatures would be near pristine but ${}^3\text{He}$ would be low since this mantle is outgassed.

St. Helena (IV). Also included in this group are Ascension, the Australs, and Guadalupe. These OIB are characterized by very large lead loss as shown by the $\beta_p(\text{Pb})$ – $\alpha_p(\text{Pb})$

correlation in Figure 12.18 indicative of the strong U/Pb enrichment attributed to this group. Large U–Pb ratios imply a large value for μ (12.5.1), and this end member is referred to as high μ (HIMU). These OIB can be attributed to imperfect mixing between depleted mantle and delaminated old continental crust. An alternative explanation for the origin of HIMU has been given by Christensen and Hofmann (1994). These authors segregate subducted oceanic crust into the D'' layer where the observed isotopic anomalies develop.

Society (V). The end member of this group is denoted as the enriched mantle member number two (EMII). The group also includes the Marquesas, Samoa, the Azores including Sao Miguel, Rapa Ridge, MacDonald, and Bouvet. The OIB from the Society Islands and Samoa are particularly anomalous in Nd–Sr systematics as shown in Figure 12.16. The Azores have a large spread that can be associated with a mixing line between the depleted mantle and subducted or delaminated young continental crust. The large lead loss shown in the $\beta_p(\text{Pb})-\alpha_p(\text{Pb})$ correlation (Figure 12.18) can be associated with subducted radiogenic sediments from the upper continental crust.

Zindler and Hart (1986) have considered the isotope systematics illustrated in Figures 12.16–12.19 in terms of mixing lines between end-member reservoirs. Three end members are the N-type MORB or DMR (depleted mantle reservoir), the bulk silicate Earth (BSE) reservoir, and the HIMU (St. Helena) reservoir. However, some OIB fall outside the mixing areas associated with these three reservoirs, so these authors introduced two additional end-member reservoirs EMI and EMII (enriched mantle reservoirs).

The OIB of the Kerguelen, St. Helena, and Society types are associated with weak plumes that do not entrain pristine rock. However, all the OIB will include fractions of N-type MORB due to pressure-release melting of upper mantle material entrained in the plume. This component will have the characteristic depleted isotope signature. The Nd–Sr correlation given in Figure 12.16 shows a strong mixing-line trend between depleted MORB and bulk silicate Earth. This trend is strong evidence for the existence of a near-pristine reservoir. Only the Society type OIB show a significant deviation from the trend. As shown in Figure 12.18 all OIB lie to the right of the geochron. This characteristic lead signature may have developed in the continental crust (Meijer, 1985).

Another isotope system that has been used to study OIB systematics is the Lu–Hf system (Salters and Hart, 1991). Blichert-Toft and Albarede (1997) have used Lu–Hf versus Sm–Nd systematics to conclude that OIB do not show a primordial trend. This is at odds with the conclusions drawn from ${}^3\text{He}/{}^4\text{He}$ systematics.

Question 12.3: What is the mantle source region of the chemically heterogeneous OIB?

Question 12.4: Do the 2 Gyr isotope anomalies associated with OIB develop in the mantle or elsewhere?

12.8 Summary

A number of simple models for the geochemical evolution of the Earth's mantle and continental crust have been presented and applied to a variety of isotopic systems. Observations on young rocks give information on the mean age of the continents and the mass of the complementary depleted mantle reservoir. Although there are many uncertainties, the mean

age of the continental crust is about $\tau_c = 2.1$ Gyr. This is the mean age that the present continental crust was separated from the mantle. The U–Th–Pb system gives somewhat younger ages. However, preferential recycling of relatively small amounts of either the parent or daughter isotope from the crust to the mantle can increase the age of the crust inferred from the isotope data.

A mean age for the continental crust of 2.1 Gyr is consistent with a rapid creation of the crust at that time or a uniform rate of creation from 4.2 Ga to the present. However, neither of these hypotheses is consistent with geological observations that the average height of the continents above sea level (freeboard) has been approximately constant for the last 2.5 Gyr. As discussed in Section 13.7, the volume of the continental crust at 3.5 Ga was probably greater than 50% of the present volume. Thus, the young mean age of the continental crust requires substantial rates of crustal recycling. This can be accomplished by delamination of the lower continental crust and by subduction of entrained sediments from the upper continental crust.

The isotope systematics of the Sm–Nd and Rb–Sr systems can also be used to infer the mass of the depleted mantle reservoir from which MORB is extracted. Isotopic data are consistent with a reservoir mass that is equal to or greater than the mass of the upper mantle but less than the mass of the whole mantle. Mass balances for radiogenic argon and helium also favor a depleted mantle reservoir with a similar mass. Thus, these isotopic studies favor layered mantle convection. However, the errors in the isotope values are sufficiently large that the data do not rule out whole mantle convection.

There are other independent geochemical studies that strongly favor a second mantle reservoir with a nearly primordial character. The Sm–Nd and Rb–Sr isotope systematics from Hawaii and Iceland are consistent with a mixing line between the depleted upper mantle reservoir and a second reservoir with nearly bulk Earth isotope values. A favored hypothesis is that these strong plumes entrain material from a lower mantle reservoir beneath their source at an internal thermal boundary layer. This hypothesis is also supported by the substantial quantities of primordial ^3He and ^{36}Ar found in OIB from Hawaii and Iceland. Any comprehensive model for mantle convection must explain the large excess values of primordial noble gases found in these OIB.

Further evidence for major differences between the MORB source reservoir and the OIB source reservoir (or reservoirs) comes from U–Th–Pb isotope systematics. Isotopic studies of normal MORB show that the U–Th ratio in the source region is $\kappa_p = 2.5 \pm 0.2$. Essentially all determinations of U–Th ratios from lead isotopes give $\kappa_p = 4 \pm 0.5$. This range also covers the U–Th ratios for the upper continental crust and the bulk silicate Earth. Simple mass balances for uranium and thorium preclude a whole mantle reservoir with $\kappa_p = 2.5 \pm 0.2$. Thus, either the mantle must be strongly vertically stratified in κ_p or there must be a lower mantle reservoir with near primordial concentrations of uranium and thorium and $\kappa_p \approx 4$. Since it is difficult to reconcile a stratification of κ_p with mantle mixing (van Keken and Ballentine, 1998), the U–Th systematics also supports layered mantle convection.

It is concluded that the geochemical evidence favors the hypothesis that the mantle is not efficiently mixed and that there are distinct MORB source and nearly primordial reservoirs. However, the geochemical evidence must be reconciled with seismic tomographic data that show the penetration of slabs deep into the lower mantle (see Chapter 3). A model to reconcile the geochemical results and slab penetration into the lower mantle has been proposed by Kellogg et al. (1999), who hypothesize a compositional barrier to convection embedded within the lower mantle. This barrier is the boundary between a near-pristine lower mantle reservoir and the MORB source reservoir. A density discontinuity of about 4% is associated

with the proposed boundary at a mean depth of about 1,600 km, though the boundary could have extensive topography and possibly extend to the D'' layer. Seismic evidence in support of this hypothesis has been given by van der Hilst and Kárason (1999) and by Kaneshima and Helffrich (1999).

OIB have significant isotopic heterogeneities. These heterogeneities probably arise from two sources: (1) nearly primitive rock which is entrained from the lower mantle and (2) continental crust and mantle which have recently been subducted or delaminated. Hawaii and Iceland are examples of the entrainment of lower mantle material. The OIB from these islands lie on mixing lines between depleted and primitive isotopic ratios and have excess primordial rare gas isotopes. Other OIB are divided into three types. The Kerguelen group is characterized by a near-pristine signature for the isotope ratios and is associated with a contribution from recently delaminated continental lithosphere. The St. Helena group is characterized by a very large lead loss. This can be attributed to old, radiogenic continental crust. The Society group has anomalous Nd–Sr systematics and a large lead loss and is attributed to subducted young continental crust.

13

Thermal History of the Earth

13.1 Introduction

Mantle convection plays an essential role in determining the evolution of the Earth's temperature through geologic time because it is the primary mechanism by which the Earth transfers heat from its deep interior to its surface. Once the internally generated heat reaches the surface it is transferred to the ocean–atmosphere system by a variety of processes including conduction and hydrothermal circulation through the oceanic crust and is eventually radiated to space. From the perspective of studying the changes in the Earth's interior temperature over geologic time, we can ignore the relatively rapid transport of internal heat through the atmosphere and oceans and assume that all heat delivered to the Earth's surface from below immediately escapes the Earth. The heat lost through the Earth's surface tends to cool the interior, and heat produced within the Earth by the decay of radioactive elements tends to warm it. The thermal evolution of the Earth is a consequence of the competition between internal energy sources producing heat and mantle convection removing it. A quantitative description of the Earth's thermal history is the application of basic energy conservation in a convecting mantle.

While the basic approach to modeling the Earth's thermal history is straightforward, its implementation is a major challenge because of the complexity of a realistic model and available computer resources that limit detailed numerical calculations of three-dimensional, time-dependent convection at the very high Rayleigh numbers applicable to the Earth's present mantle and at the even higher Rayleigh numbers appropriate to the Earth's early mantle. These limitations were discussed in detail in Chapter 10. All the complexities of mantle convection discussed in the previous chapters of this book indicate the severe limitations of any attempt to model the thermal evolution of the Earth. However, despite these limitations, relatively simple models of the Earth's thermal evolution have provided very useful results.

Concepts and results from boundary layer theories of convection and from a large number of numerical and laboratory experiments on convection have been incorporated into Earth thermal history models as a way of accounting for the effects of convective heat transfer across the mantle. This approach is known as parameterized convection and has made possible the study of the thermal evolution of the Earth with essentially analytic models (Sharpe and Peltier, 1978, 1979; Schubert, 1979; Schubert et al., 1979a,b, 1980; Stevenson and Turner, 1979; Turcotte et al., 1979; Davies, 1980; Turcotte, 1980b). The approach uses simple parameterizations between the amount of heat generated in the mantle and the vigor of mantle convection required to extract this heat.

13.2 A Simple Thermal History Model

13.2.1 Initial State

It is now generally accepted that the Earth formed by accretion (Safronov, 1969; Levin, 1972; Greenberg et al., 1978; Wetherill, 1985; Ahrens, 1990), and that upon completion of the accumulation process the Earth was hot and fully differentiated into a mantle and core with the core superliquidus and the mantle near its solidus (Schubert, 1979; Schubert et al., 1979a, b, 1980; Stevenson et al., 1983; Stevenson, 1989b, 1990). The early heat source is gravitational potential energy made available by accretion (Wetherill, 1976, 1985; Weidenschilling, 1976; Safronov, 1978; Kaula, 1979a) and core formation (Birch, 1965; Tozer, 1965b; Flasar and Birch, 1973; Shaw, 1978) contemporaneous with or shortly following accretion (Stevenson, 1981, 1989b, 1990).

The gravitational potential energy per unit mass released upon accretion can be estimated using $E = 3GM/5R$, the gravitational potential energy per unit mass of a constant density body of mass M and radius R (here, G is the universal gravitational constant). For the Earth, $E = 3.75 \times 10^7 \text{ J kg}^{-1}$. The equivalent temperature T^* is found using $E = cT^*$, and for $c = 1 \text{ kJ kg}^{-1}$, $T^* = 37,500 \text{ K}$. The key requirement for core formation during or just after accretion is the retention of a small fraction, say 20%, of the energy of impacting planetesimals by the Earth. The likelihood of this is high if large impactors played a significant role in accretion, since large impacts lead to deep burial of a substantial fraction of the impactor's kinetic energy (Wetherill, 1976, 1985, 1986; Kaula, 1979a; Melosh, 1990). Formation of the Moon may have been one of the consequences of such a large impact with a planetesimal the size of Mars in the late stages of Earth's accretion (Hartmann and Davis, 1975; Cameron and Ward, 1976; papers in Hartmann et al. (1986) discuss the Great Impact Hypothesis for the origin of the Moon; see also Stevenson, 1987) (see the discussion in Chapter 14 on the Moon). The collision of the Earth with a Mars size impactor would release about $7.5 \times 10^6 \text{ J kg}^{-1}$ and raise the average temperature of the Earth by 7,500 K if all this energy went into heating the Earth (Melosh, 1990). This energy is enough to have melted, even vaporized, a large part of the Earth. The Moon is supposed to have accreted in orbit around the Earth from terrestrial and impactor material ejected during the cataclysmic collision event. It is generally assumed that the Earth was already differentiated into a core and mantle at the time of the giant impact in order to explain the chemical similarity between the Moon and the Earth's mantle (e.g., Wänke and Dreibus, 1986). Spohn and Schubert (1991) estimate that the Earth would have re-equilibrated (thermally and structurally) on a time scale of 1–10 Myr after the giant impact. This rapid adjustment makes the giant impact event inconsequential for the long-term thermal evolution of the Earth. Though truly cataclysmic at the time, the only trace of the giant impact at the present may be the Moon itself and a slightly altered chemical composition of the Earth's mantle.

The gravitational potential energy released upon core formation is also large, enough to raise the temperature of the whole Earth by 2,000 K (e.g., Birch, 1965; Tozer, 1965b; Flasar and Birch, 1973). Radioactivity could also contribute to heating of the Earth early in its evolution if significant amounts of certain extinct radionuclides, i.e., Aluminum 26, were incorporated into the accreting Earth.

There are many fundamental but unanswered questions about the early evolution of the Earth. For example, the amount of energy available from the sources discussed above would be more than sufficient to melt the entire Earth. However, if the entire mantle were molten it would be expected that solidification would lead to a chemically fractionated planet, a thick

enriched crust, and a depleted mantle. There is no evidence that this occurred (Ringwood, 1990). There may have been a global magma ocean beneath a massive protoatmosphere of water (Abe and Matsui, 1985, 1986, 1988; Matsui and Abe, 1986a,b,c, 1987; Ahrens, 1990), but very rapid subsolidus mantle convection could have maintained most of the mantle at a temperature just below its solidus (Davies, 1990). In addition, convection in the magma ocean may have prevented fractionation by keeping crystals in suspension as the magma ocean solidified (Tonks and Melosh, 1990; Solomatov and Stevenson, 1993a,b). From this point of view, the magma ocean could have been very deep, i.e., a large part of the mantle could have been molten, without fractionation occurring on solidification.

Question 13.1: Was the Earth's mantle fractionated at the end of accretion?

On the basis of the above considerations, we adopt a simplified Earth thermal history model consisting of a two-layer Earth with a core and a compositionally homogeneous mantle. The structure is established at time zero (the start of the thermal history) and is unchanged throughout the evolution. The initial thermal state is hot; the core is superliquidus and the mantle is at the solidus. It will be seen that the subsequent thermal evolution of the model Earth consists of an early period of rapid cooling lasting several hundred million years followed by more gradual cooling over most of geologic time. After the period of rapid cooling the subsequent thermal evolution is nearly independent of the initial temperature distribution.

13.2.2 Energy Balance and Surface Heat Flow Parameterization

In this section we derive a thermal history model for the mantle using the assumption that no heat enters the mantle from the core. This assumption, made here to obtain the simplest possible model, is relaxed in the more sophisticated models discussed later in the chapter. From the viewpoint of the energy balance, this assumption leads to a one-layer Earth model.

An integration of the heat equation (e.g., 6.9.13) over the whole mantle gives

$$Mc \frac{\partial T}{\partial t} = MH - Aq \quad (13.2.1)$$

where M is the mass of the mantle, c is the specific heat of the mantle, T is the volume-averaged mantle temperature, H is the average rate of energy release in the mantle per unit mass due to the decay of long-lived radioactive elements (^{238}U , ^{235}U , ^{40}K , and ^{232}Th), A is the outer surface area of the mantle, and q is the average heat flux at the top of the mantle. The integrated energy balance (13.2.1) simply states that the time rate of change of mantle internal thermal energy is balanced by the difference between the heat production rate in the mantle and the rate of heat loss through the surface. In performing this integration we characterize the mantle with a single uniform temperature T and a uniform distribution of radiogenic heat sources. Long-lived radioactivity is an important source of heat for the mantle over geologic time; it is widely accepted that mantle radioactivity is the source of most (e.g., 80%) of the heat flowing through the Earth's surface at present (Turcotte and Schubert, 1982).

Question 13.2: What fraction of the Earth's surface heat flow can be attributed to radioactive heat generation and what fraction to secular cooling of the Earth?

We now assume that the specific radiogenic heat production rate H decays with time according to an exponential decay law with a single rate constant λ :

$$H = H_0 e^{-\lambda t} \quad (13.2.2)$$

where H_0 is the specific heat production rate at $t = 0$.

Substitution of (13.2.2) into (13.2.1) gives

$$Mc \frac{\partial T}{\partial t} = MH_0 e^{-\lambda t} - Aq \quad (13.2.3)$$

In order to solve (13.2.3) we require a heat transfer law relating q to the other model variables and parameters, especially the average mantle temperature T . We follow Schubert et al. (1979a, 1980) and specify this dependence in the following parameterized form:

$$q = \frac{k(T - T_s)}{d} \left(\frac{Ra}{Ra_{cr}} \right)^\beta \quad (13.2.4)$$

where k is the thermal conductivity of the model mantle, d is the thickness of the mantle, T_s is the surface temperature, Ra is the Rayleigh number given by

$$Ra = \frac{g\alpha(T - T_s)d^3}{\kappa\nu} \quad (13.2.5)$$

Ra_{cr} is the critical value of the Rayleigh number for the onset of convection in the spherical shell, and β is a constant. In (13.2.5), g is the acceleration of gravity in the model mantle, taken to be a constant as is appropriate to the real mantle, α is the assumed constant value of thermal expansivity in the model mantle, κ is the mantle thermal diffusivity also assumed constant, and ν is the kinematic viscosity in the mantle. The viscosity ν is a function of temperature, a dependence that controls the thermal evolution, as elaborated below.

Equation (13.2.4) is the $Nu-Ra$ relation ($Nu = qd/k(T - T_s)$) characteristic of boundary layer theories of convection and of numerous numerical and laboratory experiments on convection as discussed in Section 8.6. A constant of order unity has been tacitly incorporated into Ra_{cr} which typically has a value of order 10^3 . The power-law exponent β generally has a value of about 0.3 according to boundary layer theory and a large number of numerical experiments. Boundary layer theory gives $\beta = 1/3$ (Sections 8.6 and 13.5), while experiments give a slightly smaller value of β . The specific form (13.2.4) of the surface heat flow parameterization is suggested by boundary layer theory and experiments on convection of a constant viscosity, Boussinesq fluid in a plane layer heated from below. Its applicability to other situations is surprisingly robust and has been discussed in detail by Schubert et al. (1979a, 1980). The $Nu-Ra$ relations of other heating modes (e.g., internal heating) and geometries (e.g., spherical geometry) can all be written in the form of (13.2.4) by appropriate definitions and identifications of Ra_{cr} and β . The use of (13.2.4) for convection with temperature-dependent viscosity is generally appropriate if T is identified with the characteristic temperature of the convecting part of the fluid, Ra_{cr} and β are properly interpreted, and T_s is chosen as either the surface temperature or the temperature near the

base of any stagnant lid that forms over the convecting system (Schubert et al., 1979a, 1980). For the parameterization of Earth's mantle convection, T_s is properly taken as the surface temperature since the plates are mobile and do not form a stagnant lid over the convecting system.

Criticism of the use of (13.2.4) in Earth thermal history studies has been provided by both Richter and McKenzie (1981) and Christensen (1984c, 1985b) concerning effects of strongly temperature dependent viscosity. The former paper was mainly concerned with the influence of a stagnant upper thermal boundary layer, which does not occur on Earth. The application of (13.2.4) to the Earth or to another planet depends on a proper identification of T_s and T , as discussed above. If there are large viscosity variations within thermal boundary layers that lie within the convecting part of the fluid, e.g., the hot, low-viscosity thermal boundary layer at the bottom of the fluid, then the use of (13.2.4) can be modified appropriately as discussed below. Christensen (1985b) was also concerned with the effects of a sluggish or nearly stagnant lid and on the basis of numerical experiments inferred a very small value of β (about 0.1). This result would make Earth thermal history rather insensitive to Ra or the viscosity of the mantle.

It is now recognized that there are distinct modes of convection in fluids with strongly temperature dependent viscosity – the small viscosity contrast regime, the sluggish-lid regime, and the stagnant-lid regime (Moresi and Solomatov, 1995; Solomatov, 1995; Ratcliff et al., 1997). Separate $Nu-Ra$ parameterizations have been developed for each flow regime (Solomatov, 1995; Reese et al., 1998, 1999). These parameterizations will be discussed in more detail later in this chapter and in Chapter 14 where application is made to the thermal histories of terrestrial planets. The $Nu-Ra$ parameterizations for the sluggish-lid and stagnant-lid convection regimes are relevant to other planets, e.g., Venus, Mars, and the Moon, which lack plate tectonics and are in these convection regimes. Plate tectonics places the Earth in the small viscosity contrast convection regime and (13.2.4) applies. Parameterized convection based on (13.2.4), with a value of β around 0.3, provides the most physically plausible representation of the Earth's thermal evolution (Gurnis, 1989).

13.2.3 Temperature Dependence of Mantle Viscosity and Self-regulation

The strong dependence of mantle viscosity on temperature exerts a controlling influence on the evolution of the mantle. It is consistent with the approximate nature of parameterized convection modeling to assume a Newtonian rheology with a kinematic viscosity ν related to mantle temperature by

$$\nu = \nu_0 \exp\left(\frac{A_0}{T}\right) \quad (13.2.6)$$

where ν_0 and A_0 are constants (e.g., Weertman and Weertman, 1975; Carter, 1976; Poirier, 1985). The parameter A_0 is an activation temperature related to the activation energy E^* of the subsolidus creep deformation by $A_0 = E^*/R$, where R is the universal gas constant, as discussed in Chapter 5. The temperature dependence of mantle viscosity acts as a thermostat regulating the average mantle temperature (Tozer, 1967). Initially, when the Earth is hot, mantle viscosity is low, and extremely vigorous convection rapidly cools the Earth. Later in its evolution, when the Earth is relatively cool, its mantle viscosity is higher and more modest convection cools the planet at a reduced rate. Self-regulation tends to bring the viscosity of the mantle to a value that facilitates efficient removal by convection of the heat generated in the mantle. The temperature of the mantle adjusts to maintain or reach this preferred value

of viscosity. If the mantle is excessively hot to start with, e.g., because of accretional heating and the heat released by core formation, it will rapidly cool to bring its viscosity in line with the value preferred by its internal heat generation. The farther the mantle is from the preferred viscosity, the more rapid is the adjustment. Thus the specific value of the initial temperature $T(0)$ chosen for modeling the thermal history is unimportant. If it is too high, the adjustment by self-regulation rapidly rids the mantle of excess heat. Though not realistic, even an initially cold mantle would heat by radioactivity until the self-regulated viscosity was reached, a process that would have a billion year time scale. Self-regulation indicates that the present state of the convecting mantle has little or no memory of initial conditions, a circumstance which makes thermal evolution models applicable. As mantle radiogenic heat sources decay with time, convection transfers less heat, the preferred mantle viscosity gradually increases, and the mantle undergoes secular cooling. The gradual decrease of mantle temperature with time is a fundamental aspect of mantle evolution and requires that secular cooling contribute to the heat flow through the Earth's surface.

By combining (13.2.3)–(13.2.6) we obtain a single differential equation that contains explicitly the average mantle temperature T in all terms except the heat source:

$$\frac{\partial T}{\partial t} = f_1 e^{-\lambda t} - f_2 (T - T_s)^{1+\beta} \exp\left(\frac{-\beta A_0}{T}\right) \quad (13.2.7)$$

where

$$f_1 = H_0/c \quad (13.2.8)$$

and

$$f_2 = \frac{Ak}{Mcd} \left(\frac{\alpha g d^3}{\kappa v_0 Ra_{cr}} \right)^\beta \quad (13.2.9)$$

Equation (13.2.7) is solved subject to the initial condition $T = T(0)$ at $t = 0$. The solutions discussed in the next and subsequent sections will demonstrate the self-regulation imposed on mantle evolution by the temperature dependence of viscosity.

13.2.4 Model Results

The numerical integration of (13.2.7)–(13.2.9) subject to the initial condition $T = T(0)$ at $t = 0$ is straightforward. Some results from Schubert et al. (1980) are shown in Figures 13.1 and 13.2. Parameter values for this example are $T(0) = 3,273$ K, $T_s = 273$ K, $\beta = 0.3$, $\lambda = 1.42 \times 10^{-17}$ s $^{-1}$, $A_0 = 7 \times 10^4$ K, $f_1 = H_0/c = 4.317 \times 10^{-14}$ K s $^{-1}$, $k = 4.18$ W m $^{-1}$ K $^{-1}$, $\kappa = 10^{-6}$ m 2 s $^{-1}$, $\alpha = 3 \times 10^{-5}$ K $^{-1}$, $d = 2.8 \times 10^6$ m, $g = 10$ m s $^{-2}$, $v_0 = 1.65 \times 10^2$ m 2 s $^{-1}$, $Ra_{cr} = 1,100$, and $A/Mc = 1.377 \times 10^{-13}$ m 2 K J $^{-1}$. These values give $f_2 = 1.91 \times 10^{-14}$ (in SI units).

The kinematic viscosity of the mantle as a function of time is given in Figure 13.1; it increases monotonically from 3.2×10^{11} m 2 s $^{-1}$ at the start of the model thermal history to 3.4×10^{17} m 2 s $^{-1}$ after 4.5 Gyr. With $\rho = 3,400$ kg m $^{-3}$, the latter value of ν gives a viscosity $\mu = 1.2 \times 10^{20}$ Pa s in good agreement with inferred values of mantle viscosity. The mantle temperature is also given in Figure 13.1. Temperature decreases monotonically with time but by less than 50% of its initial value because of the very strong temperature dependence of the viscosity. The temperature after 4.5 Gyr, $T = 1,950$ K, is representative

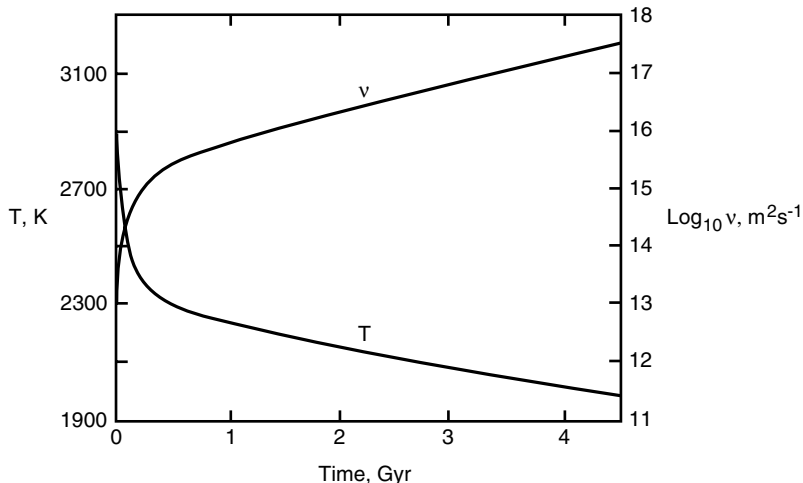


Figure 13.1. Mantle temperature T and kinematic viscosity v as functions of time in a simple thermal history model of the Earth (after Schubert et al., 1980).

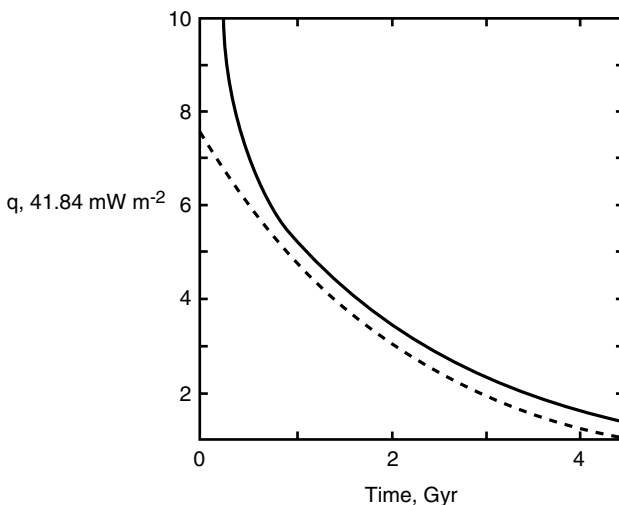


Figure 13.2. Mean surface heat flux q (solid curve) and total internal heat production per unit surface area (dashed curve) versus time for the thermal evolution calculation of Figure 13.1 (after Schubert et al., 1980).

of present temperatures in the mantle. The large drop in temperature and the enormous increase in viscosity during the first few hundred million years of model thermal evolution is a consequence of the self-regulation discussed above. The model mantle rapidly adjusts by early vigorous convection to a viscosity (temperature) that is higher (lower) than the viscosity (temperature) of its initial state. At the end of this early adjustment phase, the model mantle has gotten rid of most of its initial excess heat (Figure 13.2), and it has come into a state in which temperature and viscosity have adjusted to the convective removal of the remaining “primordial” heat and the energy produced by radioactivity. During the rest of geologic time the model mantle undergoes a more gradual secular cooling, with an attendant viscosity increase. The surface heat flow (solid line in Figure 13.2) declines throughout most

of the evolution, tracking the decay in the total radiogenic heat production per unit surface area (dashed line in Figure 13.2), but always remaining in excess of the internal heat release. The predicted surface heat flow after 4.5 Gyr is $q = 60 \text{ mW m}^{-2}$, in reasonable agreement with the present average value ($q = 72 \text{ mW m}^{-2}$) for the heat flow from the mantle (Earth's surface heat flow with the crustal component removed, see Sections 4.1.3 and 4.1.5 wherein the mean surface heat flow of 87 mW m^{-2} is reduced by 17%, the contribution of heat production in the continental crust to yield 72 mW m^{-2} for the mean mantle heat flux). The difference between the surface heat flow and the decay of radiogenic heat is due to the loss of primordial heat (or heat produced earlier by previous radioactive decay). The loss of primordial heat, or secular cooling, contributes 25% of the surface heat flow in the model of Figure 13.2. This difference will be discussed in some detail in the next section.

An analytic solution to (13.2.7)–(13.2.9) can be found for the early phase of rapid adjustment to the self-regulated state. Since the adjustment period lasts only a few hundred million years, λt is smaller than about 0.13 (for $t = 300 \text{ Myr}$) and $\exp(-\lambda t) \approx 1$. At $t = 0$, the ratio of the second term to the first term in (13.2.7) is about 25:1. Thus we can neglect the first term on the right of (13.2.7) and solve

$$\frac{\partial T}{\partial t} \approx -f_2(T - T_s)^{1+\beta} \exp\left(\frac{-\beta A_0}{T}\right) \quad (13.2.10)$$

subject to $T = T(0)$ at $t = 0$. The analytic solution to (13.2.10), valid approximately during the early rapid adjustment period, is given by the simple quadrature

$$-f_2 t = \int_{T(0)}^T \frac{ds \exp(\beta A_0/s)}{(s - T_s)^{1+\beta}} \quad (13.2.11)$$

The solution given by (13.2.11) neglects radiogenic heating during the early period of rapid cooling. The dependence of temperature on time for the first 200 Myr of Earth's history is shown in Figure 13.3 for the same parameter values as used above in the example of

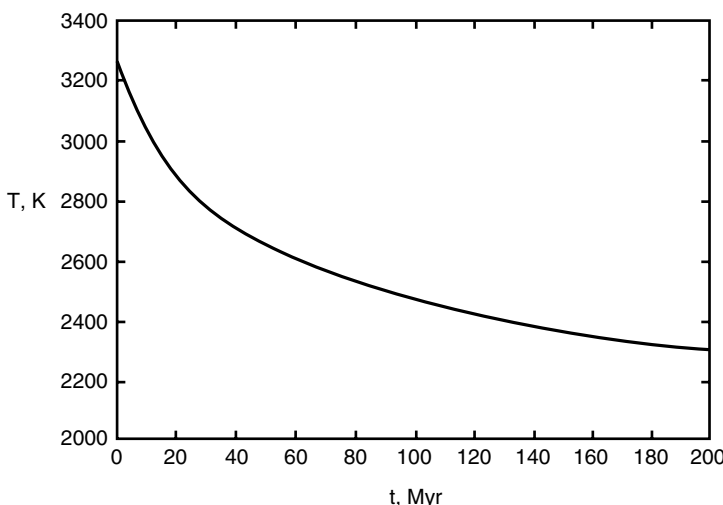


Figure 13.3. The decrease of mantle temperature with time during the early phase of vigorous convection and rapid cooling from (13.2.11). Adjustment to the self-regulated state and loss of most of the primordial heat occurs in only about 100 Myr.

Figures 13.1 and 13.2, namely $T_s = 273\text{ K}$, $\beta A_0 = 2.1 \times 10^4\text{ K}$, $T(0) = 3,273\text{ K}$, and $f_2 = 1.91 \times 10^{-14}$ (SI units). The temperature decreases by about 1,000 K in only 200 Myr. By about $t = 200$ Myr, the second term on the right of (13.2.7) is comparable to the first term (the radiogenic heating term), as can be seen by comparing Figures 13.1 and 13.3, and the approximation used in obtaining (13.2.11) is no longer valid.

13.2.5 Surface Heat Flow, Internal Heating, and Secular Cooling

Prior to the discovery of radioactivity, the heat flow through the Earth's surface was attributed to the cooling of the Earth's interior. Lord Kelvin used this hypothesis to estimate the age of the Earth as described in Section 4.1. After the discovery of radioactivity but before the widespread acceptance of mantle convection, it was realized that much of the geothermal heat loss had its origin in the decay of radioactive isotopes. Nevertheless, it was also believed that a substantial fraction (say, 25%) of the surface heat flow was due to secular cooling of the Earth (Holmes, 1916; Slichter, 1941). Unfortunately, this idea lost favor upon acceptance of convection as the mode of heat transfer in the deep mantle since it was thought that convection would be so efficient as to establish a balance between radiogenic heat production in the mantle and surface heat flow (Tozer, 1965a; Turcotte and Oxburgh, 1972b). After Lord Kelvin, who attributed 100% of the Earth's heat loss to secular cooling, opinions in the geophysical community underwent a complete reversal regarding the significance of whole-Earth cooling. A century later it was considered to contribute negligibly to the surface geothermal heat flow. The proposed equality of internal heat production and surface heat loss was used as a basis for estimating the abundances of uranium, thorium, and potassium in the Earth and Moon from measurements of surface heat flow (e.g., Langseth et al., 1976).

The idea that vigorous convection in the Earth's mantle established a balance between radiogenic heat production and surface heat flow was generally accepted throughout the 1970s. The use of parameterized convection to study the thermal evolution of the Earth was instrumental in re-establishing that secular cooling contributed importantly to Earth's surface heat flow even with efficient mantle convection. The parameterized convection models of Sharpe and Peltier (1978, 1979) showed that cooling of the Earth by mantle convection could account for Earth's surface heat flow even in the absence of any radiogenic heating in the mantle. Schubert (1979), Schubert et al. (1979a, b, 1980), Stevenson and Turner (1979), Turcotte et al. (1979), Davies (1980), Turcotte (1980b), and Peltier and Jarvis (1982) included mantle radiogenic heat production in their parameterized convection models which, as seen in Figure 13.2 and explained further below, yielded a contribution of secular cooling to surface heat flow as a natural consequence of the cooling Earth model.

The idea that secular cooling contributes significantly to the heat flow at the Earth's surface has already been seen in the model thermal history results of Figure 13.2 (after Schubert et al., 1980). The main reason is the secular decline in radioactive heat sources. There is no difficulty in having a close balance between internal heat production and surface heat flow in a convecting system with steady internal heat sources. Indeed, energy conservation requires this, if internal heating is the only source of energy for the system. However, when the internal heat sources decay with time, as is the case for radiogenic heat sources in the Earth's mantle, the surface heat loss and convection must also decline with time, and the system must cool. The secular decline in internal thermal energy must, by energy conservation, contribute to the flow of heat through the surface. No matter how efficiently convection transports heat through the mantle, the decay with time in the rate of internal heat production insures that secular cooling contributes to surface heat loss. The analyses

of Schubert et al. (1980), Davies (1980), and Stacey (1980) show that the magnitude of this contribution is substantial; about 25% of the Earth's surface heat flow is due to cooling of the Earth. This conclusion is a robust result, drawn from numerous calculations with wide variations in the values of parameters entering the thermal history models (Schubert et al., 1980).

The inequality between surface heat flow and interior heat production is expressed in terms of the Urey ratio,

$$Ur = \frac{MH}{Aq} \quad (13.2.12)$$

the ratio of the heat production term to the heat loss term on the right of (13.2.1). A Urey ratio less than unity implies a net loss of heat and a temperature decrease in the mantle, given by the following relation:

$$\frac{\partial T}{\partial t} = \frac{-Aq}{Mc}(1 - Ur) \quad (13.2.13)$$

The present value of the Urey ratio is 0.75, according to the results in Figure 13.2. This value, and estimates of the other quantities on the right of (13.2.13), give the mantle cooling rate. Substitution of $Ur = 0.75$, $q = 72 \text{ mW m}^{-2}$ (mean mantle heat flux, see Section 13.2.4), and $A/Mc = 1.38 \times 10^{-13} \text{ m}^2 \text{ KJ}^{-1}$ into (13.2.13) gives a present mantle cooling rate of about 80 K Gyr^{-1} ($-\partial T/\partial t$). The sensitivity of the Earth's Urey ratio to different assumptions about the mix of radiogenic elements in the mantle has been explored in the parameterized thermal history calculations of Jackson and Pollack (1984).

It should be stressed that mantle cooling is inevitable because of convection. Even the assumption of equality between mantle heat loss and heat production leads to an estimate of the mantle cooling rate in accord with the above. With the assumption $MH = Aq$, (13.2.4) and (13.2.5) yield the following expression for mantle temperature in terms of mantle heat production:

$$T - T_s = \frac{\rho Hd^2}{k} \left(\frac{M}{\rho Ad} \right)^{1/1+\beta} \left(\frac{k\kappa v Ra_{cr}}{\alpha g \rho Hd^5} \right)^{\beta/1+\beta} \quad (13.2.14)$$

For $\beta = 1/3$, (13.2.14) gives the dimensionless temperature $(T - T_s)/(\rho Hd^2/k)$ of an internally heated convecting fluid directly proportional to $Ra_H^{-1/4}$, where Ra_H is the Rayleigh number for internal heating (7.4.6):

$$Ra_H = \frac{\alpha g \rho H d^5}{k \kappa v} \quad (13.2.15)$$

Equation (13.2.14) provides an alternative form of parameterization for thermal history models (Turcotte et al., 1979; Turcotte, 1980b; Cook and Turcotte, 1981).

An equation for $\partial T/\partial t$ can be obtained by differentiating (13.2.14) with respect to time, noting that both H and v are functions of t . With the help of (13.2.2) and (13.2.6), we obtain

$$\frac{\partial T}{\partial t} = \frac{-\lambda(T - T_s)}{(1 + \beta)} \left\{ 1 + \frac{\beta A_0}{(1 + \beta)} \frac{(T - T_s)}{T^2} \right\}^{-1} \quad (13.2.16)$$

The second term in the parenthesis on the right of (13.2.16) is about 10 times the first term ($\beta A_0 = 2.1 \times 10^4 \text{ K}$, $\beta = 0.3$, $T \approx 2,000 \text{ K}$) and (13.2.16) can be reduced to the simple

equation

$$\frac{\partial T}{\partial t} = \frac{-\lambda T^2}{\beta A_0} \quad (13.2.17)$$

Equation (13.2.17) gives a cooling rate dependent only on mantle temperature, the radioactive decay constant, the activation temperature of the mantle viscosity, and the power-law exponent in the $Nu-Ra$ relation, all reasonably well known parameters. With $\lambda = 1.42 \times 10^{-17} \text{ s}^{-1}$, $\beta = 0.3$, $T = 2,500 \text{ K}$, and $A_0 = 7 \times 10^4 \text{ K}$ we find $\partial T/\partial t \approx -135 \text{ K Gyr}^{-1}$ from (13.2.17), in reasonable agreement with the above estimate of the mantle cooling rate. Our theoretical estimates of the Earth's secular cooling rate are in agreement with the $\approx 100 \text{ K Gyr}^{-1}$ cooling rates derived by considering the liquidus temperatures and formation mechanisms of Archean komatiites in relation to similar properties of present basalts (Sleep, 1979).

13.2.6 Volatile Dependence of Mantle Viscosity and Self-regulation

Mantle viscosity is not only a strong function of temperature, but it also depends sensitively on the mantle volatile content as well (Jackson and Pollack, 1987; McGovern and Schubert, 1989; Hirth and Kohlstedt, 1996). Dissolved volatiles in the mantle tend to lower the creep activation energy and thus reduce the viscosity at a given temperature. A loss of volatiles from the mantle (degassing or outgassing) would stiffen the mantle, requiring an increase in mantle temperature to maintain the requisite vigor of convection. Conversely, volatile recharging of the mantle (regassing) by tectonic processes such as subduction, overthrusting, and delamination would soften the mantle, requiring a decrease in mantle temperature to maintain the requisite convective vigor. The dependence of mantle viscosity on both temperature and volatile content produces a strong coupling between the evolution of the mantle and the atmosphere–hydrosphere system (Schubert et al., 1989b).

The effects of a volatile-dependent mantle viscosity on thermal evolution can be quantified with a simple extension of our elementary model, along the lines suggested by McGovern and Schubert (1989). The available data on the reduction of the activation temperature for solid-state creep by dissolved volatiles such as water can be represented by

$$A_0 = \alpha_1 + \alpha_2 f \quad (13.2.18)$$

where f is the volatile mass fraction and α_1 and α_2 are empirical constants (α_2 is negative so that mantle viscosity decreases with increasing f). The variable mass fraction of volatiles f adds an additional dependent variable in the model. To represent the physical processes of degassing and regassing that determine the volatile content of the mantle, a parameterization is required.

The rate of mantle degassing $\partial M_v^d / \partial t$ (M_v is the mass of volatiles in the mantle and d indicates degassing) can be expressed as

$$\frac{\partial M_v^d}{\partial t} = \rho_m f d_m S \quad (13.2.19)$$

where ρ_m is the mantle density, d_m is the average depth from which volatiles are released from the mantle (assuming complete outgassing to this depth), and S is the area spreading rate for the Earth's mid-ocean ridges. The parameter d_m can be thought of as an "equivalent depth," combining the actual depth of melting with an efficiency factor for the release of

volatiles. Regassing is assumed to take place through subduction. Similar to degassing, the rate of mantle regassing $\partial M_v^r / \partial t$ (r indicates regassing) can be expressed as

$$\frac{\partial M_v^r}{\partial t} = f_c \rho_c d_c \chi_r S \quad (13.2.20)$$

where f_c is the mass fraction of volatiles in the basaltic oceanic crust, ρ_c is the density of the crust, d_c is the average crustal thickness, and χ_r is an efficiency factor representing the fraction of volatiles that actually enters the deep mantle instead of returning to the surface through arc volcanism. The value of d_c can be chosen to reflect the added contribution of a subducted sediment layer.

Both degassing and regassing rates have been taken to be proportional to the vigor of mantle convection as expressed in the seafloor spreading rate S . This is related to the average age of subduction of oceanic crust τ by

$$S = \frac{A_{ob}(t)}{\tau} \quad (13.2.21)$$

where $A_{ob}(t)$ is the area of the ocean basins at time t . The heat flux through the ocean floor q (the heat flow from mantle convection) is related to τ by (8.6.8)

$$q = \frac{2k(T - T_s)}{(\pi \kappa \tau)^{1/2}} \quad (13.2.22)$$

Combination of (13.2.21) and (13.2.22) gives the seafloor spreading rate as

$$S = \frac{q^2 \pi \kappa A_{ob}(t)}{\{2k(T - T_s)\}^2} \quad (13.2.23)$$

Reymer and Schubert (1984) have proposed an expression for $A_{ob}(t)$ based on the assumption of constant continental freeboard (mean elevation of the continents above sea level) over the last 500 million years:

$$A_{ob}(t) = A_{ob}^* \left[\frac{V_{0a}^*}{V_0} + \frac{V_{0b}^* q^*}{V_0 q(t)} \right]^{-1} \quad (13.2.24)$$

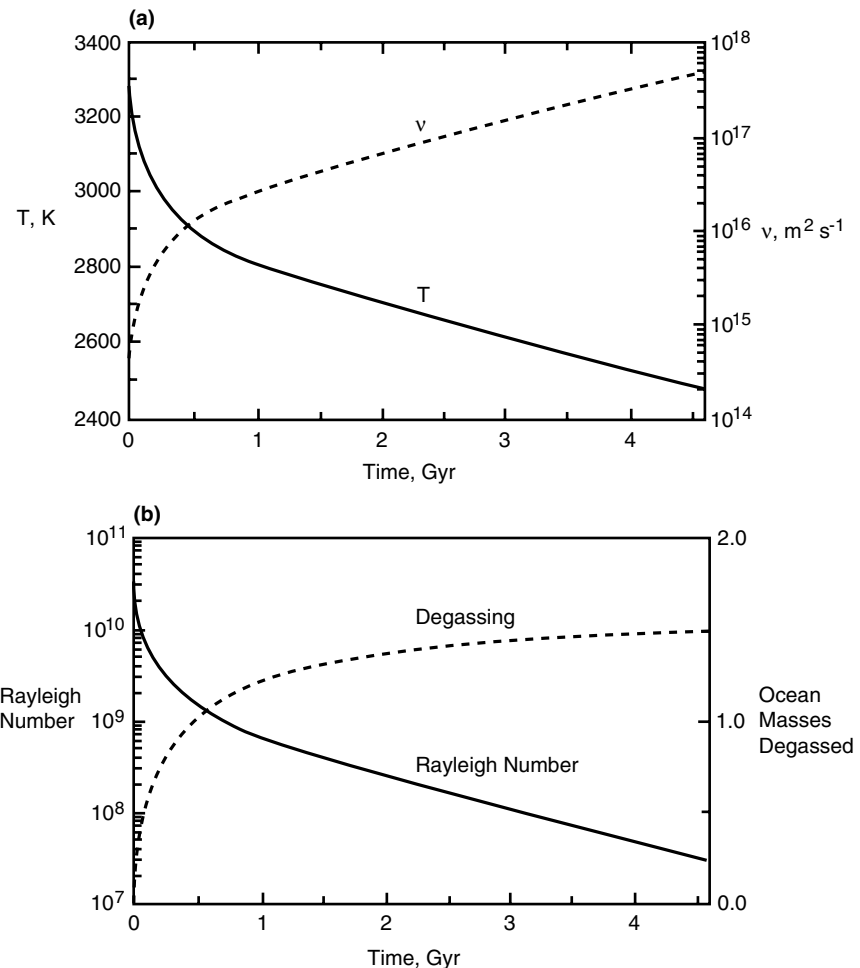
where V_0 is the total volume of water in the oceans (assumed constant in time), V_{0a} is the volume of the ocean basins above the peak ridge height, V_{0b} is the volume of the ocean basins below the peak ridge height, and asterisks denote present values. By combining (13.2.19)–(13.2.24) with the mass balance equation for the volatile content of the mantle,

$$\frac{\partial M_v}{\partial t} = \frac{\partial M_v^r}{\partial t} - \frac{\partial M_v^d}{\partial t} \quad (13.2.25)$$

we obtain

$$\frac{\partial M_v}{\partial t} = (f_c \rho_c d_c \chi_r - \rho_m f d_m) \frac{q^2 \pi \kappa A_{ob}^*}{4k^2(T - T_s)^2} \left(\frac{V_{0a}^*}{V_0} + \frac{V_{0b}^*}{V_0 q} \right)^{-1} \quad (13.2.26)$$

The addition of (13.2.18) and (13.2.26) to (13.2.3)–(13.2.6) together with an initial condition for M_v extends the simple thermal history model to a mantle with degassing and regassing and a volatile-dependent viscosity.



The results of a typical thermal history calculation with degassing are summarized in Figure 13.4 (after McGovern and Schubert, 1989). The parameter values used in the calculation are listed in Table 13.1. The values of α_1 and α_2 which give the dependence of viscosity on volatile content are based on laboratory data of Chopra and Paterson (1984) for wet dunite. The dependence of mantle viscosity on volatile (water) content has been discussed more recently by Hirth and Kohlstedt (1996). The value of the depth of melting d_m is derived from an estimate of the depth of the basalt eutectic in the Archean (Sleep, 1979). This value is too large to reflect present conditions, but it is intended to model conditions prevalent in the early history of the Earth when the convective vigor was much greater. Since rates of volatile exchange in the model (and presumably in the Earth) are much greater in the early part of the calculation than they are toward the end of the calculation, the value

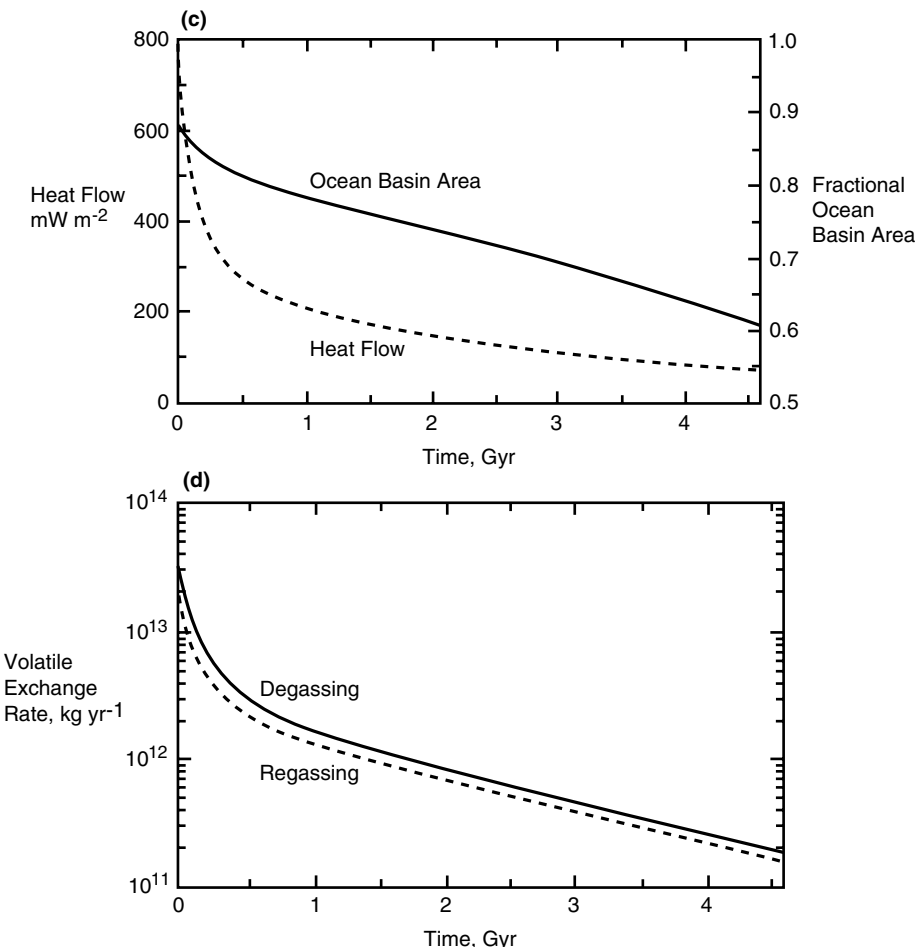


Figure 13.4. (a) Mantle temperature and kinematic viscosity as functions of time for a thermal history model with degassing and a volatile-dependent and temperature-dependent mantle viscosity. (b) Mantle Rayleigh number and amount of outgassing from the mantle (in units of ocean masses) versus time. (c) Heat flow from the mantle and normalized area of the ocean basins as functions of time (normalization is with respect to total surface area of the Earth). (d) Time dependence of mantle degassing and regassing rates (after McGovern and Schubert, 1989).

of d_m should represent conditions early in the Earth's evolution. Ringwood (1966, 1975) has estimated that the mass of dissolved water in the mantle is approximately 3 times that currently in the oceans. With the assumption that the total amount of water in the mantle–hydrosphere–atmosphere system is conserved, we set $n_m = 4$ (n_m is the number of ocean masses in the model mantle at time $t = 0$). The value of $H_0/c = f_1$ is iteratively adjusted so that the heat flow q at $t = 4.6$ Gyr is equal to the present value of about $q^* = 70 \text{ mW m}^{-2}$. For the calculation of Figure 13.4, H_0/c turns out to be $3.4 \times 10^{-14} \text{ K s}^{-1}$. It is assumed that the mass of volatiles on the surface is initially zero, i.e., $n_s = 0$ (n_s is the number of ocean masses initially in surface volatile reservoirs).

The degassing history of the mantle (Figure 13.4b) is characterized by an early period of rapid outgassing (more than one ocean mass in the first 500 Myr), followed by a gradual

Table 13.1. Parameter Values for a Thermal History Model with Degassing and a Volatile-dependent Mantle Viscosity

Parameter	Value	Reference
v_0	$2.21 \times 10^7 \text{ m}^2 \text{ s}^{-1}$	Jackson and Pollack (1987)
k	$4.2 \text{ W m}^{-1} \text{ K}^{-1}$	Schubert et al. (1980)
		Jackson and Pollack (1987)
g	9.8 m s^{-2}	
λ	$3.4 \times 10^{-10} \text{ yr}^{-1}$	Jackson and Pollack (1984)
α	$3 \times 10^5 \text{ K}^{-1}$	Schubert et al. (1980)
		Jackson and Pollack (1987)
κ	$10^{-6} \text{ m}^2 \text{ s}^{-1}$	Jackson and Pollack (1987)
R_m	6,271 km	Jackson and Pollack (1987)
R_c	3,471 km	Jackson and Pollack (1987)
T_s	273 K	Jackson and Pollack (1987)
Ra_{cr}	1,100	Jackson and Pollack (1987)
ρ_c	$4.2 \text{ MJ m}^3 \text{ K}^{-1}$	Jackson and Pollack (1987)
β	0.3	Jackson and Pollack (1987)
α_1	$6.4 \times 10^4 \text{ K}$	McGovern and Schubert (1989)
α_2	$-6.1 \times 10^6 \text{ K}$	McGovern and Schubert (1989)
	(weight fraction) $^{-1}$	McGovern and Schubert (1989)
M_{mantle}	$4.06 \times 10^{24} \text{ kg}$	Schubert et al. (1980)
d_m	100 km	Sleep (1979)
f_c	0.03	Schubert et al. (1989b)
d_c	5 km	Schubert et al. (1989b)
ρ_c	$2,950 \text{ kg m}^{-3}$	Turcotte and Schubert (1982)
χ_r	0.8	
M_{ocean}	$1.39 \times 10^{21} \text{ kg}$	Walker (1977)
n_m	4.0	Ringwood (1966, 1975)
n_s	0	
A_0^*	$3.1 \times 10^{14} \text{ m}^2$	Reymer and Schubert (1984)
V_{0a}^*	$7.75 \times 10^{17} \text{ m}^3$	Reymer and Schubert (1984)
V_{0b}^*	$3.937 \times 10^{17} \text{ m}^3$	Reymer and Schubert (1984)
V_0	$1.1687 \times 10^{18} \text{ m}^3$	Reymer and Schubert (1984)
q^*	70 mW m^{-2}	Turcotte and Schubert (1982)

leveling off in the outgassed mass for the remaining 4 Gyr. The change in activation temperature A_0 exhibits similar behavior due to its dependence on mantle volatile content. A comparison of Figures 13.4a and b shows that the time scales for degassing and for rapid initial cooling are approximately the same.

Figure 13.4c shows the area of the Earth's ocean basins A_{ob} (normalized to the total surface area) as a function of time. Although the assumption of constant freeboard is only known to be valid for the last 500 million years (Wise, 1974; Reymer and Schubert, 1984), application of this assumption over the entire thermal history calculation results in a monotonic decrease in ocean basin area (increase in continental area) over geologic time, in qualitative agreement with many crustal growth models (Reymer and Schubert, 1984, Figure 6) (see also Section 13.7). By (13.2.24) and our requirement that the present heat flow q^* matches the measured value, the present value of A_{ob} necessarily agrees with today's area of the ocean basins.

Figure 13.4d shows the mantle degassing and regassing rates as functions of time. The degassing curve of Figure 13.4b is just the integral of the area between these two curves. As implied by Figure 13.4b, these rates start out significantly different, but converge with time.

The Rayleigh number (Figure 13.4b) is very large initially (about 3.5×10^{10}) reflecting the low value of initial kinematic viscosity (about $4 \times 10^{14} \text{ m}^2 \text{ s}^{-1}$). Mantle convection during the period of early rapid heat loss is indeed vigorous. The Rayleigh number falls by about one and a half orders of magnitude during the first 500 Myr, while viscosity increases by about the same amount. The mantle adjusts to its self-regulated state in about 500 Myr, after which the Rayleigh number decreases with time (while viscosity increases with time) by about another one and a half orders of magnitude over the next 4 Gyr reaching a present value of about 3×10^7 (with a present kinematic viscosity of about $5 \times 10^{17} \text{ m}^2 \text{ s}^{-1}$). The Rayleigh number decreases approximately exponentially with time and the viscosity increases approximately exponentially with time after the initial period of rapid cooling.

In order to identify the major effects of mantle degassing or regassing on the thermal evolution of the Earth, we compare in Figure 13.5 the results of the model calculation of

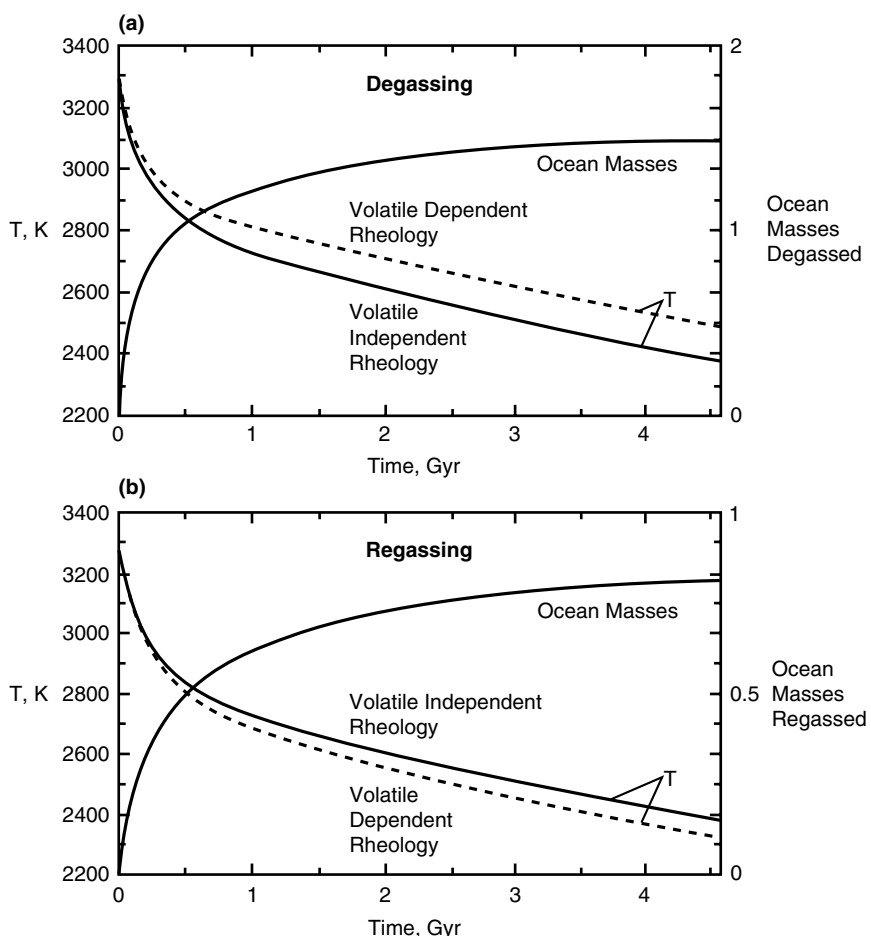


Figure 13.5. (a) The effect of degassing on mantle temperature. Thermal histories for volatile-dependent (dotted line) and volatile-independent (solid line) rheologies are plotted along with the degassing history for the volatile-dependent case. Degassing with volatile dependence raises the present temperature of the mantle. (b) The effect of regassing on mantle temperature. Thermal histories for volatile-dependent (dotted line) and volatile-independent (solid line) rheologies are plotted along with the regassing history for the volatile-dependent case. Regassing with volatile dependence lowers the present temperature of the mantle.

Figure 13.4 with one in which there is no volatile dependence of the rheology (parameters are identical to those in Figure 13.4 except $\alpha_1 = 5.6 \times 10^4$ K and $\alpha_2 = 0$). In addition, Figure 13.5 compares the results of a regassing scenario with volatile-dependent rheology (parameters are identical to those in Figure 13.4 except $d_c = 6$ km, $d_m = 50$ km, $n_m = 4$, $n_s = 2$) to the thermal history with no volatile dependence of viscosity. (In all the cases in Figure 13.5, H_0/c has essentially the same value as it does in the calculation of Figure 13.4.) Outgassing (Figure 13.5a) dries out the interior and tends to increase its viscosity. However, the tendency for devolatilization to increase viscosity is compensated by the effect of temperature on viscosity. Higher viscosity tends to reduce heat flow, allowing heat generated by radiogenic sources to build up and increase mantle temperature. But then the higher temperature tends to reduce viscosity and enhance heat flow. Thus, the mantle adjusts to maintain the required rate of heat loss by increasing temperature, reducing viscosity, and maintaining the level of convective vigor. The net result of degassing is a hotter mantle, but mantle heat flow, viscosity, and convective vigor are essentially the same as in a mantle with volatile-independent rheology. With degassing and a volatile-dependent rheology the mantle is hotter and cools more slowly than it would with a volatile-independent rheology. Regassing (Figure 13.5b) increases the volatile content of the interior and tends to decrease its viscosity. However, as in the degassing case, the tendency for revolatilization to decrease viscosity is compensated by a reduction in mantle temperature so as to maintain viscosity, heat flow, and convective vigor approximately constant. In addition, Figure 13.5b shows the amount of water regassed into the mantle. The evolution, in terms of the amount of cooling and the quantity of water reabsorbed into the mantle, is rapid during the first several hundred million years, becoming more gradual afterwards. In the regassing case about three-quarters of an ocean mass of volatiles (water) is reinjected into the mantle over geologic time, with the bulk of this occurring in the first billion years. The main effect of the volatile-dependent mantle viscosity is a cooler mantle, compared to the case where viscosity depends on temperature only. As in the degassing case, mantle viscosity and heat flow are essentially the same for both the volatile-dependent and volatile-independent viscosities. In both the regassing and degassing scenarios, the time rate of change of temperature eventually tends to the same value for the volatile-dependent and volatile-independent rheologies; during the latter stages of thermal evolution only a constant temperature offset distinguishes the volatile-dependent mantle cooling rate from the volatile-independent one.

Figure 13.6 shows the evolution of the Urey ratio for the degassing case of Figure 13.4. The Urey ratio Ur starts with a relatively low value at $t = 0$ because of the dominance of primordial heat in the initially hot mantle. The ratio quickly reaches a maximum and then slowly and steadily decreases as the mantle volatile exchange rates equilibrate and the value of A_0 approaches its self-regulated value. Because of the decay of the radiogenic heat sources, Ur will tend to zero as $t \rightarrow \infty$; Ur is less than unity throughout the entire time.

13.3 More Elaborate Thermal Evolution Models

13.3.1 A Model of Coupled Core–Mantle Thermal Evolution

While the simple models of the previous section are adequate for demonstrating many of the important aspects of the Earth's evolution, more elaborate models are needed if, for example, the evolution of the core is to be included. We now consider a more complex model developed by Stevenson et al. (1983) with a coupled core and mantle. Thermal evolution

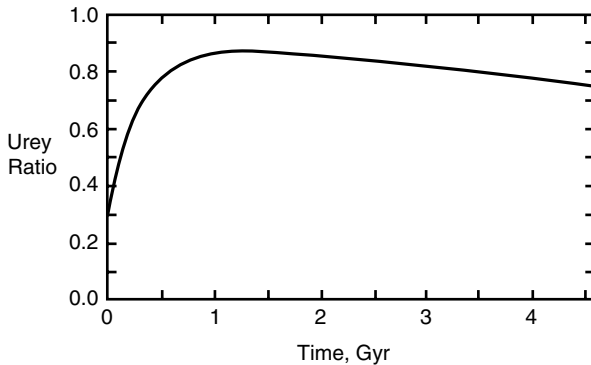


Figure 13.6. Urey ratio versus time in the thermal history calculation of Figure 13.4.

calculations including core–mantle coupling have also been given by Sleep et al. (1988) and by Davies (1993). A core thermal history model has been presented by Buffett et al. (1996). As sketched in Figure 13.7, the model of Stevenson et al. (1983) consists of a spherical shell mantle surrounding a concentric spherical core. The core has radius R_c and density ρ_c and the mantle has outer radius R_p and density ρ_m . There is a solid inner core of radius R_i and a liquid outer core.

Figure 13.7b is a schematic of the radial profile of spherically averaged temperature $T(r)$ for the coupled model. There are thermal boundary layers at the top and bottom of the convecting mantle of thickness δ_s and δ_c , respectively. Temperature is assumed to vary linearly with radius in the boundary layers. The change in temperature across the top cold thermal boundary layer is ΔT_s and the temperature change across the lower hot thermal boundary layer is ΔT_c . Mantle temperature is T_u at the base of the upper thermal boundary layer and T_l at the top of the lower thermal boundary layer. Temperature at the core–mantle boundary is T_{cm} . The surface temperature is T_s . Temperature is assumed to increase adiabatically with depth in the mantle between the values of T_u and T_l in the region outside the boundary layers. The temperature in the fluid outer core is taken to increase adiabatically with depth from T_{cm} to T_{mio} , the liquidus temperature of the core alloy. Nonadiabatic temperature differences or boundary layers are negligible in the convective outer core because of its low viscosity. The dashed curve in Figure 13.7b is the depth or pressure $p(r)$ dependent liquidus temperature of the core alloy $T_m(r)$ (r is the radial distance from the center of the model). In the liquid outer core $T(r) > T_m(r)$ while the reverse is true in the solid inner core.

The solid inner core is assumed to be pure iron while the outer core contains a light alloying element that we take to be sulfur (the model can be trivially modified to deal with other possible light constituents in the core, for example, oxygen). We neglect inner–outer core density differences in computing $p(r)$, but we do take into account the gravitational energy release upon freezing of outer core liquid and growth of the solid inner core, a process which excludes the light alloying element from the solid inner core and concentrates it in the liquid outer core. The gravitational potential energy release upon differentiation of the core is responsible for the convective motions in the outer core that generate the Earth’s magnetic field by dynamo action (Braginsky, 1963; Gubbins, 1977a; Loper, 1978a, b; Loper and Roberts, 1979; Stevenson et al., 1983; Glatzmaier and Roberts, 1997). The latent heat release that also occurs with inner core growth provides a thermal drive for convective

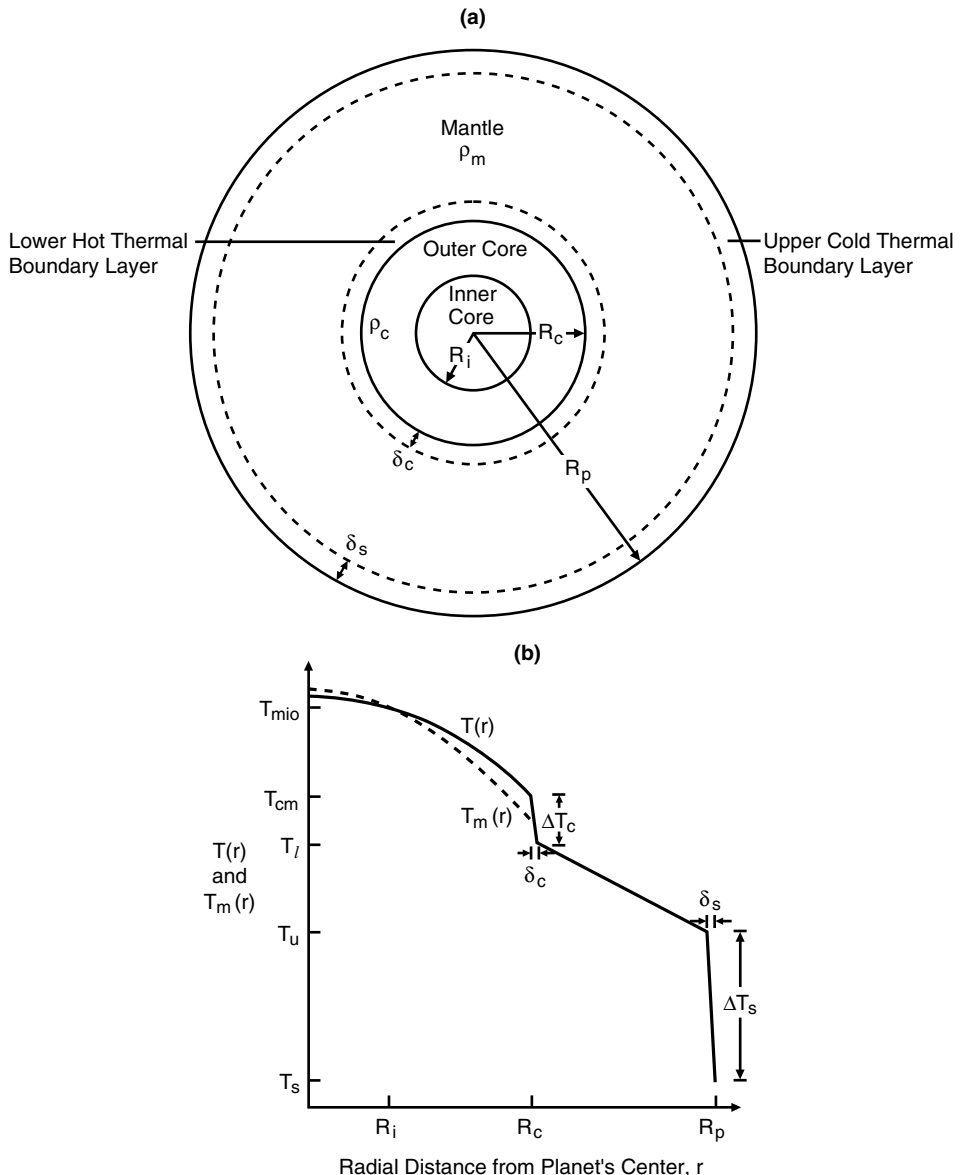


Figure 13.7. (a) Geometry of Earth thermal history model for coupled core–mantle evolution. (b) Schematic of the radial profile of spherically averaged temperature in the coupled core–mantle Earth thermal evolution model.

motions in the liquid outer core (Verhoogen, 1961). Because of the Carnot efficiency factor, a thermally driven dynamo is less thermodynamically efficient than one driven by chemical buoyancy.

The liquidus temperature $T_m(r)$ of the core alloy is expressed as a quadratic in the pressure $p(r)$ (Stevenson et al., 1983):

$$T_m(r) = T_{m0}(1 - 2\chi)(1 + T_{m1}p(r) + T_{m2}p^2(r)) \quad (13.3.1)$$

where T_{m0} , T_{m1} , and T_{m2} are constants, χ is the mass fraction of light alloying constituent in the liquid outer core and it is assumed that $\chi \ll 1$. The temperature along the outer core adiabat $T_c(r)$ is similarly represented by

$$T_c(r) = T_{cm} \left\{ \frac{1 + T_{a1}p(r) + T_{a2}p^2(r)}{1 + T_{a1}p_{cm} + T_{a2}p_{cm}^2} \right\} \quad (13.3.2)$$

where T_{a1} and T_{a2} are constants and p_{cm} is the pressure at the core–mantle boundary.

The simultaneous solution of (13.3.1) and (13.3.2) gives the pressure p_{io} at the inner core–outer core boundary. The radius of the inner core R_i is then obtained by assuming that the acceleration of gravity in the core is rg/R_c (g is the surface value of gravity):

$$R_i = \left\{ \frac{2(p_c - p_{io})R_c}{\rho_c g} \right\}^{1/2} \quad (13.3.3)$$

where p_c is the pressure at the center of the Earth. The mass of the inner core m_{ic} is

$$m_{ic} = \frac{4}{3}\pi R_i^3 \rho_c \quad (13.3.4)$$

Initially the core is superliquidus and $R_i = 0$. As the Earth cools, inner core nucleation begins when the liquidus temperature is reached at the center of the Earth. The inner core grows upon further cooling of the Earth. The liquidus temperature of the outer core decreases as the inner core grows and the light alloying constituent is concentrated in the outer core. The decrease in outer core liquidus upon inner core freezing is important in retarding the rate of inner core growth and in preventing complete freezing of the core (not applicable to the Earth but perhaps significant in other planets such as Mercury or Jupiter's moon Ganymede). Conservation of the light constituent mass gives

$$\chi = \frac{\chi_0 R_c^3}{R_c^3 - R_i^3} \quad (13.3.5)$$

where χ_0 is the initial concentration of the light element in the core.

Separate energy balance equations are required for the mantle and core. These are given by

$$\frac{4}{3}\pi (R_p^3 - R_c^3) \left\{ \rho_m H - \rho_m c_m \frac{\partial}{\partial t} \langle T_{\text{mantle}} \rangle \right\} = 4\pi \left\{ R_p^2 q_s - R_c^2 q_c \right\} \quad (13.3.6)$$

$$\frac{4}{3}\pi R_c^3 \left\{ -\rho_c c_c \frac{\partial}{\partial t} \langle T_c \rangle \right\} + (L + E_G) \frac{\partial m_{ic}}{\partial t} = 4\pi R_c^2 q_c \quad (13.3.7)$$

where c_m and c_c are the specific heats of the mantle and core, H is the rate of internal heating per unit mass in the mantle as given by (13.2.2) (it is assumed that there are no radiogenic heat sources in the core), $\langle T_{\text{mantle}} \rangle$ and $\langle T_c \rangle$ are the volume-averaged mantle and core temperatures, and q_s and q_c are the heat fluxes through the surface and core–mantle boundary, respectively. The temperature $\langle T_{\text{mantle}} \rangle$ can be related to T_u by

$$\langle T_{\text{mantle}} \rangle = \eta_m T_u \quad (13.3.8)$$

where η_m is a constant, while $\langle T_c \rangle$ can be similarly related to T_{cm} by

$$\langle T_c \rangle = \eta_c T_{cm} \quad (13.3.9)$$

where η_c is a constant. Use of (13.3.8) and (13.3.9) provides a convenient representation of the quantities $\partial \langle T_{\text{mantle}} \rangle / \partial t$ and $\partial \langle T_c \rangle / \partial t$ in the energy equations in terms of the time rates of change of the single temperatures T_u and T_{cm} . The quantity $\partial m_{ic} / \partial t$ that appears in the core energy balance equation can be related to $\partial T_{cm} / \partial t$ through the use of (13.3.1)–(13.3.4).

The heat fluxes q_s and q_c are given by parameterizations similar to (13.2.4) and (13.2.5). We note that $d(Ra_{cr}/Ra)^\beta$ in (13.2.4) is the thermal boundary layer thickness δ and that (13.2.4) is just Fourier's law of heat conduction for the boundary layer $q = k(T - T_s)/\delta$. Accordingly, we can write the expressions for q_s and q_c as (Figure 13.7)

$$q_s = \frac{k \Delta T_s}{\delta_s} = \frac{k(T_u - T_s)}{\delta_s} \quad (13.3.10)$$

$$q_c = \frac{k \Delta T_c}{\delta_c} = \frac{k(T_{cm} - T_l)}{\delta_c} \quad (13.3.11)$$

The thickness of the surface boundary layer δ_s is expressed, using the global Rayleigh number

$$Ra = \frac{g \alpha (\Delta T_s + \Delta T_c)(R_p - R_c)^3}{\nu \kappa} \quad (13.3.12)$$

as

$$\delta_s = (R_p - R_c) \left(\frac{Ra_{cr}}{Ra} \right)^\beta \quad (13.3.13)$$

If the mantle were a constant viscosity fluid layer, then the lower thermal boundary layer would have the same thickness as the upper boundary layer $\delta_c = \delta_s$ and δ_c would also be given by (13.3.13). In this case the heat fluxes q_s and q_c would be different only because of differences in the temperature drops ΔT_s and ΔT_c across the boundary layers. However, due to the strongly temperature dependent viscosity of the mantle, it is possible that the lower boundary layer is thinner, on the average, than the upper boundary layer (Daly, 1980; Nataf and Richter, 1982). The lower boundary layer might also be thinned by the ejection of plumes and thermals as a consequence of buoyancy instability enhanced by a reduction in viscosity (Howard, 1966; Richter, 1978; Yuen and Peltier, 1980; Olson et al., 1988). We can account for a reduction in boundary layer thickness at the core–mantle boundary by determining its thickness locally whenever the heat flux from the core is sufficiently large. The experiments of Booker and Stengel (1978) suggest that the local critical Rayleigh number for the breakdown of the boundary layer is

$$Ra_{crb} = \frac{g \alpha \Delta T_c \delta_c^3}{\nu_c \kappa} \approx 2 \times 10^3 \quad (13.3.14)$$

Richter (1978) finds that ν_c should be based on the average temperature within the boundary layer. Hence,

$$\nu_c \equiv \nu_r \exp \left(\frac{A_r}{T_l + \Delta T_c/2} \right) \quad (13.3.15)$$

We use (13.3.14) instead of (13.3.13) to calculate δ_c whenever (13.3.14) gives a smaller thickness. The viscosity ν used in (13.3.13) to get δ_s is given by (13.2.6) with the temperature evaluated at the upper mantle temperature T_u .

The thermal history of this coupled core–mantle model is obtained by integrating with respect to time the energy balance equations and the equation for the rate of inner core growth. The main dependent variables of the model are the upper mantle temperature $T_u(t)$, the core–mantle boundary temperature $T_{cm}(t)$, and the radius of the inner core $R_i(t)$. The boundary and initial conditions for the model are $T(R_p) = T_s$, $T_u(t = 0) = T_{u0}$, $T_{cm}(t = 0) = T_{cm0}$, $R_i(t = 0) = 0$.

13.3.2 Core Evolution and Magnetic Field Generation

The cooling history of the mantle in this coupled core–mantle thermal evolution model is similar to that of the simpler model presented in Section 13.2. Here we focus on the new aspects of the coupled model and describe the thermal evolution of the core and its implications for magnetic field generation by dynamo action. We discuss two models presented by Stevenson et al. (1983), the parameter values for which are given in Table 13.2. The rheological parameters were chosen to give a present mantle kinematic viscosity of about $10^{17} \text{ m}^2 \text{ s}^{-1}$ (Cathles, 1975; Peltier, 1981), and the value of $\rho_m H_0$, together with the chondritic value for λ , gives a present heat flux from the model mantle of about 60 mW m^{-2} . Internal heating in this model contributes about 75% of the present surface heat loss, in agreement with the discussion in Section 13.2 of the contribution of secular cooling to the Earth’s surface heat flow.

Table 13.2. Parameter Values for Two Coupled Core–Mantle Thermal Evolution Models of the Earth

Parameter	Value
Parameters Common to Both Models	
α	$2 \times 10^{-5} \text{ K}^{-1}$
k	$4 \text{ W m}^{-1} \text{ K}^{-1}$
κ	$10^{-6} \text{ m}^2 \text{ s}^{-1}$
$\rho_m c_m = \rho_c c_c$	$4 \text{ MJ m}^{-3} \text{ K}^{-1}$
$\rho_m H_0$	$0.17 \mu\text{W m}^{-3}$
λ	$1.38 \times 10^{-17} \text{ s}^{-1}$
A_0	$5.2 \times 10^4 \text{ K}$
v_0	$4 \times 10^3 \text{ m}^2 \text{ s}^{-1}$
Ra_{cr}	500
β	0.3
R_p	6,371 km
g	10 m s^{-2}
T_s	293 K
T_{m1}	6.14 K TPa^{-1}
T_{m2}	-4.5 K TPa^{-2}
T_{a1}	3.96 K TPa^{-1}
T_{a2}	-3.3 K TPa^{-2}
η_m, η_c	1.3, 1.2
Parameter	Value, E1, E2
Parameters Different for the Two Models	
$L + E_G$	$1,2 \text{ MJ kg}^{-1}$
T_{m0}	1,950, 1,980 K

The main difference between the models in Table 13.2 is the value for $L + E_G$, the total energy (latent heat plus gravitational energy) released per unit mass on inner core solidification. Model E1 uses $L + E_G = 1 \text{ MJ kg}^{-1}$, while model E2 assumes $L + E_G = 2 \text{ MJ kg}^{-1}$. The quantity $L + E_G$ is uncertain because of our lack of knowledge of the exact composition of the core and of its thermodynamic properties. In addition, the gravitational energy release E_G depends on core size. Models E1 and E2 also differ in their values of T_{m0} which are chosen to reproduce the correct inner core radius at present. Since the models are constrained to give the present value of R_i they are not sensitive to uncertainties in our precise knowledge of the core melting curve. Melting temperatures in the core are uncertain despite recent experiments to determine the melting point of iron at high pressures (Boehler, 1993, 1994, 1996; Anderson and Ahrens, 1996; Chen and Ahrens, 1996; Anderson and Duba, 1997; Boehler and Ross, 1997) in part because of our lack of knowledge of core composition.

The initial concentration of light constituent in the core χ_0 is taken to be 0.1, consistent with sulfur being the light element (Ahrens, 1979). However, the exact identification of the light constituent in the core is not essential in the model and other possibilities such as silicon and oxygen (Ringwood, 1977b; Poirier, 1994a, b) can be accommodated by adjusting the numerical coefficient of χ in (13.3.1). The parameters T_{a1} and T_{a2} for the core adiabat are based on Stacey's (1977b) value for the Grüneisen parameter γ . The choice of core and mantle adiabats following Stacey (1977b) determines the values of η_m and η_c . Core–mantle boundary layer thickness δ_c is calculated using (13.3.14).

Question 13.3: What is the major light alloying element in the Earth's core?

The core evolution according to models E1 and E2 is shown in Figure 13.8 in terms of the time dependence of the heat flux from the core. Heat flow from the core initially decreases very rapidly with time during the period when early vigorous mantle convection removes heat quickly from the core. Inner core solidification begins at $t \approx 2.7 \text{ Gyr}$ and 2.3 Gyr in models E1 and E2, respectively, when the core has cooled sufficiently that the core adiabat drops to the core melting temperature at the center of the Earth. Core freezing occurs later in model E1 since it has a lower core melting temperature than model E2 (see the values of T_{m0} in Table 13.2). The present inner core radii in models E1 and E2 are 1,234 km and 1,207 km, respectively; the present inner core radius in model E1 is larger than in model E2 despite the later onset of inner core freezeout in model E1 because twice the mass can be solidified in model E1 for every unit of $L + E_G$ removed from the core by mantle convection.

Were it not for inner core freezing, the monotonic decrease in core heat flux q_c would continue through geologic time (dashed curve in Figure 13.8) and eventually q_c would fall below the value necessary to supply the conductive heat flow along the core adiabat (estimated at 15 mW m^{-2} , horizontal dash-dot line in Figure 13.8). Thermal convection in the core is not possible if q_c falls below the heat flux conducted along the core adiabat; a thermally driven dynamo would also not be possible were q_c to drop below the conductive heat flux along the adiabat. Figure 13.8 shows that thermal convection and thermal forcing of a core dynamo would have ceased at about 3.2 Gyr in the Earth models E1 and E2 if not for inner core solidification. However, the cores in the models do begin to solidify at about 2.5 Gyr and the decrease in core heat flow with time is arrested by this event. Once core freezing begins, the release of latent heat and gravitational energy contributes to the heat flow from the core

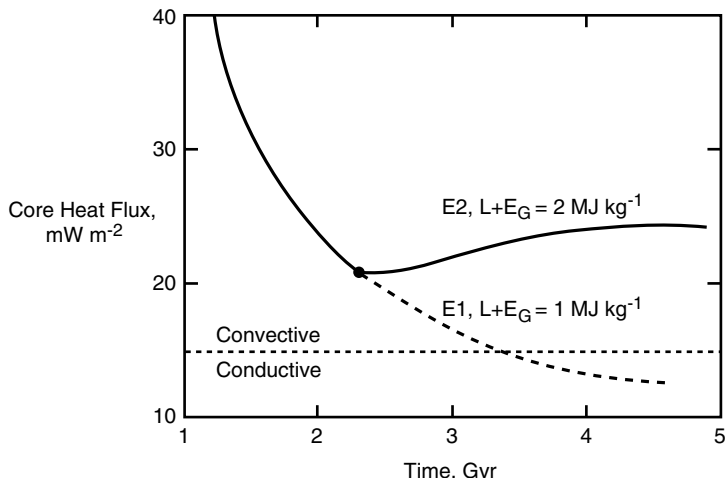


Figure 13.8. The heat flux from the core q_c versus time in a coupled core–mantle thermal history model (after Stevenson et al., 1983) for two values of $L + E_G$, the total energy liberated per unit mass upon core solidification. The horizontal dotted line gives the value of conductive heat flow along the core adiabat. For q_c above this value the core is thermally convecting while for lower values of q_c thermal convection is not possible. Onset of inner core solidification occurs at the filled circles where q_c undergoes an abrupt change in variation with time. The dashed curve indicates the thermal evolution without inner core freezing.

which is maintained above the conductive heat flow along the core adiabat for the rest of geologic time (Figure 13.8). Core heat flow tends toward a plateau at late times, depending on the particular value of $L + E_G$. Convection in the outer core is driven both thermally and compositionally subsequent to inner core freezing, an important implication of these models for the maintenance of core convection and dynamo generation of the geomagnetic field. Gravitational energy release may be more important in driving the dynamo than latent heat release since the mechanical energy is almost entirely available for dynamo generation (Gubbins, 1977a). Other models of the evolution of the Earth's core and dynamo action within it suggest that thermal convection and compositional convection are both important in the generation of the Earth's magnetic field (Braginsky and Roberts, 1995; Buffett et al., 1996).

Question 13.4: What is the dominant energy source for driving convection and dynamo action in the Earth's outer core?

One aspect of our model that is more important for other terrestrial planets than for the Earth (see the next chapter for a discussion of the thermal histories of other planets) is the dependence of the core melting temperature on the concentration of the light alloying element. The core melting temperature decreases with increasing concentration of the light constituent. Since the light element in the core is excluded from the solidifying inner core, its concentration in the liquid outer core increases with time as the inner core freezes. The melting temperature of the outer core accordingly decreases with time, thereby retarding inner core growth. Inner core growth rates in models E1 and E2 at present are 0.25 and 0.20 m Myr^{-1} , respectively.

The dependence of the core melting temperature on the minor constituent concentration can have important consequences during core formation. If core differentiation occurs contemporaneous with accretion of the Earth, then increasingly lighter material would segregate into the core as the Earth grows and the melting temperature of the iron alloy material increases with pressure in the growing Earth. This could result in a compositionally stratified core with lighter material on top of heavier material and a form of layered double diffusive convection in the core (Stevenson, 1998). The core evolution model discussed above would require modification to account for this style of core convection.

Present core heat flow values in models E1 and E2 are 18.6 and 24.4 mW m⁻², respectively. At the surface of the model Earth, these heat flows would be about 5.6 and 7.3 mW m⁻² based on $q \propto R^{-2}$ and $R_c = 3,485$ km in these models. These values of heat flow from the core are in qualitative accord with estimates of the heat advected by mantle plumes (Davies, 1988b; Sleep, 1990), assuming that all the heat lost from the core is transported through the mantle by advection in plumes.

The core thermal history predicted by these models has interesting implications for the Earth's magnetic field. The model shows the onset of inner core freezing relatively late in the Earth's thermal history, about 2 Gyr ago. Since the Earth's magnetic field is at least 3.5 Gyr old (McElhinny and Senanayake, 1980), the mode of powering the dynamo may have changed during the Earth's evolution. Early in the Earth's thermal history, the magnetic field was probably powered by thermal convection with the heat derived from secular cooling of the fluid core. After initiation of inner core growth, the dominant source of energy for the dynamo became gravitational energy release upon concentration of the light element into the liquid outer core. Latent heat release also contributes to the maintenance of the dynamo, but with diminished effectiveness compared with gravitational energy release because of the Carnot efficiency factor associated with any purely thermal energy source (Gubbins, 1977a). The energy released by gravitational and latent heat over the entire time of inner core growth in models E1 and E2 exceeds the energy made available by secular cooling of the outer core during this time interval by about a factor of 6. The energy release rate on core freezing in both models amounts to several terawatts, the level of power estimated to be necessary to drive the dynamo (Gubbins et al., 1979). The models thus indicate that while inner core solidification can power the dynamo, secular cooling by itself cannot.

An estimate of the Earth's magnetic field strength through geologic time can be derived from the model by equating the energy available for dynamo generation to the Ohmic dissipation rate Φ (Stevenson et al., 1983):

$$\Phi = E_G \frac{dm_{ic}}{dt} + \eta \left(L \frac{dm_{ic}}{dt} - \frac{dE_{th}}{dt} - 4\pi R_c^2 q_{ac} \right) \quad (13.3.16)$$

where η is the Carnot efficiency factor (≈ 0.6 if $E_G > L$), dE_{th}/dt is the rate of change of core thermal energy, and q_{ac} is the heat flow conducted along the core adiabat. Since Ohmic dissipation scales as the square of the current or field, Φ provides an estimate of a nominal nondimensional magnetic field strength $H_m(t)$ through

$$H_m(t) \equiv \{\Phi(t)/\Phi(4.5 \text{ Gyr})\}^{1/2} \quad (13.3.17)$$

Figure 13.9 from Stevenson et al. (1983) shows the nominal field strength based on (13.3.17) as a function of time for models E1 and E2. Caution must be used in interpreting this nominal field strength since changes can occur in either the toroidal or poloidal part of the Earth's magnetic field with or without changes in the other part. Nevertheless, the model result

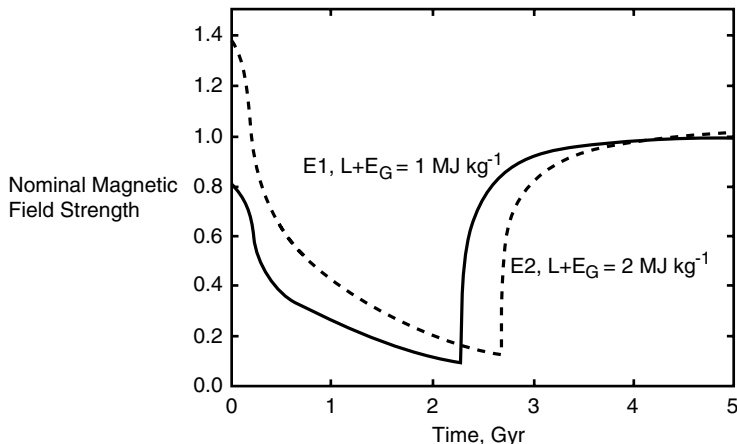


Figure 13.9. Nominal magnetic field strength from (13.3.16) and (13.3.17) versus time for coupled core–mantle thermal evolution models E1 and E2. Magnetic field generation is thermally driven early in the evolution and predominantly gravitationally driven late in the evolution. The abrupt increases in field strength at about 2.5 Gyr mark the switch from a thermally driven dynamo to a gravitationally powered dynamo with the onset of inner core freezing.

gives some indication of possible changes in the Earth’s magnetic dipole moment through geologic time. The magnetic field strength declines with time during the first two billion years of evolution as the thermally driven core dynamo decays. Prior to the onset of inner core freezing, magnetic field strengths are low. Upon inner core freezing, the source of energy for the dynamo changes to predominantly gravitational and there is a rapid rise to present magnetic field strengths within about 500 Myr. At present, the paleomagnetic evidence neither supports nor refutes this scenario (Merrill and McElhinny, 1983).

Question 13.5: Has the Earth always had a geodynamo?

13.4 Two-layer Mantle Convection and Thermal Evolution

Another generalization of the simple one-layer thermal history model allows us to explore how temperature in the Earth would have evolved in time with separate upper and lower mantle convection systems. This style of mantle convection requires that some component of the density change near 660 km depth be due to a difference in composition between the upper and lower mantle or that a large increase in viscosity between the upper and lower mantle occurs at the 660 km seismic discontinuity. The relative merits of whole-mantle convection versus layered mantle convection are discussed in other chapters. Here we simply explore the consequences of the different styles of convection for Earth thermal history. We will follow the layered mantle convection thermal history model of Spohn and Schubert (1982a). McKenzie and Richter (1981) and Richter (1985) have also analyzed layered mantle convection thermal history models and Christensen (1981) has obtained numerical solutions of convection in a chemically layered mantle. Honda (1995) has studied a parameterized thermal history model in which the mantle, initially in a state of layered convection, undergoes a transition to whole-mantle or one-layer convection. The coupled core–mantle thermal history model of the previous section is similar to the layered mantle

model of this section in the sense that both are coupled two-layer models. Some of the general results we arrive at with the layered mantle model can also be obtained with the coupled core–mantle model.

The model is sketched in Figure 13.10. It consists of two concentric spherical shells surrounding a spherical core. The outer spherical shell coincides with the upper mantle and the inner spherical shell corresponds to the lower mantle. There are thermal boundary layers at the top and bottom of both spherical shells as appropriate for vigorously convecting layers heated partly from below. Accordingly, there are two thermal boundary layers immediately

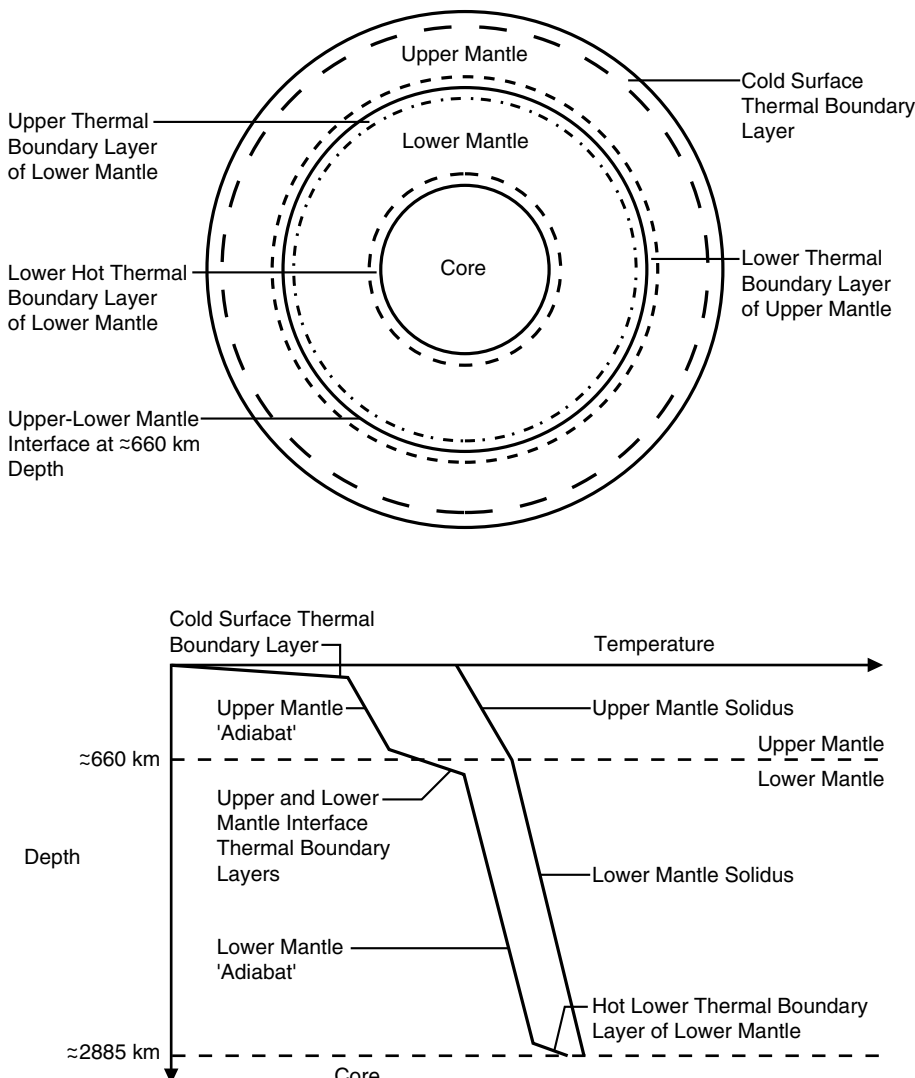


Figure 13.10. Sketch of the two-layer mantle convection thermal history model and the temperature distribution in the model. There are thermal boundary layers on both sides of the upper–lower mantle interface and thermal boundary layers at the surface and the core–mantle interface. The adiabatic temperature profiles in the upper and lower mantle are assumed to parallel the increase in temperature with depth of the upper and lower mantle solidus temperature profiles.

adjacent to the interface between the shells, the lower thermal boundary layer of the upper mantle and the upper thermal boundary layer of the lower mantle. Heat transfer across the boundary layers is by thermal conduction, while outside the boundary layers heat transfer is mainly by advection. The interface boundary layers are therefore additional sources of thermal resistance that are not present in a whole mantle model of convection. For this reason, two-layer mantle convection is less efficient than single-layer or whole-mantle convection, and results in higher mantle temperatures.

Temperature is taken to be a linear function of depth within each boundary layer. Temperature is also assumed to vary linearly with radius in the adiabatic interiors of the shells; the same assumption is made for the solidus temperature of the mantle rocks. For simplicity, the depth profiles of interior temperature are assumed to be parallel to the depth profiles of the mantle solidus. We allow the upper and lower mantle solidus temperatures to have different radial gradients, but it is assumed that solidus temperature is continuous at the upper-lower mantle interface. An interior temperature that is a fixed fraction of the solidus temperature is consistent with isoviscous upper and lower mantles (Weertman, 1970). The ratio of mantle temperature to mantle solidus temperature, known as the homologous temperature, can take different values in the upper mantle and lower mantle of the model. The upper and lower mantle homologous temperatures are functions only of time in the model. Mantle viscosity in the model is proportional to the exponential of the inverse homologous temperature, similar to the dependence of viscosity on actual temperature in (13.2.6).

The model contains internal radiogenic heat sources that are distributed uniformly in the upper and lower mantle shells. The heat source densities in the upper and lower shells of the model are generally unequal and decay with time according to the simple exponential decay law in (13.2.2). Separate energy balance equations govern the cooling histories of the two shells and the core. The shell energy balance equations are identical to (13.3.6) while the core energy balance equation is given by (13.3.7) with $L + E_G = 0$.

Heat fluxes across the thermal boundary layers are given by Fourier's law of heat conduction as in (13.3.10) and (13.3.11) and boundary layer thicknesses are specified as in (13.3.13) with the Rayleigh number of each shell defined in terms of the nonadiabatic temperature rise across each shell and the geometric, thermal, and rheological properties of each shell.

The model equations are integrated forward in time assuming that the mantle is initially at the solidus. Continuity of temperature is applied at interfaces and the surface temperature is held constant at 300K. Parameter values for the two-layer model of this section are listed in Table 13.3. In addition to the parameters given in Table 13.3, the depth profile of the solidus temperature has the same slope in both upper and lower mantle shells to facilitate comparison with a whole-layer mantle convection model having the same solidus temperature (this whole-layer model has $v_0 = 100 \text{ m}^2 \text{ s}^{-1}$). The radiogenic heat source densities in the upper and lower mantle shells are determined by requiring the model to have a present surface heat flux of about 60 mW m^{-2} and an approximately isoviscous mantle with a kinematic viscosity of about $10^{17} \text{ m}^2 \text{ s}^{-1}$.

Results of the calculations are presented in Table 13.4 and in Figures 13.11 and 13.12. According to Table 13.4 the concentration of radiogenic heat sources in the lower mantle shell of the two-layer model is only about 1.5% of the average heat source concentration in the entire mantle. We infer that in two-layer convection the lower mantle must be strongly depleted in radiogenic heat sources, because the thermal boundary layers at the upper mantle-lower mantle interface are limited in the amount of heat they can conduct across the interface. The limitation arises because the combined temperature difference across the boundary layers cannot exceed the difference between the solidus temperature and the upper mantle adiabatic

Table 13.3. Parameter Values for Two-layer Mantle Convection Thermal Evolution Models of the Earth^a

Parameter	Value
ρc	$4.2 \text{ MJ m}^{-3} \text{ K}^{-1}$
ρc (core)	$10.9 \text{ MJ m}^{-3} \text{ K}^{-1}$
k	$4.2 \text{ W m}^{-1} \text{ K}^{-1}$
κ	$10^{-6} \text{ m}^2 \text{ s}^{-1}$
α	$3 \times 10^{-5} \text{ K}^{-1}$
g	10 m s^{-2}
λ	$1.23 \times 10^{-17} \text{ s}^{-1}$
R_p	6,371 km
Radius of upper-lower mantle interface	5,671 km
Core radius	3,485 km
v_0 (upper mantle)	$100 \text{ m}^2 \text{ s}^{-1}$
v_0 (lower mantle)	$6 \times 10^3 \text{ m}^2 \text{ s}^{-1}$
β	$1/3$
Ra_{cr}	10^3
Solidus temperature at surface	1,500 K
Solidus temperature at core–mantle boundary	3,900 K
Activation parameter for the homologous temperature in the viscosity law	30

^a Unless otherwise stated, upper and lower mantle parameter values are the same.

Table 13.4. Characteristics of Two-layer and Whole-mantle Convection Thermal History Models with Similar Values of Surface Heat Flux and Mantle Viscosity^a

	Two-layer Mantle Convection Model		Whole-mantle Convection Model
	Upper Mantle	Lower Mantle	
ρH ($\mu\text{W m}^{-3}$)	0.44	0.25×10^{-2}	0.13
Surface heat flux (mW m^{-2})		58.6	58.6
v ($\text{m}^2 \text{ s}^{-1}$)	1.4×10^{17}	1.6×10^{17}	1.6×10^{17}
Urey ratio		84.3%	69.4%

^a All quantities are present values except for ρH , the initial rate of heat production per unit volume.

temperature without melting the lower mantle. Schubert and Spohn (1981) have shown that if the mantle convects in two layers, the lower mantle could not be solid at present if it contained more than about 10% of all mantle radiogenic heat sources.

In comparison, whole-mantle convection is much more efficient at removing heat from the Earth's interior. An initial heat generation rate per unit volume of only $0.13 \mu\text{W m}^{-3}$ is required to balance the average present surface heat flux in the whole-mantle model. This is about 17% less than the mantle average for the two-layer model. Thus, the present ratio of heat generation to heat loss, the Urey ratio, is only 69%, about 15% less than the value for two-layer convection. The whole-mantle convection model removes about $2 \times 10^{30} \text{ J}$

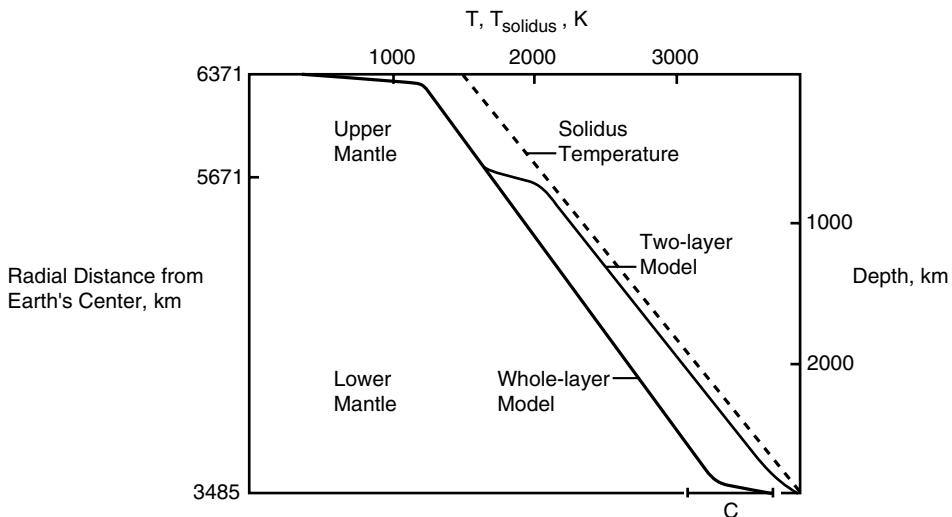


Figure 13.11. Present geotherms (solid curves) in the two-layer and whole-layer mantle convection models of Table 13.4. The mantle solidus temperature (dashed line) is the same in both thermal history models. The two-layer convection model has a hotter lower mantle than does the whole-layer model primarily due to the temperature increases across the interface thermal boundary layers in the two-layer model.

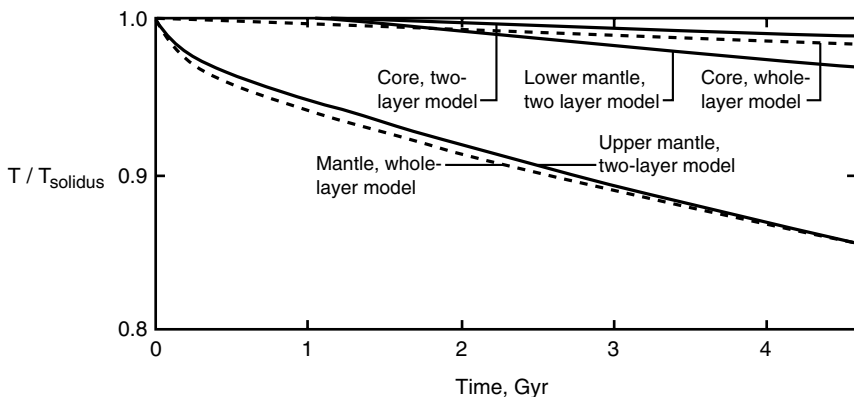


Figure 13.12. Thermal histories in the two-layer and whole-layer mantle convection models. The core temperatures are normalized relative to the value of the solidus temperature at the core–mantle boundary.

of primordial heat over its entire thermal history, while the two-layer model removes only about 6×10^{29} J, about a factor of 3 less. A larger fraction of the Earth's present surface heat flow would have to be attributed to radiogenic heating if the Earth's mantle convects in two or more layers than if it convects as a single layer.

The model results summarized in Table 13.4 have shown that the two-layer mode of mantle convection is less efficient at cooling the Earth than is the whole-layer mode of mantle convection and that the lower mantle must be strongly depleted in radiogenic heat sources if the mantle convects in two layers. Spohn and Schubert (1982a) have shown that these conclusions are robust to variations in the values of upper mantle and lower mantle rheological parameters, depth profiles of solidus temperature including unequal slopes of the

solidus curves in the upper mantle and lower mantle, assumptions about the thicknesses of the lower thermal boundary layers including the complete disappearance of these layers, and choices for the relative slopes of the depth profiles of the upper and lower mantle adiabats and solidus temperatures.

The present geotherms for the two-layer and whole-layer mantle convection thermal history models of Table 13.4 are shown in Figure 13.11, together with the mantle solidus curve. Both models have a surface thermal boundary layer or lithosphere about 80 km thick, with a temperature rise of about 940 K. Temperatures in the upper mantle are essentially the same for both models, approximately 0.80 of the solidus temperature. However, in the two-layer model temperature increases by ≈ 480 K across the thermal boundary layers separating the upper and lower mantles. Therefore, temperatures in the lower mantle of the two-layer model are about 360 K higher than those in the whole-layer model. Core temperatures in these models differ by ≈ 220 K. The lower mantle temperature rises by ≈ 330 K across the lower thermal boundary layer in the whole-mantle model compared with ≈ 170 K in the two-layer model. This boundary layer is ≈ 140 km thick in the two-layer model but only 80 km thick in the whole-mantle model. The present heat flux from the core is therefore about 3.5 times larger for the whole-mantle model. The core heat flux was even larger earlier in the Earth's thermal history since its time integral is ≈ 6 times larger for the whole-mantle model. Figure 13.11 clearly shows that whole-mantle convection not only removes more heat from the core, but it also removes more primordial heat from the mantle. The primordial heat removed after 4.5 Gyr is proportional to the area between the geotherm and the solidus curve. Thus the excess primordial heat removed by whole-mantle convection is proportional to the area between the two geotherms and amounts to about 10^{30} J after correction for differences in radiogenic heat production.

The thermal histories of the models of Table 13.4 are illustrated in Figure 13.12. The thermal evolution of the upper mantle for two-layer convection is very similar to that of the entire mantle for single-layer convection. However, the whole-mantle convection model cools the Earth's interior much more efficiently because of the absence of internal boundary layers. The lower mantle thermal history in the two-layer model is quite similar to the thermal evolutions of the cores in both the one- and two-layer models. The upper mantle of the two-layer system and the entire mantle of the single-layer model cool off very fast initially; the initial high cooling rate decays exponentially with time, and the cooling rate becomes approximately steady after the first billion years.

The cooling histories of upper mantle and whole mantle, and lower mantle and core, reflect fundamental differences between thermally insulated layers and freely cooling layers driven by large nonadiabatic temperature differences. The nonadiabatic temperature difference across the lower mantle increases as the upper mantle cools. Similarly, cooling of the core depends on the development of boundary layers at the core–mantle interface and is restricted by the temperature increase across these boundary layers. Because of the strong temperature dependence of mantle viscosity, most of the total nonadiabatic temperature rise occurs across the surface boundary layer, even late in the thermal history.

Question 13.6: Did layered mantle convection ever occur in the Earth's thermal history?

13.5 Scaling Laws for Convection with Strongly Temperature Dependent Viscosity

As already noted in Section (13.2.2), the heat flow–Rayleigh number parameterization (13.2.4) is valid only for convection with constant viscosity. Application of this parameterization to studies of planetary thermal history is therefore limited by the fact that mantle viscosity is strongly temperature dependent. One major effect of the strong temperature dependence of viscosity on thermal convection is the creation of a high-viscosity region near the upper surface where temperatures are relatively cold. The high-viscosity near-surface layer can participate sluggishly in the convection or “freeze up” to form an immobile or stagnant lid, depending on the “strength” of the viscosity variation with temperature and the temperature difference across the layer. Formation of a sluggish or rigid lid in convection with strongly temperature dependent viscosity reduces the efficiency of heat transport across the layer because cold near-surface material cannot be effectively circulated to deeper and hotter parts of the layer. Methods for incorporating this reduction in heat transfer efficiency into (13.2.4) have been mentioned in Section 13.2.2. One way is to interpret T in (13.2.4) and (13.2.5) as the temperature of the efficiently convecting material below the sluggish or rigid lid.

The sluggish or rigid lid of a convecting system with strongly temperature dependent viscosity is the analogue of the lithosphere on the Earth and other planets. In contrast to other planets however, Earth’s lithosphere does not act as a globally intact rigid lid. Nonviscous deformation mechanisms (e.g., faulting) allow it to break up into pieces (plates), many of which (oceanic plates) are subductible. The net result is that the Earth’s “rigid lid” can be circulated deeply into the hot mantle and mantle convective heat transfer is essentially as efficient as if the mantle were convecting as a constant viscosity fluid. Thus, for the Earth, (13.2.4) suffices to study its thermal evolution. However in the absence of plate tectonics, the other terrestrial planets do possess globally intact lithospheres which must behave as the sluggish or rigid lids of convection with strongly temperature dependent viscosity. Accordingly, thermal history investigations of the other planets (Chapter 14) can benefit from heat flow–Rayleigh number parameterizations specifically formulated to account for the strong temperature dependence of mantle viscosity. We discuss these parameterizations here and in the next chapter.

Parameterization of heat transport by convection in a constant viscosity fluid layer heated from below with isothermal and stress-free top and bottom boundaries requires only two dimensionless parameters, the Nusselt number Nu and the Rayleigh number Ra . When the viscosity μ of the fluid is strongly temperature T dependent, however, an additional dimensionless parameter is needed to characterize $\mu(T)$. Further, since viscosity enters the formula for Ra , it is necessary to specify the temperature at which the viscosity is evaluated in Ra . With temperature-dependent viscosity, the definitions of Ra and the Nu – Ra relation become nonunique, and the literature on convection with strongly temperature dependent viscosity reflects this nonuniqueness. In one approach, the Rayleigh number Ra_0 is defined in terms of the viscosity μ_0 evaluated at the temperature T_0 of the upper surface:

$$Ra_0 \equiv \frac{\rho g \alpha \Delta T d^3}{\kappa \mu(T_0)} = \frac{\rho g \alpha \Delta T d^3}{\kappa \mu_0} \quad (13.5.1)$$

where ΔT is the total temperature change across the fluid layer of thickness d

$$\Delta T \equiv T_1 - T_0 \quad (13.5.2)$$

and T_1 is the temperature of the lower surface. The Rayleigh number Ra_1 has also been defined in terms of the viscosity μ_1 evaluated at the temperature T_1 of the lower surface:

$$Ra_1 \equiv \frac{\rho g \alpha \Delta T d^3}{\kappa \mu (T_1)} = \frac{\rho g \alpha \Delta T d^3}{\kappa \mu_1} \quad (13.5.3)$$

A Rayleigh number $Ra_{1/2}$ based on the viscosity $\mu_{1/2}$ evaluated at the average temperature $(T_0 + T_1)/2$ of the upper and lower surfaces is often used:

$$Ra_{1/2} \equiv \frac{\rho g \alpha \Delta T d^3}{\kappa \mu ((T_0 + T_1)/2)} = \frac{\rho g \alpha \Delta T d^3}{\kappa \mu_{1/2}} \quad (13.5.4)$$

Finally, a Rayleigh number Ra_i based on the viscosity μ_i evaluated at the nearly uniform temperature of the actively convecting layer beneath the sluggish or rigid lid is also widely employed:

$$Ra_i \equiv \frac{\rho g \alpha \Delta T d^3}{\kappa \mu (T_i)} = \frac{\rho g \alpha \Delta T d^3}{\kappa \mu_i} \quad (13.5.5)$$

The specific form of $\mu(T)$ adopted in some studies is the Arrhenius law (13.2.6), but a linearized version of this law

$$\frac{\mu}{\mu_{\text{ref}}} = \exp\{-E(T - T_{\text{ref}})\} \quad (13.5.6)$$

is commonly used. In (13.5.6), T_{ref} and μ_{ref} are the reference temperature and viscosity values used in the definition of the Rayleigh number. With (13.5.6), the viscosity ratio across the layer r_μ is given by

$$r_\mu \equiv \frac{\mu_0}{\mu_1} = \exp(E \Delta T) \quad (13.5.7)$$

independent of the choice of T_{ref} and μ_{ref} . The Frank-Kamenetskii parameter θ is

$$\theta = \ln r_\mu = E \Delta T \quad (13.5.8)$$

For the viscosity law (13.5.6) the heat flow (Nusselt number)-Rayleigh number parameterization can be written as

$$Nu = Nu(\theta, Ra) \quad (13.5.9)$$

where Ra in (13.5.9) is one of the Rayleigh numbers defined above. The Rayleigh numbers Ra_1 , $Ra_{1/2}$, and Ra_0 are related to each other by

$$Ra_1 = Ra_{1/2} \sqrt{r_\mu} = r_\mu Ra_0 \quad (13.5.10)$$

Before discussing heat flow-Rayleigh number parameterizations appropriate to convection with strongly temperature dependent viscosity, we first describe the nature of this type of convection using the following thought experiment. Imagine that $Ra_{1/2}$ is kept constant at some large value (so that convection occurs) in a sequence of experiments in which

r_μ is increased from 1. At small viscosity contrasts, the cold fluid near the upper boundary is entirely mobile and participates freely in the convective motions. This is the small viscosity contrast regime and it occurs for values of r_μ less than about 10^2 . As viscosity contrasts grow larger (r_μ in the range 10^2 – 10^3), cold fluid near the upper boundary becomes increasingly more viscous and is less able to participate in convective overturning; a sluggish lid of cold viscous fluid develops. This is the sluggish-lid convection regime. When the viscosity contrast is increased still further (r_μ about 10^4), the cold fluid at the upper surface becomes so viscous as to form a stagnant lid, effectively ceasing to participate in the convective motions that occur below it. This is the stagnant-lid mode of convection. In addition to differences in the style of lid deformation, each of these convective regimes has a distinct horizontal planform. The small viscosity contrast convection regime has a horizontal wavelength comparable to the depth of the fluid layer. The sluggish-lid regime of convection has a larger horizontal scale. However, the horizontal scale of the stagnant-lid convection regime is small compared to the fluid layer depth. The morphologies of the upflows and downflows are also different in the different convection regimes. The dominant mechanism by which strongly temperature dependent viscosity influences the planform and morphology of convection is through the depth dependence of horizontally averaged viscosity. This picture summarizes results by Ratcliff et al. (1997) for fully three dimensional convection with strongly temperature dependent viscosity in both spherical shells and Cartesian boxes. Their results are discussed in the context of planetary convection in Chapter 14. The styles of convection in the different regimes are shown in Figures 14.12 and 14.13.

Different heat flow-Rayleigh number parameterizations apply in the separate convection regimes. Solomatov (1995) and Moresi and Solomatov (1995) use the differences in Nu – Ra relationships from numerical calculations of variable viscosity convection in two-dimensional geometry to identify the different convection regimes. Figure 13.12 shows approximate regime boundaries on a plot of $\log_{10} r_\mu$ versus $\log_{10} Ra_1$ (Solomatov, 1995). Points representing the three-dimensional calculations of Ratcliff et al. (1997) for $Ra_{1/2} = 10^5$ and $r_\mu = 1, 10^3, 10^4$, and 10^5 are indicated in the figure. According to Ratcliff et al. (1997) convection should be in the small viscosity contrast regime for $r_\mu = 1$ (point a, region I), in the sluggish-lid regime for $r_\mu = 10^3$ (point b, region II), and in the stagnant-lid regime for $r_\mu = 10^3$ and 10^4 (points c and d, respectively, region III). The locations of the approximate regime boundaries are in accord with the positions of these points. Regime diagrams for non-Newtonian viscous convection with strongly temperature dependent viscosity have been given in Solomatov (1995) and Reese et al. (1998, 1999). These are similar to the regime diagram of Newtonian viscous convection except that the regime boundaries are shifted to much larger temperature-dependent viscosity contrasts.

The heat flow-Rayleigh number parameterization that applies in the small viscosity contrast regime (Figure 13.13, region I) is given by (13.2.4) with T given by T_i and μ given by μ_i (Solomatov, 1995). Simple scaling arguments lead to (13.2.4) with $\beta = 1/3$ (Schubert et al., 1979a; Solomatov, 1995). For example, if the temperature drop across the layer is distributed equally between the upper and lower boundary layers and if these boundary layers each have the same thickness δ (Figure 13.14a), then the heat flow q from Fourier's law of heat conduction gives

$$q \sim \frac{k \Delta T}{\delta} \quad (13.5.11)$$

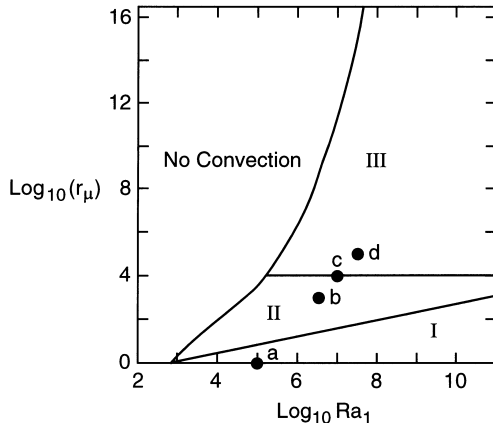


Figure 13.13. A diagram of the approximate boundaries of the small viscosity contrast (I), sluggish-lid (II), and stagnant-lid (III) convection regimes (regime boundaries are redrawn from Solomatov, 1995). The approximate boundary for the onset of convection is also shown. The diagram applies strictly to two-dimensional convection in a layer heated from below with isothermal, stress-free boundaries, but may be qualitatively applied to more general situations. Points a through d represent the three-dimensional convection simulations of Ratcliff et al. (1997) (in a Cartesian box and a spherical shell) for $\text{Ra}_{1/2} = 10^5$ and $r_\mu = 1, 10^3, 10^4$, and 10^5 ($\text{Ra}_1 = 10^5, 10^{6.5}, 10^7, 10^{7.5}$) which were in the small viscosity contrast, sluggish-lid, and stagnant-lid convection regimes, respectively.

Further, if δ scales as

$$\delta \sim \left(\frac{\kappa d}{u} \right)^{1/2} \quad (13.5.12)$$

where u is the magnitude of the horizontal velocity in the upper and lower thermal boundary layers (velocities in the boundary layers are equal in magnitude, Figure 13.14a), then

$$q \sim k \Delta T \left(\frac{u}{\kappa d} \right)^{1/2} \quad (13.5.13)$$

The velocity scale u can be found by equating the integral dissipation rate in the layer to the integral mechanical work done by thermal convection per unit time

$$\mu_i \left(\frac{u}{d} \right)^2 \sim \frac{\alpha g q}{c_p} \quad (13.5.14)$$

or

$$u \sim \left(\frac{\alpha g q d^2}{\mu_i c_p} \right)^{1/2} \quad (13.5.15)$$

Substitution of this velocity scale into (13.5.13) gives

$$q \sim \frac{k \Delta T}{d} \left(\frac{\rho g \alpha \Delta T d^3}{\kappa \mu_i} \right)^{1/3} \quad (13.5.16)$$

or

$$Nu = \frac{q}{(k \Delta T / d)} \sim R_{a_i}^{1/3} \quad (13.5.17)$$

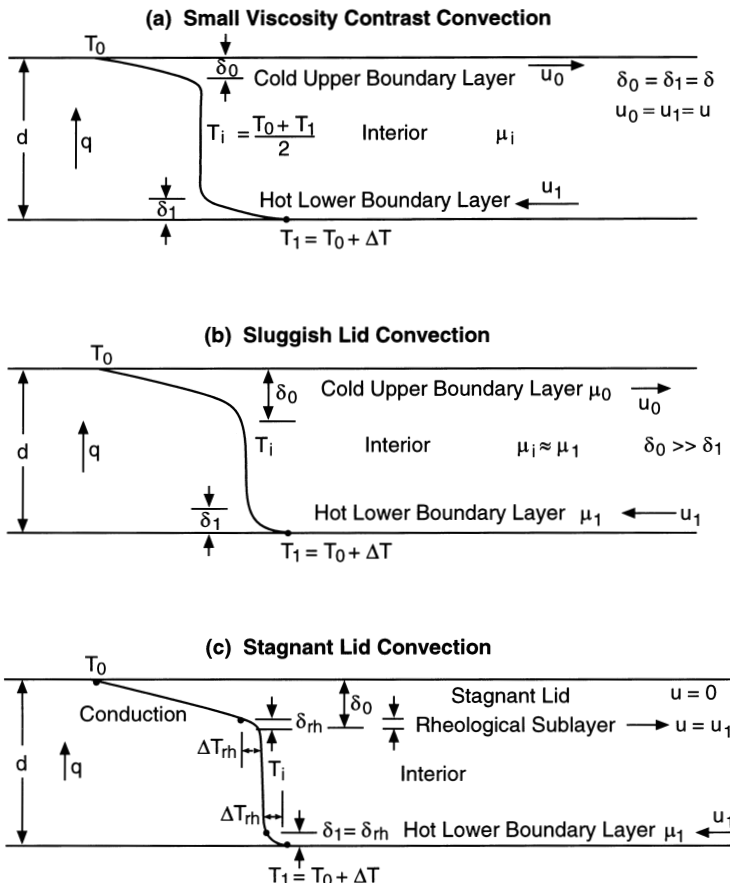


Figure 13.14. Sketch of the different regimes of thermal convection with strongly temperature dependent viscosity; (a) small viscosity: contrast convection regime; (b) sluggish-lid convection regime; (c) stagnant-lid convection regime. As the viscosity contrast across the convecting layer increases, convection undergoes transitions from the small viscosity contrast regime to the sluggish-lid regime and finally to the stagnant-lid regime. The temperature of the convecting interior increases as the viscosity contrast across the layer increases.

In the sluggish-lid convection regime (Figure 13.14b) the scaling proceeds as follows Solomatov (1995). It is assumed that half of the convective rate of doing work $\frac{1}{2}(\alpha g q / c_p)$ is balanced by the rate of dissipation in the nearly isothermal convecting region beneath the sluggish lid:

$$\mu_i \left(\frac{u_1}{d} \right)^2 \sim \frac{1}{2} \frac{\alpha g q}{c_p} \quad (13.5.18)$$

where u_1 is the horizontal velocity scale in the interior convecting region (similar to the velocity u_1 in the lower hot thermal boundary layer, Figure 13.14b). The other half of the convective work is assumed to overcome dissipation in the cold upper boundary layer:

$$\mu_0 \left(\frac{u_0}{d} \right)^2 \sim \frac{1}{2} \frac{\alpha g q}{c_p} \quad (13.5.19)$$

where subscript zero refers to the cold upper boundary layer. The upper and lower boundary layer thicknesses, δ_0 and δ_1 , respectively, are

$$\delta_0 \sim \left(\frac{\kappa d}{u_0} \right)^{1/2} \quad \text{and} \quad \delta_1 \sim \left(\frac{\kappa d}{u_1} \right)^{1/2} \quad (13.5.20)$$

Substitution of (13.5.18) and (13.5.19) into (13.5.20) gives

$$\delta_0 \sim \left(\frac{\alpha g q}{\mu_0 c_p \kappa^2} \right)^{-1/4} \quad (13.5.21)$$

$$\delta_1 \sim \left(\frac{\alpha g q}{\mu_i c_p \kappa^2} \right)^{-1/4} \quad (13.5.22)$$

From Fourier's law of heat conduction and the concept of thermal resistances in series

$$q = \frac{k \Delta T}{d} \left(\frac{\delta_0}{d} + \frac{\delta_1}{d} \right)^{-1} \quad (13.5.23)$$

Substitution of (13.5.23) into (13.5.21) and (13.5.22) together with the assumption $\delta_0 \gg \delta_1$ yields

$$\frac{\delta_0}{d} \sim Ra_0^{-1/3} \quad (13.5.24)$$

and

$$\frac{\delta_1}{d} \sim Ra_i^{-1/4} \left(\frac{\delta_0}{d} \right)^{1/4} = Ra_i^{-1/4} Ra_0^{-1/12} \quad (13.5.25)$$

From (13.5.23) we can write

$$q \sim \frac{(k \Delta T / d)}{(\delta_0/d + \delta_1/d)} \quad (13.5.26)$$

or

$$Nu \sim \frac{1}{(\delta_0/d + \delta_1/d)} \quad (13.5.27)$$

The interior temperature can be determined from the temperature drop across the cold upper boundary layer:

$$T_i - T_0 = \delta_0 \frac{q}{k} = \frac{\delta_0 \Delta T}{\delta_0 + \delta_1} \quad (13.5.28)$$

In the stagnant-lid convection regime (Figure 13.14c) most of the cold upper boundary layer is an immobile conductive region across which almost the entire ΔT occurs (Solomatov, 1995). Convection penetrates only a small distance into the lid given by the rheological length scale δ_{rh} (Morris and Canright, 1984; Fowler, 1985)

$$\delta_{rh} \sim \frac{\delta_0}{E \Delta T} = \frac{\delta_0}{\theta} \quad (13.5.29)$$

and only the small temperature difference across this rheological sublayer ΔT_{rh} is available to drive convection in the underlying region (Figure 13.14c) (Davaille and Jaupart, 1993)

$$\Delta T_{rh} \sim \frac{\Delta T}{\theta} \quad (13.5.30)$$

Convection beneath the stagnant lid is essentially constant viscosity convection driven by the temperature difference ΔT_{rh} . By replacing ΔT with ΔT_{rh} in (13.5.16) we can immediately write

$$q \sim \frac{k \Delta T}{d} \theta^{-4/3} Ra_i^{1/3} \quad (13.5.31)$$

or

$$Nu \sim \theta^{-4/3} Ra_i^{1/3} \quad (13.5.32)$$

Since q is also given by

$$q \sim \frac{k \Delta T}{\delta_0} \quad (13.5.33)$$

we find

$$\frac{\delta_0}{d} \sim \theta^{4/3} Ra_i^{-1/3} \quad (13.5.34)$$

The heat flux q is also given by

$$q \sim \frac{k \Delta T_{rh}}{\delta_1} \quad (13.5.35)$$

which, together with (13.5.30) and (13.5.33), results in

$$\frac{\delta_1}{d} \sim \frac{1}{\theta} \frac{\delta_0}{d} \quad (13.5.36)$$

Heat flow-Rayleigh number parameterizations and scaling relationships for non-Newtonian viscous convection with strongly temperature dependent viscosity have been given by Solomatov (1995) and Reese et al. (1998, 1999). The heat flow-Rayleigh number parameterizations for the different convection regimes can be used to study the thermal histories of other terrestrial planets, as discussed in Chapter 14. Such studies rely on the convection regime appropriate for a planet at each stage in its evolution. The regime

diagram of Figure 13.13 provides the information necessary to determine the style of convection. Transitions between different styles of convection could occur as a planet evolves with perhaps discernible consequences at its surface (see the discussion of Venus' thermal history in the next chapter).

The heat flow-Rayleigh number parameterizations discussed above pertain to convection in fluid layers heated from below. Grasset and Parmentier (1998) have studied convection in volumetrically heated fluid layers with strongly temperature dependent viscosity and Davaille and Jaupart (1993) have studied the closely related problem of the transient cooling of fluids with strongly temperature dependent viscosity. With volumetric heating the appropriate form of the Rayleigh number Ra_0 is

$$Ra_0 = \frac{\alpha g \rho^2 H d^5}{\kappa k \mu_0} \quad (13.5.37)$$

where H is the rate of internal heating per unit mass (see 13.2.15). For Ra_0 sufficiently small, convection occurs in a stagnant-lid regime similar to that of bottom-heated convection: a stagnant conductive lid forms at the surface and convection occurs below the lid (Figure 13.15). The convective region is essentially isothermal with temperature T_i . The temperature difference between the isothermal interior and the bottom of the stagnant conductive lid $T_i - T_c$ (T_c is the temperature at the base of the conductive lid) is a rheological temperature difference given by an equation analogous to (13.5.30) (Davaille and Jaupart, 1993; Grasset and Parmentier, 1998):

$$T_i - T_c = 2.23 \left(\frac{-\mu}{(d\mu/dT)} \right)_{T=T_i} \quad (13.5.38)$$

For the viscosity law (13.5.6), $T_i - T_c$ is $2.23E^{-1}$ and the viscosity ratio $\mu(T = T_c)/\mu(T = T_i)$ is $\exp(2.23)$ or nearly a factor of 10. For an Arrhenius viscosity law (13.2.6), $T_i - T_c$ is $2.23 RT_i^2/E^*$, where E^* is the activation energy.

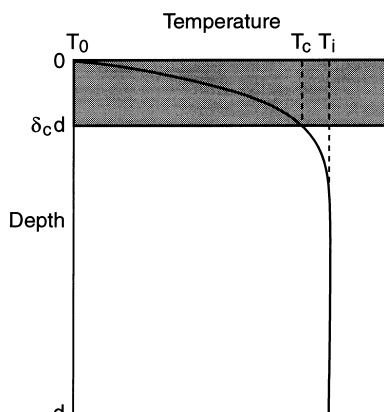


Figure 13.15. Illustration of the nature of stagnant-lid convection in an internally heated fluid layer with strongly temperature dependent viscosity (redrawn from Grasset and Parmentier, 1998).

The heat flow–Rayleigh number parameterization for stagnant-lid, heated from within, convection with strongly temperature dependent viscosity is of the form

$$\frac{T_i - T_c}{H(d - \delta_c d)^2 / k} = a \left\{ \frac{\alpha g \rho^2 H (d - \delta_c d)^5}{\kappa k \mu_i} \right\}^\beta \quad (13.5.39)$$

where $\delta_c d$ is the thickness of the conducting lid and interior temperature replaces heat flux in the parameterization for fluids heated volumetrically. This is identical to the parameterization for constant viscosity fluids; the appropriate value of β is also the same as it is in constant viscosity internally heated convection.

According to Grasset and Parmentier (1998), constant viscosity parameterized convection laws can be applied to the stagnant-lid convection regime if the quantities in the parameterization are properly identified with those of the convecting region beneath the stagnant conducting lid and if the temperature difference between the convecting region and the base of the lid is given by (13.5.38). Application of this approach to planetary thermal evolution requires that the temperature difference $T_i - T_c$ be calculated from (13.5.38) implying that T_c must evolve with T_i and not be specified a priori at some constant value. In other words, the temperature at the base of the conducting lid T_c evolves with the mantle temperature and T_c is not a constant. Mantle convection evolves so as to maintain a temperature difference below the conducting lid given by the characteristic rheological temperature difference. The conducting lid (lithosphere) will thicken as the mantle cools but the temperature at the base of the lid will also decrease with time. This effect will result in model lithospheres that are thicker than those predicted in models where lid basal temperature is held fixed. An example of this will be given in Chapter 14 when we discuss the thermal history of Mars.

Numerical calculations of steady, two-dimensional convection with strongly temperature dependent viscosity for very large values of Ra_0 show that transitions can occur among the modes of variable viscosity convection. Hansen and Yuen (1993) have found a transition from stagnant-lid convection to a small viscosity contrast regime at Ra_0 around 10^7 for fixed $r_\mu = 10^3$. In this small viscosity contrast regime at high Ra_0 , Nusselt numbers are about 100 and surface temperatures are around 1,000 K or more. Such a mode of convection might have been relevant to the early Earth shortly after the end of accretion when a dense water-dominated atmosphere might have produced high surface temperatures through the greenhouse effect (see Section 13.2.1 and references therein for a discussion of an early massive water atmosphere near the end of accretion). This high Ra_0 mode of convection might also be relevant to mantle convection in Venus at present (surface temperature on Venus is about 700 K).

Question 13.7: Has convection in the Earth's mantle always occurred in the small viscosity contrast regime?

13.6 Episodicity in the Thermal Evolution of the Earth

A major characteristic of the simple parameterized convection models of the Earth's thermal history presented in this chapter is the monotonic decline in mantle temperature, surface heat flow, and convective vigor. While the Earth has undoubtedly undergone gradual cooling over geologic time, there probably have been periods in Earth history when this secular decline was interrupted by intervals of enhanced convective vigor and surface heat flow. For example,

we know from the geologic record that major flood basalt events have occurred and plate motions have undergone rapid changes.

Numerical models show that mantle convection may be an inherently chaotic phenomenon capable of unpredictable spurts of enhanced or decreased activity. Convection models also demonstrate that the mantle is capable of sudden and perhaps catastrophic movements of material and heat. The most dramatic examples are the so-called avalanches of cold material piled up on the phase change at 660 km depth (Machetel and Weber, 1991; Tackley et al., 1993; Honda et al., 1993b, a; Solheim and Peltier, 1994b), plume or diapir release from the thermal boundary layer at the base of the mantle and plume arrival at the base of the lithosphere, plate tectonic flux variability due to ridge subduction events and continental collisions, and delamination of parts of the lithosphere.

Question 13.8: Is convection in the Earth's mantle chaotic?

Question 13.9: Have avalanches occurred in the Earth's mantle?

One way of studying nonmonotonicity in Earth thermal history is to incorporate the physical processes responsible for such behavior into numerical models. Another way is to add ad hoc conditions to parameterized convection models that allow them to change behaviors in a priori specified ways. The disadvantage of this approach is that the model behaves in a way that is forced upon it by the externally imposed conditions. We will discuss studies of the Earth's thermal history that use both approaches. Major changes have also occurred in the thermal histories of other planets and Chapter 14 discusses such an event for Venus.

As noted above, mantle avalanches have the potential to change the Earth in major ways (Weinstein, 1993). Avalanches could occur on a global scale and cause layered mantle convection to suddenly change to a whole-mantle convection pattern. Less dramatic but still significant would be the occurrence of avalanches on a regional scale in a partially layered mantle. The sudden arrival of cold avalanche material at the core–mantle boundary would displace hot material in the thermal boundary layer and might cause the ejection of massive hot plumes. The enhanced heat flow from the core into the suddenly cold overlying mantle would affect motions in the core and cause changes in the geomagnetic field; the effect might result in changes in the frequency of magnetic field reversals (Larson and Olson, 1991). Hot material from the lower mantle would be rapidly injected into the upper mantle in order to conserve mass in an avalanche with attendant thermal consequences at the surface. The sudden arrival of hot material beneath the plates from the mass-compensating injection of hot lower mantle material into the upper mantle or from massive hot plumes ejected from the core–mantle boundary layer could cause abrupt changes in plate motion and the creation of new plate margins (Brunet and Machetel, 1998; Ratcliff et al., 1998). A global avalanche or flush instability causing a change in mantle convection from the two-layer to the whole-mantle mode has been invoked by Breuer and Spohn (1995) to explain the Archean–Proterozoic transition. The late Archean was a time of profound geologic change and rapid continental growth (Taylor and McLennan, 1995).

The possibility that plumes can dramatically influence plate motions by lubricating the undersides of plates is, of course, not necessarily linked to the occurrence of mantle avalanches. Plumes are a fundamental feature of thermal convection; they occur whenever

there is some heating from below. Plume activity is naturally variable in time-dependent convection and it can be expected that large plumes in a chaotically convecting mantle will aperiodically impinge on the bottom of the lithosphere, spread hot material beneath it, and change plate velocities (Larsen et al., 1996b; Larsen and Yuen, 1997a; Ratcliff et al., 1998).

The tendency of the spinel–perovskite + magnesiowüstite phase transition to promote layering in mantle convection has been found to be stronger at higher Rayleigh number (Christensen and Yuen, 1985; Zhao et al., 1992). Accordingly, mantle convection in the early Earth may have been layered because of more vigorous convection at higher Rayleigh number than at present. If mantle convection is not layered or is only partially layered today then the Earth would have experienced a transition from two-layer mantle convection to whole-mantle convection at some time in its evolution. As discussed above, such a transition might have had a profound impact on the geologic record. The same idea has been applied to Venus by Steinbach and Yuen (1992), who suggested that this transition from layered to whole-mantle convection could have caused the major resurfacing of Venus some 750 Myr ago (see Chapter 14 for a discussion of Venus and its thermal history).

The general decrease in Rayleigh number with time as the Earth evolved could have led to another transition in convective style with thermal and tectonic consequences. At extremely high Rayleigh numbers (greater than about 10^7) thermal convection occurs in a regime of hard turbulence (Hansen et al., 1990, 1992b, a). Convection in this regime involves the rise of disconnected thermals or plumes or diapirs from the lower hot boundary layer. In the regime of soft turbulence that occurs at lower Rayleigh numbers, plumes remain connected to their source in the lower boundary layer. The vigorously convecting mantle in the early Earth could have been in the regime of hard turbulence while the transition to the less time-dependent chaotic state as the vigor of convection waned left the present mantle in the regime of soft turbulence (Yuen et al., 1993).

A parameterized convection approach to study the effects of phase-change-induced layering and associated mantle avalanches on Earth thermal history has been put forward by Davies (1995b). His model assumes that the mantle convects in two layers with ad hoc conditions for the breakdown of layering based on the attainment of either a critical temperature difference between the layers or a sufficiently cold upper mantle temperature. The Earth cools through geologic time in this model, but it can do so while experiencing periods of layered and nonlayered convection separated by major overturns of the mantle. Periods of layered convection in this model occur more often in the early evolution of the Earth and are gradually replaced by whole-mantle convection as the Earth evolves to the present. Episodic overturns could result in major spurts of tectonic activity and continental crustal formation.

Question 13.10: What dynamical processes in the mantle are responsible for episodicity in the geological record?

13.7 Continental Crustal Growth and Earth Thermal History

One of the major products of the Earth's thermal evolution is the formation of the continental crust. The continental crust is also the only accessible repository of information about the Earth's thermal state billions of years ago. In order to decipher the record of the Earth's thermal evolution contained in the continental crust, it is necessary to characterize the age distribution of the crust (Figure 13.16) and understand the processes involved in crustal

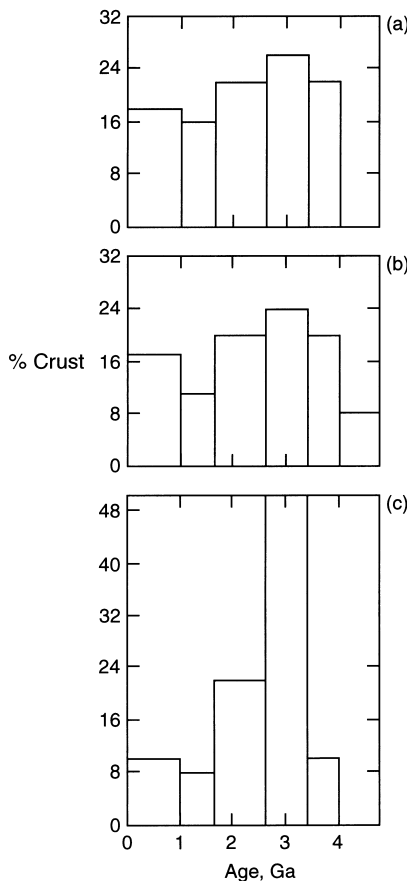


Figure 13.16. Age distribution of the crust based on Nd model ages (a, b, and c) and the freeboard constraint (c). Models (a) and (c) assume no crust at 4 Ga, model (b) assumes 8% crust at 4 Ga. Data are from Taylor and McLennan (1995). The episodic nature of crustal growth is evident particularly in model (c) which shows a strong spurt of crustal growth in the late Archean.

growth and their regulation by mantle convection. Formation of continental crust and its geochemical consequences are discussed in Sections 2.7 and 2.10 and Chapter 12. Here we discuss some aspects of crustal growth and its relation to mantle convection and the Earth's thermal evolution.

One of the major questions about continental crust is whether its growth has been continuous or episodic; related to this is the question of whether the continental crustal volume has increased with time, decreased with time from a maximum volume reached earlier in the Earth's history, remained approximately constant with time following early rapid growth, or oscillated with time.

Question 13.11: Has continental crustal growth occurred continuously or episodically?

Question 13.12: How has the volume of the continents changed through geologic time?

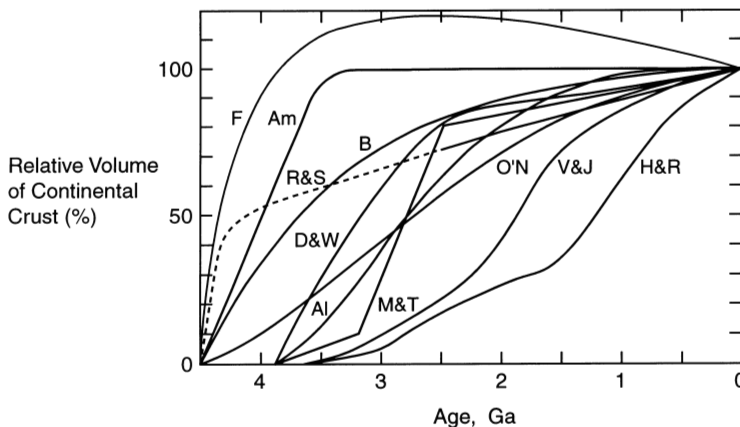


Figure 13.17. Crustal growth curves versus age (after Reymer and Schubert, 1984). The relative crustal volume is with respect to the current volume of continental crust. V & J, Veizer and Jansen (1979); M & T, McLennan and Taylor (1982); H & R, Hurley and Rand (1969); Al, Allègre (1982); O'N, O'Nions et al. (1979); R & S, Reymer and Schubert (1984); D & W, Dewey and Windley (1981); B, Brown (1979); Am, Armstrong (1981); F, Fyfe (1978).

Continental growth (the net gain in the volume or mass of the continental crust) is the net result of processes which both add and subtract material from the continents (Section 2.7). While continental growth is controlled by mantle convection, it is not clear whether enhanced mantle convective activity results in a net gain or loss of continental crust since both the addition processes (island arc and hot spot magmatic activity) and subtraction processes (sediment subduction and delamination) are more active with increased convective vigor. Figure 13.17 shows the variety of proposed continental crustal growth curves. The crustal growth curve of Fyfe (1978) shows rapid crustal growth early in the Earth's history and a decline in crustal volume since 2.5 Ga. The crustal growth curve of Armstrong (1981) shows a constant crustal volume for the last 3.5 Gyr. Reymer and Schubert (1984) proposed early accumulation of about 50% of the continental crust (within a few hundred million years of the end of accretion) followed by more gradual crustal growth over most of geologic history to the present. Many of the proposed crustal growth curves do not feature early rapid crustal growth and some delay crustal growth until 3.8 Ga. While considerable crustal differentiation probably occurred in the early, hot, vigorously convecting Earth, early crustal growth is not assured because the survivability of that crust is an open question.

Note that none of the curves shown in Figure 13.17 show episodic crustal growth. However, there is isotopic evidence that the continental crust has accumulated in spurts of activity (Moorbath, 1978; Patchett et al., 1981; Page et al., 1984; Nelson and DePaolo, 1985; DePaolo et al., 1991; Taylor and McLennan, 1995; Sylvester et al., 1997). Episodic crustal growth is suggested by the crustal age distribution models of Figure 13.16, especially model (c) which has a large spurt of crustal growth in the late Archean. The apparent episodicity in crustal growth suggested by isotopic data could be a consequence of inadequate and incomplete sampling of the crust. On the other hand, the discussion of the previous section emphasized that mantle convection can result in episodic crustal growth through its inherent chaotic behavior and through associated processes such as mantle avalanches (Stein and Hofmann, 1994). O'Nions and Tolstikhin (1996) have argued that ^{36}Ar and ^{40}Ar abundances in the

atmosphere together with estimates of the He and Ar isotopic composition of the upper and lower mantle and estimates of U, K, and Th in the mantle severely limit mass exchange between the upper mantle and lower mantle and the possibility that mantle avalanches could be responsible for episodic crustal growth.

The crustal growth curve derived by Reymer and Schubert (1984) is based on the secular cooling of the Earth and the assumption of constancy of freeboard since the Archean. Freeboard is defined as the average height of the continents above sea level. There is geological evidence that freeboard has been approximately constant since the end of the Archean at 2.5 Ga (Ambrose, 1964; Wise, 1974; Windley, 1977). The constancy of freeboard has been used to argue that no growth of the continents occurred during the Proterozoic and Phanerozoic (Armstrong, 1968, 1981, 1991). However, the secular decline in the heat production of the mantle causes the ocean basins to deepen and the volume of the oceans to increase with time; accordingly, growth of the continental crust is necessary to maintain constant freeboard (Reymer and Schubert, 1984; Schubert and Reymer, 1985; Galer, 1991). The growth of the continents can be quantified by utilizing the principle of isostasy and the relation between the depth of the ocean basins and surface heat flow (Schubert and Reymer, 1985); the resulting crustal growth curve is labeled R & S in Figure 13.17 (see also the discussion in 13.2.6). The constancy of freeboard constraint applies strictly only in the Phanerozoic and Proterozoic; its extrapolation into the Archean is speculative.

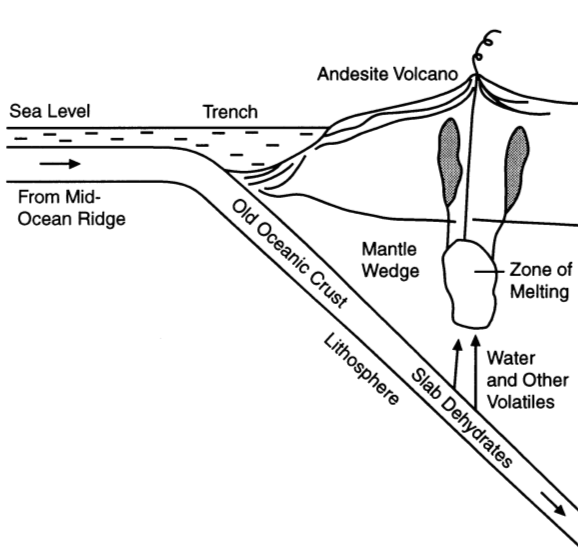
Gurnis and Davies (1985) combined the present distribution of crustal ages and crustal growth curves with a parameterized convection Earth thermal history model. They assumed that crustal production is related to the Earth's heat flux through plate velocities and that crustal removal (recycling into the mantle) is related to both heat flux and existing crustal volume. Their work emphasizes the sensitivity of the present crustal age distribution to the nature and variability of crustal production and recycling processes. For example, they show how a late-Archean peak in the crustal age distribution may have resulted from preferential removal of younger crust rather than a peak in production.

Another major question concerning the formation of the continental crust is whether crustal generation in the Archean involved processes similar to those at present. At present, continental crust is produced in island arcs and at hot spots with the former process dominant. However, the relative importance of these two processes may have changed since the Archean. The evolution of Archean and some younger terrains, such as the Arabian–Nubian Shield, may have involved a large amount of hot spot type addition in order to explain the very rapid addition rates that prevailed in these areas (Reymer and Schubert, 1984). Puchtel et al. (1998) propose continental growth by accretion of an oceanic plateau in the Archean.

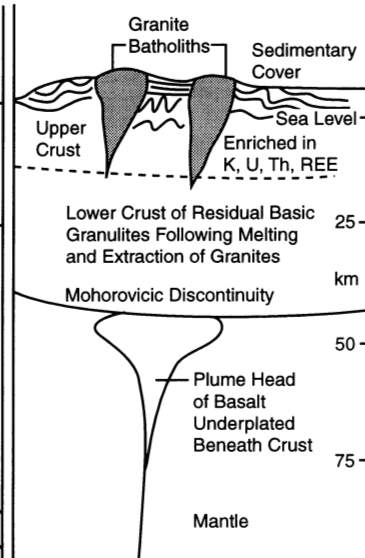
Differences in the composition of Archean and post-Archean crustal rocks suggest different crustal production mechanisms (Rudnick, 1995; Taylor and McLennan, 1995). Archean tonalities and trondhjemites may have resulted from slab or mantle wedge melting at higher temperatures and lower pressures than occur in the present mantle. At the higher temperatures that prevailed in the Archean, there would have been more rapid subduction of young hot slabs than occurs at present and slabs could have melted before undergoing complete dehydration (Martin, 1986; Defant and Drummond, 1990, 1993; Drummond and Defant, 1990; Abbott et al., 1994; Taylor and McLennan, 1995). At present, subducted old oceanic crust dehydrates, driving fluids into the overlying mantle wedge. These fluids induce further melting of the wedge in a poorly understood process (see Section 2.7.3). The resulting basic magmas pond in the continental crust and generate silicic granitic and andesitic magmas as secondary melts.

Crustal subtraction processes may also have been different in the Archean. The relative importance of sediment subduction and delamination in returning crustal material to the mantle may have been different in the Archean compared to the present. Rudnick (1995) has suggested that delamination of the lower crust may have been an important recycling process in the Archean. Figure 13.18 illustrates the possible differences between Archean

Post-Archean Growth of New Continental Crust



Mature Cratonic Crust



Growth of New Continental Crust During the Archean

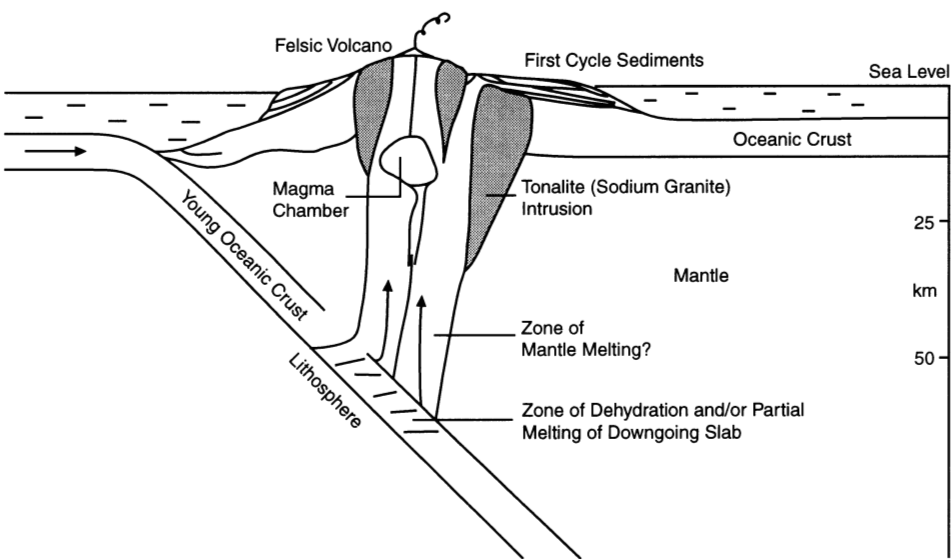


Figure 13.18. Sketch of possible differences between subduction-related crustal growth processes in the Archean and post-Archean (after Taylor and McLennan, 1995).

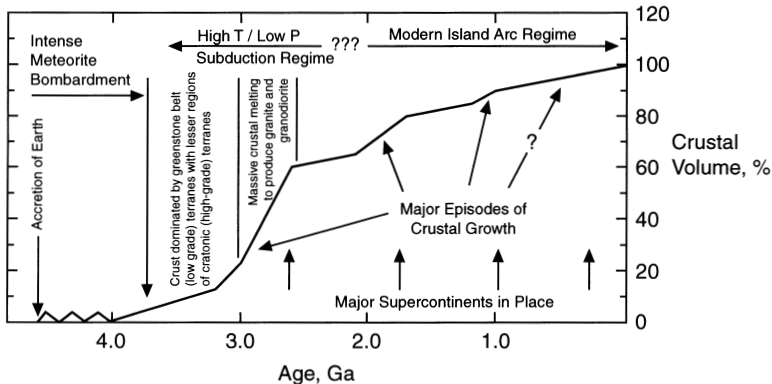


Figure 13.19. Sketch of possible crustal growth through geologic time with periods of enhanced growth indicated. The sketch suggests a possible connection between crustal growth episodes and assembly phases of supercontinents (after Taylor and McLennan, 1995).

and post-Archean crustal formation and Figure 13.19 summarizes the ideas discussed above regarding crustal growth and episodicity over geologic time.

Question 13.13: *What processes acted in the Archean to produce and recycle continental crust?*

14

Convection in the Interiors of Solid Planets and Moons

14.1 Introduction

Space missions have provided extensive information on the other planets and the planetary satellites of the solar system. Like the individual islands in an archipelago, the terrestrial planets share many characteristics and yet retain striking individuality. For example, it appears that active plate tectonics is unique to the Earth. In contrast, the Moon and Mercury have continuous lithospheres, with surfaces shaped largely by impacts and volcanic processes. Although impact cratering and volcanism have also been prevalent on Mars, its surface has also been modified by its atmosphere and the flow of a surface fluid, presumably water. Cloud-covered Venus has been exposed to the eyes of Earth-based and spacecraft radar systems. Cratering and volcanism have apparently left their marks on its surface, but there is no direct evidence of plate tectonic features such as extensive ridge or trench systems. The Galilean satellites of Jupiter are different from the inner planets and each other in puzzling ways. Ganymede and Callisto are icy satellites (half ice and half rock) whose surfaces have been modified by impacts, and, in the case of Ganymede, by tectonism. Callisto's surface shows no signs of endogenic activity, while Ganymede's surface shows no evidence of plate tectonics. Both of these Jovian moons have continuous water ice lithospheres. Europa is a mainly silicate moon of Jupiter, but Europa also has an outer layer of water ice/liquid. The surface of Europa is covered by ice, but there is a possibility that a liquid water ocean may exist beneath the ice. Europa's surface has been altered by impacts, tectonism, and cryovolcanism, but there is no evidence of global plate tectonics. Io is a silicate body, apparently lacking water. It is intensely heated by tidal dissipation and its recently formed surface is a volcanologist's paradise. Io is the only body in the solar system, other than the Earth, on which we have observed active silicate volcanism; Io may be the most volcanically active body in the solar system. Lithospheric plate evolution has destroyed much of the evidence of the early evolution of the Earth by continuously creating new surface rocks and returning old surface rocks to the mantle. The pervasive volcanism of Io has had the same effect by blanketing the surface with recently formed lavas. However, bodies such as Mercury, the Moon, the satellites of Mars, and Callisto preserve the early records of their evolutions in their cratered surfaces and thereby provide information on the early history of the solar system.

Limitations of space have precluded us from discussing all the solid planets and moons of the solar system. For example, we have not discussed Pluto and its moon Charon, Saturn's large satellite Titan, and Neptune's moon Triton. Our focus on the inner planets, the Moon, and the Galilean satellites, in part reflects the enormous increase in our knowledge of these bodies from spacecraft missions such as Magellan (Venus), Clementine

(Moon), Lunar Prospector (Moon), Mars Global Surveyor, and Galileo (Galilean satellites of Jupiter). Ongoing and future missions such as Cassini (Titan) and the planned Pluto-Kuiper Express will dramatically increase our knowledge of Titan and Pluto-Charon; comprehensive discussions of these bodies will then be appropriate.

14.1.1 The Role of Subsolidus Convection in the Solar System

Subsolidus mantle convection controls not only the cooling of the Earth, but it has also largely regulated the thermal evolution of all the other inner planets – Mercury, Venus and Mars, the Moon, and the larger satellites of the outer planets (Schubert, 1979; Schubert et al., 1986). While the Earth is unique in revealing its internal convection through the motions of its surface plates, the other planets and satellites provide only indirect evidence of past or present dynamically active interiors through surface features of tectonic and volcanic origin. The possibility of subsolidus mantle convection inside other planets and satellites is based mainly on our general understanding of how large bodies with Earth-like concentrations of radiogenic heat sources in the rocky parts of their interiors must transfer their internal heat to the surface. Table 14.1 lists some properties of those planets and satellites whose thermal histories have been likely controlled by subsolidus mantle convection. Table 14.2 gives the properties of outer planet satellites whose thermal histories have likely involved periods of subsolidus mantle convection in the past.

Question 14.1: *Is mantle convection occurring in the terrestrial planets, the Moon, and satellites of the giant planets?*

Planetary bodies are basically thermodynamic engines; the energy source is the heat produced by the radioactive decay of the isotopes of uranium, thorium and potassium and the secular cooling of the body (tidal dissipation is also an important heat source

Table 14.1. Properties of Planets and Satellites Whose Thermal Histories Have Likely Been Controlled by Subsolidus Mantle Convection

Planet or Satellite	Radius (km)	Mass (kg)	Density (kg m^{-3})	Acceleration of Gravity at the Surface (m s^{-2})	Approximate Silicate–Metal Mass Fraction
Mercury	2,439	3.30×10^{23}	5,420	3.78	1
Venus	6,050	4.87×10^{24}	5,250	8.60	1
Mars	3,398	6.42×10^{23}	3,940	3.72	1
Moon (Earth)	1,738	7.35×10^{22}	3,340	1.62	1
Io (Jupiter)	1,815	8.92×10^{22}	3,550	1.80	1
Europa (Jupiter)	1,565	4.80×10^{22}	2,989	1.32	0.85–1
Ganymede (Jupiter)	2,634	1.48×10^{23}	1,936	1.44	0.45–0.75
Callisto (Jupiter)	2,410	1.08×10^{23}	1,835	1.25	0.40–0.65
Titan (Saturn)	2,575	1.35×10^{23}	1,880	1.35	0.4–0.7
Triton (Neptune)	1,355	2.14×10^{22}	2,055	0.78	0.65–0.75

Table 14.2. Properties of Outer Planet Satellites Whose Thermal Histories Have Likely Involved Periods of Subsolidus Mantle Convection

Planet or Satellite	Radius (km)	Mass (kg)	Density (kg m^{-3})	Acceleration of Gravity at the Surface (m s^{-2})	Approximate Silicate–Metal Mass Fraction
Dione (Saturn)	560	1.05×10^{21}	1,430	0.22	0.45–0.55
Rhea (Saturn)	765	2.49×10^{21}	1,330	0.28	0.35–0.45
Tethys (Saturn)	530	7.55×10^{20}	1,210	0.18	0.3–0.35
Iapetus (Saturn)	730	1.88×10^{21}	1,150	0.24	0.25–0.30
Ariel (Uranus)	580	$\approx 1.35 \times 10^{21}$	$\approx 1,650$	≈ 0.27	
Umbriel (Uranus)	595	$\approx 1.27 \times 10^{21}$	$\approx 1,440$	≈ 0.24	
Titania (Uranus)	805	$\approx 3.48 \times 10^{21}$	$\approx 1,590$	≈ 0.36	
Oberon (Uranus)	775	$\approx 2.92 \times 10^{21}$	$\approx 1,500$	≈ 0.32	

for Io and perhaps for Europa). The escape of this heat drives thermal convection in planetary mantles. On the Earth, the tectonic plates are the thermal boundary layers of mantle convection cells; the subduction of the cold plates at ocean trenches transports about 70% of the mantle heat flux. Much of the remainder is attributed to the ascent of hot plumes through the mantle. Alternative mechanisms of heat transfer are partial delamination of the cold lithosphere and, as yet undefined, forms of secondary mantle convection.

It is quite clear that plate tectonics is not occurring on Venus. An essential question is how the heat is extracted from that planet without active plate tectonics. The recognized global resurfacing event is an important constraint on alternative models. A variety of models have been proposed but each remains speculative.

Question 14.2: How does Venus lose its heat?

The Moon and Mars appear to be planetary bodies which have essentially died in terms of surface tectonics and volcanism. One explanation is that the heat-producing elements have been fractionated into the crust and heat is now being lost by conduction. If there is little heat production at depth at present, active mantle convection is not required. Without active mantle convection there is little or no ongoing surface tectonics and volcanism. This model has also been proposed for Venus. Prior to any such extensive depletion of radiogenic elements from the deep interiors of these bodies, mantle convection would be expected to occur. Extensive volcanism and tectonism in the early history of Mars supports this view, as does the discovery of large-scale remanent magnetization in the ancient Martian southern hemisphere crust.

14.1.2 Surface Ages and Hypsometry of the Terrestrial Planets

We will first consider the surface age distribution and hypsometry (distribution of elevations) for the four planetary bodies. On the Earth both the age distribution and hypsometry are bimodal, reflecting the old, high-standing continental crust and the young, low-standing oceanic crust. Surface ages on Venus are primarily associated with the global resurfacing

event. Hypsometry on Venus provides some evidence for high-standing “continental” crust. Both Mars and the Moon are characterized by hemispheric dichotomies; one hemisphere is primarily composed of older, high-standing primitive crust, and the other younger, low-standing volcanic plains.

The distribution of surface ages on the Earth is dominated by the ocean–continent dichotomy. The oceanic lithosphere participates in the plate tectonic cycle of accretion at ocean ridges and subduction at ocean trenches. To a first approximation seafloor is created at a uniform rate of $3 \text{ km}^2 \text{ yr}^{-1}$ and is subducted at a rate proportional to age, such that the oldest seafloor has an age of 180 Myr (Parsons, 1982). Thus the oceanic lithosphere, 60% of the Earth’s surface, has a mean age of just over $\sim 60 \text{ Ma}$. This is illustrated in Figure 14.1.

In order to complete the age specification of the surface of the Earth, it is necessary to consider the age distribution of the continents (see the discussion in Section 13.7). This is not easy since erosion has greatly modified the surface and metamorphic reworking of continental rocks is common. The volume of the continental crust has grown by about 40% since 3 Ga. This is based on the freeboard argument that relates sea level to the volume of the continents (see Section 13.7) (Wise, 1974; Reymer and Schubert, 1984; Schubert and Reymer, 1985; Hallam, 1992; Taylor and McLennan, 1995). The mean age of extraction of the continents from the mantle can be obtained from the isotope systematics of mid-ocean ridge basalts (Allègre et al., 1983b) and it is found that the age is $\tau_c = 2.1 \pm 0.5 \text{ Gyr}$. Consistency of this relatively young age with the somewhat older age implied by the freeboard constraint requires recycling of continental crust into the mantle. Based on isotopic studies, DePaolo (1983) suggests that the recycling rate is $2.5 \pm 1.2 \text{ km}^3 \text{ yr}^{-1}$, but this rate is uncertain (see Section 13.7).

A basic controversy in geology is whether the creation of continental crust is nearly constant (uniformitarian) or is strongly episodic (Question 13.11). At the very least, this episodicity involves the Wilson cycle of ocean opening and closing and the assembly and dispersal of supercontinents. This episodicity since 600 Ma is well documented, and variations in the plate tectonic flux are attributed to it (Veevers, 1989). Associated with these variations are changes in many geological observations, both qualitative and quantitative.

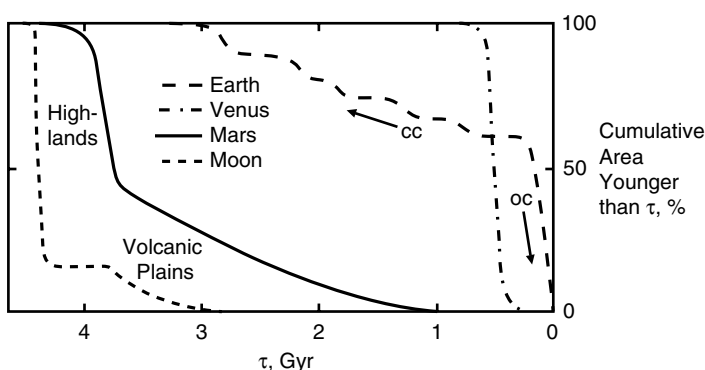


Figure 14.1. Cumulative surface area, in percent, younger than τ as a function of the age τ for the Earth, Venus, Mars, and the Moon. For the Earth, crustal ages younger than 125 Myr are principally oceanic (oc), whereas older crust is entirely continental (cc). For Mars and the Moon the older highlands are distinguished from the younger, lower-lying volcanic plains. For Venus and Mars the ages are based solely on crater counts, so that relative ages are reasonably accurate but absolute ages are subject to considerable error.

Examples include strontium isotope ratios in seawater, stable isotope ratios in carbonates and sulfates, occurrence of evaporites, and the temporal variations in the quantity and compositions of continental volcanics. This evidence has been summarized by Nance et al. (1986). The inferred age progression for the continents is combined with the age progression for the oceans in Figure 14.1. The bimodal distribution is clearly illustrated.

Without direct age determinations, the age of the surface of Venus must be determined from crater statistics. Schaber et al. (1992) demonstrated that the spatial distribution of craters on Venus does not statistically differ from a random distribution. This led these authors to postulate that a global resurfacing event occurred on Venus about 500 Ma. Strom et al. (1994) point out that only 2.5% of craters and crater-related features are embayed by lava, that only 3.5% are heavily fractured, and that 84% of the craters are completely pristine. Using Monte Carlo simulations, these authors conclude that the resurfacing event ended in less than 10 Myr and that only 4–6% of the planet has been resurfaced since that time. Bullock et al. (1993), Namiki and Solomon (1994), Price and Suppe (1994), and Hauck et al. (1998) have also studied this problem and arrive at somewhat higher rates of late resurfacing. But the conclusion that a global resurfacing event took place and that the surface has received little modification since is inescapable. The time history of the surface of Venus is illustrated in Figure 14.1. More recent studies of cratering on Venus that account for atmospheric deceleration and flattening of impactors place the resurfacing somewhat further back in time at about 750 Ma (McKinnon et al., 1997).

Comparison of the surface age distributions of the Earth and Venus raises several basic questions. Was the resurfacing event on Venus the termination of an early period of extensive surface tectonism and volcanism, followed by an indefinite period of surface stability? Or, alternatively, was the resurfacing event evidence of extreme episodicity in the evolution of the planet? If this is the case another resurfacing event can be expected.

Question 14.3: *What caused the major resurfacing of Venus about 500–750 Myr ago?*

Another question is whether some parts of the crust of Venus are much older but were reworked at the time of the global resurfacing much as the Earth's continental crust has been reworked. Particular candidates are the high-standing regions of Ishtar Terra and western Aphrodite, where Airy compensation of light crust may be applicable.

We next consider Mars. The most striking feature of the Martian surface is its hemispheric asymmetry, in some ways rather similar to that of the Moon. Much of the southern hemisphere is covered by a densely cratered terrain similar to the highlands of the Moon, whereas most of the northern hemisphere is made up of lightly cratered volcanic plains. The heavily cratered terrain in the south is probably the remnant of the post-accretional surface of the planet. The northern plains are generally similar to the volcanic plains of Venus; however, large volcanic constructs are a major exception. The largest shield volcanoes in the solar system lie on the Tharsis uplift and four of them rise 21 km above the reference level. The most spectacular of these is Olympus Mons with a mean diameter of 600 km and a summit caldera 80 km in diameter.

Since no rocks are available to date, the age distribution of the surface of Mars must be deduced from cratering statistics. Although it is possible to determine relative ages with some certainty, absolute ages are much more controversial. One estimate for the age distribution of

the surface of Mars is given in Figure 14.1 (Tanaka et al., 1992). The entire age progression could be compressed to earlier times by a factor of 2 within accepted error bounds. The hemispheric dichotomy of ages on Mars is illustrated in Figure 14.2. The boundary is between the upper Hesperian and older ages and lower Hesperian and younger ages; the age of this boundary is estimated to be 3.1 Gyr. The hemispheric dichotomy is clearly illustrated with the older terrain lying systematically to the south.

Question 14.4: *What caused the hemispheric dichotomy on Mars?*

The distribution of surface ages on the Moon is constrained by the age determinations of rocks returned during the Apollo project. The evolution of the Moon can be divided into three phases: (1) highlands formation, (2) mare formation, and (3) surface quiescence. The highlands of the Moon formed early in its evolution; one hypothesis is that the highlands crystallized rather rapidly from a global magma ocean. The highland rocks returned during the Apollo missions were highly differentiated and highly altered by surface bombardment. It is difficult to date the crystallization of the lunar highlands exactly but it certainly terminated by 4.0 Ga and probably before 4.4 Ga. The terminal bombardment, between 3.8 and 4.0 Ga,

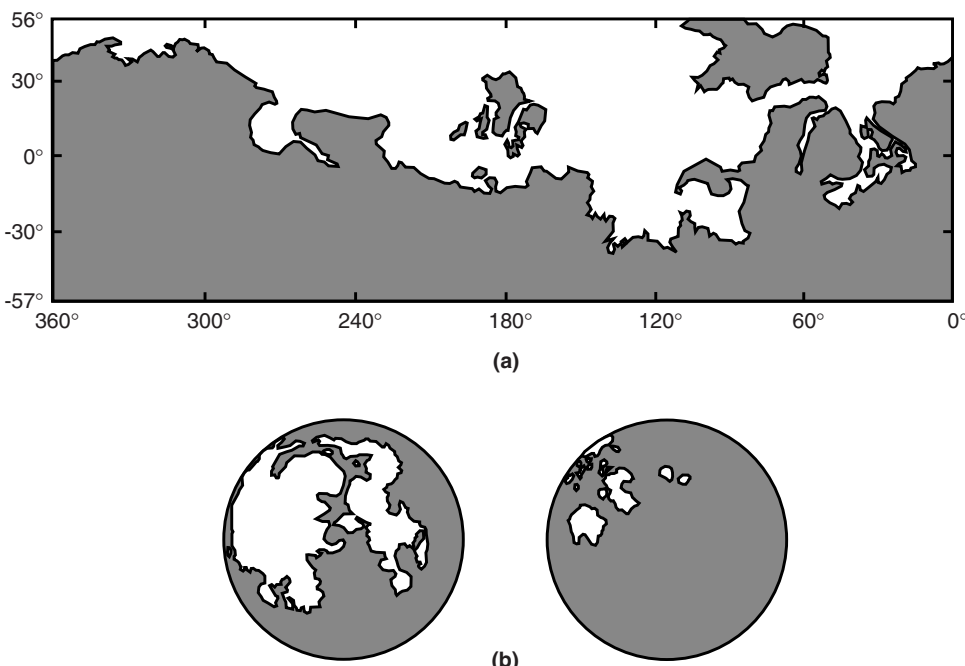


Figure 14.2. Illustration of the hemispheric dichotomies for (a) Mars and (b) the Moon. For Mars the older upland (shaded) terrains lie principally in the southern hemisphere, and the younger (unshaded) terrains, mainly low-lying volcanic constructs, are in the northern hemisphere (Tanaka, 1986). The boundary, based on crater counts, is between upper Hesperian and lower Hesperian times; the age is estimated to be 3.1 Gyr (Tanaka et al., 1992). For the Moon the distinction is between the (shaded) highlands and the low-lying (unshaded) volcanic plains (mare). The mare are principally on the nearside (left).

resulted in the excavation of many large, deep basins. These basins, particularly on the nearside, were subsequently filled by mare basaltic volcanism. The lunar mare constitute some 17% of the surface area and, based on mare basalts returned during the Apollo missions, date between 3.8 and 3.1 Ga. These basalts strongly resemble typical terrestrial basalts in major element composition and were probably produced by pressure-release melting in ascending mantle flows.

The age distribution of the surface of the Moon is given in Figure 14.1 (Heiken et al., 1991). The rapid crystallization of the highlands was followed by the slow emplacement of the mare basalts. Since 3 Ga, the Moon has been essentially a dead planet. An important aspect of lunar evolution that any comprehensive model must explain is the delay between the creation of the impact basins and the mare basalt volcanism that filled them.

The hypsometry of the Earth is primarily dependent upon the continent–ocean dichotomy and a basic level for erosion. Erosion bevels the high-standing continental crust to sea level in a relatively short time span. The result is that old continental crust has a thickness of ~ 40 km. The ocean floor is relatively low lying because the oceanic crust is dense and thin (~ 6 km) in comparison with the continental crust. In terms of comparative planetology, it is of interest to consider what the hypsometry of the Earth would be without oceans and/or without erosion. With erosion but without oceans (or oceans with a small volume of water), the thickness of old continental crust would be reduced to the thickness of the oceanic crust, and the ocean–continent dichotomy of elevation would be greatly reduced if not eliminated entirely. Without erosion, it would be expected that the continents would remain high standing. The high-standing mountains associated with young continental terrains would be expected to be maintained over geologic time. This binary split in the hypsometry is unique to the Earth, as is illustrated in Figure 14.3. Any comprehensive model for planetary evolution must explain this striking difference.

The hypsometry of Venus is better known than that of the Earth because of the high-resolution altimetry obtained during the Magellan mission (Ford and Pettengill, 1992; Rappaport and Plaut, 1994; Rappaport et al., 1999). As can be seen in Figure 14.3, variations in elevation are relatively subdued compared with the Earth, and this can be attributed to the high surface temperatures. Nevertheless, there are fairly extensive highlands in the

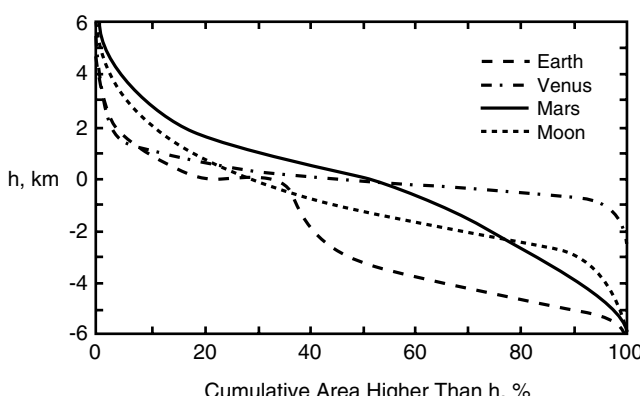


Figure 14.3. Hypsometric curves for the Earth, Venus, Mars, and the Moon. The cumulative surface area higher than h is given as a function of h . For the Earth, elevation is referred to sea level, for Venus and the Moon the reference is to the mean elevation, and for Mars the reference is arbitrary.

equatorial region and some very high topography, ~ 10 km, in Ishtar Terra. However, the strong distinction between the high-standing continents and the remainder of the Earth is not seen on Venus.

Hypsometry on Mars had been far less accurate than on the other bodies, but the situation has changed with laser altimetry data from the Mars Global Surveyor spacecraft (Smith et al., 1998, 1999a). Martian hypsometry is generally similar to that of the Moon as shown in Figure 14.3. The low-lying topography is associated with the low-lying northern plains. However, some of these plains units are covered with volcanic constructs which have the highest topography on the planet. The old southern highlands are systematically above the planetary mean.

The major question in understanding the evolution of Mars is the origin of the north–south dichotomy. Based on the low-lying volcanic plains (mare) on the Moon, one hypothesis is an initial excavation of the northern hemisphere by one or more impact basins (Wilhelms and Squyres, 1984; Frey and Schultz, 1988). The alternatives to collisional excavation are that the initial northern crust was thin or that it was thinned either partially or entirely by internal processes such as mantle convection (Lingenfelter and Schubert, 1973; Schubert and Lingenfelter, 1973; Smith et al., 1999a). Wise et al. (1979a) and McGill and Dimitriou (1990) suggest that the crust was tectonically thinned, whereas Sleep (1994b) suggests that the crust was subducted and that an episode of plate tectonics followed.

Hypsometry on the Moon is primarily associated with the systematic difference in elevation between the farside and the nearside. Excellent global topography has been obtained by the lidar instrument on the Clementine mission (Lucey et al., 1994; Zuber et al., 1994; Smith et al., 1997). The resulting hypsometry is given in Figure 14.3. Certainly many of the regions with low topography can be attributed to large impact basins. And most of the lowest-lying areas in these basins have been filled by mare basalts. An exception is the South Pole–Aitken basin with very little basaltic fill; much of the lowest-lying topography on the Moon is associated with this basin.

Just as with Mars, a major question regarding the Moon is whether the general nearside–farside dichotomy in elevation and crustal thickness can be attributed to massive impacts or to other effects such as mantle convection early in the Moon’s history (Lingenfelter and Schubert, 1973; Schubert and Lingenfelter, 1973) or hemispheric differences in the solidification of the early magma ocean (Wasson and Warren, 1980). Zuber et al. (1994) suggest that the crustal nearside thinning can be associated with crustal erosion due to mantle convection.

Question 14.5: What caused the nearside–farside dichotomy on the Moon?

14.2 Venus

14.2.1 Comparison of Two Sisters: Venus versus Earth

In terms of size, mass, and density, Venus is the planet most similar to the Earth (Table 14.1). An obvious working hypothesis would be that the tectonics of Venus would be similar to the tectonics of the Earth and that there would be plate tectonics on Venus. We know that this is not the case and that mantle convection on Venus must be substantially different from mantle convection on the Earth.



Figure 14.4. Global view of the surface of Venus centered at 180° east longitude based on Magellan synthetic aperture radar mosaics and Pioneer Venus Orbiter data.

For a color version of this figure, see plate section.

Question 14.6: *What is the nature of mantle convection in Venus?*

The cloud cover on Venus has prevented optical observations; however, Pioneer Venus radar, Earth-based radar observations, Venera 15–16 orbital imaging radar, and Magellan radar images have provided clear views of the surface of Venus (Figure 14.4). These views, along with topography and gravity data (Figures 14.5 and 14.6, respectively), indicate that the two planets are in fact quite different. On the Earth, the global oceanic rift system and the arcuate ocean trenches are the primary surface manifestations of plate tectonics. The almost total absence of these features on Venus has led to the conclusion that active plate tectonics is not occurring on that planet (Kaula and Phillips, 1981). Clearly, any comprehensive

Venus Topography

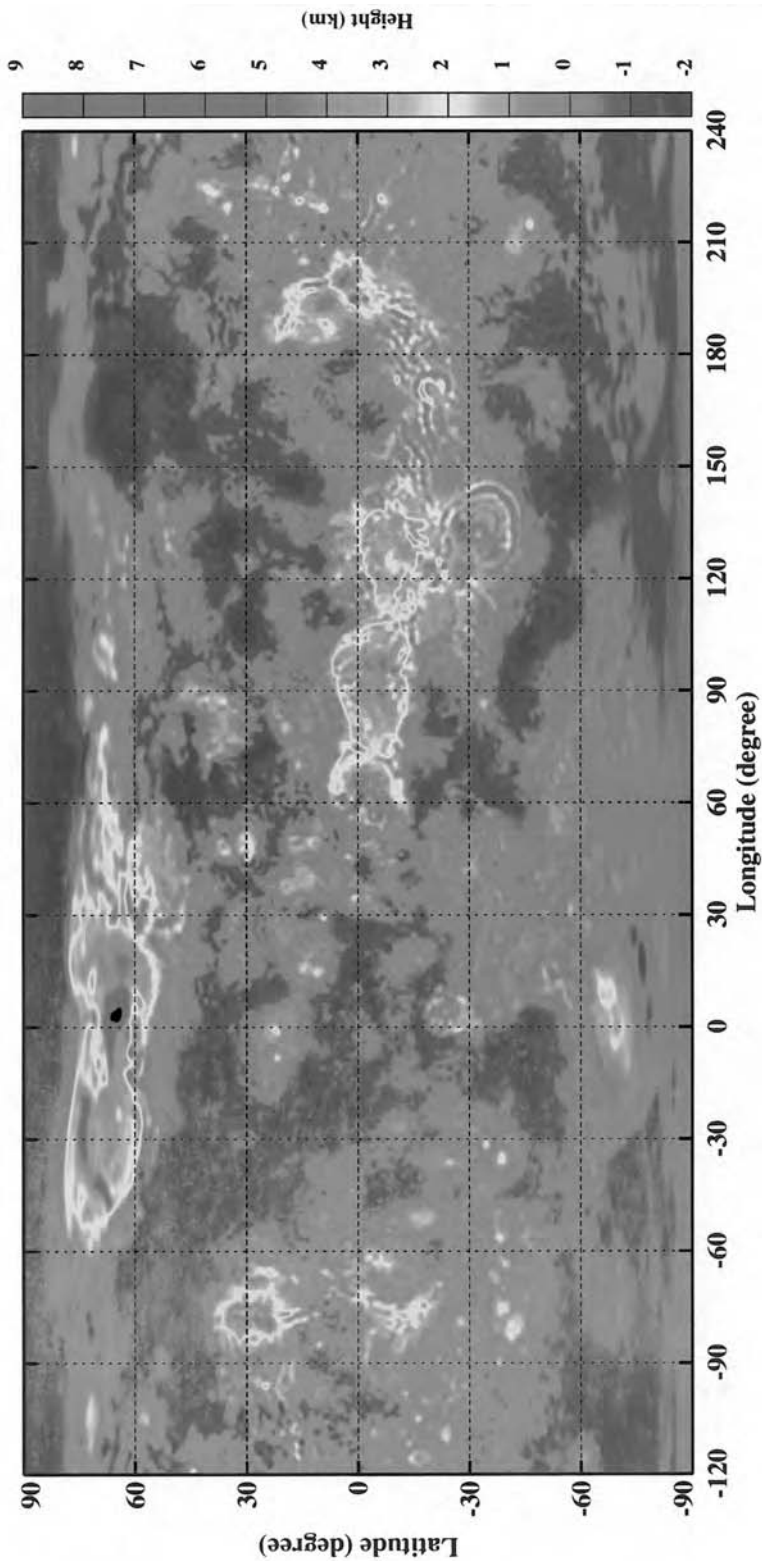


Figure 14.5. Venus topography from a 360 degree and order spherical harmonic model (Rappaport et al., 1999). The plot is based on a truncation of the model to degree and order 180.

For a color version of this figure, see plate section.

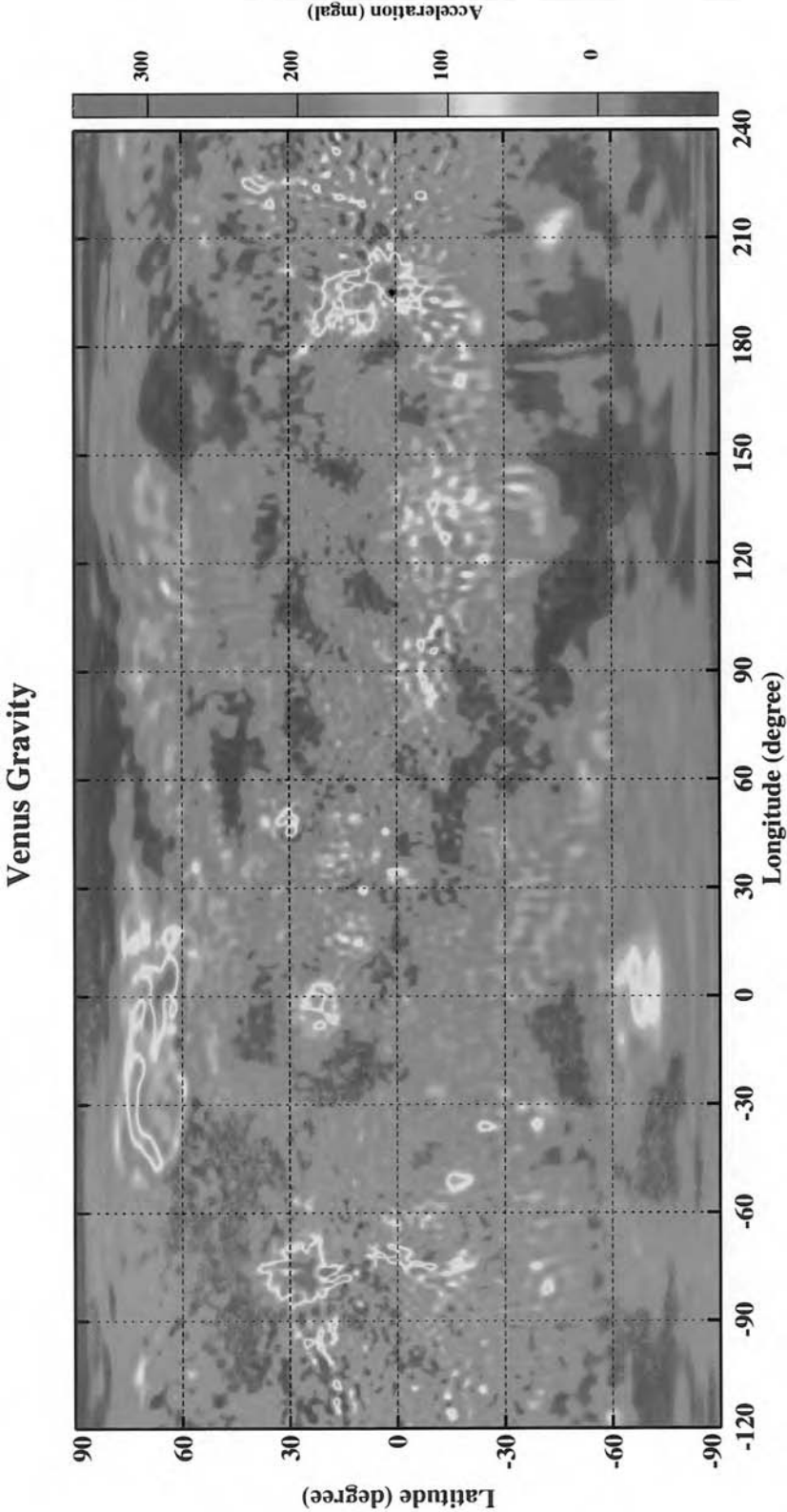


Figure 14.6. Venus gravity field from a 180 degree and order spherical harmonic model (Konopliv et al., 1999). The plot is based on a truncation of the model to degree and order 150.

For a color version of this figure, see plate section.

understanding of tectonism and volcanism on Venus requires an understanding of how heat is transported in the absence of plate tectonics.

One important difference between the planets is surface temperature. The dense atmosphere and cloud cover on Venus produce a greenhouse effect that results in a surface temperature that is 475 K higher than on the Earth (Seiff, 1983). The thickness of the lithosphere on Venus can be estimated if three assumptions are made. First, assume that the rates of internal heat generation on the two planets due to the decay of the radioactive isotopes of uranium, thorium, and potassium are nearly equal. This would appear to be a reasonable hypothesis based on the general similarities in composition of the two planets. Second, assume that the mean mantle temperatures of the two planets are approximately equal. Because of the exponential temperature dependence of the solid-state mantle viscosity, near-equal mantle temperatures are expected. Finally, assume that surface heat loss has a weak time dependence and neglect heat production in the crust. With these assumptions, a simple conduction calculation shows that the mean thickness of the lithosphere on Venus would be about 60% of the thickness on the Earth or about 40 km. One implication of a thin, hot lithosphere is that it would be weak and could not support high topography or large gravity anomalies. Another is that relaxation of large impact craters would be expected.

Topography and gravity data obtained by Pioneer Venus show serious inconsistencies with these expectations. Although the mean surface roughness (height to wavelength ratio) on Venus is a factor of 3 or 4 less than on the Earth, the maximum elevations are nearly equal (Pettengill et al., 1980; Bills and Kobrick, 1985; Turcotte, 1987; Ford and Pettengill, 1992).

The Magellan mission has provided a wealth of data on Venusian tectonism and volcanism (Solomon et al., 1992; Phillips and Hansen, 1994; Crumpler et al., 1997; Hansen et al., 1997; Nimmo and McKenzie, 1998). The radar images of the surface (Figure 14.4) are complemented by global topography (Figure 14.5) (Rappaport and Plaut, 1994; Rappaport et al., 1999) and gravity anomaly data (Figure 14.6) (Konopliv and Sjogren, 1994; Sjogren et al., 1997; Konopliv et al., 1999). It is clear that plate tectonics, as it is known on the Earth, does not occur on Venus (Kaula, 1994a). At the present time Venus is a one-plate planet. Nevertheless, there are tectonic features on Venus that certainly resemble major tectonic features on the Earth. Beta Regio has many of the features of a continental rift on Earth. It has a domal structure with a diameter of about 2,000 km and a swell amplitude of about 2 km. It has a well-defined central rift valley with a depth of 1–2 km and there is some evidence for a three-armed planform (aulacogen). Alta, Eistla, and Bell Regiones have similar rift zone characteristics (Grimm and Phillips, 1992; Senske et al., 1992). Aphrodite Terra, with a length of some 1,500 km, is reminiscent of major continental collision zones on the Earth, such as the mountain belt that extends from the Alps to the Himalayas. Ishtar Terra is a region of elevated topography with a horizontal scale of 2,000–3,000 km. A major feature is Lakshmi Planum, which is an elevated plateau similar to Tibet with a mean elevation of about 4 km. This plateau is surrounded by linear mountain belts, Akna, Danu, Freyja, and Maxwell montes, reaching elevations of 10 km, similar in scale and elevation to the Himalayas (Kaula et al., 1997).

The gravity anomalies associated with major topographic features provide information on their origin (Figures 14.5 and 14.6). Gravity anomalies obtained from tracking Pioneer Venus and Magellan revealed major surprises (Sjogren et al., 1980, 1983, 1997; Reasenberg et al., 1981; Mottinger et al., 1985; Bills et al., 1987; Konopliv and Sjogren, 1994). Unlike on Earth, gravity anomalies correlate with high topography on Venus. Large positive gravity anomalies are directly associated with Beta Regio (Esposito et al., 1982; Reasenberg et al., 1982) and eastern Aphrodite Terra (Herrick et al., 1989; Black et al., 1991) (Figures 14.5

and 14.6). These features are at least 75% compensated but the associated gravity anomalies are much larger than those found on the Earth. On the basis of Airy compensation, eastern Aphrodite Terra requires a 230 km depth of compensation (Herrick et al., 1989). Although Ishtar Terra has the highest topography on Venus, the associated gravity anomalies are somewhat smaller with an estimated 150 km depth of compensation (Sjogren et al., 1984); however, the uncertainties are large at this high northern latitude. Smrekar and Phillips (1991) have obtained ratios of geoid anomalies to topography (GTR) for elevated regions on Venus. They find that Beta Regio has the highest value with a GTR = 31 ± 2 m/km. Any explanation for the high topography on Venus must also be able to explain the large associated gravity anomalies. Geoid anomalies on Venus have been directly related to lithospheric stresses by Sandwell et al. (1997).

Question 14.7: *What produced the high topography on Venus and why are the topography and gravity strongly correlated?*

Explanations of the high topography on Venus generally fall into two classes. The first is compensated topography in analogy to the Earth. On Earth, most high topography is attributed to Airy isostasy associated with crustal thickening; high elevations have thick crustal roots. Thickened crust can be due to volcanic and magmatic construction or horizontal compression. With a thin, hot lithosphere on Venus the amount of crustal thickening would be strongly limited. Some relative topographic highs on Earth such as the mid-ocean ridges are associated with thermal isostasy or lithospheric thinning. Lithospheric thinning could produce elevated topography on Venus but a relatively thick lithosphere would be required. A thin Venusian lithosphere implies shallow depths of compensation, inconsistent with observations of Venus.

These difficulties led to the consideration of a second class of models associated with the dynamic support of topography (Phillips, 1990; Bindschadler et al., 1992a). These models depend on dynamic interactions with mantle convection in order to generate topography and the associated gravity anomalies. The equatorial highlands on Venus are generally associated with ascending mantle plumes (Morgan and Phillips, 1983; Phillips and Malin, 1983, 1984; Herrick and Phillips, 1990; Phillips et al., 1991). Grimm and Phillips (1990, 1991) also associate Ishtar Terra with mantle upwelling. However, Bindschadler and Parmentier (1990) and Bindschadler et al. (1990) associate Ishtar Terra with mantle downwelling. Bindschadler et al. (1992b) also associate Alpha, Ovda and Theta Regio with mantle downwelling.

Kiefer et al. (1986) and Kiefer and Hager (1991a,b, 1992) considered quantitative dynamic models for the topography and associated gravity anomalies on Venus. Dynamic topography would be expected to be smooth and without sharp escarpments. Although Beta Regio has a broad domal structure, it also has well-defined rift valleys. The topography associated with these rift valleys must be supported by lithospheric stresses. Ishtar Terra is bounded by escarpments several kilometers high with slopes up to 30° . This topography must also be supported by lithospheric stresses. Three kilometer high escarpments require stresses of the order of 100 MPa. There is no evidence that these surfaces are relaxing so the stresses are most likely elastic. Also, the near absence of crater relaxation on Venus requires a thick elastic lithosphere (Grimm and Solomon, 1988). These observations appear

to preclude a thin steady-state lithosphere dominated by dynamic topography and associated geoid anomalies.

Long-wavelength dynamic topography on the Earth, if it exists, must have amplitude less than a few hundred meters (Colin and Fleitout, 1990; Stein and Stein, 1992; Kido and Seno, 1994; Le Stunff and Ricard, 1995). Almost all topography on the Earth can be attributed to either Airy, Pratt, or thermal isostasy. Of course, topographic features on the Earth, unlike those on Venus, have very small associated gravity anomalies. While there is limited expression of global-scale dynamic topography on the Earth, there may be topographic signatures of dynamic topography on a regional scale. A possible example is the African superswell. Lithgow-Bertelloni and Silver (1998) have attributed the excess elevation (about 750 m) of the southern African plateau and surrounding oceans and the eastern African plateau to dynamical support by a mantle flow upwelling from great depth (the bottom of the lower mantle) beneath the African plate. The absence of global-scale dynamic topography on the Earth with amplitude more than a few hundred meters is puzzling, because mantle flow models derived from seismic tomographic buoyancy distributions and numerical convection models predict dynamic topography of order kilometers (e.g., Le Stunff and Ricard, 1997).

One of the most important observational constraints on the geodynamics of Venus comes from studies of impact cratering on the surface (McKinnon et al., 1997). Approximately 900 impact craters have been identified from Magellan images with diameters ranging from 2 to 280 km (Herrick et al., 1997). Correlations of this impact flux with craters on the Moon, the Earth, and Mars indicate a mean surface age of 0.5 ± 0.3 Gyr. Another important observation is that 52% of the craters are slightly fractured, and only 4.5% are embayed by lava flows. These observations led Schaber et al. (1992) to hypothesize that a global volcanic resurfacing event had occurred at about 500 Myr ago and that relatively little volcanism has occurred since (see also Basilevsky et al., 1997). Impact cratering studies that account for the effects of the dense Venus atmosphere (deceleration and impactor flattening) place the global resurfacing event closer to 750 Ma (McKinnon et al., 1997).

Statistical tests have confirmed the global resurfacing hypothesis (Bullock et al., 1993; Strom et al., 1994). Although there has certainly been some volcanism since the major resurfacing event, it is clear that a large fraction ($\sim 80\text{--}90\%$) of Venus' surface was covered by volcanism during a relatively short period of time (Namiki and Solomon, 1994; Hauck et al., 1998). This observation is direct evidence that the geologic evolution of Venus has been far more catastrophic than that of the Earth (Herrick, 1994).

A major geologic feature that is unique to Venus is the corona (Stofan et al., 1991, 1992, 1997; Squyres et al., 1992). Coronae are quasi-circular features, 100–2,600 km in diameter, with raised interiors and elevated rims, often with annular troughs. McKenzie et al. (1992) and Sandwell and Schubert (1992a, b) have argued that the perimeters of several large coronae on Venus, specifically Artemis, Latona, and Eithinoa, resemble terrestrial subduction zones in both planform and topography. Artemis chasma has a radius of curvature similar to that of the South Sandwich subduction zone on the Earth. Sandwell and Schubert (1992a) propose a model in which the large coronae are incipient circular subduction zones. The foundering lithosphere is replaced by ascending hot mantle in a manner similar to back-arc spreading on the Earth.

Question 14.8: Is there limited subduction or lithospheric foundering on Venus?

Sandwell and Schubert (1992b) have also shown that the morphology of several coronae are in good agreement with lithosphere flexure models that have been successful in explaining the seafloor morphology at ocean trenches on the Earth. Their flexural topographic profiles yield elastic lithosphere thicknesses of 37 km for Artemis Corona, 35 km for Latona Corona, 15 km for Eithinoa Corona, 40 km for Heng-O Corona, and 18 km for Freyja Montes. If a global lithosphere stabilized 500 Myr ago and has been thickening ever since by thermal conduction, the temperature distribution in the lithosphere would be given by (4.2.4). From this relation, temperatures at depths of 15–35 km in a stable, 500 Myr old lithosphere are 840–960 K; these are reasonable values for the base of an elastic lithosphere.

Question 14.9: What is the thickness of the lithosphere on Venus?

14.2.2 Heat Transport in Venus

An important constraint on any model for the thermal evolution of Venus is that it must explain how Venus loses its heat (Question 14.2) (Turcotte, 1995). On the Earth some 70% of the heat transfer through the mantle is attributed to the subduction of the cold oceanic lithosphere at ocean trenches. The remainder is primarily attributed to the ascent of hot mantle plumes and possibly secondary convection with a minor contribution from the partial subduction (delamination) of the lower continental lithosphere. Without active plate tectonics, the evolution of Venus is significantly different from that of the Earth. Three end-member models have been proposed, each of which will be discussed in turn.

The first model is the uniformitarian model. In this model the transport of heat through the mantle and lithosphere of Venus is in a near-steady-state balance with the heat generated by the heat-producing elements and the secular cooling of the planet. This requires a relatively thin, stable lithosphere with heat transport to its base by mantle convection. Heat transport through the lithosphere must be by conduction or another unspecified mechanism.

The second model is the catastrophic model. In this model the present loss of heat to the surface of Venus is not in balance with its internal heat generation. The global lithosphere stabilized about 500 Myr ago, and the interior of the planet has been heating up since then. Heat is lost in episodes of global subduction of the thickened lithosphere.

The third model is the differentiated planet. In this model the heat-producing elements have been almost entirely fractionated into the crust and the heat generated is lost by conduction to the surface.

In the first model, Venus is in a near-steady-state balance between radioactive heat production and secular cooling and the surface heat loss. Many of the arguments for such a hypothesis have been given by Phillips and Hansen (1994). For a near-steady-state heat loss model, a logical estimate for the present surface heat flow on Venus is obtained by scaling the Earth's heat loss ($Q_E = 3.55 \times 10^{13}$ W) to Venus using the masses of the two planets ($M_E = 5.97 \times 10^{24}$ kg, $M_V = 4.87 \times 10^{24}$ kg). The result is that the present heat loss from Venus is $Q_V = 2.91 \times 10^{13}$ W, and the mean surface heat flux is $q_V = 63$ mW m⁻². This calculation implicitly assumes that Venus and the Earth have similar concentrations of heat-producing elements, a reasonable assumption in terms of present models of planetary accretion. We will return to this point when we discuss the measurements of the surface concentrations of heat-producing elements on Venus. With the steady-state hypothesis and a thermal conductivity $k = 3.3$ W m⁻¹ K⁻¹, the mean surface thermal gradient on Venus is $dT/dy = 19$ K km⁻¹. With the assumption of a linear conduction gradient through the

lithosphere and a temperature drop across the lithosphere $\Delta T = 850$ K, the mean lithosphere thickness is $y_L = 45$ km. Mechanical arguments against such a thin lithosphere on Venus have been given by Turcotte (1993); here we are concerned with the thermal implications. The lithosphere of a planet can be thickened if a significant fraction of the planet's heat-producing elements is concentrated in it. This model will be discussed in a later section.

If Venus behaves like the Earth, the relative contributions of radioactive heat generation and secular cooling are likely to be nearly equal on the two planets. The expected secular cooling of Venus for the last 500 Myr is given in Figure 14.7 for Urey numbers $Ur = 0.8$ and 0.6. A typical rate of cooling is 70 K Gyr $^{-1}$.

Since plate tectonics is not available to transport heat through the mantle of Venus, alternate mechanisms for heat transport must be found if a near-steady-state hypothesis is to be viable. Without the participation of cold subducted lithosphere, the temperature differences associated with ascending hot material and descending cold material through the mantle of Venus will be considerably less than on the Earth. In order to transport the same amount of heat, larger material fluxes through the mantle are required. The implication is that the Rayleigh number will be higher on Venus. Since the Rayleigh number is principally sensitive to the viscosity, the conclusion is that the mean viscosity in the mantle of Venus must be considerably less than on the Earth in order to provide the necessary steady-state heat transport. Based on our understanding of heat transfer in the Earth, we consider two nonplate tectonic mechanisms, plumes and lithospheric delamination, for heat transfer in Venus. Plumes can arise from instabilities in a hot basal boundary layer and lithospheric delamination can result from partial instabilities in the cold surficial boundary layer, i.e., the lithosphere.

The geology, topography, and associated gravity anomalies of the equatorial highlands on Venus have been attributed to the dynamic processes associated with mantle plumes by a number of authors (McGill et al., 1981; Kiefer and Hager, 1991a, b, 1992; Phillips et al., 1991; Smrekar and Phillips, 1991; Bindschadler et al., 1992b; Moore and Schubert, 1995, 1997b; Stofan et al., 1995; Smrekar et al., 1997). The large number of coronae that cover the planet have also been attributed to mantle plumes (Stofan et al., 1991, 1992, 1997; Janes et al., 1992; Squyres et al., 1992). While there is substantial observational evidence for the impingement of mantle plumes on the base of the Venusian lithosphere (Koch, 1994), the

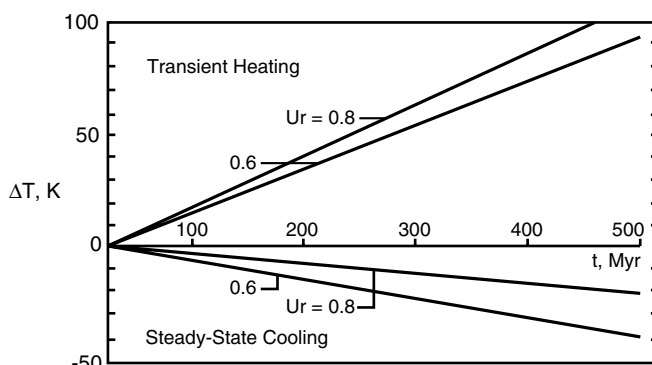


Figure 14.7. The change in temperature ΔT of the interior of Venus is given as a function of time t for the last 500 Myr. The steady-state cooling results are applicable for a uniformitarian model, and the rate of cooling is given by the Urey number Ur . The transient heating would be applicable to the episodic subduction hypotheses during periods of lithospheric stability and conductive thickening when no heat loss to the surface is assumed.

important question is whether the plumes are sufficiently large and numerous to transport the required heat. About 80 plumes with the strength of the Hawaiian plume ($Q_{pH} = 3.6 \times 10^{11}$ W) would be required to carry a substantial fraction of the total heat ($Q_V = 2.9 \times 10^{13}$ W). With a thin hot lithosphere, evidence of such a large number of strong plumes, such as extensive volcanism, would be expected to be seen on the surface; however these signatures are not seen. A quantitative study of the strengths of active plumes on Venus indicates that the present plume flux is less than on the Earth (Smrekar and Phillips, 1991).

Plumes are associated with the instability of hot basal boundary layers, but for a fluid heated from within, heat is transported primarily by instabilities in near-surface cold boundary layers (e.g., Parmentier et al., 1994). For Venus this means, for the steady-state model, that heat would be transported primarily by delamination of the cold lithosphere. A mechanism for lithospheric delamination on Venus has been proposed by Buck (1992). He decouples the upper crust from the upper mantle with a low-viscosity lower crust, a lower crustal asthenosphere. The upper mantle participates in a plate tectonic subduction cycle but the upper crust behaves as a scum that floats and does not participate in the subduction. A similar model has been proposed by Arkani-Hamed (1993). McKenzie et al. (1992), Sandwell and Schubert (1992a, b), Schubert et al. (1994), and Schubert and Sandwell (1995) have suggested that foundering of the crust and lithosphere, a form of subduction, has occurred on Venus at certain coronae and chasmata such as Artemis Corona. The arcuate trenches associated with a number of coronae and chasmata strongly resemble the trenches at subduction zones on the Earth.

The equivalent surface heat flux due to the subduction or delamination of cold lithosphere is easily estimated. The energy associated with a global subduction event is given by (Turcotte and Schubert, 1982, p. 281)

$$E_S = 8\pi R_V^2 \rho c (T_m - T_s) \left(\frac{\kappa t}{\pi} \right)^{1/2} \quad (14.2.1)$$

where R_V is the radius of Venus, T_s is surface temperature, T_m is mantle temperature, ρ is density, c is specific heat, and κ is thermal diffusivity. Equation (14.2.1) assumes that the lithosphere has cooled and thickened conductively from zero thickness for a period t . This is clearly a limiting case in that any basal heating of the lithosphere has been neglected. The equivalent mean surface heat loss Q_S is obtained by dividing (14.2.1) by t with the result

$$Q_S = 8\pi R_V^2 \rho c (T_m - T_s) \left(\frac{\kappa}{\pi t} \right)^{1/2} \quad (14.2.2)$$

The heat loss is given as a function of t in Figure 14.8, for $R_V = 6,050$ km, $T_m - T_s = 880$ K, $\rho = 3,300$ kg m⁻³, $c = 1$ kJ kg⁻¹ K⁻¹, and $\kappa = 1$ mm² s⁻¹. If the total required heat loss from the interior of Venus (2.9×10^{13} W) were associated with subduction, then the lithosphere would have to subduct, on average, at an age of $t = 85$ Myr.

The above result can also be used to determine the efficiency of delamination in transporting heat through the lithosphere of Venus. If the temperature separating delaminating lithosphere from stable lithosphere is T_D , then we define

$$\vartheta_D = \frac{(T_D - T_s)}{(T_m - T_s)} \quad (14.2.3)$$

and the mean surface heat loss due to delaminating lithosphere is given by

$$Q_D = 8\pi R_V^2 \rho c (T_m - T_s) (1 - \vartheta_D) \left(\frac{\kappa}{\pi t} \right)^{1/2} \quad (14.2.4)$$

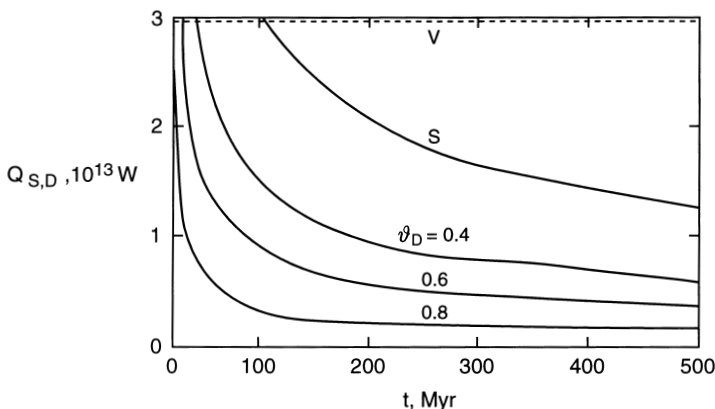


Figure 14.8. The mean surface heat flux $Q_{S,D}$ is given for lithospheric subduction (S) and delamination (D) at intervals t . The curve S is for total subduction of the lithosphere. The parameter ϑ_D is a measure of the fraction of the lithosphere that participates in delamination; $\vartheta_D = 0$ is equivalent to total subduction. The heat loss denoted by V is the required steady-state value by scaling from the Earth.

The equivalent mean surface heat losses Q_D for $\vartheta_D = 0.4, 0.6, 0.8$ are given in Figure 14.8 as a function of the delamination time interval t . If the entire mantle heat flux is attributed to delamination, then it must occur sufficiently often to transmit $Q_D = 2.91 \times 10^{13}$ W. With $T_D = 1,470$ K ($\vartheta_D = 0.8$), the entire lithosphere would have to delaminate, on average, at intervals of $t_D = 1.2$ Myr, with $T_D = 1,290$ K ($\vartheta_D = 0.6$), the required interval $t = 6$ Myr, and with $T_D = 1,110$ K ($\vartheta_D = 0.4$), $t_D = 19$ Myr. It seems highly unlikely that global delamination events could take place at such short time intervals. Also, global delamination events would be expected to disrupt the upper crust resulting in intensive volcanism that is not observed. This is not to say, however, that delamination or subduction is not occurring. Delamination may play a role in creating the high plateau topography of Ishtar Terra. As discussed above, lithospheric foundering or subduction may also be associated with the formation of some coronae and chasmata. Nevertheless, it seems implausible that delamination could make a significant contribution to the global heat flow. This is consistent with our understanding of the role of delamination on the Earth.

We now turn to the second model for Venus, which is strongly time-dependent or catastrophic. In fact, there are several alternative models that can be postulated. In one model, plate tectonics simply ceased some 500 Myr ago (Arkani-Hamed and Toksöz, 1984; Arkani-Hamed et al., 1993; Arkani-Hamed, 1994). According to this hypothesis, the global lithosphere stabilized at that time and will remain stable. The principal problem with this hypothesis is that the interior temperature will increase without plate tectonics or alternative heat transport mechanisms. The rate of temperature increase is given in Figure 14.7 for two values of the Urey number, $Ur = 0.6$ and 0.8 . Over 500 Myr the mantle temperature increases about 100 K; the corresponding decrease in viscosity is about an order of magnitude.

An alternative model is that this temperature increase will eventually trigger another episode of global volcanism and tectonics. Without sufficient surface heat loss the lithosphere on Venus will thicken during the period of surface quiescence. One suggestion is that the thickening lithosphere eventually becomes sufficiently unstable that a global subsidence event is triggered (Turcotte, 1993). Heat stored in the interior during the period of surface

quiescence is lost to the subducted lithosphere and lost during the period of volcanic activity and tectonism that would follow. An alternative explanation is that mantle convection is episodic due to chemical differentiation (Parmentier and Hess, 1992; Herrick and Parmentier, 1994).

The limiting behavior of the lithosphere during surface quiescence is conductive cooling and thickening through time with no significant convective heat flux to its base. In this limit, the thickness of the lithosphere after about 500 Myr is near 300 km. Such a thick lithosphere at present is consistent with a number of observations: (1) it provides support for the high topography, up to 10 km; (2) it is consistent with the high observed geoid-topography ratios, up to 33 m km^{-1} (Smrekar and Phillips, 1991; Kucinskas and Turcotte, 1994; Moore and Schubert, 1997b); (3) it is consistent with the observed unrelaxed craters (Grimm and Solomon, 1988); and (4) it is consistent with the thick elastic lithospheres inferred from flexural studies (Sandwell and Schubert, 1992a, b; Johnson and Sandwell, 1994).

There is also direct observational evidence that episodic subduction is an applicable mechanism for heat transfer in a convecting system with a very viscous (rigid) upper thermal boundary layer. A natural analogue for mantle convection is thermal convection in a lava lake. Atmospheric cooling creates a “solid” crust which is gravitationally unstable with respect to the molten magma beneath. Episodic subduction has been observed in lava lakes. Wright et al. (1968) describe the behavior of the Makaopuhi lava lake during the eruption of the Kilauea volcano in March 1965. They describe a particularly graphic episode of episodic subduction of the stabilized upper thermal boundary layer: “During the night of March 5 the entire, apparently stable crust of the lava lake founded in a spectacular overturn.” and “Crustal foundering was observed repeatedly during the eruption.” These authors also describe in some detail the subduction (foundering) mechanism: “Most major foundering began at a point or line near the margin of the lake. The foundering propagated along a series of arcs of increasing circumference away from the point of origin. The beginning of foundering was marked by the appearance of a crack in the lake surface, which exposed fresh magma. Either from loading behind or from upward pressure in front of the crack a second fracture opened ahead of the first, and the crust bounded by the two cracks tilted upward along the edge bounded by the second crack and then slid backward beneath lava welling out of the first crack. Formation of a third crack ahead of the second was followed by tilting of the crust between the second and third cracks, the crust then slid beneath the new lava behind the second crack, and so forth.”

Although there is no direct evidence for global subduction on Venus, there is evidence for subduction on a regional scale. As discussed above, Sandwell and Schubert (1992a, b) and Schubert et al. (1994) have proposed a model in which the large coronae on Venus are incipient circular subduction zones. The foundering lithosphere is replaced by ascending hot mantle in a manner similar to back-arc spreading on Earth.

As an approximate model for episodic subduction on Venus, we assume that the global lithosphere thickens conductively for 500 Myr; basal heating of the lithosphere is neglected. The corresponding thickness of the subducted lithosphere from (4.2.5) is $y_L = 290 \text{ km}$. The mean heat loss due to the global subduction of this lithosphere is, from (14.2.2), $Q_S = 1.23 \times 10^{13} \text{ W}$. This is only 42% of the total required heat flux ($2.91 \times 10^{13} \text{ W}$) during the time interval. The 58% deficit must be made up during a period of active volcanism and tectonics. While the global lithosphere is stable, the only cooling to the interior is due to the heating of the previously subducted lithosphere. This heating is likely to be spread over several hundred million years. From the results given in Figure 14.7, the net increase in temperature of the mantle during the 500 Myr of stable lithosphere is estimated to be about

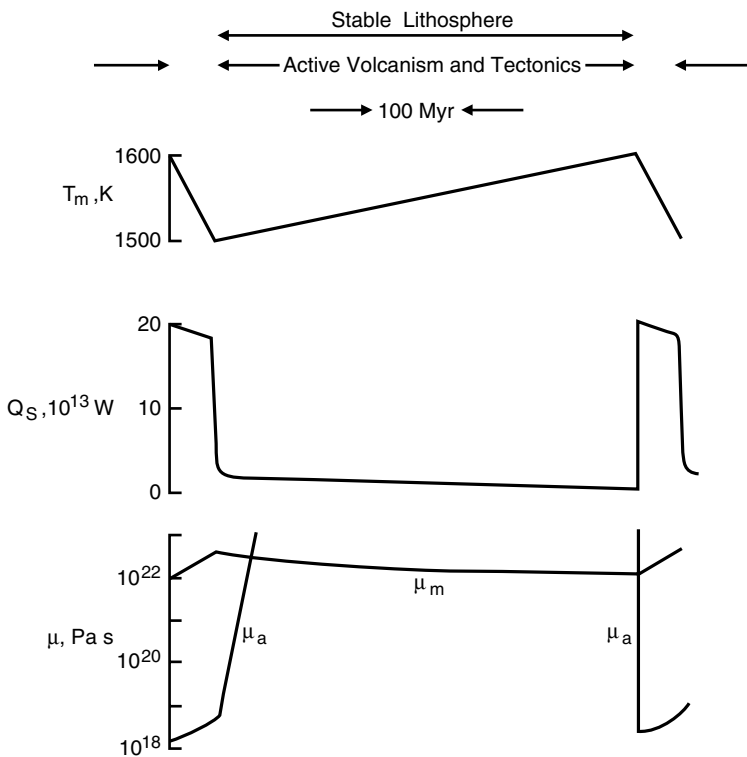


Figure 14.9. Schematic representation of a cycle of episodic subduction on Venus. The upper mantle temperature T_m , total surface heat loss Q_S , and viscosities of the asthenosphere μ_a and upper mantle μ_m are shown.

60 K; the corresponding decrease in mantle viscosity is about a factor of 5. This model is illustrated in Figure 14.9.

We assume that the period of rapid plate tectonics lasts for 50 Myr. In order to make up the deficit in heat loss during the period of lithospheric stability, the mean loss of heat is $Q = 20 \times 10^{13}$ W. From (4.2.6), this corresponds to an age of subduction of $t = 1.9$ Myr. From (4.2.5) the corresponding thickness of the subducted lithosphere is $y_L = 18$ km.

The final model for Venus is a differentiated planet (Kaula, 1994a, b). In this model the heat-producing elements have been fractionated into the crust and the resulting heat is lost to the surface by heat conduction. Prior to the general acceptance of plate tectonics and mantle convection, it was widely believed that virtually all the heat-producing elements in the Earth were concentrated in the continental crust. This upward concentration was required because conductive processes could not get the heat out of the mantle without melting it.

Proponents of this model argue that the lack of water on Venus will greatly increase the rock viscosities at a given temperature. Experimental verification of this, in terms of its application to Venus, has been given by Mackwell et al. (1998).

In order to quantify this model, we must consider the constraints on the concentrations of the heat-producing elements both in the mantle of Venus and in its crust. Overall concentrations of uranium, thorium, and potassium in Venus are estimated from terrestrial values. Values for the crust of Venus are obtained directly from data collected by the Vega and Venera landers. Estimates of the concentrations of the heat-producing elements and rates of heat

generation for the Earth are given in Table 14.3 for Urey numbers $Ur = 0.8$ and 0.6 . The values of mean heat generation for the bulk silicate Earth range from $H = 7 \times 10^{-12}$ to $5.2 \times 10^{-12} \text{ W kg}^{-1}$. Mean values for the chondritic meteorites are also given in Table 14.3. It is seen that the Earth is enriched in the refractory elements U and Th relative to the volatile element K. In the absence of other constraints, we assume that the range of concentrations associated with the Earth is also applicable to Venus.

Mid-ocean ridge basalts (MORBs) are interpreted as direct melt products of the Earth's mantle. However, the upper mantle is certainly depleted in incompatible elements relative to the bulk silicate Earth due to the concentration of these elements in the continental crust. Sun and McDonough (1989) argue that N-type or normal MORB represents the melting of this depleted source region; as evidence they give the consistent depletion of the light rare earth elements in those rocks relative to chondrites. On the other hand, they point out that E-type or enriched MORB approaches chondritic rare Earth distributions and may represent the partial melting of a source region that has near bulk Earth concentrations. Some 90% of the mid-ocean ridge basalts are N-type MORB while E-type MORB is generally associated with basalts from near-ridge hot spots such as Iceland and the Azores. The concentrations of the heat-producing elements in E-type MORB, given in Table 14.3, are about 7 times the estimated bulk Earth values, leading to a reasonable 12% basaltic component in the undepleted mantle with complete transfer of incompatible elements to the liquid fraction. Also given in Table 14.3 are typical concentrations of heat-producing elements in ocean island basalts (OIBs). Clearly these basalts have enriched concentrations of the incompatible elements.

The concentrations of heat-producing elements and heat production rates for five landing sites on Venus (Vega 1, 2, Venera 8, 9, 10) are given in Table 14.3 (Surkov et al., 1987). Potassium values are given for two additional sites. Venera 8 and 13 sampled upland plains with weekly differentiated melanocratic alkaline gabbrooids with high potassium content. Venera 14 sampled a lowland area covered with tholeiitic basaltic tuff with a low potassium content. Young shield structures were sampled by Venera 9 and 10 with lavas close in composition to tholeiitic basalts but with a calc-alkaline trend.

The Venus data are certainly less reliable than the laboratory studies of terrestrial and lunar rocks. However, the results are generally consistent with values expected for basic rocks. Five landers gave values that can be associated with moderately radiogenic basaltic rocks, 2–3 times higher than the E-type MORB, but lower than typical OIB. Two landers gave values more typical of silicic rocks on the Earth. In terms of modeling, an essential question is whether these surface values are typical of crustal values at depth. Certainly, fractionation and crystallization are likely to lead to an upward concentration of the incompatible heat-producing elements. In the continents of the Earth, the concentrations of the heat-producing elements decay exponentially with depth on a scale of 10 km. But it is impossible to estimate such variations in the crust of Venus.

As a limiting case we assume that all the heat-producing elements in Venus are concentrated uniformly in a crust of thickness y_c . Secular cooling is also neglected so that the heat flow to the base of the crust is taken to be zero. In this limit the temperature distribution in the crust is (Turcotte and Schubert, 1982, p. 145)

$$T = T_s + (T_m - T_s) \left(\frac{y}{y_c} \right) \left(2 - \frac{y}{y_c} \right) \quad (14.2.5)$$

where y is the depth below the surface ($y = 0$), T_s is the surface temperature, and T_m is the uniform temperature of the mantle. In addition, we require a balance between surface heat

Table 14.3. Concentrations of Heat-producing Elements and Rates of Heat Generation H for a Variety of Planetary Basalts and Source Rocks

		Uranium U (ppm)	Thorium Th (ppm)	Potassium K (ppm)	K/U	Th/U	Heat Production H ($10^{-12} \text{ W kg}^{-1}$)	
Chondrite [1]		0.008	0.029	545	3.6	68,000	3.5	
Bulk silicate Earth	Ur = 0.8 [2]	0.029	0.116	290	4.0	10,000	7	
	Ur = 0.6 [1]	0.021	0.085	250	4.0	11,900	5.2	
Basalts								
Earth	N-type MORB [1]	0.047	0.12	600	2.6	12,800	10	
	E-type MORB [1]	0.18	0.60	2,100	3.3	11,700	41	
	OIB [1]	1.02	4.20	12,000	4.1	11,800	255	
	Low-Ti olivine	12002 [3]	0.22	415	3.4	1,900	43	
Moon	15545 [3]	0.13	0.43	330	3.3	2,500	25	
	12064 [3]	0.22	0.84	580	3.8	2,600	46	
	Low-Ti pigeonite	15597 [3]	0.1	500	3.8	3,600	30	
	70215 [3]	0.13	0.34	415	2.6	3,200	23	
	High-Ti low-K	10049 [3]	0.81	4,03	3,000	5.0	3,700	197
	High-Ti high-K							
	Low-Ti aluminous	14035 [3]	0.59	2.1	830	3.6	1,400	117
Venus	Vega 1 [4]	0.64	1.5	4,500	2.3	7,000	118	
	Vega 2 [4]	0.68	2.0	4,000	2.9	5,900	134	
	Venera 8 [4]	2.2	6.5	40,000	3.0	18,000	531	
	Venera 9 [4]	0.60	3.65	4,700	6.1	7,800	172	
	Venera 10 [4]	0.46	0.70	3,000	1.5	6,500	74	
	Venera 13 [5]	—	—	33,000	—	—	—	
	Venera 14 [5]	—	—	1,700	—	—	—	

[1] Sun and McDonough (1989), [2] Turcotte and Schubert (1982), [3] Heiken et al. (1991), pp. 261–3, [4] Surkov et al. (1987), [5] Surkov et al. (1984).

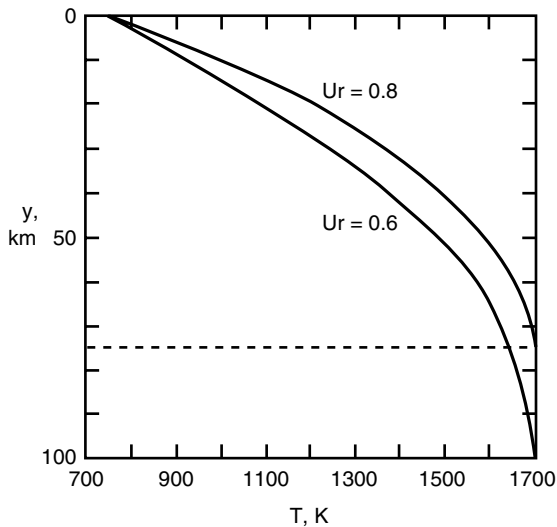


Figure 14.10. Depth profiles of temperature through a thick Venusian crust with a uniform concentration of heat-producing elements and zero mantle heat flow. For Urey number $Ur = 0.8$ the crust is 75 km thick (dashed horizontal line) while for $Ur = 0.6$ the crustal thickness is 100 km.

flow q_S and crustal radiogenic heat production

$$q_S = \rho_c H_c y_c \quad (14.2.6)$$

and use Fourier's law of heat conduction to relate q_S to $T_m - T_s$

$$T_m - T_s = \frac{1}{2} q_S \frac{y_c}{k_c} \quad (14.2.7)$$

where H_c is the rate of heat production per unit mass in the crust, ρ_c is the density of the crust, and k_c is the crustal thermal conductivity.

For a steady-state heat balance and $Ur = 0.8$, surface heat flow is $q_S = 50 \text{ mW m}^{-2}$; with $Ur = 0.6$, q_S is 38 mW m^{-2} . We also take $T_s = 750 \text{ K}$, $k_c = 2 \text{ W m}^{-1} \text{ K}^{-1}$, and $\rho_c = 2,900 \text{ kg m}^{-3}$. If the crust is thick, the temperature within it will exceed its liquidus (assumed to be undesirable). If the crust is thin, the heat production H_c will be large (exceeding the observed values). Solutions for the crustal temperature profile in the two cases in which the basal temperature approaches the liquidus ($T_m \approx 1,700 \text{ K}$) are given in Figure 14.10. For $Ur = 0.8$ we have $y_c = 75 \text{ km}$ and $H_c = 230 \times 10^{-12} \text{ W kg}^{-1}$, and for $Ur = 0.6$ we have $y_c = 100 \text{ km}$ and $H_c = 130 \times 10^{-12} \text{ W kg}^{-1}$. A comparison of these rates of heat generation with the Venusian values given in Table 14.3 shows that the values for $Ur = 0.6$ are generally consistent with the inferred heat production rates on Venus.

Thus, it is possible to construct a model for the upward concentration of the heat-producing elements that has a mantle temperature below the solidus and rates of heat generation compatible with the surface observations. However, this does require extreme assumptions: (1) almost complete transfer of the heat-producing elements to the crust, (2) negligible secular cooling of Venus, and (3) uniform concentrations of the heat-producing elements through the crust.

Presumably, if this model were valid, the crust of Venus would have thickened with time with little crustal recycling. Expected consequences of this process would include the systematic depletion of the mantle heat-producing elements with time; this should lead to a reduction in the content of the heat-producing elements in the most recent volcanics and

a gradual decay of volcanism with time. A valid question would be whether this type of decay could be consistent with the crater counts.

Any model for the evolution of Venus must satisfy the constraints of the global resurfacing event and still be able to extract the required heat from the interior of the planet. Although each of the three models given above can be considered plausible, the weight of the evidence favors a strongly time-dependent “catastrophic” evolution of the planet.

Question 14.10: Has the thermal evolution of Venus involved catastrophic events?

14.2.3 Venusian Highlands and Terrestrial Continents

An important product of the Magellan mission is the data it provided for comparing the tectonic and volcanic evolution of Venus and the Earth (Turcotte, 1996). One of the major features of the Earth is continents. The continents are older than the oceans because continental crust is not systematically subducted like oceanic crust; this is clearly illustrated in Figure 14.1. The continental crust is significantly thicker than the oceanic crust (40 km versus 6 km) and is significantly lighter (a density of $2,600 \text{ kg m}^{-3}$ versus $2,900 \text{ kg m}^{-3}$). The difference in density is due to the more silicic composition of the continental crust. The distinction between oceanic and continental crust on the Earth is clear, but do the other planetary bodies have “continents?”

Some highland regions on Venus may have continental affinities. Ishtar Terra (Kaula et al., 1997) is a primary candidate; other possibilities include the plateau highlands Alpha, Tellus, and Ovda Regiones (Grimm, 1994a; Moore and Schubert, 1997b). The boundaries of Ishtar Terra resemble continental margins and its high elevations are most easily attributed to a silicic composition. However, there is no evidence of an Earth-like bimodal hypsometry for Venus.

The origin of the continents on Earth remains somewhat controversial, but a hypothesis that is widely accepted is a two-stage origin (Section 2.7.3). Granite and granidioritic rocks typical of the continental crust are found in the volcanic lines associated with subduction zones if the subduction zone magmas pass through pre-existing continental crust as in the Andes. The volcanics associated with island arcs in an oceanic setting, however, have a near-basaltic composition as in the Aleutians. Thus, it is concluded that silicic continental rocks are not produced directly from the mantle in an island arc setting. The magmas from the mantle underplate and melt the continental crust; the resulting intracrustal differentiation creates a silicic upper crust and a more mafic lower crust. The lower crust is then recycled into the mantle by the delamination process, creating a more silicic bulk crust (Kay and Kay, 1988, 1993).

Intracrustal differentiation appears to play an essential role in the formation of the silicic continental crust. Campbell and Taylor (1983) published a paper entitled “No water, no granites, –no ocean, no continents.” They argue that the absence of water on Venus precluded the formation of extensive continental crust. They further pointed out that the conditions on Venus throughout its evolution resembled the conditions on the early Earth. Thus Ishtar Terra and Aphrodite Terra could contain some felsic igneous rocks resembling terrestrial Archean continental nuclei (Jull and Arkani-Hamed, 1995).

Question 14.11: What is the composition of the rocks in the plateau highlands of Venus?

The Earth is certainly the only planetary body that currently has plate tectonics. Also, with the possible exception of Mars (discussed later), there is no direct evidence that any of the other bodies have had plate tectonics in the past. It has long been recognized that plate tectonics cannot evolve in time without internal deformation of the plates (Dewey, 1975). It is certainly possible to create a configuration of ocean ridges, subduction zones, and transform faults that is compatible with rigid plates. However, as the plate tectonic process evolves in time both gaps between plates and overlaps of plates will develop.

On the Earth this problem of incompatibility is overcome by internal plate deformation. Much of this deformation occurs in the continents, but some occurs on accretional plate boundaries where ridge jumps occur and new plate geometries evolve. Changes in plate geometry can also be partially accommodated by new subduction zones. However, the bulk of the deformation associated with the geometrical incompatibilities of plate evolution is accommodated within broad zones of deformation in the continents adjacent to recognized plate boundaries. One example is the western United States. Although the San Andreas fault is the primary boundary between the Pacific and North American plates, extensive intraplate deformation takes place throughout the western United States. Other examples include southern Europe, much of the Middle East, and throughout China. Very little deformation occurs within the interiors of oceanic plates.

It appears reasonable to conclude that plate tectonics could not occur on Venus because there are no large continents to absorb the necessary deformation. Thus no water leads to no granites, no granites lead to no continents, and no continents lead to no plate tectonics.

Question 14.12: Why is there no plate tectonics on Venus?

14.2.4 Models of Convection in Venus

A few numerical studies of global-scale mantle convection have specifically addressed Venus. Three-dimensional spherical models were presented by Schubert et al. (1990), who showed that a rigid upper boundary (representing the base of Venus' lithosphere) decreases the temporal durability of downwellings compared to a free-slip boundary condition (representing an average boundary condition for the Earth, where the plates are free to move). The internal temperature is also higher when a rigid lid is present. Similar models in two-dimensional spherical axisymmetric geometry were presented by Leitch and Yuen (1991) and Leitch et al. (1992), who found that a rigid lid can decrease the width of convective cells in the upper mantle. Neither of these models includes the effects of an endothermic phase transition in the mantle of Venus.

A two-dimensional Cartesian model of phase-change-modulated convection in Venus (Steinbach and Yuen, 1992) found that the exothermic phase transition expected to occur at around 440 km depth in Venus increases the degree of layering; however, the greater depth of phase transitions in the Venus model compared with the Earth and the presence of a rigid conductive lid in the Venus model decrease the degree of layering. Steinbach and Yuen (1992)

also suggested that a global transition from whole mantle to layered convection might be responsible for the global resurfacing event 500 Myr ago on Venus.

Schubert et al. (1997) computed models of three-dimensional, phase-change-modulated convection in Venus' mantle. The model includes both an exothermic phase change at a depth of 440 km (410 km depth in the Earth) and an endothermic phase change at a depth of 740 km (660 km depth in the Earth); the Clapeyron slope of the exothermic phase change was 3 MPa K^{-1} and that of the endothermic phase change was -4 MPa K^{-1} . The computational domain was a spherical shell with isothermal boundaries; the inner boundary was free-slip and the outer boundary was rigid. The model was compressible, anelastic and self-gravitating, and thermodynamic and rheological properties varied with hydrostatic pressure or depth; parameter values and variations of properties with hydrostatic pressure were similar to those in the Earth's mantle. In particular, viscosity had a power-law dependence on density and increased by a factor of 17 over the depth of the model mantle. Heating was both from within and from below at realistic rates for Venus; the thermal forcing was described by volume-averaged Rayleigh numbers for internal heating Ra_H and superadiabaticity Ra_T . Results were presented for two cases. Case 1 had a rigid upper boundary and case 2 a free-slip upper boundary. For case 1, Ra_H was 1.4×10^8 and Ra_T was 4.8×10^6 ; for case 2, Ra_H was 7×10^7 and Ra_T was 2.4×10^6 .

These Venus mantle convection models have heat fluxes in the range $50\text{--}60 \text{ mW m}^{-2}$, with approximately 30% of the heat coming from the core and 70% from internal heating by radioactive decay. The heat flux is slightly lower than that of the Earth and may be realistic for Venus as discussed above. Maximum velocities are around 25 mm yr^{-1} , with values of 50 mm yr^{-1} being reached in the upper mantle of the free-slip boundary case 2.

Typical convective states in the two cases are illustrated in Figure 14.11, which shows hot and cold residual temperature anomalies corresponding to upwellings and downwellings, respectively (residual temperatures are the temperature differences from the horizontally averaged temperature at a particular radius). The broad-scale structure of convection is similar to that observed in three-dimensional spherical models of phase-change-modulated convection in the Earth's mantle (Tackley et al., 1993). The upper mantle contains a network of interconnected downwelling sheets, which do not initially penetrate the endothermic phase transition, but are deflected, resulting in pools of cold material in the transition zone (left panels in Figure 14.11). These pools build up until sufficient negative buoyancy has accumulated to overcome the buoyancy associated with phase change deflection, at which point cold material falls catastrophically into the lower mantle in the form of broad cylindrical avalanches, which empty the local transition zone contents into broad cold pools at the base of the mantle. Avalanches at different places around the sphere overlap in time, so that the system is never completely layered or completely whole mantle on a global scale.

Comparison of these simulations to previous three-dimensional spherical Venus calculations (Schubert et al., 1990) shows that the characteristic horizontal wavelengths are significantly larger than observed when no phase transitions are present. Particularly surprising in these results is that the rigid boundary case 1 (upper panels in Figure 14.11) displays greater wavelengths of flow than the free-slip boundary case 2 (lower panels in Figure 14.11). This is opposite to previous calculations with no phase changes, in which a rigid upper boundary tends to induce shorter wavelengths of flow, with more closely spaced features (Schubert et al., 1990). It also appears that the rigid boundary case is more layered.

Hot upwellings illustrated in the right panels of Figure 14.11 display less clear structure than the cold downwellings. Near the core–mantle boundary, hot ridges are observed, separating the pools of cold material deposited by various avalanches. A few hot plumes penetrate

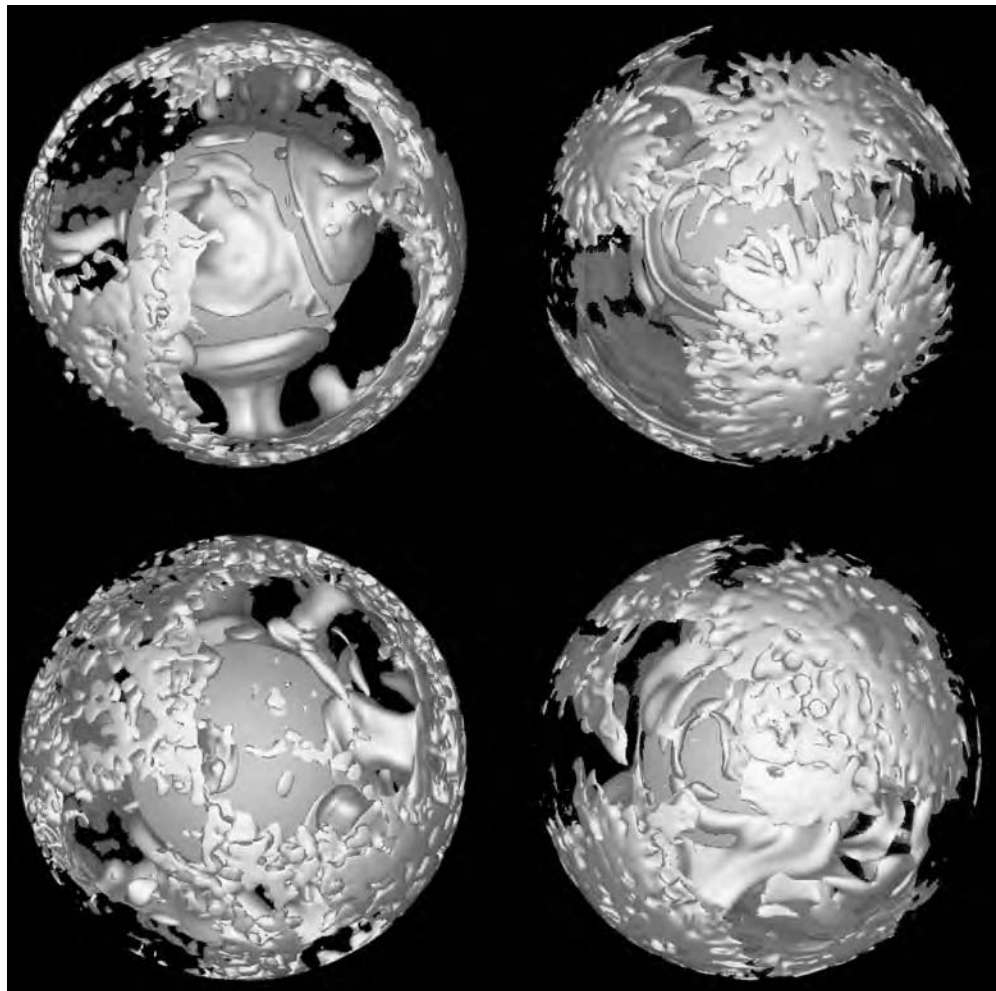


Figure 14.11. Cold downwellings (left) and hot upwellings (right) in the two spherical convection models of Venusian mantle convection. Illustrated are isosurfaces of residual temperature (temperature difference from the horizontally averaged geotherm), showing where the temperature is 110K lower (left) or 110K higher (right) than the geotherm. The upper plots show case 1, with the rigid upper surface; the lower plots show case 2, with the free-slip upper surface. Convection in these models is time dependent; the time step shown is typical of the convective state. After Schubert et al. (1997).

For a color version of this figure, see plate section.

the mid-mantle region and easily penetrate into the upper mantle. The upper mantle displays considerable long-wavelength hot structure.

Three distinct regions of the mantle can thus be identified on the basis of their thermal structure: (1) the upper mantle, containing downwelling sheets and pools of cold material in the transition zone, (2) the mid-mantle, between 740 and $\sim 2,000$ km depth, containing upwelling and broad downwelling plumes, and (3) the deep mantle, containing large pools of cold material above the core–mantle boundary separated by ridges of hot material.

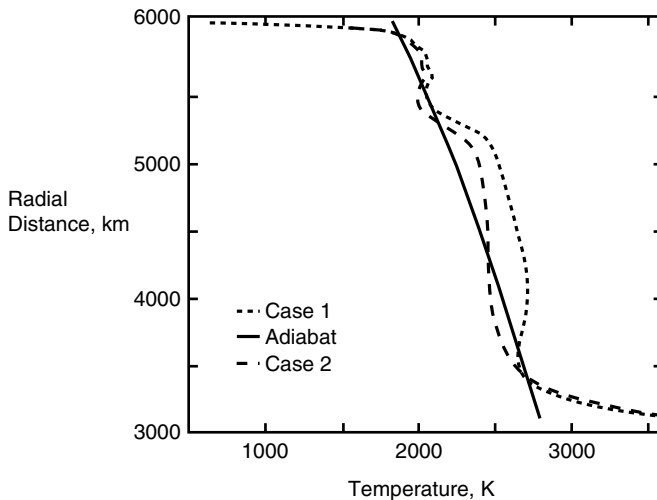


Figure 14.12. Horizontally averaged radial temperature profiles for cases 1 and 2 in Figure 14.8 and the reference state adiabat. The temperature profile is generally subadiabatic, with boundary layers visible at the surface, at the lower boundary and at 740 km depth, the location of the endothermic phase transition.

Radial profiles of horizontally averaged temperature are plotted for the two cases in Figure 14.12, which also shows the reference state adiabat. In addition to the expected thermal boundary layers at the top and bottom of the mantle, another thermal boundary layer around the endothermic phase transition is clearly visible due to the partial layering of the flow by this phase transition. This temperature drop is larger for case 1 (rigid upper boundary), implying a greater degree of layering in this case, and is around 300–400 K, compared to $\sim 1,300$ K for the upper boundary layer and ~ 900 –1,000 K for the lower boundary layer.

Away from these boundary layers the temperature profile is generally subadiabatic, i.e., the temperature increase with depth is less than that displayed by an adiabat. This may seem surprising since it is commonly assumed that the interior of a convecting mantle is adiabatic; however, this assumption is only true for systems which are predominantly heated from below – subadiabatic temperature stratification is a fundamental property of convection for systems which are heated predominantly from within (Schubert et al., 1993; Parmentier et al., 1994; Travis and Olson, 1994).

In addition to the general subadiabaticity, a temperature minimum is displayed in the deep mantle, just above the lower thermal boundary layer. This feature, which is particularly pronounced in case 1 (rigid upper boundary), is caused by the pooling of cold avalanche material at this depth. Another feature is a temperature high in the mid-mantle, just below the endothermic phase transition. This reduces the temperature anomaly of upwelling plumes relative to the deep mantle, making it more difficult for them to penetrate into the upper mantle. Overall, departures from adiabaticity of up to 300 K, i.e., around 10% of the total temperature drop, are observed in the interior of the mantle.

A useful measure of the degree of flow stratification is the normalized radial mass flux $F(r)$ (Peltier and Solheim, 1992), defined as the radial mass flux through a spherical surface at radius r , normalized so that the integral over nondimensional depth is equal to unity. Radial profiles of $F(r)$ for the two cases, averaged over a simulated period of several hundred million years, are illustrated in Figure 14.13. The important feature here is the minimum in

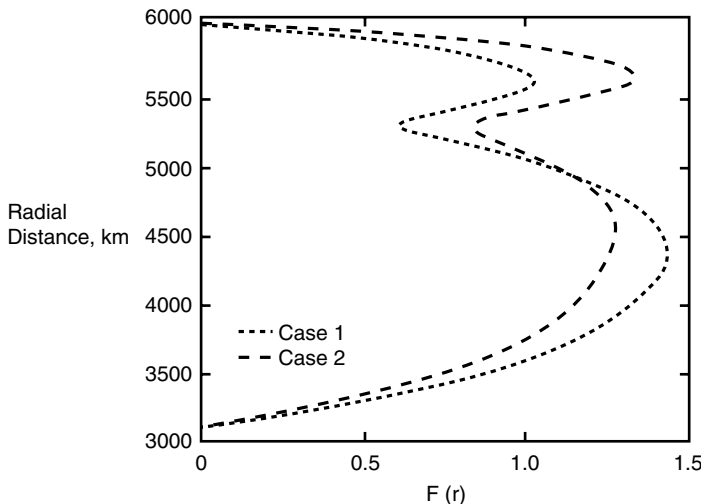


Figure 14.13. Normalized radial mass flux $F(r)$ for the two cases of Figure 14.8 averaged over a time of several hundred million years.

radial mass flux at 740 km depth caused by the inhibiting effect of the endothermic phase transition on radial flow. Although the curves in Figure 14.13 are averaged over a long period of time, they do not change much with time because of the weakness of global episodicity, even though strong episodicity may be exhibited in local regions (Tackley et al., 1994).

Comparison of the two cases in Figure 14.13 shows that the degree of layering is greater with a rigid upper boundary (case 1) than with a free-slip upper boundary (case 2). Both the flow in the upper mantle and the flow through the phase boundary are more restricted in the presence of a rigid upper boundary than a free-slip upper boundary. This confirms the impression from visual examination of the temperature field (Figure 14.11) and horizontally averaged temperature profiles (Figure 14.12) that the degree of layering is greater in case 1. If case 1 can be taken to be more representative of Venus, and case 2 more representative of the Earth, Venus' mantle may currently exhibit a greater degree of flow stratification than the Earth's mantle.

14.2.5 Topography and the Geoid: Constraints on Convection Models

The long-wavelength gravity field (Figure 14.6) and topography (Figure 14.5) are perhaps the most important surface manifestations of Venusian mantle convection, offering strong, albeit ambiguous, constraints on the physical properties and dynamics of the mantle and lithosphere. On Venus (unlike the Earth) a strong positive correlation between geoid and topography is observed, admittance ratios are high, and inferred depths of compensation are large. As discussed above, large compensation depths can be taken to represent the thickness of the lithosphere. Such an interpretation leads to estimates for the thickness of Venus' lithosphere (200–300 km) much larger than expected for quasi-steady-state convection with a similar heat flux to that of the Earth (Turcotte, 1993). The convection solutions discussed here allow us to evaluate whether compensation by deep dynamic heterogeneities that arise in a self-consistent, time-dependent, dynamically convecting system with reasonable heat

flux can provide an alternative explanation for the large admittance ratios (Kiefer and Hager, 1992; McKenzie, 1994).

The geoid, topography, and admittance ratios for the two models and Venus data are plotted in Figure 14.14. The graphs show total amplitude for each spherical harmonic degree, not the rms amplitude of the coefficient as plotted in some other papers (Konopliv et al., 1993). The Venus data are a degree 75 version of the gravity model by Konopliv and Sjogren (1994) and the degree 360 topography model of Rappaport and Plaut (1994). Admittance ratios are calculated using the usual assumption that the total gravity for each spherical harmonic is given by correlated and uncorrelated components (Kiefer et al., 1986; Simons et al., 1994, 1997):

$$G_{lm} = F_l T_{lm} + I_{lm} \quad (14.2.8)$$

where G_{lm} and T_{lm} are spherical harmonic coefficients of the geoid and topography, respectively, I_{lm} is the part of the geoid that is not correlated with topography, F_l is the admittance ratio for each degree, and there is no summation over l in the term $F_l T_{lm}$. The admittance ratio can be simply determined by

$$F_l = \text{Re} \left(\frac{\sigma_{gt}^2}{\sigma_{tt}^2} \right) \quad (14.2.9)$$

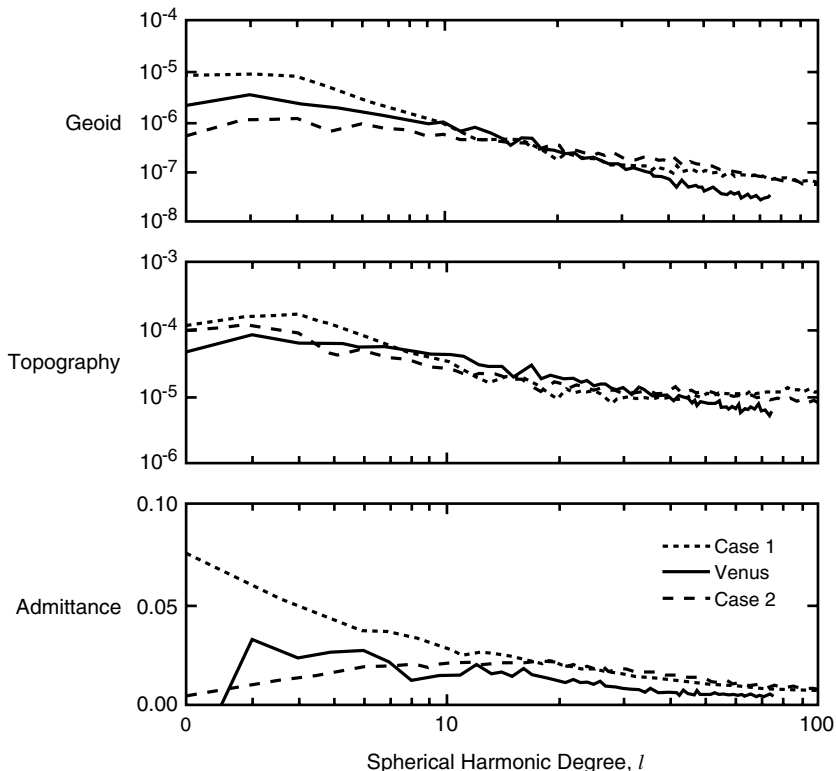


Figure 14.14. Frequency spectrum of geoid, topography, and admittance ratios for the two cases of Figure 14.8 plotted against Venus data. Geoid and topography are normalized by planetary radius and plotted as total amplitude for each spherical harmonic degree. The calculation of admittance ratios is described in the text.

where Re indicates the real part, σ_{gt} is the cross-covariance of geoid and topography, and σ_{tt} is the covariance of topography. The calculated admittance ratios are significantly different from those calculated using the earlier Pioneer Venus data set (Kiefer et al., 1986), although the overall magnitude and trend are similar.

For the geoid and topography, the two simulations appear to straddle the Venus data for the long wavelengths (spherical harmonic degrees less than about $l = 30\text{--}40$) at which these quantities are accurately known (Konopliv et al., 1993). The upper rigid boundary case 1 exhibits greater geoid and topography than the upper free-slip boundary case 2, probably because of the stronger coupling between convection and the surface. The admittance ratios straddle the Venus data for spherical harmonics less than $l = 7$ (except for $l = 2$ which is poorly determined), but are higher than Venus data, by around a factor of 2, for larger spherical harmonic degrees.

These results show that realistically large geoid, dynamic topography, and admittance ratios can be obtained on a global scale in a fully dynamical calculation even with a high heat flux thought to be appropriate to a steady-state Venus model. The upper boundary layer thickness, which would correspond to the thermal lithosphere thickness if temperature-dependent viscosity were included in the model, can be seen from the temperature profiles to be less than $\sim 90\text{ km}$, much smaller than the thickness required if admittance ratios are explained entirely by variations in lithospheric thickness. Thus, deeper mass anomalies associated with thermal convection in the interior are also important in determining large-scale geoid and topography. Since a rigid upper boundary condition gives a geoid signal which is too large, the results imply that the most appropriate upper boundary condition for Venus lies between the extremes of rigid and free slip.

Even though the calculations discussed above show that high admittance ratios are possible for the large scale of a convective model of Venus' mantle with a terrestrial-like complement of radiogenic heat sources and a relatively thin lithosphere ($\lesssim 100\text{ km}$ thick), the inference of a much thicker lithosphere (200–300 km) on Venus rests not only on large-scale admittance ratios but on the gravity and topography of many individual features of smaller scale (e.g., volcanic highlands, coronae, chasmata segments) and the deformation or lack thereof of small-scale structures (e.g., craters and flexural outer rises). Thus, a thick Venus lithosphere remains a viable interpretation of a large amount of data on the planet's gravity, topography, and geology.

Question 14.13: Do the large-scale geoid, topography, and admittance ratios on Venus imply a thick lithosphere or a convecting mantle beneath a thin lithosphere?

Because of the stronger tendency for phase-change-induced layering in Venus' mantle as compared with the Earth's mantle exhibited by the above calculations, mantle overturn due to an avalanche of global scale is a credible explanation for the resurfacing event on Venus some 500 Myr ago. Although such a globally synchronous transition has not been observed in the fully three-dimensional spherical calculations described above, these computations do not include the secular cooling of the planet which may enforce a globally synchronous transition from layered to whole-mantle convection (Steinbach et al., 1993; Steinbach and Yuen, 1994b).

14.2.6 Convection Models with a Sluggish or Stagnant Lid

The solutions discussed above do not take into account the strong dependence of the viscosity of mantle material on temperature, an effect likely to have a major influence on the style of convection. When temperature-dependent viscosity is included in models, a rigid lithosphere arises naturally due to the very high viscosity in the upper boundary layer, provided the viscosity contrast is sufficiently large. Indeed, simple temperature-dependent viscosity models may resemble Venus much better than they resemble the Earth (Ratcliff et al., 1995), where highly complex rheological behavior is required in order to describe the brittle failure (Moresi and Solomatov, 1998) and ductile localization (Bercovici, 1993, 1995b, 1996; Tackley, 1998a) processes that cause plate boundaries.

Here we discuss two sets of calculations in Cartesian geometry: one illustrates the effect of systematically increasing the viscosity contrast up to a factor of 10^5 , the other illustrates the interaction of variable viscosity flow with mantle phase transitions (Tackley, 1993, 1996b). We also discuss results of three-dimensional variable viscosity convection in a spherical shell with a viscosity contrast up to a factor of 10^4 (Ratcliff et al., 1995, 1997).

Figure 14.15 shows the effect that viscosity variation has on the form of convection. The results are from calculations in an $8 \times 8 \times 1$ rectangular box with periodic side boundaries and free-slip, isothermal top and bottom boundaries. Heating is from below and viscosity depends strongly on temperature according to an Arrhenius law. In these calculations the Rayleigh number based on the viscosity at the mean of the top and bottom boundary temperatures is 10^5 . The viscosity contrasts are 1, 10^1 , 10^2 , 10^3 , 10^4 , and 10^5 in Figures 14.15a–f, respectively. Three convective regimes are clearly visible: (i) the small viscosity contrast regime at viscosity contrasts of 1– 10^1 , characterized by a fairly symmetrical spoke pattern of upwelling and downwelling sheets which break up into plumes as they ascend or descend Figures 14.15a and b; (ii) the sluggish-lid regime at intermediate viscosity contrasts of 10^2 – 10^3 , characterized by a very long wavelength flow pattern consisting of a huge cylindrical downwelling plume surrounded by narrow upwelling sheets under a slowly deforming lithosphere (Figures 14.15c and d); and (iii) the stagnant-lid regime at large viscosity contrasts of 10^4 – 10^5 , characterized by a very small wavelength pattern of upwelling plumes and downwelling sheets under an immobile stagnant lid (Figures 14.15e and f).

With increasing viscosity contrast, Nusselt number (heat flux in units of the heat flux that would be conducted in the absence of convection) progressively decreased from 8.8 for the constant viscosity case to 4.8 for the case with a viscosity contrast of 10^5 . Velocities, however, increased significantly with increasing viscosity contrast; rms velocity (nondimensionalized to the conductive velocity κ/D , where κ is the thermal diffusivity and D is the height of the box) increased from 197 to 293, and peak velocity increased from 763 to 1813. As the viscosity contrast is increased, convection below the lithosphere becomes more vigorous but with smaller temperature contrasts, so that heat flux decreases and velocity increases.

These two fundamental transitions in convective style have been discussed from a theoretical perspective by Solomatov (1995) and identified numerically in two-dimensional, small-domain experiments (Christensen, 1984a; Moresi and Solomatov, 1995) on the basis of changes in the Nusselt number–Rayleigh number relationship. The transition to the stagnant-lid convection regime was also identified in the three-dimensional simulations of Ogawa et al. (1991) on the basis of the velocity distribution, but the small aspect ratio of their computational domain precluded the change in preferred convective planform from occurring.

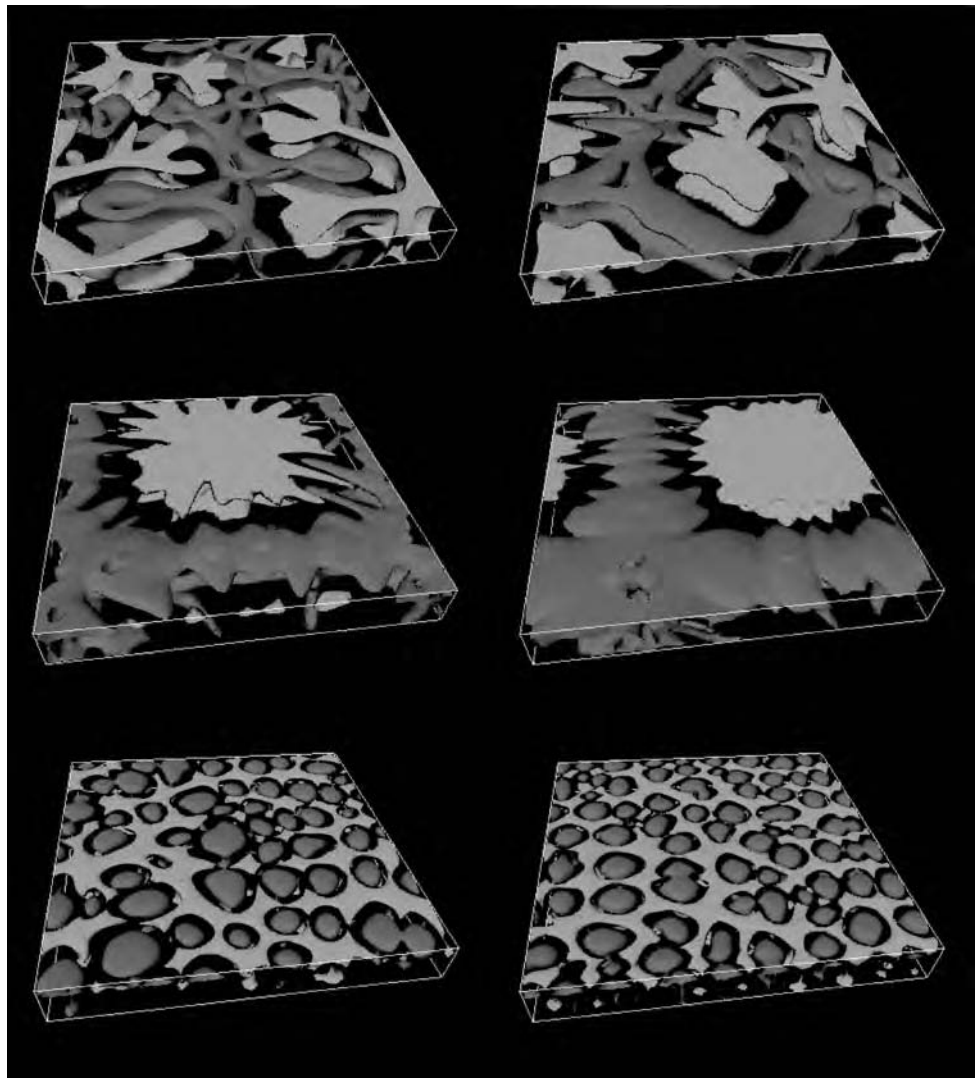


Figure 14.15. A series of Boussinesq calculations in an $8 \times 8 \times 1$ Cartesian box with fixed Rayleigh number based on the viscosity at the mean of the top and bottom boundary temperatures of 10^5 and increasing viscosity contrast. Figures show isosurfaces of residual temperature ΔT , i.e., temperature relative to a horizontally averaged temperature profile, with green (dark) surfaces representing cold (downwelling) material and red (light) surfaces representing hot (upwelling) material. (a) Constant viscosity, surfaces show $\Delta T = \pm 0.1$; (b) $\Delta\eta = 10$, $\Delta T = \pm 0.1$; (c) $\Delta\eta = 100$, $\Delta T = \pm 0.1$; (d) $\Delta\eta = 1,000$, $\Delta T = \pm 0.1$; (e) $\Delta\eta = 10^4$, $\Delta T = \pm 0.075$; and (f) $\Delta\eta = 10^5$, $\Delta T = \pm 0.05$.

For a color version of this figure, see plate section.

The transition from the small viscosity contrast mode of convection to the sluggish-lid mode of convection and the transition from sluggish-lid to stagnant-lid convection have also been found to occur in a numerical model of three-dimensional convection in a spherical shell (Ratcliff et al., 1995, 1996b, 1997). In this model the upper and lower boundaries are

isothermal and free-slip and heating is from below. The Boussinesq approximation is made and the viscosity depends exponentially on temperature according to a linearized Arrhenius law. The Rayleigh number based on the mean of the top and bottom boundary temperatures is 10^5 and the viscosity varies by up to 10^4 . The parameters for the spherical shell model are essentially the same as for the Cartesian model discussed above.

Figure 14.16 compares the spherical shell convection patterns for constant viscosity convection (also at a Rayleigh number of 10^5) and variable viscosity convection. The different convection patterns for the constant viscosity and variable viscosity cases show the transition from the small viscosity contrast regime of convection to the sluggish-lid mode of convection and from the sluggish-lid mode of convection to the stagnant-lid convection mode. In the isoviscous case, illustrative of the small viscosity contrast convection regime, flow is dominated by arcuate downwelling sheets and plume-like upflow. In the sluggish-lid mode of convection that occurs for a viscosity ratio of 10^3 , downwelling occurs as two large quasi-cylindrical structures at the poles. Finger-like spokes radiate asymmetrically from these features, reminiscent of the “spider planform” observed in the experimental work of Weinstein and Christensen (1991). Upwellings take the form of a nearly linear chain of partially connected plumes which encircle the equator. The flow pattern has a dominant degree 2 spherical harmonic signature and the dominant wavelengths of the flow are increased dramatically compared with the isoviscous case. In the stagnant-lid mode of convection that occurs for a viscosity ratio of 10^4 , upwelling flow is dominated by numerous, small-scale cylindrical plumes and downwelling flow occurs as an interconnected network of short, sheet-like features. The predominant flow wavelengths in the stagnant-lid convection mode are markedly reduced from the wavelengths of the sluggish-lid convection mode (the stagnant-lid mode of convection is dominated by spherical harmonic degrees $l = 6-8$). Comparison of the horizontally averaged profiles of temperature, velocity, and viscosity with those of the isoviscous case in Fig. 14.17 illustrates the warming of the interior due to formation of a cold, thickening, and increasingly immobile viscous lid adjacent to the upper boundary. The sluggish-lid and stagnant-lid styles of convection in the spherical shell are

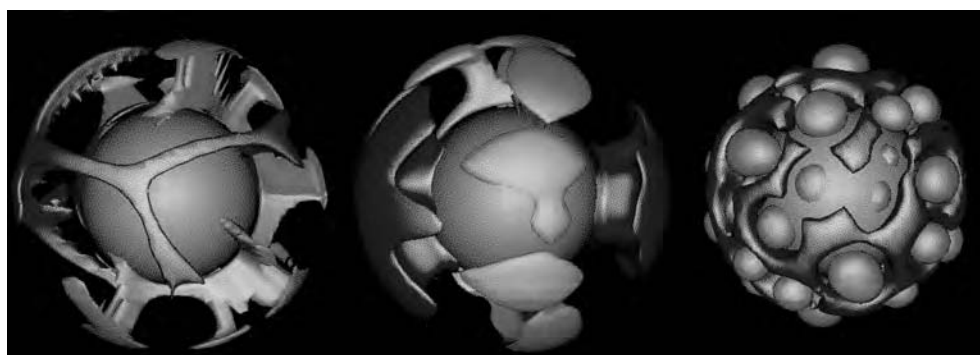


Figure 14.16. Similar to Figure 14.15 but for convection in a spherical shell with a ratio of inner radius to outer radius of 0.55. The viscosity contrasts, from left to right, are 1, 10^3 , and 10^4 . The residual temperature surfaces, from left to right, are $(+0.2, -0.15)$, $(+0.2, -0.15)$, and ± 0.15 . Blue surfaces represent cold (downwelling) material and red or orange surfaces represent hot (upwelling) material. The green sphere represents the inner boundary of the model.

For a color version of this figure, see plate section.

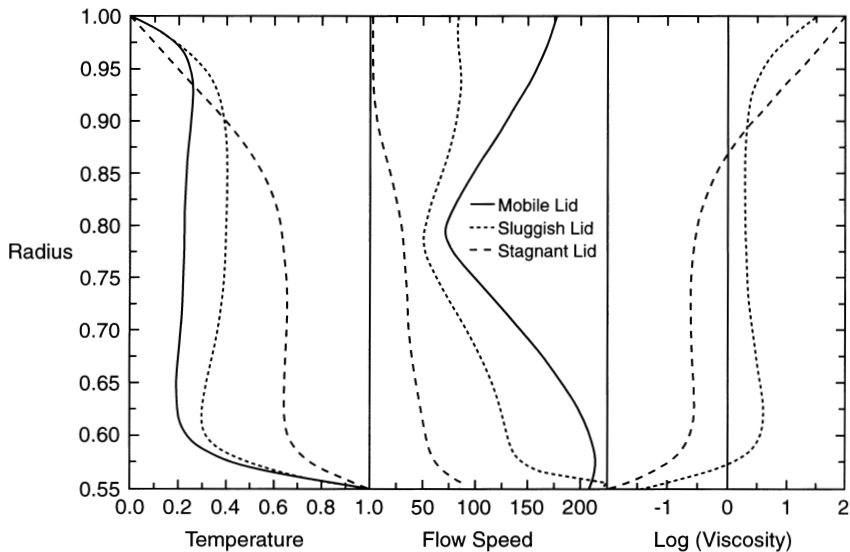


Figure 14.17. Horizontally averaged profiles of temperature (left), velocity (center), and viscosity (right) in the spherical-shell variable viscosity convection models. Solid curves are for the constant viscosity case and the dashed curves represent the variable viscosity case with viscosity contrast 10^3 (after Ratcliff et al., 1995, 1996b).

quite similar to their counterparts in the Cartesian geometry (compare Figures 14.15 and 14.16) in terms of planform and dominant length scales; the transitions among the modes of convection in spherical and Cartesian geometries also occur at similar values of the Rayleigh number (Ratcliff et al., 1997).

Figure 14.18 compares the spherical shell convection patterns with the topography of Venus. The band of upwelling with its plume concentrations in the variable viscosity computation corresponds to Venus' equatorial highlands while the polar downwellings in the computation may be analogous to the northern hemisphere high latitude plateau highland Ishtar Terra on Venus (Bindschadler et al., 1990; Kaula et al., 1997). The mode of Venusian convection has important implications for its thermal evolution as we discuss later in this chapter.

14.2.7 Convection Models with Phase Changes and Variable Viscosity

The convection models discussed above show how the strong temperature dependence of rock viscosity can significantly influence the style of mantle convection on Venus. We have also discussed earlier how phase transitions have a major effect on the nature of Venusian mantle convection. We now examine model results in which both variable viscosity and phase changes are simultaneously taken into account. Variable viscosity and phase changes, when acting together, may influence convection differently than they do when acting separately.

We base the discussion of this section on calculations of three-dimensional, variable viscosity, phase-change-modulated convection in a $4 \times 4 \times 1$ box heated from below with reflecting side boundaries and isothermal, free-slip upper and lower boundaries. The model uses the compressible anelastic liquid approximation and material properties are depth

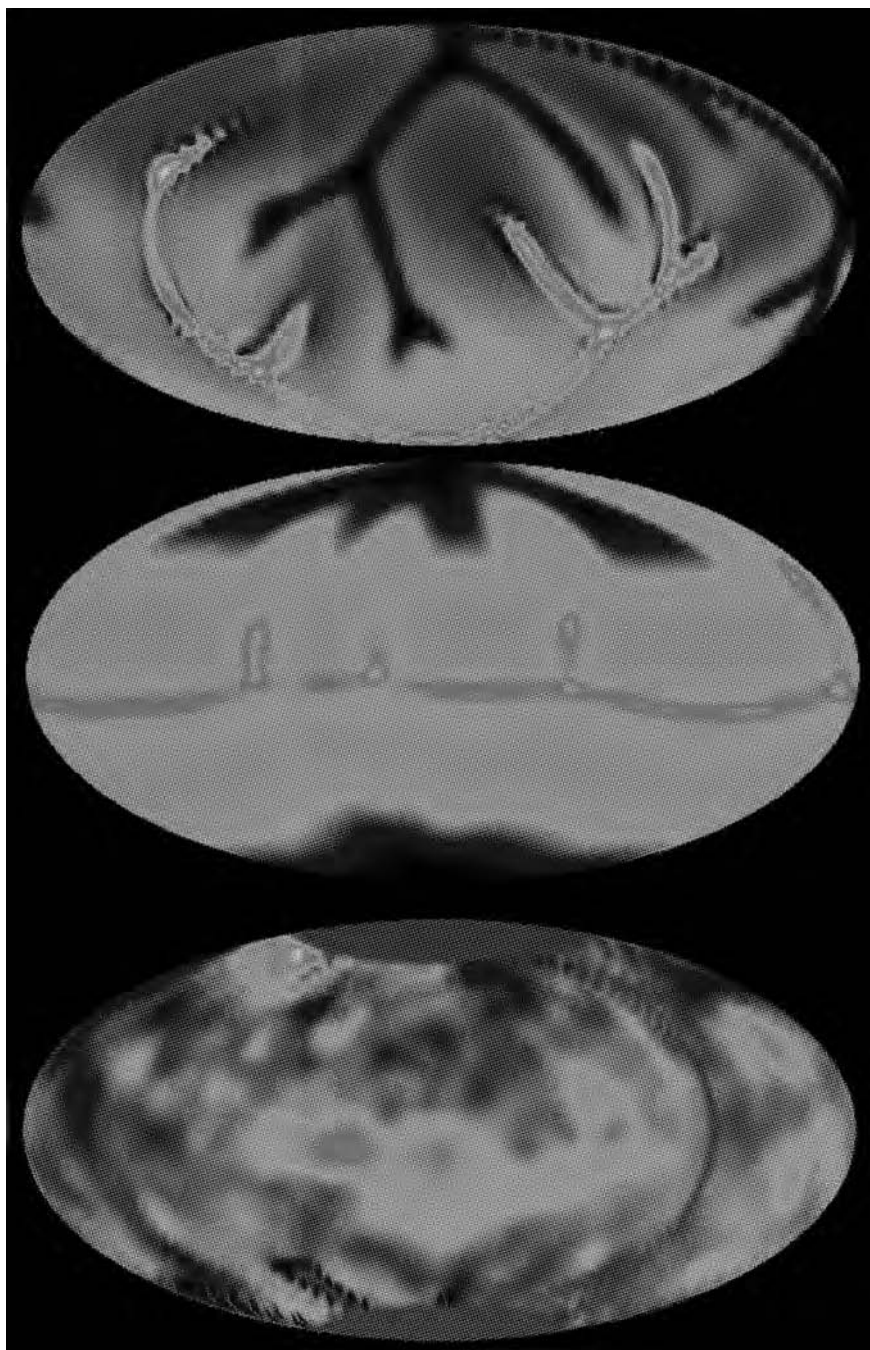


Figure 14.18. Patterns of convection in a spherical shell for constant viscosity (top), variable viscosity with a viscosity contrast of 10^3 (middle), and the topography of Venus (bottom). The convection patterns are illustrated by the temperature variations at mid-depth. Blue (dark) indicates either cold (downwelling) fluid or low topography. Red (light) indicates either hot (upwelling) fluid or high topography. The temperature fields and topography are displayed on a Hammer-Aitoff equal-area projection (after Ratcliff et al., 1995).

For a color version of this figure, see plate section.

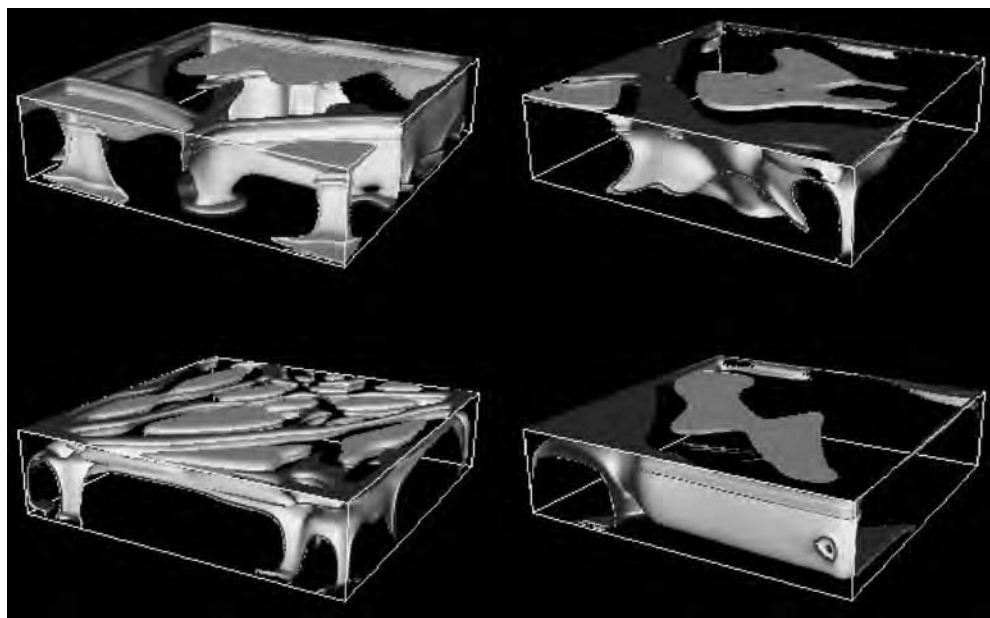


Figure 14.19. Cold downwellings (blue) and hot upwellings (red) for the three variable viscosity phase change cases. Plotted are isosurfaces of residual temperature, i.e., temperature relative to the horizontally averaged temperature profile, showing where the temperature is ± 0.1 from the horizontal average. (a) (Top left) constant viscosity case 1, (b) (lower left) variable viscosity case 2, (c) and (d) (right) variable viscosity with a yield stress (case 3) at two different times.

For a color version of this figure, see plate section.

dependent, except for viscosity which has an Arrhenius dependence on temperature. Both the exothermic and endothermic phase changes are included in the model with Clapeyron slopes of 2 and -4 MPa K^{-1} , respectively. Incorporation of a yield stress in some calculations allows comparison with an Earth-like model which simulates aspects of nonviscous lithospheric deformation involved in plate tectonics (Weinstein and Olson, 1992; Bercovici, 1993).

Results for three cases, constant viscosity (case 1), variable viscosity (case 2), and variable viscosity with a yield stress (case 3), are presented. In all cases the Rayleigh number, based on temperature, surface properties, and the viscosity of the reference adiabat at the surface, is 10^6 . Viscosity varies by about a factor of 500 near the surface of the model and by about a factor of 2,000 near the lower boundary. The patterns of convection in the three cases are shown in Figure 14.19. Case 1 (with constant viscosity, top left in Figure 14.19) displays a weakly time dependent, whole-mantle mode of convection, with the broad, plume-like upwellings and interconnected sheet-like downwellings penetrating the endothermic phase transition with ease. This pattern is similar to previous convection calculations with no phase changes (Balachandar et al., 1992; Ratcliff et al., 1997). The heat flux is 40.5 mW m^{-2} , about 20% lower than cases with similar parameters but no phase transitions reported in (Ratcliff et al., 1997); this is due to the effect of the endothermic phase transition in inhibiting flow.

Case 2 (with temperature-dependent viscosity, lower left in Figure 14.19) also exhibits only weak time dependence, but in this case an appreciable degree of layering is apparent,

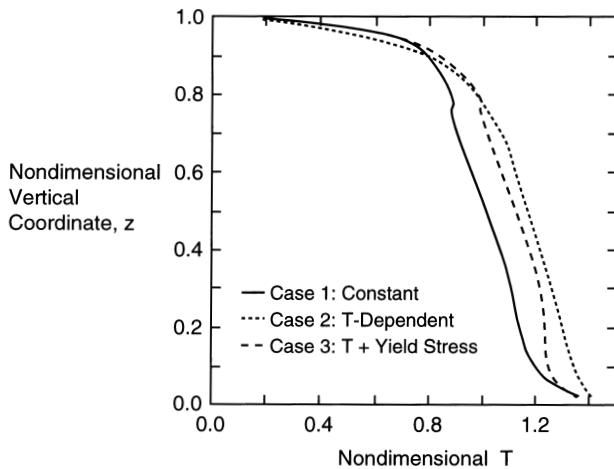


Figure 14.20. Profiles of horizontally averaged temperature for the three variable viscosity phase change cases.

with the sheet-like downwellings not penetrating the phase transition, but cold plumes at their intersections penetrating into the lower mantle. In contrast to the constant viscosity calculations, these cold plumes do not display time-dependent “avalanche” behavior. This result is similar to that of a two-dimensional calculation by Zhong and Gurnis (1994b) and corroborates the conclusion that a viscosity that is dependent only on temperature substantially increases the propensity of the mantle towards layering compared to constant viscosity. The heat flux, 22.8 mW m^{-2} , is substantially lower than in case 1 due to both the effect of a strong sluggish lithosphere in reducing heat flow, and to the greater degree of layering: layered convection is less efficient in transporting heat than whole-mantle convection.

Case 3 (similar to case 2 but with the addition of a yield stress, right panels in Figure 14.19) exhibits very strong time dependence, with heat flux and velocity varying by more than a factor of 2 (heat flux varies between 20 and 45 mW m^{-2}). Two representative frames are illustrated in Figure 14.19. The dominant feature in this case is a linear zone of downwelling, somewhat reminiscent of a terrestrial subduction zone, along the near and left edges of the box. Sections of this intermittently penetrate the phase transition into the lower mantle, with the form of penetration varying; the upper frame shows a large amorphous cold blob falling through the lower mantle, whereas the lower frame shows a coherent, linear slab-like feature extending from the surface to the core–mantle boundary. However, no cylindrical lower mantle avalanches, as observed in constant viscosity studies, occur.

Profiles of the horizontally averaged temperature for these cases are compared in Figure 14.20. The important features in case 1 are the boundary layers near the upper and lower surfaces, the approximately adiabatic increase of temperature in the interior, and a jump in temperature at the depth of the endothermic phase transition due to the adiabatic release or absorption of latent heat by material passing through the transition. The lower boundary layer is much smaller than the surface boundary layer despite the 100% basal heating; this is a consequence of the increase of thermal diffusivity with depth in the model. In case 2, the interior temperature has increased greatly so that the lower boundary layer is almost imperceptible. The temperature step observed at the phase transition depth has disappeared because there is less vertical advection through the phase transition: much of the heat transport is now conducted. The yield stress introduced in case 3 mitigates the effects

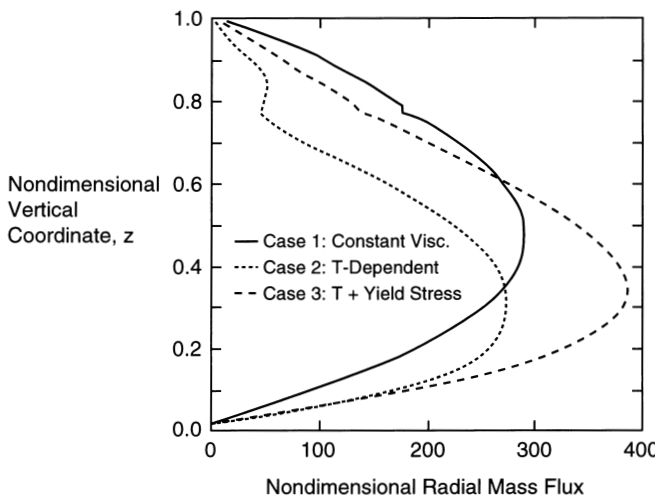


Figure 14.21. Profiles of horizontally averaged vertical mass flux for the three variable viscosity phase change cases. Note that this is the mean of the absolute mass flux; conservation of mass requires the mean of the actual mass flux to be zero.

of temperature-dependent viscosity and brings the temperature profile back in the direction of case 1, with a distinct lower boundary layer and kink in the profile at the phase transition.

A more quantitative assessment of the degree of layering can be obtained from the radial mass flux (Figure 14.21), here shown in absolute terms rather than normalized as in Figure 14.13. Case 1, constant viscosity, displays a smooth, symmetrical curve characteristic of whole-mantle convection. The endothermic phase transition has a huge effect in the variable viscosity case 2; it reduces mass flux in the upper part of the mantle and causes a minimum in the mass flux at the endothermic phase transition depth, characteristic of partially layered convection. In case 3, the signature of the phase transition is greatly reduced; only a slight change in the gradient of the curve is visible at the endothermic phase change depth. The curves for cases 1 and 2 are quite stable in time, whereas the curve for case 3 fluctuates by a factor of 2–3 in overall amplitude, though maintaining a similar profile.

These results illustrate the first-order effects of temperature-dependent viscosity on phase-change-modulated mantle convection. Since the degree of layering increases with Rayleigh number (Christensen and Yuen, 1985; Yuen et al., 1994), all cases would be more layered at the higher Rayleigh numbers realistic for Venus.

As noted above, a comparison of cases 1 and 2 indicates clearly that inclusion of a viscosity which is dependent solely on temperature greatly increases the propensity of the system towards layering, a result previously indicated in two dimensions (Zhong and Gurnis, 1994b). In such temperature-dependent viscosity convection, downwellings are broad and symmetric (i.e., two-sided), with considerable stress occurring where they leave the upper boundary layer (Tackley, 1993; Steinbach and Yuen, 1994b). Thus, the negative buoyancy of the downwellings is largely used up in overcoming stress in the upper boundary layer, and is not available for overcoming the positive buoyancy associated with phase change deflection. This style of convection may be relevant to Venus, which does not display plate tectonics.

The “Earth-like” case (case 3) with a yield stress displays two main differences: (1) the degree of layering is reduced compared to that with a purely temperature dependent viscosity

and (2) the form of phase-change-modulated convection is greatly changed compared to constant viscosity cases, with the high viscosity reducing the ability of cold material to spread in the transition zone, forcing avalanches to be linear.

Since plate tectonics is not observed on Venus it may be that case 2 is representative of Venus while case 3 is representative of the Earth. This implies that Venus' mantle may be more layered than Earth's mantle, including the possibility that Venus' mantle convection may currently be layered whereas Earth's mantle convection may be predominantly whole mantle. The spherical cases discussed above also suggest such a conclusion: the rigid-lid case was more layered than the free-slip case. A layered convection scenario for Venus would allow plumes from the upper/lower mantle interface to transport most of the heat (because they transport the heat from the lower mantle), which would be compatible with the plume-dominated tectonics favored by some researchers. The resurfacing event some 500 Myr ago might correspond to a brief episode of whole-mantle convection.

Question 14.14: Is mantle convection in Venus layered?

14.2.8 Thermal History Models of Venus

The numerical models of convection discussed above are probably most relevant to the present state of Venus' mantle although some of the results may be applicable to past states and the numerical results do suggest possible explanations for the global resurfacing event on Venus more than 500 Myr ago (mantle overturns due to a transition in convective mode or due to an avalanche). However, realistic three-dimensional convection models are too computationally demanding to be run in a thermal evolution mode. Instead, the history of Venus is most readily explored in a quantitative manner using the parameterized convection approach. This technique accounts for the contribution of mantle convective heat transfer to the overall energy balance of a planet by a Nusselt number-Rayleigh number relation. The approach has been exploited for about two decades in studies of planetary thermal evolution (Schubert, 1979; Schubert et al., 1979a; Turcotte et al., 1979). Venus-specific thermal evolution studies using the parameterized convection approach include those of Schubert et al. (1979a), Stevenson et al. (1983), Solomatov et al. (1987), Solomatov and Zharkov (1990), Zharkov and Solomatov (1992), and Solomatov (1993). The thermal evolution study of Stevenson et al. (1983) is noteworthy in providing an explanation for the nonexistence of a Venusian intrinsic magnetic field – the likely absence of inner core solidification in Venus implies the lack of an energy source to drive convection in the liquid part of the core. However, Arkani-Hamed's (1994) investigation of Venus' thermal history attributes the absence of a Venusian magnetic field to the freezing of Venus' core as a result of more efficient past heat removal on Venus compared with Earth. At present, with the Earth in the small viscosity contrast convective regime and Venus in the sluggish-lid or stagnant-lid convective regime, the Earth is more efficient at heat removal.

We discuss the thermal evolution of a Venus model cooling from a hot initial state following Solomatov (1995). Theories of the formation of the planets suggest that Venus, like the Earth, must have been extensively heated by large impacts during its accretion (Safronov, 1978; Wetherill, 1990). This, and the addition of gravitational energy release due to core formation, heating by adiabatic compression, heating by short-lived radioactive isotopes, and thermal blanketing by an atmospheric greenhouse (Abe and Matsui, 1985; Zahnle et al.,

1988) all imply a very hot interior after the early formation period. The period of post-accretional cooling, melt differentiation and convective remixing is short compared to the entire evolution (Solomatov and Stevenson, 1993b). The thermal evolution controlled by solid-state convection, which we discuss here, started around 4.5 Gyr ago and the initial potential temperature of Venus could not have been much higher than the solidus.

The parameterized thermal evolution model assumes that the mantle of Venus contains a terrestrial-like complement of radiogenic heat sources. The influence of Venus' core on the thermal evolution of its mantle is minimal and the model does not include the core. The thermal evolution of Venus is found by integrating a simple energy balance equation for the average temperature T of the mantle forward in time.

The appropriate form of the Nusselt number–Rayleigh number relation for convection with temperature-dependent viscosity depends on the regime of convection. In the small viscosity contrast regime, convection is controlled by the interior viscosity and is described by formulae identical to those for constant viscosity convection, provided the viscosity is calculated at the average temperature (Schubert et al., 1979a; Stevenson et al., 1983).

In the sluggish-lid convection regime the heat transport depends almost entirely on the surface viscosity. Investigations in the parameter range corresponding to this regime led Christensen (1984c, 1985b) to conclude that the surface velocity and Nusselt number are almost constant during the evolution of the Earth provided the surface temperature and the surface viscosity are constant. The initial conditions control the entire evolution in this regime, while in traditional models the initial conditions are not important after about 1 Gyr of evolution. In this regime, convection depends entirely on the rheology of the lithosphere.

In the stagnant-lid regime the efficiency of heat transport depends only on the rheology in the hot part of the cell where the viscosity variations do not exceed one order of magnitude, and convective heat transfer no longer depends on the rheology of the lid.

In order to calculate a thermal history for Venus with the parameterized convection approach, we must first identify the thermal regime in which Venus is found at different stages of its evolution. On the basis of theoretical estimates of viscosity contrasts, mantle convection in any terrestrial planet should be in the stagnant-lid regime. This convective regime might be most consistent with a Venusian lithosphere as thick as 200–300 km and the small surface deformation rates on Venus (Grimm, 1994b; Solomatov and Moresi, 1996; Reese et al., 1998). However, as discussed earlier in this chapter, a comparison of features on the surface of Venus with numerically computed patterns of convection suggests that Venus may be in the sluggish-lid mode of convection.

Question 14.15: Is mantle convection on Venus in the sluggish-lid or stagnant-lid convection regime?

For purposes of “bounding” the thermal evolution of Venus we present results for two end-member thermal history models: one model assumes a thermal evolution controlled by small viscosity contrast convection and the other model assumes that stagnant-lid convection dominates the thermal history. Details of the models and values of parameters can be found in Solomatov (1995). The thermal evolution of Venus models with mobile plates (small viscosity contrast regime) and with a stagnant lid are shown in Figure 14.22. Three different initial temperatures are chosen to show the effect of initial conditions.

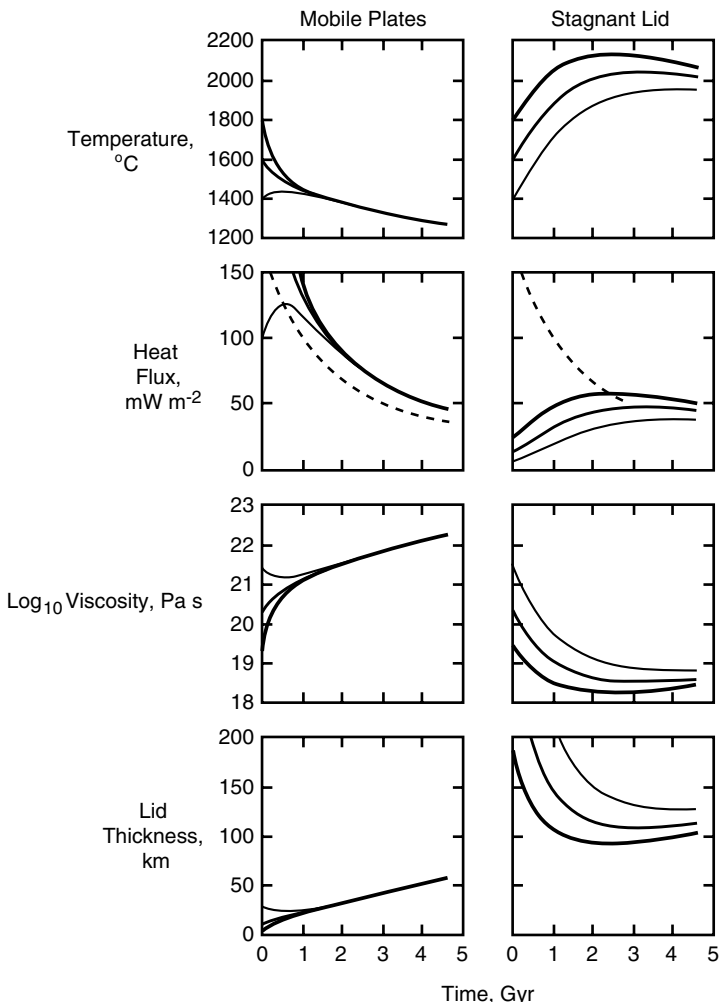


Figure 14.22. Parameterized convection calculations of the thermal evolution of Venus under the assumption that the convective regime on Venus was the same during the entire evolution. The regime with mobile plates (small viscosity contrast regime) is shown on the left, and the stagnant-lid regime is on the right. The following convective parameters are calculated: the mantle temperature T , the surface heat flux, the viscosity at temperature T , and the thickness of the lithosphere (the cold thermal boundary layer). The dashed line shows the surface heat flux that would be in equilibrium with radiogenic heat production in the mantle. The three different curves correspond to different choices of initial temperature.

The regime with mobile plates (small viscosity contrast regime) gives evolution scenarios in which the present mantle temperature is close to that of the Earth. In the stagnant-lid regime, the temperature has to increase to more than 2,000°C for the surface heat loss rate to become comparable with the radiogenic heating rate. This exceeds the melting temperature by several hundred degrees. A low rate of volcanism on Venus (at least 10 times smaller than on the Earth) seems to be in contradiction with a higher temperature of the Venusian mantle.

Another problem with both solutions is that the lithospheric thickness (the thermal boundary layer) is much less than the 200–300 km value inferred from topography and gravity

data. Even with a very depleted mantle, the lithosphere thickness would still be too small (Solomatov and Moresi, 1996).

The problem with the lithosphere thickness prediction of these parameterized convection models has been discussed earlier (Question 14.9). The numerical convection models show that the global gravity and topography data can be consistent with a lithosphere only about 100km thick overlying a convecting mantle and transporting a terrestrial-like heat flux. However, gravity and topography data on a smaller scale and the nature of small-scale lithospheric deformation on Venus also suggest that Venus has a very thick lithosphere. In the following sections we discuss two ad hoc thermal evolution scenarios that might explain the thick lithosphere dilemma.

One possible explanation for both the global resurfacing event more than 500 Myr ago and a thick lithosphere at present is a change in convective style at the time of the event from plate tectonics (similar to small viscosity contrast convection because of lithospheric subduction) to the stagnant-lid regime. The parameterized convection model of the previous section can be used to quantitatively evaluate this possibility. We first consider the consequences of the hypothesized transition and then discuss why plate tectonics could have stopped on Venus about 500 Myr ago.

If a plate tectonic-like convective regime prevailed on Venus prior to about 500 Myr ago and then ceased at that time, the deep interior of Venus would have heated up and a thicker lithosphere would have grown after the cessation of plate-like motions. Prior to the event of about 500 Myr ago, the surface heat flux would have slightly exceeded the internal radiogenic heating as a result of a small contribution to the heat flux from secular cooling. After the plates stop, convective instabilities would begin to develop near the bottom of the lithosphere after a short incubation period (Davaille and Jaupart, 1994). This is the stagnant-lid form of convective motion. It is much less efficient than plate-like convection and implies a substantial drop in the surface heat loss rate. The heat loss rate becomes smaller than the radiogenic heat production rate by almost an order of magnitude and the net result is that the interior of the planet heats up.

The cooling of the lithosphere is due to the difference between the large near-surface thermal gradients left over from the plate tectonics regime and the small heat flux carried by instabilities at the bottom of the lithosphere. As a result, the lithosphere is cooled from the top much faster than it is heated from below. The half-space cooling model adopted by Turcotte (1993) can be used to calculate the thermal regime of the lithosphere for the first few hundred million years after the cessation of plate tectonics (assuming the absence of secondary convection that would prevent continued lithospheric thickening). Accordingly, the surface heat flux F and the lithosphere thickness δ change with time as

$$F = \frac{k(T - T_s)}{\delta(t)}, \quad \delta(t) = [\pi \kappa(t - t_0)]^{1/2} \quad (14.2.10)$$

where κ is the thermal diffusivity, T_s is the surface temperature, and t_0 is a time slightly smaller than the time when plate motion stopped and is found from the requirement of a continuous change in the boundary layer thickness and the surface heat flux.

A sketch of this scenario is shown in Figure 14.23, while Figure 14.24 gives quantitative results from a thermal evolution calculation that a priori imposes the change in convective regime 500 Myr ago. The plots in Figure 14.24 show an increase in interior temperature, a drop in surface heat flux, and a dramatic thickening of the lithosphere since the hypothesized change in the convective regime 500 Myr ago. The magma production rate would also decrease after cessation of plate tectonics due to a drop in the convective velocity and

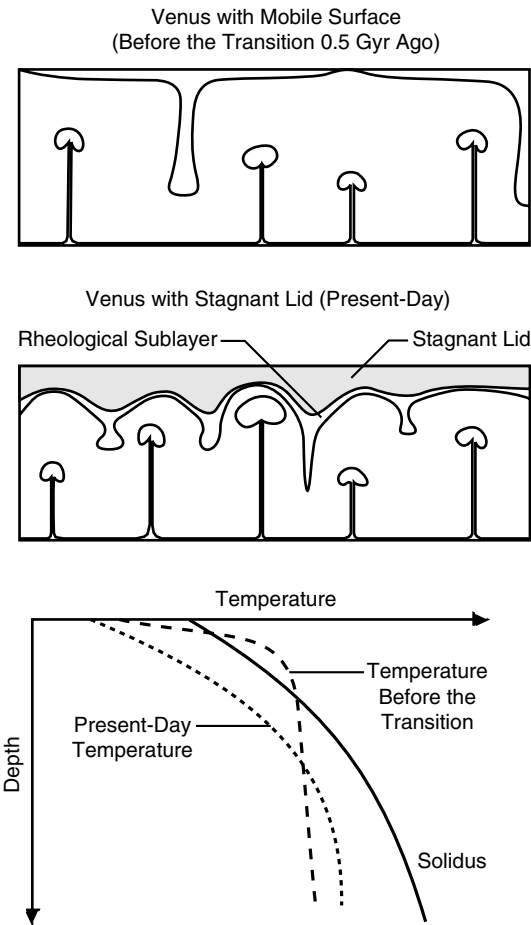


Figure 14.23. A schematic of convection in Venus before the cessation of the mobile plate regime around 0.5 billion years ago and at present, and a sketch of the depth profiles of temperature before and after the event.

an increase in the lithospheric thickness. A thicker lithosphere prevents convective flow from reaching close to the surface, thereby substantially reducing melting due to adiabatic decompression (Figure 14.23). Therefore, a decrease in the resurfacing rate on Venus would result not only from the change from mobile plates to a stagnant lid, but also from a large decrease in the rate of melt production. This is in agreement with the estimates of a very low level of present-day volcanism on Venus (Fegley and Prinn, 1989; Head et al., 1991, 1992; Basilevsky et al., 1997; Namiki and Solomon, 1998). A continuing decay in the rate of volcanism due to gradual development of the stagnant lid is also in agreement with Price and Suppe's (1994) suggestion that limited volcanism continued after the resurfacing event.

Why would a plate tectonic-like regime on Venus cease to operate about 500 Myr ago? A possible answer lies in the gradual thickening of the plates with time throughout the evolution of Venus. The thickening of the lithosphere with time increases its strength while the stresses in the lithosphere are decreasing with time (Solomatov and Moresi, 1996). Early in the evolution of Venus the stresses could have been large enough to break the lithosphere, perhaps by faulting, and result in a plate tectonic-like convective regime. When the stresses in the lid dropped below a critical value associated with the increasing strength of the lithosphere, perhaps about 500 Myr ago, active surface motion would cease. This

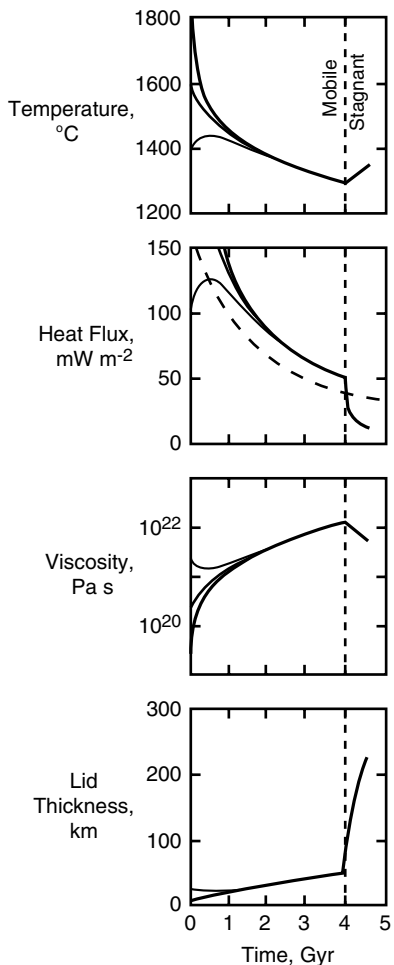


Figure 14.24. Parameterized convection calculations of the thermal evolution of Venus with the hypothesized change from the regime with mobile plates to the stagnant-lid regime 0.5 billion years ago.

mechanical explanation of the cessation of subduction and initiation of the stagnant-lid convective regime is similar to a model suggested by Fowler (1993).

In the scenario of the preceding section we have seen how the lithosphere would grow to a thickness of several hundred kilometers (Figure 14.24) following the event at about 500 Myr ago. It is possible that this overthickened, gravitationally unstable lithosphere would overturn, release heat stored in the interior during surface quiescence, and resurface the planet. If Venus is presently in a stagnant-lid, nonsteady convective regime with an already thick and thickening lithosphere, global lithospheric overturn by gravitational instability could lie in Venus' future. The event at about 500 Ma could in fact have been such a lithospheric overturn if episodic mantle overturning interspersed with long periods of stagnant-lid convection characterized Venus' thermal evolution (Turcotte, 1993). Mantle overturning and episodicity can also arise from effects of chemical differentiation (Parmentier and Hess, 1992; Herrick and Parmentier, 1994).

It is one thing to hypothesize the global overturn of a thick and gravitationally unstable lithosphere on Venus. However, a mechanism to initiate and facilitate such an overturn needs to be found. Before the strong, thick Venusian lithosphere can subduct, it must be broken.

Schubert and Sandwell (1995) have identified extension and rifting as the mechanism for initiating lithospheric foundering and subduction on Venus. Mantle plumes of unusual vigor could arise in the overheated deep interior of a planet with an overthickened lithosphere and substantially weaken, thin, upwarp, and crack the lithosphere. Rifts propagating away from the center of such hot spot sites could break nearby lithosphere thick enough to be gravitationally unstable and initiate retrograde lithospheric foundering or subduction. If there are a sufficient number of such sites, a global lithospheric overturn could occur. Venus may be on the verge of such an event. The evidence consists of the major volcanic rises such as Atla Regio and Beta Regio, the chasmata (rifts) emanating from the hot spot centers and extending into the lowlands away from the rises, and the possible occurrence of subduction along major segments of the chasmata far from the rises (Schubert and Sandwell, 1995).

14.2.9 Why is There no Dynamo in Venus?

One of the major differences between the Earth and Venus is the lack of an intrinsic magnetic field on Venus (Russell, 1980; Phillips and Russell, 1987; Donahue and Russell, 1997). We now explore the possibility that Venus' lack of an intrinsic magnetic field can be understood in terms of the thermal evolution of the core–mantle system in an Earth-like planet slightly smaller and slightly less massive than the Earth. The differences in mass and radius between Venus and Earth, though small, are crucial for the thermal evolution of the core, which freezes out a solid inner core in the case of the Earth, but remains entirely liquid in the case of Venus. We have discussed in Chapter 13 how the solidification of an inner core is essential for generation of the Earth's magnetic field by dynamo action, so that the absence of core solidification in Venus provides a straightforward explanation for the lack of a Venus magnetic field.

This explanation, suggested by Stevenson et al. (1983), is an attractive one because it does not hypothesize arbitrary differences between Venus and the Earth, but explains the differences in planetary magnetic fields as a natural consequence of thermal evolution. Other explanations for the lack of a Venus magnetic field (Arkani-Hamed, 1994) are less plausible. The rotation rate of Venus, though slow, is nevertheless large enough that Coriolis forces are important for large-scale motions in the core and should be sufficient for dynamo generation of a magnetic field in the presence of an adequate energy source (Stevenson et al., 1983). The possibility that Venus lacks a magnetic field because its core is completely frozen (Arkani-Hamed, 1994) cannot be excluded with certainty, but is considered unlikely. Complete solidification of a core in any of the terrestrial planets is likely precluded by the reduction in the freezing point that occurs upon the concentration of light alloying core elements (e.g., sulfur or oxygen) into the yet unfrozen portions of the core (Stevenson et al., 1983). Accordingly, we proceed next to discuss a coupled core–mantle thermal history model for Venus with the purpose of explaining the lack of a Venus magnetic field in terms of the absence of inner core solidification in Venus.

Question 14.16: Why does Venus not have a magnetic field?

The model we use to study the thermal history of Venus is that of Stevenson et al. (1983) and is identical to the model used in Chapter 13 to investigate the coupled core–mantle thermal evolution of the Earth. In accordance with the assumption of similarity between

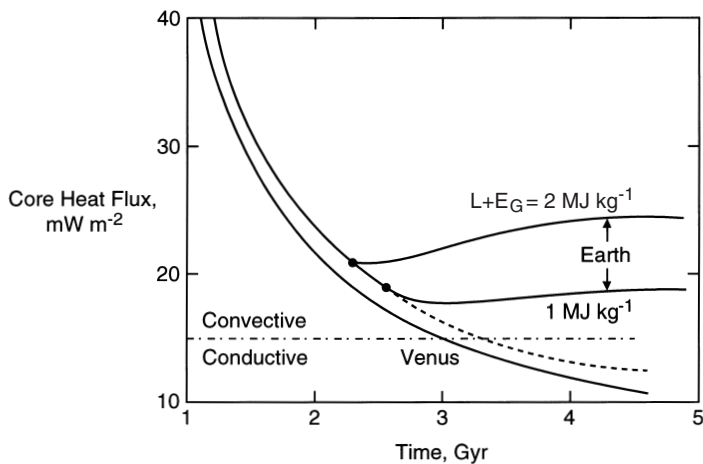


Figure 14.25. Core heat flux versus time for the Venus thermal history model. Similar results for the Earth thermal history model of Chapter 13 are included for comparison. The horizontal line is the value of heat flux conducted upward along a core adiabat. The core is superadiabatic and convection is possible if core heat flux exceeds this value, but it is subadiabatic and nonconvecting if core heat flux falls below this value. The small circles mark the onset of core solidification in the Earth models. There is no core solidification in the Venus model. The dashed curve indicates how the Earth model would continue to cool without inner core freezeout. Venus' core becomes subadiabatic and nonconvective after 3 Gyr in the model.

Venus and the Earth, we adopt the same model parameter values for Venus as for the Earth, except where differences are known or can be reasonably inferred. The Venus model discussed here assumes the following parameter values: planetary radius = 6,051 km, surface gravity = 9 m s^{-2} , surface temperature = 730 K, core radius = 3,110 km, core density = $12.5 \times 10^3 \text{ kg m}^{-3}$, central pressure = 290 GPa (360 GPa for the Earth model of Chapter 13), core-mantle boundary pressure = 130 GPa (140 GPa for the Earth model of Chapter 13), and $L + E_G = 1 \text{ MJ kg}^{-1}$. Other model parameter values are the same as in the Earth model of Chapter 13 (see also Stevenson et al., 1983).

The Venus thermal history calculation is illustrated by the plot of core heat flux versus time in Figure 14.25. The results of the Earth thermal history calculations of Figure 13.8 are included for ease of comparison. In the Venus model, core heat flux decreases monotonically with time as the planet cools, and, unlike the Earth models, there is no core solidification. The Venus core in the model of Figure 14.25 is entirely liquid at present. Venus core heat flux dropped below the value necessary to sustain thermal convection in the core about 1.5 Gyr ago. A thermally driven dynamo that might have been operative in Venus' core at earlier times would have ceased to function 1.5 Gyr ago. In this model Venus' core has been subadiabatic, nonconvective and unable to sustain dynamo action for the last 1.5 Gyr. Inner core freezing in the Earth models (onset between 2 and 3 Gyr) maintains convection and dynamo action in the liquid part of the core, as discussed in Chapter 13.

Figure 14.26 (after Stevenson et al., 1983) compares present temperatures in the cores of the Earth and Venus models of Figure 14.25 (for the Earth model with $L + E_G = 1 \text{ MJ kg}^{-1}$). Although Venus is a smaller planet, the temperatures are very similar, partly because of Venus' high surface temperature. In the models, Venus' mantle is about 100 K hotter than the Earth's mantle. Venus does not nucleate an inner core in the model mainly because of the lower pressure at the center of Venus compared with the Earth's central pressure. Because

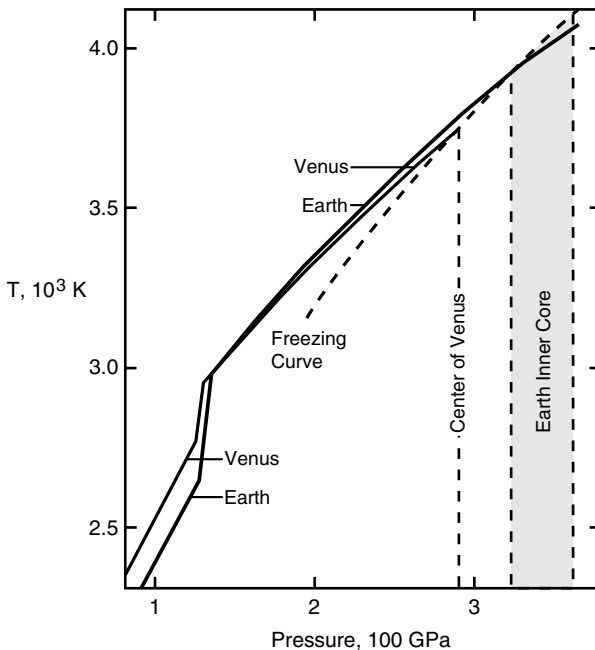


Figure 14.26. Present temperature as a function of pressure in the lower mantles and cores of Venus and Earth models with $L + E_G = 1 \text{ MJ kg}^{-1}$. The models are those of Section 14.2 and Chapter 13. The dashed curve is the freezing curve of the alloy. The dashed vertical lines give the pressures at the centers of the Venus and Earth models and at the inner–outer core boundary in the Earth model. Temperature increases with pressure along the mantle adiabat, the lower mantle thermal boundary layer, and the core adiabat. The Venus model has the core just on the verge of solidification at its center.

of the lower central pressure in the Venus model, the freezing temperature at the center of the Venus is lower than at the center of the Earth, and the Venus model needs to cool longer than the Earth model for solidification to occur (first at the planet's center). Figure 14.26 shows that the Venus model is at the onset of inner core solidification at present.

According to the Venus model, the planet had an intrinsic magnetic field until about 1.5 Gyr ago. This points to the possibility that the real planet had a magnetic field for several billion years of its evolution, a possibility that must be accounted for in studies involving the solar wind interactions with Venus and the evolution of Venus' atmosphere. Equally intriguing, from a speculative point of view, is the possibility suggested by the model that Venus may be on the verge of core solidification and rejuvenation of its magnetic field by compositionally driven convection in the core. It must be kept in mind that Venus' thermal history calculations with a variety of outcomes, including inner core solidification with present magnetic field generation and nearly complete solidification of the core, are possible with changes in the values of model parameters (see Stevenson et al., 1983) for additional Venus thermal history calculations). However, the Venus models that can be constructed with partially frozen cores and present magnetic fields are incompatible with observations of Venus that show it lacks a magnetic field. The Venus models that have nearly completely frozen cores are possible models for the real Venus, but they require very low core concentrations of light alloying elements compared to the Earth and, as discussed above, are therefore considered unlikely. It is significant that application of an Earth-like thermal history model to Venus predicts a

different Venus core structure at present and provides a natural explanation for the lack of a Venus magnetic field.

14.3 Mars

14.3.1 Surface Tectonic and Volcanic Features

The first detailed photographs of the Martian surface were returned from the flybys of Mariner 4 (1965) and Mariner 6 and 7 (1969) spacecraft. These photographs showed a heavily cratered surface much like that of the Moon. However, the photographs of the Mariner 9 orbiter (1971) revealed that the earlier spacecraft had photographed only a single type of terrain on a planet of great geological diversity. There are volcanoes that dwarf the largest volcanic structures on Earth, a huge canyon complex comparable to the East African Rift system, meandering channels with multiple braided features and stream-lined islands, sand dunes, and polar caps (Figure 14.27). The richness and variety of Martian geologic forms was not fully realized prior to the pictures returned by the Viking 1 and 2 orbiters

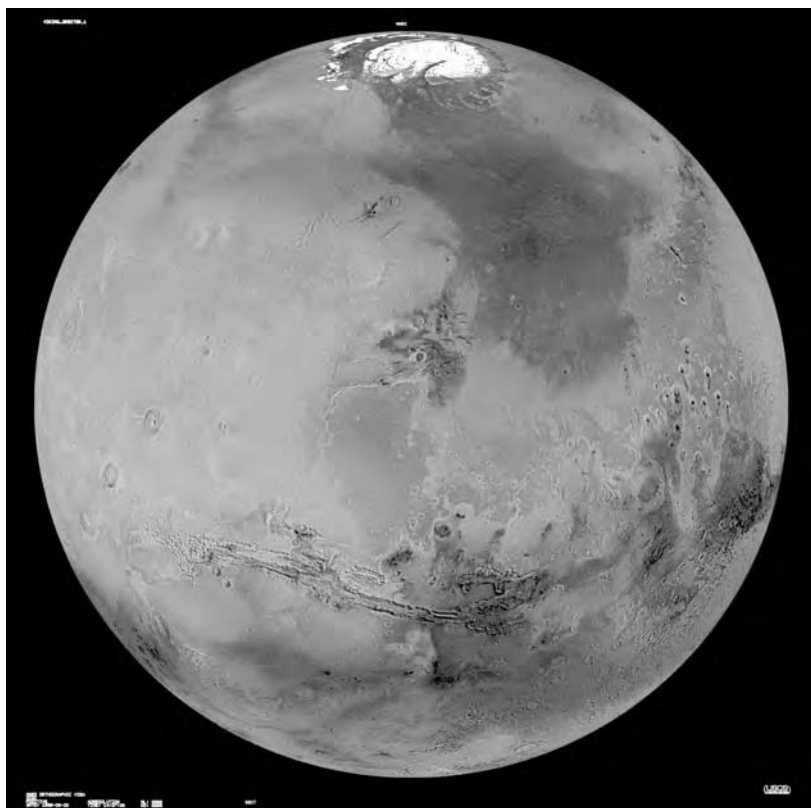


Figure 14.27. View of Mars from Viking Orbiter mosaics. The orthographic view is centered at 20° latitude and 60° longitude. The north polar cap is visible at the top of the image, the equatorial canyon system Valles Marineris is below the center, and the four Tharsis volcanoes are at the left. The view shows the heavily cratered southern hemisphere highlands and the younger, less heavily cratered terrains in the northern hemisphere.

For a color version of this figure, see plate section.

Table 14.4. Martian Epochs and Absolute-age Ranges Based on Hartmann–Tanaka (HT) and Neukum–Wise (NW) Ages, Which Represent the Two Different Time Scale Models (Tanaka et al., 1992)

Epoch	Absolute-age Range (Gyr)	
	HT	NW
Late Amazonian	0.25–0.00	0.70–0.00
Middle Amazonian	0.70–0.25	2.50–0.70
Early Amazonian	1.80–0.70	3.55–2.50
Late Hesperian	3.10–1.80	3.70–3.55
Early Hesperian	3.50–3.10	3.80–3.70
Late Noachian	3.85–3.50	4.30–3.80
Middle Noachian	3.92–3.85	4.50–4.30
Early Noachian	4.60–3.92	4.60–4.50

and landers (1976). The surface is characterized by a wide variety of volcanic and tectonic landforms. However, there is no evidence for the global system of ridges and trenches that are characteristic of active plate tectonics. Thus, it is concluded that Mars, like Venus, does not have active plate tectonics at this time. However, data on crustal magnetization from the Mars Global Surveyor, discussed below, may indicate that plate tectonics occurred on Mars early in its evolution.

In order to interpret the observed surface features of Mars in terms of the thermal and tectonic evolution of the planet, it is necessary to prescribe absolute age estimates for the various geological provinces. The density of impact craters can be used to specify relative ages with reasonable reliability. Using measurements of crater densities, the geological time is divided into three periods – Noachian, Hesperian, and Amazonian, from old to young (see Table 14.4). The Noachian and Amazonian periods are further divided into early, middle, and late epochs, while the Hesperian period is divided into early and late epochs. The surface of Mars has a much greater variation in ages than the surface of Venus. This has been illustrated in Figure 14.1. The specification of absolute ages has considerable uncertainties related to the impact rate on Mars. The age progression can be compressed by a factor of 2 within current error bars. Two estimates for absolute ages on Mars are given in Table 14.4 (Tanaka et al., 1992).

The most striking global feature of the Martian surface is its hemispheric dichotomy (Figures 14.27–14.29). Much of the southern hemisphere of Mars is covered by densely cratered terrain, whereas most of the northern hemisphere is made up of lightly covered plains. This highland–lowland boundary is a large, irregular circle centered at latitude 50°N, as illustrated in Figure 14.2 (see also Figures 14.28 and 14.29). The heavily cratered terrain in the southern hemisphere is probably the remnant of the post-accretionary surface of the planet, and younger northern plains are probably volcanic in origin.

The southern highlands cover more than 60% of the surface of Mars. Most of the highland terrain consists of ancient, rough, densely cratered rocks (largely impact breccias) formed early in the planet's history when impact rates were high. Extensive lava flows have covered large areas within the highlands. Although highland rocks range in age from Early Noachian to Late Amazonian, most formed or were emplaced during the Noachian Period. The large,

Mars Topography from MOLA

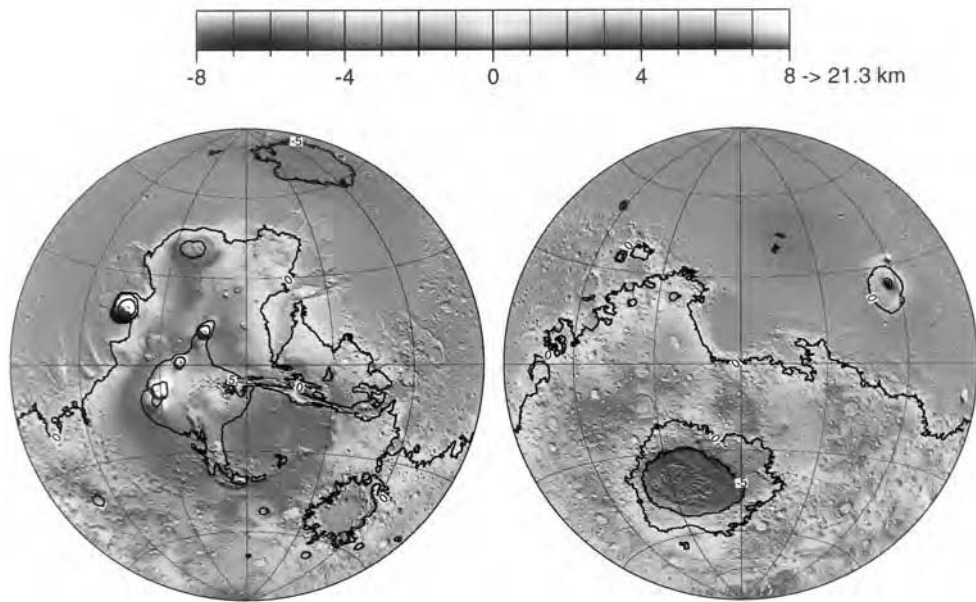


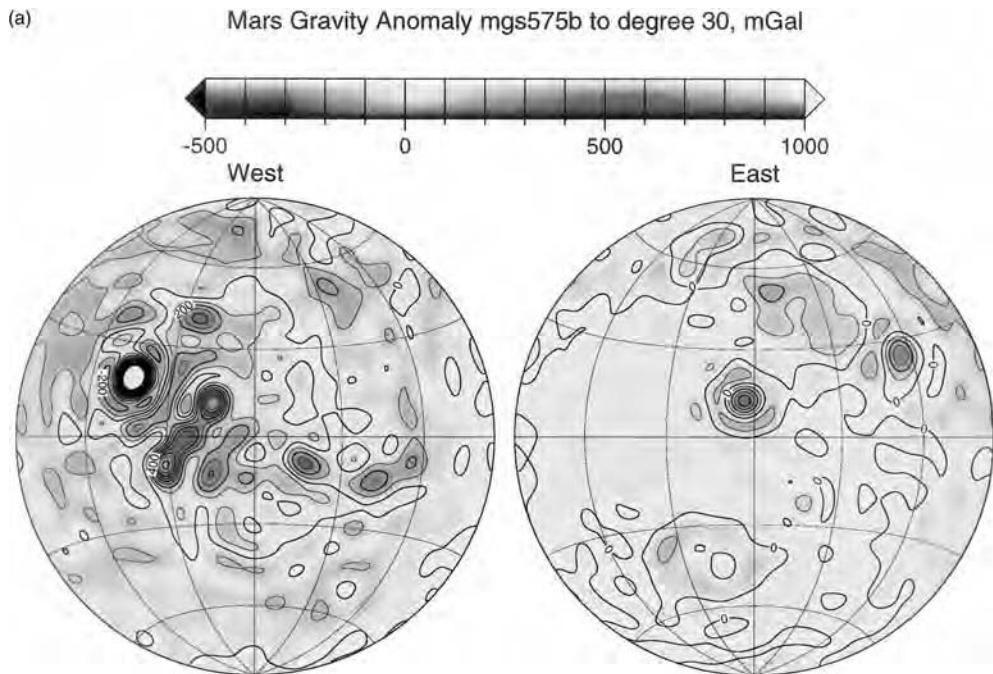
Figure 14.28. A $1^\circ \times 1^\circ$ global map of the topography of Mars from the Mars Orbiter Laser Altimeter (MOLA) on the Mars Global Surveyor spacecraft. One degree corresponds to 59 km at the equator. The global accuracy of the map is 13 m. The zero level of topography is the average radius (3,396.0 km) of the equatorial aeroid. Based on data reported in Smith et al. (1999a).

For a color version of this figure, see plate section.

roughly circular basins of Argyre and Hellas are located in the southern hemisphere and are believed to be impact basins similar to the mare basins on the Moon. The Hellas basin has a rim diameter of $\sim 2,300$ km and is one of the largest impact structures in the solar system. It is the dominant surface feature of the Martian southern highlands with a total relief of more than 9 km (Smith et al., 1999a). Material excavated from Hellas accounts for a significant amount of the southern hemisphere highlands (Smith et al., 1999a). The Argyre basin has a diameter in excess of 1,500 km.

Volcanic plains cover much of the northern lowlands of Mars. These volcanic plains are similar to the volcanic plains that dominate the surface of Venus and are much less cratered than the southern highlands. The oldest and most extensive formation in the northern lowlands is dated as Late Hesperian. Other volcanic flows span the Amazonian Period.

The approximately hemispherical dichotomy is generally held to be an ancient, first-order feature of the Martian crust. The dichotomy has been ascribed variously to a very long wavelength mantle convective planform (Lingenfelter and Schubert, 1973; Schubert and Lingenfelter, 1973), to subcrustal erosion due to mantle convection (Wise et al., 1979a; McGill and Dimitriou, 1990), to post-accretional core formation (Davies and Arvidson, 1981), to a large impact (Wilhelms and Squyres, 1984), and to several impact events (Frey and Schultz, 1988). Sleep (1994b) has proposed that the lowland crust was formed in an episode of seafloor spreading on Mars. He hypothesized a hemispheric subduction event



that destroyed the original primitive crust in the northern hemisphere. Such an event would be similar to the occurrence of episodic subduction that we have discussed for Venus. Sleep (1994b) has proposed a well-defined sequence of seafloor spreading events that created the northern volcanic plains.

One of the major tectonic features on Mars is the Tharsis region, which is an elevated domal structure composed of relatively young volcanics (Figures 14.27–14.29). The horizontal scale is some 3,000 km, with the elevation rising some 10 km above the mean surface elevation. The region exhibits a complex history of episodic tectonism, closely associated with volcanism, on local and regional scales. The most intense deformation on Tharsis occurred during the Noachian and Hesperian Periods. The entire Tharsis uplift appears to be the result of extensive volcanism. Theories for the origin of the domal structure include isostatic uplift followed by flexural loading (Banerdt et al., 1982), thick volcanic accumulations extruded through a locally thin lithosphere (Solomon and Head, 1982), and crustal thickening by intrusion (Willemann and Turcotte, 1982).

Question 14.17: What internal process produced the Tharsis uplift on Mars?

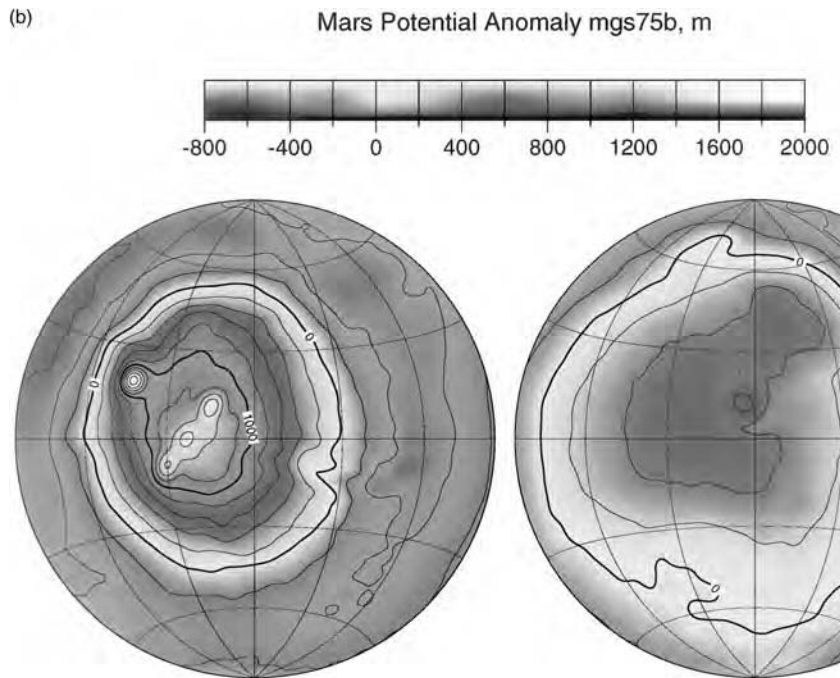


Figure 14.29. (a) Free-air gravity map of Mars from a 30th degree and order spherical harmonic representation of Mars Global Surveyor Doppler tracking data (Smith et al., 1999b). The spatial resolution is about 350 km. The gravity field has 95% of J_2 removed since 5% of J_2 is assumed to be nonhydrostatic in origin. (b) Aeroid of Mars from the spherical harmonic representation of the gravitational field described in (a).

For a color version of this figure, see plate section.

Three immense volcanic shields (Arsia, Pavonis, and Ascraeus Montes) form the Tharsis Montes, a linear chain of volcanoes extending northeastward across the Tharsis rise (Figures 14.27 and 14.28). These three shields have gentle slopes of a few degrees (the upper slopes are commonly steeper than the lower slopes), wide calderas, and flank vents. The shields appear to be formed largely of basaltic flows and are similar to the intraplate shield volcanoes of the Hawaiian Islands. The Martian shields crest 10–18 km above the Tharsis Rise and attain elevations of 18–26 km above the reference surface. Along the Tharsis axial trend, volcanoes stretch from Arsia Mons to near Tempe Patera, some 4,000 km. Lava flows that were erupted from the Tharsis Montes and surrounding vents make up volcanic plains of Late Hesperian to Late Amazonian age; these flows cover nearly 7×10^6 km².

Olympus Mons is a shield volcano nearly 600 km in diameter and over 26 km high, the tallest mountain known in the solar system. Flows on the flank of the volcano and adjacent volcanic plains that were erupted from fissures east of the volcano are among the youngest flows on Mars. The extreme height of the Martian volcanoes can probably be attributed to the low surface gravity and the lack of relative motion between the lithosphere and the magma source. The presence of shield volcanoes on Mars and their absence on the Moon may be due to differences in the viscosities of the erupted lavas.

Another spectacular tectonic feature on Mars is an enormous canyon system, Valles Marineris, extending eastward from Tharsis for about 4,500 km (Figure 14.27). Individual

canyons are up to 200 km wide and several kilometers deep. The canyon system and associated outflow channels developed mainly during the Hesperian Period. All of the canyons occur along grabens having parallel strike; in places, the valley faults were associated with volcanic activity (Lucchitta, 1987). In comparison, East African rift valleys are narrower and have extensive associated volcanoes. Rifting, magma withdrawal, and tension fracturing have been proposed as possible processes involved in the initiation and development of the canyons (Sharp, 1973; Frey, 1979; Tanaka and Golombeck, 1989).

Question 14.18: How did the Valles Marineris canyon system on Mars form?

14.3.2 Internal Structure

Unlike the case for Venus, a value of the principal moment of inertia C of Mars about its rotation axis can be inferred from observations of the gravitational field of the planet because Mars rotates rapidly on its axis (length of day $\simeq 24.6$ h) and it is nearly in hydrostatic equilibrium. The principal moment of inertia C is inferred from the hydrostatic part of the observed value of J_2 , the second degree zonal coefficient in the spherical harmonic representation of the Martian gravitational potential, through model-dependent assumptions of the relative hydrostatic and nonhydrostatic contributions to J_2 . The assumption that the nonhydrostatic part of J_2 is due only to the Tharsis bulge leads to $C = 0.365M_pR_p^2$ (Reasenberg, 1977; Kaula, 1979b), where M_p and R_p are the mass and radius of the planet, respectively. Other assumptions about the relative hydrostatic and nonhydrostatic contributions to J_2 are possible (e.g., Bills, 1989), but the assumption that the Tharsis bulge dominates the nonhydrostatic contribution to J_2 is the most physically plausible assumption since Tharsis dominates the topography (Figure 14.28) and gravity (Figure 14.29) of Mars (Kaula et al., 1989). Zuber and Smith (1997) have isolated the contribution of Tharsis to the planet's gravitational field, and by removing the Tharsis signal from Mars' overall gravitational field they have constrained $C/M_pR_p^2$ to be between 0.361 and 0.366. The actual value of $C/M_pR_p^2$ for Mars has been settled by results from the Mars Pathfinder mission. Radio Doppler and range measurements to the Mars Pathfinder lander have been combined with similar data from the Viking landers to determine the precession of Mars' spin axis. The precession is driven by the Sun's gravitational torque acting on Mars' rotational bulge, and together with a knowledge of J_2 it gives directly $C/M_pR_p^2$ without any consideration of the nonhydrostatic gravitational field. The value of $C/M_pR_p^2$ from the Mars Pathfinder is 0.3662 ± 0.0017 (Folkner et al., 1997a,b), consistent with values inferred in earlier studies that assumed Tharsis to be the predominant contributor to the nonhydrostatic gravity field of Mars. Models of the interior of Mars consistent with the moment of inertia determined by the Mars Pathfinder are not consistent with a bulk C1 chondrite Fe/Si ratio (Sohl and Spohn, 1997; Bertka and Fei, 1998a,b). Any internal structural model of Mars is constrained by the measured value of C and by the overall density of Mars.

We adopt a simple two-layer model for the Martian interior (see Schubert and Spohn, 1990). The density in each layer is constant. It is ρ_c in the core (of radius R_c) and ρ_m in the mantle (mantle thickness is $R_p - R_c$). Spherically symmetric structural models of a planet can only be constrained by the mean moment of inertia I which is an average of the three principal moments of inertia, one of which is the axial moment of inertia C . Thus, the values of I and C are slightly different. For simplicity, we constrain I by the inferred value of C .

**Table 14.5. Two-layer Structural Model of Mars for
 $M_p = 6,430 \times 10^{20} \text{ kg}$, $R_p = 3,390 \text{ km}$, and $I = 0.365 M_p R_p^2$
 (after Schubert and Spohn, 1990)**

x_S	x_{FeS}	ρ_c (kg m^{-3})	ρ_m (kg m^{-3})	R_c (km)	p_{cm} (GPa)	p_c (GPa)
0.365	1.0	5,770	3,381.06	2,082.67	15.26	35.44
0.316	0.866	6,000	3,407.60	1,993.68	16.29	36.29
0.267	0.732	6,250	3,429.01	1,911.61	17.24	37.19
0.222	0.608	6,500	3,445.40	1,841.18	18.05	38.07
0.180	0.494	6,750	3,458.37	1,779.81	18.75	38.93
0.141	0.387	7,000	3,468.92	1,725.66	19.38	39.77
0.105	0.288	7,250	3,477.68	1,677.37	19.93	40.60
0.071	0.196	7,500	3,485.08	1,633.93	20.44	41.42
0.040	0.109	7,750	3,491.43	1,594.56	20.90	42.24
0.010	0.028	8,000	3,496.93	1,558.63	21.32	43.05
0	0	8,090	3,498.74	1,546.44	21.46	43.34

With R_p assumed known, the mean density and moment of inertia constraints provide two equations for the three variables R_c , ρ_c , and ρ_m of the two-layer structural model. We can thus determine R_c and ρ_m as functions of the structural model parameter ρ_c . We assume that the core is a mixture of Fe and FeS and use the mass fraction of S in the core x_S as a model parameter alternate to ρ_c (H and C could also have been incorporated into the Martian core: Zharkov, 1996; Bertka and Fei, 1998b). The mass fraction of FeS in the core x_{FeS} (FeS undergoes a phase transformation to FeS-III at the pressures in the Martian core) is related to ρ_c by

$$x_{\text{FeS}} = 1 - \frac{1 - \rho_c / \rho_{\text{FeS}}}{\rho_c / \rho_{\text{Fe}} - \rho_c / \rho_{\text{FeS}}} \quad (14.3.1)$$

where $\rho_{\text{Fe}} = 8,090 \text{ kg m}^{-3}$ and $\rho_{\text{FeS}} = 5,770 \text{ kg m}^{-3}$ are the densities of Fe and FeS, respectively. The sulfur concentration x_S is related to the FeS concentration by

$$x_S = 0.365 x_{\text{FeS}} \quad (14.3.2)$$

where 0.365 is the ratio of the atomic weights of S and S + Fe.

The parameters ρ_c , ρ_m , R_c , p_{cm} (pressure at the core–mantle interface), and p_c (central pressure) of the two-layer structural model of Mars are given in Table 14.5 for different assumed values of the mass fraction of sulfur in the core. The values of x_S range from 0 for a pure Fe core to 0.365 for a pure FeS core. The radius of the model core increases with x_S , while ρ_c , ρ_m , p_{cm} , and p_c all decrease with an increase in x_S . Large, sulfur-rich, low-density cores, or small, sulfur-poor, high-density cores are consistent with the known mean density and moment of inertia constraints on Mars (see also Folkner et al., 1997a, b; Sohl and Spohn, 1997).

14.3.3 The Martian Lithosphere

Large-scale patterns of tectonic deformation on a planetary surface can be direct signatures of global thermal evolution. For a planet with a globally continuous lithosphere, such as

Mars, warming or cooling of the interior will give rise to net global expansion or contraction and thus, respectively, to extensional or compressional horizontal stress and strain near the planetary surface. The magnitude σ_t of thermal stress accumulated in any time interval is given by

$$\sigma_t = [E/(1 - \nu)] (\Delta R/R) \quad (14.3.3)$$

where E and ν are the Young's modulus and Poisson's ratio of near-surface material, and $\Delta R/R$ is the fractional change in radius during that time interval (Solomon, 1986). The fractional radius change is related to the radial distribution of temperature change $\Delta T(r)$ by

$$\Delta R/R = (1/R^3) \int_0^R r^2 \alpha(r) \Delta T(r) dr \quad (14.3.4)$$

where α is the volumetric coefficient of thermal expansion. For $\alpha = 3 \times 10^{-5} \text{ K}^{-1}$, a change ΔT in average interior temperature of 100 K yields $\Delta R/R = 10^{-3}$ or $\Delta R = 3 \text{ km}$. From (14.3.3), with $E = 80 \text{ GPa}$ and $\nu = 0.25$, such a radius change corresponds to $\sigma_t = 100 \text{ MPa}$ (1 kbar). Sufficiently large thermal stress and strain should be visible in globally distributed tectonic features whose timing and sense of deformation yield strong constraints on the history of internal temperatures (see, e.g., Solomon and Chaiken, 1976). Large-scale tectonic features confined to a regional, rather than global, scale are also important indicators of thermal evolution, particularly of the characteristics of heat and strain imparted to the lithosphere by mantle dynamic processes.

Much of the evidence for lithospheric extension on Mars is provided from tectonic features in and near the Tharsis area. Although the extensional fractures radiating from the center of Tharsis span a region more than 8,000 km across, Tharsis may nonetheless be regarded as a regional feature rather than part of a response to global stress. Further, there are important compressional features located in the ridged plains of Tharsis and oriented approximately circumferential to the center of activity (Wise et al., 1979b). Considerable effort has gone into understanding the evolution of the Tharsis province from this regional perspective. The long-wavelength gravity and topography of the region are not consistent with complete isostatic compensation by a single mechanism, such as crustal thickness variations (Phillips and Saunders, 1975). Complete local isostasy is possible, however, if a combination of Airy (crustal thickness variations) and Pratt (mantle density variations) mechanisms act in concert; but this is possible only if the crust is relatively thin (or is pervasively intruded by high-density plutonic material) beneath the Tharsis Rise and substantial density anomalies persist to at least 300–400 km depth (Sleep and Phillips, 1979, 1985; Finnerty et al., 1988). Alternatively, a portion of the high topography of Tharsis can be supported by membrane stresses in the elastic lithosphere (Banerdt et al., 1982; Willemann and Turcotte, 1982).

These compensation models have been used to predict lithospheric stresses for comparison with the observed distribution of tectonic features. The isostatic model for Tharsis predicts stresses in approximate agreement with the distribution and orientation of extensional fractures in the central Tharsis region and of compressive wrinkle ridges, while the model involving lithospheric support of a topographic load predicts stresses consistent with the more distal extensional features in regions adjacent to the Tharsis Rise (Sleep and Phillips, 1985). An evolution in the nature of the support of Tharsis topography has been suggested (Banerdt et al., 1982; Solomon and Head, 1982), though the sequence depends upon the relative ages of distal and proximal tectonic features. If the distal features are older, then viscoelastic relaxation of stresses associated with an early episode of lithospheric loading

may have led to an essentially isostatic state at present; if the distal features are younger, then a progression from local isostasy to lithospheric support as the Tharsis Rise was constructed may have been the natural consequence of global interior cooling and lithospheric thickening (Sleep and Phillips, 1985). This distinction is complicated by the fact that superimposed global thermal stress is apparently required to account for the formation of many of the graben and wrinkle ridges, particularly in regions where both types of features are present.

The Martian tectonic history most consistent with all of these findings is one in which Tharsis evolved after the end of heavy bombardment from a primarily isostatic state to one with long-term lithospheric support. Superimposed on the stresses associated with the Tharsis Rise was a globally compressive stress produced by significant interior cooling in the interval 3–4 Gyr ago. Any additional cooling (or warming) in the last 3 Gyr has been sufficiently modest so that further changes in planetary volume have not led to widespread development of young compressive (or extensional) features.

Estimates of lithospheric thickness on Mars provide important constraints on near-surface thermal gradients and thus on heat flux. The thickness of the thermal lithosphere may be inferred approximately from the heights of volcanic constructs, and the thickness of the elastic lithosphere may be inferred from the response to volcanic loads.

Question 14.19: What is the thickness of the Martian lithosphere?

Volcanic constructs on Mars show a tendency to increase in height with time of formation, in that the oldest such features are a few kilometers high and the youngest shields are approximately 20 km high with respect to surrounding terrain (Carr, 1974; Blasius and Cutts, 1976). This relationship has been ascribed to an increase in the hydrostatic head of the magma with time because of a progressive deepening of the source region (Vogt, 1974; Carr, 1976). Assuming a relative density contrast of 10% between magma and average overburden, and ignoring viscous head loss, these heights give depths to magma chambers varying from perhaps as little as a few tens of kilometers to somewhat over 200 km over the history of Martian shield formation.

The thickness l of the elastic lithosphere of Mars has been estimated from the tectonic response to individual loads (Thurber and Toksöz, 1978; Comer et al., 1985) and from the global response to the long-wavelength load of the Tharsis Rise (Banerdt et al., 1982; Willemann and Turcotte, 1982). The spacing of graben circumferential to the major volcanoes Ascraeus Mons, Pavonis Mons, Arsia Mons, Alba Patera, and Elysium Mons indicates values for T_e of 20–50 km – equivalently, values of flexural rigidity D of 10^{23} – 10^{24} N m (10^{30} – 10^{31} dyn cm) at the times of graben formation (Comer et al., 1985). For the Isidis basin region, the elastic lithosphere thickness is inferred to have exceeded 120 km ($D > 10^{25}$ N m) at the time of mascon loading and graben formation (Comer et al., 1985). The absence of circumferential graben around Olympus Mons requires the elastic lithosphere to have been at least 150 km thick ($D > 3 \times 10^{25}$ N m) at the time of loading (Thurber and Toksöz, 1978; Comer et al., 1985; Janle and Janssen, 1986). Models of the response of Mars to the long-wavelength topography of the Tharsis Rise provide a reasonable fit to the geoid and to the distribution of tectonic features in the Tharsis province if the elastic lithosphere of Mars is globally ~ 100 –400 km thick, corresponding to $D = 10^{25}$ to 7×10^{26} N m (Banerdt et al., 1982; Willemann and Turcotte, 1982).

The values for l_e derived for individual loads are not consistent with a simple progressive increase with time in the thickness of the elastic lithosphere of Mars. The largest estimates of l_e , for instance, are for perhaps the oldest (Isidis mascon) and youngest (Olympus Mons) features considered (Tanaka et al., 1988). Spatial variations in elastic lithosphere thickness must have been at least as important as temporal variations (Comer et al., 1985). In particular, there appears to have been a dichotomy in lithosphere thickness that spanned a significant interval of time, with comparatively thin elastic lithosphere ($l_e = 20\text{--}50\text{ km}$) beneath the central regions of major volcanic provinces and substantially thicker elastic lithosphere (l_e in excess of 100 km) beneath regions more distant from volcanic province centers and appropriate for the planet as a whole.

The values of l_e may be converted to estimates of the lithospheric thermal gradient and heat flow, given a representative strain rate and a flow law for ductile deformation of material in the lower lithosphere and estimates of lithospheric thermal conductivity. Under the assumption that the large values of elastic lithosphere thickness determined from the local response to the Isidis mascon and Olympus Mons and from the global response to the Tharsis Rise exceed the thickness of the Martian crust, the depth to the base of the mechanical lithosphere is determined by the ductile strength of the mantle. The minimum values of l_e for the Isidis mascon and Olympus Mons correspond, by this line of reasoning, to mean lithospheric thermal gradients of no greater than $5\text{--}6\text{ K km}^{-1}$ and heat flow values $< 17\text{--}24\text{ mW m}^{-2}$ (Solomon and Head, 1990). For the Tharsis Montes and Alba Patera, the mechanical lithosphere thickness is likely governed by the strength of crustal material. The mean thermal gradients consistent with the values of l_e for these loads under this assumption fall in the range $10\text{--}14\text{ K km}^{-1}$ and heat flow values in the range $25\text{--}35\text{ mW m}^{-2}$ (Solomon and Head, 1990). Essentially contemporaneous temperature differences of at least 300 K at 30–40 km depth are implied at a late stage in the development of the Tharsis province. Such temperature differences are too large to be solely the effect of large impacts that occurred some Gyr earlier (Bratt et al., 1985), but they are similar to the temperature variations associated with lithospheric reheating beneath hot spot volcanic centers on Earth (McNutt, 1987). The temperature and heat flow anomalies beneath the central regions of major volcanic provinces on Mars are presumably also related to mantle dynamic processes, such as convective upwelling plumes and magmatism. Lithospheric thinning beneath the central regions of major volcanic provinces by hot, upwelling mantle plumes can account for the different estimates of elastic lithosphere thickness in these regions as compared with the global average.

14.3.4 Radiogenic Heat Production

Of particular importance to the thermal evolution of Mars are the concentrations of the radiogenic heat-producing elements K, Th, and U in the Martian mantle. Estimates of the abundances of these elements have been made by Taylor (1986), Treiman et al. (1986), and Laul et al. (1986) using SNC meteorites. Taylor (1986) plots analyses of the meteorites on a K/U versus K diagram and shows that the SNC meteorite data are consistent with terrestrial data. The K/U ratio in Mars is not distinguishable from the Earth's, but this analysis does not yield information on the bulk K abundance in Mars.

Treiman et al. (1986) and Laul et al. (1986) have estimated abundances of K, Th, and U using their correlation with other refractory lithophile elements. The database used by the two sets of authors is substantially the same. Correlations of K with La show that the mantle of Mars has a K/La ratio of ~ 0.3 of the CI ratio. The corresponding Th/La and U/La ratios are ~ 1.7 and 2 times the CI ratio, respectively (Treiman et al., 1986). Uncertainties

Table 14.6. Radiogenic Element Abundance Estimates for the Mantles of Mars and Earth

Planet	K (ppm)	Th (ppb)	U (ppb)	K/U	Th/U
Mars ^a	170	48	16	10^4	3
Mars ^b	315	56	16	2×10^4	3.5
Earth ^c	257	102	25.7	10^4	4

^a Treiman et al. (1986).

^b Laul et al. (1986).

^c Turcotte and Schubert (1982).

in each estimate are factors of 2, 1.7, and 2, respectively. The abundances of K, Th, and U, assuming that the Martian mantle has CI abundances of La, are summarized in Table 14.6. If the Martian mantle has higher abundances of La, the abundance of K, Th, and U must be scaled upward accordingly. The bulk Martian abundances must be reduced in proportion to the mass of the core, assuming that these elements are excluded from the core. The ratios of K/U and Th/U are $\sim 10^4$ and 3, respectively, the former being indistinguishable from the Earth's ratio while the latter is lower than the terrestrial value of ~ 4 . There is uncertainty in each ratio of about a factor of 2 based on the scatter in the raw data and the lack of knowledge of the absolute values of refractory-element abundances such as La in Mars relative to CI chondrites. Given the uncertainties in these values, we conclude that radiogenic element abundances in the mantles of Mars and Earth are similar.

14.3.5 Martian Thermal History: Effects of Crustal Differentiation

The acceptance of Mars as the parent body of the SNC meteorites (Bogard et al., 1984; McSween, 1985) changed our view of the planet's evolution. Martian thermal history models of the late 1970s and early 1980s were largely dominated by the idea that the core of Mars formed subsequent to its accretion, after radioactive heating had raised the temperatures in the planet's interior sufficiently above the relatively cold initial temperatures to initiate melting and gravitational separation of Fe–FeS (Solomon and Chaiken, 1976; Johnston and Toksöz, 1977; Toksöz and Hsui, 1978b; Solomon, 1979; Davies and Arvidson, 1981). Core formation in these models occurred as late as a few Gyr after Mars accreted, and the segregation of the core lasted for up to 1 Gyr. Late core formation was supported by the notion that Martian surface geology was dominated by extensional tectonics (e.g., formation of the Valles Marineris canyon system), requiring global heating and planetary expansion until late in the planet's evolution. However, the U/Pb isotopic composition of SNC meteorites requires core formation at about 4.6 Gyr ago (Chen and Wasserburg, 1986), either contemporaneous with accretion or within a few 100 Myr of the end of accretion. Thermal evolution scenarios of Mars with cold initial temperatures and late core formation are not possible; instead, accretional heating raised temperatures inside Mars sufficiently high that the core formed early, prior to the end of accretion or within a few 100 Myr thereof and Mars began its post-accretional evolution fully differentiated and hot. Early Mars was similar to the larger terrestrial planets Venus and Earth, whose cores formed early as a consequence of high accretional temperatures. Early core formation in a hot Mars is further supported by the discovery of remanent magnetization in the ancient crust of the southern hemisphere

highlands (Acuña et al., 1999; Connerney et al., 1999). The southern hemisphere crust must have been magnetized in a magnetic field generated by a dynamo in the molten metallic core of Mars during the first several hundred million years of Martian evolution (Acuña et al., 1999; Connerney et al., 1999).

Heat transport by subsolidus mantle convection must have played an important role in the cooling of Mars from its hot, fully differentiated initial state. The internal convective activity was somehow responsible for the creation of the north–south crustal dichotomy (Smith and Zuber, 1996; Smith et al., 1999a), the Tharsis Rise, the center of mass–center of figure offset (dominated by a nearly 3 km southward shift of the center of figure from the center of mass along the polar axis) (Esposito et al., 1992; Schubert et al., 1992; Smith et al., 1999a), and global tectonic patterns (Banerdt et al., 1992). A core dynamo existed for perhaps the first 500 Myr of Martian history, after which Mars had cooled sufficiently for either the core dynamo to cease operating or the mantle to cease producing lavas whose cooling could record an existing magnetic field (Acuña et al., 1998, 1999; Connerney et al., 1999). Mars does not have a magnetic field at present (Acuña et al., 1998, 1999), so the core dynamo has not survived the passage of time. The persistence of mantle convection in Mars to the present depends on the extent to which the interior has been depleted of radiogenic heat sources by crustal differentiation.

Effects of crustal differentiation on planetary thermal history have been studied by Schubert et al. (1992) and Spohn (1991). Crustal formation is an important influence on planetary thermal history because the process of forming the crust by magmatism and volcanism removes heat-producing radiogenic elements from the mantle and concentrates them in the crust. The reduction in mantle heat sources allows the mantle to cool more rapidly and increases the lithosphere thickness. This in turn decreases mantle magmatism and crustal production, processes which occur proportionately with mantle convective vigor. In this section we present the simple crustal differentiation parameterization discussed in Schubert et al. (1992) appropriate to crustal formation on one-plate planets such as Mars where crustal recycling is likely to be minimal. A more sophisticated crustal differentiation model would be needed for Earth to account for crustal recycling by such processes as subduction of oceanic crust and subduction of sediments. For Earth, crustal growth is usually taken to mean growth of the continental crust (Taylor and McLennan, 1985), whereas for application to Mars, the model of this section refers to a primary basaltic crust. Our model assumes no crustal recycling, although even on a one-plate planet like Mars processes such as delamination (Bird, 1979) could recycle some crust back into the mantle. From the perspective of planetary thermal history, crustal recycling remixes radiogenic heat sources back into the mantle. Crustal recycling may have been important even on one-plate planets such as Mars in the early phases of evolution as is assumed by Spohn (1991), who limits early crustal growth to the growth of the lithosphere.

As a consequence of irreversible basaltic crustal differentiation, the decrease with time in the specific radiogenic mantle heat production rate H is assumed to be given by

$$\frac{dH}{dt} = -\lambda H - \frac{\chi u}{R_p} H \quad (14.3.5)$$

where λ is the radioactive decay rate, χ is a crustal fractionation parameter, and u is a mean convective velocity in the mantle. The parameter χ is the ratio of the characteristic turnover time for mantle convection to the characteristic time for crustal fractionation. The first term on the right side of (14.3.5) is the ordinary radioactive decay term.

If χ is sufficiently large, then the planet can be fully differentiated. The parameter f is introduced to specify the mass fraction of the mantle that is available as crust. A simple mass balance that ignores the volume of the core gives the maximum crustal thickness $l_{cr,max}$ as

$$l_{cr,max} = \frac{f\rho_m R_p}{3\rho_{cr}} \quad (14.3.6)$$

where ρ_{cr} is the density of the crust. With $f = 0.1$, $\rho_m = 3,940 \text{ kg m}^{-3}$, $\rho_{cr} = 2,900 \text{ kg m}^{-3}$, and $R_p = 3,398 \text{ km}$ (Schubert et al., 1992), (14.3.6) gives $l_{cr,max} = 154 \text{ km}$.

A radiogenic element mass balance relates the thickness of the evolving crust l_{cr} to the specific radiogenic mantle heat production rate according to

$$\frac{l_{cr}}{l_{cr,max}} = 1 - \frac{H}{H_{ne}} \quad (14.3.7)$$

where H_{ne} is the mantle radiogenic heat production rate in the absence of crustal differentiation (given by the right side of (14.2.2)). In writing (14.3.7) it has been assumed that the mantle radiogenic heat source density is zero when all the crust has been extracted from the mantle and that the concentration of radiogenic elements in the crust is a constant (except for radioactive decay).

Lithosphere thickness l in the crustal differentiation model of Schubert et al. (1992) is calculated on the basis of steady conductive heat flow across l :

$$l = \frac{T_{\text{lithos}} - T_s}{(R_p/3) \{ \rho_m H/k - (1/\kappa) dT/dt \}} \quad (14.3.8)$$

where T_{lithos} is the temperature at the base of the lithosphere, T_s is the surface temperature, k is thermal conductivity, and κ is thermal diffusivity. The denominator on the right side of (14.3.8) is related to the heat flow from the mantle (see (13.2.3), for example) and T is the temperature of the mantle in this one-layer thermal history model. In writing (14.3.8) it is assumed that heat-producing elements in the crust are sufficiently near the surface that they do not influence the conductive gradient in the lithosphere. The calculation of lithosphere thickness from (14.3.8) is only approximate; integration of (13.3.3) through time provides a more accurate determination of l .

The volumetric rate of addition of magma to the crust dV_{cr}/dt can be determined from the rate of change of crustal thickness by

$$\frac{dV_{cr}}{dt} = 4\pi R_p^2 \frac{dl_{cr}}{dt} \quad (14.3.9)$$

The crustal thermal history model can also provide the record of planetary radius as a function of time from

$$\frac{\Delta R_p}{R_p} = -\frac{\alpha}{3} \left\{ T(t=0) - T \left(1 - \frac{3}{2} \frac{l}{R_p} \right) \right\} + \frac{l_{cr} \Delta \rho}{3l_{cr,max}} \quad (14.3.10)$$

where $\Delta \rho = \rho_m - \rho_{cr}$ (Schubert et al., 1992). The first term on the right side of (14.3.10) represents the decrease of planetary radius with time due to cooling of the mantle and is calculated from (14.3.4), where the integration is over the entire body, including the conductive lithosphere. The second term on the right side of (14.3.10) represents the increase in volume of the planet due to formation of a low-density crust.

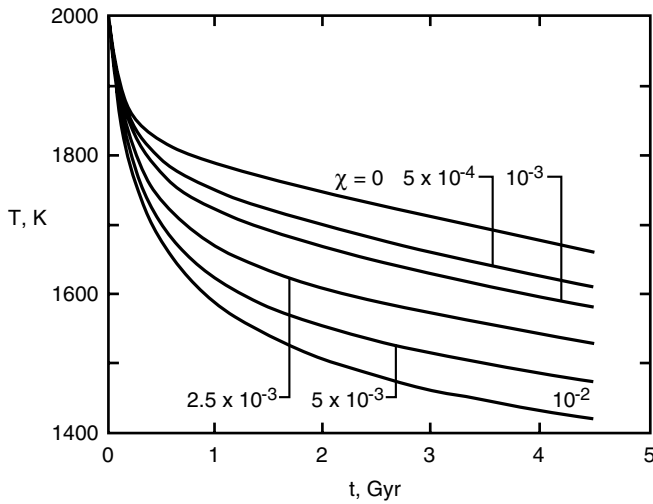


Figure 14.30. Mean temperature of the Martian mantle versus time for different values of the crustal fractionation parameter χ (after Schubert et al., 1992). Crustal formation cools a planet by removing heat sources from the interior to the surface.

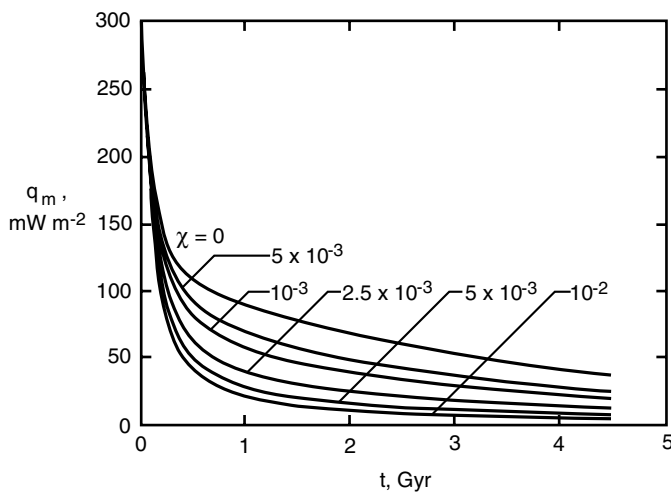


Figure 14.31. Heat flux from the mantle versus time in the Mars thermal history model with crustal differentiation for several values of χ (after Schubert et al., 1992). The decrease in mantle heat flux with increasing χ is due to the removal of mantle heat sources to the crust.

The consequences of crustal differentiation on the thermal evolution of a planet such as Mars can be determined by coupling the equations of this section with a thermal history model for the dependence of mean mantle temperature T on time. Schubert et al. (1992) carry this out for a simple one-layer thermal history model similar to that of Section 14.2. Their results are presented in Figures 14.30–14.35 for the following parameter values: $\kappa = 10^{-6} \text{ m}^2 \text{ s}^{-1}$, $k = 4 \text{ W m}^{-1} \text{ K}^{-1}$, $T_{\text{lithos}} = 1,000 \text{ K}$, $T_s = 255 \text{ K}$, $T(t = 0) = 2,000 \text{ K}$, $\alpha = 3 \times 10^{-5} \text{ K}^{-1}$, $\Delta\rho = 80 \text{ kg m}^{-3}$, $\lambda = 2.77 \times 10^{-10} \text{ yr}^{-1}$, and $H_0 = 2.47 \times 10^{-11} \text{ W kg}^{-1}$.

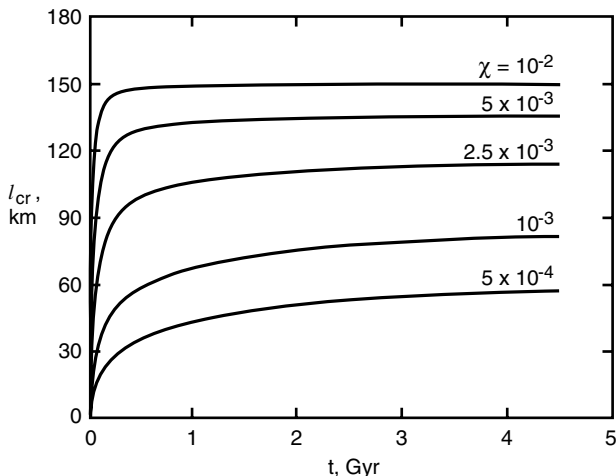


Figure 14.32. Crustal thickness as a function of time for different values of the crustal fractionation parameter χ in a Mars thermal history model (after Schubert et al., 1992). Crustal production occurs mainly in the first few hundred million years of planetary evolution.

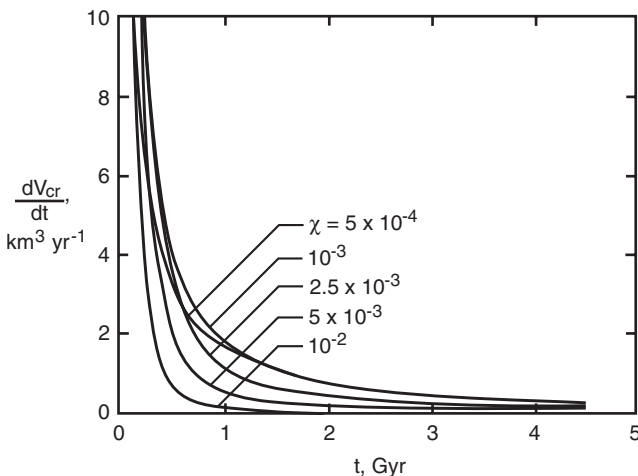


Figure 14.33. The volumetric rate of crustal growth versus time in the Mars thermal history model with χ as a parameter (after Schubert et al., 1992). Crustal production rates are large early in the thermal evolution and they fall to small values and decline very slowly after about 1 Gyr.

The effect of crustal formation on mean mantle temperature is shown in Figure 14.30 for values of the crustal fractionation parameter χ between 0 and 10^{-2} . The values of χ are based on an estimate of χ for the Earth. Oceanic crust on the Earth is created at a rate of about $3 \text{ km}^2 \text{ yr}^{-1}$ (Turcotte and Schubert, 1982). If the formation of oceanic crust involves melting of mantle material to a depth of about 60 km, then the mantle is processed at a rate of about $180 \text{ km}^3 \text{ yr}^{-1}$. Since the volume of the Earth's mantle is about $9 \times 10^{11} \text{ km}^3$, the characteristic mantle fractionation time is about $9 \times 10^{11} \text{ km}^3 / 180 \text{ km}^3 \text{ yr}^{-1} = 5 \text{ Gyr}$. With a characteristic mantle convection speed $u = 0.1 \text{ m yr}^{-1}$ and $R_p = 6 \times 10^3 \text{ km}$ (about twice the mantle thickness), the characteristic mantle turnover time is $6 \times 10^3 \text{ km} / 0.1 \text{ m yr}^{-1} = 60 \text{ Myr}$. From

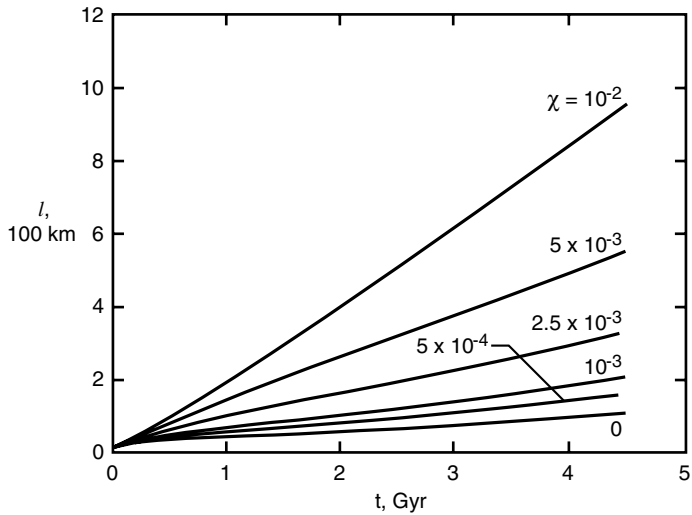


Figure 14.34. Lithosphere thickness as a function of time in the thermal history of Mars with crustal differentiation for several values of the crustal fractionation parameter (after Schubert et al., 1992). Crustal formation tends to thicken the lithosphere by enhanced planetary cooling due to upward removal of heat sources from the mantle to the surface crust.

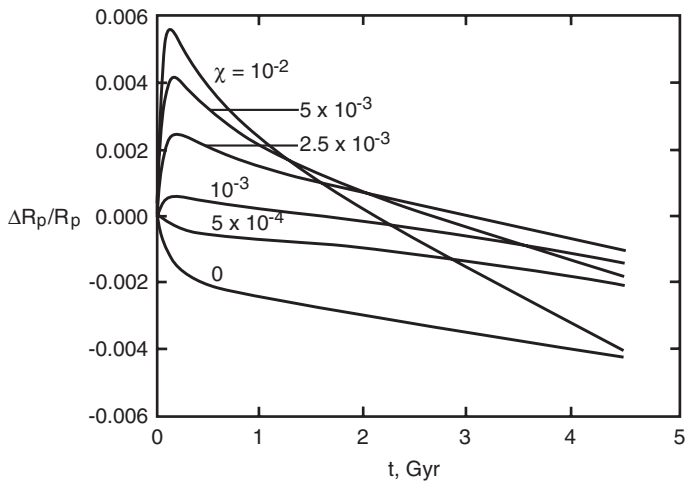


Figure 14.35. Fractional change in planetary radius with time in the Martian thermal evolution model with crustal differentiation for several values of the crustal fractionation parameter χ (after Schubert et al., 1992). The increase in planetary radius with time in the models with crustal production ($\chi \neq 0$) is due to global expansion accompanying early crustal formation. The decrease in planetary radius with time in all models is due to global contraction upon planetary cooling.

In the discussion following (14.3.5), χ is the ratio of these two time scales, $60 \text{ Myr} / 5 \times 10^3 \text{ Myr}$, or about 10^{-2} . Mantle convection is likely less vigorous in Mars than it is in the Earth (Schubert, 1979) and χ for Mars is probably less than about 10^{-2} . The model treats χ as a constant, although it has undoubtedly varied during planetary thermal evolution. In particular, χ may have been larger than 10^{-2} on Earth and Mars early in the evolution of

these bodies when they were hotter and more vigorously convecting and degrees of partial melting in the mantle were larger.

Crustal differentiation decreases mantle temperature (Figure 14.30) and heat flux from the mantle (Figure 14.31) because it removes heat sources from the mantle to the surface, where essentially direct heat loss from the surface can occur. The model predicts a drop in the present temperature of the Martian mantle by up to about 200 K for χ as large as 10^{-2} .

Crustal thickness as a function of time for different values of χ is shown in Figure 14.32. According to the model, most of the Martian crust is produced in the first few hundred million years of evolution; crustal production rates fall to very low values after the initial period of rapid crustal growth (Figure 14.33). For χ as large as 10^{-2} , present crustal thickness reaches as much as 150 km.

The crustal thickness on Mars has been estimated using gravity data and the assumption of Airy isostasy. For Hellas Planitia, as noted above, Sjogren and Wimberley (1981) estimated that the depth of compensation is 130 km. Using similar data and assumptions for the crater Antoniadi, Sjogren and Ritke (1982) found that the depth of compensation is 115 km. From gravity profiles across the highland–lowland escarpment, Janle (1983) found that the depth of compensation is also 115 km. Taking the present crustal thickness to be $D_c = 120$ km, we find from Figure 14.32 that the corresponding crustal fractionation factor is $\chi = 0.003$, about a factor of 3 less than for the Earth. This estimate of χ is uncertain because of the poorly constrained value of the mean crustal thickness on Mars.

Accepting, for purposes of discussion, that the crustal fractionation factor for Mars is $\chi = 0.003$, we can determine rates of crustal addition from Figures 14.32 and 14.33. The average amount of crust added in the last 1 Gyr was 600 m, that added between 1 and 2 Gyr ago was 1.8 km, and that added between 2 and 3 Gyr ago was 2.9 km. The volumetric rate of crustal magmatism was much higher early in the evolution of Mars. The decline to the lower values of crustal production rate characteristic of most of Martian geologic history occurred with about a 100 Myr time scale.

The most recent volcanism on Mars during the Upper Amazonian Period (Tanaka, 1986; Tanaka et al., 1992) occurred in the Arcadia, Olympus Mons, Medusae Fossae, and Tharsis Montes Formations, but the principal volcanics are flood basalts in the southern Elysium Planitia. These have an area of 10^5 km^2 , but Tanaka (1986) suggests that the thickness is only a few tens of meters. For a thickness of 50 m, this is only 0.03 m when averaged over the surface of Mars.

Greeley (1987) has estimated that $26 \times 10^6 \text{ km}^3$ of volcanics erupted during the Middle and Upper Amazonian. This corresponds to a mean thickness of 200 m when averaged over the entire surface of Mars. From the estimate of cratering rates given by Hartmann et al. (1981), the Upper Amazonian extended from 0 to 0.7 Gyr ago and the Middle Amazonian from 0.7 to 2.3 Gyr ago. Thus, the volume of young volcanics on Mars is broadly consistent with the model results above as volcanism represents only a part of crustal addition. It should be emphasized, however, that there are considerable uncertainties in the absolute ages (Strom et al., 1992) and in the crustal fractionation parameter.

The growth of the lithosphere with time in the thermal history model of Mars with crustal differentiation is depicted in Figure 14.34. A present lithosphere thickness of only about 100 km is predicted by the model for no crustal production ($\chi = 0$). This thickness is at least a factor of 2 smaller than estimates of Martian lithosphere thickness from observations of surface tectonic deformation (Schubert et al., 1992). Figure 14.34 shows how crustal formation results in considerable thickening of the lithosphere as a consequence of enhanced planetary cooling due to upward differentiation of mantle heat sources. Lithosphere thicknesses

of several hundred kilometers to as much as 900 km for $\chi = 0.01$ are predicted by the model. Depletion of mantle heat sources by crustal production in the model of this section leads to lithospheres of comparable thickness to those predicted by the models of Schubert et al. (1979a) that contained no internal heating in the mantle. However, the calculation of lithosphere thickness in the Martian thermal history model of Spohn (1991) with crustal differentiation gives much thinner lithosphere. Nevertheless, lithospheres at least about 200 km thick, as required by geological inference, are predicted by Martian thermal history models, although such a thick lithosphere in the model of Spohn (1991) is due more to an assumed smaller value of mantle radioactivity than to depletion of mantle heat sources by crustal differentiation.

Other predictions of the calculations using $\chi = 0.003$ are a lithospheric thickness $l = 400$ km and a net global contraction corresponding to $\Delta R_p/R_p = -0.001$. From Figure 14.35 we see that a global expansion of $\Delta R_p = 10$ km occurred in the first 200 Myr of the evolution of Mars. This expansion was caused by the density change associated with the generation of the early crust. For the remainder of the evolution of Mars, a nearly steady contraction occurred associated with the cooling of the interior. The total contraction subsequent to the period of early crustal differentiation was $\Delta R_p = -13$ km. All models in Figure 14.35 with substantial crustal fractionation show an early period of planetary expansion followed by a larger amount of planetary contraction.

As noted earlier, large-scale surface tectonic features of Mars include both extensional and compressional structures. The graben systems in and near the Tharsis region are likely the result of stresses generated by the Tharsis load. Compressive wrinkle ridges occur commonly throughout ancient terrains. These can be attributed to the phase of thermal contraction illustrated in Figure 14.35.

14.3.6 Martian Thermal History: Magnetic Field Generation

As is the case for Venus, the present absence of an intrinsic magnetic field (Acuña et al., 1998, 1999) is a major constraint on Martian thermal history. Early magnetic field measurements from the Mars 2, 3, and 5 spacecraft were interpreted by Dolginov et al. (1973, 1976) and Dolginov (1987) to imply that Mars had a small magnetic field with a dipole moment 3×10^{-4} times the Earth's magnetic dipole moment, tilted about 15° with respect to the rotation axis of Mars and oriented in the opposite sense to the Earth's magnetic dipole. However, Russell (1978a,b) and Russell et al. (1984) challenged this interpretation of the data and concluded that if Mars had a magnetic field, then its dipole moment would be less than about 3×10^{-5} times the Earth's magnetic dipole moment. Phobos spacecraft observations of the Martian magnetotail gave no indication of an intrinsic planetary magnetic field (Riedler et al., 1989). Data from the Mars Global Surveyor (Acuña et al., 1998, 1999) have settled the question of the existence of a global Martian magnetic field – there is none, but the crust of Mars has strong concentrations of remanent magnetism implying that Mars had a global magnetic field in the past (Acuña et al., 1999; Connerney et al., 1999). Crustal magnetization on Mars is mainly confined to the ancient highlands of the southern hemisphere (Acuña et al., 1999), and it is largely organized into east–west-trending linear features of alternating polarity extending over distances as large as 2,000 km (Connerney et al., 1999). The magnetization features are reminiscent of the magnetic stripes on the Earth's seafloor, and suggest the possibility of a plate tectonic regime with seafloor spreading early in the history of Mars (Connerney et al., 1999). The absence of crustal magnetism near large impact basins such as Hellas and Argyre implies that the early Martian dynamo ceased to operate about 4 Gyr

ago (Acuña et al., 1999). We use this knowledge of the Martian magnetic field, together with the coupled core–mantle thermal history model of Chapter 13 (Stevenson et al., 1983), to further investigate possible scenarios for the thermal evolution of Mars. The thermal history model of Stevenson et al. (1983) has been extended and applied to Mars by Schubert and Spohn (1990), and the discussion of this section relies heavily on the latter paper and the review of Martian thermal history by Schubert et al. (1992). The thermal history model of Mars we have already discussed includes crustal differentiation but not core evolution. The thermal evolution model discussed next includes the history of the Martian core but does not account for crustal differentiation.

The application of the thermal history model of Stevenson et al. (1983) to Mars requires that the planet is initially hot and completely differentiated into a superliquidus core and a mantle essentially at its solidus temperature. We have already discussed the evidence that supports this view of Martian thermal history. The major evidence for an initially hot and differentiated Mars is the acceptance of Mars as the parent body of the SNC meteorites (Becker and Pepin, 1984; Bogard et al., 1984; McSween, 1985), the whole-rock Rb–Sr model ages for SNC meteorites of about 4.6 Gyr (Shih et al., 1982), the U/Pb isotopic composition of SNC meteorites requiring core formation about 4.6 Gyr ago (Chen and Wasserburg, 1986), the old age (≥ 4 Gyr) of the southern hemisphere highlands suggesting early crustal differentiation, and the magnetization of this ancient southern hemisphere crust (Acuña et al., 1998, 1999). Other evidence of a hot early Mars includes water-carved features in the Martian surface (Carr, 1987, 1996a, b) suggesting early outgassing and an early atmosphere (see also Owen, 1992), and global ridge systems (Chicarro et al., 1985) suggesting planetary cooling over geologic time. The case for an early hot Mars is discussed at length by Schubert et al. (1992).

Parameter values for the Martian thermal history calculations of this section are those of Schubert and Spohn (1990) and are summarized in Table 14.7. The model uses a core liquidus temperature of 1,880 K for minor constituent (sulfur) core concentration by weight percent $x = 0$ and $p(r) = 0$, close to the 1 bar melting point of pure iron. The parameterization of the core melting temperature is based on the data of Liu and Bassett (1975) for the melting of iron at high pressure. The choice of the core adiabat is for the Grüneisen γ of Stacey (1977b). For a small planet such as Mars, the adiabatic temperature difference across the mantle is small and the value of η_m for the mantle (see (13.3.8)) is assumed to be unity. Abundances of radiogenic elements in the Martian mantle inferred from SNC meteorite data (Laul et al., 1986; Taylor, 1986; Treiman et al., 1987) are similar to radiogenic element concentrations in the Earth’s mantle, so the model uses the same mantle heat source density parameters for the Mars thermal history calculations as used in the Earth thermal history models (Tables 13.2 and 14.7).

Mars is a one-plate planet with a lithosphere that has thickened with time during the course of its thermal evolution (Solomon, 1978; Schubert et al., 1979a). The model already discussed provided an example of lithosphere thickening in Figure 14.34. In the model presently under discussion, the equation for lithosphere thickening is (Schubert et al., 1979a; Spohn and Schubert, 1982b, 1983)

$$\rho_m c_m (T_u - T_{\text{lithos}}) \frac{dl}{dt} = -q_m + k \left(\frac{\partial T}{\partial z} \right)_{z=l} \quad (14.3.11)$$

where T_{lithos} is the temperature of the lower boundary of the lithosphere, l is the lithosphere thickness, q_m is the heat flow from the convecting mantle (q_s in (13.3.6)), z is depth, and T_u is the average mantle temperature defined in (13.3.8). Equation (14.3.11) equates the difference in heat flow into the base of the lithosphere from the convective mantle and out of the base

Table 14.7. Parameter Values for Thermal History Models of Mars

Parameter	Value
<i>Global Parameters</i>	
Radius	3,389 km
Mass	$6,430 \times 10^{20}$ kg
Acceleration of gravity	3.7 m s^{-2}
<i>Core Parameters</i>	
Liquidus temperature (K)	$T_m(r) = 1,880(1 - 2x)(1 + 1.36 \times 10^{-11}P(r) - 6.2 \times 10^{-23}P^2(r))$
Adiabat (K)	$T_c(r) = T_{cm}(r) \frac{\{1 + 8.0 \times 10^{-12}P(r) - 3.9 \times 10^{-23}P^2(r)\}}{\{1 + 8 \times 10^{-12}P_{cm} - 3.9 \times 10^{-23}P_{cm}^2\}}$
Thermal conductivity	$40 \text{ W m}^{-1}\text{K}^{-1}$
Latent heat per unit mass, L	0.25 MJ kg^{-1}
Gravitational energy per unit mass, E_g	0.25 MJ kg^{-1}
η_c	1.1
<i>Mantle Parameters</i>	
Initial lithosphere thickness	1.4 km
Thermal conductivity	$4 \text{ W m}^{-1}\text{K}^{-1}$
Thermal diffusivity	$10^{-6} \text{ m}^2\text{s}^{-1}$
v_0	$4,000 \text{ m}^2\text{s}^{-1}$
A	52,000 K
Thermal expansivity	$2 \times 10^{-5} \text{ K}^{-1}$
Heat source density	$(1.7 \times 10^{-7}) \exp(-1.38 \times 10^{-17}t) \text{ W m}^{-3}$
η	1
ϵ	1
Critical Rayleigh number	500
Power law exponent in Nusselt number–Rayleigh number relation	0.3
<i>Initial Values and Boundary Values</i>	
Mantle temperature	2,573 K
Core–mantle boundary temperature	3,000 K
Surface temperature	220 K
Temperature at base of lithosphere	1,073 K
<i>Other Parameters</i>	
Number of grid points in lithosphere	100

of the lithosphere by upward conduction to the energy released or needed to convert hotter mantle into colder lithosphere or vice versa. The lithosphere defined here is a rheological lithosphere and T_{lithos} is the temperature below which rocks do not deform on a geologic time scale (taken as 1073 K in Table 14.7). On a one-plate planet, the lithosphere does not participate in mantle convection and the effective ‘surface’ temperature for this parameterized mantle convection calculation is T_{lithos} . Heat transfer in the lithosphere is by conduction and the surface temperature T_s listed in Table 14.7 is the actual average surface temperature on Mars. Schubert and Spohn (1990) couple a numerical finite difference solution of (14.3.11) with the solution of the parameterized mantle convection problem. The thermal lithosphere

of Mars, comprising both the rheological lithosphere and the underlying thermal boundary layer of mantle convection, is thicker than the rheological lithosphere.

The cooling of the Martian mantle and the thickening of its lithosphere with time are illustrated by the model results of Figures 14.36–14.38 for mantle temperature, mantle heat flux, and lithosphere thickness, respectively. These characteristics of the mantle and lithosphere are insensitive to the concentration of sulfur in the core. During the first several hundred million years of evolution, when the planet is hot and convecting particularly vigorously, there is a dramatic decrease in mantle temperature and heat flow (Figures 14.36 and 14.38). Following the early period of rapid cooling is a phase of gradual, slow cooling lasting most of the geologic life of the planet. The present mantle heat flow in these models is about 30 mW m^{-2} . The present surface heat flow is about 40 mW m^{-2} . Because of lithosphere thickening and cooling, surface heat flow is approximately 10 mW m^{-2} larger than the present mantle heat flow.

The lithosphere in this model thickens with time, reaching a present thickness of about 100 km (Figure 14.38), in agreement with the previous model for $\chi = 0$. We have already

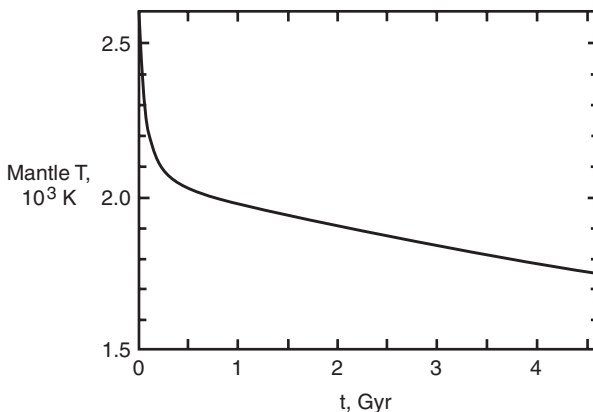


Figure 14.36. Mantle temperature versus time from the Martian thermal history model of Schubert and Spohn (1990).

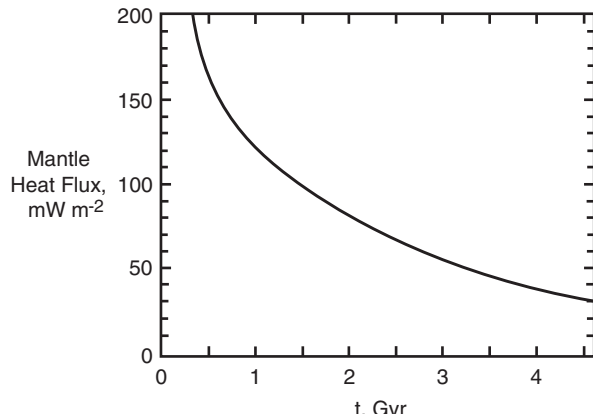


Figure 14.37. Heat flux from the mantle as a function of time for a model Martian thermal history (after Schubert and Spohn, 1990).

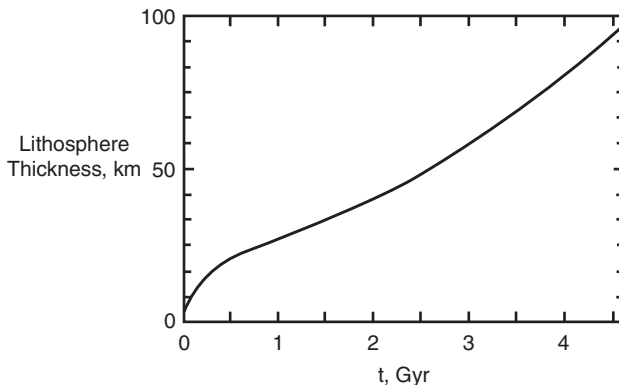


Figure 14.38. Thickening of the lithosphere with time during the model thermal evolution of Mars (after Schubert and Spohn, 1990).

noted that this is smaller, by perhaps a factor of 2 or more, than estimates of Martian lithosphere thickness based on tectonic deformation of the surface (Schubert et al., 1992). Present model lithosphere thickness could be increased by assuming a smaller mantle heat source density, but one still consistent with estimates of mantle heat source concentration from SNC meteorite data, and by accounting for upward differentiation of radiogenic heat sources from the mantle into the crust (as in the previous model, Figure 14.34) and magmatic heat transfer across the lithosphere (Spohn, 1991; Schubert et al., 1992). The present lithosphere thickness calculated in the models of Schubert et al. (1979a) is representative of maximum thicknesses since these models contained no mantle heat sources.

The thermal history of the Martian core depends strongly on its sulfur content. Though geochemical modeling based on the compositions of SNC meteorites suggests core sulfur concentrations of 12–14 wt% (Laul et al., 1986; Treiman et al., 1987), the value of x_S for the Martian core must be considered uncertain. Figure 14.39 illustrates the sensitivity of Martian core thermal evolution to the initial weight percent of sulfur in the core x_S by the time history of core heat flux for two values of x_S , 7 and 14%. There is a rapid loss of heat from the core during the first several hundred million years of core thermal evolution that is not emphasized by the plot of Figure 14.39, which focuses instead on the later phase of more gradual cooling. The sudden change in the rate of core cooling at about 750 Myr for $x_S = 0.07$ marks the onset of inner core solidification. With $x_S = 0.14$, there is no freezeout of an inner core. When inner core solidification occurs, the rate of decline in heat flow from the core is reduced because of latent heat and gravitational potential energy release, the latter occurring as a consequence of the exclusion of the light element S from the growing inner core and the concentration of S in the shrinking liquid outer core.

The dashed curve in Figure 14.39 represents the heat flux conducted along the core adiabat. When core heat flux falls below this curve, thermal convection can no longer be sustained within the core. This occurs in the model with $x_S = 0.14$ at about a time $t = 2.2$ Gyr. In this model, there would be no thermal convection in the core and no dynamo action and magnetic field generation after about 2.2 Gyr. Thermal convection in the core of the model with $x_S = 0.07$ is possible beyond $t = 4.6$ Gyr. In this model, core convection after $t = 750$ Myr is compositional as well as thermal. Indeed, the compositionally driven convection (i.e., convection driven by the release of latent heat and gravitational potential energy on inner core solidification) is responsible for the relatively slow cooling of the core

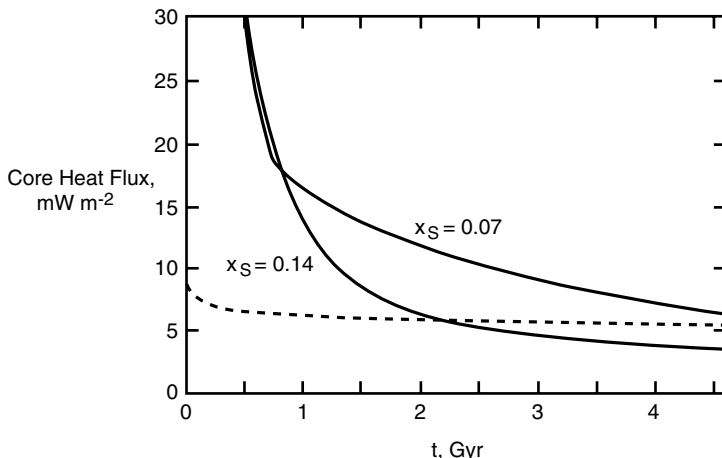


Figure 14.39. The decrease with time in heat flow from the core of the Martian thermal history model of Schubert and Spohn (1990) for two values of initial weight percent sulfur in the core $x_S = 7$ and 14%. The dashed curve is the heat flux conducted along the core adiabat. The sharp bend in the heat flux curve for $x_S = 0.07$ at $t \cong 750$ Myr marks the onset of inner core freezeout.

and the maintenance of the core heat flux above the critical value associated with conduction along the adiabat. Core convection in the $x_S = 0.07$ model could occur even after the core heat flux curve falls below the dashed curve (at some time $t > 4.6$ Gyr) as a consequence of chemical compositional buoyancy. Thermal convective transport during that time would actually be downward in the core, but compositional buoyancy would be more than adequate to offset the slightly stable state. Core convection, either thermal or compositional, could produce a magnetic field throughout the history of the model with $x_S = 0.07$. However, once the core heat flux falls below the conductive value along the adiabat, compositional convection driven by inner core freezing would be necessary for dynamo action and magnetic field generation. The Martian core thermal history with $x_S = 0.07$ is similar to the thermal evolution of the Earth's core in the model of Chapter 13. With $x_S = 0.14$, the Martian core evolves similarly to the core in the Venus model of Figure 14.25.

Initial core sulfur concentration x_S and mantle viscosity ν are the primary model parameters influencing core thermal history. Figure 14.40 shows how inner core growth in the Martian model depends on these parameters. Present inner core radius increases with decreasing x_S for a given ν , since decreasing x_S increases the core melting temperature resulting in earlier inner core freezeout and a longer period of inner core growth. Present inner core radius also increases with decreasing mantle viscosity at fixed x_S , since cooling is more rapid with lower ν again resulting in earlier inner core freezeout and a longer period of inner core growth. For mantle viscosity about $10^{16} \text{ m}^2 \text{ s}^{-1}$ (or about $3.5 \times 10^{19} \text{ Pa s}$ for a mantle density of $3,500 \text{ kg m}^{-3}$), 16 wt% is a good estimate of the minimum core sulfur concentration required for no core freezing through geologic time (see also Stevenson et al., 1983). However, with increasing mantle viscosity, the minimum core sulfur concentration for no core solidification through geologic time decreases; for $\nu = 5 \times 10^{16} \text{ m}^2 \text{ s}^{-1}$, the minimum x_S is about 10 wt%. Figure 14.40 indicates that relatively small, sulfur-poor Martian cores would be largely solid at present, while relatively large, sulfur-rich cores would be largely liquid at present.

Figure 14.41 shows normalized inner core radius versus time for three different initial S concentrations. Inner core growth is very rapid once freezeout begins; the inner core is almost

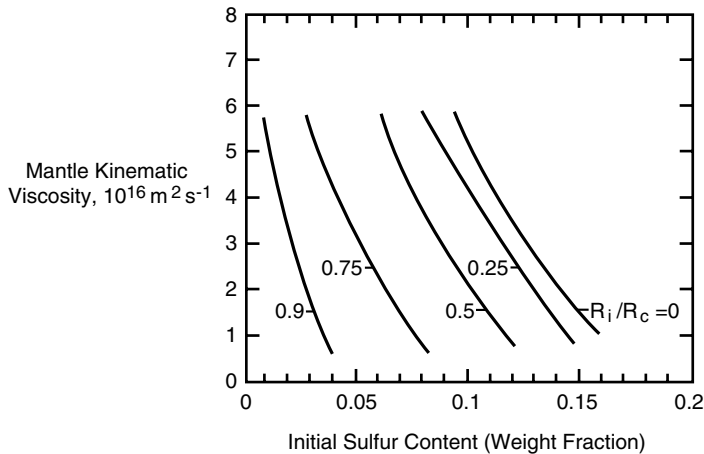


Figure 14.40. Contours of present normalized inner core radius for different values of mantle viscosity and initial weight percent of sulfur in the core (after Schubert and Spohn, 1990).

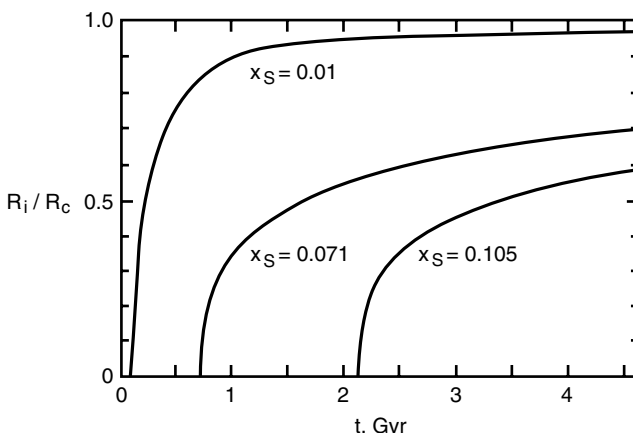


Figure 14.41. Fractional radius of the inner core as a function of time in the Martian thermal history model of Schubert and Spohn (1990) for three values of initial sulfur mass concentration x_S in the core. Inner core freezeout occurs rapidly near the onset of solidification and more slowly in the later stages of core evolution.

completely grown within about 1 Gyr of initial freezeout, particularly when core solidification occurs early, as is the case for small x_S . The depression of the melting temperature in the outer core as the sulfur concentrates there with progressive inner core growth and the slowing of the cooling rate as the planet evolves both contribute to the reduction in inner core growth rate with time. With increasing x_S , the time of initial core freezeout is delayed and present inner core radius decreases. Figure 14.40 shows that nearly complete core solidification at present requires $x_S \lesssim 0.01$, while the present core is nearly all liquid if $x_S \gtrsim 0.11$.

We can use (13.3.16) and (13.3.17) together with the Martian thermal history model to estimate the evolution of the Martian magnetic dipole moment μ_M from the equation

$$\frac{\mu_M}{\mu_E} = 10^{-9} (R_c - R_{ic}) (\Phi)^{1/2} (R_c + R_{ic})^{3/2} \quad (14.3.12)$$

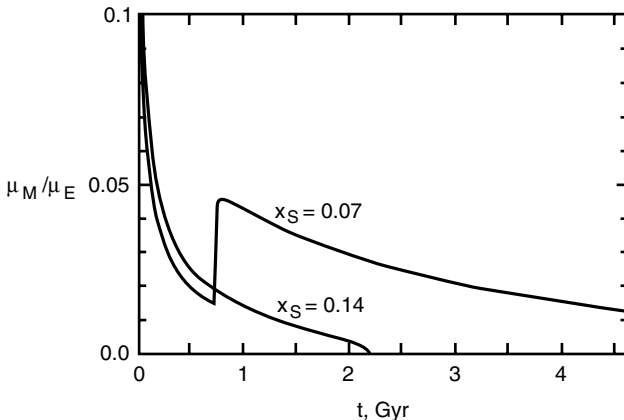


Figure 14.42. Evolution of the normalized Martian magnetic dipole moment from (14.3.12) for two values of core sulfur concentration (after Schubert and Spohn, 1990). The sudden jump in μ_M / μ_E at about 750 Myr for $x_S = 0.07$ coincides with initiation of inner core solidification. No dynamo action is possible after about 2.2 Gyr in the model with $x_S = 0.14$ since thermal convection in the core of this model does not occur subsequent to 2.2 Gyr and there is no inner core freezeout in the model.

(see Schubert et al., 1988, and Schubert and Spohn, 1990), where μ_E is the Earth's present magnetic dipole moment, R_{ic} is the inner core radius (in km), R_c (core radius) is in units of km, and Φ , the power associated with Ohmic dissipation in the Martian core, has units of TW (it has been assumed that the present value of Φ in the Earth's core is 2.5 TW, Schubert and Spohn, 1990). The results of applying (14.3.12) to the Martian thermal history model are shown in Figure 14.42 for $x_S = 0.07$ and 0.14. The magnetic dipole moment decreases rapidly during the first several hundred million years of evolution following the early rapid cooling of the planet and the rapid decline in core heat flow. With $x_S = 0.07$, there is a sudden increase in μ_M at about 750 Myr coincident with inner core formation. Prior to 750 Myr, the model dynamo is driven by thermal convection in the core; subsequent to 750 Myr the dynamo is driven by both thermal and chemical compositional convection as the inner core solidifies and releases gravitational potential energy.

With $x_S = 0.14$ there is no inner core solidification and the dynamo is driven solely by thermal convection until about $t = 2.2$ Gyr when dynamo action ceases because the core heat flux falls below the conductive heat flux along the core adiabat and thermal convection can no longer occur in the core. There is no present magnetic field in this model of Martian evolution because thermal convection is not possible in the present liquid core and there is no source of chemical convection in the core.

If the estimates of Laul et al. (1986) and Treiman et al. (1987) of 14 and 12.5 wt% sulfur in the Martian core reflect the actual sulfur content of the core, then the previous results (e.g., Figures 14.41 and 14.42) suggest that the present Martian core is all liquid or contains only a small solid inner core and the lack of a present magnetic field is due to the absence of thermal convection in a completely liquid core or the inefficient operation of a compositionally driven dynamo in the presence of a small solid inner core. With this amount of sulfur in the core, thermal convection would have driven a dynamo during the first two billion years of Mars' history, thereby allowing for the magnetization of the ancient Martian crust as required by observations of crustal remanent magnetization on Mars (Acuña et al., 1998, 1999). If x_S in the Martian core is larger than the Laul et al. (1986) and Treiman et al.

(1987) estimates, the lack of a present Martian magnetic field is explained by the absence of thermal convection in an entirely liquid core, similar to the probable cause of the lack of a magnetic field on Venus. In this case too, a core dynamo driven by thermal convection could have magnetized the crust of Mars early in its evolution. If x_S in the Martian core is less than the estimates of Laul et al. (1986) and Treiman et al. (1987), then the absence of a present Martian magnetic field requires nonoperation of a compositionally driven dynamo in a partially to nearly solidified core (Young and Schubert, 1974). Here again, there is no difficulty in accounting for crustal remanent magnetization produced by an operative dynamo early in the history of Mars. However, none of the above models has dynamo action ceasing after only several hundred million years of Martian evolution, as has been suggested by Acuña et al. (1999) in order to explain the concentration of crustal magnetization in the southern hemisphere highlands and the lack of crustal magnetization near the large Hellas and Argyre impact basins.

Question 14.20: *What is the explanation for the absence, at present, of a Martian magnetic field?*

14.3.7 Martian Thermal History Models with a Stagnant Lid

Thermal history models of Mars, based on a parameterization of mantle heat transfer by stagnant-lid convection, have been explored by Reese et al. (1998, 1999). Stagnant-lid convection is a plausible state for the Martian mantle given that Mars is a one-plate planet with a thick lithosphere. The $Nu-Ra_i$ parameterization used by Reese et al. (1999) for the stagnant-lid Newtonian convection of a fluid with strongly temperature dependent viscosity is

$$Nu = \theta^{-1.6} Ra_i^{0.6} \quad (14.3.13)$$

where θ , the Frank–Kamenetskii parameter, is the natural logarithm of the viscosity contrast across the convecting layer due to the temperature dependence of the viscosity (this definition of θ applies if a linearized version of the Arrhenius law for the dependence of viscosity on temperature is used, see (13.5.8)) and Ra_i is based on the total temperature drop across the layer and the viscosity evaluated at the temperature of the interior. The Nusselt number is the ratio of the heat flux at the top of the layer to the conductive heat flux. Stagnant-lid convection occurs when the viscosity contrast across the layer due to the temperature change is very large (about 10^8 for non-Newtonian convection according to Reese et al. (1999) and about 10^4 – 10^5 for Newtonian convection, see (14.2.6)). The large viscosity near the surface causes a stagnant lid to form as shown in Figure 14.43. Within the stagnant lid the fluid velocity is zero, the temperature is conductive and varies linearly with depth, and the viscosity varies essentially exponentially with depth (Figure 14.43). Convection is mainly confined to the isothermal interior beneath the lid, but it penetrates the lid a short distance (θ^{-1} times the lid thickness); the effective temperature difference that drives interior convection is $\Delta T/\theta$, where ΔT is the total temperature drop across the layer (Figure 14.43). Most of the overall temperature drop occurs across the largely conducting stagnant lid and only a small fraction of ΔT is available to drive convection. Stagnant-lid convection has been discussed in more detail in Section 13.5.

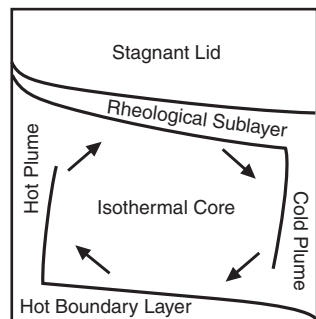
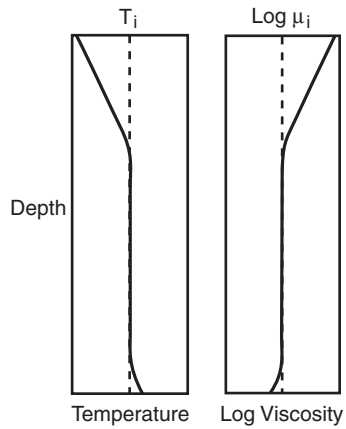


Figure 14.43. Schematic of stagnant-lid convection in a fluid heated from below with strongly temperature dependent viscosity. Modified from Reese et al. (1999).



The Reese et al. (1999) thermal history model of Mars also accounts for non-Newtonian rheological behavior (power-law viscosity or dislocation creep) and the removal of radiogenic heat sources to a crust formed by differentiation of the mantle. In accordance with model results described earlier, Reese et al. (1999) find that hot early Mars models undergo substantial crustal differentiation within a few hundred million years at the onset of evolution and substantially deplete their interiors of radiogenic heat sources. The rest of the evolution subsequent to crustal formation involves a steady decline of mantle temperature and a thickening of the lithosphere to present values of around 500 km.

Grasset and Parmentier (1998) have presented another thermal history model of Mars based on the parameterization of mantle heat transfer by stagnant-lid convection in an internally heated fluid layer with strongly temperature dependent viscosity. Their approach to the parameterization of stagnant-lid convective heat transfer has been summarized in Section 13.5. Their model gives a substantially thicker lithosphere at present than the models discussed above, in agreement with the thickness of the Martian lithosphere inferred from observations (Figure 14.44). They attribute the thicker lithosphere in their model to the requirement that the temperature of the base of the lithosphere decreases in time together with the mantle temperature so as to maintain through time about a factor of 10 contrast in viscosity between the base of the lithosphere and the convecting mantle. The Martian thermal history models with thinner lithospheres (discussed above) assumed a fixed temperature at the lithosphere base throughout time. A possible difficulty in applying a stagnant-lid convection parameterization to Mars throughout its thermal history is that early Mars may not have been in the stagnant-lid convection regime.

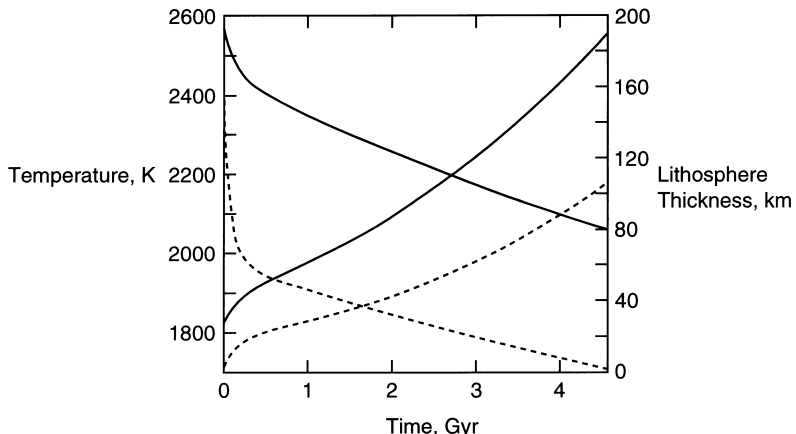


Figure 14.44. Mantle temperature and lithosphere thickness versus time in a Martian thermal history calculation by Grasset and Parmentier (1998). Mantle temperature decreases with time and lithosphere thickness increases with time. The model with higher temperature and thicker lithosphere (solid lines) allows the basal lithosphere temperature to decrease with time to maintain a viscosity contrast across the convecting mantle of about a factor of 10. The other model (dashed lines) assumes a fixed temperature at the base of the lithosphere.

14.3.8 Convection Patterns in Mars

Numerical calculations of fully three dimensional convection in a spherical shell have been carried out by Schubert et al. (1990) to simulate possible convective planforms in the Martian mantle. These results have important implications for proposed convective origins of major geologic features on Mars, such as the crustal dichotomy. In the model of Schubert et al. (1990), the spherical shell Martian mantle consists of a Boussinesq fluid that is heated both internally and from below to account for secular cooling, radiogenic heating, and heat flow from the core. The lower boundary of the shell is assumed to be isothermal and stress free, as appropriate to the interface between the mantle and a liquid outer core. The upper boundary of the shell is rigid and isothermal, as appropriate to the base of a thick, immobile lithosphere. The ratio of the inner radius of the shell to its outer radius is 0.55, in accordance with possible core radii in Mars. We discuss results for two different modes of heating. In one case, 20% of the surface heat flow originates in the core, and in the other case the percentage of heating from below is 94%. The Rayleigh numbers of both cases are approximately 100 times the critical Rayleigh numbers that characterize the onset of convection in the constant viscosity spherical shells. These Rayleigh numbers may be an order of magnitude or more smaller than the Rayleigh number of the Martian mantle. However, the Rayleigh number of the Martian mantle is unknown because of uncertainties in the thickness of the mantle and its material properties, viscosity in particular. Other uncertainties include the thickness of the lithosphere and the extent of depletion of the mantle's radiogenic heat sources. The numerical approach is described in detail in Glatzmaier (1988) and Bercovici et al. (1989b). Table 14.8 lists the parameter values for the calculations discussed here.

The horizontal planforms of convection for both modes of heating are illustrated in Figure 14.45 by contours of radial velocity on spherical surfaces midway through the shells. Meridional cross-sections of entropy contours (equivalent to isotherms in these Boussinesq calculations) for both heating modes are shown in Figure 14.46. The prominent form of

Table 14.8. Parameter Values for Three-dimensional Spherical Convection Models of the Martian Mantle

Outer radius	3,200 km
Inner radius	1,762 km
Density	$3,450 \text{ kg m}^{-3}$
Core mass	$1,490 \times 10^{20} \text{ kg}$
Kinematic viscosity	$10^{18} \text{ m}^2 \text{ s}^{-1}$
Thermal diffusivity	$10^{-6} \text{ m}^2 \text{ s}^{-1}$
Specific heat at constant pressure	$1.2 \text{ kJ kg}^{-1} \text{ K}^{-1}$
Thermal expansivity	$2 \times 10^{-5} \text{ K}^{-1}$
Temperature difference across the mantle	800 K
Internal heating rate (94% from below)	$1.5 \times 10^{13} \text{ W kg}^{-1}$
Internal heating rate (20% from below)	$5.3 \times 10^{12} \text{ W kg}^{-1}$

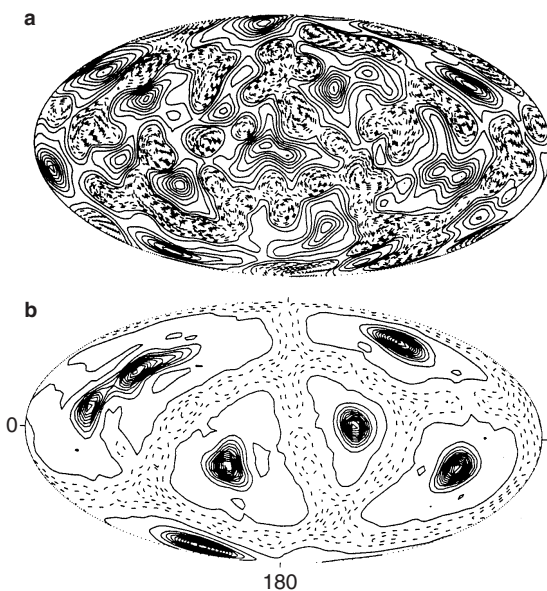


Figure 14.45. Contours of radial velocity at mid-depth in the Martian mantle in numerical models of three-dimensional mantle convection with (a) 20% and (b) 94% heating from below. The projection is an equal-area projection extending 360° in longitude and over all latitudes. Model parameter values are listed in Table 14.8 (after Schubert et al., 1990). Solid contours indicate radially outward motion, and dashed contours denote radially inward motion.

upwelling in the Martian mantle is the cylindrical plume. The number of upwelling plumes is strongly influenced by the mode of heating; with only 20% heating from below, there are a dozen plumes, while 94% bottom heating produces only six plumes. There are fewer, stronger plumes as the proportion of bottom heating increases. Plumes carry the heat flow from the core and arise from instability of the lower thermal boundary layer at the core–mantle interface. In general, the fraction of mantle heating delivered from the core has probably decreased with time as the core cooled to temperatures not much greater than those of the

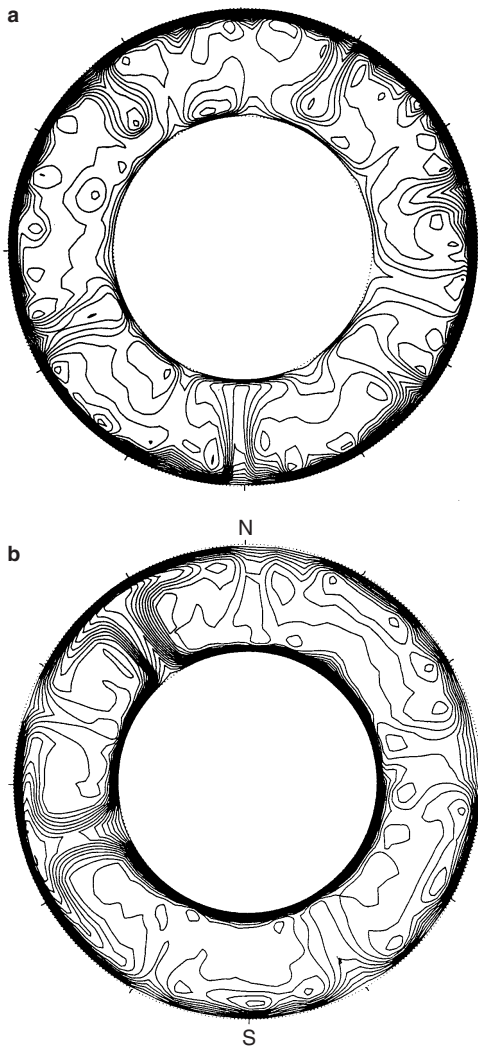


Figure 14.46. Meridional cross-sections of temperature in the numerical models of Figure 14.45 for (a) 20% and (b) 94% heating from below.

lower mantle (see, e.g., Figure 14.39). The isotherm cross-sections of Figure 14.46 show several plumes originating in the lower thermal boundary layer. Convective downwelling occurs in planar sheets that form an interconnected network surrounding the upwelling plumes. The downwellings also show cylindrical concentrations along the sheets and even distinct cylindrical downwellings.

The patterns of Figure 14.45 have evolved through many overturns of the mantle and the solutions appear to be fundamentally time dependent. However, the basic nature of the convective planform, i.e., cylindrical upwelling plumes surrounded by planar downwelling sheets, does not change with time. Thus, we can expect major volcanic provinces on Mars, like Tharsis and Elysium, to reflect the cylindrical nature of upwelling mantle plumes, similar to hot spots on the Earth. There are no sheet-like upwelling features in the Martian mantle to produce a pattern similar to the linear global system of mid-ocean ridges on the Earth. Even the mid-ocean ridges on the Earth are not connected to deep sheet-like

upwellings in the Earth's mantle (Bercovici et al., 1989a). The deep upwellings in models of convection in the Earth's mantle are also cylindrical plumes. The Earth's mid-ocean ridges are shallow, passive upwellings occurring in response to the tearing of lithospheric plates by the pull of descending slabs (Bercovici et al., 1989a). The nonviscous rheology of the Earth's lithosphere is essential for the occurrence of plate tectonics. Mars is a one-plate planet with a thick lithosphere (Solomon, 1978; Schubert et al., 1979a) beneath which mantle upwellings are in the form of cylindrical plumes.

The results of the spherical convection models have implications for proposed explanations of the crustal dichotomy and the concentrations of volcanism at Tharsis and Elysium. If the crustal dichotomy was caused by a convective system dominated by spherical harmonic degree $l = 1$ (Lingenfelter and Schubert, 1973; Schubert and Lingenfelter, 1973; Wise et al., 1979a) with upwelling under the northern hemisphere, then convection must have been driven strongly from below. Such strong heating concentrated deep within Mars can arise from the heating pulse accompanying core formation or from the flow of heat from a hot core. Indeed, the overturning accompanying core formation could in itself be an $l = 1$ mode (Stevenson, 1980), obviating the need for a thermally driven motion.

Core size is another important factor in determining the number of convective plumes. With smaller cores there is a tendency toward fewer upwelling plumes (Zebib et al., 1983). This is confirmed by the results of Figure 14.47, which shows mid-depth radial velocity contours and isotherms in meridional cross-section in the mantle of a Mars model with a core radius of 0.2 times the radius of Mars (too small for present Mars but perhaps relevant for early Mars) (Schubert et al., 1990). The model has settled into a predominantly $l = 2$ (not $l = 1$, however) convection pattern. During the early stages of core formation, the effective core radius would have been smaller than the radius at present, favoring a thermally forced convection with perhaps just one dominant upwelling. Since the Martian core formed contemporaneously with accretion or within a few 100 Myr of the end of accretion, conditions favoring $l = 1$ convection, i.e., a small core and a deep heat source, occur very early in the evolution of Mars. If a convective mechanism is responsible for the crustal dichotomy, then the dichotomy must also be a very ancient feature.

It is not obvious from the above models why there should be only two major volcanic centers (Tharsis and Elysium) on Mars. The models predict several to ~ 10 major mantle plumes. Perhaps the above models are not realistic enough to predict the actual number of major hot spots on Mars. On the other hand, there may be many plumes in the Martian mantle, but the properties of the lithosphere may select only one or two of them for prominent surface expression. Plume activity could be focused beneath Tharsis if fracturing or thinning of the lithosphere in this region has facilitated magma and heat transport across the lithosphere. The temperature dependence of mantle viscosity will strongly influence the structure of plumes and their number, through the control that variable viscosity exerts on the nature and vigor of small-scale convective activity in the lower thermal boundary layer (Olson et al., 1987).

Question 14.21: Why are there two major volcanic centers on Mars?

The numerical solutions discussed above can be used to infer that several kilometers of dynamic topography could be associated with plumes in the Martian mantle (Schubert et al., 1990). Dynamic uplift is insufficient to account for the 10 km of topography in the Tharsis

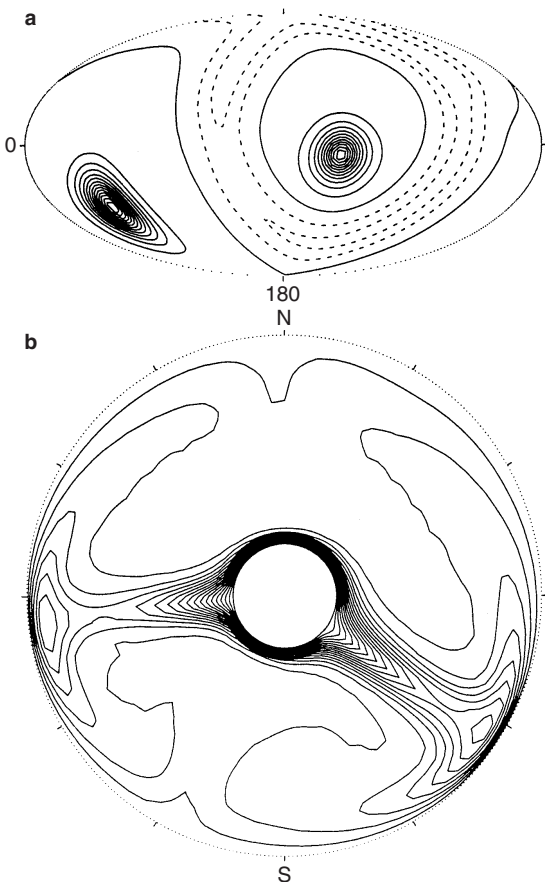


Figure 14.47. Panels (a) and (b) are similar to Figures 14.45 and 14.46 but for a small Martian core of radius 0.2 times the radius of Mars. In the model, 90% of the heating is from below.

region. This large topographic excess must be largely the result of other processes, such as volcanic construction, magmatic thickening of the crust, or depletion of the underlying mantle (see, e.g., Sleep and Phillips, 1979, 1985; Solomon and Head, 1982). Nevertheless, it is likely that the Tharsis Rise and its volcanic constructs are a consequence of a strong mantle plume (or grouping of plumes) beneath the region.

An explanation for the concentration of volcanism at Tharsis and Elysium on Mars might be found in the influence of major mantle phase transitions on the style of convection in the Martian mantle. The endothermic phase transition from spinel to perovskite and magnesiowüstite could occur near the base of the Martian mantle if the core in Mars is small enough. Harder (1998) estimates a depth of about 1,910 km for the endothermic phase transition in Mars. Thus, the phase transition could be present in Mars if its core is smaller than about 45% of the Martian radius. A core of this size is consistent with the cosmochemical estimate of around 14 wt% sulfur in the core, especially if account is taken of the high-density phase of FeS at high temperature and pressure found by Fei et al. (1995). Numerical simulations of three-dimensional spherical convection in the mantle of Mars

show that an endothermic phase change near the base of the mantle exerts a strong control on the style of Martian mantle convection (Harder and Christensen, 1996; Harder, 1998). The phase change imposes a convective pattern with only one or two strong mantle plumes. The number of plumes decreases with time during the evolution of Mars, consistent with a history of planetary volcanism that evolved from planet-wide to a single center of volcanism at Tharsis (Harder, 1998).

The endothermic phase change acts to suppress the upward passage of plumes emanating from the hot thermal boundary layer at the base of the mantle (Schubert et al., 1995) mainly due to the upward deflection of the phase change by the plume (Schubert et al., 1975). The extra amount of heavy material (perovskite) beneath the upwarped phase boundary relative to the undisturbed surroundings (spinel) produces a downward body force opposing the upwelling of the plume. Latent heat release contributes a positive buoyancy that promotes plume upwelling (Schubert et al., 1975), but phase boundary displacement is dominant in the dynamics, and the endothermic phase change acts to retard the plume (Schubert et al., 1995). Figure 14.48 shows the form of three-dimensional convection in models of Martian mantle convection with (right) and without (left) the endothermic phase change (Harder, 1998). The tendency of the phase change to suppress upwelling plumes focuses the hot material near the base of the mantle into fewer and more buoyant plumes that more readily penetrate through the phase change. Only two plumes dominate the final stages of the evolving flow in the calculation of Figure 14.48 that includes the endothermic phase change. Only one plume dominates the mantle flow in the late stages of the model shown in Figure 14.49 (left) which is at a higher Rayleigh number and has the phase change closer to the core–mantle boundary than the model of Figure 14.48 (Harder, 1998). The flow in the right panel of Figure 14.49 shows the effect of removing the endothermic phase transition from the model in the left panel. The focusing of the flow near the core–mantle boundary into a single upwelling plume by the phase change is evident. The focusing of mantle upwelling into a small number of plumes by a very deep endothermic phase change was demonstrated by Weinstein (1995) in a study carried out in two-dimensional, cylindrical geometry.

The influence of phase changes on Martian mantle convection has also been investigated by Breuer et al. (1996, 1997, 1998), who incorporated effects of the shallower olivine–spinel exothermic phase change in their models. The olivine to β -spinel and β -spinel to γ -spinel phase transitions occur deeper in the Martian mantle than in the Earth's mantle because of the smaller size of Mars and the lower pressures in its mantle. The olivine to β -spinel transition occurs at a pressure of about 13 GPa (at a radius of about 0.7 Mars radius or a depth of about 1,000 km) and the β -spinel to γ -spinel transition occurs at a pressure of about 18 GPa (near a radius of 0.6 Mars radius or a depth of about 1,350 km) (Bertka and Fei, 1996, 1997, 1998a, b; Sohl and Spohn, 1997; Spohn et al., 1998). The three-dimensional convection model of Breuer et al. (1998) shows that the exothermic phase changes alone can focus plume activity into one area by creating thermal barriers for weak plumes through the absorption of latent heat and consequent reduction of plume buoyancy (Schubert et al., 1975) (weak plumes tend to merge into stronger ones in order to penetrate the exothermic phase changes). They also point out that a deep perovskite layer in the lower mantle is more likely to exist early in the evolution of Mars when the mantle is hotter.

The importance of mantle phase transitions to the thermal history of Mars has been emphasized by Spohn et al. (1998), who point out that the phase transitions might not only focus mantle upwellings into one or two plumes but also provide a source of nonmonotonicity in Mars' thermal evolution and in the generation of a Martian magnetic field by dynamo action in the core of Mars. Phase transitions in the Martian mantle are responsible for

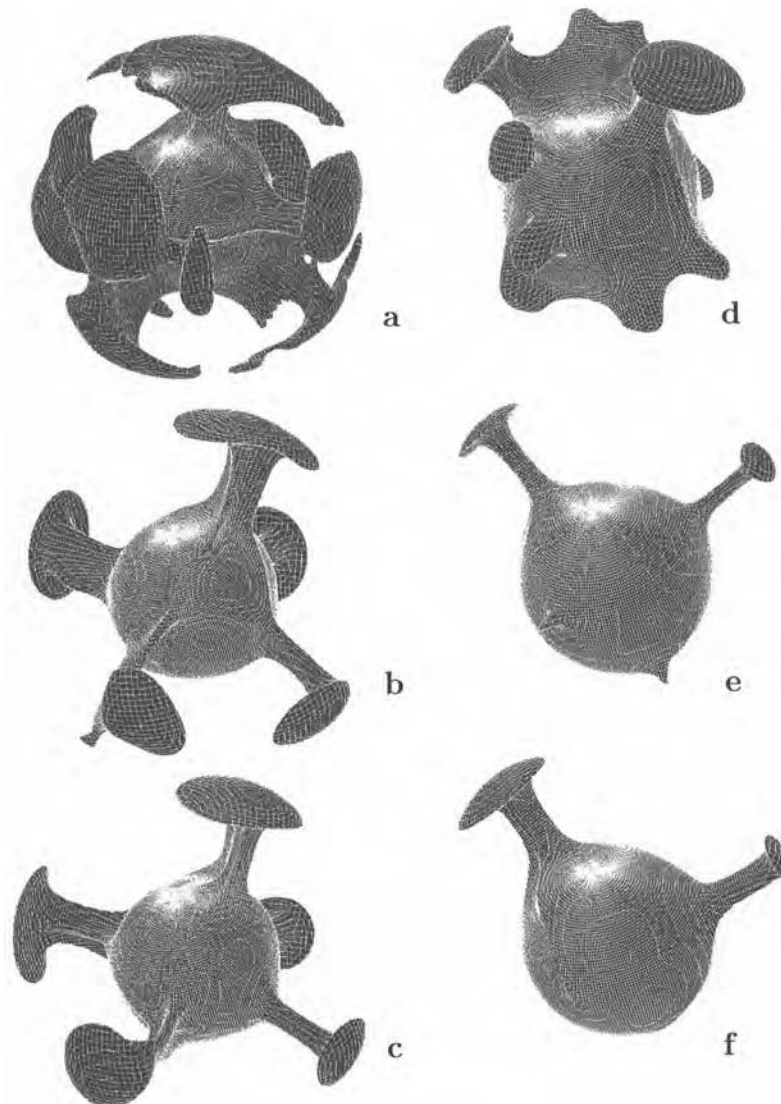


Figure 14.48. Temperature isosurfaces (nondimensional temperature = 0.55) in a model of Martian mantle convection with (right) and without (left) a deep endothermic phase transition. The phase boundary for the isosurfaces on the right is located a nondimensional height = 0.09 above the core–mantle boundary. Each plot represents a different time in the calculation with time increasing downward. The spherical shell model has an inner dimensionless radius = 0.4. Heating is both from within and from below with internal heating Rayleigh number = 10^6 and basal heating Rayleigh number = 2.5×10^5 . The upper and lower surfaces of the shell are isothermal. The lower surface is free-slip and the upper surface is no-slip. All material properties are constant. After Harder (1998).

enhanced temporal variability in models of Martian mantle convection. The modulation of core activity would occur through the regulation of heat loss from the core by the varying thermal conditions in the lower mantle of Mars. The temperature of the lower mantle of Mars and the heat flux from the core could change abruptly if the deep mantle endothermic

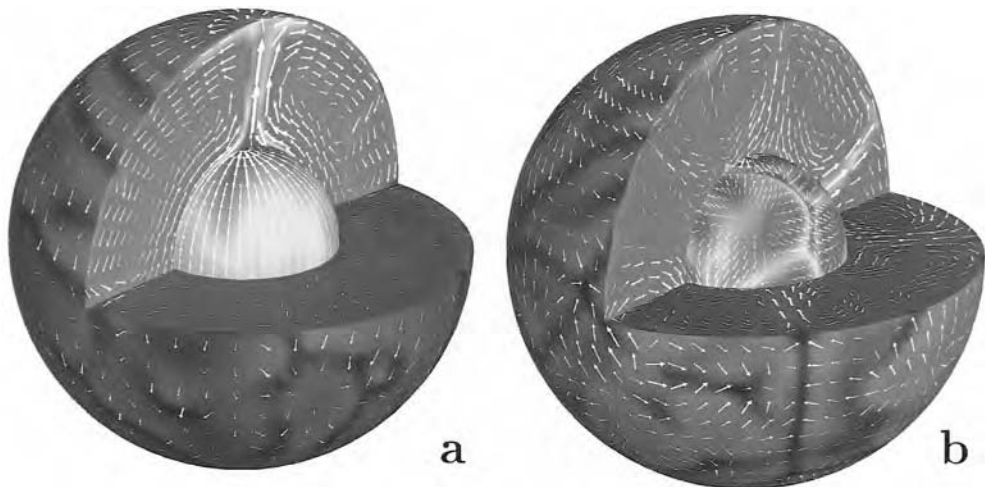


Figure 14.49. Cutaway views of the temperature and velocity field in a Martian mantle convection model with (a) and without (b) an endothermic phase change near the base of the model. The model is similar to the one described in Figure 14.48 except for the phase change which is only a nondimensional height of 0.04 (80 km) above the core–mantle boundary. In addition, the internal heating Rayleigh number is 6.5×10^6 and the basal heating Rayleigh number is 10^6 . Only one plume dominates the mantle flow when the phase change is present. After Harder (1998).

For a color version of this figure, see plate section.

phase change disappeared upon the cooling of Mars from its hot initial state. Whether the phase transition from spinel to perovskite occurs in the present Martian mantle is uncertain. Bertka and Fei (1996, 1997, 1998a) have determined the possible mineralogy of the Martian mantle from high-pressure experiments involving materials similar in composition to SNC meteorites. Their studies show that perovskite and magnesiowüstite can be present in the lower mantle of Mars. The existence of these dense silicate phases depends sensitively on mantle temperature, the overall composition of Mars, the thickness of the Martian crust, and the radius of the core.

Question 14.22: What is the structure of the Martian mantle?

14.3.9 Summary

Several general conclusions emerge from the studies of Martian thermal history and Martian mantle convection discussed in this section. The first is the hot initial state of the planetary interior and the sharp contrasts that can be drawn between the first 1 Gyr of Martian history and the subsequent 3.5 Gyr. As a result of accretional heating and core formation essentially contemporaneous with planetary formation, the early history of Mars was characterized by high internal temperatures, a vigorously convecting mantle, and high surface fluxes of heat and magma. Dynamo action in the core apparently generated a magnetic field in which the early crust was magnetized. Outgassing contributed to an early atmosphere, and widespread magmatism may have helped trigger the release of subsurface water and large-scale floods. Parameterized convection models indicate, however, that on a time scale of

only a few 100 Myr the mantle convective engine slowed, as primordial interior heat was lost and as radioactive heat production decayed or was concentrated into the shallow crust. Rapid interior cooling led to a globally thick lithosphere and was accompanied by global contraction, recorded in the pervasive formation of wrinkle ridges now preserved on ancient geologic units. The last 3.5 Gyr of Martian history was marked, in contrast, by slow cooling and by the concentration of volcanic and tectonic activity in ever more limited regions.

A second major conclusion of the above studies is the strong role of plumes expected for mantle convection in Mars. As long as a significant fraction of mantle heating comes from the core, three-dimensional convection calculations indicate that plumes dominate the upwelling portions of the flow. At least some of those plumes would be expected to have strong signatures in the surface topography and volcanic flux. The Tharsis and Elysium volcanic provinces are probably the consequences of plume-delivered heat and magma. The number and characteristics of plumes depend on the relative contributions of radioactivity and core cooling to the mantle heat budget, as well as the size of the core and the existence of major mantle phase transitions. Development of Tharsis and Elysium very early in Martian history, when core cooling occurred at its highest rate, is favored.

A third general conclusion to derive from the above studies is the dominating influence of core sulfur concentration on the thermal evolution of the core and the history of the Martian magnetic field. A core with more than ~ 15 wt% sulfur probably would not crystallize a solid inner core and probably would not be thermally convecting at present. This critical S concentration is tantalizingly close to estimates of the core sulfur content from elemental abundances of SNC meteorites. Therefore, a nearly completely fluid core that is nonconvecting or only weakly thermally or chemically convecting may provide an explanation for the lack of a present Martian magnetic field. Such a core would have been thermally convecting and could have sustained a dynamo in the past, providing a mechanism for magnetizing the crust and accounting for the remanent magnetization observed on Mars today.

Question 14.23: Is the core of Mars entirely liquid?

14.4 The Moon

14.4.1 *The Lunar Crust: Evidence from the Apollo Missions*

Early telescopic observations showed that the nearside of the Moon is composed of two types of surface: topographically low, dark areas referred to as maria (or seas) and topographically elevated, light areas known as highlands (Figure 14.50). This division has been illustrated in Figure 14.2. The highlands are more heavily cratered and were therefore presumed to be older because the flux of meteorites is known to have decreased with time. Because of its synchronous rotation with respect to the Earth, the farside of the Moon was first observed from spacecraft in lunar orbit. Highland terrain dominates the farside of the Moon; there are no extensive maria on the farside lunar surface.

The first manned landing on the Moon took place on 20 July 1969. This Apollo 11 mission as well as the subsequent Apollo 12, 15, and 17 missions landed on the lunar maria. Chemical studies of the rocks returned on these missions showed that the maria are composed of basaltic rocks similar in major element chemistry to the basalts of the oceanic crust. Radiometric dating of these rocks gives ages of 3.16–3.9 Gyr.



Figure 14.50. View of the lunar surface obtained by the Galileo spacecraft in 1992 on its way to the Jovian system. The distinct bright ray crater at the bottom of the image is the Tycho impact basin. The dark areas are basalt-covered regions Oceanus Procellarum (on the left) and basalt-filled impact basins, Mare Imbrium (center left), Mare Serenitatis and Mare Tranquillitatis (center), and Mare Crisium (near the right edge).

For a color version of this figure, see plate section.

The Apollo 14 and 16 missions returned samples from the lunar highlands. These rocks have a much more complex chemical history than the mare rocks. They have been extensively altered by meteorite bombardment. Detailed chemical studies have shown, however, that these rocks are highly fractionated igneous rocks. Radioactive dating of the highland rocks shows that they crystallized at about 4.5 Ga, close to the estimated age of the solar system.

The distribution of surface ages on the Moon is constrained by the age determinations made on the rocks returned during the Apollo project. The evolution of the Moon can be divided into three phases: (1) highlands formation, (2) mare formation, and (3) surface quiescence. The highlands of the Moon formed early in its evolution, one hypothesis being that they crystallized from a global magma ocean. The highland rocks returned during the Apollo missions are highly differentiated and greatly altered by surface bombardment. It is difficult to date the crystallization of the highlands exactly, but it certainly terminated

by 4.0 Ga and probably before 4.4 Ga. The terminal bombardment between 3.8 and 4.0 Ga resulted in the excavation of many large, deep basins. These basins, particularly on the nearside, were subsequently filled by mare basaltic volcanism. The lunar maria constitute some 17% of the surface area and, based on mare basalts returned during the Apollo missions, date between 3.8 and 3.1 Ga. These basalts strongly resemble typical terrestrial basalts in major element composition and were probably produced by pressure-release melting in ascending mantle flows.

One of the fundamental discoveries of the Apollo program was that the Moon is made up of a variety of igneous rock types that differ widely in both their chemistry and mineral composition (Heiken et al., 1991). The first-order differences are between the dark basalts of the maria and the lighter-colored feldspar-rich rocks of the highlands. There is also a great diversity among the highland rocks themselves. Three major types have been identified: (1) Ferroan anorthosites, which are rich in Ca and Al and composed largely of plagioclase feldspar, are one of the most ancient of highland rock types. Ferroan anorthosites are relatively common among samples from the Apollo 16 landing site. (2) Magnesium-rich rocks which are clearly distinct from the ferroan anorthosites. They may contain nearly as much plagioclase but they also contain Mg-rich grains of olivine and pyroxene. (3) KREEP rocks are crystalline highland rocks that contain a chemical component enriched in such elements as potassium (K), the rare earth elements (REE), and phosphorus (P). The KREEP component is also generally accompanied by relatively high concentrations of the radioactive elements U and Th. The appearance of KREEP in lunar rocks indicates extensive chemical separation within the Moon, and the enrichment of the heat-producing elements U and Th makes KREEP-bearing rocks important in understanding the Moon's thermal history.

14.4.2 Differentiation of the Lunar Interior: A Magma Ocean

The major differences between the lunar maria and highlands indicate large-scale chemical differentiation of the Moon. There is general agreement on this point, but the details of differentiation are still controversial. Early recognition of the fact that the highlands are composed mostly of plagioclase, a relatively light mineral, led to the suggestion that this mineral represents crystal flotation at the top of a deep “magma ocean” (Wood et al., 1970).

Question 14.24: Did the Moon have a magma ocean early in its history?

The basic argument for a “magma ocean” is the need for a mechanism to float a plagioclase-rich crust, while denser minerals such as olivine and pyroxene sank. As the Moon formed, its outer portions consisted of a layer of molten silicate magma in which plagioclase floated and accumulated into the first stable lunar crust. At the same time, the heavier olivine and pyroxene sank. Estimates of the depth of the lunar magma ocean vary from about 100 km to the radius of the Moon. Calculations of the depth of the magma ocean based on mass balance arguments (Warren, 1985) favor a depth greater than about 250 km but probably no more than 1,000 km.

The nature of the magma ocean is also uncertain. It is not known whether it would have been a melt of whole-Moon composition or a partial melt. The ability of partial melts to ascend from their source regions and for a solid–melt system to convect suggests that total melting is unlikely. Although some authors have developed models to explain how both

anorthosites and the Mg-suite rocks could come from a magma ocean (Longhi and Boudreau, 1979), it is likely that most Mg-suite magmas are the products of melting events that postdate the magma ocean. Nevertheless, some of them might have formed even before the magma ocean had totally solidified. Chemical data and petrologic modeling indicate that Mg-suite magmas assimilated ferroan anorthosites, with different amounts of assimilation producing the diversity seen within the Mg-suite. The sources of these magmas are not known; they could represent partial melts of previously undifferentiated material at depth in the Moon or they may be partial melts of Mg-rich mineral cumulates deep in the magma ocean.

The formation of KREEP basalts is associated with the concentration of incompatible elements in a residual melt. The residual material remaining after 99% of the magma ocean had crystallized would have been rich in FeO and trace elements and enriched somewhat in silica.

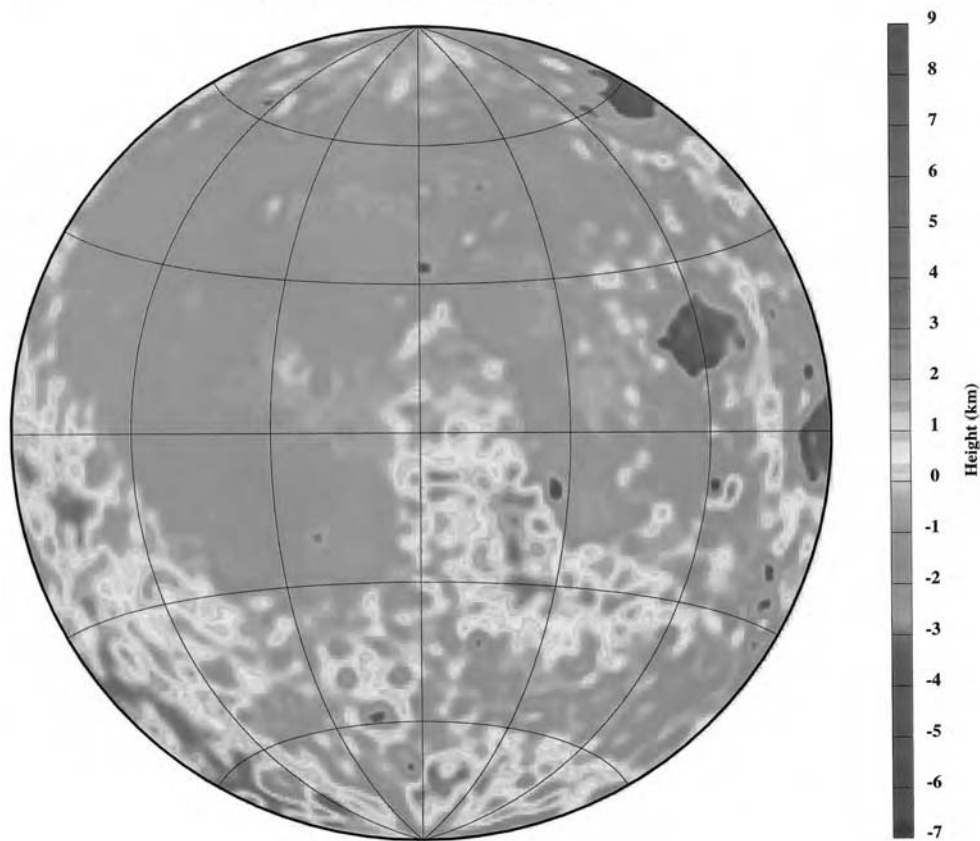
14.4.3 Lunar Topography and Gravity

Hypsometry on the Moon is primarily associated with the systematic difference in elevation between the farside and the nearside. Excellent global topography was obtained during the Clementine mission (Figure 14.51) (Lucey et al., 1994; Zuber et al., 1994; Smith et al., 1997). The resulting hypsometry is given in Figure 14.3. Certainly, many of the regions with low topography can be attributed to large impact basins and most of the lowest-lying areas in these basins have been filled by mare basalts. An exception is the South Pole-Aitken basin (2,250 km diameter, Figure 14.51) with very little basaltic fill; much of the lowest-lying topography on the Moon is associated with this basin. The scale bar in Figure 14.51 shows that topographic highs and lows on the Moon are about 8 km in amplitude relative to the mean lunar radius of 1,737.1 km. The maximum and minimum topography both occur on the lunar farside in the areas of the Korolev and South Pole-Aitken basins, respectively (Smith et al., 1997). The center of the lunar figure is displaced from its center of mass by about 1.9 km; the displacement is on a line that deviates slightly from the Earth–Moon line (on the farside of the Moon the line is displaced about 25° towards the western limb and slightly north of the equator, the center of mass of the Moon is shifted toward the Earth along this line relative to the center of figure) (Smith et al., 1997). The gravity field of the Moon (Figures 14.52 and 14.53) is not offset from the Earth–Moon line, indicating that the global-scale topography of the Moon is isostatically compensated probably by variations in crustal thickness (Kaula et al., 1974; Zuber et al., 1994; Smith et al., 1997). A relatively thin nearside crust compared to a relatively thick farside crust is one of the major features of the hemispheric dichotomy on the Moon.

The flooding of mare basins on the nearside of the Moon and the general lack of basin infilling on the lunar farside has been attributed to the difference in elevation of the selenoid with respect to floors of the impact basins. Essentially, mare basalts rise to a hydrostatic level which is above original basin floors on the nearside but below basin floors on the farside due to the thick farside lunar crust (Runcorn, 1974). Smith et al. (1997) and Arkani-Hamed et al. (1999) have tested this idea against the gravity and topography data from Clementine, and find that the explanation generally holds except for the South Pole-Aitken basin which is so deep that its floor lies below the selenoid associated with the filled basins. Apparently, the region of the South Pole-Aitken basin is compositionally or thermally distinct from other regions of the Moon (Smith et al., 1997).

The gravity fields given in Figures 14.52 and 14.53 show strong positive gravity anomalies associated with the nearside mare basins. These mascons were discovered in 1968 through

(a)

Nearside Lunar Topography

analysis of Lunar Orbiter data by P. Muller and W. L. Sjogren (Muller and Sjogren, 1968). The source of the positive gravity anomaly in a topographic depression is some combination of the mare infill and the upward emplacement of dense mantle rocks beneath the basin (Wise and Yates, 1970; Phillips et al., 1972; Bratt et al., 1985; Arkani-Hamed, 1998). Lunar Prospector gravity data (Konopliv et al., 1998) have revealed three new large mascons on the lunar nearside at Mare Humboldtianum, Mendel-Ryberg, and Schiller-Zucchiuss; significantly, the latter basin has no visible mare fill. Lunar Prospector has also given indications of mascons on the farside of the Moon at the basins Hertzsprung, Coulomb-Sarton, Freundlich-Sharonov, and Mare Muscoviense; only the latter basin has mare fill. The lunar gravity data from Clementine and Lunar Prospector (Figures 14.52 and 14.53) show rings of negative gravity anomaly surrounding the positive anomaly centers of the mascons (Lemoine et al., 1997; Konopliv et al., 1998). The negative gravity rings have been attributed to flexure (Zuber et al., 1994) and crustal thickening (Lemoine et al., 1997), but they are not well understood.

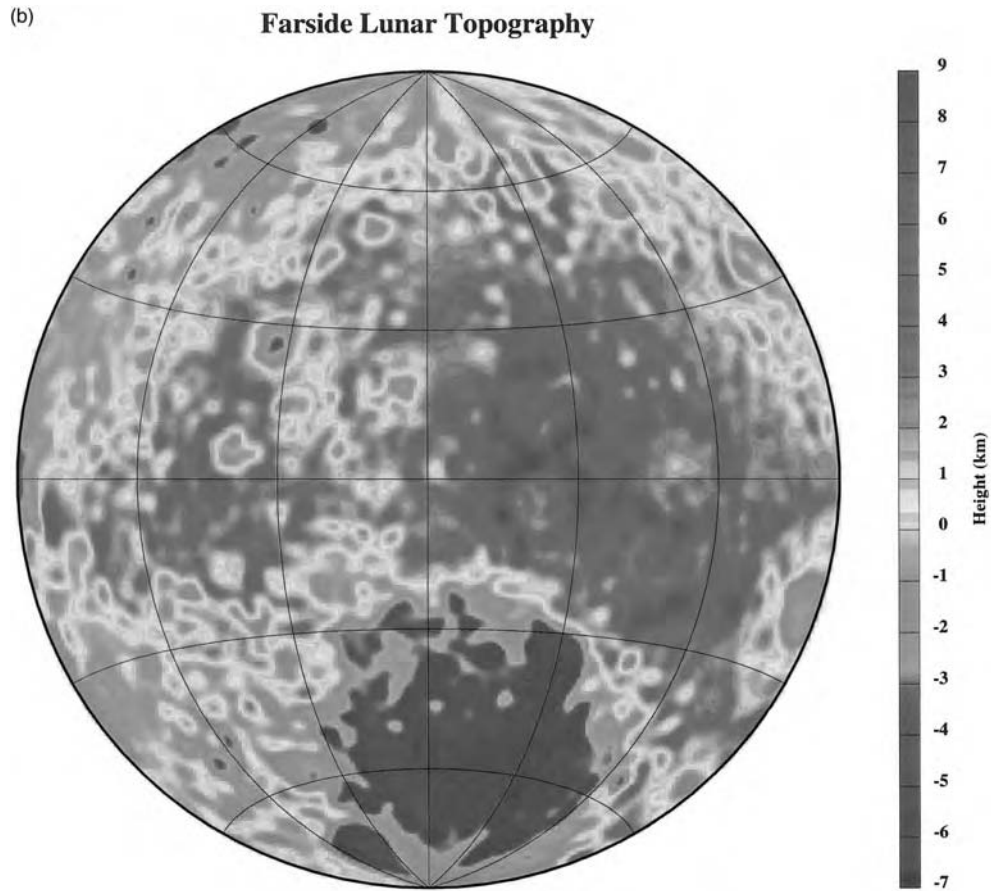
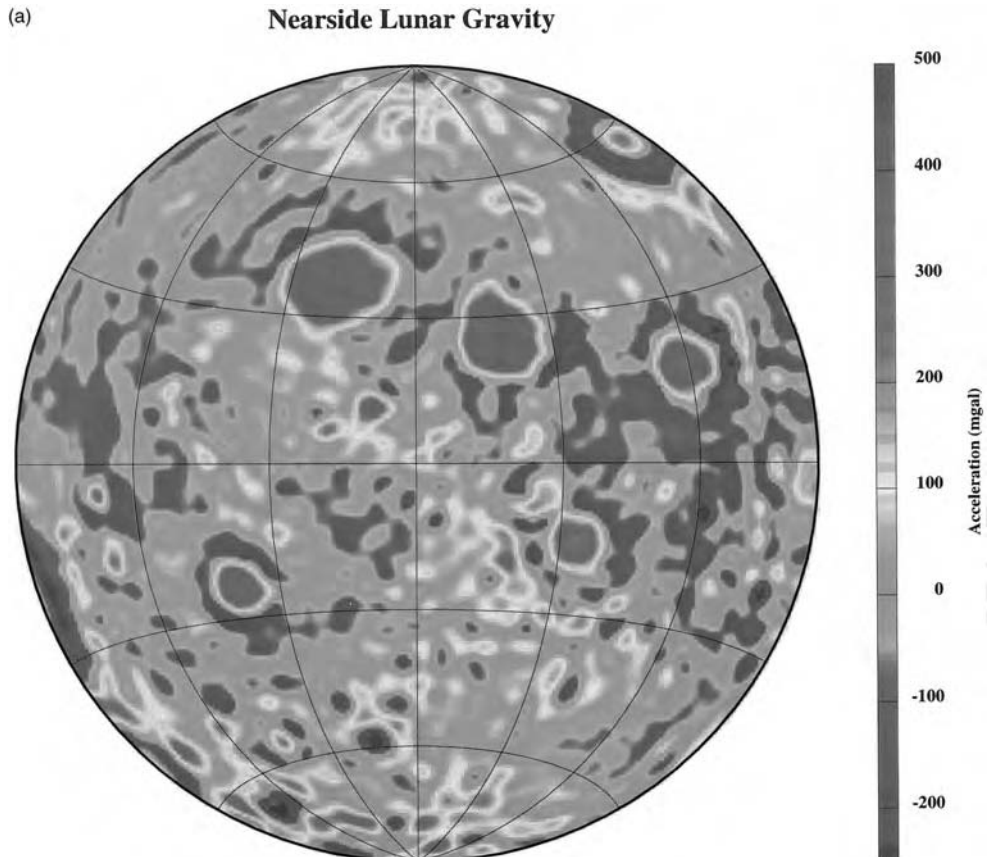


Figure 14.51. Topography of the lunar surface from Clementine lidar data (Smith et al., 1997). Nearside hemisphere (a), farside hemisphere (b). Topographic heights are with respect to a sphere of radius 1,737.1 km, the mean lunar radius. The large region of low-lying topography on the farside is the South Pole-Aitken basin. The topography is based on a spherical harmonic representation to degree and order 90.

For a color version of this figure, see plate section.

Question 14.25: What is the origin of lunar mascons?

The gravity and topography maps shown in Figures 14.51–14.53 have been used to construct a Bouguer gravity map (the gravitational attraction of the surface topography is removed from the free-air gravity) and a crustal thickness map (assigning Bouguer gravity anomalies to crustal thickness variations) of the Moon (Zuber et al., 1994). The crustal thickness map shows a farside crust of average thickness 68 km and a nearside crust of average thickness 60 km. Very thin crust underlies Mare Crisium (near-zero thickness), Mare Orientale (4 km thick), Mare Smythii (15 km thick), and the South Pole-Aitken basin (20 km). The thickest crust (107 km) is on the farside near Korolev basin (also the highest topography). The thickened farside crust contributes significantly to the lunar center of mass–center of figure offset.



A major question regarding the Moon is whether the nearside–farside dichotomy in elevation and crustal thickness can be attributed to massive impacts or to other effects. Lingenfelter and Schubert (1973) and Schubert and Lingenfelter (1973) suggested that mantle convection could cause a preferential accumulation of crust in the farside hemisphere. Wasson and Warren (1980) proposed that earlier or more rapid solidification of the lunar magma ocean occurred in the farside hemisphere. Zuber et al. (1994) suggested that the crustal nearside thinning can be associated with crustal erosion due to mantle convection. The cause of the lunar hemispheric asymmetry remains a problem (Question 14.5).

14.4.4 Early Lunar History

Subsequent to the solidification of the magma ocean, the morphology of the lunar surface was strongly affected by collisions with the remaining planetesimals and large meteorites. These collisions created large basins; the largest of the colliding bodies created the Imbrium

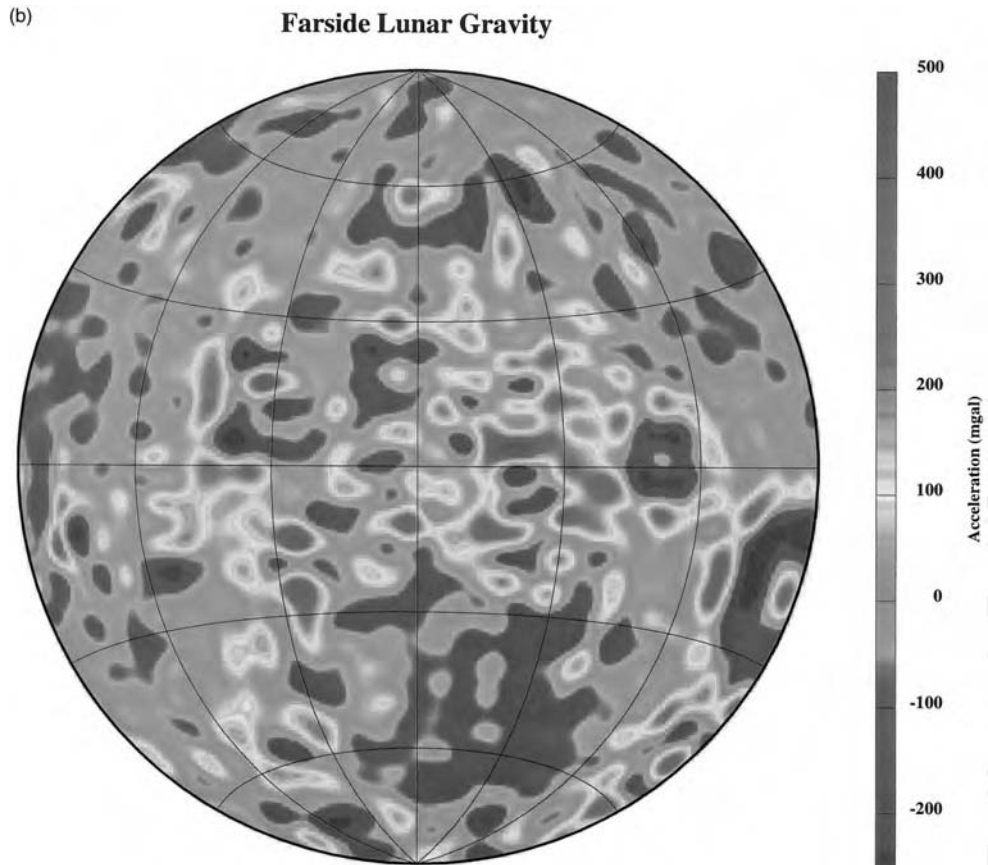
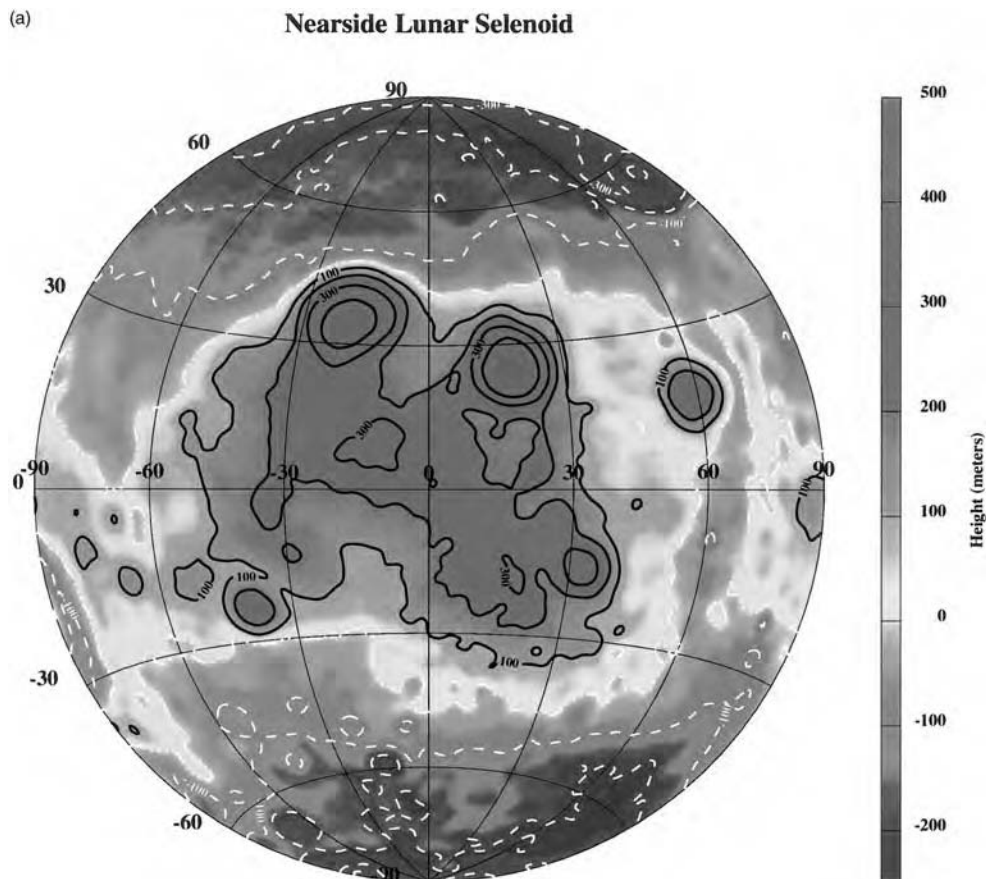


Figure 14.52. Gravity anomalies on the Moon. Lunar nearside (a), lunar farside (b). The gravity field is based on a spherical harmonic model of Lunar Prospector and other data to degree and order 100. After Konopliv and Yuan (1999).

For a color version of this figure, see plate section.

basin, an event that has been dated at 3.86 Ga. A period of volcanism lasting 1 Gyr then filled the floors of these pre-existing impact basins with the dark basaltic rocks that form the lunar maria. This volcanism terminated about 3 Ga. Since then the lunar surface has remained virtually unaltered. The chemical diversity of mare basalts demonstrates that their genesis is very complicated. Their europium anomalies indicate that they formed by partial melting of cumulates that developed from the magma ocean after plagioclase had crystallized. Experiments at elevated temperatures and pressures on melts thought to represent primary magmas indicate that they formed at depths ranging from 100 to 500 km from source rocks rich in olivine and orthopyroxene sometimes accompanied by clinopyroxene. The abundances of the source rock minerals and the percentage of partial melting varied. Most of the magmas produced began to crystallize and therefore fractionated before reaching the surface.

Mare volcanism is known to have been active by about 3.9 Ga, while the Moon was still being heavily bombarded. However, at about 3.9 Ga the rate and scale of cratering decreased. There followed a period of perhaps 1 Gyr in which many of the larger craters on the lunar



nearside were flooded by mare basalts. From ~ 3 Ga to the present it appears that igneous activity on the Moon was very sparse.

Question 14.26: Why was there a time delay in the onset of mare volcanism?

Question 14.27: What caused the termination of mare volcanism?

All of the smooth, dark regions visible on the Moon's nearside consist of mare lavas that partly or completely fill the multi-ring basins. Basaltic lavas cover an area of $7 \times 10^6 \text{ km}^2$, 17% of the Moon's surface (Head, 1976). Nearly all of the basalts occur on the nearside. Significant time elapsed between the formation of a large mare basin by impact and its subsequent filling with basaltic lava flows to form the dark lunar maria. Current information dates the Imbrium basin at about 3.9 Ga but the lavas that fill it at about 3.3 Ga. The primary

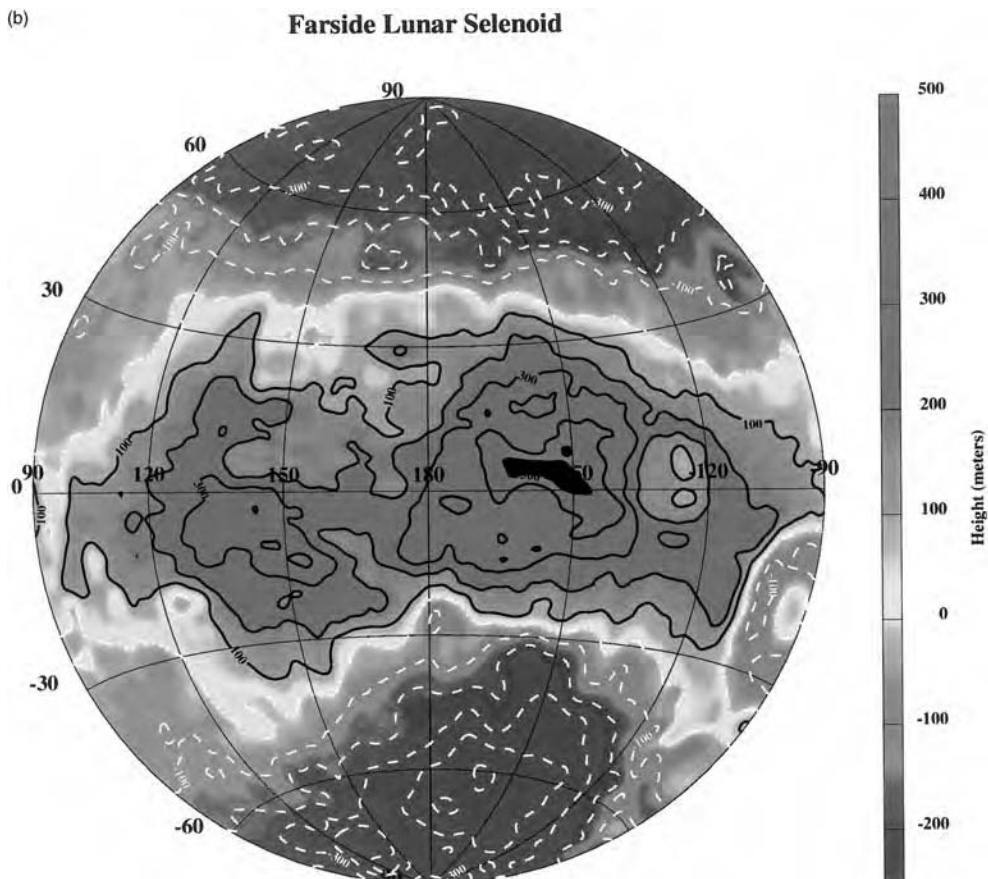


Figure 14.53. The lunar geoid or selenoid based on the gravity field in Figure 14.52. Nearside of the Moon (a) and farside (b). Selenoid heights are with respect to a reference radius of 1,738 km. After Konopliv and Yuan (1999).

For a color version of this figure, see plate section.

landforms resulting from lunar basaltic volcanism are vast, smooth plains, indicating low lava viscosities and high eruption rates. Major basaltic eruptions lasted a minimum of 800 Myr, i.e., from 3.9 to 3.1 Ga (Head, 1976). On the basis of low crater densities on some formations, minor eruptions could have continued until as recently as 2 Ga (Schultz and Spudis, 1983). The onset of basaltic volcanism is also not clearly defined. The oldest mare basalt sample crystallized at 4.2 Ga (Taylor et al., 1983).

The solidification of the magma ocean must have occurred in about 100 Myr after the formation of the solar system because of the ages of the returned lunar samples. Seismic studies carried out on the Apollo missions (Nakamura et al., 1976; Goins et al., 1979, 1981; Nakamura, 1983) showed that the lunar crust has a thickness between 60 and 100 km. Seismic velocities and the mean density of the Moon indicate that the lunar mantle is composed primarily of peridotite similar to the Earth's mantle. It is hypothesized that the lunar crust represents about a 20% partial melt fraction of a primitive lunar mantle with a composition similar to pyrolite. It is expected that there is a layer of depleted mantle rock beneath the lunar crust with a thickness of about 300 km.

14.4.5 Is There a Lunar Core?

Although lunar rocks are similar to igneous rocks on the Earth, there are significant differences between the two bodies. Unlike the Earth, the Moon does not have a large iron core. The Moon may have a small iron core, but its radius is constrained by the measured values of lunar mass, radius, and moment of inertia to have a value less than about 400 km. Since the mean density of the Moon is only $3,340 \text{ kg m}^{-3}$, the missing iron cannot be distributed through the lunar mantle. It is therefore concluded that the Moon is deficient in metallic iron relative to the Earth. The scaled lunar moment of inertia (C/MR^2), 0.3904 ± 0.0023 (Ferrari et al., 1980) (0.3935 ± 0.0011 , lunar Doppler gravity and laser ranging data, Dickey et al., 1994; 0.3932 ± 0.0002 , Lunar Prospector value, Konopliv et al., 1998) allows for but does not require an FeS (Fe) core with a radius as large as about 400–500 km (300 km) (Hood, 1986; Dickey et al., 1994; Konopliv et al., 1998). The measured induced magnetic dipole moment in the geomagnetic tail (Russell et al., 1981) and the observed small advance in the lunar rotation axis from the Cassini state (Yoder, 1981; Dickey et al., 1994) have been attributed to the existence of a lunar core about 300–400 km in radius.

Question 14.28: Does the Moon have a metallic core?

14.4.6 Crustal Magnetization: Implications for a Lunar Core and Early Dynamo

Magnetic field measurements were made by small satellites left in lunar orbit by the Apollo 15 and 16 missions (Coleman et al., 1972). Although localized regions of magnetized rock were detected by these subsatellites, no global lunar magnetic field could be measured. A lunar magnetic dipole moment can be no larger than 10^{16} A m^2 (Russell et al., 1974a, b). This is nearly seven orders of magnitude smaller than the Earth's dipole moment. The absence of a present-day global lunar magnetic field is presumably due to the absence of an active dynamo in the Moon. This may indicate that the Moon has no core; on the other hand, a small lunar core could have cooled, or solidified, sufficiently that convective motions in it are no longer possible. It has been suggested that the localized areas of remanent lunar magnetism were magnetized in the ambient field of an ancient lunar dynamo.

Question 14.29: How was the lunar crust magnetized?

The remanent magnetization of lunar surface rocks may also indicate a hot early Moon if the source of the magnetizing field was a hydromagnetic dynamo in a molten iron core (Runcorn, 1983; Hood, 1986). The core could have formed by differentiation of the Moon during or shortly after its formation, perhaps in association with the formation of the magma ocean. However, the existence of a metallic core in the Moon is uncertain.

Concentrations of crustal magnetic fields have been found in regions antipodal to the Imbrium, Serenitatis, Crisium, and Orientale impact basins (Lin et al., 1988). A magnetometer/electron reflector experiment on Lunar Prospector has also detected strong surface magnetic fields at the antipodes of Mare Imbrium and Mare Serenitatis (Lin et al., 1998). The implication is that the impacts caused the magnetization of the crust at the locations antipodal to the basins. Shock remanent magnetization associated with the focusing of seismic

energy at the antipode of a major impact might have been the mechanism for magnetic field emplacement in the surface rocks (Hood and Vickery, 1984). If the rocks were magnetized in the ambient field of a lunar dynamo, then the dynamo would have been active at least until 3.85–3.6 Ga, the ages of the Imbrium and Serenitatis basins (Lin et al., 1998).

14.4.7 Origin of the Moon

Theories for the origin of the Moon have been debated for more than a century (Brush, 1986; Wood, 1986). The classic theories include capture from an independent heliocentric orbit, co-accretion from a swarm of planetesimals in geocentric orbit, and fission from a rapidly rotating Earth (Wood, 1986). None of these theories has been able to satisfy all the major constraints on lunar origin which include the large prograde angular momentum of the Earth–Moon system relative to the other planets and the Moon’s depletion in volatile elements and iron compared with its cosmic (chondritic) abundance. It has also been proposed that the Moon formed by accreting from a disc of ejecta orbiting the Earth after the impact of a Mars-size body with the Earth (Hartmann and Davis, 1975; Cameron and Ward, 1976; Wetherill, 1986). The giant impact origin of the Moon has gained widespread support because it does not violate any of the major observational constraints on lunar origin (Cameron, 1986; Hartmann, 1986; Wood, 1986; Stevenson, 1987). One of the major consequences of the giant impact hypothesis of lunar origin is a hot, partially molten (or perhaps completely molten) Moon upon accretion from the circumterrestrial ejecta disk (Thompson and Stevenson, 1983; Cameron, 1984).

Question 14.30: Did the Moon form from an impact of a Mars-size body with the Earth?

14.4.8 Lunar Heat Flow and Convection

The Moon is the only body other than the Earth for which we have *in situ* determinations of the surface heat flux. Two lunar heat flow measurements were made, one on the Apollo 15 mission and the other on Apollo 17. The measured heat flow values are 31 mW m^{-2} and 22 mW m^{-2} (Langseth et al., 1976). Although these two determinations may not be representative of the average lunar heat flow, the values are consistent with the Earth’s surface heat loss if the differences in the sizes of the planets are accounted for. Although it is the smallest of the terrestrial bodies (Table 14.1), the Moon is large enough that with a mantle radiogenic heat source concentration similar to the Earth, heat transfer in the deep interior is expected to be by subsolidus convection (Schubert et al., 1969). The suggestion that convection might be important in the lunar interior dates back to Runcorn (1962b). The significance of mantle convection for the present state of the Moon has been considered by Turcotte and Oxburgh (1970) and Schubert et al. (1977), while its implications for thermal history have been discussed by Cassen and Reynolds (1973, 1974) and Toksöz et al. (1978). Schubert et al. (1979a) calculated thermal evolution models for the Moon that incorporated many of the features already discussed for the other planets, i.e., subsolidus convective heat transport in the mantle parameterized by (13.2.4), a strongly temperature dependent mantle viscosity given by (13.2.6), and the growth with time of a conductive lithosphere. Similar calculations were also carried out by Cassen et al. (1979), who included mantle radiogenic heat sources and upward differentiation of these heat sources upon melting.

As was the case for Mars, convection in the Moon at present depends on the extent to which the radiogenic heat sources have been removed from the mantle and concentrated into the crust. The next section explores the effects of crustal differentiation on lunar thermal history.

14.4.9 Lunar Thermal Evolution with Crustal Differentiation

The thermal history model with crustal differentiation given for Mars in Section 14.3.5 can also be applied to the Moon. The crustal differentiation model is given in (14.3.5)–(14.3.10) and the thermal history model is given in Section 13.2. Results for the Moon are presented in Figures 14.54–14.59 for the following parameter values: $\kappa = 10^{-6} \text{ m s}^{-2}$, $k = 4 \text{ W m}^{-1} \text{ K}^{-1}$, $T_{\text{lithos}} = 1,000 \text{ K}$, $T_s = 255 \text{ K}$, $T(t=0) = 2,000 \text{ K}$, $\alpha = 3 \times 10^{-5} \text{ K}^{-1}$, $\Delta\rho = 80 \text{ kg m}^{-3}$, $\lambda = 2.77 \times 10^{-10} \text{ yr}^{-1}$, and $H_0 = 2.47 \times 10^{-11} \text{ W kg}^{-1}$. The maximum crustal thickness on the Moon is obtained from (14.3.6) with $f = 0.1$, $\rho_m = 3,340 \text{ kg m}^{-3}$, $\rho_c = 2,900 \text{ kg m}^{-3}$, and $R_p = 1,738 \text{ km}$; the result is $l_{\text{cr,max}} = 67 \text{ km}$. The Apollo seismic network was used to determine the crustal structure of the Moon. Based on a review of the available data, Hood (1986) suggests that the mean crustal thickness is $55 \pm 10 \text{ km}$. If a pristine crustal fraction $f = 0.10$ is accepted, the observed crustal thickness $55 \pm 10 \text{ km}$ is close to the maximum allowed value $l_{\text{cr,max}} = 67 \text{ km}$. From the results shown in Figure 14.55, this value of crustal thickness requires that $\chi = 0.010$.

Question 14.31: What is the degree of differentiation of the Moon?

It is not certain that a convection fractionation model is appropriate for the origin of the lunar crust. An alternative hypothesis involves a global magma ocean at the time of formation of the Moon. The fractionation of the magma ocean resulted in the formation of the anorthositic highland crust. From Figure 14.55 it is seen that for our model 90% of

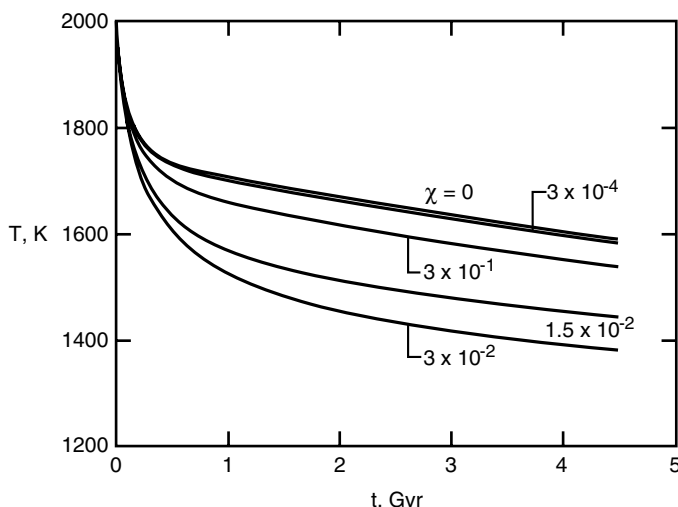


Figure 14.54. Dependence of the mean mantle temperature T in the Moon on time t for several values of the crustal fractionation parameter χ .

the lunar crust was generated by mantle convection in the first 100 Myr of lunar evolution. This would look much like a magma ocean. From Figure 14.56 with $\chi = 0.01$, we see that significant lunar volcanism lasts for about 2 Gyr. This is in good agreement with our present understanding of the chronology of lunar mare volcanism.

If we assume the applicability of the crustal fractionation parameter $\chi = 0.01$, several predictions can be made based on the results in Figures 14.54–14.59. The mean temperature of the lunar mantle at the present time is $T = 1,425$ K from Figure 14.54. The thickness of the lunar lithosphere is $l = 650$ km from Figure 14.57. This is reasonably consistent

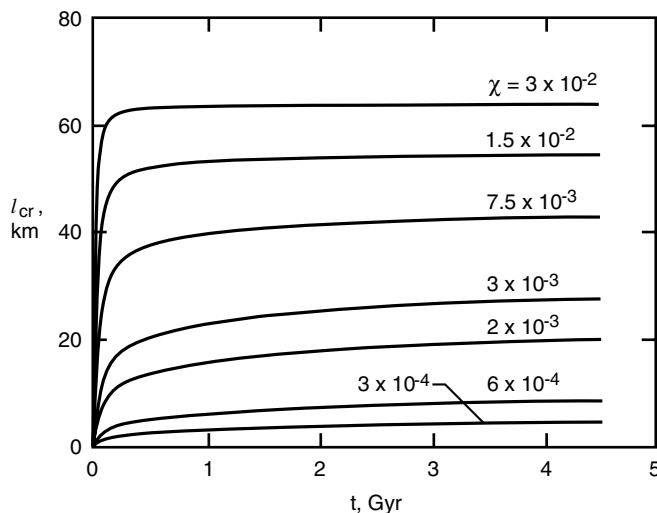


Figure 14.55. Dependence of the thickness of the lunar crust l_{cr} on time t for several values of the crustal fractionation parameter χ . The crustal thickness for a fully differentiated Moon is $l_{cr,max} = 67$ km.

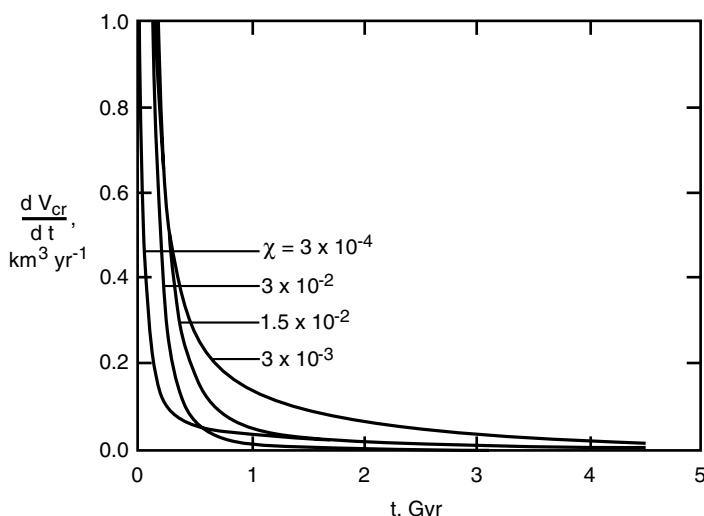


Figure 14.56. Dependence of the volumetric flux of lunar volcanism V_{cr} on time t for several values of the crustal fractionation parameter χ .

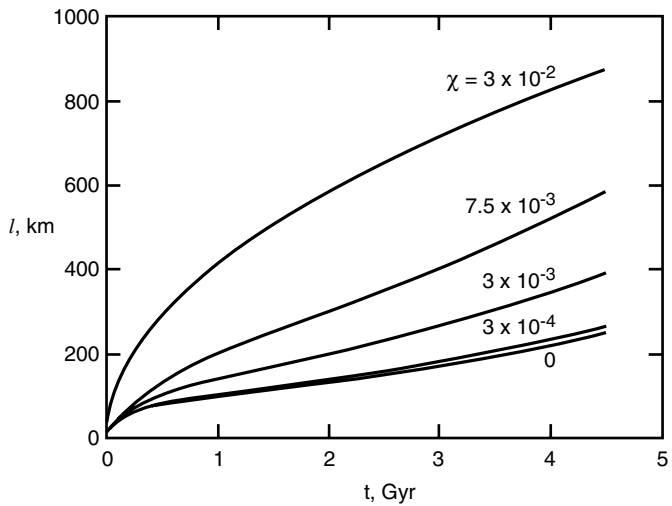


Figure 14.57. Dependence of the thickness of the lunar lithosphere l on time t for several values of the crustal fractionation parameter χ .

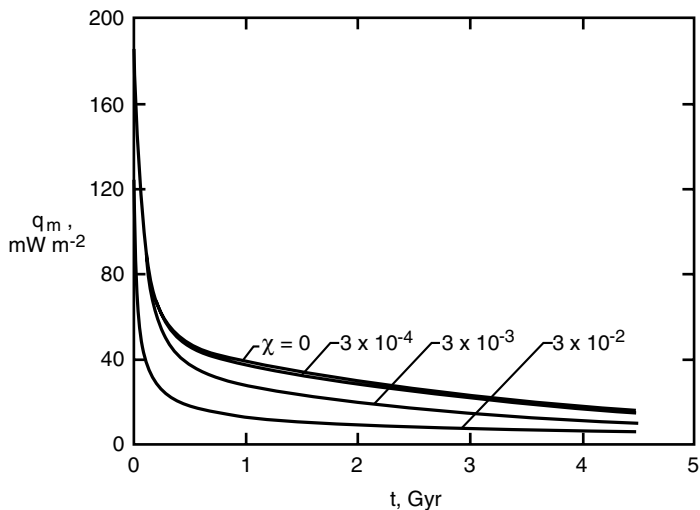


Figure 14.58. Dependence of the lunar mantle heat flux q_m on time t for several values of the crustal fractionation parameter χ .

with the minimum thickness of 300 km given by Nakamura et al. (1976) based on seismic observations.

The predicted contraction of the Moon $\Delta R_p/R_p = 0.007$ from Figure 14.59 can be compared with observations. Contraction or expansion of the lunar interior would be expected to result in compressional or extensional features on the body. It has long been recognized that the Moon does not have surface features indicative of large changes in radius. Our results predict that ΔR_p over the last 4.5 Gyr has been -12 km. This compares with $\Delta R_p = -16$ km obtained by Solomon and Chaiken (1976) and Solomon (1977) for hot initial conditions. These results were based on heat transport by conduction, but a similar value was obtained

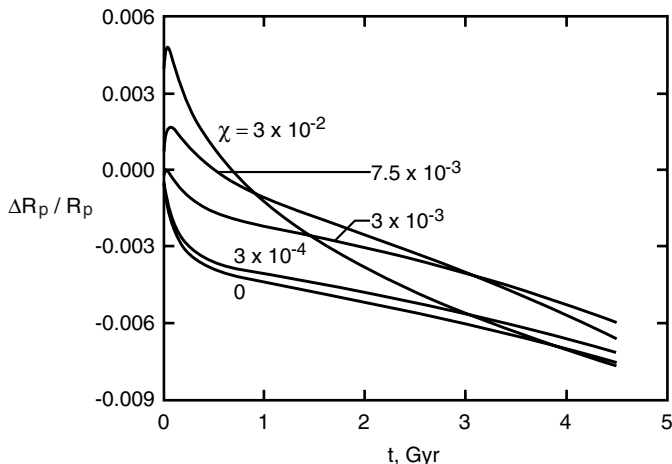


Figure 14.59. Dependence of the radial expansion (or contraction) $\Delta R_p / R_p$ for the Moon on time t for several values of the crustal fractionation parameter χ .

by Cassen et al. (1979) who also included convective transport. The difference between 12 and 16 km can be attributed to the inclusion of the density differences due to fractionation in our calculation. Kirk and Stevenson (1989) argue that this difference can cancel the thermal contraction effect. However, they take $f = 0.4$ and do not carry out thermal evolution calculations. From Figure 14.59 it is seen that the expansion associated with differentiation occurs early in the evolution of the Moon while the thermal contraction is associated with the secular cooling occurring throughout lunar history.

A direct interpretation of surface features leads to the conclusion that $\Delta R_p = \pm 1$ km for the Moon. Solomon and Chaiken (1976) satisfy this condition by taking cold initial conditions. However, hot initial conditions are preferred, particularly if the collision hypothesis for the origin of the Moon is accepted.

14.4.10 Lunar Isotope Ratios: Implications for the Moon's Evolution

Measurements of isotope ratios and the associated concentration ratios have provided a wealth of data on the age of lunar rocks as well as constraints on the origin of the Moon (Turcotte and Kellogg, 1986b; Lee et al., 1997). On the Earth the uniformity of isotope and concentration ratios for mid-ocean ridge basalts has been taken as strong evidence for vigorous mantle convection. This convection mixes and homogenizes the upper mantle beneath the lithospheric plates. Isotope and concentration ratios for lunar mare basalts show much more variability. This has been taken as evidence for distinct source regions. Heterogeneity of the source regions implies little or no mixing of the source region of the mare basalts.

We first consider the samarium–neodymium (Sm–Nd) system. The values of initial Sm–Nd isotope ratio ϵ_i (12.4.2) are given as a function of age τ in Figure 14.60. The values of Sm–Nd fractionation factor f (12.4.4) are given as a function of age in Figure 14.61. These values are referenced to a chondritic or bulk silicate Earth value $\mu_s = 0.1967$ (Jacobsen and Wasserburg, 1980b; Allègre et al., 1983b). Also included in Figure 14.60 is the predicted evolution of a reservoir from (12.4.21) for $Q = 25.3$, $\tau_c = 4.4$ Ga (age of crust formation), and various values of f .

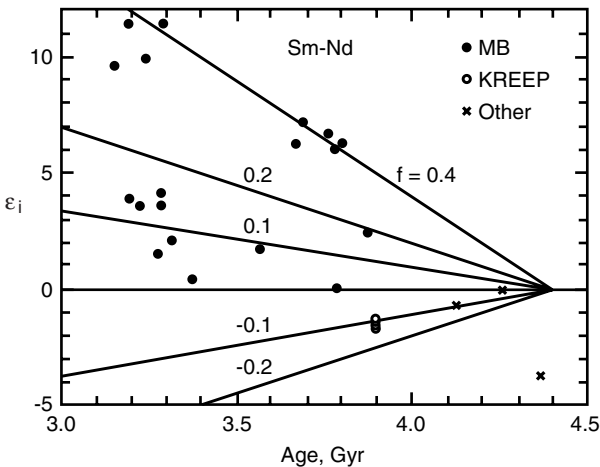


Figure 14.60. The measured initial Sm–Nd isotope ratios ϵ_i for a variety of lunar rocks are given as a function of their age. Also included is the predicted evolution of a mantle reservoir from (12.4.21) for $Q = 25.3$, $\tau_c = 4.4$ Gyr, and various values of the fractionation factor f .

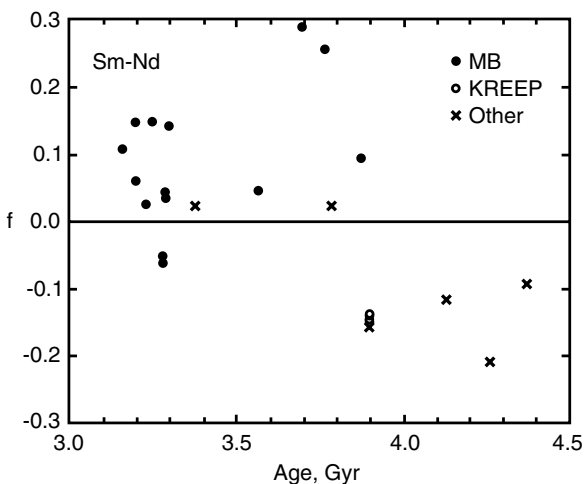


Figure 14.61. The measured Sm–Nd fractionation factors f for a variety of lunar rocks are given as a function of their age. The values are referenced to a chondritic or bulk silicate Earth value $\mu_s = 0.1967$.

First, it is necessary to make several assumptions. It is assumed that the f and ϵ_i values of lunar mare basalts are equal to the values in the depleted source region. This is a good approximation for ϵ since isotope fractionation is insignificant, but it may be a bad approximation for f if the degree of partial melting is low. With a substantial degree of partial melting, essentially all the incompatible elements go into the melt. It is also necessary to assume that the mare basalts were not contaminated when they passed through the pre-existing lunar crust.

It is seen in Figure 14.60 that there is considerable scatter in the data. Discrete groups appear to correlate with variations in major element chemistry. Several authors

(Papanastassiou et al., 1977; Lugmair and Marti, 1978; Nyquist et al., 1979) argue that this variation in ϵ_i values for the lunar basalts indicates early lunar differentiation into multiple distinct reservoirs. Lugmair and Marti (1978) identify at least three reservoirs, the first of which is the source of KREEP basalts whose initial ϵ is negative. The remaining samples have positive initial ϵ . Lugmair and Marti (1978) distinguish between green glass (nearly chondritic) and mare basalts with high initial ϵ . Papanastassiou et al. (1977) present a model of early differentiation of the upper Moon (crust formation at about 4.4 Ga). They propose that the lunar mantle may have undergone further differentiation at later ages, and that the varying ϵ 's of the mare basalts reflect different source layers. They also observe that the Sm/Nd ratios of lunar rocks differ widely from chondritic values. The lunar ratios contrast with those of terrestrial basalts, whose Sm/Nd ratios are very nearly chondritic. Papanastassiou et al. (1977) point out that this variation makes estimation of the bulk Sm/Nd ratios of the Moon extremely difficult, and argue that to assume a chondritic bulk Moon may be wrong. Nyquist et al. (1979) argue that a plot of initial Sr ratios against Nd ratios for lunar rocks confirms the layered nature of the lunar mantle. The plot shows a lack of correlation between initial Nd and Sr ratios in the rocks, indicating that the rocks came from distinct sources. A correlation would have indicated that the variations in ϵ could be an artifact of mixing of the magma sources of the rocks.

It is seen from Figure 14.61 that the measured values of fractionation factors are not consistent with the values inferred from the isotope evolution diagram (Figure 14.60). For a model of instantaneous formation of the lunar crust, a number of data points in Figure 14.60 require $f > 0.3$. However, no measured values for f are this high. Acceptance of the validity of the measured values implies that this difference can be attributed to either a low degree of partial melting that leads to a fractionation of samarium and neodymium or to contamination during eruption. For comparison, the preferred value for the Sm–Nd fractionation in the MORB source is $f = 0.19$.

We next consider the rubidium–strontium (Rb–Sr) system. The values of initial ϵ are given as a function of age τ in Figure 14.62. The values of initial f are given as a function of age τ in Figure 14.63. These values are referenced to a mean silicate Earth value $\mu_s = 0.0892$, given by Allègre et al. (1983b) based on a cross-correlation of the Sm–Nd and Rb–Sr systems. Also included in Figure 14.62 is the predicted evolution of a reservoir from (12.4.21) for $Q = 17.7$, $\tau_c = 4.4$ Ga, and $f = -0.78$. The values of f measured directly are in quite good agreement with the values inferred from isotope evolution. However, a word of caution is in order. The maximum negative value of f is -1 , corresponding to the complete removal of rubidium. Nevertheless, the behavior of the Rb–Sr system seems to be more systematic than the behavior of the Sm–Nd system.

The results in Figures 14.62 and 14.63 show a strong depletion in rubidium relative to strontium. This could be associated with either the formation of the Moon or the differentiation of the lunar crust. Clearly the KREEP basalts are enriched in rubidium and may represent a complementary enriched reservoir. However, the Moon is generally depleted in volatiles and this general depletion during formation would be expected to lead to a relative depletion in rubidium.

Our best value of f for the lunar mare basalts, $f = -0.78$, is identical to the best-fit value for MORB given by Allègre et al. (1983b). Since the processes leading to the depletion of MORB must have been different from the processes leading to the depletion of the lunar mantle, it is difficult to provide a chemical basis for this similarity.

We also consider the uranium–thorium–lead (U–Th–Pb) system. Initial values of α and β were obtained using (12.5.3) and (12.5.4) and ages obtained independently (usually

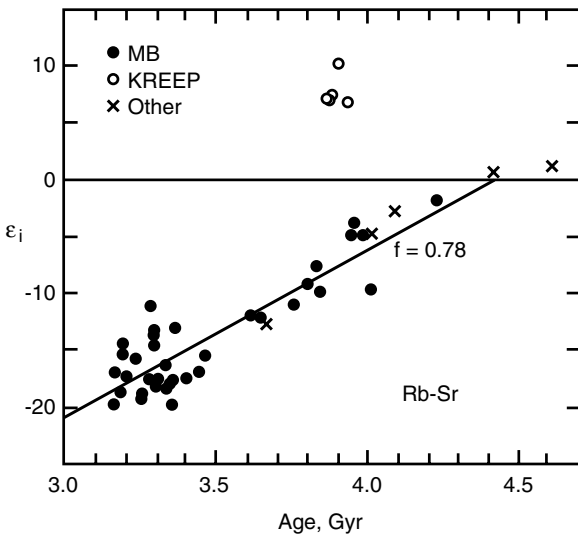


Figure 14.62. The measured initial Rb–Sr isotope ratios ϵ_i for a variety of lunar rocks are given as a function of their age. Also included is the predicted evolution of a mantle reservoir from (12.4.21) for $Q = 17.7$, $\tau_c = 4.4$ Gyr, and $f = -0.78$.

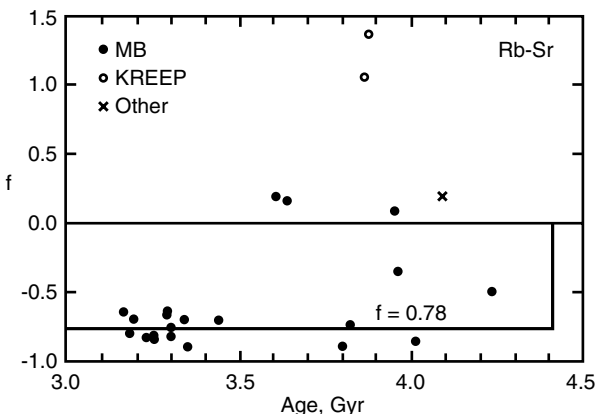


Figure 14.63. The measured Rb–Sr fractionation factors for a variety of lunar rocks are given as a function of their age. These values are referenced to a mean silicate Earth value $\mu_s = 0.0892$.

using Rb–Sr data). The initial values α_i and β_i for a variety of mare basalts are plotted in Figure 14.64. If the lunar mantle reservoirs were uniform, all the data would lie on a $\mu = \text{constant}$ curve at the intersection of the time line corresponding to the age of the basalt.

The large values of α_i and β_i indicate a strong depletion of naturally occurring lead relative to uranium. This leads to severe measurement problems concerning the reference lead isotope ^{204}Pb . Some of the scatter in the data can be attributed to this difficulty. Apollo 17 data have a particularly large scatter and a particularly low μ value. There appears to be a weak correlation of the data with $\mu = 250$. This compares with $\mu = 9$ for the Earth's mantle. Clearly the lunar mantle was strongly depleted in lead, probably prior to its formation. It is difficult to envision a lunar reservoir for the missing lead.

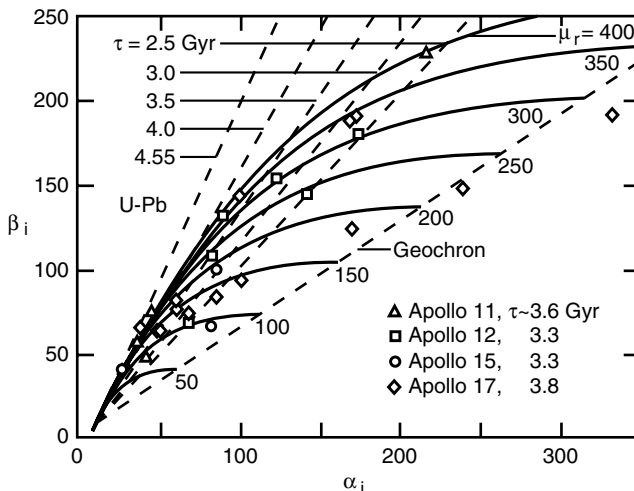


Figure 14.64. The measured initial U-Pb isotope ratios β_i for a variety of mare basalts are given as a function of the initial U-Pb isotope ratios α_i . The solid lines are evolution curves obtained from (12.5.3) and (12.5.4) for various values of the reference composition ratio μ_r . The dashed lines give the expected initial values (β_i and α_i) corresponding to the time τ when the mare basalts were erupted.

Isotope data on lunar rocks for the Rb-Sr system show the least variability. Both isotope and concentration data show a strong depletion of rubidium relative to terrestrial values in the source region for mare basalts. The KREEP basalts show enrichment. It is interesting that the mean depletion in mare basalts is equal to the mean depletion in mid-ocean ridge basalts. However, the significance of this equality, if any, is not clear. The depletion of rubidium in the source region for mare basalts is probably due to fractionation during the formation of the Moon. The systematic depletion of rubidium in the Moon relative to terrestrial values would seem to favor a hot origin for the Moon; however, this does not seem to be consistent with the concept of multiple source regions as discussed above.

The isotope and concentration data for the Sm-Nd system show considerable variability. This variability has led a number of authors to postulate distinct source regions for the mare basalts. As in the case of the source region for MORB, neodymium is depleted relative to samarium and the magnitude of the depletion is about the same as on the Earth.

The U-Pb system also shows considerable scatter. However, it is clear that the source region for mare basalts is strongly depleted in lead relative to the Earth's mantle; an estimated $\mu \sim 250$ versus $\mu = 9$. It is difficult to envision a reservoir on the Moon for this missing lead, and thus the fractionation must have occurred prior to the formation of the Moon. The low concentrations of the reference stable lead isotope ^{204}Pb cause serious experimental difficulties. Thus the scatter in the lead data cannot be taken as strong evidence for distinct source regions for the mare basalts, but it is certainly consistent with this hypothesis.

The isotope data from lunar rocks show much more variability than similar data from terrestrial rocks. In particular, mid-ocean ridge basalts yield consistent isotope signatures on a worldwide basis. This is taken as strong evidence that vigorous mantle convection has mixed and homogenized the upper mantle beneath the lithosphere plates. The variability of the lunar data is taken as evidence for distinct source regions. It is also evidence that mantle convection did not mix and homogenize the lunar mantle prior to the eruption of the mare basalts.

Question 14.32: Is the lunar mantle chemically heterogeneous?

Lee et al. (1997) have used the hafnium–tungsten isotopic system to study the evolution of the Moon. In this system the hafnium isotope ^{182}Hf decays to the tungsten daughter ^{182}W with a half-life of nine million years. Hafnium is a lithophile element so that it is found in silicate rocks, whereas tungsten is siderophile so that it fractionates into a metallic core. If this fractionation takes place during the lifetime of ^{182}Hf , then the silicate reservoir will have an excess abundance of the radiogenic daughter ^{182}W , i.e., a high or radiogenic $^{182}\text{W}/^{184}\text{W}$ ratio.

Studies of $^{182}\text{W}/^{184}\text{W}$ ratios show strong variability for both highland and mare rocks (Lee et al., 1997). Ratios vary from chondritic (no core formation) to highly radiogenic (core formation). The studies provide evidence that the sources of these lunar rocks were not homogenized by mantle convection.

Hess and Parmentier (1995) and Alley and Parmentier (1998) have proposed a model for a chemically stratified Moon that they argue satisfies the isotopic constraints for a heterogeneous source of mare basalts. In their model the crystallization of the lunar magma ocean creates a chemically stratified Moon consisting of an anorthositic crust and magma ocean cumulates overlying the primitive lunar interior. Within the magma ocean, the last liquids to crystallize form dense, ilmenite-rich cumulates that contain high concentrations of incompatible radioactive elements. The underlying olivine–orthopyroxene cumulates are also stratified with later crystallized, denser, more Fe-rich compositions at the top. Rayleigh–Taylor instability causes the dense ilmenite-rich cumulate layer and underlying Fe-rich cumulates to sink toward the center of the Moon, forming a dense lunar core. After this overturn, radioactive heating within the ilmenite-rich cumulate core heats the overlying mantle, causing it to melt. In this model, the source region for high- TiO_2 mare basalts is a convectively mixed layer above the core–mantle boundary which would contain small and variable amounts of admixed ilmenite and KREEP. This deep high-pressure melting, as required for the generation of mare basalts, occurs after a reasonable time interval to explain the onset of mare basalt volcanism if the content of radioactive elements in the core and the chemical density gradients above the core are sufficiently high but within a range of values that might have been present in the Moon. Regardless of details implied by particular model parameters, gravitational overturn driven by the high density of magma ocean Fe-rich cumulates should concentrate high- TiO_2 mare basalt sources, and probably a significant fraction of radioactive heating, toward the center of the Moon.

14.5 Io

14.5.1 Volcanism and Heat Sources: Tidal Dissipation

Although it is similar in size to the Earth’s Moon, Jupiter’s satellite Io is remarkable for its intense volcanic activity (Figure 14.65) (Morabito et al., 1979; Masursky et al., 1979; Smith et al., 1979a,b; Strom et al., 1979; Pearl and Sinton, 1982; Nash et al., 1986; Spencer and Schneider, 1996; McEwen et al., 1998a,b; see Table 14.1 for some general properties of Io). Infrared telescopic observations of Io indicate that the satellite is losing heat at the extraordinary rate of about 100 TW corresponding to a surface heat flux of about 2.5 W m^{-2} (Morrison and Telesco, 1980; Matson et al., 1981; Sinton, 1981; Pearl and Sinton, 1982;

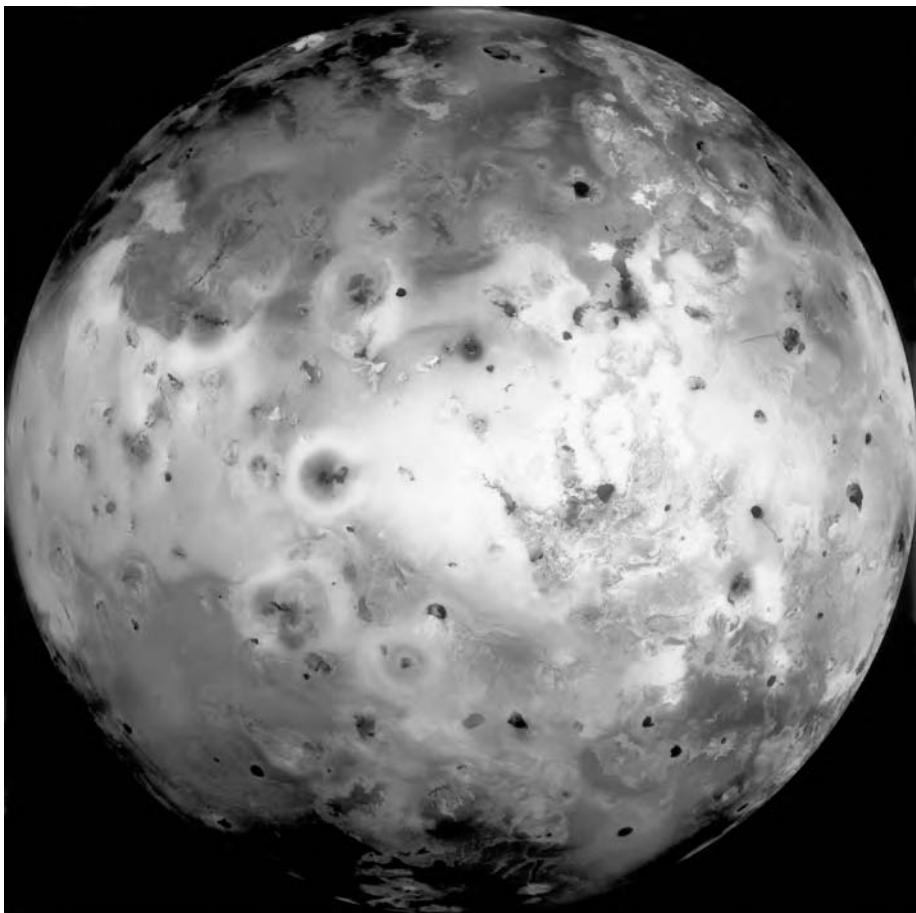


Figure 14.65. Global view of Jupiter's satellite Io from high-resolution (1.3 km per pixel) images obtained by the Galileo spacecraft on 3 July 1999. This false color mosaic uses near-infrared, green, and violet filters of the spacecraft's camera to enhance more subtle color variations. Surface features include mountains several kilometers high, layered materials forming plateaus, and irregular depressions or volcanic calderas. Some volcanic centers have bright, colorful flows possibly due to lavas with predominantly sulfur composition. Dark flow-like features may be silicate lava flows. Volcanic resurfacing has erased any evidence of impact craters. The picture is centered at 0.3° north latitude and 137.5° west longitude. North is to the top of the picture and the sun illuminates the surface from almost directly behind the spacecraft.

For a color version of this figure, see plate section.

Nash et al., 1986; Veeder et al., 1994). Io's surface heat loss of about 100 TW is about 2.8 times larger than the total heat flow through the Earth's surface of about 35.5 TW (Turcotte and Schubert, 1982) even though the Earth's radius is 3.5 times larger than Io's radius. Io's surface heat flux of about $2,500 \text{ mW m}^{-2}$ is approximately 35 times larger than the Earth's surface heat flux of about 70 mW m^{-2} (Turcotte and Schubert, 1982). The heat flow from the Moon, based on the mean of two lunar heat flux measurements by Apollo 15 and 17 (18 mW m^{-2} , Langseth et al., 1976), is about 0.7 TW, less than 1% of Io's heat loss. Clearly, no cosmochemically reasonable concentration of radiogenic elements in Io's interior can account for the enormous amount of heat that must be generated inside the

satellite. Io undoubtedly possesses a terrestrial-like inventory of radiogenic elements which would contribute at most about 1 TW to its surface heat flow, similar to the lunar heat flow. However, most of Io's surface heat loss originates from an energy source that is unimportant for the Earth and the other terrestrial planets. It is this energy source that distinguishes Io from other solar system bodies and is of particular interest here in connection with planetary thermal history.

The major source of Io's internally generated heat is widely accepted to be tidal dissipation (Peale et al., 1979; Yoder, 1979; Schubert et al., 1981, 1986; Yoder and Peale, 1981; Cassen et al., 1982; Ross and Schubert, 1985, 1986; Burns, 1986; Nash et al., 1986; Peale, 1986; Segatz et al., 1988). Although Io is rotating around Jupiter synchronously with its orbital period, its relatively large eccentricity, forced by an orbital resonance with Europa and Ganymede (known as the Laplace resonance), causes the tide-raising potential of Jupiter on Io's surface to oscillate. The periodic distortion of Io in response to the time-varying tidal potential gives rise to tidal dissipation and heating in its interior. Tidal friction in Io tends to reduce its orbital eccentricity, but circularization of Io's orbit is prevented by the orbital resonance. The energy dissipated as heat in Io's interior derives from orbital energy, the ultimate source being the rotational energy of Jupiter. Tides raised on Jupiter by Io produce torques which decelerate the planet's spin.

Two principal tides are raised on Io due to its synchronous but eccentric motion. One is radial and is due to the varying distance of the satellite to the planet; the other, the dominant tide (Yoder, 1979; Segatz et al., 1988), moves back and forth across the mean subplanetary point and is due to the libration of the satellite which results from variations of the orbital angular velocity along the elliptic orbit. The mean dissipation rate due to both these tides \dot{E}_T is given by (Segatz et al., 1988; see also Yoder and Peale, 1981)

$$\dot{E}_T = \frac{21}{2} \frac{R_{\text{Io}}^5}{G} n^5 e^2 \text{Im}(k) \quad (14.5.1)$$

where R_{Io} is the radius of Io (Table 14.1), G is the universal gravitational constant, n is Io's mean motion (i.e., 2π divided by its orbital period), e is the orbital eccentricity, and $\text{Im}(k)$ is the imaginary part of Io's complex second degree tidal potential Love number (Love, 1927; k is the ratio of the component of the second degree potential at Io's displaced surface arising solely from Io's tidal deformation to the second degree component of the imposed tidal potential). Equation (14.5.1) can be rewritten in terms of the frequently used dissipation factor Q

$$Q \equiv \frac{|k|}{\text{Im}(k)} \quad (14.5.2)$$

as

$$\dot{E}_T = \frac{21}{2} |k| \frac{R_{\text{Io}}^5 n^5 e^2}{G Q} \quad (14.5.3)$$

The complex second degree tidal potential Love number of a body depends on its structure and rheology. It is possible to determine k for bodies with sufficiently simple structure and rheology by solving the equilibrium equations for the deformation of the body subject to an imposed tidal potential. For a homogeneous elastic body with density ρ and modulus of rigidity μ , the second degree potential Love number is real and is given by

$$k = \frac{3/2}{1 + 19\mu/(2g\rho R)} \quad (14.5.4)$$

where R is the body's radius and g is surface gravity (Love, 1927; Jeffreys, 1962). Tidal dissipation in an almost elastic body can be calculated from (14.5.3) with k given by (14.5.4) and Q regarded as an independent property of the body (Peale and Cassen, 1978). However, in reality, both k and Q depend in a complex way on a body's internal structure (e.g., layering, molten regions) and rheology, and choosing k and Q as independent parameters may lead to inconsistent models (e.g., a large k is inconsistent with a small Q). Also, use of (14.5.4) together with an assumed value of Q to calculate dissipation, bases the calculation on purely elastic and inviscid deformation rates; both the amplitude and phase angle of the deformation rate of a viscoelastic body are affected by the dissipation. Accordingly, Segatz et al. (1988) have calculated tidal dissipation in Io based on layered models of the satellite with Maxwell viscoelastic rheology.

Deformation of a Maxwell body is governed by the constitutive relation (Peltier, 1974)

$$\dot{\tau}_{kl} + \frac{\mu}{\eta} (\tau_{kl} - \frac{1}{3} \tau_{jj} \delta_{kl}) = 2\mu \dot{e}_{kl} + \lambda \dot{e}_{jj} \delta_{kl} \quad (14.5.5)$$

where τ_{kl} and e_{kl} are the stress and strain tensors, respectively, δ_{kl} is the Kronecker delta, λ is the Lamé constant, η is the dynamic viscosity, and the dot denotes a derivative with respect to time. Hooke's law is obtained by taking the Laplace transform of (14.5.5) and assuming incompressibility:

$$\bar{\tau}_{kl} = 2\mu(s) \bar{e}_{kl} \quad (14.5.6)$$

where $\bar{\tau}_{kl}$ is the Laplace transform of the deviatoric stress tensor, \bar{e}_{kl} is the Laplace transform of the strain tensor, $\mu(s) = \mu s / (s + \mu/\eta)$ is the complex shear modulus, and s is the Laplace variable. The imaginary part of $\mu(s)$ gives the phase lag between stress and strain. Application of the correspondence principle (Cathles, 1975) formally reduces the viscoelastic problem to an elastic problem with well-known methods of solution for layered bodies (e.g., Alterman et al., 1959; Takeuchi et al., 1962). The ratio η/μ defines the Maxwell time τ_M . With a Maxwell time much less than the period of forcing, the body deforms viscously; it deforms elastically if τ_M is much larger than the forcing period. The tidal response of a layered Maxwell satellite depends on the layer thicknesses and material parameters. The amount and spatial distribution of tidal heating in Io is therefore a sensitive function of the satellite's internal structure.

14.5.2 Some Consequences of Tidal Dissipation

There is too much tidal dissipation in Io for its interior to be entirely solid with material parameters similar to those of the Earth or Moon. Peale et al. (1979) and Peale and Cassen (1978) have suggested that Io is a solid shell surrounding a liquid interior, a structure formed as a consequence of runaway melting due to tidal heating. Runaway melting could occur if melting were initiated near the center of Io by tidal dissipation and heat transfer in the surrounding solid part of Io was unable to remove the tidally generated heat because tidal dissipation would increase with the radius of the molten region. However, Schubert et al. (1981) have pointed out that the thermostat effect of subsolidus mantle convection should prevent runaway melting. Even if runaway melting occurred, efficient liquid-state convection would solidify the satellite in a few hundred million years leaving a differentiated satellite with a possibly molten iron-rich core, a solid mantle, and a partially molten asthenosphere (Schubert et al., 1981, 1986). The partially molten asthenosphere would exist because tidal

dissipation in a silicate partial melt layer increases as the layer thickness decreases, thereby preventing complete solidification of the asthenosphere.

While a largely molten Io cannot be entirely ruled out, it seems most plausible that Io has a hot, low- Q , near-solidus mantle and a partially molten asthenosphere. The major uncertainty in Io's present structure concerns the existence and nature of the asthenosphere. As we will see below, it is possible to generate 0 (100 TW) of tidal dissipation in a model of Io without an asthenosphere but with a mantle having a Maxwell rheology and viscosity a few times 10^{16} Pa s (Ross and Schubert, 1985, 1986; Segatz et al., 1988). Most of the tidal heating occurs deep in the mantle, just above the core–mantle boundary. It is also possible to generate this amount of heat by tidal dissipation in a model of Io with a partially molten asthenosphere about 20–100 km thick with viscosity about 10^6 – 10^9 Pa s (Ross and Schubert, 1985; Segatz et al., 1988). In this model the tidal heating occurs mainly in the asthenosphere. Voyager-based observations of a basin and swell pattern in Io's equatorial long-wavelength topography (Gaskell et al., 1988) strongly support the existence of an asthenosphere in Io. The basin and swell topography is only consistent with tidal dissipation models of Io in which substantial heating occurs in an asthenosphere (Ross et al., 1990). However, Galileo limb profiles of Io have not confirmed the longitudinal variations in topography (Thomas et al., 1998).

Question 14.33: Does Io have a partially molten asthenosphere?

14.5.3 Io's Internal Structure

Io's mean density and hydrostatic shape strongly suggest that it has an Fe–FeS core about 1,000 km in radius (Gaskell et al., 1988; Segatz et al., 1988). The mean density of Io (Table 14.1) is larger than densities of terrestrial rocks, and core radii between 700 and 1,000 km have accordingly been proposed (Consolmagno, 1981; Dermott, 1984; Nash et al., 1986). Segatz et al. (1988) developed a structural model of Io with a core radius of 980 km, a mantle density of $3,200 \text{ kg m}^{-3}$, and a core density of $5,150 \text{ kg m}^{-3}$. The core radius and the densities were derived from an adiabatic model of Io with STP mantle and core densities of $3,450$ and $5,400 \text{ kg m}^{-3}$, respectively. These are the STP densities of the Earth's upper mantle and eutectic Fe–FeS melt (Usselman, 1975). A lithosphere basal temperature of 1,600 K was also assumed. The assumption of a eutectic core maximizes the core radius and because the eutectic temperature at Io's central pressure is 1,250 K (Usselman, 1975), the core was assumed to be liquid.

Io's density is compatible with that of a dehydrated C2 chondrite and this composition has been proposed for Io (Consolmagno, 1981; Lewis, 1982) to explain free sulfur on the surface. Most of the sulfur, however, would differentiate into the core (Consolmagno, 1981), resulting in a eutectic core if the concentration of sulfur is a little less than 5% of Io's mass. Io's core may be smaller if it contains less sulfur; a pure iron core would have a radius of about 700 km. Because the liquidus temperature of pure iron at Io's central pressure is around 2,000 K (Boehler, 1986), Io might then have a solid inner core.

Segatz et al. (1988) have also calculated the hydrostatic figure of the above structural model of Io. The figure can be calculated from the solution of the equation of motion by determining the second degree surface deformation Love number for the fluid limit h_f (Jeffreys, 1962). The Love number h_f is the ratio of the second degree surface displacement of a tidally deformed fluid body to the second degree imposed tidal potential at the surface

divided by surface gravity. For a constant density body h_f is 2.5 (Jeffreys, 1962), but h_f for the Io model is less than 2.5 because density increases with depth in the model. For the Segatz et al. (1988) structural model, the tidal disturbance potential and Io's rotation give a triaxial equilibrium figure with principal radii $a = 1,833.3$ km, $b = 1,822.6$ km, $c = 1,819.1$ km, and $h_f = 2.3$. The radii agree well with those determined from Voyager observations by Gaskell et al. (1988); the observations give $a = 1,830.0$ km, $b = 1,818.7$ km, and $c = 1,815.3$ km. The agreement supports the existence of an Fe–FeS core in Io. The observed figure is nearly in hydrostatic equilibrium; $(b-c)/(a-c)$ is 0.23, very close to the hydrostatic value of 0.25.

Galileo gravity (Anderson et al., 1996a) and shape measurements (Thomas et al., 1998) have confirmed and further constrained the basic internal structure model of Io discussed above. Analysis of the radio Doppler data from the flyby of Io by the Galileo spacecraft on 7 December 1995 yielded values of the gravitational coefficients J_2 and C_{22} equal to $(1,863 \pm 90) \times 10^{-6}$ and $(559 \pm 27) \times 10^{-6}$, respectively. The analysis of the radio Doppler data assumed that Io was in rotational and tidal equilibrium so that J_2 and C_{22} were not independently determined (for a body in hydrostatic equilibrium $J_2 = \frac{10}{3}C_{22}$). The degree 2 gravitational coefficients of a planet can be used to infer the planet's axial moment of inertia C if the degree 2 gravitational field has its origin in the equilibrium ellipsoidal distortion of the body to rotational and tidal forcing. Under this assumption, the value of C/MR^2 for Io (M is the mass of Io and R is Io's radius) turns out to be 0.378 ± 0.007 (Anderson et al., 1996a). With the assumption of hydrostatic equilibrium, the degree 2 gravitational coefficients also determine the ellipsoidal shape of the body; the shape of Io derived from the gravity field is given by $(a - c)/c = 7.897 \times 10^{-3}$ and $(b - c)/c = 1.974 \times 10^{-3}$. These values are consistent with the shape of Io derived from Voyager data (Gaskell et al., 1988). Moreover, the shape of Io inferred from Galileo limb profiles is indistinguishable from an equilibrium figure and consistent with the gravity shape (Thomas et al., 1998). The proximity of Io to Jupiter, the strong heating of Io by tidal flexing, and the measured shape of Io all argue strongly that Io is in hydrostatic equilibrium. This is important verification of a key assumption made in the interpretation of Galileo gravity data to yield the axial moment of inertia of Io.

The value of $C/MR^2 = 0.378$ for Io means that there is a concentration of mass toward the center of the satellite (C/MR^2 for a sphere of uniform density is 0.4). Anderson et al. (1996a) have used a simple two-layer model of Io to explore the consequences of the measured value of C/MR^2 . In a two-layer model with core radius r_c , core density ρ_c , mantle density ρ_m , and outer radius R , mean density $\bar{\rho}$ and C/MR^2 are given by

$$\bar{\rho} = \left(\frac{r_c}{R}\right)^3 (\rho_c - \rho_m) + \rho_m \quad (14.5.7)$$

$$\frac{C}{MR^2} = \frac{2}{5} \left[\frac{\rho_m}{\bar{\rho}} + \left(1 - \frac{\rho_m}{\bar{\rho}}\right) \left(\frac{r_c}{R}\right)^2 \right] \quad (14.5.8)$$

For $C/MR^2 = 0.378$ and $\bar{\rho}$ given in Table 14.1, there are two constraints ((14.5.7) and (14.5.8)) on the three model parameters ρ_c , ρ_m , and r_c . Thus it is not possible, even with a knowledge of both $\bar{\rho}$ and C/MR^2 , to uniquely determine the size and density of Io's core. With an additional assumption about core density (or composition), r_c can be determined. If Io's core is a eutectic mixture of iron and iron sulfide ($\rho_c = 5,150 \text{ kg m}^{-3}$), $r_c/R = 0.52$ and the core mass is about 20% of Io's mass; if the core is pure iron ($\rho_c = 8,090 \text{ kg m}^{-3}$), $r_c/R = 0.36$ and the core mass is about 10% of Io's mass. The conclusion that Io has a

metallic core is a robust one and its size is consistent with pre-Galileo estimates based on Io's shape. Not only does Io have a metallic core, but it also might have an active dynamo or magnetoconvective engine in its core (Sarson et al., 1997) responsible for the observed magnetic field perturbation measured by Galileo during its flyby of Io (Kivelson et al., 1996a; Khurana et al., 1997a).

14.5.4 Models of Tidal Dissipation in Io

The theory and structural models discussed above can be combined to yield predictions of the amount and distribution of tidal heating in Io. We describe here the results obtained by Segatz et al. (1988).

Figure 14.66 shows the spatial distribution of surface heat flow obtained by integrating the volumetric tidal dissipation rate in the mantle over radial distance in an Io model with no asthenosphere. To balance the observed surface heat loss by tidal dissipation requires a mantle viscosity η between 4×10^{12} Pas and 6×10^{16} Pas and a shear modulus μ in excess of 80 MPa. The model used in Figure 14.66 produces the observed heat loss and has $\eta = 2 \times 10^{16}$ Pas and $\mu = 10^{10}$ Pa. This viscosity is about the minimum solid-state viscosity of rock (Tullis, 1979) and it is also the viscosity required to transfer the observed heat flux by subsolidus convection (Schubert et al., 1981). The value of the shear modulus is compatible with the shear moduli of rock (Berckhemer et al., 1982). The dissipation factor in the model of Figure 14.66 is about 36 and the magnitude of the Love number k is 0.25. Surface heat flux in the mantle dissipation model of Figure 14.66 is symmetrical in latitude and longitude (about the meridional plane through the sub- and anti-Jovian points), has minima of about 0.6 W m^{-2} at the sub- and anti-Jovian points, and maximizes at the poles.

Surface heat flow due to radially integrated tidal dissipation in an Io model with an asthenosphere is shown in Figure 14.67. The model has a 30 km thick elastic lithosphere and a 50 km thick asthenosphere with a viscosity of 100 MPa and a shear modulus of 10 MPa. Io's observed heat loss is also produced by tidal dissipation in the asthenosphere of this model. In contrast to the model of Figure 14.66 with no asthenosphere, the maximum tidal heat production and heat flux (2.4 W m^{-2}) occur 30° north and south of the sub- and anti-Jovian

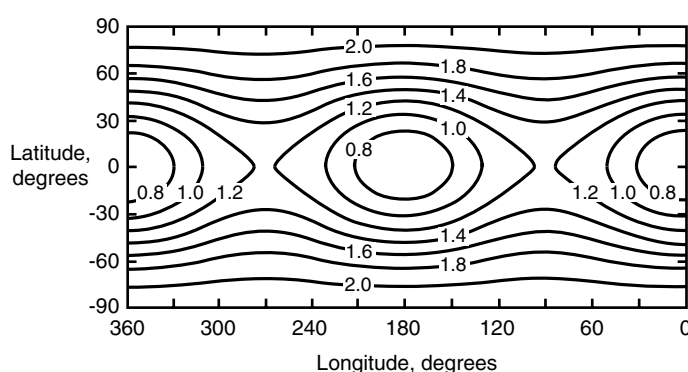


Figure 14.66. Spatial distribution of surface heat flux due to radially integrated tidal dissipation in a model of Io with no asthenosphere and $\eta = 2 \times 10^{16}$ Pas, $\mu = 10^{10}$ Pa (after Segatz et al., 1988). Latitude and longitude are Iographic coordinates. The sub- and anti-Jovian points are at longitudes 0° and 180° . The contours are curves of constant heat flux (W m^{-2}). Maximum heat flux occurs at the poles and heat flux minima are at the sub- and anti-Jovian points.

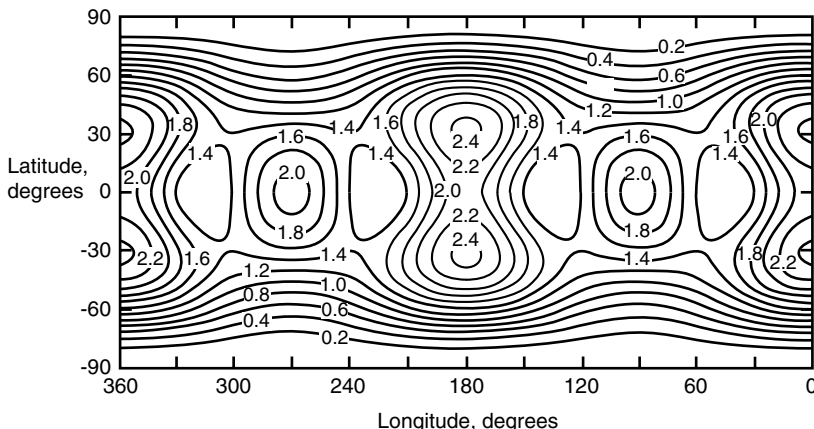


Figure 14.67. Contours of surface heat flow (W m^{-2}) in an Io model with an asthenosphere obtained by integrating the volumetric tidal dissipation rate in the asthenosphere over radial distance. Dissipation in the asthenosphere results in heat flow maxima near the equator and near-zero heat flow at the poles. Latitudes and longitudes are Iographic coordinates. Asthenosphere thickness is 50 km and viscosity is 100 MPa (after Segatz et al., 1988).

points. Smaller local maxima are located at the orbit tangent points (longitude 90° and 270° and latitude 0°). On the equator between these points and the sub- and anti-Jovian points, the surface heat flux has local minima with half values of the maximum heat flux. The heat flux at the poles is close to zero.

The asthenosphere model of Figure 14.67 is not unique in the sense that tidal dissipation in other viscoelastic models of Io can also generate the observed heat loss from Io. For example, if the asthenosphere thickness in the model of Figure 14.67 is doubled to 100 km, the requisite amount of tidal dissipation can be achieved if the asthenosphere viscosity is 10^9 Pa s. These viscosities agree well with the lower bound for the sublithospheric viscosity given by Webb and Stevenson (1987) using subsidence velocities of topographic features. For a given dissipation rate, asthenosphere viscosity increases with asthenosphere thickness. In general, asthenosphere thickness and viscosity are the primary parameters determining the tidal dissipation rate in Io models that contain an asthenosphere. The shear modulus of the asthenosphere must be such that the Maxwell time roughly equals or is smaller than the orbital period of Io.

In the model of Figure 14.67, most of the dissipation occurs in the asthenosphere. Tidal dissipation in the asthenosphere is largest near the mantle–asthenosphere and asthenosphere–lithosphere boundaries. This results from tangential movement of asthenosphere material to compensate tidally forced thickness variations. In the model of Figure 14.66 with no asthenosphere, the volumetric dissipation rate generally decreases with radial distance from the core–mantle boundary.

Because of the prominent differences in the spatial distribution of radially integrated tidal dissipation rates between Io models with and without an asthenosphere, Figures 14.67 and 14.66, respectively, it might be expected that the observed surface distributions of plumes and hot spots would provide an indicator of Io's internal structure. There is some observational support for asthenospheric heating although the data are not conclusive (Spencer and Schneider, 1996). Plume activity may be concentrated toward the equator and diffuse glows are seen in eclipse at both the sub- and anti-Jovian points (McEwen et al., 1998a). A major

problem is lack of global infrared observations of uniformly adequate spatial resolution by Earth-based telescopes and spacecraft experiments. For example, Io's polar regions are very poorly covered, if at all.

Io's surface topography might also be expected to reveal the pattern of internal tidal heating especially if the heating was in an asthenosphere close to the surface. According to Voyager observations, Io's equatorial topography is dominated by a series of four alternating high and low regions spaced roughly equally in longitude (Gaskell et al., 1988). Its polar topography is moderately high in the north and nearly at the average radius in the south. The near-equatorial highs and lows in the tidal heating pattern of Figure 14.67 have a similar longitude distribution as the observed topography and suggest that the pattern of tidal heating in a viscous asthenosphere controls the large-scale equatorial topography (Gaskell et al., 1988; Ross et al., 1990).

Ross et al. (1990) have used the tidal heating model of Segatz et al. (1988) to calculate global topography for multilayer viscoelastic models of Io with dissipation occurring in a viscous asthenosphere and a solid mantle. Topography is calculated from the surface heat flux (radially integrated tidal dissipation rate) by assuming isostasy and either a "thermal" lithosphere, i.e., one denser than the underlying asthenosphere because of thermal contrasts, or a "differentiated" lithosphere, i.e., one lighter than the underlying asthenosphere because of compositional differences. The Io model which most closely matches the observed topography is one in which about two-thirds of the tidal heating occurs in the asthenosphere and about one-third occurs in the underlying solid mantle. Other considerations suggest that Io's lithosphere is differentiated. In a differentiated lithosphere model consistent with topography, the asthenosphere must be at least 50 km thick and less than about 100 km thick, with viscosity at least about 100 MPa s and less than about 1 TPa s. The asthenosphere viscosity suggests a crystal-rich magma (McBirney and Murase, 1984). The asthenosphere must be about 7% more dense than the lithosphere. Tidal dissipation in the mantle requires that its density exceeds the asthenosphere density by at least 10%. The viscosity of the mantle must lie between about 10^{16} and 4×10^{17} Pa s consistent with a solid mantle but allowing for some partial melt. The mean thickness of the lithosphere is about 35 km. Regions of greater (lesser) than average surface heat flow are depressed (elevated) with respect to the hydrostatic ellipsoid of Io's figure and the lithosphere in such regions is thinner (thicker) than the mean lithosphere thickness. Heat is transferred across the lithosphere by both conduction and magma migration (O'Reilly and Davies, 1981). Tidal dissipation in the asthenosphere is focused strongly at the lithosphere–asthenosphere and asthenosphere–mantle interfaces. Figure 14.68 illustrates the differentiated lithosphere model of Io.

The differentiated lithosphere model discussed just above is consistent with a number of observations of Io. Io must be extensively differentiated if, over geologic time, it has been heated on average at even 10% of the present heating rate; Io could have been melted 40 times over with this amount of heating (Keszthelyi and McEwen, 1997). Silicate volcanism is common on Io (Carr, 1986; Johnson et al., 1988; Blaney et al., 1995; Davies, 1996; Howell, 1997; McEwen et al., 1998a, b). Inferred temperatures of some lavas on Io exceed 1,700 K and may be as large as 2,000 K, hotter than the highest temperature basaltic eruptions on Earth today (McEwen et al., 1998b). A possible explanation for these high temperatures is that these lavas are melts of ultramafic (magnesium-rich) silicates with high melting temperature (McEwen et al., 1998b). Geochemical modeling of a strongly differentiated Io predicts a 50 km thick low-density crust rich in alkali elements, silica, and aluminum, and a mantle rich in magnesium, iron, and calcium (Keszthelyi and McEwen, 1997). The mantle could be further differentiated into a less dense magnesium-rich upper part and a more dense iron- and

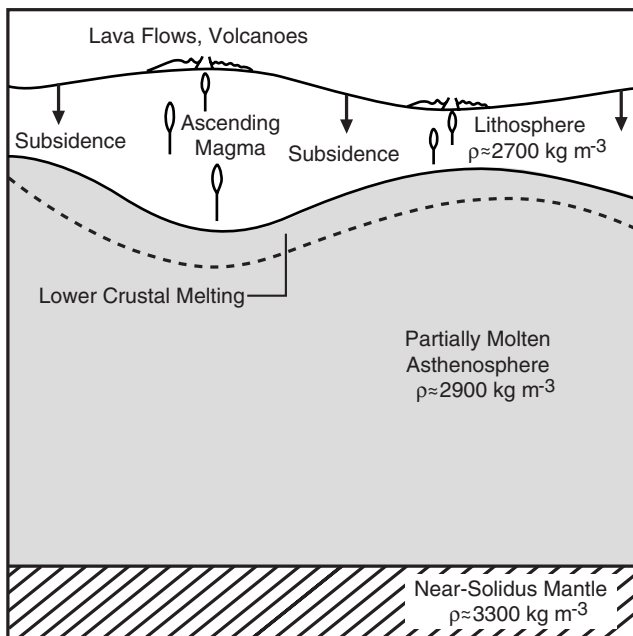


Figure 14.68. A sketch of the differentiated lithosphere model of Io (after Ross et al., 1990). The lithosphere subsides at a rate that balances the resurfacing rate of Io. Reheating of the subsiding lithosphere contributes importantly to the near-surface heat balance.

calcium-rich lower part; melts from such an upper mantle could have temperatures as high as 2,100 K (McEwen et al., 1998b). Other explanations for the high lava temperatures on Io include the possibility of strong superheating of magmas by the intense tidal dissipation in Io and large degrees of partial melting of a mantle that has undergone little differentiation after core formation. Io's mantle could have maintained such a primitive composition if the lithosphere has been efficiently recycled and mixed back into the mantle (Carr et al., 1998a; McEwen et al., 1998b). The substantial rate at which Io is resurfaced (about 10 cm yr^{-1}) suggests that the lithosphere may be subsiding and remelting at its base sufficiently rapidly to enable the recycling to occur (Carr et al., 1998a) (see Fig. 14.68).

Though Io is intensely heated by tidal deformation, its lithosphere must be thick enough to support isolated, high-standing mountains distributed widely and evenly over its surface (Carr et al., 1998a). The mountains are polygonal in shape with widths of 50–150 km, up to 15 km high, and have an uncertain origin; some mountains may be volcanic while others show extensive tectonic disruption. Schenk and Bulmer (1998) suggest that the mountains are due to thrust faulting and block rotation caused by the compression at depth resulting from the subsidence of Io's crust. Their detailed study of the morphology of mountains such as Euboea Montes (about 10 km high and about 175 km \times 240 km in base planform) revealed no evidence of volcanic associations such as lava flows, vents, and calderas. The 35 km average lithosphere thickness in the model discussed above would suffice to support the mountains, but an even thicker lithosphere is possible. The high rate of resurfacing and the deposition of tidal heating in the asthenosphere and underlying mantle suggests relatively low temperature gradients in the upper lithosphere and steeper thermal gradients in the lower lithosphere (Carr et al., 1998a).

The differentiated lithosphere model of Io was originally motivated by the basin-swell longitudinal topographic variations deduced from Voyager data. So far, Io topographic data based on Galileo limb profiles have not confirmed the Voyager basin-swell topography (Thomas et al., 1998). Even should the Voyager topography not prove to be robust, the differentiated lithosphere model of Io is a reasonable one for such a volcanically active, intensely heated satellite.

Question 14.34: How thoroughly has Io been differentiated?

14.5.5 Models of the Thermal and Orbital Dynamical History of Io

The preceding discussion of Io has dealt mainly with its present internal structure and the physics of its principal internal energy source, i.e., tidal dissipation. It remains to integrate this material into a thermal history model of Io. A major difficulty in developing a theory of Io's thermal history is in the coupling of this history to Io's orbital evolution because the source of Io's internal heat is its orbital energy. In turn, Io's orbital history depends on its rheology which is a function of its thermal state. In fact, Io's orbital–thermal evolution is coupled to that of Europa and Ganymede, through the Laplace resonance. So the evolution of the three inner Galilean satellites really needs to be considered as that of a single system. Both Ojakangas and Stevenson (1986) and Fischer and Spohn (1990) have presented models of the coupled thermal–orbital evolution of Io. In the following, we summarize the model and major results of Fischer and Spohn (1990).

Tidal dissipation couples Io's thermal and orbital evolution because it is a sink of energy in the orbital energy balance and a source of energy in the thermal balance. The tidal dissipation rate (see (14.5.1) and (14.5.3)) depends on the orbital parameters (mainly eccentricity and mean motion) and Io's internal temperature through the temperature dependence of the rheological parameters. The orbital evolution in the model of Fischer and Spohn (1990) is based on the theory of the Laplace resonance of Yoder and Peale (1981) and includes the effects of dissipation in both Io and Europa. The orbital evolution theory provides a nonlinear first-order ordinary differential equation for the secular variation of Io's mean motion, the integration of which, together with other dynamical relations, leads to the determination of Io's eccentricity. The thermal evolution in the model of Fischer and Spohn (1990) incorporates the tidal dissipation calculation of Segatz et al. (1988) for a three-layer model of Io with a 980 km radius Fe–FeS core, a Maxwell rheology mantle, and a 30 km thick elastic lithosphere. The thermal model also parameterizes convective mantle heat transfer and the secular variation in Io's temperature following the approach of Schubert et al. (1979a) by equations similar to those in Section 13.2.2 with the radiogenic heating term replaced by tidal heating.

Fischer and Spohn (1990) assume temperature-dependent mantle shear modulus μ and viscosity η . An important aspect of the model is the allowance for partial melt in Io's mantle through the dependence of μ and η on temperature T for temperatures in excess of the solidus temperature. Both shear modulus and viscosity decrease strongly with increasing temperature above a characteristic T slightly higher than the solidus temperature. Below the solidus temperature μ is a constant and η has the characteristic subsolidus temperature dependence of (13.2.6).

The main results of Fischer and Spohn's (1990) model thermal–orbital history calculations are as follows. Io may presently be in a hot, high dissipation state with approximate

equilibrium between tidal heat production and heat loss. An exact equilibrium cannot pertain because Io's internal temperature and orbital eccentricity are slowly evolving with time. For this state to be stable against small perturbations in temperature and eccentricity, tidal dissipation must decrease with increasing T . This is accomplished in the model by the decrease of shear modulus with increasing T above the solidus and requires Io's mantle to be partially molten. In an Io model with an asthenosphere, tidal dissipation would also decrease with increasing T because asthenosphere thickness increases with increasing T (Segatz et al., 1988). Thus, Io's partial melt can be concentrated in an asthenosphere as is preferred in the differentiated lithosphere model of Ross et al. (1990).

The hot high dissipation state (perhaps the present Io) will eventually be replaced by one involving oscillations with time in the orbital and thermal properties of Io (see also Ojakangas and Stevenson, 1986). The time of onset of the oscillatory evolutionary stage depends on Io's rheological and heat flow parameter values. The onset time could be a Gyr in the future or Io could already have entered this phase of its evolution. The oscillatory phase of Io's evolution will also be eventually replaced by runaway cooling to a cold, low dissipation state. The duration of the oscillatory phase of evolution also depends sensitively on model parameters and is uncertain. Whereas the thermal histories of the terrestrial planets involve simple secular cooling, the thermal–orbital history of Io involves transitions among three characteristically distinct states, one of which is oscillatory in time as sketched in Figure 14.69.

Which of the three thermal–orbital states characterizes the present Io is uncertain. While Io is presumably not in the cold, low dissipation state, it might be in the hot, high dissipation state or in the oscillatory state. In the former state there is a near-equilibrium between tidal heating and surface heat loss and in the latter state tidal heating and surface heat loss oscillate out of phase with the present Io, being at a peak in the surface heat loss and a minimum in the tidal dissipation rate. There is some difficulty in accepting that Io is in a near-equilibrium state because its heat flow is so large and dynamical considerations place an approximate upper bound of 9×10^{13} W on the average tidal heating rate of Io over the age of the solar system (Schubert et al., 1986), close to the observed value of present heat loss on Io. It is also difficult to understand how energy could be dissipated in Jupiter (the ultimate source of Io's heat flow is the slowing of Jupiter's rotation) at the rate it is observed to flow from Io, although dissipation mechanisms in Jupiter are not well understood (Ioannou and Lindzen, 1993). It is also difficult to believe that we are observing Io in a phase of its oscillatory state that occurs only 10% of the time (Ojakangas and Stevenson, 1986). Perhaps Io is in a transient state of enhanced mantle activity similar to that of Venus during its global resurfacing event.

Question 14.35: What is the nature of Io's present thermal, orbital-dynamical state?

Wienbruch and Spohn (1995) have studied the thermal–orbital evolution of Io with emphasis on the evolution of Io's metallic core and the possibility of dynamo magnetic field generation in the core. They concluded that Io could not have a dynamo at present if the satellite were in the near-equilibrium state because too much heat is generated in the mantle for the core to cool sufficiently to convect and undergo dynamo action. A dynamo would also be unlikely in this state because Io's interior would be too hot for inner core solidification to

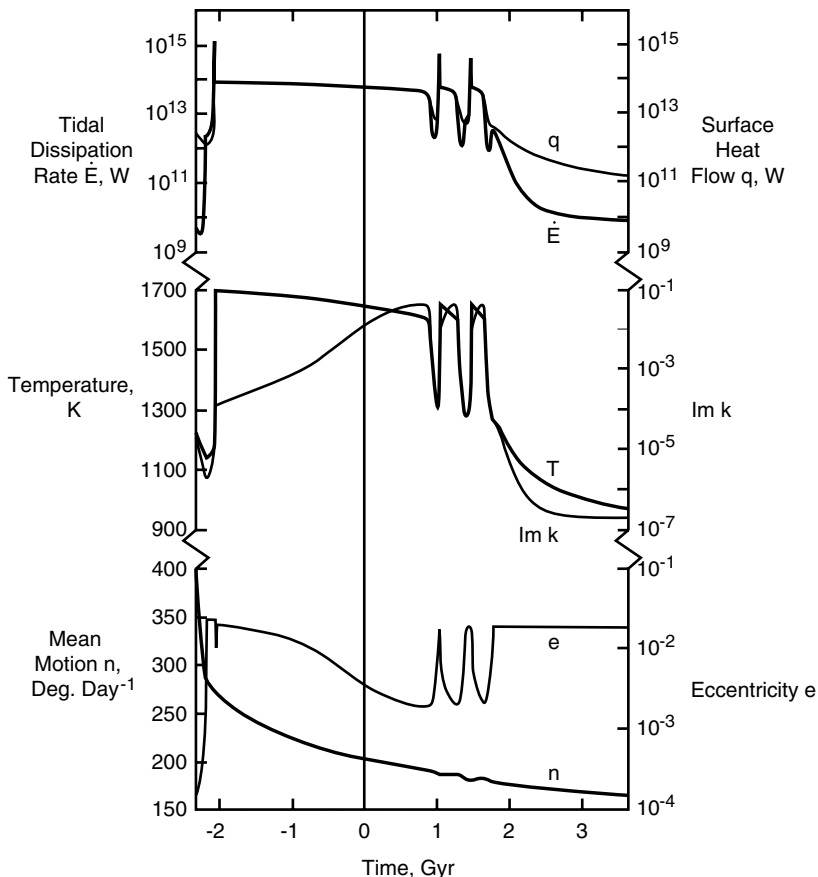


Figure 14.69. Coupled thermal–orbital evolution of an Io model with an Fe–FeS core, a Maxwell viscoelastic model, and an elastic lithosphere (after Fischer and Spohn, 1990). The origin of the time axis is the present. The reader is referred to Fischer and Spohn (1990) for more details about the model and for model parameter values.

have occurred, precluding the possibility of compositionally driven convection and dynamo action. Their analysis did allow for an Io dynamo during certain phases of the oscillatory state. As noted above, the Galileo spacecraft did detect a magnetic perturbation associated with Io (Kivelson et al., 1996a; Khurana et al., 1997a), but the source of this signal (an Io dynamo or currents in the ambient Ionian plasma) has not been definitively identified and its implications for the state of Io’s interior and the satellite’s thermal evolution are uncertain.

Question 14.36: Does Io have a magnetic field?

14.6 Mercury

14.6.1 Composition and Internal Structure

Although it is the smallest of the terrestrial planets, Mercury (Figure 14.70) is the densest of the inner planets (Table 14.1). If the planet has the cosmic abundances of heavy elements,

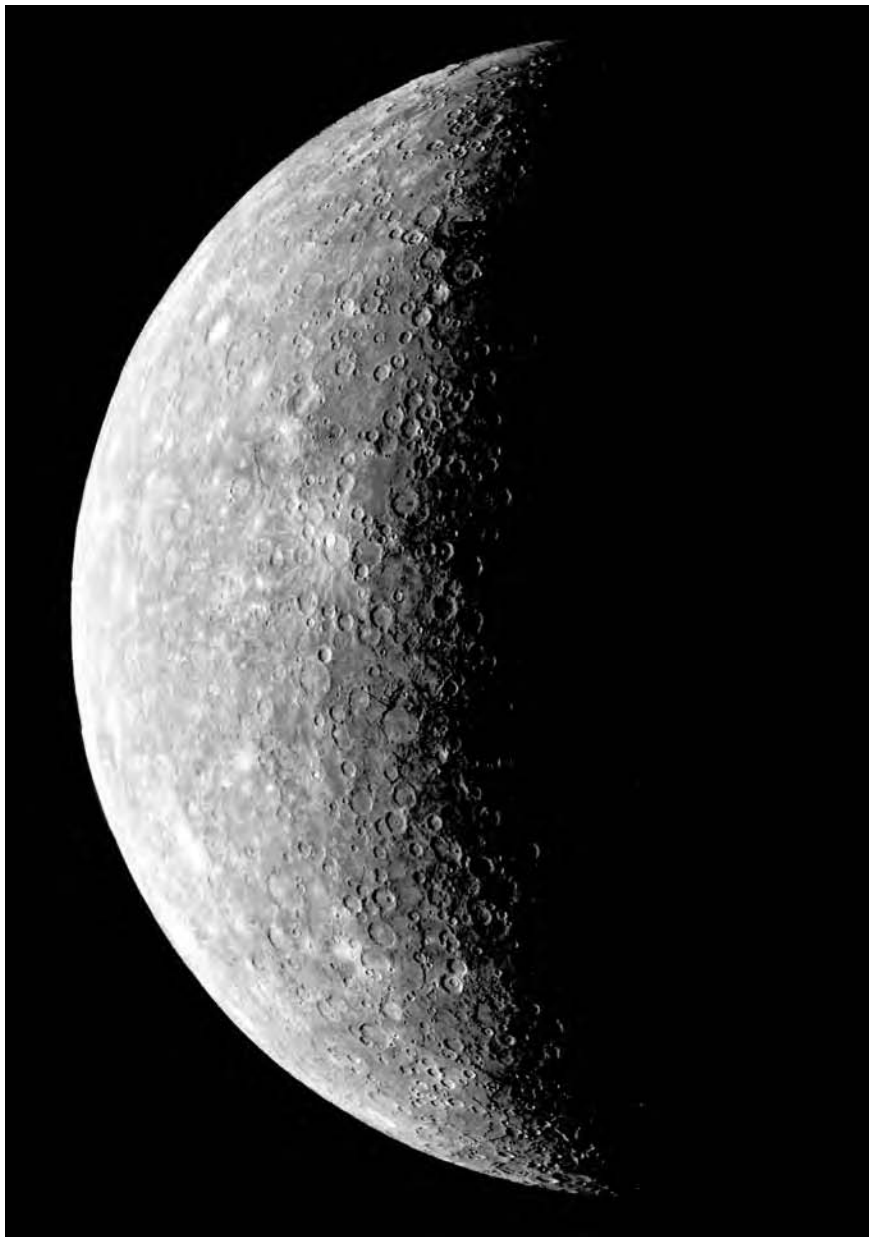


Figure 14.70. Mariner 10 image of Mercury acquired on 24 March 1974.

For a color version of this figure, see plate section.

then its large density requires that Mercury is 60–70% Fe by mass (Urey, 1951, 1952; Kozlovskaya, 1969; Reynolds and Summers, 1969; Siegfried and Solomon, 1974). With the iron concentrated in a central core, Mercury could best be described as a ball of iron surrounded by a thin silicate shell. In the model of Siegfried and Solomon (1974), the radius of Mercury's iron core is about 75% of the planet's radius. Its large iron core and thin

silicate mantle set Mercury apart from the other planets and distinguish its thermal history in interesting ways. In particular, tidal heating in a Mercurian inner core could influence the operation of a Mercurian dynamo. Planetary magnetism once again provides an important constraint on thermal history modeling, but unlike the situations for Venus and Mars, Mercury has a magnetic field with a dipole moment about 4×10^{-4} of the Earth's magnetic dipole moment (Ness et al., 1974, 1975; Connerney and Ness, 1988). The following discussion of Mercury's thermal history follows the papers of Stevenson et al. (1983) and Schubert et al. (1988).

The major uncertainty about Mercury's internal structure is whether the planet is differentiated into an iron core and silicate mantle or whether the iron is more homogeneously mixed.

Question 14.37: What is the structure of Mercury's interior?

If it is assumed that Mercury has a metallic core, then the core size can be inferred from the planet's known density and assumptions about its composition, as above, but the lack of basic dynamical data about the planet precludes a direct determination of its axial moment of inertia and possible core radius. The gravitational coefficients J_2 and C_{22} of Mercury are known from radio tracking of the Mariner 10 flybys of the planet (Anderson et al., 1987), but the moment of inertia cannot be inferred from these data since Mercury cannot be assumed a priori to be in hydrostatic equilibrium. Earth-based radar ranging data have determined the equatorial ellipsoidal shape, the center of figure–center of mass offset in the equatorial plane, and the equatorial topography of Mercury (Harmon and Campbell, 1988; Anderson et al., 1996b). Comparison of the equatorial ellipticity of Mercury with its gravitational equatorial ellipticity has yielded an estimate of the thickness of Mercury's crust of 100–300 km (assuming Airy isostatic compensation of the crust, Anderson et al., 1996b). The existence of a planetary magnetic field points to the existence of a core if the magnetic field is generated by a hydromagnetic dynamo and not by permanent magnetism, as is argued in Schubert et al. (1988).

Question 14.38: What is the source of Mercury's magnetic field?

Reflectance spectra of Mercury's surface (Vilas, 1988) limit the amount of iron in orthopyroxenes at the surface and suggest the concentration of Fe into a core. An actual measurement of Mercury's moment of inertia and core radius may be possible if a future Mercury orbiter can measure the amplitude of the 88-day libration of the outer solid mantle due to torques from the Sun and refine our knowledge of Mercury's obliquity (Peale, 1988). The following discussion of Mercury's thermal history assumes that Mercury consists of a large Fe core surrounded by a thin silicate mantle.

14.6.2 Accretion, Core Formation, and Temperature

Core separation should have occurred early in Mercury's evolution, prior to the end of the period of heavy bombardment (about 4 Gyr ago), because there is no evidence in the surface geology of the large-scale extension that would have accompanied the later differentiation

of the planet (Solomon, 1977). Accretional heating can provide the energy required for core formation. As discussed in Section 13.2 in connection with the early evolution of the Earth, the gravitational potential energy per unit mass made available for heating upon homogeneous accretion of a planet is $0.6 GM/R$. For Mercury, this is enough energy to raise the temperature of the entire planet by 5,500 K, assuming a specific heat of $1 \text{ kJ kg}^{-1} \text{ K}^{-1}$. There is a surfeit of energy for melting and differentiation because the silicate melting temperature in Mercury rises to only about 2,500 K at great depth and the accumulating planetesimals may have initial temperatures of about 1,000 K (Schubert et al., 1988). As discussed in Section 13.2, core formation contemporaneous with accretion requires retention of a fraction of the available accretional energy as heat within the planet while the rest of it is radiated away. A plausible retention efficiency h of 20% (Kaula, 1979a, 1980) would suffice to insure accretional melting of nearly all of Mercury.

Accretional radial r temperature profiles T_{acc} for Mercury based on the model equation (Kaula, 1980; Schubert et al., 1986)

$$T_{\text{acc}}(r) = \frac{hGM(r)}{cr} \left\{ 1 + \frac{ru^2}{2GM(r)} \right\} + T_e \quad (14.6.1)$$

are shown in Figure 14.71. In (14.6.1) T_e is the ambient temperature during accretion, $M(r)$ is the mass of the planet internal to r , c is specific heat, and $u^2/2$ is the approach kinetic energy per unit mass of planetesimals forming Mercury. The calculations for Figure 14.71 assume $ru^2/(2GM) \ll 1$ and $c = 1 \text{ kJ kg}^{-1} \text{ K}^{-1}$. The equation for T_{acc} is based on the assumption that the retained fraction of impact heating is distributed uniformly over the instantaneous surface of the growing planet and that no radial redistribution of heat occurs. The high near-surface temperatures in Figure 14.71 would be reduced by radiative heat loss from the surface and smearing out of the temperature by radial heat transfer in the actual

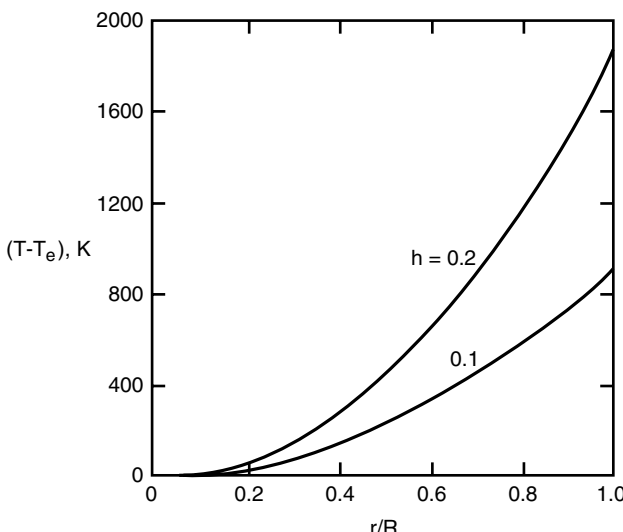


Figure 14.71. Model radial temperature T profile for the accretional heating of Mercury. T_e is the background temperature of planetesimals accumulating to form Mercury and r/R is the radius normalized by the planetary radius. The parameter h is the fraction of gravitational potential energy retained within the growing planet as internal thermal energy.

planet. According to Figure 14.71, melting and differentiation would first occur in the outer portions of the planet after it had grown to a considerable fraction of its final radius.

Core separation contemporaneous with or shortly after accretion releases additional gravitational potential energy. A comparison of the gravitational potential energy of a two-layer model of a planet consisting of a mantle and core with the gravitational potential energy of a homogeneous model of a planet gives the energy of differentiation U_{diff} as (Schubert et al., 1986)

$$U_{\text{diff}} = \frac{16}{15}\pi^2 GR^5 \left\{ \rho_m^2 + \frac{5}{2}\rho_m(\rho_p - \rho_m) + \left(\frac{3}{2}\rho_m - \rho_c \right) (\rho_m - \rho_c) \left(\frac{\rho_p - \rho_m}{\rho_c - \rho_m} \right)^{5/3} - 1 \right\} \quad (14.6.2)$$

where ρ_p is the overall density of the planet and ρ_m and ρ_c are the mantle and core densities, respectively. The energy of differentiation is retained as heat within the planet and will raise Mercury's temperature by about 700 K (Solomon, 1976). Accretional energy and energy of differentiation are likely to have set Mercury on its evolutionary path as a hot, differentiated planet similar to the other terrestrial planets. The energies involved may have been even larger than estimated above if Mercury lost part of its silicate mantle early in its evolution by vaporization or a giant impact. Such events have been suggested as explanations of Mercury's large density (Cameron et al., 1988; Wetherill, 1988).

Question 14.39: Why is Mercury's density so high?

14.6.3 Thermal History

The thermal evolution model of Mercury assumes a fully differentiated initial state with the mantle at the solidus temperature and the core at a near-liquidus adiabat. The cooling of the planet is calculated with the coupled core–mantle model of Stevenson et al. (1983) as modified by Schubert et al. (1988). The basic model has been discussed in Section 13.3 in connection with the thermal evolution of the Earth and it has also been employed in our discussions of the thermal histories of Venus and Mars. Modifications to the basic model by Schubert et al. (1988) include a thickening lithosphere and tidal heating in the solid inner core. The temperature profile in the lithosphere is approximated by a conductive steady state. Tidal dissipation in the core is determined similarly to the calculation of tidal heating in Io, as discussed in the previous section.

The inclusion of tidal dissipation as a heat source in the inner core requires that the basic model of Section 13.3 be extended to provide separate energy balance equations for the inner and outer cores. Instead of (13.3.7) we use (Schubert et al., 1988)

$$\frac{4}{3}\pi R_c^3 \left\{ -\rho_c c_c \eta_c \frac{dT_{cm}}{dt} \right\} + (L + E_G)4\pi R_i^2 \rho_c \frac{dR_i}{dt} = 4\pi \left\{ R_c^2 q_c - R_i^2 q_i \right\} \quad (14.6.3)$$

and

$$\frac{4}{3}\pi R_i^3 \left(-\rho_c c_c \eta_i \frac{dT_i}{dt} \right) + \dot{E}_T = 4\pi R_i^2 q_i \quad (14.6.4)$$

The energy balance for the outer core (14.6.3) differs from (13.3.7) only in the term involving q_i , the heat flux from the inner core. In the energy balance equation for the inner core (14.6.4),

\dot{E}_T is the total power generated by the inner core tidal heat source, T_i is the temperature at the inner–outer core boundary, and η_i accounts for the adiabatic temperature rise in the inner core. Insofar as the energy balance equations are concerned, it is assumed that the density and specific heat are identical in the inner and outer cores.

Tidal dissipation in Mercury’s inner core might be an important heat source for the core because Mercury’s dynamical state is dominated by the tidal interaction with the Sun. Present tidal heating in Mercury is a consequence of rotation with respect to the Sun (period = 175.94 days) and the eccentricity of the orbit (0.175). (Tidal heating in Mercury’s mantle is not an important heat source at present.) Schubert et al. (1988) calculate tidal dissipation in Mercury’s inner core for a three-layer model of Mercury with an elastic mantle, an inviscid outer liquid core, and a Maxwell viscoelastic inner core with temperature-dependent viscosity and shear modulus using the formalism of Zschau (1978), Sabadini et al. (1982), and Ross and Schubert (1986). Inner core tidal heating might be significant in Mercury because the solid iron Maxwell time could be near the tidal forcing period.

The parameter values used in the Mercury thermal history calculations of Schubert et al. (1988) are similar to parameter values used in the thermal evolution models of the other terrestrial planets discussed previously. The mass, radius, and surface gravity of Mercury are given in Table 14.1. Core radius is 1,840 km. Core density and mantle density are, respectively, 8,600 and 3,300 kg m⁻³. The expressions for core liquidus temperature and core adiabat are the ones used in the Mars model of Table 14.7. The constant η_m (see (13.3.8)), which accounts for the adiabatic rise of mantle temperature with depth, is taken as 1, while the similar constants for the inner and outer cores η_i and η_c are 1.1. Other mantle parameters are $k = 4 \text{ W m}^{-1} \text{ K}^{-1}$, $\alpha = 3 \times 10^{-5} \text{ K}^{-1}$, $\beta = 0.3$, $\kappa = 10^{-6} \text{ m}^2 \text{ s}^{-1}$, and $Ra_{cr} = 1,000$. The mantle radiogenic heat source density is the one given in Table 14.7 for the Mars model as is the value of the latent heat release per unit mass L upon inner core freezing.

Schubert et al. (1988) show that the gravitational energy release per unit mass E_G as a consequence of exclusion of the light alloying element in the core (assumed to be S in the Mercury model) from the solid inner core is given by

$$E_G = \frac{2\pi G R_c^2 \chi_0 (\rho_{\text{Fe}} - \rho_S)}{(1 - \xi^3)^2} \left(\frac{\rho_{ic}}{\rho_S} \right) \left\{ \frac{1}{5}(1 - \xi^5) - \frac{\xi^2}{3}(1 - \xi^3) \right\} \quad (14.6.5)$$

where $\xi = R_i/R_c$, χ_0 is the initial mass concentration of S in the core, ρ_{ic} is the density of the inner core, and ρ_S and ρ_{Fe} are the densities of sulfur and iron. According to (14.6.5), E_G varies with the size of the inner core ξ and with χ_0 . Equation (14.6.5) is used to evaluate E_G in the Mercury thermal history calculations.

Mantle kinematic viscosity is given by (13.2.6) with T evaluated at the temperature T_u just below the upper thermal boundary layer. The value of v_0 for the mantle is the one given in Table 14.7 for the Martian mantle, while A_0 is taken to be 57,000 K, corresponding to a stiffer Mercurian mantle compared with the Earth-like Martian mantle of Table 14.7. This large value of A_0 for Mercury’s mantle is based on the assumption that the melting temperature in Mercury’s mantle is higher than in the Earth’s mantle (at the same pressure) because of the likely refractory nature of Mercurian silicates. At a given temperature and pressure, Mercury’s mantle would have a larger viscosity than the Earth’s mantle.

A major unknown, insofar as assessing the potential importance of inner core tidal heating is concerned, is the rheology of solid iron at high temperature and pressure. Frost and Ashby (1982) summarize low-pressure creep data for γ -Fe that suggest deformation by grain boundary diffusion at high temperature. Grain boundary diffusion viscosity is linear

in stress and directly proportional to the cube of the mean iron grain size δ . The temperature dependence of grain boundary viscosity for iron can also be represented by (13.2.6), and for application to the Mercury thermal history model T is evaluated at the temperature just below the upper thermal boundary layer in the inner core. Extrapolation of the data in Frost and Ashby (1982) to the stress appropriate for Mercurian solar tides gives $v_0 = 3.6 \times 10^6 \delta^3$ (δ in mm). The grain size in Mercury's core is unknown. It will be seen that only a small range of grain sizes results in significant inner core tidal heating. The grain boundary activation temperature A_0 for the high-temperature diffusion creep of γ -Fe is taken to be 19,000 K (Frost and Ashby, 1982). The shear modulus of iron as a function of temperature T is $\mu = 81(1 - 0.91T/T_m)$ GPa (Frost and Ashby, 1982). Initial and boundary temperatures for the results discussed below are $T(R_p) = T_s = 440$ K, $T_u(t = 0) = 2,000$ K, $T_{cm}(t = 0) = 2,600$ K; at $t = 0$ the core is entirely liquid.

The results of the Mercury thermal history modeling are similar in many respects to those obtained in the models of the thermal histories of the other terrestrial planets already discussed. We will emphasize here only those aspects of the results of special interest for Mercury, e.g., the effects of tidal heating in the inner core. As we found in our discussion of Martian thermal history, the evolution of the core is particularly sensitive to the initial sulfur weight fraction χ_0 in the core. Schubert et al. (1988) present Mercury thermal histories for χ_0 equal to 0.002, 0.01, and 0.05. Cosmochemical arguments give plausible values of χ_0 ranging from 0 in a strict equilibrium condensation model (Grossman, 1972; Lewis, 1972) up to about 0.5 if substantial mixing occurred among planetesimals in the inner solar system (Basaltic Volcanism Study Project, 1981; Goettl, 1988; Lewis, 1988; Wetherill, 1988).

Figure 14.72 shows how the growth of Mercury's solid inner core varies with time and initial weight percent sulfur. For $\chi_0 = 0.002$ and 0.01, inner core solidification begins before 1 Gyr and at present the core is substantially solid. For $\chi = 0.05$, however, the onset of inner core freezeout is delayed until about 2.5 Gyr and at present the solid inner core is relatively small. A number of early papers on Mercury's thermal history (e.g., Siegfried and Solomon, 1974; Solomon, 1976) predicted rapid solidification of the core, thereby creating a problem for a core dynamo explanation of the present magnetic field. The studies of Cassen et al. (1976), Gubbins (1977b), and Toksöz et al. (1978) emphasized that subsolidus

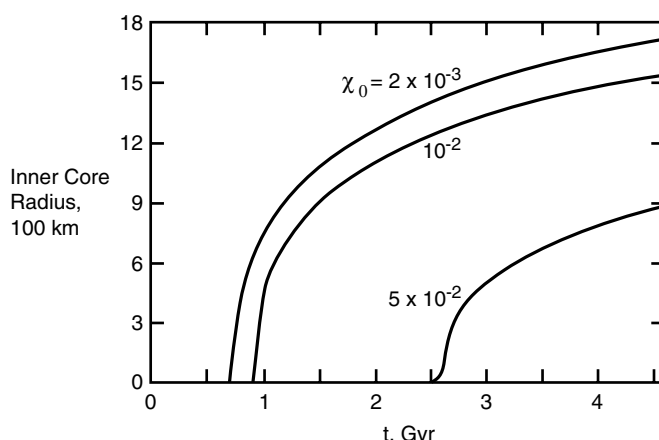


Figure 14.72. Inner core radius versus time in the Mercury thermal history model of Schubert et al. (1988). The parameter χ_0 is the initial mass fraction of sulfur in the core.

mantle convection exacerbated the problem of early core solidification. Figure 14.72 shows, however, that complete core freezing is precluded by even small amounts of sulfur in the core. Nevertheless, for small sulfur concentrations in the core, the liquid outer core is very thin at present and the efficiency of a dynamo operating in a thin shell may be reduced, a point we return to below. Inner core growth is rapid at first and then more gradual with time (Figure 14.72) as the rate of planetary cooling decreases with the decreasing vigor of mantle convection and with the increasing concentration of light constituent in the outer core. Mercury's core would still be liquid at present if χ_0 were greater than about 7%. Inner core growth is not significantly influenced by tidal dissipation in the solidified part of the core.

The cooling of Mercury's mantle and the thickening of its lithosphere with time are typical of thermal histories already discussed and are relatively insensitive to core sulfur concentration and inner core tidal heating. The lithosphere thickens to a present value of about 200 km in the models of Schubert et al. (1988); the larger lithosphere thickness in the models of Schubert et al. (1979a) results from the absence of mantle radioactivity in those models.

Mercury's cooling history can be translated into a prediction of planetary contraction and compared with the contraction inferred from the surface geologic record. The amount of post-heavy bombardment contraction inferred from the heights and lengths of lobate scarps (compressional structures) on Mercury is a couple of kilometers (Strom et al., 1975; Strom, 1979). Solomon (1976, 1977, 1979) has argued that this observation places a limit of about 1,100 km on the radial extent of core solidification for a core entirely fluid 4 Gyr ago. However, much depends on how early core freezing begins and how rapidly it proceeds. If a substantial amount of core freezing occurs prior to the end of heavy bombardment and preservation of terrain about 4 Gyr ago, then the geologic constraint on the extent of core freezing is weakened.

Schubert et al. (1988) have computed the decrease in planetary radius with time in the Mercury thermal history model as the result of mantle cooling and inner core solidification. The change in planetary radius ΔR_p due to inner core freezing is given by (Solomon, 1977)

$$\Delta R_p = \frac{1}{R_p^2} \int_0^{R_i} \frac{\Delta V_{l \rightarrow \gamma}}{V_\gamma} r^2 dr \quad (14.6.6)$$

where $\Delta V_{l \rightarrow \gamma}$ is the specific volume change upon solidification of liquid Fe to the γ phase and V_γ is the specific volume of γ -Fe at relevant pressures. The secular cooling of the mantle results in a change of planetary radius given by (14.3.10) with $l = 0$ and $\Delta\rho = 0$. The thermal history results of Schubert et al. (1988) favor models of Mercury with initial core sulfur mass concentrations χ_0 greater than about 2%. Models with smaller amounts of S in the core give planetary contractions greater than about 2 km since 1 Gyr.

For χ_0 in the range 0.002–0.05, the thermal history model of Schubert et al. (1988) predicts that the present heat flux out of Mercury's core is subadiabatic. Convection in the liquid outer core and dynamo generation of a magnetic field at present must be driven by chemical stirring due to inner core freezing in these models. Equation (14.3.12) has been used to estimate the Mercurian magnetic dipole moment from the model thermal history results. Present magnetic fields are predicted for initial core sulfur concentrations $\gtrsim 0.1\%$ but $\lesssim 7\%$. More than about 7% initial sulfur concentration precludes any inner core growth and there is insufficient thermal energy to drive a dynamo in such a model at present. For relatively large values of initial core sulfur concentration, e.g., $\chi_0 = 5\%$, the models give long periods of time (i.e., a billion years or more) when Mercury would have had no

magnetic field. These intervals of no dynamo magnetic field generation take place subsequent to the occurrence of core subadiabaticity (cessation of thermal convection) but prior to inner core solidification and outer core chemical convection. The simultaneous consideration of the constraints that a viable Mercury thermal history model must be capable of present magnetic field generation in a liquid outer core and be limited to about 2 km of post-heavy bombardment thermal contraction suggests a preferred core sulfur concentration of several weight percent. The magnetic dipole moment estimates of such models are larger than the observed dipole moment of Mercury. Our inability to quantitatively predict the strength of hydromagnetic dynamos in the planets is clear in these models.

Effects of tidal dissipation in the inner core are significant for the evolution of Mercury's core only for relatively large inner cores and only for a small range of inner core viscosities (iron grain sizes). The maximum inner core tidal heating in the models of Schubert et al. (1988) occurs for an iron grain size of about 2.5 mm (viscosity about 10^{16} Pa s) and contributes about 4% to the heat flux escaping from the core. The major effect of this additional core heat source is to prolong somewhat the occurrence of thermal convection in the outer liquid core.

The Mercury thermal history models of Schubert et al. (1988) did not consider crustal formation and upward differentiation of mantle heat sources. Removal of heat sources from Mercury's mantle by crustal growth would cool the mantle more efficiently and increase the rate of inner core solidification. However, according to the model calculations of Spohn (1991), only about 10% of the initial inventory of mantle heat sources is fractionated into a Mercurian crust and there is not a major effect on planetary thermal history.

14.7 Europa, Ganymede, and Callisto

14.7.1 Introduction

Io, Europa (Figure 14.73), Ganymede (Figure 14.74), and Callisto (Figure 14.75), moons of Jupiter, were discovered by Galileo in about 1610 when he directed his telescope at the giant planet. Accordingly, these moons are collectively referred to as the Galilean satellites. We have already discussed Io in Section 14.5. Here, we briefly describe the other Galilean moons, particularly with regard to aspects of their properties and characteristics relevant to mantle convection. Our knowledge of the Galilean satellites has increased enormously through the close-up observations by the Galileo spacecraft. Table 14.1 summarizes the basic properties of Europa, Ganymede, and Callisto.

14.7.2 Europa

Europa is the smallest of the Galilean moons with a radius about 173 km smaller than that of our own Moon. From its mean density (Table 14.1) and normalized axial moment of inertia ($C/MR^2 = 0.346 \pm 0.005$, C is the axial moment of inertia, M is the satellite's mass, and R is the moon's radius), we can infer that Europa has a metal-silicate interior surrounded by an ice-liquid water shell about 80–170 km thick (Anderson et al., 1998a). The metal-silicate interior is most likely in the form of a central metallic core surrounded by a rock mantle shell, but the possibility that the deep interior is a uniform mixture of dense silicate and metal cannot be ruled out (Anderson et al., 1998a). The core radius is uncertain; it depends on the composition, and hence the density of the core. The core radius could be

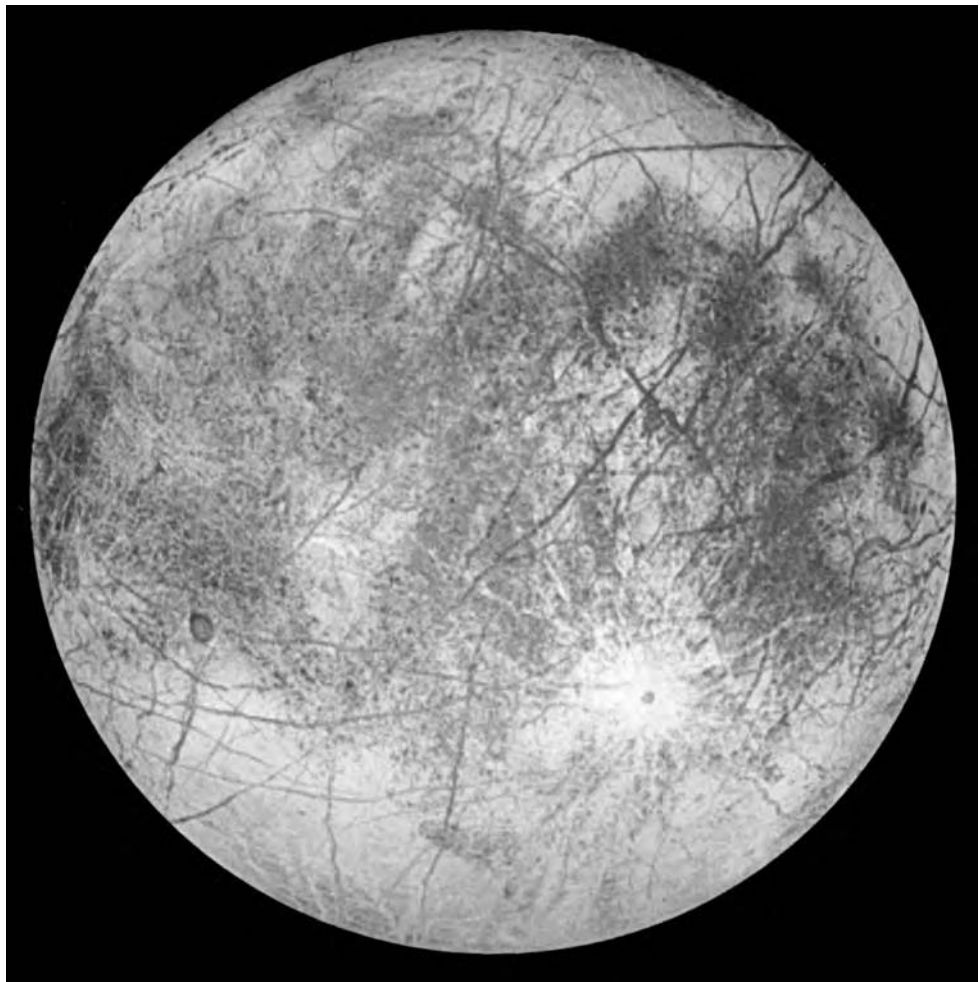


Figure 14.73. Global view of the trailing hemisphere of Europa. This false color image enhances the color differences in the predominantly icy surface. Dark areas are regions of higher concentration of rocky materials derived from the interior or implanted by impact. Bright plains are shown in tones of blue to distinguish possibly coarse-grained ice from fine-grained ice. Long dark lines are fractures in the icy crust possibly produced by tidal stresses. The bright feature containing a central dark spot in the lower third of the image is the impact crater Pwyll (about 50 km in diameter). This image of Europa was taken on 7 September 1996 by the solid-state imaging camera on the Galileo spacecraft.

For a color version of this figure, see plate section.

as large as about 50% of Europa's radius for an Fe–FeS core. The core would be smaller if it is pure iron.

The Galileo spacecraft measured a magnetic field perturbation in its flyby of Europa (Kivelson et al., 1997). It is thought that the magnetic signal is due to electromagnetic induction in the satellite's interior as apparently occurs inside Callisto (Khurana et al., 1998; Kivelson et al., 1999) (see below). If this interpretation is correct, then Europa does not have its own dynamo-generated magnetic field.

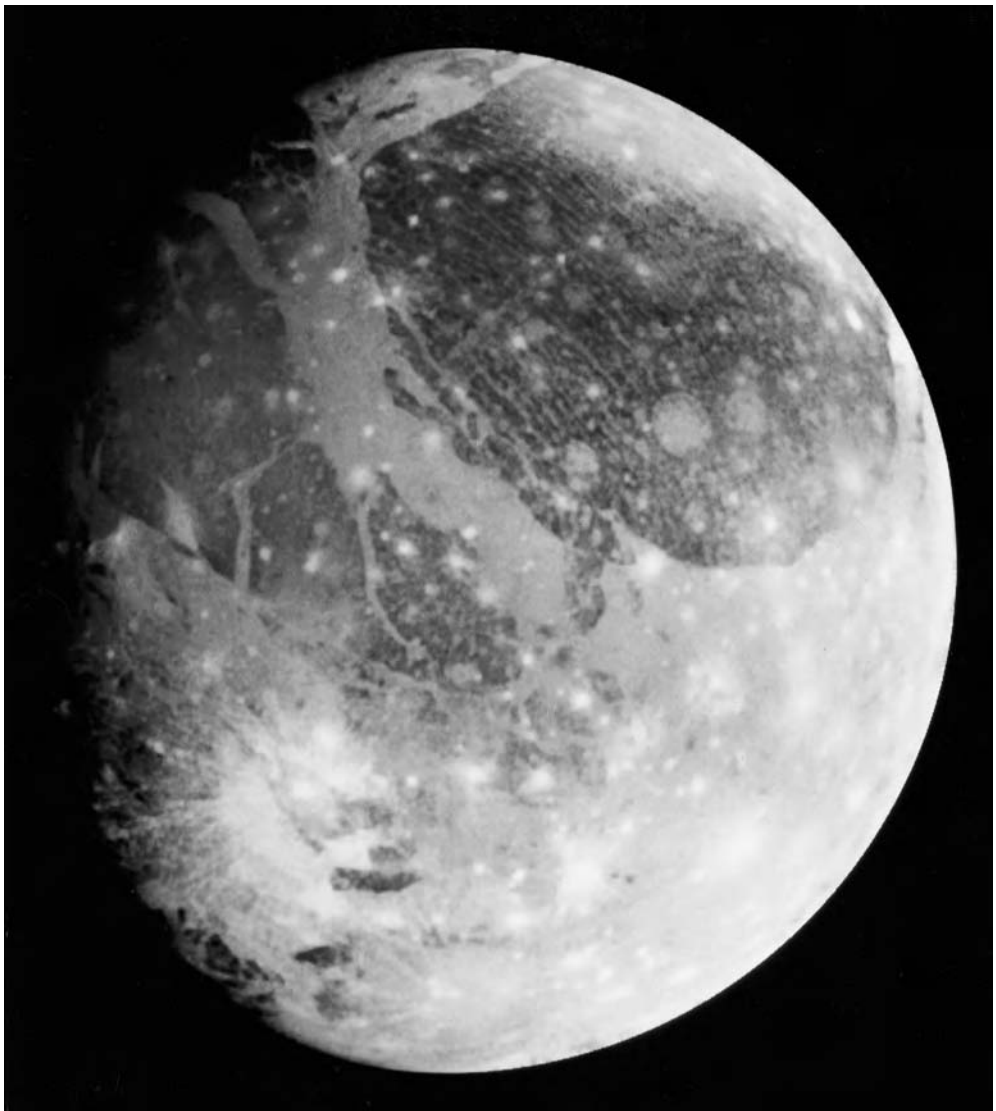


Figure 14.74. Global image of Ganymede (natural color) obtained by the Galileo spacecraft on 26 June 1996. North is to the top of the picture and the sun illuminates the surface from the right. The dark areas are older, more heavily cratered regions and the lighter areas are younger, tectonically deformed regions. The brownish-gray color is due to mixtures of rocky material, probably derived from impacts, and water ice. Bright spots are geologically recent impact craters.

For a color version of this figure, see plate section.

Europa's surface is mainly covered by water ice (Pilcher et al., 1972; Fink et al., 1973). The surface is relatively smooth (Malin and Pieri, 1986; Pappalardo et al., 1999); principal terrains are plains units of different albedo and mottled regions (areas of chaos and lenticulae, see below). There are long (up to thousands of kilometers) surface markings called lineae, many of which are ridges or ridge-complexes and plausibly of

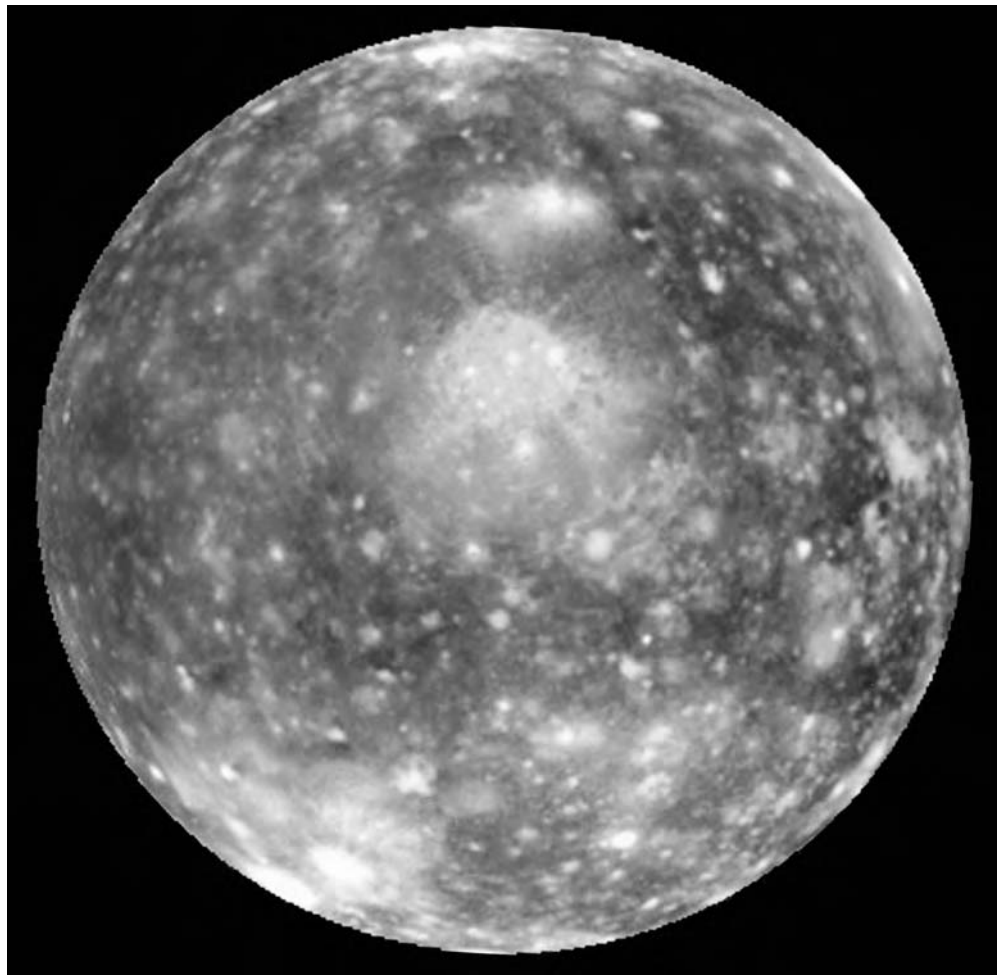


Figure 14.75. Global view of Callisto (false color). The image is centered at 0.5° south latitude and 56.3° longitude. North is to the top of the image and the sun illuminates the surface from near center. The images were taken on 5 November 1997 by the Galileo spacecraft on its 11th orbit of Jupiter. The large bright feature near the center is the ancient, multi-ring impact structure Valhalla, about 600 km in diameter and surrounded by concentric rings 3,000–4,000 km in diameter. The surface is predominantly ice with admixtures of rocky material from impacts. Brighter regions are areas of cleaner ice possibly exposed by impact excavation.

For a color version of this figure, see plate section.

tectonic origin (Greeley et al., 1998; Greenberg et al., 1998) (Figure 14.73). Some of the lineae are unusual ridge complex structures known as triple bands and consist of low albedo stripes typically 10–20 km wide with a medial high albedo band (Greeley et al., 1998). The darker, brownish parts of triple bands and mottled terrain are areas with the highest fraction of non-ice components on Europa's surface. Some areas of the surface are tectonically disrupted (Conamara Chaos) and show signs of relative displacement (translation and rotation) of blocks of icy crust as small as a kilometer across (Carr et al., 1998b; Greeley et al., 1998; Pappalardo et al., 1999). There are relatively few impact craters on

Europa (Moore et al., 1998a) and there is a possibility that Europa's surface is geologically young, although the age of the surface is controversial due to the unknown impact cratering rate in the Jovian system (Greeley et al., 1998; Neukum et al., 1998; Zahnle et al., 1998; Pappalardo et al., 1999). Despite the general lack of large impact craters on Europa, some have been identified, e.g., the craters Pwyll and Mannann'an, each about 26 km in diameter, and two multi-ringed structures, Callanish and Tyre, are inferred to be of impact origin (Moore et al., 1998a). Tyre and Callanish are similar in appearance to larger, degraded multi-ringed structures on Ganymede and Callisto known as palimpsests. One interpretation of the multi-ring structures on Europa is that they represent impacts which penetrated to relatively low viscosity ice or liquid water (Moore et al., 1998a; Pappalardo et al., 1999).

Many of the lineae and long ridges on Europa's surface are believed to be caused by tidal stresses acting on the ice lithosphere (Greenberg et al., 1998); lineae may also form in response to stresses associated with the possible nonsynchronous rotation of Europa (Greenberg and Weidenschilling, 1984; Helfenstein and Parmentier, 1985; McEwen, 1986; Ojakangas and Stevenson, 1989a; Leith and McKinnon, 1996; Geissler et al., 1998a,b; Greenberg et al., 1998). As discussed in connection with the heating of Io, the inner three Galilean satellites (Io, Europa, and Ganymede) are in an orbital dynamical resonance, the Laplace resonance, and like Io, Europa is subjected to tidal stresses that are large enough to deform the surface. The tidal stresses may also be large enough to heat Europa's interior and prevent the complete freezing of Europa's water ice–liquid shell (Cassen et al., 1982; Squyres et al., 1983; Schubert et al., 1986; Ross and Schubert, 1987; Ojakangas and Stevenson, 1989b).

The geology of Europa's surface is consistent with the existence of a liquid water layer beneath an outer ice shell (Carr et al., 1998b; Pappalardo et al., 1998a, 1999). The evidence includes the relatively young age of the icy surface, small rotated and tilted blocks of icy crust in regions like Conamara Chaos, the existence of pull-apart bands (zones of limited extension), signs of resurfacing by mobile ice or liquid water extruded onto the surface (cryovolcanism), the appearance of flow fronts, and dark spots, domes, and quasi-circular pits, collectively known as lenticulae (as large as 20 km across and spaced as much as 20 km apart) that may be indicative of subsolidus convection in the icy shell. The major question about Europa is whether an internal liquid water ocean does survive beneath Europa's icy surface.

Question 14.40: Does Europa have a subsurface liquid water ocean?

14.7.3 *Ganymede*

Ganymede is the largest of the Galilean satellites. It is larger than the planet Mercury (Table 14.1). Its mean density (Table 14.1) and normalized axial moment of inertia ($C/MR^2 = 0.3105 \pm 0.0028$) require that Ganymede be differentiated into a metallic core surrounded by a silicate mantle. The deep metal–rock interior of Ganymede is covered by a thick (800 km) ice–liquid water shell. Ganymede thus has a three-layer internal structure consisting of an inner metal core (radius 400–1,300 km depending on the composition and hence the density of the metal), a middle rock shell, and an outer water (ice–liquid) shell (Anderson et al., 1996c). Ganymede is known as an icy satellite because its relatively low mean density requires that it is made of about equal amounts, by mass, of water ice

and rock–metal (actually, about 60% rock and 40% ice). Ganymede has a magnetic field large enough to create its own magnetosphere within the Jovian magnetosphere (Kivelson et al., 1996b); the source of Ganymede’s magnetic field is likely dynamo action within a still liquid part of Ganymede’s metallic core (Schubert et al., 1996). The existence of a large Ganymedean magnetic field supports the inference from the gravity measurements by the Galileo spacecraft that Ganymede has a metallic core.

Ganymede’s surface is covered by ice and rock (Figure 14.74). It is not as smooth or as geologically youthful in appearance as the surface of Europa, but neither is it a primordial surface. The craters on Ganymede’s surface suggest surface ages between about 4.2 Gyr for Galileo Regio, a large expanse of dark terrain, and about 3.7 Gyr for the youngest sulcus (an area of grooved terrain) (Greeley et al., 1998). As with Europa, estimates of surface ages on Ganymede based on crater counts are uncertain, mainly due to the lack of knowledge of the cratering flux in the Jovian system (Neukum et al., 1998; Zahnle et al., 1998; Pappalardo et al., 1999). There are clear signs of endogenic modification of Ganymede’s surface with tectonism the dominant process.

The principal geologic units on Ganymede’s surface are bright and dark terrains (Squyres and Croft, 1986), with each unit comprising about half of the surface. The dark terrain occurs in roughly polygonal units that are cut through and separated by bands of bright terrain. The dark terrain is hummocky and heavily cratered and some dark units, most notably Galileo Regio, have a distinct linear texture consisting of shallow, subparallel linear depressions called furrows (Squyres and Croft, 1986; Prockter et al., 1998). Furrows have wide (5–10 km) flat floors, are bounded by sharp raised rims, and range from 50 km to several hundred kilometers long (Shoemaker et al., 1982). They are believed to have formed through tectonism. Dark terrain has a higher content of materials other than ice compared with the bright terrain, and processes like sublimation and mass wasting may have acted to concentrate the low albedo material (Prockter et al., 1998). The bright terrain is less heavily cratered than the dark areas, indicative of a younger age, and consists predominantly of a complex pattern of long (hundreds of kilometers) and narrow (several kilometers wide) grooves (sets of subparallel ridges and troughs). Some areas of bright terrain are free of grooves. The grooves on Ganymede most likely have a tectonic origin with extension playing a major role (Shoemaker et al., 1982); there is little evidence for compressional deformation on Ganymede (Squyres and Croft, 1986). High-resolution images of Ganymede by the Galileo spacecraft suggest that the grooved terrain of Uruk Sulcus (an ≈ 300 km wide and 2,500 km long swath of bright grooved terrain crossing low northern latitudes) formed by both horst-and-graben-style normal faulting and tilt-block-style normal faulting with icy volcanism at most having a minor role (Pappalardo et al., 1998b).

14.7.4 Callisto

Callisto, the outermost of the Galilean satellites, is only slightly smaller than Ganymede (Table 14.1), but differs from it in a number of significant ways. Though the mean density of Callisto and Ganymede are similar (Table 14.1), Callisto has a larger value of $C/(MR^2)$ ($C/(MR^2) = 0.359 \pm 0.005$), implying a very different interior structure for Callisto compared with the interior of Ganymede. Unlike Ganymede, Callisto is only partially differentiated and consists of a water ice–liquid shell less than 350 km thick surrounding a primordial or undifferentiated ice–rock–metal core (Anderson et al., 1998b). The rock and ice in Callisto are not completely separated and Callisto does not have a central metallic core.

The gravitational data obtained by the Galileo spacecraft in a flyby past Callisto cannot absolutely rule out the existence of a small metallic core in Callisto with a radius less than 25% of the satellite's radius. However, geophysical arguments and other properties of Callisto make the existence of a small metallic core in the moon highly unlikely (Anderson et al., 1998b). Callisto is characterized as an icy satellite because, like Ganymede, its relatively low density requires that it be about half water ice and half rock–metal by mass. Consistent with the absence of a metallic core, Callisto does not have an intrinsic magnetic field (Khurana et al., 1997b, 1998). The surface of Callisto (Figure 14.75) is heavily cratered; there is a lack of clear geological evidence of endogenic modification of Callisto's surface (Klemaszewski et al., 1998) consistent with the relatively small degree of differentiation of its interior.

Most of the surface of Callisto is similar in appearance to the dark cratered terrain on Ganymede, but Callisto's surface is even darker and more heavily cratered (Squyres and Croft, 1986). The most prominent features on Callisto are large multi-ring impact structures, the largest of which are Valhalla (over 4,000 km across) and Asgard (over 1,600 km in diameter). Adlinda is another multi-ring structure probably older than Valhalla and Asgard because of its highly degraded appearance and the relatively high spatial density of superposed impact craters (Klemaszewski et al., 1998). At scales of hundreds of meters to kilometers, Callisto's surface appears smooth and slightly undulating with a low spatial density of small (< 10km diameter) impact craters (Klemaszewski et al., 1998). A dark non-ice material appears to blanket the surface and result in its relative smoothness; how this dark material might be redistributed over the surface, infilling low-lying topography, is not understood. Impact craters on Callisto exhibit a range of morphologies from fresh to highly degraded. Mass wasting of crater walls appears to be a dominant degradational process; deposits within craters appear to be the result of inward debris slides (Klemaszewski et al., 1998). The degradation of crater walls and rims is likely responsible for the production of the ubiquitous dark material.

Though Callisto lacks its own magnetic field, the Galileo spacecraft has detected the magnetic perturbation associated with electromagnetic induction in Callisto. Induction occurs when the satellite experiences time periodic changes in the ambient magnetic field of the Jovian magnetosphere due to its orbital motion around Jupiter, the rotation of Jupiter, and the tilt of the Jovian magnetic field (Kivelson et al., 1999). The magnitude of the electromagnetic induction signal requires that there be a global layer of high electrical conductivity in close proximity to Callisto's surface (Khurana et al., 1998; Kivelson et al., 1999). The only explanation for such a layer is that it is a subsurface liquid water ocean with a salinity similar to that of terrestrial seawater (Khurana et al., 1998; Kivelson et al., 1999). Unlike the surface of Europa, Callisto's surface provides no hint that a liquid water ocean might hide beneath. The induction signal is the only indirect evidence that Callisto might have a subsurface liquid water ocean. The existence of such an internal ocean in Callisto is difficult to reconcile with the lack of endogenic modification of its surface. Curiously, the source of the magnetic field perturbations detected by the Galileo spacecraft on its first several flybys of Europa could not be definitively attributed to electromagnetic induction. However, there is now unambiguous confirmation that magnetic field signals from Europa are due to electromagnetic induction in the satellite (Kivelson et al., 2000). Both Callisto and Europa, geologically and structurally very different satellites, have induction signals indicative of subsurface liquid water oceans. We may ask a similar question about Callisto that we asked about Europa.

Question 14.41: Does Callisto have a subsurface liquid water ocean?

Callisto is not part of the Laplace resonance of the inner three Galilean satellites and it is therefore not tidally heated. Without such a heat source it is difficult to understand how a subsurface liquid water ocean in Callisto could be prevented from freezing solid over geologic time. At least in the case of Europa, tidal dissipation is a possible source of heat to maintain a subsurface water layer in a liquid state. Tidal heating in the distant past may also explain why Ganymede is completely internally differentiated while Callisto is only partially differentiated. After all, both these moons are comparable in size and mass, have similar amounts of radiogenic heat sources, and experienced similar amounts of accretional heating on formation.

Question 14.42: Why are Ganymede and Callisto so different?

14.7.5 Convection in Icy Satellites

Subsolidus convection in the ice-dominated outer layers of Europa, Ganymede, and Callisto plays a major role in controlling the evolution and present internal state of each of these satellites (Schubert et al., 1986; McKinnon, 1998). Provided the rock fraction is not larger than about 60% by volume, the deformation of an ice–rock mixture is controlled by the rheology of the ice matrix in which the silicates are imbedded. The outermost layers of Europa, Ganymede, and Callisto are predominantly water ice and the deformation of these layers is almost certainly governed by the rheology of ice. Even in the deep undifferentiated (no ice–rock separation) interior of Callisto, the rock fraction should be small enough for ice deformation to dominate.

The rheological behavior of ice is similar to that of rock in many respects. Ice can flow by a number of micromechanical processes including the motion of dislocations, diffusion of atoms, and sliding of grain boundaries (see Chapter 5). Goldsby and Kohlstedt (1997a, b) have deformed ice I in the laboratory and have quantified its flow properties over broad ranges of temperature, stress, and grain size. Deformation by any of the basic flow mechanisms can be described by a power-law rheological equation of the form

$$\dot{\epsilon} = A \frac{\tau^n}{d^p} \exp\left(\frac{-Q}{RT}\right) \quad (14.7.1)$$

where $\dot{\epsilon}$ is strain rate, A , n , and p are material parameters, τ is the differential stress, d is the grain size, Q is the activation energy, T is absolute temperature, and R is the universal gas constant (compare with (5.9.3)). At high differential stress the creep rate is controlled by the motion of dislocations on the hard slip system in ice. At intermediate differential stress, grain boundary sliding controls flow. At low stress the creep rate is controlled by dislocation motion on the easy (basal) slip system in ice.

All the ice I creep data can be represented by a constitutive law of the form (Goldsby and Kohlstedt, 1997a, b)

$$\dot{\epsilon}_{\text{total}} = \left[\frac{1}{(\dot{\epsilon}_{hs} + \dot{\epsilon}_{es})} + \frac{1}{\dot{\epsilon}_{gbs}} \right]^{-1} + \left[\frac{1}{\dot{\epsilon}_{hs}} + \frac{1}{\dot{\epsilon}_{es}} \right]^{-1} \quad (14.7.2)$$

where the subscripts hs , es , and gbs refer to the strain rate due to slip on the hard slip system, the strain rate due to slip on the easy slip system, and the strain rate due to grain boundary

Table 14.9. Rheological Parameter Values for the Deformation of Ice I^a

Basic Flow Mechanism	n	Q (kJ mol ⁻¹)	p
Dislocation motion on hard slip system	4.5	60	0
Dislocation motion on easy slip system	2.4	60	0
Grain boundary sliding	1.8	49	1.4

^a After Goldsby and Kohlstedt (1997a).

sliding, respectively. Each of the terms \dot{e}_{hs} , \dot{e}_{es} , and \dot{e}_{gbs} is given by (14.7.1) with parameters A , n , and p listed in Table 14.9.

Diffusion creep is not a significant creep mechanism for ice under any of the conditions encountered in the icy satellites. Instead, grain boundary sliding in combination with dislocation motion (superplastic flow) is the dominant mechanism of deformation in these bodies (Goldsby and Kohlstedt, 1997a, b).

According to (14.7.1) and (14.7.2), at temperatures sufficiently close to its melting temperature, ice deforms in a fluid-like manner on long time scales. The flow of glaciers and ice sheets on Earth illustrates the fluid-like, subsolidus deformation of ice on time scales of years or less. Temperatures are lower, about 100 K, at the surfaces of Europa, Ganymede, and Callisto than they are in ice sheets on Earth, so near-surface ice should be rather stiff on these satellites. However, temperature will increase with depth in the outer ice layers of these moons, rising even to the melting temperature if liquid water exists near the bases of the layers or in their interiors. The discussion above has indicated that liquid water layers might exist in Europa and Callisto, in which case a liquid water layer is also probable in Ganymede. The temperature gradient in the conductive part of the ice layer is determined by its thermal conductivity and the heat flux through the ice. A minimum heat flow is set by the radioactive heat generation in the silicate component of the satellite. Additional contributions to the heat flow come from the secular cooling of the satellite and, in the cases of Europa and possibly Ganymede, from tidal dissipation. With a temperature difference across the ice layer as large as 273 K – 100 K = 173 K, the ice layer will undergo subsolidus convection if it is thick enough for the Rayleigh number to exceed the minimum value for the onset of convection. An ice layer on the outer planet moons will convect if it is thicker than about 10 km; the outer ice shells on Europa, Ganymede, and Callisto are at least 100 km thick and as much as 800 km thick in the cases of Ganymede and Callisto. As it is in the Earth's mantle, subsolidus convection is the dominant heat transfer mechanism in the ice layers of the Galilean satellites.

It is clear from (14.7.1) that the rheology of ice, like that of rock, is strongly temperature dependent. The effective viscosity μ_{eff} of ice is given by

$$\mu_{\text{eff}} = \frac{\tau}{2\dot{e}} \quad (14.7.3)$$

Elimination of τ between (14.7.1) and (14.7.3) gives

$$\mu_{\text{eff}} = \frac{1}{2} \left\{ \frac{d^p}{A} \exp \left(\frac{Q}{RT} \right) \right\}^{1/n} \dot{e}^{1/n-1} \quad (14.7.4)$$

Figure 14.76 shows the dependence of μ_{eff} on T for the grain boundary sliding rheological parameters of Table 14.9, $A = 0.008$, $\dot{e} = 2 \times 10^{-10} \text{ s}^{-1}$ (a representative strain rate for tidal

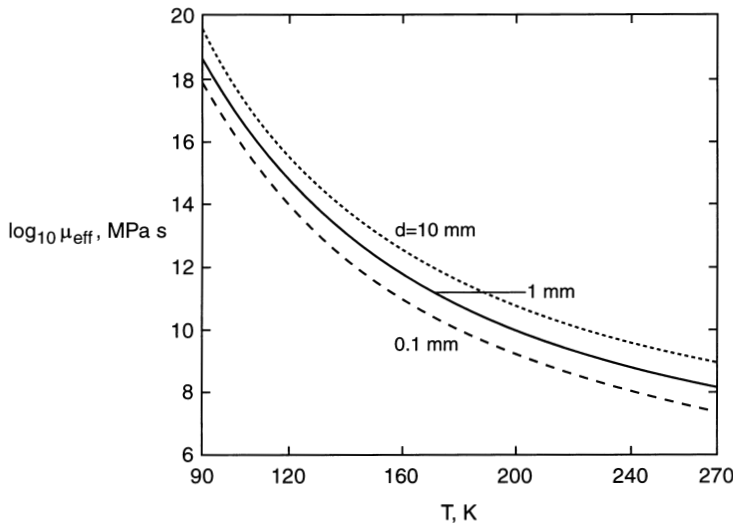


Figure 14.76. The dependence of effective viscosity μ_{eff} on temperature T for ice deformation by grain boundary sliding according to (14.7.4) with $A = 0.008$, $\dot{\epsilon} = 2 \times 10^{-10} \text{ s}^{-1}$, and other parameters from Table 14.9. The parameter d is the grain size.

deformation on Europa; Ojakangas and Stevenson, 1989b; Pappalardo et al., 1998a), and a range of grain sizes considered appropriate for ice on Europa (Pappalardo et al., 1998a). With the above values of p , n , and A , μ_{eff} has units of MPa s, d must have units of m, and $\dot{\epsilon}$ needs to have units of s^{-1} . The grain boundary sliding viscosity of ice is quite high at temperatures less than 150 K, but for T between 230 K and 270 K, for example, the viscosity of ice is only between about 10^{13} and 10^{16} Pa s (depending on grain size).

Because of the strong temperature dependence of ice rheology, convection in the ice layers of Galilean moons should be described by the formalism developed earlier in this chapter and in Chapter 13 for convection in fluid layers with viscosity a strong function of temperature. Thus, the ideas of stagnant lids and underlying convective regions are directly applicable to convection in the ice layers of the Jovian moons. There are yet other similarities between convection in the Earth's mantle and convection in the ice layers of Galilean satellites. Most notably, the phase changes to high-pressure dense forms of ice, both exothermic (ice I–ice II) and endothermic (ice I–ice III, ice II–ice V), might be found in the thick outer ice shells of Ganymede and Callisto and could influence convection in these layers in ways similar to the effects of transition layer phase changes on mantle convection (Thurber et al., 1980; Bercovici et al., 1986; Schubert et al., 1986; Sotin and Parmentier, 1989; McKinnon, 1998).

The major question about Europa is whether it has a subsurface liquid water ocean (Schubert et al., 1986; Pappalardo et al., 1999). If it is assumed that Europa had such an ocean in the past, then the question reduces to the survivability of the ocean as Europa cools with time and the ice layer at the surface thickens. When the ice layer thickens enough for convection to occur in it, convection transports more heat through the ice, leading to faster cooling and thickening of the ice layer (Cassen et al., 1982; Schubert et al., 1986). Subsolidus convective heat transfer in the ice layer at Europa's surface acts to enhance the freezing of any liquid water at the bottom of the ice and destroy the liquid water ocean. This process could freeze a 100 km thick water layer in a few hundred million years. Only

tidal heating in the ocean or the ice could prevent complete freezing of the water layer. The amount of tidal heating in Europa is unknown; models of the competition between tidal heating and convective cooling have provided ambiguous results (Squyres et al., 1983; Ross and Schubert, 1987; McKinnon, 1999). Tidal heating depends on the magnitude of tidal deformation and the rheology of the ice at tidal periods (Durham et al., 1997; Goldsby and Kohlstedt, 1997a, b). Importantly, tidal dissipation is expected to be greatest where the ice is warmest and most deformable, most likely near the base of the ice layer (Ojakangas and Stevenson, 1989b). The magnitude of tidal deformation depends on Europa's internal structure, in particular on the existence of a liquid ocean beneath the ice layer; deformation is large (tens of meters) only if the ice layer is decoupled from Europa's interior, as would occur if there is an internal ocean. Convective cooling depends on the viscosity, which depends on temperature, which in turn depends on tidal dissipation. Clearly, the complex interplay of highly nonlinear feedback mechanisms controls the survivability of an internal liquid water ocean on Europa. To complicate matters even further, the occurrence of minor constituents in the ice and ocean such as salts (Kargel, 1991; McCord et al., 1998) and ammonia (Schubert et al., 1986; Kargel, 1992; Grasset and Sotin, 1996) would affect the rheology of the ice and the freezing temperature of the ocean.

The differentiation of Ganymede that separated ice from rock and rock from metal must have completely melted the ice component. Whether this occurred early in Ganymede's evolution during or just after accretion (Schubert et al., 1986), or later in the passage of Ganymede through some dynamical resonance, is not known (Schubert et al., 1996; Showman and Malhotra, 1997; Showman et al., 1997). Nevertheless, as with Europa, we are faced with the question of the survivability of a water layer through time as Ganymede has cooled. Subsolidus convection would be even more efficient in the thicker ice layer of Ganymede, compared with Europa, and any liquid water below the ice at Ganymede's surface should have frozen in a few hundred million years. Tidal heating in Ganymede at present is even smaller than it is in Europa and it is difficult to account for the maintenance of a subsurface liquid water layer in Ganymede through geologic time.

Similar arguments can be made for Callisto, which experiences essentially no tidal heating. Moreover, with only partial separation of ice and rock in the outer part of Callisto (Anderson et al., 1998b), it is problematic, though possible, that a liquid water region ever existed beneath the ice cover. Yet, we are faced with the dilemma of explaining the electromagnetic induction signal measured by the Galileo spacecraft, the only explanation for which apparently requires the existence of a subsurface salty water ocean on Callisto (Khurana et al., 1998; Kivelson et al., 1999).

As in the Earth and in other terrestrial planets, subsolidus convection has been a dominant process inside all the Galilean moons. Models of the larger Saturnian satellites (Ellsworth and Schubert, 1983; Forni et al., 1991; McKinnon, 1998) show its importance in the thermal histories of these moons as well. There are arguments that subsolidus convection is also occurring at present in Saturn's large moon Titan and Neptune's moon Triton (Schubert et al., 1986; McKinnon, 1998). The more we explore our solar system, the more we realize how subsolidus convection has controlled the evolution and internal states of all its major solid planets and satellites.

15

Nature of Convection in the Mantle

15.1 Introduction

Our understanding of mantle convection is derived from a wide range of geological, geo-physical, and geochemical observations, laboratory data on material properties, numerical and laboratory convection experiments, plus the theory for thermal convection of Earth's mantle and the other terrestrial planets and processes related to it. In this chapter we attempt a synthesis of all this information, to create a picture of how the mantle circulates and why it does so. Many aspects of the picture remain somewhat blurred, even some of the major ones. Nevertheless, our present knowledge of the mantle and our current understanding of the fundamental physics and chemistry are adequate to bring some parts of the picture into focus, at least for the Earth.

Throughout this book we have listed major questions concerning mantle convection and the many related subjects we have considered. A summary of these questions is provided in Table 15.1. For some of the questions we have provided definitive answers, for others the answers are either uncertain or completely unknown. The most far-reaching of these questions are addressed in this chapter.

Table 15.1. Major Questions Concerning Mantle Convection

Question Number	Question
1.1	What is the source of energy for the tectonics and volcanism of the solid Earth?
1.2	How is this energy converted into the tectonic and volcanic phenomena we are familiar with?
2.1	Why do accretional plate margins develop the orthogonal ridge segment-transform fault geometry?
2.2	What is the rheology of the lithosphere at a subduction zone?
2.3	What determines the subduction dip angle?
2.4	What is the fate of descending slabs?
2.5	Do slabs that cross 660 km depth sink all the way to the core-mantle boundary or do they come to rest at some shallower depth?
2.6	Why do subduction zones have arcuate structures?
2.7	What is the mechanism for subduction zone volcanism?
2.8	Why do back-arc basins form?
2.9	Are there plumes in the mantle beneath hot spots, and if so, from what depth(s) do they originate?
2.10	How were the continents formed?
2.11	Does delamination play an important role in recycling continental crust and lithosphere?

Question Number	Question
2.12	How is continental crust formed?
2.13	What are the forces that drive plate tectonics?
2.14	How is toroidal motion generated in mantle convection?
2.15	How are accretional plate margins formed?
2.16	How are subduction zones formed?
2.17	Is the temporal variability of plate tectonics stochastic or is it driven by episodicity in mantle convection?
3.1	Is the LVZ partially molten?
3.2	What is the thickness of the continental lithosphere? Do the continents have roots that extend to depths of several hundred kilometers in the mantle?
3.3	What is the nature of the Lehmann seismic discontinuity at a depth of 220 km?
3.4	What is the nature of the 660 km seismic discontinuity?
3.5	Is the composition of the lower mantle different from that of the upper mantle?
3.6	Is the D'' layer a purely thermal boundary layer or does it have a compositional component?
3.7	Is there partial melt at the base of the mantle?
3.8	What is the composition of the core? What is the major light element in the core?
3.9	What is the relative importance of thermal and compositional convection in powering the geodynamo?
3.10	How deep do the upwellings beneath mid-ocean ridges extend into the mantle? What are the implications for the passivity of mid-ocean ridges?
3.11	Do subducted slabs penetrate into the lower mantle?
3.12	Do some subducted slabs sink all the way to the core–mantle boundary?
3.13	What is the topography of the core–mantle boundary?
4.1	Why are there deviations from the half-space cooling model for the oceanic lithosphere at seafloor ages greater than about 80 Myr?
4.2	How thick is old oceanic lithosphere?
4.3	How thick is the continental lithosphere?
4.4	What is the fate of buoyant depleted mantle material created together with the continental crust?
4.5	What mechanism provides heat to the base of the continental lithosphere?
4.6	What causes the seismic LVZ beneath the oceanic lithosphere?
4.7	How is magma focused into a narrow region in the vicinity of a ridge crest?
4.8	How does magma rise through the lithosphere?
4.9	What causes volcanism at subduction zones?
4.10	Is there a wedge of metastable olivine in old descending slabs?
4.11	Is the olivine–spinel phase boundary in descending slabs shallower or deeper than it is in the surrounding mantle?
4.12	What is the cause of deep earthquakes?
4.13	How do the major phase transitions between 410 and 660 km depth influence the style of mantle convection?
4.14	What is the heat flow from the core?
4.15	What is the temperature change across the thermal boundary layer at the base of the mantle?
4.16	Are there internal thermal boundary layers in the transition zone?
5.1	Is there a low-viscosity asthenosphere beneath some plates? What is the viscosity of the asthenospheric material?

(continued)

Table 15.1 (continued)

Question Number	Question
5.2	What is the relationship between density anomalies and seismic velocity anomalies in the mantle?
5.3	What is the dynamical topography associated with mantle convection?
5.4	What is the difference between the viscosity of the upper mantle and the viscosity of the lower mantle?
5.5	What is the dependence of grain size on deviatoric stress in the mantle?
5.6	Is dislocation creep or diffusion creep the dominant deformation mechanism associated with mantle convection?
5.7	Does the mantle behave like a Newtonian or a non-Newtonian fluid on geological time scales?
5.8	Are there changes in viscosity associated with the solid–solid phase changes in the transition zone?
7.1	What is the influence of the olivine–spinel and spinel–perovskite + magnesiowüstite phase changes on mantle convection?
7.2	How supercritical is the mantle?
7.3	Is there secondary or small-scale thermal convection in the oceanic asthenosphere due to gravitational instability of the lower part of the oceanic lithosphere?
7.4	Is there mantle convection in the lunar interior?
8.1	Is mantle convection chaotic?
8.2	Is mantle convection turbulent?
8.3	Is the subducted oceanic lithosphere mixed and homogenized in the mantle?
9.1	What are the multi-rheological laws governing deformation of the crust and mantle?
9.2	How are mantle seismic velocity heterogeneities partitioned among temperature, composition, and melting?
9.3	Is mantle convection turbulent?
9.4	How does the emergence of plates in mantle convection influence the nature of that convection?
9.5	Are there compositional changes as well as phase changes in the transition zone?
9.6	To what extent is the mantle layered by the phase changes and possible compositional gradients of the transition zone?
9.7	How is mantle convection influenced by the temperature and pressure dependence of rock viscosity?
9.8	How does subduction initiate?
9.9	How do descending slabs interact with the spinel → perovskite + magnesiowüstite phase change at a depth of 660 km?
9.10	How do mantle plumes interact with the endothermic phase change at a depth of 660 km?
9.11	How is mantle convection influenced by the power-law viscosity of rocks?
9.12	How is mantle convection influenced by changes with depth in its thermodynamic and transport properties?
9.13	What are the effects of viscous heating on mantle dynamics?
9.14	What are the consequences of continents for the nature of mantle convection?
9.15	Is the D'' layer a chemical boundary layer as well as a thermal boundary layer?
9.16	Is there small-scale convection in the D'' layer?
10.1	What is the style of three-dimensional thermal convection in the mantle and how does it relate to the plates and the major structures of the mantle?
10.2	Do the properties of the endothermic phase change at a depth of 660 km explain the seismically observed morphological diversity in slabs near the base of the upper mantle and the top of the lower mantle?

Question Number	Question
10.3	Is the 660 km phase change responsible for imposing the long-wavelength spectral character of mantle seismic heterogeneity?
10.4	Do the avalanches that occur in mantle convection models also occur in the Earth's mantle?
10.5	Is mantle convection in the Earth partially layered by effects of the 660 km phase change?
10.6	Is the 660 km phase change responsible for the dominance of long-wavelengths in the Earth's nonhydrostatic geoid?
10.7	Why are tectonic plates so large?
10.8	Is an increase of viscosity with depth responsible for the long-wavelength dominance of the Earth's geoid and mantle seismic velocity heterogeneity?
10.9	Was the Earth's mantle divided into separately convecting upper and lower layers early in the Earth's evolution?
10.10	How important is viscous heating in the Earth's mantle?
10.11	Does compressibility in the Earth's mantle significantly affect the nature of mantle convection?
10.12	What essential rheological behavior needs to be incorporated into models of mantle convection for plate tectonics to arise from the model in a natural, self-consistent way?
11.1	Do mantle plumes exist?
11.2	Which "hot spots" are associated with mantle plumes?
11.3	What mechanism is responsible for the formation of hot spot swells?
11.4	What is the depth of the source of mantle plumes?
11.5	How much heat is transported by mantle plumes?
11.6	What is the physical mechanism for the generation of mantle plumes?
11.7	What causes massive flood basalt eruptions?
11.8	What is the structure of a mantle plume?
11.9	Do conduit waves occur in the Earth's mantle?
11.10	Are mass extinctions related to flood basalt events?
12.1	Do the isotope systematics of MORB require separate upper mantle and lower mantle reservoirs indicative of layered mantle convection?
12.2	Do the ^3He anomalies observed in some OIB indicate that there is a "primitive" mantle reservoir?
12.3	What is the mantle source region of the chemically heterogeneous OIB?
12.4	Do the 2 Gyr isotope anomalies associated with OIB develop in the mantle or elsewhere?
13.1	Was the Earth's mantle fractionated at the end of accretion?
13.2	What fraction of the Earth's surface heat flow can be attributed to radioactive heat generation and what fraction to secular cooling of the Earth?
13.3	What is the major light alloying element in the Earth's core?
13.4	What is the dominant energy source for driving convection and dynamo action in the Earth's outer core?
13.5	Has the Earth always had a geodynamo?
13.6	Did layered mantle convection ever occur in the Earth's thermal history?
13.7	Has convection in the Earth's mantle always occurred in the small viscosity contrast regime?
13.8	Is convection in the Earth's mantle chaotic?
13.9	Have avalanches occurred in the Earth's mantle?
13.10	What dynamical processes in the mantle are responsible for episodicity in the geological record?
13.11	Has continental crustal growth occurred continuously or episodically?

(continued)

Table 15.1 (continued)

Question Number	Question
13.12	How has the volume of the continents changed through geologic time?
13.13	What processes acted in the Archean to produce and recycle continental crust?
14.1	Is mantle convection occurring in the terrestrial planets, the Moon, and satellites of the giant planets?
14.2	How does Venus lose its heat?
14.3	What caused the major resurfacing of Venus about 500–750 Myr ago?
14.4	What caused the hemispheric dichotomy on Mars?
14.5	What caused the nearside–farside dichotomy on the Moon?
14.6	What is the nature of mantle convection in Venus?
14.7	What produced the high topography on Venus and why are the topography and gravity strongly correlated?
14.8	Is there limited subduction or lithospheric foundering on Venus?
14.9	What is the thickness of the lithosphere on Venus?
14.10	Has the thermal evolution of Venus involved catastrophic events?
14.11	What is the composition of the rocks in the plateau highlands of Venus?
14.12	Why is there no plate tectonics on Venus?
14.13	Do the large-scale geoid, topography, and admittance ratios on Venus imply a thick lithosphere or a convecting mantle beneath a thin lithosphere?
14.14	Is mantle convection in Venus layered?
14.15	Is mantle convection on Venus in the sluggish-lid or stagnant-lid convection regime?
14.16	Why does Venus not have a magnetic field?
14.17	What internal process produced the Tharsis uplift on Mars?
14.18	How did the Valles Marineris canyon system on Mars form?
14.19	What is the thickness of the Martian lithosphere?
14.20	What is the explanation for the absence, at present, of a Martian magnetic field?
14.21	Why are there two major volcanic centers on Mars?
14.22	What is the structure of the Martian mantle?
14.23	Is the core of Mars entirely liquid?
14.24	Did the Moon have a magma ocean early in its history?
14.25	What is the origin of lunar mascons?
14.26	Why was there a time delay in the onset of mare volcanism?
14.27	What caused the termination of mare volcanism?
14.28	Does the Moon have a metallic core?
14.29	How was the lunar crust magnetized?
14.30	Did the Moon form from an impact of a Mars-size body with the Earth?
14.31	What is the degree of differentiation of the Moon?
14.32	Is the lunar mantle chemically heterogeneous?
14.33	Does Io have a partially molten asthenosphere?
14.34	How thoroughly has Io been differentiated?
14.35	What is the nature of Io's present thermal, orbital-dynamical state?
14.36	Does Io have a magnetic field?
14.37	What is the structure of Mercury's interior?
14.38	What is the source of Mercury's magnetic field?
14.39	Why is Mercury's density so high?
14.40	Does Europa have a subsurface liquid water ocean?
14.41	Does Callisto have a subsurface liquid water ocean?
14.42	Why are Ganymede and Callisto so different?

The starting point in a discussion of mantle convection is a description of the energy sources responsible for mantle convection. Heat is by far the most important form of energy available in the mantle for convection and other dynamical processes. The primary sources of thermal energy for mantle convection are internal heating due to the decay of the radioactive isotopes of uranium, thorium, and potassium, the long-term secular cooling of the Earth, and heat from the core [Question 1.1]. The relative importance of these three heat sources is still a matter of debate [Question 13.2], but a reasonable estimate is that radioactive heating contributes more than half of the total, and the other two contribute most of the remainder. Locally, heating due to viscous dissipation may be important [Question 10.10].

The transfer of this thermal energy from the Earth's interior to the surface occurs by several mechanisms, including thermal conduction, hydrothermal and magmatic circulation, and subsolidus thermal convection. Subsolidus convection can occur because of solid-state creep (diffusion or dislocation) in the mantle [Question 1.3]. The heat transport by subsolidus convection dominates the other mechanisms at all depths in the mantle below the lithosphere and above the D'' layer with the possible exception of a dividing region between an upper mantle convecting layer and lower mantle convection. Accordingly, the processes that actively shape the Earth's surface, including tectonism, volcanism, and seismicity, are all byproducts of subsolidus convection in the mantle. We could also add the Earth's magnetic field to the list of byproducts, since mantle convection controls the rate of heat loss from the core, which in turn controls the power available to drive the geodynamo [Questions 3.8, 3.9, 13.3, 13.4, 13.5].

At the most fundamental level, mantle convection is adequately described in terms of convection in an ordinary viscous fluid. The three necessary ingredients for thermal convection are present in the mantle: a fluid layer in a gravitational field that is cooled from above, a positive thermal expansivity, and relatively low values of the viscosity and thermal conductivity. In the mantle, the required adverse temperature gradient is maintained by the difference between the interior and surface temperatures, and the viscosity is finite because of thermally activated creep processes that operate at the high temperatures of the interior. To first order then, the mantle behaves like a viscous fluid that is heated from within and from below, and cooled from above, all within its own gravitational field. Convection occurs in such a fluid when the Rayleigh number exceeds a critical value, which is typically about 1,000. As we have shown, the Rayleigh number for the whole mantle is about 10,000 times this value. Therefore, according to theory, the mantle is not just marginally unstable to convection; it convects vigorously.

At a general level, the theory of thermal convection provides a remarkably unified explanation for the structure and behavior of the mantle. We know from theoretical, numerical, and laboratory studies that thermal convection at high Rayleigh number exhibits a flow pattern that is, at each instant in time, generally cellular (although the flow pattern changes continuously in time) and that the kinetic energy-containing scale of the flow is proportional to the depth of the convecting region. This explains why motions in the mantle are global in scale. These studies also demonstrate that the temperature variations which drive the flow are concentrated in boundary layer structures that are significantly smaller in scale compared to the circulation. Cold thermal boundary layers form on the upper surface, become gravitationally unstable, and separate from the surface, driving descending flows. In the mantle, the cold thermal boundary layer is the lithosphere and subduction is the expression of surface boundary layer separation to initiate the descending flows. The best evidence for a hot thermal boundary layer is found in the D'' layer at the base of the mantle. In comparison with the lithosphere, we know much less about the character of this layer and how it fits into

the overall scheme of mantle convection. Numerical and laboratory experiments indicate that thermal plumes are generated in the hot basal boundary layer of a convecting fluid that is heated from below. For this reason, the D'' layer is considered a likely site for generation of mantle plumes.

In order of importance, the forces that drive mantle convection are (1) the negative buoyancy force on the cold subducted lithosphere (slab pull); (2) gravitational sliding and its associated pressure gradient that accompanies thickening of the lithosphere by conductive cooling as it diverges from the mid-ocean ridges (ridge push); and (3) large-scale, distributed density heterogeneity, especially in the lower mantle, as imaged by seismic tomography [Question 2.13]. The forces that resist mantle convection are (1) the friction provided by mantle viscosity; (2) frictional forces at plate boundaries, especially convergent plate boundaries; and (3) stabilizing buoyancy forces associated with compositional heterogeneity, especially in the continental crust and continental lithosphere. In addition to these, deflection of the phase transition boundaries at 410 and 660 km in the transition zone provide a driving force and a resisting force, respectively.

The seismicity of the Earth is concentrated at plate margins and is a direct result of the resistive forces there. In addition, pressure-release melting associated with ascending mantle convection directly explains a large fraction of the Earth's volcanism. Thus, the tectonics and volcanism on the Earth's surface can be readily accounted for as byproducts of mantle convection [Question 1.2].

In treating the mantle as a viscous fluid, we are able to explain the fundamentals of heat loss and motion in the Earth's interior. However, the viscous fluid model does not explain the existence of plates. The simple fluid model of the mantle predicts distributed deformation at the Earth's surface, rather than deformation concentrated at the margins of mobile plates. This shortcoming of the basic theory highlights the complex role of plates in mantle convection. Although plate tectonics is a consequence of mantle convection, the two phenomena are distinct to some degree. Plate tectonics requires mantle convection in order to support a thin lithosphere and to provide a driving force. However, the converse is not true: mantle convection does not require plate tectonics. Our survey of the solar system indicates that plate tectonics is a uniquely terrestrial surface expression of subsolidus convection. As numerical and laboratory experiments have demonstrated, mantle convection could be associated with an entirely different form of surface tectonics, such as sluggish-lid or stagnant-lid deformation. These alternative forms of convection are evident from the surfaces of other planets and satellites. The resolution of this paradox lies in the complex rheology of the lithosphere. Although mantle convection can be adequately modeled using a viscous fluid rheology, the behavior of the plates requires both a viscous and an elastic/plastic behavior. Brittle deformation and fracture, which lead to slip on faults, is also important.

We still do not have an adequate knowledge of the rheology of the lithosphere to fully explain how plate tectonics arises from mantle convection, but we can make some general inferences. For example, it is clear that the generation of plates by the convecting mantle feeds back strongly on the rest of the convection. Plates enforce their scale on the convection, they govern the symmetry of the flow at plate boundaries, and suppress instabilities in the upper thermal boundary layer. Though the influence of plates is strongest in the upper mantle and decreases with depth, the global scale of the largest plates insures that they are felt throughout the mantle.

Major aspects of mantle convection have remained controversial since the idea was first introduced. Most notable is the controversy concerning layered versus whole mantle convection. As the subject has developed, the prevailing opinion has oscillated between these

two rather extreme hypotheses. The initial assumption was that the whole mantle is a single convective system. This view changed with the observation that subduction zone seismicity terminates at a depth of 660 km, which was taken as evidence for layered mantle convection. Recently the pendulum of opinion has swung back, mostly because of seismic tomographic images beneath convergent plate boundaries, which are now interpreted as providing compelling evidence that at least some slabs penetrate deeply into the lower mantle. This is interpreted to mean that some form of whole mantle convection occurs. But it must be noted that geochemical constraints preclude a mantle that has been well mixed by convection. It has also been suggested that a barrier to convection within the lower mantle is consistent with both seismic tomographic and geochemical constraints.

15.2 Form of Downwelling

We begin our description of the nature of mantle convection by examining the major downwellings. The most important mantle downwellings occur in connection with convergent plate margins. They are marked by negative surface topography at the ocean trenches, collisional mountain belts on the continents, and by deep seismicity in the Wadati–Benioff zones. All major downwellings are associated with subduction of the oceanic lithosphere, either at present or in the past. Although the subducted lithosphere is rheologically distinct from the bulk of the viscous mantle, a fact that complicates our efforts to understand them in terms of viscous thermal convection, they play a role in mantle convection analogous to the cold sheet-like downwellings observed in three-dimensional convection in a viscous fluid. Theory indicates that convection in internally heated fluids is driven largely by these cold downwellings, which separate from the upper thermal boundary layer and sink due to their negative buoyancy. We infer, then, that the negative buoyancy of the descending lithospheric slabs is the main driving force for convection in the predominantly internally heated mantle.

In numerical models the downflows begin as instabilities from the cold thermal boundary layer, as seen in Figures 10.34 and 10.38. Depending on the rheology of the surface layer and the relative proportions of internal to basal heating in the model, these instabilities can form either isolated cylindrical-shaped downwellings or, alternatively, larger structures consisting of networks of partially connected, tabular-shaped downwellings.

Of these two alternatives, the second one is more similar to the pattern of major downwellings in the mantle. Viewed from the surface, the major downflow in the Earth's mantle consists of a ring of descending material enclosing the Pacific Ocean basin, with a branch extending westward from this ring beneath southern Asia. The surface expression of this structure is the network of oceanic trenches that surround the Pacific Ocean on its north, east, and west sides, the trench system along Indonesia, and the Alpine–Himalayan mountain belt. These major downwellings are identified with the belts of seismically fast material in the lower mantle seen in Figures 15.1 and 15.2.

15.2.1 Subduction

Several first-order questions remain in regard to the fate of downwelling material in the deep mantle [Question 2.4]. One major question is the depth of penetration of descending slab material [Questions 2.5, 3.11, 3.12]. As seen in Figure 15.2, and the images in Chapter 3, mantle seismic tomography is equivocal on this question. In some places the images provide strong evidence that some slabs stall at the 660 km seismic discontinuity, while beneath other convergent margins the slab material appears to penetrate into the lower mantle. But

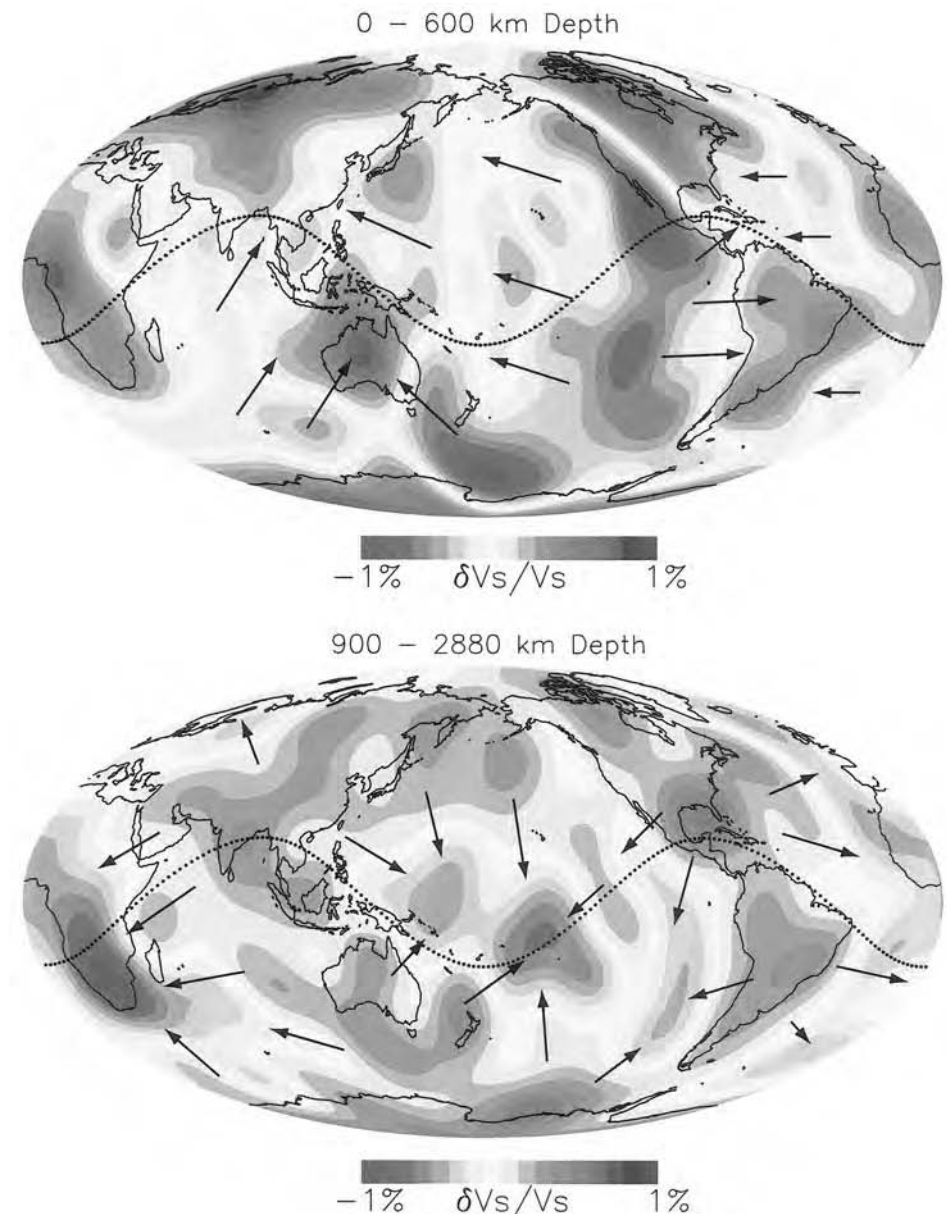


Figure 15.1. The pattern of large-scale mantle heterogeneity with the possible pattern of mantle convection. Top panel: Contours of seismic shear wave heterogeneity from Li and Romanowicz (1996) averaged over the upper mantle (0–600 km depth). The arrows indicate the direction and relative magnitude of horizontal transport in the upper mantle, inferred from the direction of plate motions and the pattern of seismic heterogeneity. Bottom panel: Contours of heterogeneity from the same seismic tomography model, averaged over the lower mantle (900–2,880 km depth). The arrows indicate the direction of horizontal transport in the lower mantle, assuming the seismic heterogeneity is proportional to density heterogeneity. The dotted curve indicates the cross-section shown in Figure 15.2.

For a color version of this figure, see plate section.

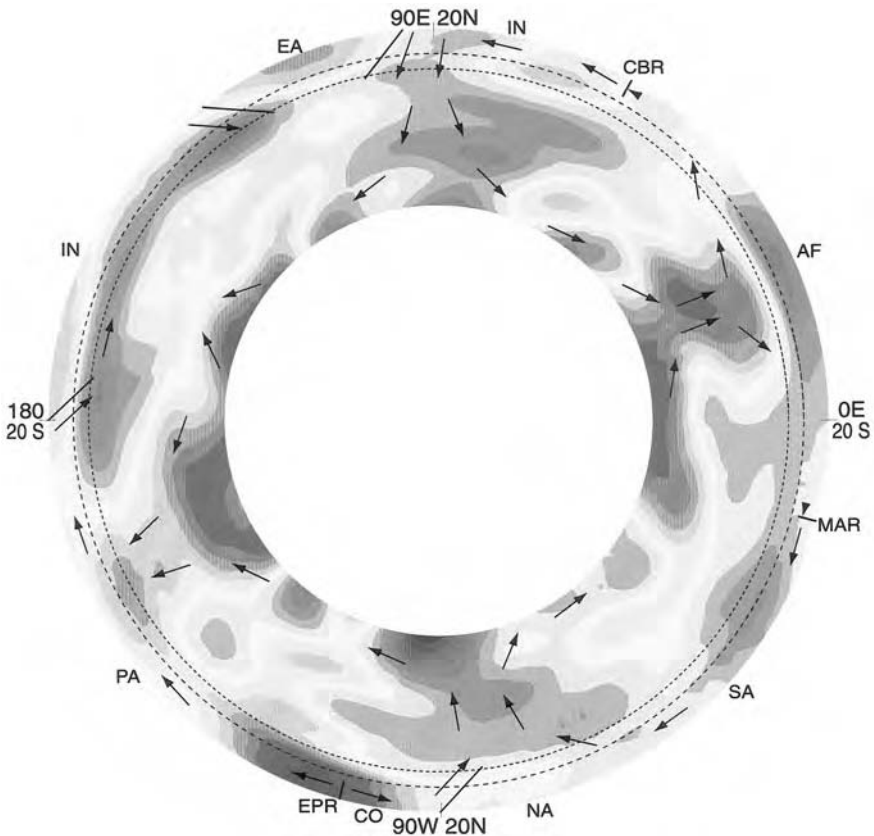


Figure 15.2. Cross-section of the Li and Romanowicz (1996) seismic tomography model along the slice shown in Figure 15.1. Color contours are the same as in Figure 15.1. The 410 and 660 km seismic discontinuities are shown as long and short dashed lines, respectively. The latitude of the slice θ varies with longitude ϕ as $\theta_0 \cos(2\phi)$ with θ_0 corresponding to -20° . The slice latitude is 20°N at longitudes 90°E and 90°W , and is 20°W at longitudes 0° and 180° , at the locations indicated on the diagram. This slice intersects the major seismic anomalies in the lower mantle and is oblique to the direction of plate motions. The plates, spreading centers, and subduction zones along the slice are shown for reference. Subduction zones are indicated by dipping line segments. Plate motion at spreading centers is indicated by double arrows, with direction of ridge migration indicated by parallel arrows. EPR = East Pacific Rise; MAR = Mid-Atlantic Ridge; CBR = Carlsburg Ridge. Plates: EA = Eurasian; IN = Indian; PA = Pacific; NA = North American; SA = South American; AF = African; CO = Cocos. The arrows indicate the pattern of large-scale flow assuming whole mantle convection, with the seismic heterogeneity proportional to density heterogeneity.

For a color version of this figure, see plate section.

even in these zones, the behavior of the slab material does not appear to conform to a simple steady-state downwelling. Beneath the Indonesia–Pacific convergence zone, for example, the seismically fast belt appears to terminate at mid-mantle depths, without reaching the core–mantle boundary. At other convergence zones, for example beneath India and the Americas, the seismic velocity anomalies extend throughout the lower mantle, indicating that downwelling there may be continuous to the core–mantle boundary.

A related major question concerning the fate of descending slabs is the degree to which they are mixed and homogenized into the mantle [Question 8.3]. After the subducted basaltic oceanic crust is converted to its high-pressure eclogitic phase there is a significant density contrast between the relatively heavy subducted crust and the relatively light depleted mantle [Question 4.4]. We have discussed two alternative hypotheses for how this two-layer lithosphere structure behaves after subduction: (1) the dense eclogite crust sinks to the base of the mantle and the light depleted mantle rises to the upper mantle; and (2) the crust and mantle are stretched and thinned by kinematic mixing until homogenization is completed by diffusion on the centimeter scale. A variety of evidence favors the latter hypothesis. The inference that the MORB source in the upper mantle is chemically depleted requires rehomogenization of the subducted crust and lithosphere.

Some of the thermal aspects of subduction zones are poorly represented in the fluid convection model. Island arc volcanism is ubiquitous at subduction zones. However, subduction zones are essentially cold and pressure-release melting cannot occur in downwellings. Thus, the origin of the volcanism associated with the volcanic lines lying parallel to subduction zones remains enigmatic from a thermal perspective [Questions 2.7, 4.9]. Back-arc basins are found behind a substantial fraction of the subduction zones. These basins are generally attributed to subduction zone rollback or to induced secondary subduction zones, either of which imply tensional forces in a region where the fluid model predicts the forces should be primarily compressional. Clearly the fluid convection model does not provide a detailed understanding of the process or processes in back-arc basin formation [Question 2.8].

Many subduction zones exhibit an arcuate structure. This is the origin of the term “island arc,” of which the Aleutian arc is an example. An explanation of this arcuate planform is provided by the “ping-pong ball” analogy. The arcuate structure minimizes distortions of the descending slab [Question 2.6].

Although cylindrical downwellings occur in numerical computations of convection in a viscous fluid with internal heat generation, no such structures have been resolved in the Earth’s mantle. Either cylindrical downflows in the mantle are not easily detected, or they do not occur. The latter is likely if account is taken of the influence of plate rheology on mantle convection. The tabular-shaped mode of downwelling in viscous convection is enhanced by the presence of mechanically strong subducted lithosphere slabs and by the tendency of the lithosphere to break in a brittle fashion along linear zones. Conversely, the mechanically strong lithosphere cannot easily deform so as to produce cylindrical downwellings. In other words, the arcuate shape of subducted slabs of oceanic lithosphere favors the development of tabular-shaped downwellings, while the mechanical strength of the lithosphere suppresses the development of cylindrical downwellings.

We have argued that the pattern of plate convergence, Wadati–Benioff zone geometry, and the pattern of mantle seismic heterogeneity all indicate that major mantle downwellings are compatible, on a large scale, with convection in a viscous fluid. However, a closer examination of mantle downwellings reveals several important discrepancies with a purely fluid model of this process. Most of the major shortcomings in fluid models of mantle convection stem from their oversimplified treatment of the mechanical behavior of the subducted lithosphere.

One important disagreement between mantle downwellings and downwellings in a viscous fluid is the nonvertical descent of lithospheric slabs into the mantle. Descending lithosphere slabs dip into the mantle at angles ranging from nearly horizontal to nearly vertical, but predominantly at angles near 45°. In contrast, descending sheets in a convecting fluid tend to sink vertically (Figure 10.36) [Question 2.3]. Although several mechanisms

have been proposed to explain this effect, the fundamental reason for nonvertical subduction in the Earth is not understood.

Another area of disagreement is the process of initiating a downwelling. In a viscous fluid, downwellings begin as thermal boundary layer instabilities and tend to be roughly symmetric, with either a vertical symmetry axis (in the case of cylindrical instabilities) or a vertical symmetry plane (in the case of two-dimensional instabilities). In contrast, the processes of subduction zone initiation [Question 2.16] and lithospheric deformation at ocean trenches lead to asymmetric downwelling in the mantle, with only one plate subducted [Question 2.2]. The issues of slab dip and one-sided subduction are clearly related. The sinking plate bends through 45° or more at subduction zones while the overriding plate remains on the surface. This asymmetric deformation is more characteristic of brittle or plastic failure processes, rather than fluid deformation.

15.2.2 Delamination

Although the dominant form of downwelling in the mantle is related to subduction, there is indirect evidence of downwelling in other environments. Delamination of the continental lithosphere, a form of small-scale convection, is likely to be important locally beneath the continents [Question 2.11]. Under a variety of circumstances the negative buoyancy of the continental lithosphere and lower continental crust delaminates these from the upper continental crust. Although not important to total heat transport of the whole mantle, delamination is significant in the evolution of the continental crust and for the isotopic balance of the mantle.

15.3 Form of Upwelling

There is direct surface evidence for two forms of mantle upwelling: flows associated with accretional plate margins, which we also refer to as spreading centers and mid-ocean ridges, and localized upwellings beneath volcanic hot spots, which we refer to as mantle plumes. In addition, seismic tomography provides some evidence for larger-scale upwellings at depth.

15.3.1 Accretional Plate Margins

First we discuss the character of upwellings beneath spreading centers, the mid-ocean ridges. The central question on their role in mantle convection is whether the upwellings at spreading centers are active or passive [Question 3.10]. Here the term “active” refers to upwellings driven primarily by their own buoyancy, whereas the term “passive” refers to upwellings driven primarily by stresses derived from plate divergence. This is an important distinction in the theory of mantle convection. Since active upwellings represent dynamically complementary structures to the negatively buoyant downwellings in a convecting fluid, we should expect the upwellings beneath spreading centers to extend to the base of the convecting region, if they are active. In contrast, there is no such restriction on the depth extent of passive upwellings beneath spreading centers.

The observable characteristics of spreading centers favor the passive upwelling hypothesis. As shown in Figures 15.1 and 15.2, seismic tomographic images of the mantle clearly indicate the presence of seismically slow and presumably hot regions beneath mid-ocean ridges. However, with the exception of the East Pacific Rise, these anomalies do not extend deeper than about 350 km into the mantle. This observation suggests that, in most places,

upwelling beneath mid-ocean ridges has a shallow origin. Even in the case of the East Pacific Rise, the anomaly is confined to the upper mantle. In addition, the mid-ocean ridges have a negligible geoid signature, implying that they are compensated isostatically at shallow depths. If the upwellings beneath spreading centers were active, then at least some part of their topography would be dynamically supported at depth. This would result in a measurable geoid anomaly, which is not observed.

It is important to note in this context that the role of the mid-ocean ridges as the major source of magmatic and volcanic activity on the Earth does not require active upwelling. Mid-ocean ridge magmatism can be explained by pressure-release melting in a passive upwelling beneath spreading centers. Upper mantle material contains a low melting temperature component. This component is about 20% of the total and melting of this component forms the 6 km thick basaltic oceanic crust. The melt is produced at depths of less than 50 km and rises to the surface due to its positive buoyancy, by some combination of porous flow and magma fracture. Although magma is generated over a relatively wide zone in a passive upwelling, the ocean crust is actually formed in a narrow region in the vicinity of a ridge crest; the mechanism or mechanisms responsible for this focusing have not been established [Question 4.7].

Although geophysical evidence favors the interpretation of shallow and rather passive upwellings beneath the global system of spreading centers, it is not obvious from the theory of convection why this should be the case. For example, in a homogeneous fluid, upwellings beneath regions of large-scale surface divergence typically extend to all depths, even if they are passive.

What causes the upwellings beneath mantle spreading centers to be shallow? The likely explanation can be found in the accretional process at the ridges and the effects of the transition zone on passive upwellings. The mechanism of accretion at spreading centers imposes kinematic constraints on mantle flow that are fundamentally incompatible with convective upwellings in a viscous fluid. First, the geometry of spreading centers consists of diverging ridge segments alternating with transform faults, across which the motion is transverse [Question 2.1]. In a viscous fluid, the divergent motion of the boundary induces a poloidal flow, whereas transverse boundary motion induces a toroidal flow. Only the poloidal part of the motion is compatible with convection. Second, spreading centers migrate over the Earth's surface in response to the stress distribution in the plates, rather than in response to buoyancy forces deeper in the mantle. Ridges evolve by rift propagation along strike, and by rapidly migrating in the spreading direction, sometimes jumping to new locations almost discontinuously. These observations indicate that brittle failure, rather than distributed viscous flow, governs the deformation in the oceanic lithosphere. Spreading centers can migrate away from mantle upwellings in response to the forces in the plates.

We therefore conclude that mid-ocean ridges represent a shallow, passive upwelling of the mantle in response to the tearing of tectonic plates under the pull of sinking slabs. Mid-ocean ridges do not represent deep active upwelling sheets of hot mantle material. Unlike the surface pattern of subduction zones which reveal the sites of deep mantle downwelling, the surface pattern of mid-ocean ridges says little about active deep mantle upwelling. Mid-ocean ridges reflect a pattern of shallow passive mantle circulation forced upon the deep mantle convection system by the brittle rheology of the plates. In order to produce concentrated linear regions of shallow upwelling and divergence, models of mantle convection would have to incorporate a mechanically strong layer at the surface to act as a stress guide for the tension supplied by the slabs, and a brittle-fracture or plastic rheology of the layer to give sharp or discontinuous features of extensional strain.

In concluding that spreading centers generally represent shallow mantle upwellings, we beg the question: Where do deep mantle upwellings occur? Clearly they must exist, in order to balance the mass flux into the lower mantle from slabs. There is in fact evidence for two types of deep mantle upwelling structures. One type is the broad-scale lower mantle upwellings inferred from the pattern of seismic heterogeneity. As shown in Figures 15.1 and 15.2, there are two mushroom-shaped low-velocity anomalies in the lower mantle, one beneath Africa, the other beneath the Southwest Pacific, that extend from the core–mantle boundary to the transition zone. These structures are more or less surrounded by a sheet of high-velocity (cold) material that we identify as (at least in part) former lithospheric material. Assuming that seismic velocity heterogeneities correlate with density heterogeneities, these low-velocity structures represent positively buoyant material and large-scale upwellings in the lower mantle. They appear to deflect near the base of the transition zone (especially the structure beneath Africa), suggesting that mantle upwellings are impeded by phase transitions or perhaps a subtle compositional stratification between the upper and lower mantle.

15.3.2 Mantle Plumes

We now turn to the second generally accepted form of mantle upwelling, mantle plumes beneath volcanic hot spots. Seismic evidence for the existence of mantle plumes is beginning to emerge, but remains fragmentary. Most of the ideas about mantle plumes derive from the widespread and long-held interpretation that many hot spots are the surface expressions of mantle plumes [Question 11.1]. Theory and numerical models of convection indicate that mantle plumes originate from instabilities of a thermal boundary layer at the base of the lower mantle, the base of the upper mantle, or both [Questions 2.9, 11.4]. Another question is whether all plumes produce volcanic hot spots [Question 11.2]. The surface volcanism of hot spots associated with mantle plumes requires the penetration of magma through thick oceanic and continental lithospheres. It is entirely possible that some mantle plumes rise to the base of the lithosphere but fail to produce a hot spot, either because they do not produce sufficient magma, or because the magma, which must fracture its way through the lithosphere, does not reach the surface [Question 4.8].

Temperature-dependent mantle viscosity focuses the thermal and velocity anomalies of plumes into small diameter cylindrical structures and helps to maintain their narrowness. In a fluid with a thermally activated viscosity of the Arrhenius type, steady plumes consist of a narrow cylindrical high-velocity conduit imbedded within a broader cylindrical thermal halo [Question 11.8]. The high-velocity cylindrical core is typically several tens of kilometers in diameter with upward motions at speeds of nearly a meter per year. The cylindrical thermal anomaly is about twice as broad with excess temperatures of perhaps several hundred Kelvin. Because of the strong temperature dependence of mantle viscosity, plumes in the mantle could have dimensions as small as 10 km.

The narrowness of ascending plumes is destroyed by the interaction of plumes with the lithosphere. The lithosphere deflects the upward plume flow horizontally along its base, resulting in a broad flattened flow region. Major hot spots are usually associated with lithospheric swells. These are broad elliptical zones of elevated topography with diameters of about 1,000 km. The widely accepted hypothesis is that this elevated topography is the compensation of the excess buoyancy of the deflected plume [Question 11.3]. This association has allowed a quantitative determination of the heat transported in the mantle by plumes [Question 11.5]. It is estimated that mantle plumes beneath recognized hot spots carry about 10% of the Earth's surface heat flux. The heat flux from the core to the mantle is estimated

to be about this amount, so the energetics of hot spots are consistent with plumes originating at the core–mantle boundary [Question 4.14]. Support for a core–mantle boundary origin of at least some mantle plumes comes from the correlation between the locations of some of the most energetic hot spots at the surface and seismic ultra-low velocity zones at the base of the mantle. However, some surface hot spots are so small, in terms of their heat transport, that it is difficult to envision them originating at such great depth.

The precise relationship between mantle plumes and the general mantle circulation remains an open question. The large-scale images of mantle structure obtained from global seismic tomography such as Figures 15.1 and 15.2 do not show evidence of mantle plume structures that would produce localized hot spots. For the most part, mantle plumes are envisioned as secondary scale flows arising from an instability in a hot, low-viscosity, basal thermal boundary layer, perhaps located at the core–mantle interface [Question 11.6]. The observation of near-stationary hot spots – that the motion of hot spots relative to one another is generally small compared to the velocities of the overlying plates and the plate boundaries – has been interpreted to mean that plumes are decoupled from the large-scale flows that drive the plates. According to this view, plumes drift in response to the “mantle wind” beneath the plates, and the relative motion of hot spots reflects the time variations in total mass flux beneath the plates. This is likely an oversimplified picture of the real situation, however.

Models of convection with boundary layer instabilities and plumes indicate that mantle plumes interact more strongly with larger-scale components of mantle motion. In particular, convection models indicate that plumes modify their local environment in a large-scale convective flow, in effect creating conditions more conducive for stationary hot spots. They cast doubt on the concept of hot spots originating from unconnected plumes that rise at random locations in the mantle irrespective of the general circulation pattern. Instead, convection models suggest that mantle plumes may be connected by a network of thermal ridges in the basal thermal boundary layer and that the plumes form at the intersection points of the thermal ridges. According to this interpretation, it is these ridge intersections, from which the plumes originate, that map into hot spot locations at the surface. Mantle plumes do not simply arise from the instability of an otherwise undisturbed lower thermal boundary layer. Their locations are influenced by the large-scale flow, in particular the sinking and spreading out of the relatively cold downflows which modulate the lower thermal boundary layer and determine where the thermal ridges form. These downflows thin and even remove the hot lower boundary layer where they descend, suppressing plume formation there. The hot material is driven laterally in the boundary layer, where it converges into thermal ridges. Where the ridges intersect, upwelling plumes form.

Mantle isotope ratios indicate that the source region for ocean island basalts (OIB) is more enriched and much more heterogeneous than the source region for mid-ocean ridge basalts (MORB). The OIB cannot be obtained from the same source region as MORB. In addition, some OIB have isotope signatures indicating a primordial component. For example, high concentrations of ^{3}He found in Hawaii and elsewhere appear to require a source region that has not been previously differentiated. This is a strong argument for an isolated lower mantle reservoir [Questions 12.1, 12.2]. The variety of isotope signatures found in OIB requires about 2 Gyr to develop. Thus, the source regions must have been isolated for this length of time. Two explanations have been given for this isolation: (1) significant volumes of the mantle have remained isolated on this time scale, and (2) isolation has occurred in the continental crust and underlying lithosphere [Question 12.4]. Studies of mantle mixing appear to preclude the isolation of sufficient volumes of the mantle on the required time scale. The preferred explanation is the relatively recent delamination of continental crust

and lithosphere which can produce the required isotope signatures. The delaminated material becomes part of an ascending plume from the basal boundary layer [Question 12.3].

The mantle plume hypothesis offers compelling explanations for several long-standing problems in lithosphere dynamics. One of these is the elevated heat flow in old lithosphere. Heat transfer from plumes to the base of the lithosphere significantly contributes to the surface heat flow in old oceanic lithosphere and in continental lithosphere. However, even the plume contribution is not enough to explain why the old lithosphere reaches thermal equilibrium. This indicates one of two possibilities: (1) there are more mantle plumes than surface hot spots, or (2) there are secondary convection cells beneath the plates. Mantle plumes have been assigned an important role in the initiation of an accretional plate boundary [Question 2.15]. The lithospheric swells associated with plume-initiated hot spots in the continents result in three-armed rift systems. Where these systems interact, they rupture the continental lithosphere resulting in the formation of a new ocean. Another important aspect of the ascending flows associated with plumes is the concept of plume heads, a concept primarily drawn from laboratory experiments. Several hot spot tracks appear to have been initiated with a massive flood basalt eruption. According to the plume head model, flood basalts form by the partial melting in a large-volume plume head as it impinges on the base of the continental lithosphere [Questions 11.7, 11.10].

15.4 Horizontal Boundary Layers

The recognition that regions of the mantle with strongly superadiabatic temperature gradients are thermal boundary layers of convection must be regarded as one of the major contributions of fluid mechanical modeling to our understanding of the mantle. This insight came originally through the results of asymptotic boundary layer theories and two-dimensional numerical models of steady convection. Subsequently, two-dimensional models and three-dimensional models of time-dependent convection have helped clarify the nature of mantle boundary layers. Originally conceived as steady features with regular spatial structure, we now recognize that they are highly time dependent and dynamic, with spatially varying structure. Examples of such temporal and spatial variability in mantle boundary layer structures are lithospheric thinning by mantle plumes, delamination of overthickened or weakened lithosphere, rifting, and lateral variations in seismic properties of the D'' layer.

15.4.1 *The Lithosphere*

The association of the Earth's lithosphere with the upper cold thermal boundary layer of a convecting system provides a means of predicting a number of geophysical observables and thereby testing the validity of the lithosphere as a thermal boundary layer concept. The dependences of surface topography, geoid height, and surface heat flux on distance from the center of upwelling can be inferred from the dependence of temperatures on horizontal distance and depth in boundary layer and numerical two-dimensional solutions of convection. Comparisons of such predictions with observations of oceanic topography (bathymetry), geoid height, and heat flux as a function of the age of the seafloor or distance from a mid-ocean ridge generally result in good agreement and validate the idea that the Earth's oceanic lithosphere is the upper thermal boundary layer of a convecting mantle.

Some areas of disagreement remain, however. Although the predictions of the half-space cooling model are in good agreement with observations for seafloor ages of less than about 80 Myr, there are significant differences for older seafloor [Question 4.1]. The

oceanic lithosphere appears to approach an asymptotic maximum thickness [Question 4.2]. Estimates of this maximum thickness range from about 95 to 125 km. The reason for this maximum thickness remains controversial. Two hypotheses have been proposed. The first is that the impingement of plumes heats the base of the lithosphere. The second is that there is secondary convection involving the instability of the lower part of the oceanic lithosphere, a form of delamination [Question 7.3]. This second hypothesis assumes an active role for the asthenosphere, usually identified with the seismic low-velocity zone (LVZ), which underlies a large fraction of the oceanic lithosphere, particularly where it is thin. The low seismic velocities and seismic attenuation associated with the LVZ are usually attributed to partial melting [Questions 3.1, 4.5]. A sufficiently low viscosity in the asthenosphere promotes decoupling of the plates from the underlying flow of the mantle and the secondary convection necessary for delamination.

What do the results of convection studies say about the dynamical role of the oceanic lithosphere? Originally it was thought that convection in a fluid with a strongly temperature dependent viscosity would be a satisfactory model for mantle convection and would yield a fully dynamical theory for plate tectonics. Unfortunately this has not turned out to be the case. Although the viscosity of the mantle is strongly temperature dependent, the mechanical behavior of the Earth's lithosphere does not resemble that of the cold upper boundary layer of convection in a fluid with temperature dependent viscosity. The top thermal boundary layer of such a fluid is a stagnant lid, and does not consist of mobile plates. Furthermore, stagnant lid convection does not exhibit an analog to subduction. Instead, the downwellings are more analogous to delamination, because they involve only the high temperature and less viscous portion of the lid. In mantle convection the upper thermal boundary layer, in spite of its high viscosity, is transformed directly into descending slabs by the mechanism of subduction. Subduction, which involves deformation by nonviscous processes such as faulting and strain concentration, is the key difference between convection in a temperature-dependent viscous fluid and convection in the mantle.

In some ways, the behavior of the continental lithosphere resembles more the stagnant lid in temperature dependent viscous convection. Continental crust and lithosphere resist subduction [Question 9.14]. They couple to mantle convection through viscous tractions on the base of the lithosphere and through the mechanism of delamination, which involves convection-driven entrainment and lithosphere erosion [Question 4.4]. The thickness of the continental lithosphere remains uncertain, with estimates ranging from 150 to 300 km [Questions 3.2, 4.3]. This is the range of thicknesses predicted by stagnant-lid convection models.

15.4.2 The D'' Layer

Another achievement of mantle convection studies is identifying the D'' layer at the base of the mantle as a hot thermal boundary layer. Although the full picture of this layer is far from complete, seismic studies have provided considerable information on its structure. It seems to be a compound boundary layer, with superimposed temperature and compositional variations. Based on the extreme lateral variations in seismic properties, it appears to be as dynamical as the crust–lithosphere system at the surface. There is topography on the core–mantle boundary just as there is topography at the Earth's surface [Question 3.13]. This topography is clearly associated with the dynamic behavior of this boundary layer. Several first-order questions remain in regard to the D'' layer: What is the change in temperature across it [Question 4.15]? What is the source of the compositional variation [Questions 3.6,

9.15]? Is there partial melt in the layer [Question 3.7]? Is there small-scale convection in the layer [Question 9.16]? Does this small-scale convection result in mantle plumes [Question 11.6]?

15.4.3 Internal Boundary Layers

Other than the lithosphere and the D'' layer, there is no compelling geophysical evidence at this time for other mantle thermal boundary layers. However, geochemical evidence must also be considered when models of mantle convection are constructed. Geochemical studies preclude a well-stirred, homogeneous mantle. A variety of geochemical observations require that a significant fraction of the mantle preserve primordial concentrations of trace elements and noble gases. While the upper mantle must be a near-homogeneous reservoir to provide the source region for MORB, there must be other parts of the mantle that can provide primordial isotopic signatures and high concentrations of primordial noble gases. One of the most important considerations is the thorium–uranium ratio. From both direct observations and isotopic evidence, it is known that the MORB source region has a thorium–uranium ratio of 2.5. From heat flow considerations and lead isotope studies it is also known that this cannot be the thorium–uranium ratio for the entire mantle. Parts of the mantle must be either heterogeneous or layered. Studies of mantle mixing generally favor a well-stirred mantle unless it is layered. Layering and an internal thermal boundary layer could exist in the transition zone, perhaps at the depth of the 660 km seismic discontinuity, but observed slab penetration into the lower mantle appears to preclude strictly layered convection at this depth. Partial layering due to the temporary stalling and deflection of slabs in the transition zone keeps open the possibility of spatially limited or regional transient thermal boundary layers yet to be discovered. It has recently been proposed that layering occurs within the lower mantle; although this can explain geochemical observations, it remains a controversial hypothesis.

15.5 The General Circulation

The upwelling, downwelling, and boundary layer structures described in the previous sections combine to form the general circulation of the mantle [Question 10.1]. It likely consists of distinctive shallow and deep components, each with its own character determined by dynamical conditions in that part of the mantle. Understanding the exact nature of this linkage represents a major challenge for the future.

In order to illustrate the essential parts of the general circulation, we have superimposed schematic velocity arrows on mantle seismic tomography images in Figures 15.1 and 15.2. Figure 15.1 shows mantle shear wave tomography averaged over the upper mantle and the lower mantle, respectively. The arrows indicate the directions and relative magnitudes of the horizontal transport, the integrated horizontal velocity over the layer.

In the upper mantle the general circulation is dominated by the nearly rigid motion of the major plates, particularly the fast Pacific, Nazca, Cocos, and Indian plates. Vertical motions in the upper 200–300 km of the mantle are greatest beneath the fast spreading centers, especially the East Pacific Rise. The existence of the low-viscosity asthenosphere beneath the lithosphere explains how ridge-imposed upwellings can be largely confined to the upper few hundred kilometers of the mantle [Question 5.1]. The return flow to the ridge does not consist of closed cells in the upper mantle and does not directly involve the descending slabs, which penetrate to greater depths. Hence the mass transport in the upper

mantle is away from the spreading centers and toward the convergent plate boundaries on average, as shown in the figures. The fact that the upper mantle flow is strongly concentrated beneath the four fastest moving plates, which comprise only about one half of the surface area, is an indication of the time-dependent, open cell character of mantle convection. Ridge and trench migration, which enlarge some plates at the expense of others and transfer mass from beneath one plate to another, are surface expressions of this time-dependent, open cell convection. It is clear that the motion of the plates strongly influences flows in the mantle [Question 9.4]. Plates are also responsible for generating the toroidal component of mantle convection [Question 2.14].

Much of the Earth's topography can be associated with changes in the thicknesses of the crust and lithosphere. A controversial question is whether a significant component of Earth's topography is dynamically induced by convective flows at depth [Question 5.3].

The deeper circulation of the mantle consists of the descending slabs, large-scale upflows, and, by assumption, concentrated ascending plumes which are not resolved by seismic tomography. The slabs appear to penetrate into the lower mantle though some may stall in the transition zone above the endothermic phase change at 660 km depth. Some slabs are deflected horizontally near the 660 km seismic discontinuity before sinking into the lower mantle. After entering the lower mantle, slabs may fold under compression into thicker structures before sinking all the way to the core–mantle boundary or, alternatively, some may become assimilated into the lower mantle before reaching the base. An interesting question is whether layered mantle convection dominated early in the Earth's evolution [Question 10.9].

As inferred from the pattern of high seismic velocities in Figures 15.1 and 15.2, at least some accumulations of subducted slab material may sink all the way to the bottom of the mantle, especially in the great ring beneath the Pacific basin. Slab material reaching the core–mantle boundary would displace hot material laterally in the D'' layer. This heated material would then accumulate at locations far from the major descending currents to form thick masses of seismically low-velocity material such as those beneath Africa and the south-central Pacific shown in the figures. The net buoyancy of these low seismic velocity masses depends on their composition relative to the rest of the mantle. If their source region in the D'' layer has a composition denser than the rest of the lower mantle, then their combination of temperature and composition may make them nearly isopycnal with respect to the lower mantle. Under these conditions, they will ascend to a level of approximate neutral buoyancy and spread out. In the case of the low-velocity structure beneath Africa, this material appears to spread out near the base of the transition zone. There is some indication in the seismic tomography that material from the upflow beneath the south Pacific crosses into the upper mantle. In other places around the core–mantle boundary, the inferred upflows appear to terminate within the lower mantle.

Similar dynamical considerations apply on a smaller scale to upwelling plumes. These may rise all the way to the surface forming hot spots such as Hawaii and Iceland, they may be trapped or stalled at the top of the lower mantle, or they may rise to some intermediate depth before becoming incorporated into the general circulation. Ultimately their fate depends on their buoyancy flux and the maintenance of a connection to the source of hot material perhaps at the base of the mantle.

A comparison of the inferred downflow and upflow structures imaged in seismic tomography with those of numerical models suggests what may happen to descending slabs in the deep mantle and to lower mantle upflows. Downflow sheets in the models broaden and break up into more equidimensional structures as they approach the lower boundary. Descending slabs may similarly broaden by folding and break apart along strike.

This is a purely viscous effect and would happen even to those slabs that penetrate the 660 km phase change with little deformation. Slab folding followed by breakup along strike could be effective in the deep lower mantle and could promote slab assimilation into the lower mantle instead of slab pile-up on the core–mantle boundary. The tendency of the endothermic phase change at 660 km depth to resist slab sinking can force the slab to strongly deform in the transition zone long before it encounters the lower mantle. A substantial increase in viscosity with depth at the transition from the upper mantle to the lower mantle at a depth of about 660 km or deeper in the lower mantle could also cause the folding of slabs descending through this depth.

By arguing that the negative buoyancy in subducted slab material provides the main driving force for mantle convection, and that the seismic tomography images show where large concentrations of slab material presently reside, it is possible to construct a schematic picture of the general mantle circulation. Figure 15.2 shows such a schematic, based on the presumption of some form of convection through the whole mantle, but with the transition zone acting as a partial filter. We emphasize this is just a schematic of what is in reality a highly time variable flow pattern with multiple spatial scales of motion present simultaneously.

The cross-section in Figure 15.2 is a cut along the path shown in Figure 15.1. This section was chosen to cut the two largest high seismic velocity anomalies and the two largest low seismic velocity anomalies in the lower mantle. It therefore approximates a longitudinal flow section in the lower mantle. Note that it does not correspond to a flow section for the upper mantle. The section runs along plate boundaries at some places and through plate interiors at other places. The fact that a longitudinal flow section in the lower mantle is not the same for the upper mantle is a geometrical illustration of the main point of this chapter: there is a change in style of convection with depth through the mantle due to the plates' depth-dependent properties and the effects of the transition zone.

The flow shown in Figure 15.2 is dominated by a spherical harmonic degree 2 pattern, particularly in the lower mantle. The major descending flows correspond to the high seismic velocity ring surrounding the Pacific and extending beneath southern Asia. The major upflows appear to be roughly cylindrically shaped low seismic velocity structures beneath Africa and the south-central Pacific. The inferred upper mantle flow in the same section is compatible with quasi-cellular whole mantle convection at some places, such as beneath the Indian Ocean, but not at other places, such as beneath the eastern half of the Pacific Plate.

15.6 Time Dependence

The chaotic and turbulent nature of convective motions in even very viscous fluids suggests that the mantle may also be a chaotic system exhibiting thermal turbulence [Questions 8.1, 8.2, 9.3, 13.7]. Many geological observations provide support for a highly time dependent or chaotic mantle. These include changes with time in the number, geometry, directions and speeds of motion of tectonic plates, related changes in plate boundary structures including the propagation, extinction, initiation, and subduction of ridges and the drift and creation of subduction zones, and possible episodicity in hot spot and flood basalt activity and continental growth.

Mantle avalanches are prominent sporadic downflow events in models of mantle convection; their occurrence in the real mantle would likely have produced major changes in the geological record such as the Archean–Proterozoic transition. Indirect support for the reality of mantle avalanches is provided by seismic tomographic observations of slabs that appear

to have stalled and piled up on the 660 km endothermic phase transition and slabs that have entered the lower mantle as broadened downwellings [Questions 10.4, 13.10].

Mantle convection models undergo transitions from one style of convection to another. Examples include the possible transition from layered to whole mantle convection and the transition from constant-viscosity-like convection to stagnant-lid or sluggish-lid convection; of course, such transitions can also occur in the opposite directions. The occurrence of such transitions in the evolving Earth would have had profound global consequences for the planet. Transitions of this type might also have taken place in other planets providing an explanation for global catastrophic events such as the resurfacing of Venus some 500–750 Myr ago. While all this is speculative, the important point is that the temporal complexity of mantle convection provides an abundance of behaviors that could literally turn over the mantle and reshape the surface. Impacts are not the only way to change the course of planetary evolution; the source of global change can also lie within a body, in the dynamics of a vigorously convecting mantle.

The interactions of the plates with the mantle also have important implications for time dependence. So far it has not been possible to systematically include the breakup and coalescence of plates in three-dimensional models of mantle convection. Thus, we do not know if the creation and destruction of plates is a stochastic process associated with the creation of new accretional margins where plumes randomly impinge on continental lithosphere and the initiation of subduction zones at randomly weak passive margins. If plate creation and destruction do occur this way, then the random surface boundary condition may dominate the time dependence of convection at depth. An alternative is that plate geometries are strongly influenced by internal flows [Question 2.17]. A related question concerns the statistical distribution of plate sizes: Why are plates so large [Question 10.7]?

Fully three-dimensional models of mantle convection exhibit variations with time that, while less spectacular, may have analogous behaviors in the mantle [Question 10.1]. The drift of downwelling sheets in numerical models (Chapter 10) and in laboratory experiments is similar to the lateral migration (perpendicular to strike) of descending slabs through the mantle. The along-axis lengthening of downwellings in the numerical models suggests the possibility that subduction zones on Earth may evolve by propagation along their strike. The random and spatially sporadic initiation of downwelling in models of convection is difficult to relate to subduction on the Earth since subduction is strongly influenced by plate rheology and initiation of subduction is not well understood.

The strong temperature dependence of mantle viscosity could enhance the temporal (and spatial) variability of mantle convection in yet other ways. An example is the possible occurrence of vigorous sub-boundary layer scale convection in the D'' layer [Question 9.16]. Two-dimensional numerical models with strongly temperature dependent viscosity show small-scale convective activity in the hot lower thermal boundary layer. Small-scale convection in the D'' layer could be responsible for lateral heterogeneity in the structure of the layer and roughness, or small-scale topography, of the core–mantle boundary. Vigorous sub-boundary layer scale convection in the D'' layer also introduces temporal variability in the structure of the layer on a time scale as short as several million years.

15.7 Special Effects in Mantle Convection

Here we summarize special physical effects that give mantle convection its unique character. The often subtle interplay between these effects may hold the key to the further understanding of mantle convection.

15.7.1 Solid-state Phase Transformations

From depths of 220–660 km there are increases in density and density discontinuities that require deviations from the adiabatic behavior of an iso-mineralic mantle; this is the transition zone. The behavior of the transition zone can be attributed to either phase changes or changes in composition [Question 9.5]. The shallowest density change at a depth of 220 km is known as the Lehmann seismic discontinuity. Both its existence and its origin are controversial [Question 3.3].

The stronger density and seismic discontinuity at a depth of 410 km is attributed to the transformation of olivine to the spinel phase. In equilibrium, the phase boundary would be elevated in the descending slab and would provide additional slab pull. However, if the phase transformation is slow (out of equilibrium), a metastable wedge of olivine could develop in the slab below 410 km depth [Questions 4.10, 4.11]. In any case, there is no evidence that this phase boundary significantly influences mantle convection.

The density and seismic discontinuity at a depth of 660 km is another matter. It has long been debated whether this is simply a transformation from spinel to perovskite or if it also includes a change in composition [Questions 3.4, 3.5]. This question is directly related to the question of whether this discontinuity is a barrier to convection [Questions 7.1, 9.6, 9.9, 13.6]. It is certainly a partial barrier and it definitely has an important influence on mantle convection [Questions 4.13, 10.5]. Seismic tomographic data appear to indicate that some, but not all, descending slabs penetrate through this boundary into the lower mantle. If there is a substantial interchange of material between the upper and lower mantle, the mantle will be homogenized and any compositional difference between the upper and lower mantle would be reduced. In this case, the morphological diversity of slab behavior at this boundary must be attributed to the phase change [Question 10.2]. Related questions are whether the partial blockage of convection at this depth (1) requires a thermal boundary layer [Question 4.16], (2) has an influence on the penetration of plumes [Question 9.10], (3) explains the long-wavelength variations in seismic velocity [Question 10.3] and the long-wavelength geoid anomalies [Question 10.6]. Deep earthquakes are also associated with the phase changes, but questions remain about the details of this association [Question 4.12].

Numerical studies of mantle convection indicate that the 660 km phase change may trigger avalanches of material transport between the upper mantle and the lower mantle [Question 10.4]. If these avalanches occur they could explain the episodicity associated with the geological record on the continents [Question 13.10]. Whether or not mantle avalanches are real, models of mantle convection emphasize that the endothermic phase change at 660 km depth has a profound influence on the style of mantle convection. The spinel–perovskite phase change tends to oppose the downwelling of cold material and provides an explanation for the seismic tomographic observations of bent and thickened slabs in the transition zone [Question 10.2]. A viscosity increase from the upper mantle to the lower mantle could also account for slab distortion around 660 km depth so it is not certain that the endothermic nature of the spinel–perovskite phase change is the entire explanation of the seismic observations.

The temporary ponding of cold downwelling material above the 660 km phase change imposes a long-wavelength signature on models of mantle convection that can explain the dominance of long wavelengths in spectra of mantle seismic heterogeneity and the geoid [Questions 10.3, 10.6]. Again, it is not certain that the observational data are fully explained by the action of the endothermic phase change alone since other things such as an increase in mantle viscosity with depth, the size of plates, and the ocean–continent dichotomy also impose a long-wavelength pattern on mantle convection.

15.7.2 Variable Viscosity: Temperature, Pressure, Depth

Variations of mantle viscosity with temperature, pressure, mineralogy, and volatile content combine to produce lateral and radial changes in mantle viscosity. Together with the phase changes in the transition zone, viscosity variations with temperature and depth provide the most important control on the nature of mantle convection [Questions 9.7, 9.12]. We have already noted in the previous section how an increase of viscosity from the upper mantle to the lower mantle could deform and broaden slabs and impose a long-wavelength structure on mantle convection. An important question is whether the 660 km phase change results directly in an increase in viscosity [Question 5.8]. A high viscosity in the lower mantle could also reduce the amount of convective mixing by the mantle and preserve geochemical reservoirs over long periods of time; a high lower mantle viscosity could also help to explain the relative fixity of mantle plumes. The present consensus about mantle viscosity is that the lower mantle is more viscous than the upper mantle, but the amount of the increase and other details about the variation of mantle viscosity with depth are uncertain [Questions 5.4, 13.5]. Studies using postglacial rebound data tend to indicate some viscosity increase with depth in the mantle, whereas inversions of geoid data favor a larger increase [Question 10.8].

Models of mantle convection with strongly temperature dependent viscosity reveal three regimes of convection – constant viscosity, sluggish lid, and stagnant lid. The different convection regimes feature different convective planforms and efficiencies of heat transfer. The Earth is in the constant viscosity convection regime, because nonviscous crustal and lithospheric deformation facilitates plate subduction. The sluggish-lid or stagnant-lid convection regimes may pertain to other planets such as Venus.

15.7.3 Nonlinear Viscosity

An important question is whether the mantle viscosity is Newtonian (linear) or non-Newtonian (nonlinear) [Question 5.7]. This is directly related to the question of whether the dominant mechanism for solid-state creep in the mantle is diffusion creep or dislocation creep [Question 5.6]. Diffusion creep gives a Newtonian behavior and dislocation creep gives a nonlinear, non-Newtonian behavior. Studies of postglacial rebound strongly favor a linear rheology, whereas laboratory studies suggest the applicability of the nonlinear dislocation creep mechanism. If the governing mechanism is diffusion creep there may be a significant dependence on grain size [Question 5.5]. In order to do detailed and realistic numerical calculations of mantle convection, it is also necessary to specify the rheology of the crust and mantle lithosphere [Question 9.1].

Two-dimensional Cartesian models of convection with non-Newtonian viscosity emphasize the importance of simultaneously accounting for the dependence of viscosity on temperature and pressure when assessing effects of the stress dependence of viscosity on convection [Question 9.11]. When viscosity depends on temperature, pressure, and stress, the effect of the stress dependence is to moderate the influence of temperature and pressure. Stated another way, a convective flow with temperature-, pressure-, and stress-dependent viscosity has a Newtonian viscous counterpart with a viscosity that depends more weakly on temperature and pressure. Convection with non-Newtonian viscosity has smaller internal viscosity variation than would be predicted on the basis of temperature and pressure variations alone. If the dependence of viscosity on temperature and pressure is of the Arrhenius type with an activation enthalpy, then the Newtonian analogue of the non-Newtonian flow has an activation enthalpy only about half as large as that of the nonlinear flow.

The effects of nonlinear viscosity on convection need to be determined for three-dimensional flows. A few steady-state three-dimensional solutions with non-Newtonian, power-law viscosity are in the literature and the effect of a non-Newtonian surface sheet on three-dimensional convection has also been studied. However, there are no studies of three-dimensional convection with non-Newtonian viscosity in vigorously convecting, time-dependent cases. It is possible that nonlinear viscosity will influence three-dimensional convection in unanticipated ways because of the spatial complexity of flow patterns in three dimensions. However, as the two-dimensional calculations emphasize, this should be done by simultaneously incorporating the temperature and pressure dependence of viscosity and probably compressibility as well. Compressibility and nonlinear viscosity are tied together through the influence of viscous dissipation on compressible convection and through the dependence of viscosity on temperature and pressure. If the combined effect of all the variables which influence viscosity is to moderate viscosity variations in the flow, then mantle convection may be closer to constant viscosity convection than would be expected on the basis of the individual dependences of mantle viscosity on temperature, pressure, and stress.

15.7.4 Compressibility

Compressibility is significant in mantle convection because the density of the Earth's mantle increases by about 60% from the top of the mantle to the bottom (accounting for phase and/or compositional changes). The effects of compressibility have been considered in two-dimensional Cartesian and axisymmetric studies of convection and in three-dimensional studies. Compressible models of convection must also incorporate viscous dissipation to be valid [Question 10.11].

Compressibility has dramatic effects on convection only when the superadiabatic temperature change across the spherical shell is small compared with the adiabatic temperature change. In the Earth's mantle, the superadiabatic temperature change is comparable to the adiabatic temperature change and compressibility should not particularly influence convection.

The results of some numerical models suggest that compressibility might stabilize the bottom of the mantle and lead to penetrative convection. In some two-dimensional, plane layer, liquid anelastic models the dissipation number is assumed constant and the magnitude of the adiabatic temperature gradient increases exponentially with depth. The stabilization of the bottom of the layer in this model is a consequence of the steep adiabat. The adiabat in the Earth's mantle does not steepen in this manner with depth and compressibility does not stabilize the lower mantle. A form of penetrative convection in the Earth's lower mantle has been suggested, but this is associated with density changes across 660 km depth. Realistic variations with depth in the density and thermal structure of the deep mantle as a consequence of compressibility do not lead to stabilization and penetrative convection in the lower mantle.

Laboratory experiments and theoretical studies have shown that thermal expansivity in the Earth's mantle decreases with depth due to the compressibility of rocks under high pressure [Question 9.12]. This effect has been incorporated into two-dimensional numerical models of compressible convection which show that it is a significant influence on the style of convection (e.g., the occurrence and structure of plumes). A decrease of thermal expansivity with depth is a standard feature in most three-dimensional compressible convection models. While the depth dependence of thermal expansivity must be accounted for in realistic models of mantle convection, the variation of thermal expansivity with depth is not a major influence

on the style of compressible convection. Variations in viscosity with depth are much more important.

Compressibility affects convection through the complex interplay of a number of material properties and the distribution of heat sources, but overall, the effects of compressibility on mantle convection appear to be relatively minor. The interpretation of the seismic velocity anomalies obtained in mantle tomography requires an understanding of the relative roles of temperature, composition, and melting [Questions 5.2, 9.2].

15.7.5 Viscous Dissipation

The role of viscous heating in mantle convection has been studied in several compressible convection models. Viscous dissipation in these models is significant in small-scale structures such as boundary layers, plumes, and sheet-like downflows [Question 9.13]. Viscous heating is strong where upwelling plumes meet the top thermal boundary layer. Accordingly, viscous heating could play an important role in lithospheric thinning.

15.8 Plates and Continents

Future progress in modelling thermal convection in the Earth's mantle must address two issues. The first is the behavior of the plates. An important aspect of this is the mechanism or mechanisms responsible for the initiation of subduction. A second issue is the presence of the continents. The formation of the continents must follow from any comprehensive model of mantle convection.

15.8.1 Plates

There is no satisfactory way of incorporating plate behavior into models of mantle convection at this time [Question 10.12]. In some models, the effects of plates on mantle convection have been inferred by the simple expedient of imposing surface velocity or surface stress boundary conditions on the model. In other models, plate-like behavior has been simulated by the imposition of weakened zones at the surface and at faults. However, plates are an integral part of the multi-rheological mantle, and in a truly realistic model of mantle convection, the number and geometry of the plates and their velocities would be determined by the model itself.

The key to the self-consistent generation of plate-like behavior in mantle convection models is the incorporation of rheological behavior that results in the localization of deformation to narrow shear zones, either faults or ductile shear zones. This can be accomplished by rheological laws that exhibit strain-rate weakening, but no self-consistent convection simulations with a strain-rate weakening rheology have yet been carried out. Furthermore, there is yet no way of relating the parameters of idealized strain-rate weakening rheologies to the rheological properties of real rocks which localize deformation by faulting in the brittle and elastic part of the lithosphere and by ductile shear localization below this layer. The basic problem is to determine where faults and ductile shear zones will develop in order to accommodate subduction [Question 9.8]. There is no indication that this problem can be solved in a deterministic context. It may be a purely statistical aspect of mantle convection.

Tectonic plates impose a large scale on mantle convection. Because of their large sizes, the non-subductibility of continental plates, and the thermal and mechanical contrasts between

continental and oceanic plates, tectonic plates also have a strong influence on the large-scale mantle circulation. The derivation of plate-tectonic behavior from a model of mantle convection remains the principal challenge to our understanding of mantle dynamics.

15.8.2 Continents

Any comprehensive model for the Earth must include the formation of the continents [Question 2.10]. The continental crust is composed of light silicic rocks that have evolved from the mantle in a relatively complex cycle. Basaltic rocks in the continents can represent a melt fraction of the mantle just as the basaltic rocks of the oceanic crust. But a substantial fraction of continental rocks have a more silicic, granitic, or rhyolitic composition. These rocks are produced by secondary melting within the continental crust.

The most widely accepted model for the creation of continental crust involves the addition of mafic basaltic or near-basaltic rocks in island arc or plume (hot spot) volcanics [Question 2.12]. These rocks are altered by the hydrologic cycle. When these altered rocks are remelted by intrusive island arc or hot spot volcanism, the result is the granitic or rhyolitic rocks which are so common in the continental crust. However, this internal fractionation process would produce a more mafic lower crust and a mean continental crustal composition that is mafic (basaltic). Since the mean crustal composition is much more silicic, there must be a process that removes the mafic lower mantle. This process is delamination, which recycles lower continental crust and lithosphere into the mantle. There is strong isotopic evidence for the presence of the recycled material in plume-generated OIB.

Isotopic evidence gives a mean age of continental crustal rocks of about 2.1 Gyr. Accordingly, without recycling of continental crust into the mantle, the volume of continental crust would have been about 50% of its present value 2 Gyr ago. But evidence from sea level (freeboard) is that the volume of continental crust 2 Gyr ago was essentially the same as today [Question 13.12]. This requires the recycling of substantial volumes of continental crust into the mantle. Certainly, new rocks are being added continuously through island arc and hot spot volcanism, but age dating of continental rocks indicates that there have been episodic additions of large volumes [Question 13.11]. These can be attributed to the Wilson cycle and/or to mantle avalanches [Question 13.10]. Another interesting question is whether a different crustal generation process was operative in the Archean [Question 13.13]. Also, was the Earth's mantle fractionated to form a crust and/or a layered mantle at the end of accretion [Question 13.1]?

15.9 Comparative Planetology

Potentially one of the most important sources of information on how the Earth evolves is the evolution of the other rocky planets and moons. As data have accumulated over the past 40 years from various space missions and Earth-based observations, the major differences between the bodies have become striking. It is generally accepted that the inner planets, Mercury, Venus, Earth, and Mars, were formed from accretion in the solar nebula. In terms of density these planets are similar except for the excess density of Mercury [Question 14.39], which remains anomalous. The presence of the Earth's Moon has also long been considered an anomaly. At the present time, the favored hypothesis for the origin of the Moon is that it resulted from a giant impact with a Mars-size object during planetary accretion [Question 14.27]. Although there are problems with this hypothesis, alternative hypotheses have far greater problems.

One question associated with comparative planetology is the presence or absence of an internally generated magnetic field in a planet or moon. Why do not Mars and Venus have magnetic fields [Questions 14.16, 14.20]? Is this due to slow rates of rotation, different internal temperatures, or different physical states of the planets' cores [Question 14.23]? In the case of Venus, a strong argument can be made that Venus' core is liquid at present and not undergoing thermal convection. Why does Mercury have a magnetic field [14.38]? Is it due to the large size of the core or thermochemical convection in a partially solidified core? Why is the lunar crust magnetized [Questions 14.25, 14.26]? Does Io have an internally generated magnetic field [Question 14.36]?

15.9.1 Venus

It is generally accepted that the primary mechanism responsible for the tectonic and volcanic evolution of rocky planetary bodies is the escape of heat from their interiors. This heat is generated by radioactive isotopes and secular cooling. The escape of heat from planetary interiors will certainly depend on the size of the body. The smaller the body, the larger the ratio of surface area to volume, the more efficient is the loss of heat. Thus, in terms of understanding the Earth, Venus, because of its similar size, is the body of most interest.

In the absence of evidence to the contrary, it is generally accepted that the concentrations of heat-producing elements in Venus are similar to those in the Earth. This heat generation plus secular cooling escapes from Venus' deep interior by mantle convection [Question 14.1]. It was widely assumed that a consequence of this convection would be plate tectonics on Venus. But it is now clear that plate tectonics is not occurring on Venus [Question 14.12]. A major question is: How is heat lost from the interior of Venus without plate tectonics [Question 14.2]? The near-uniform distribution of craters on Venus implies a near-global, volcanic resurfacing event about 500–750 Myr ago [Question 14.3]. This event has been interpreted in terms of a near-global, catastrophic subduction event or in terms of the termination of plate tectonics on Venus [Question 14.10].

In the absence of plate tectonics, a steady-state loss of heat on Venus would require a very thin lithosphere (≈ 25 km). There are various lines of evidence that with the high surface temperature, the lithosphere on Venus cannot be this thin [Question 14.9]. The high topography on Venus requires high stresses to support it. The associated gravity anomalies can be interpreted in terms of a deep depth of compensation [Questions 14.7, 14.13]. Also, large craters are not relaxed.

The conclusion is that the interior of Venus is presently being heated by the decay of the radioactive isotopes. It has been hypothesized that this heating could lead to a future global subduction event. The structure of the major coronae on Venus has been associated with incipient subduction events.

Another major difference between Venus and the Earth is the absence of “continents” on Venus. There are plateau highlands on Venus, but they have a much smaller area than the continents on the Earth. These highlands could be more silicic than the basaltic volcanic plains [Question 14.11]. But it is consistent with our understanding of the Earth that oceans and erosion play an essential role in the silicic (granitic, rhyolitic) volcanism responsible for our continents. It is tempting to further hypothesize that without the rheologically “soft” continents, it is not possible to absorb the area changes associated with the geometrical incompatibilities of plate tectonics. The major question regarding Venus is: How is heat lost on Venus without plate tectonics [Questions 14.2, 14.15]? Is there subduction on Venus

without accretionary plate boundaries [Question 14.8]? Major questions concerning layered versus whole mantle convection can also be asked for Venus [Questions 14.6, 14.14].

15.9.2 Mars

We next turn our attention to Mars. Mars is significantly smaller than the Earth and Venus and, for this reason, its tectonic and volcanic evolution would be expected to be different. It is generally accepted that Mars is presently a dead planet. Two reasons can be given for this: (1) Due to the large surface area to volume ratio more heat has been lost and the interior has cooled. (2) Crustal differentiation on Mars has been more efficient and a large fraction of the incompatible heat-producing elements are now near the surface where heat can be lost by conduction [Question 14.22].

Two major aspects of the surface tectonics and volcanism on Mars can be associated with mantle convection within Mars. The first is the hemispheric dichotomy between the ancient, heavily cratered southern hemisphere and the younger, low-lying volcanic plains of the northern hemisphere [Question 14.4]. This could be related to the dominance of a low degree spherical harmonic pattern of mantle convection early in Mars' geologic history or, possibly, with a period of plate tectonics. The second is the origin of the Tharsis uplift and the associated great shield volcanoes on Mars [Questions 14.17, 14.21]. The localized nature of this volcanism can be attributed to pressure-release melting in a single large plume within Mars. The spinel–perovskite or olivine–spinel transformation in the Martian mantle could enforce a convection mode dominated by a single plume. The great height of the shield volcanoes is one argument for a very thick lithosphere on Mars [Question 14.19]. Another major question concerning Mars is the origin of the Valles Marineris canyon system [Question 14.18].

15.9.3 The Moon

Because of its small size, it is not surprising that the Moon is presently a dead planet. Because of the many surface samples returned on Apollo missions, we have a better data base for the Moon than for the other rocky planetary bodies. Age dating has shown that surface volcanism on the Moon ceased about 1.5 Gyr ago. Seismic studies and gravity and topography mapping have shown that the lunar crust has an average thickness in excess of 60 km so that the Moon is essentially fully differentiated into a mafic crust and a depleted mantle [Question 14.31]. Thus, it can be concluded that the heat-producing elements lie near the surface where the heat can be lost by conduction. If this is the case, then it would be doubtful that there is mantle convection within the Moon [Question 7.4].

A major aspect of the Moon is a hemispheric dichotomy similar to that on Mars [Question 14.5]. The farside of the Moon is almost entirely composed of heavily cratered highlands. The nearside of the Moon is dominated by the younger, low-lying volcanic plains of the mare, although there are significant highland regions. The lunar hemispheric dichotomy, like the one on Mars, could be due to mantle convection early in the Moon's evolution.

The dating of highland rocks indicates that they formed within a few hundred million years of the formation of the Moon. They are highly differentiated and are attributed to the solidification of a global, or near-global, magma ocean [Question 14.24]. Convection in the global magma ocean could also explain the nearside–farside crustal dichotomy.

The basaltic volcanic plains of the mare fill large, pre-existing impact craters. The ages of the mare date from about 1.8 to 2.8 Ga. Isotope studies on these rocks indicate they come from a chemically heterogeneous lunar mantle [Question 14.32]. The implication is that mantle convection has not homogenized the interior of the Moon. Although the volume of the extrusive volcanics associated with mare fill can be estimated, the volume of intrusive volcanism remains unknown. Extensive crustal underplating over this age range of basaltic volcanism could have occurred. There are other major questions concerning this basaltic volcanism. Why was its onset delayed [Question 14.26]? Why was it terminated [Question 14.27]? Was mare volcanism produced by *in situ* radioactive heating or was it produced by pressure-release melting associated with ascending mantle convection? Another major question concerns the origin of mascons [Question 14.25] whose large gravity anomalies are associated with many of the filled basins. The gravity anomalies imply buried high-density rock. Two alternatives are (1) diapirs of dense mantle rock intruded into the lighter crust, and (2) the transformation of lighter basalt to denser eclogite.

15.9.4 Mercury and Io

Mercury is another small rocky planet. It is certainly a dead planet now and its entire surface appears to be primordial. We have very little information on either internal structure or internal processes except for the large iron core [Question 14.37]. On the other hand, Io is a very active, though small, rocky planetary body. This is attributed to tidal heating [Question 14.35]. Io is differentiated into a metallic core and silicate mantle [Question 14.34] and it may have a partially molten asthenosphere [Question 14.33] as indicated by its extensive high-temperature volcanism. It is not known with certainty whether Io has its own magnetic field [Question 14.36].

15.9.5 Icy Satellites

Icy satellites of the outer planets are admixtures of water ice and rock/metal. Subsolidus convection is plausibly occurring in the interiors of large icy satellites such as Ganymede and the viscosity of ice is likely controlling the dynamics. Major questions about these bodies concern the extent of internal differentiation. It is known that Ganymede is fully differentiated into a metallic core and rock and ice shells while the similar-sized moon Callisto is only partially differentiated and does not have a metallic core. Ganymede is the only moon in our solar system known to have an active core dynamo and a magnetic field. Why similar-sized bodies such as Ganymede and Callisto are so different internally and so different in appearance are lingering dilemmas [Question 14.42]. Internal structure and dynamics and thermal evolution of outer planet satellites have a unique aspect not encountered with terrestrial planets, namely a close interplay with orbital dynamics in which tidal dissipation can be a major source of heat [Question 14.35]. It remains to be resolved whether Europa and Callisto have subsurface liquid water oceans [Questions 14.40 and 14.41].

References

- Abbott, D., Burgess, L., Longhi, J., & Smith, W. H. F. (1994). An empirical thermal history of the Earth's upper mantle. *J. Geophys. Res.* **99**, 13835–50.
- Abe, Y. & Matsui, T. (1985). The formation of an impact-generated H₂O atmosphere and its implications for the early thermal history of the Earth. *J. Geophys. Res.* **90**, 545–59.
- (1986). Early evolution of the Earth: Accretion, atmosphere formation, and thermal history. *J. Geophys. Res.* **91**, E291–E302.
- (1988). Evolution of an impact-generated H₂O–CO₂ atmosphere and formation of a hot proto-ocean on Earth. *J. Atmos. Sci.* **45**, 3081–101.
- Abers, G. A. (1992). Relationship between shallow- and intermediate-depth seismicity in the eastern Aleutian subduction zone. *Geophys. Res. Lett.* **19**, 2019–22.
- (1996). Plate structure and the origin of double seismic zones. In *Subduction: Top to Bottom*, pp. 223–8, eds. G. E. Bebout, D. W. Scholl, S. H. Kirby, & J. P. Platt, Geophysical Monograph 96. American Geophysical Union, Washington, DC.
- Abramowitz, M. & Stegun, I. A., editors (1964). *Handbook of Mathematical Functions*. Applied Mathematics Series 55. National Bureau of Standards, Washington, DC, 1046 pp.
- Acuña, M. H., Connerney, J. E. P., Wasilewski, P., Lin, R. P., Anderson, K. A., Carlson, C. W., McFadden, J., Curtis, D. W., Mitchell, D., Rème, H., Mazelle, C., Sauvaud, J. A., d'Uston, C., Cros, A., Medale, J. L., Bauer, S. J., Cloutier, P., Mayhew, M., Winterhalter, D., & Ness, N. F. (1998). Magnetic field and plasma observations at Mars: Initial results of the Mars Global Surveyor mission. *Science* **279**, 1676–80.
- Acuña, M. H., Connerney, J. E. P., Ness, N. F., Lin, R. P., Mitchell, D., Carlson, C. W., McFadden, J., Anderson, K. A., Rème, H., Mazelle, C., Vignes, D., Wasilewski, P., & Cloutier, P. (1999). Global distribution of crustal magnetization discovered by the Mars Global Surveyor MAG/ER experiment. *Science* **284**, 790–3.
- Aharonov, E., Whitehead, J. A., Kelemen, P. B., & Spiegelman, M. (1995). Channeling instability of upwelling melt in the mantle. *J. Geophys. Res.* **100**, 20433–50.
- Ahern, J. L. & Turcotte, D. L. (1979). Magma migration beneath an ocean ridge. *Earth Planet. Sci. Lett.* **45**, 115–22.
- Ahrens, T. J. (1979). Equations of state of iron sulfide and constraints on the sulfur content of the Earth. *J. Geophys. Res.* **84**, 985–98.
- Ahrens, T. (1990). Earth accretion. In *Origin of the Earth*, pp. 211–27, eds. H. E. Newsom & J. H. Jones. Oxford University Press, New York.
- Akaogi, M., Navrotsky, A., Yagi, T., & Akimoto, S. (1987). Pyroxene-garnet transformation: Thermochemistry and elasticity of garnet solid solutions, and application to a pyrolite mantle. In *High-Pressure Research in Mineral Physics*, pp. 251–60, eds. M. H. Manghnani & Y. Syono, Geophysical Monograph 39. American Geophysical Union, Washington, DC.
- Akaogi, M., Ito, E., & Navrotsky, A. (1989). Olivine-modified spinel-spinel transitions in the system Mg₂SiO₄–Fe₂SiO₄: Calorimetric measurements, thermochemical calculation, and geophysical application. *J. Geophys. Res.* **94**, 15671–85.

- Aki, K. & Richards, P. G. (1980). *Quantitative Seismology: Theory and Methods*, Vols. I and II. W. H. Freeman & Co., San Francisco, 932 pp.
- Akimoto, S.-I. & Fujisawa, H. (1968). Olivine–spinel solid solution equilibria in the system Mg_2SiO_4 – Fe_2SiO_4 . *J. Geophys. Res.* **73**, 1467–79.
- Albers, M. & Christensen, U. R. (1996). The excess temperature of plumes rising from the core–mantle boundary. *Geophys. Res. Lett.* **23**, 3567–70.
- Alder, B. J. (1966). Is the mantle soluble in the core? *J. Geophys. Res.* **71**, 4973–9.
- Allègre, C. J. (1982). Chemical geodynamics. *Tectonophysics* **81**, 109–32.
- (1987). Isotope geodynamics. *Earth Planet. Sci. Lett.* **86**, 175–203.
- Allègre, C. J. & Rousseau, D. (1984). The growth of the continent through geological time studied by Nd isotope analysis of shales. *Earth Planet. Sci. Lett.* **67**, 19–34.
- Allègre, C. J. & Turcotte, D. L. (1985). Geodynamic mixing in the mesosphere boundary layer and the origin of oceanic islands. *Geophys. Res. Lett.* **12**, 207–10.
- (1986). Implications of a two-component marble-cake mantle. *Nature* **323**, 123–7.
- Allègre, C. J., Brevart, O., Dupré, B., & Minster, J. F. (1980). Isotopic and chemical effects produced in a continuously differentiating convecting Earth mantle. *Phil. Trans. Roy. Soc. London A* **297**, 447–77.
- Allègre, C. J., Hart, S. R., & Minster, J.-F. (1983a). Chemical structure and evolution of the mantle and continents determined by inversion of Nd and Sr isotopic data, I. Theoretical methods. *Earth Planet. Sci. Lett.* **66**, 177–90.
- (1983b). Chemical structure and evolution of the mantle and continents determined by inversion of Nd and Sr isotopic data, II. Numerical experiments and discussion. *Earth Planet. Sci. Lett.* **66**, 191–213.
- Allègre, C. J., Staudacher, T., Sarda, P., & Kurz, M. (1983c). Constraints on evolution of Earth's mantle from rare gas systematics. *Nature* **303**, 762–6.
- Allègre, C. J., Dupré, B., & Lewin, E. (1986). Thorium/uranium ratio of the Earth. *Chem. Geol.* **56**, 219–21.
- Allègre, C. J., Staudacher, T., & Sarda, P. (1987). Rare gas systematics: Formation of the atmosphere, evolution and structure of the Earth's mantle. *Earth Planet. Sci. Lett.* **81**, 127–50.
- Allègre, C. J., Sarda, P., & Staudacher, T. (1993). Speculations about the cosmic origin of He and Ne in the interior of the Earth. *Earth Planet. Sci. Lett.* **117**, 229–33.
- Allègre, C. J., Moreira, M., & Staudacher, T. (1995). 4He / 3He dispersion and mantle convection. *Geophys. Res. Lett.* **22**, 2325–8.
- Allègre, C. J., Hofmann, A., & O'Nions, K. (1996). The Argon constraints on mantle structure. *Geophys. Res. Lett.* **23**, 3555–7.
- Alley, K. M. & Parmentier, E. M. (1998). Numerical experiments on thermal convection in a chemically stratified viscous fluid heated from below: Implications for a model of lunar evolution. *Phys. Earth Planet. Int.* **108**, 15–32.
- Alterman, Z., Jarosch, H., & Pekeris, C. L. (1959). Oscillations of the Earth. *Proc. Roy. Soc. London A* **252**, 80–95.
- Alvarez, L. W., Asaro, F., Michel, H. V., & Alvarez, W. (1980). Extraterrestrial cause for the Cretaceous-Tertiary extinction. *Science* **208**, 1095–108.
- Alvarez, W., Kauffman, E. G., Surlyk, F., Alvarez, L. W., Asaro, F., & Michel, H. V. (1984). Impact theory of mass extinctions and the invertebrate fossil record. *Science* **223**, 1135–41.
- Ambrose, J. W. (1964). Exhumed paleoplains of the Precambrian shield of North America. *Am. J. Sci.* **262**, 817–57.
- Anderson, D. L. (1970). Petrology of the mantle. *Mineral. Soc. Am. Spec. Pap.* **3**, 85–93.
- (1982). Hotspots, polar wander, Mesozoic convection and the geoid. *Nature* **297**, 391–3.
- (1987a). Thermally induced phase changes, lateral heterogeneity of the mantle, continental roots, and deep slab anomalies. *J. Geophys. Res.* **92**, 13968–80.
- (1987b). A seismic equation of state. II. Shear properties and thermoamics of the lower mantle. *Phys. Earth Planet. Int.* **45**, 307–23.
- (1989). *Theory of the Earth*. Blackwell Sci. Publ., Boston, MA, 366 pp.
- (1993). Helium-3 from the mantle: Primordial signal or cosmic dust? *Science* **261**, 170–6.
- (1998a). The helium paradoxes. *Proc. Natl. Acad. Sci. USA* **95**, 4822–7.

- Anderson, D. L. (1998b). A model to explain the various paradoxes associated with mantle noble gas geochemistry. *Proc. Natl. Acad. Sci. USA* **95**, 9087–92.
- Anderson, D. L. & Bass, J. D. (1984). Mineralogy and composition of the upper mantle. *Geophys. Res. Lett.* **11**, 637–40.
- Anderson, D. L. & Given, J. W. (1982). Absorption band Q model for the Earth. *J. Geophys. Res.* **87**, 3893–904.
- Anderson, J. D., Colombo, G., Esposito, P. B., Lau, E. L., & Trager, G. B. (1987). The mass, gravity field, and ephemeris of Mercury. *Icarus* **71**, 337–49.
- Anderson, J. D., Sjogren, W. L., & Schubert, G. (1996a). Galileo gravity results and the internal structure of Io. *Science* **272**, 709–12.
- Anderson, J. D., Jurgens, R. F., Lau, E. L., Slade, M. A., & Schubert, G. (1996b). Shape and orientation of Mercury from radar ranging data. *Icarus* **124**, 690–7.
- Anderson, J. D., Lau, E. L., Sjogren, W. L., Schubert, G., & Moore, W. B. (1996c). Gravitational constraints on the internal structure of Ganymede. *Nature* **384**, 541–3.
- Anderson, J. D., Schubert, G., Jacobson, R. A., Lau, E. L., Moore, W. B., & Sjogren, W. L. (1998a). Europa's differentiated internal structure: Inferences from four Galileo encounters. *Science* **281**, 2019–22.
- (1998b). Distribution of rock, metals, and ices in Callisto. *Science* **280**, 1573–6.
- Anderson, O. L. (1967). Equation for thermal expansivity in planetary interiors. *J. Geophys. Res.* **72**, 3661–8.
- (1978). The role of magma vapors in volcanic tremors and rapid eruptions. *Bull. Volcanol.* **41–4**, 341–53.
- (1979). Evidence supporting the approximation $\gamma\rho = \text{const}$ for the Grüneisen parameter of the Earth's lower mantle. *J. Geophys. Res.* **84**, 3537–42.
- Anderson, O. L. & Duba, A. (1997). Experimental melting curve of iron revisited. *J. Geophys. Res.* **102**, 22659–69.
- Anderson, O. L. & Grew, P. C. (1977). Stress corrosion theory of crack propagation with applications to geophysics. *Rev. Geophys. Space Phys.* **15**, 77–104.
- Anderson, O. L., Schreiber, E., Liebermann, C., & Soga, N. (1968). A model for the computation of thermal expansivity at high compression and high temperatures: MgO as an example. *Rev. Geophys.* **6**, 491–524.
- Anderson, O. L., Chopelas, A., & Boehler, R. (1990). Thermal expansivity versus pressure at constant temperature: A re-examination. *Geophys. Res. Lett.* **17**, 685–8.
- Anderson, O. L., Oda, H., & Isaak, D. (1992). A model for the computation of thermal expansivity at high compression and high temperatures: MgO as an example. *Geophys. Res. Lett.* **19**, 1987–90.
- Anderson, R. N., Uyeda, S., & Miyashiro, A. (1976). Geophysical and geochemical constraints at converging plate boundaries – Part 1: Dehydration in the downgoing slab. *Geophys. J. Roy. Astron. Soc.* **44**, 333–57.
- Anderson, W. W. & Ahrens, T. J. (1996). Shock temperature and melting in iron sulfides at core pressures. *J. Geophys. Res.* **101**, 5627–42.
- Arkani-Hamed, J. (1993). On the tectonics of Venus. *Phys. Earth Planet. Int.* **76**, 75–96.
- (1994). On the thermal evolution of Venus. *J. Geophys. Res.* **99**, 2019–33.
- (1998). The lunar mascons revisited. *J. Geophys. Res.* **103**, 3709–39.
- Arkani-Hamed, J. & Toksöz, M. N. (1984). Thermal evolution of Venus. *Phys. Earth Planet. Int.* **34**, 232–50.
- Arkani-Hamed, J., Schaber, G. G., & Strom, R. G. (1993). Constraints on the thermal evolution of Venus inferred from Magellan data. *J. Geophys. Res.* **98**, 5309–15.
- Arkani-Hamed, J., Konopliv, A. S., & Sjogren, W. L. (1999). On the equipotential surface hypothesis of lunar maria floors. *J. Geophys. Res.* **104**, 5921–31.
- Armstrong, R. L. (1968). A model for the evolution of strontium and lead isotopes in a dynamic Earth. *Rev. Geophys.* **6**, 175–99.
- (1969). Correction to "A model for the evolution of strontium and lead isotopes in a dynamic Earth," 1968. *Rev. Geophys.* **7**, 665.

- Armstrong, R. L. (1981). Radiogenic isotopes: The case for crustal recycling on a near-steady-state no-continental-growth Earth. *Phil. Trans. Roy. Soc. London A* **301**, 443–72.
- (1991). The persistent myth of crustal growth. *Aust. J. Earth Sci.* **38**, 613–30.
- Armstrong, R. L. & Hein, S. M. (1973). Computer simulation of Pb and Sr isotope evolution of the Earth's crust and upper mantle. *Geochim. Cosmochim. Acta* **37**, 1–18.
- Ashby, M. F. & Verrall, R. A. (1977). Micromechanisms of flow and fracture, and their relevance to the rheology of the upper mantle. *Phil. Trans. Roy. Soc. London A* **288**, 59–95.
- Ashwal, L. D. & Burke, K. (1989). African lithospheric structure, volcanism, and topography. *Earth Planet. Sci. Lett.* **96**, 8–14.
- Atkinson, B. K. (1984). Subcritical crack growth in geological materials. *J. Geophys. Res.* **89**, 4077–114.
- Atwater, T. (1970). Implications of plate tectonics for the Cenozoic tectonic evolution of western North America. *Geol. Soc. Am. Bull.* **81**, 3513–35.
- Aurnou, J. M., Brito, D., & Olson, P. L. (1996). Mechanics of inner core super-rotation. *Geophys. Res. Lett.* **23**, 3401–4.
- Backus, G. E. (1955). On the application of eigenfunction equations to the problem of the thermal instability of a fluid sphere heated within. *Phil. Mag. Ser. 7* **46**, 1310–27.
- Bacon, F. (1620). *Novum Organum*. Open Court Publishing Company., Chicago and LaSalle, Illinois, p. 194, Translated and edited by P. Urbach and J. Gibson, 1994.
- Balachandar, S. & Yuen, D. A. (1994). Three-dimensional fully spectral numerical method for mantle convection with depth-dependent properties. *J. Comp. Phys.* **113**, 62–74.
- Balachandar, S., Yuen, D. A., & Reuteler, D. (1992). Time-dependent three dimensional compressible convection with depth-dependent properties. *Geophys. Res. Lett.* **19**, 2247–50.
- (1993). Viscous and adiabatic heating effects in three-dimensional compressible convection at infinite Prandtl number. *Phys. Fluids A* **5**, 2938–45.
- (1995a). Localization of toroidal motion and shear heating in 3-D high Rayleigh number convection with temperature-dependent viscosity. *Geophys. Res. Lett.* **22**, 477–80.
- Balachandar, S., Yuen, D. A., Reuteler, D. M., & Lauer, G. S. (1995b). Viscous dissipation in three-dimensional convection with temperature-dependent viscosity. *Science* **267**, 1150–3.
- Banerdt, W. B., Phillips, R. J., Sleep, N. H., & Saunders, R. S. (1982). Thick shell tectonics on one-plate planets: Applications to Mars. *J. Geophys. Res.* **87**, 9723–33.
- Banerdt, W. B., Golombek, M. P., & Tanaka, K. L. (1992). Stress and tectonics on Mars. In *Mars*, pp. 249–97, eds. H. H. Kieffer, B. M. Jakosky, C. W. Snyder, & M. S. Matthews. The University of Arizona Press, Tucson and London.
- Barazangi, M. & Brown, L., editors (1986). *Reflection Seismology: The Continental Crust*, volume 14 of *Geodynamics Series*. American Geophysical Union, Washington, DC, 339 pp.
- Barcilon, V. & Lovera, O. M. (1989). Solitary waves in magma dynamics. *J. Fluid Mech.* **204**, 121–33.
- Barcilon, V. & Richter, F. M. (1986). Nonlinear waves in compacting media. *J. Fluid Mech.* **164**, 429–48.
- Barenblatt, G. I. (1962). Mathematical theory of equilibrium cracks. *Adv. App. Mech.* **7**, 55–129.
- Bargar, K. E. & Jackson, E. D. (1974). Calculated volumes of individual shield volcanoes along the Hawaiian-Emperor chain. *J. Res. U.S. Geol. Surv.* **2**, 545–50.
- Barrett, P. H. & Freeman, R. B., editors (1987). *The Geology of the Voyage of H.M.S. Beagle. Part II: Geological Observations on the Volcanic Islands*. In *The Works of Charles Darwin*, volume 8. New York University Press, New York.
- Barron, T. H. K. (1979). A note on Anderson–Grüneisen functions. *J. Phys. C* **12**, L155–L159.
- Basaltic Volcanism Study Project (1981). *Basaltic Volcanism on the Terrestrial Planets*. Pergamon Press, New York, 1286 pp.
- Basilevsky, A. T., Head, J. W., Schaber, G. G., & Strom, R. G. (1997). The resurfacing history of Venus. In *Venus II: Geology, Geophysics, Atmosphere, and Solar Wind Environment*, pp. 1047–84, eds. S. W. Bougher, D. M. Hunten, & R. J. Phillips. The University of Arizona Press, Tucson.
- Bataille, K. & Flatté, S. M. (1988). Inhomogeneities near the core-mantle boundary inferred from short-period scattered PKP waves recorded at the Global Digital Seismograph Network. *J. Geophys. Res.* **93**, 15057–64.

- Batchelor, G. K. (1967). *An Introduction to Fluid Dynamics*. Cambridge University Press, Cambridge, England, 615 pp.
- Baumgardner, J. R. (1985). Three-dimensional treatment of convective flow in the Earth's mantle. *J. Statist. Phys.* **39**, 501–11.
- (1988). Application of supercomputers to 3-d mantle convection. In *The Physics of the Planets: Their Origin, Evolution and Structure*, pp. 199–231, ed. S. K. Runcorn. J. Wiley & Sons, Ltd., New York.
- Bear, J. (1972). *Dynamics of Fluids in Porous Media*. American Elsevier, New York, 764 pp.
- Becker, R. H. & Pepin, R. O. (1984). The case for a Martian origin of the shergottites: Nitrogen and noble gases in EETA 79001. *Earth Planet. Sci. Lett.* **69**, 225–42.
- Bell, D. R. & Rossman, G. R. (1992). Water in Earth's mantle: The role of nominally anhydrous minerals. *Science* **255**, 1391–7.
- Bénard, H. (1900). Les tourbillons cellulaires dans une nappe liquide. *Revue Generale des Sciences Pures et Appliquées* **11**, 1261–71; 1309–28.
- (1901). Les tourbillons cellulaires dans une nappe liquide transportant de la chaleur par convection en régime permanent. *Ann. Chim. Phys.* **23**, 62–144.
- Benioff, H. (1949). Seismic evidence for the fault origin of oceanic deeps. *Geol. Soc. Am. Bull.* **60**, 1837–56.
- Benz, H. M. & Vidale, J. E. (1993). Sharpness of upper-mantle discontinuities determined from high-frequency reflections. *Nature* **365**, 147–50.
- Berckhemer, H., Kampfmann, W., Aulbach, E., & Schmeling, H. (1982). Shear modulus and Q of forsterite and dunite near partial melting from forced-oscillation experiments. *Phys. Earth Planet. Int.* **29**, 30–41.
- Bercovici, D. (1993). A simple model of plate generation from mantle flow. *Geophys. J. Int.* **114**, 635–50.
- (1995a). On the purpose of toroidal motion in a convecting mantle. *Geophys. Res. Lett.* **22**, 3107–10.
- (1995b). A source-sink model of the generation of plate tectonics from non-Newtonian mantle flow. *J. Geophys. Res.* **100**, 2013–30.
- (1996). Plate generation in a simple model of lithosphere-mantle flow with dynamic self-lubrication. *Earth Planet. Sci. Lett.* **144**, 41–51.
- (1998). Generation of plate tectonics from lithosphere-mantle flow and void-volatile self-lubrication. *Earth Planet. Sci. Lett.* **154**, 139–51.
- Bercovici, D. & Kelly, A. (1997). The non-linear initiation of diapirs and plume heads. *Phys. Earth Planet. Int.* **101**, 119–30.
- Bercovici, D. & Lin, J. (1996). A gravity current model of cooling mantle plume heads with temperature-dependent buoyancy and viscosity. *J. Geophys. Res.* **101**, 3291–309.
- Bercovici, D. & Mahoney, J. (1994). Double flood basalts and plume head separation at the 660-kilometer discontinuity. *Science* **266**, 1367–9.
- Bercovici, D., Schubert, G., & Reynolds, R. T. (1986). Phase transitions and convection in icy satellites. *Geophys. Res. Lett.* **13**, 448–51.
- Bercovici, D., Schubert, G., & Glatzmaier, G. A. (1989a). Three-dimensional spherical models of convection in the Earth's mantle. *Science* **244**, 950–5.
- Bercovici, D., Schubert, G., Glatzmaier, G. A., & Zebib, A. (1989b). Three-dimensional thermal convection in a spherical shell. *J. Fluid Mech.* **206**, 75–104.
- Bercovici, D., Schubert, G., & Glatzmaier, G. A. (1989c). Influence of heating mode on three-dimensional mantle convection. *Geophys. Res. Lett.* **16**, 617–20.
- (1991). Modal growth and coupling in three-dimensional spherical convection. *Geophys. Astrophys. Fluid Dyn.* **61**, 149–59.
- (1992). Three-dimensional convection of an infinite-Prandtl-number compressible fluid in a basally heated spherical shell. *J. Fluid Mech.* **239**, 683–719.
- Bercovici, D., Schubert, G., & Tackley, P. J. (1993). On the penetration of the 660 km phase change by mantle downflows. *Geophys. Res. Lett.* **20**, 2599–602.
- Bernal, J. D. (1936). Hypothesis on the 20° discontinuity. *Observatory* **59**, 268.
- Bertka, C. M. & Fei, Y. (1996). Constraints on the mineralogy of an iron-rich Martian mantle from high-pressure experiments. *Planet. Space Sci.* **44**, 1269–76.

- Bertka, C. M. & Fei, Y. (1997). Mineralogy of the Martian interior up to core–mantle boundary pressures. *J. Geophys. Res.* **102**, 5251–64.
- (1998a). Density profile of an SNC model Martian interior and the moment-of-inertia factor of Mars. *Earth Planet. Sci. Lett.* **157**, 79–88.
- (1998b). Implications of Mars Pathfinder data for the accretion history of the terrestrial planets. *Science* **281**, 1838–40.
- Bijwaard, H. & Spakman, W. (1999). Tomographic evidence for a narrow whole mantle plume below Iceland. *Earth Planet. Sci. Lett.* **166**, 121–6.
- Bills, B. G. (1989). The moments of inertia of Mars. *Geophys. Res. Lett.* **16**, 385–8.
- Bills, B. G. & Kobrick, M. (1985). Venus topography: A harmonic analysis. *J. Geophys. Res.* **90**, 827–36.
- Bills, B. G. & May, G. M. (1987). Lake Bonneville: Constraints on lithospheric thickness and upper mantle viscosity from isostatic warping of Bonneville, Provo, and Gilbert stage shorelines. *J. Geophys. Res.* **92**, 11493–508.
- Bills, B. G., Kiefer, W. S., & Jones, R. L. (1987). Venus gravity: A harmonic analysis. *J. Geophys. Res.* **92**, 10335–51.
- Bills, B. G., Currey, D. R., & Marshall, G. A. (1994). Viscosity estimates for the crust and upper mantle from patterns of lacustrine shoreline deformation in the Eastern Great Basin. *J. Geophys. Res.* **99**, 22059–86.
- Bina, C. R. (1996). Phase transition buoyancy contributions to stresses in subducting lithosphere. *Geophys. Res. Lett.* **23**, 3563–6.
- Bina, C. R. & Helffrich, G. (1994). Phase transition Clapeyron slopes and transition zone seismic discontinuity topography. *J. Geophys. Res.* **99**, 15853–60.
- Bina, C. R. & Liu, M. (1995). A note on the sensitivity of mantle convection models to composition-dependent phase relations. *Geophys. Res. Lett.* **22**, 2565–8.
- Bina, C. R. & Wood, B. J. (1987). Olivine-spinel transitions: Experimental and thermodynamic constraints and implications for the nature of the 400-km seismic discontinuity. *J. Geophys. Res.* **92**, 4853–66.
- Bindschadler, D. L. & Parmentier, E. M. (1990). Mantle flow tectonics: The influence of a ductile lower crust and implications for the formation of topographic uplands on Venus. *J. Geophys. Res.* **95**, 21329–44.
- Bindschadler, D. L., Schubert, G., & Kaula, W. M. (1990). Mantle flow tectonics and the origin of Ishtar Terra, Venus. *Geophys. Res. Lett.* **17**, 1345–8.
- Bindschadler, D. L., Decharon, A., Beratan, K. K., Smrekar, S. E., & Head, J. W. (1992a). Magellan observations of Alpha Regio: Implications for formation of complex ridged terrains on Venus. *J. Geophys. Res.* **97**, 13563–77.
- Bindschadler, D. L., Schubert, G., & Kaula, W. M. (1992b). Coldspots and hotspots: Global tectonics and mantle dynamics of Venus. *J. Geophys. Res.* **97**, 13495–532.
- Birch, F. (1939). The variation of seismic velocities within a simplified Earth model, in accordance with the theory of finite strain. *Seismol. Soc. Am. Bull.* **29**, 463–79.
- (1952). Elasticity and constitution of the Earth's interior. *J. Geophys. Res.* **57**, 227–86.
- (1963). Some geophysical applications of high-pressure research. In *Solids Under Pressure*, pp. 137–62, eds. W. Paul & D. M. Warschauer. McGraw Hill, New York.
- (1965). Energetics of core formation. *J. Geophys. Res.* **70**, 6217–21.
- (1968). Thermal expansion at high pressures. *J. Geophys. Res.* **73**, 817–19.
- Bird, P. (1978a). Stress and temperature in subduction shear zones: Tonga and Mariana. *Geophys. J. Roy. Astron. Soc.* **55**, 411–34.
- (1978b). Initiation of intracontinental subduction in the Himalaya. *J. Geophys. Res.* **83**, 4975–87.
- (1979). Continental delamination and the Colorado Plateau. *J. Geophys. Res.* **84**, 7561–71.
- (1998). Testing hypotheses on plate-driving mechanisms with global lithosphere models including topography, thermal structure, and faults. *J. Geophys. Res.* **103**, 10115–29.
- Bird, P. & Baumgardner, J. (1981). Steady propagation of delamination events. *J. Geophys. Res.* **86**, 4891–903.

- Black, M. T., Zuber, M. T., & McAdoo, D. C. (1991). Comparison of observed and predicted gravity profiles over Aphrodite Terra, Venus. *J. Geophys. Res.* **96**, 301–15.
- Blackett, P. M. S. (1956). *Lectures on Rock Magnetism*. Weizmann Sci. Press of Israel, Jerusalem, 131 pp.
- Blaney, D. L., Johnson, T. V., Matson, D. L., & Veedor, G. J. (1995). Volcanic eruptions on Io: Heat flow, resurfacing, and lava composition. *Icarus* **113**, 220–5.
- Blasius, K. R. & Cutts, J. A. (1976). Shield volcanism and lithospheric structure beneath the Tharsis plateau, Mars. *Proc. Lunar Sci. Conf. 7th*, 3561–73.
- Blichert-Toft, J. & Albarede, F. (1997). The Lu–Hf isotope geochemistry of chondrites and the evolution of the mantle–crust system. *Earth Planet. Sci. Lett.* **148**, 243–58.
- Blum, J. D. (1995). Isotopic decay data. In *Global Earth Physics: A Handbook of Physical Constants*, pp. 271–82, ed. T. J. Ahrens. American Geophysical Union, Washington, DC.
- Boehler, R. (1986). The phase diagram of iron to 430 kbar. *Geophys. Res. Lett.* **13**, 1153–6.
- (1992). Melting of the Fe–FeO and Fe–FeS systems at high pressure: Constraints on core temperatures. *Earth Planet. Sci. Lett.* **111**, 217–27.
- (1993). Temperatures in the Earth's core from melting-point measurements of iron at high static pressures. *Nature* **363**, 534–6.
- (1994). The phase diagram of iron to 2 Mbar: New static measurements. In *High-Pressure Science and Technology – 1993*, pp. 919–22, eds. S. C. Schmidt, J. W. Shaner, G. A. Samara, & M. Ross. American Institute of Physics, Woodbury, NY AIP Conference Proceedings 309, Part 1.
- (1996). Melting of mantle and core materials at very high pressures. *Phil. Trans. Roy. Soc. London* **354**, 1265–78.
- Boehler, R. & Ross, M. (1997). Melting curve of aluminum in a diamond cell to 0.8 Mbar: Implications for iron. *Earth Planet. Sci. Lett.* **153**, 223–7.
- Bogard, D. D., Nyquist, L. E., & Johnson, P. (1984). Noble gas contents of shergottites and implications for the Martian origin of SNC meteorites. *Geochim. Cosmochim. Acta* **48**, 1723–39.
- Bolt, B. A. (1993). *Earthquakes*. W. H. Freeman & Co., New York, 331 pp.
- Bonneville, A., Von Herzen, R. P., & Lucaleau, F. (1997). Heat flow over Reunion hot spot track: Additional evidence for thermal rejuvenation of oceanic lithosphere. *J. Geophys. Res.* **102**, 22731–47.
- Booker, J. R. (1976). Thermal convection with strongly temperature-dependent viscosity. *J. Fluid Mech.* **76**, 741–54.
- Booker, J. R. & Stengel, K. C. (1978). Further thoughts on convective heat transport in a variable-viscosity fluid. *J. Fluid Mech.* **86**, 289–91.
- Bottinga, Y. & Allègre, C. J. (1978). Partial melting under spreading ridges. *Phil. Trans. Roy. Soc. London A* **228**, 501–25.
- Boudier, F. (1978). Structure and petrology of the Lanzo peridotite massif (Piedmont Alps). *Geol. Soc. Am. Bull.* **89**, 1574–91.
- Bougault, H., Joron, J. L., & Treuil, M. (1980). The primordial chondritic nature and large-scale heterogeneities in the mantle: Evidence from high and low partition coefficient elements in oceanic basalts. *Phil. Trans. Roy. Soc. London A* **297**, 203–13.
- Boyd, F. R. (1973). A pyroxene geotherm. *Geochim. Cosmochim. Acta* **37**, 2533–46.
- (1989). Compositional distinction between oceanic and cratonic lithosphere. *Earth Planet. Sci. Lett.* **96**, 15–26.
- Boyd, F. R. & Meyer, H. O. A., editors (1979). *The Mantle Sample: Inclusions in Kimberlites and Other Volcanics*. American Geophysical Union, Washington, DC, 424 pp.
- Boyd, F. R., Gurney, J. J., & Richardson, S. H. (1985). Evidence for a 150–200-km thick Archaean lithosphere from diamond inclusion thermobarometry. *Nature* **315**, 387–9.
- Braginsky, S. I. (1963). Structure of the F layer and reasons for convection in the Earth's core. *Doklady Akad. Nauk. SSSR* **149**, 1311–4. Translation published by American Geological Institute, ibid. pp. 8–10.
- Braginsky, S. I. & Roberts, P. H. (1995). Equations governing convection in Earth's core and the geodynamo. *Geophys. Astrophys. Fluid Dyn.* **79**, 1–97.

- Bratt, S. R., Solomon, S. C., Head, J. W., & Thurber, C. H. (1985). The deep structure of lunar basins: Implications for basin formation and modification. *J. Geophys. Res.* **90**, 3049–64.
- Breuer, D. & Spohn, T. (1995). Possible flush instability in mantle convection at the Archaean-Proterozoic transition. *Nature* **378**, 608–10.
- Breuer, D., Zhou, H., Yuen, D. A., & Spohn, T. (1996). Phase transitions in the Martian mantle: Implications for the planet's volcanic history. *J. Geophys. Res.* **101**, 7531–42.
- Breuer, D., Yuen, D. A., & Spohn, T. (1997). Phase transitions in the Martian mantle: Implications for partially layered convection. *Earth Planet. Sci. Lett.* **148**, 457–69.
- Breuer, D., Yuen, D. A., Spohn, T., & Zhang, S. (1998). Three dimensional models of Martian mantle convection with phase transitions. *Geophys. Res. Lett.* **25**, 229–32.
- Brown, G. C. (1977). Mantle origin of Cordilleran granites. *Nature* **265**, 21–4.
- (1979). The changing pattern of batholith emplacement during Earth history. In *Origin of Granite Batholiths: Geochemical Evidence*, pp. 106–15, eds. M. P. Atherton & J. Tarney. Shiva Publishing Limited, Nantwich, U.K.
- Brown, J. M. & Shankland, T. J. (1981). Thermodynamic parameters in the Earth as determined from seismic profiles. *Geophys. J. Roy. Astron. Soc.* **66**, 579–96.
- Brown, L. D. (1991). A new map of crustal 'terranes' in the United States from COCORP deep seismic reflection profiling. *Geophys. J. Int.* **105**, 3–13.
- Brown, S. C. (1957). Count Rumford discovers thermal convection. *Daedalus* **86**, 340–3.
- Bruce, P. M. & Huppert, H. E. (1989). Thermal control of basaltic fissure eruptions. *Nature* **342**, 665–7.
- Brunet, D. & Machetel, P. (1998). Large-scale tectonic features induced by mantle avalanches with phase, temperature, and pressure lateral variations of viscosity. *J. Geophys. Res.* **103**, 4929–45.
- Brush, S. G. (1986). Early history of selenogony. In *Origin of the Moon*, pp. 3–15, eds. W. K. Hartmann, R. J. Phillips, & G. J. Taylor. Lunar and Planetary Institute, Houston, Texas.
- Buck, W. R. (1985). When does small-scale convection begin beneath oceanic lithosphere? *Nature* **313**, 775–7.
- (1992). Global decoupling of crust and mantle: Implications for topography, geoid and mantle viscosity on Venus. *Geophys. Res. Lett.* **19**, 2111–4.
- Buck, W. R. & Parmentier, E. M. (1986). Convection beneath young oceanic lithosphere: Implications for thermal structure and gravity. *J. Geophys. Res.* **91**, 1961–74.
- Buck, W. R. & Su, W. (1989). Focused mantle upwelling below mid-ocean ridges due to feedback between viscosity and melting. *Geophys. Res. Lett.* **16**, 641–4.
- Buffett, B. A. & Glatzmaier, G. A. (2000). Gravitational braking of inner-core rotation in geodynamo simulations. *Geophys. Res. Lett.* **27**, 3125–8.
- Buffett, B. A., Huppert, H. E., Lister, J. R., & Woods, A. W. (1996). On the thermal evolution of the Earth's core. *J. Geophys. Res.* **101**, 7989–8006.
- Bühler, F., Axford, W. I., Chivers, H. J. A., & Marti, K. (1976). Helium isotopes in an aurora. *J. Geophys. Res.* **81**, 111–5.
- Bull, A. J. (1921). A hypothesis of mountain building. *Geol. Mag.* **58**, 364–7.
- (1931). The convection current hypothesis of mountain building. *Geol. Mag.* **68**, 495–8.
- Bullard, E. C. (1954). The flow of heat through the floor of the Atlantic Ocean. *Proc. Roy. Soc. London A* **222**, 408–29.
- Bullard, E. C., Maxwell, A. E., & Revelle, R. (1956). Heat flow through the deep sea floor. In *Advances in Geophysics*, pp. 153–81, ed. H. E. Landsberg, volume 3. Academic Press, New York.
- Bullard, E., Everett, J. E., & Smith, A. G. (1965). The fit of continents around the Atlantic. *Phil. Trans. Roy. Soc. London A* **258**, 41–51.
- Bullen, K. E. (1936). The variation in density and the ellipticities of strata of equal density within the Earth. *Mon. Not. Roy. Astron. Soc., Geophys. Suppl.* **3**, 395–401.
- (1940). The problem of the Earth's density variation. *Seismol. Soc. Am. Bull.* **30**, 235–50.
- (1946). A hypothesis on compressibility at pressures of the order of a million atmospheres. *Nature* **157**, 405.
- Bullock, M. A., Grinspoon, D. H., & Head, J. W. (1993). Venus resurfacing rates: Constraints provided by 3-D Monte Carlo simulations. *Geophys. Res. Lett.* **20**, 2147–50.

- Bunge, H.-P. & Richards, M. A. (1996). The origin of large scale structure in mantle convection: Effects of plate motions and viscosity stratification. *Geophys. Res. Lett.* **23**, 2987–90.
- Bunge, H.-P., Richards, M. A., & Baumgardner, J. R. (1996). Effect of depth-dependent viscosity on the planform of mantle convection. *Nature* **379**, 436–8.
- (1997). A sensitivity study of three-dimensional spherical mantle convection at 10^8 Rayleigh number: Effects of depth-dependent viscosity, heating mode, and an endothermic phase change. *J. Geophys. Res.* **102**, 11991–2007.
- Burchfiel, B. C. (1983). The continental crust. *Sci. Am.* **249**, 130–42.
- Burchfield, J. D., editor (1975). *Lord Kelvin and the Age of the Earth*. Sci. Hist. Pub., New York, 260 pp.
- Burke, K. (1977). Aulacogens and continental breakup. *Ann. Rev. Earth Planet. Sci.* **5**, 371–96.
- Burke, K. & Dewey, J. F. (1973). Plume-generated triple junctions: Key indicators in applying plate tectonics to old rocks. *J. Geol.* **81**, 406–33.
- Burke, K., Dewey, J. F., & Kidd, W. S. F. (1977). World distribution of sutures – the sites of former oceans. *Tectonophysics* **40**, 69–99.
- Burns, J. A. (1986). The evolution of satellite orbits. In *Satellites*, pp. 117–58, eds. J. A. Burns & M. S. Matthews. The University of Arizona Press, Tucson.
- Busse, F. H. (1967). On the stability of two-dimensional convection in a layer heated from below. *J. Math. Phys.* **46**, 140–50.
- (1975). Patterns of convection in spherical shells. *J. Fluid Mech.* **72**, 67–85.
- (1978). Non-linear properties of thermal convection. *Rep. Prog. Phys.* **41**, 1929–67.
- (1981). On the aspect ratios of two-layer mantle convection. *Phys. Earth Planet. Int.* **24**, 320–4.
- (1989). Fundamentals of thermal convection. In *Mantle Convection: Plate Tectonics and Global Dynamics*, pp. 23–95, ed. W. R. Peltier, volume 4 of *The Fluid Mechanics of Astrophysics and Geophysics*. Gordon and Breach Science Publishers, New York.
- Busse, F. H. & Riahi, N. (1982). Patterns of convection in spherical shells. Part 2. *J. Fluid Mech.* **123**, 283–301.
- Busse, F. H. & Schubert, G. (1971). Convection in a fluid with two phases. *J. Fluid Mech.* **46**, 801–12.
- Busse, F. H., Christensen, U., Clever, R., Cserepes, L., Gable, C., Giannandrea, E., Guillou, L., Houseman, G., Nataf, H.-C., Ogawa, M., Parmentier, M., Sotin, C., & Travis, B. (1994). 3D convection at infinite Prandtl number in cartesian geometry – A benchmark comparison. *Geophys. Astrophys. Fluid Dyn.* **75**, 39–59.
- Butler, R. W. H. (1986). Thrust tectonics, deep structure and crustal subduction in the Alps and Himalayas. *J. Geol. Soc. London* **143**, 857–73.
- Byerly, P. (1926). The Montana earthquake of June 28, 1925, GMCT. *Seismol. Soc. Am. Bull.* **16**, 209–65.
- Čadek, O. & Ricard, Y. (1992). Toroidal/poloidal energy partitioning and global lithospheric rotation during Cenozoic time. *Earth Planet. Sci. Lett.* **109**, 621–32.
- Caldwell, J. G., Haxby, W. F., Karig, D. E., & Turcotte, D. L. (1976). On the applicability of a universal elastic trench profile. *Earth Planet. Sci. Lett.* **31**, 239–46.
- Calvert, A. J. (1995). Seismic evidence for a magma chamber beneath the slow-spreading Mid-Atlantic Ridge. *Nature* **377**, 410–14.
- Cameron, A. G. W. (1984). Formation of the prelunar accretion disk (abstract). In *Papers Presented to the Conference on the Origin of the Moon*, p. 58. Lunar and Planetary Institute, Houston, Texas.
- (1986). The impact theory for origin of the Moon. In *Origin of the Moon*, pp. 609–16, eds. W. K. Hartmann, R. J. Phillips, & G. J. Taylor. Lunar and Planetary Institute, Houston, Texas.
- Cameron, A. G. W. & Ward, W. R. (1976). The origin of the Moon (abstract). In *Lunar and Planetary Science VII*, pp. 120–2. Lunar and Planetary Institute, Houston, Texas.
- Cameron, A. G. W., Fegley, B., Benz, W., & Slattery, W. L. (1988). The strange density of Mercury: Theoretical considerations. In *Mercury*, pp. 692–708, eds. F. Vilas, C. R. Chapman, & M. S. Matthews. The University of Arizona Press, Tucson.
- Campbell, I. H. & Griffiths, R. W. (1990). Implications of mantle plume structure for the evolution of flood basalts. *Earth Planet. Sci. Lett.* **99**, 79–93.
- Campbell, I. H. & Taylor, S. R. (1983). No water, no granites – no oceans, no continents. *Geophys. Res. Lett.* **10**, 1061–4.

- Campbell, I. H., Griffiths, R. W., & Hill, R. I. (1989). Melting in an Archaean mantle plume: Heads it's basalts, tails it's komatiites. *Nature* **339**, 697–9.
- Cann, J. R. (1974). A model for oceanic crustal structure developed. *Geophys. J. Roy. Astron. Soc.* **39**, 169–87.
- Cardin, P. & Olson, P. (1992). An experimental approach to thermochemical convection in the Earth's core. *Geophys. Res. Lett.* **19**, 1995–8.
- Carey, S. W. (1955). Wegener's South America–Africa assembly, fit or misfit? *Geol. Mag.* **92**, 196–200.
- (1958). The tectonic approach to continental drift. In *Continental Drift, A Symposium*, pp. 177–355, ed. S. W. Carey, University of Tasmania, Hobart, Tasmania.
- (1976). *The Expanding Earth: A Symposium*. Elsevier Scientific Pub. Co., Amsterdam, 488 pp.
- Carr, M. H. (1974). Tectonism and volcanism of the Tharsis region of Mars. *J. Geophys. Res.* **79**, 3943–9.
- (1976). Change in height of Martian volcanoes with time. *Geol. Rom.* **15**, 421–2.
- (1986). Silicate volcanism on Io. *J. Geophys. Res.* **91**, 3521–32.
- (1987). Water on Mars. *Nature* **326**, 30–5.
- (1996a). *Water on Mars*. Oxford University Press, New York, 229 pp.
- (1996b). Channels and valleys on Mars: Cold climate features formed as a result of a thickening cryosphere. *Planet. Space Sci.* **44**, 1411–23.
- Carr, M. H., McEwen, A. S., Howard, K. A., Chuang, F. C., Thomas, P., Schuster, P., Oberst, J., Neukum, G., Schubert, G., & the Galileo Imaging Team (1998a). Mountains and calderas on Io: Possible implications for lithosphere structure and magma generation. *Icarus* **135**, 146–65.
- Carr, M. H., Belton, M. J. S., Chapman, C. R., Davies, M. E., Geissler, P., Greenberg, R., McEwen, A. S., Tufts, B. R., Greeley, R., Sullivan, R., Head, J. W., Pappalardo, R. T., Klaasen, K., Johnson, T. V., Kaufman, J., Senske, D., Moore, J., Neukum, G., Schubert, G., Burns, J. A., Thomas, P., & Everka, J. (1998b). Evidence for a subsurface ocean on Europa. *Nature* **391**, 363–5.
- Carrigan, C. R. (1982). Multiple-scale convection in the Earth's mantle: A three-dimensional study. *Science* **215**, 965–7.
- (1985). Convection in an internally heated, high Prandtl number fluid: A laboratory study. *Geophys. Astrophys. Fluid Dyn.* **32**, 1–21.
- Carrigan, C. R. & Eichelberger, J. C. (1990). Zoning of magmas by viscosity in volcanic conduits. *Nature* **343**, 248–51.
- Carrigan, C. R., Schubert, G., & Eichelberger, J. C. (1992). Thermal and dynamical regimes of single- and two-phase magmatic flow in dikes. *J. Geophys. Res.* **97**, 17377–92.
- Carslaw, H. S. & Jaeger, J. C. (1984). *Conduction of Heat in Solids*. Clarendon Press, Oxford, 2nd edition, 510 pp.
- Carter, N. L. (1976). Steady state flow of rocks. *Rev. Geophys. Space Phys.* **14**, 301–60.
- Casey, J. F. & Dewey, J. F. (1984). Initiation of subduction zones along transform and accreting plate boundaries, triple-junction evolution, and forearcspreading centres – Implications for ophiolitic geology and obduction. In *Ophiolites and Oceanic Lithosphere*, pp. 269–90, eds. I. G. Gass, S. J. Lippard, & A. W. Shelton, volume 13. Geol. Soc. Special Publ., London.
- Cassen, P. & Reynolds, R. T. (1973). Role of convection in the Moon. *J. Geophys. Res.* **78**, 3203–15.
- (1974). Convection in the Moon: Effect of variable viscosity. *J. Geophys. Res.* **79**, 2937–44.
- Cassen, P., Young, R. E., Schubert, G., & Reynolds, R. T. (1976). Implications of an internal dynamo for the thermal history of Mercury. *Icarus* **28**, 501–8.
- Cassen, P., Reynolds, R. T., Graziani, F., Summers, A., McEllis, J., & Blalock, L. (1979). Convection and lunar thermal history. *Phys. Earth Planet. Int.* **19**, 183–96.
- Cassen, P. M., Peale, S. J., & Reynolds, R. T. (1982). Structure and thermal evolution of the Galilean satellites. In *Satellites of Jupiter*, pp. 93–128, ed. D. Morrison. The University of Arizona Press, Tucson.
- Castillo, P. (1988). The Dupal anomaly as a trace of the upwelling lower mantle. *Nature* **336**, 667–70.
- Castle, J. C. & Creager, K. C. (1997). Seismic evidence against a mantle chemical discontinuity near 660 km depth beneath Izu-Bonin. *Geophys. Res. Lett.* **24**, 241–4.
- (1998). Topography of the 660-km seismic discontinuity beneath Izu-Bonin: Implications for tectonic history and slab deformation. *J. Geophys. Res.* **103**, 12511–27.

- Cathles, L. M. (1975). *The Viscosity of the Earth's Mantle*. Princeton University Press, Princeton, New Jersey, 386 pp.
- (1980). Interpretation of postglacial isostatic adjustment phenomena in terms of mantle rheology. In *Earth Rheology, Isostasy and Eustasy*, pp. 11–43, ed. N.-A. Mörner. John Wiley & Sons, Chichester.
- Cazenave, A. (1984). Thermal cooling of the oceanic lithosphere: New constraints from geoid height data. *Earth Planet. Sci. Lett.* **70**, 395–406.
- Cazenave, A., Lago, B., & Dominh, K. (1983). Thermal parameters of the oceanic lithosphere estimated from geoid height data. *J. Geophys. Res.* **88**, 1105–18.
- Cazenave, A., Parsons, B., & Calcagno, P. (1995). Geoid lineations of 1000 km wavelength over the Central Pacific. *Geophys. Res. Lett.* **22**, 97–100.
- Chandrasekhar, S. (1952). The thermal instability of a fluid sphere heated within. *Phil. Mag. Ser. 7* **43**, 1317–29.
- (1953). The onset of convection by thermal instability in spherical shells. *Phil. Mag. Ser. 7* **44**, 233–41; also, The onset of convection by thermal instability in spherical shells – (A correction), *ibid*, 1129–30.
- (1961). *Hydrodynamic and Hydromagnetic Stability*. International Series of Monographs on Physics. Oxford University Press, London, 654 pp.
- Chase, C. G. (1978). Extension behind island arcs and motions relative to hot spots. *J. Geophys. Res.* **83**, 5385–7.
- (1979a). Subduction, the geoid, and lower mantle convection. *Nature* **282**, 464–8.
- (1979b). Asthenospheric counterflow: A kinematic model. *Geophys. J. Roy. Astron. Soc.* **56**, 1–18.
- (1981). Oceanic island Pb: Two-stage histories and mantle evolution. *Earth Planet. Sci. Lett.* **52**, 277–84.
- Chen, G. Q. & Ahrens, T. J. (1996). High-pressure melting of iron: New experiments and calculations. *Phil. Trans. Roy. Soc. London A* **354**, 1251–63.
- Chen, J. H. & Wasserburg, G. J. (1986). Formation ages and evolution of Shergotty and its parent planet from U–Th–Pb systematics. *Geochim. Cosmochim. Acta* **50**, 955–68.
- Chicarro, A. F., Schultz, P. H., & Masson, P. (1985). Global and regional ridge patterns on Mars. *Icarus* **63**, 153–74.
- Chopelas, A. & Boehler, R. (1989). Thermal expansion measurements at very high pressure, systematics, and a case for a chemically homogeneous mantle. *Geophys. Res. Lett.* **16**, 1347–50.
- (1992). Thermal expansivity in the lower mantle. *Geophys. Res. Lett.* **19**, 1983–6.
- Chopelas, A., Boehler, R., & Ko, T. (1994). Thermodynamics and behavior of γ -Mg₂SiO₄ at high pressure – Implications for Mg₂SiO₄ phase-equilibrium. *Phys. Chem. Miner.* **21**, 351–9.
- Chopra, P. N. & Paterson, M. S. (1984). The role of water in the deformation of dunite. *J. Geophys. Res.* **89**, 7861–76.
- Christensen, N. I. & Salisbury, M. H. (1979). Seismic anisotropy in the oceanic upper mantle: Evidence from the Bay of Islands ophiolite complex. *J. Geophys. Res.* **84**, 4601–10.
- Christensen, U. (1981). Numerical experiments on convection in a chemically layered mantle. *J. Geophys. Res.* **49**, 82–4.
- (1983a). Convection in a variable-viscosity fluid: Newtonian versus power-law rheology. *Earth Planet. Sci. Lett.* **64**, 153–62.
- (1983b). A numerical model of coupled subcontinental and oceanic convection. *Tectonophysics* **95**, 1–23.
- (1984a). Convection with pressure- and temperature-dependent non-Newtonian rheology. *Geophys. J. Roy. Astron. Soc.* **77**, 343–84.
- (1984b). Instability of a hot boundary layer and initiation of thermo-chemical plumes. *Ann. Geophysicae* **2**, 311–20.
- Christensen, U. R. (1984c). Heat transport by variable viscosity convection and implications for the Earth's thermal evolution. *Phys. Earth Planet. Int.* **35**, 264–82.
- (1985a). Heat transport by variable viscosity convection II: Pressure influence, non-Newtonian rheology and decaying heat sources. *Phys. Earth Planet. Int.* **37**, 183–205.
- (1985b). Thermal evolution models for the Earth. *J. Geophys. Res.* **90**, 2995–3007.

- Christensen, U. R. (1987). Time-dependent convection in elongated Rayleigh-Benard cells. *Geophys. Res. Lett.* **14**, 220–3.
- (1989a). Mantle rheology, constitution and convection. In *Mantle Convection: Plate Tectonics and Global Dynamics*, pp. 595–655, ed. W. R. Peltier, volume 4 of *The Fluid Mechanics of Astrophysics and Geophysics*. Gordon and Breach Science Publishers, New York.
- Christensen, U. (1989b). Mixing by time-dependent convection (in mantle). *Earth Planet. Sci. Lett.* **95**, 382–94.
- Christensen, U. R. (1989c). The heat transport by convection rolls with free boundaries at high Rayleigh number. *Geophys. Astrophys. Fluid Dyn.* **46**, 93–103.
- Christensen, U. (1995). Effects of phase transitions on mantle convection. *Ann. Rev. Earth Planet. Sci.* **23**, 65–87.
- Christensen, U. R. (1996). The influence of trench migration on slab penetration into the lower mantle. *Earth Planet. Sci. Lett.* **140**, 27–39.
- (1997). Influence of chemical buoyancy on the dynamics of slabs in the transition zone. *J. Geophys. Res.* **102**, 22435–43.
- Christensen, U. & Harder, H. (1991). 3-D convection with variable viscosity. *Geophys. J. Int.* **104**, 213–26.
- Christensen, U. R. & Hofmann, A. W. (1994). Segregation of subducted oceanic crust in the convecting mantle. *J. Geophys. Res.* **99**, 19867–84.
- Christensen, U. R. & Yuen, D. A. (1984). The interaction of a subducting lithospheric slab with a chemical or phase boundary. *J. Geophys. Res.* **89**, 4389–402.
- (1985). Layered convection induced by phase transitions. *J. Geophys. Res.* **90**, 10291–300.
- (1989). Time-dependent convection with non-Newtonian viscosity. *J. Geophys. Res.* **94**, 814–20.
- Clark, S. P., editor (1966). *Handbook of Physical Constants*. Geol. Soc. America Mem. 97. Geol. Soc. America, revised edition.
- Clauser, C. & Huenges, E. (1995). Thermal conductivity of rocks and minerals. In *Rock Physics and Phase Relations: A Handbook of Physical Constants*, pp. 105–26, ed. T. J. Ahrens. American Geophysical Union, Washington, DC.
- Clayton, R. W. & Comer, R. P. (1983). A tomographic analysis of mantle heterogeneities from body wave travel times. *EOS Trans. AGU* **64**, 776.
- Clemens, J. D. (1998). Observations on the origins and ascent mechanisms of granitic magmas. *J. Geol. Soc. London* **155**, 843–51.
- Clever, R. M. (1977). Heat transfer and stability properties of convection rolls in an internally heated fluid layer. *Zeitschrift für Angewandte Mathematik und Physik* **28**, 585–97.
- Cloetingh, S. A. P. L., Wortel, M. J. R., & Vlaar, N. J. (1984). Passive margin evolution, initiation of subduction and the Wilson cycle. *Tectonophysics* **109**, 147–63.
- Cloetingh, S., Wortel, R., & Vlaar, N. J. (1989). On the initiation of subduction zones. *Pure Appl. Geophys.* **129**, 7–25.
- Coleman, P. J., Lichtenstein, B. R., Russell, C. T., Sharp, L. R., & Schubert, G. (1972). Magnetic fields near the moon. *Proc. Lunar Sci. Conf. 3rd*, 2271–86.
- Colin, P. & Fleitout, L. (1990). Topography of the ocean floor: Thermal evolution of the lithosphere and interaction of deep mantle heterogeneities with the lithosphere. *Geophys. Res. Lett.* **17**, 1961–4.
- Collerson, K. D. & Kamber, B. S. (1999). Evolution of the continents and the atmosphere inferred from Th–U–Nb systematics of the depleted mantle. *Science* **283**, 1519–22.
- Collette, B. J. (1974). Thermal contraction joints in a spreading seafloor as origin of fracture zones. *Nature* **251**, 299–300.
- Comer, R. P., Solomon, S. C., & Head, J. W. (1985). Mars: Thickness of the lithosphere from the tectonic response to volcanic loads. *Rev. Geophys.* **23**, 61–92.
- Comte, D., Dorbath, L., Pardo, M., Monfret, T., Haessler, H., Rivera, L., Frogneux, M., Glass, B., & Meneses, C. (1999). A double-layered seismic zone in Arica, northern Chile. *Geophys. Res. Lett.* **26**, 1965–8.
- Condie, K. C. (1998). Episodic continental growth and supercontinents: A mantle avalanche connection? *Earth Planet. Sci. Lett.* **163**, 97–108.

- Connerney, J. E. P. & Ness, N. F. (1988). Mercury's magnetic field and interior. In *Mercury*, pp. 494–513, eds. F. Vilas, C. R. Chapman, & M. S. Matthews. The University of Arizona Press, Tucson.
- Connerney, J. E. P., Acuña, M. H., Wasilewski, P. J., Ness, N. F., Rème, H., Mazelle, C., Vignes, D., Lin, R. P., Mitchell, D. L., & Cloutier, P. A. (1999). Magnetic lineations in the ancient crust of Mars. *Science* **284**, 794–8.
- Consolmagno, G. J. (1981). Io: Thermal models and chemical evolution. *Icarus* **47**, 36–45.
- Cook, F. A. & Turcotte, D. L. (1981). Parameterized convection and the thermal evolution of the Earth. *Tectonophysics* **75**, 1–17.
- Cook, F. A., Albaugh, D. S., Brown, L. D., Kaufman, S., Oliver, J. E., & Hatcher, R. D. (1979). Thin-skinned tectonics in the crystalline southern Appalachians: COCORP seismic-reflection profiling of the Blue Ridge and Piedmont. *Geology* **7**, 563–7.
- Cormier, V. F. & Richards, P. G. (1976). Comments on 'The damping of core waves' by Anthony Qamar and Alfredo Eisenberg. *J. Geophys. Res.* **81**, 3066–8.
- Corriu, V., Ricard, Y., & Froidevaux, C. (1994). Converting mantle tomography into mass anomalies to predict the Earth's radial viscosity. *Phys. Earth Planet. Int.* **84**, 3–13.
- Couillette, D. L. & Loper, D. E. (1995). Experimental, numerical and analytical models of mantle starting plumes. *Phys. Earth Planet. Int.* **92**, 143–67.
- Courtillot, V. (1994). Mass extinctions in the last 300 million years; One impact and seven flood basalts? *Israel J. Earth Sci.* **43**, 255–66.
- (1995). *La Vie en Catastrophes*. Fayard, Paris, 278 pp.
- Courtillot, V., Jaeger, J.-J., Yang, Z., Féraud, G., & Hofmann, C. (1996). The influence of continental flood basalts on mass extinctions: Where do we stand? In *The Cretaceous-Tertiary Event and Other Catastrophes in Earth History*, pp. 513–25, eds. G. Ryder, D. Fastovsky, & S. Gartner, Geol. Soc. Am. Spec. Pap. 307. The Geological Society of America, Boulder, CO.
- Cox, A., Doell, R. R., & Dalrymple, G. B. (1963). Geomagnetic polarity epochs and Pleistocene geochronometry. *Nature* **198**, 1049–51.
- (1964). Reversals of the Earth's magnetic field. *Science* **144**, 1537–43.
- Cox, J. P. & Giuli, R. T. (1968). *Principles of Stellar Structure*, volume 2. Applications to Stars. Gordon and Breach, Science Publishers, New York, 1327 pp.
- Craig, H. & Lupton, J. E. (1981). Helium-3 and mantle volatiles in the ocean and the oceanic crust. In *The Oceanic Lithosphere*, pp. 391–428, ed. C. Emiliani, volume 7. J. Wiley and Sons, New York.
- Craig, H., Clarke, W. B., & Beg, M. A. (1975). Excess ^3He in deep water on the East Pacific Rise. *Earth Planet. Sci. Lett.* **26**, 125–32.
- Creager, K. C. (1992). Anisotropy of the inner core from differential travel times of the phases PKP and PKIKP. *Nature* **356**, 309–14.
- Creager, K. C. & Jordan, T. H. (1984). Slab penetration into the lower mantle. *J. Geophys. Res.* **89**, 3031–49.
- (1986a). Slab penetration into the lower mantle beneath the Mariana and other island arcs of the northwest Pacific. *J. Geophys. Res.* **91**, 3573–89.
- (1986b). Aspherical structure of the core–mantle boundary from PKP travel times. *Geophys. Res. Lett.* **13**, 1497–500.
- Crittenden, M. D. (1963). Effective viscosity of the Earth derived from isostatic loading of Pleistocene Lake Bonneville. *J. Geophys. Res.* **68**, 5517–30.
- Crough, S. T. (1978). Thermal origin of mid-plate hot-spot swells. *Geophys. J. Roy. Astron. Soc.* **55**, 451–69.
- (1983). Hotspot swells. *Ann. Rev. Earth Planet. Sci.* **11**, 165–93.
- Crough, S. T. & Jurdy, D. M. (1980). Subducted lithosphere, hotspots and the geoid. *Earth Planet. Sci. Lett.* **48**, 15–22.
- Crough, S. T., Morgan, W. J., & Hargraves, R. B. (1980). Kimberlites: Their relation to mantle hotspots. *Earth Planet. Sci. Lett.* **50**, 260–74.
- Crumpler, L. S., Aubele, J. C., Senske, D. A., Keddie, S. T., Magee, K. P., & Head, J. W. (1997). Volcanoes and centers of volcanism on Venus. In *Venus II: Geology, Geophysics, Atmosphere, and*

- Solar Wind Environment*, pp. 697–756, eds. S. W. Bougher, D. M. Hunten, & R. J. Phillips. The University of Arizona Press, Tucson.
- Cserepes, L. (1982). Numerical studies of non-Newtonian mantle convection. *Phys. Earth Planet. Int.* **30**, 49–61.
- Cserepes, L. & Christensen, U. (1990). Three-dimensional convection under drifting plates. *Geophys. Res. Lett.* **17**, 1497–500.
- Cserepes, L. & Rabinowicz, M. (1985). Gravity and convection in a two-layer mantle. *Earth Planet. Sci. Lett.* **76**, 193–207.
- Cserepes, L. & Yuen, D. A. (1997). Dynamical consequences of mid-mantle viscosity stratification on mantle flows with an endothermic phase transition. *Geophys. Res. Lett.* **24**, 181–4.
- Cserepes, L., Rabinowicz, M., & Rosemburg-Borot, C. (1988). Three-dimensional infinite Prandtl number convection in one and two layers with implications for the Earth's gravity field. *J. Geophys. Res.* **93**, 12009–25.
- Cumming, G. L. & Richards, J. R. (1975). Ore lead isotope ratios in a continuously changing Earth. *Earth Planet. Sci. Lett.* **28**, 155–71.
- Daessler, R. & Yuen, D. A. (1996). The metastable olivine wedge in fast subducting slabs: Constraints from thermo-kinetic coupling. *Earth Planet. Sci. Lett.* **137**, 109–18.
- D'Agostino, G., Spada, G., & Sabadini, R. (1997). Postglacial rebound and lateral viscosity variations: A semi-analytical approach based on a spherical model with Maxwell rheology. *Geophys. J. Int.* **129**, F9–F13.
- Daines, M. J. & Kohlstedt, D. L. (1994). The transition from porous to channelized flow due to melt/rock reaction during melt migration. *Geophys. Res. Lett.* **21**, 145–8.
- Daines, M. J. & Richter, F. M. (1988). An experimental method for directly determining the interconnectivity of melt in a partially molten system. *Geophys. Res. Lett.* **15**, 1459–62.
- Daly, R. A. (1934). *The Changing World of the Ice Age*. Yale University Press, New Haven, 271 pp.
- Daly, S. F. (1980). The vagaries of variable viscosity convection. *Geophys. Res. Lett.* **7**, 841–4.
- Daniels, L. R. M., Gurney, J. J., & Harte, B. (1996). A crustal mineral in a mantle diamond. *Nature* **379**, 153–6.
- Darwin, G. H. (1898). *The Tides and Kindred Phenomena in the Solar System*. Houghton Mifflin and Company, Boston and New York, 378 pp.; see also same title, W. H. Freeman and Co., 1962.
- Davaille, A. & Jaupart, C. (1993). Transient high-Rayleigh-number thermal convection with large viscosity variations. *J. Fluid Mech.* **253**, 141–66.
- (1994). Onset of thermal convection in fluids with temperature-dependent viscosity: Application to the oceanic mantle. *J. Geophys. Res.* **99**, 19853–66.
- Davies, A. G. (1996). Io's volcanism: Thermo-physical models of silicate lava compared with observations of thermal emission. *Icarus* **124**, 45–61.
- Davies, G. F. (1980). Thermal histories of convective Earth models and constraints on radiogenic heat production in the Earth. *J. Geophys. Res.* **85**, 2517–30.
- (1984). Geophysical and isotopic constraints on mantle convection: An interim synthesis. *J. Geophys. Res.* **89**, 6017–40.
- (1986). Mantle convection under simulated plates: Effects of heating modes and ridge and trench migration, and implications for the core–mantle boundary, bathymetry, the geoid and Benioff zones. *Geophys. J. Roy. Astron. Soc.* **84**, 153–83.
- (1988a). Role of the lithosphere in mantle convection. *J. Geophys. Res.* **93**, 10451–66.
- (1988b). Ocean bathymetry and mantle convection. 1. Large-scale flow and hotspots. *J. Geophys. Res.* **93**, 10467–80.
- (1989). Mantle convection model with a dynamic plate: Topography, heat flow and gravity anomalies. *Geophys. J. Int.* **98**, 461–4.
- (1990). Heat and mass transport in the early Earth. In *Origin of the Earth*, pp. 175–94, eds. H. E. Newsom & J. H. Jones. Oxford University Press, New York.
- (1992). Temporal variation of the Hawaiian plume flux. *Earth Planet. Sci. Lett.* **113**, 277–86.
- (1993). Cooling the core and mantle by plume and plate flows. *Geophys. J. Int.* **115**, 132–46.
- (1994). Thermomechanical erosion of the lithosphere by mantle plumes. *J. Geophys. Res.* **99**, 15709–22.

- Davies, G. F. (1995a). Penetration of plates and plumes through the mantle transition zone. *Earth Planet. Sci. Lett.* **133**, 507–16.
- (1995b). Punctuated tectonic evolution of the Earth. *Earth Planet. Sci. Lett.* **136**, 363–79.
- Davies, G. F. & Arvidson, R. E. (1981). Martian thermal history, core segregation, and tectonics. *Icarus* **45**, 339–46.
- Davies, G. F. & Dziewonski, A. M. (1975). Homogeneity and constitution of the Earth's lower mantle and outer core. *Phys. Earth Planet. Int.* **10**, 336–43.
- Davies, G. F. & Gurnis, M. (1986). Interaction of mantle dregs with convection: Lateral heterogeneity at the core–mantle boundary. *Geophys. Res. Lett.* **13**, 1517–20.
- Davies, G. F. & Richards, M. A. (1992). Mantle convection. *J. Geol.* **100**, 151–206.
- Davies, J. H. (1999). The role of hydraulic fractures and intermediate-depth earthquakes in generating subduction-zone magmatism. *Nature* **398**, 142–5.
- Davies, J. H. & Stevenson, D. J. (1992). Physical model of source region of subduction zone volcanics. *J. Geophys. Res.* **97**, 2037–70.
- De Bremaecker, J. C. (1977). Is the oceanic lithosphere elastic or viscous? *J. Geophys. Res.* **82**, 2001–4.
- De Bresser, J. H. P., Peach, C. J., Reijss, J. P. J., & Spiers, C. J. (1998). On dynamic recrystallization during solid state flow: Effects of stress and temperature. *Geophys. Res. Lett.* **25**, 3457–60.
- Defant, M. J. & Drummond, M. S. (1990). Derivation of some modern arc magmas by melting of young subducted lithosphere. *Nature* **347**, 662–5.
- (1993). Mount St. Helens: Potential example of the partial melting of the subducted lithosphere in a volcanic arc. *Geology* **21**, 547–50.
- DeFazio, T. L. (1974). Island-arc and underthrust-plate geometry. *Tectonophysics* **23**, 149–54.
- Delaney, P. T. & Pollard, D. D. (1982). Solidification of basaltic magma during flow in a dike. *Am. J. Sci.* **282**, 856–85.
- DeLong, S. E., Fox, P. J., & McDowell, F. W. (1978). Subduction of the Kula Ridge at the Aleutian Trench. *Geol. Soc. Am. Bull.* **89**, 83–95.
- DeLong, S. E., Schwarz, W. M., & Anderson, R. N. (1979). Thermal effects of ridge subduction. *Earth Planet. Sci. Lett.* **44**, 239–46.
- DeMets, C., Gordon, R. G., Argus, D. F., & Stein, S. (1990). Current plate motions. *Geophys. J. Int.* **101**, 425–78.
- (1994). Effect of recent revisions to the geomagnetic reversal time scale on estimates of current plate motions. *Geophys. Res. Lett.* **21**, 2191–4.
- DePaolo, D. J. (1979). Implications of correlated Nd and Sr isotopic variations for the chemical evolution of the crust and mantle. *Earth Planet. Sci. Lett.* **43**, 201–11.
- (1980). Crustal growth and mantle evolution: Inferences from models of element transport and Nd and Sr isotopes. *Geochim. Cosmochim. Acta* **44**, 1185–96.
- (1983). The mean life of continents: Estimates of continent recycling rates from Nd and Hf isotopic data and implications for mantle structure. *Geophys. Res. Lett.* **10**, 705–8.
- (1988). *Neodymium Isotope Geochemistry: An Introduction*. Springer-Verlag, Berlin, 187 pp.
- DePaolo, D. J. & Wasserburg, G. J. (1976). Nd isotopic variations and petrogenetic models. *Geophys. Res. Lett.* **3**, 249–52.
- DePaolo, D. J., Linn, A. M., & Schubert, G. (1991). The continental crust age distribution: Methods of determining mantle separation ages from Sm–Nd isotopic data and application to the southwestern United States. *J. Geophys. Res.* **96**, 2071–88.
- Dermott, S. F. (1984). Rotation and the internal structures of the major planets and their inner satellites. *Phil. Trans. Roy. Soc. London A* **313**, 123–39.
- Detrick, R. S. (1981). An analysis of geoid anomalies across the Mendocino fracture zone: Implications for thermal models of the lithosphere. *J. Geophys. Res.* **86**, 11751–62.
- Detrick, R. S. & Crough, S. T. (1978). Island subsidence, hot spots, and lithospheric thinning. *J. Geophys. Res.* **83**, 1236–44.
- Detrick, R. S., Von Herzen, R. P., Crough, S. T., Epp, D., & Fehn, U. (1981). Heat flow on the Hawaiian Swell and lithospheric reheating. *Nature* **292**, 142–3.

- Detrick, R. S., Von Herzen, R. P., Parsons, B., Sandwell, D., & Dougherty, M. (1986). Heat flow observations of the Bermuda rise and thermal models of midplate swells. *J. Geophys. Res.* **91**, 3701–23.
- Detrick, R. S., Buhl, P., Vera, E., Mutter, J., Orcutt, J., Madsen, J., & Brocher, T. (1987). Multi-channel seismic imaging of a crustal magma chamber along the East Pacific Rise. *Nature* **326**, 35–41.
- Devaux, J. P., Schubert, G., & Anderson, C. (1997). Formation of a metastable olivine wedge in a descending slab. *J. Geophys. Res.* **102**, 24627–37.
- Devoti, R., Fermi, M., Luceri, V., Rutigliano, P., Sciarretta, C., & Bianco, G. (1997). Estimation of low degree geopotential coefficients using slr data. *Ann. Geophysicae, Suppl. I* **15(I)**, C126.
- Dewey, J. F. (1975). Finite plate implications: Some implications for the evolution of rock masses at plate margins. *Am. J. Sci.* **275-A**, 260–84.
(1977). Suture zone complexities: A review. *Tectonophysics* **40**, 53–67.
- Dewey, J. F. & Bird, J. M. (1970). Mountain belts and the new global tectonics. *J. Geophys. Res.* **75**, 2625–47.
- Dewey, J. F. & Windley, B. F. (1981). Growth and differentiation of the continental crust. *Phil. Trans. Roy. Soc. London A* **301**, 189–206.
- Dick, H. J. B. (1989). Abyssal peridotites, very slow spreading ridges and ocean ridge magmatism. In *Magmatism in the Ocean Basins*, pp. 71–105, eds. A. D. Saunders & M. J. Norry, Geological Society Special Publication No. 42. Published for The Geological Society by Blackwell Scientific Publications, Oxford.
- Dicke, R. H. (1969). Average acceleration of the Earth's rotation and the viscosity of the deep mantle. *J. Geophys. Res.* **74**, 5895–902.
- Dickey, J. O., Bender, P. L., Faller, J. E., Newhall, X. X., Ricklefs, R. L., Ries, J. G., Shelus, P. J., Veillet, C., Whipple, A. L., Wiant, J. R., Williams, J. G., & Yoder, C. F. (1994). Lunar laser ranging: A continuing legacy of the Apollo program. *Science* **265**, 482–90.
- Dickin, A. P. (1995). *Radiogenic Isotope Geology*. Cambridge University Press, Cambridge, England, 452 pp.
- Dickinson, W. R. & Luth, W. C. (1971). A model for plate tectonic evolution of mantle layers. *Science* **174**, 400–4.
- Dickman, S. R. (1977). Secular trend of the Earth's rotation pole: Consideration of motion of the latitude observatories. *Geophys. J. Roy. Astron. Soc.* **51**, 229–44.
- Dickson, G. O., Pitman, W. C., & Heirtzler, J. R. (1968). Magnetic anomalies in the South Atlantic and ocean floor spreading. *J. Geophys. Res.* **73**, 2087–100.
- Dietz, R. S. (1961). Continent and ocean basin evolution by spreading of the sea floor. *Nature* **190**, 854–7.
- Doe, B. R. & Zartman, R. E. (1979). Plumbotectonics, the Phanerozoic. In *Geochemistry of Hydrothermal Ore Deposits*, pp. 22–70, ed. H. L. Barnes. J. Wiley, New York, second edition.
- Doin, M.-P. & Fleitout, L. (1996). Thermal evolution of the oceanic lithosphere: An alternative view. *Earth Planet. Sci. Lett.* **142**, 121–36.
- Doin, M.-P., Fleitout, L., & McKenzie, D. (1996). Geoid anomalies and the structure of continental and oceanic lithospheres. *J. Geophys. Res.* **101**, 16119–35.
- Doin, M.-P., Fleitout, L., & Christensen, U. (1997). Mantle convection and stability of depleted and undepleted continental lithosphere. *J. Geophys. Res.* **102**, 2771–87.
- Dolginov, Sh. Sh. (1987). What we have learned about the Martian magnetic field. *Earth Moon and Planets* **37**, 17–52.
- Dolginov, Sh. Sh., Yeroshenko, Ye. G., & Zhuzgov, L. N. (1973). Magnetic field in the very close neighborhood of Mars according to data from the Mars 2 and Mars 3 spacecraft. *J. Geophys. Res.* **78**, 4779–86.
(1976). The magnetic field of Mars according to the data from the Mars 3 and Mars 5. *J. Geophys. Res.* **81**, 3353–62.
- Donahue, T. M. & Russell, C. T. (1997). The Venus atmosphere and ionosphere and their interaction with the solar wind: An overview. In *Venus II: Geology, Geophysics, Atmosphere, and Solar Wind*

- Environment*, pp. 3–31, eds. S. W. Bougher, D. M. Hunten, & R. J. Phillips. The University of Arizona Press, Tucson.
- Doornbos, D. J. (1974). The anelasticity of the inner core. *Geophys. J. Roy. Astron. Soc.* **38**, 397–415.
- Doornbos, D. J. & Hilton, T. (1989). Models of the core–mantle boundary and the travel times of internally reflected core phases. *J. Geophys. Res.* **94**, 15741–51.
- Doornbos, D. J. & Mondt, J. C. (1979). P and S waves diffracted around the core and the velocity structure at the base of the mantle. *Geophys. J. Roy. Astron. Soc.* **57**, 381–95.
- Driscoll, M. L. & Parsons, B. (1988). Cooling of the oceanic lithosphere—evidence from geoid anomalies across the Uditsev and Eltanin fracture zones. *Earth Planet. Sci. Lett.* **88**, 289–307.
- Drummond, M. S. & Defant, M. J. (1990). A model for trondjemite-tonalite-dacite genesis and crustal growth via slab melting: Archean to modern comparisons. *J. Geophys. Res.* **95**, 21503–21.
- Drury, M. J. (1989). The heat flow–heat generation relationship: Implications for the nature of continental crust. *Tectonophysics* **164**, 93–106.
- Drury, M. R. & Fitz Gerald, J. D. (1998). Mantle rheology: Insights from laboratory studies of deformation and phase transition. In *The Earth's Mantle: Composition, Structure, and Evolution*, pp. 503–59, ed. I. Jackson. Cambridge University Press, Cambridge, England.
- Drury, M. R., Vissers, R. L. M., van der Wal, D., & Strating, E. H. H. (1991). Shear localisation in upper mantle peridotites. *Pure Appl. Geophys.* **137**, 439–61.
- du Toit, A. L. (1937). *Our Wandering Continents: An Hypothesis of Continental Drifting*. Oliver and Boyd, Edinburgh, 366 pp.
- Dumoulin, C., Bercovici, D., & Wessel, P. (1998). A continuous plate-tectonic model using geophysical data to estimate plate-margin widths, with a seismicity-based example. *Geophys. J. Int.* **133**, 379–89.
- Duncan, C. C. & Turcotte, D. L. (1994). On the breakup and coalescence of continents. *Geology* **22**, 103–6.
- Duncan, R. A. & Richards, M. A. (1991). Hotspots, mantle plumes, flood basalts, and true polar wander. *Rev. Geophys.* **29**, 31–50.
- Dupeyrat, L., Sotin, C., & Parmentier, E. M. (1995). Thermal and chemical convection in planetary mantles. *J. Geophys. Res.* **100**, 497–520.
- Dupré, B. & Allègre, C. J. (1983). Pb-Sr isotope variation in Indian Ocean basalts and mixing phenomena. *Nature* **303**, 142–6.
- Durham, W. B., Kirby, S. H., & Stern, L. A. (1997). Creep of water ices at planetary conditions: A compilation. *J. Geophys. Res.* **102**, 16293–302.
- Dziewonski, A. M. (1984). Mapping the lower mantle: Determination of lateral heterogeneity in P velocity up to degree and order 6. *J. Geophys. Res.* **89**, 5929–52.
- Dziewonski, A. M. & Anderson, D. L. (1981). Preliminary reference Earth model. *Phys. Earth Planet. Int.* **25**, 297–356.
- Dziewonski, A. M. & Woodhouse, J. H. (1987). Global images of the Earth's interior. *Science* **236**, 37–48.
- Dziewonski, A. M., Hales, A. L., & Lapwood, E. R. (1975). Parametrically simple Earth models consistent with geophysical data. *Phys. Earth Planet. Int.* **10**, 12–48.
- Dziewonski, A. M., Hager, B. H., & O'Connell, R. J. (1977). Large-scale heterogeneities in the lower mantle. *J. Geophys. Res.* **82**, 239–55.
- Eaton, G. P. (1980). Geophysical and geological characteristics of the crust of the Basin and Range Province. In *Continental Tectonics*, pp. 96–113, B. C. Burchfiel, J. E. Oliver and L. T. Silver, Panel Co-Chairmen. Natl. Acad. Sci., Washington, DC.
- Ebinger, C. J. & Sleep, N. H. (1998). Cenozoic magmatism throughout east Africa resulting from impact of a single plume. *Nature* **395**, 788–91.
- Ellsworth, K. & Schubert, G. (1983). Saturn's icy satellites: Thermal and structural models. *Icarus* **54**, 490–510.
- (1988). Numerical models of thermally and mechanically coupled two-layer convection of highly viscous fluids. *Geophys. J.* **93**, 347–63.
- Ellsworth, K., Schubert, G., & Sammis, C. G. (1985). Viscosity profile of the lower mantle. *Geophys. J. Roy. Astron. Soc.* **83**, 199–213.

- Elsasser, W. M., Olson, P., & Marsh, B. D. (1979). The depth of mantle convection. *J. Geophys. Res.* **84**, 147–55.
- Emeran, S. H. & Turcotte, D. L. (1983). Stagnation flow with a temperature-dependent viscosity. *J. Fluid Mech.* **127**, 507–17.
- Emeran, S. H., Turcotte, D. L., & Spence, D. A. (1986). Transport of magma and hydrothermal solutions by laminar and turbulent fluid fracture. *Phys. Earth Planet. Int.* **41**, 249–59.
- Engdahl, E. R. & Gubbins, D. (1987). Simultaneous travel time inversion for earthquake location and subduction zone structure in the central Aleutian Islands. *J. Geophys. Res.* **92**, 13855–62.
- Engdahl, E. R. & Johnson, L. E. (1974). Differential PcP travel times and the radius of the core. *Geophys. J. Roy. Astron. Soc.* **39**, 435–56.
- Engdahl, E. R. & Scholz, C. H. (1977). A double Benioff zone beneath the central Aleutians: An unbending of the lithosphere. *Geophys. Res. Lett.* **4**, 473–6.
- Engdahl, E. R., Flinn, A., & Massé, P. (1974). Differential PKiKP travel times and the radius of the inner core. *Geophys. J. Roy. Astron. Soc.* **39**, 457–63.
- Engdahl, E. R., van der Hilst, R., & Buland, R. (1998). Global teleseismic earthquake relocation with improved travel times and procedures for depth determination. *Seismol. Soc. Am. Bull.* **88**, 722–43.
- Engebretson, D. C., Kelly, K. P., Cashman, H. J., & Richards, M. A. (1992). 180 million years of subduction. *GSA Today* **2**, 93–5.
- England, P. & Houseman, G. (1986). Finite strain calculations of continental deformation. 2. Comparison with the India-Asia collision zone. *J. Geophys. Res.* **91**, 3664–76.
- England, P. C., Oxburgh, E. R., & Richardson, S. W. (1980). Heat refraction and heat production in and around granite plutons in north-east England. *Geophys. J. Roy. Astron. Soc.* **62**, 439–55.
- Erickson, S. G. (1993). Sedimentary loading, lithospheric flexure, and subduction initiation at passive margins. *Geology* **21**, 125–8.
- Erickson, S. G. & Arkani-Hamed, J. (1993). Subduction initiation at passive margins: The Scotian Basin, eastern Canada as a potential example. *Tectonics* **12**, 678–87.
- Esposito, P. B., Sjogren, W. L., Mottinger, N. A., Bills, B. G., & Abbott, E. (1982). Venus gravity: Analysis of Beta Regio. *Icarus* **51**, 448–59.
- Esposito, P. B., Banerdt, W. B., Lindal, G. F., Sjogren, W. L., Slade, M. A., Bills, B. G., Smith, D. E., & Balmino, G. (1992). Gravity and topography. In *Mars*, pp. 209–48, eds. H. H. Kieffer, B. M. Jakosky, C. W. Snyder, & M. S. Matthews. The University of Arizona Press, Tucson and London.
- Estabrook, C. H. & Kind, R. (1996). The nature of the 660-kilometer upper-mantle seismic discontinuity from precursors to the PP phase. *Science* **274**, 1179–82.
- Evans, B. & Kohlstedt, D. L. (1995). Rheology of rocks. In *Rock Physics and Phase Relations: A Handbook of Physical Constants*, pp. 148–65, ed. T. J. Ahrens. American Geophysical Union, Washington, DC.
- Faccenna, C., Giardini, D., Davy, P., & Argentieri, A. (1999). Initiation of subduction at Atlantic-type margins: Insights from laboratory experiments. *J. Geophys. Res.* **104**, 2749–66.
- Farley, K. A. & Neroda, E. (1998). Noble gases in the Earth's mantle. *Ann. Rev. Earth Planet. Sci.* **26**, 189–218.
- Farnetani, C. G. (1997). Excess temperature of mantle plumes: The role of chemical stratification across D''. *Geophys. Res. Lett.* **24**, 1583–6.
- Faure, G. (1986). *Principles of Isotope Geology*. John Wiley, New York, 2nd edition, 589 pp.
- Fegley, B. & Prinn, R. G. (1989). Estimation of the rate of volcanism on Venus from reaction rate measurements. *Nature* **337**, 55–8.
- Fei, Y. (1995). Thermal expansion. In *Mineral Physics and Crystallography: A Handbook of Physical Constants*, pp. 29–44, ed. T. J. Ahrens. American Geophysical Union, Washington, DC.
- Fei, Y., Prewitt, C. T., Mao, H.-K., & Bertka, C. M. (1995). Structure and density of FeS at high pressure and high temperature and the internal structure of Mars. *Science* **268**, 1892–4.
- Feighner, M. A. & Richards, M. A. (1995). The fluid dynamics of plume–ridge and plume–plate interactions: An experimental investigation. *Earth Planet. Sci. Lett.* **129**, 171–82.
- Feighner, M. A., Kellogg, L. H., & Travis, B. J. (1995). Numerical modeling of chemically buoyant mantle plumes at spreading ridges. *Geophys. Res. Lett.* **22**, 715–8.

- Ferrachat, S. & Ricard, Y. (1998). Regular vs. chaotic mantle mixing. *Earth Planet. Sci. Lett.* **155**, 75–86.
- Ferrari, A. J., Sinclair, W. S., Sjogren, W. L., Williams, J. G., & Yoder, C. F. (1980). Geophysical parameters of the Earth–Moon system. *J. Geophys. Res.* **85**, 3939–51.
- Fink, U., Dekkers, N. H., & Larson, H. P. (1973). Infrared spectra of the Galilean satellites of Jupiter. *Astrophys. J.* **179**, L155–L159.
- Finnerty, A. A. & Boyd, F. R. (1987). Thermobarometry for garnet peridotites: Basis for the determination of thermal and compositional structure of the upper mantle. In *Mantle Xenoliths*, pp. 381–402, ed. P. H. Nixon. John Wiley & Sons, Chichester, England.
- Finnerty, A. A., Phillips, R. J., & Banerdt, W. B. (1988). Igneous processes and closed system evolution of the Tharsis region of Mars. *J. Geophys. Res.* **93**, 10225–35.
- Fischer, H. J. & Spohn, T. (1990). Thermal–orbital histories of viscoelastic models of Io (J1). *Icarus* **83**, 39–65.
- Fisher, O. (1881). *Physics of the Earth's Crust*. Macmillan, London, 299 pp.
- Flanagan, M. P. & Shearer, P. M. (1998a). Global mapping of topography on transition zone velocity discontinuities by stacking SS precursors. *J. Geophys. Res.* **103**, 2673–92.
- (1998b). Topography on the 410-km seismic velocity discontinuity near subduction zones from stacking of sS, sP, and pP precursors. *J. Geophys. Res.* **103**, 21165–82.
- (1999). A map of topography on the 410-km discontinuity from PP precursors. *Geophys. Res. Lett.* **26**, 549–52.
- Flasar, F. M. & Birch, F. (1973). Energetics of core formation: A correction. *J. Geophys. Res.* **73**, 6101–3.
- Fleitout, L. & Froidevaux, C. (1980). Thermal and mechanical evolution of shear zones. *J. Struct. Geol.* **2**, 159–64.
- Fleitout, L. & Yuen, D. A. (1984). Secondary convection and the growth of the oceanic lithosphere. *Phys. Earth Planet. Int.* **36**, 181–212.
- Folkner, W. M., Kahn, R. D., Preston, R. A., Yoder, C. F., Standish, E. M., Williams, J. G., Edwards, C. D., Hellings, R. W., Eubanks, T. M., & Bills, B. G. (1997a). Mars dynamics from Earth-based tracking of the Mars Pathfinder lander. *J. Geophys. Res.* **102**, 4057–64.
- Folkner, W. M., Yoder, C. F., Yuan, D. N., Standish, E. M., & Preston, R. A. (1997b). Interior structure and seasonal mass redistribution of Mars from radio tracking of Mars Pathfinder. *Science* **278**, 1749–52.
- Ford, P. G. & Pettengill, G. H. (1992). Venus topography and kilometer-scale slopes. *J. Geophys. Res.* **97**, 13103–14.
- Forni, O., Coradini, A., & Federico, C. (1991). Convection and lithospheric strength in Dione, an icy satellite of Saturn. *Icarus* **94**, 232–45.
- Forsyth, D. W. (1975). The early structural evolution and anisotropy of the oceanic upper mantle. *Geophys. J. Roy. Astron. Soc.* **43**, 103–62.
- (1993). Crustal thickness and the average depth and degree of melting in fractional melting models of passive flow beneath mid-ocean ridges. *J. Geophys. Res.* **98**, 16073–9.
- Forsyth, D. & Uyeda, S. (1975). On the relative importance of the driving forces of plate motion. *Geophys. J. Roy. Astron. Soc.* **43**, 163–200.
- Forte, A. M. & Mitrovica, J. X. (1996). New inferences of mantle viscosity from joint inversion of long-wavelength mantle convection and post-glacial rebound data. *Geophys. Res. Lett.* **23**, 1147–50.
- Forte, A. M., Peltier, W. R., & Dziewonski, A. M. (1991). Inferences of mantle viscosity from tectonic plate velocities. *Geophys. Res. Lett.* **18**, 1747–50.
- Forte, A. M., Dziewonski, A. M., & Woodward, R. L. (1993). Aspherical structure of the mantle, tectonic plate motions, nonhydrostatic geoid, and topography of the core–mantle boundary. In *Dynamics of Earth's Deep Interior and Earth Rotation*, pp. 135–66, eds. J.-L. Le Mouël, D. E. Smylie, & T. Herring, Geophysical Monograph 72, IUGG Volume 12. American Geophysical Union, Washington, DC.
- Fowler, A. C. (1985). Fast thermoviscous convection. *Stud. Appl. Math.* **72**, 189–219.
- (1993). Boundary layer theory and subduction. *J. Geophys. Res.* **98**, 21997–2005.
- Frank, F. C. (1967). Defects in diamonds. In *Science and Technology of Industrial Diamonds*, pp. 119–35, ed. J. Burls, volume 1. Science. Industrial Diamond Information Bureau, London.
- (1968a). Curvature of island arcs. *Nature* **220**, 363.

- Frank, F. C. (1968b). Two-component flow model for convection in the Earth's upper mantle. *Nature* **220**, 350–2.
- Freedman, A. P. & Parsons, B. (1990). Geoid anomalies over two South Atlantic fracture zones. *Earth Planet. Sci. Lett.* **100**, 18–41.
- Freer, R. (1981). Diffusion in silicate minerals and glasses: A data digest and guide to the literature. *Contrib. Mineral. Petrol.* **76**, 440–54.
- Frey, H. (1979). Martian canyons and African rifts: Structural comparisons and implications. *Icarus* **37**, 142–55.
- Frey, H. & Schultz, R. A. (1988). Large impact basins and the mega-impact origin for the crustal dichotomy on Mars. *Geophys. Res. Lett.* **15**, 229–32.
- Frost, C. D. & O'Nions, R. K. (1984). Nd evidence for Proterozoic crustal development in the Belt-Purcell Supergroup. *Nature* **312**, 53–6.
- Frost, H. J. & Ashby, M. F. (1982). *Deformation-Mechanism Maps: The Plasticity and Creep of Metals and Ceramics*. Pergamon Press, Oxford, England, 166 pp.
- Fuchs, K. (1986). Reflections from the subcrustal lithosphere. In *Reflection Seismology: The Continental Crust*, pp. 67–76, eds. M. Barazangi & L. Brown, volume 14 of *Geodynamics Series*. American Geophysical Union, Washington, DC.
- Fujii, N. & Uyeda, S. (1974). Thermal instabilities during flow of magma in volcanic conduits. *J. Geophys. Res.* **79**, 3367–9.
- Fukao, Y. (1977). Upper mantle P structure on the ocean side of the Japan-Kurile Arc. *Geophys. J. Roy. Astron. Soc.* **50**, 621–42.
- Fukao, Y., Obayashi, M., Inoue, H., & Nenbai, M. (1992). Subducting slabs stagnant in the mantle transition zone. *J. Geophys. Res.* **97**, 4809–22.
- Fyfe, W. S. (1978). The evolution of the Earth's crust: Modern plate tectonics to ancient hot spot tectonics? *Chem. Geol.* **23**, 89–114.
- Gable, C. W., O'Connell, R. J., & Travis, B. J. (1991). Convection in three dimensions with surface plates: Generation of toroidal flow. *J. Geophys. Res.* **96**, 8391–405.
- Gaherty, J. B. & Jordan, T. H. (1995). Lehmann discontinuity as the base of an anisotropic layer beneath continents. *Science* **268**, 1468–71.
- Galer, S. J. G. (1991). Interrelationships between continental freeboard, tectonics and mantle temperature. *Earth Planet. Sci. Lett.* **105**, 214–28.
- Galer, S. J. G. & O'Nions, R. K. (1985). Residence time of thorium, uranium and lead in the mantle with implications for mantle convection. *Nature* **316**, 778–82.
- (1986). Magmagenesis and the mapping of chemical and isotopic variations in the mantle. *Chem. Geol.* **56**, 45–61.
- Gao, S., Zhang, B.-R., Jin, Z.-M., Kern, H., Luo, T.-C., & Zhao, Z.-D. (1998). How mafic is the lower continental crust? *Earth Planet. Sci. Lett.* **161**, 101–17.
- Garfunkel, Z., Anderson, C. A., & Schubert, G. (1986). Mantle circulation and the lateral migration of subducted slabs. *J. Geophys. Res.* **91**, 7205–23.
- Garnero, E. J. & Helmberger, D. V. (1995). On seismic resolution of lateral heterogeneity in the Earth's outermost core. *Phys. Earth Planet. Int.* **88**, 117–30.
- (1996). Seismic detection of a thin laterally varying boundary layer at the base of the mantle beneath the central-Pacific. *Geophys. Res. Lett.* **23**, 977–80.
- Garnero, E., Helmberger, D., & Engen, G. (1988). Lateral variations near the core-mantle boundary. *Geophys. Res. Lett.* **15**, 609–12.
- Garnero, E. J., Revenaugh, J., Williams, Q., Lay, T., & Kellogg, L. H. (1998). Ultralow velocity zone at the core-mantle boundary. In *The Core-Mantle Boundary Region*, pp. 319–34, eds. M. Gurnis, M. E. Wysession, E. Knittle, & B. A. Buffett, volume 28 of *Geodynamics Series*. American Geophysical Union, Washington, DC.
- Gaskell, R. W., Synnott, S. P., McEwen, A. S., & Schaber, G. G. (1988). Large-scale topography of Io: Implications for internal structure and heat transfer. *Geophys. Res. Lett.* **15**, 581–4.
- Gast, P. W. (1968). Trace element fractionation and the origin of tholeiitic and alkaline magma types. *Geochim. Cosmochim. Acta* **32**, 1057–86.

- Geertsma, J. & DeKlerk, F. (1969). A rapid method of predicting width and extent of hydraulically induced fracture. *J. Petrol. Technol.* **21**, 1571–81.
- Geertsma, J. & Haafkens, R. (1979). A comparison of the theories for predicting width and extent of vertical hydraulically induced fractures. *J. Energy Res. Technol.* **101**, 8–19.
- Geissler, P. E., Greenberg, R., Hoppa, G., Helfenstein, P., McEwen, A., Pappalardo, R., Tufts, R., Ockert-Bell, M., Sullivan, R., Greeley, R., Belton, M. J. S., Denk, T., Clark, B., Burns, J., Veverka, J., & the Galileo Imaging Team (1998a). Evidence for non-synchronous rotation of Europa. *Nature* **391**, 368–70.
- Geissler, P. E., Greenberg, R., Hoppa, G., McEwen, A., Tufts, R., Phillips, C. B., Clark, B., Ockert-Bell, M., Helfenstein, P., Burns, J., Veverka, J., Sullivan, R., Greeley, R., Pappalardo, R. T., Head, J. W., Belton, M. J. S., & Denk, T. (1998b). Evolution of lineaments on Europa: Clues from Galileo multispectral imaging observations. *Icarus* **135**, 107–26.
- Gianandrea, E. & Christensen, U. (1993). Variable viscosity convection experiments with a stress-free upper boundary and implications for the heat transport in the Earth's mantle. *Phys. Earth Planet. Int.* **78**, 139–52.
- Giardini, D. & Woodhouse, J. H. (1984). Deep seismicity and modes of deformation in Tonga subduction zone. *Nature* **307**, 505–9.
- Gilbert, F. & Dziewonski, A. M. (1975). An application of normal mode theory to the retrieval of structural parameters and source mechanisms from seismic spectra. *Phil. Trans. Roy. Soc. London A* **278**, 187–269.
- Gilbert, G. K. (1890). *Lake Bonneville*, volume 1 of *U.S. Geol. Survey Monograph*. U.S. Government Printing Office, Washington, DC, 438 pp.
- Giunchi, C., Spada, G., & Sabadini, R. (1997). Lateral viscosity variations and post-glacial rebound: Effects on present-day VLBI baseline deformations. *Geophys. Res. Lett.* **24**, 13–16.
- Glatzmaier, G. A. (1988). Numerical simulations of mantle convection: Time-dependent, three-dimensional, compressible, spherical shell. *Geophys. Astrophys. Fluid Dyn.* **43**, 223–64.
- Glatzmaier, G. A. & Roberts, P. H. (1995). A three-dimensional convective dynamo solution with rotating and finitely conducting inner core and mantle. *Phys. Earth Planet. Int.* **91**, 63–75.
- (1996). Rotation and magnetism of Earth's inner core. *Science* **274**, 1887–91.
- (1997). Simulating the geodynamo. *Contemporary Physics* **38**, 269–88.
- Glatzmaier, G. A. & Schubert, G. (1993). Three-dimensional spherical models of layered and whole mantle convection. *J. Geophys. Res.* **98**, 21969–76.
- Glatzmaier, G., Schubert, G., & Bercovici, D. (1990). Chaotic, subduction-like downflows in a spherical model of convection in the Earth's mantle. *Nature* **347**, 274–7.
- Goettel, K. A. (1988). Present bounds on the bulk composition of Mercury: Implications for planetary formation processes. In *Mercury*, pp. 613–21, eds. F. Vilas, C. R. Chapman, & M. S. Matthews. The University of Arizona Press, Tucson.
- Goetze, C. & Kohlstedt, D. L. (1973). Laboratory study of dislocation climb and diffusion in olivine. *J. Geophys. Res.* **26**, 5961–71.
- Goins, N. R., Toksöz, M. N., & Dainty, A. M. (1979). The lunar interior: A summary report. *Proc. Lunar Planet. Sci. Conf. 10th*, 2421–39.
- Goins, N. R., Dainty, A. M., & Toksöz, M. N. (1981). Lunar seismology: The internal structure of the Moon. *J. Geophys. Res.* **86**, 5061–74.
- Goldsby, D. L. & Kohlstedt, D. L. (1997a). Flow of ice I by dislocation, grain boundary sliding, and diffusion processes (abstract). In *Lunar and Planetary Science XXVIII*, pp. 429–30. Lunar and Planetary Institute, Houston, Texas.
- (1997b). Grain boundary sliding in fine-grained ice I. *Scripta Materialia* **37**, 1399–406.
- Goldschmidt, V. M. (1933). Grundlagen der quantitativen Geochemie. *Fortschr. Miner. Krist. Petrog.* **17**, 112–56.
- Gorbatov, A., Suárez, G., Kostoglodov, V., & Gordeev, E. (1994). A double-planed seismic zone in Kamchatka from local and teleseismic data. *Geophys. Res. Lett.* **21**, 1675–8.
- Gordon, R. B. (1965). Diffusion creep in the Earth's mantle. *J. Geophys. Res.* **70**, 2413–8.

- Gordon, R. B. (1967). Thermally activated processes in the Earth: Creep and seismic attenuation. *Geophys. J. Roy. Astron. Soc.* **14**, 33–43.
- (1998). The plate tectonic approximation: Plate nonrigidity, diffuse plate boundaries, and global plate reconstructions. *Ann. Rev. Earth Planet. Sci.* **26**, 615–42.
- Gor'kov, L. P. (1958). Stationary convection in a plane liquid layer near the critical heat transfer point. *Sov. Phys. JETP* **6**, 311–5.
- Goto, K., Suzuki, Z., & Hamaguchi, H. (1987). Stress distribution due to olivine–spinel phase transition in descending plate and deep focus earthquakes. *J. Geophys. Res.* **92**, 13811–20.
- Gough, D. O. (1969). The anelastic approximation for thermal convection. *J. Atmos. Sci.* **26**, 448–56.
- Grand, S. P. (1987). Tomographic inversion for shear velocity beneath the North American plate. *J. Geophys. Res.* **92**, 14065–90.
- (1994). Mantle shear structure beneath the Americas and surrounding oceans. *J. Geophys. Res.* **99**, 11591–621.
- Grand, S. P. & Helmberger, D. V. (1984a). Upper mantle shear structure of North America. *Geophys. J. Roy. Astron. Soc.* **76**, 399–438.
- (1984b). Upper mantle shear structure beneath the northwest Atlantic Ocean. *J. Geophys. Res.* **89**, 11465–75.
- Grand, S. P., van der Hilst, R. D., & Widjiantoro, S. (1997). Global seismic tomography: A snapshot of convection in the Earth. *Geol. Soc. Amer. Today* **7**, 1–7.
- Grasset, O. & Parmentier, E. M. (1998). Thermal convection in a volumetrically heated, infinite Prandtl number fluid with strongly temperature-dependent viscosity: Implications for planetary thermal evolution. *J. Geophys. Res.* **103**, 18171–81.
- Grasset, O. & Sotin, C. (1996). The cooling rate of a liquid shell in Titan's interior. *Icarus* **123**, 101–12.
- Greeley, R. (1987). Release of juvenile water on Mars: Estimated amounts and timing associated with volcanism. *Science* **236**, 1653–4.
- Greeley, R., Sullivan, R., Klemaszewski, J., Homan, K., Head, J. W., Pappalardo, R. T., Veverka, J., Clark, B. E., Johnson, T. V., Klaasen, K. P., Belton, M., Moore, J., Asphaug, E., Carr, M. H., Neukum, G., Denk, T., Chapman, C. R., Pilcher, C. B., Geissler, P. E., Greenberg, R., & Tufts, R. (1998). Europa: Initial Galileo geological observations. *Icarus* **135**, 4–24.
- Green, D. H. & Falloon, T. J. (1998). Pyrolite: A Ringwood concept and its current expression. In *The Earth's Mantle: Composition, Structure, and Evolution*, pp. 311–78, ed. I. Jackson. Cambridge University Press, Cambridge, England.
- Green, H. W. & Houston, H. (1995). The mechanics of deep earthquakes. *Ann. Rev. Earth Planet. Sci.* **23**, 169–213.
- Greenberg, R. & Weidenschilling, S. J. (1984). How fast do Galilean satellites spin? *Icarus* **58**, 186–96.
- Greenberg, R., Wacker, J. F., Hartmann, W. K., & Chapman, C. R. (1978). Planetesimals to planets: Numerical simulation of collisional evolution. *Icarus* **35**, 1–26.
- Greenberg, R., Geissler, P., Hoppa, G., Tufts, B. R., Durda, D. D., Pappalardo, R., Head, J. W., Greeley, R., Sullivan, R., & Carr, M. H. (1998). Tectonic processes on Europa: Tidal stresses, mechanical response, and visible features. *Icarus* **135**, 64–78.
- Griffiths, R. W. (1986). Thermals in extremely viscous fluids, including the effects of temperature-dependent viscosity. *J. Fluid Mech.* **166**, 115–38.
- Griffiths, R. W. & Campbell, I. H. (1990). Stirring and structure in mantle starting plumes. *Earth Planet. Sci. Lett.* **99**, 66–78.
- (1991a). Interaction of mantle plume heads with the Earth's surface and onset of small-scale convection. *J. Geophys. Res.* **96**, 18295–310.
- (1991b). On the dynamics of long-lived plume conduits in the convecting mantle. *Earth Planet. Sci. Lett.* **103**, 214–27.
- Griffiths, R. W., Hackney, R. I., & van der Hilst, R. D. (1995). A laboratory investigation of effects of trench migration on the descent of subducted slabs. *Earth Planet. Sci. Lett.* **133**, 1–17.
- Griggs, D. T. (1939). A theory of mountain-building. *Am. J. Sci.* **237**, 611–50.
- (1972). The sinking lithosphere and the focal mechanism of deep earthquakes. In *The Nature of the Solid Earth*, pp. 361–84, ed. E. C. Robertson. McGraw-Hill, New York.

- Grimm, R. E. (1994a). The deep structure of Venusian plateau highlands. *Icarus* **112**, 89–103.
- (1994b). Recent deformation rates on Venus. *J. Geophys. Res.* **99**, 23163–71.
- Grimm, R. E. & Phillips, R. J. (1990). Tectonics of Lakshmi Planum, Venus: Tests for Magellan. *Geophys. Res. Lett.* **17**, 1349–52.
- (1991). Gravity anomalies, compensation mechanisms, and the geodynamics of western Ishtar Terra, Venus. *J. Geophys. Res.* **96**, 8305–24.
- (1992). Anatomy of a Venusian hot spot: Geology, gravity, and mantle dynamics of Eistla Regio. *J. Geophys. Res.* **97**, 16035–54.
- Grimm, R. E. & Solomon, S. C. (1988). Viscous relaxation of impact crater relief on Venus: Constraints on crustal thickness and thermal gradient. *J. Geophys. Res.* **93**, 11911–29.
- Grossman, L. (1972). Condensation in the primitive solar nebula. *Geochim. Cosmochim. Acta* **36**, 597–619.
- Gubbins, D. (1977a). Energetics of the Earth's core. *J. Geophys.* **43**, 453–64.
- (1977b). Speculations on the origin of the magnetic field of Mercury. *Icarus* **30**, 186–91.
- (1981). Rotation of the inner core. *J. Geophys. Res.* **86**, 11695–9.
- Gubbins, D., Masters, T. G., & Jacobs, J. A. (1979). Thermal evolution of the Earth's core. *Geophys. J. Roy. Astron. Soc.* **59**, 57–99.
- Guillou, L. & Jaupart, C. (1995). On the effect of continents on mantle convection. *J. Geophys. Res.* **100**, 24217–38.
- Guillou-Frottier, L., Buttles, J., & Olson, P. (1995). Laboratory experiments on the structure of subducted lithosphere. *Earth Planet. Sci. Lett.* **133**, 19–34.
- Gurnis, M. (1986a). Stirring and mixing in the mantle by plate-scale flow: Large persistent blobs and long tendrils coexist. *Geophys. Res. Lett.* **13**, 1474–7.
- (1986b). The effects of chemical density differences on convective mixing in the Earth's mantle. *J. Geophys. Res.* **91**, 407–19.
- (1986c). Quantitative bounds on the size spectrum of isotopic heterogeneity within the mantle. *Nature* **323**, 317–20.
- (1988). Large-scale mantle convection and the aggregation and dispersal of supercontinents. *Nature* **332**, 695–9.
- (1989). A reassessment of the heat transport by variable viscosity convection with plates and lids. *Geophys. Res. Lett.* **16**, 179–82.
- Gurnis, M. & Davies, G. F. (1985). Simple parametric models of crustal growth. *J. Geodynamics* **3**, 105–35.
- (1986a). Mixing in numerical models of mantle convection incorporating plate kinematics. *J. Geophys. Res.* **91**, 6375–95.
- (1986b). The effect of depth-dependent viscosity on convective mixing in the mantle and the possible survival of primitive mantle. *Geophys. Res. Lett.* **13**, 541–4.
- Gurnis, M. & Hager, B. H. (1988). Controls of the structure of subducted slabs. *Nature* **335**, 317–21.
- Gurnis, M. & Zhong, S. (1991). Generation of long wavelength heterogeneity in the mantle by the dynamic interaction between plates and convection. *Geophys. Res. Lett.* **18**, 581–4.
- Gurnis, M., Eloy, C., & Zhong, S. (1996). Free-surface formulation of mantle convection – II. Implication for subduction-zone observables. *Geophys. J. Int.* **127**, 719–27.
- Gutenberg, B. (1913). Über die konstitution des Erdinnern, erschlossen aus Erdbebenbeobachtungen. *Phys. Z.* **14**, 1217–18.
- Gwinn, C. R., Herring, T. A., & Shapiro, I. I. (1986). Geodesy by radio interferometry: Studies of the forced nutations of the Earth: 2. Interpretation. *J. Geophys. Res.* **91**, 4755–65.
- Haddon, R. A. W. (1982). Evidence for inhomogeneities near the core–mantle boundary. *Phil. Trans. Roy. Soc. London A* **306**, 61–70.
- Haddon, R. A. W. & Buchbinder, G. G. R. (1987). S-wave scattering by 3-D heterogeneities at the base of the mantle. *Geophys. Res. Lett.* **14**, 891–4.
- Hadley, D. & Kanamori, H. (1977). Seismic structure of the Transverse Ranges, California. *Geol. Soc. Am. Bull.* **88**, 1469–78.

- Hager, B. H. (1984). Subducted slabs and the geoid: Constraints on mantle rheology and flow. *J. Geophys. Res.* **89**, 6003–15.
- (1991). Mantle viscosity: A comparison of models from postglacial rebound and from the geoid, plate driving forces, and advected heat flux. In *Glacial Isostasy, Sea-Level and Mantle Rheology*, pp. 493–513, eds. R. Sabadini, K. Lambeck, & E. Boschi. Kluwer Academic Publishers, Dordrecht, The Netherlands.
- Hager, B. H. & Clayton, R. W. (1989). Constraints on the structure of mantle convection using seismic observations, flow models, and the geoid. In *Mantle Convection: Plate Tectonics and Global Dynamics*, pp. 657–763, ed. W. R. Peltier, volume 4 of *The Fluid Mechanics of Astrophysics and Geophysics, Geodynamics Series*. Gordon and Breach Science Publishers, New York.
- Hager, B. H. & O'Connell, R. J. (1978). Subduction zone dip angles and flow driven by plate motion. *Tectonophysics* **50**, 111–33.
- (1979). Kinematic models of large-scale flow in the Earth's mantle. *J. Geophys. Res.* **84**, 1031–48.
- (1981). A simple global model of plate dynamics and mantle convection. *J. Geophys. Res.* **86**, 4843–67.
- Hager, B. H. & Richards, M. A. (1989). Long-wavelength variations in Earth's geoid: Physical models and dynamical implications. *Phil. Trans. Roy. Soc. London A* **328**, 309–27.
- Hager, B. H., Clayton, R. W., Richards, M. A., Comer, R. P., & Dziewonski, A. M. (1985). Lower mantle heterogeneity, dynamic topography and the geoid. *Nature* **313**, 541–5.
- Hales, A. L. (1936). Convection currents in the Earth. *Mon. Not. Roy. Astron. Soc., Geophys. Suppl.* **3**, 372–9.
- Hall, A. (1987). *Igneous Petrology*. Longman Scientific & Technical, Essex, U.K., 573 pp.
- Hallam, A. (1977). Secular changes in marine inundation of USSR and North America through the Phanerozoic. *Nature* **269**, 769–72.
- (1992). *Phanerozoic Sea-Level Changes*. Perspectives in Paleobiology and Earth History Series. Columbia Univ. Press, New York, 266 pp.
- Hamelin, B. & Allègre, C. J. (1988). Lead isotope study of orogenic lherzolite massifs. *Earth Planet. Sci. Lett.* **91**, 117–31.
- Hanan, B. B. & Graham, D. W. (1996). Lead and helium isotope evidence from oceanic basalts for a common deep source of mantle plumes. *Science* **272**, 991–5.
- Hansen, U. & Yuen, D. A. (1988). Numerical simulations of thermal–chemical instabilities at the core–mantle boundary. *Nature* **334**, 237–49.
- (1989). Dynamical influences from thermal–chemical instabilities at the core–mantle boundary. *Geophys. Res. Lett.* **16**, 629–32.
- (1990). Nonlinear physics of double-diffusive convection in geological systems. *Earth Sci. Rev.* **29**, 385–99.
- (1993). High Rayleigh number regime of temperature-dependent viscosity convection and the Earth's early thermal history. *Geophys. Res. Lett.* **20**, 2191–4.
- (1994). Effects of depth-dependent thermal expansivity on the interaction of thermal-chemical plumes with a compositional boundary. *Phys. Earth Planet. Int.* **86**, 205–21.
- Hansen, U., Yuen, D. A., & Kroening, S. E. (1990). Transition to hard turbulence in thermal convection at infinite Prandtl number. *Phys. Fluids A* **2**, 2157–63.
- (1991). Effects of depth-dependent thermal expansivity on mantle circulations and lateral thermal anomalies. *Geophys. Res. Lett.* **18**, 1261–4.
- (1992a). Mass and heat transport in strongly time-dependent thermal convection at infinite Prandtl number. *Geophys. Astrophys. Fluid Dyn.* **63**, 67–89.
- Hansen, U., Yuen, D. A., & Malevsky, A. V. (1992b). Comparison of steady-state and strongly chaotic thermal convection at high Rayleigh number. *Phys. Rev. A* **46**, 4742–55.
- Hansen, U., Yuen, D. A., Kroening, S. E. & Larsen, T. B. (1993). Dynamical consequences of depth-dependent thermal expansivity and viscosity on mantle circulations and thermal structure. *Phys. Earth Planet. Int.* **77**, 205–23.
- Hansen, V. L., Willis, J. J., & Banerdt, W. B. (1997). Tectonic overview and synthesis. In *Venus II: Geology, Geophysics, Atmosphere, and Solar Wind Environment*, pp. 797–844, eds. S. W. Bougher, D. M. Hunten & R. J. Phillips. The University of Arizona Press, Tucson.

- Hardee, H. C. (1986). Replenishment rates of crustal magma and their bearing on potential sources of thermal energy. *J. Volcanol. Geotherm. Res.* **28**, 275–96.
- Hardee, H. C. & Larson, D. W. (1977). Viscous dissipation effects in magma conduits. *J. Volcanol. Geotherm. Res.* **2**, 299–308.
- Harder, H. (1998). Phase transitions and the three-dimensional planform of thermal convection in the Martian mantle. *J. Geophys. Res.* **103**, 16775–97.
- Harder, H. & Christensen, U. R. (1996). A one-plume model of martian mantle convection. *Nature* **380**, 507–9.
- Harding, A. J., Orcutt, J. A., Kappus, M. E., Vera, E. E., Mutter, J. C., Buhl, P., Detrick, R. S., & Brocher, T. M. (1989). Structure of young oceanic crust at 13°N on the East Pacific Rise from expanding spread profiles. *J. Geophys. Res.* **94**, 12163–96.
- Harmon, J. K. & Campbell, D. B. (1988). Radar observations of Mercury. In *Mercury*, pp. 101–17, eds. F. Vilas, C. R. Chapman, & M. S. Matthews. The University of Arizona Press, Tucson.
- Harris, J. W. (1987). Recent physical, chemical, and isotopic research of diamond. In *Mantle Xenoliths*, pp. 477–500, ed. P. H. Nixon. J. Wiley & Sons, Chichester, England.
- Hart, S. R. (1984). A large-scale isotope anomaly in the Southern Hemisphere mantle. *Nature* **309**, 753–7.
- (1988). Heterogeneous mantle domains: Signatures, genesis and mixing chronologies. *Earth Planet. Sci. Lett.* **90**, 273–96.
- (1993). Equilibration during mantle melting: A fractal tree model. *Proc. Natl. Acad. Sci.* **90**, 11914–8.
- Hartmann, W. K. (1986). Moon origin: The impact-trigger hypothesis. In *Origin of the Moon*, pp. 579–608, eds. W. K. Hartmann, R. J. Phillips & G. J. Taylor. Lunar and Planetary Institute, Houston, Texas.
- Hartmann, W. K. & Davis, D. R. (1975). Satellite-sized planetesimals and lunar origin. *Icarus* **24**, 504–15.
- Hartmann, W. K., Strom, R. G., Weidenschilling, S. J., Blasius, K. R., Woronow, A., Dence, M. R., Grieve, R. A. F., Diaz, J., Chapman, C. R., Shoemaker, E. N., & Jones, K. L. (1981). Chronology of planetary volcanism by comparative studies of planetary cratering. In *Basaltic Volcanism on the Terrestrial Planets*, pp. 1049–127. Pergamon Press, New York.
- Hartmann, W. K., Phillips, R. J., & Taylor, G. J., editors (1986). *Origin of the Moon*. Lunar and Planetary Institute, Houston, Texas, 781 pp.
- Hasegawa, A., Umino, N. & Takagi, A. (1978a). Double-planed deep seismic zone and upper-mantle structure in the northeastern Japan Arc. *Geophys. J. Roy. Astron. Soc.* **54**, 281–96.
- (1978b). Double-planed structure of the deep seismic zone in the northeastern Japan Arc. *Tectonophysics* **47**, 43–58.
- Haskell, N. A. (1935). The motion of a viscous fluid under a surface load. *Physics* **6**, 265–9.
- (1936). The motion of a viscous fluid under a surface load. Part II. *Physics* **1**, 56–61.
- (1937). The viscosity of the asthenosphere. *Am. J. Sci.* **33**, 22–8.
- Hauck, S. A., Phillips, R. J., & Price, M. H. (1998). Venus: Crater distribution and plains resurfacing models. *J. Geophys. Res.* **103**, 13635–42.
- Hauri, E. H., Whitehead, J. A. & Hart, S. R. (1994). Fluid dynamic and geochemical aspects of entrainment in mantle plumes. *J. Geophys. Res.* **99**, 24275–300.
- Hawkesworth, C. J., Kempton, P. D., Rogers, N. W., Ellam, R. M., & van Calsteren, P. W. (1990). Continental mantle lithosphere, and shallow level enrichment processes in the Earth's mantle. *Earth Planet. Sci. Lett.* **96**, 256–68.
- Hawkesworth, C. J., Gallagher, K., Hergt, J. M. & McDermott, F. (1994). Destructive plate margin magmatism: Geochemistry and melt generation. *Lithos* **33**, 169–88.
- Haxby, W. F. & Turcotte, D. L. (1978). On isostatic geoid anomalies. *J. Geophys. Res.* **83**, 5473–8.
- Haxby, W. F. & Weissel, J. K. (1986). Evidence for small-scale mantle convection from Seasat altimeter data. *J. Geophys. Res.* **91**, 3507–20.
- Hays, J. D. & Pitman, W. C. (1973). Lithospheric plate motion, sea level changes and climatic and ecological consequences. *Nature* **246**, 18–22.
- Head, J. W. (1976). Lunar volcanism in space and time. *Rev. Geophys. Space Phys.* **14**, 265–300.

- Head, J. W., Campbell, D. B., Elachi, C., Guest, J. E., McKenzie, D. P., Saunders, R. S., Schaber, G. G., & Schubert, G. (1991). Venus volcanism: Initial analysis from Magellan data. *Science*, **252**, 276–88.
- Head, J. W., Crumpler, L. S., Aubele, J. C., Guest, J. E., & Saunders, R. S. (1992). Venus volcanism: Classification of volcanic features and structures, associations, and global distribution from Magellan data. *J. Geophys. Res.*, **97**, 13153–97.
- Heiken, G., Vaniman, D. & French, B. M. (1991). *Lunar Sourcebook: A User's Guide to the Moon*. Cambridge University Press, Cambridge, England, 736 pp.
- Heimpel, M. & Olson, P. (1994). Buoyancy-driven fracture and magma transport through the lithosphere: Models and experiments. In *Magmatic Systems*, pp. 223–40, ed. M. P. Ryan, volume 57 of *International Geophysics Series*. Academic Press, New York.
- Heinz, D. L. & Jeanloz, R. (1987). Measurement of the melting curve of $Mg_{0.9}Fe_{0.1}SiO_3$ at lower mantle conditions and its geophysical implications. *J. Geophys. Res.*, **92**, 11437–44.
- Heirtzler, J. R., Dickson, G. O., Herron, E. M., Pitman, W. C., & Le Pichon, X. (1968). Marine magnetic anomalies, geomagnetic field reversals, and motions of the ocean floor and continents. *J. Geophys. Res.*, **73**, 2119–36.
- Helfenstein, P. & Parmentier, E. M. (1985). Patterns of fracture and tidal stresses due to nonsynchronous rotation: Implications for fracturing on Europa. *Icarus*, **61**, 175–84.
- Helmburger, D. V., Wen, L., & Ding, X. (1998). Seismic evidence that the source of the Iceland hotspot lies at the core–mantle boundary. *Nature*, **396**, 251–5.
- Helmstaedt, H. & Gurney, J. J. (1984). Kimberlites of Southern Africa: Are they related to subduction processes? In *Kimberlites: I. Kimberlites and Related Rocks*, pp. 425–34, ed. J. Kornprobst, volume 11A. Elsevier, Amsterdam.
- Hemley, R. J. & Cohen, R. E. (1992). Silicate perovskite. *Ann. Rev. Earth Planet. Sci.*, **20**, 553–600.
- Herrick, D. L. & Parmentier, E. M. (1994). Episodic large-scale overturn of two-layer mantles in terrestrial planets. *J. Geophys. Res.*, **99**, 2053–62.
- Herrick, R. R. (1994). Resurfacing history of Venus. *Geology*, **22**, 703–6.
- Herrick, R. R. & Phillips, R. J. (1990). Blob tectonics: A prediction for Western Aphrodite Terra, Venus. *Geophys. Res. Lett.*, **17**, 2129–32.
- Herrick, R. R., Bills, B. G., & Hall, S. A. (1989). Variations in effective compensation depth across Aphrodite Terra, Venus. *Geophys. Res. Lett.*, **16**, 543–6.
- Herrick, R. R., Sharpton, V. L., Malin, M. C., Lyons, S. N., & Feely, K. (1997). Morphology and morphometry of impact craters. In *Venus II: Geology, Geophysics, Atmosphere, and Solar Wind Environment*, pp. 1015–46, eds. S. W. Bougher, D. M. Hunten, & R. J. Phillips. The University of Arizona Press, Tucson.
- Herring, J. R. (1963). Investigation of problems in thermal convection. *J. Atmos. Sci.*, **20**, 325–38.
- (1964). Investigation of problems in thermal convection: Rigid boundaries. *J. Atmos. Sci.*, **21**, 277–90.
- Hess, H. H. (1962). History of ocean basins. In *Petrologic Studies – A Volume in Honor of A. F. Buddington*, pp. 599–620, eds. A. Engeln, H. L. James, & B. F. Leonard. Geol. Soc. America, New York.
- (1965). Mid-oceanic ridges and tectonics of the sea-floor. In *Submarine Geology and Geophysics*, pp. 317–32, eds. W. F. Whittard & R. Bradshaw, Colston Research Society Symposium 17th, London. Butterworths.
- Hess, P. C. & Parmentier, E. M. (1995). A model for the thermal and chemical evolution of the Moon's interior: Implications for the onset of mare volcanism. *Earth and Planet. Sci. Lett.*, **134**, 501–14.
- Hewitt, J. M., McKenzie, D. P., & Weiss, N. O. (1975). Dissipative heating in convective flows. *J. Fluid Mech.*, **68**, 721–38.
- Hewitt, J. M., McKenzie, D. P., & Weiss, N. O. (1980). Large aspect ratio cells in two-dimensional thermal convection. *Earth Planet. Sci. Lett.*, **51**, 370–80.
- Hey, R., Duennbier, F. K., & Morgan, W. J. (1980). Propagating rifts on midocean ridges. *J. Geophys. Res.*, **85**, 3647–58.
- Hildebrand, R. S. & Bowring, S. A. (1999). Crustal recycling by slab failure. *Geology*, **27**, 11–14.
- Hill, R. I. (1991). Starting plumes and continental break-up. *Earth Planet. Sci. Lett.*, **104**, 398–416.

- Hill, R. I., Campbell, I. H., Davies, G. F., & Griffiths, R. W. (1992). Mantle plumes and continental tectonics. *Science* **256**, 186–93.
- Hirs, G. G. (1974). A systematic study of turbulent film flow. *J. Lubric. Technol.* **96**, 118–26.
- Hirth, G. & Kohlstedt, D. L. (1995a). Experimental constraints on the dynamics of the partially molten upper mantle: Deformation in the diffusion creep regime. *J. Geophys. Res.* **100**, 1981–2001.
- (1995b). Experimental constraints on the dynamics of the partially molten upper mantle: 2. Deformation in the dislocation creep regime. *J. Geophys. Res.* **100**, 15441–9.
- (1996). Water in the oceanic upper mantle: Implications for rheology, melt extraction and the evolution of the lithosphere. *Earth Planet. Sci. Lett.* **144**, 93–108.
- Hiyagon, H. & Ozima, M. (1986). Partition of noble gases between olivine and basalt melt. *Geochim. Cosmochim. Acta* **50**, 2045–57.
- Hiyagon, H., Ozima, M., Marty, B., Zashu, S., & Sakai, H. (1992). Noble gases in submarine glasses from mid-oceanic ridges and Loihi seamount: Constraints on the early history of the Earth. *Geochim. Cosmochim. Acta* **56**, 1301–16.
- Hobson, E. W. (1955). *The Theory of Spherical and Ellipsoidal Harmonics*. Chelsea, New York, 500 pp.
- Hoffman, N. R. A. & McKenzie, D. P. (1985). The destruction of geochemical heterogeneities by differential fluid motions during mantle convection. *Geophys. J. Roy. Astron. Soc.* **82**, 163–206.
- Hofmann, A. W. & White, W. M. (1982). Mantle plumes from ancient oceanic crust. *Earth Planet. Sci. Lett.* **57**, 421–36.
- Hofmann, A. W., Jochum, K. P., Seufert, M., & White, W. M. (1986). Nb and Pb in oceanic basalts: New constraints on mantle evolution. *Earth Planet. Sci. Lett.* **79**, 33–45.
- Hofmeister, A. M. (1999). Mantle values of thermal conductivity and the geotherm from phonon lifetimes. *Science* **283**, 1699–706.
- Holland, J. G. & Lambert, R. St. J. (1972). Major element chemical composition of shields and the continental crust. *Geochim. Cosmochim. Acta* **36**, 673–83.
- Holland, K. G. & Ahrens, T. J. (1997). Melting of $(\text{Mg},\text{Fe})_2\text{SiO}_4$ at the core–mantle boundary of the Earth. *Science* **275**, 1623–5.
- Holmes, A. (1915a). Radio-activity and the Earth's thermal history. I. The concentration of the radio-active elements in the Earth's crust. *Geol. Mag.* **2**, 60–71.
- (1915b). Radio-activity and the Earth's thermal history. II. Radio-activity and the Earth as a cooling body. *Geol. Mag.* **2**, 102–12.
- (1916). Radio-activity and the Earth's thermal history. III. Radio-activity and isostasy. *Geol. Mag.* **3**, 265–74.
- (1931). Radioactivity and Earth movements, XVII. *Trans. Geol. Soc. Glasgow, Vol. XVIII – Part III, 1928–31* **18**, 559–606.
- (1933). The thermal history of the Earth. *J. Wash. Acad. Sci.* **23**, 169–95.
- (1945). *Principles of Physical Geology*. Ronald Press, New York, 532 pp.
- (1946). An estimate of the age of the Earth. *Nature* **157**, 680–4.
- Holzer, T. E. & Axford, W. I. (1971). Interaction between interstellar helium and the solar wind. *J. Geophys. Res.* **76**, 6965–70.
- Honda, S. (1995). A simple parameterized model of Earth's thermal history with the transition from layered to whole mantle convection. *Earth Planet. Sci. Lett.* **131**, 357–69.
- Honda, S. & Yuen, D. A. (1994). Model for convective cooling of mantle with phase changes: Effects of aspect ratios and initial conditions. *J. Phys. Earth* **42**, 165–86.
- Honda, S., Balachandar, S., Yuen, D. A., & Reuteler, D. (1993a). Three-dimensional mantle dynamics with an endothermic phase transition. *Geophys. Res. Lett.* **20**, 221–4.
- Honda, S., Yuen, D. A., Balachandar, S., & Reuteler, D. (1993b). Three-dimensional instabilities of mantle convection with multiple phase transitions. *Science* **259**, 1308–11.
- Hood, L. L. (1986). Geophysical constraints on the lunar interior. In *Origin of the Moon*, pp. 361–410, eds. W. K. Hartmann, R. J. Phillips, & G. J. Taylor. Lunar and Planetary Institute, Houston, Texas.
- Hood, L. L. & Vickery, A. (1984). Magnetic field amplification and generation in hypervelocity meteoroid impacts with application to lunar paleomagnetism. *J. Geophys. Res.* **89**, 211–23.

- Horai, K. & Simmons, G. (1970). An empirical relationship between thermal conductivity and Debye temperature for silicates. *J. Geophys. Res.* **75**, 978–82.
- Houseman, G. (1988). The dependence of convection planform on mode of heating. *Nature* **332**, 346–9.
- Houseman, G. & England, P. (1986). Finite strain calculations of continental deformation: 1. Method and general results for convergent zones. *J. Geophys. Res.* **91**, 3651–63.
- Houseman, G. A., McKenzie, D. P., & Molnar, P. (1981). Convective instability of a thickened boundary layer and its relevance for the thermal evolution of continental convergent belts. *J. Geophys. Res.* **86**, 6115–32.
- Houston, M. H. & De Bremaecker, J.-C. (1975). Numerical models of convection in the upper mantle. *J. Geophys. Res.* **80**, 742–51.
- Houtermans, F. G. (1946). Die istopenhaufigkeiten im natürlichen blei und das alter des urans. *Naturwiss.* **33**, 185–6, 219.
- Howard, L. N. (1966). Convection at high Rayleigh number. In *Proc. 11th Intl. Cong. Appl. Mech.*, pp. 1109–15, ed. H. Görtler, Springer-Verlag, Berlin.
- Howell, R. R. (1997). Thermal emission from lava flows on Io. *Icarus* **127**, 394–407.
- Hsui, A. T. (1981). Some remarks on the thermal consequences of ridge subduction. *Geophys. Res. Lett.* **8**, 1031–4.
- Hsui, A. T. & Toksöz, M. N. (1979). The evolution of thermal structures beneath a subduction zone. *Tectonophysics* **60**, 43–60.
- (1981). Back-arc spreading: Trench migration, continental pull or induced convection? *Tectonophysics* **74**, 89–98.
- Hsui, A. T., Marsh, B. D., & Toksöz, M. N. (1983). On melting of the subduction oceanic crust: Effects of subduction induced mantle flow. *Tectonophysics* **99**, 207–20.
- Hsui, A. T., Yang, W.-S., & Baumgardner, J. R. (1995). A preliminary study of the effects of some flow parameters in the generation of poloidal and toroidal energies within a 3-D spherical thermal-convective system with variable viscosity. *PAGEOPH* **145**, 487–503.
- Humphreys, E. D. & Clayton, R. W. (1990). Tomographic image of the Southern California mantle. *J. Geophys. Res.* **95**, 19725–46.
- Humphreys, E. D. & Dueker, K. G. (1994). Physical state of the western U.S. upper mantle. *J. Geophys. Res.* **99**, 9635–50.
- Huppert, H. E. & Sparks, R. S. J. (1988). The generation of granitic magmas by intrusion of basalt into continental crust. *J. Petrol.* **29**, 599–624.
- Hurley, P. & Rand, J. R. (1969). Pre-drift continental nuclei. *Science* **164**, 1229–42.
- Hynes, A. & Mott, J. (1985). On the causes of back-arc spreading. *Geology* **13**, 387–9.
- Inoue, H., Fukao, Y., Tanabe, K., & Ogata, Y. (1990). Whole mantle P-wave travel time tomography. *Phys. Earth Planet. Int.* **59**, 294–328.
- Ioannou, P. J. & Lindzen, R. S. (1993). Gravitational tides in the outer planets. II. Interior calculations and estimation of the tidal dissipation factor. *Astrophys. J.* **406**, 266–78.
- Irifune, T. & Ringwood, A. E. (1987). Phase transformations in primitive MORB and pyrolite compositions to 25 GPa and some geophysical implications. In *High-Pressure Research in Mineral Physics*, pp. 231–42, eds. M. H. Manghnani & Y. Syono, Geophysical Monograph 39. American Geophysical Union, Washington, DC.
- Irwin, G. R. (1957). Analysis of stresses and strains near the end of a crack traversing a plate. *J. Appl. Mech.* **24**, 361–4.
- Isacks, B. L. & Barazangi, M. (1977). Geometry of Benioff zones: Lateral segmentation and downwards bending of the subducted lithosphere. In *Island Arcs, Deep Sea Trenches, and Back-Arc Basins*, pp. 99–114, eds. M. Talwani & W. C. Pitman, III, Maurice Ewing Series 1. American Geophysical Union, Washington, DC.
- Isacks, B. & Molnar, P. (1971). Distribution of stresses in the descending lithosphere from a global survey of focal-mechanism solutions of mantle earthquakes. *Rev. Geophys. Space Phys.* **9**, 103–74.
- Isacks, B., Oliver, J., & Sykes, L. R. (1968). Seismology and the new global tectonics. *J. Geophys. Res.* **73**, 5855–99.

- Ita, J. & King, S. D. (1994). Sensitivity of convection with an endothermic phase change to the form of governing equations, initial conditions, boundary conditions, and equation of state. *J. Geophys. Res.* **99**, 15919–38.
- Ito, E. (1989). Stability relations of silicate perovskite under subsolidus conditions. In *Perovskite: A Structure of Great Interest to Geophysics and Materials Science*, pp. 27–32, eds. A. Navrotsky & D. Weidner, Geophysical Monograph 45. American Geophysical Union, Washington, DC.
- Ito, E. & Katsura, T. (1989). A temperature profile of the mantle transition zone. *Geophys. Res. Lett.* **16**, 425–8.
- Ito, E. & Takahashi, E. (1989). Postspinel transformations in the system Mg_2SiO_4 – Fe_2SiO_4 and some geophysical implications. *J. Geophys. Res.* **94**, 10637–46.
- Ito, E., Akaogi, M., Topor, L., & Navrotsky, A. (1990). Negative pressure-temperature slopes for reactions forming $MgSiO_3$ perovskite from calorimetry. *Science* **249**, 1275–8.
- Ito, G., Lin, J., & Gable, C. W. (1997). Interaction of mantle plumes and migrating mid-ocean ridges: Implications for the Galapagos plume–ridge system. *J. Geophys. Res.* **102**, 15403–17.
- Ivins, E. R., Sammis, C. G., & Yoder, C. F. (1993). Deep mantle viscous structure with prior estimate and satellite constraint. *J. Geophys. Res.* **98**, 4579–609.
- Iwamori, H. (1997). Heat sources and melting in subduction zones. *J. Geophys. Res.* **102**, 14803–20.
- Iwamori, H., McKenzie, D., & Takahashi, E. (1995). Melt generation by isentropic mantle upwelling. *Earth Planet. Sci. Lett.* **134**, 253–66.
- Iwase, Y. & Honda, S. (1997). An interpretation of the Nusselt–Rayleigh number relationship for convection in a spherical shell. *Geophys. J. Int.* **130**, 801–4.
- Iyer, H. M. (1979). Deep structure under Yellowstone National Park, USA: A continental ‘hot spot’. *Tectonophys.* **56**, 165–97.
- (1984). Geophysical evidence for the locations, shapes and sizes, and internal structures of magma chambers beneath regions of Quaternary volcanism. *Phil. Trans. Roy. Soc. London A* **310**, 473–510.
- Jackson, M. J. & Pollack, H. N. (1984). On the sensitivity of parameterized convection to the rate of decay of internal heat sources. *J. Geophys. Res.* **89**, 10103–8.
- (1987). Mantle devolatilization and convection: Implications for the thermal history of the Earth. *Geophys. Res. Lett.* **14**, 737–40.
- Jacob, D., Jagoutz, E., Lowry, D., Mattey, D., & Kudrjavtseva, G. (1994). Diamondiferous eclogites from Siberia: Remnants of Archean oceanic crust. *Geochim. Cosmochim. Acta* **58**, 5191–207.
- Jacobsen, S. B. & Wasserburg, G. J. (1979). The mean age of mantle and crustal reservoirs. *J. Geophys. Res.* **84**, 7411–27.
- (1980a). A two-reservoir recycling model for mantle–crust evolution. *Proc. Nat. Acad. Sci. USA* **77**, 6298–302.
- (1980b). Sm–Nd isotopic evolution of chondrites. *Earth Planet. Sci. Lett.* **50**, 139–55.
- (1981). Transport models for crust and mantle evolution. *Tectonophysics* **75**, 163–79.
- Jacoby, W. R. & Schmeling, H. (1982). On the effects of the lithosphere on mantle convection and evolution. *Phys. Earth Planet. Int.* **29**, 305–19.
- Jakeš, P. & Taylor, S. R. (1974). Excess europium content in Precambrian sedimentary rocks and continental evolution. *Geochim. Cosmochim. Acta* **38**, 739–45.
- Jakeš, P. & White, A. J. R. (1971). Composition of island arcs and continental growth. *Earth Planet. Sci. Lett.* **12**, 224–30.
- Jambon, A., Weber, H., & Braun, O. (1986). Solubility of He, Ne, Ar, Kr and Xe in a basalt melt in the range 1250–1600 degrees C. *Geochim. Cosmochim. Acta* **50**, 401–8.
- James, T. S. & Ivins, E. R. (1997). Global geodetic signatures of the Antarctic ice sheet. *J. Geophys. Res.* **102**, 605–33.
- James, D. M., Squyres, S. W., Bindschadler, D. L., Baer, G., Schubert, G., Sharpton, V. L., & Stofan, E. R. (1992). Geophysical models for the formation and evolution of coronae on Venus. *J. Geophys. Res.* **97**, 16055–67.
- Janle, P. (1983). Bouguer gravity profiles across the highland–lowland escarpment on Mars. *Moon and Planets* **28**, 55–67.

- Janle, P. & Jannsen, D. (1986). Isostatic gravity and elastic bending models of Olympus Mons, Mars. *Ann. Geophysicae* **4**, 537–46.
- Jarchow, C. M. & Thompson, G. A. (1989). The nature of the Mohorovicic discontinuity. *Ann. Rev. Earth Planet. Sci.* **17**, 475–506.
- Jaroslow, G. E., Hirth, G., & Dick, H. J. B. (1996). Abyssal peridotite mylonites: Implications for grain-size sensitive flow and strain localization in the oceanic lithosphere. *Tectonophysics* **256**, 17–37.
- Jarrard, R. D. (1986). Relations among subduction parameters. *Rev. Geophys.* **24**, 217–84.
- Jarvis, G. T. (1984). Time-dependent convection in the Earth's mantle. *Phys. Earth Planet. Int.* **36**, 305–27.
- Jarvis, G. T. & McKenzie, D. P. (1980). Convection in a compressible fluid with infinite Prandtl number. *J. Fluid Mech.* **96**, 515–83.
- Jarvis, G. T. & Peltier, W. R. (1982). Mantle convection as a boundary layer phenomenon. *Geophys. J. Roy. Astron. Soc.* **68**, 389–427.
- Jaupart, C. (1983). Horizontal heat transfer due to radioactivity contrasts: Causes and consequences of the linear heat flow relation. *Geophys. J. Roy. Astron. Soc.* **75**, 411–35.
- Jaupart, C. & Parsons, B. (1985). Convective instabilities in a variable viscosity fluid cooled from above. *Phys. Earth Planet. Int.* **39**, 14–32.
- Jaupart, C., Slater, J. G., & Simmons, G. (1981). Heat flow studies: Constraints on the distribution of uranium, thorium and potassium in the continental crust. *Earth Planet. Sci. Lett.* **52**, 328–44.
- Jaupart, C., Mann, J. R. & Simmons, G. (1982). A detailed study of the distribution of heat flow and radioactivity in New Hampshire (USA). *Earth Planet. Sci. Lett.* **59**, 267–87.
- Jaupart, C., Mareschal, J. C., Guillou-Frottier, L., & Davaille, A. (1998). Heat flow and thickness of the lithosphere in the Canadian Shield. *J. Geophys. Res.* **103**, 15269–86.
- Jeanloz, R. & Knittle, E. (1989). Density and composition of the lower mantle. *Phil. Trans. Roy. Soc. London A* **328**, 377–89.
- Jeanloz, R. & Morris, S. (1986). Temperature distribution in the crust and mantle. *Ann Rev. Earth Planet. Sci.* **14**, 377–415.
- Jeanloz, R. & Richter, F. M. (1979). Convection, composition, and the thermal state of the lower mantle. *J. Geophys. Res.* **84**, 5497–504.
- Jeanloz, R. & Thompson, A. B. (1983). Phase transitions and mantle discontinuities. *Rev. Geophys. Space Phys.* **21**, 51–74.
- Jeffreys, H. (1929). *The Earth, its Origin, History, and Physical Constitution*. Cambridge Univ. Press, Cambridge, 2nd edition.
- (1930). The instability of a compressible fluid heated from below. *Proc. Cambridge Phil. Soc.* **26**, 170–2.
- (1939). The times of P, S and SKS, and the velocities of P and S. *Mon. Not. Roy. Astron. Soc., Geophys. Suppl.* **4**, 498–533.
- (1962). *The Earth, its Origin, History, and Physical Constitution*. Cambridge Univ. Press, Cambridge, England, fourth edition, 420 pp.
- Jeffreys, H. & Bland, M. E. M. (1951). The instability of a fluid sphere heated within. *Mon. Not. Roy. Astron. Soc., Geophys. Suppl.* **6**, 148–58.
- Jeffreys, H. & Bullen, K. E. (1940). *Seismological Tables*. British Assoc. Adv. Sci., London, 48 pp.
- Jephcoat, A. & Olson, P. (1987). Is the inner core of the Earth pure iron? *Nature* **325**, 332–5.
- Jin, D., Karato, S.-I., & Obata, M. (1998). Mechanisms of shear localization in the continental lithosphere: Inference from the deformation microstructures of peridotites from the Ivrea zone, northwestern Italy. *J. Struct. Geol.* **20**, 195–209.
- Johnson, C. L. & Sandwell, D. T. (1994). Lithospheric flexure on Venus. *Geophys. J. Int.* **119**, 627–47.
- Johnson, H. P. & Carlson, R. L. (1992). Variation of sea floor depth with age: A test of models based on drilling results. *Geophys. Res. Lett.* **19**, 1971–4.
- Johnson, L. R. (1967). Array measurements of P velocities in the upper mantle. *J. Geophys. Res.* **72**, 6309–25.

- Johnson, T. V., Veeder, G. J., Matson, D. L., Brown, R. H., Nelson, R. M., & Morrison, D. (1988). Io: Evidence for silicate volcanism in 1986. *Science* **242**, 1280–3.
- Johnston, D. H. & Toksöz, M. N. (1977). Internal structure and properties of Mars. *Icarus* **32**, 73–84.
- Jones, G. M. (1977). Thermal interaction of the core and the mantle and long-term behavior of the geomagnetic field. *J. Geophys. Res.* **82**, 1703–9.
- Jordan, T. H. (1975). The continental tectonosphere. *Rev. Geophys. Space Phys.* **13**, 1–12.
- (1977). Lithospheric slab penetration into the lower mantle beneath the Sea of Okhotsk. *J. Geophys.* **43**, 473–96.
- (1981). Continents as a chemical boundary layer. *Phil. Trans. Roy. Soc. London A* **301**, 359–73.
- (1988). Structure and formation of the continental tectosphere. *J. Petrol.* **1988**, 11–37.
- Jordan, T. H., Puster, P., Glatzmaier, G. A., & Tackley, P. J. (1993). Comparisons between seismic Earth structures and mantle flow models based on radial correlation functions. *Science* **261**, 1427–31.
- Julian, B. R. & Sengupta, M. K. (1973). Seismic travel time evidence for lateral inhomogeneity in the deep mantle. *Nature* **242**, 443–7.
- Jull, M. G. & Arkani-Hamed, J. (1995). The implications of basalt in the formation and evolution of mountains on Venus. *Phys. Earth Planet. Int.* **89**, 163–75.
- Jurdy, D. M. & Gordon, R. G. (1984). Global plate motions relative to the hot spots 64 to 56 Ma. *J. Geophys. Res.* **89**, 9927–36.
- Jurdy, D. M. & Stefanick, M. (1990). Models for the hotspot distribution. *Geophys. Res. Lett.* **17**, 1965–8.
- (1991). The forces driving the plates: Constraints from kinematics and stress observations. *Phil. Trans. Roy. Soc. London A* **337**, 127–39.
- Kameyama, M., Yuen, D. A., & Fujimoto, H. (1997). The interaction of viscous heating with grain-size dependent rheology in the formation of localized slip zones. *Geophys. Res. Lett.* **24**, 2523–6.
- Kanamori, H., Anderson, D. L., & Heaton, T. H. (1998). Frictional melting during the rupture of the 1994 Bolivian earthquake. *Science* **279**, 839–42.
- Kanasewich, E. R. (1968). The interpretation of lead isotopes and their geological significance. In *Radiometric Dating for Geologists*, pp. 147–223, eds. E. I. Hamilton & R. M. Farquhar. Interscience Publishers, London and New York.
- Kaneshima, S. & Helffrich, G. (1999). Dipping low-velocity layer in the mid-lower mantle: Evidence for geochemical heterogeneity. *Science* **283**, 1888–91.
- Kao, H. & Chen, W.-P. (1994). The double seismic zone in Kuril-Kamchatka: The tale of two overlapping single zones. *J. Geophys. Res.* **99**, 6913–30.
- (1995). Transition from interplate slip to double seismic zone along the Kuril-Kamchatka arc. *J. Geophys. Res.* **100**, 9881–903.
- Karato, S.-I. (1992). On the Lehmann discontinuity. *Geophys. Res. Lett.* **19**, 2255–8.
- (1993). Magnetic-field-induced preferred orientation of iron. *Science* **262**, 1708–11.
- (1997). Phase transformations and rheological properties of mantle minerals. In *Earth's Deep Interior: The Doornbos Memorial Volume*, pp. 223–72, ed. D. J. Crossley. Gordon and Breach Science Publ., Amsterdam.
- (1998). Micro-physics of post glacial rebound. *GeoResearch Forum* **3–4**, 351–64. Trans. Tech. Publications, Switzerland.
- (1999). Private communication.
- Karato, S.-I. & Wu, P. (1993). Rheology of the upper mantle: A synthesis. *Science* **260**, 771–8.
- Karato, S., Toriumi, M., & Fujii, T. (1980). Dynamic recrystallization of olivine single crystals during high-temperature creep. *Geophys. Res. Lett.* **7**, 649–52.
- Karato, S.-I., Paterson, M. S., & FitzGerald, J. D. (1986). Rheology of synthetic olivine aggregates: Influence of grain size and water. *J. Geophys. Res.* **91**, 8151–76.
- Karato, S., Zhang, S., & Wenk, H.-R. (1995a). Superplasticity in the Earth's lower mantle: Evidence from seismic anisotropy and rock physics. *Science* **270**, 458–61.
- Karato, S.-I., Wang, Z., Liu, B., & Fujino, K. (1995b). Plastic deformation of garnets: Systematics and implications for the rheology of the mantle transition zone. *Earth Planet. Sci. Lett.* **130**, 13–30.
- Kargel, J. S. (1991). Brine volcanism and the interior structures of asteroids and icy satellites. *Icarus* **94**, 368–90.

- Kargel, J. S. (1992). Ammonia-water volcanism on icy satellites: Phase relations at 1 atmosphere. *Icarus* **100**, 556–74.
- Karig, D. E. (1971). Origin and development of marginal basins in the western Pacific. *J. Geophys. Res.* **76**, 2542–61.
- Karig, D. E. & Kay, R. W. (1981). Fate of sediments on the descending plate at convergent margins. *Phil. Trans. Roy. Soc. London A* **301**, 233–51.
- Katsura, T. (1995). Thermal diffusivity of olivine under upper mantle conditions. *Geophys. J. Int.* **122**, 63–9.
- Katsura, T. & Ito, E. (1989). The system Mg_2SiO_4 – Fe_2SiO_4 at high pressures and temperatures: Precise determination of stabilities of olivine, modified spinel, and spinel. *J. Geophys. Res.* **94**, 15663–70.
- Kaula, W. M. (1979a). Thermal evolution of Earth and Moon growing by planetesimal impacts. *J. Geophys. Res.* **84**, 999–1008.
- (1979b). The moment of inertia of Mars. *Geophys. Res. Lett.* **6**, 194–6.
- (1980). The beginning of the Earth's thermal evolution. In *The Continental Crust and Its Mineral Deposits*, pp. 25–34, ed. D. W. Strangway, Special Paper 20. Geol. Assn. Canada.
- (1994a). The tectonics of Venus. *Phil. Trans. Roy. Soc. London A* **349**, 345–55.
- (1994b). Comment on “An episodic hypothesis for Venusian tectonics” by Donald L. Turcotte. *J. Geophys. Res.* **99**, 19095–6.
- Kaula, W. M. & Phillips, R. J. (1981). Quantitative tests for plate tectonics on Venus. *Geophys. Res. Lett.* **8**, 1187–90.
- Kaula, W. M., Schubert, G., Lingenfelter, R. E., Sjogren, W. L., & Wollenhaupt, W. R. (1974). Apollo laser altimetry and inferences as to lunar surface structure. *Proc. Lunar Sci. Conf. 5th*, 3049–58.
- Kaula, W. M., Sleep, N. H., & Phillips, R. J. (1989). More about the moment of inertia of Mars. *Geophys. Res. Lett.* **16**, 1333–6.
- Kaula, W. M., Lenardic, A., Bindschadler, D. L., & Arkani-Hamed, J. (1997). Ishtar Terra. In *Venus II – Geology, Geophysics, Atmosphere, and Solar Wind Environment*, pp. 879–900, eds. S. W. Bougher, D. M. Hunten, & R. J. Phillips. The University of Arizona Press, Tucson.
- Kawakatsu, H. (1986). Double seismic zones: Kinematics. *J. Geophys. Res.* **91**, 4811–25.
- Kawasaki, I. (1986). Azimuthally anisotropic model of the oceanic upper mantle. *Phys. Earth Planet. Int.* **43**, 1–21.
- Kay, R. W. (1980). Volcanic arc magmas: Implications of a melting-mixing model for element recycling in the crust-upper mantle system. *J. Geol.* **88**, 497–522.
- Kay, R. W. & Kay, S. M. (1988). Crustal recycling and the Aleutian Arc. *Geochim. Cosmochim. Acta* **52**, 1351–9.
- (1991). Creation and destruction of lower continental crust. *Geol. Rundsch.* **80**, 259–78.
- (1993). Delamination and delamination magmatism. *Tectonophysics* **219**, 177–89.
- Kay, S. M., Kay, R. W., & Citron, G. P. (1982). Tectonic controls on tholeiitic and calc-alkaline magmatism in the Aleutian arc. *J. Geophys. Res.* **87**, 4051–72.
- Kay, S. M., Ramos, V. A., & Marquez, M. (1993). Evidence in Cerro Pampa volcanic rocks for slab-melting prior to ridge-trench collision in southern South America. *J. Geol.* **101**, 703–14.
- Kelemen, P. B. & Dick, H. J. B. (1995). Focused melt flow and localized deformation in the upper mantle: Juxtaposition of replacive dunite and ductile shear zones in the Josephine peridotite, SW Oregon. *J. Geophys. Res.* **100**, 423–38.
- Kelemen, P. B., Shimizu, N., & Salters, V. J. M. (1995a). Extraction of mid-ocean-ridge basalt from the upwelling mantle by focused flow of melt in dunite channels. *Nature* **375**, 747–53.
- Kelemen, P. B., Whitehead, J. A., Aharonov, E., & Jordahl, K. A. (1995b). Experiments on flow focusing in soluble porous media, with applications to melt extraction from the mantle. *J. Geophys. Res.* **100**, 475–96.
- Kelemen, P. B., Hirth, G., Shimizu, N., Spiegelman, M., & Dick, H. J. B. (1997). A review of melt migration processes in the adiabatically upwelling mantle beneath oceanic spreading ridges. *Phil. Trans. Roy. Soc. London A* **355**, 283–318.
- Kellogg, L. H. (1992). Mixing in the mantle. *Ann. Rev. Earth Planet Sci.* **20**, 365–88.

- Kellogg, L. H. (1993). Chaotic mixing in the Earth's mantle. In *Advances in Geophysics*, pp. 1–33, eds. R. Dmowska & B. Saltzman, volume 34. Academic Press, San Diego.
- (1997). Growing the Earth's D'' layer: Effect of density variations at the core-mantle boundary. *Geophys. Res. Lett.* **24**, 2749–52.
- Kellogg, L. H. & Stewart, C. A. (1991). Mixing by chaotic convection in an infinite Prandtl number fluid and implications for mantle convection. *Phys. Fluids A* **3**, 1374–8.
- Kellogg, L. H. & Turcotte, D. L. (1987). Homogenization of the mantle by convective mixing and diffusion. *Earth Planet. Sci. Lett.* **81**, 371–8.
- (1990). Mixing and the distribution of heterogeneities in a chaotically convecting mantle. *J. Geophys. Res.* **95**, 421–32.
- Kellogg, L. H., Hager, B. H., & van der Hilst, R. D. (1999). Compositional stratification in the deep mantle. *Science* **283**, 1881–4.
- Kemp, D. V. & Stevenson, D. J. (1996). A tensile, flexural model for the initiation of subduction. *Geophys. J. Int.* **125**, 73–94.
- Kendall, J. M. & Shearer, P. M. (1994). Lateral variations in D'' thickness from long-period shear wave data. *J. Geophys. Res.* **99**, 11575–90.
- Kennett, B. L. N. (1991). *IASPEI 1991 Seismological Tables*. Research School of Earth Sciences, Australian National University, Canberra, Australia.
- Kennett, B. L. N. & van der Hilst, R. D. (1998). Seismic structure of the mantle: From subduction zone to craton. In *The Earth's Mantle: Composition, Structure, and Evolution*, pp. 381–404, ed. I. Jackson. Cambridge University Press, Cambridge, England.
- Kennett, B. L. N., Widjiantoro, S., & van der Hilst, R. D. (1998). Joint seismic tomography for bulk sound and shear wave speed in the Earth's mantle. *J. Geophys. Res.* **103**, 12469–93.
- Kenyon, P. M. (1998). The effect of channel spacing during magma migration on trace element and isotopic ratios. *Geophys. Res. Lett.* **25**, 3995–8.
- Kenyon, P. M. & Turcotte, D. L. (1983). Convection in a two-layer mantle with a strongly temperature-dependent viscosity. *J. Geophys. Res.* **88**, 6403–14.
- (1987). Along-strike magma mixing beneath mid-ocean ridges: Effects on isotopic ratios. *Earth Planet. Sci. Lett.* **84**, 393–405.
- Keszthelyi, L. & McEwen, A. (1997). Magmatic differentiation of Io. *Icarus* **130**, 437–48.
- Khodakovskii, G., Rabinowicz, M., Genton, P., & Ceuleneer, G. (1998). 2D modeling of melt percolation in the mantle: The role of a melt dependent mush viscosity. *Geophys. Res. Lett.* **25**, 683–6.
- Khurana, K. K., Kivelson, M. G., & Russell, C. T. (1997a). Interaction of Io with its torus: Does Io have an internal magnetic field? *Geophys. Res. Lett.* **24**, 2391–4.
- Khurana, K. K., Kivelson, M. G., Russell, C. T., Walker, R. J., & Southwood, D. J. (1997b). Absence of an internal magnetic field at Callisto. *Nature* **387**, 262–4.
- Khurana, K. K., Kivelson, M. G., Stevenson, D. J., Schubert, G., Russell, C. T., Walker, R. J., Joy, S., & Polanskey, C. (1998). Induced magnetic fields as evidence for subsurface oceans in Europa and Callisto. *Nature* **395**, 777–80.
- Kidd, R. G. W. (1977). A model for the process of formation of the upper oceanic crust. *Geophys. J. Roy. Astron. Soc.* **50**, 149–83.
- Kido, M. & Seno, T. (1994). Dynamic topography compared with residual depth anomalies in oceans and implications for age-depth curves. *Geophys. Res. Lett.* **21**, 717–20.
- Kiefer, W. S. & Hager, B. H. (1991a). A mantle plume model for the equatorial highlands of Venus. *J. Geophys. Res.* **96**, 20947–66.
- (1991b). Mantle downwelling and crustal convergence: A model for Ishtar Terra, Venus. *J. Geophys. Res.* **96**, 20967–80.
- (1992). Geoid anomalies and dynamic topography from convection in cylindrical geometry: Applications to mantle plumes on Earth and Venus. *Geophys. J. Int.* **108**, 198–214.
- Kiefer, W. S., Richards, M. A., Hager, B. H., & Bills, B. G. (1986). A dynamic model of Venus' gravity field. *Geophys. Res. Lett.* **13**, 14–17.

- Kieffer, S. W. (1976). Lattice thermal conductivity within the Earth and considerations of a relationship between the pressure dependence of the thermal diffusivity and the volume dependence of the Grüneisen parameter. *J. Geophys. Res.* **81**, 3025–30.
- Kincaid, C. & Olson, P. (1987). An experimental study of subduction and slab migration. *J. Geophys. Res.* **92**, 13832–40.
- Kincaid, C. & Sacks, I. S. (1997). Thermal and dynamical evolution of the upper mantle in subduction zones. *J. Geophys. Res.* **102**, 12295–315.
- Kincaid, C., Ito, G., & Gable, C. (1995). Laboratory investigation of the interaction of off-axis mantle plumes and spreading centres. *Nature* **376**, 758–61.
- Kincaid, C., Sparks, D. W., & Detrick, R. (1996). The relative importance of plate-driven and buoyancy-driven flow at mid-ocean ridges. *J. Geophys. Res.* **101**, 16177–93.
- King, S. D. (1995a). Models of mantle viscosity. In *Mineral Physics and Crystallography: A Handbook of Physical Constants*, pp. 227–36, ed. T. J. Ahrens. American Geophysical Union, Washington, DC.
- (1995b). The viscosity structure of the mantle. *Rev. Geophys.* **33**, 11–17.
- King, S. D. & Hager, B. H. (1990). The relationship between plate velocity and trench viscosity in Newtonian and power-law subduction calculations. *Geophys. Res. Lett.* **17**, 2409–12.
- (1994). Subducted slabs and the geoid. *J. Geophys. Res.* **99**, 19843–52.
- King, S. D. & Ita, J. (1995). Effect of slab rheology on mass transport across a phase transition boundary. *J. Geophys. Res.* **100**, 20211–22.
- King, S. D. & Masters, G. (1992). An inversion for radial viscosity structure using seismic tomography. *Geophys. Res. Lett.* **19**, 1551–4.
- King, S. D., Gable, C. W., & Weinstein, S. A. (1992). Models of convection-driven tectonic plates: A comparison of methods and results. *Geophys. J. Int.* **109**, 481–7.
- Kirby, S. H. & McCormick, J. W. (1979). Creep of hydrolytically weakened synthetic quartz crystals oriented to promote 2110–0001 slip: A brief summary of work to date. *Bull. Minéral.* **102**, 124–37.
- Kirby, S. H., Stein, S., Okal, E. A., & Rubie, D. C. (1996). Metastable mantle phase transformations and deep earthquakes in subducting oceanic lithosphere. *Rev. Geophys.* **34**, 261–306.
- Kirk, R. L. & Stevenson, D. J. (1989). The competition between thermal contraction and differentiation in the stress history of the Moon. *J. Geophys. Res.* **94**, 12133–44.
- Kivelson, M. G., Khurana, K. K., Walker, R. J., Russell, C. T., Linker, J. A., Southwood, D. J., & Polanskey, C. (1996a). A magnetic signature at Io: Initial report from the Galileo magnetometer. *Science* **273**, 337–40.
- Kivelson, M. G., Khurana, K. K., Russell, C. T., Walker, R. J., Warnecke, J., Coroniti, F. V., Polanskey, C., Southwood, D. J., & Schubert, G. (1996b). Discovery of Ganymede's magnetic field by the Galileo spacecraft. *Nature* **384**, 537–41.
- Kivelson, M. G., Khurana, K. K., Joy, S., Russell, C. T., Southwood, D. J., Walker, R. J., & Polanskey, C. (1997). Europa's magnetic signature: Report from Galileo's pass on 19 December 1996. *Science* **276**, 1239–41.
- Kivelson, M. G., Khurana, K. K., Stevenson, D. J., Bennett, L., Joy, S., Russell, C. T., Walker, R. J., Zimmer, C., & Polanskey, C. (1999). Europa and Callisto: Induced or intrinsic fields in a periodically varying plasma environment. *J. Geophys. Res.* **104**, 4609–25.
- Kivelson, M. G., Khurana, K. K., Russell, C. T., Volwerk, M., Walker, R. J., & Zimmer, C. (2000). Galileo magnetometer measurements: A stronger case for a subsurface ocean at Europa. *Science* **289**, 1340–3.
- Klein, E. M. & Langmuir, C. H. (1987). Global correlations of ocean ridge basalt chemistry with axial depth and crustal thickness. *J. Geophys. Res.* **92**, 8089–115.
- Klemaszewski, J. E., Greeley, R., Homan, K. S., Bender, K. C., Chuang, F. C., Kadel, S., Sullivan, R. J., Chapman, C., Merline, W. J., Moore, J., Wagner, R., Denk, T., Neukum, G., Head, J., Pappalardo, R., Prockter, L., Belton, M., Johnson, T. V., Pilcher, C., & the Galileo Team (1998). Galileo at Callisto: Overview of nominal mission results (CD-ROM, abstract 1866). In *Lunar and Planetary Science XXIX*, Lunar and Planetary Institute, Houston, Texas.
- Knittle, E. & Jeanloz, R. (1986). High-pressure metallization of FeO and implications for the Earth's core. *Geophys. Res. Lett.* **13**, 1541–4.

- Knittle, E. & Jeanloz, R. (1991). Earth's core–mantle boundary: Results of experiments at high pressures and temperatures. *Science* **251**, 1438–43.
- Knittle, E., Jeanloz, R., & Smith, G. L. (1986). Thermal expansion of silicate perovskite and stratification of the Earth's mantle. *Nature* **319**, 214–6.
- Koch, D. M. (1994). A spreading drop model for plumes on Venus. *J. Geophys. Res.* **99**, 2035–52.
- Kohlstedt, D. L. & Goetze, C. (1974). Low-stress high-temperature creep in olivine single crystals. *J. Geophys. Res.* **79**, 2045–51.
- Kohlstedt, D. L. & Zimmerman, M. E. (1996). Rheology of partially molten mantle rocks. *Ann. Rev. Earth Planet. Sci.* **24**, 41–62.
- Kohlstedt, D. L., Evans, B., & Mackwell, S. J. (1995). Strength of the lithosphere: Constraints imposed by laboratory experiments. *J. Geophys. Res.* **100**, 17587–602.
- Konopliv, A. S. & Sjogren, W. L. (1994). Venus spherical harmonic gravity model to degree and order 60. *Icarus* **112**, 42–54.
- Konopliv, A. S. & Yuan, D. N. (1999). Lunar Prospector 100th degree gravity model development (CD-ROM, abstract 1067). In *Lunar and Planetary Science XXX*, Lunar and Planetary Institute, Houston, Texas.
- Konopliv, A. S., Borderies, N. J., Chodas, P. W., Christensen, E. J., Sjogren, W. L., Williams, B. G., Balmino, G., & Barriot, J. P. (1993). Venus gravity and topography – 60th degree and order model. *Geophys. Res. Lett.* **20**, 2403–6.
- Konopliv, A. S., Binder, A. B., Hood, L. L., Kucinskas, A. B., Sjogren, W. L., & Williams, J. G. (1998). Improved gravity field of the Moon from Lunar Prospector. *Science* **281**, 1476–80.
- Konopliv, A. S., Banerdt, W. B., & Sjogren, W. L. (1999). Venus gravity: 180th degree and order model. *Icarus* **139**, 3–18.
- Korenaga, J. & Kelemen, P. B. (1998). Melt migration through the oceanic lower crust: A constraint from melt percolation modeling with finite solid diffusion. *Earth Planet. Sci. Lett.* **156**, 1–11.
- Kozlovskaya, S. V. (1969). On the internal constitution and chemical composition of Mercury. *Astrophys. Lett.* **4**, 1–4.
- Kucinskas, A. B. & Turcotte, D. L. (1994). Isostatic compensation of equatorial highlands on Venus. *Icarus* **112**, 104–16.
- Kunz, J., Staudacher, T., & Allegre, C. J. (1998). Plutonium-fission xenon found in Earth's mantle. *Science* **280**, 877–80.
- Kurz, M. D. & Jenkins, W. J. (1981). The distribution of helium in oceanic basalt glasses. *Earth Planet. Sci. Lett.* **53**, 41–54.
- (1982). Helium partitioning in basaltic glass: Reply to comment by R. Poreda. *Earth Planet. Sci. Lett.* **59**, 439–40.
- Kurz, M. D., Jenkins, W. J., & Hart, S. R. (1982a). Helium isotopic systematics of oceanic islands and mantle heterogeneity. *Nature* **297**, 43–7.
- Kurz, M. D., Jenkins, W. J., Schilling, J. G. & Hart, S. R. (1982b). Helium isotopic variations in the mantle beneath the central North Atlantic Ocean. *Earth Planet. Sci. Lett.* **58**, 1–14.
- Kurz, M. D., Jenkins, W. J., Hart, S. R., & Clague, D. (1983). Helium isotopic variations in volcanic rocks from Loihi Seamount and the Island of Hawaii. *Earth Planet. Sci. Lett.* **66**, 388–406.
- Kushiro, I., Yoder, H. S. & Mysen, B. O. (1976). Viscosities of basalt and andesite melts at high pressures. *J. Geophys. Res.* **81**, 6351–6.
- Lachenbruch, A. H. (1970). Crustal temperature and heat production: Implications of the linear heat-flow relation. *J. Geophys. Res.* **75**, 3291–300.
- Lachenbruch, A. H. & Sass, J. H. (1978). Models of an extending lithosphere and heat flow in the Basin and Range Province. *Geol. Soc. Am. Mem.* **152**, 209–50.
- Lambeck, K. (1988). *Geophysical Geodesy: The Slow Deformations of the Earth*. Clarendon Press, Oxford, England, 718 pp.
- Lambeck, K. & Johnston, P. (1998). The viscosity of the mantle: Evidence from analyses of glacial-rebound phenomena. In *The Earth's Mantle: Composition, Structure, and Evolution*, pp. 461–502, ed. I. Jackson. Cambridge University Press, Cambridge, England.

- Lambeck, K. & Nakada, M. (1990). Late Pleistocene and Holocene sea-level change along the Australian coast. *Palaeogeogr. Palaeoclimatol. Palaeoecol.* **89**, 143–76.
- Lambeck, K., Johnston, P., & Nakada, M. (1990). Holocene glacial rebound and sea-level change in NW Europe. *Geophys. J. Int.* **103**, 451–68.
- Langseth, M. G., Keihm, S. J., & Peters, K. (1976). Revised lunar heat-flow values. *Proc. Lunar Sci. Conf. 7th*, 3143–71.
- Laravie, J. A. (1975). Geometry and lateral strain of subducted plates in island arcs. *Geology* **3**, 484–6.
- Larsen, T. B. & Yuen, D. A. (1997a). Ultrafast upwelling bursting through the upper mantle. *Earth Planet. Sci. Lett.* **146**, 393–9.
- (1997b). Fast plumeheads: Temperature-dependent versus non-Newtonian rheology. *Geophys. Res. Lett.* **24**, 1995–8.
- Larsen, T. B., Yuen, D. A., Malevsky, A. V., & Smedsmo, J. L. (1996a). Dynamics of strongly time-dependent convection with non-Newtonian temperature-dependent viscosity. *Phys. Earth Planet. Int.* **94**, 75–103.
- Larsen, T. B., Yuen, D. A., Smedsmo, J. L., & Malevsky, A. V. (1996b). Thermomechanical modeling of pulsation tectonics and consequences on lithospheric dynamics. *Geophys. Res. Lett.* **23**, 217–20.
- Larson, R. L. (1991). Latest pulse of Earth: Evidence for a mid-Cretaceous superplume. *Geology* **19**, 547–50.
- Larson, R. L. & Olson, P. (1991). Mantle plumes control magnetic reversal frequency. *Earth Planet. Sci. Lett.* **107**, 437–47.
- Laske, G. & Masters, G. (1999). Limits on differential rotation of the inner core from an analysis of the Earth's free oscillations. *Nature* **402**, 66–9.
- Laubscher, H. P. (1988). Material balance in Alpine orogeny. *Geol. Soc. Am. Bull.* **100**, 1313–28.
- Laul, J. C., Smith, M. R., Wänke, H., Jagoutz, E., Dreibus, G., Palme, H., Spettel, B., Burghel, A., Lipschutz, M. E., & Verkouteren, R. M. (1986). Chemical systematics of the Shergotty meteorite and the composition of its parent body (Mars). *Geochim. Cosmochim. Acta* **50**, 909–26.
- Lay, T. (1989). Mantle, lower: Structure. In *The Encyclopedia of Solid Earth Geophysics*, pp. 770–5, ed. D. E. James. Van Nostrand Reinhold, New York.
- (1994a). The fate of descending slabs. *Ann. Rev. Earth Planet. Sci.* **22**, 33–61.
- (1994b). Seismological Structure of Slabs. In *Advances in Geophysics*, pp. 1–185, eds. R. Dmowska & B. Saltzman, volume 35. Academic Press, San Diego.
- (1994c). *Structure and Fate of Subducting Slabs*. Academic Press, San Diego, 185 pp.
- Lay, T. & Helmberger, D. V. (1983). A lower mantle S-wave triplication and the shear velocity structure of D''. *Geophys. J. Roy. Astron. Soc.* **75**, 799–837.
- Lay, T., Williams, Q., & Garnero, E. J. (1998). The core–mantle boundary layer and deep Earth dynamics. *Nature* **392**, 461–8.
- Le Pichon, X. (1968). Sea-floor spreading and continental drift. *J. Geophys. Res.* **73**, 3661–97.
- Le Stunff, Y. & Ricard, Y. (1995). Topography and geoid due to lithospheric mass anomalies. *Geophys. J. Int.* **122**, 982–90.
- (1997). Partial advection of equidensity surfaces: A solution for the dynamic topography problem? *J. Geophys. Res.* **102**, 24655–67.
- Lee, D.-C., Halliday, A. N., Snyder, G. A., & Taylor, L. A. (1997). Age and origin of the Moon. *Science* **278**, 1098–103.
- Lees, A. C., Bukowski, M. S. T., & Jeanloz, R. (1983). Reflection properties of phase transition and compositional change models of the 670-km discontinuity. *J. Geophys. Res.* **88**, 8145–59.
- Lehmann, I. (1936). "P." *Publ. Bur. Cent. Seism. Int. A* **14**, 87–115.
- Leitch, A. M. & Yuen, D. A. (1991). Compressible convection in a viscous Venusian mantle. *J. Geophys. Res.* **96**, 15551–62.
- Leitch, A. M., Yuen, D. A., & Lausten, C. L. (1992). Axisymmetric spherical shell models of mantle convection with variable properties and free and rigid lids. *J. Geophys. Res.* **97**, 20899–923.
- Leitch, A. M., Davies, G. F., & Wells, M. (1998). A plume head melting under a rifting margin. *Earth Planet. Sci. Lett.* **161**, 161–77.

- Leith, A. C. & McKinnon, W. B. (1996). Is there evidence for polar wander on Europa? *Icarus* **120**, 387–98.
- Lemoine, F. G. R., Smith, D. E., Zuber, M. T., Neumann, G. A., & Rowlands, D. D. (1997). A 70th degree lunar gravity model (GLGM-2) from Clementine and other tracking data. *J. Geophys. Res.* **102**, 16339–59.
- Lemoine, F. G., Kenyon, S. C., Factor, J. K., Trimmer, R. G., Palvis, N. K., Chinn, D. S., Cox, C. M., Klosko, S. M., Luthcke, S. B., Torrence, M. H., Wang, Y. M., Williamson, R. G., Palvis, E. C., Rapp, R. H., & Olson, T. R. (1998). The development of the Joint NASA GSFC and the National Imagery and Mapping Agency (NIMA) Geopotential Model EGM96. Technical report, NASA/TP-1998-206861.
- Lenardic, A. (1997). On the heat flow variation from Archean cratons to Proterozoic mobile belts. *J. Geophys. Res.* **102**, 709–21.
- (1998). On the partitioning of mantle heat loss below oceans and continents over time and its relationship to the Archean paradox. *Geophys. J. Int.* **134**, 706–20.
- Lenardic, A. & Kaula, W. M. (1995a). More thoughts on convergent crustal plateau formation and mantle dynamics with regard to Tibet. *J. Geophys. Res.* **100**, 15193–203.
- (1995b). Mantle dynamics and the heat flow into the Earth's continents. *Nature* **378**, 709–11.
- (1996). Near-surface thermal/chemical boundary layer convection at infinite Prandtl number: Two-dimensional numerical experiments. *Geophys. J. Int.* **126**, 689–711.
- Leerch, F. J., Klosko, S. M., & Patch, G. B. (1983). A refined gravity model from LAGEOS (GEM-L2). Technical report, NASA/TM-84, 986.
- Leven, J. H. (1985). The application of synthetic seismograms to the interpretation of the upper mantle P-wave velocity structure in northern Australia. *Phys. Earth Planet. Int.* **38**, 9–27.
- Levin, B. J. (1972). Origin of the Earth. In *The Upper Mantle*, pp. 7–30, ed. A. R. Ritsema. Elsevier, Amsterdam.
- Levitt, D. A. & Sandwell, D. T. (1995). Lithospheric bending at subduction zones based on depth soundings and satellite gravity. *J. Geophys. Res.* **100**, 379–400.
- (1996). Modal depth anomalies from multibeam bathymetry: Is there a South Pacific superswell? *Earth Planet. Sci. Lett.* **139**, 1–16.
- Lewis, J. S. (1972). Metal/silicate fractionation in the solar system. *Earth Planet. Sci. Lett.* **15**, 286–90.
- (1982). Io: Geochemistry of sulfur. *Icarus* **50**, 103–14.
- (1988). Origin and composition of Mercury. In *Mercury*, pp. 651–66, eds. F. Vilas, C. R. Chapman, & M. S. Matthews. The University of Arizona Press, Tucson.
- Li, X.-D. & Romanowicz, B. (1996). Global mantle shear velocity model developed using nonlinear asymptotic coupling theory. *J. Geophys. Res.* **101**, 22245–72.
- Lin, J., Purdy, G. M., Schouten, H., Sempere, J.-C., & Zervas, C. (1990). Evidence from gravity data for focused magmatic accretion along the Mid-Atlantic Ridge. *Nature* **344**, 627–32.
- Lin, R. P., Anderson, K. A., & Hood, L. L. (1988). Lunar surface magnetic field concentrations antipodal to young large impact basins. *Icarus* **74**, 529–41.
- Lin, R. P., Mitchell, D. L., Curtis, D. W., Anderson, K. A., Carlson, C. W., McFadden, J., Acuña, M. H., Hood, L. L., & Binder, A. (1998). Lunar surface magnetic fields and their interaction with the solar wind: Results from Lunar Prospector. *Science* **281**, 1480–4.
- Lingenfelter, R. E. & Schubert, G. (1973). Evidence for convection in planetary interiors from first-order topography. *The Moon* **7**, 172–80.
- Lister, C. R. B. (1980). Heat flow and hydrothermal circulation. In *Annual Review of Earth and Planetary Sciences*, pp. 95–117, eds. F. A. Donath, F. G. Stehli, & G. Wetherill, volume 8. Annual Reviews, Palo Alto, CA.
- Lister, C. R. B., Sclater, J. G., Davis, E. E., Villinger, H., & Nagihara, S. (1990). Heat flow maintained in ocean basins of great age: Investigations in the north-equatorial West Pacific. *Geophys. J. Int.* **102**, 603–30.
- Lister, J. R. (1990a). Buoyancy-driven fluid fracture: The effects of material toughness and of low-viscosity precursors. *J. Fluid Mech.* **210**, 263–80.
- (1990b). Buoyancy-driven fluid fracture: Similarity solutions for the horizontal and vertical propagation of fluid-filled cracks. *J. Fluid Mech.* **217**, 213–39.

- Lister, J. R. (1991). Steady solutions for feeder dikes in a density-stratified lithosphere. *Earth Planet Sci. Lett.* **107**, 233–42.
- Lister, J. R. & Buffett, B. A. (1995). The strength and efficiency of thermal and compositional convection in the geodynamo. *Phys. Earth Planet. Int.* **91**, 17–30.
- Lister, J. R. & Kerr, R. C. (1991). Fluid-mechanical models of crack propagation and their application to magma transport in dykes. *J. Geophys. Res.* **96**, 10049–77.
- Lithgow-Bertelloni, C. & Silver, P. G. (1998). Dynamic topography, plate driving forces and the African superswell. *Nature* **395**, 269–72.
- Lithgow-Bertelloni, C., Richards, M. A., Ricard, Y., O'Connell, R. J., & Engebretson, D. C. (1993). Toroidal-poloidal partitioning of plate motions since 120 Ma. *Geophys. Res. Lett.* **20**, 375–8.
- Liu, L. (1974). Silicate perovskite from phase transformations of pyrope-garnet at high pressure and temperature. *Geophys. Res. Lett.* **1**, 277–80.
- Liu, L.-G. & Bassett, W. A. (1975). The melting of iron up to 200 kbar. *J. Geophys. Res.* **80**, 3777–82.
- Liu, M. (1994). Asymmetric phase effects and mantle convection patterns. *Science* **264**, 1904–7.
- Liu, M. & Chase, C. G. (1989). Evolution of midplate hotspot swells: Numerical solutions. *J. Geophys. Res.* **94**, 5571–84.
- Liu, M., Yuen, D. A., Zhao, W., & Honda, S. (1991). Development of diapiric structures in the upper mantle due to phase transitions. *Science* **252**, 1836–9.
- Lognonné, P. & Romanowicz, B. (1990). Effect of a global plume distribution on Earth normal modes. *Geophys. Res. Lett.* **17**, 1493–6.
- Longhi, J. & Boudreau, A. E. (1979). Complex igneous processes and the formation of the primitive lunar crustal rocks. *Proc. Lunar Planet. Sci. Conf.* **10th**, 2085–105.
- Loper, D. E. (1978a). The gravitationally powered dynamo. *Geophys. J. R. Astron. Soc.* **54**, 389–404.
- (1978b). Some thermal consequences of a gravitationally powered dynamo. *J. Geophys. Res.* **83**, 5961–70.
- (1984a). Structure of the core and lower mantle. *Adv. Geophys.* **26**, 1–34.
- (1984b). The dynamical structures of D'' and deep plumes in a non-Newtonian mantle. *Phys. Earth Planet. Int.* **34**, 57–67.
- Loper, D. E. & Eltayeb, I. A. (1986). On the stability of the D'' layer. *Geophys. Astrophys. Fluid Dyn.* **36**, 229–55.
- Loper, D. E. & Lay, T. (1995). The core–mantle boundary region. *J. Geophys. Res.* **100**, 6397–420.
- Loper, D. E. & Roberts, P. H. (1979). Are planetary dynamos driven by gravitational settling? *Phys. Earth Planet. Int.* **20**, 192–3.
- Loper, D. E. & Stacey, F. D. (1983). The dynamical and thermal structure of deep mantle plumes. *Phys. Earth Planet. Int.* **33**, 304–17.
- Lord Rayleigh (1916). On convection currents in a horizontal layer of fluid, when the higher temperature is on the under side. *Phil. Mag.* **32**, 529–46.
- Lorenz, E. N. (1963). Deterministic non-periodic flow. *J. Atmos. Sci.* **20**, 130–41.
- Loubet, M. & Allègre, C. J. (1982). Trace elements in orogenic lherzolites reveal the complex history of the upper mantle. *Nature* **298**, 809–14.
- Love, A. E. H. (1927). *A Treatise on the Mathematical Theory of Elasticity*. Dover Publications, New York, fourth edition, 643 pp.
- Lowman, J. P. & Jarvis, G. T. (1995). Mantle convection models of continental collision and breakup incorporating finite thickness plates. *Phys. Earth Planet. Int.* **88**, 53–68.
- (1996). Continental collisions in wide aspect ratio and high Rayleigh number two-dimensional mantle convection models. *J. Geophys. Res.* **101**, 25485–97.
- Luais, B. & Hawkesworth, C. J. (1994). The generation of continental crust: An integrated study of crust-forming processes in the Archaean of Zimbabwe. *J. Petrol.* **35**, 43–93.
- Lucchitta, B. K. (1987). Recent mafic volcanism on Mars. *Science* **235**, 565–7.
- Lucey, P. G., Spudis, P. D., Zuber, M., Smith, D., & Malaret, E. (1994). Topographic-compositional units on the Moon and the early evolution of the lunar crust. *Science* **266**, 1855–8.
- Lugmair, G. W. & Marti, K. (1978). Lunar initial $^{143}\text{Nd}/^{144}\text{Nd}$: Differential evolution of the lunar crust and mantle. *Earth Planet. Sci. Lett.* **39**, 349–57.

- Lux, G. E. (1987). The behavior of noble gases in silicate liquids: Solution, diffusion, bubbles and surface effects, with applications to natural samples. *Geochim. Cosmochim. Acta* **51**, 1549–60.
- Lux, R. A., Davies, G. F., & Thomas, J. H. (1979). Moving lithospheric plates and mantle convection. *Geophys. J. Roy. Astron. Soc.* **58**, 209–28.
- Lyakhovsky, V., Ben-Zion, Y., & Agnon, A. (1997a). Distributed damage, faulting, and friction. *J. Geophys. Res.* **102**, 27635–49.
- Lyakhovsky, V., Reches, Z., Weinberger, R., & Scott, T. E. (1997b). Non-linear elastic behaviour of damaged rocks. *Geophys. J. Int.* **130**, 157–66.
- MacGregor, I. D. & Manton, W. I. (1986). Roberts Victor eclogites: Ancient oceanic crust. *J. Geophys. Res.* **91**, 14063–79.
- Machetel, P. & Weber, P. (1991). Intermittent layered convection in a model mantle with an endothermic phase change at 670 km. *Nature* **350**, 55–7.
- Machetel, P. & Yuen, D. A. (1987). Chaotic axisymmetrical spherical convection large-scale mantle circulation. *Earth Planet. Sci. Lett.* **86**, 93–104.
- (1989). Penetrative convective flows induced by internal heating and mantle compressibility. *J. Geophys. Res.* **94**, 10609–26.
- Machetel, P., Rabinowicz, M., & Bernardet, P. (1986). Three-dimensional convection in spherical shells. *Geophys. Astrophys. Fluid Dyn.* **37**, 57–84.
- Machetel, P., Thoraval, C., & Brunet, D. (1995). Spectral and geophysical consequences of 3-D spherical mantle convection with an endothermic phase change at the 670 km discontinuity. *Phys. Earth Planet. Int.* **88**, 43–51.
- Mackwell, S. J., Zimmerman, M. E., & Kohlstedt, D. L. (1998). High-temperature deformation of dry diabase with application to tectonics on Venus. *J. Geophys. Res.* **103**, 975–84.
- Malevsky, A. V. & Yuen, D. A. (1992). Strongly chaotic non-Newtonian mantle convection. *Geophys. Astrophys. Fluid Dyn.* **65**, 149–71.
- Malin, M. C. & Pieri, D. C. (1986). Europa. In *Satellites*, pp. 689–717, eds. J. A. Burns & M. S. Matthews. The University of Arizona Press, Tucson.
- Malkus, W. V. R. & Veronis, G. (1958). Finite amplitude cellular convection. *J. Fluid Mech.* **4**, 225–60.
- Mamyrin, B. A. & Tolstikhin, L. N. (1984). *Helium Isotopes in Nature*, volume 3 of *Developments in Geochemistry*. Elsevier, Amsterdam.
- Manga, M. & Jeanloz, R. (1996). Implications of a metal-bearing chemical boundary layer in D'' for mantle dynamics. *Geophys. Res. Lett.* **23**, 3091–4.
- (1997). Thermal conductivity of corundum and periclase and implications for the lower mantle. *J. Geophys. Res.* **102**, 2999–3008.
- Manghnani, M. H., Ramananandro, R., & Clark, S. P. (1974). Compressional and shear wave velocities in granulite facies rocks and eclogites to 10 kbar. *J. Geophys. Res.* **79**, 5427–46.
- Manglik, A. & Christensen, U. R. (1997). Effect of mantle depletion buoyancy on plume flow and melting beneath a stationary plate. *J. Geophys. Res.* **102**, 5019–28.
- Mao, H. K., Wu, Y., Chen, L. C., Shu, J. F., & Jephcoat, A. P. (1990). Static compression of iron to 300 GPa and $\text{Fe}_{0.8}\text{Ni}_{0.2}$ alloy to 260 GPa: Implications for composition of the core. *J. Geophys. Res.* **95**, 21737–42.
- Mao, H. K., Hemley, R. J., Fei, Y., Shu, J. F., Chen, L. C., Jephcoat, A. P., Wu, Y., & Bassett, W. A. (1991). Effect of pressure, temperature, and composition on lattice parameters and density of $(\text{Fe}, \text{Mg})\text{SiO}_3$ -perovskites to 30 GPa. *J. Geophys. Res.* **96**, 8069–79.
- Marsh, B. D. (1979). Island arc development: Some observations, experiments, and speculations. *J. Geol.* **87**, 687–713.
- Marsh, B. (1983). Satellite altimetry. *Rev. Geophys. Space Phys.* **21**, 10955–64.
- Martin, H. (1986). Effect of steeper Archean geothermal gradient on geochemistry of subduction-zone magmas. *Geology* **14**, 753–6.
- Marton, F. C., Bina, C. R., Stein, S., & Rubie, D. C. (1999). Effects of slab mineralogy on subduction rates. *Geophys. Res. Lett.* **26**, 119–22.
- Marty, J., Cazenave, A., & Lago, B. (1988). Geoid anomalies across Pacific fracture zones. *Geophys. J. Int.* **93**, 1–23.

- Marzoli, A., Renne, P. R., Piccirillo, E. M., Ernesto, M., Bellieni, G., & De Min, A. (1999). Extensive 200-million-year-old continental flood basalts of the Central Atlantic Magmatic Province. *Science* **284**, 616–8.
- Mason, R. G. (1958). A magnetic survey of the west coast of the United States between latitudes 32° and 36° N, longitudes 121° and 128° W. *Geophys. J. Roy. Astron. Soc.* **1**, 320–9.
- Masters, G. (1979). Observational constraints on the chemical and thermal structure of the Earth's deep interior. *Geophys. J. Roy. Astron. Soc.* **57**, 507–34.
- (1989). Seismic modelling of the Earth's large-scale three-dimensional structure. *Phil. Trans. Roy. Soc. A* **238**, 329–49.
- Masters, G., Jordan, T. H., Silver, G., & Gilbert, F. (1982). Aspherical Earth structure from fundamental spheroidal-mode data. *Nature* **298**, 609–13.
- Masters, G., Johnson, S., Laske, G., & Bolton, H. (1996). A shear-velocity model of the mantle. *Phil. Trans. Roy. Soc. London* **354**, 1385–411.
- Masters, T. G. & Shearer, P. M. (1990). Summary of seismological constraints on the structure of the Earth's core. *J. Geophys. Res.* **95**, 21691–5.
- Masursky, H., Schaber, G. G., Soderblom, L. A., & Strom, R. G. (1979). Preliminary geological mapping of Io. *Nature* **280**, 725–9.
- Matson, D. L., Ransford, G. A., & Johnson, T. V. (1981). Heat flow from Io (JI). *J. Geophys. Res.* **86**, 1664–72.
- Matsui, M. & Anderson, O. L. (1997). The case for a body-centered cubic phase (α') for iron at inner core conditions. *Phys. Earth Planet. Int.* **103**, 55–62.
- Matsui, T. & Abe, Y. (1986a). Impact-induced atmospheres and oceans on Earth and Venus. *Nature* **322**, 526–8.
- (1986b). Evolution of an impact-induced atmosphere and magma ocean on the accreting Earth. *Nature* **319**, 303–5.
- (1986c). Formation of a 'magma ocean' on the terrestrial planets due to the blanketing effect of an impact-induced atmosphere. *Earth, Moon, Planets* **34**, 223–30.
- (1987). Evolutionary tracks of the terrestrial planets. *Earth, Moon, Planets* **39**, 207–14.
- Matthews, D. & Smith, C. (1987). Deep seismic reflection profiling of the continental lithosphere. *Geophys. J. Roy. Astron. Soc.* **89**, vii–xii.
- Maxwell, A. E., Von Herzen, R. P., Hsu, K. J., Andrews, J. E., Saito, T., Percival, S. F., Milow, E. D., & Boyce, R. E. (1970). Deep sea drilling in the south Atlantic. *Science* **168**, 1047–59.
- McAdoo, D. C., Caldwell, J. G., & Turcotte, D. L. (1978). On the elastic-perfectly plastic bending of the lithosphere under generalized loading with application to the Kuril Trench. *Geophys. J. Roy. Astron. Soc.* **54**, 11–26.
- McBirney, A. R. & Murase, T. (1984). Rheological properties of magmas. *Ann. Rev. Earth Planet. Sci.* **12**, 337–57.
- McCarthy, D. D. & Luzum, B. J. (1996). Path of the mean rotational pole from 1899 to 1994. *Geophys. J. Int.* **125**, 623–9.
- McCartney, K. & Loper, D. E. (1989). Emergence of a rival paradigm to account for the Cretaceous/Tertiary event. *J. Geol. Ed.* **37**, 36–48.
- McClain, J. S., Orcutt, J. A., & Burnett, M. (1985). The East Pacific Rise in cross section: A seismic model. *J. Geophys. Res.* **90**, 8627–39.
- McCord, T. B., Hansen, G. B., Fanale, F. P., Carlson, R. W., Matson, D. L., Johnson, T. V., Smythe, W. D., Crowley, J. K., Martin, P. D., Ocampo, A., Hibbits, C. A., Granahan, J. C., & the NIMS Team (1998). Salts on Europa's surface detected by Galileo's near infrared mapping spectrometer. *Science* **280**, 1242–5.
- McDonough, W. F. & Sun, S. S. (1995). The composition of the earth. *Chem. Geol.* **120**, 223–53.
- McDougall, I. & Honda, M. (1998). Primordial solar noble-gas component in the Earth: Consequences for the origin and evolution of the Earth and its atmosphere. In *The Earth's Mantle: Composition, Structure, and Evolution*, pp. 159–87, ed. I. Jackson. Cambridge University Press, Cambridge, England.

- McElhinny, M. W. & Senanayake, W. E. (1980). Paleomagnetic evidence for the existence of the geomagnetic field 3.5 Ga ago. *J. Geophys. Res.* **85**, 3523–8.
- McEwen, A. S. (1986). Tidal reorientation and the fracturing of Jupiter's moon Europa. *Nature* **321**, 49–51.
- McEwen, A. S., Keszthelyi, L., Geissler, P., Simonelli, D. P., Carr, M. H., Johnson, T. V., Klaasen, K. P., Breneman, H. H., Jones, T. J., Kaufman, J. M., Magee, K. P., Senske, D. A., Belton, M. J. S., & Schubert, G. (1998a). Active volcanism on Io as seen by Galileo SSI. *Icarus* **135**, 181–219.
- McEwen, A. S., Keszthelyi, L., Spencer, J. R., Schubert, G., Matson, D. L., Lopes-Gautier, R., Klaasen, K. P., Johnson, T. V., Head, J. W., Geissler, P., Fagents, S., Davies, A. G., Carr, M. H., Breneman, H. H., & Belton, M. J. S. (1998b). High-temperature silicate volcanism on Jupiter's moon Io. *Science* **281**, 87–90.
- McGill, G. E. & Dimitriou, A. M. (1990). Origin of the Martian global dichotomy by crustal thinning in the late Noachian or early Hesperian. *J. Geophys. Res.* **95**, 12595–605.
- McGill, G. E., Steenstrup, S. J., Barton, C., & Ford, P. G. (1981). Continental rifting and the origin of Beta Regio, Venus. *Geophys. Res. Lett.* **8**, 737–40.
- McGovern, P. J. & Schubert, G. (1989). Thermal evolution of the Earth: Effects of volatile exchange between atmosphere and interior. *Earth Planet. Sci. Lett.* **96**, 27–37.
- McKenzie, D. P. (1967). Some remarks on heat flow and gravity anomalies. *J. Geophys. Res.* **72**, 6261–73.
- (1969). Speculations on the consequences and causes of plate motions. *Geophys. J. Roy. Astron. Soc.* **18**, 1–32.
- (1970). Temperature and potential temperature beneath island arcs. *Tectonophysics* **10**, 357–66.
- McKenzie, D. (1977a). Surface deformation, gravity anomalies and convection. *Geophys. J. Roy. Astron. Soc.* **48**, 211–38.
- McKenzie, D. P. (1977b). The initiation of trenches: A finite amplitude instability. In *Island Arcs, Deep Sea Trenches and Back-Arc Basins*, pp. 57–61, eds. M. Talwani & W. C. Pitman, III, Maurice Ewing Series 1. American Geophysical Union, Washington, DC, second edition.
- McKenzie, D. (1979). Finite deformation during fluid flow. *Geophys. J. Roy. Astron. Soc.* **58**, 689–715.
- (1984a). A possible mechanism for epeirogenic uplift. *Nature* **307**, 616–8.
- (1984b). The generation and compaction of partially molten rock. *J. Petrol.* **25**, 713–65.
- (1985). The extraction of magma from the crust and mantle. *Earth Planet. Sci. Lett.* **74**, 81–91.
- (1988). The symmetry of convective transitions in space and time. *J. Fluid Mech.* **191**, 287–339.
- (1989). Some remarks on the movement of small melt fractions in the mantle. *Earth Planet. Sci. Lett.* **95**, 53–72.
- (1994). The relationship between topography and gravity on Earth and Venus. *Icarus* **112**, 55–88.
- McKenzie, D. & Bickle, M. J. (1988). The volume and composition of melt generated by extension of the lithosphere. *J. Petrol.* **29**, 625–79.
- McKenzie, D. P. & Morgan, W. J. (1969). Evolution of triple junctions. *Nature* **224**, 125–33.
- McKenzie, D. & O'Nions, R. K. (1983). Mantle reservoirs and ocean island basalts. *Nature* **301**, 229–31.
- (1991). Partial melt distributions from inversion of rare earth element concentrations. *J. Petrol.* **32**, 1021–91.
- McKenzie, D. P. & Parker, R. L. (1967). The north Pacific, an example of tectonics on a sphere. *Nature* **216**, 1276–80.
- McKenzie, D. & Richter, F. M. (1981). Parameterized thermal convection in a layered region and the thermal history of the Earth. *J. Geophys. Res.* **86**, 11667–80.
- McKenzie, D. & Sclater, J. G. (1968). Heat flow inside the island arcs of the northwestern Pacific. *J. Geophys. Res.* **73**, 3173–9.
- McKenzie, D., Roberts, J., & Weiss, N. (1973). Numerical models of convection in the Earth's mantle. *Tectonophysics* **19**, 89–103.
- McKenzie, D. P., Roberts, J. M., & Weiss, N. O. (1974). Convection in the Earth's mantle: Towards a numerical simulation. *J. Fluid Mech.* **62**, 465–538.
- McKenzie, D., Ford, P. G., Johnson, C., Parsons, B., Sandwell, D., Saunders, S., & Solomon, S. C. (1992). Features on Venus generated by plate boundary processes. *J. Geophys. Res.* **97**, 13533–44.

- McKinnon, W. B. (1998). Geodynamics of icy satellites. In *Solar System Ices*, pp. 525–50, eds. B. Schmitt, C. DeBergh, & M. Festou. Kluwer Acad. Pub., Dordrecht, Holland.
- (1999). Convective instability in Europa's floating ice shell. *Geophys. Res. Lett.* **26**, 951–4.
- McKinnon, W. B., Zahnle, K. J., Ivanov, B. A., & Melosh, H. J. (1997). Cratering on Venus: Models and observations. In *Venus II: Geology, Geophysics, Atmosphere, and Solar Wind Environment*, pp. 969–1014, eds. S. W. Bougher, D. M. Hunten, & R. J. Phillips. The University of Arizona Press, Tucson.
- McLennan, S. M. (1988). Recycling of the continental crust. *Pure Appl. Geophys.* **128**, 683–724.
- McLennan, S. M. & Taylor, S. R. (1982). Geochemical constraints on the growth of the continental crust. *J. Geol.* **90**, 347–61.
- McNutt, M. (1987). Temperature beneath midplate swells: The inverse problem. In *Seamounts, Islands, and Atolls*, pp. 123–32, eds. B. H. Keating, P. Fryer, R. Batiza, & G. W. Boehlert, Geophysical Monograph 43. American Geophysical Union, Washington, DC.
- McNutt, M. K. (1998). Superswells. *Rev. Geophys.* **36**, 211–44.
- McNutt, M. K. & Fischer, K. M. (1987). The South Pacific superswell. In *Seamounts, Islands, and Atolls*, pp. 25–34, eds. B. H. Keating, P. Fryer, R. Batiza, & G. W. Boehlert, Geophysical Monograph 43. American Geophysical Union, Washington, DC.
- McSween, H. Y. (1985). SNC meteorites: Clues to Martian petrologic evolution? *Rev. Geophys.* **23**, 391–416.
- Meijer, A. (1985). Pb isotope evolution in the Earth: A proposal. *Geophys. Res. Lett.* **12**, 741–4.
- Meissner, R. (1986). *The Continental Crust: A Geophysical Approach*, volume 34 of *International Geophysics Series*. Academic Press, London, 426 pp.
- Meissner, R. & Wever, T. (1989). Continental crustal structure. In *The Encyclopedia of Solid Earth Geophysics*, pp. 75–89, ed. D. E. James, Encyclopedia of Earth Sciences. Van Nostrand Reinhold, New York.
- Melosh, H. J. (1990). Giant impacts and the thermal state of the early Earth. In *Origin of the Earth*, pp. 69–83, eds. H. E. Newsom & J. H. Jones. Oxford University Press, New York.
- Melosh, H. J. & Raefsky, A. (1980). The dynamical origin of subduction zone topography. *Geophys. J. Roy. Astron. Soc.* **60**, 333–54.
- Mercier, J.-C., Anderson, D. A., & Carter, N. L. (1977). Stress in the lithosphere: Inferences from steady state flow of rocks. *Pure Appl. Geophys.* **115**, 199–226.
- Meriaux, C. & Jaupart, C. (1998). Dike propagation through an elastic plate. *J. Geophys. Res.* **103**, 18295–314.
- Meriaux, C., Lister, J. R., Lyakhovsky, V., & Agnon, A. (1999). Dyke propagation with distributed damage of the host rock. *Earth Planet. Sci. Lett.* **165**, 177–85.
- Merrill, R. T. & McElhinny, M. W. (1983). *The Earth's Magnetic Field: Its History, Origin and Planetary Perspective*. Academic Press, London, 401 pp.
- Meyer, H. O. A. (1987). Inclusions in diamond. In *Mantle Xenoliths*, pp. 501–23, ed. P. H. Nixon. J. Wiley & Sons, Chichester, England.
- Mihaljan, J. M. (1962). A rigorous exposition of the Boussinesq approximations applicable to a thin layer of fluid. *Astrophys. J.* **136**, 1126–33.
- Milne, G. A., Mitrovica, J. X., & Forte, A. M. (1998). The sensitivity of glacial isostatic adjustment predictions to a low-viscosity layer at the base of the upper mantle. *Earth Planet. Sci. Lett.* **154**, 265–78.
- Mimouni, A. & Rabinowicz, M. (1988). The old continental shields stability related to mantle convection. *Geophys. Res. Lett.* **15**, 68–71.
- Mitrovica, J. X. (1996). Haskell [1935] revisited. *J. Geophys. Res.* **101**, 555–69.
- Mitrovica, J. X. & Forte, A. M. (1997). Radial profile of mantle viscosity: Results from the joint inversion of convection and postglacial rebound observables. *J. Geophys. Res.* **102**, 2751–69.
- Mitrovica, J. X. & Jarvis, G. T. (1987). A numerical study of thermal convection between rigid horizontal boundaries. *Geophys. Astrophys. Fluid Dyn.* **38**, 193–223.
- Mitrovica, J. X. & Peltier, W. R. (1991). Radial resolution in the inference of mantle viscosity from observations of glacial isostatic adjustment. In *Glacial Isostasy, Sea-Level and Mantle Rheology*,

- pp. 63–78, eds. R. Sabadini, K. Lambeck, & E. Boschi. Kluwer Academic Publishers, Dordrecht, The Netherlands.
- Mitrovica, J. X. & Peltier, W. R. (1995). Constraints on mantle viscosity based upon the inversion of post-glacial uplift data from the Hudson Bay region. *Geophys. J. Int.* **122**, 353–77.
- Miyashiro, A., Aki, K., & Celâl Şengör, A. (1982). *Orogeny*. John Wiley & Sons, New York, 242 pp.
- Mohorovicic, A. (1909). Das Beben vom 8.X. *Jb. met. Obs. Zagreb* **9**, 1–63.
- Molnar, P. & Atwater, T. (1973). Relative motion of hot spots in the mantle. *Nature* **246**, 288–91.
- (1978). Interarc spreading and cordilleran tectonics as alternates related to the age of subducted oceanic lithosphere. *Earth Planet. Sci. Lett.* **41**, 330–40.
- Molnar, P. & Stock, J. (1987). Relative motions of hotspots in the Pacific, Atlantic and Indian oceans since late Cretaceous time. *Nature* **327**, 587–91.
- Molnar, P. & Tapponnier, P. (1975). Cenozoic tectonics of Asia: Effects of a continental collision. *Science* **189**, 419–26.
- (1978). Active tectonics of Tibet. *J. Geophys. Res.* **83**, 5361–75.
- (1981). A possible dependence of tectonic strength on the age of the crust in Asia. *Earth Planet. Sci. Lett.* **52**, 107–14.
- Monnereau, M. & Rabinowicz, M. (1996). Is the 670 km phase transition able to layer the Earth's convection in a mantle with depth-dependent viscosity? *Geophys. Res. Lett.* **23**, 1001–4.
- Monnereau, M., Rabinowicz, M., & Arquis, E. (1993). Mechanical erosion and reheating of the lithosphere: A numerical model for hotspot swells. *J. Geophys. Res.* **98**, 809–23.
- Montagner, J. (1994). Can seismology tell us anything about convection in the mantle? *Rev. Geophys.* **32**, 115–37.
- Montague, N. L., Kellogg, L. H. & Manga, M. (1998). High Rayleigh number thermo-chemical models of a dense boundary layer in D'' . *Geophys. Res. Lett.* **25**, 2345–8.
- Mooney, W. D. & Brocher, T. M. (1987). Coincident seismic reflection/refraction studies of the continental lithosphere: A global review. *Rev. Geophys.* **25**, 723–42.
- Mooney, W. D., Laske, G., & Masters, T. G. (1998). CRUST 5.1: A global crustal model at $5^\circ \times 5^\circ$. *J. Geophys. Res.* **103**, 727–47.
- Moorbath, S. (1978). Age and isotope evidence for the evolution of continental crust. *Phil. Trans. Roy. Soc. London A* **288**, 401–13.
- Moorbath, S., O'Nions, R. K., Pankhurst, R. J., Gale, N. H. & McGregor, V. R. (1972). Further rubidium-strontium age determination on very early Precambrian rocks of the Godthaab district, West Greenland. *Nature Phys. Sci.* **240**, 78–82.
- Moore, D. R. & Weiss, N. O. (1973). Two-dimensional Rayleigh-Bénard convection. *J. Fluid Mech.* **58**, 289–312.
- Moore, J. M., Asphaug, E., Sullivan, R. J., Klemaszewski, J. E., Bender, K. C., Greeley, R., Geissler, P. E., McEwen, A. S., Turtle, E. P., Phillips, C. B., Tufts, B. R., Head, J. W., Pappalardo, R. T., Jones, K. B., Chapman, C. R., Belton, M. J. S., Kirk, R. L., & Morrison, D. (1998a). Large impact features on Europa: Results of the Galileo nominal mission. *Icarus* **135**, 127–45.
- Moore, W. B. & Schubert, G. (1995). Lithospheric thickness and mantle/lithosphere density contrast beneath Beta Regio, Venus. *Geophys. Res. Lett.* **22**, 429–32.
- (1997a). Lithospheric thinning and chemical buoyancy beneath the Hawaiian Swell. *Geophys. Res. Lett.* **24**, 1287–90.
- (1997b). Venusian crustal and lithospheric properties from nonlinear regressions of highland geoid and topography. *Icarus* **128**, 415–28.
- Moore, W. B., Schubert, G., & Tackley, P. J. (1998b). Three-dimensional simulations of plume-lithosphere interaction at the Hawaiian Swell. *Science* **279**, 1008–11.
- (1999). The role of rheology in lithospheric thinning by mantle plumes. *Geophys. Res. Lett.* **26**, 1073–6.
- Morabito, L. A., Synnott, S. P., Kupferman, P. N., & Collins, S. A. (1979). Discovery of currently active extraterrestrial volcanism. *Science* **204**, 972.
- Morelli, A. (1993). Teleseismic tomography: Core–mantle boundary. In *Seismic Tomography: Theory and Practice*, pp. 163–89, eds. H. M. Iyer & K. Hirahara. Chapman and Hall, London.

- Morelli, A. & Dziewonski, A. M. (1987). Topography of the core-mantle boundary and lateral homogeneity of the liquid core. *Nature* **325**, 678–83.
- Morelli, A., Dziewonski, A. M., & Woodhouse, J. H. (1986). Anisotropy of the inner core inferred from PKIP travel-times. *Geophys. Res. Lett.* **13**, 1545–8.
- Moresi, L. & Gurnis, M. (1996). Constraints on the lateral strength of slabs from three-dimensional dynamic flow models. *Earth Planet. Sci. Lett.* **138**, 15–28.
- Moresi, L.-N. & Lenardic, A. (1997). Three-dimensional numerical simulations of crustal deformation and subcontinental mantle convection. *Earth Planet. Sci. Lett.* **150**, 233–43.
- Moresi, L.-N. & Solomatov, V. S. (1995). Numerical investigation of 2D convection with extremely large viscosity variations. *Phys. Fluids* **7**, 2154–62.
- Moresi, L. & Solomatov, V. (1998). Mantle convection with a brittle lithosphere: Thoughts on the global tectonic styles of the Earth and Venus. *Geophys. J. Int.* **133**, 669–82.
- Morgan, P. & Phillips, R. J. (1983). Hot spot heat transfer: Its application to Venus and implications to Venus and Earth. *J. Geophys. Res.* **88**, 8305–17.
- Morgan, W. J. (1968). Rises, trenches, great faults, and crustal blocks. *J. Geophys. Res.* **73**, 1959–82.
- (1971). Convection plumes in the lower mantle. *Nature* **230**, 42–3.
- (1972). Plate motions and deep mantle convection. *Geol. Soc. Am. Man.* **132**, 7–22.
- (1981). Hotspot tracks and the opening of the Atlantic and Indian oceans. In *The Oceanic Lithosphere*, pp. 443–87, ed. C. Emiliani, volume 7 of *The Sea*. J. Wiley & Sons, New York.
- (1983). Hotspot tracks and the early rifting of the Atlantic. *Tectonophysics* **94**, 123–9.
- Mori, J. & Helmberger, D. V. (1995). Localized boundary layer below the mid-Pacific velocity anomaly identified from a Pcp precursor. *J. Geophys. Res.* **100**, 20359–65.
- Morris, G. B., Raitt, R. W., & Shor, G. G. (1969). Velocity anisotropy and delay-time maps of the mantle near Hawaii. *J. Geophys. Res.* **74**, 4300–16.
- Morris, S. (1982). The effects of a strongly temperature-dependent viscosity on slow flow past a hot sphere. *J. Fluid Mech.* **124**, 1–26.
- Morris, S. & Canright, D. (1984). A boundary-layer analysis of Benard convection in a fluid of strongly temperature-dependent viscosity. *Phys. Earth Planet. Int.* **36**, 355–73.
- Morrison, D. & Telesco, C. M. (1980). Io: Observational constraints on internal energy and thermophysics of the surface. *Icarus* **44**, 226–33.
- Mottinger, N. A., Sjogren, W. L., & Bills, B. G. (1985). Venus gravity: A harmonic analysis and geophysical implications. *J. Geophys. Res.* **90**, 739–56.
- Mueller, R. D., Roest, W. R., Royer, J.-Y., Gahagan, L. M. & Sclater, J. G. (1997). Digital isochrons of the world's ocean floor. *J. Geophys. Res.* **102**, 3211–4.
- Mueller, S. (1977). A new model of the continental crust. In *The Earth's Crust: Its Nature and Physical Properties*, pp. 289–317, eds. J. G. Heacock, G. V. Keller, J. E. Oliver, & G. Simmons, Geophysical Monograph 20. American Geophysical Union, Washington, DC.
- Mueller, S. & Phillips, R. J. (1991). On the initiation of subduction. *J. Geophys. Res.* **96**, 651–65.
- Muller, P. M. & Sjogren, W. L. (1968). Mascons: Lunar mass concentrations. *Science* **161**, 680–4.
- Munk, W. H. & MacDonald, G. J. F. (1960). *The Rotation of the Earth: A Geophysical Discussion*. Cambridge University Press, London, 323 pp.
- Murase, T. & McBirney, A. R. (1973). Properties of some common igneous rocks and their melts at high temperatures. *Geol. Soc. Am. Bull.* **84**, 3563–92.
- Murnaghan, F. D. (1951). *Finite Deformation of an Elastic Solid*. John Wiley & Sons, New York, 140 pp.
- Mutter, C. Z. & Mutter, J. C. (1993). Variations in thickness of layer 3 dominate oceanic crustal structure. *Earth Planet. Sci. Lett.* **117**, 295–317.
- Nakada, M. & Lambeck, K. (1989). Late Pleistocene and Holocene sea-level change in the Australian region and mantle rheology. *Geophys. J.* **96**, 497–517.
- Nakakuki, T. & Fujimoto, H. (1994). Interaction of the upwelling plume with the phase and chemical boundaries (2) – Effects of the pressure-dependent viscosity. *J. Geomag. Geoelectr.* **46**, 587–602.

- Nakakuki, T., Sato, H., & Fujimoto, H. (1994). Interaction of the upwelling plume with the phase and chemical boundary at the 670 km discontinuity: Effects of temperature-dependent viscosity. *Earth Planet. Sci. Lett.* **121**, 369–84.
- Nakakuki, T., Yuen, D. A. & Honda, S. (1997). The interaction of plumes with the transition zone under continents and oceans. *Earth Planet. Sci. Lett.* **146**, 379–91.
- Nakamura, Y. (1983). Seismic velocity structure of the lunar mantle. *J. Geophys. Res.* **88**, 677–86.
- Nakamura, Y., Duennebier, F. K., Latham, G. V., & Dorman, H. J. (1976). Structure of the lunar mantle. *J. Geophys. Res.* **81**, 4818–24.
- Nakiboglu, S. M. & Lambeck, K. (1983). A reevaluation of the isostatic rebound of Lake Bonneville. *J. Geophys. Res.* **88**, 10439–47.
- Namiki, N. & Solomon, S. C. (1994). Impact crater densities on volcanoes and coronae on Venus: Implications for volcanic resurfacing. *Science* **265**, 929–33.
- (1998). Volcanic degassing of argon and helium and the history of crustal production on Venus. *J. Geophys. Res.* **103**, 3655–77.
- Nance, R. D., Worsley, T. R., & Moody, J. B. (1986). Post-Archean biogeochemical cycles and long-term episodicity in tectonic processes. *Geology* **14**, 514–8.
- Nansen, F. (1928). *The Earth's Crust, Its Surface-Forms, and Isostatic Adjustment*. I Kommisjon Hos Jacob Dybwab, Oslo, Norway, Avhandlinger Utgitt Av Det Norske Videnskaps-Akademii I Oslo I. Mat. Naturv. Klasse 1927. No. 12, 121 pp.
- Nash, D. B., Carr, M. H., Gradie, J., Hunten, D. M. & Yoder, C. F. (1986). Io. In *Satellites*, pp. 629–88, eds. J. A. Burns & M. S. Matthews. The University of Arizona Press, Tucson.
- Nataf, H.-C. (1991). Mantle convection, plates, and hotspots. *Tectonophysics* **187**, 361–71.
- Nataf, H.-C. & Houard, S. (1993). Seismic discontinuity at the top of D'': A world-wide feature? *Geophys. Res. Lett.* **20**, 2371–4.
- Nataf, H. C. & Richter, F. M. (1982). Convection experiments in fluids with highly temperature-dependent viscosity and the thermal evolution of the planets. *Phys. Earth Planet. Int.* **29**, 320–9.
- Nataf, H.-C. & VanDecar, J. (1993). Seismological detection of a mantle plume? *Nature* **364**, 115–20.
- Nataf, H., Nakanishi, I., & Anderson, D. L. (1986). Measurements of mantle wave velocities and inversion for lateral heterogeneities and anisotropy: 3. Inversion. *J. Geophys. Res.* **91**, 7261–307.
- Navon, O. & Stolper, E. (1987). Geochemical consequences of melt percolation: The upper mantle as a chromatographic column. *J. Geol.* **95**, 285–307.
- Navrotsky, A. (1995). Thermodynamic properties of minerals. In *Mineral Physics and Crystallography: A Handbook of Physical Constants*, pp. 18–28, ed. T. J. Ahrens. American Geophysical Union, Washington, DC.
- Nelson, B. K. & DePaolo, D. J. (1984). 1700-Myr greenstone volcanic successions in southwestern North America and isotopic evolution of Proterozoic mantle. *Nature* **312**, 143–6.
- (1985). Rapid production of continental crust 1.7 to 1.9 b.y. ago: Nd isotopic evidence from the basement of the North American mid-continent. *Geol. Soc. Am. Bull.* **96**, 746–54.
- Ness, N. F., Behannon, K. W., Lepping, R. P., Whang, Y. C., & Schatten, K. H. (1974). Magnetic field observations near Mercury: Preliminary results from Mariner 10. *Science* **185**, 151–60.
- Ness, N. F., Behannon, K. W., Lepping, R. P., & Whang, Y. C. (1975). The magnetic field of Mercury, 1. *J. Geophys. Res.* **80**, 2708–16.
- Neukum, G., Wagner, R., Wolf, U., Ivanov, B. A., Head, J. W., Pappalardo, R. T., Klemaszewski, J. E., Greeley, R., & Belton, M. J. S. (1998). Cratering chronology in the Jovian system and derivation of absolute ages (CD-ROM, abstract 1742). In *Lunar and Planetary Science XXIX*, Lunar and Planetary Institute, Houston, Texas.
- Nicolas, A. (1986). A melt extraction model based on structural studies in mantle peridotites. *J. Petrol.* **27**, 999–1022.
- (1990). Melt extraction from mantle peridotites: Hydrofracturing and porous flow, with consequences for oceanic ridge activity. In *Magma Transport and Storage*, pp. 159–73, ed. M. P. Ryan. John Wiley & Sons, Chichester, England.
- Nicolas, A. & Jackson, M. (1982). High temperature dikes in peridotites: Origin by hydraulic fracturing. *J. Petrol.* **23**, 568–82.

- Nicolaysen, L. O. (1985). On the physical basis for the extended Wilson cycle, in which most continents coalesce and then disperse again. *Trans. Geol. Soc. South Africa* **88**, 562–80.
- Nimmo, F. & McKenzie, D. (1998). Volcanism and tectonics on Venus. *Ann. Rev. Earth Planet. Sci.* **26**, 23–51.
- Niu, F. & Kawakatsu, H. (1995). Direct evidence for the undulation of the 660-km discontinuity beneath Tonga: Comparison of Japan and California array data. *Geophys. Res. Lett.* **22**, 531–4.
- Nockolds, S. R. (1954). Average chemical compositions of some igneous rocks. *Geol. Soc. Am. Bull.* **65**, 1007–32.
- Nyquist, L. E., Shih, C.-Y., Wooden, J. L., Bansal, B. M., & Wiesmann, H. (1979). The Sr and Nd isotopic record of Apollo 12 basalts: Implications for lunar geochemical evolution. *Proc. Lunar Planet. Sci. Conf. 10th*, 77–114.
- Obata, M. & Karato, S. (1995). Ultramafic pseudotachylite from the Balmuccia peridotite, Ivrea–Verbano zone, northern Italy. *Tectonophysics* **242**, 313–28.
- O'Connell, R. J., Gable, C. W., & Hager, B. H. (1991). Toroidal-poloidal partitioning of lithospheric plate motions. In *Glacial Isostasy, Sea-Level and Mantle Rheology*, pp. 535–51, eds. R. Sabadini, K. Lambeck & E. Boschi. Kluwer Academic Publishers, Dordrecht.
- Officer, C. & Page, J. (1993). *Tales of the Earth: Paroxysms and Perturbations of the Blue Planet*. Oxford University Press, New York, 226 pp.
- Officer, C. B., Hallam, A., Drake, C. L., & Devine, J. D. (1987). Late Cretaceous and paroxysmal Cretaceous/Tertiary extinctions. *Nature* **326**, 143–9.
- Ogawa, M., Schubert, G. & Zebib, A. (1991). Numerical simulations of three-dimensional thermal convection in a fluid with strongly temperature-dependent viscosity. *J. Fluid Mech.* **233**, 299–328.
- Ogura, Y. & Phillips, N. A. (1962). Scale analysis of deep and shallow convection in the atmosphere. *J. Atmos. Sci.* **19**, 173–9.
- Ohtani, E. & Ringwood, A. E. (1984). Composition of the core. I. Solubility of oxygen in molten iron at high temperatures. *Earth Planet. Sci. Lett.* **71**, 85–93.
- Ojakangas, G. W. & Stevenson, D. J. (1986). Episodic volcanism of tidally heated satellites with application to Io. *Icarus* **66**, 341–58.
- (1989a). Polar wander of an ice shell on Europa. *Icarus* **81**, 242–70.
- (1989b). Thermal state of an ice shell on Europa. *Icarus* **81**, 220–41.
- Oldenburg, D. W. & Brune, J. N. (1972). Ridge transform fault spreading pattern in freezing wax. *Science* **178**, 301–4.
- (1975). An explanation for the orthogonality of ocean ridges and transform faults. *J. Geophys. Res.* **80**, 2575–85.
- Oldham, R. D. (1906). The constitution of the interior of the Earth, as revealed by earthquakes. *Quart. J. Geol. Soc. London* **62**, 456–75.
- Oliver, D. S. & Booker, J. R. (1983). Planform of convection with strongly temperature-dependent viscosity. *Geophys. Astrophys. Fluid Dyn.* **27**, 73–85.
- Olson, P. (1981). Mantle convection with spherical effects. *J. Geophys. Res.* **86**, 4881–90.
- (1984). An experimental approach to thermal convection in a two-layered mantle. *J. Geophys. Res.* **89**, 11293–301.
- (1987). A comparison of heat transfer laws for mantle convection at very high Rayleigh numbers. *Phys. Earth Planet. Int.* **48**, 153–60.
- (1990). Hot spots, swells and mantle plumes. In *Magma Transport and Storage*, pp. 33–51, ed. M. P. Ryan. John Wiley & Sons Ltd., Chichester, U.K.
- Olson, P. & Bercovici, D. (1991). On the equipartition of kinetic energy in plate tectonics. *Geophys. Res. Lett.* **18**, 1751–4.
- Olson, P. & Christensen, U. (1986). Solitary wave propagation in a fluid conduit within a viscous matrix. *J. Geophys. Res.* **91**, 6367–74.
- Olson, P. & Corcos, G. M. (1980). A boundary layer model for mantle convection with surface plates. *Geophys. J. Roy. Astron. Soc.* **62**, 195–219.
- Olson, P. & Kincaid, C. (1991). Experiments on the interaction of thermal convection and compositional layering at the base of the mantle. *J. Geophys. Res.* **96**, 4347–54.

- Olson, P. & Singer, H. (1985). Creeping plumes. *J. Fluid Mech.* **158**, 511–31.
- Olson, P. & Yuen, D. A. (1982). Thermochemical plumes and mantle phase transitions. *J. Geophys. Res.* **87**, 3993–4002.
- Olson, P., Yuen, D. A., & Balsiger, D. (1984a). Convective mixing and the fine structure of mantle heterogeneity. *Phys. Earth Planet. Int.* **36**, 291–304.
- (1984b). Mixing of passive heterogeneities by mantle convection. *J. Geophys. Res.* **89**, 425–36.
- Olson, P., Schubert, G., & Anderson, C. (1987). Plume formation in the D''-layer and the roughness of the core–mantle boundary. *Nature* **327**, 409–13.
- Olson, P., Schubert, G., Anderson, C. & Goldman, P. (1988). Plume formation and lithosphere erosion: A comparison of laboratory and numerical experiments. *J. Geophys. Res.* **93**, 15065–84.
- Olson, P., Schubert, G., & Anderson, C. (1993). Structure of axisymmetric mantle plumes. *J. Geophys. Res.* **98**, 6829–44.
- O’Nions, R. K. (1987). Relationships between chemical and convective layering in the Earth. *J. Geol. Soc. London* **144**, 259–74.
- O’Nions, R. K. & Hamilton, P. J. (1981). Isotope and trace element models of crustal evolution. *Phil. Trans. Roy. Soc. London A* **301**, 473–87.
- O’Nions, R. K. & Oxburgh, E. R. (1983). Heat and helium in the Earth. *Nature* **306**, 429–31.
- O’Nions, R. K. & Pankhurst, R. J. (1974). Petrogenetic significance of isotope and trace element variations in volcanic rocks from the Mid-Atlantic. *J. Petrol.* **15**, 603–34.
- O’Nions, R. K. & Tolstikhin, I. N. (1996). Limits on the mass flux between lower and upper mantle and stability of layering. *Earth Planet. Sci. Lett.* **139**, 213–22.
- O’Nions, R. K., Evensen, N. M., & Hamilton, P. J. (1979). Geochemical modeling of mantle differentiation and crustal growth. *J. Geophys. Res.* **84**, 6091–101.
- O’Nions, R. K., Hamilton, P. J. & Hooker, P. J. (1983). A Nd isotope investigation of sediments related to crustal development in the British Isles. *Earth Planet. Sci. Lett.* **63**, 229–40.
- Orcutt, J. A., McClain, J. S., & Burnett, M. (1984). Evolution of the ocean crust: Results from recent seismic experiments. In *Ophiolites and Oceanic Lithosphere*, pp. 7–16, eds. I. G. Gass, S. J. Lippard & A. W. Shelton, volume 13. Geol. Soc. Special Publ., London.
- O'Reilly, T. C. & Davies, G. F. (1981). Magma transport of heat on Io: A mechanism allowing a thick lithosphere. *Geophys. Res. Lett.* **8**, 313–6.
- Orowan, E. (1964). Continental drift and the origin of mountains – Hot creep and creep fracture are crucial factors in the formation of continents and mountains. *Science* **146**, 1003–10.
- (1965). Convection in a non-Newtonian mantle, continental drift, and mountain building. *Phil. Trans. Roy. Soc. London A* **258**, 284–313.
- Osako, M. & Ito, E. (1991). Thermal diffusivity of MgSiO₃ perovskite. *Geophys. Res. Lett.* **18**, 239–42.
- Ottino, J. M. (1989). *The Kinematics of Mixing: Stretching, Chaos, and Transport*. Cambridge University Press, Cambridge, England, 364 pp.
- (1990). Mixing, chaotic advection, and turbulence. *Ann. Rev. Fluid Mech.* **22**, 207–53.
- Owen, T. (1992). The composition and early history of the atmosphere of Mars. In *Mars*, pp. 818–34, eds. H. H. Kieffer, B. M. Jakosky, C. W. Snyder, & M. S. Matthews. The University of Arizona Press, Tucson.
- Oxburgh, E. R. (1972). Flake tectonics and continental collision. *Nature* **239**, 202–4.
- Oxburgh, E. R. & O’Nions, R. K. (1987). Helium loss, tectonics, and the terrestrial heat budget. *Science* **237**, 1583–8.
- Oxburgh, E. R. & Parmentier, E. M. (1977). Compositional and density stratification in oceanic lithosphere: Causes and consequences. *J. Geol. Soc. London* **133**, 343–55.
- Oxburgh, E. R. & Turcotte, D. L. (1968). Problem of high heat flow and volcanism associated with zones of descending mantle convective flow. *Nature* **218**, 1041–3.
- (1970). Thermal structure of island arcs. *Geol. Soc. Am. Bull.* **81**, 1665–88.
- Ozima, M. (1975). Ar isotopes and Earth–atmosphere evolution models. *Geochim. Cosmochim. Acta* **39**, 1127–34.
- (1994). Noble gas state in the mantle. *Rev. Geophys.* **32**, 405–26.

- Page, R. W., McCulloch, M. T., & Black, L. P. (1984). Isotopic record of major Precambrian events in Australia. *Precam. Geol. 27th Int. Geol. Congr.* **5**, 25–72.
- Pakiser, L. C. & Robinson, R. (1966). Composition of the continental crust as estimated from seismic observations. In *The Earth Beneath the Continents – A Volume of Geophysical Studies in Honor of Merle A. Tuve*, pp. 620–6, eds. J. S. Steinhart & T. J. Smith, Geophysical Monograph 10. American Geophysical Union, Washington, DC.
- Palm, E. (1960). On the tendency towards hexagonal cells in steady convection. *J. Fluid Mech.* **8**, 183–92.
- Palm, E. & Øiann, H. (1964). Contribution to the theory of cellular thermal convection. *J. Fluid Mech.* **19**, 353–65.
- Palm, E., Ellingsen, T., & Gjevik, B. (1967). On the occurrence of cellular motion in Bénard convection. *J. Fluid Mech.* **30**, 651–61.
- Papanastassiou, D. A., DePaolo, D. J., & Wasserburg, G. J. (1977). Rb–Sr and Sm–Nd chronology and genealogy of mare basalts from the Sea of Tranquillity. *Proc. Lunar Planet. Sci. Conf. 8th*, 1639–72.
- Pappalardo, R. T., Head, J. W., Greeley, R., Sullivan, R. J., Pilcher, C., Schubert, G., Moore, W. B., Carr, M. H., Moore, J. M., Belton, M. J. S. & Goldsby, D. L. (1998a). Geological evidence for solid-state convection in Europa's ice shell. *Nature* **391**, 365–8.
- Pappalardo, R. T., Head, J. W., Collins, G. C., Kirk, R. L., Neukum, G., Oberst, J., Giese, B., Greeley, R., Chapman, C. R., Helfenstein, P., Moore, J. M., McEwen, A., Tufts, B. R., Senske, D. A., Breneman, H. H., & Klaasen, K. (1998b). Grooved terrain on Ganymede: First results from Galileo high-resolution imaging. *Icarus* **135**, 276–302.
- Pappalardo, R. T., Belton, M. J. S., Breneman, H. H., Carr, M. H., Chapman, C. R., Collins, G. C., Denk, T., Fagents, S., Geissler, P. E., Giese, B., Greeley, R., Greenberg, R., Head, J. W., Helfenstein, P., Hoppa, G., Kadel, S. D., Klaasen, K. P., Klemaszewski, J. E., Magee, K., McEwen, A. S., Moore, J. M., Moore, W. B., Neukum, G., Phillips, C. B., Prockter, L. M., Schubert, G., Senske, D. A., Sullivan, R. J., Tufts, B. R., Turtle, E. P., Wagner, R., & Williams, K. K. (1999). Does Europa have a subsurface ocean? Evaluation of the geological evidence. *J. Geophys. Res.* **104**, 24015–55.
- Pari, G. & Peltier, W. R. (1996). The free-air gravity constraint on subcontinental mantle dynamics. *J. Geophys. Res.* **101**, 28105–32.
- Parise, J. B., Wang, Y., Yeganeh-Haeri, A., Cox, D. E., & Fei, Y. (1990). Crystal structure and thermal expansion of (Mg,Fe)SiO₃ perovskite. *Geophys. Res. Lett.* **17**, 2089–92.
- Parmentier, E. M. (1978). A study of thermal convection in non-Newtonian fluids. *J. Fluid Mech.* **84**, 1–11.
- Parmentier, E. M. & Haxby, W. F. (1986). Thermal stresses in the oceanic lithosphere: Evidence from geoid anomalies at fracture zones. *J. Geophys. Res.* **91**, 7193–204.
- Parmentier, E. M. & Hess, P. C. (1992). Chemical differentiation of a convecting planetary interior: Consequences for a one plate planet such as Venus. *Geophys. Res. Lett.* **19**, 2015–8.
- Parmentier, E. M. & Morgan, III, J. (1982). Thermal convection in non-Newtonian fluids: Volumetric heating and boundary layer scaling. *J. Geophys. Res.* **87**, 7757–62.
- Parmentier, E. M. & Turcotte, D. L. (1978). Two-dimensional mantle flow beneath a rigid accreting lithosphere. *Phys. Earth Planet. Int.* **17**, 281–9.
- Parmentier, E. M., Turcotte, D. L., & Torrance, K. E. (1975). Numerical experiments on the structure of mantle plumes. *J. Geophys. Res.* **80**, 4417–24.
- (1976). Studies of finite amplitude non-Newtonian thermal convection with application to convection in the Earth's mantle. *J. Geophys. Res.* **81**, 1839–46.
- Parmentier, E. M., Sotin, C., & Travis, B. J. (1994). Turbulent 3-D thermal convection in an infinite Prandtl number, volumetrically heated fluid: Implications for mantle dynamics. *Geophys. J. Int.* **116**, 241–51.
- Parsons, B. (1981). The rates of plate creation and consumption. *Geophys. J. Roy. Astron. Soc.* **67**, 437–48.
- (1982). Causes and consequences of the relation between area and age of the ocean floor. *J. Geophys. Res.* **87**, 289–302.
- Parsons, B. & McKenzie, D. (1978). Mantle convection and the thermal structure of the plates. *J. Geophys. Res.* **83**, 4485–96.

- Parsons, B. & Sclater, J. G. (1977). An analysis of the variation of ocean floor bathymetry and heat flow with age. *J. Geophys. Res.* **82**, 803–27.
- Patchett, J. & Chauvel, C. (1984). The mean life of continents is currently not constrained by Nd and Hf isotopes (comment). *Geophys. Res. Lett.* **11**, 151–3.
- Patchett, P. J., Kouvo, O., Hedge, C. E., & Tatsumoto, M. (1981). Evolution of continental crust and mantle heterogeneity: Evidence from Hf isotopes. *Contrib. Mineral. Petrol.* **78**, 279–97.
- Patterson, C. C. (1956). Age of meteorites and the Earth. *Geochim. Cosmochim. Acta* **10**, 230–7.
- Peacock, S. M., Rushmer, T. & Thompson, A. B. (1994). Partial melting of subducting oceanic crust. *Earth Planet. Sci. Lett.* **121**, 227–44.
- Peale, S. J. (1986). Orbital resonances, unusual configurations and exotic rotation states among planetary satellites. In *Satellites*, pp. 159–223, eds. J. A. Burns & M. S. Matthews. The University of Arizona Press, Tucson.
- (1988). The rotational dynamics of Mercury and the state of its core. In *Mercury*, pp. 461–93, eds. F. Vilas, C. R. Chapman, & M. S. Matthews. The University of Arizona Press, Tucson.
- Peale, S. J. & Cassen, P. (1978). Contribution of tidal dissipation to lunar thermal history. *Icarus* **36**, 245–69.
- Peale, S. J., Cassen, P., & Reynolds, R. T. (1979). Melting of Io by tidal dissipation. *Science* **203**, 892–4.
- Pearl, J. C. & Sinton, W. M. (1982). Hot spots of Io. In *Satellites of Jupiter*, pp. 724–55, ed. D. Morrison. The University of Arizona Press, Tucson.
- Pearson, D. G., Davies, G. R., Nixon, P. H., & Milledge, H. J. (1989). Graphitized diamonds from a peridotite massif in Morocco and implications for anomalous diamond occurrences. *Nature* **338**, 60–2.
- Pekeris, C. L. (1935). Thermal convection in the interior of the Earth. *Mon. Not. Roy. Astron. Soc., Geophys. Suppl.* **3**, 343–67.
- Pellew, A. & Southwell, R. V. (1940). On maintained convective motion in a fluid heated from below. *Proc. Roy. Soc. London A* **176**, 312–43.
- Peltier, W. R. (1974). The impulse response of a Maxwell Earth. *Rev. Geophys. Space Phys.* **12**, 649–69.
- (1981). Ice age geodynamics. *Ann. Rev. Earth Planet. Sci.* **9**, 199–225.
- (1989). Mantle viscosity. In *Mantle Convection: Plate Tectonics and Global Dynamics*, pp. 389–478, ed. W. R. Peltier, volume 4 of *The Fluid Mechanics of Astrophysics and Geophysics*. Gordon and Breach Science Publishers, New York, 881 pp.
- (1996a). Mantle viscosity and ice-age ice sheet topography. *Science* **273**, 1359–64.
- (1996b). Phase-transition modulated mixing in the mantle of the Earth. *Phil. Trans. Roy. Soc. London A* **354**, 1425–47.
- Peltier, W. R. & Jarvis, G. T. (1982). Whole mantle convection and the thermal evolution of the Earth. *Phys. Earth Planet. Int.* **29**, 281–304.
- Peltier, W. R. & Jiang, X. (1996). Glacial isostatic adjustment and Earth rotation: Refined constraints on the viscosity of the deepest mantle. *J. Geophys. Res.* **101**, 3269–90.
- Peltier, W. R. & Solheim, L. P. (1992). Mantle phase transitions and layered chaotic convection. *Geophys. Res. Lett.* **19**, 321–4.
- Peltier, W. R., Jarvis, G. T., Forte, A. M., & Solheim, L. P. (1989). The radial structure of the general mantle circulation. In *Mantle Convection: Plate Tectonics and Global Dynamics*, pp. 765–815, ed. W. R. Peltier, volume 4 of *The Fluid Mechanics of Astrophysics and Geophysics*. Gordon and Breach Science Publishers, New York, 881 pp.
- Pettengill, G. H., Eliason, E., Ford, P. G., Loriot, G. B., Masursky, H. & McGill, G. E. (1980). Pioneer Venus radar results: Altimetry and surface properties. *J. Geophys. Res.* **85**, 8261–70.
- Phillips, J. L. & Russell, C. T. (1987). Upper limit on the intrinsic magnetic field of Venus. *J. Geophys. Res.* **92**, 2253–63.
- Phillips, R. J. (1990). Convection-driven tectonics on Venus. *J. Geophys. Res.* **95**, 1301–16.
- Phillips, R. J. & Hansen, V. L. (1994). Tectonic and magmatic evolution of Venus. *Ann. Rev. Earth Planet. Sci.* **22**, 597–654.

- Phillips, R. J. & Malin, M. C. (1983). The interior of Venus and tectonic implications. In *Venus*, pp. 159–214, eds. D. M. Hunten, L. Colin, T. M. Donahue, & V. I. Moroz. The University of Arizona Press, Tucson.
- (1984). Tectonics of Venus. *Ann. Rev. Earth Planet. Sci.* **12**, 411–43.
- Phillips, R. J. & Saunders, R. S. (1975). The isostatic state of Martian topography. *J. Geophys. Res.* **80**, 2893–8.
- Phillips, R. J., Conel, J. E., Abbott, E. A., Sjogren, W. L., & Morton, J. B. (1972). Mascons: Progress toward a unique solution for mass distribution. *J. Geophys. Res.* **77**, 7106–14.
- Phillips, R. J., Grimm, R. E., & Malin, M. C. (1991). Hot-spot evolution and the global tectonics of Venus. *Science* **252**, 651–8.
- Phipps Morgan, J. (1987). Melt migration beneath mid-ocean spreading centers. *Geophys. Res. Lett.* **14**, 1238–41.
- Phipps Morgan, J., Morgan, W. J. & Price, E. (1995). Hotspot melting generates both hotspot volcanism and a hotspot swell? *J. Geophys. Res.* **100**, 8045–62.
- Pilcher, C. B., Ridgway, S. T., & McCord, T. B. (1972). Galilean satellites: Identification of water frost. *Science* **178**, 1087–9.
- Pinet, C. & Jaupart, C. (1987). The vertical distribution of radiogenic heat production in the Precambrian crust of Norway and Sweden: Geothermal implications. *Geophys. Res. Lett.* **14**, 260–3.
- Pinet, C., Jaupart, C., Mareschal, J.-C., Gariepy, C., Bienfait, G., & Lapointe, R. (1991). Heat flow and structure of the lithosphere in the eastern Canadian Shield. *J. Geophys. Res.* **96**, 19941–63.
- Pitman, W. C. & Heirtzler, J. R. (1966). Magnetic anomalies over the Pacific-Antarctic ridge. *Science* **154**, 1164–71.
- Poirier, J.-P. (1985). *Creep of Crystals: High-Temperature Deformation Processes in Metals, Ceramics and Minerals*. Cambridge University Press, Cambridge, England, 260 pp.
- (1994a). Light elements in the Earth's outer core: A critical review. *Phys. Earth Planet. Int.* **85**, 319–37.
- (1994b). Physical properties of the Earth's core. *Comptes Rendus de l'Academie des Sciences* **318**, 341–50.
- Poirier, J. (1995). Plastic rheology of crystals. In *Mineral Physics and Crystallography: A Handbook of Physical Constants*, pp. 237–47, ed. T. J. Ahrens. American Geophysical Union, Washington, DC.
- Pollack, H. N. (1986). Cratonization and thermal evolution of the mantle. *Earth Planet. Sci. Lett.* **80**, 175–82.
- Pollack, H. N., Hurter, S. J., & Johnson, J. R. (1993). Heat flow from the Earth's interior: Analysis of the global data set. *Rev. Geophys.* **31**, 267–80.
- Pollack, J. B., Toon, O. B., Sagan, C., Summers, A., & Van Camp, W. J. (1976). Volcanic explosions and climatic change: A theoretical assessment. *J. Geophys. Res.* **81**, 1071–83.
- Polve, M. & Allègre, C. J. (1980). Orogenic Iherzolite complexes studied by ^{87}Rb - ^{87}Sr : A clue to understand the mantle convection processes? *Earth Planet. Sci. Lett.* **51**, 71–93.
- Ponko, S. C. & Peacock, S. M. (1995). Thermal modeling of the southern Alaska subduction zone: Insight into the petrology of the subducting slab and overlying mantle wedge. *J. Geophys. Res.* **100**, 22117–28.
- Porcelli, D. & Wasserburg, G. J. (1995). Mass transfer of helium, neon, argon, and xenon through a steady-state upper mantle. *Geochim. Cosmochim. Acta* **59**, 4921–37.
- Poupinet, G., Pillet, R., & Souriau, A. (1983). Possible heterogeneity of the Earth's core deduced from PKIKP travel times. *Nature* **305**, 204–6.
- Price, M. & Suppe, J. (1994). Mean age of rifting and volcanism on Venus deduced from impact crater densities. *Nature* **372**, 756–9.
- Prinzofer, A., Lewin, E., & Allègre, C. J. (1989). Stochastic melting of the marble cake mantle: Evidence from local study of the East Pacific Rise at $12^{\circ}50' \text{N}$. *Earth Planet. Sci. Lett.* **92**, 189–206.
- Prockter, L. M., Head, J. W., Pappalardo, R. T., Senske, D. A., Neukum, G., Wagner, R., Wolf, U., Oberst, J., Giese, B., Moore, J. M., Chapman, C. R., Helfenstein, P., Greeley, R., Breneman, H. H., & Belton, M. J. S. (1998). Dark terrain on Ganymede: Geological mapping and interpretation of Galileo Regio at high resolution. *Icarus* **135**, 317–44.
- Prout, W. (1834). *Bridgewater Treatises*, volume 8. W. Pickering, London, Page 65.

- Puchtel, I. S., Hofmann, A. W., Mezger, K., Jochum, K. P., Shchipansky, S. S., & Samsonov, A. V. (1998). Oceanic plateau model for continental crustal growth in the Archaean: A case study from the Kostomuksha greenstone belt, NW Baltic Shield. *Earth Planet. Sci. Lett.* **155**, 57–74.
- Pudovkin, M. I., Tolstikhin, I. N. & Golovchanskaya, I. V. (1981). Recent achievements in helium isotope dissipation research. *Geochem. J.* **15**, 51–61.
- Purdy, G. M. & Ewing, J. (1986). Seismic structure of the ocean crust. In *The Geology of North America: Vol. M, The Western North Atlantic Region*, pp. 313–30, eds. P. R. Vogt & B. E. Tucholke. Geol. Soc. Am., Boulder, CO.
- Puster, P. & Jordan, T. H. (1997). How stratified is mantle convection? *J. Geophys. Res.* **102**, 7625–46.
- Pysklywec, R. N. & Mitrovica, J. X. (1997). Mantle avalanches and the dynamic topography of continents. *Earth Planet. Sci. Lett.* **148**, 447–55.
- Qamar, A. & Eisenberg, A. (1974). The damping of core waves. *J. Geophys. Res.* **79**, 758–65.
- Quarenii, F. & Yuen, D. A. (1984). Time-dependent solutions of mean-field equations with applications for mantle convection. *Phys. Earth Planet. Int.* **36**, 337–53.
- (1988). Mean-field methods in mantle convection. In *Mathematical Geophysics: A Survey of Recent Developments in Seismology and Geodynamics*, pp. 227–64, eds. N. J. Vlaar, G. Nolet, M. J. R. Wortel, & S. A. P. L. Cloetingh. D. Reidel, Dordrecht, Holland.
- Rabinowicz, M., Lago, B., & Froidevaux, C. (1980). Thermal transfer between the continental asthenosphere and the oceanic subducting lithosphere: Its effect on subcontinental convection. *J. Geophys. Res.* **85**, 1839–53.
- Rabinowicz, M., Ceuleneer, G. & Nicolas, A. (1987). Melt segregation and flow in mantle diapirs below spreading centers: Evidence from the Oman ophiolite. *J. Geophys. Res.* **92**, 3475–86.
- Rabinowicz, M., Rouzo, S., Sempere, J.-C., & Rosemberg, C. (1993). Three-dimensional mantle flow beneath mid-ocean ridges. *J. Geophys. Res.* **98**, 7851–69.
- Raitt, R. W., Shor, G. G., Francis, T. J. G., & Morris, G. B. (1969). Anisotropy of the Pacific upper mantle. *J. Geophys. Res.* **74**, 3095–109.
- Ranalli, G. (1995). *Rheology of the Earth*. Chapman and Hall, London, second edition, 413 pp.
- Rappaport, N. & Plaut, J. J. (1994). A 360-degree and -order model of Venus topography. *Icarus* **112**, 27–33.
- Rappaport, N. J., Konopliv, A. S., & Kucinskas, A. B. (1999). An improved 360 degree and order model of Venus topography. *Icarus* **139**, 19–31.
- Ratcliff, J. T., Schubert, G., & Zebib, A. (1995). Three-dimensional variable viscosity convection of an infinite Prandtl number Boussinesq fluid in a spherical shell. *Geophys. Res. Lett.* **22**, 2227–30.
- (1996a). Steady tetrahedral and cubic patterns of spherical shell convection with temperature-dependent viscosity. *J. Geophys. Res.* **101**, 25473–84.
- (1996b). Effects of temperature-dependent viscosity on thermal convection in a spherical shell. *Physica D* **97**, 242–52.
- Ratcliff, J. T., Tackley, P. J., Schubert, G., & Zebib, A. (1997). Transitions in thermal convection with strongly variable viscosity. *Phys. Earth Planet. Int.* **102**, 201–12.
- Ratcliff, J. T., Bercovici, D., Schubert, G., & Kroenke, L. W. (1998). Mantle plume heads and the initiation of plate tectonic reorganizations. *Earth Planet. Sci. Lett.* **156**, 195–207.
- Raup, D. M. & Sepkoski, J. J. (1986). Periodic extinction of families and genera. *Science* **231**, 833–6.
- Ray, T. W. & Anderson, D. L. (1994). Spherical disharmonics in the Earth sciences and the spatial solution: Ridges, hotspots, slabs, geochemistry and tomography correlations. *J. Geophys. Res.* **99**, 9605–14.
- Reasenberg, R. D. (1977). The moment of inertia and isostasy of Mars. *J. Geophys. Res.* **82**, 369–75.
- Reasenberg, R. D., Goldberg, Z. M., MacNeil, P. E., & Shapiro, I. I. (1981). Venus gravity: A high-resolution map. *J. Geophys. Res.* **86**, 7173–9.
- Reasenberg, R. D., Goldberg, Z. M., & Shapiro, I. I. (1982). Venus: Comparison of gravity and topography in the vicinity of Beta Regio. *Geophys. Res. Lett.* **9**, 637–40.
- Reese, C. C., Solomatov, V. S., & Moresi, L.-N. (1998). Heat transport efficiency for stagnant lid convection with dislocation viscosity: Application to Mars and Venus. *J. Geophys. Res.* **103**, 13643–57.

- Reese, C. C., Solomatov, V. S., & Moresi, L.-N. (1999). Non-Newtonian stagnant lid convection and magmatic resurfacing on Venus. *Icarus* **139**, 67–80.
- Regan, J. & Anderson, D. L. (1984). Anisotropic models of the upper mantle. *Phys. Earth Planet. Int.* **35**, 227–63.
- Regenauer-Lieb, K. (1999). Dilatant plasticity applied to Alpine collision: Ductile void growth in the intraplate area beneath the Eifel volcanic field. *J. Geodyn.* **27**, 1–21.
- Renkin, M. L. & Sclater, J. G. (1988). Depth and age in the North Pacific. *J. Geophys. Res.* **93**, 2919–35.
- Revelle, R. & Maxwell, A. E. (1952). Heat flow through the floor of the eastern North Pacific Ocean. *Nature* **170**, 199–200.
- Revenaugh, J. & Jordan, T. H. (1991). Mantle layering from ScS reverberations: 2, The transition zone. *J. Geophys. Res.* **96**, 19763–80.
- Revenaugh, J. & Meyer, R. (1997). Seismic evidence of partial melt within a possibly ubiquitous low-velocity layer at the base of the mantle. *Science* **277**, 670–3.
- Reymer, A. & Schubert, G. (1984). Phanerozoic addition rates to the continental crust and crustal growth. *Tectonics* **3**, 63–77.
- Reynolds, R. T. & Summers, A. L. (1969). Calculations on the composition of the terrestrial planets. *J. Geophys. Res.* **74**, 2494–511.
- Riahi, N., Geiger, G., & Busse, F. H. (1982). Finite Prandtl number convection in spherical shells. *Geophys. Astrophys. Fluid Dyn.* **20**, 307–18.
- Ribe, N. M. (1985a). The deformation and compaction of partial molten zones. *Geophys. J. Roy. Astron. Soc.* **83**, 487–501.
- (1985b). The generation and composition of partial melts in the Earth's mantle. *Earth Planet. Sci. Lett.* **73**, 361–76.
- (1986). Melt segregation driven by dynamic forcing. *Geophys. Res. Lett.* **13**, 1462–5.
- (1987). Theory of melt segregation – A review. *J. Volcan. Geotherm. Res.* **33**, 241–53.
- (1988). On the dynamics of mid-ocean ridges. *J. Geophys. Res.* **93**, 429–36.
- (1992). The dynamics of thin shells with variable viscosity and the origin of toroidal flow in the mantle. *Geophys. J. Int.* **110**, 537–52.
- Ribe, N. M. & Christensen, U. R. (1994). Three-dimensional modeling of plume–lithosphere interaction. *J. Geophys. Res.* **99**, 669–82.
- Ribe, N. M. & de Valpine, D. P. (1994). The global hotspot distribution and instability of D''. *Geophys. Res. Lett.* **21**, 1507–10.
- Ribe, N. M., Christensen, U. R., & Theißing, J. (1995). The dynamics of plume–ridge interaction, 1: Ridge-centered plumes. *Earth Planet. Sci. Lett.* **134**, 155–68.
- Ricard, Y. & Vigny, C. (1989). Mantle dynamics with induced plate tectonics. *J. Geophys. Res.* **94**, 17543–59.
- Ricard, Y. & Wuming, B. (1991). Inferring the viscosity and the 3-D density structure of the mantle from geoid, topography and plate velocities. *Geophys. J. Int.* **105**, 561–71.
- Ricard, Y., Fleitout, L., & Froidevaux, C. (1984). Geoid heights and lithospheric stresses for a dynamic Earth. *Ann. Geophysicae* **2**, 267–86.
- Ricard, Y., Vigny, C., & Froidevaux, C. (1989). Mantle heterogeneities, geoid, and plate motion: A Monte Carlo inversion. *J. Geophys. Res.* **94**, 13739–54.
- Ricard, Y., Sabadini, R., & Spada, G. (1992). Isostatic deformations and polar wander induced by redistribution of mass within the Earth. *J. Geophys. Res.* **97**, 14223–36.
- Ricard, Y., Richards, M., Lithgow-Bertelloni, C., & Le Stunff, Y. (1993). A geodynamic model of mantle density heterogeneity. *J. Geophys. Res.* **98**, 21895–909.
- Richards, M. A. & Griffiths, R. W. (1989). Thermal entrainment by deflected mantle plumes. *Nature* **342**, 900–2.
- Richards, M. A. & Hager, B. H. (1984). Geoid anomalies in a dynamic Earth. *J. Geophys. Res.* **89**, 5987–6002.
- Richards, M. A. & Lithgow-Bertelloni, C. (1996). Plate motion changes, the Hawaiian–Emperor bend, and the apparent success and failure of geodynamic models. *Earth Planet. Sci. Lett.* **137**, 19–27.

- Richards, M. A. & Wicks, C. W. (1990). S-P conversion from the transition zone beneath Tonga and the nature of the 670 km discontinuity. *Geophys. J. Int.* **101**, 1–35.
- Richards, M. A., Duncan, R. A., & Courtillot, V. E. (1989). Flood basalts and hot-spot tracks: Plume heads and tails. *Science* **246**, 103–7.
- Richards, M. A., Ricard, Y., Lithgow-Bertelloni, C., Spada, G., & Sabadini, R. (1997). An explanation for Earth's long-term rotational stability. *Science* **275**, 372–5.
- Richards, P. G. (1972). Seismic waves reflected from velocity gradient anomalies within the Earth's upper mantle. *Z. Geophys.* **38**, 517–27.
- Richardson, C. N. (1998). Melt flow in a variable viscosity matrix. *Geophys. Res. Lett.* **25**, 1099–102.
- Richardson, R. M., Solomon, S. C., & Sleep, N. H. (1979). Tectonic stress in the plates. *Rev. Geophys. Space Phys.* **17**, 981–1019.
- Richardson, S. H., Gurney, J. J., Erlank, A. J., & Harris, J. W. (1984). Origin of diamonds in old enriched mantle. *Nature* **310**, 198–202.
- Richardson, W. P., Stein, S., Stein, C. A., & Zuber, M. T. (1995). Geoid data and thermal structure of the oceanic lithosphere. *Geophys. Res. Lett.* **22**, 1913–6.
- Richter, F. M. (1973). Dynamical models for sea floor spreading. *Rev. Geophys. and Space Phys.* **11**, 223–87.
- (1978). Experiments on the stability of convection rolls in fluids whose viscosity depends on temperature. *J. Fluid Mech.* **89**, 553–60.
- (1985). Models for the Archean thermal regime. *Earth Planet. Sci. Lett.* **73**, 350–60.
- (1986). Simple models for trace element fractionation during melt segregation. *Earth Planet. Sci. Lett.* **77**, 333–44.
- Richter, F. M. & McKenzie, D. P. (1981). On some consequences and possible causes of layered mantle convection. *J. Geophys. Res.* **86**, 6133–42.
- (1984). Dynamical models for melt segregation from a deformable matrix. *J. Geol.* **92**, 729–40.
- Richter, F. M. & Parsons, B. (1975). On the interaction of two scales of convection in the mantle. *J. Geophys. Res.* **80**, 2529–41.
- Richter, F. M. & Ribe, N. M. (1979). On the importance of advection in determining the local isotopic composition of the mantle. *Earth Planet. Sci. Lett.* **43**, 212–22.
- Richter, F. M., Daly, S. F., & Nataf, H. C. (1982). A parameterized model for the evolution of isotopic heterogeneities in a convecting system. *Earth Planet. Sci. Lett.* **60**, 178–94.
- Richter, F. M., Nataf, H. C., & Daly, S. F. (1983). Heat transfer and horizontally averaged temperature of convection with large viscosity variations. *J. Fluid Mech.* **129**, 173–92.
- Riedel, M. R. & Karato, S. (1997). Grain-size evolution in subducted oceanic lithosphere associated with the olivine–spinel transformation and its effects on rheology. *Earth Planet. Sci. Lett.* **148**, 27–43.
- Riedler, W., Möhlmann, D., Oraevsky, V. N., Schwingenschuh, K., Yeroshenko, Y., Rustenbach, J., Aydogar, O., Berghofer, G., Lichtenegger, H., Delva, M., Schelch, G., Pirsch, K., Fremuth, G., Steller, M., Arnold, H., Raditsch, T., Auster, U., Fornacon, K.-H., Schenk, H. J., Michaelis, H., Motschmann, U., Roatsch, T., Sauer, K., Schröter, R., Kurths, J., Lenners, D., Linthe, J., Kobzev, V., Styashkin, V., Achache, J., Slavin, J., Luhmann, J. G., & Russell, C. T. (1989). Magnetic fields near Mars: First results. *Nature* **341**, 604–7.
- Ringwood, A. E. (1966). The chemical composition and origin of the Earth. In *Advances in Earth Science*, pp. 287–356, ed. P. M. Hurley. The M.I.T. Press, Cambridge, MA.
- (1970). Phase transformations and the constitution of the mantle. *Phys. Earth Planet. Int.* **3**, 109–55.
- (1975). *Composition and Petrology of the Earth's Mantle*. Mc-Graw Hill, Inc., New York, 618 pp.
- (1977a). Petrogenesis in island arc systems. In *Island Arcs, Deep Sea Trenches, and Back-Arc Basins*, pp. 311–24, eds. M. Talwani & W. C. Pitman, III, Maurice Ewing Series 1. American Geophysical Union, Washington, DC.
- (1977b). Composition of the core and implications for the origin of the Earth. *Geophys. J.* **11**, 111–35.
- (1979). *Origin of the Earth and Moon*. Springer-Verlag, New York, 295 pp.
- (1990). Earliest history of the Earth–Moon system. In *Origin of the Earth*, pp. 101–34, eds. H. E. Newsom & J. H. Jones. Oxford University Press, New York.

- Ringwood, A. E. & Major, A. (1970). The system Mg_2SiO_4 – Fe_2SiO_4 at high pressures and temperatures. *Phys. Earth Planet. Int.* **3**, 89–108.
- Rison, W. & Craig, H. (1983). Helium isotopes and mantle volatiles in Loihi Seamount and Hawaiian Island basalts and xenoliths. *Earth Planet. Sci. Lett.* **66**, 407–26.
- Ritzwoller, M. H. & Lavelle, E. M. (1995). Three-dimensional seismic models of the Earth's mantle. *Rev. Geophys.* **33**, 1–66.
- Roberts, G. O. (1979). Fast viscous Benard convection. *Geophys. Astrophys. Fluid Dyn.* **12**, 235–72.
- Roberts, P. H. (1965a). Convection in a self-gravitating fluid sphere. *Mathematika* **12**, 128–37.
- (1965b). On nonlinear Benard convection. In *Non-Equilibrium Thermodynamics, Variational Techniques and Stability*, pp. 125–62, eds. R. Donnelly, R. Hermann, & I. Prigogine. University of Chicago Press, Chicago.
- (1967). Convection in horizontal layers with internal heat generation. Theory. *J. Fluid Mech.* **30**, 33–49.
- Robinson, E. M. & Parsons, B. (1988). Effect of a shallow low-viscosity zone on the formation of midplate swells. *J. Geophys. Res.* **93**, 3144–56.
- Robinson, E. M., Parsons, B., & Daly, S. F. (1987). The effect of a shallow low viscosity zone on the apparent compensation of mid-plate swells. *Earth Planet. Sci. Lett.* **82**, 335–48.
- Rodgers, A. & Wahr, J. (1993). Inference of core–mantle boundary topography from ISC Pcp and PKP traveltimes. *Geophys. J. Int.* **115**, 991–1011.
- Romanowicz, B. (1991). Seismic tomography of the Earth's mantle. *Ann. Rev. Earth Planet. Sci.* **19**, 77–99.
- Romanowicz, B., Li, X.-D., & Durek, J. (1996). Anisotropy in the inner core: Could it be due to low-order convection? *Science* **274**, 963–6.
- Ronov, A. B. (1972). Evolution of rock composition and geochemical processes in the sedimentary shell of the Earth. *Sedimentology* **19**, 157–72.
- Ronov, A. B. & Yaroshevsky, A. A. (1969). Chemical composition of the Earth's crust. In *The Earth's Crust and Upper Mantle*, pp. 37–57, Geophysical Monograph 13. American Geophysical Union, Washington, DC.
- Ross, M. N. & Schubert, G. (1985). Tidally forced viscous heating in a partially molten Io. *Icarus* **64**, 391–400.
- Ross, M. & Schubert, G. (1986). Tidal dissipation in a viscoelastic planet. *J. Geophys. Res.* **91**, D447–D452.
- Ross, M. N. & Schubert, G. (1987). Tidal heating in an internal ocean model of Europa. *Nature* **325**, 133–4.
- Ross, M. N., Schubert, G., Spohn, T., & Gaskell, R. W. (1990). Internal structure of Io and the global distribution of its topography. *Icarus* **85**, 309–25.
- Rubie, D. C. & Ross, C. R. (1994). Kinetics of the olivine–spinel transformation in subducting lithosphere: Experimental constraints and implications for deep slab processes. *Phys. Earth Planet. Int.* **86**, 223–41.
- Rubincam, D. P. (1984). Postglacial rebound observed by Lageos and the effective viscosity of the lower mantle. *J. Geophys. Res.* **89**, 1077–87.
- Rudnick, R. L. (1995). Making continental crust. *Nature* **378**, 571–8.
- Rudnick, R. L. & Fountain, D. M. (1995). Nature and composition of the continental crust: A lower crustal perspective. *Rev. Geophys.* **33**, 267–309.
- Ruff, L. J. (1996). Large earthquakes in subduction zones: Segment interaction and recurrence times. In *Subduction: Top to Bottom*, pp. 91–104, eds. G. E. Bebout, D. W. Scholl, S. H. Kirby, & J. P. Platt, Geophysical Monograph 96. American Geophysical Union, Washington, DC.
- Ruff, L. J. & Helmberger, D. V. (1982). The structure of the lowermost mantle determined by short-period P-wave amplitudes. *Geophys. J. Roy. Astron. Soc.* **68**, 95–119.
- Runcorn, S. K. (1956). Palaeomagnetic comparisons between Europe and North America. *Proc. Geol. Assoc. Canada* **8**, 77–85.
- (1962a). Palaeomagnetic evidence for continental drift and its geophysical cause. In *Continental Drift*, pp. 1–40, ed. S. K. Runcorn, Int. Geophys. Ser., **3**. Academic Press, New York.
- (1962b). Convection in the Moon. *Nature* **195**, 1150–1.

- Runcorn, S. K. (1974). On the origin of mascons and moonquakes. *Proc. Lunar Planet. Sci. Conf. 5th*, 3115–26.
- (1983). Lunar magnetism, polar displacements and primeval satellites in the Earth–Moon system. *Nature* **304**, 589–96.
- Russell, C. T. (1978a). The magnetic field of Mars: Mars 3 evidence reexamined. *Geophys. Res. Lett.* **5**, 81–4.
- (1978b). The magnetic field of Mars: Mars 5 evidence re-examined. *Geophys. Res. Lett.* **5**, 85–8.
- (1980). Planetary magnetism. *Rev. Geophys. Space Phys.* **18**, 77–106.
- Russell, C. T., Coleman, P. J., & Schubert, G. (1974a). Lunar magnetic field: Permanent and induced dipole moments. *Science* **186**, 825–6.
- Russell, C. T., Coleman, P. J., Lichtenstein, B. R., & Schubert, G. (1974b). The permanent and induced magnetic dipole moment of the Moon. *Proc. Lunar Sci. Conf. 5th*, 2747–60.
- Russell, C. T., Coleman, P. J., & Goldstein, B. E. (1981). Measurements of the lunar induced magnetic moment in the geomagnetic tail: Evidence for a lunar core? *Proc. Lunar Planet. Sci. Conf. 12th*, 831–6.
- Russell, C. T., Luhmann, J. G., Spreiter, J. R., & Stahara, S. S. (1984). The magnetic field of Mars: Implications from gas dynamic modeling. *J. Geophys. Res.* **89**, 2997–3003.
- Russell, R. D. (1972). Evolutionary model for lead isotopes in conformable ores and in ocean volcanics. *Rev. Geophys. Space Phys.* **10**, 529–49.
- Russell, S. A., Lay, T., & Garnero, E. J. (1998). Seismic evidence for small-scale dynamics in the lowermost mantle at the root of the Hawaiian hotspot. *Nature* **396**, 255–8.
- Ryan, M. P. & Blevins, J. Y. K. (1987). The viscosity of synthetic and natural silicate melts and glasses at high temperatures and 1 bar (10^5 Pascals) pressure and at higher pressures. *U.S. Geol. Surv. Bull.* **1764**, 563 pp.
- Ryerson, F. J., Weed, H. C., & Piwinski, A. J. (1988). Rheology of subliquidus magmas. *J. Geophys. Res.* **93**, 3421–36.
- Sabadini, R. & Yuen, D. A. (1989). Mantle stratification and long-term polar wander. *Nature* **339**, 373–5.
- Sabadini, R., Yuen, D. A., & Boschi, E. (1982). Polar wandering and the forced responses of a rotating, multilayered, viscoelastic planet. *J. Geophys. Res.* **87**, 2885–903.
- Sacks, I. S. & Snook, J. A. (1984). Seismological determinations of the subcrustal continental lithosphere. *Phys. Chem. Earth* **15**, 3–37.
- Sacks, P. E. & Secor, D. T. (1990). Delamination in collisional orogens. *Geology* **18**, 999–1002.
- Safronov, V. S. (1969). *Evolution of the Protoplanetary Cloud and Formation of the Earth and Planets*. Nauka, Moscow, Translation by the Israel Program for Scientific Translation, 1972.
- (1978). The heating of the Earth during its formation. *Icarus* **33**, 3–12.
- Salters, V. J. M. & Hart, S. R. (1989). The hafnium paradox and the role of garnet in the source of mid-ocean-ridge basalts. *Nature* **342**, 420–2.
- (1991). The mantle sources of ocean ridges, islands and arcs: The Hf-isotope connection. *Earth Planet. Sci. Lett.* **104**, 364–80.
- Saltzman, B. (1962). Finite amplitude free convection as an initial value problem. *J. Atmos. Sci.* **19**, 329–41.
- Sammis, C. G., Smith, J. C., Schubert, G., & Yuen, D. A. (1977). Viscosity-depth profile of the Earth's mantle: Effects of polymorphic phase transitions. *J. Geophys. Res.* **82**, 3747–61.
- Sammis, C. G., Smith, J. C., & Schubert, G. (1981). A critical assessment of estimation methods for activation volume. *J. Geophys. Res.* **86**, 10707–18.
- Samowitz, I. R. & Forsyth, D. W. (1981). Double seismic zone beneath the Mariana Island arc. *J. Geophys. Res.* **86**, 7013–21.
- Sandwell, D. T. (1982). Thermal isostasy: Response of a moving lithosphere to a distributed heat source. *J. Geophys. Res.* **87**, 1001–14.
- (1986). Thermal stress and the spacings of transform faults. *J. Geophys. Res.* **91**, 6405–17.
- Sandwell, D. T. & MacKenzie, K. R. (1989). Geoid height versus topography for oceanic plateaus and swells. *J. Geophys. Res.* **94**, 7403–18.

- Sandwell, D. & Schubert, G. (1980). Geoid height versus age for symmetric spreading ridges. *J. Geophys. Res.* **85**, 7235–41.
- Sandwell, D. T. & Schubert, G. (1982). Geoid height–age relation from SEASAT altimeter profiles across the Mendocino fracture zone. *J. Geophys. Res.* **87**, 3949–58.
- (1992a). Flexural ridges, trenches, and outer rises around coronae on Venus. *J. Geophys. Res.* **97**, 16069–83.
- (1992b). Evidence for retrograde lithospheric subduction on Venus. *Science* **257**, 766–70.
- Sandwell, D. T., Johnson, C. L., Bilotti, F., & Suppe, J. (1997). Driving forces for limited tectonics on Venus. *Icarus* **129**, 232–44.
- Sarda, P., Staudacher, T., & Allègre, C. J. (1985). $^{40}\text{Ar}/^{36}\text{Ar}$ in MORB glasses: Constraints on atmosphere and mantle evolution. *Earth Planet. Sci. Lett.* **72**, 357–75.
- Sarda, P., Moreira, M., & Staudacher, T. (1999). Argon–lead isotopic correlation in Mid-Atlantic Ridge basalts. *Science* **283**, 666–8.
- Sarson, G. R., Jones, C. A., Zhang, K., & Schubert, G. (1997). Magnetoc convection dynamos and the magnetic fields of Io and Ganymede. *Science* **276**, 1106–8.
- Sawamoto, H. (1987). Phase diagram of MgSiO_3 at pressures up to 24 GPa and temperatures up to 2,200°C: Phase stability and properties of tetragonal garnet. In *High-Pressure Research in Mineral Physics*, pp. 209–19, eds. M. H. Manghnani & Y. Syono, Geophysical Monograph 39. American Geophysical Union, Washington, DC.
- Saxena, S. K., Shen, G., & Lazor, P. (1994). Temperatures in Earth's core based on melting and phase transformation experiments on iron. *Science* **264**, 405–7.
- Schaber, G. G., Strom, R. G., Moore, H. J., Soderblom, L. A., Kirk, R. L., Chadwick, D. J., Dawson, D. D., Gaddis, L. R., Boyce, J. M., & Russell, J. (1992). Geology and distribution of impact craters on Venus: What are they telling us? *J. Geophys. Res.* **97**, 13257–301.
- Schatz, J. F. & Simmons, G. (1972). Thermal conductivity of Earth materials at high temperatures. *J. Geophys. Res.* **77**, 6966–83.
- Schenk, P. M. & Bulmer, M. H. (1998). Origin of mountains on Io by thrust faulting and large-scale mass movements. *Science* **279**, 1514–7.
- Schilling, J.-G. (1973). Iceland mantle plume: Geochemical study of Reykjanes Ridge. *Nature* **242**, 565–71.
- (1991). Fluxes and excess temperatures of mantle plumes inferred from their interaction with migrating mid-ocean ridges. *Nature* **352**, 397–403.
- Schilling, J.-G., Thompson, G., Kingsley, R., & Humphris, S. (1985). Hotspot–migrating ridge interaction in the South Atlantic. *Nature* **313**, 187–91.
- Schmalzl, J., Houseman, G. A., & Hansen, U. (1995). Mixing properties of three-dimensional (3-D) stationary convection. *Phys. Fluids* **7**, 1027–33.
- (1996). Mixing in vigorous, time-dependent three-dimensional convection and application to Earth's mantle. *J. Geophys. Res.* **101**, 21847–58.
- Schmeling, H. & Jacoby, W. R. (1981). On modelling the lithosphere in mantle convection with non-linear rheology. *J. Geophys.* **50**, 89–100.
- Schmeling, H., Monz, R., & Rubie, D. C. (1999). The influence of olivine metastability on the dynamics of subduction. *Earth Planet. Sci. Lett.* **165**, 55–66.
- Schubert, G. (1979). Subsolidus convection in the mantles of terrestrial planets. *Ann. Rev. Earth Planet. Sci.* **7**, 289–342.
- (1992). Numerical models of mantle convection. *Ann. Rev. Fluid Mech.* **24**, 359–94.
- Schubert, G. & Anderson, C. A. (1985). Finite element calculations of very high Rayleigh number thermal convection. *Geophys. J. Roy. Astron. Soc.* **80**, 575–601.
- Schubert, G. & Garfunkel, Z. (1984). Mantle upwelling in the Dead Sea and Salton Trough-Gulf of California leaky transforms. *Ann. Geophysicae* **2**, 633–48.
- Schubert, G. & Hey, R. N. (1986). Mantle viscosity beneath the Galapagos 95.5°W propagating rift. *Geophys. Res. Lett.* **13**, 329–32.
- Schubert, G. & Lingenfelter, R. E. (1973). Martian centre of mass – centre of figure offset. *Nature* **242**, 251–2.

- Schubert, G. & Reymer, A. P. S. (1985). Continental volume and freeboard through geological time. *Nature* **316**, 336–9.
- Schubert, G. & Sandwell, D. (1989). Crustal volumes of the continents and of oceanic and continental submarine plateaus. *Earth Planet. Sci. Lett.* **92**, 234–46.
- Schubert, G. & Sandwell, D. T. (1995). A global survey of possible subduction sites on Venus. *Icarus* **117**, 173–96.
- Schubert, G. & Spohn, T. (1981). Two-layer mantle convection and the depletion of radioactive elements in the lower mantle. *Geophys. Res. Lett.* **8**, 951–4.
- (1990). Thermal history of Mars and the sulfur content of its core. *J. Geophys. Res.* **95**, 14095–104.
- Schubert, G. & Tackley, P. J. (1995). Mantle dynamics: The strong control of the spinel–perovskite transition at a depth of 660 km. *J. Geodyn.* **20**, 417–28.
- Schubert, G. & Turcotte, D. L. (1971). Phase changes and mantle convection. *J. Geophys. Res.* **76**, 1424–32.
- Schubert, G. & Zebib, A. (1980). Thermal convection of an internally heated infinite Prandtl number fluid in a spherical shell. *Geophys. Astrophys. Fluid Dyn.* **15**, 65–90.
- Schubert, G. & Zhang, K. (1997). Foundering of the lithosphere at the onset of subduction. *Geophys. Res. Lett.* **24**, 1527–9.
- Schubert, G., Turcotte, D. L., & Oxburgh, E. R. (1969). Stability of planetary interiors. *Geophys. J. Roy. Astron. Soc.* **18**, 441–60.
- (1970). Phase change instability in the mantle. *Science* **169**, 1075–7.
- Schubert, G., Yuen, D. A., & Turcotte, D. L. (1975). Role of phase transitions in a dynamic mantle. *Geophys. J. Roy. Astron. Soc.* **42**, 705–35.
- Schubert, G., Young, R. E., & Cassen, P. (1977). Solid state convection models of the lunar internal temperature. *Phil. Trans. Roy. Soc. London A* **285**, 523–36.
- Schubert, G., Cassen, P., & Young, R. E. (1979a). Subsolidus convective cooling histories of terrestrial planets. *Icarus* **38**, 192–211.
- (1979b). Core cooling by subsolidus mantle convection. *Phys. Earth Planet. Int.* **20**, 194–208.
- Schubert, G., Stevenson, D., & Cassen, P. (1980). Whole planet cooling and the radiogenic heat source contents of the Earth and Moon. *J. Geophys. Res.* **85**, 2511–8.
- Schubert, G., Stevenson, D. J., & Ellsworth, K. (1981). Internal structures of the Galilean satellites. *Icarus* **47**, 46–59.
- Schubert, G., Spohn, T., & Reynolds, R. T. (1986). Thermal histories, compositions and internal structures of the moons of the solar system. In *Satellites*, pp. 224–92, eds. J. A. Burns & M. S. Matthews. The University of Arizona Press, Tucson.
- Schubert, G., Ross, M. N., Stevenson, D. J., & Spohn, T. (1988). Mercury's thermal history and the generation of its magnetic field. In *Mercury*, pp. 429–60, eds. F. Vilas, C. R. Chapman, & M. S. Matthews. The University of Arizona Press, Tucson.
- Schubert, G., Olson, P., Anderson, C., & Goldman, P. (1989a). Solitary waves in mantle plumes. *J. Geophys. Res.* **94**, 9523–32.
- Schubert, G., Turcotte, D. L., Solomon, S. C., & Sleep, N. H. (1989b). Coupled evolution of the atmospheres and interiors of planets and satellites. In *Origin and Evolution of Planetary and Satellite Atmospheres*, pp. 450–83, eds. S. K. Atreya, J. B. Pollack & M. S. Matthews. The University of Arizona Press, Tucson.
- Schubert, G., Bercovici, D., & Glatzmaier, G. A. (1990). Mantle dynamics in Mars and Venus: Influence of an immobile lithosphere on three-dimensional mantle convection. *J. Geophys. Res.* **95**, 14105–29.
- Schubert, G., Solomon, S. C., Turcotte, D. L., Drake, M. J., & Sleep, N. H. (1992). Origin and thermal evolution of Mars. In *Mars*, pp. 147–83, eds. H. H. Kieffer, B. M. Jakosky, C. W. Snyder, & M. S. Matthews. The University of Arizona Press, Tucson and London.
- Schubert, G., Glatzmaier, G. A., & Travis, B. (1993). Steady, three-dimensional, internally heated convection. *Phys. Fluids A* **5**, 1928–32.
- Schubert, G., Moore, W. B., & Sandwell, D. T. (1994). Gravity over coronae and chasmata on Venus. *Icarus* **112**, 130–46.

- Schubert, G., Anderson, C., & Goldman, P. (1995). Mantle plume interaction with an endothermic phase change. *J. Geophys. Res.* **100**, 8245–56.
- Schubert, G., Zhang, K., Kivelson, M. G., & Anderson, J. D. (1996). The magnetic field and internal structure of Ganymede. *Nature* **384**, 544–5.
- Schubert, G., Solomatov, V. S., Tackley, P. J., & Turcotte, D. L. (1997). Mantle convection and the thermal evolution of Venus. In *Venus II: Geology, Geophysics, Atmosphere, and Solar Wind Environment*, pp. 1245–87, eds. S. W. Bougher, D. M. Hunten, & R. J. Phillips. The University of Arizona Press, Tucson.
- Schlitz, P. H. & Spudis, P. D. (1983). Beginning and end of lunar mare volcanism. *Nature* **302**, 233–6.
- Sclater, J. G., Jaupart, C. & Galson, D. (1980). The heat flow through oceanic and continental crust and the heat loss of the Earth. *Rev. Geophys. Space Phys.* **18**, 269–311.
- Sclater, J. G., Parsons, B., & Jaupart, C. (1981). Oceans and continents: Similarities and differences in the mechanisms of heat loss. *J. Geophys. Res.* **86**, 11535–52.
- Scott, D. R. (1988). The competition between percolation and circulation in a deformable porous medium. *J. Geophys. Res.* **93**, 6451–62.
- Scott, D. R. & Stevenson, D. J. (1984). Magma solitons. *Geophys. Res. Lett.* **11**, 1161–4.
- (1986). Magma ascent by porous flow. *J. Geophys. Res.* **91**, 9283–96.
- (1989). A self-consistent model of melting, magma migration and buoyancy-driven circulation beneath mid-ocean ridges. *J. Geophys. Res.* **94**, 2973–88.
- Scott, D. R., Stevenson, D. J., & Whitehead, J. A. (1986). Observations of solitary waves in a viscously deformable pipe. *Nature* **319**, 759–61.
- Secor, D. T. & Pollard, D. D. (1975). On the stability of open hydraulic fractures in the Earth's crust. *Geophys. Res. Lett.* **2**, 510–3.
- Segatz, M., Spohn, T., Ross, M. N., & Schubert, G. (1988). Tidal dissipation, surface heat flow, and figure of viscoelastic models of Io. *Icarus* **75**, 187–206.
- Segel, L. A. (1965). The non-linear interaction of a finite number of disturbances to a layer of fluid heated from below. *J. Fluid Mech.* **21**, 359–84.
- Segel, L. A. & Stuart, J. T. (1962). On the question of the preferred mode in cellular thermal convection. *J. Fluid Mech.* **13**, 289–306.
- Seiff, A. (1983). Thermal structure of the atmosphere of Venus. In *Venus*, pp. 215–79, eds. D. M. Hunten, L. Colin, T. M. Donahue, & V. I. Moroz. The University of Arizona Press, Tucson.
- Senske, D. A., Schaber, G. G., & Stofan, E. R. (1992). Regional topographic rises on Venus: Geology of Western Eistla Regio and comparison to Beta Regio and Atla Regio. *J. Geophys. Res.* **97**, 13395–420.
- Shankland, T. J. & Brown, J. M. (1985). Homogeneity and temperatures in the lower mantle. *Phys. Earth Planet. Int.* **38**, 51–8.
- Sharp, R. P. (1973). Mars: Troughed terrain. *J. Geophys. Res.* **78**, 4063–72.
- Sharp, W. E. (1974). A plate tectonic origin for diamond-bearing kimberlites. *Earth Planet. Sci. Lett.* **21**, 351–4.
- Sharpe, H. N. & Peltier, W. R. (1978). Parameterized mantle convection and the Earth's thermal history. *Geophys. Res. Lett.* **5**, 737–40.
- (1979). A thermal history model for the Earth with parameterized convection. *Geophys. J. Roy. Astron. Soc.* **59**, 171–203.
- Shaw, D. M., Cramer, J. J., Higgins, M. D., & Truscott, M. G. (1986). Composition of the Canadian Precambrian shield and the continental crust of the Earth. In *The Nature of the Lower Continental Crust*, pp. 275–82, eds. J. B. Dawson, D. A. Carswell, J. Hall & K. H. Wedepohl, Geological Society Special Publication No 24. Blackwell Scientific Publications, Oxford.
- Shaw, G. H. (1978). Effects of core formation. *Phys. Earth Planet. Int.* **16**, 361–9.
- Shaw, H. R. (1969). Rheology of basalt in the melting range. *J. Petrol.* **10**, 510–35.
- Shearer, P. M. (1990). Seismic imaging of upper-mantle structure with new evidence for a 520-km discontinuity. *Nature* **344**, 121–6.
- (1991). Constraints on upper mantle discontinuities from observations of long-period reflected and converted phases. *J. Geophys. Res.* **96**, 18147–82.
- (1996). Transition zone velocity gradients and the 520-km discontinuity. *J. Geophys. Res.* **101**, 3053–66.

- Shearer, P. M. & Masters, T. G. (1992). Global mapping of topography on the 660-km discontinuity. *Nature* **355**, 791–6.
- Shearer, P. M. & Toy, K. M. (1991). PKP(BC) versus PKP(DF) differential travel times and aspherical structure in the Earth's inner core. *J. Geophys. Res.* **96**, 2233–47.
- Shearer, P. M., Toy, K. M., & Orcutt, J. A. (1988). Axi-symmetric Earth models and inner-core anisotropy. *Nature* **333**, 228–32.
- Shemenda, A. I. (1992). Horizontal lithosphere compression and subduction: Constraints provided by physical modeling. *J. Geophys. Res.* **97**, 11097–116.
- (1993). Subduction of the lithosphere and back arc dynamics: Insights from physical modeling. *J. Geophys. Res.* **98**, 16167–85.
- Shen, G. & Lazor, P. (1995). Measurement of melting temperatures of some minerals under lower mantle pressures. *J. Geophys. Res.* **100**, 17699–713.
- Shen, Y., Solomon, S. C., Bjarnason, I. T., & Wolfe, C. J. (1998). Seismic evidence for a lower-mantle origin of the Iceland plume. *Nature* **395**, 62–5.
- Shih, C.-Y., Nyquist, L. E., Bogard, D. D., McKay, G. A., Wooden, J. L., Bansal, B. M., & Wiesmann, H. (1982). Chronology and petrogenesis of young achondrites, Shergotty, Zagami, and ALHA 77005: Late magmatism on a geologically active planet. *Geochim. Cosmochim. Acta* **46**, 2323–44.
- Shoemaker, E. M., Lucchitta, B. K., Wilhelms, D. E., Plescia, J. B., & Squyres, S. W. (1982). The geology of Ganymede. In *Satellites of Jupiter*, pp. 435–520, ed. D. Morrison. The University of Arizona Press, Tucson.
- Shore, M. J. (1984). A seismic *Q*-profile for the lower mantle from short-period P waves. *Nature* **310**, 399–401.
- Showman, A. P. & Malhotra, R. (1997). Tidal evolution into the Laplace resonance and the resurfacing of Ganymede. *Icarus* **127**, 93–111.
- Showman, A. P., Stevenson, D. J., & Malhotra, R. (1997). Coupled orbital and thermal evolution of Ganymede. *Icarus* **129**, 367–83.
- Sichoix, L., Bonneville, A., & McNutt, M. K. (1998). The seafloor swells and Superswell in French Polynesia. *J. Geophys. Res.* **103**, 27123–33.
- Siegfried, R. W. & Solomon, S. C. (1974). Mercury: Internal structure and thermal evolution. *Icarus* **23**, 192–205.
- Sigmarsdóttir, O., Condomines, M., Morris, J. D., & Harmon, R. S. (1990). Uranium and ^{10}Be enrichments by fluids in Andean arc magmas. *Nature* **346**, 163–5.
- Silver, P. G. (1996). Seismic anisotropy beneath the continents: Probing the depths of geology. *Ann. Rev. Earth Planet. Sci.* **24**, 385–432.
- Silver, P. G., Carlson, R. W., & Olson, P. (1988). Deep slabs, geochemical heterogeneity, and the large-scale structure of mantle convection: Investigation of an enduring paradox. *Ann. Rev. Earth Planet. Sci.* **16**, 477–541.
- Simons, M., Hager, B. H., & Solomon, S. C. (1994). Global variations in the geoid/topography admittance of Venus. *Science* **264**, 798–803.
- Simons, M., Solomon, S. C., & Hager, B. H. (1997). Localization of gravity and topography: Constraints on the tectonics and mantle dynamics of Venus. *Geophys. J. Int.* **131**, 24–44.
- Sinton, J. M. & Detrick, R. S. (1992). Mid-ocean ridge magma chambers. *J. Geophys. Res.* **97**, 197–216.
- Sinton, W. M. (1981). The thermal emission spectrum of Io and a determination of the heat flux from its hot spots. *J. Geophys. Res.* **86**, 3122–8.
- Sisson, T. W. & Bronto, S. (1998). Evidence for pressure-release melting beneath magmatic arcs from basalt at Galunggung, Indonesia. *Nature* **391**, 833–86.
- Sjogren, W. L. & Ritke, S. J. (1982). Mars: Gravity data analysis of the crater Antoniadi. *Geophys. Res. Lett.* **9**, 739–42.
- Sjogren, W. L. & Wimberley, R. N. (1981). Mars: Hellas Planitia gravity analysis. *Icarus* **45**, 331–8.
- Sjogren, W. L., Phillips, R. J., Birkeland, P. W., & Wimberly, R. N. (1980). Gravity anomalies on Venus. *J. Geophys. Res.* **85**, 8295–302.

- Sjogren, W. L., Bills, B. G., Birkeland, P. W., Esposito, P. B., Konopliv, A. R., Mottinger, N. A., Ritke, S. J., & Phillips, R. J. (1983). Venus gravity anomalies and their correlations with topography. *J. Geophys. Res.* **88**, 1119–28.
- Sjogren, W. L., Bills, B. G., & Mottinger, N. A. (1984). Venus: Ishtar gravity anomaly. *Geophys. Res. Lett.* **11**, 489–91.
- Sjogren, W. L., Banerdt, W. B., Chodas, P. W., Konopliv, A. S., Balmino, G., Barriot, J. P., Arkani-Hamed, J., Colvin, T. R., & Davies, M. E. (1997). The Venus gravity field and other geodetic parameters. In *Venus II: Geology, Geophysics, Atmosphere, and Solar Wind Environment*, pp. 1125–61, eds. S. W. Bouger, D. M. Hunten, & R. J. Phillips. The University of Arizona Press, Tucson.
- Skilbeck, J. N. & Whitehead, J. A. (1978). Formation of discrete islands in linear island chains. *Nature* **272**, 499–501.
- Sleep, N. H. (1971). Thermal effects of the formation of Atlantic continental margins by continental break up. *Geophys. J. Roy. Astron. Soc.* **24**, 325–50.
- (1974). Segregation of magma from a mostly crystalline mush. *Geol. Soc. Am. Bull.* **85**, 1225–32.
- (1979). Thermal history and degassing of the Earth: Some simple calculations. *J. Geology* **87**, 671–86.
- (1987). Lithospheric heating by mantle plumes. *Geophys. J. Roy. Astron. Soc.* **91**, 1–11.
- (1988a). Tapping of melt by veins and dikes. *J. Geophys. Res.* **93**, 10255–72.
- (1988b). Gradual entrainment of a chemical layer at the base of the mantle by overlying convection. *Geophys. J.* **95**, 437–47.
- (1990). Hotspots and mantle plumes: Some phenomenology. *J. Geophys. Res.* **95**, 6715–36.
- (1992). Hotspot volcanism and mantle plumes. *Ann. Rev. Earth Planet. Sci.* **20**, 19–43.
- (1994a). Lithospheric thinning by midplate mantle plumes and the thermal history of hot plume material ponded at sublithospheric depths. *J. Geophys. Res.* **99**, 9327–43.
- (1994b). Martian plate tectonics. *J. Geophys. Res.* **99**, 5639–55.
- (1996). Lateral flow of hot plume material ponded at sublithospheric depths. *J. Geophys. Res.* **101**, 28065–83.
- (1997). Lateral flow and ponding of starting plume material. *J. Geophys. Res.* **102**, 10001–12.
- Sleep, N. H. & Phillips, R. J. (1979). An isostatic model for the Tharsis province, Mars. *Geophys. Res. Lett.* **6**, 803–6.
- (1985). Gravity and lithospheric stress on the terrestrial planets with reference to the Tharsis region of Mars. *J. Geophys. Res.* **90**, 4469–89.
- Sleep, N. H., Richards, M. A., & Hager, B. H. (1988). Onset of mantle plumes in the presence of preexisting convection. *J. Geophys. Res.* **93**, 7672–89.
- Slichter, L. B. (1941). Cooling of the Earth. *Geol. Soc. Am. Bull.* **52**, 561–600.
- Smith, B. A., Soderblom, L. A., Johnson, T. V., Ingersoll, A. P., Collins, S. A., Shoemaker, E. M., Hunt, G. E., Masursky, H., Carr, M. H., Davies, M. E., Cook, A. F., Boyce, J., Danielson, G. E., Owen, T., Sagan, C., Beebe, R. F., Veverka, J., Strom, R. G., McCauley, J. F., Morrison, D., Briggs, G. A., & Suomi, V. E. (1979a). The Jupiter system through the eyes of Voyager 1. *Science* **204**, 951–71.
- Smith, B. A., Soderblom, L. A., Beebe, R., Boyce, J., Briggs, G., Carr, M., Collins, S. A., Cook, A. F., Danielson, G. E., Davies, M. E., Hunt, G. E., Ingersoll, A., Johnson, T. V., Masursky, H., McCauley, J., Morrison, D., Owen, T., Sagan, C., Shoemaker, E. M., Strom, R., Suomi, V. E., & Veverka, J. (1979b). The Galilean satellites and Jupiter: Voyager 2 imaging science results. *Science* **206**, 927–50.
- Smith, D. E. & Zuber, M. T. (1996). The shape of Mars and the topographic signature of the hemispheric dichotomy. *Science* **271**, 184–8.
- Smith, D. E., Zuber, M. T., Neumann, G. A., & Lemoine, F. G. (1997). Topography of the Moon from the Clementine lidar. *J. Geophys. Res.* **102**, 1591–611.
- Smith, D. E., Zuber, M. T., Frey, H. V., Garvin, J. B., Head, J. W., Muhleman, D. O., Pettengill, G. H., Phillips, R. J., Solomon, S. C., Zwally, H. J., Banerdt, W. B., & Duxbury, T. C. (1998). Topography of the northern hemisphere of Mars from the Mars Orbiter Laser Altimeter. *Science* **279**, 1686–92.
- Smith, D. E., Zuber, M. T., Solomon, S. C., Phillips, R. J., Head, J. W., Garvin, J. B., Banerdt, W. B., Muhleman, D. O., Pettengill, G. H., Neumann, G. A., Lemoine, F. G., Abshire, J. B., Aharonson, O.,

- Brown, C. D., Hauck, S. A., Ivanov, A. B., McGovern, P. J., Zwally, H. J., & Duxbury, T. C. (1999a). The global topography of Mars and implications for surface evolution. *Science* **284**, 1495–503.
- Smith, D. E., Sjogren, W. L., Tyler, G. L., Balmino, G., Lemoine, F. G., & Konopliv, A. S. (1999b). The gravity field of Mars: Results from Mars Global Surveyor. *Science* **286**, 94–7.
- Smith, G. M. & Banerjee, S. K. (1986). Magnetic structure of the upper kilometer of the marine crust at Deep Sea Drilling Project Hole 504B, eastern Pacific Ocean. *J. Geophys. Res.* **91**, 10337–54.
- Smith, W. H. F. & Sandwell, D. T. (1997). Global sea floor topography from satellite altimetry and ship depth soundings. *Science* **277**, 1956–62.
- Smithson, S. B. (1978). Modeling continental crust: Structural and chemical constraints. *Geophys. Res. Lett.* **5**, 749–52.
- Smithson, S. B. & Decker, E. R. (1974). A continental crustal model and its geothermal implications. *Earth Planet. Sci. Lett.* **22**, 215–25.
- Smrekar, S. E. & Phillips, R. J. (1991). Venusian highlands: Geoid to topography ratios and their implications. *Earth Planet. Sci. Lett.* **107**, 582–97.
- Smrekar, S. E., Kiefer, W. S., & Stofan, E. R. (1997). Large volcanic rises on Venus. In *Venus II: Geology, Geophysics, Atmosphere, and Solar Wind Environment*, pp. 845–78, eds. S. W. Bougher, D. M. Hunten, & R. J. Phillips. The University of Arizona Press, Tucson.
- Smythe, W. R. (1968). *Static and Dynamic Electricity*. McGraw-Hill, New York, Third edition, 623 pp.
- Sohl, F. & Spohn, T. (1997). The interior structure of Mars: Implications from SNC meteorites. *J. Geophys. Res.* **102**, 1613–35.
- Solheim, L. P. & Peltier, W. R. (1990). Heat transfer and the onset of chaos in a spherical, axisymmetric, anelastic model of whole mantle convection. *Geophys. Astrophys. Fluid Dyn.* **53**, 205–55.
- (1993). Mantle phase transitions and layered convection. *Canad. J. Earth Sci.* **30**, 881–92.
- (1994a). Phase boundary deflections at 660-km depth and episodically layered isochemical convection in the mantle. *J. Geophys. Res.* **99**, 15861–75.
- (1994b). Avalanche effects in phase transition modulated thermal convection: A model of Earth's mantle. *J. Geophys. Res.* **99**, 6997–7018.
- Solomatov, V. S. (1993). Parameterization of temperature- and stress-dependent viscosity convection and the thermal evolution of Venus. In *Flow and Creep in the Solar System: Observations, Modeling and Theory*, pp. 131–45, eds. D. B. Stone & S. K. Runcorn. Kluwer Academic Publishers, Dordrecht, Netherlands.
- (1995). Scaling of temperature- and stress-dependent viscosity convection. *Phys. Fluids* **7**, 266–74.
- Solomatov, V. S. & Moresi, L.-N. (1996). Stagnant lid convection on Venus. *J. Geophys. Res.* **101**, 4737–53.
- Solomatov, V. S. & Stevenson, D. J. (1993a). Suspension in convective layers and style of differentiation of a terrestrial magma ocean. *J. Geophys. Res.* **98**, 5375–90.
- (1993b). Nonfractional crystallization of a terrestrial magma ocean. *J. Geophys. Res.* **98**, 5391–406.
- Solomatov, V. S. & Zharkov, V. N. (1990). The thermal regime of Venus. *Icarus* **84**, 280–95.
- Solomatov, V. S., Leontjev, V. V., & Zharkov, V. N. (1987). Models of thermal evolution of Venus in the approximation of parameterised convection. *Gerlands Beitr. Geophysik Leipzig* **96**, 73–96.
- Solomon, S. C. (1976). Some aspects of core formation in Mercury. *Icarus* **28**, 509–21.
- (1977). The relationship between crustal tectonics and internal evolution in the Moon and Mercury. *Phys. Earth Planet. Int.* **15**, 135–45.
- (1978). On volcanism and thermal tectonics on one-plate planets. *Geophys. Res. Lett.* **5**, 461–4.
- (1979). Formation, history and energetics of cores in the terrestrial planets. *Phys. Earth Planet. Int.* **19**, 168–82.
- (1986). On the early thermal state of the Moon. In *Origin of the Moon*, pp. 435–52, eds. W. K. Hartmann, R. J. Phillips, & G. J. Taylor. Lunar and Planetary Institute, Houston, Texas.
- Solomon, S. C. & Chaiken, J. (1976). Thermal expansion and thermal stress in the Moon and terrestrial planets: Clues to early thermal history. *Proc. Lunar Planet. Sci. Conf. 7th*, 3229–43.
- Solomon, S. C. & Head, J. W. (1982). Evolution of the Tharsis province of Mars: The importance of heterogeneous lithospheric thickness and volcanic construction. *J. Geophys. Res.* **87**, 9755–74.

- Solomon, S. C. & Head, J. W. (1990). Heterogeneities in the thickness of the elastic lithosphere of Mars: Constraints on heat flow and internal dynamics. *J. Geophys. Res.* **95**, 11073–83.
- Solomon, S. C., Smrekar, S. E., Bindschadler, D. L., Grimm, R. E., Kaula, W. M., McGill, G. E., Phillips, R. J., Saunders, R. S., Schubert, G., Squyres, S. W., & Stofan, E. R. (1992). Venus tectonics: An overview of Magellan observations. *J. Geophys. Res.* **97**, 13199–255.
- Song, X. & Helmberger, D. V. (1993). Anisotropy of Earth's inner core. *Geophys. Res. Lett.* **20**, 2591–4.
- Song, X. & Richards, P. G. (1996). Seismological evidence for differential rotation of the Earth's inner core. *Nature* **382**, 221–4.
- Sotin, C. & Parmentier, E. M. (1989). On the stability of a fluid layer containing a univariant phase transition: Application to planetary interiors. *Phys. Earth Planet. Int.* **55**, 10–25.
- Souriau, A. & Romanowicz, B. (1997). Anisotropy in the inner core: Relation between P-velocity and attenuation. *Phys. Earth Planet. Int.* **101**, 33–47.
- Souriau, A. & Souriau, M. (1989). Ellipticity and density at the inner core boundary from subcritical PK_iKP and P_cP data. *Geophys. J. Int.* **98**, 39–54.
- Souriau, A., Roudil, P., & Moynot, B. (1997). Inner core differential rotation: Facts and artefacts. *Geophys. Res. Lett.* **24**, 2103–6.
- Spada, G., Sabadini, R., & Boschi, E. (1996). Long-term rotation and mantle dynamics of the Earth, Mars, and Venus. *J. Geophys. Res.* **101**, 2253–66.
- Spakman, W. (1986). Subduction beneath Eurasia in connection with the Mesozoic Tethys. *Geol. Mijnbouw* **65**, 145–53.
- Spakman, W., van der Lee, S., & van der Hilst, R. (1993). Travel-time tomography of the European-Mediterranean mantle down to 1400 km. *Phys. Earth Planet. Int.* **79**, 3–74.
- Sparks, D. W. & Parmentier, E. M. (1991). Melt extraction from the mantle beneath spreading centers. *Earth Planet. Sci. Lett.* **105**, 368–77.
- (1993). The structure of three-dimensional convection beneath oceanic spreading centres. *Geophys. J. Int.* **112**, 81–91.
- Sparks, D. W., Parmentier, E. M., & Phipps Morgan, J. (1993). Three-dimensional mantle convection beneath a segmented spreading center: Implications for along-axis variations in crustal thickness and gravity. *J. Geophys. Res.* **98**, 21977–95.
- Sparrow, C. (1982). *The Lorenz Equations: Bifurcations, Chaos, and Strange Attractors*. Springer-Verlag, New York, 269 pp.
- Sparrow, E. M., Goldstein, R. J., & Jonsson, V. K. (1964). Thermal instability in a horizontal fluid layer: Effect of boundary conditions and non-linear temperature profile. *J. Fluid Mech.* **18**, 513–28.
- Spence, D. A. & Sharp, P. (1985). Self-similar solutions for elastohydrodynamic cavity flow. *Proc. Roy. Soc. London A* **400**, 289–313.
- Spence, D. A. & Turcotte, D. L. (1985). Magma-driven propagation of cracks. *J. Geophys. Res.* **90**, 575–80.
- (1990). Buoyancy-driven magma fracture: A mechanism for ascent through the lithosphere and the emplacement of diamonds. *J. Geophys. Res.* **95**, 5113–9.
- Spence, D. A., Sharp, P. W., & Turcotte, D. L. (1987). Buoyancy-driven crack propagation: A mechanism for magma migration. *J. Fluid Mech.* **174**, 135–53.
- Spencer, J. R. & Schneider, N. M. (1996). Io on the eve of the Galileo mission. *Ann. Rev. Earth Planet. Sci.* **24**, 125–90.
- Spera, F. J. (1984). Carbon dioxide in petrogenesis: III. Role of volatiles in the ascent of alkaline magma with special reference to xenolith-bearing mafic lavas. *Contrib. Mineral. Petrol.* **88**, 217–32.
- (1987). Dynamics of translithospheric migration of metasomatic fluid and alkaline magma. In *Mantle Metasomatism*, pp. 1–20, eds. M. A. Menzies & C. J. Hawkesworth. Academic Press, London.
- Spiegel, E. A. & Veronis, G. (1960). On the Boussinesq approximation for a compressible fluid. *Astrophys. J.* **131**, 442–7.
- Spiegelman, M. (1993a). Flow in porous media. Part 1: Simple analysis. *J. Fluid Mech.* **247**, 17–38.
- (1993b). Flow in porous media. Part 2: Numerical analysis – the relationship between shock waves and solitary waves. *J. Fluid Mech.* **247**, 39–63.

- Spiegelman, M. (1993c). Physics of melt extraction: Theory, implications, applications. . *Trans. Roy. Soc. London A* **342**, 23–41.
- (1994). Geochemical effects of magmatic solitary waves – II. Some analysis. *Geophys. J. Int.* **117**, 296–300.
- (1996). Geochemical consequences of melt transport in 2-D: The sensitivity of trace elements to mantle dynamics. *Earth Planet. Sci. Lett.* **139**, 115–32.
- Spiegelman, M. & Kenyon, P. (1992). The requirements for chemical disequilibrium during magma migration. *Earth Planet. Sci. Lett.* **109**, 611–20.
- Spiegelman, M. & McKenzie, D. (1987). Simple 2-D models for melt extraction at mid-ocean ridges and island arcs. *Earth Planet. Sci. Lett.* **83**, 137–52.
- Spohn, T. (1991). Mantle differentiation and thermal evolution of Mars, Mercury, and Venus. *Icarus* **90**, 222–36.
- Spohn, T. & Schubert, G. (1982a). Modes of mantle convection and the removal of heat from the Earth's interior. *J. Geophys. Res.* **87**, 4682–96.
- (1982b). Convective thinning of the lithosphere: A mechanism for the initiation of continental rifting. *J. Geophys. Res.* **87**, 4669–81.
- (1983). Convective thinning of the lithosphere: A mechanism for rifting and mid-plate volcanism on Earth, Venus, and Mars. *Tectonophys.* **94**, 67–90.
- (1991). Thermal equilibration of the Earth following a giant impact. *Geophys. J. Int.* **107**, 163–70.
- Spohn, T., Sohl, F., & Breuer, D. (1998). Mars. *Astron. Astrophys. Rev.* **8**, 181–236.
- Squyres, S. W. & Croft, S. K. (1986). The tectonics of icy satellites. In *Satellites*, pp. 293–341, eds. J. A. Burns & M. S. Matthews. The University of Arizona Press, Tucson.
- Squyres, S. W., Reynolds, R. T., Cassen, P. M., & Peale, S. J. (1983). Liquid water and active resurfacing on Europa. *Nature* **301**, 225–6.
- Squyres, S. W., Janes, D. M., Baer, G., Bindschadler, D. L., Schubert, G., Sharpton, V. L., & Stofan, E. R. (1992). The morphology and evolution of coronae on Venus. *J. Geophys. Res.* **97**, 13611–34.
- Stacey, F. D. (1977a). A thermal model of the Earth. *Phys. Earth Planet. Int.* **15**, 341–8.
- (1977b). *Physics of the Earth*. John Wiley & Sons, New York, Second edition, 414 pp.
- (1980). The cooling Earth: A reappraisal. *Phys. Earth Planet. Int.* **22**, 89–96.
- (1992). *Physics of the Earth*. Brookfield Press, Brisbane, Third edition, 513 pp.
- Stacey, F. D. & Loper, D. E. (1983). The thermal boundary-layer interpretation of D'' and its role as a plume source. *Phys. Earth Planet. Int.* **33**, 45–55.
- Stacey, J. S. & Kramers, J. D. (1975). Approximation of terrestrial lead isotope evolution by a two-stage model. *Earth Planet. Sci. Lett.* **26**, 207–21.
- Stark, P. B. & Frohlich, C. (1985). The depths of the deepest deep earthquakes. *J. Geophys. Res.* **90**, 1859–69.
- Staudacher, T. & Allègre, C. J. (1982). Terrestrial xenology. *Earth Planet. Sci. Lett.* **60**, 389–406.
- Staudacher, T., Moreira, M., & Allègre, C. J. (1994). Heterogeneity and scatter of helium isotopic ratios in MORB. *Mineral. Mag.* **58A**, 874–5.
- Staudigel, H. & King, S. D. (1992). Ultrafast subduction: The key to slab recycling efficiency and mantle differentiation? *Earth Planet. Sci. Lett.* **109**, 517–30.
- Staudigel, H., Park, K.-H., Pringle, M., Rubenstein, J. L., Smith, W. H. F., & Zindler, A. (1991). The longevity of the South Pacific isotopic and thermal anomaly. *Earth Planet. Sci. Lett.* **102**, 24–44.
- Stefan, J. (1891). Ueber die theorie der eisbildung, insbesondere über die Eisbildung im Polarmeere. *Annalen der Physik und Chem.* **42**, 269–86.
- Stein, C. A. & Stein, S. (1992). A model for the global variation in oceanic depth and heat flow with lithospheric age. *Nature* **359**, 123–9.
- Stein, M. & Hofmann, A. W. (1994). Mantle plumes and episodic crustal growth. *Nature* **372**, 63–68.
- Stein, S. & Stein, C. A. (1996). Thermo-mechanical evolution of oceanic lithosphere: Implications for the subduction process and deep earthquakes. In *Subduction: Top to Bottom*, pp. 1–17, eds. G. E. Bebout, D. W. Scholl, S. H. Kirby, & J. P. Platt, Geophysical Monograph 96. American Geophysical Union, Washington, DC.

- Steinbach, V. & Yuen, D. A. (1992). The effects of multiple phase transitions on Venusian mantle convection. *Geophys. Res. Lett.* **19**, 2243–6.
- (1994a). Melting instabilities in the transition zone. *Earth Planet. Sci. Lett.* **127**, 67–75.
- (1994b). Effects of depth-dependent properties on the thermal anomalies produced in flush instabilities from phase transitions. *Phys. Earth Planet. Int.* **86**, 165–83.
- (1995). The effects of temperature-dependent viscosity on mantle convection with the two major phase transitions. *Phys. Earth Planet. Int.* **90**, 13–36.
- (1997). Dynamical effects of a temperature- and pressure-dependent lower-mantle rheology on the interaction of upwellings with the transition zone. *Phys. Earth Planet. Int.* **103**, 85–100.
- Steinbach, V., Yuen, D. A., & Zhao, W. (1993). Instabilities from phase transitions and the timescales of mantle thermal evolution. *Geophys. Res. Lett.* **20**, 1119–22.
- Steinberger, B. & O'Connell, R. J. (1997). Changes of the Earth's rotation axis owing to advection of mantle density heterogeneities. *Nature* **387**, 169–73.
- (1998). Advection of plumes in mantle flow: Implications for hotspot motion, mantle viscosity and plume distribution. *Geophys. J. Int.* **132**, 412–34.
- Stengel, K. C., Oliver, D. S., & Booker, J. R. (1982). Onset of convection in a variable-viscosity fluid. *J. Fluid Mech.* **120**, 411–31.
- Stephen, R. A. (1985). Seismic anisotropy in the upper oceanic crust. *J. Geophys. Res.* **90**, 11383–96.
- Stevenson, D. J. (1980). Lunar asymmetry and paleomagnetism. *Nature* **287**, 520–21.
- (1981). Models of the Earth's core. *Science* **214**, 611–19.
- (1987). Origin of the Moon – The collision hypothesis. *Ann. Rev. Earth Planet. Sci.* **15**, 271–315.
- (1989a). Spontaneous small-scale melt segregation in partial melts undergoing deformation. *Geophys. Res. Lett.* **16**, 1067–70.
- (1989b). Formation and early evolution of the Earth. In *Mantle Convection: Plate Tectonics and Global Dynamics*, pp. 817–73, ed. W. R. Peltier, volume 4 of *The Fluid Mechanics of Astrophysics and Geophysics*. Gordon and Breach Science Publishers, New York.
- (1990). Fluid dynamics of core formation. In *Origin of the Earth*, pp. 231–49, eds. H. E. Newsom & J. H. Jones. Oxford University Press, New York.
- (1998). Private communication.
- Stevenson, D. J. & Scott, D. R. (1991). Mechanics of fluid-rock systems. *Ann. Rev. Fluid Mech.* **23**, 305–39.
- Stevenson, D. J. & Turner, J. S. (1977). Angle of subduction. *Nature* **270**, 334–6.
- (1979). Fluid models of mantle convection. In *The Earth: Its Origin, Structure and Evolution*, pp. 227–63, ed. M. W. McElhinny. Academic Press, London.
- Stevenson, D. J., Spohn, T., & Schubert, G. (1983). Magnetism and thermal evolution of the terrestrial planets. *Icarus* **54**, 466–89.
- Stewart, C. A. & Turcotte, D. L. (1989). The route to chaos in thermal convection at infinite Prandtl number. *J. Geophys. Res.* **94**, 13707–17.
- Stixrude, L., Hemley, R. J., Fei, Y., & Mao, H. K. (1992). Thermoelasticity of silicate perovskite and magnesiowüstite and stratification of the Earth's mantle. *Science* **257**, 1099–101.
- Stoddard, P. R. & Abbott, D. (1996). Influence of the tectosphere upon plate motion. *J. Geophys. Res.* **101**, 5425–33.
- Stofan, E. R., Bindschadler, D. L., Head, J. W., & Parmentier, E. M. (1991). Corona structures on Venus: Models of origin. *J. Geophys. Res.* **96**, 20933–46.
- Stofan, E. R., Sharpton, V. L., Schubert, G., Baer, G., Bindschadler, D. L., Janes, D. M., & Squyres, S. W. (1992). Global distribution and characteristics of coronae and related features on Venus: Implications for origin and relation to mantle processes. *J. Geophys. Res.* **97**, 13347–78.
- Stofan, E. R., Smrekar, S. E., Bindschadler, D. L., & Senske, D. A. (1995). Large topographic rises on Venus: Implications for mantle upwelling. *J. Geophys. Res.* **100**, 23317–27.
- Stofan, E. R., Hamilton, V. E., Janes, D. M., & Smrekar, S. E. (1997). Coronae on Venus: Morphology and origin. In *Venus II: Geology, Geophysics, Atmosphere, and Solar Wind Environment*, pp. 931–65, eds. S. W. Bougher, D. M. Hunten & R. J. Phillips. The University of Arizona Press, Tucson.

- Stolper, E. (1980). A phase diagram for mid-ocean ridge basalts: Preliminary results and implications for petrogenesis. *Contrib. Mineral. Petrol.* **74**, 13–27.
- Stolper, E., Walker, D., Hager, B. H., & Hays, J. F. (1981). Melt segregation from partially molten source regions: The importance of melt density and source region size. *J. Geophys. Res.* **86**, 6261–71.
- Strom, R. G. (1979). Mercury: A post-Mariner 10 assessment. *Space Sci. Rev.* **24**, 3–70.
- Strom, R. G., Trask, N. J., & Guest, J. E. (1975). Tectonism and volcanism on Mercury. *J. Geophys. Res.* **80**, 2478–507.
- Strom, R. G., Terrile, R. J., Masursky, H., & Hansen, C. (1979). Volcanic eruption plumes on Io. *Nature* **280**, 733–6.
- Strom, R. G., Croft, S. K., & Barlow, N. G. (1992). The Martian impact cratering record. In *Mars*, pp. 383–423, eds. H. H. Kieffer, B. M. Jakosky, C. W. Snyder, & M. S. Matthews. The University of Arizona Press, Tucson and London.
- Strom, R. G., Schaber, G. G., & Dawson, D. D. (1994). The global resurfacing of Venus. *J. Geophys. Res.* **99**, 10899–926.
- Su, W. & Buck, W. R. (1993). Buoyancy effects on mantle flow under mid-ocean ridge. *J. Geophys. Res.* **98**, 12191–205.
- Su, W. & Dziewonski, A. M. (1991). Predominance of long-wavelength heterogeneity in the mantle. *Nature* **352**, 121–6.
- (1995). Inner core anisotropy in three dimensions. *J. Geophys. Res.* **100**, 9831–52.
- (1997). Simultaneous inversion for 3-D variations in shear and bulk velocity in the mantle. *Phys. Earth Planet. Int.* **100**, 135–56.
- Su, W., Woodward, R. L., & Dziewonski, A. M. (1992). Joint inversions of travel-time and waveform data for the 3-D models of the Earth up to degree 12 (Abstract). *EoS Trans. AGU* **73**, 201–2.
- (1994). Degree 12 model of shear velocity heterogeneity in the mantle. *J. Geophys. Res.* **99**, 6945–80.
- Su, W., Dziewonski, A. M., & Jeanloz, R. (1996). Planet within a planet: Rotation of the inner core of Earth. *Science* **274**, 1883–7.
- Sun, S. S. (1980). Lead isotopic study of young volcanic rocks from mid-ocean ridges, ocean islands and island arcs. *Phil. Trans. Roy. Soc. London A* **297**, 409–45.
- Sun, S. S. & Hanson, G. N. (1975). Evolution of the mantle: Geochemical evidence from alkali basalt. *Geology* **3**, 297–302.
- Sun, S.-S. & McDonough, W. F. (1989). Chemical and isotopic systematics of oceanic basalts: Implications for mantle composition and processes. In *Magmatism in the Ocean Basins*, pp. 313–45, eds. A. D. Saunders & M. J. Norry. Geol. Soc. Spec. Publ. No. 42, Oxford.
- Sung, C. & Burns, R. G. (1976). Kinetics of high-pressure phase transformations: Implications to the evolution of the olivine → spinel transition in the downgoing lithosphere and its consequences on the dynamics of the mantle. *Tectonophysics* **31**, 1–32.
- Surkov, Y., Barsukov, V. L., Moskalyeva, L. P., Kharyukova, V. P., & Kemurdzhian, A. L. (1984). New data on the composition, structure, and properties of Venus rock obtained by Venera 13 and Venera 14. *J. Geophys. Res., Suppl.* **89**, B393–B402.
- Surkov, Y., Kirnozov, F. F., Glazov, V. N., Dunchenko, A. G., Tatsy, L. P., & Soborov, O. P. (1987). Uranium, thorium, and potassium in the Venusian rocks at the landing sites of Vega 1 and 2. *J. Geophys. Res.* **92**, E537–E540.
- Sykes, L. R. (1966). The seismicity and deep structure of island arcs. *J. Geophys. Res.* **71**, 2981–3006.
- Sylvester, P. J., Campbell, L. H., & Bowyer, D. A. (1997). Niobium/uranium evidence for early formation of the continental crust. *Science* **275**, 521–3.
- Tackley, P. J. (1993). Effects of strongly temperature-dependent viscosity on time-dependent, three-dimensional models of mantle convection. *Geophys. Res. Lett.* **20**, 2187–90.
- (1995). On the penetration of an endothermic phase transition by upwellings and downwellings. *J. Geophys. Res.* **100**, 15477–88.
- (1996a). On the ability of phase transitions and viscosity layering to induce long wavelength heterogeneity in the mantle. *Geophys. Res. Lett.* **23**, 1985–8.
- (1996b). Effects of strongly variable viscosity on three-dimensional compressible convection in planetary mantles. *J. Geophys. Res.* **101**, 3311–32.

- Tackley, P. J. (1997). Effects of phase transitions on three-dimensional mantle convection. In *Earth's Deep Interior: The Doornbos Memorial Volume*, pp. 273–335, ed. D. J. Crossley. Gordon and Breach Science Publ., Amsterdam.
- (1998a). Self-consistent generation of tectonic plates in three-dimensional mantle convection. *Earth Planet. Sci. Lett.* **157**, 9–22.
- (1998b). Three-dimensional simulations of mantle convection with a thermo-chemical basal boundary layer: D''? In *The Core–Mantle Boundary Region*, pp. 231–53, eds. M. Gurnis, M. E. Wysession, E. Knittle, & B. A. Buffett, volume 28 of *Geodynamics Series*. American Geophysical Union, Washington, DC.
- Tackley, P. J., Stevenson, D. J., Glatzmaier, G. A., & Schubert, G. (1993). Effects of an endothermic phase transition at 670 km depth in a spherical model of convection in the Earth's mantle. *Nature* **361**, 699–704.
- (1994). Effects of multiple phase transitions in a three-dimensional spherical model of convection in Earth's mantle. *J. Geophys. Res.* **99**, 15877–901.
- Tajima, F. & Grand, S. P. (1998). Variation of transition zone high-velocity anomalies and depression of 660 km discontinuity associated with subduction zones from the southern Kuriles to Izu-Bonin and Ryukyu. *J. Geophys. Res.* **103**, 15015–36.
- Takahashi, E. & Kushiro, I. (1983). Melting of a dry peridotite at high pressures and basalt magma genesis. *Am. Mineral.* **68**, 859–79.
- Takeuchi, H., Saito, M., & Kobayashi, N. (1962). Statical deformations and free oscillations of a model Earth. *J. Geophys. Res.* **67**, 1141–54.
- Tanaka, K. L. (1986). The stratigraphy of Mars. *J. Geophys. Res.* **91**, E139–E158.
- Tanaka, K. L. & Golombeck, M. P. (1989). Martian tension fractures and the formation of grabens and collapse features at Valles Marineris. *Proc. Lunar Planet. Sci. Conf. 19th*, 383–96.
- Tanaka, K. L., Isbell, N. K., Scott, D. H., Greeley, R., & Guest, J. E. (1988). The resurfacing history of Mars: A synthesis of digitized, Viking-based geology. *Proc. Lunar Planet. Sci. Conf. 18th*, 665–78.
- Tanaka, K. L., Scott, D. H., & Greeley, R. (1992). Global stratigraphy. In *Mars*, pp. 345–82, eds. H. H. Kieffer, B. M. Jakosky, C. W. Snyder, & M. S. Matthews. The University of Arizona Press, Tucson and London.
- Tanaka, S. & Hamaguchi, H. (1997). Degree one heterogeneity and hemispherical variation of anisotropy in the inner core from PKP(BC)-PKP(DF) times. *J. Geophys. Res.* **102**, 2925–38.
- Tanimoto, T. (1990). Long-wavelength S-wave velocity structure throughout the mantle. *Geophys. J. Int.* **100**, 327–36.
- Tanimoto, T. & Anderson, D. L. (1985). Lateral heterogeneity and azimuthal anisotropy of the upper mantle: Love and Rayleigh waves 100–250 s. *J. Geophys. Res.* **90**, 1842–58.
- Tarbuck, E. J. & Lutgens, F. K. (1988). *Earth Science*. Merrill, Columbus, OH, fifth edition, 612 pp.
- Tatsumi, Y. & Eggins, S. (1995). *Subduction Zone Magmatism*. Blackwell Science, Cambridge, 211 pp.
- Tatsumi, Y. & Isoyama, H. (1988). Transportation of beryllium with H₂O at high pressures: Implication for magma genesis in subduction zones. *Geophys. Res. Lett.* **15**, 180–3.
- Tatsumoto, M., Knight, R. J., & Allègre, C. J. (1973). Time differences in the formation of meteorites as determined from the ratio of lead-207 to lead-206. *Science* **180**, 1279–83.
- Tatsumoto, M., Hegner, E., & Unruh, D. M. (1987). Origin of the West Maui volcanic rocks inferred from Pb, Sr, and Nd isotopes and a multicomponent model for oceanic basalt. *U.S. Geol. Surv. Prof. Pap. P 1350*, 723–44.
- Taylor, F. B. (1910). Bearing of the Tertiary mountain belt on the origin of the Earth's plan. *Geol. Soc. Am. Bull.* **21**, 179–226.
- Taylor, L. A., Shervais, J. W., Hunter, R. H., Shih, C.-Y., Bansal, B. M., Wooden, J., Nyquist, L. E., & Laul, L. C. (1983). Pre-4.2 AE mare-basalt volcanism in the lunar highlands. *Earth Planet. Sci. Lett.* **66**, 33–47.
- Taylor, S. R. (1967). The origin and growth of continents. *Tectonophysics* **4**, 17–34.
- (1977). Island arc models and the composition of the continental crust. In *Island Arcs, Deep Sea Trenches, and Back-Arc Basins*, pp. 325–35, eds. M. Talwani & W. C. Pitman, III, Maurice Ewing Series 1. American Geophysical Union, Washington, DC.

- Taylor, S. R. (1986). The origin of the Moon: Geochemical considerations. In *Origin of the Moon*, pp. 125–43, eds. W. K. Hartmann, R. J. Phillips, & G. J. Taylor. Lunar and Planetary Institute, Houston, Texas.
- Taylor, S. R. & McLennan, S. M. (1981). The composition and evolution of the continental crust: Rare earth element evidence from sedimentary rocks. *Phil. Trans. Roy. Soc. London A* **301**, 381–99.
- (1985). *The Continental Crust: Its Composition and Evolution, An Examination of the Geochemical Record Preserved in Sedimentary Rocks*. Blackwell Scientific Publ., Oxford, 312 pp.
- (1995). The geochemical evolution of the continental crust. *Rev. Geophys.* **33**, 241–65.
- Taylor, S. R. & White, A. J. R. (1965). Geochemistry of andesites and the growth of continents. *Nature* **208**, 271–3.
- Ten, A. A., Podladchikov, Y. Yu., Yuen, D. A., Larsen, T. B., & Malevsky, A. V. (1998). Comparison of mixing properties in convection with the particle-line method. *Geophys. Res. Lett.* **25**, 3205–8.
- Tera, F., Brown, L., Morris, J., Sacks, I. S., Klein, J., & Middleton, R. (1986). Sediment incorporation in island-arc magmas: Inferences from ^{10}Be . *Geochim. Cosmochim. Acta* **50**, 535–50.
- Thomas, P. C., Davies, M. E., Colvin, T. R., Oberst, J., Schuster, P., Neukum, G., Carr, M. H., McEwen, A., Schubert, G., Belton, M. J. S., & the Galileo Imaging Team (1998). The shape of Io from Galileo limb measurements. *Icarus* **135**, 175–80.
- Thompson, A. C. & Stevenson, D. J. (1983). Two-phase gravitational instabilities in thin disks with application to the origin of the Moon (abstract). In *Lunar and Planetary Science XIV*, pp. 787–8. Lunar and Planetary Institute, Houston, Texas.
- Thompson, J. (1882). On a changing tesselated structure in certain liquids. *Proc. Phil. Soc. Glasgow* **13**, 464–8.
- Thoraval, C. & Richards, M. A. (1997). The geoid constraint in global geodynamics: Viscosity structure, mantle heterogeneity models and boundary conditions. *Geophys. J. Int.* **131**, 1–8.
- Thurber, C. H. & Toksöz, M. N. (1978). Martian lithospheric thickness from elastic flexure theory. *Geophys. Res. Lett.* **5**, 977–80.
- Thurber, C. H., Hsui, A. T., & Toksöz, M. N. (1980). Thermal evolution of Ganymede and Callisto: Effects of solid-state convection and constraints from Voyager imagery. *Proc. Lunar Planet. Sci. Conf.* **11th**, 1957–77.
- Toksöz, M. N. & Hsui, A. T. (1978a). Numerical studies of back-arc convection and the formation of marginal basins. *Tectonophysics* **50**, 177–96.
- (1978b). Thermal history and evolution of Mars. *Icarus* **34**, 537–47.
- Toksöz, M. N., Minear, J. W., & Julian, B. R. (1971). Temperature field and geophysical effects of a downgoing slab. *J. Geophys. Res.* **76**, 1113–38.
- Toksöz, M. N., Hsui, A. T., & Johnston, D. H. (1978). Thermal evolutions of the terrestrial planets. *Moon and Planets* **18**, 281–320.
- Tonks, W. B. & Melosh, H. J. (1990). The physics of crystal settling and suspension in a turbulent magma ocean. In *Origin of the Earth*, pp. 151–74, eds. H. E. Newsom & J. H. Jones. Oxford University Press, New York.
- Toth, J. & Gurnis, M. (1998). Dynamics of subduction initiation at preexisting fault zones. *J. Geophys. Res.* **103**, 18053–67.
- Tovich, A. & Schubert, G. (1978). Island arc curvature, velocity of convergence and angle of subduction. *Geophys. Res. Lett.* **5**, 329–32.
- Tovich, A., Schubert, G., & Luyendyk, B. P. (1978). Mantle flow pressure and the angle of subduction: Non-Newtonian corner flows. *J. Geophys. Res.* **83**, 5892–8.
- Tozer, D. C. (1965a). Heat transfer and convection currents. *Phil. Trans. Roy. Soc. London A* **258**, 252–71.
- (1965b). Thermal history of the Earth. I. The formation of the core. *Geophys. J. Roy. Astron. Soc.* **9**, 95–112.
- (1967). Towards a theory of thermal convection in the mantle. In *The Earth's Mantle*, pp. 325–53, ed. T. F. Gaskell. Academic Press, London.
- Travis, B. & Olson, P. (1994). Convection with internal heat sources and thermal turbulence in the Earth's mantle. *Geophys. J. Int.* **118**, 1–19.

- Travis, B., Olson, P., & Schubert, G. (1990a). The transition from two-dimensional to three-dimensional planforms in infinite-Prandtl-number thermal convection. *J. Fluid Mech.* **216**, 71–91.
- Travis, B., Weinstein, S., & Olson, P. (1990b). Three-dimensional convection planforms with internal heat generation. *Geophys. Res. Lett.* **17**, 243–6.
- Treiman, A. H., Drake, M. J., Janssens, M.-J., Wolf, R., & Ebihara, M. (1986). Core formation in the Earth and Shergottite parent body(SPB): Chemical evidence from basalts. *Geochim. Cosmochim. Acta* **50**, 1071–91.
- Treiman, A. H., Jones, J. H., & Drake, M. J. (1987). Core formation in the Shergottite parent body and comparison with the Earth. *J. Geophys. Res.* **92**, E627–E632.
- Trompert, R. & Hansen, U. (1998). Mantle convection simulations with rheologies that generate plate-like behaviour. *Nature* **395**, 686–9.
- Trubitsyn, V. P. & Rykov, V. V. (1997). Mechanism of formation of an inclined subduction zone. *Izvest. Phys. Solid Earth* **33**, 427–37.
- Tsenn, M. C. & Carter, N. L. (1987). Upper limits of power law creep of rocks. *Tectonophysics* **136**, 1–26.
- Tullis, J. A. (1979). High temperature deformation of rocks and minerals. *Rev. Geophys. Space Phys.* **17**, 1137–54.
- Turcotte, D. L. (1974). Are transform faults thermal contraction cracks? *J. Geophys. Res.* **79**, 2573–7. (1979). Flexure. *Adv. Geophys.* **21**, 51–86.
- (1980a). Models for the evolution of sedimentary basins. In *Dynamics of Plate Interiors*, pp. 21–6, eds. A. W. Bally, P. L. Bender, T. R. McGechin, & R. I. Walcott, volume 1. American Geophysical Union, Washington, D. C.
- (1980b). On the thermal evolution of the Earth. *Earth Planet. Sci. Lett.* **48**, 53–58.
- (1982). Magma migration. *Ann. Rev. Earth Planet. Sci.* **10**, 397–408.
- (1983). Mechanisms of crustal deformation. *J. Geol. Soc. London* **140**, 701–24.
- (1987). A fractal interpretation of topography and geoid spectra on the Earth, Moon, Venus, and Mars. *J. Geophys. Res.* **92**, E597–E601.
- (1989a). Dynamics of recycling. In *Crust/Mantle Recycling at Convergence Zones*, pp. 245–57, eds. S. R. Hart & L. Gülen. Kluwer Academic Publishers, Dordrecht.
- (1989b). Geophysical processes influencing the lower continental crust. In *Properties and Processes of Earth's Lower Crust*, pp. 321–9, eds. R. F. Mereu, S. Mueller, & D. M. Fountain, Geophysical Monograph 51, IUGG Vol. 6. American Geophysical Union and International Union of Geodesy and Geophysics, Washington, DC.
- (1990). On the role of laminar and turbulent flow in buoyancy driven magma fractures. In *Magma Transport and Storage*, pp. 103–11, ed. M. P. Ryan. John Wiley & Sons, Chichester, England.
- (1993). An episodic hypothesis for Venusian tectonics. *J. Geophys. Res.* **98**, 17061–8.
- (1995). How does Venus lose heat? *J. Geophys. Res.* **100**, 16931–40.
- (1996). Magellan and comparative planetology. *J. Geophys. Res.* **101**, 4765–73.
- Turcotte, D. L. & Ahern, J. L. (1978). A porous flow model for magma migration in the asthenosphere. *J. Geophys. Res.* **83**, 767–72.
- Turcotte, D. L. & Burke, K. (1978). Global sea-level changes and the thermal structure of the Earth. *Earth Planet. Sci. Lett.* **41**, 341–6.
- Turcotte, D. L. & Emerman, S. H. (1983). Mechanisms of active and passive rifting. *Tectonophysics* **94**, 39–50.
- Turcotte, D. L. & Kellogg, L. H. (1986a). Isotopic modelling of the evolution of the mantle and crust. *Rev. Geophys.* **24**, 311–28.
- (1986b). Implications of isotope data for the origin of the Moon. In *Origin of the Moon*, pp. 311–29, eds. W. K. Hartmann, R. J. Phillips, & G. J. Taylor. Lunar and Planetary Institute, Houston, Texas.
- Turcotte, D. L. & McAdoo, D. C. (1979). Geoid anomalies and the thickness of the lithosphere. *J. Geophys. Res.* **84**, 2381–7.
- Turcotte, D. L. & Oxburgh, E. R. (1967). Finite amplitude convective cells and continental drift. *J. Fluid Mech.* **28**, 29–42.

- Turcotte, D. L. & Oxburgh, E. R. (1968). A fluid theory for the deep structure of dip-slip fault zones. *Phys. Earth Planet. Int.* **1**, 381–6.
- (1970). Lunar convection. *J. Geophys. Res.* **75**, 6549–52.
- (1972a). Statistical thermodynamic model for the distribution of crustal heat sources. *Science* **176**, 1021–2.
- (1972b). Mantle convection and the new global tectonics. *Ann. Rev. Fluid Mech.* **4**, 33–68.
- Turcotte, D. L. & Phipps Morgan, J. (1992). The physics of magma migration and mantle flow beneath a mid-ocean ridge. In *Mantle Flow and Melt Generation at Mid-Ocean Ridges*, pp. 155–82, eds. J. Phipps Morgan, D. K. Blackman, & J. M. Sinton, Geophysical Monograph 71. American Geophysical Union, Washington, DC.
- Turcotte, D. L. & Schubert, G. (1971). Structure of the olivine–spinel phase boundary in the descending lithosphere. *J. Geophys. Res.* **76**, 7980–7.
- (1972). Correction. *J. Geophys. Res.* **77**, 2146.
- (1973). Frictional heating of the descending lithosphere. *J. Geophys. Res.* **78**, 5876–86.
- (1982). *Geodynamics: Applications of Continuum Physics to Geological Problems*. John Wiley, New York, 450 pp.
- (1988). Tectonic implications of radiogenic noble gases in planetary atmospheres. *Icarus* **74**, 36–46.
- Turcotte, D. L., Hsui, A. T., Torrance, K. E., & Schubert, G. (1974). Influence of viscous dissipation on Bénard convection. *J. Fluid Mech.* **64**, 369–74.
- Turcotte, D. L., Haxby, W. F., & Ockendon, J. R. (1977). Lithospheric instabilities. In *Island Arcs, Deep Sea Trenches, and Back-Arc Basins*, pp. 63–9, eds. M. Talwani & W. C. Pitman, III, Maurice Ewing Series 1. American Geophysical Union, Washington, DC.
- Turcotte, D. L., Cooke, F. A., & Willeman, R. J. (1979). Parameterized convection within the Moon and the terrestrial planets. *Proc. Lunar Planet. Sci. Conf.* **10th**, 2375–92.
- Turcotte, D. L., Liu, J. Y., & Kulhawy, F. H. (1984). The role of an intracrustal asthenosphere on the behavior of major strike-slip faults. *J. Geophys. Res.* **89**, 5801–16.
- Turcotte, D. L., Emerman, S. H., & Spence, D. A. (1987). Mechanics of dyke injection. In *Mafic Dyke Swarms*, pp. 25–9, eds. H. C. Halls & W. F. Fahrig, Special Paper 34. Geol. Assn. Canada.
- Turekian, K. K. (1959). The terrestrial economy of helium and argon. *Geochim. Cosmochim. Acta* **17**, 37–43.
- Tushingham, A. M. & Peltier, W. R. (1992). Validation of the ICE-3G model of Würm-Wisconsin deglaciation using a global data base of relative sea level histories. *J. Geophys. Res.* **97**, 3285–304.
- Tveitereid, M. (1978). Thermal convection in a horizontal fluid layer with internal heat sources. *Int. J. Heat Mass Trans.* **21**, 335–9.
- Tveitereid, M. & Palm, E. (1976). Convection due to internal heat sources. *J. Fluid Mech.* **76**, 481–99.
- Twiss, R. J. & Moores, E. M. (1992). *Structural Geology*. W. H. Freeman and Company, New York, 532 pp.
- Unrug, R. (1992). The supercontinent cycle and Gondwanaland assembly: Component cratons and the timing of suturing events. *J. Geodynam.* **16**, 215–40.
- Urakawa, S., Kato, M., & Kumazawa, M. (1987). Experimental study on the phase relations in the system Fe-Ni-O-S to 15 GPa. In *High-Pressure Research in Mineral Physics*, pp. 95–111, eds. M. H. Manghnani & Y. Syono, Geophysical Monograph 39. American Geophysical Union, Washington, DC.
- Urey, H. C. (1951). The origin and development of the Earth and other terrestrial planets. *Geochim. Cosmochim. Acta* **1**, 209–77.
- Urey, H. (1952). *The Planets: Their Origin and Development*. Yale University Press, New Haven, Conn., 245 pp.
- Usselman, T. M. (1975). Experimental approach to the state of the core. Part I. The liquidus relations of the Fe-rich portion of the Fe-Ni-S system from 30 to 100 kb. *Am. J. Sci.* **275**, 278–90.
- Utsu, T. (1971). Seismological evidence for anomalous structure of island arcs with special reference to the Japanese region. *Rev. Geophys. Space Phys.* **9**, 839–90.
- Uyeda, S. & Kanamori, H. (1979). Back-arc opening and the mode of subduction. *J. Geophys. Res.* **84**, 1049–61.

- van Bemmelen, R. W. & Berlage, H. P. (1934). Versuch einer mathematischen Behandlung geotektonischer Bewegungen unter besonderer Berücksichtigung der Undationstheorie. *Gerlands Beitr. Geophys.* **43**, 19–55.
- van den Berg, A. P. & Yuen, D. A. (1997). The role of shear heating in lubricating mantle flow. *Earth Planet. Sci. Lett.* **151**, 33–42.
- van der Hilst, R. (1995). Complex morphology of subducted lithosphere in the mantle beneath the Tonga trench. *Nature* **374**, 154–57.
- van der Hilst, R. D. & Kárasón, H. (1999). Compositional heterogeneity in the bottom 1,000 kilometers of Earth's mantle: Toward a hybrid convection model. *Science* **283**, 1885–88.
- van der Hilst, R., Engdahl, R., Spakman, W., & Nolet, G. (1991). Tomographic imaging of subducted lithosphere below northwest Pacific island arcs. *Nature* **353**, 37–43.
- van der Hilst, R. D., Widjiantoro, S., & Engdahl, E. R. (1997). Evidence for deep mantle circulation from global tomography. *Nature* **386**, 578–84.
- van der Hilst, R. D., Widjiantoro, S., Creager, K. C., & McSweeney, T. J. (1998). Deep subduction and aspherical variations in *P*-wavespeed at the base of Earth's mantle. In *The Core-Mantle Boundary Region*, pp. 5–20, eds. M. Gurnis, M. E. Wysession, E. Knittle, & B. A. Buffett, volume 28 of *Geodynamics Series*. American Geophysical Union, Washington, DC.
- van der Lee, S. & Nolet, G. (1997). Upper mantle *S* velocity structure of North America. *J. Geophys. Res.* **102**, 22815–38.
- van Keken, P. (1997). Evolution of starting mantle plumes: A comparison between numerical and laboratory models. *Earth Planet. Sci. Lett.* **148**, 1–11.
- van Keken, P. E. & Ballentine, C. J. (1998). Whole-mantle versus layered mantle convection and the role of a high-viscosity lower mantle in terrestrial volatile evolution. *Earth Planet. Sci. Lett.* **156**, 19–32.
- van Keken, P. E. & Yuen, D. A. (1995). Dynamical influences of high viscosity in the lower mantle induced by the steep melting curve of perovskite: Effects of curvature and time dependence. *J. Geophys. Res.* **100**, 15233–48.
- van Keken, P., Yuen, D. A., & van den Berg, A. (1992). Pulsating diapiric flows: Consequences of vertical variations in mantle creep laws. *Earth Planet. Sci. Lett.* **112**, 179–94.
- van Keken, P. E., Yuen, D. A., & van den Berg, A. P. (1994). Implications for mantle dynamics from the high melting temperature of perovskite. *Science* **264**, 1417–39.
- Vasco, D. W. & Johnson, L. R. (1998). Whole Earth structure estimated from seismic arrival times. *J. Geophys. Res.* **103**, 2633–71.
- Vassiliou, M. S. & Hager, B. H. (1988). Subduction zone earthquakes and stress in slabs. *Pure Appl. Geophys.* **128**, 547–624.
- Veeder, G. J., Matson, D. L., Johnson, T. V., Blaney, D. L., & Goguen, J. D. (1994). Io's heat flow from infrared radiometry: 1983–1993. *J. Geophys. Res.* **99**, 17095–162.
- Veevers, J. J. (1989). Middle/Late Triassic (230 ± 1 Ma) singularity in the stratigraphic and magmatic history of the Pangean heat anomaly. *Geology* **17**, 784–7.
- Veizer, J. & Jansen, S. L. (1979). Basement and sedimentary recycling and continental evolution. *J. Geology* **87**, 341–70.
- Vening Meinesz, F. A. (1937). Results of maritime gravity research, 1923–32. In *International Aspects of Oceanography: Oceanographic Data and Provisions for Oceanographic Research*, pp. 61–69. National Academy of Sciences, Washington, DC.
- (1948). Major tectonic phenomena and the hypothesis of convection currents in the Earth. *Quart. J. Geol. Soc. London* **103**, 191–207.
- Verhoogen, J. (1951). The adiabatic gradient in the mantle. *Trans. Am. Geophys. Un.* **32**, 41–3.
- (1954). Petrological evidence on temperature distribution in the mantle of the Earth. *Trans. Am. Geophys. Un.* **35**, 85–92.
- (1961). Heat balance of the Earth's core. *Geophys. J. Roy. Astron. Soc.* **4**, 276–81.
- (1965). Phase changes and convection in the Earth's mantle. *Phil. Trans. Roy. Soc. London A* **258**, 276–83.
- (1973). Thermal regime of the Earth's core. *Phys. Earth Planet. Int.* **7**, 47–58.
- (1980). *Energetics of the Earth*. National Academy of Sciences, Washington, DC, 139 pp.

- Vermeersen, L. L. A., & Vlaar, N. J. (1993). Changes in the Earth's rotation by tectonic movements. *Geophys. Res. Lett.* **20**, 81–4.
- Vermeersen, L. L. A., Sabadini, R., Spada, G., & Vlaar, N. J. (1994). Mountain building and Earth rotation. *Geophys. J. Int.* **117**, 610–24.
- Vermeersen, L. L. A., Fournier, A., & Sabadini, R. (1997). Changes in rotation induced by Pleistocene ice masses with stratified analytical Earth models. *J. Geophys. Res.* **102**, 27689–702.
- Vidale, J. E. & Benz, H. M. (1992). Upper-mantle seismic discontinuities and the thermal structure of subduction zones. *Nature* **356**, 678–83.
- Vidale, J. E. & Hedlin, M. A. H. (1998). Evidence for partial melt at the core–mantle boundary north of Tonga from the strong scattering of seismic waves. *Nature* **391**, 682–5.
- Vilas, F. (1988). Surface composition of Mercury from reflectance spectrophotometry. In *Mercury*, pp. 59–76, eds. F. Vilas, C. R. Chapman, & M. S. Matthews. The University of Arizona Press, Tucson.
- Vincent, A. P. & Yuen, D. A. (1988). Thermal attractor in chaotic convection with high-Prandtl-number fluids. *Phys. Rev. A* **38**, 328–34.
- (1989). Multimode mean-field filtering experiments for chaotic thermal convection. *Geophys. Astrophys. Fluid Dyn.* **47**, 131–56.
- Vine, F. J. (1966). Spreading of the ocean floor – New evidence. *Science* **154**, 1405–15.
- Vine, F. J. & Matthews, D. H. (1963). Magnetic anomalies over oceanic ridges. *Nature* **199**, 947–9.
- Vine, F. J. & Wilson, J. T. (1965). Magnetic anomalies over a young oceanic ridge off Vancouver Island. *Science* **150**, 485–9.
- Vinogradov, A. P. (1962). Average contents of chemical elements in the principal types of igneous rocks of the Earth's crust. *Geochemistry* **7**, 641–64.
- Vissers, R. L. M., Drury, M. R., Strating, E. H. H., Spiers, C. J., & van der Wal, D. (1995). Mantle shear zones and their effect on lithosphere strength during continental breakup. *Tectonophysics* **249**, 155–71.
- Vogt, P. R. (1974). Volcano height and plate thickness. *Earth Planet. Sci. Lett.* **23**, 337–48.
- (1979). Global magmatic episodes: New evidence and implications for the steady-state mid-ocean ridge. *Geology* **7**, 93–98.
- (1981). On the applicability of thermal conduction models to mid-plate volcanism: Comments on a paper by Gass et al. *J. Geophys. Res.* **86**, 950–60.
- Vollmer, R. (1977). Terrestrial lead isotopic evolution and formation time of the Earth's core. *Nature* **270**, 144–7.
- Von Herzen, R. P., Detrick, R. S., Crough, S. T., Epp, D., & Fehn, U. (1982). Thermal origin of the Hawaiian swell: Heat flow evidence and thermal models. *J. Geophys. Res.* **87**, 6711–23.
- Von Herzen, R. P., Cordery, M. J., Detrick, R. S., & Fang, C. (1989). Heat flow and the thermal origin of hot spot swells: The Hawaiian Swell revisited. *J. Geophys. Res.* **94**, 13783–99.
- von Huene, R. & Scholl, D. W. (1991). Observations at convergent margins concerning sediment subduction, subduction erosion, and the growth of continental crust. *Rev. Geophys.* **29**, 279–316.
- Wada, Y. (1994). On the relationship between dike width and magma viscosity. *J. Geophys. Res.* **99**, 17743–55.
- Wadati, K. (1928). Shallow and deep earthquakes. *Geophys. Mag.* **1**, 161–202.
- (1934/35). On the activity of deep-focus earthquakes in the Japan Islands and neighbourhoods. *Geophys. Mag.* **8**, 305–25.
- Wahr, J. & de Vries, D. (1989). The possibility of lateral structure inside the core and its implications for nutation and Earth tide observations. *Geophys. J. Int.* **97**, 511–9.
- Walcott, R. I. (1972a). Late quaternary vertical movements in eastern North America: Quantitative evidence of glacio-isostatic rebound. *Rev. Geophys. Space Phys.* **10**, 849–84.
- (1972b). Past sea levels, eustasy and deformation of the Earth. *Quaternary Res.* **2**, 1–14.
- (1973). Structure of the Earth from glacio-isostatic rebound. *Ann. Rev. Earth Planet. Sci.* **1**, 15–37.
- Walker, D., Stolper, E. M., & Hays, J. F. (1978). A numerical treatment of melt/solid segregation: Size of the ecrite parent body and stability of the terrestrial low-velocity zone. *J. Geophys. Res.* **83**, 6005–13.
- Walker, J. C. G. (1977). *Evolution of the Atmosphere*. Macmillan, New York, 318 pp.

- Walzer, U. & Hendel, R. (1997). Time-dependent thermal convection, mantle differentiation and continental-crust growth. *Geophys. J. Int.* **130**, 303–25.
- Wang, K. & Reeber, R. R. (1995). A simplified model for predicting high pressure thermal expansion of MgO. *Geophys. Res. Lett.* **22**, 1297–300.
- Wänke, H. & Dreibus, G. (1986). Geochemical evidence for the formation of the Moon by impact-induced fission of the proto-Earth. In *Origin of the Moon*, pp. 649–72, eds. W. K. Hartmann, R. J. Phillips, & G. J. Taylor. Lunar and Planetary Institute, Houston, Texas.
- Warren, P. H. (1985). The magma ocean concept and lunar evolution. *Ann. Rev. Earth Planet. Sci.* **13**, 201–40.
- Wasserburg, G. J. & DePaolo, D. J. (1979). Models of Earth structure inferred from neodymium and strontium isotopic abundances. *Proc. Nat. Acad. Sci. USA* **76**, 3594–8.
- Wasson, J. T. & Warren, P. H. (1980). Contribution of the mantle to the lunar asymmetry. *Icarus* **44**, 752–71.
- Watson, S. & McKenzie, D. (1991). Melt generation by plumes: A study of Hawaiian volcanism. *J. Petrol.* **32**, 501–37.
- Watson, S. & Spiegelman, M. (1994). Geochemical effects of magmatic solitary waves. *Geophys. J. Int.* **117**, 284–95.
- Watts, A. B. (1976). Gravity and bathymetry in the central Pacific Ocean. *J. Geophys. Res.* **81**, 1533–53.
- Weaver, B. L. & Tarney, J. (1984). Empirical approach to estimating the composition of the continental crust. *Nature* **310**, 575–7.
- Webb, E. K. & Stevenson, D. J. (1987). Subsidence of topography on Io. *Icarus* **70**, 348–53.
- Weber, M. (1993). P- and S-wave reflections from anomalies in the lowermost mantle. *Geophys. J. Int.* **115**, 183–210.
- Wedepohl, K. H. (1994). The composition of the continental crust. *Mineral. Mag.* **58A**, 959–60.
- Weertman, J. (1970). The creep strength of the Earth's mantle. *Rev. Geophys. Space Phys.* **8**, 145–68.
- (1971). Theory of water-filled crevasses in glaciers applied to vertical magma transport beneath oceanic ridges. *J. Geophys. Res.* **76**, 1171–83.
- Weertman, J. & Weertman, J. R. (1975). High temperature creep of rock and mantle viscosity. *Ann. Rev. Earth Planet. Sci.* **3**, 293–315.
- Wegener, A. (1915). *Die Entstehung der Kontinente und Ozeane*. Vieweg, Braunschweig, 94 pp.
- (1924). *The Origin of Continents and Oceans*. E. P. Dutton, New York, 212 pp. Trans. from 3rd German ed. by J. G. A Skerl.
- (1929). *Die Entstehung der Kontinente und Ozeane*. Vieweg, Braunschweig, fourth edition.
- Weidenschilling, S. J. (1976). Accretion of the terrestrial planets. II. *Icarus* **27**, 161–70.
- Weidner, D. J. (1985). A mineral physics test of a pyrolite mantle. *Geophys. Res. Lett.* **12**, 417–20.
- Weidner, D. V. (1986). Mantle model based on measured physical properties of minerals. In *Chemistry and Physics of Terrestrial Planets*, pp. 251–74, ed. S. K. Saxena, Springer-Verlag, New York.
- Weidner, D. J. & Wang, Y. (1988). Chemical- and Clapeyron-induced buoyancy at the 660 km discontinuity. *J. Geophys. Res.* **103**, 7431–41.
- Weijermars, R. (1988a). Convection experiments in high Prandtl number silicones, Part 1. Rheology, equipment, nomograms and dynamic scaling of stress- and temperature-dependent convection in a centrifuge. *Tectonophysics* **154**, 71–96.
- (1988b). Convection experiments in high Prandtl number silicones, Part 2. Deformation, displacement and mixing in the Earth's mantle. *Tectonophysics* **154**, 97–123.
- Weinberg, R. F. (1997). Rise of starting plumes through mantle of temperature-, pressure-, and stress-dependent viscosity. *J. Geophys. Res.* **102**, 7613–23.
- Weinstein, S. A. (1992). Induced compositional layering in a convecting fluid layer by an endothermic phase transition. *Earth Planet. Sci. Lett.* **113**, 23–39.
- (1993). Catastrophic overturn of the Earth's mantle driven by multiple phase changes and internal heat generation. *Geophys. Res. Lett.* **20**, 101–4.
- (1995). The effects of a deep mantle endothermic phase change on the structure of thermal convection in silicate planets. *J. Geophys. Res.* **100**, 11719–28.

- Weinstein, S. A. (1998). The effect of convection planform on the toroidal-poloidal energy ratio. *Earth Planet. Sci. Lett.* **155**, 87–95.
- Weinstein, S. A. & Christensen, U. (1991). Convection planforms in a fluid with a temperature-dependent viscosity beneath a stress-free upper boundary. *Geophys. Res. Lett.* **18**, 2035–8.
- Weinstein, S. & Olson, P. (1990). Planforms in thermal convection with internal heat sources at large Rayleigh and Prandtl numbers. *Geophys. Res. Lett.* **17**, 239–42.
- Weinstein, S. A. & Olson, P. L. (1992). Thermal convection with non-Newtonian plates. *Geophys. J. Int.* **111**, 515–30.
- Wessel, P., Kroenke, L. W., & Bercovici, D. (1996). Pacific Plate motion and undulations in geoid and bathymetry. *Earth Planet. Sci. Lett.* **140**, 53–66.
- Wetherill, G. W. (1976). The role of large bodies in the formation of the Earth and Moon. *Proc. Lunar Planet. Sci. Conf. 7th*, 3245–57.
- (1985). Occurrence of giant impacts during the growth of the terrestrial planets. *Science* **228**, 877–9.
- (1986). Accumulation of the terrestrial planets and implications concerning lunar origin. In *Origin of the Moon*, pp. 519–50, eds. R. J. Phillips & G. J. Taylor. Lunar and Planetary Institute, Houston, Texas.
- (1988). Accumulation of Mercury from planetesimals. In *Mercury*, pp. 670–91, eds. F. Vilas, C. R. Chapman, & M. S. Matthews. The University of Arizona Press, Tucson.
- (1990). Formation of the Earth. *Ann. Rev. Earth Planet. Sci.* **18**, 205–56.
- White, D. B. (1988). The planforms and onset of convection with a temperature-dependent viscosity. *J. Fluid Mech.* **191**, 247–86.
- White, R. S. (1993). Melt production rates in mantle plumes. *Phil. Trans. Roy. Soc. London A* **342**, 137–53.
- White, R. & McKenzie, D. (1989). Magmatism at rift zones: The generation of volcanic continental margins and flood basalts. *J. Geophys. Res.* **94**, 7685–729.
- White, R. S. & McKenzie, D. (1995). Mantle plumes and flood basalts. *J. Geophys. Res.* **100**, 17543–85.
- White, W. (1985). Sources of oceanic basalts: Radiogenic isotopic evidence. *Geology* **13**, 115–8.
- Whitehead, J. A. (1982). Instabilities of fluid conduits in a flowing Earth—are plates lubricated by the asthenosphere? *Geophys. J. Roy. Astron. Soc.* **70**, 415–33.
- (1987). A laboratory demonstration of solitons using a vertical watery conduit in syrup. *Am. J. Phys.* **55**, 998–1003.
- (1988). Fluid models of geological hotspots. *Ann. Rev. Fluid Mech.* **20**, 61–87.
- Whitehead, J. A. & Helffrich, K. R. (1988). Wave transport of deep mantle material. *Nature* **336**, 59–61.
- (1990). Magma waves and diapiric dynamics. In *Magma Storage and Transport*, pp. 53–76, ed. M. L. Ryan, John Wiley & Sons, Chichester, England.
- Whitehead, J. A. & Luther, D. S. (1975). Dynamics of laboratory diapir and plume models. *J. Geophys. Res.* **80**, 705–17.
- Whitehead, J. A. & Parsons, B. (1978). Observations of convection at Rayleigh numbers up to 760000 in a fluid with large Prandtl number. *Geophys. Astrophys. Fluid Dyn.* **9**, 201–17.
- Wicks, C. W. & Richards, M. A. (1993). A detailed map of the 660-kilometer discontinuity beneath the Izu-Bonin subduction zone. *Science* **261**, 1424–7.
- Widiyantoro, S. & van der Hilst, R. (1996). Structure and evolution of lithospheric slab beneath the Sunda arc, Indonesia. *Science* **271**, 1566–70.
- Wienbruch, U. & Spohn, T. (1995). A self-sustained magnetic field on Io? *Planet. Space Sci.* **43**, 1045–57.
- Wilhelms, D. E. & Squyres, S. W. (1984). The Martian hemispheric dichotomy may be due to a giant impact. *Nature* **309**, 138–40.
- Willemann, R. J. & Turcotte, D. L. (1982). The role of lithospheric stress in the support of the Tharsis rise. *J. Geophys. Res.* **87**, 9793–801.
- Williams, Q. & Garnero, E. J. (1996). Seismic evidence for partial melt at the base of Earth's mantle. *Science* **273**, 1528–30.
- Williams, Q., Jeanloz, R., Bass, J., Svendsen, B., & Ahrens, T. J. (1987). The melting curve of iron to 250 gigapascals: A constraint on the temperature at Earth's center. *Science* **236**, 181–2.

- Williams, Q., Revenaugh, J., & Garnero, E. (1998). A correlation between ultra-low basal velocities in the mantle and hot spots. *Science* **281**, 546–9.
- Williamson, E. D. & Adams, L. H. (1923). Density distribution in the earth. *J. Washington Acad. Sci.* **13**, 413–31.
- Wilshire, H. G. & Kirby, S. H. (1989). Dikes, joints, and faults in the upper mantle. *Tectonophys.* **161**, 23–31.
- Wilson, J. T. (1963a). Hypothesis of Earth's behaviour. *Nature* **198**, 925–9.
- (1963b). Evidence from islands on the spreading of ocean floors. *Nature* **197**, 536–8.
- (1963c). A possible origin of the Hawaiian islands. *Canad. J. Phys.* **41**, 863–70.
- (1965a). A new class of faults and their bearing on continental drift. *Nature* **207**, 343–7.
- (1965b). Transform faults, oceanic ridges, and magnetic anomalies southwest of Vancouver Island. *Science* **150**, 482–5.
- (1966). Did the Atlantic close and then re-open? *Nature* **211**, 676–81.
- (1973). Mantle plumes and plate motions. *Tectonophysics* **19**, 149–64.
- Wilson, J. T. & Burke, K. (1972). Two types of mountain building. *Nature* **239**, 448–9.
- Wilson, J. T. & Head, J. W. (1981). Ascent and eruption of basaltic magma on the Earth and Moon. *J. Geophys. Res.* **86**, 2971–3001.
- Windley, B. F. (1977). Timing of continental growth and emergence. *Nature* **270**, 426–8.
- (1995). *The Evolving Continents*. John Wiley & Sons, Chichester, England, 3rd edition, 526 pp.
- Wise, D. U. (1974). Continental margins, freeboard and the volumes of continents and oceans through time. In *The Geology of Continental Margins*, pp. 45–58, eds. C. A. Burk & C. L. Drake. Springer-Verlag, New York.
- Wise, D. U. & Yates, M. T. (1970). Mascons as structural relief on a lunar 'Moho'. *J. Geophys. Res.* **75**, 261–8.
- Wise, D. U., Golombek, M. P., & McGill, G. E. (1979a). Tectonic evolution of Mars. *J. Geophys. Res.* **84**, 7934–9.
- (1979b). Tharsis province of Mars: Geologic sequence, geometry, and a deformation mechanism. *Icarus* **38**, 456–72.
- Wolfe, C. J., Bjarnason, I. T., VanDecar, J. C., & Solomon, S. C. (1997). Seismic structure of the Iceland mantle plume. *Nature* **385**, 245–7.
- Wood, J. A. (1986). Moon over Mauna Loa: A review of hypotheses of formation of Earth's Moon. In *Origin of the Moon*, pp. 17–55, eds. W. K. Hartmann, R. J. Phillips, & G. J. Taylor. Lunar and Planetary Institute, Houston, Texas.
- Wood, J. A., Dickey, J. S., Marvin, U. B., & Powell, B. N. (1970). Lunar anorthosites and a geophysical model of the moon. *Proc. Apollo 11 Lunar Sci. Conf.* **1**, 965–88.
- Woodhouse, J. H. & Dziewonski, A. M. (1984). Mapping the upper mantle: Three-dimensional modeling of Earth structure by inversion of seismic waveforms. *J. Geophys. Res.* **89**, 5953–86.
- (1989). Seismic modelling of the Earth's large-scale three-dimensional structure. *Phil. Trans. Roy. Soc. London A* **328**, 291–308.
- Woods, M. T. & Okal, E. A. (1996). Rayleigh-wave dispersion along the Hawaiian Swell: A test of lithospheric thinning by thermal rejuvenation at a hotspot. *Geophys. J. Int.* **125**, 325–39.
- Worsley, T. R., Nance, D., & Moody, J. B. (1984). Global tectonics and eustasy for the past 2 billion years. *Marine Geology* **58**, 373–400.
- Wright, J. A., Jessop, A. M., Judge, A. S., & Lewis, T. J. (1980). Geothermal measurements in Newfoundland. *Canad. J. Earth Sci.* **17**, 1370–6.
- Wright, T. L., Kinoshita, W. T., & Peck, D. L. (1968). March 1965 eruption of Kilauea volcano and the formation of Makaopuhi lava lake. *J. Geophys. Res.* **73**, 3181–205.
- Wu, P. (1995). Can observations of postglacial rebound tell whether the rheology of the mantle is linear or nonlinear? *Geophys. Res. Lett.* **22**, 1645–8.
- Wu, P. & Peltier, W. R. (1983). Glacial isostatic adjustment and the free air gravity anomaly as a constraint on deep mantle viscosity. *Geophys. J. Roy. Astron. Soc.* **74**, 377–449.
- Wyllie, P. J. (1971). *The Dynamic Earth: Textbook in Geosciences*. John Wiley & Sons, Inc., New York, 416 pp.

- Wysession, M. E., Lay, T., Revenaugh, J., Williams, Q., Garnero, E. J., Jeanloz, R., & Kellogg, L. H. (1998). The D'' discontinuity and its implications. In *The Core–Mantle Boundary Region*, pp. 273–97, eds. M. Gurnis, M. E. Wysession, E. Knittle, & B. A. Buffett, volume 28 of *Geodynamics Series*. American Geophysical Union, Washington, DC.
- Yale, L. B. & Carpenter, S. J. (1998). Large igneous provinces and giant dike swarms: Proxies for supercontinent cyclicity and mantle convection. *Earth Planet. Sci. Lett.* **163**, 109–22.
- Yamaoka, K. & Fukao, Y. (1987). Why do island arcs form cusps at their junctions? *Geology* **15**, 34–6.
- Yamaoka, K., Fukao, Y., & Kumazawa, M. (1986). Spherical shell tectonics: Effects of sphericity and inextensibility on the geometry of the descending lithosphere. *Rev. Geophys.* **24**, 27–53.
- Yeats, R. S. (1981). Quaternary flake tectonics of the California Transverse Ranges. *Geology* **9**, 16–20.
- Yoder, C. F. (1979). How tidal heating in Io drives the Galilean orbital resonance locks. *Nature* **279**, 767–70.
- (1981). The free librations of a dissipative Moon. *Phil. Trans. Roy. Soc. London A* **303**, 327–38.
- Yoder, C. F. & Peale, S. J. (1981). The tides of Io. *Icarus* **47**, 1–35.
- Yoder, C. F., Williams, J. G., Dickey, J. O., Schutz, B. E., Eanes, R. J., & Tapley, B. D. (1983). Secular variation of Earth's gravitational harmonic J_2 coefficient from Lageos and nontidal acceleration of Earth rotation. *Nature* **303**, 757–62.
- Yokokura, T. (1981). On subduction dip angles. *Tectonophysics* **77**, 63–77.
- Yoshida, S., Sumita, I. & Kumazawa, M. (1996). Growth model of the inner core coupled with the outer core dynamics and the resulting elastic anisotropy. *J. Geophys. Res.* **101**, 28085–103.
- Yoshioka, S. & Wortel, M. J. R. (1995). Three-dimensional numerical modeling of detachment of subducted lithosphere. *J. Geophys. Res.* **100**, 20223–44.
- Young, C. J. & Lay, T. (1987). The core–mantle boundary. *Ann. Rev. Earth Planet. Sci.* **15**, 25–46.
- (1990). Multiple phase analysis of the shear velocity structure in the d'' region beneath Alaska. *J. Geophys. Res.* **95**, 17385–402.
- Young, R. E. (1974). Finite-amplitude thermal convection in a spherical shell. *J. Fluid Mech.* **63**, 695–721.
- Young, R. E. & Schubert, G. (1974). Temperatures inside Mars: Is the core liquid or solid? *Geophys. Res. Lett.* **1**, 157–60.
- Yuen, D. A. & Fleitout, L. (1984). Stability of the oceanic lithosphere with variable viscosity: An initial-value approach. *Phys. Earth Planet. Int.* **34**, 173–85.
- Yuen, D. A. & Peltier, W. R. (1980). Mantle plumes and the thermal stability of the D'' layer. *Geophys. Res. Lett.* **7**, 625–8.
- Yuen, D. A. & Sabadini, R. (1984). Secular rotational motions and the mechanical structure of a dynamical viscoelastic Earth. *Phys. Earth Planet. Int.* **36**, 391–412.
- (1985). Viscosity stratification of the lower mantle as inferred by the J_2 observation. *Ann. Geophysicae* **3**, 647–54.
- Yuen, D. A. & Schubert, G. (1976). Mantle plumes: A boundary layer approach for Newtonian and non-Newtonian temperature-dependent rheologies. *J. Geophys. Res.* **81**, 2499–510.
- Yuen, D. A., Fleitout, L., Schubert, G., & Froidevaux, C. (1978). Shear deformation zones along major transform faults and subducting slabs. *Geophys. J. Roy. Astron. Soc.* **54**, 93–119.
- Yuen, D. A., Peltier, W. R., & Schubert, G. (1981). On the existence of a second scale of convection in the upper mantle. *Geophys. J. Roy. Astron. Soc.* **65**, 171–90.
- Yuen, D. A., Sabadini, R., & Boschi, E. V. (1982). Viscosity of the lower mantle as inferred from rotational data. *J. Geophys. Res.* **87**, 10745–62.
- Yuen, D. A., Hansen, U., Zhao, W., Vincent, A. P., & Malevsky, A. V. (1993). Hard turbulent thermal convection and thermal evolution of the mantle. *J. Geophys. Res.* **98**, 5355–73.
- Yuen, D. A., Reuteler, D. M., Balachandar, S., Steinbach, V., Malevsky, A. V., & Smedsø, J. J. (1994). Various influences on three-dimensional mantle convection with phase transitions. *Phys. Earth Planet. Int.* **86**, 185–203.
- Yuen, D. A., Balachandar, S., Steinbach, V. C., Honda, S., Reuteler, D. M., Smedsø, J. J., & Lauer, G. S. (1995). Non-equilibrium effects of core-cooling and time-dependent internal heating on mantle flush events. *Nonlinear Processes in Geophysics* **2**, 206–21.

- Zahnle, K. J., Kasting, J. F., & Pollack, J. B. (1988). Evolution of a steam atmosphere during Earth's accretion. *Icarus* **74**, 62–97.
- Zahnle, K., Dones, L., & Levison, H. F. (1998). Cratering rates on the Galilean satellites. *Icarus* **136**, 202–22.
- Zartman, R. E. & Doe, B. R. (1981). Plumbotectonics: The model. *Tectonophysics* **75**, 135–62.
- Zebib, A., Schubert, G., & Straus, J. M. (1980). Infinite Prandtl number thermal convection in a spherical shell. *J. Fluid Mech.* **97**, 257–77.
- Zebib, A., Schubert, G., Dein, J. L., & Paliwal, R. C. (1983). Character and stability of axisymmetric thermal convection in spheres and spherical shells. *Geophys. Astrophys. Fluid Dyn.* **23**, 1–42.
- Zebib, A., Goyal, A. K., & Schubert, G. (1985). Convective motions in a spherical shell. *J. Fluid Mech.* **152**, 39–48.
- Zerr, A. & Boehler, R. (1993). Melting of (Mg,Fe)SiO₃-perovskite to 625 kilobars: Indication of a high melting temperature in the lower mantle. *Science* **262**, 553–5.
- (1994). Constraints on the melting temperature of the lower mantle from high-pressure experiments on MgO and magnesiowüstite. *Nature* **371**, 506–8.
- Zerr, A., Serghiou, G., & Boehler, R. (1997). Melting of CaSiO₃ perovskite to 430 kbar and first in-situ measurements of lower mantle eutectic temperatures. *Geophys. Res. Lett.* **24**, 909–12.
- Zerr, A., Diegeler, A., & Boehler, R. (1998). Solidus of Earth's deep mantle. *Science* **281**, 243–6.
- Zhang, K., Hager, B. H., & Raefsky, A. (1985). A critical assessment of viscous models of trench topography and corner flow. *Geophys. J. Roy. Astron. Soc.* **83**, 451–75.
- Zhang, S. & Yuen, D. A. (1995). The influences of lower mantle viscosity stratification on 3D spherical-shell mantle convection. *Earth Planet. Sci. Lett.* **132**, 157–66.
- (1996a). Various influences on plumes and dynamics in time-dependent, compressible mantle convection in 3-D spherical shell. *Phys. Earth Planet. Int.* **94**, 241–67.
- (1996b). Intense local toroidal motion generated by variable viscosity compressible convection in 3-D spherical-shell. *Geophys. Res. Lett.* **23**, 3115–8.
- Zhang, Y. S. & Tanimoto, T. (1989). Three-dimensional modelling of upper mantle structure under the Pacific Ocean and surrounding area. *Geophys. J. Int.* **98**, 255–69.
- (1992). Ridges, hotspots and their interaction as observed in seismic velocity maps. *Nature* **355**, 45–9.
- (1993). High-resolution global upper mantle structure and plate tectonics. *J. Geophys. Res.* **98**, 9793–823.
- Zhang, Y. & Zindler, A. (1989). Noble gas constraints on the evolution of the Earth's atmosphere. *J. Geophys. Res.* **94**, 13719–37.
- Zhao, W., Yuen, D. A., & Honda, S. (1992). Multiple phase transitions and the style of mantle convection. *Phys. Earth Planet. Int.* **72**, 185–210.
- Zharkov, V. N. (1996). The internal structure of Mars: A key to understanding the origin of terrestrial planets. *Solar System Research* **30**, 456–65.
- Zharkov, V. N. & Solomatov, V. S. (1992). Models of the thermal evolution of Venus. In *Venus Geology, Geochemistry and Geophysics: Research Results From the USSR*, pp. 280–319, eds. V. L. Barsukov, A. T. Basilevsky, V. P. Volkov, & V. N. Zharkov. The University of Arizona Press, Tucson and London.
- Zharkov, V. N., Karpov, P. B., & Leontjev, V. V. (1985). On the thermal regime of the boundary layer at the bottom of the mantle. *Phys. Earth Planet. Int.* **41**, 138–42.
- Zhong, S. & Gurnis, M. (1993). Dynamic feedback between a continentlike raft and thermal convection. *J. Geophys. Res.* **98**, 12219–32.
- (1994a). Controls on trench topography from dynamic models of subducted slabs. *J. Geophys. Res.* **99**, 15683–95.
- (1994b). Role of plates and temperature-dependent viscosity in phase change dynamics. *J. Geophys. Res.* **99**, 15903–17.
- (1995a). Mantle convection with plates and mobile, faulted plate margins. *Science* **267**, 838–43.
- (1995b). Towards a realistic simulation of plate margins in mantle convection. *Geophys. Res. Lett.* **22**, 981–4.
- Zhong, S. D. & Gurnis, M. (1996). Interaction of weak faults and non-Newtonian rheology produces plate tectonics in a 3D model of mantle flow. *Nature* **383**, 245–7.

- Zhong, S., Gurnis, M., & Moresi, L. (1998). Role of faults, nonlinear rheology, and viscosity structure in generating plates from instantaneous mantle flow models. *J. Geophys. Res.* **103**, 15255–68.
- Zhou, H. & Anderson, D. L. (1989). Search for deep slabs in the Northwest Pacific mantle. *Proc. Natl. Acad. Sci. USA* **86**, 8602–6.
- Zindler, A. & Hart, S. (1986). Chemical geodynamics. *Ann. Rev. Earth Planet Sci.* **14**, 493–571.
- Zindler, A., Jagoutz, E., & Goldstein, S. (1982). Nd, Sr and Pb isotopic systematics in a three-component mantle: A new perspective. *Nature* **298**, 519–23.
- Zindler, A., Staudigel, H., Hart, S. R., Endres, R., & Goldstein, S. (1983). Nd and Sr isotopic study of a mafic layer from Ronda ultramafic complex. *Nature* **304**, 226–30.
- Zindler, A., Staudigel, H., Langmuir, C., Goldstein, S., Weaver, S., & Batiza, R. (1984). Nd and Sr isotope variations in young Pacific seamounts: Implications for the scale of mantle heterogeneity. *Earth Planet. Sci. Lett.* **70**, 175–82.
- Zschau, J. (1978). Tidal friction in the solid Earth: Loading tide vs. body tides. In *Tidal Friction and the Earth's Rotation*, pp. 62–94, eds. P. Brosche & J. Sündermann. Springer-Verlag, Berlin.
- Zuber, M. T. & Smith, D. E. (1997). Mars without Tharsis. *J. Geophys. Res.* **102**, 28673–85.
- Zuber, M. T., Smith, D. E., Lemoine, F. G., & Neumann, G. A. (1994). The shape and internal structure of the Moon from the Clementine mission. *Science* **266**, 1839–43.

Appendix: Table of Variables

Variable	SI Units	Definition	Eq. No.	Page
a	m	radius of the Earth	(2.8.1)	51
a	m^{-1}	proportionality factor	(5.3.1)	231
a	m	Earth's equatorial radius	(5.3.3)	231
a	m	outer radius of mantle shell	(6.12.2)	274
a	m	radius of sphere	(7.7.2)	309
a	m	semi-major axis		346
a^*		ratio of inner radius of shell to its outer radius (the dimensionless inner radius)	(8.7.40)	366
A	$\text{m}^2 \text{s}^{-1}$	volumetric rate of injection per unit depth	(4.5.43)	168
A	m^2	surface area	(5.2.34)	222
A		amplitude coefficient in Lorenz eigenmode expansion	(8.3.1)	332
A	K^{-1}	rheological constant in viscosity law	(10.8.3)	495
A	m^2	cross-sectional area of conduit	(11.8.1)	525
A	m^2	outer surface area of mantle	(13.2.1)	588
A_c	m^2	area of continents	(4.1.38)	128
A_o	m^2	area of ocean	(4.1.38)	128
A_{ob}	m^2	area of ocean basins	(13.2.21)	597
A_{ps}	m^2	cross-sectional area of swell in vertical plane normal to hot spot track	(11.5.2)	510
A_0	K	activation temperature	(13.2.6)	590
b	m	side length of cubic structure	(4.5.1)	154
b	m	magnitude of Burgers vector	(5.9.3)	243
b	m	depth of convecting region		266
b		maximum depth of reference state	(6.12.17)	276

(continued)

Variable	SI Units	Definition	Eq. No.	Page
b	m	thickness of infinite horizontal fluid layer		290
b	m	semi-minor axis		346
b	m	Burgers vector		242
B		amplitude coefficient in Lorenz eigenmode expansion	(8.3.1)	332
B		buoyancy number	(9.13.1)	415
c	$\text{J kg}^{-1} \text{K}^{-1}$	specific heat	(4.1.1)	119
c	m	core radius		274
c		coefficient in Nusselt number–Rayleigh number relation	(9.2.4)	381
c		wave propagation speed	(11.10.8)	535
c_p	$\text{J kg}^{-1} \text{K}^{-1}$	specific heat at constant pressure	(4.8.1)	193
c_v	$\text{J kg}^{-1} \text{K}^{-1}$	specific heat at constant volume	(4.11.13)	209
c_0		average fluid velocity in conduit	(11.10.10)	536
C		mass concentration of radioactive isotope	(4.1.40)	130
C	kg m^2	moment of inertia about rotation axis	(5.3.3)	231
C		amplitude coefficient in Lorenz eigenmode expansion	(8.3.1)	332
C_{22}		gravitational coefficient		741
d	m	depth		235
d	m	grain size	(5.9.3)	243
d	m	shell thickness	(10.2.3)	427
d	m	overall thickness of region of flow	(10.4.5)	468
d	m	thickness of mantle	(13.2.4)	589
d_c	m	average crustal thickness	(13.2.20)	597
d_{lc}	m	thickness of lower crust	(4.3.9)	149
d_m	m	average depth from which volatiles are released from the mantle	(13.2.19)	596
d_{oc}	m	thickness of oceanic crust	(4.3.9)	149
d_{uc}	m	thickness of upper crust	(4.3.9)	148
d_v	m	distance above slip zone		178
d_{wr}	m	depth of oceanic ridge	(4.3.9)	149
D	m	slab length	(4.8.41)	200
D	m	depth of convecting region	(4.11.14)	209
D	$\text{m}^2 \text{s}^{-1}$	viscous diffusion coefficient of asthenosphere channel	(5.2.45)	227
D	$\text{m}^2 \text{s}^{-1}$	diffusion coefficient	(5.9.1)	240
D		dissipation number	(6.10.18)	268
D	m	height of box		664
D	N m	flexural rigidity		689
D		enrichment factor	(12.4.13)	554

Variable	SI Units	Definition	Eq. No.	Page
D		recycling enrichment ratio	(12.4.38)	562
D_0	$\text{m}^2 \text{s}^{-1}$	frequency factor	(5.9.1)	240
Di		dissipation number	(4.11.14)	209
e	J kg^{-1}	specific internal energy	(4.11.13)	209
e		orbital eccentricity	(14.5.1)	738
\dot{e}	s^{-1}	strain rate	(5.9.3)	243
$\underline{\dot{e}}$	s^{-1}	strain rate tensor	(10.8.1)	491
e_e		elastic strain	(5.1.1)	212
e_f		fluid strain	(5.1.2)	212
\dot{e}_{ij}	s^{-1}	strain rate tensor	(5.2.34)	222
e_{kl}		strain tensor	(14.5.5)	739
E	Pa	Young's modulus	(5.1.1)	212
E	K^{-1}	activation parameter		421
E	J kg^{-1}	gravitational potential energy per unit mass		587
E^*	J mol^{-1}	activation energy per mole	(5.9.1)	240
E_G	J kg^{-1}	gravitational energy release per unit mass	(14.6.5)	753
\dot{E}_T	W	mean tidal dissipation rate	(14.5.1)	738
\dot{E}_T	W	total power generated by inner core tidal heat source	(14.6.4)	753
f		degree of partial melting	(4.5.6)	155
f	J kg^{-1}	specific Helmholtz free energy	(6.8.12)	260
f		fractionation factor	(12.4.4)	551
f		volatile mass fraction	(13.2.18)	596
f		mass fraction of mantle available as crust	(14.3.6)	693
f_c		mass fraction of volatiles in basaltic oceanic crust	(13.2.20)	597
F	W m^{-2}	surface heat flux	(14.2.10)	675
F_b	N m^{-1}	downward buoyancy force per unit depth on cold plume	(8.6.25)	356
F_l		admittance ratio for spherical harmonic degree l	(14.2.8)	662
$F(r)$		normalized radial mass flux		660
$F_{^4\text{He}}$	kg s^{-1}	mass flux of ${}^4\text{He}$	(12.6.1)	574
g	m s^{-2}	magnitude of the acceleration of gravity	(3.2.8)	65
g	J kg^{-1}	specific Gibbs free energy	(6.8.13)	260
g_i	m s^{-2}	acceleration of gravity	(6.4.1)	254
\bar{g}_i	m s^{-2}	acceleration of gravity in reference state	(6.10.3)	265

(continued)

Variable	SI Units	Definition	Eq. No.	Page
g'		diapir buoyancy	(11.7.8)	521
G	$\text{m}^3 \text{ kg}^{-1} \text{ s}^{-2}$	universal constant of gravitation	(3.2.10)	66
G_{lm}		spherical harmonic coefficient of geoid	(14.2.8)	662
h	m	depth of compensation	(4.2.16)	137
h	J kg^{-1}	specific enthalpy	(4.11.12)	209
h	m	change in surface elevation	(5.2.35)	222
h	m	change in relative sea level	(5.3.2)	230
h	m	scale depth of viscosity variation	(7.6.1)	307
h		retention efficiency	(14.6.1)	751
h	m	crack half-width	(4.5.43)	168
h	m	thickness of two-phase region		197
h_c	m	average crustal thickness		146
\bar{h}_d	m	local density scale height	(6.10.14)	268
h_f		second-degree surface deformation Love number for fluid limit		740
h_{ps}	m	elevation of plume swell relative to surrounding seafloor	(11.5.2)	510
h_r	m	length scale for decrease with depth in heat production rate per unit mass	(4.3.1)	144
h_{uc}	m	thickness of upper continental crust		146
H	W kg^{-1}	internal heat production rate per unit mass	(4.1.32)	125
H	m	full or present crack opening	(5.2.50)	230
H	J mol^{-1}	activation enthalpy	(9.9.1)	404
H_c	W kg^{-1}	rate of crustal internal heat production per unit mass	(14.2.6)	655
H_m		nondimensional magnetic field strength	(13.3.17)	610
H_r	W kg^{-1}	representative internal heating rate per unit mass	(6.10.25)	270
H_T	m	adiabatic temperature scale height	(4.7.4)	188
$H(x)$		Heaviside step function	(5.2.46)	228
i	mol kg^{-1}	mole density of nonradiogenic reference isotope	(12.4.1)	551
i^*	mol kg^{-1}	mole density of radiogenic daughter isotope	(12.4.1)	551
I	kg m^2	mean moment of inertia		686
I_{lm}		part of geoid not correlated with topography	(14.2.8)	662
j	mol kg^{-1}	mole density of radioactive parent isotope	(12.4.3)	551

Variable	SI Units	Definition	Eq. No.	Page
J_2		second-degree zonal coefficient in spherical harmonic representation of gravitational potential		686
\dot{J}_2	s^{-1}	time rate of change of J_2		231
k	$W m^{-1} K^{-1}$	thermal conductivity	(4.1.1)	119
k	m^{-1}	horizontal wave number		227
k		second-degree tidal potential Love number	(14.5.1)	738
k_B	Pas	bulk viscosity	(6.5.3)	256
k_c	$W m^{-1} K^{-1}$	crustal thermal conductivity	(14.2.7)	655
k_p	m^2	permeability	(4.5.2)	154
K	$Pa m^{1/2}$	stress intensity factor	(4.5.49)	169
K	Pa	bulk modulus		207
K		geoid response kernel	(5.5.1)	234
K'		coefficient of pressure in linear expression for bulk modulus as function of pressure		477
K_a	Pa	adiabatic bulk modulus	(3.2.2)	65
K_T	Pa	isothermal bulk modulus	(6.8.32)	262
l		spherical harmonic degree		103
l	m	height of material in crack	(5.2.50)	230
l	m	lithosphere thickness	(14.3.8)	693
l		half-length of a propagating dike		168
l_{cr}	m	crustal thickness	(14.3.7)	693
L	m	distance from ocean ridge		132
L	m	characteristic length scale of mantle flow		165
L	m	plate thickness		230
L	$J kg^{-1}$	latent heat release per unit mass	(4.1.27)	124
L_H	$J kg^{-1}$	latent heat of phase change	(4.6.12)	181
L^2		horizontal differential operator	(7.8.14)	328
m		order of spherical harmonic	(5.5.1)	233
m_{ic}	kg	mass of inner core	(13.3.4)	605
M	kg	mass of heat-producing material in Earth	(4.1.39)	128
M	kg	Earth's mass	(5.3.3)	231
M	kg	mass of mantle	(13.2.1)	588
\dot{M}	$kg s^{-1}$	mass flux processed at mid-ocean ridges	(8.5.2)	344
M_c	kg	mass of continental crust		553
M_E	kg	mass of Earth		647
M_m	kg	mass of mantle		306

(continued)

Variable	SI Units	Definition	Eq. No.	Page
M_m	kg	mass of complementary mantle reservoir	(8.5.1)	344
M_m	kg	mass of depleted mantle reservoir	(12.6.1)	574
M_p	kg	mass of primitive mantle	(8.5.6)	345
M_p	kg	mass of planet		686
\dot{M}_{pc}	kg s^{-1}	compositional buoyancy flux	(11.5.7)	513
\dot{M}_{ps}	kg s^{-1}	mass flux of plume hot spot swell	(11.5.1)	510
$M(r)$	kg	mass of planet internal to r	(14.6.1)	751
$\bar{M}(r)$	kg	mass internal to radius r	(6.12.2)	274
M_v	kg	mass of volatiles in mantle	(13.2.19)	596
M_V	kg	mass of Venus		647
\dot{M}_0	kg s^{-1}	current rate at which mantle is being processed at oceanic ridges	(8.5.1)	344
M^2		dimensionless parameter measuring the influence of compressibility. A Mach number squared	(6.10.8)	266
n		rheological parameter	(5.9.3)	243
n		polytropic index	(6.12.28)	278
n	s^{-1}	Io's mean motion	(14.5.1)	738
N	m	geoid height	(4.2.17)	137
Nu		Nusselt number	(8.3.18)	334
p	Pa	pressure	(3.2.1)	64
p_c	Pa	pressure at center of Earth	(13.3.3)	605
p_{cm}	Pa	pressure at core–mantle boundary	(13.3.2)	605
p_{io}	Pa	pressure at inner core–outer core boundary	(13.3.3)	605
p_0	Pa	surface pressure	(7.3.6)	291
p'	Pa	dynamic pressure variation	(6.10.2)	265
P		phase buoyancy parameter	(7.4.13)	300
Pe		Péclet number	(4.7.2)	188
$P_l(\cos \theta)$		Legendre polynomial	(7.8.4)	323
$P_l^m(\cos \theta)$		associated Legendre function	(7.8.2)	323
P_n		P waves critically refracted along the Moho		76
Pr		Prandtl number	(6.10.8)	266
q	W m^{-2}	magnitude of heat flux	(4.6.1)	178
\mathbf{q}	W m^{-2}	conductive heat flux vector	(4.11.15)	210
\bar{q}	W m^{-2}	mean heat flux across layer	(8.6.6)	351
\underline{q}	$\text{m}^3 \text{s}^{-1}$	volume flux in asthenosphere	(5.2.42)	227
\underline{q}	$\text{m}^2 \text{s}^{-1}$	horizontal plume flux	(11.11.2)	539
q_{ac}	W m^{-2}	heat flow conducted along core adiabat	(13.3.16)	610

Variable	SI Units	Definition	Eq. No.	Page
q_b	W m^{-2}	upward heat flux at lower boundary		295
q_c	W m^{-2}	upward heat flux in conductive reference state	(7.3.2)	291
q_c	W m^{-2}	heat flux through core–mantle boundary	(13.3.6)	605
\bar{q}_c	W m^{-2}	mean continental heat flux	(4.1.38)	128
q_i	W m^{-2}	heat flux vector	(6.9.2)	262
q_i	W m^{-2}	heat flux from inner core	(14.6.3)	752
q_m	W m^{-2}	heat flow from convecting mantle	(14.3.11)	699
\bar{q}_o	W m^{-2}	mean oceanic heat flux	(4.1.38)	128
q_r	W m^{-2}	reduced heat flow		144
q_s	W m^{-2}	heat flux through surface	(13.3.6)	605
\bar{q}_s	W m^{-2}	mean surface heat flow for Earth		128
q_V	W m^{-2}	mean surface heat flux on Venus		647
Q	W	Earth's global heat flow		61
Q	$\text{m}^2 \text{s}^{-1}$	vertical flow rate	(4.5.64)	173
Q		dimensionless internal heat production rate	(9.1.2)	378
Q	W m^{-3}	volumetric density of rate of internal heating	(10.2.3)	427
Q	J kg^{-1}	latent heat per unit mass	(10.4.2)	464
Q	W	total heat transport in plume	(11.5.5)	512
Q	W	heat flow in conduit	(11.9.14)	531
Q		dissipation factor	(14.5.2)	738
Q	J mol^{-1}	activation energy	(14.7.1)	763
Q_B	$\text{m}^3 \text{s}^{-1}$	volume flux of volcanics		510
Q_c	W	total heat flow from continents		128
Q_D	$\text{m}^3 \text{s}^{-1}$	volume flux of depleted plume material	(11.5.7)	513
Q_D	W	mean surface heat loss due to delaminating lithosphere	(14.2.4)	650
Q_E	W	Earth's heat loss		647
Q_f	W m^{-3}	heat loss due to melting	(4.5.12)	156
Q_m	W	total heat flow from mantle		297
Q_o	W	total heat flow from oceans		128
Q_{pH}	W	heat of Hawaiian plume		649
Q_S		shear wave attenuation factor		79
Q_S	W	mean surface heat loss	(14.2.2)	649
Q_V	$\text{m}^3 \text{s}^{-1}$	plume volume flux		510
Q_V	W	present heat loss from Venus		647
r	m	radial coordinate	(3.2.1)	64

(continued)

Variable	SI Units	Definition	Eq. No.	Page
r		ratio of Rayleigh number to critical Rayleigh number	(8.3.4)	332
\hat{r}		radial unit vector	(7.7.17)	310
\tilde{r}		dimensionless radial coordinate	(10.7.2)	484
r_{bot}	m	inner radius of shell		478
r_c	m	core radius	(5.2.39)	222
r_e	m	Earth's radius	(5.5.1)	234
r_s	m	radius of reference outer surface	(5.2.35)	222
r_{top}	m	outer radius of shell		478
\tilde{r}_0		dimensionless outer radius of shell	(10.7.8)	485
r_μ		viscosity ratio across layer	(13.5.7)	618
R		dimensionless buoyancy parameter	(4.5.36)	163
R	J mol ⁻¹ K ⁻¹	universal gas constant	(5.9.1)	590
R	m	initial radius of incipient diapir	(11.7.5)	520
R	m	radius		587
R		mass concentration ratio	(12.6.1)	574
R_c	m	core radius		603
R_i	m	initial diapir radius		523
R_i	m	radius of solid inner core		603
R_{ic}	m	inner core radius	(14.3.12)	705
R_p	m	outer radius of mantle		603
R_p	m	radius of planet		686
R_s	m	diapir radius at separation	(11.7.9)	522
R_t		top boundary Rayleigh number		435
R_V	m	radius of Venus	(14.2.1)	649
Ra		Rayleigh number	(6.10.20)	269
Ra_{cr}		critical Rayleigh number for onset of convection	(7.3.28)	294
$Ra_{cr}(\text{min})$		minimum critical Rayleigh number for onset of convection	(7.3.28)	294
Raf		Rayleigh number based on bottom heat flux	(9.3.1)	382
Ra_H		internal heating Rayleigh number	(6.10.26)	270
Rai		Rayleigh number based on viscosity μ_i evaluated at nearly uniform temperature of actively convecting layer beneath a sluggish or rigid lid	(13.5.5)	618
R_{Io}	m	radius of Io	(14.5.1)	738
Ra_{LH}		Rayleigh number based on the temperature difference L_H/c_p	(7.4.12)	299
Raq		Rayleigh number based on heat flux lower boundary condition	(7.3.37)	296

Variable	SI Units	Definition	Eq. No.	Page
$Ra_{\bar{q}}$		Rayleigh number based on the layer thickness b and the mean heat flux \bar{q}	(8.6.11)	352
Ra_Q		Rayleigh number for an internally heated spherical shell	(10.2.3)	427
Ra_{sp}		Rayleigh number for an internally heated sphere	(7.7.34)	312
Rat		volume-averaged Rayleigh number for superadiabaticity		658
$Ra_{(T)}$		Rayleigh number based on viscosity at temperature $\langle T \rangle$		393
$Ra_{y_T,cr}$		critical value of Rayleigh number based on critical boundary layer thickness	(8.6.4)	351
Ra_δ		Rayleigh number based on boundary layer thickness δ	(11.7.1)	519
Ra_0		Rayleigh number based on the viscosity evaluated at the temperature of the upper surface	(13.5.1)	617
Ra_1		Rayleigh number based on viscosity at the temperature of the lower boundary	(13.5.3)	618
$Ra_{1/2}$		Rayleigh number based on viscosity at the average temperature	(13.5.4)	618
Re		Reynolds number	(4.5.47)	169
Re		real part	(14.2.9)	663
s	$\text{J kg}^{-1}\text{K}^{-1}$	specific entropy	(3.2.1)	64
s		as subscript, isentropic variation	(3.2.1)	64
s		as subscript, bulk silicate Earth	(12.4.2)	551
s	m	radius in plane perpendicular to cylindrical axis	(6.2.8)	253
s	s^{-1}	Laplace variable	(14.5.6)	739
\hat{s}		unit vector in cylindrical coordinate system		530
S	m	channel thickness	(5.2.42)	227
S		dimensionless parameter closely related to phase buoyancy parameter	(7.4.11)	300
S	m	thickness of horizontally spreading plume		539
S	$\text{m}^2 \text{ s}^{-1}$	area spreading rate for Earth's mid-ocean ridges	(13.2.19)	596

(continued)

Variable	SI Units	Definition	Eq. No.	Page
\underline{S}		poloidal vector field	(7.8.18)	328
\underline{S}_{lm}		spherical harmonic component of poloidal vector field	(7.8.24)	329
t	s	time	(4.1.1)	119
t	s	age of slab entering trench	(4.6.13)	185
t	s	time measured forward from creation of Earth	(8.5.2)	344
\bar{t}	s	mean age of crust at fracture zone		138
t_c	s	time at which boundary-layer breakaway occurs	(8.6.5)	351
t_{cr}	s	onset time for boundary-layer instability	(11.7.4)	520
t_{c0}	s	time at which crustal growth began	(12.4.27)	557
t_D	s	time constant		227
t_e	s	age of Earth	(8.5.2)	344
t_p	s	mantle processing time	(8.5.1)	344
t_r	s	relaxation time		223
t_R	s	characteristic time for decay of heat-producing elements in Earth	(8.5.2)	344
t_s	s	time for diapir separation	(11.7.10)	522
t_S	s	total time of crack opening	(5.2.50)	230
t_{ve}	s	viscoelastic relaxation time	(5.1.7)	213
$t_{1/2}$	s	half-life	(12.4.9)	552
t_2	s	spherical harmonic degree $l = 2$	(5.3.2)	231
		relaxation time constant		
T	K	temperature	(3.6.3)	93
\overline{T}	K	reference state temperature	(6.10.1)	265
\underline{T}		toroidal vector field	(7.8.19)	328
\underline{T}_{lm}		spherical harmonic component of toroidal vector field	(7.8.23)	329
T_a	K	mantle adiabat		196
T_{acc}	K	accretionary temperature	(14.6.1)	751
T_c	K	conductive temperature		291
T_c	K	core or interior temperature	(8.6.1)	350
T_c	K	temperature at base of conductive lid	(13.5.38)	624
T_{cm}	K	temperature at the core–mantle boundary		603
$\langle T_c \rangle$	K	volume-averaged core temperature	(13.3.9)	605
$T_c(r)$	K	temperature along outer core adiabat	(13.3.2)	605
T_D	K	Debye temperature		207
T_D	K	temperature separating delaminating lithosphere from stable lithosphere	(14.2.3)	649

Variable	SI Units	Definition	Eq. No.	Page
T_e	K	ambient temperature during accretion	(14.6.1)	751
T_i	K	temperature at inner–outer core boundary	(14.6.4)	753
T_l	K	mantle temperature at top of lower thermal boundary layer		603
T_{lithos}	K	temperature at base of lithosphere	(14.3.8)	693
T_{lm}		spherical harmonic coefficient of topography	(14.2.8)	662
T_m	K	mantle temperature beneath boundary layer		26
T_m	K	melting temperature of crystalline solid	(5.9.2)	242
T_m	K	uniform temperature of mantle	(14.2.5)	653
T_{mio}	K	liquidus temperature of core alloy		603
$\langle T \rangle_{\text{mantle}}$	K	volume-averaged mantle temperature	(13.3.8)	605
T_p	m	thermal parameter of slab	(4.6.13)	185
T_0	K	surface temperature	(4.6.10)	179
T_1	K	temperature of lower boundary	(8.6.1)	351
T_1	K	isothermal interior or core temperature	(8.6.13)	352
\underline{u}	m s^{-1}	velocity vector		328
u_0	m s^{-1}	velocity of seafloor spreading	(4.2.1)	132
\bar{u}	m s^{-1}	mean flow velocity in x -direction	(4.5.43)	168
\underline{u}'		dynamically induced infinitesimal perturbation velocity	(7.7.16)	310
$\hat{\underline{u}}$		unit vector in direction of plate motion	(11.11.6)	540
\underline{u}_i	m s^{-1}	fluid velocity vector	(5.2.34)	222
(u_r, u_θ, u_ϕ)	m s^{-1}	components of velocity in (r, θ, ϕ) directions of spherical coordinate system		252
u_m	m s^{-1}	plate speed relative to “fixed” hot spot	(11.5.1)	510
\underline{u}_p	m s^{-1}	horizontal velocity of spreading plume material	(11.11.1)	539
(u_s, u_z, u_ϕ)	m s^{-1}	components of velocity in (s, z, ϕ) directions of cylindrical coordinate system	(6.2.8)	253
u_x	m s^{-1}	horizontal component of velocity	(5.2.2)	218
u_y	m s^{-1}	vertical component of velocity	(5.2.2)	218

(continued)

Variable	SI Units	Definition	Eq. No.	Page
(u_x, u_y, u_z)	m s^{-1}	components of velocity in (x, y, z) directions of Cartesian coordinate system		252
$u^2/2$	J kg^{-1}	kinetic energy per unit mass of element of fluid	(6.9.20)	264
$u^2/2$	J kg^{-1}	approach kinetic energy per unit mass of accreting planetesimals		751
U	m s^{-1}	characteristic velocity scale associated with mantle flow		165
U	m s^{-1}	surface speed	(9.4.1)	386
U	$\text{m}^2 \text{s}^{-2}$	gravitational potential	(4.2.16)	137
U	m s^{-1}	half-spreading rate of plates	(11.12.1)	545
Ur		Urey ratio	(13.2.12)	595
U_{diff}	J	energy of differentiation	(14.6.2)	752
U_∞	m s^{-1}	Stokes velocity of buoyant fluid sphere	(11.7.8)	521
v	m s^{-1}	down-dip descent velocity of slab	(4.6.13)	185
v	m s^{-1}	downward flow velocity		193
v	m s^{-1}	seismic velocity	(5.5.2)	235
v	m s^{-1}	vertical velocity	(8.6.24)	355
v	$\text{m}^3 \text{kg}^{-1}$	specific volume	(6.8.1)	259
v_{crit}	m s^{-1}	critical value of downward velocity	(4.8.10)	194
v_l	m s^{-1}	magma vertical velocity	(4.5.4)	155
v_0	m s^{-1}	mantle ascent velocity below melt zone	(4.5.5)	155
V	m s^{-1}	vertical velocity of the matrix	(4.5.4)	155
V	m^3	shell volume	(5.2.34)	222
V	$\text{m}^2 \text{s}^{-2}$	gravitational potential	(6.13.1)	279
V	m^3	volume of diapir	(11.7.6)	521
V	m^3	volume of material transported by wave	(11.10.12)	536
V_m	m^3	total flow volume	(4.5.68)	173
V_P	m s^{-1}	seismic compressional wave velocity	(3.2.3)	65
V_S	m s^{-1}	seismic shear wave velocity	(3.2.4)	65
V_V	m^3	volume of erupted volcanics		527
V_0	m^3	total volume of water in oceans	(13.2.24)	597
V_{0a}	m^3	volume of ocean basins above peak ridge height	(13.2.24)	597
V_{0b}	m^3	volume of ocean basins below peak ridge height	(13.2.24)	597
V^*	$\text{m}^3 \text{ mol}^{-1}$	activation volume per mole	(5.9.1)	240

Variable	SI Units	Definition	Eq. No.	Page
V_∞	m^3	steady state or terminal volume of plume head	(11.8.4)	525
V_γ	$\text{m}^3 \text{ kg}^{-1}$	specific volume of γ -Fe	(14.6.6)	755
w	m	depth of ocean floor below ridge crest	(4.2.9)	135
w	m	length		173
w	m	displacement of surface, topography	(5.2.20)	220
w_e	m	equilibrium depth of old ocean basins	(4.2.31)	141
w_m	m	initial displacement of surface	(5.2.1)	217
W	m	Pratt depth of compensation	(11.3.1)	505
W_0	m	plume width	(11.12.1)	543
x	m	horizontal coordinate	(4.2.1)	132
\underline{x}	m	position vector	(11.11.3)	539
x_i	m	position vector	(6.2.1)	252
x_{FeS}		mass fraction of FeS in core	(14.3.1)	687
x_m	m	distance along slip zone where melting first occurs		179
x_S		mass fraction of S in core	(14.3.2)	687
(x, y, z)	m	Cartesian coordinates	(6.2.2)	252
X		mass fraction of spinel	(4.8.1)	193
X_{Mg}		magnesium number, the molar concentration of Mg normalized by the molar concentration of Mg plus Fe		84
y	m	depth	(4.1.1)	119
y_c	m	thickness of Venusian crust	(14.2.5)	653
y_L	m	thickness of lithosphere	(4.2.7)	135
Y_l		spherical harmonic of degree l	(5.2.39)	222
y_m	m	depth of solidification interface	(4.1.25)	123
$Y_l^m(\theta, \phi)$		spherical harmonic of degree l and order m	(7.8.1)	323
y_T	m	thickness of boundary layer	(4.1.22)	122
$y_{T,cr}$	m	critical value of boundary layer thickness	(8.6.4)	351
y_0	m	base of the melt zone	(4.5.19)	157
z	m	distance parallel to cylindrical axis, cylindrical coordinate	(6.2.8)	253
z	m	depth	(14.3.11)	699
α	K^{-1}	thermal expansivity, volume coefficient of thermal expansion	(4.11.1)	207

(continued)

Variable	SI Units	Definition	Eq. No.	Page
α		dimensionless strain rate	(8.5.12)	348
α		isotope ratio	(12.4.1)	551
α		aspect ratio		173
β	K m^{-1}	temperature gradient	(7.4.2)	298
β		isotope ratio	(12.5.2)	566
β_{ad}	K m^{-1}	magnitude of adiabatic temperature gradient	(7.4.16)	300
β_c	K m^{-1}	radial temperature gradient in conductive reference state	(7.7.7)	309
γ		Grüneisen ratio	(6.9.12)	263
γ	Pa K^{-1}	Clapeyron slope		457
γ		rheological parameter	(11.9.1)	529
γ		isotope ratio	(12.5.2)	566
Γ	Pa K^{-1}	Clapeyron slope	(4.6.12)	180
Γ		dimensionless phase or composition variable	(9.1.3)	378
δ	m	channel diameter		154
δ		dip of slab	(4.6.13)	185
δ		delta function		539
δ	m	thermal boundary layer thickness	(13.3.10)	606
δ	m	lithosphere thickness	(14.2.10)	675
δ	m	mean iron grain size		754
δ_c	m	radius of high velocity conduit		530
δ_{rh}	m	rheological length scale	(13.5.29)	622
δ_T		Anderson–Grüneisen parameter	(4.11.2)	207
δ_T	m	plume thermal halo radius	(11.9.16)	532
Δ		angle subtended at center of Earth by pole of rotation P and point on plate boundary	(2.8.1)	51
ϵ		dimensionless parameter	(4.8.34)	197
ϵ		aspect ratio of strain marker		346
ϵ_i		initial samarium–neodymium isotope ratio		731
ε		isotope ratio	(12.4.2)	551
ε_c		crustal isotope ratio		554
ε_m		mantle isotope ratio		554
ζ_i	s^{-1}	vorticity vector	(6.6.1)	257
ζ_s	Pas	bulk viscosity of the matrix	(4.5.27)	162
η		Bullen inhomogeneity parameter	(3.6.1)	93
η	m	vertical displacement of distorted phase boundary	(7.4.9)	299
η		Carnot efficiency factor	(13.3.16)	610
η	Pas	dynamic viscosity	(14.5.5)	739
η	Pas	mantle viscosity		741
η		similarity variable	(4.1.3)	119

Variable	SI Units	Definition	Eq. No.	Page
θ		angle		176
θ		colatitude, spherical polar coordinate	(6.2.7)	252
θ		orientation of strain marker		346
θ		dimensionless plume temperature anomaly	(11.9.7)	531
θ		Frank–Kamenetskii parameter	(13.5.8)	618
$\theta_{m,n}^*$		Fourier coefficients of temperature	(8.4.2)	337
θ'	K	dynamically induced infinitesimal temperature perturbation	(7.7.18)	310
Θ		colatitude of rotation pole	(2.8.2)	51
Θ		ratio of temperature difference with convection to temperature difference without convection	(8.6.10)	352
κ	$\text{m}^2 \text{s}^{-1}$	thermal diffusivity	(4.1.3)	119
κ		composition ratio	(12.5.1)	566
λ	m	wavelength	(5.2.1)	217
λ	Pa s	second viscosity	(6.5.2)	256
λ	m	pulse length of conduit	(11.10.9)	535
λ	s^{-1}	decay constant	(12.4.5)	552
λ	Pa	Lamé constant	(14.5.5)	739
λ_{cr}	m	critical wavelength	(10.4.5)	468
λ_1		maximum Lyapunov exponent		348
μ	Pa	shear modulus or rigidity of a solid	(3.2.3)	65
μ	Pa s	viscosity	(5.1.2)	212
μ	Pa s	mantle viscosity		216
μ	Pa s	dynamic viscosity	(6.5.2)	256
μ		composition ratio	(12.4.3)	551
μ_E	A m^2	Earth's present magnetic dipole moment	(14.3.12)	705
μ_{eff}		effective viscosity	(9.9.2)	404
μ_l		magma viscosity	(4.5.4)	155
$\mu_{1/2}$		viscosity evaluated at average temperature of upper and lower surfaces	(13.5.4)	618
μ_M	A m^2	Martian magnetic dipole moment	(14.3.12)	704
$\mu(s)$		complex shear modulus	(14.5.6)	739
ν		Poisson's ratio		168
ν	$\text{m}^2 \text{s}^{-1}$	kinematic viscosity		266
ν		composition ratio	(12.5.1)	566
ξ	m	coordinate axis		346
Π'	Pa	dynamically induced pressure perturbation	(7.7.17)	310

(continued)

Variable	SI Units	Definition	Eq. No.	Page
ρ	kg m^{-3}	density	(3.2.1)	64
$\underline{\underline{\sigma}}$	Pa	stress tensor	(10.8.1)	491
σ_d	kg m^{-2}	mass per unit area		235
σ_{gt}		cross-covariance of geoid and topography	(14.2.9)	663
σ_n	Pa	normal stress exerted by exterior fluid on conduit wall	(11.10.1)	535
σ_s	Pa	surface normal load	(5.2.36)	222
σ_t	Pa	magnitude of thermal stress	(14.3.3)	688
σ_{tt}		covariance of topography	(14.2.9)	663
σ_{yield}	Pa	yield stress	(10.8.1)	491
τ	Pa	shear stress	(4.6.2)	178
τ	Pa	stress	(5.1.1)	212
τ	Pa	deviatoric stress	(5.9.3)	243
τ		nondimensional time		334
τ	s	average age of subduction of oceanic crust	(13.2.21)	597
τ	Pa	differential stress	(14.7.1)	763
τ_c	s	age of crustal separation		554
τ_h	Pa	shear stress on horizontal boundaries	(8.6.32)	357
τ_{ij}	Pa	deviatoric stress tensor	(6.4.1)	254
τ_l	s	relaxation time constant	(5.2.41)	223
τ_r	s	characteristic time for exponential relaxation of initial displacement	(5.2.32)	221
τ_r	s	recycling time	(12.4.40)	562
τ_v	Pa	shear stress on vertical boundaries	(8.6.31)	357
τ_{xx}, τ_{yy}	Pa	deviatoric normal stresses		255
τ_{xy}, τ_{yx}	Pa	deviatoric shear stresses		255
τ_2	Pa	square root of second invariant of deviatoric stress tensor	(5.10.1)	249
$\tau_{1/2}$	s	half-life of radioactive isotope	(4.1.41)	130
ϕ		porosity	(4.5.1)	154
ϕ	$\text{m}^2 \text{s}^{-2}$	seismic parameter	(4.7.5)	189
ϕ		longitude, spherical polar coordinate (cylindrical coordinate)	(6.2.7) (6.2.8)	252
Φ	$\text{m}^2 \text{s}^{-2}$	seismic parameter	(3.2.5)	65
Φ	Pa s^{-1}	viscous dissipation function	(6.9.3)	262
Φ	$\text{m}^3 \text{s}^{-1}$	poloidal scalar	(7.7.21)	311
Φ	W	ohmic dissipation rate	(13.3.16)	610
χ		mass fraction of light alloying constituent in liquid outer core	(13.3.1)	605
χ		crustal fractionation parameter		692
χ_a	Pa^{-1}	adiabatic compressibility	(3.2.2)	65

Variable	SI Units	Definition	Eq. No.	Page
χ_r		efficiency factor for volatile recycling	(13.2.20)	597
χ_T	Pa^{-1}	isothermal compressibility	(6.8.3)	259
ψ	$\text{m}^2 \text{s}^{-1}$	stream function	(5.2.5)	218
Ψ		east longitude of rotation pole	(2.8.2)	51
Ψ'	$\text{m}^2 \text{s}^{-1}$	toroidal scalar function	(7.7.21)	311
Ψ'		east longitude of a point on plate boundary	(2.8.2)	51
$\tilde{\Psi}$		dimensionless geopotential function	(10.7.3)	484
ω	s^{-1}	angular velocity	(2.8.1)	51
ω^*		component of nondimensional strain-rate tensor	(8.5.11)	346
$\underline{\omega}'$	s^{-1}	perturbation vorticity	(7.7.19)	310
Ω	s^{-1}	Earth's spin rate	(5.3.1)	231

Author Index

- Abbott et al. (1994), 630, 797
Abe and Matsui (1985), 588, 672, 797
Abe and Matsui (1986), 588, 797
Abe and Matsui (1988), 588, 797
Abers (1992), 33, 797
Abers (1996), 33, 797
Abramowitz and Stegun (1964), 179, 323, 797
Acuña et al. (1998), 692, 698, 699, 705, 797
Acuña et al. (1999), 692, 698, 699, 705, 706, 797
Aharonov et al. (1995), 165, 797
Ahern and Turcotte (1979), 154, 161, 164, 797
Ahrens (1979), 608, 797
Ahrens (1990), 587, 588, 797
Akaoogi et al. (1987), 85, 797
Akaoogi et al. (1989), 84, 85, 302, 464, 797
Aki and Richards (1980), 66, 798
Akimoto and Fujisawa (1968), 84, 798
Albers and Christensen (1996), 529, 532, 533, 798
Alder (1966), 99, 798
Allègre (1982), 547, 550, 556, 629, 798
Allègre (1987), 547, 798
Allègre and Rousseau (1984), 559, 560, 798
Allègre and Turcotte (1985), 350, 550, 580–582, 798
Allègre and Turcotte (1986), 349, 350, 550, 798
Allègre et al. (1980), 549, 550, 798
Allègre et al. (1983a), 550, 798
Allègre et al. (1983b), 550, 556, 636, 731, 733, 798
Allègre et al. (1983c), 573, 575, 578, 579, 798
Allègre et al. (1986), 571, 572, 798
Allègre et al. (1987), 573, 575, 576, 798
Allègre et al. (1993), 577, 798
Allègre et al. (1995), 575, 798
Allègre et al. (1996), 578, 798
Alley and Parmentier (1998), 736, 798
Alterman et al. (1959), 739, 798
Alvarez et al. (1980), 545, 798
Alvarez et al. (1984), 545, 798
Ambrose (1964), 630, 798
Anderson (1967), 207, 209, 799
Anderson (1970), 88, 798
Anderson (1978), 176, 799
Anderson (1979), 190, 799
Anderson (1982), 61, 408, 798
Anderson (1987a), 107, 798
Anderson (1987b), 190, 455, 485, 798
Anderson (1989), 63, 81, 83, 798
Anderson (1993), 577, 798
Anderson (1998a), 577, 798
Anderson (1998b), 577, 799
Anderson and Ahrens (1996), 608, 799
Anderson and Bass (1984), 82, 83, 799
Anderson and Duba (1997), 202, 608, 799
Anderson and Given (1982), 79, 799
Anderson and Grew (1977), 168, 799
Anderson et al. (1968), 152, 799
Anderson et al. (1976), 38, 180, 799
Anderson et al. (1987), 750, 799
Anderson et al. (1990), 209, 799
Anderson et al. (1992), 208, 209, 464, 799
Anderson et al. (1996a), 741, 799
Anderson et al. (1996b), 750, 799
Anderson et al. (1996c), 760, 799
Anderson et al. (1998a), 756, 799
Anderson et al. (1998b), 761, 762, 766, 799
Arkani-Hamed (1993), 649, 799
Arkani-Hamed (1994), 650, 672, 678, 799
Arkani-Hamed (1998), 720, 799
Arkani-Hamed and Toksöz (1984), 650, 799
Arkani-Hamed et al. (1993), 650, 799
Arkani-Hamed et al. (1999), 719, 799
Armstrong (1968), 561, 569, 630, 799
Armstrong (1969), 561, 569, 799
Armstrong (1981), 45, 561, 565, 629, 630, 800
Armstrong (1991), 630, 800
Armstrong and Hein (1973), 561, 800
Ashby and Verrall (1977), 245, 800
Ashwal and Burke (1989), 61, 800
Atkinson (1984), 171, 800
Atwater (1970), 59, 800
Aurnou et al. (1996), 99, 800
Backus (1955), 314, 800

- Bacon (1620), 5, 800
 Balachandar and Yuen (1994), 482, 800
 Balachandar et al. (1992), 471, 477, 482, 483, 669, 800
 Balachandar et al. (1993), 477, 482, 483, 486, 800
 Balachandar et al. (1995a), 482, 488, 800
 Balachandar et al. (1995b), 482, 800
 Banerdt et al. (1982), 684, 688, 689, 800
 Banerdt et al. (1992), 692, 800
 Barazangi and Brown (1986), 72, 800
 Barcilon and Lovera (1989), 161, 800
 Barcilon and Richter (1986), 161, 800
 Barenblatt (1962), 169, 800
 Bargar and Jackson (1974), 503, 800
 Barrett and Freeman (1987), 41, 800
 Barron (1979), 209, 800
 Basaltic Volcanism Study Project (1981), 71, 153, 513, 754, 800
 Basilevsky et al. (1997), 646, 676, 800
 Bataille and Flatté (1988), 97, 800
 Batchelor (1967), 251, 801
 Baumgardner (1985), 417, 801
 Baumgardner (1988), 417, 801
 Bear (1972), 154, 801
 Becker and Pepin (1984), 699, 801
 Bell and Rossman (1992), 248, 801
 Bénard (1900), 3, 801
 Bénard (1901), 3, 4, 801
 Benioff (1949), 31, 801
 Benz and Vidale (1993), 86, 801
 Berckhemer et al. (1982), 742, 801
 Bercovici (1993), 389, 490, 664, 669, 801
 Bercovici (1995a), 57, 439, 801
 Bercovici (1995b), 490, 664, 801
 Bercovici (1996), 490, 491, 664, 801
 Bercovici (1998), 490, 491, 801
 Bercovici and Kelly (1997), 520, 522, 801
 Bercovici and Lin (1996), 527, 801
 Bercovici and Mahoney (1994), 525, 528, 529, 536, 801
 Bercovici et al. (1986), 765, 801
 Bercovici et al. (1989a), 41, 113, 277, 403, 417, 441, 443, 444, 446, 448, 471, 711, 801
 Bercovici et al. (1989b), 417–422, 425, 479, 708, 801
 Bercovici et al. (1989c), 417, 441, 444, 446, 449, 453, 454, 801
 Bercovici et al. (1991), 417, 801
 Bercovici et al. (1992), 417, 477–482, 801
 Bercovici et al. (1993), 390, 392, 403, 468, 801
 Bernal (1936), 84, 801
 Bertka and Fei (1996), 713, 715, 801
 Bertka and Fei (1997), 713, 715, 802
 Bertka and Fei (1998a), 686, 713, 715, 802
 Bertka and Fei (1998b), 686, 687, 713, 802
 Bijwaard and Spakman (1999), 510, 802
 Bills (1989), 686, 802
 Bills and Kobrick (1985), 644, 802
 Bills and May (1987), 228, 802
 Bills et al. (1987), 644, 802
 Bills et al. (1994), 228, 802
 Bina (1996), 185, 802
 Bina and Helffrich (1994), 88, 302, 464, 469, 802
 Bina and Liu (1995), 470, 802
 Bina and Wood (1987), 85, 86, 802
 Bindschadler and Parmentier (1990), 645, 802
 Bindschadler et al. (1990), 645, 667, 802
 Bindschadler et al. (1992a), 645, 802
 Bindschadler et al. (1992b), 645, 648, 802
 Birch (1939), 207, 802
 Birch (1952), 84, 189, 207, 802
 Birch (1963), 99, 802
 Birch (1965), 587, 802
 Birch (1968), 207, 802
 Bird (1978a), 38, 180, 802
 Bird (1978b), 45, 802
 Bird (1979), 45, 692, 802
 Bird (1998), 54, 55, 802
 Bird and Baumgardner (1981), 45, 802
 Black et al. (1991), 644, 803
 Blackett (1956), 11, 803
 Blaney et al. (1995), 744, 803
 Blasius and Cutts (1976), 689, 803
 Blichert-Toft and Albarede (1997), 583, 803
 Blum (1995), 552, 803
 Boehler (1986), 202, 740, 803
 Boehler (1992), 203, 803
 Boehler (1993), 101, 201–203, 608, 803
 Boehler (1994), 608, 803
 Boehler (1996), 202, 203, 608, 803
 Boehler and Ross (1997), 608, 803
 Bogard et al. (1984), 691, 699, 803
 Bolt (1993), 17, 34, 803
 Bonneville et al. (1997), 507, 803
 Booker (1976), 393, 803
 Booker and Stengel (1978), 606, 803
 Bottinga and Allègre (1978), 158, 803
 Boudier (1978), 349, 803
 Bougault et al. (1980), 549, 803
 Boyd (1973), 144, 803
 Boyd (1989), 151, 803
 Boyd and Meyer (1979), 81, 803
 Boyd et al. (1985), 144, 151, 803
 Braginsky (1963), 100, 603, 803
 Braginsky and Roberts (1995), 609, 803
 Bratt et al. (1985), 690, 720, 804
 Breuer and Spohn (1995), 470, 626, 804
 Breuer et al. (1996), 713, 804
 Breuer et al. (1997), 713, 804
 Breuer et al. (1998), 713, 804
 Brown (1957), 3, 804
 Brown (1977), 47, 804
 Brown (1979), 629, 804
 Brown (1991), 73, 804
 Brown and Shankland (1981), 93, 804
 Bruce and Huppert (1989), 171, 176, 804
 Brunet and Machetel (1998), 470, 626, 804
 Brush (1986), 727, 804

- Buck (1985), 143, 804
Buck (1992), 649, 804
Buck and Parmentier (1986), 143, 804
Buck and Su (1989), 165, 804
Buffett and Glatzmaier (2000), 99, 804
Buffett et al. (1996), 603, 609, 804
Bühler et al. (1976), 576, 804
Bull (1921), 8, 804
Bull (1931), 8, 804
Bullard (1954), 127, 804
Bullard et al. (1956), 127, 804
Bullard et al. (1965), 5, 6, 804
Bullen (1936), 66, 804
Bullen (1940), 66, 804
Bullen (1946), 97, 98, 804
Bullock et al. (1993), 637, 646, 804
Bunge and Richards (1996), 471, 472, 489, 805
Bunge et al. (1996), 471, 472, 476, 805
Bunge et al. (1997), 471, 805
Burchfiel (1983), 72, 805
Burchfield (1975), 118, 805
Burke (1977), 57, 805
Burke and Dewey (1973), 57, 61, 805
Burke et al. (1977), 59, 805
Burns (1986), 738, 805
Busse (1967), 307, 417, 805
Busse (1975), 418, 805
Busse (1978), 367, 368, 418, 805
Busse (1981), 474, 805
Busse (1989), 367, 370, 375, 805
Busse and Riahi (1982), 418, 427, 805
Busse and Schubert (1971), 297, 300, 301, 805
Busse et al. (1994), 429, 805
Butler (1986), 45, 805
Byerly (1926), 84, 805
- Čadek and Ricard (1992), 490, 805
Caldwell et al. (1976), 33, 805
Calvert (1995), 153, 805
Cameron (1984), 727, 805
Cameron (1986), 727, 805
Cameron and Ward (1976), 587, 727, 805
Cameron et al. (1988), 752, 805
Campbell and Griffiths (1990), 528, 805
Campbell and Taylor (1983), 47, 656, 805
Campbell et al. (1989), 527, 806
Cann (1974), 166, 806
Cardin and Olson (1992), 100, 806
Carey (1955), 5, 806
Carey (1958), 13, 806
Carey (1976), 14, 806
Carr (1974), 689, 806
Carr (1976), 689, 806
Carr (1986), 744, 806
Carr (1987), 699, 806
Carr (1996a), 699, 806
Carr (1996b), 699, 806
Carr et al. (1998a), 745, 806
- Carr et al. (1998b), 759, 760, 806
Carrigan (1982), 446, 806
Carrigan (1985), 446, 806
Carrigan and Eichelberger (1990), 176, 806
Carrigan et al. (1992), 175, 176, 806
Carslaw and Jaeger (1984), 139, 806
Carter (1976), 590, 806
Casey and Dewey (1984), 59, 806
Cassen and Reynolds (1973), 727, 806
Cassen and Reynolds (1974), 727, 806
Cassen et al. (1976), 754, 806
Cassen et al. (1979), 727, 731, 806
Cassen et al. (1982), 738, 760, 765, 806
Castillo (1988), 514, 806
Castle and Creager (1997), 89, 806
Castle and Creager (1998), 181, 806
Cathles (1975), 216, 225, 226, 228, 231, 607, 739, 807
Cathles (1980), 216, 228, 807
Cazenave (1984), 138, 807
Cazenave et al. (1983), 138, 807
Cazenave et al. (1995), 143, 807
Chandrasekhar (1952), 314, 807
Chandrasekhar (1953), 314, 807
Chandrasekhar (1961), 288, 290, 301, 314, 316, 318, 320, 328, 329, 807
Chase (1978), 39, 807
Chase (1979a), 408, 807
Chase (1979b), 489, 807
Chase (1981), 550, 807
Chen and Ahrens (1996), 608, 807
Chen and Wasserburg (1986), 691, 699, 807
Chicarro et al. (1985), 699, 807
Chopelas and Boehler (1989), 207, 209, 807
Chopelas and Boehler (1992), 91, 209, 464, 485, 807
Chopelas et al. (1994), 469, 807
Chopra and Paterson (1984), 248, 598, 807
Christensen (1981), 474, 611, 807
Christensen (1983a), 404, 807
Christensen (1983b), 413, 807
Christensen (1984a), 394, 404, 405, 664, 807
Christensen (1984b), 414, 523, 807
Christensen (1984c), 395, 590, 673, 807
Christensen (1985a), 404, 807
Christensen (1985b), 590, 673, 807
Christensen (1987), 192, 808
Christensen (1989a), 248, 404, 808
Christensen (1989b), 347, 808
Christensen (1989c), 379, 381, 808
Christensen (1995), 390, 808
Christensen (1996), 398, 399, 461, 462, 808
Christensen (1997), 399, 400, 808
Christensen and Harder (1991), 417, 432, 438, 808
Christensen and Hofmann (1994), 347, 414, 583, 808
Christensen and Salisbury (1979), 76, 807
Christensen and Yuen (1984), 35, 90, 397, 398, 808
Christensen and Yuen (1985), 300, 390, 392, 463, 473, 627, 671, 808
Christensen and Yuen (1989), 404, 808

- Clark (1966), 158, 190, 808
 Clauser and Huenges (1995), 210, 808
 Clayton and Comer (1983), 102, 808
 Clemens (1998), 176, 808
 Clever (1977), 439, 808
 Cloetingh et al. (1984), 58, 808
 Cloetingh et al. (1989), 58, 808
 Coleman et al. (1972), 726, 808
 Colin and Fleitout (1990), 646, 808
 Collerson and Kamber (1999), 572, 808
 Collette (1974), 29, 808
 Comer et al. (1985), 689, 690, 808
 Comte et al. (1999), 31, 33, 808
 Condie (1998), 62, 808
 Connerney and Ness (1988), 750, 809
 Connerney et al. (1999), 692, 698, 809
 Consolmagno (1981), 740, 809
 Cook and Turcotte (1981), 595, 809
 Cook et al. (1979), 45, 809
 Cormier and Richards (1976), 98, 809
 Corriu et al. (1994), 471, 809
 Couillette and Loper (1995), 525, 809
 Courtillot (1994), 545, 809
 Courtillot (1995), 545, 546, 809
 Courtillot et al. (1996), 546, 809
 Cox and Giuli (1968), 278, 809
 Cox et al. (1963), 12, 809
 Cox et al. (1964), 12, 13, 809
 Craig and Lupton (1981), 574, 809
 Craig et al. (1975), 574, 809
 Creager (1992), 98, 99, 809
 Creager and Jordan (1984), 107, 809
 Creager and Jordan (1986a), 107, 809
 Creager and Jordan (1986b), 117, 809
 Crittenden (1963), 228, 809
 Crough (1978), 505–507, 541, 809
 Crough (1983), 505, 809
 Crough and Jurdy (1980), 499, 500, 514, 809
 Crough et al. (1980), 508, 809
 Crumpler et al. (1997), 644, 809
 Cserepes (1982), 404, 810
 Cserepes and Christensen (1990), 417, 810
 Cserepes and Rabinowicz (1985), 474, 810
 Cserepes and Yuen (1997), 473, 810
 Cserepes et al. (1988), 417, 810
 Cumming and Richards (1975), 569, 810
- Daessler and Yuen (1996), 185, 810
 D'Agostino et al. (1997), 240, 810
 Daines and Kohlstedt (1994), 165, 810
 Daines and Richter (1988), 158, 810
 Daly (1934), 216, 810
 Daly (1980), 394, 471, 606, 810
 Daniels et al. (1996), 349, 810
 Darwin (1898), 1, 810
 Davaille and Jaupart (1993), 393, 623, 624, 810
 Davaille and Jaupart (1994), 143, 308, 675, 810
 Davies (1980), 586, 594, 595, 810
- Davies (1984), 350, 810
 Davies (1986), 389, 810
 Davies (1988a), 389, 471, 810
 Davies (1988b), 403, 510, 610, 810
 Davies (1989), 389, 489, 810
 Davies (1990), 588, 810
 Davies (1992), 502, 507, 810
 Davies (1993), 603, 810
 Davies (1994), 506, 810
 Davies (1995a), 397, 811
 Davies (1995b), 470, 627, 811
 Davies (1996), 744, 810
 Davies (1999), 168, 811
 Davies and Arvidson (1981), 683, 691, 811
 Davies and Dziewonski (1975), 88, 811
 Davies and Gurnis (1986), 414, 811
 Davies and Richards (1992), 403, 466, 811
 Davies and Stevenson (1992), 38, 811
 De Bremaecker (1977), 33, 811
 De Bresser et al. (1998), 243, 811
 Defant and Drummond (1990), 630, 811
 Defant and Drummond (1993), 630, 811
 DeFazio (1974), 36, 811
 Delaney and Pollard (1982), 172, 811
 DeLong et al. (1978), 59, 811
 DeLong et al. (1979), 59, 811
 DeMets et al. (1990), 48–50, 811
 DeMets et al. (1994), 49, 811
 DePaolo (1979), 554, 811
 DePaolo (1980), 550, 554, 811
 DePaolo (1983), 45, 560, 561, 563, 565, 636, 811
 DePaolo (1988), 556, 811
 DePaolo and Wasserburg (1976), 551, 811
 DePaolo et al. (1991), 629, 811
 Dermott (1984), 740, 811
 Detrick (1981), 138, 811
 Detrick and Crough (1978), 505, 811
 Detrick et al. (1981), 507, 811
 Detrick et al. (1986), 507, 812
 Detrick et al. (1987), 153, 812
 Devaux et al. (1997), 185–187, 812
 Devoti et al. (1997), 231, 812
 Dewey (1975), 52, 69, 657, 812
 Dewey (1977), 59, 812
 Dewey and Bird (1970), 59, 812
 Dewey and Windley (1981), 556, 629, 812
 Dick (1989), 153, 812
 Dicke (1969), 231, 812
 Dickey et al. (1994), 726, 812
 Dickin (1995), 547, 812
 Dickinson and Luth (1971), 82, 549, 812
 Dickman (1977), 232, 812
 Dickson et al. (1968), 13, 812
 Dietz (1961), 12, 812
 Doe and Zartman (1979), 571, 812
 Doin and Fleitout (1996), 142, 812
 Doin et al. (1996), 147, 812
 Doin et al. (1997), 389, 412, 812

- Dolginov (1987), 698, 812
Dolginov et al. (1973), 698, 812
Dolginov et al. (1976), 698, 812
Donahue and Russell (1997), 678, 812
Doornbos (1974), 98, 813
Doornbos and Hilton (1989), 117, 813
Doornbos and Mondt (1979), 95, 813
Driscoll and Parsons (1988), 138, 813
Drummond and Defant (1990), 38, 630, 813
Drury (1989), 146, 813
Drury and Fitz Gerald (1998), 245, 246, 813
Drury et al. (1991), 490, 813
Dumoulin et al. (1998), 56, 813
Duncan and Richards (1991), 525, 813
Duncan and Turcotte (1994), 62, 813
Dupeyrat et al. (1995), 347, 813
Dupre and Allègre (1983), 551, 813
Durham et al. (1997), 766, 813
du Toit (1937), 6, 813
Dziewonski (1984), 103, 113, 813
Dziewonski and Anderson (1981), 66–68, 77, 95, 477, 813
Dziewonski and Woodhouse (1987), 103, 813
Dziewonski et al. (1975), 68, 813
Dziewonski et al. (1977), 113, 233, 813
- Eaton (1980), 45, 813
Ebinger and Sleep (1998), 515, 813
Ellsworth and Schubert (1983), 766, 813
Ellsworth and Schubert (1988), 474, 813
Ellsworth et al. (1985), 473, 813
Elsasser et al. (1979), 97, 204, 814
Emerman and Turcotte (1983), 45, 506, 814
Emerman et al. (1986), 166, 170, 171, 814
Engdahl and Gubbins (1987), 107, 814
Engdahl and Johnson (1974), 97, 814
Engdahl and Scholz (1977), 33, 814
Engdahl et al. (1974), 98, 814
Engdahl et al. (1998), 18, 814
Engebretson et al. (1992), 108, 110, 814
England and Houseman (1986), 46, 59, 814
England et al. (1980), 146, 814
Erickson (1993), 58, 814
Erickson and Arkani-Hamed (1993), 58, 814
Esposito et al. (1982), 644, 814
Esposito et al. (1992), 692, 814
Estabrook and Kind (1996), 87, 814
Evans and Kohlstedt (1995), 245, 246, 814
- Faccenna et al. (1999), 59, 814
Farley and Neroda (1998), 573, 814
Farnetani (1997), 414, 415, 528, 533, 814
Faure (1986), 547, 814
Fegley and Prinn (1989), 676, 814
Fei (1995), 209, 814
Fei et al. (1995), 712, 814
Feighner and Richards (1995), 543, 545, 814
Feighner et al. (1995), 543, 814
- Ferrachat and Ricard (1998), 347, 815
Ferrari et al. (1980), 726, 815
Fink et al. (1973), 758, 815
Finnerty and Boyd (1987), 144, 815
Finnerty et al. (1988), 688, 815
Fischer and Spohn (1990), 746, 748, 815
Fisher (1881), 3, 815
Flanagan and Shearer (1998a), 85, 89, 90, 92, 815
Flanagan and Shearer (1998b), 85, 92, 815
Flanagan and Shearer (1999), 85, 92, 815
Flasar and Birch (1973), 587, 815
Fleitout and Froidevaux (1980), 490, 815
Fleitout and Yuen (1984), 142, 815
Folkner et al. (1997a), 686, 687, 815
Folkner et al. (1997b), 686, 687, 815
Ford and Pettengill (1992), 639, 644, 815
Forni et al. (1991), 766, 815
Forsyth (1975), 77, 815
Forsyth (1993), 154, 815
Forsyth and Uyeda (1975), 52, 53, 815
Forte and Mitrovica (1996), 471, 815
Forte et al. (1991), 237, 239, 815
Forte et al. (1993), 97, 466, 815
Fowler (1985), 622, 815
Fowler (1993), 677, 815
Frank (1967), 349, 815
Frank (1968a), 36, 815
Frank (1968b), 154, 816
Freedman and Parsons (1990), 138, 816
Freer (1981), 242, 816
Frey (1979), 686, 816
Frey and Schultz (1988), 640, 683, 816
Frost and Ashby (1982), 246, 753, 754, 816
Frost and O’Nions (1984), 559, 560, 816
Fuchs (1986), 72, 73, 816
Fujii and Uyeda (1974), 172, 816
Fukao (1977), 84, 816
Fukao et al. (1992), 107, 460, 468, 816
Fyfe (1978), 629, 816
- Gable et al. (1991), 57, 389, 489, 816
Gaherty and Jordan (1995), 79, 80, 816
Galer (1991), 630, 816
Galer and O’Nions (1985), 572, 575, 816
Galer and O’Nions (1986), 572, 816
Gao et al. (1998), 43, 816
Garfunkel et al. (1986), 39, 461, 816
Garnero and Helmberger (1995), 206, 816
Garnero and Helmberger (1996), 95, 414, 816
Garnero et al. (1988), 115, 816
Garnero et al. (1998), 206, 816
Gaskell et al. (1988), 740, 741, 744, 816
Gast (1968), 549, 816
Geertsma and DeKlerk (1969), 166, 817
Geertsma and Haafkens (1979), 166, 170, 817
Geissler et al. (1998a), 760, 817
Geissler et al. (1998b), 760, 817
Giannandrea and Christensen (1993), 393, 817

- Giardini and Woodhouse (1984), 106, 817
 Gilbert and Dziewonski (1975), 66, 817
 Gilbert (1890), 228, 817
 Giunchi et al. (1997), 240, 817
 Glatzmaier (1988), 277, 417, 708, 817
 Glatzmaier and Roberts (1995), 99, 817
 Glatzmaier and Roberts (1996), 99, 817
 Glatzmaier and Roberts (1997), 603, 817
 Glatzmaier and Schubert (1993), 473–476, 817
 Glatzmaier et al. (1990), 277, 417, 446, 449–451, 454,
 817
 Goettel (1988), 754, 817
 Goetze and Kohlstedt (1973), 246, 817
 Goins et al. (1979), 725, 817
 Goins et al. (1981), 725, 817
 Goldsby and Kohlstedt (1997a), 763, 764, 766, 817
 Goldsby and Kohlstedt (1997b), 763, 764, 766, 817
 Goldschmidt (1933), 44, 817
 Gorbatov et al. (1994), 33, 817
 Gordon (1965), 10, 817
 Gordon (1967), 240, 818
 Gordon (1998), 52, 818
 Gor'kov (1958), 367, 818
 Goto et al. (1987), 185, 818
 Gough (1969), 267, 818
 Grand (1987), 102, 108, 818
 Grand (1994), 102, 107, 108, 110, 818
 Grand and Helmberger (1984a), 76, 86, 818
 Grand and Helmberger (1984b), 76, 86, 818
 Grand et al. (1997), 107, 109, 111–113, 468, 818
 Grasset and Parmentier (1998), 394, 624, 625, 707,
 708, 818
 Grasset and Sotin (1996), 766, 818
 Greeley (1987), 697, 818
 Greeley et al. (1998), 759–761, 818
 Green and Falloon (1998), 81, 82, 818
 Green and Houston (1995), 31, 185, 818
 Greenberg and Weidenschilling (1984), 760, 818
 Greenberg et al. (1978), 587, 818
 Greenberg et al. (1998), 759, 760, 818
 Griffiths (1986), 525, 528, 818
 Griffiths and Campbell (1990), 525, 528, 818
 Griffiths and Campbell (1991a), 527, 818
 Griffiths and Campbell (1991b), 528, 818
 Griffiths et al. (1995), 399, 461, 818
 Griggs (1939), 10, 11, 818
 Griggs (1972), 177, 818
 Grimm (1994a), 656, 819
 Grimm (1994b), 673, 819
 Grimm and Phillips (1990), 645, 819
 Grimm and Phillips (1991), 645, 819
 Grimm and Phillips (1992), 644, 819
 Grimm and Solomon (1988), 645, 651, 819
 Grossman (1972), 754, 819
 Gubbins (1977a), 603, 609, 610, 819
 Gubbins (1977b), 754, 819
 Gubbins (1981), 99, 819
 Gubbins et al. (1979), 610, 819
 Guillou and Jaupart (1995), 409, 410, 819
 Guillou-Frottier et al. (1995), 398, 399, 461, 819
 Gurnis (1986a), 346, 819
 Gurnis (1986b), 346, 349, 819
 Gurnis (1986c), 349, 819
 Gurnis (1988), 409, 489, 819
 Gurnis (1989), 590, 819
 Gurnis and Davies (1985), 630, 819
 Gurnis and Davies (1986a), 346, 819
 Gurnis and Davies (1986b), 346, 819
 Gurnis and Hager (1988), 389, 399, 400, 819
 Gurnis and Zhong (1991), 471, 819
 Gurnis et al. (1996), 33, 819
 Gutenberg (1913), 63, 97, 819
 Gwynn et al. (1986), 117, 819
 Haddon (1982), 97, 819
 Haddon and Buchbinder (1987), 97, 819
 Hadley and Kanamori (1977), 45, 819
 Hager (1984), 233, 820
 Hager (1991), 233, 820
 Hager and Clayton (1989), 103, 466, 820
 Hager and O'Connell (1978), 55, 820
 Hager and O'Connell (1979), 489, 820
 Hager and O'Connell (1981), 34, 489, 820
 Hager and Richards (1989), 97, 233, 234, 236, 237,
 471, 820
 Hager et al. (1985), 233, 820
 Hales (1936), 10, 820
 Hall (1987), 71, 820
 Hallam (1977), 61, 820
 Hallam (1992), 61, 636, 820
 Hamelin and Allègre (1988), 349, 550, 820
 Hanan and Graham (1996), 573, 820
 Hansen and Yuen (1988), 414, 523, 820
 Hansen and Yuen (1989), 414, 820
 Hansen and Yuen (1990), 523, 820
 Hansen and Yuen (1993), 625, 820
 Hansen and Yuen (1994), 407, 820
 Hansen et al. (1990), 382, 384, 627, 820
 Hansen et al. (1991), 209, 384, 406, 408, 820
 Hansen et al. (1992a), 407, 627, 820
 Hansen et al. (1992b), 627, 820
 Hansen et al. (1993), 209, 407, 471, 820
 Hansen et al. (1997), 644, 820
 Hardee (1986), 172, 821
 Hardee and Larson (1977), 172, 821
 Harder (1998), 712–715, 821
 Harder and Christensen (1996), 713, 821
 Harding et al. (1989), 153, 821
 Harmon and Campbell (1988), 750, 821
 Harris (1987), 349, 821
 Hart (1984), 551, 580, 581, 821
 Hart (1988), 550, 821
 Hart (1993), 165, 821
 Hartmann (1986), 727, 821
 Hartmann and Davis (1975), 587, 727, 821
 Hartmann et al. (1981), 697, 821

- Hartmann et al. (1986), 587, 821
Hasegawa et al. (1978a), 33, 821
Hasegawa et al. (1978b), 33, 34, 821
Haskell (1935), 216, 223, 228, 231, 821
Haskell (1936), 223, 821
Haskell (1937), 9, 216, 223, 821
Hauck et al. (1998), 637, 646, 821
Hauri et al. (1994), 529, 821
Hawkesworth et al. (1990), 82, 821
Hawkesworth et al. (1994), 38, 821
Haxby and Turcotte (1978), 137, 505, 506, 821
Haxby and Weissel (1986), 143, 821
Hays and Pitman (1973), 27, 61, 821
Head (1976), 724, 725, 821
Head et al. (1991), 676, 822
Head et al. (1992), 676, 822
Heiken et al. (1991), 639, 654, 718, 822
Heimpel and Olson (1994), 167, 168, 822
Heinz and Jeanloz (1987), 205, 822
Heirtzler et al. (1968), 13, 822
Helfenstein and Parmentier (1985), 760, 822
Helmburger et al. (1998), 509, 514, 822
Helmstaedt and Gurney (1984), 349, 822
Hemley and Cohen (1992), 209, 822
Herrick (1994), 646, 822
Herrick and Parmentier (1994), 651, 677, 822
Herrick and Phillips (1990), 645, 822
Herrick et al. (1989), 644, 645, 822
Herrick et al. (1997), 646, 822
Herring (1963), 361, 822
Herring (1964), 361, 822
Hess (1962), 12, 14, 822
Hess (1965), 12, 822
Hess and Parmentier (1995), 736, 822
Hewitt et al. (1975), 408, 822
Hewitt et al. (1980), 379, 822
Hey et al. (1980), 29, 822
Hildebrand and Bowring (1999), 45, 822
Hill (1991), 527, 822
Hill et al. (1992), 527, 823
Hirs (1974), 168, 173, 823
Hirth and Kohlstedt (1995a), 248, 823
Hirth and Kohlstedt (1995b), 248, 823
Hirth and Kohlstedt (1996), 248, 596, 598, 823
Hiyagon and Ozima (1986), 579, 823
Hiyagon et al. (1992), 578, 823
Hobson (1955), 323, 823
Hoffman and McKenzie (1985), 346, 823
Hofmann and White (1982), 550, 823
Hofmann et al. (1986), 350, 823
Hofmeister (1999), 211, 823
Holland and Ahrens (1997), 96, 205, 823
Holland and Lambert (1972), 44, 823
Holmes (1915a), 125, 823
Holmes (1915b), 125, 823
Holmes (1916), 125, 594, 823
Holmes (1931), 8, 9, 295, 823
Holmes (1933), 8, 823
Holmes (1945), 9, 823
Holmes (1946), 566, 823
Holzer and Axford (1971), 576, 823
Honda (1995), 611, 823
Honda and Yuen (1994), 470, 823
Honda et al. (1993a), 455, 626, 823
Honda et al. (1993b), 455, 626, 823
Hood (1986), 726, 728, 823
Hood and Vickery (1984), 727, 823
Horai and Simmons (1970), 210, 824
Houseman (1988), 417, 445, 471, 824
Houseman and England (1986), 46, 824
Houseman et al. (1981), 46, 824
Houston and De Bremaecker (1975), 394, 417, 824
Houtermans (1946), 566, 824
Howard (1966), 350, 520, 606, 824
Howell (1997), 744, 824
Hsui (1981), 59, 824
Hsui and Toksöz (1979), 37, 824
Hsui and Toksöz (1981), 39, 824
Hsui et al. (1983), 37, 824
Hsui et al. (1995), 490, 824
Humphreys and Clayton (1990), 45, 824
Humphreys and Dueker (1994), 516, 824
Huppert and Sparks (1988), 48, 824
Hurley and Rand (1969), 556, 629, 824
Hynes and Mott (1985), 39, 824

Inoue et al. (1990), 116, 472, 824
Ioannou and Lindzen (1993), 747, 824
Irfune and Ringwood (1987), 90, 824
Irwin (1957), 169, 824
Isacks and Barazangi (1977), 32, 824
Isacks and Molnar (1971), 35, 106, 824
Isacks et al. (1968), 16, 106, 824
Ita and King (1994), 457, 825
Ito (1989), 90, 825
Ito and Katsura (1989), 127, 825
Ito and Takahashi (1989), 88, 89, 204, 455, 825
Ito et al. (1990), 455, 825
Ito et al. (1997), 543–545, 825
Ivins et al. (1993), 471, 473, 825
Iwamori (1997), 37, 825
Iwamori et al. (1995), 154, 825
Iwase and Honda (1997), 419, 825
Iyer (1979), 516, 825
Iyer (1984), 516, 825

Jackson and Pollack (1984), 595, 600, 825
Jackson and Pollack (1987), 596, 600, 825
Jacob et al. (1994), 349, 825
Jacobsen and Wasserburg (1979), 554, 825
Jacobsen and Wasserburg (1980a), 550, 554, 825
Jacobsen and Wasserburg (1980b), 550, 556, 731, 825
Jacobsen and Wasserburg (1981), 550, 825
Jacoby and Schmelting (1982), 394, 825
Jákeš and Taylor (1974), 47, 825
Jákeš and White (1971), 47, 825

- Jambon et al. (1986), 579, 825
 James and Ivins (1997), 232, 825
 Janes et al. (1992), 648, 825
 Janle (1983), 697, 825
 Janle and Jannsen (1986), 689, 826
 Jarchow and Thompson (1989), 73, 826
 Jaroslow et al. (1996), 490, 826
 Jarrard (1986), 39, 187, 826
 Jarvis (1984), 379–384, 826
 Jarvis and McKenzie (1980), 268, 408, 478, 479, 482,
 826
 Jarvis and Peltier (1982), 381, 826
 Jaupart (1983), 146, 826
 Jaupart and Parsons (1985), 143, 307, 308, 826
 Jaupart et al. (1981), 146, 826
 Jaupart et al. (1982), 146, 826
 Jaupart et al. (1998), 146, 826
 Jeanloz and Knittle (1989), 91, 826
 Jeanloz and Morris (1986), 127, 826
 Jeanloz and Richter (1979), 204, 826
 Jeanloz and Thompson (1983), 189, 826
 Jeffreys (1929), 7, 98, 826
 Jeffreys (1930), 8, 826
 Jeffreys (1939), 63, 826
 Jeffreys (1962), 739–741, 826
 Jeffreys and Bland (1951), 314, 826
 Jeffreys and Bullen (1940), 64, 826
 Jephcoat and Olson (1987), 100, 826
 Jin et al. (1998), 490, 826
 Johnson (1967), 84, 93, 826
 Johnson and Carlson (1992), 136, 826
 Johnson and Sandwell (1994), 651, 826
 Johnson et al. (1988), 744, 827
 Johnston and Toksöz (1977), 691, 827
 Jones (1977), 97, 204, 827
 Jordan (1975), 78, 79, 104, 827
 Jordan (1977), 107, 827
 Jordan (1981), 78, 104, 827
 Jordan (1988), 78, 827
 Jordan et al. (1993), 476, 827
 Julian and Sengupta (1973), 113, 827
 Jull and Arkani-Hamed (1995), 656, 827
 Jurdy and Gordon (1984), 502, 827
 Jurdy and Stefanick (1990), 514, 827
 Jurdy and Stefanick (1991), 53, 827
 Kameyama et al. (1997), 490, 827
 Kanamori et al. (1998), 36, 827
 Kanasewich (1968), 568, 827
 Kaneshima and Helffrich (1999), 585, 827
 Kao and Chen (1994), 33, 827
 Kao and Chen (1995), 33, 827
 Karato (1992), 80, 827
 Karato (1993), 98, 827
 Karato (1997), 248, 827
 Karato (1998), 215, 827
 Karato (1999), 248, 827
 Karato and Wu (1993), 246, 247, 827
 Karato et al. (1980), 490, 827
 Karato et al. (1986), 490, 827
 Karato et al. (1995a), 247, 827
 Karato et al. (1995b), 248, 827
 Kargel (1991), 766, 827
 Kargel (1992), 766, 828
 Karig (1971), 38, 39, 828
 Karig and Kay (1981), 46, 828
 Katsura (1995), 211, 828
 Katsura and Ito (1989), 84, 85, 302, 464, 828
 Kaula (1979a), 587, 751, 828
 Kaula (1979b), 686, 828
 Kaula (1980), 751, 828
 Kaula (1994a), 644, 652, 828
 Kaula (1994b), 652, 828
 Kaula and Phillips (1981), 641, 828
 Kaula et al. (1974), 719, 828
 Kaula et al. (1989), 686, 828
 Kaula et al. (1997), 644, 656, 667, 828
 Kawakatsu (1986), 33, 828
 Kawasaki (1986), 77, 828
 Kay (1980), 565, 828
 Kay and Kay (1988), 47, 656, 828
 Kay and Kay (1991), 45, 828
 Kay and Kay (1993), 45, 656, 828
 Kay et al. (1982), 38, 828
 Kay et al. (1993), 38, 828
 Kelemen and Dick (1995), 165, 828
 Kelemen et al. (1995a), 165, 828
 Kelemen et al. (1995b), 165, 828
 Kelemen et al. (1997), 166, 828
 Kellogg (1992), 346, 828
 Kellogg (1993), 346, 829
 Kellogg (1997), 414, 523, 524, 829
 Kellogg and Stewart (1991), 347, 829
 Kellogg and Turcotte (1987), 346, 349, 829
 Kellogg and Turcotte (1990), 346, 347, 829
 Kellogg et al. (1999), 94, 584, 829
 Kemp and Stevenson (1996), 59, 829
 Kendall and Shearer (1994), 115, 117, 829
 Kennett (1991), 68, 829
 Kennett and van der Hilst (1998), 103, 829
 Kennett et al. (1998), 468, 829
 Kenyon (1998), 164, 829
 Kenyon and Turcotte (1983), 350, 829
 Kenyon and Turcotte (1987), 164, 829
 Keszthelyi and McEwen (1997), 744, 829
 Khodakovskii et al. (1998), 164, 829
 Khurana et al. (1997a), 742, 748, 829
 Khurana et al. (1997b), 762, 829
 Khurana et al. (1998), 757, 762, 766, 829
 Kidd (1977), 166, 829
 Kido and Seno (1994), 136, 646, 829
 Kiefer and Hager (1991a), 645, 648, 829
 Kiefer and Hager (1991b), 645, 648, 829
 Kiefer and Hager (1992), 645, 648, 662, 829
 Kiefer et al. (1986), 645, 662, 663, 829
 Kieffer (1976), 210, 830

- Kincaid and Olson (1987), 90, 397, 398, 461, 830
Kincaid and Sacks (1997), 37, 830
Kincaid et al. (1995), 543, 545, 830
Kincaid et al. (1996), 498, 830
King (1995a), 233, 238, 471, 830
King (1995b), 471, 830
King and Hager (1990), 489, 830
King and Hager (1994), 400, 830
King and Ita (1995), 390, 397, 470, 489, 830
King and Masters (1992), 239, 466, 830
King et al. (1992), 389, 830
Kirby and McCormick (1979), 45, 830
Kirby et al. (1996), 31, 185–187, 830
Kirk and Stevenson (1989), 731, 830
Kivelson et al. (1996a), 742, 748, 830
Kivelson et al. (1996b), 761, 830
Kivelson et al. (1997), 757, 830
Kivelson et al. (1999), 757, 762, 766, 830
Kivelson et al. (2000), 762, 830
Klein and Langmuir (1987), 153, 508, 830
Klemaszewski et al. (1998), 762, 830
Knittle and Jeanloz (1986), 99, 202, 207, 830
Knittle and Jeanloz (1991), 414, 831
Knittle et al. (1986), 91, 207, 831
Koch (1994), 648, 831
Kohlstedt and Goetze (1974), 246, 831
Kohlstedt and Zimmerman (1996), 248, 831
Kohlstedt et al. (1995), 246, 248, 831
Konopliv and Sjogren (1994), 644, 662, 831
Konopliv and Yuan (1999), 723, 725, 831
Konopliv et al. (1993), 662, 663, 831
Konopliv et al. (1998), 720, 726, 831
Konopliv et al. (1999), 643, 644, 831
Korenaga and Kelemen (1998), 164, 831
Kozlovskaya (1969), 749, 831
Kucinskas and Turcotte (1994), 651, 831
Kunz et al. (1998), 579, 831
Kurz and Jenkins (1981), 575, 831
Kurz and Jenkins (1982), 575, 831
Kurz et al. (1982a), 575, 831
Kurz et al. (1982b), 575, 831
Kurz et al. (1983), 575, 831
Kushiro et al. (1976), 158, 831

Lachenbruch (1970), 144, 831
Lachenbruch and Sass (1978), 45, 831
Lambeck (1988), 231, 831
Lambeck and Johnston (1998), 216, 238, 831
Lambeck and Nakada (1990), 229, 237, 832
Lambeck et al. (1990), 238, 832
Langseth et al. (1976), 594, 727, 737, 832
Laravie (1975), 36, 832
Larsen and Yuen (1997a), 405, 407, 529, 627, 832
Larsen and Yuen (1997b), 405, 832
Larsen et al. (1996a), 404, 832
Larsen et al. (1996b), 627, 832
Larson (1991), 515, 546, 832
Larson and Olson (1991), 60, 61, 626, 832

Laske and Masters (1999), 98, 832
Laubscher (1988), 45, 832
Laul et al. (1986), 690, 691, 699, 702, 705, 706, 832
Lay (1989), 95, 832
Lay (1994a), 35, 832
Lay (1994b), 35, 832
Lay (1994c), 35, 832
Lay and Helmberger (1983), 96, 832
Lay et al. (1998), 200, 201, 204, 832
Lee et al. (1997), 731, 736, 832
Lees et al. (1983), 86, 832
Lehmann (1936), 63, 97, 832
Leitch and Yuen (1991), 657, 832
Leitch et al. (1992), 657, 832
Leitch et al. (1998), 527, 832
Leith and McKinnon (1996), 760, 833
Lemoine et al. (1997), 720, 833
Lemoine et al. (1998), 21, 833
Lenardic (1997), 412, 833
Lenardic (1998), 412, 833
Lenardic and Kaula (1995a), 59, 833
Lenardic and Kaula (1995b), 412, 833
Lenardic and Kaula (1996), 412, 833
Le Pichon (1968), 16, 832
Lerch et al. (1983), 472, 833
Le Stunff and Ricard (1995), 646, 832
Le Stunff and Ricard (1997), 646, 832
Leven (1985), 84, 833
Levin (1972), 587, 833
Levitt and Sandwell (1995), 33, 77, 78, 833
Levitt and Sandwell (1996), 515, 833
Lewis (1972), 754, 833
Lewis (1982), 740, 833
Lewis (1988), 754, 833
Li and Romanowicz (1996), 103, 105, 143, 833
Lin et al. (1988), 726, 833
Lin et al. (1990), 153, 833
Lin et al. (1998), 726, 727, 833
Lingenfelter and Schubert (1973), 640, 683, 711, 722, 833
Lister (1980), 132, 833
Lister (1990a), 168, 833
Lister (1990b), 168, 833
Lister (1991), 168, 834
Lister and Buffett (1995), 100, 834
Lister and Kerr (1991), 168, 834
Lister et al. (1990), 134, 833
Lithgow-Bertelloni and Silver (1998), 646, 834
Lithgow-Bertelloni et al. (1993), 57, 834
Liu (1974), 88, 834
Liu (1994), 470, 834
Liu and Bassett (1975), 699, 834
Liu and Chase (1989), 506, 834
Liu et al. (1991), 459, 834
Lognonne and Romanowicz (1990), 518, 834
Longhi and Boudreau (1979), 719, 834
Loper (1978a), 100, 603, 834
Loper (1978b), 603, 834

- Loper (1984a), 204, 834
 Loper (1984b), 529, 834
 Loper and Eltayeb (1986), 521, 834
 Loper and Lay (1995), 95, 97, 201, 834
 Loper and Roberts (1979), 603, 834
 Loper and Stacey (1983), 529, 834
 Lord Rayleigh (1916), 3, 290, 294, 834
 Lorenz (1963), 330, 332, 334, 834
 Loubet and Allègre (1982), 349, 834
 Love (1927), 738, 739, 834
 Lowman and Jarvis (1995), 409, 834
 Lowman and Jarvis (1996), 409, 411, 834
 Luais and Hawkesworth (1994), 48, 834
 Lucchitta (1987), 686, 834
 Lucey et al. (1994), 640, 719, 834
 Lugmair and Marti (1978), 733, 834
 Lux (1987), 579, 835
 Lux et al. (1979), 387, 388, 417, 835
 Lyakhovsky et al. (1997a), 490, 835
 Lyakhovsky et al. (1997b), 490, 835
- MacGregor and Manton (1986), 349, 835
 Machetel and Weber (1991), 390, 457, 468, 626, 835
 Machetel and Yuen (1987), 454, 835
 Machetel and Yuen (1989), 478, 479, 482, 835
 Machetel et al. (1986), 417, 418, 835
 Machetel et al. (1995), 455, 457, 835
 Mackwell et al. (1998), 652, 835
 Malevsky and Yuen (1992), 404–406, 835
 Malin and Pieri (1986), 758, 835
 Malkus and Veronis (1958), 367, 370, 835
 Mamyrin and Tolstikhin (1984), 573, 574, 835
 Manga and Jeanloz (1996), 211, 414, 835
 Manga and Jeanloz (1997), 211, 835
 Manghnani et al. (1974), 190, 835
 Manglik and Christensen (1997), 541, 835
 Mao et al. (1990), 99–101, 835
 Mao et al. (1991), 209, 835
 Marsh (1979), 37, 835
 Marsh (1983), 21, 22, 835
 Martin (1986), 630, 835
 Marton et al. (1999), 185, 835
 Marty et al. (1988), 138, 139, 835
 Marzoli et al. (1999), 546, 836
 Mason (1958), 13, 836
 Masters (1979), 66, 836
 Masters (1989), 103, 836
 Masters and Shearer (1990), 98, 836
 Masters et al. (1982), 103, 836
 Masters et al. (1996), 103, 113–116, 836
 Masursky et al. (1979), 736, 836
 Matson et al. (1981), 736, 836
 Matsui and Abe (1986a), 588, 836
 Matsui and Abe (1986b), 588, 836
 Matsui and Abe (1986c), 588, 836
 Matsui and Abe (1987), 588, 836
 Matsui and Anderson (1997), 202, 836
 Matthews and Smith (1987), 72, 836
- Maxwell et al. (1970), 13, 836
 McAdoo et al. (1978), 33, 836
 McBirney and Murase (1984), 744, 836
 McCarthy and Luzum (1996), 232, 836
 McCartney and Loper (1989), 545, 836
 McClain et al. (1985), 153, 836
 McCord et al. (1998), 766, 836
 McDonough and Sun (1995), 80, 81, 836
 McDougall and Honda (1998), 573, 836
 McElhinny and Senanayake (1980), 610, 837
 McEwen (1986), 760, 837
 McEwen et al. (1998a), 736, 743, 744, 837
 McEwen et al. (1998b), 736, 744, 745, 837
 McGill and Dimitriou (1990), 640, 683, 837
 McGill et al. (1981), 648, 837
 McGovern and Schubert (1989), 579, 596, 598–600, 837
 McKenzie (1967), 139, 837
 McKenzie (1969), 177, 837
 McKenzie (1970), 177, 837
 McKenzie (1977a), 33, 837
 McKenzie (1977b), 58, 837
 McKenzie (1979), 346, 837
 McKenzie (1984a), 48, 837
 McKenzie (1984b), 158, 161, 164, 837
 McKenzie (1985), 164, 837
 McKenzie (1988), 307, 837
 McKenzie (1989), 164, 837
 McKenzie (1994), 662, 837
 McKenzie and Bickle (1988), 154, 837
 McKenzie and Morgan (1969), 16, 837
 McKenzie and O’Nions (1983), 45, 837
 McKenzie and O’Nions (1991), 154, 837
 McKenzie and Parker (1967), 16, 837
 McKenzie and Richter (1981), 611, 837
 McKenzie and Sclater (1968), 36, 177, 837
 McKenzie et al. (1973), 379, 837
 McKenzie et al. (1974), 379, 837
 McKenzie et al. (1992), 646, 649, 837
 McKinnon (1998), 763, 765, 766, 838
 McKinnon (1999), 766, 838
 McKinnon et al. (1997), 637, 646, 838
 McLennan (1988), 46, 838
 McLennan and Taylor (1982), 556, 629, 838
 McNutt (1987), 690, 838
 McNutt (1998), 515, 838
 McNutt and Fischer (1987), 514, 838
 McSween (1985), 691, 699, 838
 Meijer (1985), 583, 838
 Meissner (1986), 72, 838
 Meissner and Wever (1989), 74, 838
 Melosh (1990), 587, 838
 Melosh and Raefsky (1980), 33, 838
 Mercier et al. (1977), 158, 838
 Meriaux and Jaupart (1998), 168, 838
 Meriaux et al. (1999), 168, 838
 Merrill and McElhinny (1983), 611, 838
 Meyer (1987), 349, 838

- Mihaljan (1962), 268, 838
Milne et al. (1998), 473, 838
Mimouni and Rabinowicz (1988), 413, 838
Mitrovica (1996), 231, 471, 838
Mitrovica and Forte (1997), 473, 838
Mitrovica and Jarvis (1987), 353, 838
Mitrovica and Peltier (1991), 237, 838
Mitrovica and Peltier (1995), 238, 839
Miyashiro et al. (1982), 74, 839
Mohorovicic (1909), 63, 839
Molnar and Atwater (1973), 502, 839
Molnar and Atwater (1978), 39, 839
Molnar and Stock (1987), 502, 504, 839
Molnar and Tapponnier (1975), 59, 839
Molnar and Tapponnier (1978), 59, 839
Molnar and Tapponnier (1981), 45, 839
Monnercieu and Rabinowicz (1996), 401, 839
Monnercieu et al. (1993), 506, 839
Montagner (1994), 103, 839
Montague et al. (1998), 414–416, 839
Mooney and Brocher (1987), 72, 73, 839
Mooney et al. (1998), 74, 75, 839
Moorbath (1978), 629, 839
Moorbath et al. (1972), 553, 839
Moore and Schubert (1995), 648, 839
Moore and Schubert (1997a), 506, 507, 839
Moore and Schubert (1997b), 648, 651, 656, 839
Moore and Weiss (1973), 358, 417, 839
Moore et al. (1998a), 760, 839
Moore et al. (1998b), 45, 506, 507, 527, 543, 839
Moore et al. (1999), 506, 527, 839
Morabito et al. (1979), 736, 839
Morelli (1993), 117, 839
Morelli and Dziewonski (1987), 117, 840
Morelli et al. (1986), 98, 840
Moresi and Gurnis (1996), 461, 840
Moresi and Lenardic (1997), 412, 498, 840
Moresi and Solomatov (1995), 394, 590, 619, 664, 840
Moresi and Solomatov (1998), 664, 840
Morgan (1968), 16, 840
Morgan (1971), 39, 499, 840
Morgan (1972), 499, 501, 840
Morgan (1981), 509, 525, 840
Morgan (1983), 502, 840
Morgan and Phillips (1983), 645, 840
Mori and Helmberger (1995), 206, 840
Morris (1982), 530, 840
Morris and Canright (1984), 360, 393, 622, 840
Morris et al. (1969), 76, 840
Morrison and Telesco (1980), 736, 840
Mottinger et al. (1985), 644, 840
Mueller (1977), 45, 840
Mueller and Phillips (1991), 59, 840
Mueller et al. (1997), 19, 840
Muller and Sjogren (1968), 720, 840
Munk and MacDonald (1960), 230, 840
Murase and McBirney (1973), 175, 840
Murnaghan (1951), 277, 840
Mutter and Mutter (1993), 71, 840
Nakada and Lambeck (1989), 229, 237, 471, 840
Nakakuki and Fujimoto (1994), 401, 840
Nakakuki et al. (1994), 401, 841
Nakakuki et al. (1997), 401, 841
Nakamura (1983), 725, 841
Nakamura et al. (1976), 725, 730, 841
Nakiboglu and Lambeck (1983), 228, 841
Namiki and Solomon (1994), 637, 646, 841
Namiki and Solomon (1998), 676, 841
Nance et al. (1986), 637, 841
Nansen (1928), 216, 841
Nash et al. (1986), 736, 738, 740, 841
Nataf (1991), 393, 841
Nataf and Houard (1993), 96, 841
Nataf and Richter (1982), 393, 489, 606, 841
Nataf and VanDecar (1993), 518, 841
Nataf et al. (1986), 106, 841
Navon and Stolper (1987), 164, 841
Navrotsky (1995), 209, 841
Nelson and DePaolo (1984), 561, 841
Nelson and DePaolo (1985), 629, 841
Ness et al. (1974), 750, 841
Ness et al. (1975), 750, 841
Neukum et al. (1998), 760, 761, 841
Nicolas (1986), 165, 841
Nicolas (1990), 165, 841
Nicolas and Jackson (1982), 349, 841
Nicolaysen (1985), 59, 842
Nimmo and McKenzie (1998), 644, 842
Niu and Kawakatsu (1995), 89, 842
Nockolds (1954), 44, 842
Nyquist et al. (1979), 733, 842
Obata and Karato (1995), 490, 842
O'Connell et al. (1991), 57, 490, 842
Officer and Page (1993), 545, 842
Officer et al. (1987), 545, 842
Ogawa et al. (1991), 417, 428, 429, 432, 435, 436, 438, 664, 842
Ogura and Phillips (1962), 267, 842
Ohtani and Ringwood (1984), 202, 842
Ojakangas and Stevenson (1986), 746, 747, 842
Ojakangas and Stevenson (1989a), 760, 842
Ojakangas and Stevenson (1989b), 760, 765, 766, 842
Oldenburg and Brune (1972), 29, 842
Oldenburg and Brune (1975), 29, 842
Oldham (1906), 97, 842
Oliver and Booker (1983), 428, 842
Olson (1981), 362, 364, 366, 842
Olson (1984), 392, 842
Olson (1987), 379, 842
Olson (1990), 534, 539, 842
Olson and Bercovici (1991), 57, 842
Olson and Christensen (1986), 534–536, 842
Olson and Corcos (1980), 353, 389, 489, 842
Olson and Kincaid (1991), 115, 523, 842

- Olson and Singer (1985), 525, 526, 537, 538, 843
 Olson and Yuen (1982), 192, 843
 Olson et al. (1984a), 346, 843
 Olson et al. (1984b), 346, 843
 Olson et al. (1987), 413, 414, 520–522, 580, 711, 843
 Olson et al. (1988), 507, 606, 843
 Olson et al. (1993), 529, 530, 843
 O'Nions (1987), 550, 843
 O'Nions and Hamilton (1981), 571, 843
 O'Nions and Oxburgh (1983), 573–575, 843
 O'Nions and Pankhurst (1974), 71, 843
 O'Nions and Tolstikhin (1996), 579, 629, 843
 O'Nions et al. (1979), 550, 556, 629, 843
 O'Nions et al. (1983), 559, 560, 843
 Orcutt et al. (1984), 69, 843
 O'Reilly and Davies (1981), 744, 843
 Orowan (1964), 16, 843
 Orowan (1965), 16, 843
 Osako and Ito (1991), 211, 455, 843
 Ottino (1989), 346, 843
 Ottino (1990), 346, 843
 Owen (1992), 699, 843
 Oxburgh (1972), 45, 59, 843
 Oxburgh and O'Nions (1987), 573, 843
 Oxburgh and Parmentier (1977), 151, 549, 843
 Oxburgh and Turcotte (1968), 36, 177, 843
 Oxburgh and Turcotte (1970), 37, 177, 843
 Ozima (1975), 573, 843
 Ozima (1994), 573, 843
- Page et al. (1984), 629, 844
 Pakiser and Robinson (1966), 44, 844
 Palm (1960), 307, 844
 Palm and Øiann (1964), 307, 844
 Palm et al. (1967), 307, 844
 Papanastassiou et al. (1977), 733, 844
 Pappalardo et al. (1998a), 760, 765, 844
 Pappalardo et al. (1998b), 761, 844
 Pappalardo et al. (1999), 758–761, 765, 844
 Pari and Peltier (1996), 46, 844
 Parise et al. (1990), 207, 844
 Parmentier (1978), 404, 844
 Parmentier and Haxby (1986), 29, 844
 Parmentier and Hess (1992), 651, 677, 844
 Parmentier and Morgan (1982), 404, 844
 Parmentier and Turcotte (1978), 417, 844
 Parmentier et al. (1975), 529, 844
 Parmentier et al. (1976), 394, 404, 844
 Parmentier et al. (1994), 466, 649, 660, 844
 Parsons (1981), 52, 844
 Parsons (1982), 636, 844
 Parsons and McKenzie (1978), 142, 350, 844
 Parsons and Sclater (1977), 132, 141, 845
 Patchett and Chauvel (1984), 561, 563, 845
 Patchett et al. (1981), 629, 845
 Patterson (1956), 566, 567, 845
 Peacock et al. (1994), 37, 845
 Peale (1986), 738, 845
 Peale (1988), 750, 845
 Peale and Cassen (1978), 739, 845
 Peale et al. (1979), 738, 739, 845
 Pearl and Sinton (1982), 736, 845
 Pearson et al. (1989), 349, 845
 Pekeris (1935), 10, 233, 845
 Pellew and Southwell (1940), 295, 845
 Peltier (1974), 216, 739, 845
 Peltier (1981), 607, 845
 Peltier (1989), 216, 226, 845
 Peltier (1996a), 238, 845
 Peltier (1996b), 390, 845
 Peltier and Jarvis (1982), 594, 845
 Peltier and Jiang (1996), 238, 845
 Peltier and Solheim (1992), 390, 457, 466, 468, 660, 845
 Peltier et al. (1989), 303, 845
 Pettengill et al. (1980), 644, 845
 Phillips (1990), 645, 845
 Phillips and Hansen (1994), 644, 647, 845
 Phillips and Malin (1983), 645, 846
 Phillips and Malin (1984), 645, 846
 Phillips and Russell (1987), 678, 845
 Phillips and Saunders (1975), 688, 846
 Phillips et al. (1972), 720, 846
 Phillips et al. (1991), 645, 648, 846
 Phipps Morgan (1987), 165, 846
 Phipps Morgan et al. (1995), 507, 513, 539, 541, 846
 Pilcher et al. (1972), 758, 846
 Pinet and Jaupart (1987), 144, 846
 Pinet et al. (1991), 144, 146, 846
 Pitman and Heirtzler (1966), 13, 846
 Poirier (1985), 245, 590, 846
 Poirier (1994a), 99, 100, 202, 608, 846
 Poirier (1994b), 608, 846
 Poirier (1995), 245, 846
 Pollack (1986), 413, 846
 Pollack et al. (1976), 545, 846
 Pollack et al. (1993), 24, 128, 143, 147, 512, 846
 Polve and Allègre (1980), 349, 846
 Ponko and Peacock (1995), 37, 846
 Porcelli and Wasserburg (1995), 573, 846
 Poupinet et al. (1983), 98, 846
 Price and Suppe (1994), 637, 676, 846
 Prinzhofer et al. (1989), 550, 846
 Prockter et al. (1998), 761, 846
 Prout (1834), 3, 846
 Puchtel et al. (1998), 630, 847
 Pudovkin et al. (1981), 577, 847
 Purdy and Ewing (1986), 69, 847
 Puster and Jordan (1997), 392, 847
 Pysklywec and Mitrovica (1997), 390, 847
- Qamar and Eisenberg (1974), 98, 847
 Quarenii and Yuen (1984), 363, 364, 847
 Quarenii and Yuen (1988), 366, 847
- Rabinowicz et al. (1980), 413, 847

- Rabinowicz et al. (1987), 165, 847
Rabinowicz et al. (1993), 498, 847
Raitt et al. (1969), 76, 847
Ranalli (1995), 245, 847
Rappaport and Plaut (1994), 639, 644, 662, 847
Rappaport et al. (1999), 639, 642, 644, 847
Ratcliff et al. (1995), 664, 665, 667, 668, 847
Ratcliff et al. (1996a), 421–427, 847
Ratcliff et al. (1996b), 665, 667, 847
Ratcliff et al. (1997), 393, 394, 489, 590, 619, 620,
 664, 665, 667, 669, 847
Ratcliff et al. (1998), 527, 626, 627, 847
Raup and Sepkoski (1986), 546, 847
Ray and Anderson (1994), 472, 847
Reasenberg (1977), 686, 847
Reasenberg et al. (1981), 644, 847
Reasenberg et al. (1982), 644, 847
Reese et al. (1998), 590, 619, 623, 673, 706, 847
Reese et al. (1999), 590, 619, 623, 706, 707, 848
Regan and Anderson (1984), 77, 78, 848
Regenauer-Lieb (1999), 490, 848
Renkin and Slater (1988), 136, 141, 848
Revelle and Maxwell (1952), 127, 848
Revenaugh and Jordan (1991), 92, 848
Revenaugh and Meyer (1997), 206, 848
Reymer and Schubert (1984), 45, 556, 564, 565, 597,
 600, 629, 630, 636, 848
Reynolds and Summers (1969), 749, 848
Riahi et al. (1982), 427, 848
Ribe (1985a), 161, 848
Ribe (1985b), 161, 164, 848
Ribe (1986), 165, 848
Ribe (1987), 166, 848
Ribe (1988), 165, 848
Ribe (1992), 57, 489, 848
Ribe and Christensen (1994), 507, 539, 541–543, 848
Ribe and de Valpine (1994), 521, 848
Ribe et al. (1995), 543, 545, 848
Ricard and Vigny (1989), 233, 237, 848
Ricard and Wuming (1991), 471, 848
Ricard et al. (1984), 466, 848
Ricard et al. (1989), 233, 235, 239, 848
Ricard et al. (1992), 232, 471, 848
Ricard et al. (1993), 21, 848
Richards (1972), 86, 849
Richards and Griffiths (1989), 528, 848
Richards and Hager (1984), 233, 235, 466, 848
Richards and Lithgow-Bertelloni (1996), 501, 848
Richards and Wicks (1990), 89, 849
Richards et al. (1989), 61, 525, 527, 849
Richards et al. (1997), 232, 849
Richardson (1998), 164, 849
Richardson et al. (1979), 54, 849
Richardson et al. (1984), 151, 849
Richardson et al. (1995), 138, 849
Richter (1973), 417, 849
Richter (1978), 393, 417, 606, 849
Richter (1985), 611, 849
Richter (1986), 164, 849
Richter and McKenzie (1981), 392, 474, 590, 849
Richter and McKenzie (1984), 161, 849
Richter and Parsons (1975), 142, 389, 849
Richter and Ribe (1979), 346, 849
Richter et al. (1982), 346, 849
Richter et al. (1983), 393, 849
Riedel and Karato (1997), 185, 849
Riedler et al. (1989), 698, 849
Ringwood (1966), 599, 600, 849
Ringwood (1970), 88, 849
Ringwood (1975), 63, 80–82, 156, 158, 599, 600, 849
Ringwood (1977a), 38, 180, 849
Ringwood (1977b), 608, 849
Ringwood (1979), 63, 81, 849
Ringwood (1990), 588, 849
Ringwood and Major (1970), 84, 850
Rison and Craig (1983), 575, 850
Ritzwoller and Lavelle (1995), 103, 850
Roberts (1965a), 314, 850
Roberts (1965b), 361, 850
Roberts (1967), 306, 439, 850
Roberts (1979), 353, 850
Robinson and Parsons (1988), 507, 850
Robinson et al. (1987), 507, 850
Rodgers and Wahr (1993), 117, 850
Romanowicz (1991), 103, 850
Romanowicz et al. (1996), 98, 850
Ronov (1972), 44, 850
Ronov and Yaroshevsky (1969), 44, 850
Ross and Schubert (1985), 738, 740, 850
Ross and Schubert (1986), 738, 740, 753, 850
Ross and Schubert (1987), 760, 766, 850
Ross et al. (1990), 740, 744, 745, 747, 850
Rubie and Ross (1994), 185, 850
Rubincam (1984), 231, 850
Rudnick (1995), 630, 631, 850
Rudnick and Fountain (1995), 44, 73, 146, 150, 850
Ruff (1996), 31, 850
Ruff and Helmberger (1982), 95, 850
Runcorn (1956), 12, 850
Runcorn (1962a), 12, 850
Runcorn (1962b), 727, 850
Runcorn (1974), 719, 851
Runcorn (1983), 726, 851
Russell (1972), 569, 851
Russell (1978a), 698, 851
Russell (1978b), 698, 851
Russell (1980), 678, 851
Russell et al. (1974a), 726, 851
Russell et al. (1974b), 726, 851
Russell et al. (1981), 726, 851
Russell et al. (1984), 698, 851
Russell et al. (1998), 510, 518, 851
Ryan and Blevins (1987), 158, 173, 175, 851
Ryerson et al. (1988), 175, 851

Sabadini and Yuen (1989), 231, 851

- Sabadini et al. (1982), 753, 851
 Sacks and Secor (1990), 45, 851
 Sacks and Snoke (1984), 79, 851
 Safronov (1969), 587, 851
 Safronov (1978), 587, 672, 851
 Salters and Hart (1989), 164, 851
 Salters and Hart (1991), 583, 851
 Saltzman (1962), 331, 851
 Sammis et al. (1977), 473, 851
 Sammis et al. (1981), 473, 851
 Samowitz and Forsyth (1981), 33, 851
 Sandwell (1982), 506, 851
 Sandwell (1986), 29, 851
 Sandwell and MacKenzie (1989), 505, 851
 Sandwell and Schubert (1980), 132, 138, 852
 Sandwell and Schubert (1982), 138, 139, 852
 Sandwell and Schubert (1992a), 646, 649, 651, 852
 Sandwell and Schubert (1992b), 646, 647, 649, 651, 852
 Sandwell et al. (1997), 645, 852
 Sarda et al. (1985), 573, 852
 Sarda et al. (1999), 578, 579, 852
 Sarson et al. (1997), 742, 852
 Sawamoto (1987), 87, 852
 Saxena et al. (1994), 202, 852
 Schaber et al. (1992), 637, 646, 852
 Schatz and Simmons (1972), 210, 852
 Schenk and Bulmer (1998), 745, 852
 Schilling (1973), 543, 852
 Schilling (1991), 508, 543, 852
 Schilling et al. (1985), 543, 852
 Schmalzl et al. (1995), 347, 852
 Schmalzl et al. (1996), 347, 852
 Schmeling and Jacoby (1981), 489, 852
 Schmeling et al. (1999), 185, 852
 Schubert (1979), 586, 587, 594, 634, 672, 696, 852
 Schubert (1992), 440, 466, 495, 852
 Schubert and Anderson (1985), 379, 381, 432, 440, 852
 Schubert and Garfunkel (1984), 229, 230, 852
 Schubert and Hey (1986), 230, 852
 Schubert and Lingenfelter (1973), 640, 683, 711, 722, 852
 Schubert and Reymer (1985), 27, 630, 636, 853
 Schubert and Sandwell (1989), 43, 46, 853
 Schubert and Sandwell (1995), 649, 678, 853
 Schubert and Spohn (1981), 614, 853
 Schubert and Spohn (1990), 686, 687, 699–705, 853
 Schubert and Tackley (1995), 455, 462, 463, 853
 Schubert and Turcotte (1971), 192, 297, 299, 301, 463, 464, 853
 Schubert and Zebib (1980), 316, 318, 319, 417, 853
 Schubert and Zhang (1997), 59, 853
 Schubert et al. (1969), 307, 727, 853
 Schubert et al. (1970), 297, 300, 301, 853
 Schubert et al. (1975), 35, 181, 185, 192, 297, 302, 401, 463, 464, 470, 713, 853
 Schubert et al. (1977), 727, 853
 Schubert et al. (1979a), 586, 587, 589, 590, 594, 619, 672, 673, 698, 699, 702, 711, 727, 746, 755, 853
 Schubert et al. (1979b), 586, 587, 594, 853
 Schubert et al. (1980), 586, 587, 589–592, 594, 595, 600, 853
 Schubert et al. (1981), 738, 739, 742, 853
 Schubert et al. (1986), 634, 738, 739, 747, 751, 752, 760, 763, 765, 766, 853
 Schubert et al. (1988), 705, 750–756, 853
 Schubert et al. (1989a), 534, 853
 Schubert et al. (1989b), 596, 600, 853
 Schubert et al. (1990), 417, 657, 658, 708, 709, 711, 853
 Schubert et al. (1992), 692–697, 699, 702, 853
 Schubert et al. (1993), 427–429, 439, 660, 853
 Schubert et al. (1994), 649, 651, 853
 Schubert et al. (1995), 401, 402, 458, 461, 529, 713, 854
 Schubert et al. (1996), 761, 766, 854
 Schubert et al. (1997), 470, 658, 659, 854
 Schultz and Spudis (1983), 725, 854
 Sclater et al. (1980), 132, 150, 854
 Sclater et al. (1981), 150, 854
 Scott (1988), 165, 854
 Scott and Stevenson (1984), 161, 535, 854
 Scott and Stevenson (1986), 161, 854
 Scott and Stevenson (1989), 165, 854
 Scott et al. (1986), 534, 854
 Secor and Pollard (1975), 168, 854
 Segatz et al. (1988), 738–744, 746, 747, 854
 Segel (1965), 307, 854
 Segel and Stuart (1962), 307, 854
 Seiff (1983), 644, 854
 Senske et al. (1992), 644, 854
 Shankland and Brown (1985), 90, 94, 854
 Sharp (1973), 686, 854
 Sharp (1974), 349, 854
 Sharpe and Peltier (1978), 586, 594, 854
 Sharpe and Peltier (1979), 586, 594, 854
 Shaw (1969), 175, 854
 Shaw (1978), 587, 854
 Shaw et al. (1986), 44, 146, 854
 Shearer (1990), 79, 84, 92, 854
 Shearer (1991), 84, 92, 854
 Shearer (1996), 92, 854
 Shearer and Masters (1992), 87, 89, 855
 Shearer and Toy (1991), 99, 855
 Shearer et al. (1988), 98, 855
 Shemenda (1992), 399, 855
 Shemenda (1993), 399, 855
 Shen and Lazor (1995), 205, 473, 855
 Shen et al. (1998), 510, 517, 518, 855
 Shih et al. (1982), 699, 855
 Shoemaker et al. (1982), 761, 855
 Shore (1984), 97, 855
 Showman and Malhotra (1997), 766, 855
 Showman et al. (1997), 766, 855
 Sichoix et al. (1998), 515, 855

- Siegfried and Solomon (1974), 749, 754, 855
Sigmarsson et al. (1990), 38, 855
Silver (1996), 77, 855
Silver et al. (1988), 514, 855
Simons et al. (1994), 662, 855
Simons et al. (1997), 662, 855
Sinton (1981), 736, 855
Sinton and Detrick (1992), 153, 855
Sisson and Bronto (1998), 38, 855
Sjogren and Ritke (1982), 697, 855
Sjogren and Wimberley (1981), 697, 855
Sjogren et al. (1980), 644, 855
Sjogren et al. (1983), 644, 856
Sjogren et al. (1984), 645, 856
Sjogren et al. (1997), 644, 856
Skilbeck and Whitehead (1978), 537, 856
Sleep (1971), 147, 148, 856
Sleep (1974), 154, 856
Sleep (1979), 596, 598, 600, 856
Sleep (1987), 506, 856
Sleep (1988a), 165, 856
Sleep (1988b), 414, 523, 856
Sleep (1990), 403, 510, 511, 610, 856
Sleep (1992), 505, 856
Sleep (1994a), 143, 856
Sleep (1994b), 640, 683, 684, 856
Sleep (1996), 527, 856
Sleep (1997), 527, 856
Sleep and Phillips (1979), 688, 712, 856
Sleep and Phillips (1985), 688, 689, 712, 856
Sleep et al. (1988), 603, 856
Slichter (1941), 594, 856
Smith and Banerjee (1986), 71, 857
Smith and Sandwell (1997), 23, 502, 857
Smith and Zuber (1996), 692, 856
Smith et al. (1979a), 736, 856
Smith et al. (1979b), 736, 856
Smith et al. (1997), 640, 719, 721, 856
Smith et al. (1998), 640, 856
Smith et al. (1999a), 640, 683, 692, 856
Smith et al. (1999b), 685, 857
Smithson (1978), 44, 857
Smithson and Decker (1974), 150, 857
Smrekar and Phillips (1991), 645, 648, 649, 651, 857
Smrekar et al. (1997), 648, 857
Smythe (1968), 325, 857
Sohl and Spohn (1997), 686, 687, 713, 857
Solheim and Peltier (1990), 482, 857
Solheim and Peltier (1993), 390, 857
Solheim and Peltier (1994a), 390, 457, 463, 468, 857
Solheim and Peltier (1994b), 390, 457, 463, 468, 626,
857
Solomatov (1993), 672, 857
Solomatov (1995), 393, 489, 590, 619–623, 664, 672,
673, 857
Solomatov and Moresi (1996), 673, 675, 676, 857
Solomatov and Stevenson (1993a), 588, 857
Solomatov and Stevenson (1993b), 588, 673, 857
Solomatov and Zharkov (1990), 672, 857
Solomatov et al. (1987), 672, 857
Solomon (1976), 752, 754, 755, 857
Solomon (1977), 730, 751, 755, 857
Solomon (1978), 699, 711, 857
Solomon (1979), 691, 755, 857
Solomon (1986), 688, 857
Solomon and Chaiken (1976), 688, 691, 730, 731, 857
Solomon and Head (1982), 684, 688, 712, 857
Solomon and Head (1990), 690, 858
Solomon et al. (1992), 644, 858
Song and Helmberger (1993), 98, 858
Song and Richards (1996), 98, 858
Sotin and Parmentier (1989), 765, 858
Souriau and Romanowicz (1997), 98, 858
Souriau and Souriau (1989), 97, 858
Souriau et al. (1997), 98, 858
Spada et al. (1996), 232, 858
Spakman (1986), 107, 858
Spakman et al. (1993), 107, 108, 858
Sparks and Parmentier (1991), 165, 858
Sparks and Parmentier (1993), 498, 858
Sparks et al. (1993), 498, 858
Sparrow (1982), 333, 858
Sparrow et al. (1964), 296, 858
Spence and Sharp (1985), 166, 170, 858
Spence and Turcotte (1985), 166, 171, 858
Spence and Turcotte (1990), 168, 858
Spence et al. (1987), 168, 858
Spencer and Schneider (1996), 736, 743, 858
Spera (1984), 176, 858
Spera (1987), 166, 858
Spiegel and Veronis (1960), 268, 858
Spiegelman (1993a), 161, 858
Spiegelman (1993b), 161, 858
Spiegelman (1993c), 161, 859
Spiegelman (1994), 161, 859
Spiegelman (1996), 165, 859
Spiegelman and Kenyon (1992), 164, 859
Spiegelman and McKenzie (1987), 165, 859
Spohn (1991), 692, 698, 702, 756, 859
Spohn and Schubert (1982a), 611, 615, 859
Spohn and Schubert (1982b), 699, 859
Spohn and Schubert (1983), 699, 859
Spohn and Schubert (1991), 587, 859
Spohn et al. (1998), 713, 859
Squyres and Croft (1986), 761, 762, 859
Squyres et al. (1983), 760, 766, 859
Squyres et al. (1992), 646, 648, 859
Stacey (1977a), 190, 859
Stacey (1977b), 608, 699, 859
Stacey (1980), 595, 859
Stacey (1992), 326, 859
Stacey and Kramers (1975), 569, 859
Stacey and Loper (1983), 519, 859
Stark and Frohlich (1985), 106, 859
Staudacher and Allègre (1982), 579, 859
Staudacher et al. (1994), 575, 859

- Staudigel and King (1992), 551, 859
 Staudigel et al. (1991), 551, 859
 Stefan (1891), 123, 859
 Stein and Hofmann (1994), 62, 629, 859
 Stein and Stein (1992), 132, 134, 140, 646, 859
 Stein and Stein (1996), 132, 134, 140, 859
 Steinbach and Yuen (1992), 463, 627, 657, 860
 Steinbach and Yuen (1994a), 401, 403, 860
 Steinbach and Yuen (1994b), 663, 671, 860
 Steinbach and Yuen (1995), 401, 403, 860
 Steinbach and Yuen (1997), 401, 403, 860
 Steinbach et al. (1993), 470, 663, 860
 Steinberger and O'Connell (1997), 232, 860
 Steinberger and O'Connell (1998), 502, 860
 Stengel et al. (1982), 489, 860
 Stephen (1985), 71, 860
 Stevenson (1980), 711, 860
 Stevenson (1981), 100, 204, 587, 860
 Stevenson (1987), 587, 727, 860
 Stevenson (1989a), 165, 860
 Stevenson (1989b), 587, 860
 Stevenson (1990), 587, 860
 Stevenson (1998), 610, 860
 Stevenson and Scott (1991), 166, 860
 Stevenson and Turner (1977), 34, 860
 Stevenson and Turner (1979), 586, 594, 860
 Stevenson et al. (1983), 587, 602–604, 607, 610, 672,
 673, 678–680, 699, 703, 750, 752, 860
 Stewart and Turcotte (1989), 337, 860
 Stixrude et al. (1992), 91, 860
 Stoddard and Abbott (1996), 53, 860
 Stofan et al. (1991), 646, 648, 860
 Stofan et al. (1992), 646, 648, 860
 Stofan et al. (1995), 648, 860
 Stofan et al. (1997), 646, 648, 860
 Stolper (1980), 153, 861
 Stolper et al. (1981), 154, 861
 Strom (1979), 755, 861
 Strom et al. (1975), 755, 861
 Strom et al. (1979), 736, 861
 Strom et al. (1992), 697, 861
 Strom et al. (1994), 637, 646, 861
 Su and Buck (1993), 165, 861
 Su and Dziewonski (1991), 103, 472, 861
 Su and Dziewonski (1995), 98, 861
 Su and Dziewonski (1997), 113, 861
 Su et al. (1992), 462, 463, 861
 Su et al. (1994), 79, 95, 103, 104, 115, 116, 143, 462,
 463, 861
 Su et al. (1996), 98, 861
 Sun (1980), 565, 861
 Sun and Hanson (1975), 550, 861
 Sun and McDonough (1989), 653, 654, 861
 Sung and Burns (1976), 185, 861
 Surkov et al. (1984), 654, 861
 Surkov et al. (1987), 653, 654, 861
 Sykes (1966), 32, 861
 Sylvester et al. (1997), 629, 861
 Tackley (1993), 393, 394, 471, 664, 671, 861
 Tackley (1995), 467, 468, 861
 Tackley (1996a), 455, 472, 473, 861
 Tackley (1996b), 455, 486, 664, 861
 Tackley (1997), 391, 392, 455, 862
 Tackley (1998a), 390, 491–496, 664, 862
 Tackley (1998b), 414, 473, 862
 Tackley et al. (1993), 390, 391, 403, 455, 456, 458–460,
 463, 626, 658, 862
 Tackley et al. (1994), 403, 455, 462–468, 661, 862
 Tajima and Grand (1998), 468, 862
 Takahashi and Kusiro (1983), 152, 862
 Takeuchi et al. (1962), 739, 862
 Tanaka (1986), 638, 697, 862
 Tanaka and Golombeck (1989), 686, 862
 Tanaka and Hamaguchi (1997), 99, 862
 Tanaka et al. (1988), 690, 862
 Tanaka et al. (1992), 638, 682, 697, 862
 Tanimoto (1990), 103, 116, 862
 Tanimoto and Anderson (1985), 106, 862
 Tarbuck and Lutgens (1988), 37, 862
 Tatsumi and Eggins (1995), 36, 862
 Tatsumi and Isoyama (1988), 38, 862
 Tatsumoto et al. (1973), 566, 862
 Tatsumoto et al. (1987), 580, 581, 862
 Taylor (1910), 5, 862
 Taylor (1967), 47, 862
 Taylor (1977), 47, 862
 Taylor (1986), 690, 699, 863
 Taylor and McLennan (1981), 556, 863
 Taylor and McLennan (1985), 44, 48, 72, 146, 575,
 578, 692, 863
 Taylor and McLennan (1995), 626, 628–632, 636, 863
 Taylor and White (1965), 47, 863
 Taylor et al. (1983), 725, 862
 Ten et al. (1998), 347, 863
 Tera et al. (1986), 38, 863
 Thomas et al. (1998), 740, 741, 746, 863
 Thompson (1882), 3, 863
 Thompson and Stevenson (1983), 727, 863
 Thoraval and Richards (1997), 233, 863
 Thurber and Toksöz (1978), 689, 863
 Thurber et al. (1980), 765, 863
 Toksöz and Hsui (1978a), 39, 863
 Toksöz and Hsui (1978b), 691, 863
 Toksöz et al. (1971), 37, 863
 Toksöz et al. (1978), 727, 754, 863
 Tonks and Melosh (1990), 588, 863
 Toth and Gurnis (1998), 59, 396, 863
 Tovich and Schubert (1978), 36, 863
 Tovich et al. (1978), 34, 863
 Tozer (1965a), 16, 594, 863
 Tozer (1965b), 587, 863
 Tozer (1967), 590, 863
 Travis and Olson (1994), 384–386, 660, 863
 Travis et al. (1990a), 417, 428, 430–434, 440, 441, 864
 Travis et al. (1990b), 417, 440, 442, 449, 452, 864
 Treiman et al. (1986), 690, 691, 864

- Treiman et al. (1987), 699, 702, 705, 706, 864
Trompert and Hansen (1998), 495, 497, 498, 864
Trubitsyn and Rykov (1997), 411, 864
Tsenn and Carter (1987), 246, 864
Tullis (1979), 742, 864
Turcotte (1974), 29, 864
Turcotte (1979), 33, 864
Turcotte (1980a), 147, 864
Turcotte (1980b), 586, 594, 595, 864
Turcotte (1982), 152, 864
Turcotte (1983), 46, 864
Turcotte (1987), 644, 864
Turcotte (1989a), 45, 864
Turcotte (1989b), 45, 864
Turcotte (1990), 166, 864
Turcotte (1993), 648, 650, 661, 675, 677, 864
Turcotte (1995), 647, 864
Turcotte (1996), 656, 864
Turcotte and Ahern (1978), 154, 864
Turcotte and Burke (1978), 27, 61, 864
Turcotte and Emerman (1983), 57, 864
Turcotte and Kellogg (1986a), 551, 864
Turcotte and Kellogg (1986b), 731, 864
Turcotte and McAdoo (1979), 147, 864
Turcotte and Oxburgh (1967), 16, 353, 864
Turcotte and Oxburgh (1968), 36, 177, 865
Turcotte and Oxburgh (1970), 727, 865
Turcotte and Oxburgh (1972a), 146, 865
Turcotte and Oxburgh (1972b), 594, 865
Turcotte and Phipps Morgan (1992), 166, 865
Turcotte and Schubert (1971), 35, 184, 192, 196, 865
Turcotte and Schubert (1972), 194, 865
Turcotte and Schubert (1973), 37, 865
Turcotte and Schubert (1982), 45, 175, 236, 274, 588,
 600, 649, 653, 654, 691, 695, 737, 865
Turcotte and Schubert (1988), 573, 865
Turcotte et al. (1974), 408, 485, 865
Turcotte et al. (1977), 59, 865
Turcotte et al. (1979), 586, 594, 595, 672, 865
Turcotte et al. (1984), 45, 865
Turcotte et al. (1987), 166, 865
Turekian (1959), 573, 865
Tushingham and Peltier (1992), 238, 865
Tveitereid (1978), 439, 865
Tveitereid and Palm (1976), 439, 865
Twiss and Moores (1992), 241–245, 865

Unrug (1992), 59, 865
Urakawa et al. (1987), 203, 865
Urey (1951), 749, 865
Urey (1952), 749, 865
Usselman (1975), 202, 203, 740, 865
Uttsu (1971), 31, 865
Uyeda and Kanamori (1979), 39, 865

van Bemmelen and Berlage (1934), 866
van den Berg and Yuen (1997), 408, 866
van der Hilst (1995), 107–109, 468, 866
van der Hilst and Kárasoñ (1999), 468, 585, 866
van der Hilst et al. (1991), 102, 107, 460, 468, 866
van der Hilst et al. (1997), 102, 107, 113, 468, 866
van der Hilst et al. (1998), 468, 866
van der Lee and Nolet (1997), 516, 866
van Keeken (1997), 525, 526, 528, 866
van Keeken and Ballantine (1998), 584, 866
van Keeken and Yuen (1995), 473, 866
van Keeken et al. (1992), 404, 866
van Keeken et al. (1994), 473, 866
Vasco and Johnson (1998), 102, 117, 866
Vassiliou and Hager (1988), 33, 866
Veeder et al. (1994), 737, 866
Veevers (1989), 59, 60, 636, 866
Veizer and Jansen (1979), 556, 629, 866
Vening Meinesz (1937), 15, 866
Vening Meinesz (1948), 15, 866
Verhoogen (1951), 190, 866
Verhoogen (1954), 190, 866
Verhoogen (1961), 100, 604, 866
Verhoogen (1965), 16, 192, 866
Verhoogen (1973), 97, 204, 866
Verhoogen (1980), 100, 202, 203, 866
Vermeersen and Vlaar (1993), 232, 867
Vermeersen et al. (1994), 232, 867
Vermeersen et al. (1997), 231, 232, 867
Vidale and Benz (1992), 89, 867
Vidale and Hedlin (1998), 95, 206, 867
Vilas (1988), 750, 867
Vincent and Yuen (1988), 454, 867
Vincent and Yuen (1989), 366, 867
Vine (1966), 13, 867
Vine and Matthews (1963), 13, 15, 867
Vine and Wilson (1965), 13, 867
Vinogradov (1962), 44, 867
Visser et al. (1995), 490, 867
Vogt (1974), 689, 867
Vogt (1979), 504, 536, 867
Vogt (1981), 499, 867
Vollmer (1977), 571, 867
Von Herzen et al. (1982), 507, 867
Von Herzen et al. (1989), 132, 507, 867
von Huene and Scholl (1991), 31, 867

Wada (1994), 176, 867
Wadati (1928), 31, 867
Wadati (1934/35), 31, 867
Wahr and de Vries (1989), 117, 867
Walcott (1972a), 224, 225, 867
Walcott (1972b), 224, 867
Walcott (1973), 216, 224, 867
Walker (1977), 600, 867
Walker et al. (1978), 154, 867
Walzer and Hendel (1997), 413, 868
Wang and Reeber (1995), 209, 868
Wänke and Dreibus (1986), 587, 868
Warren (1985), 718, 868
Wasserburg and DePaolo (1979), 550, 868

- Wasson and Warren (1980), 640, 722, 868
 Watson and McKenzie (1991), 508, 868
 Watson and Spiegelman (1994), 161, 868
 Watts (1976), 504, 868
 Weaver and Tarney (1984), 44, 146, 868
 Webb and Stevenson (1987), 743, 868
 Weber (1993), 96, 868
 Wedepohl (1994), 146, 868
 Weertman (1970), 245, 613, 868
 Weertman (1971), 168, 868
 Weertman and Weertman (1975), 249, 590, 868
 Wegener (1915), 5, 868
 Wegener (1924), 5, 868
 Wegener (1929), 8, 868
 Weidenschilling (1976), 587, 868
 Weidner (1985), 85, 868
 Weidner (1986), 189, 868
 Weidner and Wang (1988), 470, 868
 Weijermars (1988a), 393, 868
 Weijermars (1988b), 393, 868
 Weinberg (1997), 525, 868
 Weinstein (1992), 392, 868
 Weinstein (1993), 390, 457, 468, 626, 868
 Weinstein (1995), 713, 868
 Weinstein (1998), 57, 869
 Weinstein and Christensen (1991), 393, 666, 869
 Weinstein and Olson (1990), 446, 447, 454, 869
 Weinstein and Olson (1992), 389, 404, 489, 669, 869
 Wessel et al. (1996), 143, 869
 Wetherill (1976), 587, 869
 Wetherill (1985), 587, 869
 Wetherill (1986), 587, 727, 869
 Wetherill (1988), 752, 754, 869
 Wetherill (1990), 672, 869
 White (1985), 350, 570, 571, 580, 581, 869
 White (1988), 393, 428, 869
 White (1993), 508, 869
 White and McKenzie (1989), 71, 508, 509, 525, 869
 White and McKenzie (1995), 508, 869
 Whitehead (1982), 525, 536, 869
 Whitehead (1987), 534, 869
 Whitehead (1988), 534, 869
 Whitehead and Helfrich (1988), 534, 869
 Whitehead and Helfrich (1990), 534, 536, 869
 Whitehead and Luther (1975), 521, 525, 869
 Whitehead and Parsons (1978), 440, 869
 Wicks and Richards (1993), 89, 869
 Widjiantoro and van der Hilst (1996), 108, 110, 869
 Wienbruch and Spohn (1995), 747, 869
 Wilhelms and Squyres (1984), 640, 683, 869
 Willemann and Turcotte (1982), 684, 688, 689, 869
 Williams and Garnero (1996), 95, 206, 414, 869
 Williams et al. (1987), 202, 869
 Williams et al. (1998), 509, 514, 870
 Williamson and Adams (1923), 64, 870
 Wilshire and Kirby (1989), 176, 870
 Wilson (1963a), 16, 870
 Wilson (1963b), 16, 870
 Wilson (1963c), 499, 870
 Wilson (1965a), 16, 870
 Wilson (1965b), 16, 870
 Wilson (1966), 57, 870
 Wilson (1973), 499, 870
 Wilson and Burke (1972), 39, 870
 Wilson and Head (1981), 172, 870
 Windley (1977), 630, 870
 Windley (1995), 72, 870
 Wise (1974), 600, 630, 636, 870
 Wise and Yates (1970), 720, 870
 Wise et al. (1979a), 640, 683, 711, 870
 Wise et al. (1979b), 688, 870
 Wolfe et al. (1997), 42, 43, 500, 516, 517, 870
 Wood (1986), 727, 870
 Wood et al. (1970), 718, 870
 Woodhouse and Dziewonski (1984), 103, 870
 Woodhouse and Dziewonski (1989), 103, 870
 Woods and Okal (1996), 541, 870
 Worsley et al. (1984), 59, 870
 Wright et al. (1968), 651, 870
 Wright et al. (1980), 146, 870
 Wu (1995), 249, 870
 Wu and Peltier (1983), 217, 870
 Wyllie (1971), 152, 870
 Wysession et al. (1998), 95, 871
 Yale and Carpenter (1998), 62, 871
 Yamaoka and Fukao (1987), 36, 871
 Yamaoka et al. (1986), 36, 871
 Yeats (1981), 45, 871
 Yoder (1979), 738, 871
 Yoder (1981), 726, 871
 Yoder and Peale (1981), 738, 746, 871
 Yoder et al. (1983), 231, 871
 Yokokura (1981), 34, 871
 Yoshida et al. (1996), 98, 871
 Yoshioka and Wortel (1995), 461, 871
 Young (1974), 418, 871
 Young and Lay (1987), 95, 96, 871
 Young and Lay (1990), 96, 871
 Young and Schubert (1974), 706, 871
 Yuen and Fleitout (1984), 143, 871
 Yuen and Peltier (1980), 606, 871
 Yuen and Sabadini (1984), 231, 871
 Yuen and Sabadini (1985), 471, 871
 Yuen and Schubert (1976), 529, 871
 Yuen et al. (1978), 36, 180, 490, 871
 Yuen et al. (1981), 143, 308, 871
 Yuen et al. (1982), 231, 871
 Yuen et al. (1993), 382, 384, 387, 627, 871
 Yuen et al. (1994), 455, 469, 470, 473, 671, 871
 Yuen et al. (1995), 470, 871
 Zahnle et al. (1988), 672, 872
 Zahnle et al. (1998), 760, 761, 872
 Zartman and Doe (1981), 569, 872
 Zebib et al. (1980), 320, 322, 324, 418, 872

- Zebib et al. (1983), 314, 315, 318, 320–323, 711, 872
Zebib et al. (1985), 381, 872
Zerr and Boehler (1993), 205, 473, 872
Zerr and Boehler (1994), 205, 473, 872
Zerr et al. (1997), 473, 872
Zerr et al. (1998), 205, 473, 872
Zhang and Tanimoto (1989), 515, 872
Zhang and Tanimoto (1992), 515, 872
Zhang and Tanimoto (1993), 515, 872
Zhang and Yuen (1995), 471, 477, 872
Zhang and Yuen (1996a), 482, 483, 485–489, 872
Zhang and Yuen (1996b), 487, 488, 490, 872
Zhang and Zindler (1989), 573, 872
Zhang et al. (1985), 33, 872
Zhao et al. (1992), 390, 391, 463, 627, 872
Zharkov (1996), 687, 872
Zharkov and Solomatov (1992), 672, 872
Zharkov et al. (1985), 201, 872
Zhong and Gurnis (1993), 409, 411, 872
Zhong and Gurnis (1994a), 33, 872
Zhong and Gurnis (1994b), 470, 471, 670, 671, 872
Zhong and Gurnis (1995a), 389, 872
Zhong and Gurnis (1995b), 489, 872
Zhong and Gurnis (1996), 489, 872
Zhong et al. (1998), 396, 873
Zhou and Anderson (1989), 107, 873
Zindler and Hart (1986), 71, 580, 583, 873
Zindler et al. (1982), 550, 580, 581, 873
Zindler et al. (1983), 349, 873
Zindler et al. (1984), 550, 873
Zschau (1978), 753, 873
Zuber and Smith (1997), 686, 873
Zuber et al. (1994), 640, 719–722, 873

Subject Index

The abbreviation “f” is used to denote reference to a figure, “t” to denote reference to a table.

- abyssal peridotites, 153
- acceleration of fluid particle, 254
- acceleration of gravity, 65, 66, 155, 222, 230, 254, 265, 269, 274, 275, 279–281, 290, 316, 320, 427, 464, 477, 478, 484, 519, 589, 605, 700, 700t
- accretion, 25f, 26, 74, 559, 559f, 573, 579, 587, 588, 610, 625, 629, 630, 636, 647, 672, 691, 711, 727, 750–752, 766, 770, 779, 792
- Earth, 573, 587, 588, 610, 625, 770
- Ganymede, 766
- Mars, 691
- Moon, 727
- planetary, 647, 792
- Venus, 672
- accretionary heating, 591
 - Callisto, 763
 - Ganymede, 763
 - Mars, 691, 715
 - Mercury, 751, 751f
 - Venus, 672
- accretionary plate boundaries, 25f, 27–29, 36, 38, 52, 57, 58f, 59, 132, 657, 767, 768, 778, 782, 787
 - formation of, 57
 - Venus, 794
- accretionary ridge segments, 59
- accretionary prisms, 31, 31f, 46, 47, 72
- acid rain, 545
- activation energy, 240, 246, 246t, 393, 590, 596, 624, 763
- activation enthalpy, 404, 405f, 789
- activation temperature, 590, 596, 600, 754
- activation volume, 240, 246, 246t, 406
- Adams–Williamson equation, 65, 90, 276, 482, 483, 485
- Aden, Gulf of, 57
- adiabat, 28, 91, 91f, 153, 191, 191t, 192, 196, 200, 201, 203, 204, 206, 211, 270, 271, 403, 458, 458f, 480, 482, 508, 605, 608, 609, 609f, 610, 660, 660f, 669, 679, 679f, 680, 680f, 699, 700, 700t, 702, 703, 703f, 705, 752, 753, 790
- adiabatic bulk modulus, 65, 66, 68f, 262, 277
- adiabatic compressibility, 65, 261, 262, 276
- adiabatic compression, 188, 193, 194, 264, 455, 580
- adiabatic cooling, 264, 441, 478, 483, 484, 486, 487
- adiabatic expansion, 264
- adiabatic heating, 185, 264, 441, 477, 478, 484–487, 489f
- adiabatic hydrostatic polytropic reference state, 277
- adiabatic lower mantle, 66
- adiabatic process, 260
- adiabatic regions of the mantle, 127
- adiabatic temperature gradient, 8, 93, 131, 153, 190, 264, 265, 270, 271, 277, 300, 482, 485, 790
- adiabatic temperature increase across the mantle, 153, 188, 190, 267, 603
- adiabatic temperature scale height, 188, 190, 203, 209, 540
- advective heat transport, 127, 188, 290, 423, 438, 610, 613
- age distribution of crust, 19f
- age of a rock, 552, 792
- age of crustal separation from mantle, 554, 570
- age of Earth, 13, 344, 554, 567, 577, 579, 594
- age progression
 - of continents, 637
 - of Hawaiian islands, 16
 - of Hawaiian–Emperor island-seamount chain, 41
 - of hot spots, 501, 504f, 510
 - of oceans, 637
- ages of lunar rocks, 638
- Alps, 45, 59, 644
- Altiplano, 45
- aluminum
 - extinct ^{26}Al , 587
- Anderson–Grüneisen parameter, 207
- Andes, 45, 47, 59, 74, 656
- anelastic approximation, 268–271, 455, 483
 - liquid, 268
- anelastic conservation of mass equation, 267, 268, 477
- anelastic energy equation, 270, 271

- anelasticity, 68
 angular momentum, 215
 Earth, 215, 232
 of Earth–Moon system, 727
 angular velocity, 48f, 49, 51, 215, 255, 738
 Earth, 215
 of an infinitesimal fluid parcel, 255
 of plate rotation, 48, 48f
 Arabian–Nubian Shield, 630
 Archean processes, 47, 564, 626, 630, 631, 631f, 632, 771, 792
 argon, 548, 573, 577–579, 584
 ^{36}Ar , 573
 ^{40}Ar , 573, 574, 577, 578, 578f, 579
 $^{40}\text{Ar}/^{36}\text{Ar}$ ratio, 577–579
 in Earth’s atmosphere, 577–579
 outgassing from mantle, 578, 578f
 solubility in melts, 579
 Arrhenius law, 240, 413, 618, 624, 664, 666, 706
 for viscosity dependence on temperature, 413, 664, 666, 706
 ascent time from D'' to base of lithosphere, 527
 aseismic extension of slabs, 107
 aspect ratio of convection cell, 295
 associated Legendre functions, 323, 324, 325t, 327, 328
 asthenosphere, 25, 25f, 27f, 46, 46f, 76, 83, 142, 161, 165, 308, 507, 537–539, 649, 652f, 652f, 739, 740, 742, 742f, 743, 743f, 744, 745, 747, 768, 769, 771, 783, 784, 795
 Io, 739, 740, 742–745
 melt migration, 161, 165
 rebound model, 227
 viscosity, 143, 216, 227–230, 240, 250, 308, 507, 540, 652f, 740, 742, 743, 743f, 744, 768, 783, 784
 atmosphere, 257, 547, 548, 572–574, 576, 576f, 577–579, 586, 596, 599, 625, 630, 699
 Earth, 577–579
 Mars, 633, 715
 Venus, 644, 646, 680
 aulacogens, 57
 avalanches, 390–392, 454, 456–458, 461–464, 466–469, 469f, 473, 626, 627, 629, 630, 658, 670, 672, 770, 786, 788, 792
 axial magma chamber, 27f, 153
 axial moment of inertia
 Io, 741
 axisymmetric flow, 253, 530

 back-arc basins, 38, 767, 777
 back-arc seafloor spreading, 31, 31f, 38, 646, 651
 basal heating, 139, 142, 143, 147, 151, 382, 383f, 385f, 462, 482, 529, 649, 651, 670, 774
 basal tractions, 52–55
 basalt geochemistry, 579
 basaltic crust production rate, 513
 basaltic dike, 171, 175
 basaltic dike complex, 70
 basaltic magma, 13, 47, 70, 82, 173, 175, 176, 574
 bathymetry, 75, 75f, 138–141, 153, 377, 505, 506f, 782
 Baysian inference, 239
 Bénard, Henri, 4f
 Bénard cells, 3
 Bénard’s experiment, 3
 bifurcation diagram, 335, 335f, 341f
 biharmonic equation, 218, 219, 356, 468
 Biot number, 412
 body force, 15, 27, 34, 52, 53, 102, 177, 181–183, 185, 254, 256, 264, 280, 357, 401, 713
 body wave, 64, 66, 79, 95, 102
 Bonneville, Lake, 228
 boundary layer, 26, 113, 122, 123f, 127, 131, 163, 164f, 206, 307, 353, 376, 395, 398, 414, 421, 423, 444, 479, 480, 482, 580, 603, 606, 613, 648, 649, 660f, 664, 670, 753
 chemical, 412, 416, 769
 cold thermal, 16, 97, 143, 351, 354, 355, 379, 393, 404, 445, 446, 449, 603, 621, 622, 674f, 772, 774
 compositional, 414, 415
 instability, 143, 307, 308, 342, 382, 384, 388, 406, 413, 519, 520, 521f, 649, 778, 780, 781
 internal, 204, 616
 model of thermal convection, 16
 Rayleigh number, 380f, 423, 424, 519, 606
 theory of convection, 359, 379, 589
 thermal, 26, 42, 76, 77, 94, 95, 121, 122, 127, 131, 132, 143, 176, 190, 204, 211, 307, 308, 335, 336, 350, 351, 380f, 414f, 527, 533, 534f, 580, 581, 584, 612f, 615f, 635, 680f, 754, 768, 769, 773, 774, 781, 788, 791
 and plume formation, 500, 518, 519
 D'' layer, 190, 201, 204, 211, 413, 414, 416
 evolution of sedimentary basins, 147
 in Earth thermal history models, 590, 603, 606, 612, 626
 in three-dimensional convection, 418, 419, 423, 427, 432, 438, 440, 444, 446
 in two-dimensional convection, 379, 381, 382, 393, 395, 401, 402, 405, 411, 412
 stability, 350–352
 transition zone, 127, 190, 204
 Venus, 651, 660
 Boussinesq approximation, 162, 268–271, 274, 275, 288, 308, 331, 350, 367, 377, 666
 box model of chemical geodynamics, 547
 buckling of slabs, 399, 468
 bulk modulus, 65–67, 207, 450f, 477
 bulk silicate Earth (BSE), 551, 553t, 554, 555, 562, 566, 570, 571, 572f, 575, 580, 583, 584, 653, 654t
 bulk viscosity, 158t, 162, 256, 262, 263
 Bullen Earth models, 66, 68, 84, 95, 108f
 buoyancy number, 415
 buoyancy support, 543
 Burgers vector, 242, 242f, 243, 244f, 245
 butterfly effect, 377

- Callisto, 633, 634t, 756, 757, 759f, 760–766, 771, 795
 subsolidus convection, 763
 topography, 762
catastrophic subduction event, 793
centrifugal force, 6, 254
Chandler wobble, 98
channel flow equation, 539
channelized flow, 165
chaos, 758
chaotic mantle convection, 330, 337, 377, 626, 627, 769, 770
chaotic mantle mixing, 347
chaotic thermal convection, 251, 334, 336, 337, 342, 342f, 366, 384, 454
characteristic equation, 333
chemical buoyancy, 412, 413, 507, 547, 703
 geodynamo, 604
 stabilizing effect, 92
chemical compositional change with depth in mantle, 72, 89
chemical diffusion in mantle, 346, 349
chemical geodynamics, 547, 548
chemical heterogeneity in the D'' layer, 523
chondrites, 81t, 574, 653, 654t
 CI, 80, 81t, 691
chondritic meteorites, 71, 131, 131t, 556, 653
chondritic uniform reservoir (CHUR), 556
chromatographic column, 164
Clapeyron curve, 181, 182f, 184, 193–195, 297–299
 endothermic phase change, 181
 exothermic phase change, 181
Clapeyron slope, 85, 88, 180, 181f, 182, 182f, 195, 197, 199t, 298, 302, 398, 401, 402, 402f, 455, 457, 463, 464, 469, 470, 658, 669
of 660 km phase change and mantle convection, 182, 390
clastic sediments, 44, 44t
clinopyroxene, 81, 81t, 246, 723
Coble creep, 240
coefficient of thermal expansion, 135, 165, 207, 210, 259, 279, 298, 406, 408f, 688
Colorado Plateau, 45
compaction layer, 163, 164, 164f
compaction length, 163, 164
comparative planetology, 639, 792, 793
complementary error function, 120, 121, 121t, 122f
complementary nature of continental crust and MORB source reservoir, 549
composition of crust, 548, 656, 792
composition ratio, 551, 552, 553t, 554, 555, 565, 566, 569, 571f, 574, 735f
composition variable, 378
compositional buoyancy, 100, 107, 204, 507, 513, 703
compositional convection, 680, 702, 768
compositional density jump at 660 km phase change, 611
compositional gradient, 77, 392, 393, 769
compositional heterogeneity in D'', 204
compositional layering, 92, 93, 414, 415, 780
compositional stratification, 523
compressibility, 64, 209, 210, 224, 259, 267, 269, 377, 408, 477, 480, 482, 770, 790, 791
 mantle, 265
compressional wave velocity, 63–65, 82, 83f, 110f
concentration of light alloying element into outer core as inner core freezes, 603, 605
conductive heat flow along core adiabat, 608, 609, 609f, 610
conduits
 shearing of, 536
 tilt-induced instability, 537, 537f
conformable lead deposits, 568, 568f
conservation equations
 approximate, 265
conservation of energy, 251, 259, 262, 265, 272, 273, 286, 366
conservation of mass, 251–253, 267, 268, 272, 273
 Lagrangian form, 252
conservation of momentum, 251, 254, 264, 265, 272, 273
conservation of phase or composition, 377
constancy of freeboard, 584, 597, 600, 628f, 630
constitutive law, 248, 256
continental aggregation, 59
continental collisions, 52, 58f, 59–62
continental crust, 2, 8, 10, 13, 15, 25, 36, 43, 44, 44t, 45, 46, 46f, 47, 48, 53, 59, 60, 64f, 69, 69t, 71, 72f, 73, 74f, 79, 123, 126, 127, 131t, 146, 148, 149, 149f, 150, 151, 632
as a geochemical reservoir, 547–550, 556, 559f, 560, 560f, 561, 562, 564, 564f, 565, 570–573, 575, 578, 580, 582–585
formation, 559f
crustal growth and Earth thermal history, 600, 627, 630
density, 73
formation, 47, 130, 548, 553, 555, 563, 627, 628, 630
heat production, 129, 130
mass, 557
structure, 71–74
temperatures, 144, 146, 147
continental dispersal, 59, 60f
continental drift, 4–13, 15, 408, 409
 arguments in favor of, 6f, 42
cause, 9f
convection currents, 295
cyclic, 57
Jeffreys, 7f
plate tectonics, 16
relationship to mantle convection, 16
supercontinent formation, 409
Wegener, 7f
continental flood basalts, 61, 525, 527, 536, 545, 546
continental freeboard, 597, 630
continental geoid height, 149, 150f

- continental geotherms, 144, 150f
 continental growth, 74, 558, 559t, 561, 565, 626, 629, 630
 continental lithosphere, 25, 26, 37f, 43, 45–47, 53, 57, 58, 71, 76, 79, 104, 127, 131, 143, 144, 146–149, 149f, 150, 150f, 151, 248
 thickness, 143, 146–149, 149f, 150, 150f, 151
 continental margins, 43, 57–59, 61, 72, 128, 228, 229, 229f, 237t
 continental Moho, 73
 continental rafts, 377
 continental roots, 79, 80, 103
 continental shields, 73, 78, 82, 103, 104, 143
 continents, 1, 9, 10, 12, 13, 15, 43, 44, 47, 52, 53, 55, 60f, 61, 66, 69, 72, 77, 79, 101, 149, 150f, 297, 408–413, 471, 505, 545, 597, 636, 637, 639, 640, 653, 657, 767–769, 771, 774, 778, 782, 788, 791–793
 age of, 559, 563, 583
 area, 128
 composition, 42, 43
 continental drift, 5, 6
 crustal growth, 628–630
 Earth, 656, 657
 formation, 46–48, 558, 565
 geochemical reservoirs, 547, 558, 559, 561–563, 574, 583, 584
 geoid anomalies, 149
 heat flow, 128, 296
 lithospheric thickness, 147
 mean surface heat flow, 147
 thermal regime, 127, 129
 Venus, 656, 657
 Wilson cycle, 57, 59
 continents and convection, 408
 continuum theory, 251
 convection, 3, 8, 10, 39f, 63, 65, 68, 82, 95, 127, 129, 143, 200, 206, 206f, 277, 279, 280, 330, 342, 352, 368, 369, 373, 422, 457
 approximate equations, 265, 267, 269
 boundary layer theory, 355, 358
 cell, 39, 330, 335, 350, 354f, 357f, 359f, 360, 372, 413
 chaotic mixing, 346, 349
 compositional, 100, 609, 703, 705
 compressible, 209, 269, 408, 443f, 477, 478, 482, 483, 483f, 486f, 487, 487f, 488, 490f, 790, 791
 core, 99
 effect of depth-dependent thermodynamic and transport properties, 405, 407, 408f
 in D'' layer, 413, 414
 internal heat sources and time dependence, 382, 384
 layered mantle, 306, 344, 345, 345f, 359, 360, 366, 378, 556, 575, 576f, 578, 578f, 584, 611, 616, 626, 770, 774, 785, 794
 linear stability, 288–290, 294, 295, 295f, 296t, 300–302, 307, 308, 312, 314, 315, 315f, 316, 318, 318t, 319, 319t, 320f, 321, 321t, 322, 322f, 324f
 Lorenz equations, 333, 334, 336
 lower mantle, 113
 mantle, 1, 2, 7–11, 13, 102, 330, 336, 337, 344, 347, 350, 354, 355, 537
 basic equations, 251, 265–269, 274, 276, 279
 calculation of geoid in model, 279
 chemical geodynamics, 547, 549, 550, 580, 584
 Earth thermal history, 586, 588, 590, 594, 597, 601, 608, 611, 612f, 615, 625–629
 Galilean satellites, 756, 765
 Io, 739
 linear stability, 288, 295–297, 303, 306, 315, 323
 Mars, 683, 692, 700, 701, 709f, 713, 714, 714f, 715, 716
 melt under ridges, 165
 Mercury, 755
 models of, 87
 Moon, 722, 727, 729, 731, 735, 736
 nature of, 199, 200, 767–774, 775f, 777–779, 783–795
 planets and moons, 634, 635, 640, 641
 plate tectonics, 16, 26, 35, 36, 39f, 42, 55, 56, 62
 structure and composition, 63, 68, 69, 71, 73, 83, 95, 97, 100, 102, 104, 106, 113, 116
 structure of, 92
 subsolidus, 8, 9f
 temperatures, 127–129, 143, 147, 153, 165, 176, 191, 201, 204
 thermodynamic properties, 209, 210
 three-dimensional, 417, 438, 454–457, 460, 463, 464, 465f, 466–468, 470–474, 477, 480, 482, 488, 489, 498
 two-dimensional, 376, 377, 379, 381, 382, 384, 385, 386f, 388–390, 392, 394, 396, 403, 405, 407–409, 411–413
 Venus, 645, 647, 651, 652, 657, 659f, 661, 667, 671–673
 viscosity, 213, 215, 232, 235, 240, 245–247, 247f, 248, 249, 250f
 mean field approximation, 361, 362, 364
 nonlinear theory, 366, 367, 370, 371
 partially layered, 206f
 phase transformations, 35, 191, 192, 200
 plane layer heated from within, 303
 plate tectonics, 16, 42
 Rayleigh–Bénard, 346, 386
 secondary, 139, 142, 143, 151
 small viscosity contrast regime, 590, 619, 620, 621f, 625
 stagnant lid, 308
 strongly temperature-dependent viscosity, 425, 425f, 427f, 438, 487
 style, 68
 subcrustal, 3
 surface plates, 55, 377, 385
 thermal, 3, 8, 9, 16, 55, 100, 767, 769, 772, 774, 791, 793

- convection (*cont.*)
 thermal (*cont.*)
 approximate solutions, 330, 336, 343, 347, 350, 353, 358, 360–362, 367
 basic equations, 265, 266, 269
 Earth thermal history, 608, 609, 609f, 610, 617, 620, 626, 627
 linear stability, 288, 290, 291f, 294f, 297, 303, 307, 308, 313, 314t, 316, 317t, 318, 320
 mantle temperatures, 207
 Mars, 702, 705, 705f, 706
 melting temperatures, 177, 188
 Mercury, 756
 planets and moons, 635
 strongly temperature-dependent viscosity, 621f
 three-dimensional, 417, 418, 441, 448f, 450f, 452f, 454, 489
 two-dimensional, 376, 379, 381, 385, 385f, 389, 390, 392, 393, 404, 406, 407f, 408, 408–411f, 412
 Venus, 651, 663, 679
 thermal and compositional in core and geodynamo, 609
 thermal compositional, 705
 thermochemical, 100
 three-dimensional, 408
 two-dimensional, 376–379, 380f, 381, 382, 383f, 384, 384f, 385, 386f, 387, 387f, 388, 388f, 389, 389f, 390, 391, 391f, 393, 394, 394f, 395, 395f, 397f, 398, 403–405, 405f, 406, 408, 408f, 409, 411–415, 415f, 416
 two-layer mantle, 575, 613, 627
 upper mantle, 297, 306
 viscosity increase with depth, 472, 482
 whole mantle, 113, 204, 206, 206f, 295, 306, 345, 350, 360, 556, 575, 576f, 577, 578, 578f, 579, 584, 773, 774, 776f, 787, 794
 chaotic mixing, 344, 345
 D'' layer, 204
 Earth thermal history, 611, 613, 614, 616, 627
 three-dimensional, 474
 two-dimensional, 345f, 378
 Venus, 663, 670–672
 convective mixing, 345, 346, 349
 convergent plate boundaries, 10, 22
 coral reefs and island subsidence, 41, 42f
 core, 1, 2, 35, 61–63, 64f, 80t, 93, 94, 97, 98, 101f, 127, 128, 176, 191t, 200, 202, 204, 206, 211, 267, 306, 403, 414, 415, 436, 679f, 703–705f, 712f, 754f, 768, 770–772, 780, 793, 795
 blanketing by mantle downflows, 456, 456f, 457, 466
 complete solidification in terrestrial planets, 678
 composition, 66, 80, 98–100, 127, 206, 608
 convection, 100
 cooling, 702, 716
 density, 66, 99, 679, 740, 741, 753, 756
 dynamo, 100
 Earth, 679, 703, 705
 Earth thermal history, 587, 588, 602, 603, 605–609, 609f, 610, 612, 613, 614t, 616, 626
 energetics, 100
 formation, 99, 587, 591, 610, 672, 683, 691, 699, 705, 711, 715, 736, 745, 750
 Galilean satellites, 756, 757, 760–762
 geochemical reservoir, 547, 549, 550, 571, 573
 gravitational energy release upon exclusion of light element from solidifying core, 587, 603, 610, 702, 753
 growth of solid inner core, 603, 605
 heat flow, 201, 382, 403, 610
 heat flow vs. time in Earth thermal history model, 608
 inner, 63, 64f, 66, 69t, 97–100, 101f, 103, 549, 603, 605, 607, 609, 678, 679, 702, 703, 704f, 705, 716, 740, 750, 753, 754, 756, 760
 Io, 739–742
 Mars, 686, 687, 691–693, 699, 701–706, 708, 709, 711–716
 melting temperature, 200, 608–610, 699, 703, 704
 Mercury, 749, 753–756
 Moon, 726, 736
 outer, 64f, 66, 69t, 97–100, 101f, 127, 200, 201f, 203, 204, 254, 549, 603–605, 609, 610, 702, 704, 708, 753, 755, 756, 770
 structure and composition, 98–100
 temperatures, 200
 Venus, 658, 672, 673, 678, 679, 679f, 680, 680f, 703
 core–mantle boundary (CMB), 35, 61, 62, 66, 73, 93, 94, 215, 265, 378, 379, 403, 455, 456, 456f, 457, 458f, 465f, 486, 509, 518, 580, 603, 605, 606, 614t, 615f, 767, 768, 776, 780, 781, 785–787
 chemical reactions, 549
 cold downflows on CMB, 457, 462, 466, 471, 474, 626
 heat flow, 303, 482
 Io, 740, 743
 Mars, 713, 714, 715f
 Moon, 736
 plume generation, 518, 519
 slabs on the CMB, 112
 temperature, 191t, 203
 thermal conductivity, 211
 thermal expansivity, 209
 topography, 116, 233, 413, 414f, 783
 ultra-low velocity zone (ULVZ), 95
 Venus, 658, 659, 670
 core–mantle mass exchange, 549
 core–mantle thermal evolution, 602, 604f, 607, 607t, 611f, 678
 coriolis acceleration, 103
 coriolis forces, 254, 678
 corner flow, 34, 429, 436, 439, 491
 correspondence principle, 739
 crack propagation, 166, 168, 169, 229
 crack tip, 168, 169

- cratering, 633
 on Mars, 637
 on the Moon, 723
 on Venus, 637
 cratons, 73, 78, 79, 148, 151, 508
 creation in back-arc basins, 38
 creep activation energy and volatile content, 596
 creep viscosity, 214, 215, 243, 248
 Cretaceous magnetic polarity superchron, 61
 critical Rayleigh number for convection onset, 294, 294f, 296t, 301, 301f, 302, 302f, 314t, 318, 319t, 320f, 321t, 330, 367, 368, 373
 crust
 age distribution of, 627, 628f, 629, 630
 bimodality, 69
 composition of, 38, 43, 44, 44t, 47, 48, 69, 71, 73, 80
 thickness, 64f, 69, 70, 70t, 71, 73, 74, 75f
 crustal addition, 555, 564, 565, 629
 crustal doubling in Tibet, 45
 crustal growth, 556–559, 559f, 560, 560, 561f, 563–565, 600, 627, 628, 628f, 629, 629f, 630, 632, 632f
 Archean, 628f, 629, 631f
 crustal recycling, 548, 556, 561–564, 564f, 565, 584
 crustal reflection studies, 69, 72, 73
 crustal subtraction, 565, 629, 631
 crustal xenoliths, 43, 94
 crystalline lattice, 240, 241f, 242, 242–244f
 cubic patterns of steady three-dimensional convection, 421
 Curie temperature, 13
 cylindrical coordinates, 253, 255, 256, 264, 280–282, 285, 286, 530
 D'' layer, 66, 93, 96f, 117f, 127, 190, 191t, 414f, 473, 527, 768, 769, 772, 773, 782–785, 787
 chemical heterogeneity, 523, 533, 583
 mantle plumes, 509, 520, 532
 small-scale convection, 413, 414, 416
 structure and properties, 93–97, 115, 117
 temperature, 200, 201, 204, 519
 thermal boundary layer, 500
 thermal properties, 209, 211
 viscosity, 239
 damage equation, 490
 Darcy flow, 161
 Darcy resistance, 162, 164
 Darcy velocity, 155
 Darcy's law, 154, 155, 162, 163
 Debye temperature, 207, 209
 decay constant, 125, 552, 552t, 565, 566, 573t, 575, 596
 Deccan Traps, 527
 declination, 11, 12
 deep earthquakes, 106, 107
 deep seismicity, 16, 18f, 33, 106, 107
 defect migration, 240
 deformation map, 246, 247, 247f
 deformation of ice I, 763, 764t
 deformation of Maxwell body, 212, 213, 739
 degassing, 596–598, 599f, 600, 600t, 601, 601f, 602
 and mantle temperature, 596, 601f, 602
 effects on rheology, 596
 degassing history, 599
 deglaciation, 215, 216, 224, 226f, 229f, 231, 232
 of Fennoscandia, 217f
 degree of partial melting, 153, 155–158, 158f, 159, 159f, 160, 160f, 508, 513
 dehydration of subducted oceanic crust, 38
 delamination, 45, 46, 582, 626, 650, 767, 778, 783, 792
 and crustal recycling, 44, 45, 561
 and downwellings, 783
 and global heat flow, 650, 650f
 and heat loss on Venus, 649
 and high plateau topography of Ishtar Terra, 650
 and high seismic velocities, 45
 and magmatism, 45
 and partial layer instability, 308
 and secondary convection, 783
 and subtraction of continental crust, 629
 and volatile recharging of mantle, 596
 as mechanism for heat transfer in Venus, 648, 649
 as mechanism of heat transfer, 635
 at intracrustal weak zone, 45
 at island arcs, 45
 continental, 43–45, 46f, 561
 crustal recycling, 631
 in Archean, 631
 in continental collision zones, 45
 in evolution of continental crust and for isotopic balance of mantle, 778
 of continental crust and lithosphere
 isotope signatures, 781
 of continental lithosphere, 45, 47, 647, 778
 of lithosphere, 143, 648, 650f
 of lower continental crust, 45, 48, 548, 584
 on Mars, 692
 density scale height, 268, 276, 277
 depleted mantle reservoir (DMR), 71, 550, 558, 560, 560f, 561, 561f, 564f, 570–572, 574, 575, 579, 580, 583, 584
 depth of compensation, 135, 137
 depth of ocean floor, 132, 133f, 135, 136, 136f, 137, 140, 207, 210
 vs. age, 41, 132, 136, 136f, 140, 207, 210
 descending lithosphere, 31, 32f, 33–36, 39, 52, 53, 176, 181f
 descending slab
 fate, 106, 767, 774, 777
 deterministic chaos, 330, 336
 deviatoric stress tensor, 254–256, 282
 diapirs, 38, 413, 520–523, 528, 536, 537, 580, 627, 795
 buoyancy, 521, 527
 chains, 533, 536, 537f

- diapirs (*cont.*)
 growth, 520, 522
 separation from thermal boundary layer, 521, 522
- diatremes, 43, 246
- differential uplift, 228, 229
- differentiation, 771, 794, 795
 core, 603, 610
 crust, 47, 146, 629
 Earth, 587
 Galilean satellites, 762, 766
 geochemical reservoirs, 547, 548, 553, 570
 incompatible elements, 130
 Io, 745
 mantle, 68
 Mars, 691–694, 694f, 696f, 697–699, 702, 707, 728
 Mercury, 756
 Moon, 718, 726, 728, 731, 733
 MORB parent material, 71
 Venus, 647, 651, 652, 673, 677
- diffusion coefficient, 227, 228, 240, 242
- diffusion creep, 240, 241f, 243, 244, 246, 246t, 247, 247f, 248–250, 250f
- dike injection, 166, 171, 171f
- dike propagation, 168f, 171, 176
- dilatation rate, 255
- diopside, 81
- dip angle, 15, 32, 34, 36, 107, 108, 180, 397, 777
 subduction, 34, 767
- dipole moment of density distribution, 137
- dislocation climb, 243, 245f
- dislocation creep, 240, 242, 242f, 243, 243f, 244, 244, 245f, 246, 246t, 247, 247f, 248, 249, 250f
- dissipation number, 268, 273, 276, 477, 478, 482, 484
- double seismic zones, 33
- downwelling convective sheets, 418, 423, 424, 429, 432, 436, 437, 441, 444–446, 449, 452, 454, 455, 457, 461, 471, 474, 477, 479, 482, 486, 487, 498, 498f
- drilling program, 13
- driving force for plate tectonics, 31, 52, 53
- DUPAL isotopic anomaly, 350, 514, 551
- dynamic recrystallization, 243, 244, 390, 490
- dynamic topography, 233, 234f, 235, 413, 466, 646, 711
- dynamic viscosity, 256, 257, 262, 263, 289, 298, 450f, 455
- dynamo generation, 609, 610, 678
- Earth, 2f, 8, 10, 14f, 23f, 45, 60f, 61, 63, 64f, 66, 68f, 69, 75f, 87, 98, 99, 122–125, 128–130, 215, 216, 231, 234, 265, 315, 316, 318, 467, 548f, 576f, 577, 578f, 579, 583, 592f, 599f, 605, 607t, 614, 614t, 633, 634, 634t, 635, 636, 636f, 637, 639f, 640, 650f, 654t, 691t, 727, 764, 767, 770–774, 777–780, 782, 783, 785, 787, 789–794
- accretionary heating, 587
- age, 13, 554, 567, 577, 579, 594
- Airy isostasy, 212, 645, 646
- area of continents, 43
- boundary layer model of mantle convection, 353–355
- comparison with Galilean satellites, 738, 739, 744, 764, 766
- comparison with Mars, 690–692, 695–697, 710
- comparison with Mercury, 752
- comparison with Moon, 681, 716, 719, 726, 727, 731, 735
- comparison with Venus, 640, 641, 644–653, 656–658, 661, 664, 672, 674, 678–680
- continental crust, 71–73
- cooling, 588, 589, 591, 594–596, 605, 607, 630
- core, 97–100
- coupled core–mantle thermal history, 602, 604f, 607, 607t, 609f, 611, 611f, 678
- D'' layer, 94
- density, 63, 67, 69
- early differentiation, 587
- effects of degassing or regassing on thermal evolution, 601
- evolution, 3f, 547, 565, 587, 633, 673, 696, 770, 785, 787, 792
- expansion, 14
- geochemical reservoirs, 547–549, 556
- global magma ocean on early Earth, 588
- gravitational potential, 279
- heat conduction and age, 118, 121, 122, 125
- heat flow and heat production, 128, 129t, 131
- heat flow distribution, 22
- heat production, 125, 129, 130, 131f, 143–145, 145f, 146
- historical ideas, 1–3
- hypsometry, 639
- lower mantle, 94
 composition, 92
- magnetic field strength vs. time, 610, 611, 611f
- mantle avalanches and thermal evolution, 627
- mantle mixing, 344, 349
- mantle plumes, 514, 519, 533, 537, 545
- mass, 66, 68, 69t, 92, 128, 215, 231
- melt migration, 153, 161
- models, 16, 104, 105f, 108f, 110f, 189, 588, 594, 604f, 607t, 608, 609, 609f, 610, 611f, 630, 679, 679f, 680, 680f, 792
- mantle convection, 463, 466–468, 471
- seismic, 66, 67, 67f, 68, 68f, 74, 79, 84, 86, 90, 91f, 92–94, 94f, 95, 96, 98, 100, 101f
- tomographic, 102, 103
- viscosity, 231, 232
- moment of inertia, 66, 215, 230, 231
- noble gases, 573–575, 577–579
- ocean ridges, 28
- oceanic lithosphere geoid anomaly, 137
- origin of continents, 656
- paleomagnetism, 11
- plate driving forces, 52
- plate motions, 48, 51

- Earth (*cont.*)
- plate tectonics, 22, 25
 - Prandtl number, 267
 - Pratt isostasy, 646
 - Rayleigh number, 295, 296
 - reference state models, 277, 278
 - rheology, 213, 214, 216, 217, 245
 - rotation, 6, 14, 103, 117, 215, 230, 231, 254, 471, 727
 - seafloor spreading, 13
 - secular acceleration, 231
 - silicic crust, 656
 - slab temperature, 176
 - structure and composition, 63, 66, 68, 69, 69t, 80t, 101, 103
 - subduction, 29, 31
 - surface ages, 636, 637
 - temperature, 127, 190, 191t, 200
 - thermal history, 201, 586–588, 590, 591, 592f, 593–595, 597, 598, 600, 601, 601f, 602, 603f, 605, 607, 609–611, 615–617, 627, 679, 679f, 699, 770
 - and coupled core–mantle evolution, 604f, 607, 607t, 609f, 611f
 - and degassing, 598, 599f, 600t
 - and two-layer mantle convection, 611, 612f, 614t, 615f, 616
 - crustal growth, 629, 630
 - episodicity, 625–627
 - of core, 588, 603, 608, 610
 - strongly temperature-dependent viscosity, 617
 - thermal isostasy, 645, 646
 - thermal resistance in two-layer mantle convection model, 613
 - three-dimensional mantle convection models, 438, 441, 446, 454, 455, 457, 461, 462, 468–472, 474, 477, 478, 480, 482, 488, 490, 495, 498
 - topography, 645
 - two-dimensional mantle convection models, 376, 379, 392, 395, 403, 408, 411, 412
 - upper mantle, 75, 76, 80, 81
 - viscosity, 232, 233
 - Wilson cycle, 61
 - earthquakes, 1, 8, 15, 16, 18f, 22, 31, 32, 32f, 34f, 35, 69, 98, 103, 106, 107, 185–187, 187t, 188, 768, 788
 - focal mechanisms, 53, 106
 - East African Rift, 57
 - eclogite, 75, 81, 82, 190t, 199t, 349, 795
 - Roberts Victor, 349
 - eclogitic xenoliths, 81
 - edge dislocation, 242, 242f, 243, 243–245f
 - effective viscosity, 250
 - eigenmode expansions, 330–332
 - elastic bending, 26
 - at subduction zones, 33
 - elastic lithosphere, 25, 26, 57
 - elastic rigidity, 7
 - elastic solid, 212
 - elastic strain, 169, 212
 - elastic stresses, 26, 645
 - elastic waves, 212
 - elastic–perfectly plastic rheology, 33
 - elasticity, 1, 65, 189t, 224
 - electromagnetic induction, 757, 762, 766
 - elevated beach terraces, 223
 - energetics of core, 100
 - energy balance of mantle, 588, 605, 673
 - energy barrier, 240–242
 - enriched mantle reservoir, 583
 - enrichment factor, 553t, 554, 558, 562, 569
 - enstatite, 81, 85
 - entropy, 64, 188, 260, 261, 263, 443f, 448f
 - entropy equation, 188
 - episodicity in crustal growth, 627, 628, 628f, 629, 630, 632f
 - equation of state, 64, 84, 91, 91f, 251, 259, 265–267, 278, 279, 455
 - erosion, 69, 145, 413, 506, 560, 561, 563, 565, 577, 636, 639, 640, 683, 783, 793
 - error function, 120, 121t, 122f, 150f, 179
 - error function integral, 120, 179
 - Ethiopian swell, 57
 - Euler's theorem, 48, 48f
 - Eulerian form of mass conservation, 252
 - Europa, 633, 634t, 635, 738, 746, 756, 757, 757f, 758–766, 771, 795
 - subsolidus convection, 760, 763
 - tidal dissipative heating, 763, 766
 - exchange of stabilities, 290, 316
 - exclusion of light alloying element from solid inner core, 603, 753
 - exothermic reaction, 85, 88, 192, 193, 196, 199, 200, 390
 - exotic terranes, 47
 - exsolution of light elements from outer core into lower mantle, 549
 - failed arm, 57
 - fayalite, 81, 84
 - Fe melting, 202, 203f
 - Fe–FeO melting, 202, 203f
 - Fe–FeS melting, 202, 203f
 - Fennoscandian ice sheet, 216, 223, 224, 232, 232f
 - Ferroan anorthosites, 718, 719
 - fertile mantle rocks, 38, 82, 513
 - fine structure, 66–68, 73, 84, 90, 92, 102, 416, 516
 - finite difference, 378, 417
 - finite element, 378, 417
 - first law of thermodynamics, 259
 - fixed mantle plumes, 41
 - fixed points, 334, 335, 335f, 336–340, 340t, 341f, 342, 342f, 539
 - unstable, 339
 - fixed surface boundary condition, 295, 296, 306, 307, 314

- flake tectonic model, 59
flexure, 33, 720
flood basalts, 60, 61, 509f, 525, 527, 527t, 528, 536, 545, 546
fluid-driven fracture propagation, 166
focal mechanisms
 down-dip compressional, 33
 down-dip extensional, 33
 of deep earthquakes, 106
focusing of magma, 165
force balance, 254, 256, 271
forced convection, 387
forsterite, 81
fossil conduit, 537, 538f
foundering, 34, 39, 39f, 59, 646, 649–651, 678, 771
Fourier's law of heat conduction, 122, 124, 210, 262, 309, 606, 613, 619, 622, 655
fractionation factor, 551, 554, 559, 562, 564, 733
 crustal, 559, 559f, 559t, 563, 697
 Mars, 697
 mantle, 553t, 559t, 560f, 564
 rubidium–strontium, 734f
 samarium–neodymium, 732f
fracture resistance, 169–171
fracture zone, 28f, 29, 138, 139f, 142
 Mendocino, 138
Frank–Kamenetskii parameter, 618, 706
Frank's hypothesis for island arcs, 36
freeboard, 584, 597, 600, 630, 792
free-surface boundary condition, 306, 307, 351
freezing of inner core, 100, 605, 608, 609, 609f, 610, 611, 611f
frictional heating, 36
 on slip zone, 176–178, 180, 181f
- Galapagos rift, 230
Galerkin technique, 417
Galilean satellites, 633, 634, 746, 756, 760, 761, 763–765
 subsolidus convection, 764
Ganymede, 605, 633, 634t, 738, 746, 756, 758f, 760–766, 771, 795
 subsolidus convection, 763, 766
garnet lherzolite, 81
garnet–perovskite phase change, 90
gas–melt partitioning, 579
general mantle circulation, 376, 382, 580, 781, 784–786
geochemical cycles, 547, 565
geochemical reservoirs, 95, 547, 548f, 551, 579, 789
geochron, 567, 567f, 570, 571, 571, 572f, 583
geodynamo, 98, 100, 611, 768, 770, 772
geoid, 21f, 22, 22f, 26, 139f, 151, 234f, 237t, 239f, 279, 514, 514f, 540, 543f
mantle viscosity, 212, 215, 232, 233, 237–239
Mars, 689
oceanic lithosphere, 138, 140–143
Venus, 661–663
- geoid anomalies, 33, 137, 138, 138f, 141, 147, 149, 215, 233, 233f, 235–237, 505, 506f, 541, 645, 646
 internal loads, 235, 236
geoid height, 16, 21f, 132, 148, 149, 150f, 207
 topography ratio over swell, 505, 506f, 540
 vs. age, 132, 210
geoid highs, 39, 233, 514
geoid response kernel, 234
geothermal gradient, 27, 118, 119, 122, 152
giant impact hypothesis, 587, 792
Gibbs free energy, 260
glacial isostatic adjustment, 216
glacial loading and unloading, 214, 228, 231
glaciation, 60f, 213, 215, 216, 218f, 224, 231
 of Fennoscandia, 223
glide plane, 242, 243, 244f
global isostatic adjustment, 216
global seismicity, 16, 18f, 31
Gondwanaland, 6
grain boundaries, 78, 154, 240, 243, 244, 763
grain boundary diffusion viscosity of iron, 753
grain size, 154, 155, 158t, 243–245, 245f, 246, 247, 249, 754, 756, 763, 765, 765f, 769, 789
granites
 origin of, 44
 region of, 656
granitoid production rates, 60
gravitational field, 8, 257, 290, 307, 772
 Earth, 137
gravitational instability, 8
 crust, 651
 of continental lithosphere, 45
 of lithosphere, 25, 46, 506
 of oceanic lithosphere, 29, 308, 769
 of thermal boundary layer, 360, 452, 772
gravitational potential anomaly, 137
gravitational potential energy, 587
 release upon accretion, 587
 release upon core formation, 587
gravitational sliding, 27, 52, 773
gravity, 66, 155, 215, 222, 230, 254–256, 265, 269, 274, 275, 279–281, 308, 418, 419f, 512t, 635t
 Io, 741
 Mars, 686, 688
 Mercury, 753
 Venus, 662, 663, 679, 685
gravity anomalies, 2, 15, 215, 228, 236, 644–646, 648, 719–721, 723f, 793, 795
gravity–topography correlation on Venus, 645, 771
Great Salt Lake, 228
greenhouse, 546, 672
Griggs experiment, 10, 11f
growth curve, 567, 568, 568f, 571f
 crustal, 629, 630
Grüneisen parameter, 128, 188, 190, 191f, 209, 210, 263, 266, 268, 277, 450f, 455, 477, 485, 608
acoustical, 190

- hafnium–tungsten isotopic system and lunar rocks, 736
 half-life, 129, 129t, 130, 552, 579, 736
 half-space cooling model, 132, 134, 134f, 136f, 138, 138f, 139, 139f, 141, 142, 147, 151, 675, 768, 782
 hard thermal turbulence, 387f, 627
 harzburgite, 81
 Hawaii, 39, 354, 499, 500t, 501, 501f, 508, 510, 511t, 513, 513t, 515, 533, 536, 541t, 550, 581f, 781
 basalt geochemistry, 578, 580, 584, 585
 Hawaii (II), 580
 Hawaiian hot spot, 502, 505, 506, 510, 512, 518, 522, 527, 529, 533, 541, 542f, 543, 578–580, 584, 585, 785
 Hawaiian Island chain, 41, 41f
 Hawaiian Islands, 26, 685
 Hawaiian Swell, 45, 505, 507
 Hawaiian–Emperor island-seamount chain, 41, 59, 499, 501, 502, 503f
 heat conduction along adiabat, 201, 608, 609, 609f, 610, 679f, 702, 703, 703f, 705
 heat conduction equation with heat sources, 125
 heat diffusion, 121, 540
 heat flow distribution, 22
 heat flow vs. age, 133, 134f
 heat flux boundary condition, 296, 382
 heat flux Rayleigh number, 382
 heat flux vector, 210, 262
 heat generation, 9, 129, 145f, 146, 148, 151, 344, 385f, 447f, 450f, 635, 654t, 770, 777, 793
 boundary layer analysis of convection, 359, 360
 conductive cooling, 125
 continental crust, 143, 144, 146, 297
 Earth thermal history, 589, 591, 592f, 593–595, 614, 614t, 616, 630
 energy equation, 262, 270
 Ganymede, 764
 Io, 742
 Mars, 690, 716
 rare gas isotopes, 573
 Rayleigh number, 378
 stability of plane layer, 303, 306
 surface heat flow, 128–130
 time-dependent convection, 382, 384
 Venus, 644, 647, 648, 653, 655, 674f
 heat transfer, 2, 45, 64, 782, 789
 convection onset, 288
 from core, 211
 hexagonal convection, 375
 in Earth thermal history models, 586, 591, 594, 613, 617
 in planets and moons, 634, 635, 765
 in three-dimensional convection, 423, 432
 in two-dimensional convection, 381, 393, 411, 413
 Io, 739, 744
 mantle, 127
 mantle plumes, 513
 Mars, 700, 702, 706, 707
 mean field theory, 364
- Mercury, 751
 Moon, 727
 Nusselt number, 334
 to base of lithosphere, 142, 143
 Venus, 647, 648, 651, 672, 673
 heat transport law, 197, 379, 381
 helium, 573, 574, 579, 582f
 ^3He , 573–577, 582, 584, 781
 ^4He , 573, 573t, 574–576, 576f, 577, 579
 $^4\text{He}/^3\text{He}$ ratio, 574, 575
 mass of ^3He in atmosphere, 576
 radiogenic, 548, 574, 584
- Helmholtz free energy, 260
 hemispheric asymmetry of Mars, 637
 hemispheric dichotomy, 638
 Mars, 636, 638, 638f, 682, 771, 794
 Moon, 636, 638f, 719, 722, 794
- Herring–Nabarro creep, 240, 241f
 highland rocks, 638, 682, 717, 718
 Himalayas, 59, 72, 644
 HIMU, 583
 hinge, 33
 Holmes, Arthur, 8, 9, 9f
 Holmes–Houtermans model, 566
 homologous temperature of mantle, 473, 613, 614t
 Hooke’s law, 739
 Hopf bifurcation, 334, 335, 335f, 339, 340, 341f, 342
 hot spots, 22, 39, 40f, 42, 48, 153, 201, 499, 501, 501f, 502, 505, 507–510, 512–514, 514f, 515, 516, 518, 522, 527, 529, 532, 533, 539–541, 542f, 543, 544f, 545
 clusters, 514
 energetics, 510, 511t, 512
 geoid highs, 514
 heat transfer, 511t, 512, 513, 536
 locations, 39, 499, 500t, 501f, 514, 515, 515f, 516, 518, 543
 magma production, 513
 mantle plumes, 201, 499, 500, 502, 511, 515, 518, 527, 532, 537
 motion, 501, 502
 rate of production of volcanic rocks, 510
 reference frame, 52
 source strength, 507
 strength, 510
 swell shape parameter I , 539, 540, 541t
 swells, 499, 505–507, 510, 513, 514, 516, 537, 540, 541, 541t
 tracks, 40f, 499, 501, 501f, 502, 505, 507–509, 509f, 510, 515, 516, 525, 527, 537, 541
 volcanism, 39, 47, 501, 502, 505, 510, 527
- Hutton, James, 2, 3f
 hydraulically driven fracture propagation, 166
 hydrologic cycle, 72, 792
 hydrostatic compression, 265
 hydrostatic equation, 65, 93, 264, 265, 268, 269, 274, 276, 278, 485
 hydrostatic equilibrium, 2, 135, 212, 686

- hydrothermal circulation, 132, 134, 146, 574, 577, 579, 586
 hydrothermal processes, 132, 574
 hypsometry, 635, 640, 719
 of Mars, 640
 of the Earth, 639
 of the Moon, 640, 719
 of Venus, 636, 639, 656
- ice in glaciers, 10, 212
 ice load histories, 224, 225
 Iceland, 28, 39, 43f, 153, 166, 172, 354, 499, 500t, 501f, 506f, 508–510, 511t, 516, 517f, 518, 527, 527t, 536, 543, 545, 549, 550, 575, 578, 580, 584, 585, 653, 785
 ilmenite, 189t
 ilmenite–perovskite phase change, 198, 199t
 impact basins, 639, 640, 683, 706, 717f, 719, 723, 726
 impact flux, 646
 inclination, 11, 12
 incompatible elements, 69, 71, 130, 547, 548, 653, 719, 732, 794
 radioactive, 736
 trace, 164, 508
 incompressible fluid, 218, 222, 251, 252, 263
 incremental heat addition, 259
 incremental work done, 259
 India–Asia collision, 59, 501
 inertial force, 256, 269, 271, 281
 infertile mantle rock, 82
 inhomogeneity parameter, 93, 94f, 98
 initiation of subduction, 58, 58f, 59
 inner core, 64f, 69t, 101f, 103
 discovery, 63
 energy release on solidification, 609
 Galilean satellites, 760
 geochemical reservoir, 549
 growth in thermal history model, 603, 605, 607
 in Martian thermal history models, 702, 703, 704f, 705, 716
 Io, 740
 Mercury, 750, 753, 754, 756
 rotation, 98, 99
 seismic model, 66
 structure and composition, 97–100
 Venus, 678, 679
- inner core boundary (ICB), 98, 200, 202
 interfacial thermal boundary layer, 127, 204
 interior plate deformation, 52, 657
 internal heating Rayleigh number, 270, 273, 304, 312, 319, 378, 445, 447f, 450f, 471, 473
 internal loads, 232, 233, 235, 236, 236f, 237
 internal structure
 Europa, 766
 Ganymede, 760
 Io, 739–741, 743, 746
 Mars, 686
 Mercury, 750
- internally heated sphere, 312, 313, 314t, 315f, 321
 intracrustal asthenosphere, 25
 intracrustal decollement, 45
 intracrustal differentiation, 656
 intracrustal weak zone, 45, 46f
 intraplate deformation, 69, 657
 intrusion equation, 539
 inverse continents, 117
 inverse methods, 238
 Io, 633, 634t, 635, 736, 737, 737f, 738–742, 742f, 743–745, 745f, 746, 756, 760, 771, 793, 795
 asthenosphere, 740, 742, 743, 743f
 basin and swell topography, 740, 746
 C/MR^2 , 741
 coupled orbital–thermal evolution, 746, 748f
 dependence of shear modulus and viscosity on temperature in mantle, 746
 differentiation of interior, 739, 744
 ellipsoidal shape, 741, 744
 Galileo gravity measurements, 741, 761, 762
 Galileo shape determination, 741
 heat flow and dissipation in Jupiter, 747
 high-temperature lavas, 744
 hydrostatic equilibrium, 741
 hydrostatic figure, 744
 J_2 and C_{22} , 741
 lithosphere thickness, 742, 744, 745
 magnetic field, 742
 metallic core, 740–742
 models of tidal dissipative heating, 740, 742–744
 mountains, 737f, 745
 oscillations in time history of thermal–orbital state, 747
 present thermal–orbital state, 747
 runaway melting, 739
 silicate volcanism, 633, 737f, 744
 subsolidus mantle convection, 634t, 739, 742
 surface heat flow, 738, 742, 743f, 744
 surface topography and tidal heating in asthenosphere, 740, 744
 thermal lithosphere, 744
 thermal–orbital evolution, 746, 748f
 tidal and rotational distortion, 741
 tidal dissipative heating, 633, 634, 736, 738–740, 742, 742f, 743, 743f, 744–746
 tidal friction, 738
 tidal potential Love number, 738
 tides raised on, 738
 topography, 740, 744
 two-layer model, 741
 volcanic activity, 633, 736, 737f, 744, 746
- iodine
 extinct ^{129}I , 579
- iridium anomaly, 545
- isentropic process, 64, 65, 260
- island arcs, 36, 37f, 47, 567, 777
 arcuate structure, 36
- cusps, 36

- island arcs (*cont.*)
 formation of continental crust, 47, 630
 volcanism, 36, 37, 37f, 38, 46, 47, 60, 177, 548, 597, 777, 792
- isobaric process, 64
- isostasy, 135, 148, 149, 230, 630
 on Io, 744
 on Mars, 689
- isostatic compensation, 79, 505, 511, 688
- isostatic equilibrium, 137, 228, 231
- isostatic geoid height anomaly of swell, 540
- isostatic topography above intrusion, 540
- isothermal bulk modulus, 207, 262, 278
- isothermal compressibility, 259
- isotope ratios, 59, 553t, 559t, 566, 567, 567f, 569, 571, 571, 572f, 585, 637, 731, 732f, 734, 735f, 781
 geochemical evolution, 551
 models, 554, 555, 559, 563
 geochemical reservoirs, 547, 549
- hot spot basalts, 508
- mantle mixing, 349
- models for interpretation, 551
- MORB, 549, 550
- noble gas systems, 574, 577, 579
- of lunar rocks, 731
- of mid-ocean ridge basalts, 731
- radioactive decay, 551, 552
- U, Th, Pb system, 565, 566
- isotope studies, 349, 547, 784, 795
- isotope systematics, 547, 550, 561, 565, 583, 584
 of mid-ocean ridge basalts, 636
 of OIB, 580
- isotopic composition, 47, 508, 536, 549, 630, 691, 699
- isotopic signature, 349, 350, 784
- isotropic fluid, 255
- jadite, 81
- JB tables, 64
- Jeffreys, Harold, 6, 7, 7f
- K/T extinctions, 545
- Kerguelen, 511t, 541t, 550, 581f, 583
- Kerguelen (III), 582
- Kerguelen Plateau, 501f
- kimberlite, 81, 349, 508
- kinematic mixing, 550, 777
- kinematic viscosity, 427, 478, 519, 521, 525, 535, 539, 591, 592f, 599f, 601, 607, 613, 709t, 753
 definition, 266
- Rayleigh number, 293, 298, 589, 590
- kinetic energy, 56, 100, 264, 382, 393, 454, 587
 of elementary fluid parcel, 264
 of plates, 52
- KREEP, 718, 736
- Kronecker delta, 256, 739
- laminar dike, 170
- laminar flow, 168–171, 171f, 172, 172f, 173, 174, 174f, 175, 251, 525
- Lane–Emden equation, 278
- Laplace resonance of Io, Europa and Ganymede, 738, 760, 763
- Laplace's equation, 326, 327
 in spherical coordinates, 326, 327
- large impact, 587, 672, 683, 690
- latent heat, 124, 183, 184, 184t, 186, 186f, 191, 195, 196, 297, 300, 401, 403, 458, 464, 608, 670, 700t, 702, 713
- of fusion, 156, 158, 158t, 171
- of phase change, 181, 194, 458
- release on core solidification, 608
- lattice diffusion, 243
- Laurasia, 6
- Laurentide ice sheet, 216, 226f, 232f
- lava lake, 651
- layering of mantle convection due to endothermic phase change, 390
- layers, 70f
 conduction, 127
 diffusive, 190
- lead isotope ratio, 568f
- Legendre function, 325t, 327, 328
- Legendre polynomial, 323, 324, 325t
- Lehmann seismic discontinuity, 79, 80, 768, 788
- length of day, 215, 230, 686
- light constituent in core, 603, 605, 608, 609, 755
- linear stability, 288
- linear viscosity, 753, 789
- lithosphere, 16, 22, 25, 25f, 26, 27, 27f, 29, 31, 31f, 32–36, 37f, 38, 39, 39f, 46f, 134f, 148, 149f, 160, 160f, 181f, 700t, 767–769, 771–774, 777–785, 787, 789, 791–794
- above mantle plumes, 499, 500, 505, 516, 517, 525, 527, 528, 532, 536–538, 540, 541, 543, 626, 627
- basal tractions, 53
- continental, 71, 143, 145, 147–149, 151, 409, 410, 410f, 411–413
- deformation, 73, 376
- delamination, 44–47, 561, 582, 650f
- in mantle convection models, 385, 389, 390, 492f
- Io, 745t, 748t
- LID, 78, 101
- Mars, 708t
- mechanical, 25
- mixing back into mantle, 344, 345, 350, 547, 549, 550, 580, 581, 585
- Moon, 730f
- negative buoyancy, 88
- oceanic, 131–133, 135, 137–139, 141–144, 147, 151, 152, 207, 210, 211, 215, 308, 410f, 412, 413, 636, 647
 magma migration, 166, 168
- rheology, 490–492, 495, 498
- rigid lid, 617, 625
- seismic observations, 104, 106, 106f
 slab penetration through 660 km depth, 397, 399, 400f, 401

- lithosphere (*cont.*)
 slab pull, 52
 subduction, 57–59, 61, 650f
 surface thermal boundary layer, 76, 119, 127, 355, 360, 616
 temperatures, 190, 191t
 temperatures in subducting slabs, 176, 178, 180, 188
 thermal, 25, 26
 thickness, 59, 78f, 133f, 135, 139, 146, 147, 149, 150, 150f, 151, 674f, 696f, 700t, 702f, 708f, 773
 thinning, 45, 403, 458, 463, 505–508, 513
 viscosity, 216, 220, 222, 227, 229–231, 237, 237t, 238, 240, 248, 250, 473
 lithospheric flexure, 33, 45, 77, 540
 lithospheric foundering, 34, 39, 39f, 59
 lithospheric stoping, 46, 46f
 lithospheric swells, 57
 lithostatic pressure, 135
 local density scale height, 268
 localization of deformation, 490
 Lord Kelvin, 118, 118f, 122, 123
 and cooling of Earth, 594
 Lord Rayleigh, 5f
 Lorenz attractor, 336, 338, 347
 Lorenz equations, 330, 332, 333, 334, 335f, 336, 361, 370
 Love number, 738, 740, 742
 Love waves, 66, 76, 77
 low-velocity zone (LVZ), 76, 96, 151, 783
 low-viscosity asthenosphere, 226f, 227–230, 240, 308, 507, 768, 783, 784
 low-viscosity channel, 227, 545
 low-viscosity transition zone, 239
 low-viscosity zone, 473, 495
 lower continental crust, 25, 73, 584, 778, 792
 composition, 43–45, 46f, 548
 crustal formation, 46–48, 656
 delamination, 43–45, 46f, 631, 649, 656
 density, 148, 149f, 150
 geochemical reservoirs, 556, 561
 geoid height, 148
 heat production, 146
 missing lead paradox, 571
 seismic structure, 72, 73
 lower mantle, 35, 42, 45, 66, 84, 99, 612f, 614t, 615f, 680f, 768, 769, 773, 774, 775f, 776, 776f, 780, 784–790, 792
 adiabaticity, 93–95, 188–190, 200, 201
 avalanches, 455–457, 461–463, 626, 630
 composition, 87, 88, 90–93
 D'' layer, 97
 degree two residual geoid, 514
 geochemical reservoirs, 549, 550, 572, 575, 578, 578f, 579, 580, 584, 585
 mantle flow, 646
 Mars, 710, 713–715
 penetration by subducted slabs, 106–109, 112–115, 117, 397, 399
 plume upflow, 401, 403
 plumes, 499, 518–520
 properties, 69t
 seismic structure, 66, 90, 91, 91f, 92–95, 103, 106–109, 112–115, 117
 thermal evolution and two-layer mantle convection, 611–616
 thermal properties, 209–211
 thermal properties and convection, 406–408, 457
 thermal state, 127, 201f, 204–207
 three-dimensional convection models, 456f, 466–468, 470–473, 486
 two-layer convection, 379, 391, 392
 Venus, 658, 670, 672
 viscosity, 231, 233, 235, 237–240, 247, 248, 250, 522
 lower mantle reservoir, 549, 550, 571, 573, 575, 576, 578, 580, 584, 770
 lubrication approximation, 168, 169
 lubrication equation, 539
 lubrication theory, 229, 539
 lunar core, 726, 736, 771
 lunar crust, 716, 718, 719, 725, 726, 728, 729, 729f, 732, 733, 771, 793, 794
 lunar differentiation into multiple reservoirs, 733
 lunar evolution, 639, 729
 lunar heat flow, 727, 738
 lunar highlands, 638, 717
 lunar laser ranging data, 231, 726
 lunar magma ocean, 718, 722, 736, 771
 lunar mare basalts, 639, 731–733
 lunar mascons, 721
 lunar moment of inertia, 726
 lunar rocks, 653, 718, 726, 731, 732f, 733, 734f, 735, 736
 lunar thermal evolution, 728
 lutetium–hafnium isotope systematics, 561, 583
 Lyapunov exponent, 348
- Mach number, 267
 mafic composition, 548, 656, 792, 794
 magma chamber, 27f, 70, 70f, 71, 153, 165, 166, 172, 689
 magma channel, 154f
 magma flow through channel, 155, 172, 174
 magma generation, 153, 527
 magma injection rate, 171
 magma ocean, 588, 638, 640, 717–719, 723, 725, 726, 728, 729, 794
 magma ocean cumulates, 719, 723, 736
 magma transport through lithosphere, 711, 768, 780
 magma viscosity, 155, 158, 159, 175, 176
 magma-driven fracture propagation, 166, 651, 780
 magmons, 161
 magnesium number X_{Mg} , 84
 magnetic anomaly, 13
 magnetic declination, 11, 12

- magnetic field, 11–13, 60f, 98, 603, 609, 610, 678, 762, 771, 772, 793
 Callisto, 762
 Europa, 757
 Ganymede, 761, 795
 Io, 742, 771, 793, 795
 Mars, 698, 699, 705, 706, 713, 715, 716, 771, 793
 Mercury, 750, 754–756
 Moon, 726, 727
 Venus, 672, 678, 680, 681, 706, 771, 793
 magnetic field anomalies, 13, 16, 19f, 49, 71, 132
 magnetic field generation by motions in core, 603, 678
 magnetic inclination, 11, 12
 magnetic pole, 11
 magnetic reversals, 12, 13, 50f
 time scale, 50f
 major element petrology, 547
 majorite, 85, 189t, 199t
 mantle
 degassing rate, 573, 596, 597, 599f, 600
 marble cake structure, 349
 regassing rate, 597, 599f, 600
 mantle ascent velocity, 153, 155, 158, 158t, 160
 mantle avalanches, 391, 403, 454–457, 463, 466–469, 469f, 473, 626, 627, 629, 630, 658, 670, 770, 786, 788, 792
 modeling in three dimensions, 468
 mantle convection, 586, 696, 773, 788
 mantle creep, 215, 240, 393, 529
 mantle deformation by surface load, 216, 217
 mantle downwelling, 46, 113, 115, 391, 407, 408, 415, 456f, 466, 471, 645, 659, 774, 777–779
 mantle heat flow, 147, 150, 152, 588, 593, 599f, 602
 mantle heterogeneity, 103, 108, 113, 115, 232, 233, 234f, 237, 238, 239f, 344–347, 349, 350, 399, 408, 457, 462, 463, 470, 472, 514, 515, 770, 773, 775f, 777, 788, 926
 mantle layers, 113
 mantle mixing, 113, 344, 346, 347, 350, 550, 584, 781, 784, 789
 mantle mixing time, 345, 346, 349
 mantle outgassing and effects on rheology, 596
 mantle phase changes and layering, 390, 391, 393, 467, 469f, 470, 473, 474, 627
 mantle phase transitions on Mars, 470, 712, 713, 714f, 715, 716
 mantle plumes, 61, 94, 95, 409, 526f, 528f, 533f, 647, 767, 769, 770, 773, 778, 780–782, 784, 789
 and hot spots, 39, 41, 42, 354, 355, 499, 500, 502
 at base of lithosphere, 57, 142, 147
 breakup of Pangea, 61
 conduit waves, 533, 534
 core heat flow, 201, 610
 evidence from seismology and geoid, 514–519
 hot spot swells, 545
 hot spots, 153
 in three-dimensional mantle convection models, 457, 463, 466
 initiation as instability, 413
 interaction with endothermic phase change, 182, 183, 401–404, 769
 interaction with exothermic phase change, 182, 183
 isotope systematics of OIB, 580, 581
 lithospheric thinning, 143
 on Mars, 690, 710–713
 on Venus, 645, 648, 649, 678
 plume generation, 523, 537, 538
 plume heads, 528, 529
 plume heat flux, 635
 source region, 42, 94, 95, 403, 454, 509, 510, 514, 515, 518, 519, 528, 529
 temperatures, 533
 trailing conduit, 525, 527, 528
 mantle processing time, 344
 mantle reservoirs, 71, 344, 345, 547, 549, 550, 553–556, 558, 560, 561, 563, 570, 572–575, 577, 580, 581, 583, 584, 732f, 734f, 770, 781
 mantle stirring, 346
 mantle upwellings, 26, 28, 41, 104, 115, 153, 229, 230, 408, 415, 459, 495, 508, 645, 646, 709, 711, 713, 778–780
 mantle viscosity, 26, 250f, 267, 315, 472f, 492f, 512t, 704f, 769, 772, 773, 780, 783, 786–789
 and magma migration, 164, 165
 dependence on temperature, 129
 dependence on volatile content, 596, 598
 early estimates, 8–10
 Earth rotation, 214–217, 230–233
 geoid, 214–217, 235, 237–240
 in Earth thermal history models, 589, 591, 599f, 600t, 602, 606, 607, 611, 613, 614t, 616, 617
 increase at 660 km depth, 107
 increase with depth, 471–473, 482
 inverse methods, 237–240
 Io, 740, 742, 744
 laboratory experiments, 214–217
 lower mantle, 522, 523
 Mars, 703, 711
 Mercury, 753
 Moon, 727
 postglacial rebound, 214–217, 221, 223–225, 229
 radial profile, 215, 423, 424, 424f, 425, 426f, 667f
 self-regulation, 590
 strain rate weakening, 491
 temperature and pressure dependence, 393, 403, 425, 457, 461, 590, 591
 Venus, 644, 648, 649, 652, 664
 viscosity functions, 248–250
 mantle xenoliths, 80, 81, 94, 144, 151
 marble cake structure, 550
 mare basaltic volcanism, 639, 718, 736
 mare basalts, 639, 640, 719, 723, 724, 731–733, 735, 735f, 736
 marginal basins, 31, 31f, 38, 39, 39f, 128, 297
 maria, 716, 718, 723, 724

- Mars, 482, 587, 590, 633, 634, 634t, 635, 636, 636f, 638, 639f, 646, 657, 681, 681f, 682, 683, 683f, 684, 685, 685f, 686, 687, 687t, 688–691, 691t, 692, 694, 696, 696f, 697–700, 700t, 702f, 705–708, 710–712, 712f, 713–716, 728, 750, 771, 792–794
 Airy isostasy, 688, 697
 change in planetary radius with time, 693
 compensation of Tharsis, 688
 concentration of volcanism at Tharsis, 711, 712
 control of mantle convection by endothermic phase change, 712, 713
 convection and concentration of volcanism at Tharsis and Elysium, 711, 712
 convection and crustal dichotomy, 683, 692, 708, 711
 convection patterns, 708, 711, 713
 crustal differentiation, 691–694, 697–699, 707
 crustal thickness, 688, 690, 693, 697, 715
 depth to magma chambers beneath volcanoes, 689
 dynamo generation of magnetic field, 692
 effect of core size on mantle convection, 711, 716
 elastic lithosphere, 688–690
 endothermic spinel to perovskite and magnesiowüstite transition, 712
 evidence for hot, early Mars, 699
 extensional and compressional features, 688, 689, 698
 flexural rigidity, 689
 global contraction, 688, 696f, 698, 716
 global expansion, 688, 696f, 698
 Global Surveyor, 634
 heat flow and thermal gradients, 689, 690
 hemispheric dichotomy, 638, 640, 682, 683, 771, 794
 highly cratered terrain, 637, 682
 hypsometry, 640
 influence of core concentration on core thermal history, 716
 initially hot and differentiated, 691, 692, 699
 lithosphere thickening, 689, 692, 696f, 697, 699, 701, 702f, 707
 lithosphere thickness, 689, 690, 693, 696f, 697–699, 700t, 701, 702, 707, 708, 708f
 magnetic field, 692, 698, 699, 702, 703, 705, 706, 713, 715, 716
 mantle, 690, 691, 697, 699, 701, 706, 708, 709, 709f, 710–713, 715, 753, 771, 794
 mantle convection and phase transitions, 712, 714, 714f, 716
 mantle phase transitions, 470
 mantle plumes, 690, 709–713, 716
 mantle structure, 715
 mantle temperature vs. time, 694f
 northern hemisphere plains, 637, 640, 682–684
 perovskite in mantle, 712, 713, 715
 phase transitions and mantle convection, 712, 714
 radiogenic heat sources in mantle, 692, 702, 707, 708
 Rayleigh number of mantle, 708
 rheological lithosphere, 700, 701
 solidification of inner core, 702, 704f, 705, 705f
 southern hemisphere highlands, 637, 638f, 681f, 683, 692, 698, 699, 706
 subsolidus mantle convection, 692
 surface, 633, 637, 638, 794
 surface age, 637, 638
 tectonic patterns of deformation, 687
 Tharsis Montes, 685, 690
 Tharsis Rise, 637, 684–686, 688–690, 692, 698, 710–713, 716, 771, 794
 thermal contraction, 698
 thermal history, 625, 691, 694, 694–696f, 697–699, 700t, 701f, 703f, 704, 704f, 705, 707, 708f, 713, 715, 728, 754
 thermal history based on parameterization of stagnant lid convection, 706, 707
 thermal history of core, 699, 702, 703
 thermal lithosphere, 689, 700
 thermal stresses, 688, 689
 thickness of elastic lithosphere, 689, 690
 three-dimensional modes of convection in mantle, 708, 709f, 709t, 712, 713, 716
 topography, 640, 683, 686, 688, 689
 topography and mantle convection, 711, 716
 two-layer model of interior structure, 686, 687, 687t
 Valles Marineris, 681f, 685, 686, 691
 volcanic constructs, 637, 638f, 640, 689, 712
 volcanism, 633, 635, 771, 794
 wrinkle ridges, 688, 689, 698, 716
 mascons, 719–721, 771, 795
 mass extinctions, 545, 546, 770
 mass flux, 155, 252, 298, 299, 344, 467, 479, 510, 512, 533, 574, 660, 661, 661f, 671, 671f, 780, 781
 mass flux vector, 253
 massive eruptions, 525, 545, 546, 782
 flood basalt, 525, 770
 global change, 545, 546
 matrix compaction, 154, 161, 163
 matrix viscosity, 158t, 162
 Maxwell model, 212
 Maxwell relations, 261
 Maxwell time, 739, 743, 753
 Maxwell viscoelastic rheology, 739
 Maxwell–Boltzmann distribution, 241, 243
 mean age of crustal reservoir, 556
 mean field theory for spherical convection, 364, 366
 mean heat flux through upper mantle, 296, 297
 mechanical energy equation, 264
 mechanical lithosphere, 25, 26, 690
 mechanical strength of subducted slabs, 381, 390, 391, 396
 mechanical thickness, 77, 78f
 mechanically weak zones in plates, 389, 398
 melt ascent, 154
 melt fraction, 130, 153, 156, 156f, 161, 725, 792
 melt migration, 153, 154, 156, 159, 165, 166
 melt zone, 155, 157, 158, 158t, 159, 159, 160f, 161
 melting and dehydration of subducting slabs in the Archean, 630

- melting of early Earth, 587
 melting of silicate perovskite, 205
 melting temperature of core, 200, 202, 203, 608–610, 699, 703, 704
Mercury, 605, 633, 634, 634t, 749, 749f, 750, 751f, 752–756, 760, 771, 792, 793, 795
 compressional tectonics, 755
 crustal thickness, 750
 density, 752, 771, 792
 dynamo generation of magnetic field, 755, 756
 early core differentiation, 750
 effects of tidal dissipation on thermal history, 753
 energy balance of inner core, 752, 753
 energy balance of outer core, 752, 753
 equatorial center of figure–center of mass offset, 750
 equatorial ellipsoidal shape, 750
 equatorial topography, 750
 geologic constraint on core freezing, 755
 giant impact, 752
 gravity, 753
 growth of solid inner core, 754, 755
 lithosphere thickening, 755
 lithosphere thickness, 755
 lobate scarps, 755
 magnetic field, 750, 754–756, 771, 793
 Maxwell time in core, 753
 metallic core, 749
 planetary contraction, 755
 subsolidus mantle convection, 755
 thermal contraction, 756
 thermal history, 634, 634t, 750, 753, 754, 754f, 755, 756
 tidal dissipative heating in solid inner core, 753, 755, 756
 viscosity of mantle, 753
metamorphism, 47, 636
metastability of olivine–spinel phase change, 184, 185
meteorite impact hypothesis for K/T extinctions, 545
mid-Atlantic ridge, 12, 13, 15f, 104, 508, 579, 581f, 776f
mid-ocean ridge, 12, 15, 23f, 47, 52, 207, 344, 349, 354, 495, 499, 508, 512, 543, 547, 549, 597, 645, 710, 711, 768, 773, 778, 779
 underlying mantle structure, 83, 104
mid-ocean ridge basalt (MORB), 69, 508
midplane symmetry, 418, 428, 432, 444
minimum Rayleigh number for convection onset, 427, 439
missing lead paradox, 571
Moho, 63, 64f, 66, 68, 72–76, 79
Mohorovicic seismic discontinuity, 64f
moment of inertia, 66, 215, 230, 231, 686, 687, 726, 741, 756, 760
Europa, 756
Ganymede, 760
Io, 741
Mars, 686
Mercury, 750
 momentum diffusivity, 266
 Monte Carlo inversion, 239, 239f
 Monte Carlo simulations, 637
 Moon, 314, 315, 587, 633, 634, 634t, 635, 636, 636f, 637, 638, 638f, 639, 639f, 640, 646, 654t, 681, 685, 716–723, 723f, 724, 725, 725f, 726–728, 728, 729f, 730, 731, 731f, 733, 735–737, 756, 771, 792, 794, 795
 chemical stratification, 718, 736
 Clementine, 634
 comparison with Galilean satellites, 739
 convection, 590, 640, 722, 727–729, 735, 736
 depth of magma ocean, 718
 differentiation
 lunar mantle, 727, 733
 distribution of surface ages, 638, 717
 dynamo, 726, 727
 evolution, 638, 639
 flotation of plagioclase crystals in magma ocean, 718
 formation, 726, 728, 733, 735
 formation of lunar highlands, 638, 717
 giant impact hypothesis for origin, 587, 727
 gravity, 719–721, 723f, 725f, 726
 hemispheric dichotomy, 636, 638f, 640, 719, 722
 hypsometry, 640, 719
 Imbrium Basin, 723, 724, 727
 impact basins, 639, 640, 683, 717f, 719, 723, 726
 infilling of mare basins, 719
 lead depletion, 734, 735
 lithosphere thickness, 729, 730, 730f
 Lunar Prospector, 634
 magnetic field, 726, 727
 mantle convection and isotope data, 735
 maria, 716, 718, 723, 724
 origin, 727, 731, 735
 potassium, 718
 rubidium depletion in lunar rocks, 735
 rubidium enrichment in KREEP basalts, 733
 rubidium–strontium system and lunar rocks, 735
 South Pole Aitken basin, 640, 719, 721, 721f
 subsolidus convection, 727
 surface age distribution, 638, 639, 717
 surface heat flow, 594
 thermal contraction, 731
 thermal history, 718, 727, 728
 thermal history with crustal differentiation, 728
 topography, 640, 716, 719, 721, 721f
 uranium, 734
 uranium–thorium–lead system, 733
 MORB, 71, 154, 571, 572f, 581, 582f, 583, 584, 733, 735, 770
 E-type, 154, 653, 654t
 formation by partial melting, 69, 80, 82, 153
 geochemical reservoirs, 549–551
 isotope ratios, 350
 lead isotopes, 568, 570, 571
 N-type, 154, 580, 583, 653, 654t
 parent material, 71

- MORB (*cont.*)
 rare gases, 573, 578
 relation to hot spot basalts, 508, 579, 580
 source region, 71, 82, 154, 349, 781, 784
- MORB (I), 580
- mountain building, 8
 mountain ranges, 1, 2, 12, 23f, 72
 Murnaghan equation, 277, 455, 477
- Navier–Stokes equations, 255–258, 269, 272, 273, 281–284
 negative buoyancy, 25, 52, 184, 356, 382, 399, 464, 658, 671, 774, 778, 786
 neodymium–samarium system and lunar rocks, 732f, 735
 neovolcanic zone, 153
 Newton's second law of motion, 254
 Newtonian viscous fluid, 168, 213, 243, 247, 248, 255, 262, 263, 404, 405f, 412, 438, 491, 769, 789
 Newtonian–Stokesian fluid, 256
 Niger Rift, 57
 nodal lines of Y_l^m , 325
 nonhydrostatic geoid, 232, 234f, 237, 470, 770
 nonlinear viscosity and plate behavior, 389
 non-Newtonian convection, 405, 619, 623, 706
 non-Newtonian fluid, 248
 non-Newtonian viscosity, 227, 404, 405f, 789, 790
 nonrigid rate of deformation, 255
 normal mode, 66, 98, 103, 518
 normal mode frequency, 66, 98, 102
 normal MORB, 549, 550, 584
 normal stresses, 255, 256
 normalized isotope ratio, 553t
 Nusselt number, 389f, 395f, 422f, 427f, 439f, 706
 definition, 334
 Earth, 673
 in boundary layer analysis of cellular convection, 358
 in boundary layer stability analysis, 352, 353
 in Earth thermal history model, 589, 625
 in mean field approximation, 364, 364f, 366
 in three-dimensional convection, 419, 425
 in two-dimensional convection at high Ra , 379, 381
 in weakly nonlinear stability theory, 370
 temperature-dependent viscosity, 394, 617
 Venus, 664
 Nusselt number–Rayleigh number relation, 370, 381, 425, 589, 596, 617, 672, 673, 700t
 sluggish-lid convection, 590
 stagnant-lid convection, 590
 temperature-dependent viscosity, 425, 673
 NUVEL-1 model of plate motions, 48, 49, 49t, 50f, 51
 NUVEL-1A model of plate motions, 49, 49t
- ocean basin area, 128
 ocean basins, 13, 52, 79, 141, 515, 597, 599f, 630
 area, 600
 development and plate tectonics, 42
 equilibrium depth beneath ridge crests, 141
- evolution, 13
 geoid anomaly, 505
 geoid height, 148, 149, 150f
 high shear wave velocities, 103
 hot spots, 505
 LVZ, 78
 origin, 1
 subsidence, 136
 systematic variations in LVZ structure, 77
 topographic flattening, 151
 variable density, 505
 volume, 597
- ocean crust, 19f, 28, 29, 31, 31f, 43, 45–47, 52, 57, 59, 60, 64f, 70f, 82, 127, 136f, 149, 152, 166f, 349, 409, 495, 586, 597, 635, 636f, 639, 656, 692, 695, 716, 777, 779, 792
 age, 15f, 16
 argon flux, 577
 as part of oceanic lithosphere, 25
 at hot spots, 153, 154
 creation, 13, 15, 160, 165, 166, 344, 547
 creation in back-arc basins, 37, 38, 180
 exposed at surface, 75, 76
 geochemical reservoirs, 547–550, 561, 583
 heat loss, 132, 134
 heat production, 130
 helium flux, 574, 577
 hydrothermal circulation, 132, 134, 577
 layer 1, 70, 70f
 layer 2, 70f, 71
 layer 3, 70f, 71
 melting and dehydration on subduction, 37, 38, 177, 180
 mixing with mantle, 349, 350
 properties, 69t
 rate of production, 153
 structure and composition, 69–72
 thickness, 74, 344
 ocean island basalts (OIB), 508, 549, 550, 568, 571, 572f, 573, 577, 579, 580, 581, 582f, 582–585
 ocean trenches, 15, 16, 25f, 31, 32f, 45–47, 49, 635, 636, 774, 778
 and transform faults, 29
 crustal recycling at, 548
 earthquakes, 29, 31
 elastic bending, 26
 marginal basins, 39
 subduction, 22, 25, 31, 33, 52, 143, 177
 trench rollback, 39
 Venus, 641, 647
 volcanic lines, 36
 volcanism, 130, 177
 oceanic heat flow, 127, 128, 143, 297, 507
 oceanic lithosphere, 29, 31, 31f, 37f, 45, 47, 78f, 147, 215, 399, 543, 580, 636, 768, 769, 774, 777, 779, 780, 782, 783
 basal heating, 139, 142, 143, 151
 cold upper thermal boundary layer, 16, 26, 127

- oceanic lithosphere (*cont.*)
 compositional stratification, 82
 definition, 25
 deformation, 73
 deformation at subduction zones, 33, 34
 elastic, 26
 frictional heating on subduction, 180
 geoid, 132, 137–139, 141
 initiation of subduction, 59
 magma migration, 166
 mechanical, 25, 26
 Peclét number, 132
 relation to seismic LID, 76
 remixing into mantle, 549
 seismic evidence for subducted lithosphere, 108
 seismic LVZ, 151, 152
 temperature, 176
 temperature distribution, 132, 133, 134f, 135, 178, 410f
 thermal, 26
 thermal model, 119, 123, 131, 132, 135
 thermal properties, 207, 210, 211
 thickness, 25, 102, 131, 135, 412, 413
 Venus, 647
 viscosity, 240, 248
- oceanic ridges, 13, 15, 16, 22, 25f, 27, 28f, 148f, 149, 158f, 636, 657
 and back-arc spreading, 38
 and hot spots, 499
 geoid anomaly, 137, 141
 helium loss, 574, 577
 isotope ratios, 580
 magma migration, 160, 161, 165, 166
 magmas, 153
 magnetic profiles, 14f
 melting and isotope ratios, 550
 MORB, 350
 partial melting and depletion of incompatible elements, 130
 processes at, 26–29, 344
 structure, 160
 thermal model, 132, 135
 topography, 141
 oceanic spreading rate, 60
 ohmic dissipation, 610, 705
 olivine, 90, 192f, 301, 405f, 768, 788
 α phase, 84, 85, 90, 189t, 199t
 deformation, 246
 heat production, 654t
 in pyrolite, 81t
 in transition zone, 84–86
 mantle mineral, 69, 80–82
 metastability in descending slab, 185, 186
 Moon, 718, 723
 MORB, 71
 phase diagram, 84
 rheology, 246, 248
 seismic velocities, 189t
- thermal diffusivity, 211
 thermal properties, 190t
 transition to spinel, 35, 84–86, 185, 186, 518
 in descending slab, 180, 181
 model of flow through phase transition, 193
 olivine–spinel phase transformation, 84, 85, 181, 182f, 185f, 193f, 391f, 769, 788, 794
 divariant model of phase transition, 198
 in descending slab, 180, 183, 184
 mantle avalanches, 463
 Mars, 470, 713
 metastability in descending slab, 184, 185
 phase buoyancy parameter, 463
 stability of plane layer with phase transition, 297, 298, 300–303
 Venus, 470
- Olympus Mons, 637, 685, 689, 690, 697
 one-dimensional time-dependent heat conduction, 119
 onset of convection, 3, 9, 301, 302f, 314t, 443f, 448f, 450f, 453f, 620f, 708
 in fluid spheres and spherical shells, 308
 in Galilean satellites, 764
 in plane layer with phase transition, 302
 in spheres and spherical shells, 418, 422, 422t, 427, 478
 in spherical shell heated only from within, 318
 in uniformly heated sphere, 313
 in uniformly heated spherical shell, 316
 linear stability analysis, 288–290, 310
 minimum critical Ra , 294, 295, 378, 379, 381, 439–441, 589
 onset of thermal instability, 519, 520
 opening of ocean, 57, 58f, 636
 ophiolites, 166, 172, 246, 550
 orogens, 73
 orthopyroxene, 81, 81t, 189, 190t, 199t, 246, 723, 736
 outer core, 64f, 101f, 770
 adiabaticity, 127
 coriolis forces, 254
 interaction with lower mantle, 549
 Mars, 702, 704, 708
 Mercury, 753, 755, 756
 properties, 69t, 98–100
 seismic evidence for, 97
 seismic models, 66
 temperatures, 200, 201f, 203, 204
 thermal evolution, 603–605, 609, 610
- P-wave, 65, 66, 76, 83f, 84, 85, 95, 97–99, 103, 108, 109, 109–111f, 112, 112f, 113, 116f, 117
 paired belts of deep seismicity, 33
 paleomagnetism, 11
 Pangea, 60, 61, 408, 546
 breakup of, 60, 408, 546
 parameterized convection, 353, 425, 586, 590, 594, 617–619, 623–625, 674f, 727
 internal heating and strongly temperature-dependent viscosity, 707

- parameterized convection (*cont.*)
 strongly temperature-dependent viscosity, 425
- partial melt fraction, 130, 153, 156, 156f, 159, 159f, 161, 725
- partial melting, 83f, 782, 783
 basalts, 349
 beneath spreading centers, 153
 concentration of incompatible elements, 547, 548
 D'' layer, 97, 205, 206, 414
 degree of, 513
 flood basalts, 536
 in mantle plumes, 580
 in mantle wedge above descending slab, 38, 47
 in plume heads, 61
 Io, 745
 LVZ, 78, 97, 151–153
 magma migration, 155–160, 164
 mantle, 68, 69, 80, 82, 83, 158f, 160f, 206f, 516
 mantle rheology, 248
 Mars, 697
 Moon, 718, 723, 732, 733
 MORB, 508, 653
 pressure release melting, 458, 508, 513, 549
 ridges, 104, 151–153, 191
 subduction zone magmatism, 180
 ULVZ, 510
- partial subduction, 45, 647
- particle and line method, 347
- particle paths, 253, 333, 346, 347
- passive continental margins, 58, 59, 72, 787
- passive rifting, 153
- passive spreading centers, 492, 495, 778
- passive upwellings, 778, 779
- patterns of convection in spherical shells, 381, 427, 474
- Peclet number, 132, 133, 178, 188, 199, 386, 388, 389f
- Peierls flow, 389
- PEM, 68
- peridotites, 38, 73–75, 80–82, 84, 130, 131t, 144f, 152, 152t, 190t, 199t, 349, 508, 725
- peripheral bulge, 228, 229
- peripheral trough, 228
- permeability, 154, 155, 161, 162
- perovskite, 91f, 400, 463, 788
 dynamical effects on phase transition, 184t, 302, 455
 in descending slab, 180, 182
 in lower mantle, 88–91, 94
 in Mars mantle, 712, 713, 715
 mantle avalanches, 455, 458
- melting temperatures, 204, 205, 205f
- phase transition from spinel, 35, 191
- properties, 189–191t, 199t
- rheology, 248
- subsolidus temperature, 96
 thermal properties, 207, 209, 211
- perturbation quantities, 288–290
- phase buoyancy parameter, 300, 457, 463
- phase change instability, 297, 390
- phase changes and driving force for mantle convection, 199
- phase changes and layering, 390, 391, 393, 467, 469f, 470, 473, 474, 627, 657, 769, 770
- phase portraits, 334
- phase transformation, 84–88, 94, 128, 184, 185, 185f, 190–192, 192f, 193, 193f, 196, 199, 199t, 200, 687, 788, 794
- endothermic, 87, 88, 107, 180–182, 182f, 183, 184t, 192, 199, 200
 exothermic, 88, 182f, 184t, 192, 199, 200
- phase transitions and Martian mantle convection, 714f
- physics of mantle creep, 240
- pillow basalts, 70, 70f, 166
- ping-pong ball analogy, 36, 777
- pitchfork bifurcation, 333, 335, 335f, 339, 340, 341f
- PKIKP, 97
- PKJKP, 98
- planetary interiors, 426, 715, 793
- plate generation in models of mantle convection, 488
- plate margins
 accretional, 26
- plate tectonic indentor, 59
- plate tectonics, 75, 633, 657, 768, 770, 771, 773, 783, 793, 794
 and Earth thermal history, 590, 617
 and mantle plumes, 41
 basic description, 16, 22, 25, 42
 driving force, 52
 Earth comparison with Venus, 641, 644
 Europa, 633
 Ganymede, 633
 geochemical cycling, 547, 549
 history, 8, 15
 initiation of subduction, 396
 Mars, 640, 657, 682, 711
 plate deformation, 69
 relation to mantle convection, 354, 360, 376, 488, 489, 495, 498
 relation to seismic tomography, 104
 time dependence, 57
- Venus, 635, 640, 641, 644, 647, 648, 650, 652, 657, 669, 671, 672, 675
- Wilson cycle, 57, 62, 62f
- plate-like rheology, 488, 489
- plateau uplifts, 45
- plates, 17f, 25f, 27, 28f, 30f, 36, 50f, 51, 114, 228, 232, 388f, 470, 471, 489, 500t, 509, 538f, 542f, 548, 626, 635, 657, 673–675, 677f, 711, 768–770, 773, 776f, 778, 779, 781–788, 791, 792
- African plate, 646
 and Earth thermal history, 590, 617
 and mantle plumes, 41
 area, 22, 52
 basic properties, 16, 22, 25
 boundaries, 16, 17, 18f, 22, 48, 52, 57, 153, 229, 230, 257, 657, 664, 773, 774, 781, 785, 786
- accretionary, 22

- plates (*cont.*)
 boundaries (*cont.*)
 and hot spots, 533
 convergent, 29
 incorporation in mantle convection models, 388–390
 plate-like in mantle convection models, 498
 stresses at, 26
 transform, 28
 cold thermal boundary layer, 359
 deformation of, 51, 61
 dimensions, 53t
 driving forces, 27, 31, 54, 55
 flux, 61, 636
 frictional heating on slip zone, 176–180, 181f
 geometry, 48, 49t, 177f, 385, 389, 657, 787
 heat flux, 178
 hot spot swells, 514, 516
 and lithosphere thinning, 506, 507
 in mantle, 113
 incorporation in mantle convection models, 377, 381, 385, 387–390
 initiation of subduction, 396, 398
 interaction with plume, 537–541, 543, 545
 Mars, 657
 Moon, 731, 735
 motions, 16, 25, 41f, 48, 52, 53, 55, 56, 56f, 59, 385, 389, 491, 501, 502, 507, 513, 533, 537, 540, 541, 626, 675, 775, 776f
 in inversions for mantle viscosity, 237, 238
 relation to seismic tomography, 104
 true polar wander, 232
 plate velocity and mantle convection, 388
 plate-like behavior in mantle convection models, 491, 492, 495, 497
 processes at plate margins, 26–29, 31
 relation to mantle convection, 417
 rheology, 489
 rotation, 48
 seismic anisotropy, 77, 106
 temperatures of, 132, 139, 141
 thickness, 139
 Venus, 674f, 676
 platforms, 72f, 73, 74, 74f, 78, 101
 Pleistocene ice sheet, 224
 plume conduit, 423, 424, 499, 516, 518, 527–529, 533, 537, 540
 cross-sectional area, 525, 527, 535
 radius, 527, 530, 532, 536, 545
 thermal halo structure, 516, 529, 530
 waves, 533, 534, 534f, 535–537, 538f
 plume upwellings, 42, 61, 182–184, 381, 401, 418, 427, 432, 436, 441, 444, 449, 454, 457, 464, 470, 479, 480, 482, 483f, 486, 487, 495, 510
 plume–ridge interaction, 543, 545
 plumes
 approximate model of thermomechanical structure, 506
 ascent through mantle, 527, 528
 buoyancy flux, 510, 511, 532, 533f, 785
 centerline temperature anomaly, 531, 532
 centerline viscosity, 531
 density deficit, 511, 512t, 540
 entrainment, 523, 527, 528
 flux, 61, 62, 510–512, 532, 533, 533f, 539, 649
 formation, 518–520, 521f, 523, 529, 770, 773
 haloes, 427, 428, 516, 529
 heads and partial melting, 61, 782
 heat transport, 45, 452, 510, 512, 540, 610, 770, 780
 impingement on lithosphere, 506, 537
 incipient, 520
 instability, 518–520, 536, 648, 649, 709, 780, 781
 interaction with an endothermic phase change, 401
 leading diapir or plume head, 525
 lubrication of plates by hot plume material, 626
 mass flux, 510, 512, 533
 penetration through entire mantle, 532
 radius of conduit, 527, 530, 532, 536, 545
 radius of head, 527
 spreading beneath lithosphere, 507, 516, 517, 538
 steady axisymmetric structure, 529
 terminal ascent speed, 525
 thermal halo, 516, 529, 530, 532, 780
 transience, 384, 405, 519, 520
 volumetric flux, 511–513, 543
 waves, 528, 533, 534, 534f, 535–537, 538f
 point defects, 241f
 Poiseuille flow, 525, 535
 Poisson equation, 66, 279, 484
 Poisson’s ratio, 98, 168, 688
 polar wander, 11, 12, 232, 232f
 polarity, 12–14, 60f, 698
 pole of rotation, 48, 48f, 51, 51f, 501
 poloidal components, 328, 490
 poloidal energy, 487
 poloidal motion, 57, 779
 poloidal scalar, 311
 poloidal vector field, 311, 328
 poloidal velocity field, 311, 312
 polytropic index, 278, 455, 477
 porosity, 154, 155, 157, 158t, 159, 161, 161f, 162, 164, 165
 porous flow, 154, 155, 165
 position vector, 252
 postglacial rebound, 213–216, 218f, 221–223, 228, 237, 237t, 238, 247, 249, 250
 relaxation time, 221, 223
 potassium, 69, 128–131, 146, 306, 577, 578, 594, 634, 654t, 772
 ^{40}K , 573, 577
 Earth, 69, 128, 577, 578, 594, 772
 Venus, 644
 potential temperature, 82, 154, 190, 191f, 508, 673
 power-law viscosity, 389, 398, 404, 707, 790
 Prandtl number, 266, 267, 269, 273, 331, 336, 337, 343, 353, 361, 367, 370, 371, 380f, 474

- Pratt compensation, 505, 688
 pre-exponential factor, 243, 246f, 404
 precursor thermal boundary layer, 192, 193, 197, 198
 PREM, 67, 67f, 68, 68f, 79, 90, 91f, 93, 95f, 96, 100, 101f, 103, 104, 105f, 110f, 231, 455, 477
 pressure forces, 254, 256, 264, 266, 281
 pressure-release melting, 28, 36, 38, 165, 508
 primeval lead, 567
 primordial component, 350, 571, 580, 781
 primordial helium, 574, 584
 pristine reservoir, 550, 571, 573, 580, 583, 584
 pure shear, 346, 347, 349
 pyrolite, 80, 81t, 82, 88, 205, 725
 pyroxenite bands, 349
- quality factor Q , 68, 78
- radial correlation function, 392, 476, 476f
 radial mass flux diagnostic, 466, 467
 radioactive daughter isotope, 551, 552, 565
 radioactive decay, 129, 144, 146, 382, 551, 555, 577, 579, 593, 634, 658, 693
 radioactive elements, 61, 61f, 100, 125, 128, 130, 297, 586, 588, 718, 736
 radioactive isotopes, 61, 129, 129t, 130, 131f, 306, 344, 594, 644, 672, 772, 793
 radioactive parent isotope, 551, 552, 552t, 565
 radioactivity, 145, 587, 588, 591, 592, 594, 698, 716, 755
 radiogenic gases, 548
 radiogenic heating, 129, 146, 486, 593, 594, 615, 675, 691, 708, 736, 772, 795
 radiogenic helium, 574
 radiogenic noble gases, 573, 579
 rare earth element distributions, 154, 653
 Rayleigh number, 289, 291, 330, 333, 334, 378, 379, 381, 382, 384, 390, 392, 394, 395, 405, 406, 412, 455, 470, 472–474, 518, 599f, 606, 624, 665f, 772
 bifurcations of Saltzman equations, 337, 339, 340, 342, 343
 boundary layer Rayleigh number, 519, 520
 critical Rayleigh numbers, 294f, 296t, 301, 302f, 314t, 318, 319t, 320, 321f, 321t, 324f, 334
 definition, 269, 273
 Earth's early mantle, 586
 for variable viscosity convection, 393, 666
 for whole mantle convection, 378, 772
 Galilean satellites, 764
 in boundary layer analysis of cellular convection, 357–360
 in boundary layer stability analysis, 350–353
 in compressible convection, 478t, 479, 482
 in convection models with plate-like rheology, 491, 497
 in Earth thermal history models, 589, 595, 601, 606, 613, 627
 in single-mode mean field approximation, 364
 in three-dimensional convection, 417, 418, 422–425, 427, 428, 432, 435, 435f, 437f, 443f, 447, 448f, 450f, 453f, 469f, 483f, 490f
 unsteady, asymmetric, 439–441, 445, 449, 452
 in two-dimensional numerical models of convection, 380f, 383f, 388f, 395f
 in weakly nonlinear stability theory, 367, 368, 373, 375
 internal heating, 270, 273
 internally heated sphere, 312, 314
 Mars, 700t, 708, 713, 714, 715f
 plane layer heated from below, 293–297
 with univariant phase change, 300–302
 plane layer heated from within, 304, 306, 307
 spherical shell heated from below or from within, 318–322
 temperature-dependent viscosity, 392–394, 394, 395f, 410f, 423f, 425f, 427f, 471, 599f
 critical Rayleigh number, 422t
 for Mars, 706
 in Earth thermal history models, 589, 590, 606, 617–619, 623–625
 spherical shells, 425, 428
 subducting slabs, 395, 396
 upper mantle convection, 296, 297, 336
 Venus, 648, 658, 664, 666, 667, 669, 671
 whole mantle convection, 306, 336
 Rayleigh waves, 66, 76, 77
 rebound from load of ice during last ice age, 10
 rectangular patterns of three-dimensional convection, 417, 432
 recycling, 44, 45, 548, 556, 561, 563, 564, 571, 572, 578, 579, 584, 630, 636, 655, 692, 745, 767, 792, 933
 continental crust, 43–46, 548, 556, 561–564, 564f, 565, 584, 630–632
 Red Sea, 57
 reduced heat flow, 132, 144
 regassing, 596, 597, 601, 601f, 602
 relative sea level, 216, 224, 226f, 231
 relative velocity at a point, 255
 relative velocity between plates, 16, 48f, 49t, 51, 51f
 relaxation spectrum, 231
 relaxation time scale, 237
 remanent magnetism, 635, 691, 698, 705, 706, 716, 726
 residual solid matrix, 154
 retrograde trench migration, 397, 398, 461, 462
 and slab penetration of 660 km phase change, 397, 398, 461, 462
 Reunion hot spot, 499, 500t, 501f, 509, 509f, 511t, 527, 527t, 541t
 reversed polarity, 12, 14f
 reversible process, 259, 260
 reversible work, 259, 264
 Reynolds number, 169, 173
 rheological law, 213
 rheological sublayer in stagnant-lid convection, 623

- rheology of subduction, 33
 ridge-centered hot spots, 508, 543, 545
 ridge–ridge transform, 28f, 29
 ridges
 axes, 13, 16, 17f, 27f, 165
 crest elevation, 27, 28
 jumps, 29
 push, 27, 52, 53
 segments, 28, 29, 48, 48f, 52, 59
 subduction, 58f, 59, 626
 volcanism, 28, 165
 volume, 27, 60, 61
 rifting, 57, 58, 678, 686, 782
 continental, 52, 57
 passive, 57, 153
 rigid body rotation, 255
 rigid lid, 387, 393, 489, 617, 657, 672
 rigid plates, 16, 36, 48, 50f, 51, 52, 55
 rigidity, 26, 33, 36, 55
 roots, 2, 10, 78, 79, 103, 104, 212, 334, 645, 768
 rubidium–strontium system, 555, 556, 571, 584, 733, 735
- S-wave, 65, 66, 77, 78, 79f, 82, 83f, 95, 103, 104, 105f, 107, 108f, 109, 110, 111f, 112, 112f, 113, 114–116f
 saddle bifurcation, 340
 St. Helena, 500t, 501f, 511t, 550, 581f, 583
 St. Helena (IV), 582
 St. Lawrence River Valley Rift, 57
 Saltzman equation, 331, 337
 samarium–neodymium system, 555, 556, 563, 584, 731, 733, 735
 fractionation factor, 564, 731, 732f
 isotope ratio, 731, 732
 San Andreas fault, 29, 30f, 51, 59
 scaling laws for heat transport and velocity, 379
 screw dislocation, 242, 242, 243f
 sea level variations, 59, 60f, 61, 61f
 Sea of Japan, 38
 seafloor spreading, 9f, 10, 12, 13, 14f, 15, 16, 22, 29, 38, 59, 132, 133f, 143, 153, 158, 166
 rate, 13, 16, 27, 60, 60f
 seafloor swells, 499, 537
 seamounts, 550, 551
 sedimentation, 73
 seismic discontinuities
 20°, 84
 410 km depth, 64f, 82, 84–86, 92, 191t, 193, 198, 204, 248, 776f, 788
 520 km depth, 92
 660 km depth, 31, 64f, 85–90, 90f, 92, 106, 107, 113, 193, 198, 199, 204, 248, 336, 397, 473, 550, 611, 768, 774, 776f, 784, 785, 788
 Conrad, 73
 seismic layers, 64, 66, 67, 69, 71, 113
 crustal, 73
 D'' layer, 97
- seismicity
 depth of termination, 35, 87
 shear localization, 490, 491
 shear modulus, 65, 68f, 168, 739, 742, 743, 753, 754
 shear stress, 168, 169, 178, 255, 379, 422, 474, 528
 on slip zone, 177–180
 shear wave velocity, 65, 66, 79f, 82, 83f, 95, 104, 105f, 107, 108f, 110f, 112, 114–116f, 152, 392, 515, 516, 517f
 shear zones, 165, 490, 491
 sheet-like downwettings, 423, 424, 436, 446, 471, 498
 sheeted dike complex, 70, 70f, 71
 shields, 72f, 73, 74, 78, 82, 101, 104, 501, 537, 685
 Archean, 72, 74f, 151
 Canadian, 76f, 104, 144, 145f
 continental, 143
 Mars, 685, 689
 Proterozoic, 74f
 silicic composition, 43, 44, 47, 48, 64f, 71, 656
 silicic crust, 25, 43, 44, 47, 48, 64f, 69, 71, 74
 silicic volcanism, 71
 similarity solution, 119, 166, 179, 529
 similarity variable, 119, 122, 123
 SKS, 96, 509, 510
 slab deflection, 92, 107, 108
 slab dip, 38, 185, 777, 778
 slab penetration through 660 km discontinuity, 35, 88, 398, 461, 767, 786
 slab pull, 31, 52, 53, 711, 773, 788
 slip
 dislocation, 242, 243, 244f, 763
 slip zone, 176–180, 181f
 sluggish-lid convection, 426, 427, 470, 498, 590, 617–619, 620f, 621, 621f, 665, 666, 673
 Venus, 664, 666, 672, 673
 small viscosity contrast convection, 426, 590, 619, 620, 621f, 625, 664–666, 672–674, 674f, 675
 small-scale convection, 413, 414, 416, 457
 Snake River Plain, 501f, 505, 516
 SNC meteorites, 690, 691, 699, 702, 715, 716
 snowplow model, 59
 Society (V), 581f
 soft turbulence, 382, 384, 627
 solar system
 age of, 566
 solenoidal velocity, 252
 solid–solid phase transitions, 102, 128, 184, 191, 192f, 248
 solid-state creep, 596
 solidification boundary, 123, 124
 solidification of magma, 123f, 125f, 166, 174–176
 solidification of semi-infinite half-space, 123
 solidus, 78, 83, 152, 153, 160f, 161, 174, 178, 180, 199t, 205, 205f, 508, 587, 588, 613, 655, 673
 solidus temperature, 28, 38, 96, 152, 153, 156, 160, 178, 179, 205, 473, 613, 614t, 615, 615f, 616, 699
 solitary waves, 161, 528, 533, 535, 536
 duration of, 536

- South Kerguelen Plateau, 506f
 specific enthalpy, 260
 specific entropy, 263
 specific Gibbs free energy, 260
 specific heat, 209, 260
 specific heat at constant pressure, 156, 194, 196, 259
 specific heat at constant volume, 209, 259
 specific Helmholtz free energy, 260
 specific internal energy, 259
 specific volume, 259
 spectral content of mantle convection, 471, 472
 spectral-transform technique, 417
 spherical Earth model, 66, 67, 67f, 68, 68f, 92–94, 96, 98, 102, 104, 105f, 110f
 spherical harmonics, 103, 104f, 106, 113, 114, 114f, 117
 spherical polar coordinates, 252, 252f, 253, 255, 256, 264, 280, 281, 283, 285–287
 spheroidal oscillations, 66
 spinel
 β phase, 35, 84, 85, 92, 189t, 198, 199t, 200, 204, 463, 713
 γ phase, 85, 88, 89, 92, 189t, 199t, 200, 204, 713
 spinel lherzolite, 81
 spoke pattern of convection, 440, 442f, 447f, 449
 spreading centers, 39
 spreading rate, 13, 16, 27, 49, 50f, 60, 60f, 132, 153, 344, 502, 550, 597
 stagnant lid, 436f, 783, 789
 Galilean satellites, 765
 heat flow–Rayleigh number parameterization with strongly temperature-dependent viscosity, 619, 623–625
 in Earth thermal history models, 590, 617
 in fluid with depth-dependent viscosity, 308
 in fluid with temperature-dependent viscosity, 393
 spherical shells, 426
 in rectangular boxes with temperature-dependent viscosity, 432, 435
 in three-dimensional convection with strain-rate-weakening rheology, 492
 in three-dimensional convection with strongly temperature-dependent viscosity, 664
 in three-dimensional convection with temperature- and strain rate-dependent rheology, 497
 Mars, 706
 Venus, 470, 664, 673, 676, 677
 stagnant-lid convection, 707f, 783, 787
 heat flow–Rayleigh number parameterization with strongly temperature-dependent viscosity, 625
 in rectangular boxes with temperature-dependent viscosity, 432
 in spherical shells with temperature-dependent viscosity, 425
 in three-dimensional convection with strongly temperature-dependent viscosity, 665
 in three-dimensional convection with temperature- and strain rate-dependent rheology, 497, 498
 Mars, 706, 707
 Venus, 498, 673, 677
 stagnant-lid deformation, 773
 state variable, 64, 259, 260
 steady tetrahedral convection in spherical shell, 421, 427
 Stefan problem, 123
 stishovite, 80, 85, 88, 89f, 189t
 Stokes assumption, 256
 Stokes diapir, 536
 Stokes velocity, 521
 Stokesian fluid, 263
 strain evolution, 348, 348f
 strain markers, 346, 348
 strain rate, 256, 347–349, 763, 764
 strain rate tensor, 255, 282, 346
 strange attractors, 335
 stream function, 388f, 405f, 468
 definitions, 253
 in boundary layer analysis of cellular convection, 356
 in convection with non-Newtonian viscosity, 404
 in deformation of half-space by internal load, 235
 in deformation of half-space by surface load, 218, 219
 in eigenmode expansions, 331, 337
 in Lorenz equations, 333
 in onset of convection in plane layer heated from below, 292
 in onset of convection in plane layer heated from within, 305
 in semi-infinite fluid with depth-dependent viscosity, 308
 in two-dimensional convection models, 378, 383, 384f
 momentum equation in terms of stream function, 257, 258, 274
 streamline, 133f, 253, 314, 315f, 319f, 322–324f, 333, 347, 347f, 380f, 397f, 536
 stress intensity factor, 168–171
 stress singularity at crack tip, 169
 stress–strain rate relation, 256
 subducted slab, 87, 92, 102, 106, 107, 109, 112, 115, 192f, 237, 390, 399, 407, 414, 768, 777
 subducting slab, 176
 subduction, 25f, 31f, 34f, 43, 58f, 60f, 399, 408, 409, 411, 470, 635, 636, 647, 783, 786, 787
 analogous to convection model downflows, 354, 360, 376, 390, 396–398, 495, 497, 498, 498f
 and olivine metastability, 185, 188
 and recycling of continental crust, 47
 as heat loss mechanism, 176
 buoyancy, 73
 crustal subtraction, 629–631
 driving forces, 53
 episodic, 353
 general discussion, 29, 31, 33, 34
 geochemical heterogeneities, 345, 350
 geochemical recycling, 551, 565, 579, 584

- subduction (*cont.*)
 geoid anomalies, 215
 loss of surface area at ocean trenches, 13, 15, 22
 partial subduction of oceanic continental crust and lithosphere, 45
 rate of subduction of oceanic crust, 52
 regassing of mantle, 596, 597
 retrograde trench migration, 461
 role of oceanic crust in subduction zone volcanism, 38
 slab penetration into lower mantle, 106–108
 thermal instability, 142, 143, 308
 Venus, 646, 647, 649–651
 Wilson cycle, 57–61
 subduction zones, 17f, 25f, 31f, 78f, 92, 180, 399, 400, 409, 656, 657, 670, 767, 768, 776f, 777–779, 786, 787
 analogues in convection models, 354, 390, 396, 397, 454, 477
 arcuate structure, 35, 36, 767, 777
 continental crust formation, 71, 72
 formation, 58
 geochemical recycling, 548, 561, 572
 geoid anomalies, 215, 466
 mantle seismic discontinuities, 89, 90
 Mars, 657
 phase changes, 181, 198
 seismic tomography, 104, 108, 110f, 112, 114
 temperatures, 127
 Venus, 646, 649, 651
 volcanism, 36, 38, 47, 59, 177, 180
 subsolidus creep, 214
 superadiabatic temperature change, 188, 198, 204
 superplume, 515
 superswell, 514, 515, 646
 surface heat flow and secular cooling of Earth, 118
 surface heat flow–heat production correlation, 144–146
 suture zone, 58f, 59
 swells
 rate of formation, 502, 510
 shape parameter I , 539, 540, 541t
 topography, 505, 507, 540, 541, 545
- tectosphere, 79
 temperature in core, 191t, 200, 203, 603, 605, 608, 615f
 temperature in Earth's interior, 126, 586
 temperature increase across D'' , 204, 209
 temperature- and pressure-dependent rheology, 377
 temperatures in continental lithosphere, 143, 144, 148
 temperatures in transition zone, 84, 92, 204
 terminal bombardment, 638, 718
 terminal volume of plume head, 525
 Tethys (Saturn), 635t
 Tethys ocean, 6
 tetrahedral mode of convection, 418, 419, 419, 420f, 421, 421f, 422, 422, 423f, 426, 427, 427f
 thermal boundary layer, 382, 398, 401, 402, 674f, 680f
 at base of mantle, 42
 boundary layer analysis of cellular convection, 354–356, 359, 360
 boundary layer stability analysis, 350–352
 cold upper boundary layer, 176, 211, 412
 D'' layer, 94, 95, 97, 201, 204, 414, 414f, 416
 effects of non-Newtonian viscosity, 404, 405
 effects of temperature dependence of viscosity, 393, 395
 in convection with strongly temperature-dependent viscosity, 620, 621
 in Earth thermal history models, 590, 603, 606, 612, 613, 616, 626
 in mantle, 190
 in single-mode mean field theory, 362, 364, 366
 in three-dimensional convection, 418, 419, 423, 424, 432, 438, 440, 444–446, 449, 452–454, 457, 466, 474
 in two-dimensional convection models, 376, 379, 380f, 381
 in two-layer mantle convection models of Earth thermal history, 615f, 616
 instability, 143, 307, 308, 335, 336, 382, 406, 411, 413, 427, 709
 lava lakes, 635, 651
 LVZ, 83
 Mars, 701, 710, 711, 713
 Mercury, 753, 754
 oceanic lithosphere, 16, 26, 127, 131, 132, 133f, 143
 precursor thermal boundary layer, 192, 193, 197, 198
 role in mantle convection, 127
 seismic LID, 76, 77, 78f, 101, 152
 subsidence of sedimentary basins, 147
 thickness, 121, 122, 152, 351
 Venus, 651, 660, 674
 thermal buoyancy, 192, 507, 513, 523, 524f
 thermal conduction, 613
 thermal conductivity, 128, 156, 251, 271, 289, 290, 298, 403, 427, 450f, 477, 589
 depth dependence, 406, 455, 482
 Galilean satellites, 764
 in conservation of energy equation, 262
 in heat conduction equation, 119
 in melt zone model, 158t
 lower mantle, 201
 mantle values, 210, 211
 Mars, 690, 693, 700t
 of crust, 409, 412
 value for mantle plume, 512
 Venus, 647, 655
 thermal contraction, 22, 29, 132, 135, 183
 thermal convection, 177, 188, 207, 288, 331, 332, 359f, 609f, 635
 approximate solutions, 330, 336, 343, 347, 350, 353, 358, 360–362, 366, 367
 Earth thermal history, 608–610, 617, 620, 626, 627
 in core, 604, 608, 609, 609f, 610

- thermal convection (*cont.*)
 linear stability, 288, 290, 291f, 294f, 297, 301, 301f, 302, 302f, 303, 307, 308, 313, 314t, 316, 318, 320, 321t
 Mars, 702, 703, 705, 705f, 706
 Mercury, 756
 three-dimensional, 417, 418, 441, 448f, 450f, 454, 489, 491
 two-dimensional, 376, 379, 381, 385, 385f, 389, 390, 392, 393, 404, 406, 407f, 408, 408–411f, 412
 Venus, 651, 663, 679
 thermal diffusion length, 123
 thermal diffusivity, 122, 128, 171, 210, 298, 416, 427, 478, 484, 531, 589
 in Prandtl number, 266
 in Rayleigh number, 293, 519
 in similarity variable, 119
 in temperature equation for two-phase region, 193
 mantle values, 210, 211
 Mars, 693, 700t, 709t
 value for mantle plume, 512t
 Venus, 649, 664, 670, 675
 thermal energy equation, 262–264
 thermal evolution, 634
 Earth, 586–590, 592f, 596, 604f, 609f, 611f, 616
 continental crustal growth, 627, 628
 coupled core–mantle model, 607
 models with two-layer mantle convection, 607, 611, 614t, 616, 617
 parameterization with strongly temperature-dependent viscosity, 625
 temperature dependence of viscosity and self-regulation, 591, 592, 594
 with degassing, 601, 602
 Io, 746, 748
 Mars, 682, 687, 688, 690, 691, 694, 695f, 696, 696f, 699, 702, 702f, 703, 713, 716
 Mercury, 753
 Moon, 727, 728, 731
 planetary, 672
 Venus, 647, 656, 667, 672, 673, 674f, 675, 677, 677f, 678
 thermal expansion coefficient or thermal expansivity α , 128, 183, 207, 210, 279, 298, 310, 406, 408f, 468, 471, 477, 478, 482, 507, 512, 512t, 530, 541
 adiabatic temperature scale height, 188
 definition, 207, 259
 dependence on temperature and pressure, 207, 209
 in D'' layer, 414
 in phase buoyancy parameter, 300, 301
 in Rayleigh number, 427, 519, 589
 Mars, 700t, 709t
 of perovskite, 91, 92
 planetary expansion, 688
 relation to Bullen inhomogeneity parameter, 93
 relation to partial melt buoyancy, 165
 role in convection, 772
 thermally induced density changes, 135
 variation with depth, 207, 210, 406, 407, 455, 457, 464, 482, 790
 thermal halo, 516, 529, 530, 532
 thermal subsidence of sedimentary basins, 147, 148f
 thermal turbulence, 336, 384, 384f
 thermally activated creep, 240, 243
 thermochemical boundary layer, 523
 thermochemical convection, 100, 523, 524f
 thermochemical D'' layer, 473
 thermochemical plumes, 523
 thermodynamics, 64, 194, 198, 259
 first law, 259
 second law, 260, 262
 thermostat effect of mantle rheology, 590
 thickness of thermal boundary layer, 122, 147, 360, 379, 381, 412
 at onset of convection, 307, 350, 351
 boundary layer instability, 413
 definition, 121
 in parameterized convection models of thermal history, 606, 616, 619, 622
 in three-dimensional spherical convection, 418, 423
 LID depth, 152
 thermal diffusion length, 122
 Venus, 663, 674, 674f
 Thompson, William, *see* Lord Kelvin
 thorium, 306, 568f, 654t, 772
 ^{232}Th , 574, 575
 geochemical reservoirs, 572–575, 584
 heat production, 128–131, 146, 594, 634, 644
 in continental crust, 69
 U–Th–Pb isotope system, 565, 566, 571, 572, 572f
 Venus, 644
 three-dimensional convection, 419f, 431f, 433f, 435f, 443f, 450f, 453f, 469f, 477, 483f, 620f
 adiabatic heating, 441, 477, 478, 484–487, 488, 489f
 beneath spreading centers, 498
 bimodal, 432, 433f
 compressible, 441, 443f, 477, 483, 483f
 cubic convection in spherical shell, 419, 420f, 421
 in Earth-like model, 468
 internal heating, 439, 440, 446, 449, 453f, 471
 mantle avalanches, 455
 plate-like behavior, 491, 495
 rectangular box, 429, 432, 435, 439, 440
 spherical shell, 417, 418, 421
 temperature-dependent viscosity, 438, 619
 tetrahedral and cubic patterns, 421
 time-dependent, 440, 441, 586
 time-dependent and asymmetric, 440, 441, 443f, 448f
 upflow plumes and downwelling sheets, 432, 446, 449, 454, 486, 666
 variable viscosity, 664, 667
 Venus, 658, 672
 viscous heating, 441, 477, 485–487, 489f
 with an endothermic phase change, 468
 with depth-dependent viscosity, 472–474

- three-dimensional convection (*cont.*)
 with sluggish or stagnant lid, 665
- Tibetan plateau, 59
- tidal dissipation, 739, 743
 Europa, 764, 766
 Ganymede, 764
 Io, 633, 634, 736, 738–740, 742, 742f, 743, 743f, 744–746
 Mercury, 752
- Titan (Saturn)
 subsolidus mantle convection, 766
- toroidal deformation, 57, 390
- toroidal energy, 56, 57, 487
- toroidal flow with strongly temperature-dependent viscosity, 438
- toroidal oscillations, 66
- toroidal scalar, 311
- toroidal vector field, 311, 328, 329
- trace element composition, 549
- trace elements, 547, 565
- trailing conduit, 525, 527, 528
- transform faults, 16, 17f, 22, 28, 28f, 29, 30f, 48, 48f, 52, 57, 59
- transition zone, 94, 466
 avalanches, 457
 composition, 82
 composition and mantle layering, 381, 392, 393
 in seismic Earth models, 63, 66, 67, 69t
 melting temperatures, 205f
 phase transitions, 199
 plumes, 183, 403
 structure and composition, 84–86, 86f, 87, 90, 92, 112f
 subducted slabs, 106–108, 112, 113, 397f, 398, 399
 temperature and flow, 190–192
 temperatures, 127, 204–206
 thermal properties, 210
 viscosity, 406
- transport of He isotopes through mantle, crust and atmosphere, 57f
- Transverse Ranges, 45
- travel times, 66, 96, 98, 102, 113, 117
- trench migration, 34, 39, 39f, 397, 461, 462, 498
- trench rollback, 39, 399, 399f
- triple junction, 16, 29, 30f, 57
- Triton
 subsolidus mantle convection, 766
- turbulence, 176, 251, 384
 fluid, 343
 soft, 382, 627
 thermal, 336, 384, 384f, 786
- turbulent dike, 171
- two-dimensional convection, 295f, 303, 333, 354f, 359f, 376, 377, 380f, 388, 388f, 394f, 409
- Nu–Ra* relation, 358
 comparison with spherical, axisymmetric convection, 381
 convective mixing, 346, 347
- single-mode mean field approximation, 361
- temperature- and pressure-dependent rheology, 377, 381, 392–394, 394, 395f, 404, 407f, 412
- two-layer convection, 379, 397f, 411
- unit aspect ratio, 379, 380f, 393
- weakly nonlinear stability theory, 367
- two-dimensional convection with internal heat generation, 385f
- two-layer spherical convection, 474
- two-reservoir model, 553, 557t, 559t
- ultra-low velocity zone (ULVZ), 95, 206, 509, 519, 781
- unbending, 33
- underplating, 48
- uniformitarian model, 647, 648f
- uniformitarianism, 2
- uplift, 10, 57, 216, 223, 224, 224f, 225, 226f, 227–229, 684, 711
- uplift history, 216, 223
- upper crust, 43, 44, 47, 59, 72, 73
- upper mantle, 42, 66, 67, 67f, 68, 69, 69t, 70, 70t, 73–82, 84, 85, 87, 88, 91, 102–104, 106, 107, 108f, 113, 115
- upper mantle reservoir, 549, 550, 571, 575, 578, 580, 584
- uranium, 69, 128–131, 146, 306, 382, 565, 566, 568f, 571, 571f, 572, 572f, 574, 575, 584, 594, 634, 654t, 772
 ²³⁵U, 574, 575
 ²³⁸U, 574, 575
- Venus, 644
- uranium–thorium–lead isotope systems, 565, 584
- Urey number, 577, 648, 648f, 650, 653, 655f
- veins, 165, 568
- Vendian supercontinent
 breakup of, 60
- Venus, 633, 634, 634t, 635, 636, 636f, 637, 639f, 640, 641, 641f, 644–648, 648f, 649–652, 652f, 653, 654t, 655, 655f, 656, 657, 661, 662, 662f, 663, 664, 671–674, 674f, 675, 676, 676f, 677, 677f, 678, 679, 679f, 680, 680f, 681–684, 686, 691, 698, 706, 750, 789, 792–794
- accretionary heating, 672
- Airy isostasy, 637, 645
- catastrophic heat loss, 647
- change from mobile plates to stagnant lid, 676, 677f
- change in convective regime, 637
- chasmata, 649, 650, 678
- continents, 656, 657
- convection style, 671, 675
- coronae, 646, 648–651, 663, 793
- coupled core–mantle thermal history, 678
- crater relaxation, 645
- differentiated model, 647, 652
- dynamic topography, 645, 646, 663
- elastic lithosphere, 645, 651
- episodic subduction, 647, 648f, 651, 652f, 684
- equatorial highlands, 645, 648, 667

Venus (*cont.*)

geoid, topography, and admittance ratio, 661, 662, 662f, 663
global resurfacing event, 627, 635–637, 646, 656, 658, 663, 672, 675, 676, 771, 787, 793
gravity, 643f, 645, 646, 662, 663, 771
heat loss, 647–652, 675
heat production, 644, 647, 653, 655, 674f, 675
highlands, 639, 648, 656, 657, 667, 771, 793
impact cratering, 646
initiation of lithospheric foundering, 678
Ishtar Terra, 637, 640, 644, 645, 650, 656, 667
lithosphere thickening, 648f, 650, 651, 675–677
lithosphere thickness, 644, 645, 647, 648, 651, 652, 661, 663, 673, 674f, 675–677, 771, 793
lithospheric delamination, 635, 648, 649
lithospheric flexure, 647
lithospheric foundering, 646, 649–651, 678
lithospheric overturn, 677, 678
magnetic field, 672, 678, 680, 681
mantle convection, 635, 640, 641, 645, 647, 651, 652, 657, 658, 659f, 661, 661f, 663, 664, 667, 669–673, 674f, 675, 676f, 677, 677f
mantle convection avalanches, 663, 672
mantle layering, 663, 670, 671
models of convection, 657, 658, 659f
normalized radial mass flux in model of mantle convection, 660, 661f
parameterized thermal history models, 673
phase-change-induced layering in mantle, 663
phase-change-modulated convection in mantle, 658
plumes in mantle, 645, 648, 649, 658–660, 667, 670, 672, 678
potassium, 652, 653
quiescence and lithospheric thickening, 650, 651
Rayleigh number of mantle, 648, 671
silicic crust, 656
steady-state heat balance, 647
subadiabaticity in models of mantle convection, 660
subduction, 646, 647, 648f, 649–652, 652f, 675, 677, 678, 683, 684
surface age, 637
surface heat loss, 635, 644, 647, 648f, 649, 650, 652f, 674, 675
tectonics, 635, 637, 640, 641, 644, 648, 656, 657, 672, 675, 676, 771, 793
termination of plate tectonics, 637
thermal history, 624, 627, 672, 673, 678, 679, 679f, 680
with coupled core–mantle evolution, 678
thermal lithosphere, 663
thickening of lithosphere with time, 651, 675, 676
thorium, 652
topography, 640, 641, 642f, 644–646, 648, 650, 651, 661, 662, 662f, 663, 667, 668f, 674, 675, 771, 793
uranium, 652
Verhoogen effect, 192, 199

vertical vorticity in three-dimensional convection with temperature-dependent viscosity, 438
viscoelastic relaxation time, 213
viscoelasticity, 212, 213, 231
viscosity, 3, 10
dependence on depth, 216, 248, 250
temperature dependence, 249, 250, 381, 401, 403, 438, 487–490, 621f, 624f, 707f
Mars, 707
Mercury, 753
Venus, 663, 664, 669, 671, 673
water, 10
viscosity of mantle, 403, 491
creep mechanisms, 248–250
dependence on temperature and pressure, 393, 425, 461, 590, 591
dynamical topography, 235
Earth rotation, 230–233
Earth thermal evolution, 589–591, 596, 598, 602, 606, 607, 611, 613, 616, 617
low-viscosity asthenosphere channel, 229
plate motions, 237–240
postglacial rebound relaxation time, 221, 223–225
sources of data, 213–217
variation with depth, 457, 471–473, 482
viscous dissipation, 262–264, 377, 403, 408, 441, 478, 484, 486, 490f, 491
viscous forces, 256, 266
viscous snowplow models of continental collision, 59
volcanic islands, 26
volcanic line, 25f, 32, 32f, 38, 39, 39f, 46, 46f, 58f, 180
volcanic shield, 685
volcanism, 39, 767, 768, 771–773
basaltic, 349, 513t
breakup of Vendian supercontinent, 59
chemical differentiation, 547, 548
distribution, 22
energy source, 8
formation of continental crust, 47
Galilean satellites, 761
geochemical recycling, 565
hot spots, 39, 41, 499, 501, 502, 505, 510, 515, 527, 580, 780, 792
Io, 736, 744
lithospheric stoping, 46, 47
Mars, 684, 692, 697, 711–713
Moon, 315, 718, 723–725, 729, 729f, 736
on other planets, 633, 635, 637, 639, 793–795
plume heads, 527
ridges, 12, 28, 165, 574
rifting, 57
role in ^{40}Ar degassing from mantle, 577–579
silicic, 71
subduction zones, 36–38, 59, 130, 177, 179, 180, 777
Venus, 644, 646, 649–651, 656, 674, 676
Wilson cycle, 61

- volcanoes
 locations of, 22, 177
- volume of continents, 43
- volume of erupted volcanics, 527, 527t
- volumetric heat production, 146
- volumetric heat production rate due to viscous
 dissipation, 262
- vorticity, 56, 56f, 255, 257, 258, 274
- Wadati–Benioff zone, 31, 32f, 35, 102, 107
- wall rock, 171, 174, 175
- waveform method, 103
- weak coupling approximation, 362, 365
- weakly nonlinear theory, 330, 367
- Wegener, Alfred, 5, 6, 7f, 8
- West Antarctic ice sheet, 224
- whole rock isochron, 553
- Wilson cycle, 57, 58, 58f, 59
- xenoliths, 43, 80–82, 94, 144, 144f, 151
- xenon, 573, 579
 ^{129}Xe , 573t, 579
 $^{129}\text{Xe}/^{130}\text{Xe}$, 579
- Yellowstone, 499, 500t, 501f, 505, 511t, 516, 541t
- Young's modulus, 212
- Zagros, 45
- zero net force on plates, 388
- zonal harmonics, 324, 325